Remote Sensing and Digital Image Processing

Domenico Solimini

Understanding Earth Observation

The Electromagnetic Foundation of Remote Sensing

EARSeL

Springer

Remote Sensing and Digital Image Processing

Volume 23

More information about this series at http://www.springer.com/series/6477

Domenico Solimini

Understanding Earth Observation

The Electromagnetic Foundation of Remote Sensing

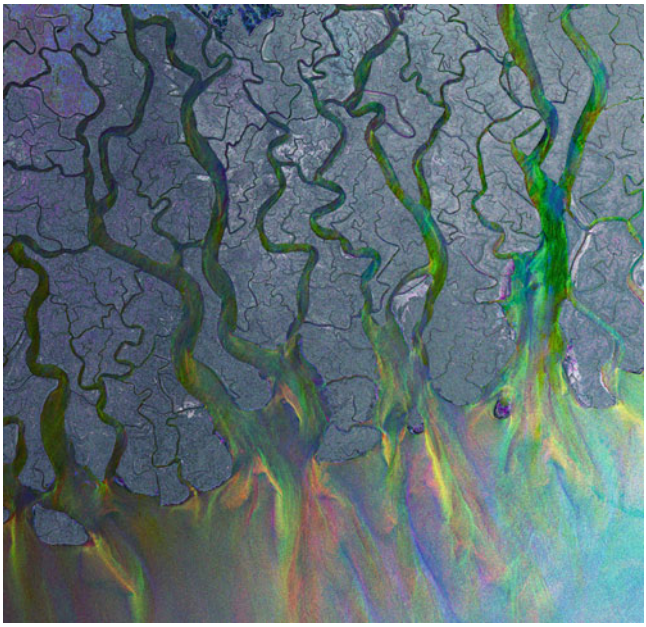

Springer

Domenico Solimini
Dipartimento di Ingegneria Civile
e Ingegneria Informatica
Tor Vergata University
Roma, Italy

ISSN 1567-3200 ISSN 2215-1842 (electronic)
Remote Sensing and Digital Image Processing
ISBN 978-3-319-25632-0 ISBN 978-3-319-25633-7 (eBook)
DOI 10.1007/978-3-319-25633-7

Library of Congress Control Number: 2016937331

Printed on acid-free paper

This Springer imprint is published by Springer Nature
The registered company is Springer International Publishing AG Switzerland

To
Leo, Vitto, Giacomo, Silvia, Νεφέλη

Preface

Understanding Earth Observation addresses the electromagnetic foundation of remote sensing. The basic fundamentals are presented in close association with the kinds of environmental targets to be monitored and with the observing techniques. It is intended for scientifically literate students and professionals who plan to gain a first understanding of remote-sensing data and of their information content.

Motivation. Clearly, value is added to Earth observation (EO) when the information contained in the measurements is watchfully selected and effectively used in the applications. Myriads of data keep streaming from the space missions that national governments, international organizations, and companies devise, develop, and launch, as well as from the variety of sensors on manned and unmanned air platforms and on the Earth's surface. The steady increase of the amount of EO products and the enhancement of their quality, as well as many other technological factors, pave the way for their pervasive assimilation into the emerging Internet of Things (C.C. Aggarwal, ed., *Managing and Mining Sensor Data*, Springer 2013, ISBN 9781461463092). However, the complex nature of remote-sensing information, together with the heterogeneity of continuously evolving systems and observing modes, makes it increasingly hard for the software developers, operators, and users to master the plethora of data and application tools. Without understanding of the data, false expectation and misinterpretation may ensue, as well as inadequate processing and occasional pitfalls. Criticality is added by the frequent demand for operational results. These results, if poor or dubious, may lead to Earth observation distrust and ultimately may jeopardize the expansion of the EO customer base. Clearly, adequate understanding of how the information on the observed target is generated and transferred from the target to the observing system is crucial toward the full exploitation of the EO potential, especially when emphasis is not only on "*what* is happening" but on "*how much* it is happening."

The above considerations made it mandatory to place the emphasis of this book on fundamentals and methods that facilitate the unified understanding of the remote-sensing data, irrespective of the application, type of sensor, acquisition mode, and spectral range. Such an approach, hopefully, will also retain its value as new

systems supersede those presently available and operational requirements evolve. The objective is pursued by providing the comprehensive frame of the interaction between electromagnetic waves and terrestrial environments and by highlighting within this unifying context the type of information that the observing systems are able to gain according to their nature and to the spectral band at which they operate.

The book addresses both academic and professional audiences. Its content aims at providing students with sufficiently sound bases to comprehend and master the applications which they are likely to encounter in the course of their professional life. Currently, EO is finding use in a steadily widening range of contexts, which encompass a host of industrial and service sectors. The ensuing heterogeneity of educational curricula demands a basic approach, but, at the same time, requires coming close to the application, since most of today's students are expected to become end users of EO products tomorrow. The subject matter and organization of the book are also intended to facilitate the present activity of professionals who carry out specialized tasks in the EO field, which in many instances are beyond their educational backgrounds. The basics-to-applications unified approach of the book is believed to make effective the process of adapting the remote-sensing principles and technology to specific education and professional interest.

In summary, a concrete end goal is to prepare future and present EO operators to properly select the sensor type, spectral range, and observational geometry able to provide the dataset containing the information they require on a given target, as well as to identify the processing tools that efficiently retrieve the values of the target parameters from the measurements.

Approach and development lines. The basic driving idea is that the information on a remote target is generated by electromagnetic wave-matter interaction and brought to the observing system by waves traveling through matter. The real scientific and technical challenge then resides in converting the observed wave features into target properties. In many cases, the retrieval approach is successful when it takes advantage of a comprehensive ensemble of analytical instruments, including electromagnetic, spectral, and statistical tools. Providing such a manifold background is laborious and time-consuming, so that the theory is sometimes abridged to expedite the applications. The ensuing risk is the fragmented and incomplete comprehension of the information content of the observations.

The book attacks this dilemma by striving to provide the needed mathematical tools within the corresponding physical context. Given the essential nature of the remote measurements, the wave-matter interactions on which remote sensing is founded are developed in a systematic manner from the basic electromagnetic models, clearly integrated by experimental results. Modeling the phenomena at the source of the observations is expected to maintain effectiveness in educating the reader, either student or professional, to understand how the data are generated, how they relate to the desired properties of the observed target, and how they can be exploited in different applications. The potential of the available observational techniques and sensors, as well as similarities and differences between measurements taken in the various portions of the electromagnetic spectrum, is intended to be

clarified by the unified theoretical background. The adoption of the mathematical view is hopefully made less daunting by interpreting and discussing the obtained analytical expressions, with the aim of suggesting the physical nature and behavior of the interaction. Some formally "dirty" mathematics of simple particular cases help in fixing several key concepts in the reader's mind. Colored diagrams and pictures, including clouds, plants, and monuments, have been inserted as appropriate to somewhat lighten the electromagnetic analytical burden.

Indeed, a critical issue is the possibly restricted physical and mathematical backgrounds of a substantial fraction of readers. This required keeping the needed analytical skills to a minimum by limiting the presentation to particularly simple, albeit significant, cases. For instance, the inhomogeneities of the materials are assumed weak enough that only single-scattering events are sufficient to characterize the electromagnetic interaction. Moreover, reference is generally made to specific significant targets, typically to those with plane average boundaries, for which simple mathematical models can be established. This choice may be a suitable compromise between a rigorous analytical approach and the mathematical manageability and convincing physical evidence that can make suggestive, rather than repulsive, a first encounter of the reader with the subject. Also, in designing a presentation that is smoothly readable by the beginner, several details that are not necessary for understanding the fundamentals have been neglected, although sometimes at the expenses of what, from a rigorous point of view, may appear oversimplified.

Basing the entire remote-sensing science and technology on the electromagnetic interaction leads to a clear conceptual interconnection among its various aspects. Extensive cross-referencing throughout the chapters emphasizes the interrelation between active and passive techniques, as well as between optical and microwave observations. Remote sensing includes a tremendous variety of particular issues, sometimes treated separately, but the disconnected presentation of these would be unavoidably bewildering, if not even superficial and rapidly outdated. In fact, since all the measured quantities stem from electromagnetic interactions, a common basic behavior is observed, when the variations of the dielectric properties with wavelength are accounted for and reciprocity is exploited. This global approach includes both deterministic and stochastic fields. The latter, as required by the essentially random nature of the terrestrial environments, leads to the concepts of correlation and coherence. Analogously, in treating the sources that provide electromagnetic power, consideration is given to the coherent waves originated by radar systems and to the incoherent radiation coming from the sun or originated by thermal emission from the terrestrial materials. With each succeeding chapter, the complexity of the material tends to increase following the design of the book. The first chapters, as well as their initial sections, present the concepts and analytical machinery that are being developed in the following chapters or sections. This tries to develop the tools able to make the subsequent matter, and especially the last chapter, intelligible to the reader with no or little specific background. Long mathematical developments are abridged when suitable, to avoid interrupting the smooth flow of concepts. Within certain limits, the details of some heavier

introductory mathematics (e.g., the first part of Chap. 9) can be given diminished attention, by focusing on the physical fundamentals. The presentation of certain topics, such as atmospheric attenuation, requires more than one chapter, following the path from the abstract electromagnetic properties to the basic mechanisms of interaction and then to the behavior of the actually observed quantities. It is not uncommon that the same subject appears more than once, since it may form the foundations of traditionally separated fields such as active and passive techniques or optical and microwave observations.

The concluding chapter discusses concisely the interaction of the electromagnetic waves with the classes of terrestrial environment of particular relevance for the applications. The main emphasis is now on converting the remote measurements into the bio-geo-physical parameters demanded by the users or, in an enlarged perspective, into pervasive information to assimilate in the Internet of Things. The wave-medium interaction is clearly the unifying key factor that singles out and explains the information on the observed targets that each type of observation contains. The presentation is organized to highlight the invariant fundamental features of the interaction with land, water, and air, which are expected to keep their value, even as new missions and sensors are developed and put in use. This last chapter, which is mainly descriptive, can be possibly regarded as a catalogue of the techniques and spectral bands (in the wide sense) to observe the environmental targets of interest and of the corresponding kind of information that is obtainable.

Genesis, sources, and nomenclature. This undertaking started several years ago as lecture notes for the PhD candidates of the GeoInformation Curriculum offered by the Tor Vergata University Doctoral School. It was the variety of backgrounds of the candidates that gave rise to the issue regarding the approach to follow in an Earth observation course. In fact, graduates in engineering were attending the course together with physicists, geologists, geographers, and mathematicians, who came from different countries of Africa, Asia, and Europe. It should be added that analogous heterogeneity of background and of interests can be expected among the professionals active in the operational use of remote sensing. The structure of the book has evolved over the years, first in response to the reactions of the students attending the lectures and then trying to adapt to the interests of the audience, assumed to be a significant sample of the general EO community. This process has resulted in the present organization of the book's content and, unavoidably, has led to including more material than a course is able to typically cover in one year.

As said, the book in its present form is expected to address a variety of readers: graduate students who include Earth observation into curricular backgrounds in technology (environmental, electrical, civil, computer engineering, etc.), as well as those studying natural sciences, meteorology, and geography; professionals who endeavor to enhance their activity in fields such as safety and security, civil protection, forestry, geology, and agricultural and marine resources, by assimilating remote-sensing data into conventional working schemes; and practitioners,

already expert in particular areas of remote sensing, who are keen to enlarge their competence by taking advantage of alternative or complementary solutions offered by different EO techniques and other types of data.

Many books exist that present the matter either from a basic perspective or from the system point of view or that follow the application-oriented approach, sometimes treating Earth observation as a self-contained field, with little contact with the underlying physics and even less with the electromagnetic formalism. Such books are listed among the references at the end of the chapters identifying the topics which happen to fall within their contents. Their location is somewhat arbitrary and can be legitimately deemed subject to limited knowledge, personal taste, and prejudice. Anyway, the reader is encouraged to extensively refer to the literature for bridging the present approach with the more conventional slant she/he could be accustomed to. Such a blending is especially advised with the texts that emphasize the practical and operational points of view, which have been left out of this book. The appendix provides a very succinct overview of the vector and operator properties that are quoted and utilized throughout the chapters. This reference material may ease just the first approach to the various topics, but must be clearly complemented and superseded by accessing the relevant literature. The books on electromagnetic fields among those listed in Chap. 1 often include sections on the algebra of vectors and operators.

It is worth recalling that the chosen approach draws on various disciplinary sectors, from electromagnetics to botany and from statistics to hydrocarbon chemistry, to mention just a few. The subject matter of the book has been assembled from a variety of sources, looking from different perspectives at the many facets of Earth observation. Thus, encountering some discrepancies of terminology and symbols was not uncommon, which raised serious issues of consistency. Decisions on the definitions and symbols that in the author's opinion were more appropriate were frequently required. Disagreement is clearly expected about both the choice and the relation with the terms in common use. Furthermore, incoherence and gaps may have possibly endured the effort to make the text comprehensive and consistent.

The symbols strive to adhere to the recommendations by the relevant organizations (A. Thompson and B.N. Taylor, *Guide for the Use of the International System of Units (SI)*. National Institute of Standards and Technology, US Department of Commerce NIST Special Publication 811, 2008; as well as *Quantities and Units – Part 2: Mathematical Signs and Symbols to be Used in the Natural Sciences and Technology*. ISO 80000-2, 2009). However, as mentioned, a serious problem is raised by the coexistence of a number of different quantities that are represented by the same letters in different disciplinary environments, sometimes not even too distant, such as radar and optics, wave propagation, and radiative transfer. To reduce the changes of notation, yet to distinguish the represented quantity, use has been made of some of the different fonts that are available (S. Pakin, *The Comprehensive LATEX Symbol List* 2009, http://www:ctan:org/) for a given letter of the Latin alphabet. Gothic letters have been also introduced in particular cases. Sub- and superscripts have contributed extensively, perhaps at the expense of overloading the

notation, thus hindering smooth reading. When the same Greek letter had to denote different quantities, upright characters have been used together with the italic ones, somewhat contravening the recommendations about the representation of variables. A further license has been taken in representing dyadic quantities by *blackboard* characters, since it was graphically suggestive of the "two-dimensional" nature of the pertinent quantities. To avoid possible misunderstanding, as well as to ease the approach of the readers unfamiliar with them, symbols with corresponding units are listed in the glossary.

The subject index that appears at the end of the book following the lists of acronyms and of symbols includes most of the entries the reader is expected to address.

Roma, Italy Domenico Solimini

Acknowledgments

It is a hard task to trace the origin of the ideas around which the book is constructed and to mention all those to whom I am indebted for stimulating the evolution of the concepts. In attempting to do so, first I think back to my late professors: Giorgio Barzilai introduced me to the electromagnetic theory, Giorgio Gerosa to microwaves, and Giovanni d'Auria pointed out the inadequacy of the deterministic approach to real-world electromagnetics. Conception, shaping, and development of the matter has benefited from extended interaction with a number of colleagues. When at La Sapienza University, collaboration with Patrizia Basili and Piero Ciotti initiated the approach to atmospheric sensing. Working with the Earth observation group at Tor Vergata University has then played a decisive role in expanding and consolidating the overall comprehension of remote sensing. Elucidating discussions with Fabio Del Frate and, especially, with Giovanni Schiavon and Leila Guerriero have greatly influenced the configuration of the book. Besides, I am particularly indebted to Paolo Ferrazzoli, whose uncommon remarkably deep and thorough understanding of antennas, wave propagation, electromagnetic interaction, and remote sensing has considerably contributed to make clear a number of primary concepts and basic definitions.

The interaction over the years with the graduate students associated with the Tor Vergata EO Lab has certainly enhanced the overall cultural heritage from which this book stems. In particular, it was a pleasant and enriching experience to get involved in the research projects carried out by some of the students attending the GeoInformation Program offered by the Tor Vergata Doctoral School. The candidates with whom I mainly interacted include Michele Iapaolo (PhD in 2006), Andrea Minchella (2006), Andrea Della Vecchia (2007), Riccardo Duca (2008), Alessandro Burini (2009), Cosimo Putignano (2009), Pasquale Sellitto (2009), Marco Lavalle (2009), Giorgio Licciardi (2010), Fabio Pacifici (2010), Rachid Rahmoune (2011), Chiara Pratola (2013), Antonio Di Noia (2013), and Gaia Vaglio Laurin (2014). An explicit mention is due to Yogesh Kumar Singh (PhD in 2014) and to Alireza Taravat Najafabadi (2014) who raised questions and voiced objections that contributed to enhance formulation and comprehensibility

of several arguments. I am also especially indebted to the PhD candidate Andrey Giardino for pointing out deficiencies and lack of clarity in my former presentation of SAR interferometry: his careful comments led to a decidedly improved content of Chap. 12.

Finally, I have to acknowledge the friendly and insightful involvement of Dr. Ed R. Westwater. Discussing with him the general planning of the work in addition to addressing some basic questions has greatly helped me to focus onto crucial issues, to clear my mind, and, all in all, has encouraged me to write the book, with the hope it is found readable and useful.

Special appreciation goes to Mr. Antonio Perrone for producing many of the figures. Thanks to his outstanding skill in handling computer graphics tools and to his tasteful competence in manipulating images, the text has been enriched with a wealth of suggestive illustrations.

As many authors know, writing a book can be an utterly demanding task: acknowledging the patience of my wife Donatella is by now badly owed.

Contents

List of Figures

List of Tables

Chapter 1
The Electromagnetic Field

Substantial information on the Earth's environment is gained from the remotely sensed properties of electromagnetic waves that interact with the observed target. The basic quantities involved in the information acquisition process are the electromagnetic field vectors, the associated power and their statistical parameters. On its side, the target exerts the imprinting on the waves according to the electric properties of the constitutive matter, which are therefore key elements to trace the physical features of interest from the measured data.

1.1 Basic Definitions and Relations

Fundamental observations about the forces acting on moving electrical charges lead to the definition of the electric, $\boldsymbol{E}(\boldsymbol{r}, t)$, and magnetic, $\boldsymbol{B}(\boldsymbol{r}, t)$, basic vectors (Appendix A.1), associated with time t and the position vector $\boldsymbol{r} = x\mathbf{x}_0 + y\mathbf{y}_0 + z\mathbf{z}_0$ that identifies a point P in space. The *electric field* $\boldsymbol{E}$ and the *magnetic induction* $\boldsymbol{B}$ are thus *vector functions* of space, i.e., of three coordinates (here the Cartesian coordinates x, y, z), and time. Two other corresponding vector fields are associated with $\boldsymbol{E}$ and $\boldsymbol{B}$: the *electric displacement* $\boldsymbol{D}$ and the *magnetic field* $\boldsymbol{H}$. The two pairs of electric ($\boldsymbol{E}$, $\boldsymbol{D}$) and magnetic ($\boldsymbol{H}$, $\boldsymbol{B}$) vectors describe the *electromagnetic field* [10, 11, 37, 38].

D. Solimini, *Understanding Earth Observation*, Remote Sensing and Digital Image Processing 23, DOI 10.1007/978-3-319-25633-7_1

1.1.1 Maxwell's Equations

The space-time variations of the electromagnetic vectors are interconnected by Maxwell's equations[1]

$$\nabla \times \boldsymbol{E} = -\frac{\partial \boldsymbol{B}}{\partial t} \; ; \tag{1.1}$$

$$\nabla \times \boldsymbol{H} = \frac{\partial \boldsymbol{D}}{\partial t} + \boldsymbol{J} \; ; \tag{1.2}$$

$$\nabla \cdot \boldsymbol{D} = \rho \; ; \tag{1.3}$$

$$\nabla \cdot \boldsymbol{B} = 0 \; , \tag{1.4}$$

which determine the properties of the fields, also relating them to the *conduction current density* $\boldsymbol{J}$ and to the *electric charge density* ρ existing in any point of space at any time. Maxwell's equations form a set of partial differential equations involving the *curl* and *divergence* operators reviewed in Appendix A.3, as well as the time partial derivative. The *Nabla* vector operator ∇ is used to denote curl and divergence as $\nabla\times$ and $\nabla\cdot$, respectively (Sect. A.4.1).

1.1.2 Electromagnetic Constitutive Relations

The pair of electric vectors are related by

$$\boldsymbol{D} = \epsilon \, \boldsymbol{E} = \tilde{\epsilon} \, \epsilon_0 \, \boldsymbol{E} \; ,$$

where the *permittivity* (or *dielectric "constant"*) ϵ expresses the dielectric behavior of the material. The subscript $_0$ in ϵ_0 denotes vacuum, while $\tilde{\epsilon}$ denotes *relative permittivity*.

The magnetic vectors are related by the analogous relation

$$\boldsymbol{H} = \frac{\boldsymbol{B}}{\mu} = \frac{\boldsymbol{B}}{\mu_0 \, \tilde{\mu}} \; ,$$

involving the magnetic properties of the material, expressed by its *permeability* μ.

The *current density* $\boldsymbol{J}$ represents the effect of a volumic net charge ρ which moves with velocity $\boldsymbol{u}$

$$\boldsymbol{J} = \rho \, \boldsymbol{u} \; .$$

[1] Actually, the equations in their field-only formalism are ascribed to O. Heaviside [13].

Since in a *passive* material the charges are put in motion by an electric field, the current density is controlled by the *conducting* properties of the material, expressed by its *conductivity* g:

$$\boldsymbol{J} = \rho \boldsymbol{u} = g \boldsymbol{E} \, . \tag{1.5}$$

When $g \to \infty$, the (reference) material is an *ideal conductor*.

As will be clarified in the following, the above proportionality relations assume linearity and *instantaneous response* of the material.

A material is characterized electromagnetically by the three parameters, ϵ, μ, and g. A specific terminology is associated with their features with respect to each parameter: the material is

- *stationary* if the parameter does not vary with time;
- *homogeneous* (or *uniform*), if the parameter is the same everywhere in space;
- *linear*, if the parameter is independent of the field intensity;
- *isotropic*, if the parameter is independent of the field direction.

If the material is *anisotropic*, the *scalar* (single) parameter ϵ is replaced by a *tensor* [27] with nine elements, e.g., in matrix notation, for permittivity,

$$[\boldsymbol{\epsilon}] = \begin{bmatrix} \epsilon_{11} & \epsilon_{12} & \epsilon_{13} \\ \epsilon_{21} & \epsilon_{22} & \epsilon_{23} \\ \epsilon_{31} & \epsilon_{32} & \epsilon_{33} \end{bmatrix} \, .$$

In anisotropic materials, corresponding vectors, i.e., $\boldsymbol{E}$ and $\boldsymbol{D}$, $\boldsymbol{E}$ and $\boldsymbol{J}$, or $\boldsymbol{H}$ and $\boldsymbol{B}$, may not be parallel, since they are related by linear transformations of the type

$$\boldsymbol{D} = [\boldsymbol{\epsilon}] \boldsymbol{E} \, .$$

Some kinds of anisotropic media are encountered in **E**arth **o**bservation (EO), including the ionosphere, canopies of oriented vegetation elements, and locally crystalline materials.

1.1.3 Electromagnetic Sources

Once the current density is related to the electric field by (1.5), Maxwell's equations,

$$\nabla \times \boldsymbol{E} = -\frac{\partial \boldsymbol{B}}{\partial t} \, ;$$

$$\nabla \times \boldsymbol{H} = \frac{\partial \boldsymbol{D}}{\partial t} + g \boldsymbol{E} \, ,$$

become a system of homogeneous equations, which yield information on the internal features of the field, but do not account for its origin and hence are not able to relate magnitude nor orientation to the external forcing.

Actually, the field is generated by some process taking place in the "source", which converts energy of "different kind" into electromagnetic energy. In nature, this happens in the sun, or, in general, in any body generating thermal emission. In classical electrodynamics, the energy conversion process is suitably modeled by an *impressed* electric current density $\boldsymbol{J}_\mathrm{s}$, with $\boldsymbol{J}_\mathrm{s} \neq g\boldsymbol{E}$, that is, independent of the electric field.[2] It is important to bear in mind that the *a-priori assigned* $\boldsymbol{J}_\mathrm{s}$ does not attempt to physically model the actual source of electromagnetic energy, which might not be described by classical electrodynamics. Rather, from a mathematical point of view, the impressed current is a known *equivalent* term that acts in the second Maxwell's equation to account for the transfer of energy from the source to the electromagnetic field and, from the practical point of view, allows one to compute the field. To this end, both electric and magnetic impressed currents are admissible, since they are equivalent quantities, not constrained by physical reality.

With the introduction of the impressed currents that account for the source, the first and second Maxwell's equations become

$$\nabla \times \boldsymbol{E} = -\frac{\partial \boldsymbol{B}}{\partial t} - \boldsymbol{J}_\mathrm{m} - \boldsymbol{J}_\mathrm{ms} \; ; \tag{1.6}$$

$$\nabla \times \boldsymbol{H} = \frac{\partial \boldsymbol{D}}{\partial t} + \boldsymbol{J} + \boldsymbol{J}_\mathrm{s} \; , \tag{1.7}$$

with $\boldsymbol{J}_\mathrm{s}, \boldsymbol{J}_\mathrm{ms}$ electric and magnetic source currents, respectively. The magnetic current $\boldsymbol{J}_\mathrm{m}$, nonexistent in nature, is introduced to make (1.6) similar to (1.7). Moreover, the source equivalence discussed in the later Sect. 3.2.2 calls for both electric and magnetic currents.

It is anticipated that the concept of impressed current will be used extensively to determine the radiating, and, by reciprocity, the receiving features of systems of interest in EO.

1.1.3.1 Electromagnetic Duality

The system (1.6)–(1.7) is now formally symmetric, so that each equation transforms into the other through the correspondences

$$\boldsymbol{E} \to \boldsymbol{H}, \quad \boldsymbol{H} \to -\boldsymbol{E}; \qquad \boldsymbol{J} \to \boldsymbol{J}_\mathrm{m}, \quad \boldsymbol{J}_\mathrm{m} \to -\boldsymbol{J}, \quad \boldsymbol{J}_\mathrm{s} \to \boldsymbol{J}_\mathrm{ms}, \quad \boldsymbol{J}_\mathrm{ms} \to -\boldsymbol{J}_\mathrm{s} \; . \tag{1.8}$$

[2] The subscript $_\mathrm{s}$ in $\boldsymbol{J}_\mathrm{s}$ stands for *source*.

The *dual* transformations (1.8), together with the biunivocal correspondence

$$\epsilon \longleftrightarrow \mu$$

leave the equations system, hence the fields it yields, unchanged.

Duality proves quite useful in practice, since expressions of electric type (e.g., $\boldsymbol{E}$) can be readily obtained from expressions of magnetic type (e.g., $\boldsymbol{H}$) and vice-versa. Given its effectiveness, extensive use of duality is made in the following.

Note that the connection expressed by the above relations signifies that electric and magnetic quantities are facets of a unique entity, that is the electromagnetic field.

1.1.4 Boundary Conditions

Many materials are present in the terrestrial environments with which the electromagnetic radiation interacts. The basic situation is the one in which the field crosses a pair of different materials. For instance, this happens when the solar radiation impinges from the air onto the soil surface, or a radar wave hits a building wall. Then, different values of the electromagnetic parameters taking account of the different physicochemical properties of the matter appear in (1.1) and (1.2). However, the particular interrelations among the fields set by Maxwell's equations constrain the electric and magnetic vectors in each material. The readily derived relations named *boundary conditions* form the grounds on which some basic properties of EO involving reflection (Chap. 6) and scattering (Chap. 7) are obtained.

Consider two materials, M_1 and M_2 with different electromagnetic parameters, separated by a thin transition region [36, Chap. 1], which is regarded as a surface of separation, with unit normal $\mathbf{n}_0$ oriented from M_1 towards M_2 (Fig. 1.1) The following conditions hold for the fields across the boundary separating M_1 from M_2.

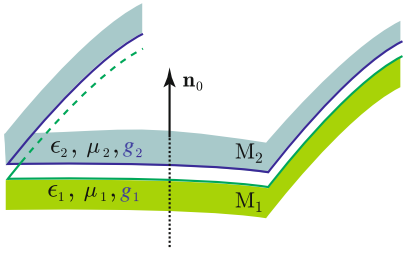

Fig. 1.1 Boundary between two different materials M_1 and M_2, characterized by the parameters ϵ_1, μ_1, g_1 and ϵ_2, μ_2, g_2, respectively, and local normal $\mathbf{n}_0$

1.1.4.1 Normal Field Components

Applying Gauss's theorem (A.15) to a boundary element yields the result that the component of the electric displacement perpendicular to the boundary undergoes a variation equal to the unbalanced areic electric charge ς_e locally present in the transition layer

$$(\boldsymbol{D}_2 - \boldsymbol{D}_1) \cdot \mathbf{n}_0 = \varsigma_e \ . \tag{1.9}$$

The constraint on the normal component of the magnetic induction is immediately obtained by duality (1.8)

$$(\boldsymbol{B}_2 - \boldsymbol{B}_1) \cdot \mathbf{n}_0 = \varsigma_m \equiv 0 \ . \tag{1.10}$$

No variation of $\boldsymbol{B}$ perpendicular to the boundary occurs, given the nonexistence of the free magnetic charge ς_m.

1.1.4.2 Tangential Field Components

Stokes' theorem (A.17) applied to an elementary loop across the boundary leads to the result that the variation of the component of the magnetic field tangential to the boundary[3] equals the conduction current density $\boldsymbol{\mathcal{J}}$ that locally flows within the boundary layer

$$\mathbf{n}_0 \times (\boldsymbol{H}_2 - \boldsymbol{H}_1) = \boldsymbol{\mathcal{J}} \ . \tag{1.11}$$

As before, duality immediately yields the constraint on the tangential component of the electric field

$$\mathbf{n}_0 \times (\boldsymbol{E}_1 - \boldsymbol{E}_2) = \boldsymbol{\mathcal{J}}_m \equiv 0 \ , \tag{1.12}$$

since the absence of free magnetic charges implies the nonexistence of the magnetic current $\boldsymbol{\mathcal{J}}_m$. Equation (1.12) expresses the important property that the tangential components of the electric field do not change across the boundary between different materials. This finding will be extensively exploited in the following.

A time-varying electromagnetic field inside an ideal conductor vanishes. Therefore, conditions (1.10) and (1.12) constrain the electric field to be perpendicular and the magnetic field to be tangential to the surface of the conductor, as sketched in Fig. 1.2. While ideal conductors are not present in nature, they are a useful reference to understand the behavior of the electromagnetic field on the boundaries of high-permittivity materials, the features of which approach those of the conductors, as discussed in the later Sect. 2.1.3.2.

[3]The component tangential to the surface is obtained by the cross-product with the normal $\mathbf{n}_0$.

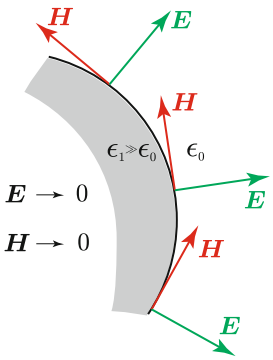

Fig. 1.2 The electric field tends to be perpendicular and the magnetic field tangential to the surface of a highly conducting material; the fields have a similar behavior on materials with high permittivity

Table 1.1 Conditions on the fields at the boundary between diverse materials

Normal components	Tangential components
$\mathbf{n}_0 \cdot (\boldsymbol{E}_2 - \frac{\epsilon_1}{\epsilon_2}\boldsymbol{E}_1) = \frac{\varsigma_e}{\epsilon_2}$	$\mathbf{n}_0 \times (\boldsymbol{E}_2 - \boldsymbol{E}_1) = 0$
$\mathbf{n}_0 \cdot (\boldsymbol{D}_2 - \boldsymbol{D}_1) = \varsigma_e$	$\mathbf{n}_0 \times (\boldsymbol{D}_2 - \frac{\epsilon_2}{\epsilon_1}\boldsymbol{D}_1) = 0$
$\mathbf{n}_0 \cdot (\boldsymbol{H}_2 - \frac{\mu_1}{\mu_2}\boldsymbol{H}_1) = 0$	$\mathbf{n}_0 \times (\boldsymbol{H}_2 - \boldsymbol{H}_1) = \boldsymbol{\jmath}$
$\mathbf{n}_0 \cdot (\boldsymbol{B}_2 - \boldsymbol{B}_1) = 0$	$\mathbf{n}_0 \times (\boldsymbol{B}_2 - \frac{\mu_2}{\mu_1}\boldsymbol{B}_1) = \mu_2 \boldsymbol{\jmath}$

A list of the boundary conditions satisfied by time-varying electric and magnetic vectors are given in Table 1.1 with reference to Fig. 1.1.

1.2 Electromagnetic Power Budget

The basic energetic features of the electromagnetic field and of its interaction with the environment are obtained directly from Maxwell's equations.

Consider a source characterized by the impressed electric and magnetic currents $\boldsymbol{J}_s$ and $\boldsymbol{J}_{ms}$ and carry out the dot products (Sect. A.1.2.1) of the terms of the first equation by the co-located magnetic field $\boldsymbol{H}$ and of the terms of the second equation by $-\boldsymbol{E}$

$$\nabla \times \boldsymbol{E} = -\frac{\partial \boldsymbol{B}}{\partial t} - \boldsymbol{J}_{ms} \qquad \cdot \boldsymbol{H} \; ;$$

$$\nabla \times \boldsymbol{H} = \frac{\partial \boldsymbol{D}}{\partial t} + \boldsymbol{J} + \boldsymbol{J}_s \qquad \cdot (-\boldsymbol{E}) \; .$$

Term-by-term addition, followed by integration over an *arbitrary* volume V contoured by the surface S and use of the vector identity (A.34)

$$\nabla \times \boldsymbol{E} \cdot \boldsymbol{H} - \boldsymbol{E} \cdot \nabla \times \boldsymbol{H} = \nabla \cdot (\boldsymbol{E} \times \boldsymbol{H})$$

and of the divergence theorem (A.15) yield

$$\begin{aligned} \iiint_V (-\boldsymbol{J}_\mathrm{s} \cdot \boldsymbol{E}_\mathrm{s} - \boldsymbol{J}_\mathrm{ms} \cdot \boldsymbol{H}_\mathrm{s}) \, \mathrm{d}V \; &= \iiint_V g \, \boldsymbol{E} \cdot \boldsymbol{E} \, \mathrm{d}V \\ &+ \iiint_V \left(\boldsymbol{H} \cdot \frac{\partial \boldsymbol{B}}{\partial t} + \boldsymbol{E} \cdot \frac{\partial \boldsymbol{D}}{\partial t} \right) \mathrm{d}V \\ &+ \oiint_S \boldsymbol{E} \times \boldsymbol{H} \cdot \mathbf{n}_0 \, \mathrm{d}S \, . \end{aligned} \tag{1.13}$$

The source term in (1.13) contains the products of the electric and magnetic *impressed* currents by the corresponding *co-located* fields $\boldsymbol{E}_\mathrm{s}$ and $\boldsymbol{H}_\mathrm{s}$.

Equation (1.13), named the integral form of *Poynting's theorem*, sets the balance among four integral terms combining electric and magnetic vectors, and source currents: three terms are expressed by volume integrals, one is an integral over the closed surface that encloses the volume. The arbitrariness of volume V, hence of surface S, which turns out particularly attractive in applications, is stressed.

Interpreting the physical meaning of the various terms in (1.13) illuminates several features of the electromagnetic power.

1.2.1 The Electromagnetic Source

The source is modeled as a volume $V_\mathrm{s} \subseteq V$ inside which a charge density ρ_s moves at an *impressed* velocity $\boldsymbol{u}_\rho$, yielding the impressed electric current density $\boldsymbol{J}_\mathrm{s}$

$$\boldsymbol{J}_\mathrm{s} = \rho_\mathrm{s} \, \boldsymbol{u}_\rho \, .$$

The electric field $\boldsymbol{E}_\mathrm{s}$ inside the source and co-located with $\boldsymbol{J}_\mathrm{s}$, exerts a force $\boldsymbol{F}_\mathrm{es} = \rho_\mathrm{s} \boldsymbol{E}_\mathrm{s}$ on the charge ρ_s; since ρ_s moves, the "application point" of the force exerted by $\boldsymbol{E}_\mathrm{s}$ moves, hence the field conveys power

$$W_\mathrm{es} = \rho_\mathrm{s} \boldsymbol{E}_\mathrm{s} \cdot \frac{\mathrm{d}\boldsymbol{r}'}{\mathrm{d}t} = \boldsymbol{J}_\mathrm{s} \cdot \boldsymbol{E}_\mathrm{s}$$

to the volumic charge moving at velocity $\boldsymbol{u}_\rho = \dfrac{\mathrm{d}\boldsymbol{r}'}{\mathrm{d}t}$. Given the negative sign of the source term,

$$-\boldsymbol{J}_\mathrm{s} \cdot \boldsymbol{E}_\mathrm{s} = -W_\mathrm{es} = W_\mathrm{se}$$

represents the power W_{se} conveyed from the impressed current density to the electric field, that is, the power that the unit volume of the source delivers to the electromagnetic field. Note that, because of the negative sign, in order that the source delivers power to the field, the current in the source must flow *against* the force exerted by the field. This requires an "external" action, therefore the intervention of *energy of different kind*.

The term involving the magnetic quantities is interpreted analogously, keeping in mind its purely equivalent character.

In conclusion, the term

$$W_s = \iiint_{V_s} (-\boldsymbol{J}_s \cdot \boldsymbol{E}_s - \boldsymbol{J}_{ms} \cdot \boldsymbol{H}_s)\ \mathrm{d}V$$

represents the power W_s that the energy conversion process acting in the volume V_s of the source and modeled through impressed electric and magnetic currents, conveys to the electromagnetic field.

Poynting's theorem indicates that the power W_s delivered by the source is divided into three parts, represented by the terms at the second member of (1.13) listed in the following.

1.2.2 Dissipated Power

The first term at the second member of (1.13) contains the non-negative[4] quantity

$$g\,\boldsymbol{E} \cdot \boldsymbol{E}\ \ \mathrm{d}V = \boldsymbol{J} \cdot \boldsymbol{E}\ ,$$

which denotes the power density that the field conveys to the conduction current in the region of space $V_g \subseteq V$ where $g \neq 0$: the electromagnetic energy is irreversibly transformed into heat (dissipated through the *Joule effect*) at the rate

$$W_g = \iiint_{V_g} g\,\boldsymbol{E} \cdot \boldsymbol{E}\,\mathrm{d}V\ . \tag{1.14}$$

Equation (1.14) yields the power W_g that the dissipating mechanisms, for the time being modeled through the conductivity g of the materials in V_g, take away from the electromagnetic field.

[4]The case of *active media* modeled by $g < 0$ is of lesser interest in Earth observation.

1.2.3 Stored Energy

The quantity

$$\boldsymbol{E}\cdot\frac{\partial \boldsymbol{D}}{\partial t}+\boldsymbol{H}\cdot\frac{\partial \boldsymbol{B}}{\partial t}=\frac{\partial \mathcal{E}_{\mathrm{e}}}{\partial t}+\frac{\partial \mathcal{E}_{\mathrm{m}}}{\partial t}$$

in the second term at the second member of (1.13) is known to represent the power associated with changes of the electric ($\mathcal{E}_{\mathrm{e}}$) and magnetic ($\mathcal{E}_{\mathrm{m}}$) energies per unit volume stored in the time-varying electromagnetic field: the power is positive when it flows to increase the field energy and negative when depleting the stored energy. Therefore,

$$W_{\mathcal{E}}=\frac{\partial \mathcal{E}_{\mathrm{em}}}{\partial t}=\iiint_V\left(\boldsymbol{E}\cdot\frac{\partial \boldsymbol{D}}{\partial t}+\boldsymbol{H}\cdot\frac{\partial \boldsymbol{B}}{\partial t}\right)\mathrm{d}V$$

denotes the power that is associated with changes of the energy $\mathcal{E}_{\mathrm{em}}$ stored in the time-varying electromagnetic field inside the volume V.

1.2.4 Electromagnetic Radiation

Unlike the other terms, which describe three-dimensional processes occurring in V, the last term in (1.13) refers to a flux (A.1.3) through the surface S contouring V. Clearly, it also denotes power, hence the scalar product $\boldsymbol{E}\times\boldsymbol{H}\cdot\mathbf{n}_0$ is the power that crosses the unit area of S. The vector

$$\boldsymbol{\mathcal{P}}=\boldsymbol{E}\times\boldsymbol{H}$$

is named *Poynting vector*: its component locally perpendicular to S yields the power that the electromagnetic field carries across the unit area of S. Consistently with the definition of flux,

- an outward component of the Poynting's vector yields a *positive* contribution to the power that crosses S *leaving* volume V,
- while an inward (*negative*) component brings power inside V.

The total flux is positive when power globally leaves V, thus indicating the presence of sources in V; it is negative when power enters S: this occurs when the sources are outside V, inside which, instead, lossy materials are located that dissipate electromagnetic energy.

The *instantaneous energy budget* (1.13) provides the electromagnetic power associated with the *radiation* produced by the sources

$$\oiint_S\boldsymbol{\mathcal{P}}\cdot\mathbf{n}_0\,\mathrm{d}S=W_{\mathrm{s}}-W_g-W_{\mathcal{E}}\ . \tag{1.15}$$

The electromagnetic field carries power out of any portion of space in which sources are located. Given the arbitrariness of S, flux of power exists however far from the source. This feature illustrates the potential of the electromagnetic field in carrying power (hence information) over large distances. The radiation received from remote stars hints at the huge paths traveled by the information carried by the field. On its side, the active manmade farthest object from Earth, the Voyager 1 space probe launched by the **N**ational **A**eronautics and **S**pace **A**dministration (NASA) on September 5, 1977, was sending information (signals) to the Earth from a distance of about 1.84×10^{10} km as of November 2012.

Concept and properties of electromagnetic radiation are clearly basic to Earth observation.

1.2.5 Power Budget for Time-Harmonic Fields

Fields which vary harmonically with time are of paramount importance in EO.

A source with an impressed electric current $\boldsymbol{J}_s$ varying sinusoidally with time at *angular frequency* $\omega = 2\pi f$ creates a time-harmonic electromagnetic field at the same frequency. It means that the current

$$\boldsymbol{J}_s = J_s \sin(\omega t)\ \mathbf{j}_0 \tag{1.16}$$

produces the fields

$$\boldsymbol{E} = E \sin(\omega t + \Phi_E)\ \boldsymbol{\mathfrak{e}}_0\ ; \tag{1.17}$$

$$\boldsymbol{H} = H \sin(\omega t + \Phi_H)\ \boldsymbol{\mathfrak{h}}_0\ . \tag{1.18}$$

The amplitudes J_s, E and H, and phases Φ_E and Φ_H of $\boldsymbol{E}$ and $\boldsymbol{H}$ are in general point functions.[5] Given the indeterminateness of the initial time, Φ_E and Φ_H are *relative* to the phase of $\boldsymbol{J}_s$, which is then assumed as reference. In (1.16), (1.17), and (1.18), $\mathbf{j}_0$, $\boldsymbol{\mathfrak{e}}_0$, and $\boldsymbol{\mathfrak{h}}_0$ are unit vectors expressing the respective orientations of current and fields.

A significant insight is obtained by separately discussing the power budget for time-harmonic fields in absence or in presence of lossy materials.

1.2.5.1 Power Balance for Non-dissipative Materials

Consider a region of space containing a time-harmonic electric source $\boldsymbol{J}_s$ and only lossless ($g = 0$) materials. Then (1.13) reduces to

$$\iiint_{V_s} -\boldsymbol{J}_s \cdot \boldsymbol{E}_s \ \mathrm{d}V = \iiint_V \left(\boldsymbol{E} \cdot \frac{\partial \boldsymbol{D}}{\partial t} + \boldsymbol{H} \cdot \frac{\partial \boldsymbol{B}}{\partial t} \right) \mathrm{d}V + \oiint_S \boldsymbol{E} \times \boldsymbol{H} \cdot \mathbf{n}_0 \, \mathrm{d}S\ .$$

[5] It should be well kept in mind that the phase has nothing to do with the angle between vectors.

By writing the explicit time dependence of current (1.16) and fields (1.17) and (1.18), the power associated with the radiation (1.15) is

$$\oiint_S \boldsymbol{E}\times\boldsymbol{H}\cdot\mathbf{n}_0\,\mathrm{d}S = -\iiint_{V_\mathrm{s}} J_\mathrm{s}E_\mathrm{s}\,\mathbf{j}_0\cdot\mathbf{e}_0\;\sin\omega t\;\sin(\omega t+\Phi_{\mathrm{Es}})\,\mathrm{d}V$$
$$-\iiint_V\left[\epsilon E^2\sin(\omega t+\Phi_\mathrm{E})\frac{\mathrm{d}\sin(\omega t+\Phi_\mathrm{E})}{\mathrm{d}t}+\mu H^2\sin(\omega t+\Phi_\mathrm{H})\frac{\mathrm{d}\sin(\omega t+\Phi_\mathrm{H})}{\mathrm{d}t}\right]\mathrm{d}V\,,$$

where Φ_{Es} denotes the phase of the electric field in the source volume V_s. Trigonometric identities readily yield

$$\oiint_S \boldsymbol{E}\times\boldsymbol{H}\cdot\mathbf{n}_0\,\mathrm{d}S = -\frac{1}{2}\iiint_{V_\mathrm{s}} J_\mathrm{s}E_\mathrm{s}\,\mathbf{j}_0\cdot\mathbf{e}_0\;[\cos\Phi_{\mathrm{Es}}-\cos(2\omega t+\Phi_{\mathrm{Es}})]\,\mathrm{d}V$$
$$-\frac{\omega}{2}\iiint_V\left[\epsilon E^2\sin 2(\omega t+\Phi_\mathrm{E})+\mu H^2\sin 2(\omega t+\Phi_\mathrm{H})\right]\mathrm{d}V\,. \tag{1.19}$$

Equation (1.19) indicates that the power created by the time-harmonic source is the sum of a term independent of time and of sinusoidal terms, two of which represent the time-variations of the energy stored in the fields. The variable terms are periodic, with frequency which is twice that of the source current.

In practice, only time-average values are significant, rather than instantaneous values.[6] The quantities of interest to users are obtained by averaging over the period T of the oscillation, so that (1.19) becomes

$$\frac{1}{T}\int_0^T\oiint_S \boldsymbol{E}\times\boldsymbol{H}\cdot\mathbf{n}_0\,\mathrm{d}S\,\mathrm{d}t$$
$$=-\frac{1}{2}\iiint_{V_s} J_\mathrm{s}E_\mathrm{s}\,\mathbf{j}_0\cdot\mathbf{e}_0\,\frac{1}{T}\int_0^T[\cos\Phi_{\mathrm{Es}}-\cos(2\omega t+\Phi_{\mathrm{Es}})]\,\mathrm{d}t\,\mathrm{d}V$$
$$-\frac{\omega}{2}\iiint_V\left[\epsilon E^2\frac{1}{T}\int_0^T\sin 2(\omega t+\Phi_\mathrm{E})\mathrm{d}t+\mu H^2\frac{1}{T}\int_0^T\sin 2(\omega t+\Phi_\mathrm{H})\mathrm{d}t\right]\mathrm{d}V$$
$$=-\frac{1}{2}\iiint_{V_\mathrm{s}} J_\mathrm{s}E_\mathrm{s}\,\mathbf{j}_0\cdot\mathbf{e}_0\;\cos\Phi_{\mathrm{Es}}\,\mathrm{d}V\,.$$

The power varying the energy in the fields has only periodic terms, hence its average vanishes, as does the periodic source term, because harmonic functions are zero-mean functions. Therefore, the average flow of power, that is the *radiation*, through S coincides with the average power $\overline{W}_\mathrm{s}$ created by the source, *provided only lossless materials are enclosed by S*

[6] Energy and time-average power are equivalent and are used alternatively.

$$\overline{W}_{\mathrm{s}} = \oiint_S \overline{\boldsymbol{\mathcal{P}}} \cdot \mathbf{n}_0 \, \mathrm{d}S \,, \tag{1.20}$$

where $\overline{\boldsymbol{\mathcal{P}}}$ denotes the time-average Poynting vector.

Let us apply (1.20) to compute the surface density of solar radiation reaching the Earth. The field radiated by the Sun is assumed to behave as a harmonic quantity, uniformly distributed in angle in a lossless interplanetary medium. The geometric surface S is chosen as a sphere centered on the Sun with radius $R_{\mathrm{SE}} \approx 1.5 \cdot 10^{11}$ m representative of the distance between Sun and Earth. Both vectors $\overline{\boldsymbol{\mathcal{P}}}$ and $\mathbf{n}_0$ are directed radially, as sketched in Fig. 1.3. The radiation intensity is the magnitude $\overline{\mathcal{P}}$ of the average Poynting vector, which is readily obtained by (1.20)

$$4\,\pi\, R_{\mathrm{SE}}^2\, \overline{\mathcal{P}} = \overline{W}_s \,.$$

From the estimated radiated power $\overline{W}_s \approx 3.85 \times 10^{26}$ W, the average areic power $\overline{\mathcal{P}} \approx 1360\,\mathrm{W\,m^{-2}}$ carried by the electromagnetic field originating from Sun is computed to reach Earth.

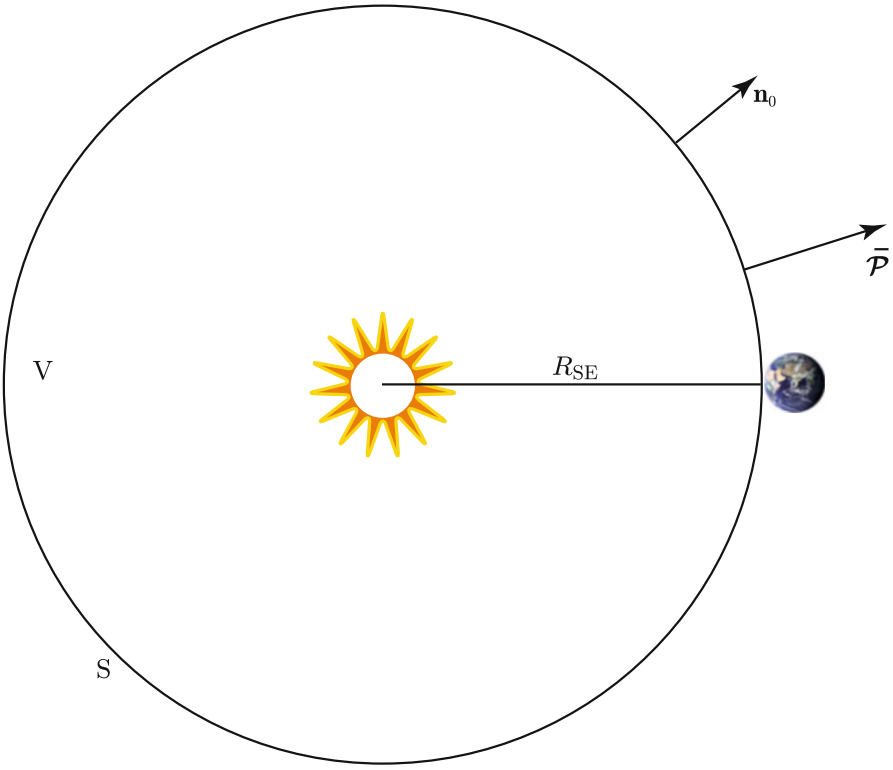

Fig. 1.3 The surface density of solar radiation reaching the Earth is readily estimated by Poynting's theorem

If the source is external to the considered lossless region of space, no average power is supplied to the field nor is subtracted from it, so

$$\oiint_S \overline{\mathcal{P}} \cdot \mathbf{n}_0 \, \mathrm{d}S = 0 \, .$$

Poyting's theorem indicates that no average power *globally* enters or leaves S: the incoming power is balanced by the leaving one. This is assumed to occur in the interplanetary "empty" space of Fig. 1.3.

1.2.5.2 Power Balance with Lossy Materials

Assume now that lossy materials, characterized, for the time being, by conductivity g, are present in regions V_g of the considered volume. The radiation is given by the balance between the time-average power terms

$$\begin{aligned}
&\oiint_S \overline{\mathcal{P}} \cdot \mathbf{n}_0 \, \mathrm{d}S \\
&= -\frac{1}{2} \iiint_{V_\mathrm{s}} J_\mathrm{s} E_\mathrm{s} \, \mathbf{j}_0 \cdot \boldsymbol{\epsilon}_0 \, \cos \Phi_\mathrm{Es} \, \mathrm{d}V - \iiint_{V_g} \frac{1}{T} \int_0^T g E^2 \sin^2(\omega t + \Phi_\mathrm{E}) \, \mathrm{d}t \, \mathrm{d}V \\
&= \overline{W}_\mathrm{s} - \iiint_{V_g} g \frac{E^2}{2} \, \mathrm{d}V \, .
\end{aligned} \tag{1.21}$$

When a source coexists with lossy materials in V, the flux of power through the contour S of V is lowered by the dissipation mechanisms of the matter: part of the energy delivered by the source heats the lossy materials at a volumic average rate

$$\overline{W}_\mathrm{gv} = g \frac{E^2}{2} > 0 \, ,$$

while the remainder leaves S. The radiation (1.21) flowing through S is then

$$\oiint_S \overline{\mathcal{P}} \cdot \mathbf{n}_0 \, \mathrm{d}S = \overline{W}_\mathrm{s} - \overline{W}_\mathrm{g} \, .$$

If the source is external to the considered lossy region of space, the power balance reduces to

$$\oiint_S \overline{\mathcal{P}} \cdot \mathbf{n}_0 \, \mathrm{d}S = -\overline{W}_\mathrm{g} \, . \tag{1.22}$$

The average power globally flowing through S is now negative: the "incoming" energy exceeds the "leaving" one by the quantity $\overline{W}_\mathrm{g}$ that the dissipation process transforms into heat.

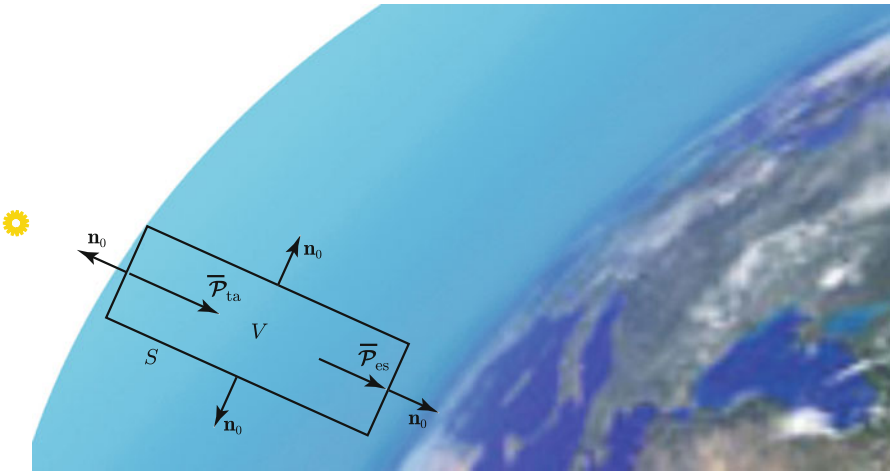

Fig. 1.4 The areic solar radiation $\overline{\mathcal{P}}_{\rm es}$ at the surface of the Earth is estimated by applying Poynting's theorem to the volume V of air crossed by the radiation

We use (1.22) to estimate in a simple way the solar radiation at ground level, i.e., below the atmospheric burden. The geometric surface S is now chosen to be that of the cylinder sketched in Fig. 1.4 with axis parallel to the direction along which the solar radiation travels and unitary cross-section. The upper section of the cylinder is assumed to be at the top of the atmosphere, while the bottom section is at ground level. Taking account of the direction of the external normal $\mathbf{n}_0$, Eq. (1.22) becomes

$$-\overline{\mathcal{P}}_{\rm ta} + \overline{\mathcal{P}}_{\rm es} = -\overline{W}_{\rm a} \,,$$

where $\overline{\mathcal{P}}_{\rm ta}$ and $\overline{\mathcal{P}}_{\rm es}$ are respectively the values of the areic power of the solar radiation at the top and bottom of the atmosphere and $\overline{W}_{\rm a}$ is the power that the atmosphere in the considered cylindrical volume removes from the radiation. As a reference, assume that the crossed volume of air subtracts 30 % of the solar radiation that arrives at the top of the atmosphere: then the direct solar power density at the Earth's surface is $\overline{\mathcal{P}}_{\rm es} = 0.7\,\overline{\mathcal{P}}_{\rm ta} \approx 950\,\mathrm{W\,m^{-2}}$. This no-cost considerable power density is the primary source utilized in optical Earth observation [7].

1.3 Polarization and Coherence

Natural and man-made electromagnetic sources in Earth observation produce fields that are deterministic or random functions of time. At a given position, the Cartesian components of the electric field are represented by the general expressions

$$E_x(t) = E_{0x}(t)\cos\left[\omega t + \Phi_x(t)\right] \ ;$$
$$E_y(t) = E_{0y}(t)\cos\left[\omega t + \Phi_y(t)\right] \ ;$$
$$E_z(t) = E_{0z}(t)\cos\left[\omega t + \Phi_z(t)\right] \ ,$$

where amplitudes E_{0p} and phases Φ_p, $(p = x, y, z)$, generally vary with time, according to the temporal properties of the source.

1.3.1 Monochromatic Fields

The basic reference is the time-harmonic source $\boldsymbol{J}_s$, at angular frequency ω, which, in a stationary and linear medium, produces a radiation the *spectrum* of which consists of a *single line*. This means that $\boldsymbol{J}_s$ generates time-harmonic electric and magnetic fields at its same angular frequency. Then, the amplitude E_{0p} and phase Φ_p of the p-component of the field are constant with respect to time: the field components vary with time in a purely sinusoidal manner at the source's angular frequency ω:

$$E_p(t) = E_{0p}\cos\left(\omega t + \Phi_p\right) \qquad p = x, y, z \ . \tag{1.23}$$

The field components are conveniently represented by the corresponding *phasors*, complex numbers $\widehat{E}_p$ *independent of time*, given by

$$\widehat{E}_p = E_{0p}\,\mathrm{e}^{\mathrm{j}\Phi_p} \qquad p = x, y, z \ .$$

The harmonic time-dependent component (1.23) is directly obtained by taking the real part of the complex spectral line $\widehat{E}_p$ multiplied (in advance) by the complex exponential $\mathrm{e}^{\mathrm{j}\omega t}$

$$E_p(t) = \Re[\widehat{E}_p\,\mathrm{e}^{\mathrm{j}\omega t}] \qquad p = x, y, z \ .$$

The phasors of the components $\widehat{E}_p$ form a *representative complex vector* independent of time

$$\begin{aligned}\widehat{\boldsymbol{E}} &= (E_{x\mathrm{r}} + \mathrm{j}E_{x\mathrm{j}})\mathbf{x}_0 + (E_{y\mathrm{r}} + \mathrm{j}E_{y\mathrm{j}})\mathbf{y}_0 + (E_{z\mathrm{r}} + \mathrm{j}E_{z\mathrm{j}})\mathbf{z}_0 \\ &= E_{x\mathrm{r}}\mathbf{x}_0 + E_{y\mathrm{r}}\mathbf{y}_0 + E_{z\mathrm{r}}\mathbf{z}_0 + \mathrm{j}(E_{x\mathrm{j}}\mathbf{x}_0 + E_{y\mathrm{j}}\mathbf{y}_0 + E_{z\mathrm{j}}\mathbf{z}_0) \\ &= \boldsymbol{E}_\mathrm{r} + \mathrm{j}\boldsymbol{E}_\mathrm{j} \ ,\end{aligned} \tag{1.24}$$

where $\boldsymbol{E}_\mathrm{r}$ and $\boldsymbol{E}_\mathrm{j}$ are ordinary vectors, with components expressed by real numbers. The vector $\widehat{\boldsymbol{E}}$ is "representative" in the sense that the time-dependent vector $\boldsymbol{E}(t)$ is obtained from it by the operation

$$\boldsymbol{E}(t) = \Re\left[\widehat{\boldsymbol{E}}\,\mathrm{e}^{\mathrm{j}\omega t}\right] . \tag{1.25}$$

By expressing $\widehat{\boldsymbol{E}}$ in terms of the "real" $\boldsymbol{E}_\mathrm{r}$ and "imaginary" $\boldsymbol{E}_\mathrm{j}$ vectors, $\boldsymbol{E}(t)$ is given by

$$\begin{aligned}\boldsymbol{E}(t) &= \Re\left[(\boldsymbol{E}_\mathrm{r} + \mathrm{j}\boldsymbol{E}_\mathrm{j})\,\mathrm{e}^{\mathrm{j}\omega t}\right] = \Re\left[(\boldsymbol{E}_\mathrm{r} + \mathrm{j}\boldsymbol{E}_\mathrm{j})\,(\cos\omega t + \mathrm{j}\sin\omega t)\right] \\ &= \boldsymbol{E}_\mathrm{r}\cos\omega t - \boldsymbol{E}_\mathrm{j}\sin\omega t\ .\end{aligned} \tag{1.26}$$

Since the time reference waveform is conventionally assumed to be $\cos\omega t$,

- the real vector $\boldsymbol{E}_\mathrm{r}$ is the *in-phase* vector component
- the imaginary vector $\boldsymbol{E}_\mathrm{j}$ is the *quadrature*[7] vector component.

In-phase and quadrature vectors of a monochromatic field depend on space, while are clearly independent of time.

1.3.1.1 Polarization of the Electromagnetic Field

Equation (1.26) indicates that at a given position in space, the terminal point of $\boldsymbol{E}(t)$ traces out the ellipse in the plane of $\boldsymbol{E}_\mathrm{r}$ and $\boldsymbol{E}_\mathrm{j}$ depicted in Fig. 1.5: $\boldsymbol{E}$ is said to have *elliptical polarization*. Two particular cases, of primary importance for Earth observation, can occur.

- When $\boldsymbol{E}_\mathrm{r}\cdot\boldsymbol{E}_\mathrm{j} = 0$ and $|\boldsymbol{E}_\mathrm{r}| = |\boldsymbol{E}_\mathrm{j}|$, the ellipse degenerates into a circle: the vector is *circularly polarized*.

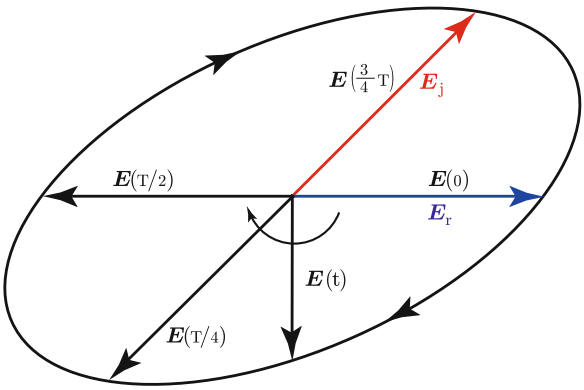

Fig. 1.5 Evolution with time of a vector with in-pase $\boldsymbol{E}_\mathrm{r}$ and quadrature $\boldsymbol{E}_\mathrm{j}$ components; $T = 2\pi/\omega$ is the period of the oscillation

[7] It should be clear that quadrature has no relationship with perpendicularity.

- If $\boldsymbol{E}_\mathrm{r} \times \boldsymbol{E}_\mathrm{j} = 0$, the ellipse degenerates into a segment and the vector is *linearly polarized*. This condition is met when either the in-phase or the quadrature component vanishes, as well as when the two components are parallel.

Although the cartesian components of $\boldsymbol{E}$ are always sinusoidal functions of time, the features of the vector change according to its polarization [5, 14, 26]. In case of linear polarization, the direction of the vector does not change, while its instantaneous magnitude varies sinusoidally; instead, a circularly polarized vector has a constant instantaneous amplitude, whereas its direction changes, uniformly, with time. Both instantaneous value and direction change with time in case of elliptical polarization.[8]

It is useful to note that elliptically and circularly polarized vectors can be regarded as linear combinations of the two linearly polarized vectors $\boldsymbol{E}_\mathrm{r}$ and $\boldsymbol{E}_\mathrm{j}$. In turn, linearly polarized vectors can be obtained as sum of two co-planar elliptically or circularly polarized vectors rotating in opposite directions and having the same amplitude. In Earth observation, a generally polarized field is usually expressed on a *linear polarization basis* (Sect. 4.2.1), sometimes on a *circular polarization basis*.

1.3.1.1.1 Modulus, "Versor" and Orthogonality of Complex Vectors

Given the widespread use of complex vectors in representing time-varying fields, the concepts of modulus, versor and orthogonality must be extended and adapted.

The representative complex vector (1.24) is

$$\widehat{\boldsymbol{E}} = E_\mathrm{r}\,\boldsymbol{e}_\mathrm{r} + \mathrm{j}E_\mathrm{j}\,\boldsymbol{e}_\mathrm{j}\ , \tag{1.27}$$

where $\boldsymbol{e}_\mathrm{r}$ and $\boldsymbol{e}_\mathrm{j}$ are the versors (real unit vectors, in this case) of the ordinary vectors $\boldsymbol{E}_\mathrm{r}$ and $\boldsymbol{E}_\mathrm{j}$ respectively. The *modulus* of $\widehat{\boldsymbol{E}}$ is obtained from[9]

$$\widehat{\boldsymbol{E}} \cdot \widehat{\boldsymbol{E}}^* = {E_\mathrm{r}}^2 + {E_\mathrm{j}}^2$$

as

$$|\widehat{\boldsymbol{E}}| = \sqrt{{E_\mathrm{r}}^2 + {E_\mathrm{j}}^2}\ .$$

Then the expression alternative to (1.27),

$$\widehat{\boldsymbol{E}} = |\widehat{\boldsymbol{E}}|\,\boldsymbol{e}_0\ ,$$

[8] Polarization is effectively depicted in animations that are found on web sites such as [8].

[9] In column-vector notation, superscript * indicates conjugate transpose.

introduces the *complex unit vector*[10]

$$\mathfrak{e}_0 = \frac{E_\mathrm{r}}{|\widehat{\boldsymbol{E}}|}\,\mathfrak{e}_\mathrm{r} + \mathrm{j}\frac{E_\mathrm{j}}{|\widehat{\boldsymbol{E}}|}\,\mathfrak{e}_\mathrm{j}$$

corresponding to the versor of an ordinary vector.

Two complex vectors $\widehat{\boldsymbol{E}}_1$ and $\widehat{\boldsymbol{E}}_2$ are *orthogonal* when

$$\widehat{\boldsymbol{E}}_1 \cdot \widehat{\boldsymbol{E}}_2^* = 0\ . \tag{1.28}$$

In case $\widehat{\boldsymbol{E}}_1 = C_1\,|\widehat{\boldsymbol{E}}_1|\,\mathfrak{e}_{01}$ and $\widehat{\boldsymbol{E}}_2 = C_2\,|\widehat{\boldsymbol{E}}_2|\,\mathfrak{e}_{02}$ are linearly polarized[11] along the directions identified by the *real* unit vectors $\mathfrak{e}_{01}$ and $\mathfrak{e}_{02}$, the orthogonality condition (1.28)

$$\widehat{\boldsymbol{E}}_1 \cdot \widehat{\boldsymbol{E}}_2^* = C\,|\widehat{\boldsymbol{E}}_1||\widehat{\boldsymbol{E}}_2|\ \mathfrak{e}_{01} \cdot \mathfrak{e}_{02} = 0$$

implies $\mathfrak{e}_{01} \perp \mathfrak{e}_{02}$: orthogonal linearly polarized vectors are perpendicular. Instead, in case of circular or elliptical polarization, orthogonality does not mean perpendicularity. In fact, the orthogonality condition for the *complex* unit vectors $\mathfrak{e}_{01} = \mathfrak{e}_{\mathrm{r}1} + \mathrm{j}\mathfrak{e}_{\mathrm{j}1}$ and $\mathfrak{e}_{02} = \mathfrak{e}_{\mathrm{r}2} + \mathrm{j}\mathfrak{e}_{\mathrm{j}2}$ yields

$$(\mathfrak{e}_{\mathrm{r}1} + \mathrm{j}\mathfrak{e}_{\mathrm{j}1}) \cdot (\mathfrak{e}_{\mathrm{r}2} - \mathrm{j}\mathfrak{e}_{\mathrm{j}2}) = \mathfrak{e}_{\mathrm{r}1} \cdot \mathfrak{e}_{\mathrm{r}2} + \mathfrak{e}_{\mathrm{j}1} \cdot \mathfrak{e}_{\mathrm{j}2} + \mathrm{j}(\mathfrak{e}_{\mathrm{j}1} \cdot \mathfrak{e}_{\mathrm{r}2} - \mathfrak{e}_{\mathrm{r}1} \cdot \mathfrak{e}_{\mathrm{j}2}) = 0\ .$$

Therefore, $\mathfrak{e}_{01}$ is orthogonal to $\mathfrak{e}_{02}$ when

$$\begin{cases} \mathfrak{e}_{\mathrm{r}1} \cdot \mathfrak{e}_{\mathrm{r}2} + \mathfrak{e}_{\mathrm{j}1} \cdot \mathfrak{e}_{\mathrm{j}2} = 0\ ; \\ \mathfrak{e}_{\mathrm{r}1} \cdot \mathfrak{e}_{\mathrm{j}2} - \mathfrak{e}_{\mathrm{j}1} \cdot \mathfrak{e}_{\mathrm{r}2} = 0\ . \end{cases}$$

It should be noted that $\mathfrak{e}_{0i}$ $(i = 1, 2)$ is a unit vector, whereas $\mathfrak{e}_{ri}$ and $\mathfrak{e}_{ji}$ $(i = 1, 2)$ *are not* unit vectors.

1.3.1.2 Polarization Parameters

The general polarization state of a vector is described by the two polarization parameters shown in Fig. 1.6:

- the *inclination angle* ψ, defined as the angle between the major semi-axis of the polarization ellipse[12] and a reference direction;

[10] It is easily checked that $\mathfrak{e}_0 \cdot \mathfrak{e}_0^* = 1$.

[11] The complex factors C_i $(i = 1, 2)$ account for the phases.

[12] The polarization ellipse includes the degenerate cases of circle for circular polarization and of segment for linear polarization.

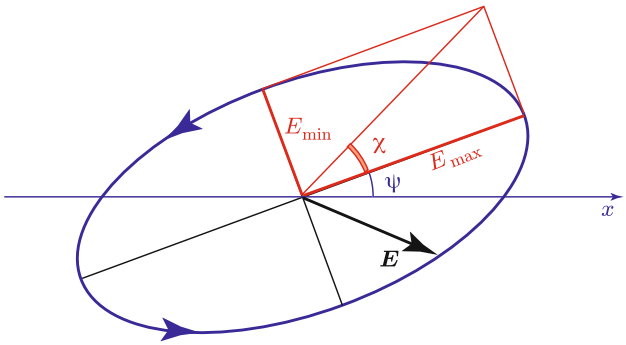

Fig. 1.6 Inclination angle ψ and ellipticity angle χ determine the polarization state of vector $\boldsymbol{E}$

- the *ellipticity angle* χ, defined as the arctangent of *ellipticity*:

$$\chi = \pm \arctan \frac{E_{\min}}{E_{\max}} \cdot$$

In Earth observation the inclination angle is commonly referred to the local horizontal direction, so that $\psi = 0$ when the major axis of the polarization ellipse is horizontal, while $\psi = \dfrac{\pi}{2}$ when it lies in the vertical plane (Sect. 4.2.1).

The ellipticity angle varies in the range $-\pi/4 \leqslant \chi \leqslant \pi/4$, with linear polarization corresponding to $\chi = 0$ and circular polarization to the extreme values. The $\pm$ sign identifies the direction of rotation of the vector, with respect to a reference versor orthogonal to the *polarization plane* identified by the plane of the ellipse. In a commonly adopted convention, the $+$ sign corresponds to a clockwise rotation (named *left polarization*) of the vector and the $-$ sign to counterclockwise rotation (*right polarization*) when the field is observed *facing* the source. Clearly the senses of rotation reverse if the field is observed *from* the source.[13]

1.3.2 Quasi-monochromatic Fields

The pure sinusoidal variation with time is an extremely useful reference in Earth observation and is widely used. However, the actual non-monochromaticity of the radiation must be taken into account in several instances. In reality, both natural and man-made radiation result from the superposition of a number of sinusoidal oscillations generated by the energy conversion process taking place in the source: the *spectrum* of the electromagnetic field does not consist of a single *line*, rather it

[13] Unfortunately, the two opposite conventions (facing the source, or looking away from the source) are both used, according to the application.

extends over a range of frequencies. The frequency spectra $\mathcal{S}$ of the electromagnetic radiation considered in practical applications have *narrow bands*,[14] that is, they differ appreciably from zero in a narrow frequency range Δf about a central frequency f_0:

$$\mathcal{S}(f) \neq 0 \quad \text{for} \quad f_0 - \frac{\Delta f}{2} < f < f_0 + \frac{\Delta f}{2}, \quad \text{with} \quad \frac{\Delta f}{f_0} \ll 1 \,. \tag{1.29}$$

A field the spectrum of which in narrow, i.e., satisfies the condition (1.29), is called *quasi-monochromatic* [2]. Narrow-band fields are of particular interest in Earth observation, since they are apt to approximately represent both man-made (e.g., radar) signals and the natural radiation passing through radiometric channels which separate the spectral components.

The *analytic signal* notation is the formalism, derived from that of the monochromatic case, used to represent quasi-monochromatic fields. Each field component *at a given point of space* is represented by the corresponding complex quantity E_p^{a}, where, as before, subscript $_p$ denotes p-component:

$$\begin{aligned} E_x^{\mathrm{a}}(t) &= E_{0x}(t)\, \mathrm{e}^{\mathrm{j}\Phi_x(t)} \,; \\ E_y^{\mathrm{a}}(t) &= E_{0y}(t)\, \mathrm{e}^{\mathrm{j}\Phi_y(t)} \,; \\ E_z^{\mathrm{a}}(t) &= E_{0z}(t)\, \mathrm{e}^{\mathrm{j}\Phi_z(t)} \,. \end{aligned}$$

The time-dependent amplitudes and phases allow one to express quantities that are not purely sinusoidal. The complex analytic components form the representative analytic vector $\boldsymbol{E}^{\mathrm{a}}(t)$ as in (1.24):

$$\begin{aligned} &\boldsymbol{E}^{\mathrm{a}}(t) = \\ &E_{0x}(t)\, \mathrm{e}^{\mathrm{j}\Phi_x(t)}\, \mathbf{x}_0 + E_{0y}(t)\, \mathrm{e}^{\mathrm{j}\Phi_y(t)}\, \mathbf{y}_0 + E_{0z}(t)\, \mathrm{e}^{\mathrm{j}\Phi_z(t)}\, \mathbf{z}_0 = \widehat{\boldsymbol{E}}(\boldsymbol{r}) \mathrm{e}^{\mathrm{a}}(t) + \mathrm{j}\, \boldsymbol{E}_{\mathrm{j}}^{\mathrm{a}}(t) \,, \end{aligned} \tag{1.30}$$

so that the field in the time domain is obtained by

$$\boldsymbol{E}(t) = \Re \left[\left(\boldsymbol{E}_{\mathrm{r}}^{\mathrm{a}}(t) + \mathrm{j}\, \boldsymbol{E}_{\mathrm{j}}^{\mathrm{a}}(t) \right) \mathrm{e}^{\mathrm{j}\omega t} \right] = \boldsymbol{E}_{\mathrm{r}}^{\mathrm{a}}(t)\, \cos \omega t - \boldsymbol{E}_{\mathrm{j}}^{\mathrm{a}}(t)\, \sin \omega t \,. \tag{1.31}$$

Given the variation with time of amplitudes and phases of the field components, the in-phase and quadrature vectors vary with time and, in turn, amplitude and polarization of the field change, following the deterministic or random variations

[14] Wide-band special systems are not considered.

of the components. However, the quasi-monochromaticity of the field implies that its amplitude and polarization state vary "slowly" with time: in general, $\boldsymbol{E}(t)$ describes an ellipse, the major axis, inclination and ellipticity of which change, but, given the condition (1.29) the changes are not appreciable over "short" time intervals, that is, of the order of $T_0 = 1/f_0$; rather, at a given point of space, variations of the field parameters become appreciable only for times $t \gg T_0$.

1.3.3 Spectral Maxwell's Equations

Introducing the fields expressed in the time-domain through the analytic vectors of the form (1.30) into Maxwell's equations leads to derivatives with respect to time of the type

$$\frac{\partial}{\partial t}\left\{\Re\left[E_0(t)\mathrm{e}^{\mathrm{j}\Phi(t)}\mathrm{e}^{\mathrm{j}\omega t}\right]\right\} = \Re\left[\left(j\omega E_0(t)\mathrm{e}^{\mathrm{j}\Phi(t)} + Q(t)\right)\mathrm{e}^{\mathrm{j}\omega t}\right] ,$$

where $Q(t)$ denotes a combination of the time derivatives $\frac{\partial}{\partial t}E_0(t)$ and $\frac{\partial}{\partial t}\Phi(t)$. It is readily realized that $Q(t) \ll \omega E_0$, because $E_0(t)$ and $\Phi(t)$ vary slowly with time, whence

$$\frac{\partial}{\partial t}\left\{\Re\left[E_0(t)\mathrm{e}^{\mathrm{j}\Phi(t)}\mathrm{e}^{\mathrm{j}\omega t}\right]\right\} \simeq \Re\left[j\omega E_0(t)\mathrm{e}^{\mathrm{j}\Phi(t)}\mathrm{e}^{\mathrm{j}\omega t}\right] .$$

Within this approximation for the time derivatives, Maxwell's equations in the frequency domain for non-monochromatic narrow-band fields represented by analytic vectors and scalars become

$$\nabla \times \boldsymbol{E}^{\mathrm{a}} = -\mathrm{j}\omega \boldsymbol{B}^{\mathrm{a}} - \boldsymbol{J}^{\mathrm{a}}_{\mathrm{ms}} ; \tag{1.32}$$

$$\nabla \times \boldsymbol{H}^{\mathrm{a}} = \mathrm{j}\omega \boldsymbol{D}^{\mathrm{a}} + \boldsymbol{J}^{\mathrm{a}} + \boldsymbol{J}_{\mathrm{s}}{}^{\mathrm{a}} ; \tag{1.33}$$

$$\nabla \cdot \boldsymbol{D}^{\mathrm{a}} = \rho^{\mathrm{a}} ; \tag{1.34}$$

$$\nabla \cdot \boldsymbol{B}^{\mathrm{a}} = 0 . \tag{1.35}$$

The relations (1.32), (1.33), (1.34) and (1.35) are called *spectral* Maxwell's equations. They relate through spatial differential operators the set of electromagnetic quantities, which are treated as functions of space only, within the narrow-band approximation. Nevertheless, it is understood that they are also deterministic or stochastic slow[15] functions of time.

[15] Again, the term "slow" means that the analytic quantities do not change appreciably over a time interval $\Delta t = 2\pi/\omega$, where ω is the angular frequency of the considered spectral component.

This approach allows the actual space-time electromagnetic vectors $\boldsymbol{E}(\boldsymbol{r}, t)$ and $\boldsymbol{H}(\boldsymbol{r}, t)$ to be readily obtained from the complex analytic vectors $\boldsymbol{E}^{\mathrm{a}}(\boldsymbol{r})$ and $\boldsymbol{H}^{\mathrm{a}}(\boldsymbol{r})$ provided by (1.32)–(1.35), as done in Sect. 1.3.1 for the purely harmonic fields:

$$\boldsymbol{E}(\boldsymbol{r}, t) = \Re\left[\boldsymbol{E}^{\mathrm{a}}(\boldsymbol{r})\mathrm{e}^{\mathrm{j}\omega t}\right]; \qquad \boldsymbol{H}(\boldsymbol{r}, t) = \Re\left[\boldsymbol{H}^{\mathrm{a}}(\boldsymbol{r})\mathrm{e}^{\mathrm{j}\omega t}\right] .$$

1.3.4 Random Electromagnetic Fields

Amplitude and phase of the fields of main interest in Earth observation are not deterministic functions of space and time. Particularly relevant examples are the natural radiation arriving from the Sun, or the optical or microwave radiation scattered by common terrestrial environments. Amplitude $E_{0p}(\boldsymbol{r}, t)$ and phase $\Phi_p(\boldsymbol{r}, t)$ of the p-component of the field in (1.30) are *random processes* [32], [24, Ch. 2] and the field $\boldsymbol{E}^{\mathrm{a}}$ at given point and time, which is regarded as a *realization* of the process, is a random complex vector function of space and time. Its value changes stochastically from point to point and from time to time. Therefore, determining single values of $\boldsymbol{E}^{\mathrm{a}}$ would be inadequate (or at least impractical) to characterize its global properties, which, rather, are suitably represented by the *moments* of the field [1, 33, Ch. 10].

The first moment of $\boldsymbol{E}^{\mathrm{a}}$ is its *mean* $\langle \boldsymbol{E}^{\mathrm{a}}(\boldsymbol{r}, t)\rangle$, that is, the average[16] over the random sequence (*ensemble*) of process realizations. When the phases of the random field components are uniformly distributed in the 0 to 2π range, the mean field vanishes

$$\langle \boldsymbol{E}^{\mathrm{a}}(\boldsymbol{r}, t)\rangle = 0 .$$

Therefore, non-vanishing higher-order moments are needed to describe the properties of $\boldsymbol{E}^{\mathrm{a}}$. The space-time second-order moment is the ensemble average of the juxtaposition of fields $\boldsymbol{E}_1^{\mathrm{a}}$ at point $\boldsymbol{r}_1$ and time t_1 and $\boldsymbol{E}_2^{\mathrm{a}}$ at point $\boldsymbol{r}_2$ and time t_2:

$$\mathbb{\Gamma}(\boldsymbol{r}_1, t_1, \boldsymbol{r}_2, t_2) := \langle \boldsymbol{E}^{\mathrm{a}}(\boldsymbol{r}_1, t_1)\boldsymbol{E}^{\mathrm{a}}(\boldsymbol{r}_2, t_2)^*\rangle , \tag{1.36}$$

where * is restated denoting[17] transpose conjugate [6]. The *dyadic* tensor (cf. A.1.2.3) $\mathbb{\Gamma}$ is sufficient to characterize the random field $\boldsymbol{E}^{\mathrm{a}}$ in a number of cases of practical importance in Earth observation.

[16] The averaging operation is denoted by the angular brackets $< >$, that, in the present context, *do not* indicate inner product.

[17] The superscript $^{\mathrm{H}}$ is also used (cf. Sect. 12.3.3).

1.3.4.1 Polarization Matrix

At a given point of space $\boldsymbol{r}$ and time t, i.e., for $\boldsymbol{r}_1 = \boldsymbol{r}_2 \equiv \boldsymbol{r}$, $t_1 = t_2 \equiv t$, the second-order moment (1.36) reduces to the *polarization dyadic*

$$\mathbb{J}(\boldsymbol{r}, t) = \langle \boldsymbol{E}^{\mathrm{a}}(\boldsymbol{r}, t)\, \boldsymbol{E}^{\mathrm{a}}(\boldsymbol{r}, t)^* \rangle \ , \tag{1.37}$$

which describes the general space-time polarization properties of the random field.

For a better insight into definition (1.37), consider the particularly relevant case of a two-component field:

$$\boldsymbol{E}^{\mathrm{a}} = E_{0x}\, \mathrm{e}^{\mathrm{j}\Phi_x} \mathbf{x}_0 + E_{0y}\, \mathrm{e}^{\mathrm{j}\Phi_y} \mathbf{y}_0 \ ,$$

the amplitudes and phases of which are random variables. The suitably arranged coefficients of the dyads in $\mathbb{J}$ form the *polarization matrix* [15], representing the *outer product*

$$\left\langle \boldsymbol{E}^{\mathrm{a}} \otimes \boldsymbol{E}^{\mathrm{a}*} \right\rangle \equiv [\mathcal{J}] := \begin{bmatrix} \langle E_{0x}^2 \rangle & \left\langle E_{0x} E_{0y}\, \mathrm{e}^{\mathrm{j}(\Phi_x - \Phi_y)} \right\rangle \\ \left\langle E_{0y} E_{0x}\, \mathrm{e}^{-\mathrm{j}(\Phi_x - \Phi_y)} \right\rangle & \langle E_{0y}^2 \rangle \end{bmatrix} \ ,$$

which is a source of valuable information on the properties of the field.

- The trace of the polarization matrix[18]

$$tr\,[\mathcal{J}] = \langle E_{0x}^2 \rangle + \langle E_{0y}^2 \rangle := 2\, \mathcal{I}_0 \tag{1.38}$$

  relates to the power carried by the field (Sect. 3.1.4.2): the quantity $\mathcal{I}_0$ defined by (1.38) is called *intensity* of $\boldsymbol{E}^{\mathrm{a}}$.
- The determinant of the polarization matrix

$$|\mathcal{J}| = \langle E_{0x}^2 \rangle \langle E_{0y}^2 \rangle - \left| \left\langle E_{0x} E_{0y} \mathrm{e}^{\mathrm{j}(\Phi_x - \Phi_y)} \right\rangle \right|^2$$

  provides information on the stochastic properties of the field:
  - The components of a deterministic field have a constant phase difference, so that $|\mathcal{J}| = 0$; a field for which the determinant of the polarization matrix vanishes has inclination and ellipticity angles that do not vary: it is said to be *completely polarized*.
  - Instead, a field the components of which have purely random amplitude and phases has $|\mathcal{J}| = \mathcal{I}_0^2$ because $\mathcal{J}_{12} = \mathcal{J}_{21} = 0$; inclination and ellipticity angles change continuously and the field is said *unpolarized*.[19]

[18] The polarization matrix is Hermitian ($\mathcal{J}_{21} = \mathcal{J}_{12}^*$).

[19] The condition $\mathcal{J}_{11} = \mathcal{J}_{22}$ ia also required.

- The form of the polarization matrix depends on the type of polarization.
  - A polarization matrix with real elements denotes a linearly polarized field.
  - Imaginary off-diagonal elements identify circular polarization[20]:

$$[\boldsymbol{\mathcal{J}}] = \mathcal{I}_0 \begin{bmatrix} 1 & \mp \mathrm{j} \\ \pm \mathrm{j} & 1 \end{bmatrix} .$$

  - A matrix of the form

$$[\boldsymbol{\mathcal{J}}] = \mathcal{I}_0 \begin{bmatrix} 1 & 0 \\ 0 & 1 \end{bmatrix}$$

    indicates no preferential orientation of the field, as it may occur in the solar radiation.

In general, the field can be regarded as the superposition of polarized and unpolarized parts and the polarization matrix as the sum of the corresponding partial matrices:

$$[\boldsymbol{\mathcal{J}}] = [\boldsymbol{\mathcal{J}}]^{(\mathrm{p})} + [\boldsymbol{\mathcal{J}}]^{(\mathrm{u})} .$$

The *degree of polarization* γ_p is defined as the ratio between the intensity of the polarized part to the total one, i.e.,

$$\gamma_\mathrm{p} := \frac{tr[\boldsymbol{\mathcal{J}}]^{(\mathrm{p})}}{tr[\boldsymbol{\mathcal{J}}]^{(\mathrm{p})} + tr[\boldsymbol{\mathcal{J}}]^{(\mathrm{u})}} = \sqrt{1 - \frac{4|\boldsymbol{\mathcal{J}}|}{(\mathcal{J}_{11} + \mathcal{J}_{22})^2}} .$$

An unpolarized field, for which $\mathcal{J}_{11} = \mathcal{J}_{22} \equiv \mathcal{J}$ and $\mathcal{J}_{12} = \mathcal{J}_{21} = 0$, has $|\boldsymbol{\mathcal{J}}| = \mathcal{J}^2$; so that $\gamma_\mathrm{p} = 0$, while a completely polarized field with $|\boldsymbol{\mathcal{J}}| = 0$, is characterized by $\gamma_\mathrm{p} = 1$.

1.3.4.2 Coherency Matrix

In the general space-time case in which $\boldsymbol{r}_1 \neq \boldsymbol{r}_2$ and $t_1 \neq t_2$, the second moment of the field (1.36) is the *coherency dyadic*[21]:

$$\begin{aligned} \boldsymbol{\Gamma}(\boldsymbol{r}_1, \boldsymbol{r}_2; t_1, t_2) &= \langle \boldsymbol{E}^\mathrm{a}(\boldsymbol{r}_1, t_1)\, \boldsymbol{E}^\mathrm{a}(\boldsymbol{r}_2, t_2)^* \rangle \equiv \left\langle \boldsymbol{E}_1^\mathrm{a}\, \boldsymbol{E}_2^{\mathrm{a}*} \right\rangle \\ &= \left\langle (E_{x1}\, \mathrm{e}^{\mathrm{j}\Phi_{x1}}\, \mathbf{x}_0 + E_{y1}\, \mathrm{e}^{\mathrm{j}\Phi_{y1}}\, \mathbf{y}_0)(E_{x2}\, \mathrm{e}^{-\mathrm{j}\Phi_{x2}}\, \mathbf{x}_0 + E_{y2}\, \mathrm{e}^{-\mathrm{j}\Phi_{y2}}\, \mathbf{y}_0) \right\rangle \\ &= \left\langle E_{x1} E_{x2}\, \mathrm{e}^{\mathrm{j}(\Phi_{x1} - \Phi_{x2})} \right\rangle \mathbf{x}_0 \mathbf{x}_0 + \left\langle E_{x1} E_{y2}\, \mathrm{e}^{\mathrm{j}(\Phi_{x1} - \Phi_{y2})} \right\rangle \mathbf{x}_0 \mathbf{y}_0 \\ &\quad + \left\langle E_{y1} E_{x2}\, \mathrm{e}^{\mathrm{j}(\Phi_{y1} - \Phi_{x2})} \right\rangle \mathbf{y}_0 \mathbf{x}_0 + \left\langle E_{y1} E_{y2}\, \mathrm{e}^{\mathrm{j}(\Phi_{y1} - \Phi_{y2})} \right\rangle \mathbf{y}_0 \mathbf{y}_0 . \end{aligned} \quad (1.39)$$

[20] The $\pm$ sign identifies the sense of rotation (Sect. 1.3.1.2).

[21] The assumption of two-component field is retained.

The coefficients of the dyads are the space-time *covariances* of the corresponding field components, which are arranged to form the *coherency matrix* [34, 42]

$$[\Gamma] = \begin{bmatrix} \Gamma_{xx} & \Gamma_{xy} \\ \Gamma_{yx} & \Gamma_{yy} \end{bmatrix} . \tag{1.40}$$

The coherency matrix for $\boldsymbol{r}_1 = \boldsymbol{r}_2$ and $t_1 = t_2$ reduces to the polarization matrix.

To simplify the notations, consider a linearly polarized field, for instance $\boldsymbol{E}^{\mathrm{a}} = E^{\mathrm{a}}\mathbf{y}_0$, the coherency matrix of which reduces to the only non-zero element

$$\Gamma = \left\langle E_1^{\mathrm{a}} E_2^{\mathrm{a}*} \right\rangle = \left\langle E_0(\boldsymbol{r}_1, t_1)\, E_0(\boldsymbol{r}_2, t_2)\, \mathrm{e}^{\,\mathrm{j}[\Phi(\boldsymbol{r}_1, t_1) - \Phi(\boldsymbol{r}_2, t_2)]} \right\rangle . \tag{1.41}$$

The statistical properties of the field can be considered either with respect to time, by setting $\boldsymbol{r}_1 = \boldsymbol{r}_2 \equiv \boldsymbol{r}$, or with respect to space ($t_1 = t_2 \equiv t$), thus leading to

- the *temporal coherence* (or temporal covariance) of the field in $\boldsymbol{r}$

$$\Gamma(\boldsymbol{r}; t_1, t_2) = \langle E^{\mathrm{a}}(\boldsymbol{r}, t_1)\, E^{\mathrm{a}}(\boldsymbol{r}, t_2)^* \rangle \ ,$$

- the *spatial coherence* at time t

$$\Gamma(\boldsymbol{r}_1, \boldsymbol{r}_2; t) = \langle E^{\mathrm{a}}(\boldsymbol{r}_1, t)\, E^{\mathrm{a}}(\boldsymbol{r}_2, t)^* \rangle \ .$$

The coherence at the same space-time point $\Gamma(\boldsymbol{r}, t)$ clearly yields the intensity (1.38) of the single-polarization field.

The degree of coherence γ is the coherence normalized to the variance [2, Chap. X]:

$$\gamma(\boldsymbol{r}_1, \boldsymbol{r}_2; t_1, t_2) = \frac{\langle E^{\mathrm{a}}(\boldsymbol{r}_1, t_1)\, E^{\mathrm{a}}(\boldsymbol{r}_2, t_2)^* \rangle}{\sqrt{\langle |E^{\mathrm{a}}(\boldsymbol{r}_1, t_1)|^2 \rangle}\, \sqrt{\langle |E^{\mathrm{a}}(\boldsymbol{r}_2, t_2)|^2 \rangle}} \cdot \tag{1.42}$$

The modulus $0 \leqslant |\gamma| \leqslant 1$ of the complex degree of coherence (1.42) represents the amount of correlation between the fluctuations of amplitudes and phases of the field at two different times and/or points. When $|\gamma| = 0$, the temporal variations of the field at the considered positions and/or the spatial variations of the field at the considered times are *statistically independent*, while $|\gamma| = 1$ indicates that the variations are fully related by deterministic relations. The phase of γ accounts for the deterministic relative phase of $\boldsymbol{E}_2^{\mathrm{a}}$ with respect to $\boldsymbol{E}_1^{\mathrm{a}}$.

The particular cases of temporal or spatial correlations are separately considered by

- the *degree of temporal coherence*

$$\gamma(\boldsymbol{r}; t_1, t_2) = \frac{\langle E^{\mathrm{a}}(\boldsymbol{r}, t_1)\, E^{\mathrm{a}}(\boldsymbol{r}, t_2)^* \rangle}{\sqrt{\langle |E^{\mathrm{a}}(\boldsymbol{r}, t_1)|^2 \rangle}\, \sqrt{\langle |E^{\mathrm{a}}(\boldsymbol{r}, t_2)|^2 \rangle}} \ ; \tag{1.43}$$

- the *degree of spatial coherence*

$$\gamma(\boldsymbol{r}_1, \boldsymbol{r}_2; t) = \frac{\langle E^{\mathrm{a}}(\boldsymbol{r}_1, t)\, E^{\mathrm{a}}(\boldsymbol{r}_2, t)^* \rangle}{\sqrt{\langle |E^{\mathrm{a}}(\boldsymbol{r}_1, t)|^2 \rangle}\, \sqrt{\langle |E^{\mathrm{a}}(\boldsymbol{r}_2, t)|^2 \rangle}} \cdot \tag{1.44}$$

The meaning is the same as highlighted previously for the space-time case.

What We Learned on the Electromagnetic Field

There are sound hints that the Earth's environment can be observed effectively by looking at the electromagnetic fields that interact with it. This means that we need some smattering of electromagnetics to develop the ambition to understand remote sensing.

So, after primary terminology, we learn basic properties and concepts, such as that the quantities we have to deal with are vectors, which need knowledge of magnitude and direction. We meet both electric and magnetic quantities, interrelated by exotic mathematical operators. Carrying on some algebra yields attractive results about the energy budget, like the presence of radiation, hence of detectable information, at "any" large distance from the electromagnetic source. We readily realize that this property is just right for observing the Earth from remote locations.

Things become more obscure when time comes into play explicitly. We refer to the sinusoidal time variation, which is the simplest harmonic case: nonetheless, we have to introduce a further item, the phase, into the representation of the field, already containing magnitude and direction information. Complex numbers then make their appearance, on which complex vectors are built. We are informed that the electromagnetic vectors evolve in time according to their polarization, i.e., they change amplitude and/or direction following peculiar configurations, linear, circular, elliptical.

At this point the basically random nature of the real world presents us with a dramatic hurdle. Complex vectors are not enough, but products of vectors are rather demanded to describe the stochastic properties that the randomly varying and fluctuating Earth's environment attributes to the interacting electromagnetic field. Then we have to endure awkward formalisms in handling dyadics and matrices. Worse yet, concepts of probability and correlation, random processes and random fields enter into play. The emergence of statistics concepts puts us in an awkward situation in the unfortunate case our background is limited to a deterministic approach to the electromagnetic theory. And we are aware that there is no room to provide us with a statistical background, except for a sort of list of compact definitions. So we are presented with the space-time second-order moment of the field, the primary quantity based on ensemble averages, which branches out into the concepts of intensity, polarization matrix, and temporal and spatial coherency that are all crucial to EO.

References

1. Boerner W-M, Mott H, Lüneburg E, Livingstone C, Brisco B, Brown R, Paterson JS (1999) Polarimetry in remote sensing – basic and applied concepts. In: Ryerson RA, Rencz AN (eds) Manual of remote sensing: remote sensing for the Earth sciences. Wiley. ISBN:9780471294054
2. Born M, Wolf E, Bhatia AB (2002) Principles of optics: electromagnetic theory of propagation, interference and diffraction of light. Cambridge University Press. ISBN:9781139643405
3. Clarke D (1974) Polarimetric definitions. In: Gehrels T (ed) Planets, stars and nebulae studied with photopolarimetry. The University of Arizona Press. ISBN:9780816504282
4. Cloude S (2009) Polarisation: applications in remote sensing. Oxford University Press. ISBN:9780191580383
5. Collett E (1993) Polarized light: fundamentals and applications. Marcel Dekker. ISBN:9780824787295
6. Courant R, Hilbert D (2008) Methods of mathematical physics, vol 1. Wiley. ISBN:9783527617227
7. Elachi C, van Zyl JJ (2006) Introduction to the physics and techniques of remote sensing. Wiley. ISBN:9780471475699
8. Electromagnetic Wave Polarization. Amanogawa digital Maestro. http://www.amanogawa.com/archive/Polarization/Polarization-2.html. Visited on 14 May 2014
9. Eyges L (2012) The classical electromagnetic field. Dover. ISBN:9780486152356
10. Feynman RP, Leighton RB, Sands M (2011) The Feynman lectures on physics: mainly electromagnetism and matter. New Millennium. ISBN:9780465024940
11. Fleisch D (2008) A student's guide to Maxwell's equations. Cambridge University Press. ISBN:9781139468473
12. Garg AK (2012) Classical electromagnetism in a nutshell. Princeton University Press. ISBN:9780691130187
13. Geselowitz M (2013) Did you know? Someone else wrote Maxwell's equations. IEEE The Institute. http://theinstitute.ieee.org/technology-focus/technology-history/did-you-know-someone-else-wrote-maxwells-equations. Visited on 03 July 2014
14. Goldstein DH (2007) Polarized light. CRC. ISBN:9781439830406
15. Gori F, Santarsiero M, Vicalvi S, Borghi R, Guattari G (1998) Beam coherence-polarization matrix. Pure Appl Opt J Eur Opt Soc A 7(5):941–951. doi:10.1088/09639659/7/5/004
16. Griffiths DJ (2012) Introduction to electrodynamics. Pearson Education. ISBN:9780321847812
17. Harrington RF (2001) Time-harmonic electromagnetic fields. Wiley. ISBN:9780471208068
18. Ishimaru A (1991) Electromagnetic wave propagation, radiation, and scattering. Prentice-Hall. ISBN:9780132490535
19. Jackson JD (1998) Classical electrodynamics. Wiley. ISBN:9780471309321
20. Kong JA (1986) Electromagnetic wave theory. Wiley. ISBN:9780471828235
21. Korotkova O (2013) Random light beams: theory and applications. Taylor & Francis. ISBN:9781439819500
22. Kraus JD, Carver KR (1981) Electromagnetics. McGraw-Hill. ISBN:9780070353961
23. Lee JS, Pottier E (2009) Polarimetric radar imaging: from basics to applications. Taylor & Francis. ISBN:9781420054989
24. Mandel L, Wolf E (1995) Optical coherence and quantum optics. Cambridge University Press. ISBN:9780521417112
25. Mott H (1986) Polarization in antennas and radar. Wiley. ISBN:9780471011675
26. Mott H (2007) Remote sensing with polarimetric radar. Wiley. ISBN:9780470074763
27. Nye JF (1972) Physical properties of crystals: their representation by tensors and matrices. Clarendon Press. ISBN:9780198511656
28. Panofsky WKH, Phillips M (2012) Classical electricity and magnetism. Dover. ISBN:9780486132259
29. Papas CH (2011) Theory of electromagnetic wave propagation. Dover. ISBN:9780486656786

30. Rao RS (2012) Electromagnetic waves and transmission lines. PHI Learning. ISBN:9788120345157
31. Rautio JC (2014) The long road to Maxwell's equations. IEEE Spectr 51(12):32–37. http://spectrum.ieee.org/telecom/wireless/the-long-road-to-maxwells-equations. Visited on 04 Dec 2014
32. Rytov SM, Kravtsov YuA, Tatarskii VI (1987) Principles of statistical radiophysics 1: elements of random process theory. Springer. ISBN:9780387125626
33. Saleh BEA, Teich MC (1991) Fundamentals of photonics. Wiley. ISBN:9780471213741
34. Sharma KK (2006) Optics: principles and applications. Elsevier. ISBN:9780080463919
35. Smith GS (1997) An introduction to classical electromagnetic radiation. Cambridge University Press. ISBN:9780521586986
36. Sommerfeld A (1949) Partial differential equations in physics. Elsevier. ISBN:9780080873091
37. Stratton JA, Adams SJ (2007) Electromagnetic theory. McGraw-Hill. ISBN:9781406765472
38. Ulaby FT, Michielssen E, Ravaioli U (2010) Fundamentals of applied electromagnetics. Prentice Hall. ISBN:9780132139311
39. Van Bladel JG (2007) Electromagnetic fields. Wiley. ISBN:9780471263883
40. Vanderlinde J (2004) Classical electromagnetic theory. Springer. ISBN:9781402026997
41. Wentworth SM (2004) Fundamentals of electromagnetics with engineering applications. Wiley. ISBN:9780471263555
42. Wolf E (2007) Introduction to the theory of coherence and polarization of light. Cambridge University Press. ISBN:9780521822114

Chapter 2
Dielectric Behavior of Terrestrial Materials

Section 1.3.3 shows that a system of differential equations in the space variables alone is obtained by introducing the analytic quantities defined in Sect. 1.3.2 into the time-domain Maxwell's equation system (1.1)–(1.4). The solutions provide the representative complex quantities from which the actually measurable electromagnetic vectors and scalars are obtained through (1.31). In simplified albeit unambiguous[1] notations,

$$\nabla \times \boldsymbol{E} = -\mathrm{j}\omega\mu\boldsymbol{H} - \boldsymbol{J}_{\mathrm{ms}} \; ; \tag{2.1}$$

$$\nabla \times \boldsymbol{H} = \mathrm{j}\omega\epsilon\boldsymbol{E} + g\boldsymbol{E} + \boldsymbol{J}_{\mathrm{s}} \; ; \tag{2.2}$$

$$\nabla \cdot \epsilon\boldsymbol{E} = \rho_{\mathrm{s}} \; ; \tag{2.3}$$

$$\nabla \cdot \mu\boldsymbol{H} = 0 \; . \tag{2.4}$$

Equations (2.1)–(2.4) interconnect electric and magnetic fields with the sources, taking into account the effects of the materials, represented by their dielectric permittivity ϵ, electrical conductivity g and magnetic permeability μ. The coefficients of the equations depend on these electromagnetic parameters, therefore the fields clearly carry the imprinting by the material.

A wide range of values of permittivity and conductivity are encountered in common terrestrial materials, while their magnetic permeability is usually quite close to that of vacuum. Therefore, given the lesser relevance that the magnetic properties of matter have in Earth observation, $\mu \approx \mu_0$ will be assumed in the following. The properties of the materials are then expressed by their conductivity

[1] The vectors are now understood to be slowly varying quantities from which the measurable (in the time domain) fields are derived. Therefore, the superscript [a] used trough (1.44) is dropped henceforth.

D. Solimini, *Understanding Earth Observation*, Remote Sensing and Digital Image Processing 23, DOI 10.1007/978-3-319-25633-7_2

and, principally, by their permittivity.[2] With some exception, linearity and isotropy of the materials (Sect. 1.1.2) are also implicitly assumed.

2.1 Permittivity in the Spectral Domain

The effect of the electric field entering a material is to change the equilibrium spatial distribution of the charges which compose the neutral matter. The modified charge arrangement generally gives rise to an electric dipole $\boldsymbol{\mathcal{P}}$. The permittivity ϵ that characterizes the dielectric properties of the (linear) material depends linearly on the normalized magnitude $\mathcal{P}$ of the volumic dielectric dipole induced by the acting field:

$$\epsilon = \epsilon_0 \left(1 + \frac{\mathcal{P}}{\epsilon_0 E}\right) = \epsilon_0(1 + \chi) \; . \tag{2.5}$$

The higher the dipole induced by a given acting field, the larger is the permittivity. In (2.5) the *susceptibility* χ accounts directly for the dipole induced into the isotropic material, in which $\boldsymbol{\mathcal{P}} \parallel \boldsymbol{E}$. The creation of the dipole by the acting electric field is named dielectric polarization.

From the relation in the time domain,[3]

$$\boldsymbol{D}(t) = \epsilon_0 \boldsymbol{E}(t) + \boldsymbol{\mathcal{P}}(t) \; ,$$

the relation between $\boldsymbol{D}$ and $\boldsymbol{E}$ in the spectral domain[4] is obtained:

$$\boldsymbol{D}(\omega) = \epsilon_0 \boldsymbol{E}(\omega) + \boldsymbol{\mathcal{P}}(\omega) = \epsilon(\omega)\boldsymbol{E}(\omega) \; . \tag{2.6}$$

The *spectral permittivity* $\epsilon(\omega)$ in (2.6) is related to the spectral susceptibility $\chi(\omega)$ by extending (2.5) into the spectral domain

$$\epsilon(\omega) = \epsilon_0 \left[1 + \chi(\omega)\right] = \epsilon_0 \, \tilde{\epsilon}(\omega) = \epsilon_0 \left[1 + \frac{\mathcal{P}(\omega)}{\epsilon_0 E(\omega)}\right] \cdot \tag{2.7}$$

Equation (2.7) indicates that the spectral dielectric behavior of a material, represented by its permittivity at angular frequency ω, depends on the electric dipole $\mathcal{P}(\omega)$ induced in the material by the acting electric field E at frequency ω.

[2] Section 2.1.3.2 links conductivity to permittivity.

[3] As said, this simplified approach assumes instantaneous response.

[4] Equation (2.6) is instrumental but incorrect in general, since a rigorous approach to spectral permittivity would require introducing convolution in the time domain.

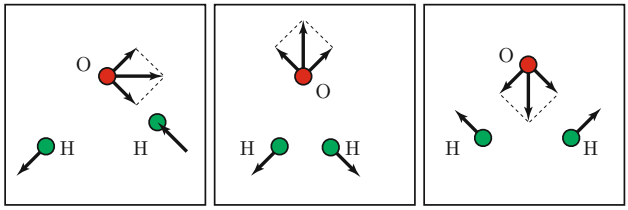

Fig. 2.1 Three modes of vibration of the water molecule; the *arrows* denote the forces acting on the atoms, as well as the corresponding relative displacements

The dipole describes the change of the spatial distribution of charges that is induced in the constituent matter by the electromagnetic field. Since the materials have more than one internal degree of freedom, they have different *modes* of changing the charge spatial distribution. As an example, Fig. 2.1 depicts three modes of deformation [3, 37, 38] of the water molecule.[5]

In general, the following mechanisms of charge pattern change are identified:

- change in the spatial arrangement of electrons (*deformation*),
- displacements between atoms (*vibration*),
- full *rotation* or partial rotation (*libration*) of charge systems,
- displacement of free ions or electrons (*conductivity*).

Equivalent charges, masses and forces involved in the electromagnetic field interactions change according to the mode, so that, given the models outlined in the following sections, the effect of each mechanism may prevail in a peculiar frequency range. Section 10.1.3 mentions that permittivity is typically affected by

- electronic modes at the highest frequencies (*ultraviolet, visible*) of interest in Earth observation,
- vibrational modes in an intermediate range (*infrared*),
- rotational modes at *relatively low* frequencies (*microwaves*),
- while at still lower frequencies, permittivity is essentially related to the free charge density.

More than one mode of interaction may occur simultaneously and, moreover, they can combine nonlinearly.

An elementary approach is followed in the following to interpret the dielectric behavior of terrestrial materials. Indeed, in spite of the microscopic nature of the field-matter interaction, classical-mechanics models are able to reproduce relevant dielectric features [10, 92], [67, Chap10] of many types of natural and man-made materials. In particular, three kinds of macroscopic mechanisms of dielectric polarization are separately considered here:

[5] Various web sites, e.g., [91, 97], show suggestive molecule animations.

- *deformation polarization*, which, although present in any material, characterizes non-polar non-conducting media in particular (for instance, rocks or dry soil);
- *orientation polarization*, that explains the behavior of polar media, especially water;
- *free-charge polarization*, that takes into account the effect of charges in conducting media such as moist soil or green vegetation.

2.1.1 Non-polar Non-conducting Materials

A non-polar non-conducting material is an aggregate of *bound* electric charges of opposite sign, the spatial distribution of which makes the "center" of positive charges to coincide with that of the negative ones *when no external electric field is applied* (Fig. 2.2a). An applied electric field exerts opposite forces on bound charges of opposite sign, thus inducing an overall displacement of positive charges with respect to the negative ones (Fig. 2.2b). The displacement results in a volumic electric dipole $\boldsymbol{\mathcal{P}}_\mathrm{d} = q_\mathrm{d}\,\ell_\mathrm{d}\,\boldsymbol{p}_{0\mathrm{d}}$ in the direction $\boldsymbol{p}_{0\mathrm{d}} = \mathfrak{e}_0$ of the field, assumed linearly polarized (Fig. 2.2c). The electric dipole $\boldsymbol{\mathcal{P}}_\mathrm{d}$ originated by deformation is computed from the displacement ℓ_d of the volumic *effective* charge q_d, according to a simple macroscopic dynamical model of the unit volume of material.

The charge q_d, with associated mass m_d, oscillates when subject to the alternating force exerted by a periodic electric field at angular frequency ω. The restoring force, which binds the charge about its equilibrium position, is assumed directly proportional to the displacement ℓ_d trough the restoring coefficient c_d, in the linear approximation. Energy is transferred from the field to the moving charges through the electrical force, the application point of which moves. In turn, the moving charges loose energy through random collisions with other particles forming the material. A *frictional* force, assumed directly proportional to velocity trough the kinetic friction coefficient s_d, takes account of the transfer of energy from the charges to the material, that is, of the heating process in this latter. Under the classical mechanics approach, the motion of q_d is determined by the dynamic equilibrium:

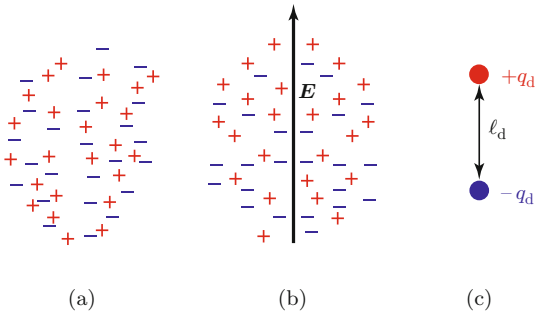

Fig. 2.2 Deformation polarization mechanism

$$F_\mathrm{i} + F_\mathrm{s} + F_\mathrm{r} = F_\mathrm{e}\ , \tag{2.8}$$

where the volumic forces in (2.8) are, respectively

$$F_\mathrm{i} = m_\mathrm{d}\ \left(\mathrm{d}^2\ell_\mathrm{d}\right) / \left(\mathrm{d}t^2\right) \qquad \text{the inertial force;} \tag{2.9}$$

$$F_\mathrm{s} = s_\mathrm{d}\ (\mathrm{d}\ell_\mathrm{d}) / (\mathrm{d}t) \qquad \text{the internal frictional force;} \tag{2.10}$$

$$F_\mathrm{r} = c_\mathrm{d}\,\ell_\mathrm{d} \qquad \text{the restoring force;} \tag{2.11}$$

$$F_\mathrm{e} = q_\mathrm{d}\,E_0\,\cos\omega t \qquad \text{the forcing by the electric field.} \tag{2.12}$$

The displacement $\ell_\mathrm{d}(t)$ is then obtained by the differential equation of motion

$$m_\mathrm{d}\frac{\mathrm{d}^2\ell_\mathrm{d}}{\mathrm{d}t^2} + s_\mathrm{d}\frac{\mathrm{d}\ell_\mathrm{d}}{\mathrm{d}t} + c_\mathrm{d}\,\ell_\mathrm{d} = q_\mathrm{d}\,E_0\,\cos\omega t\ , \tag{2.13}$$

which is readily transformed into an algebraic equation by the *phasor complex formalism* introduced in Sect. 1.3.1

$$\ell_\mathrm{d}(t) = \Re\left[\hat{\ell}_\mathrm{d}\,\mathrm{e}^{\mathrm{j}\omega t}\right]; \qquad E = \Re\left[\hat{E}\,\mathrm{e}^{\mathrm{j}\omega t}\right],$$

which yields

$$-\omega^2\hat{\ell}_\mathrm{d} + \mathrm{j}\omega\frac{s_\mathrm{d}}{m_\mathrm{d}}\hat{\ell}_\mathrm{d} + \frac{c_\mathrm{d}}{m_\mathrm{d}}\hat{\ell}_\mathrm{d} = \frac{q_\mathrm{d}}{m_\mathrm{d}}\hat{E}\ .$$

By defining

- the *damping coefficient* $\alpha_\mathrm{d} = \dfrac{s_\mathrm{d}}{2m_\mathrm{d}}$,
- the *resonant angular frequency* $\omega_0 = \sqrt{\dfrac{c_\mathrm{d}}{m_\mathrm{d}}}$,

the equation of motion becomes

$$\left(-\omega^2 + 2\mathrm{j}\omega\alpha_\mathrm{d} + {\omega_0}^2\right) q_\mathrm{d}\,\hat{\ell}_\mathrm{d} = \frac{q_\mathrm{d}^2}{m_\mathrm{d}}\,\hat{E}\ ,$$

and yields the phasor $\widehat{\mathcal{P}}_\mathrm{d} = q_\mathrm{d}\hat{\ell}_\mathrm{d}$ of the induced dipole:

$$\widehat{\mathcal{P}}_\mathrm{d} = \frac{q_\mathrm{d}^2}{m_\mathrm{d}}\ \frac{\hat{E}}{({\omega_0}^2 - \omega^2) + 2\mathrm{j}\alpha_\mathrm{d}\,\omega}\ . \tag{2.14}$$

Then the spectral susceptibility χ_d of the material due to the pure deformation mechanism, according to (2.7) and (2.14), is

$$\chi_{\mathrm{d}}(\omega) = \frac{\widehat{\mathcal{P}}_{\mathrm{d}}}{\epsilon_0 \hat{E}} = \frac{q_{\mathrm{d}}^2}{\epsilon_0 m_{\mathrm{d}}} \frac{\left(\omega_0^2 - \omega^2\right) - 2\mathrm{j}\alpha_{\mathrm{d}}\,\omega}{\left(\omega_0^2 - \omega^2\right)^2 + 4\alpha_{\mathrm{d}}^2\,\omega^2} = \chi_{\mathrm{dr}} + \mathrm{j}\chi_{\mathrm{dj}}\ . \tag{2.15}$$

It is important to note that susceptibility and, in turn, permittivity, are *complex* quantities, provided $\alpha_{\mathrm{d}} \neq 0$. Their real and imaginary parts depend on frequency according to the physical characteristics of the material, as taken into account by the parameters q_{d}, m_{d}, α_{d} and ω_0.

In analyzing the dependence of χ_{d} on ω, the following three characteristic frequency ranges are customarily singled out.

2.1.1.1 Low-Frequency Dielectric Behavior

At frequencies $\omega \ll \omega_0$, real and imaginary parts of χ_{d} are approximated by

$$\chi_{\mathrm{dr}} \simeq \frac{q_{\mathrm{d}}^2}{\epsilon_0 m_{\mathrm{d}} \omega_0^2}; \qquad -\chi_{\mathrm{dj}} \simeq \frac{q_{\mathrm{d}}^2}{\epsilon_0 m_{\mathrm{d}}} \frac{2\alpha_{\mathrm{d}}\,\omega}{\omega_0^4} \ll \chi_{\mathrm{dr}}\ , \tag{2.16}$$

because commonly encountered materials have $\alpha_{\mathrm{d}} < \omega_0$. The relatively low value of the imaginary part of the susceptibility means that at "low" frequencies, the charges in the matter follow without delay the "slowly" varying sinusoidal electric field, hence, $\mathcal{P}$ and, in turn, D, are in phase with E. Correspondingly, the permittivity of the material is (nearly) real and independent of frequency.

It should be pointed out that the "low-frequency" range is defined by $\omega \ll \omega_0$, therefore, it assumes the existence of a resonance. As shown in the following, resonances characterize the dielectric behavior of materials in which the deformation mechanism prevails, whereas resonant frequencies cannot be defined for other dielectric polarization mechanisms.

2.1.1.2 High-Frequency Dielectric Behavior

At frequencies $\omega \gg \omega_0$, (2.15) approximately yields

$$\chi_{\mathrm{dr}} \simeq -\frac{q_{\mathrm{d}}^2}{\epsilon_0 m_{\mathrm{d}} \omega^2}; \qquad -\chi_{\mathrm{dj}} \simeq \frac{q_{\mathrm{d}}^2}{\epsilon_0 m_{\mathrm{d}}} \frac{2\alpha_{\mathrm{d}}}{\omega^3} \ll |\chi_{\mathrm{dr}}|\ . \tag{2.17}$$

At "high" frequencies, the charges in the matter are not quite able to follow the rapidly varying sinusoidal electric field, given their inertia. The delay is such that $\mathcal{P}$ becomes opposite to E: the real part of the susceptibility is then negative and D is decreased compared with its low-frequency value. Permittivity is correspondingly lower and, given the relatively high value of ω, weakly dependent on frequency.

2.1.1.3 Dielectric Behavior About Resonance

When the frequency falls in the neighborhood of resonance, i.e., $\omega \simeq \omega_0$, a suitable approximation for (2.15) is

$$\chi_{\mathrm{dr}} + \mathrm{j}\chi_{\mathrm{dj}} \simeq \frac{q_{\mathrm{d}}^2}{2\epsilon_0 m_{\mathrm{d}} \omega_0} \left[\frac{\Delta\omega}{(\Delta\omega)^2 + \alpha_{\mathrm{d}}^2} - \mathrm{j} \frac{\alpha_{\mathrm{d}}}{(\Delta\omega)^2 + \alpha_{\mathrm{d}}^2} \right],$$

where $\Delta\omega = \omega_0 - \omega$ is the deviation from the resonant angular frequency. The features of χ are now quite different from those in the low- and high-frequency ranges. Real and imaginary parts of susceptibility are of the same order of magnitude, with peculiar trends with frequency: χ_{dr} sharply decreases through the resonance and changes sign, while $|\chi_{\mathrm{dj}}|$ has a bell-shaped functional form called *Lorentzian line shape*, with peak at ω_0 and line width[6] $\delta\omega = 2\,\alpha_{\mathrm{d}}$.

Note that χ_{dj} is always non-positive, since $\alpha_{\mathrm{d}} \geqslant 0$, irrespective of the frequency range. This property stems from the basic nature of friction in *passive* materials, where collisions *always* subtract energy from the moving charges.

Figure 2.3 reports the real ($\tilde{\epsilon}_{\mathrm{r}}$) and imaginary ($\tilde{\epsilon}_{\mathrm{j}}$) parts of relative permittivity $\tilde{\epsilon} = 1 + \chi$ as functions of frequency given by the Lorentzian model. At low frequencies,

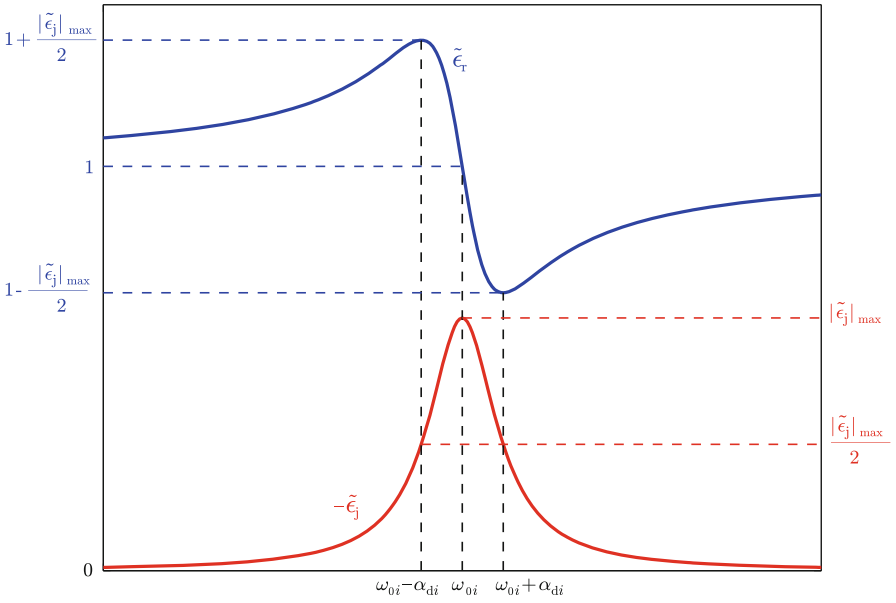

Fig. 2.3 Real (top) and imaginary parts of relative permittivity vs. angular frequency modeled by a single-resonance Lorentzian line shape (Diagram, courtesy G. Schiavon)

[6]The line width is commonly named **f**ull **w**idth at **h**alf **m**aximum (FWHM).

the permittivity is fairly independent of frequency, and practically real, given the quite low values of $\tilde{\epsilon}_j$, according to (2.16). Both real and imaginary parts increase with increasing frequency. When ω approaches the resonance value, $\tilde{\epsilon}_r$ reaches a maximum, then sharply decreases across ω_0, reaches a minimum, after which it keeps slowly increasing, consistently with (2.17). The imaginary part shows its bell-shape functional form (*Lorentzian line shape*), with the (negative) peak at ω_0 and values that tend to vanish as frequency further increases.

2.1.1.4 Permittivity of Composite Materials

As already observed for the water molecule, many pure materials change their spatial arrangement of charges according to different configurations, resulting in different permittivity patterns. In particular, resonances occur at different frequencies, since involved charges, masses, frictional and restoring forces differ according to the deformation mode. The dependence of susceptibility on frequency results from the superposition of the single modes. On the other side, apart from pure water, materials composed by single types of molecule are rarely found in the terrestrial environment, rather, media are composite, formed by different constituents, each with its own modes of deformation. The deformation susceptibility of a composite material results from the possibly nonlinear superposition of the effects of the ensemble of modes of deformation of the individual species. Therefore, a number of resonances are exhibited by materials, generally related to their complexity and microscopic structure.

The essential features of the real and imaginary parts of permittivity actually observed experimentally for a wide range of materials are satisfactorily described by the classical-mechanics macroscopic model discussed previously, as suggested by the example shown in Fig. 2.4. However, the determination of the values of the parameters do require a microscopic approach. The resonance frequencies and the corresponding values of permittivity (*line intensities and widths*) are actually related to *transitions* between both vibrational and electronic *energy levels*. A mixture of macroscopic approach and quantum (microscopic) results is generally suitable to quantitatively describe the dielectric behavior of terrestrial materials.

2.1.2 Polar Materials

Charges in some materials are organized in microscopic domains possessing permanent electric dipoles. Liquid water is a material with polar molecules (Fig. 2.5) [57, Ch. 9] of crucial importance to Earth, hence of utmost interest to EO.[7]

[7] Details on water, complemented by animations, can be found at websites such as [17, 86, 96].

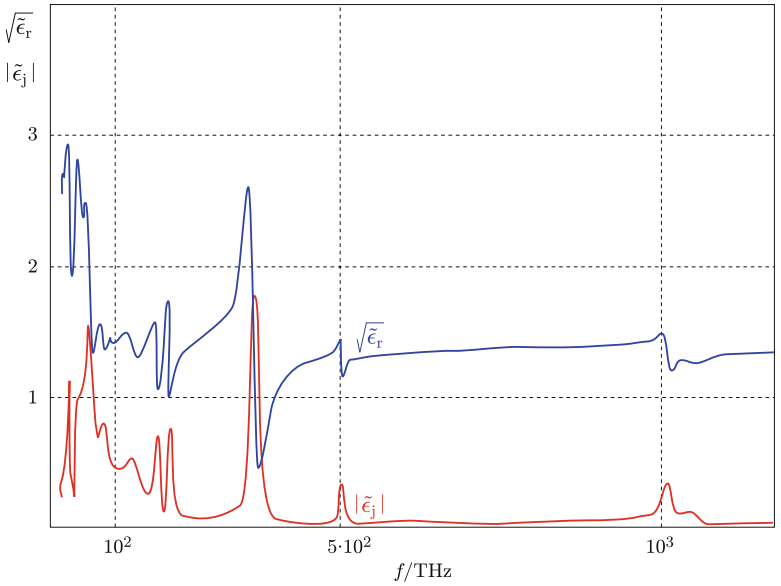

Fig. 2.4 Trend of $\sqrt{\tilde{\epsilon}_r}$ and $|\tilde{\epsilon}_j|$ of gypsum vs. frequency f, showing several resonances (Curves interpolate data from [4])

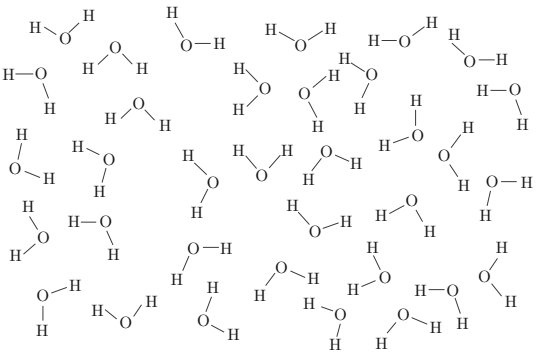

Fig. 2.5 Sketch of the polar H_2O molecules assembly in water: given the hydrogen bonding, the dipoles associated with the molecules tend to organize in microdomains [46]

With no electric field applied, the dipoles tend to orient randomly and no net dipole moment is present. An applied electric field forces the elementary permanent dipoles towards its direction, thus inducing a dipole moment $\boldsymbol{\mathcal{P}}_o$ in the unit volume of material. This mechanism gives rise to the dielectric *orientation polarization* The orientation of permanent dipoles superimposes to the charge displacement which gives rise to the deformation polarization and which is almost always present. Assuming deformation and orientation independent from each other,

$$\boldsymbol{\mathcal{P}}(t) = \boldsymbol{\mathcal{P}}_d(t) + \boldsymbol{\mathcal{P}}_o(t) \ ,$$

where $\boldsymbol{\mathcal{P}}_{\mathrm{d}}$, given by (2.14), accounts for the deformation of the charge structure and $\boldsymbol{\mathcal{P}}_{\mathrm{o}}$ for the orientation of individual permanent dipoles.

By the classical-mechanics equilibrium of torques per unit volume of material,

$$\mathcal{M}_{\mathrm{s}} + \mathcal{M}_{\mathrm{c}} = \mathcal{M}(E) \ . \tag{2.18}$$

In Eq. (2.18):

- $\mathcal{M}(E)$ is the forcing torque,
- $\mathcal{M}_{\mathrm{s}}$ is the damping torque due to "viscosity", which takes account of the energy that the interaction with the surrounding charge environment subtracts from the rotating dipole,
- $\mathcal{M}_{\mathrm{c}}$ is the torque accounting for the collisions which tend to disorganize the orientation of individual dipoles and that, depending on thermal agitation, is a function of temperature.

The terms at the first member of (2.18), which result from microscopic interactions, crucially depend on the state of aggregation of the material. Air is a *sparse* environment, such that the water vapor molecules suffer from little interaction with their surroundings, hence are put in relatively free rotation by the alternating electric field. Instead, the molecules in a *condensed* material such as liquid water, are not free to rotate because of the strong interaction with the dense charge environment. They are able to follow the alternating field when frequency is sufficiently low, but their rotation becomes only partial with increasing frequency. The incomplete rotation of the H-O-H water molecule chains in the field of force of the surrounding dipoles with consequent interaction with the bulk material is named *libration* [68].

To model libration, the torques $\mathcal{M}_{\mathrm{c}}$ and $\mathcal{M}_{\mathrm{s}}$ are assumed simply proportional to the dipole and to its angular velocity, respectively, and the forcing torque to the acting field:

$$\mathcal{M}_{\mathrm{c}} = c_{\mathrm{r}}\,\mathcal{P}_{\mathrm{o}}; \qquad \mathcal{M}_{\mathrm{s}} = s_{\mathrm{o}}\frac{\mathrm{d}\mathcal{P}_{\mathrm{o}}}{\mathrm{d}t}; \qquad \mathcal{M}(E) = c_{\mathrm{o}}\,E(t) \ .$$

Within these assumptions, (2.18) puts the orientation dipole $\mathcal{P}_{\mathrm{o}}$ into linear relation with the electric field

$$s_{\mathrm{o}}\frac{\mathrm{d}\mathcal{P}_{\mathrm{o}}}{\mathrm{d}t} + c_{\mathrm{r}}\mathcal{P}_{\mathrm{o}} = c_{\mathrm{o}}E(t) \ ,$$

or, in the spectral domain,

$$\mathrm{j}\omega s_{\mathrm{o}}\widehat{\mathcal{P}}_{\mathrm{o}} + c_{\mathrm{r}}\widehat{\mathcal{P}}_{\mathrm{o}} = c_{\mathrm{o}}\hat{E} \ .$$

whence

$$\widehat{\mathcal{P}}_{\mathrm{o}} = \frac{c_{\mathrm{o}}\,\hat{E}}{c_{\mathrm{r}} + \mathrm{j}\,\omega s_{\mathrm{o}}} \ .$$

Then, the susceptibility χ_o contributed by the *librational* orientation of permanent dipoles, according to (2.7) is

$$\chi_o(\omega) = \frac{c_o/c_r}{\epsilon_0\left(1 + j\,\omega\frac{s_o}{c_r}\right)} = \frac{\chi^0}{1 + j\,\omega\,\tau_r}\,,$$

where χ^0 is the static (i.e., for $\omega \to 0$) susceptibility, while τ_r is the *dielectric relaxation time* of the material [23, 24, 39]. In fact, if E is turned off, the equation of motion yields a volumic oriented electric dipole decaying with time t according to

$$\mathcal{P}_o(t) = \mathcal{P}_o(0)\,e^{-(t/\tau_r)}\,.$$

The relaxation time τ_r clearly decreases with increasing temperature, since the thermal agitation speeds up the disorganization process.

As for the deformation, also the susceptibility resulting from the orientation mechanism of dielectric polarization is complex

$$\chi_o = \frac{\chi^0}{1 + (\omega\,\tau_r)^2}(1 - j\,\omega\tau_r) = \chi_{or} + j\chi_{oj}\,. \tag{2.19}$$

The real part of the susceptibility contributed by the libration of permanent dipoles decreases monotonically with frequency. Again, the imaginary part is always non-positive for *passive* materials and peaks at the *relaxation angular frequency* $\omega_r = 1/\tau_r$, about which the real part decreases sharply (Fig. 2.6). It is important to note that both the real and the imaginary parts tend to vanish for angular frequencies much larger than the relaxation frequency. The absence of resonance is also observed.

By superposing deformation and orientation polarizations, the susceptibility χ_{do} of dielectric (non-conducting) materials is obtained from (2.15) and (2.19) as

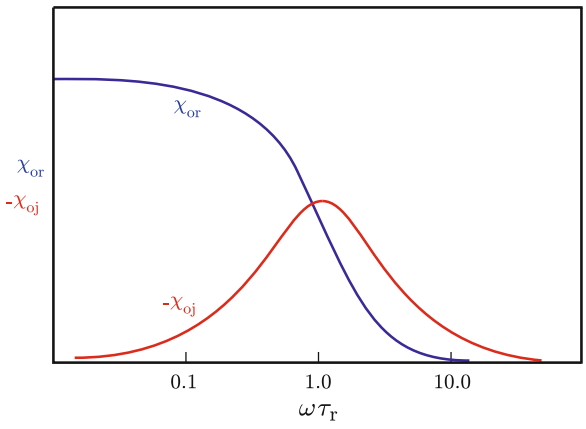

Fig. 2.6 Trends of the real (χ_{or}) and imaginary (χ_{oj}) parts of susceptibility of a polar material due to the librational mechanism vs. normalized angular frequency $\omega\tau_r$

$$\chi_{do} := \chi_d + \chi_o = \chi_{dr} + \chi_{or} + j(\chi_{dj} + \chi_{oj}) \equiv \chi_{dor} + j\chi_{doj} \ . \tag{2.20}$$

As for the deformation polarization, the orientation dielectric behavior of composite materials derives from the superposition of the possibly interacting behavior of the various constituents. Polar materials may show more than one relaxation time, analogously to the various resonances exhibited by the deformation mechanism. Water, which is the polar material of main practical interest in Earth observation, has the two leading relaxation frequencies discussed in Sect. 2.2.2.1.

2.1.3 Conducting Materials

Conducting materials have a volumic charge q_c free to move under the action of the electric field. The dielectric dipole created by the separation of the positive from the negative charges[8] induced by the field is obtained by the same equation of motion (2.13) considered for the bound charges, by setting the restoring force to zero, since the charges can move freely, and with the parameters appropriate to the charges in the conduction band

$$m_c \frac{d^2\ell}{dt^2} + s_c \frac{d\ell}{dt} = q_c E_0 \, cos\omega t \ . \tag{2.21}$$

Passing to the frequency domain,

$$-\omega^2 \hat{\ell} + j\omega \frac{s_c}{m_c} \hat{\ell} = \frac{q_c}{m_c} \hat{E} \ ,$$

or

$$\left(-\omega^2 + 2j\omega\alpha_c\right) q_c \, \hat{\ell} = \frac{q_c^2}{m_c} \hat{E} \ , \tag{2.22}$$

having defined the appropriate damping coefficient $\alpha_c = s_c/(2m_c)$. Since no restoring force acts on the free charges, obviously $\omega_0 = 0$. Equation (2.22) yields the susceptibility χ_c contributed by the free charges:

$$\chi_c = -\frac{q_c^2}{\epsilon_0 m_c} \frac{1}{\omega^2 + 4\alpha_c^2} - j\frac{q_c^2}{\epsilon_0 m_c} \frac{2\alpha_c}{\omega(\omega^2 + 4\alpha_c^2)} = \chi_{cr} + j\chi_{cj} \ . \tag{2.23}$$

Once again, the imaginary part χ_{cj} is non-positive. The susceptibility contributed by the free charge increases monotonically with decreasing frequency and, in particular, $\chi_{cj} \to \infty$ for $\omega \to 0$, since the model implicitly assumes an ideally unlimited amount of charge which is free to move in an infinite time.

[8] The origin of the dipole is clearly the same as in Sect. 2.1.1, excepted that now the charges are not bound to their zero-field equilibrium position.

2.1.3.1 Conductivity

Mainly for historical reasons, in a low-frequency/circuital approach, the effect of the free charges is sometimes taken into account by the *conductivity* of the material.

If velocity $u_c = (\mathrm{d}\ell)/(\mathrm{d}t)$ of the volumic charge is regarded as the unknown instead of displacement ℓ, the equation of motion (2.21) is written as

$$m_c \frac{\mathrm{d}u_c}{\mathrm{d}t} + s_c u_c = q_c E_0 \cos \omega t \,, \tag{2.24}$$

so that, multiplying by q_c,

$$m_c q_c \frac{\mathrm{d}u_c}{\mathrm{d}t} + s_c\, q_c u_c = q_c^2 E_0 \cos \omega t \,,$$

which relates the conduction current density $J = q_c u_c$ to the acting field E. In the spectral domain the equation is written

$$\mathrm{j}\omega m_c \hat{J} + 2\alpha_c m_c \hat{J} = q_c^2 \hat{E} \,,$$

whence

$$\hat{J} = \frac{q_c^2}{m_c(2\alpha_c + \mathrm{j}\omega)} \hat{E} \,.$$

Then the spectral conductivity is derived from the definition of g given in Sect. 1.1.2:

$$g(\omega) = \frac{q_c^2}{m_c(2\alpha_c + \mathrm{j}\omega)} = \frac{q_c^2}{m_c} \frac{2\alpha_c}{4\alpha_c^2 + \omega^2} - \mathrm{j}\frac{q_c^2}{m_c} \frac{\omega}{4\alpha_c^2 + \omega^2} \,. \tag{2.25}$$

At "low" frequency, that now means for $\omega \ll \alpha_c$,

$$g(\omega) \simeq \frac{q_c^2}{m_c} \frac{1}{2\alpha_c} - \mathrm{j}\frac{q_c^2}{m_c} \frac{\omega}{4\alpha_c^2} \,.$$

Given the quite high values of α_c of common *condensed* terrestrial materials, $|\Im[g]| \ll \Re[g]$, up to the microwave range, at least.

2.1.3.2 Permittivity vs. Conductivity

Since both susceptibility and conductivity are derived from the same model, either described by (2.21) or by (2.24), χ_c is expected to be tightly related to g. Comparing (2.23) with (2.25),

$$\chi_{cj} = -\frac{\Re[g]}{\omega} \,, \tag{2.26}$$

which shows that imaginary part of susceptibility and real part of conductivity are directly proportional. Indeed, imaginary part of susceptibility and real part of conductivity represent the same process of damping the motion of the charges through collisions, irrespective of their state, bound or free.

At radio frequencies, since the conductivity of condensed matter is almost real,

$$\chi_{\mathrm{cj}} \simeq -\frac{g}{\omega} \,. \tag{2.27}$$

In some fields of application it is still customary to provide the conductivity g of lossy materials. Then the imaginary part of permittivity is clearly obtained by (2.27) and definition (2.5). On the other hand, an *effective conductivity* g_{e} can be defined to account for the total electromagnetic dissipation even when the lossy material does not conduct[9]:

$$g_{\mathrm{e}} = -\omega \, \chi_{\mathrm{cj}} \,.$$

Conductivity is seldom considered at frequencies above the microwave range.

2.1.4 Complex Permittivity and Power Budget

The procedure followed in Sect. 1.2 to arrive at the power budget of an electromagnetic field varying with time in any way, can be applied to the representative complex field described by the spectral Maxwell's equations (2.1), (2.2), (2.3) and (2.4). By straightforward manipulation of Eqs. (2.1) and (2.2) and integration over an arbitrary volume V contoured by surface S, the *spectral Poynting's theorem* is obtained:

$$\begin{aligned} &\iiint_V \left(-\frac{\boldsymbol{J}_{\mathrm{s}}^* \cdot \boldsymbol{E}_{\mathrm{s}}}{2} - \frac{\boldsymbol{J}_{\mathrm{ms}} \cdot \boldsymbol{H}_{\mathrm{s}}^*}{2} \right) \mathrm{d}V \\ &= \iiint_V g \frac{\boldsymbol{E} \cdot \boldsymbol{E}^*}{2} \, \mathrm{d}V + \mathrm{j}\omega \iiint_V \left(\mu \frac{\boldsymbol{H} \cdot \boldsymbol{H}^*}{2} - \epsilon^* \frac{\boldsymbol{E} \cdot \boldsymbol{E}^*}{2} \right) \mathrm{d}V \\ &\quad + \frac{1}{2} \oiint_S (\boldsymbol{E} \times \boldsymbol{H}^*) \cdot \mathbf{n}_0 \, \mathrm{d}S \,. \end{aligned} \tag{2.28}$$

Following the steps of Sects. 1.2.1, 1.2.2, 1.2.3 and 1.2.4 allows understanding the meaning of the various terms in (2.28) and provides insight into the role of the complex permittivity.

[9] A reference material of this kind is de-ionized water.

2.1.4.1 Complex Source Term

If, without loss of generality, $\boldsymbol{J}_{\mathrm{ms}} = 0$ and $\boldsymbol{J}_{\mathrm{s}}$ and $\boldsymbol{E}_{\mathrm{s}}$ are assumed linearly polarized and parallel, that is,

$$\boldsymbol{J}_{\mathrm{s}} = -\mathrm{j}J_{\mathrm{s}}\,\mathbf{j}_0; \qquad \boldsymbol{E}_{\mathrm{s}} = -\mathrm{j}E_{\mathrm{s}}\,\mathrm{e}^{\mathrm{j}\Phi_{\mathrm{Es}}}\,\boldsymbol{\epsilon}_0, \qquad \mathbf{j}_0 \equiv \boldsymbol{\epsilon}_0\ ,$$

the volumic power associated with the source becomes

$$-\frac{\boldsymbol{J}_{\mathrm{s}}^{*}\cdot\boldsymbol{E}_{\mathrm{s}}}{2} = -\frac{J_{\mathrm{s}}E_{\mathrm{s}}}{2}\cos\Phi_{\mathrm{Es}} - \mathrm{j}\frac{J_0E_0}{2}\sin\Phi_{\mathrm{Es}}\ . \tag{2.29}$$

It is readily realized that the real part of (2.29) coincides with the time average of the power that the unit volume of the source irreversibly delivers to the field, determined in Sect. 1.2.5.1.

2.1.4.2 Term with Conductivity

The term containing the conductivity

$$\iiint_V g\frac{\boldsymbol{E}\cdot\boldsymbol{E}^{*}}{2}\,\mathrm{d}V\ , \tag{2.30}$$

at the frequencies at which the conductivity retains its meaning, is a real quantity which coincides with the time-average electromagnetic power dissipated (i.e., converted into heat) by the conduction mechanisms within the materials contained by the considered volume V. The dissipated power was determined in Sect. 1.2.5.2.

2.1.4.3 Term with Permittivity

Differently from the previous ones, the term

$$\mathrm{j}\omega\iiint_V\left(\mu\frac{\boldsymbol{H}\cdot\boldsymbol{H}^{*}}{2} - \epsilon^{*}\frac{\boldsymbol{E}\cdot\boldsymbol{E}^{*}}{2}\right)\mathrm{d}V\ , \tag{2.31}$$

formally corresponding to the stored energy discussed in Sect. 1.2.3, now acquires a substantially different meaning. According to (2.20), the permittivity contributed by the deformation and orientation mechanisms[10] is written

$$\epsilon = \epsilon_0(1+\chi_{\mathrm{do}}) = \epsilon_0\,\tilde{\epsilon}_{\mathrm{do}} = \epsilon_0(\tilde{\epsilon}_{\mathrm{dor}} + \mathrm{j}\tilde{\epsilon}_{\mathrm{doj}})\ .$$

[10]The spectral permittivity ϵ in (2.31) derives from the deformation and orientation contributions only, since the effect of the free charges is already taken into account by g.

The electric term in (2.31) becomes

$$-\epsilon^* \frac{\boldsymbol{E}\cdot\boldsymbol{E}^*}{2} = \frac{1}{2}\left[-\epsilon_0(\tilde{\epsilon}_{\mathrm{dor}} - \mathrm{j}\tilde{\epsilon}_{\mathrm{doj}})\,\boldsymbol{E}\cdot\boldsymbol{E}^*\right]$$
$$= \frac{1}{2}(-\epsilon_0\,\tilde{\epsilon}_{\mathrm{dor}}\,\boldsymbol{E}\cdot\boldsymbol{E}^*) + \frac{j}{2}(\epsilon_0\,\tilde{\epsilon}_{\mathrm{doj}}\,\boldsymbol{E}\cdot\boldsymbol{E}^*)\,.$$

Since $\tilde{\epsilon}_{\mathrm{doj}} \le 0$ and $\mu = \mu_0$, the real part of the electric term of (2.31)

$$\Re\left[\mathrm{j}\omega \iiint_V -\epsilon^* \frac{\boldsymbol{E}\cdot\boldsymbol{E}^*}{2}\,\mathrm{d}V\right] = \frac{1}{2}\,\omega \iiint_V \epsilon_0|\tilde{\epsilon}_{\mathrm{doj}}|\,\boldsymbol{E}\cdot\boldsymbol{E}^*\,\mathrm{d}V$$

is non-negative and adds to the power dissipated by the free charges expressed by (2.30). It represents the time-average power dissipated by the lossy deformation and orientation polarization mechanisms. Therefore, the total time-average power $\overline{W}_{\mathrm{d}}$ dissipated in the lossy volume V is

$$\overline{W}_{\mathrm{d}} = \iiint_V g\frac{\boldsymbol{E}\cdot\boldsymbol{E}^*}{2}\,\mathrm{d}V + \frac{\omega}{2}\iiint_V \epsilon_0|\tilde{\epsilon}_{\mathrm{doj}}|\,\boldsymbol{E}\cdot\boldsymbol{E}^*\,\mathrm{d}V$$
$$= \frac{\omega\,\epsilon_0}{2}\iiint_V \left(\frac{g}{\omega\epsilon_0} + |\tilde{\epsilon}_{\mathrm{doj}}|\right)\boldsymbol{E}\cdot\boldsymbol{E}^*\,\mathrm{d}V = \frac{\omega\,\epsilon_0}{2}\iiint_V \tilde{\epsilon}_{\mathrm{j}}\,\boldsymbol{E}\cdot\boldsymbol{E}^*\,\mathrm{d}V\,. \quad (2.32)$$

The imaginary part $\tilde{\epsilon}_{\mathrm{j}}$ of relative permittivity in (2.32) takes account globally of the losses caused by both dielectric polarization (deformation and orientation) and conduction. Indeed, distinguishing between dissipation by free and bound charges may be meaningless, since the basic mechanism is the same.

In the following, when not mentioned, conductivity is included into permittivity. The crucial role of $\tilde{\epsilon}_{\mathrm{j}}$ in determining the decay of the electromagnetic field with distance, which is an essential issue in Earth observation, is discussed in Sect. 4.1.2.

2.1.4.4 The Radiation Term

The meaning of the complex surface integral is now clear: the real part of the flux is the time-average power that leaves the volume V in which the source is located, flowing through the contouring surface S. The vector

$$\boldsymbol{\mathcal{P}} = \mathcal{P}\,\mathfrak{p}_0 = \frac{\boldsymbol{E}\times\boldsymbol{H}^*}{2} \quad (2.33)$$

is named *complex Poynting vector*: it measures the areic power associated with the electromagnetic field. Its real part yields the power that crosses the unit area of a surface perpendicular[11] to $\mathfrak{p}_0$.

[11] The unit vector $\mathfrak{p}_0$ is assumed real, for simplicity.

In summary, the power supplied by the source is in part dissipated by the lossy conduction *and* polarization mechanisms in the materials, which are correspondingly characterized by a complex permittivity. The remaining part flows through any surface surrounding the source, giving rise to the *radiated power*. Lossless materials have ϵ real, which clearly implies $g = 0$, provided this parameter needs consideration.

2.2 Permittivity of Relevant Terrestrial Materials

The materials in the terrestrial environment generally present all the three polarization mechanisms discussed in Sect. 2.1. The total electric dipole, on the assumption of independent isotropic processes of dielectric polarization, is

$$\mathcal{P} = \mathcal{P}_\mathrm{d} + \mathcal{P}_\mathrm{o} + \mathcal{P}_\mathrm{c} \ ,$$

with corresponding total complex susceptibility

$$\chi = \chi_\mathrm{d} + \chi_\mathrm{o} + \chi_\mathrm{c} \ .$$

In turn, the spectral permittivity (2.7)

$$\epsilon(\omega) = \epsilon_\mathrm{r}(\omega) + \mathrm{j}\epsilon_\mathrm{j}(\omega) = \epsilon_0[\tilde{\epsilon}_\mathrm{r}(\omega) + \mathrm{j}\tilde{\epsilon}_\mathrm{j}(\omega)]$$

derives from the contributions by the different mechanisms, each of them with the peculiar frequency trend previously considered [90]. It should be kept in mind that passive terrestrial materials have $\epsilon_\mathrm{j} \leqslant 0$.

2.2.1 The Atmosphere

The atmosphere is of utmost importance in Earth observation, since

- it is a quite relevant observable component of the Earth's environment, directly interacting with the anthropogenic activity;
- even when it is not direct subject of observation, it has to be taken into account because it is always crossed by the electromagnetic waves in sensing surface-based targets from elevated platforms.

The atmosphere essentially consists of nitrogen (78.1 %) and oxygen (20.9 %), a small amount of water vapor and minor quantities of other gases, among which carbon dioxide, methane, and ozone. Because of the low polarizability of nitrogen, the permittivity of the air mainly results from the dielectric polarization of the other molecular species, of which the water vapor, being polar, is particularly active.

Real and imaginary parts of the permittivity are expressed as the superposition of the contributions by the N_{H_2O} individual interaction modes of single H_2O molecules and the N_{O_2} modes of O_2 molecules, plus additional contributions [55, 60]:

$$\tilde{\epsilon}_r(\omega) = 1 + \chi_r(\omega) \simeq 1 + \sum_{i=1}^{N_{H_2O}} \left[\mathscr{S}\mathscr{F}'(\omega)\right]_i + \sum_{i=1}^{N_{O_2}} \left[\mathscr{S}\mathscr{F}'(\omega)\right]_i + \chi_{rg}(\omega) + \chi_{rc} \; ; \tag{2.34}$$

$$\tilde{\epsilon}_j(\omega) \equiv \chi_j(\omega) \simeq \sum_{i=1}^{N_{H_2O}} \left[\mathscr{S}\mathscr{F}''(\omega)\right]_i + \sum_{i=1}^{N_{O_2}} \left[\mathscr{S}\mathscr{F}''(\omega)\right]_i + \chi_{jg}(\omega) + \chi_{jc} \; . \tag{2.35}$$

The ith term $[\mathscr{S}\mathscr{F}(\omega)]_i$ is the product of the *line intensity* $\mathscr{S}_i$ peculiar of the molecule, times the normalized *line shapes* [89] $\mathscr{F}_i'(\omega)$ and $\mathscr{F}_i''(\omega)$, relative to χ_r and χ_j respectively. The line intensities and shapes are relative to the interaction modes dominant in the non-ionized atmosphere, i.e., deformation (*electronic* and *vibrational*) and full orientation (*rotational*), as well as their combinations. The additional terms χ_{rg} and χ_{jg}, having the same structure as the other terms in (2.34) and (2.35) are needed to account for the contributions by other constituents and trace gases, including O_3, CO_2, CH_4, CO, N_2O. Given the relatively low density of these molecules, the effect on $\tilde{\epsilon}_r$ is small. However, in spite of the low density, the resonances can lead to non-negligible peak values of $\tilde{\epsilon}_j$ mainly at infrared frequencies,[12] as discussed later in Sect. 10.1.2.1. Finally, the last terms χ_{rc} and χ_{jc} are needed to include possible further contributions weakly dependent on frequency, which form the *continuum* in the microwave [75] and infrared [20, 74] bands.[13]

2.2.1.1 Microwave Permittivity of Air

At microwaves, the main interactive gases are oxygen and, especially, water vapor, which determine the dominant trend with frequency of the real and imaginary parts of the air permittivity [11, 50, 64].

Figure 2.7 shows the trends of $\tilde{\epsilon}_r$ and $|\tilde{\epsilon}_j|$ with frequency up to the millimeter-wave range, of the *reference atmosphere*, assumed at pressure $p_t = 1013$ hPa (sea-level), temperature $T = 20\,°C$, relative humidity $RH = 70\,\%$.

The frequency patterns of $\tilde{\epsilon}_r$ and $|\tilde{\epsilon}_j|$ are determined by

- oxygen, which has a set of resonant lines resulting in the peak of $|\epsilon_j|$ around $f_{01}^{O_2} = 61.2$ GHz, and a line at $f_{02}^{O_2} \approx 118.8$ GHz;
- water vapor, with lines at $f_{01}^{H_2O} \approx 22.2$ GHz and $f_{02}^{H_2O} \approx 183.3$ GHz.

[12] In the "optical" spectral range, wavelength λ_0 (Sect. 3.1.1.2) is used rather than frequency f.

[13] The denomination of the spectral bands is reported in Sect. 10.1.1.

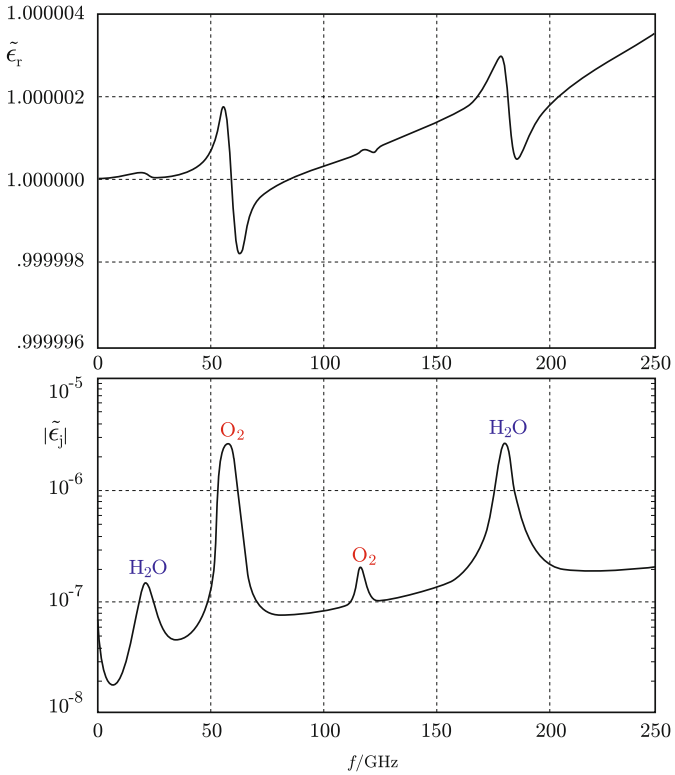

Fig. 2.7 Real ($\tilde{\epsilon}_r$) and imaginary ($\tilde{\epsilon}_j$) parts of relative permittivity of air at standard conditions modeled [52] as a function of microwave frequency f (Diagram, courtesy G. Schiavon)

The diagrams show that the Lorentzian line shapes of the single molecular species are superimposed to the pedestal (the continuum) which increases smoothly with frequency. The continuously raising trend is attributed to the far wings of broadened resonant lines at higher frequencies [51], as well as to clusters of two (dimers) or more water vapor molecules in the air [1, 79, 87, 101].

At the frequencies $f \lesssim 40$ GHz at which more common passive microwave sensors (Sect. 11.4.2.1) and **S**ynthetic **A**perture **R**adar (SAR) systems (Sect. 11.4.3.4) operate for observing the Earth, $|\chi_j| \ll \chi_r$, so that ϵ is assumed real. Moreover, the dependence on frequency is generally neglected up to the beginning of the 60-GHz oxygen resonance band. A customary way of deriving the air relative microwave permittivity from the measurable meteorological parameters is given by[14]

[14]The frequency-independent coefficients in (2.36) yield fairly accurate estimates of $\tilde{\epsilon}$ for frequencies $f < 40$ GHz. Note that slightly different values of the coefficients are found in literature, as, for instance, in [77].

$$\tilde{\epsilon} = 1 + \delta\tilde{\epsilon}_{\text{dry}} + \delta\tilde{\epsilon}_{\text{w}} \simeq 1 + 1.55 \cdot 10^{-4} \frac{p_{\text{t}}}{T} + 0.75 \frac{p_{\text{w}}}{T^2} \cdot \tag{2.36}$$

Expression (2.36) contains two contributions to the relative permittivity:

- the *dry* term $\delta\tilde{\epsilon}_{\text{dry}}$, in which the total atmospheric pressure p_{t} accounts for the total amount of all polarizable molecules;
- the *wet* term $\delta\tilde{\epsilon}_{\text{w}}$, specifically accounting for the density of the highly polarizable water molecules through the water vapor partial pressure p_{w}.

Equation (2.36) indicates that, for given pressures p_{t} and p_{w}, the permittivity decreases with T, because increasing temperature enhances thermal agitation that hinders the action of the field in inducing oriented dipoles. However, it should be considered that p_{w}, hence the water vapor density in the air, increases considerably with temperature [7], so that an overall growth of $\tilde{\epsilon}$ with T actually occurs. As an example, the dry term at the reference sea level pressure $p_{\text{t}} = 1000\,\text{hPa}$, varies between $\delta\tilde{\epsilon}_{\text{dry}} = 5.29 \cdot 10^{-4}$ (for $T = 20\,^{\circ}\text{C}$) and $\delta\tilde{\epsilon}_{\text{dry}} = 5.68 \cdot 10^{-4}$ (at $T = 0\,^{\circ}\text{C}$). In spite of the low density of water vapor (its partial pressure is of the order of a few tens of hPa), given the high polarizability of water molecules, the wet term varies between $\delta\tilde{\epsilon}_{\text{w}} = 6.2 \cdot 10^{-5}$ (at $T = 0\,^{\circ}\text{C}$) and $\delta\tilde{\epsilon}_{\text{w}} = 2.04 \cdot 10^{-4}$ (for $T = 20\,^{\circ}\text{C}$) in saturation conditions. In summary, the dry term is higher, but more stable, whereas the wet term has lower values but with high variations, given the considerable dependence of vapor density on temperature and on the type of air mass. The detrimental effect of the wet term in SAR interferometric observations is discussed in Sect. 12.3.2.1.

It is worth to point out that both $\tilde{\epsilon}_{\text{r}}$ and $|\tilde{\epsilon}_{\text{j}}|$ decrease with altitude, following the variation with height of p_{t} and p_{w}. In fact, the decreasing air density lowers the number of molecules per unit volume, hence the volumic charge q on which the line intensities depend. The height-decreasing pressure also changes the overall shape of the imaginary part of air permittivity in the neighborhood of the 60-GHz oxygen resonant complex [54]. Indeed, pressure broadening has the effect of merging single lines into a relatively smooth function of frequency, which characterizes $|\tilde{\epsilon}_{\text{j}}|$ at low altitudes. As pressure decreases with altitude, the individual lines tend to separate, as suggested by Fig. 10.9. This effect holds in general.

2.2.1.2 Optical Permittivity of Air

The diagrams in Fig. 2.7 indicate that real and imaginary parts of the air permittivity keep a generally increasing trend with increasing frequency beyond the microwave range. The growing trend is caused by the superposition of numerous resonant lines of atmospheric constituents located at higher frequencies. The high number of resonances of the atmospheric gases has the general effect of increasing the imaginary part of air permittivity especially in the infrared, as stressed in Sect. 10.1.2. In particular, the water molecule keeps contributing strongly to the air susceptibility, given the large number of resonances corresponding to rotational and roto-vibrational transitions that fall in the sub-mm wave band and in the infrared [5].

As frequency further increases towards the optical range, i.e., *near* infrared and visible, the resonances of atmospheric constituents rarefy and decrease in intensity, so that at the frequencies corresponding to visible wavelengths the air susceptibility is again approximately real. Modeling of permittivity in the visible and near infrared spectral range takes account of the main air constituents and water vapor, as well as of carbon dioxide [19]. Approximate values of $\tilde{\epsilon}$ are given in terms of measurable meteorological parameters by the simple expression

$$\tilde{\epsilon} \simeq 1 + \chi_s(f) \frac{C_1 p_t}{1 + C_2 T} , \tag{2.37}$$

where χ_s is the susceptibility of air at reference composition, pressure and temperature, and C_1 and C_2 are constants.[15] Numerical values of the optical permittivity of the air fairly close to those at microwaves are commonly encountered. The reference susceptibility $\chi_s(f)$ in (2.37) introduces a weak dependence of $\tilde{\epsilon}$ on frequency, so that, as general features, the air permittivity in the optical range:

– slightly increases with increasing frequency;
– decreases with increasing temperature.

It can be observed that the water vapor contribution, which is strong at microwaves, is quenched in the optical frequency range. Rather, $\tilde{\epsilon}$ slightly decreases with increasing partial pressure of water vapor,[16] the molecules of which take the place of the more polarizable oxygen molecules in the unit volume of air at a given pressure p_t.

Finally, at the high frequency end, that is, in the ultraviolet of interest to Earth observation, real and imaginary parts of the air susceptibility keep increasing with increasing frequency, given the approaching *electronic resonances*.

It is worth mentioning that an additional analysis of the fine effects of the atmospheric constituents and of the physical parameters of air is needed when enhanced accuracy of the optical permittivity estimations is required by particular applications, such as precise measurement of distance, for which the results yielded by (2.37), as after all by (2.36), are not adequate [78].

2.2.2 Water and Ice

Water exists on Earth in its three states, all of them playing a major environmental role. The dielectric features of vapor, of crucial relevance for the atmosphere, have been summarized in the preceding section. The main dielectric aspects of the liquid and solid phases are discussed in the following.

[15]The accuracy of (2.37) is subject to the condition that the air conditions are not far from the standard ones, i.e., dry air at $T = 15°$ C, $p_t = 1013$ hPa, with 0.045 % volume fraction of CO_2.

[16]Equation (2.37) clearly needs modification to account for the effect of water vapor.

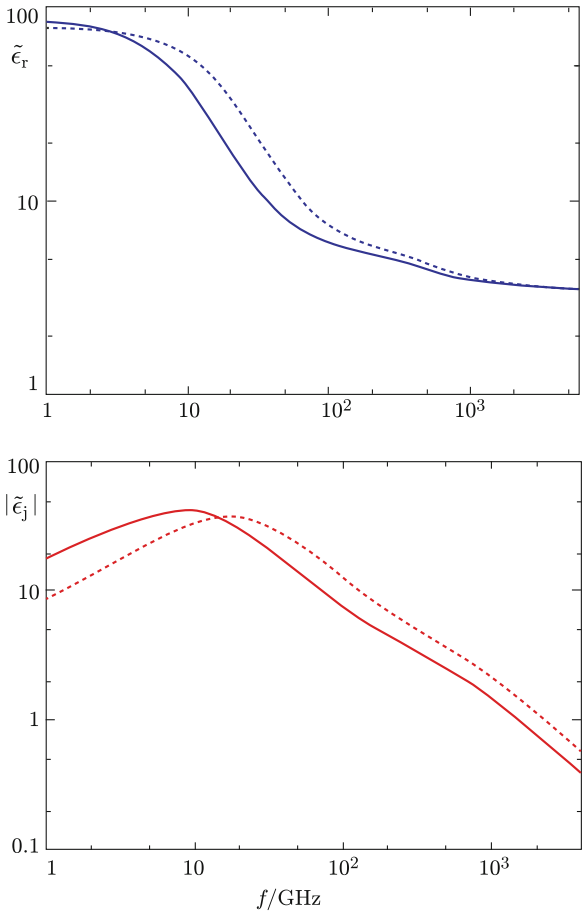

Fig. 2.8 Real ($\tilde{\epsilon}_r$) and imaginary ($\tilde{\epsilon}_j$) parts of relative permittivity of liquid water on an extended range of frequencies f from microwaves to infrared. The continuos curves refer to temperature $T = 0\,°C$, the dashed ones to $T = 20\,°C$ (Curves interpolate data from [43])

2.2.2.1 Liquid Water

Liquid water [16] is a polar material that, according to the *Debye double relaxation* model [53], displays a main relaxation around 20 GHz, at room temperature, and a secondary one around 600 GHz, as sketched in Fig. 2.8.[17] The polarizability of liquid water around its main relaxation angular frequency $\omega_r = 1/\tau_r$ is considerably higher than that associated with the secondary one. Therefore, a single-relaxation model is generally adequate to represent liquid water permittivity at microwaves.[18]

Given the value of the relaxation time τ_r, the microwave frequency range $\omega \approx \omega_r$ at which the orientation mainly contributes to the dielectric polarization falls in

[17]Note the effect of temperature, outlined in Sect. 2.1.2.

[18]The web hosts several resources, for instance, [21, 69], that provide complex permittivity of liquid water and ice.

the "low" frequency regime of the deformation polarization, which fully develops at considerably higher frequencies. In other words, at the frequencies at which $\chi_o \neq 0$, the approximations (2.16) considered in Sect. 2.1.1.1 hold. This implies that the contribution χ_d by the deformation mechanism to the susceptibility (2.20) is nearly constant, so that the frequency trend is essentially set by the single-relaxation orientation term χ_o. It is also observed that χ_d is relatively small and takes the form of a pedestal, which, together with the fairly flat contribution of the upper Debye relaxation, becomes appreciable only above $f \approx 100\,\text{GHz}$.

With further increase of frequency, vibrational modes progressively replace the partial-orientation (librational) mechanism. Given the intermolecular coupling of vibrations in the dense liquid environment (Sect. 14.2.3), the resulting bands are quite broad and overlap considerably, so as to resemble a continuum with smooth variation with frequency. Figure 2.9 shows that above $f \approx 1\,\text{THz}$, the real part

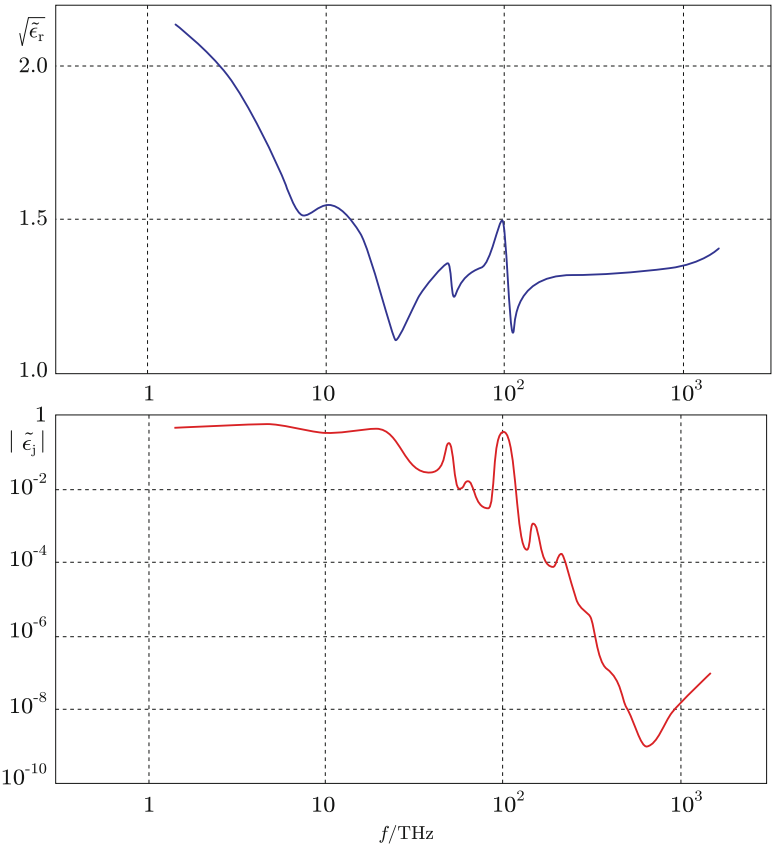

Fig. 2.9 Square root of the real ($\tilde{\epsilon}_r$) part and imaginary ($\tilde{\epsilon}_j$) part of relative permittivity of liquid water vs. frequency f in the optical range (Curves interpolate data from [35])

of susceptibility[19] decreases and that the behavior typical of individual vibrational resonances appears from about $f = 10\,\text{THz}$, up to frequencies beyond 100 THz. Afterwards, the real part of susceptibility has a fairly flat trend across the visible light spectrum. Then, it tends to further increase with frequency, since the ultraviolet electronic resonance range is being approached. The imaginary part $|\chi_j|$ follows the corresponding pattern, with a few peaks appearing in the 100 THz range and a deep minimum in the visible. It is important to realize that the values are considerably lower than those at microwaves reported in Fig. 2.8.

2.2.2.2 Ice

Although ice is composed of water molecules, its dielectric properties [59] differ substantially from those of liquid water. Indeed, the polar molecules, constrained in the ice crystalline lattice, are not free to orient under the action of the field: the contribution to susceptibility by the librational modes is quenched and values of χ_r considerably lower than those of liquid water are observed. Moreover, χ_r is fairly independent of frequency in the microwave range. Correspondingly, $\chi_j \approx 0$, particularly between 2 and 4 GHz.

Beyond the microwave band, where the orientation mechanism originates a major difference, ice tends to approach the dielectric behavior of liquid water: the real part of susceptibility increases slightly with frequency in the sub-mm frequency range, where collective vibrations occur, whereas χ_j increases by several orders of magnitude, as shown in Fig. 2.10. Individual vibrational resonances appear in the THz band, as for liquid water, but, being ice a crystalline material, its bands are sharper (Fig. 2.11). Across the visible light spectrum, i.e., from $f \approx 400\,\text{THz}$ to

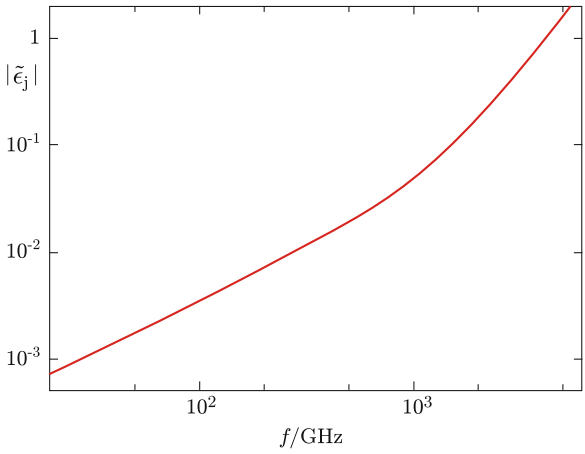

Fig. 2.10 Imaginary part $\tilde{\epsilon}_j$ of relative permittivity of ice vs. frequency f in the range from microwaves to infrared (Curves interpolate data from [43])

[19] The trend of $\sqrt{\tilde{\epsilon}_r}$ reported in Fig. 2.9 clearly follows the pattern of the real part of susceptibility.

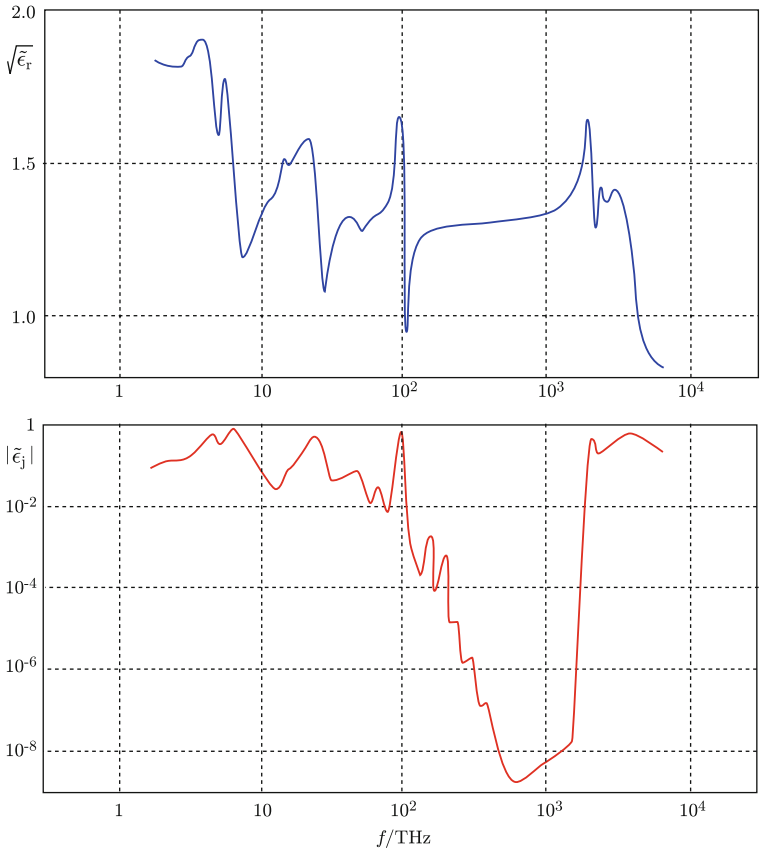

Fig. 2.11 Square root of the real part ($\sqrt{\tilde{\epsilon}_r}$) and imaginary ($\tilde{\epsilon}_j$) part of relative permittivity of ice vs. frequency f in the range from infrared to ultraviolet (Curves interpolate data from [94])

$f \approx 790\,\text{THz}$, the real part of susceptibility shows a fairly flat trend, while the imaginary part falls to quite low values. Both $\tilde{\epsilon}_r$ and $\tilde{\epsilon}_j$ increase with further increase of frequency, as shown by the liquid in Fig. 2.9. Then the curves clearly exhibit the effect of the electronic resonances in the subsequent ultraviolet range.

2.2.2.3 Sea Water

Water containing dissolved salts forms a typical *conducting* polar material. Its dielectric properties represent or model those of several classes of *aqueous materials* quite widespread on Earth, such as sea water, moist terrain, vegetal matter. Permittivity of blood [70, 100] and human tissues [31] are also well represented by water with free charges.

By assembling the models considered in the previous sections, the general expression of permittivity, is written as

$$\epsilon_r = \epsilon_0 + \frac{q_d^2}{m_d} \frac{\left(\omega_0^2 - \omega^2\right)}{\left(\omega_0^2 - \omega^2\right)^2 + 4\alpha_d^2 \omega^2} + \frac{\epsilon^0 - \epsilon_0}{(1 + \omega^2 \tau_r)} - \frac{q_c^2}{m_c} \frac{1}{\omega^2 + 4\alpha_c^2} ;$$

$$-\epsilon_j = \frac{q_d^2}{m_d} \frac{2\alpha_d \omega}{\left(\omega_0^2 - \omega^2\right)^2 + 4\alpha_d^2 \omega^2} + \frac{(\epsilon^0 - \epsilon_0)\, \omega \tau_r}{1 + \omega^2 \tau_r} + \frac{q_c^2}{m_c} \frac{2\alpha_c}{\omega(\omega^2 + 4\alpha_c^2)} ,$$

where $\epsilon^0 = \epsilon_0(1 + \chi^0)$ denotes the *static*, i.e., for $\omega \to 0$, *orientation* permittivity of the material.

All three polarization mechanisms contribute to the permittivity of a conducting polar material, although each mechanism reflects upon its peculiar frequency range. Figure 2.12 shows that the free charges affect the real and imaginary parts of sea water permittivity at the lower microwave frequencies. In particular, the effect of

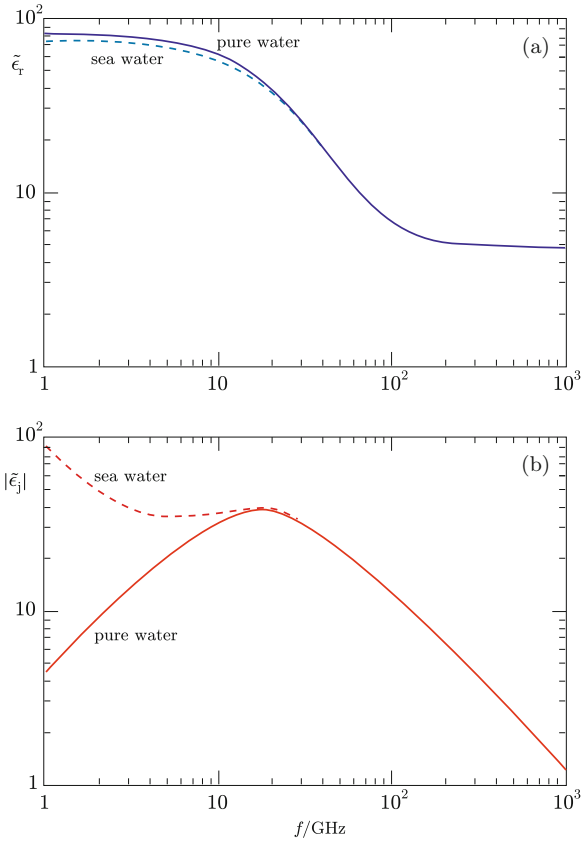

Fig. 2.12 Indicative trends of real ($\tilde{\epsilon}_r$) and imaginary ($\tilde{\epsilon}_j$) parts of relative permittivity of sea water vs. frequency f in the microwave range (Curves interpolate data from [58])

the dissolved salts is small on the real part, with a trend decreasing with increasing frequency; it is large on the imaginary part at frequencies of a few GHz and below, wile it vanishes at the first water relaxation, beyond which the trend is essentially set by the librational mechanism first and by the vibrational one for further frequency increase. Once the effect of salinity has vanished, "clean" sea water behaves like pure water (Sect. 2.2.2.1).

In summary, taking global account for the effect of free charges and of libration, at microwaves:

- $\tilde{\epsilon}_r$ is weakly dependent on salinity, since the polar properties of the water molecule prevail over the effect of the free charge;
- $\tilde{\epsilon}_j$ is strongly affected by salinity at the lower frequencies, where the dissipation associated with the orientation of the water molecules is relatively small.

Sea water generally hosts a number of substances, including suspended biological matter, sediments and bulk polluting materials. While the presence of such substances does not appreciably modify the dielectric properties of water at microwaves, resonances of impurities typically show up in the visible, as detailed in Sect. 14.2.1.

2.2.3 Vegetal Tissues

Biological living tissues, such as vegetal matter, are an important class of aqueous dielectrics [32–34, 66]. Main constituents of vegetal matter are free saline water, which is present in pores and capillary tubes, bound water in the cell walls, solid bulk substances, and air. Permittivity is determined by the density and the proportions of these constituents, measured, for instance, by the respective volume fractions.

2.2.3.1 Green Matter

2.2.3.1.1 Microwave Permittivity

As seen, the microwave permittivity of *free* water is the highest,[20] with relative real and imaginary parts of the order of a few tens, whereas dry matter has real part of a few units and imaginary part of some tenths (for instance, $\tilde{\epsilon} = 2.1 - j0.3$). Because of the relatively high contribution to susceptibility given by water, changes in moisture lead to significant changes in the dielectric properties of vegetation [56], as the diagrams of $\tilde{\epsilon}_r$ and $\tilde{\epsilon}_j$ as functions of **p**lant **w**ater **c**ontent (PWC) m_v in Fig. 2.13 suggest.Water tightly bound to the host *solid* material

[20] Among widespread natural materials.

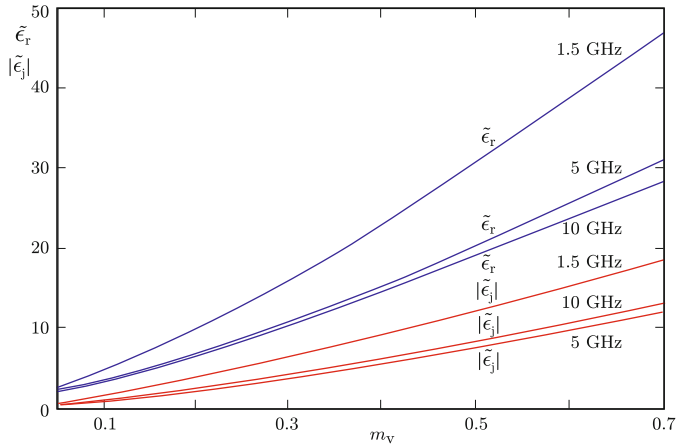

Fig. 2.13 Trends of real ($\tilde{\epsilon}_r$) and imaginary ($\tilde{\epsilon}_j$) parts of relative permittivity of maize leaves vs. PWC m_v at some EO microwave frequencies (Curves interpolate data from [88])

has a dielectric behavior similar to that of ice, because the elementary dipoles are not free to orient themselves along the field, so that permittivity is low. The solute changes the conductivity of free water, increasing permittivity, especially at the lower frequencies, at which the free ions can be fully moved by the field. Figure 2.14 shows the trends of real and imaginary parts of relative permittivity of maize leaves with frequency in the microwave band of main interest to Earth observation. The permittivity decreases as the leaves dry out. The real part shows the decreasing trend characterizing the contributions by the solute and by relaxation. The imaginary part, which is enhanced by the dissolved salts at the lower frequency end, decreases as the increasing frequency reduces the ion mobility. Once the contribution of the free charges is quenched, the trend is essentially determined by the water relaxation, as denoted by the increase at the higher frequencies, which approach the water Debye frequency (Sect. 2.2.2.1). Figure 2.15 reports the imaginary part of $\tilde{\epsilon}$ on an extended microwave frequency range to highlight that, consistently with the dielectric model of water, $|\tilde{\epsilon}_j|$ increases from C-band[21] onward, reaches a (temperature-dependent) maximum in the K_u-band, beyond which it decreases.

2.2.3.1.2 Optical Permittivity

The real part of permittivity of vegetal green matter in the optical range essentially follows that of liquid water [63], given the frequency range well above the upper relaxation of this latter. Instead, the imaginary part is affected by the resonances

[21] Please refer to Table 10.2 for the denomination of the microwave bands.

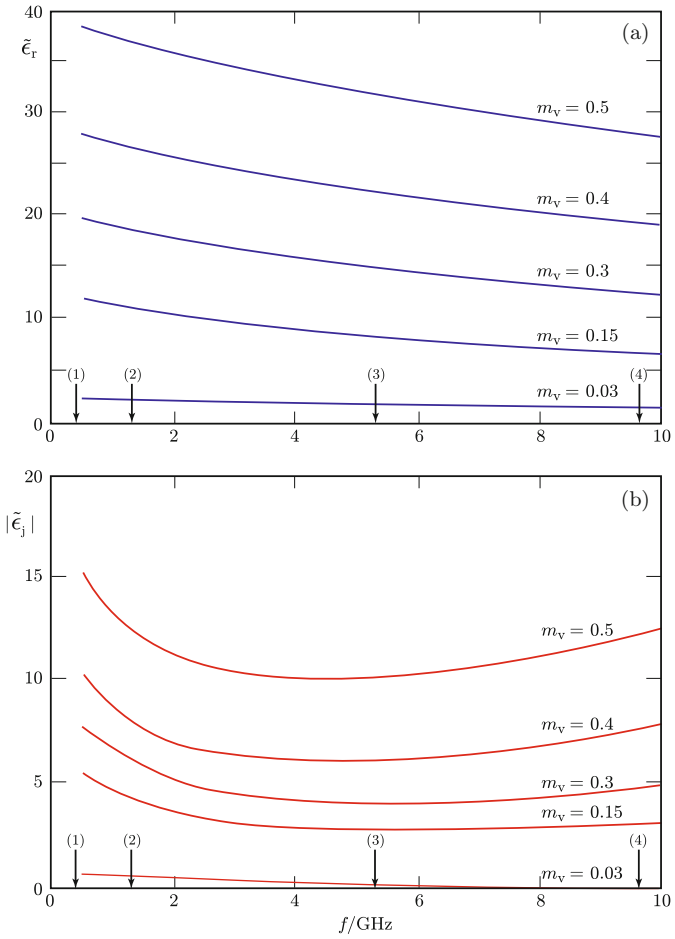

Fig. 2.14 Trends of real, (**a**), and imaginary, (**b**), parts of relative permittivity of maize leaves for various PWC m_v vs. microwave frequency f. The *arrows* indicate frequencies at which EO SAR observations are more commonly carried out: (1), P-band; (2), L-band; (3), C-band; (4), X-band (Curves interpolate data from [27])

of the various substances forming the vegetal tissues (Sect. 14.1.1.2), what also explains the general[22] trend of $\tilde{\epsilon}_r$, coarsely increasing with frequency, displayed in Fig. 2.16. However, it is worth mentioning that the specific dielectric properties are substantially affected by the microstructure of the vegetation element under consideration.

[22]High variability with the leaf composition is expected [18].

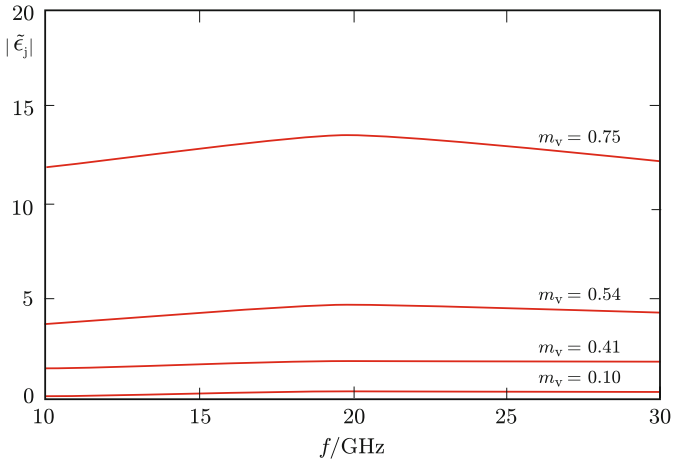

Fig. 2.15 Imaginary part of relative permittivity of alfalfa leaves in the range of frequency f from 10 to 30 GHz for various PWC m_v, hinting at the first Debye water relaxation (Curves interpolate data from [81])

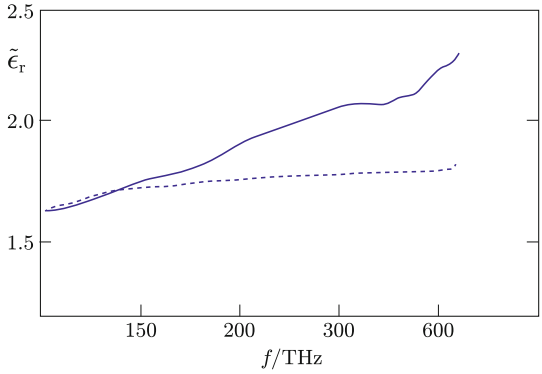

Fig. 2.16 Indicative trend of the real part $\tilde{\epsilon}_r$ of leaf relative permittivity (*continuous curve*) and of water (*dashed*) vs. frequency f in the optical range (Curves interpolate data from [42])

2.2.3.2 Ligneous Matter

The coarse composition of wood is that of vegetal matter outlined in Sect. 2.2.3, but with pigments and water content generally lower than the ones of green plant elements and relative abundance of cellulose and, especially, of lignin. Commonly encountered PWC are in the range $m_v \approx 0.1\,\mathrm{m^3\,m^{-3}}$ for naturally dried wood to $m_v \approx 0.6\,\mathrm{m^3\,m^{-3}}$ for fresh trunk wood, depending on the radial position (Fig. 2.17). The bark, which is a porous material with relatively high air fraction and little moisture, has low permittivity. The trend of wood permittivity [45] with frequency is essentially determined by water, as discussed in the previous section. The example illustrated in Fig. 2.18 refer to an aged balsam fir tree trunk with low moisture content.

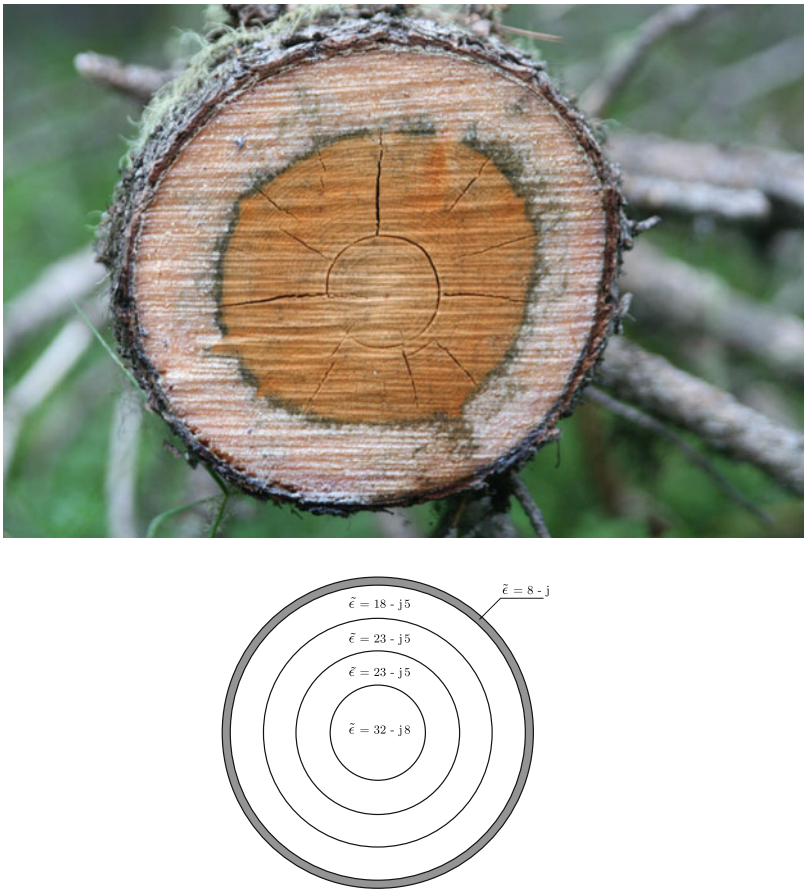

Fig. 2.17 Section of freshly cut tree (spruce) trunk and example of radial variation of microwave complex relative permittivity (poplar) (Data from [27])

2.2.3.3 Effect of Temperature

As the Debye relaxation of water is affected by temperature T, also the permittivity of the mixture forming the vegetal matter depends on T. For fresh agricultural crops, the plant temperature, which typically falls in the $0\,^{\circ}\mathrm{C} \lesssim T \lesssim 40\,^{\circ}\mathrm{C}$ must be considered. On its side, freezing of vegetal matter produces a particularly sizable effect, resulting in the dramatic decrease of microwave permittivity depicted in Fig. 2.19, caused by the reduced orientation capability of the permanent dipoles. For this reason, taking into account the freezing-thawing cycle of permittivity is crucial especially for interpreting microwave forest remote sensing data taken over high-latitude boreal areas [48, 72].

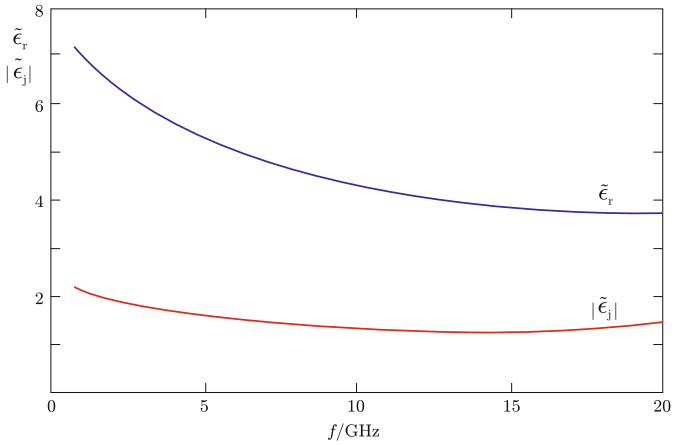

Fig. 2.18 Example of variations of real ($\tilde{\epsilon}_r$) and imaginary ($\tilde{\epsilon}_j$) parts of aged wood permittivity with microwave frequency f (Curves interpolate data from [27])

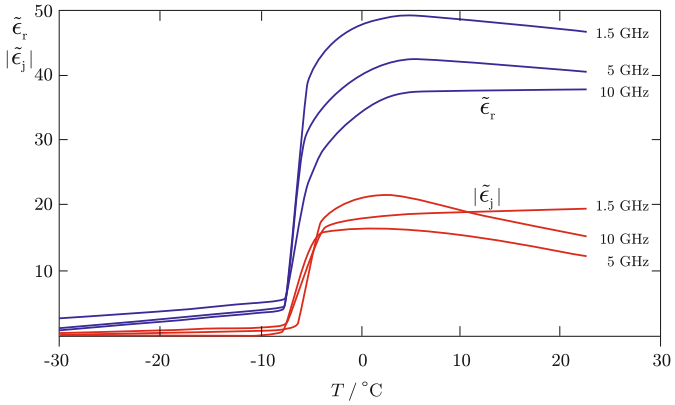

Fig. 2.19 Effect of temperature T on real ($\tilde{\epsilon}_r$) and imaginary ($\tilde{\epsilon}_j$) parts of maize leaf permittivity at various microwave frequencies f (Curves interpolate data from [27])

2.2.4 Soil

Soil is a mixture [25, 82] of free and bound water, mineral and organic matter, and air [36, Chap. 5]. The diagrams of Fig. 2.20 highlight the strong dependence of microwave permittivity on **s**oil **m**oisture **c**ontent (SMC) m_v because of the relatively high permittivity of liquid water with respect to the one of the bulk terrain material. Kind and amount of dissolved mineral salts also affect the soil dielectric properties, especially at the lower frequencies, analogously to the effect of the free charges in vegetal matter considered in Sect. 2.2.3.1.1. Permittivity of terrain typically increases slowly with increasing moisture content, then, beyond a threshold value, it

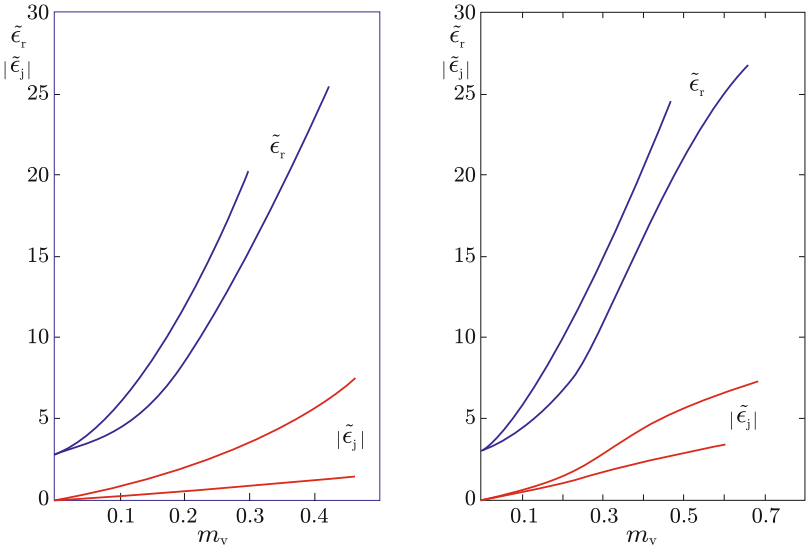

Fig. 2.20 Examples of real ($\tilde{\epsilon}_r$) and imaginary ($\tilde{\epsilon}_j$) parts of relative permittivity of two different types of soil at frequencies $f = 1.4$ GHz (*left*) and $f = 5.0$ GHz (*right*) vs. SMC m_v; note that the range of m_v for the curves at 5 GHz is wider than for those at 1.4 GHz (Curves interpolate data from [93])

increases steeply with m_v. The transition value of moisture varies with soil type and texture: for instance, it is smaller for sandy soils than for high-clay content soils. The behavior follows the state of the water molecules [61], which are mainly bound when moisture is low, and the microstructure [8] of the terrain.

The trend of soil permittivity with microwave frequency is consistent with the behavior of solutes, as shown by the diagrams in Fig. 2.21. Note that the various substances forming the soil make small resonances to appear in the microwave frequency range and that variations of moisture produce shifts of the resonance frequencies.

As expected, the temperature affects the soil permittivity in a quite similar fashion to that of vegetal matter. The diagrams in Fig. 2.22 suggest that increasing temperature increases the frequency at which the maximum of the broad relaxation peak occurs and that freezing produces drops of both $\tilde{\epsilon}_r$ and $|\tilde{\epsilon}_j|$.

Data on permittivity of soil are difficult to acquire at optical and infrared wavelengths. Indeed, soil is a loose "incoherent" ensemble of heterogeneous materials, having quite variable nature and proportions. The macroscopic parameter used at microwaves, that is the global permittivity of such a mixture, is scarcely meaningful in the optical range, at which other quantities directly related to the electromagnetic radiation are usually preferred in soil characterization (Sect. 14.1.1.1). If needed, the permittivity of single constituents can be measured. Then, by mixing the parameters describing the individual optical dielectric behavior, indications on the global

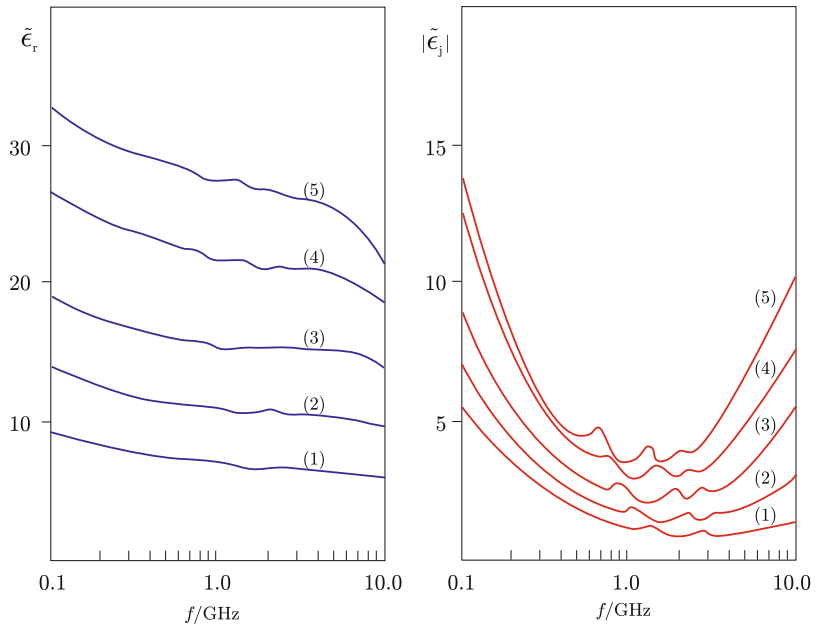

Fig. 2.21 Examples of real ($\tilde{\epsilon}_r$) and imaginary ($\tilde{\epsilon}_j$) parts of relative permittivity of silty soil with different SMC m_v vs. microwave frequency f; curves refer to: (1), $m_v = 0.12$; (2), $m_v = 0.21$; (3), $m_v = 0.31$; (4), $m_v = 0.35$; (5), $m_v = 0.48$. Temperature is $T = 20\,°C$ (Curves interpolate data from [22])

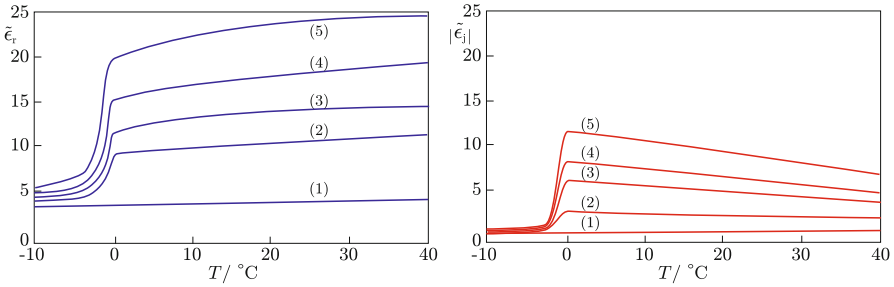

Fig. 2.22 Examples of real ($\tilde{\epsilon}_r$) and imaginary ($\tilde{\epsilon}_j$) parts of relative permittivity of silty soil with different SMC m_v vs. temperature T at $f = 10\,$GHz. Curves refer to: (1), $m_v = 0.07$; (2), $m_v = 0.23$; (3), $m_v = 0.36$; (4), $m_v = 0.41$; (5), $m_v = 0.46$ (Curves interpolate data from [22])

properties of the surface and bulk composite matter can be estimated. However, soils are generally characterized by their reflective properties instead that by the permittivity, which, rather, is a collective parameter fit to model the microwave behavior.

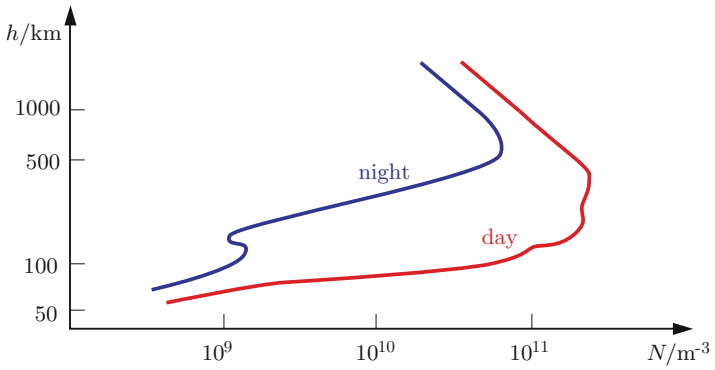

Fig. 2.23 Volumic free electron number as function of height h in the Ionosphere in presence (day) and absence (night) of solar radiation

2.2.5 *The Ionosphere*

In the middle-high atmosphere, the ionizing action of solar radiation creates free electron/ion charge couples. The region of the atmosphere in which air is ionized is named ionosphere. Its dielectric properties are essentially those of the material with free charges discussed in Sect. 2.1.3. Given the inertia of the ions, the permittivity is mainly determined by the density N_e of free electrons, which depends on local solar position, hence on location, time, season, and solar cycle (Fig. 2.23). Introductory details on the ionosphere are found at several web sites, e.g., [40, 41].

Since the ionospheric plasma is not a condensed but a tenuous material, the damping coefficient is low ($\alpha_c \approx 0.5\,\mathrm{kHz}$). At microwaves frequencies, $f \gg \alpha_c$, therefore, if q_e is the charge of the electron and m_e its mass, (2.23) yields

$$\tilde{\epsilon}_r \simeq 1 - \frac{N_e\, q_e^2}{\epsilon_0\, m_e\, \omega^2} = 1 - \left(\frac{\omega_p}{\omega}\right)^2 ,$$

where

$$\omega_p = \sqrt{\frac{N_e\, q_e^2}{\epsilon_0\, m_e}}$$

is the *plasma frequency*, dependent on N_e, hence on height, on average. Therefore, the ionosphere behaves as an inhomogeneous dielectric layer with a minimum of $\tilde{\epsilon}_r$ at the height of maximum ionization.

Since the electrons move in presence of the Earth's magnetic field $\boldsymbol{H}_E$, they are subject to the Lorentz force and follow circular patterns in planes perpendicular to $\boldsymbol{H}_E$. Coupling between charges in circular motion and circularly polarized electromagnetic fields differs according to the relative sense of rotation. This coupling difference gives rise to a dyadic permittivity: the ionosphere behaves as

an electromagnetically anisotropic medium that changes the direction of the fields propagating [12] through it (*Faraday rotation*),[23] thus introducing errors and noise when the measurements taken by the Earth observing systems are of polarimetric nature, that is, are based on measuring the complex field components. This noxious effect of the ionosphere decreases with increasing frequency: it is almost negligible from C-band onward, while it can be detrimental to L- and, especially, to P-band observations.

What We Learned About Dielectric Properties

We realize that permittivity is the basic quantity that links the observed material to the electromagnetic field which, by interacting with the target, extracts the information and carries it to the sensor. The value of ϵ is determined by the dielectric polarization mechanisms, consisting of the displacement and/or rotation of the ensemble of charges that essentially characterize the material. The dielectric polarization processes are accompanied by energy dissipation, hence the material must be characterized both in terms of the magnitude of the response to the external electric field and from the point of view of the loss of electromagnetic power. This implies that two numerical values are needed to identify the permittivity, which is then suitably represented by the complex number $\epsilon = \epsilon_\mathrm{r} + j\epsilon_\mathrm{j}$, with $\epsilon_\mathrm{j} \leq 0$.

The mechanism that is at the heart of the polarization of all materials is the elastic deformation of the spatial arrangement of the charges in the matter. The process is characterized by resonances: the real part of ϵ falls and the imaginary part peaks in correspondence of a resonant frequency. Each material is marked by its peculiar spectrum of vibrational frequencies, which typically occur at the higher frequencies at which EO systems operate. Water has a polar molecule, which reacts to the electric field also by orienting itself. This process, which occurs at lower frequencies, is characterized by dipolar relaxation. It gives a strong additional contribution both to the real and to the imaginary parts of ϵ. The presence of free charges, such as ions in liquids, is evidenced by a further increase of permittivity at the lowest frequencies. Since water is a widespread constituent of the Earth's environment, it substantially affects the dielectric behavior of a large majority of observed solid and liquid materials, the permittivity of which has a coarse but substantial decreasing trend with increasing frequency. The dielectric features of the gaseous atmosphere differ considerably, because the little interacting air molecules tend to display the individual traits of the constituents, including the rotational and roto-vibrational details of the water molecules. Details on the real and imaginary parts of the air permittivity are given both for the microwave and for the optical spectral ranges, because of the crucial role played by the atmosphere in remote sensing.

[23] Section 1.3.1.1 mentions that linearly polarized vectors can be regarded as sum of two co-planar circularly polarized vectors rotating in opposite directions.

The mixture of theoretical and experimental diagrams that follow the theoretical introduction, allows us to get an idea of the dielectric features we can expect throughout the range of frequencies at which Earth observation systems operate. Water is first examined both in its liquid and solid (ice) state and the effect of the dissolved salts is surveyed to explain the dielectric behavior of the sea, as well as to start figuring out the properties of vegetal matter and soil. The trends with frequency of the permittivity of green and ligneous matters are discussed, together with the effect of temperature, which, below the freezing point, cuts down the strong contribution by molecular orientation. We find an analogous behavior of the soil, which, after all, is a mixture of mineral and vegetal matter, and of free and bound water.

References

1. Aplin KL, McPheat RA (2005) Absorption of infra-red radiation by atmospheric molecular cluster-ions. J Atmos Solar-Terr Phys 67(8–9):775–783. doi:10.1016/j.jastp.2005.01.007
2. Baker-Jarvis J, Kim S (2012) The interaction of radio-frequency fields with dielectric materials at macroscopic to mesoscopic scales. J Res Natl Inst Stand Technol 117:1–60. http://dx.doi.org/10.6028/jres.117.001
3. Barrow GM (1963) The structure of molecules: An introduction to molecular spectroscopy. Benjamin. ISBN:9780805305210
4. Bell RJ Jr, Alexander RW, Long LL, Ordal MA, Paul R, Peacher J (1985) The optical constants of smoke materials (Naturally occurring minerals), plus iron and graphite in the millimeter and submillimeter. Technical report CRDC-CR-85057. U.S. Army AMCC, Sept 1985
5. Bernath PF (2002) The spectroscopy of water vapour: experiment, theory and applications. Phys Chem Chem Phys 4:1501–1509. doi:10.1039/b200372d
6. Bernath PF (2005) Spectra of atoms and molecules. Oxford University Press. ISBN:9780195177596
7. Bhattacharya Y, Milne M (2009) Psychrometric chart tutorial: a tool for understanding human thermal comfort conditions. In: 38th American Solar Energy Society Conference, Buffalo, 11–16 May 2009. ISBN:9781615673636. http://www.proceedings.com/05939.html. Visited on 17 May 2014
8. Bobrov PP, Mironov VL, Kondratieva OV, Repin AV (2009) Frequency dependence of permittivity of free and bound water in soils for different textures. PIERS Online 5(5):426–430. doi:10.2529/PIERS090219110307, http://piers.org/piersonline/piers.php?volume=5&number=5&page=426. Visited on 23 July 2014
9. Bone S, Zaba B (1992) Bioelectronics. Wiley. ISBN:9780335158126
10. Böttcher CJF, Bordewijk P (1978) Theory of electric polarization: dielectrics in time-dependent fields. Elsevier. ISBN:9780444600691
11. Brussaard G, Watson PA (1994) Atmospheric modelling and millimetre wave propagation. Springer. ISBN:9780412562303
12. Budden KG (1988) The propagation of radio waves: the theory of radio waves of low power in the ionosphere and magnetosphere. Cambridge University Press. ISBN:9780521369527
13. Burke LA, Jensen JO, Jensen JL, Krishnan PN (1993) Theoretical study of water clusters. I. Pentamer. Chem Phys Lett 206(1–4):293–296. doi:10.1016/0009-2614(93)85554-2
14. Carlon HR (1979) Do clusters contribute to the infrared absorption spectrum of water vapor? Infrared Phys 19(5):549–557. doi:10.1016/0020-0891(79)90072-1

15. Carlon HR (1979) Variations in emission spectra from warm water fogs: evidence for clusters in the vapor phase. Infrared Phys 19(1):49–64. doi:10.1016/0020-0891(79)90093-9
16. Chaplin M. Water structure and science. London South Bank University. http://www1.lsbu.ac.uk/water/. Visited on 15 Apr 2014
17. Chemistry Review: Water. American Chemical Society. http://www.\\inquiryinaction.org/chemistryreview/water/. Visited on 16 May 2014
18. Chen M, Weng F (2012) Kramers-Kronig analysis of leaf refractive index with the PROSPECT leaf optical property model. J Geophys Res 117:D18106, 1–9. doi:10.1029/2012JD017477
19. Ciddor PE (1996) Refractive index of air: new equations for the visible and near infrared. Appl Opt 35(9):1566–1573. doi:10.1364/AO.35.001566
20. Clough SA, Kneizys FX, Davies RW (1989) Line shape and the water vapor continuum. Atmos Res 23(3–4):229–241. doi:10.1016/0169-8095(89)90020-3
21. Complex Dielectric Constant of Water. Random science tools and calculators. http://www.random-science-tools.com/electronics/water_dielectric.htm. Visited on 12 Sept 2014
22. Curtis JO (1993) Microwave dielectric behavior of soils, report 3, Measurements and Modeling. Technical report EL-93-25. U.S. Army Corps of Engineers, Dec 1993
23. Daniel VV (1967) Dielectric relaxation. Academic. ISBN:9780122019500
24. Davidson DV (1961) Dielectric relaxation in liquids: I. The representation of relaxation behavior. Can J Chem 39(3):571–594. doi:10.1139/v61-069
25. Dobson MC, Ulaby FT, Hallikainen MT, El-Rayes MA (1985) Microwave dielectric behavior of wet soil – Part II: dielectric mixing models. IEEE Trans Geosci Remote Sens GE-23(1):35–46. doi:10.1109/TGRS.1985.289498
26. Eisenberg D, Kauzmann W (2005) The structure and properties of water. Oxford University Press. ISBN:9780198570264
27. El-Rayes MA, Ulaby FT (1987) Microwave dielectric spectrum of vegetation – Part I: experimental observations. IEEE Trans Geosci Remote Sens GE-25:541–549. doi:10.1109/TGRS.1987. 289832
28. Feldman Y. The physics of dielectrics. The Hebrew University of Jerusalem Department of Applied Physics. http://aph.huji.ac.il/courses/2008_9/83887/index.html. Visited on 17 Sept 2014
29. Feret J-B, François C, Asner GP, Gitelson AA, Martin RE, Bidel LPR, Ustin SL, le Maire G, Jacquemoud S (2008) PROSPECT-4 and 5: advances in the leaf optical properties model separating photosynthetic pigments. Remote Sens Environ 112(6):3030–3043. doi:10.1016/j.rse.2008.02.012
30. Frölich H (1949) Theory of dielectrics: dielectric constant and dielectric loss. Clarendon Press. ISBN:0198513798
31. Gabriel C (1996) Compilation of the dielectric properties of body tissues at RF and microwave frequencies. Technical report AL/OE-TR-1996-0037. Armstrong Laboratory (AFMC) Occupational and Environmental Health Directorate Radiofrequency Radiation Division
32. Gabriel C, Gabriel S, Corthout E (1996) The dielectric properties of biological tissues: I. Literature survey. Phys Med Biol 41(11):2231–2249. doi:10.1088/0031-9155/41/11/001
33. Gabriel S, Lau RW, Gabriel C (1996) The dielectric properties of biological tissues: II. Measurements in the frequency range 10 Hz to 20 GHz. Phys Med Biol 41(11):2251–2269. doi:10.1088/0031-9155/41/11/002
34. Gabriel S, Lau RW, Gabriel C (1996) The dielectric properties of biological tissues: III. Parametric models for the dielectric spectrum of tissues. Phys Med Biol 41(11):2271–2293. doi:10.1088/0031-9155/41/11/003
35. Hale GM, Querry MR (1973) Optical constants of water in the 200-nm to 200-μm wavelength region. Appl Opt 12:555–563. doi:10.1364/AO.12.000555
36. Heege HJ (ed) (2013) Precision in crop farming: site specific concepts and sensing methods: applications and results. Springer. ISBN:9789400767607
37. Herzberg G (1951) Molecular spectra and molecular structure: infrared and Raman spectra of polyatomic molecules. Van Nostrand. ISBN:9780894642692

38. Herzberg G (2007) Molecular spectra and molecular structure – vol 1: spectra of diatomic molecules. Read Books. ISBN:9781406738537
39. Hill NE, Vaughan WE, Price AH, Davies M (1969) Dielectric properties and molecular behaviour. Van Nostrand Reinhold. ISBN:9780442034115
40. Introduction to the Ionosphere. NOAA National Geophysical Data Center. http://www.ngdc.noaa.gov/stp/iono/ionointro.html. Visited on 18 May 2014
41. Ionosphere: Tutorial (2013) Royal observatory of Belgium GNSS research group. http://www.gnss.be/ionosphere_tutorial.php. Visited on 18 May 2014
42. Jacquemoud S, Baret F (1990) PROSPECT: a model of leaf optical properties spectra. Remote Sens Environ 34(2):75–91. doi:10.1016/0034-4257(90)90100-Z
43. Jiang JH, Wu DL (2004) Ice and water permittivities for millimeter and sub-millimeter remote sensing applications. Atmos Sci Lett 5:146–151. doi:10.1002/asl.77
44. Kaatze U (1989) Complex permittivity of water as a function of frequency and temperature. J Chem Eng Data 34(4):371–374. doi:10.1021/je00058a001
45. Kalinkevich AA (2013) On measuring the permittivity of "living" wood for microwave remote sensing. J Commun Technol Electron 58(9):919–925. doi:10.1134/S1064226913090052
46. Keutsch FN, Saykally RJ (2001) Water clusters: untangling the mysteries of the liquid, one molecule at a time. Proc Natl Acad Sci USA 98(19):10533–10540. doi:10.1073/pnas.191266498
47. Krishnan PN, Jensen JO, Burke LA (1994) Theoretical study of water clusters. II. Hexamer. Chem Phys Lett 217(3):311–318. doi:10.1016/0009-2614(93)E1370-V
48. Kwok R, Rignot EJM, Way JB, Freeman A, Holt J (1994) Polarization signatures of frozen and thawed forests of varying environmental state. IEEE Trans Geosci Remote Sens 32:371–381. doi:10.1109/36.295051
49. Leiphart JP, Zeek RW, Bearce LS, Toth E (1962) Penetration of the ionosphere by very-low-frequency radio signals – interim results of the LOFTI I experiment. Proc IRE 50(1):6–17. doi:10.1109/JRPROC.1962.288269
50. Liebe HJ (1981) Modeling attenuation and phase of radio waves in air at frequencies below 1000 GHz. Radio Sci 16(6):1183–1199. doi:10.1029/RS016i006p01183
51. Liebe HJ (1984) The atmospheric water vapor continuum below 300 GHz. Int J Infrared Millim Waves 5(2):207–227. doi:10.1007/BF01417651
52. Liebe HJ (1989) MPM – an atmospheric millimeter-wave propagation model. Int J Infrared Millim Waves 10:631–650. doi:10.1007/BF01009565
53. Liebe HJ, Hufford GA, Manabe T (1991) A model for the complex permittivity of water at frequencies below 1 THz. Int J Infrared Millim Waves 12:659–675. doi:10.1007/BF01008897
54. Liebe HJ, Rosenkranz PW, Hufford GA (1992) Atmospheric 60-GHz oxygen spectrum: new laboratory measurements and line parameters. J Quant Spectrosc Radiat Transf 48(5–6):629–643. doi:10.1016/0022-4073(92)90127-P
55. Liebe HJ, Hufford GA, Cotton MG (1993) Propagation modeling of moist air and suspended water/ice particles at frequencies below 1000 GHz". In: NATO/AGARD Wave Propagation Panel, 52nd Meeting Atmospheric Propagation Effects Through Natural and Man-Made Obscurants for Visible to MM-Wave Radiation, Palma de Mallorca, 17–20 May 1993, vol AGARD-CP-542. ISBN:9283507274
56. Li Z, Zeng JY, Chen Q, Bi HY (2014) The measurement and model construction of complex permittivity of vegetation. Sci China Earth Sci 57(4):729–740. doi:10.1007/s11430-013-4691-5
57. Marechal Y (2006) The hydrogen bond and the water molecule: the physics and chemistry of water, aqueous and bio-media. Elsevier. ISBN:9780080469294
58. Mathew T, Sarkar A (2010) Sensitivity of dielectric properties of ocean water to frequencies used in microwave remote sensing. Int J Earth Sci Eng 3(5):662–668. ISSN:0974-5904
59. Mätzler C (2006) Microwave dielectric properties of ice. In: Mätzler C, Rosenkranz PW, Battaglia A, Wigneron J-P (eds) Thermal microwave radiation: applications for remote sensing. Institution of Engineering and Technology. ISBN:9780863415739

60. McClatchey RA, Burch DE, Rothman LS, Benedict WS, Calfee RF, Garing JS, Clough SA, Fox K (1973) AFCRL atmospheric absorption line parameters compilation. Technical report AFCRL-TR-73-0096. U.S. Air Force Cambridge Research Laboratories
61. Mironov VL, Dobson MC, Kaupp VH, Komarov SA, Kleshchenko VN (2004) Generalized refractive mixing dielectric model for moist soils. IEEE Trans Geosci Remote Sens 42(4):773–785. doi:10.1109/TGRS.2003.823288
62. Molecular Spectroscopy. NASA Jet Propulsion Laboratory/California Institute of Technology JPL Molecular Spectroscopy Team. http://spec.jpl.nasa.gov. Visited on 17 May 2014
63. Palmer KF, Williams D (1974) Optical properties of water in the near infrared. J Opt Soc Am 64(8):1107–1110. doi:10.1364/JOSA.64.001107
64. Pickett HM, Poynter RL, Cohen EA, Delitsky ML, Pearson JC, Müller HSP (1998) Submillimeter, millimeter and microwave spectral line catalog. J Quant Spectrosc Radiat Transf 60:883–890. doi:10.1016/S0022-4073(98)00091-0
65. Pope RM, Fry ES (1997) Absorption spectrum (380–700 nm) of pure water. II. Integrating cavity measurements. Appl Opt 36(33):8710–8723. doi:10.1364/AO.36.008710
66. Presman AS (1970) Electromagnetic fields and life. Plenum Press. ISBN:9781475706376
67. Purcell EM, Morin DJ (2013) Electricity and magnetism. Cambridge University Press. ISBN:9781107014022
68. Rahman A, Stillinger FH (1971) Molecular dynamics study of liquid water. J Chem Phys 55:3336–3359. doi:10.1063/1.1676585
69. Refractive index database. Refractive Index.Info. http://refractiveindex.info/legacy/?group=LIQUIDS&material=Water; http://refractiveindex.info/legacy/?group=CRYSTALS&material=H2O-ice. Visited on 12 Sept 2014
70. Reid CB, Reese G, Gibson AP, Wallace VP (2013) Terahertz time-domain spectroscopy of human blood. IEEE J Biomed Health Inform 17(4):774–778. doi:10.1109/JBHI.2013.2255306
71. Reimers JR, Watts RO (1984) The structure and vibrational spectra of small clusters of water molecules. Chem Phys 85(1):83–112. doi:10.1016/S0301-0104(84)85175-7
72. Rignot E, Way JB (1994) Monitoring freeze-thaw cycles along North-South Alaskan transects using ERS-1 SAR. Remote Sens Environ 49:131–137. doi:10.1016/0034-4257(94)90049-3
73. Rishbeth H (1988) Basic physics of the ionosphere: a tutorial review. J Inst Electron Radio Eng 58(6):S207–S223. doi:10.1049/jiere.1988.0060
74. Roberts RE, Selby JEA, Biberman LM (1976) Infrared continuum absorption by atmospheric water vapor in the 8–12-μm window. Appl Opt 15(9):2085–2090. doi:10.1364/AO.15.002085
75. Rosenkranz PW (1998) Water vapor microwave continuum absorption: a comparison of measurements and models. Radio Sci 33:919–928. doi:10.1029/98RS01182
76. Rüeger JM (1996) Electronic distance measurement: an introduction. Springer. ISBN:9780387611594
77. Rüeger JM (2002) Refractive index formulae for radio waves. In: International Federation of Surveyors (FIG) XXII International Congress, JS 28, Washington, DC, 19–26 Apr 2002. http://www.fig.net/pub/fig_2002/procmain.htm. Visited on 08 Jan 2014
78. Rüeger JM (2002) Refractive indices of light, infrared and radio waves in the atmosphere. Technical report UNISURV S-68. School of Surveying and Spatial Information Systems University of New South Wales
79. Saykally RJ (2013) Simplest water cluster leaves behind its spectral fingerprint. Physics 6(22). doi:10.1103/Physics.6.22
80. Sediki A, Lebsir F, Martiny L, Dauchez M, Krallafa A (2008) Ab initio investigation of the topology and properties of three-dimensional clusters of water $(H_2O)_n$. Food Chem 106(4):1476–1484. doi:10.1016/j.foodchem.2007.03.080
81. Shrestha BL, Wood HC, Sokhansanj S (2007) Modeling of vegetation permittivity at microwave frequencies. IEEE Trans Geosci Remote Sens 45(2):342–348. doi:10.1109/TGRS.2006.886175
82. Sihvola AH (1999) Electromagnetic mixing formulas and applications. Institution of Electrical Engineers. ISBN:9780852967720

83. Tatartchenko VA (2010) Infrared characteristic radiation of water condensation and freezing in connection with atmospheric phenomena. Earth-Sci Rev 101(1–2):24–28. doi:10.1016/j.earscirev.2010.03.002
84. Tatartchenko VA (2011) Infrared characteristic radiation of water condensation and freezing in connection with atmospheric phenomena; Part 2: new data. Earth-Sci Rev 107(3–4):311–314. doi:10.1016/j.earscirev.2011.04.001
85. Tatartchenko VA, Liu Y, Chen W, Smirnov P (2012) Infrared characteristic radiation of water condensation and freezing in connection with atmospheric phenomena; Part 3: experimental data. Earth-Sci Rev 114(3–4):218–223. doi:10.1016/j.earscirev.2012.07.001
86. The Structure of Water: Hydrogen Bonds. Biomodel.uah.es. http://biomodel.uah.es/en/water/index.htm. Visited on 16 May 2014
87. Tretyakov MYu, Serov EA, Koshelev MA, Parshin VV, Krupnov AF (2013) Water dimer rotationally resolved millimeter-wave spectrum observation at room temperature. Phys Rev Lett PRL 110:093001. doi:10.1103/PhysRevLett.110.093001
88. Ulaby FT, Jedlika RP (1984) Microwave dielectric properties of plant materials. IEEE Trans Geosci Remote Sens GE-22(4): 406–415. doi:10.1109/TGRS.1984.350644
89. Van Vleck JH, Weisskopf VF (1945) On the shape of collision-broadened lines. Rev Mod Phys 17:227–236. doi:http://dx.doi.org/10.1103/RevModPhys.17.227
90. Variation of the Dielectric Constant in Alternating Fields. DoITPoMS University of Cambridge. http://www.doitpoms.ac.uk/tlplib/dielectrics/variation.php. Visited on 16 May 2014
91. Vibration of Molecules. U.C. Berkeley College of Chemistry CHEM Study. https://archive.org/details/vibration_of_molecules. Visited on 13 May 2014
92. Von Hippel AR (1995) Dielectrics and waves. Artech House. ISBN:9781580531221
93. Wang JR, Schmugge TJ (1980) An empirical model for the complex dielectric permittivity of soils as a function of water content. IEEE Trans Geosci Remote Sens GE-18(4):288–295. doi:10.1109/TGRS.1980.350304
94. Warren SG (1984) Optical constants of ice from the ultraviolet to the microwave. Appl Opt 23(8):1206–1225. doi:10.1029/2007JD009744
95. Warren SG, Brandt RE (2008) Optical constants of ice from the ultraviolet to the microwave: a revised compilation. J Geophys Res Atmos 113(D14). doi:10.1029/2007JD009744
96. Water: Hydrogen Bonding in Liquid Water. franklychemistry.co.uk. https://www.youtube.com/watch?v=k5q5C7sPu0c. Visited on 16 May 2014
97. Water Molecules – Part 1. Canadian Museum of Nature. http://www.youtube.com/watch?v=sBZfPmIcS-E. Visited on 13 May 2014
98. Watt AD, Mathews FS, Maxwell EL (1963) Some electrical characteristics of the Earth's crust. Proc IEEE 51(6):897–910. doi:10.1109/PROC.1963.2323
99. Weisskopf V (1933) Die Streuung des Lichts an angeregten Atomen. German. Zeitschrift für Physik 85(7–8):451–481. doi:10.1007/BF01330970, http://dx.doi.org/10.1007/BF01330970
100. Wolf M, Gulich R, Lunkenheimer P, Loidl A (2011) Broadband dielectric spectroscopy on human blood. Biochimica et Biophysica Acta 1810:727–740. doi:10.1016/j.bbagen.2011.05.012
101. Yang Y, Mandehgar M, Grischkowsky D (2014) Determination of the water vapor continuum absorption by THz-TDS and molecular response theory. Opt Exp 22(4):4388–4403. doi:10.1364/OE.22.004388

Chapter 3
Electromagnetic Sources and Radiation

Once determined some general properties of the electromagnetic field and of the dielectric characteristics of terrestrial materials, the relations between sources and field must now be established: in particular, how and to which extent the features of the source affect the properties of the field.

3.1 The Radiated Field

Starting point are the spectral Maxwell's equations (2.1) and (2.2) including the impressed electric current $\boldsymbol{J}_s$ modeling the source of electromagnetic energy at angular frequency ω:

$$\nabla \times \boldsymbol{E} = -\mathrm{j}\omega\mu_0 \boldsymbol{H} \; ; \tag{3.1}$$

$$\nabla \times \boldsymbol{H} = \mathrm{j}\omega\epsilon \boldsymbol{E} + \boldsymbol{J}_s \; . \tag{3.2}$$

The complex spectral permittivity ϵ in (3.2) takes account of all the contributions to dielectric polarization, as discussed in Sect. 2.2. Magnetic permeability is assumed to be that of vacuum everywhere. Under the assumption of linearity, each kind of source acts separately, hence, for the time being, the magnetic source is not considered. Anyway, the duality introduced in Sect. 1.1.3 allows determining the field produced by magnetic currents through straightforward transformations of the field produced by electric currents.

Auxiliary quantities are known to be useful tools for describing the electromagnetic field. A *magnetic vector potential* $\mathfrak{A}$, that can be put into more direct relation with the source current, is introduced so that

$$\boldsymbol{H} = \nabla \times \mathfrak{A} \; . \tag{3.3}$$

D. Solimini, *Understanding Earth Observation*, Remote Sensing and Digital Image Processing 23, DOI 10.1007/978-3-319-25633-7_3

Then, the first Maxwell's equation becomes

$$\nabla \times \boldsymbol{E} = -\mathrm{j}\omega\mu_0 \nabla \times \mathfrak{A} \ ,$$

from which the electric field is obtained

$$\boldsymbol{E} = -\mathrm{j}\omega\mu_0 \mathfrak{A} - \nabla \mathcal{V} \ , \tag{3.4}$$

where $\mathcal{V}$ is an arbitrary *electric scalar potential*. By substitution into the second Maxwell's equation,

$$\nabla \times (\nabla \times \mathfrak{A}) = \mathrm{j}\omega\epsilon(-\mathrm{j}\omega\mu_0 \mathfrak{A} - \nabla \mathcal{V}) + \boldsymbol{J}_\mathrm{s} \ ,$$

or, given (A.41),

$$\nabla \nabla \cdot \mathfrak{A} - \nabla^2 \mathfrak{A} = \kappa^2 \mathfrak{A} - \mathrm{j}\omega\epsilon \nabla \mathcal{V} + \boldsymbol{J}_\mathrm{s} \ ,$$

where the parameter $\kappa^2 = \omega^2 \mu_0 \epsilon$ has been defined. The degree of freedom in the choice of $\mathfrak{A}$ (any curl-free vector field can be added to $\mathfrak{A}$ without changing $\boldsymbol{H}$) is saturated by the *Lorenz (FitGerald) gauge*[1]

$$\nabla \cdot \mathfrak{A} = -\mathrm{j}\omega\epsilon \mathcal{V} \ ,$$

so that

$$\nabla^2 \mathfrak{A} + \kappa^2 \mathfrak{A} = -\mathrm{j}\omega \mathcal{V} \nabla\epsilon - \boldsymbol{J}_\mathrm{s} = -\boldsymbol{J}_\epsilon - \boldsymbol{J}_\mathrm{s} = -\boldsymbol{J}_\mathrm{ts} \ , \tag{3.5}$$

where the term contributed by the dielectric inhomogeneities,

$$\boldsymbol{J}_\epsilon := \mathrm{j}\omega \mathcal{V} \nabla\epsilon \ ,$$

has been joined to the impressed current $\boldsymbol{J}_\mathrm{s}$ to form a total source term $\boldsymbol{J}_\mathrm{ts}$, which, for the time being, is assumed to be known.

Indeed, the vector potential $\mathfrak{A}$ from which the field is obtained, is a function of both the (electric) source currents and of the dielectric inhomogeneities of the medium. The spatial variations of permittivity expressed by $\nabla\epsilon$ produce effects analogous to those of the *primary* source currents: the dielectric inhomogeneities act as *secondary* sources. This basic electromagnetic property is instrumental to the Earth observation techniques that exploit *scattering* either of solar radiation or of radar waves from the inhomogeneous terrestrial materials. This crucial issue is mainly discussed in Chap. 7.

[1] The gauge is found attributed to both Lorenz and FitGerald.

When magnetic source currents need to be considered, defining an electric vector potential and use of duality readily yield the field. If the source model requires both electric and magnetic currents, the field is the superposition of the fields contributed by each type of source current.

3.1.1 Impulse Response of Free Space

The electromagnetic *impulse response* is the space-time dependent field produced by an impressed point current, which is the elementary form of source. The field produced by impressed currents of finite dimensions, as well as by the dielectric secondary sources, is obtained from the superposition of the contributions originating from the various points of space i.e., by suitable spatial integration of the impulsive response.

Since the quasi-monochromatic case is of interest, the source current is modeled as an analytic vector at angular frequency ω, which is spatially impulsive. In turn, the electromagnetic field is represented by the complex analytic vectors functions of space introduced in Sect. 1.3.2.

To determine the basic features of the electromagnetic field, this first approach considers homogeneous materials, with particular reference to vacuum. This is actually the case of solar radiation in the interplanetary space or of radiation from space-borne antennas outside the atmosphere. A homogeneous medium is anyway a quite useful reference, able also to represent the *average* of several man-made and natural materials. Moreover, in many instances, actual terrestrial materials can be approximated by piecewise homogeneous media.

The *free space*[2] case is considered in the following, that is, the field created by a point source is sought in an unbound lossless medium characterized by the real parameter

$$\kappa^2 := \omega^2 \mu_0 \epsilon \tag{3.6}$$

constant everywhere. Extension to a homogeneous lossy material is relatively straightforward.

In free space, (3.5) reduces to the inhomogeneous *Helmholtz equation*

$$\nabla^2 \mathfrak{A} + \kappa^2 \mathfrak{A} = -\boldsymbol{J}_\mathrm{s} \ . \tag{3.7}$$

To derive the magnetic vector potential impulse response $\mathfrak{A}_\mathrm{i}$, the source current density representing the point source must be impulsive, i.e., $\boldsymbol{J}_\mathrm{s}(\boldsymbol{r}) = J_0 \, \delta(\boldsymbol{r} - \boldsymbol{r}')\mathbf{t}_0$, where $\delta(\boldsymbol{r} - \boldsymbol{r}')$ is the unitary *Dirac delta* function of space located in $\boldsymbol{r}'$, J_0 an

[2] In general, free space does not imply vacuum.

amplitude constant, and $\mathbf{t}_0$ the unit vector in direction of $\boldsymbol{J}_s$. Then the free-space impulse magnetic vector potential $\mathfrak{A}$ at the point $\boldsymbol{r}$ is obtained from (3.7) in which $J_0 = 1\,\mathrm{A\,m^{-2}}$, that is

$$\nabla^2 \mathfrak{A}_i(\boldsymbol{r}-\boldsymbol{r}') + \kappa^2 \mathfrak{A}_i(\boldsymbol{r}-\boldsymbol{r}') = -\delta(\boldsymbol{r}-\boldsymbol{r}')\mathbf{t}_0 \,.$$

The function $\mathcal{G}$ satisfying the corresponding scalar equation

$$\nabla^2 \mathcal{G}(\boldsymbol{r}-\boldsymbol{r}') + \kappa^2 \mathcal{G}(\boldsymbol{r}-\boldsymbol{r}') = -\delta(\boldsymbol{r}-\boldsymbol{r}') \tag{3.8}$$

is called the *scalar Green's function* $\mathcal{G}(\boldsymbol{r}-\boldsymbol{r}')$, such that

$$\mathfrak{A}_i = \mathcal{G}\,\mathbf{t}_0 \,.$$

Once obtained the scalar impulse response $\mathcal{G}$, the magnetic vector potential $\mathfrak{A}(\boldsymbol{r})$ produced in $\boldsymbol{r}$ by any spatial distribution of source currents $\boldsymbol{J}_s(\boldsymbol{r}')$ is given by the convolution integral

$$\mathfrak{A}(\boldsymbol{r}) = \mathcal{G}(\boldsymbol{r}-\boldsymbol{r}') \otimes \boldsymbol{J}_s(\boldsymbol{r}') = \iiint_{V'} \mathcal{G}(\boldsymbol{r}-\boldsymbol{r}')\,\boldsymbol{J}_s(\boldsymbol{r}')\,\mathrm{d}V' \,, \tag{3.9}$$

where the infinite integration domain has been reduced to the source volume V', being the impressed currents $\boldsymbol{J}_s(\boldsymbol{r}') = 0$ for $\boldsymbol{r}' \notin V'$. In turn, the electric field is formally derived from (3.4):

$$\boldsymbol{E}(\boldsymbol{r}) = (-\mathrm{j}\omega\mu_0 + \frac{\nabla\nabla\cdot}{\mathrm{j}\omega\epsilon})\,\mathfrak{A}(\boldsymbol{r}) \,. \tag{3.10}$$

Equation (3.10) points out that the relation between current and electric field is not direct: a dyadic Green's function [14] $\mathfrak{G}(\boldsymbol{r}-\boldsymbol{r}')$ is needed to transform the source current field $\boldsymbol{J}_s(\boldsymbol{r}')$ into the electric field $\boldsymbol{E}(\boldsymbol{r})$ it produces:

$$\boldsymbol{E}(\boldsymbol{r}) = \iiint_{V'} \mathfrak{G}(\boldsymbol{r}-\boldsymbol{r}') \cdot \boldsymbol{J}_s(\boldsymbol{r}')\,\mathrm{d}V' \,. \tag{3.11}$$

The linear transformation in (3.11) implies that, in general, $\boldsymbol{E} \nparallel \boldsymbol{J}_s$.

3.1.1.1 The Scalar Green's Function

The scalar Green's function is the elementary quantity in terms of which any field is expressed. To determine $\mathcal{G}$, assume the spherical coordinate system of Fig. 3.1 with the origin coincident with the impulse source point, so that $\boldsymbol{r}' = 0$. Since the *wave equation*

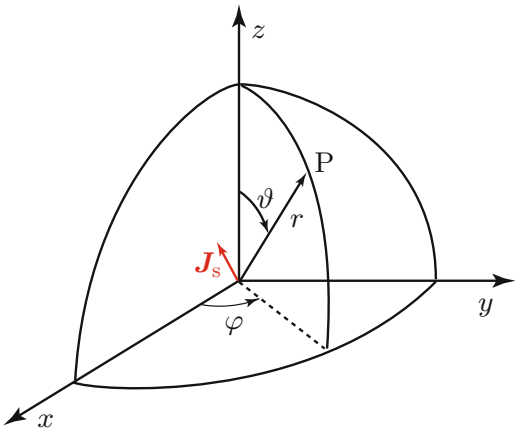

Fig. 3.1 Spherical coordinate system centered on the impulsive source current $\boldsymbol{J}_s$

$$\frac{\mathrm{d}^2}{\mathrm{d}r^2}(r\mathcal{G}) + \kappa^2(r\mathcal{G}) = 0 \tag{3.12}$$

holds in the space surrounding the source, $\mathcal{G}$ is readily obtained as

$$\mathcal{G}(r) = C_1\frac{\mathrm{e}^{-\mathrm{j}\kappa r}}{r} + C_2\frac{\mathrm{e}^{\mathrm{j}\kappa r}}{r}\,, \tag{3.13}$$

where C_1 and C_2 are quantities to be determined once magnitude and phase of the source are known. To this end, the physical meaning of (3.13) needs enlightening.

3.1.1.2 The Wave

The scalar Green's function $\mathcal{G}$ is a space-dependent complex quantity from which the space-time dependent vector potential, hence the *measurable* electromagnetic field, is obtained following the indications of Sect. 1.3.2: the space-time Green's function $\mathcal{G}(r,t)$ is

$$\mathcal{G}(r,t) = \Re\left[\mathcal{G}(r)\mathrm{e}^{\mathrm{j}\omega t}\right] = \Re\left[\frac{C_1}{r}\mathrm{e}^{-\mathrm{j}(\kappa\, r\,-\,\omega t)} + \frac{C_2}{r}\mathrm{e}^{\mathrm{j}(\kappa\, r\,+\,\omega t)}\right].$$

If, without loss of generality, C_1 and C_2 are assumed real,

$$\mathcal{G}(r,t) = \frac{C_1}{r}\cos(\kappa\, r - \omega t) + \frac{C_2}{r}\cos(\kappa\, r + \omega t) = \mathcal{G}_1 + \mathcal{G}_2\,.$$

Consider the first term $\mathcal{G}_1$ sketched in Fig. 3.2. At any distance r from the source, $\mathcal{G}_1$ is a quasi-harmonic function of time, with short-term temporal periodicity defined by the period $T = 2\pi/\omega$ of the source current (Sect. 1.3.2). Correspondingly, at a

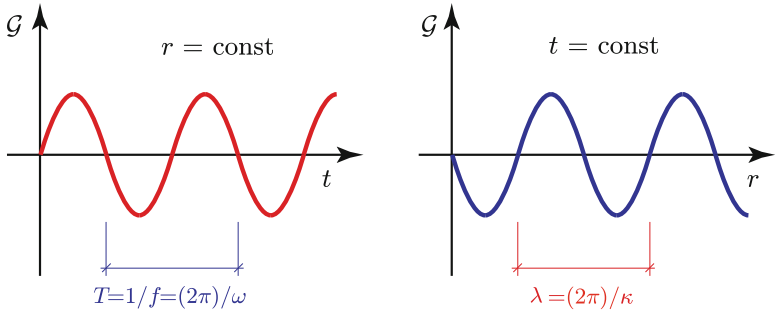

Fig. 3.2 Indicative variation with time, (**a**), and with space, (**b**), of the space-time electromagnetic potential

given time, $\mathcal{G}_1$ is a quasi-harmonic function of r with short-range spatial periodicity defined by the *wavelength*

$$\lambda = \frac{2\pi}{\kappa} = \frac{2\pi}{\omega\sqrt{\mu_0\epsilon}}\,, \tag{3.14}$$

which depends on κ, hence on frequency and on permittivity.

When the field is considered in the vacuum,

$$\lambda \equiv \lambda_0 = \frac{2\pi}{\omega\sqrt{\mu_0\epsilon_0}} = \frac{1}{f\sqrt{\mu_0\epsilon_0}}\,. \tag{3.15}$$

The wavelength *in vacuo*[3] is in a biunivocal correspondence with frequency, therefore, λ_0 can replace f and vice-versa: the wavelength is used prevalently for optical observations, while frequency at microwaves.

The quasi-sinusoid $\mathcal{G}_1$ translates with time, since increasing r makes κr to counterbalance ωt in the argument of the cosine, so as to leave $\mathcal{G}_1$ unchanged. Since $\mathcal{G}_1$ is constant if $kr{-}\omega t$ is constant, the coupled dependence on space and time makes $\mathcal{G}_1$ to move. Therefore, $\mathcal{G}_1$ represents a *wave that propagates*[4]. Figure 3.3 visualizes how $\mathcal{G}_1$ displaces along r to maintain the same values as time progresses from $t = 0$ to $t = T/4$, to $t = T/2$, and so on. The parameter κ, defined in Sect. 3.1.1, which affects the propagation features of the wave, is named *propagation constant*.

By defining the space-time total phase $\Phi_1(\boldsymbol{r}, t) = \Phi(\boldsymbol{r}) - \omega\, t$ of the wave $\mathcal{G}_1$,

[3]The wavelength λ_0 is also called *free-space* wavelength, although, as observed, free space does not generally imply vacuum.

[4]Animations suggestive of wave propagation are available from several web sites such as [3, 4].

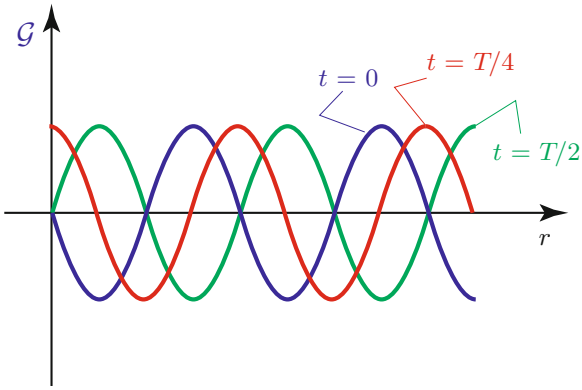

Fig. 3.3 The displacement with time of the sinusoidal potential results in the propagation of the wave

$$\mathcal{G}_1(\boldsymbol{r}, t) = \frac{C_1}{r}\, \mathrm{e}^{-\mathrm{j}\Phi_1(\boldsymbol{r}, t)}$$

represents $\mathcal{G}_1(\boldsymbol{r}, t)$ in the three-dimensional space. The space-time *wave surface* $\Phi_1(\boldsymbol{r}, t)$ is identified, over which the *phase* of $\mathcal{G}_1$ is constant. The shape of the phase surface identifies the type of wave: since, for any t, here $\Phi_1 = const$ for $r = const$, the wave surfaces are spheres centered on the impulsive current, which, therefore, is considered source of a *spherical wave*.[5]

By extending the one-dimensional previous results to the three-dimensional wave surface, $\Phi_1(\boldsymbol{r})$ translates with time, yielding the wave propagation in space. For an elementary time variation $\mathrm{d}t$, the displacement $\mathrm{d}r$ in the radial direction which cancels the total differential of the phase $\Phi_1 = \kappa r - \omega t$ is given by

$$\mathrm{d}\Phi_1 = \kappa\, \mathrm{d}r - \omega\, \mathrm{d}t = 0\ .$$

The *phase velocity* along the radial direction $\mathbf{r}_0$ is derived from this condition

$$\left.\frac{\mathrm{d}r}{\mathrm{d}t}\right|_{\mathbf{r}_0} = \frac{\omega}{\kappa} = u_1\ . \tag{3.16}$$

The *velocity of propagation* $\boldsymbol{u}_1 = u_1 \mathbf{r}_0$ of the wave represented by $\mathcal{G}_1$ is directed along $\mathbf{r}_0$: the wave propagates in the *outward* direction.

The wave surface of $\mathcal{G}_2$, representative of the second term of $\mathcal{G}$ in (3.13), is

$$\Phi_2 = \kappa\, r + \omega t\ .$$

The distance r from the source current must now decrease to counterbalance the increase of phase caused by the elapsing time, so that the condition

[5] In case the shape of the phase surface were plane, the wave would be a *plane wave* (Sect. 4.1).

$$\mathrm{d}\Phi_2 = \kappa\,\mathrm{d}r + \omega\,\mathrm{d}t = 0$$

yields a negative phase velocity of $\mathcal{G}_2$ along $\mathbf{r}_0$

$$u_2 = \left.\frac{\mathrm{d}r}{\mathrm{d}t}\right|_{\mathbf{r}_0} = -\frac{\omega}{\kappa}\,.$$

The negative velocity of propagation $\boldsymbol{u}_2 = -(\omega/\kappa)\,\mathbf{r}_0 = -\boldsymbol{u}_1$ indicates that the wave represented by $\mathcal{G}_2$ is directed inward, toward the "source". In conclusion, the two terms formally composing the scalar Green's function (3.13) represent two spherical waves which propagate in opposite directions: one, $\mathcal{G}_1$, travels outward, the other, $\mathcal{G}_2$, goes inward. Since the field is caused by a source placed in the origin of coordinates, the collapsing wave $\mathcal{G}_2$ does not meet the physical conditions of existence and must be disregarded, i.e., $C_2 = 0$, so that (3.13) reduces to

$$\mathcal{G}(r) = \frac{C}{r}\,\mathrm{e}^{-\mathrm{j}\kappa\, r}\,.$$

The wave amplitude C is readily determined as

$$C = \frac{1}{4\pi}$$

because the source is unitary, so that the scalar Green's function is finally found to be

$$\mathcal{G}(r) = \frac{1}{4\pi}\,\frac{\mathrm{e}^{-\mathrm{j}\kappa r}}{r}\,.$$

In general, the location of the point source is not the origin of coordinates, rather $\boldsymbol{r}'$: then a translation of coordinates yields

$$\mathcal{G}(\boldsymbol{r}-\boldsymbol{r}') = \frac{\mathrm{e}^{-\mathrm{j}\kappa(|\boldsymbol{r}-\boldsymbol{r}'|)}}{4\pi(|\boldsymbol{r}-\boldsymbol{r}'|)} = \frac{\mathrm{e}^{-\mathrm{j}\kappa R}}{4\pi R}\,, \tag{3.17}$$

where $R = |\boldsymbol{r}-\boldsymbol{r}'|$ is the relative distance between source and observation points. The expression (3.17) represents[6] a spherical wave emanating from $\boldsymbol{r}'$.

It is interesting to note the symmetry of $\mathcal{G}$ with respect to $\boldsymbol{r}$ and $\boldsymbol{r}'$: this feature implies *reciprocity*, in the sense that the measured field does not change if the location of the source is interchanged with the point where the field is observed.

[6]Several resources of the web provide visual representation of basic electromagnetic concepts, in addition to wave propagation; examples and links to further educational sites are found at [7, 9, 12], to mention just a few.

3.1.1.3 Doppler Effect

The results of Sect. 3.1.1.2 indicate that space-time Green's function

$$\mathcal{G}(R,t) = \Re\left[\frac{1}{4\pi R}\mathrm{e}^{-\mathrm{j}(\kappa_\mathrm{s} R - \omega_\mathrm{s} t)}\right]$$

represents the wave observed in the static case at a given distance R from a point source originating electromagnetic radiation at angular frequency $\omega_\mathrm{s} = 2\pi f_\mathrm{s}$ with corresponding propagation constant $\kappa_\mathrm{s} = \omega_\mathrm{s}\sqrt{\mu_0\epsilon}$. Assume now that the source does not remain at a fixed point, but moves with uniform velocity $\boldsymbol{u}_\mathrm{s}$ with respect to the reference system sketched in Fig. 3.1. The distance R of the source located in $\boldsymbol{r}'(t)$ from a *stationary* observation point P located in $\boldsymbol{r}$ changes with time according to

$$R(t) = R_0 - \boldsymbol{u}_\mathrm{s}\cdot\boldsymbol{R}_0\, t\ ,$$

where R_0 is a reference initial distance and $\mathbf{R}_0$ is the versor of $\boldsymbol{r} - \boldsymbol{r}'$. Then the space-time Green's function in the dynamic case is

$$\begin{aligned}\mathcal{G}(R,t) &= \Re\left[\frac{1}{4\pi R}\mathrm{e}^{-\mathrm{j}[\kappa_\mathrm{s}(R_0 - \boldsymbol{u}_\mathrm{s}\cdot\mathbf{R}_0\, t) - \omega_\mathrm{s} t]}\right] \\ &= \frac{1}{4\pi R}\cos\left[\kappa_\mathrm{s} R_0 - (\omega_\mathrm{s} + \kappa_\mathrm{s}\,\boldsymbol{u}_\mathrm{s}\cdot\mathbf{R}_0)\, t\right]\ . \end{aligned} \tag{3.18}$$

Equation (3.18) shows that the angular frequency of the wave observed in P is

$$\omega = \omega_\mathrm{s} + \kappa_\mathrm{s}\,\boldsymbol{u}_\mathrm{s}\cdot\mathbf{R}_0$$

i.e., differs from the one, ω_s, at the source by a shift

$$\omega_\mathrm{D} = \kappa_\mathrm{s}\,\boldsymbol{u}_\mathrm{s}\cdot\mathbf{R}_0\ .$$

The corresponding frequency shift

$$f_\mathrm{D} = \frac{\omega_\mathrm{D}}{2\pi} = \omega_\mathrm{s}\sqrt{\mu_0\epsilon}\,\frac{\boldsymbol{u}_\mathrm{s}\cdot\mathbf{R}_0}{2\pi} = \mathbf{R}_0\cdot\frac{\boldsymbol{u}_\mathrm{s}}{u} f_\mathrm{s} \tag{3.19}$$

is named *Doppler shift*. The shift is proportional to the *radial* velocity of the source relative to the observation point normalized to the velocity of propagation u of the electromagnetic wave, as derived from (3.16).

Inspection of (3.19) points out that

– the frequency of the observed radiation is increased when $\boldsymbol{u}_\mathrm{s}\cdot\mathbf{R}_0 > 0$, i.e., when the source moves *towards* the observation point,

– while the observed frequency is lower for sources pulling away;
– no shift is present when the source moves transversely ($\boldsymbol{u}_\mathrm{s} \cdot \mathbf{R}_0 = 0$) to the direction of observation.

Given (3.14), the shift of frequency induced by the Doppler effect translates into corresponding wavelength shift: the radiation of an approaching source exhibits shorter wavelengths, whereas the radiation of receding sources is shifted towards longer λ.

It is worth emphasizing that the Doppler effect depends on the *relative* radial velocity between source and observation point. This implies that the effect is as well observed when the measuring location approaches or moves away from a stationary source, or, in general, for any dynamic state, when the relative motion has a component in the direction passing through source and observation points. The Doppler effect is widely exploited in remote sensing, especially by radar systems.

3.1.2 Wave Interference

Coming back to the spectral domain for the static case, the vector potential at a point $\boldsymbol{r}$ created by an *extended* source $\boldsymbol{J}_\mathrm{s}(\boldsymbol{r}')$ acting in the source volume V' is obtained by spatial convolution:

$$\mathfrak{A}(\boldsymbol{r}) = \iiint_{V'} \frac{\mathrm{e}^{-\mathrm{j}\kappa(|\boldsymbol{r}-\boldsymbol{r}'|)}}{4\pi(|\boldsymbol{r}-\boldsymbol{r}'|)} \boldsymbol{J}_\mathrm{s}(\boldsymbol{r}')\,\mathrm{d}V' \,, \tag{3.20}$$

in other words, it derives from the addition of the complex vector contributions from the various (elementary) parts $\mathrm{d}V'$ of the source V'. The electromagnetic field is said to derive from the *interference*, i.e., from the superposition with their respective amplitudes and phases, of elementary spherical waves originating from the source elements $\boldsymbol{J}_\mathrm{s}\,\mathrm{d}V'$.

The role played by the relative phases of the interfering waves is crucial in determining the field. Assume that two elements $\boldsymbol{J}_\mathrm{s}(\boldsymbol{r}'_1) = J_{\mathrm{s}1}\,\mathbf{j}_0$ and $\boldsymbol{J}_\mathrm{s}(\boldsymbol{r}'_2) = J_{\mathrm{s}2}\,\mathbf{j}_0$ of the extended source contribute two elementary waves $\mathcal{G}_1$ and $\mathcal{G}_2$ having the same amplitude C, but different phases[7] Φ_1 and Φ_2 at a point $\boldsymbol{r}$. The vector potential $\mathfrak{A}(\boldsymbol{r})$ is

$$\mathfrak{A}(\boldsymbol{r}) = C\left[\mathrm{e}^{-\mathrm{j}\Phi_1} + \mathrm{e}^{-\mathrm{j}\Phi_2}\right]\mathbf{j}_0 \,.$$

The modulus of $\mathfrak{A}$ is

[7] The phases may differ either because of the different phases of the source current or because of the different distance, as outlined later.

$$|\mathfrak{A}| = 2C\cos\left(\frac{\Phi_2 - \Phi_1}{2}\right),$$

hence $|\mathfrak{A}|$, and correspondingly the field in $\boldsymbol{r}$, changes dramatically according to the relative phases of the *interfering* elementary contributions. In particular, it spans the range from

$$|\mathfrak{A}| = 0 \qquad \text{for} \quad \Phi_2 = \Phi_1 + (2n+1)\pi, \quad n = 0, 1, 2, \ldots$$

i.e., when *destructive interference* occurs, to

$$|\mathfrak{A}| = 2C \qquad \text{for} \quad \Phi_2 = \Phi_1 + 2n\pi, \quad n = 0, 1, 2, \ldots$$

for *constructive interference*.

The combination of the single contributions is effectively visualized by the corresponding phasors in the $\{\Re\ \Im\}$ complex plane depicted in Fig. 3.4. The phasors $\tilde{\mathcal{G}}_1$ and $\tilde{\mathcal{G}}_2$ produce a resulting phasor $\tilde{\mathcal{G}}$ the modulus of which depends on the angle *in the complex plane*,[8] i.e., on the phase difference $\Phi_1 - \Phi_2$ between $\tilde{\mathcal{G}}_1$ and $\tilde{\mathcal{G}}_2$, as sketched in Fig. 3.4a. The resultant $\tilde{\mathcal{G}}$ vanishes when $\Phi_2 = \Phi_1 + \pi$ as in Fig. 3.4b, while $\left|\tilde{\mathcal{G}}\right| = \left|\tilde{\mathcal{G}}_1\right| + \left|\tilde{\mathcal{G}}_2\right|$, when $\Phi_2 = \Phi_1$, as shown in Fig. 3.4c.

For the extended source, constructive interference yielding field maxima occurs where the elementary spherical waves emanating from the various portions of the source arrive with the same, or close, phase values, whereas the field is low where destructive interference between elementary spherical waves with close amplitudes and opposite phases occurs. The interfering elementary waves have amplitude and phase determined not only by the local amplitude and phase of the source current, but mainly by the distance $R = |\boldsymbol{r} - \boldsymbol{r}'|$ traveled. The phase Φ_R added by the traveled distance is

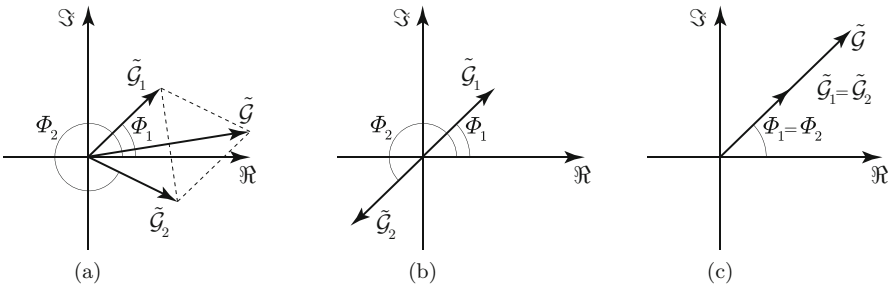

Fig. 3.4 Phasor representation of wave interference in the complex plane (**a**), with the destructive (**b**) and constructive (**c**) limiting cases

[8] The complex plane, which is a *mathematical* entity having the purpose of representing complex quantities, should not be mistaken for a plane belonging to the *"physical"* 3-D space.

$$\Phi_R = \kappa R = \frac{2\pi}{\lambda} R \,,$$

so that the phases of the waves originated from a pair of source elements differ by

$$\Delta\Phi_R = 2\pi \frac{\Delta R}{\lambda} \,, \tag{3.21}$$

where ΔR is the difference of distance between the source elements and the point in which the field is measured. Equation (3.21) points out the crucial role played by the ratio between the dimension of the source and the wavelength: for a given source geometry, interference effects are generally enhanced by increasing frequency, hence by decreasing wavelength. On the contrary, sources that are small with respect to wavelength are characterized by reduced or no interference, This concept is recalled in Sect. 7.2.1 with regard to scattering.

In summary, the spatial pattern of the field of an extended source, being produced through the interference mechanism, depends on

- shape and dimensions of the volume occupied by the source;
- amplitude, polarization, and phase distribution of the source current;
- frequency.

When interpreting the scattering behavior of natural and man-made objects, or when analyzing the features of the field radiated by an antenna, the manifold basic effects of the above parameters must be carefully considered.

The reader will have remarked the deterministic approach that has been followed in outlining the interference between a pair of monochromatic waves the relative phase of which has been assumed fixed. This is the reference approach, suitable to firmly clarify the basic concepts. However, it is worth pointing out that in Earth observation, the waves are quasi-monochromatic, so that the phase of one field fluctuates randomly with respect to the other. This may happen because of random fluctuations of the propagation medium, or when the source itself is partially coherent, or the observed fields originate from a random scattering process. Non-negligible effects can ensue, as outlined in Sect. 4.3.2 and detailed in Sect. 12.3.2 for a specific observation technique.

3.1.3 Field of Point Source

An elementary source is modeled by an impressed current density concentrated in the point $\boldsymbol{r}'$ of the source space:

$$\boldsymbol{J}_s = \mathcal{M}\,\delta(\boldsymbol{r}')\mathbf{j}_0 \,.$$

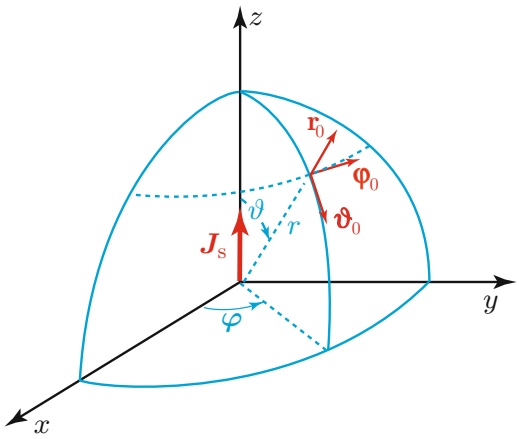

Fig. 3.5 Point source current $\boldsymbol{J}_s = J_s\,\mathbf{z}_0$ and unit vectors $\mathbf{r}_0$, $\boldsymbol{\vartheta}_0$, $\boldsymbol{\varphi}_0$ in a spherical coordinate system

The *momentum* $\boldsymbol{\mathcal{M}} = \mathcal{M}\,\mathbf{j}_0$ contains the information on the intensity and polarization of the source current. Assume $\boldsymbol{\mathcal{M}} = \mathcal{M}\,\mathbf{z}_0$ directed along the polar axis of the spherical coordinate system centered on the source, represented in Fig. 3.5. The vector potential (3.20) is parallel to the single-direction source current:

$$\mathfrak{A}(\boldsymbol{r}) = \mathcal{G}(\boldsymbol{r})\,\boldsymbol{\mathcal{M}} = \frac{\mathrm{e}^{-\mathrm{j}\kappa r}}{4\pi r}\mathcal{M}\,\mathbf{z}_0\,.$$

By definition (3.3), the magnetic field depends directly on the three-dimensional spatial variation (Sect. A.3.4.3) of the vector potential $\mathfrak{A}$. Given the axial symmetry of the source, the produced field is expected to be independent on the azimuth angle φ, so that, by suitable manipulation of the curl operator in spherical coordinates (A.29),

$$\boldsymbol{H}(\boldsymbol{r}) = \frac{\mathrm{j}\kappa\mathcal{M}}{4\pi r}\left(1 + \frac{1}{\mathrm{j}\kappa r}\right)\mathrm{e}^{-\mathrm{j}\kappa r}\sin\vartheta\;\boldsymbol{\varphi}_0\,. \tag{3.22}$$

In turn, the electric field is directly related to the spatial variations of the magnetic field, since, from the second Maxwell's equation,

$$\boldsymbol{E}(\boldsymbol{r}) = \frac{1}{\mathrm{j}\omega\epsilon}\nabla\times[H(r,\vartheta)\;\boldsymbol{\varphi}_0]\,.$$

Taking again the axial symmetry into account,

$$\begin{aligned}\boldsymbol{E}(\boldsymbol{r}) = {} & \frac{\mu_0\mathcal{M}}{2\pi\epsilon\, r^2}\left(1 + \frac{1}{\mathrm{j}\kappa r}\right)\mathrm{e}^{-\mathrm{j}\kappa r}\cos\vartheta\;\mathbf{r}_0 \\ & + \frac{\mathrm{j}\omega\mu_0\mathcal{M}}{4\pi r}\left(1 + \frac{1}{\mathrm{j}\kappa r} - \frac{1}{\kappa^2 r^2}\right)\mathrm{e}^{-\mathrm{j}\kappa r}\sin\vartheta\;\boldsymbol{\vartheta}_0\,.\end{aligned} \tag{3.23}$$

Equations (3.22) and (3.23) show that

- the magnetic field has the only $\boldsymbol{\varphi}_0$ component, hence is orthogonal to the plane formed by the source current and by the radial direction[9];
- the electric field is parallel to the source current, i.e., it lies in the meridian plane containing the radial direction.

Both electric and magnetic fields are given by sums of terms containing powers of different order of $\kappa r = 2\pi(r/\lambda)$. This feature implies that the high-order or low-order terms prevail according to the ratio between distance r and wavelength λ. The ratio affects in a crucial fashion the properties of the electromagnetic field produced by the source, because

- at distances "short" *with respect to wavelength*, electric and magnetic fields have a complicate phase dependence on distance, with steeply decreasing amplitudes;
- at "far" (always with respect to wavelength) distances, the low-order terms prevail, $E_r \ll E_\vartheta$, and the fields regularize as

$$\boldsymbol{E}(\boldsymbol{r}) \simeq \mathrm{j}\frac{\sqrt{\mu_0}\mathcal{M}}{2\sqrt{\epsilon}\lambda r}\mathrm{e}^{-\mathrm{j}\kappa r}\sin\vartheta\ \boldsymbol{\vartheta}_0\ ; \qquad \boldsymbol{H}(\boldsymbol{r}) \simeq \frac{\mathrm{j}\mathcal{M}}{2\lambda r}\mathrm{e}^{-\mathrm{j}\kappa r}\sin\vartheta\ \boldsymbol{\varphi}_0\ . \tag{3.24}$$

The *far* field, i.e., the field for $r \gg \lambda$, exhibits the fundamental properties:

- it is directly proportional to the component of the source current density orthogonal to the radial direction $\mathbf{r}_0$, so that
  - in the direction of the current (z-axis, $\vartheta = 0$) the field vanishes,
  - whereas $\boldsymbol{E}$ and $\boldsymbol{H}$ are maximum on the equatorial plane $\vartheta = \dfrac{\pi}{2}$;
- the field amplitude is
  - directly proportional to frequency,
  - inversely proportional to distance r;
- a direct relation exists between magnetic and electric fields, i.e.,

$$\boldsymbol{H} = \frac{\mathbf{r}_0 \times \boldsymbol{E}}{\eta}\ ,$$

where

$$\eta := \sqrt{\frac{\mu_0}{\epsilon}} \tag{3.25}$$

is the *intrinsic impedance* of the material in which the field is considered.

[9] The source current is linearly polarized and located in the origin of coordinates.

In regions far from the source, the expression of the Poynting vector

$$\boldsymbol{\mathcal{P}} = \frac{1}{2}\boldsymbol{E} \times \boldsymbol{H}^* = \frac{\boldsymbol{E} \cdot \boldsymbol{E}^*}{2\eta}\,\mathbf{r}_0 = \frac{\eta|\mathcal{M}|^2}{8\lambda^2 r^2}\sin^2\vartheta\,\mathbf{r}_0 \tag{3.26}$$

indicates that

- power travels in the radial direction;
- the areic power density $\mathcal{P}$ carried by the field
  - depends directly on the square of frequency,
  - depends inversely on the square of distance.

Therefore, the power that crosses a given elementary surface $\mathrm{d}S$ perpendicular to the direction $\mathbf{r}_0$ at an angle ϑ with the direction of the source current is

$$\mathrm{d}W = \boldsymbol{\mathcal{P}} \cdot \mathbf{r}_0\,\mathrm{d}S = \mathcal{P}\,\mathrm{d}S = \frac{\eta|\mathcal{M}|^2}{8\lambda^2}\sin^2\vartheta\,\frac{\mathrm{d}S}{r^2}\,,$$

hence, $\mathrm{d}W$ decreases as r^{-2}. With reference to the elementary solid angle $\mathrm{d}\Omega$ under which $\mathrm{d}S$ is seen from the source represented in Fig. 3.6,

$$\mathrm{d}W = \frac{\eta|\mathcal{M}|^2}{8\lambda^2}\sin^2\vartheta\,\mathrm{d}\Omega\,,$$

which implies that the *angular* power density $\mathcal{P}$, i.e., the power traveling within a cone with vertex on the source,

$$\mathcal{P} = \frac{dW}{d\Omega} = \frac{\eta|\mathcal{M}|^2}{8\lambda^2}\sin^2\vartheta\,,$$

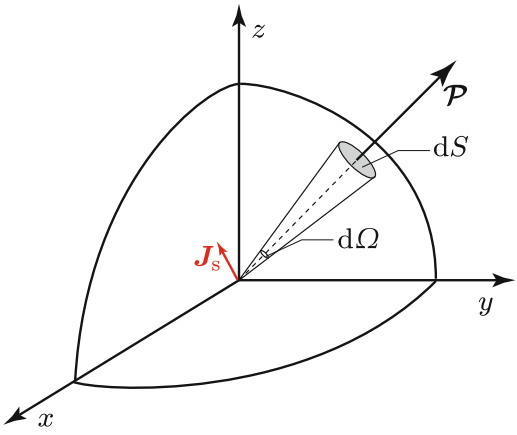

Fig. 3.6 The far-range power per unit solid angle does not vary with distance in lossless materials

is independent of distance. Therefore, far from the source, in a lossless medium, the *angular* power density $\mathcal{P}$ [W sr^{-1}] remains constant, whereas the *surface* power density $\mathcal{P}$ [W m^{-2}] decreases. The result is obviously consistent with the outcome of the Poynting's theorem discussed in Sect. 1.2.5.1.

3.1.4 Field of Finite-Dimension Sources

The radiation utilized in Earth observation originates from extended sources such as the Sun or a radar antenna. The measured radiation also originates from extended sources modeling reflecting or scattering materials.

To determine the field originated by the general three-dimensional sources, consider the spatial distribution of source electrical currents $\boldsymbol{J}_s(\boldsymbol{r}')$ acting in the volume V' sketched in Fig. 3.7. The electromagnetic field in the lossless free space is derived from the vector potential $\mathfrak{A}(\boldsymbol{r})$. According to (3.3) and (3.20), the magnetic field is

$$\boldsymbol{H}(\boldsymbol{r}) = \nabla \times \iiint_{V'} \boldsymbol{J}_s(\boldsymbol{r}')\, \mathcal{G}(R)\, \mathrm{d}V' \,, \tag{3.27}$$

where $R = |\boldsymbol{r} - \boldsymbol{r}'|$ is the distance from the *source point* identified by $\boldsymbol{r}'$, where the source current is located, to the *observation point* P, identified by $\boldsymbol{r}$, where the field is measured or computed. Since the curl (with respect to the observation coordinates $\boldsymbol{r}$) and integration (with respect to the source coordinates $\boldsymbol{r}'$) operators commute, (3.27) becomes

$$\boldsymbol{H}(\boldsymbol{r}) = \iiint_{V'} \nabla \times \left[\boldsymbol{J}_s(\boldsymbol{r}')\, \mathcal{G}(R)\right] \mathrm{d}V' \,, \tag{3.28}$$

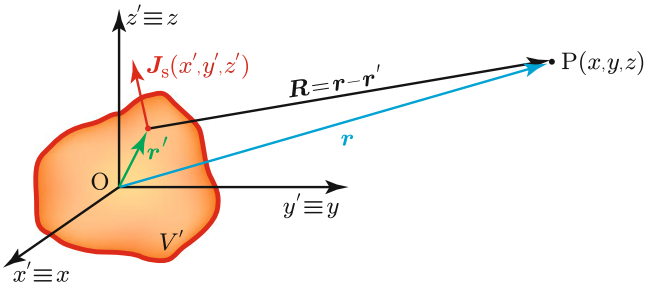

Fig. 3.7 Extended source $\boldsymbol{J}_s(\boldsymbol{r}')$ distributed in the volume V' described by the source coordinates x', y', z', and point P$(\boldsymbol{r})$ identified by the observation coordinates x, y, z, where the field is measured

where, given (A.33) and the independence of $\boldsymbol{J}_s$ from $\boldsymbol{r}$,

$$\nabla \times \left[\boldsymbol{J}_s(\boldsymbol{r}')\, \mathcal{G}(R)\right] = \nabla \mathcal{G}(R) \times \boldsymbol{J}_s(\boldsymbol{r}') \, .$$

The gradient of the Green's function is

$$\begin{aligned} \nabla \mathcal{G}(R) &= \frac{\partial}{\partial R} \frac{\mathrm{e}^{-\mathrm{j}\kappa R}}{4\pi R} \mathbf{R}_0 = \left(-\mathrm{j}\kappa \frac{\mathrm{e}^{-\mathrm{j}\kappa R}}{4\pi R} - \frac{1}{R} \frac{\mathrm{e}^{-\mathrm{j}\kappa R}}{4\pi R}\right) \mathbf{R}_0 \\ &= -\left(\mathrm{j}\kappa + \frac{1}{R}\right) \frac{\mathrm{e}^{-\mathrm{j}\kappa R}}{4\pi R} \mathbf{R}_0 \, . \end{aligned} \tag{3.29}$$

The gradient expresses the rate of spatial change of the quantity on which it operates. The Green's function depends on the traveled distance through the function κR at the exponent and $4\pi R$ at the denominator. Therefore, the variations with distance of both phase and amplitude contribute to the gradient, resulting in the two factors of (3.29):

- the first is independent of distance R and inversely proportional to the wavelength $\lambda = 2\pi/\kappa$,
- while the second is inversely proportional to R.

3.1.4.1 The Far Field

It is important to note that the relative contribution by each term depends on $\kappa R = 2\pi(R/\lambda)$, therefore, as in Sect. 3.1.3, the ratio of distance to wavelength has a crucial impact on the field. In fact, the variation of $\mathcal{G}$ is essentially due to the phase change with distance when $R \gg \lambda$, so that the expression simplifies into

$$\boldsymbol{H}(\boldsymbol{r}) \simeq -\mathrm{j}\kappa \iiint_{V'} \frac{\mathrm{e}^{-\mathrm{j}\kappa R}}{4\pi R} \mathbf{R}_0 \times \boldsymbol{J}_s(\boldsymbol{r}')\, \mathrm{d}V' \, . \tag{3.30}$$

On its side, the dimension of the source compared both with the distance and with the wavelength, has also a quite important impact on the field:

- First, when the distance is large with respect to the maximum *transverse* dimension D_s of the source, then

  $$\mathbf{R}_0 \simeq \mathbf{r}_0 \quad \text{and} \quad R \simeq r \qquad \text{in } V' \, ,$$

  where $\mathbf{r}_0$ and r are fixed quantities referred to the "center" of the source, conveniently assumed as origin of coordinates. This approximation further simplifies (3.30) in

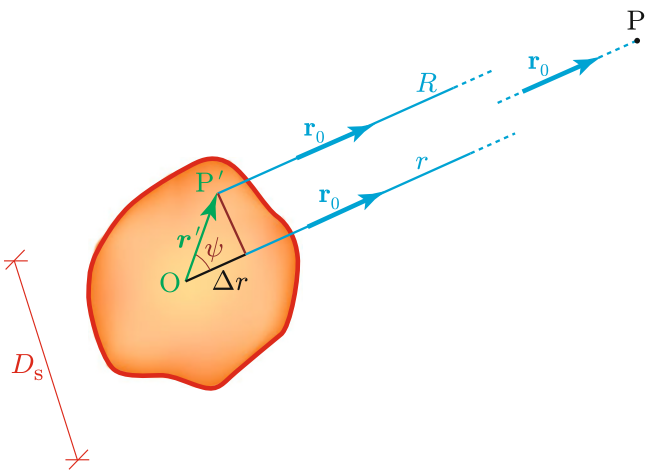

Fig. 3.8 Geometry for the far-distance approximation

$$\boldsymbol{H}(\boldsymbol{r}) \simeq -\frac{\mathrm{j}\kappa}{4\pi r}\,\mathbf{r}_0 \times \iiint_{V'} \boldsymbol{J}_\mathrm{s}(\boldsymbol{r}')\,\mathrm{e}^{-\mathrm{j}\kappa R}\,\mathrm{d}V' \ .$$

– Second, at distances large enough to satisfy the condition $R \gg 2D_\mathrm{s}^2/\lambda$, the segments that connect the source points P′ to the observation point P can be regarded as parallel (Fig. 3.8) and R approximated by a linear function of the source coordinates:

$$R \simeq r - r'\cos\psi = r - r'(\mathbf{r}_0' \cdot \mathbf{r}_0) \ .$$

Note that all the requirements involving distance, source dimension and wavelength are usually satisfied in Earth observation.

Once the conditions are met, that occurs theoretically for $r \to \infty$ and any finite-dimension sources, the far field is

$$\boldsymbol{H}_\infty(\boldsymbol{r}) = \lim_{r\to\infty} \boldsymbol{H}(\boldsymbol{r}) = -\mathrm{j}\kappa\,\frac{\mathrm{e}^{-\mathrm{j}\kappa r}}{4\pi r}\,\mathbf{r}_0 \times \iiint_{V'} \boldsymbol{J}_\mathrm{s}(\boldsymbol{r}')\,\mathrm{e}^{\mathrm{j}\kappa \boldsymbol{r}'\cdot\mathbf{r}_0}\,\mathrm{d}V' \ ; \tag{3.31}$$

$$\boldsymbol{E}_\infty(\boldsymbol{r}) = \lim_{r\to\infty} \boldsymbol{E}(\boldsymbol{r}) = \mathrm{j}\omega\mu_0\,\frac{\mathrm{e}^{-\mathrm{j}\kappa r}}{4\pi r}\,\mathbf{r}_0 \times \left[\mathbf{r}_0 \times \iiint_{V'} \boldsymbol{J}_\mathrm{s}(\boldsymbol{r}')\,\mathrm{e}^{\mathrm{j}\kappa \boldsymbol{r}'\cdot\mathbf{r}_0}\,\mathrm{d}V'\right] \ . \tag{3.32}$$

Given the properties of the cross product (Sect. A.1.2.2), only the components of the source current perpendicular to $\mathbf{r}_0$ contribute to the far field. Both Eqs. (3.31) and (3.32) contain the integral expressing the interference of the waves originating from the elements $\mathrm{d}V'$ of the source volume V', as discussed previously in Sect. 3.1.2. The contributions by the distributed impressed current add construc-

tively to enhance the field or interfere destructively to quench it, depending on the direction $\mathbf{r}_0$ in which the field is being radiated. The exponential $\exp(\mathrm{j}\kappa\, \boldsymbol{r}' \cdot \mathbf{r}_0)$ in (3.31) and (3.32) can be referred as the *diffraction phase factor*.

3.1.4.2 Properties of Field and Power at Far Distance

The *far field* (3.32) of an extended source, which is written in the compact form

$$\boldsymbol{E}_\infty(\boldsymbol{r}) = \frac{\mathrm{e}^{-\mathrm{j}\kappa r}}{r}\, \mathcal{F}(\vartheta, \varphi)\,, \tag{3.33}$$

has properties analogous to those of the point source, since it consists of the product of two factors:

- a spherical wave, with wave surface $\Phi(r) = \kappa r$ and with an r^{-1} dependence of amplitude on distance;
- a complex vector term $\mathcal{F}$, which is a *directional pattern* function of the angular coordinates ϑ, φ that identify the versor $\mathbf{r}_0$ pointing in the direction in which the field is observed, directly proportional to frequency and independent of distance.

Moreover, $\boldsymbol{E}_\infty$, $\boldsymbol{H}_\infty$, and $\mathbf{r}_0$ are mutually transverse and interrelated by the intrinsic impedance η of the material:

$$\boldsymbol{H}_\infty = \frac{\mathbf{r}_0 \times \boldsymbol{E}_\infty}{\eta}\,. \tag{3.34}$$

Figure 3.9 shows the systems of cartesian coordinates x', y', z' on which the features of the source depend, and of spherical coordinates r, ϑ, φ centered on the source, on which the radiated field depends. The electric field which lies in the plane

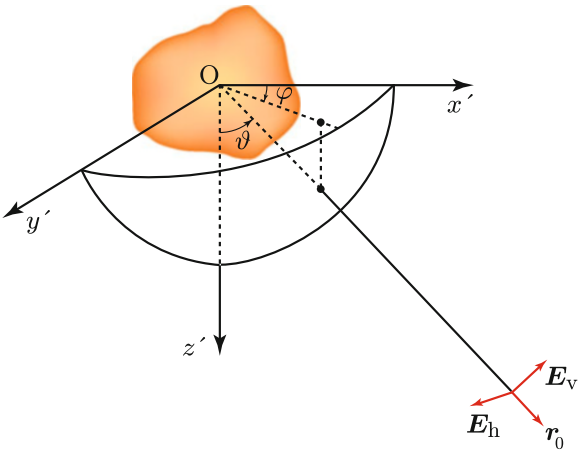

Fig. 3.9 The radiated field is represented in the spherical coordinate system (r, ϑ, φ) different from the one, for instance (x', y', z'), of the source, and the field components $\boldsymbol{E}_\mathrm{h}, \boldsymbol{E}_\mathrm{v}$ are defined with respect to a further reference (e.g., the Earth's surface, as in Fig. 4.3)

perpendicular to $\mathbf{r}_0$ is also sketched, with the pair of components $\boldsymbol{E}_\mathrm{v}$ and $\boldsymbol{E}_\mathrm{h}$ introduced later in Sect. 4.2.1 and represented in Fig. 4.3, able to represent any polarization (Sect. 1.3.1.1). Given the properties of the far field, the radial direction $\mathbf{r}_0$, locally perpendicular to the wave surface $\Phi = const$, coincides with the direction along which the radiated power flows. This feature is further discussed in Sect. 5.2 in a more general context.

The vector directional pattern in a *lossless* material characterized by parameters μ_0 and ϵ and in which the field at angular frequency ω has wavelength λ, is readily written

$$\begin{aligned}\mathcal{F}(\vartheta,\varphi) &= \mathrm{j}\frac{\omega\mu_0}{4\pi}\,\mathbf{r}_0\times\left[\mathbf{r}_0\times\iiint_{V'}\boldsymbol{J}_\mathrm{s}(\boldsymbol{r}')\,\mathrm{e}^{\mathrm{j}\kappa\boldsymbol{r}'\cdot\mathbf{r}_0}\,\mathrm{d}V'\right]\\ &= \mathrm{j}\frac{\eta}{2\lambda}\,\mathbf{r}_0\times\left[\mathbf{r}_0\times\iiint_{V'}\boldsymbol{J}_\mathrm{s}(\boldsymbol{r}')\,\mathrm{e}^{\mathrm{j}\kappa\boldsymbol{r}'\cdot\mathbf{r}_0}\,\mathrm{d}V'\right]. \qquad (3.35)\end{aligned}$$

In turn, the power density is expressed in terms of the vector directional pattern $\mathcal{F}$ by

$$\begin{aligned}\mathcal{P}_\infty &= \frac{1}{2}\boldsymbol{E}_\infty\times\boldsymbol{H}^*_\infty = \frac{\boldsymbol{E}_\infty\cdot\boldsymbol{E}^*_\infty}{2\eta}\,\mathbf{r}_0 = \frac{\mathcal{F}\cdot\mathcal{F}^*}{2\,\eta\,r^2}\,\mathbf{r}_0\\ &= \frac{\eta}{8\lambda^2 r^2}\left|\mathbf{r}_0\times\left[\mathbf{r}_0\times\iiint_{V'}\boldsymbol{J}_\mathrm{s}(\boldsymbol{r}')\,\mathrm{e}^{\mathrm{j}\kappa\boldsymbol{r}'\cdot\mathbf{r}_0}\,\mathrm{d}V'\right]\right|^2\mathbf{r}_0\,.\end{aligned}$$

The power $\mathcal{P}_\infty$ carried by the far field across the unit surface has the same expression as the one (3.26) of the point source along z, with $\mathcal{F}$ in place of $\mathcal{M}\sin\vartheta$. As predicted by the Poynting's theorem and consistently with the energy conservation, $\mathcal{P}_\infty$ decreases as r^{-2}, while the power per unit angle $\mathcal{P}_\infty = r^2\mathcal{P}_\infty$ in a given direction remains the same at any (far) distance. From the field and power point of view, an extended source at far distance behaves like a point source. The only, albeit crucial, difference resides in the directional pattern, that is, in the way the source distributes the radiated power in the various directions. The vector angular pattern $\mathcal{F}$ characterizing the radiating directional properties of the extended source depends on the spatial features of the latter and obviously differs from that of the point source.

3.1.4.3 Radiation Parameters

The radiant properties of any source[10] are contained in the complex vector radiation function independent of distance (3.35) since, for a given frequency,the spherical

[10]Equation (3.35) refers explicitly to an electric source, but, based on duality (Sect. 1.1.3.1), analogous expressions hold for magnetic or mixed-type sources.

wave factor in the field expression (3.33) does not depend on the features of the source. The *field radiation pattern*

$$\boldsymbol{\mathcal{F}}(\vartheta,\varphi) = r\,\mathrm{e}^{\mathrm{j}\kappa r}\,\boldsymbol{E}_\infty(r,\vartheta,\varphi) = \mathcal{F}_\vartheta(\vartheta,\varphi)\boldsymbol{\vartheta}_0 + \mathcal{F}_\varphi(\vartheta,\varphi)\boldsymbol{\varphi}_0 \tag{3.36}$$

provides information on how the amplitude and polarization of the far field vary with the direction identified by the pair of angles ϑ, φ. The polarimetric characterization of radiation is not always required in Earth observation. When only the directional variation of the power density is of interest, the *power radiation pattern* $\mathcal{P}$ is used. The scalar function $\mathcal{P}$ is obtained from the areic power $\mathcal{P}$ by removing its r^{-2} dependence on distance and is readily related to the field radiation pattern by

$$\mathcal{P}(\vartheta,\varphi) := r^2\,\mathcal{P}(r,\vartheta,\varphi) = r^2 \cdot \frac{1}{2}\,|\boldsymbol{E}_\infty \times \boldsymbol{H}^*_\infty| = \frac{1}{2\eta}\,|\boldsymbol{\mathcal{F}}(\vartheta,\varphi)|^2 \ . \tag{3.37}$$

The total power W_T radiated by the source is directly obtained through the Poynting theorem by computing the flow of power across a spherical far surface centered on the source[11]

$$W_\mathrm{T} = \int_0^{2\pi}\int_0^{\pi} \frac{1}{2}\,\boldsymbol{E}_\infty \times \boldsymbol{H}^*_\infty \cdot \mathbf{r}_0\, r^2 \sin\vartheta\,\mathrm{d}\vartheta\,\mathrm{d}\varphi \ . \tag{3.38}$$

Taking the definition (3.37) into account,

$$W_\mathrm{T} = \int_0^{2\pi}\int_0^{\pi} \mathcal{P}(\vartheta,\varphi)\sin\vartheta\,\mathrm{d}\vartheta\,\mathrm{d}\varphi = \iint_{4\pi} \mathcal{P}(\vartheta,\varphi)\,\mathrm{d}\Omega \ , \tag{3.39}$$

which shows that the power radiation pattern coincides with the *angular* power density

$$\mathcal{P}(\vartheta,\varphi) = \frac{\mathrm{d}W(\vartheta,\varphi)}{\mathrm{d}\Omega} \tag{3.40}$$

radiated into the elementary cone with vertex on the source "center", and axis in the ϑ, φ direction. At far distance, the center of the finite-dimension source takes the place of the point source considered in Sect. 3.1.3. In the lossless case, the angular power density $\mathcal{P}$ does not depend on distance, as observed in Sect. 3.1.4.2. This feature leads to the introduction of the radiance (8.17).

[11] The approach holds for a lossless medium as in Sect. 1.2.5.1.

3.2 Reciprocity and Equivalence

To conclude the overview of the basic properties of electromagnetic sources and of the radiation they produce, some relations relative to reciprocity of basic importance in Earth observation will be summarized. The equivalent currents will also be introduced, given the fundamental role they play in modeling primary and secondary sources of radiation.

3.2.1 Reciprocity

The structure of the Green's function considered in Sect. 3.1.1.2 has already hinted at reciprocity, since it implies the invariance of the free-space field with respect to exchanging source and measurement positions. By manipulating the respective Maxwell's equations, general analytic relations are obtained which relate in a reciprocal fashion the fields produced by *two* sources. Figure 3.10 represents two monochromatic[12] sources A_1 and A_2, generally including both electric and magnetic impressed currents at the same frequency, which radiate into linear and isotropic media. The field of the first source A_1 satisfies Maxwell's equations:

$$\nabla \times \boldsymbol{E}_1 = -\mathrm{j}\omega\mu \boldsymbol{H}_1 - \boldsymbol{J}_{\mathrm{ms1}} \; ; \tag{3.41}$$

$$\nabla \times \boldsymbol{H}_1 = \mathrm{j}\omega\epsilon \boldsymbol{E}_1 + \boldsymbol{J}_{\mathrm{s1}} \; ; \tag{3.42}$$

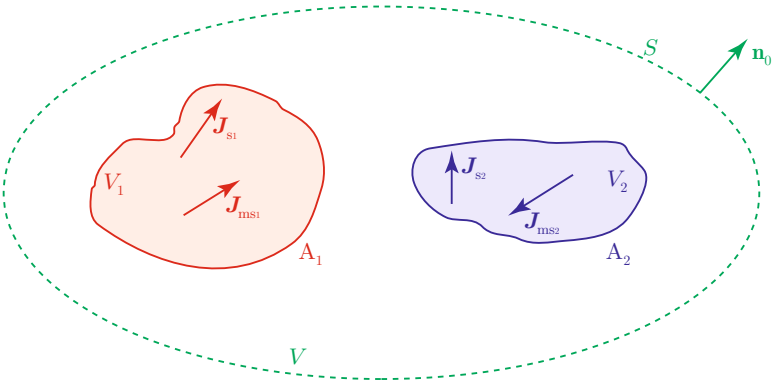

Fig. 3.10 The fields of the sources A_1 and A_2 are related by reciprocity

[12]The procedure can be extended to include sources and fields with general time dependence [6, 15].

and, analogously, for the field of the second source A_2,

$$\nabla \times \boldsymbol{E}_2 = -\mathrm{j}\omega\mu \boldsymbol{H}_2 - \boldsymbol{J}_{\mathrm{ms2}} \; ; \tag{3.43}$$

$$\nabla \times \boldsymbol{H}_2 = \mathrm{j}\omega\epsilon \boldsymbol{E}_2 + \boldsymbol{J}_{\mathrm{s2}} \; . \tag{3.44}$$

The formal expression of the *reciprocity theorem* is obtained in a straightforward way by steps analogous to those followed to arrive at the Poynting theorem. In particular, the procedure considers the dot products of the terms of Eqs. (3.41), (3.42), (3.43) and (3.44) times $\boldsymbol{H}_2$, $\boldsymbol{E}_2$, $-\boldsymbol{H}_1$, and $-\boldsymbol{E}_1$, respectively; then the resulting terms are summed up and integrated over the arbitrary volume V contoured by the surface S with outward normal $\mathbf{n}_0$, shown in Fig. 3.10. The final result is

$$\oiint_S (\boldsymbol{E}_1 \times \boldsymbol{H}_2 - \boldsymbol{E}_2 \times \boldsymbol{H}_1) \cdot \mathbf{n}_0 \, \mathrm{d}S = \iiint_{V_1} (\boldsymbol{J}_{\mathrm{s1}} \cdot \boldsymbol{E}_2 - \boldsymbol{J}_{\mathrm{ms1}} \cdot \boldsymbol{H}_2) \, \mathrm{d}V - \iiint_{V_2} (\boldsymbol{J}_{\mathrm{s2}} \cdot \boldsymbol{E}_1 - \boldsymbol{J}_{\mathrm{ms2}} \cdot \boldsymbol{H}_1) \, \mathrm{d}V \; , \tag{3.45}$$

being $\boldsymbol{J}_{\mathrm{s1}} = \boldsymbol{J}_{\mathrm{ms1}} = 0$ and $\boldsymbol{J}_{\mathrm{s2}} = \boldsymbol{J}_{\mathrm{ms2}} = 0$ for $\boldsymbol{r} \notin V_1$ and $\boldsymbol{r} \notin V_2$, respectively. The validity of the result is subject to the isotropy[13] of the materials in V, since, in general,

$$([\boldsymbol{\epsilon}] \boldsymbol{E}_1) \cdot \boldsymbol{E}_2 \neq ([\boldsymbol{\epsilon}] \boldsymbol{E}_2) \cdot \boldsymbol{E}_1 \; .$$

Therefore, reciprocity may fail in the ionosphere at the lower microwave frequencies, as mentioned in Sect. 2.2.5.

3.2.1.1 The Reaction Integrals

If the integration volume V expands to infinity, given the properties of the far field,

$$\oiint_{S_\infty} (\boldsymbol{E}_{\infty 1} \times \boldsymbol{H}_{\infty 2} - \boldsymbol{E}_{\infty 2} \times \boldsymbol{H}_{\infty 1}) \cdot \mathbf{n}_0 \, \mathrm{d}S = 0 \; ,$$

which implies that the two volume integrals in (3.45) coincide:

$$I_{12} = \iiint_{V_1} (\boldsymbol{J}_{\mathrm{s1}} \cdot \boldsymbol{E}_2 - \boldsymbol{J}_{\mathrm{ms1}} \cdot \boldsymbol{H}_2) \, \mathrm{d}V_1 = \iiint_{V_2} (\boldsymbol{J}_{\mathrm{s2}} \cdot \boldsymbol{E}_1 - \boldsymbol{J}_{\mathrm{ms2}} \cdot \boldsymbol{H}_1) \, \mathrm{d}V_2 = I_{21} \; ,$$

provided isotropy holds.

The integrals I_{12} and I_{21} are named *reactions*, or *reaction integrals* [11]. Note that, given the independence of the integrands from the particular choice of the

[13] Linearity of the materials is also assumed.

integration volume, the result $I_{12} = I_{21}$ holds in general. This implies that[14]

$$\oiint_S (\boldsymbol{E}_1 \times \boldsymbol{H}_2 - \boldsymbol{E}_2 \times \boldsymbol{H}_1) \cdot \mathbf{n}_0 \, \mathrm{d}S = 0 \, ,$$

when either $(V_i \in V, \ i = 1, 2)$ or $(V_i \notin V, \ i = 1, 2)$ hold, while

$$\oiint_S (\boldsymbol{E}_1 \times \boldsymbol{H}_2 - \boldsymbol{E}_2 \times \boldsymbol{H}_1) \cdot \mathbf{n}_0 \, \mathrm{d}S = I_{12} \, , \tag{3.46}$$

when $V_1 \in V$ and $V_2 \notin V$, or

$$\oiint_S (\boldsymbol{E}_1 \times \boldsymbol{H}_2 - \boldsymbol{E}_2 \times \boldsymbol{H}_1) \cdot \mathbf{n}_0 \, \mathrm{d}S = -I_{21} \, , \tag{3.47}$$

when $V_2 \in V$ and $V_1 \notin V$.

3.2.1.2 Test Source

The concept of test source turns out instrumental to a number of basic developments relevant to Earth observation.

The two sources considered in the previous paragraph now consist of an extended electric source A and a point source, modeled by an impressed electric current $\boldsymbol{J}_\mathrm{t}$ of momentum $\mathcal{M}_\mathrm{t}$ located at a point $\boldsymbol{r}_\mathrm{t}$, as indicated in Fig. 3.11:

$$\boldsymbol{J}_\mathrm{t} = \mathcal{M}_\mathrm{t} \, \delta(\boldsymbol{r} - \boldsymbol{r}_\mathrm{t}) \mathbf{t}_0 \, .$$

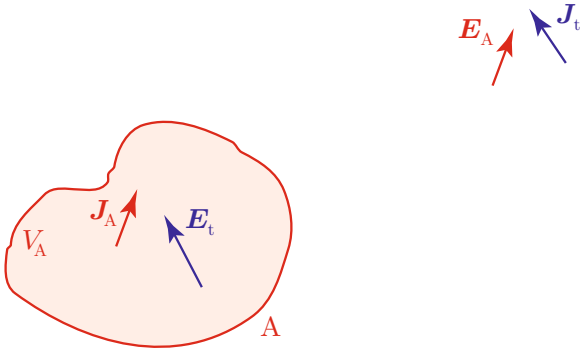

Fig. 3.11 The test source $\boldsymbol{J}_\mathrm{t}$ provides information on the field $\boldsymbol{E}_\mathrm{A}$ produced by the distributed source A

[14] The *Lorentz reciprocity theorem* $\nabla \cdot (\boldsymbol{E}_1 \times \boldsymbol{H}_2 - \boldsymbol{E}_2 \times \boldsymbol{H}_1) = 0$ holds in source-free regions of space.

The equality of reactions

$$I_{\mathrm{At}} \equiv \iiint_{V_{\mathrm{A}}} \boldsymbol{J}_{\mathrm{A}} \cdot \boldsymbol{E}_{\mathrm{t}} \, \mathrm{d}V = \iiint_{V_{\mathrm{t}}} \boldsymbol{J}_{t} \cdot \boldsymbol{E}_{\mathrm{A}} \, \mathrm{d}V \equiv I_{\mathrm{tA}} \tag{3.48}$$

yields

$$I_{\mathrm{At}} = \mathcal{M}_{\mathrm{t}} \boldsymbol{E}_{\mathrm{A}}(\boldsymbol{r}_{\mathrm{t}}) \cdot \mathbf{t}_0 \, . \tag{3.49}$$

In Eq. (3.48), $\boldsymbol{E}_{\mathrm{t}}$ is the electric field that the test source creates in the volume V_{A} of the extended source, while $\boldsymbol{E}_{\mathrm{A}}$ is the field that the source A produces in the volume $V_{\mathrm{t}} \not\ni V_{\mathrm{A}}$ explored by the test current. Equation (3.49) indicates that the electric field produced by any source A can be obtained from the reaction between the source and an electric impulse (*test source*) oriented parallel to the field:

$$\boldsymbol{E}_{\mathrm{A}}(\boldsymbol{r}_{\mathrm{t}}) = E_{\mathrm{A}} \boldsymbol{\mathfrak{e}}_{0\mathrm{A}} = \frac{I_{\mathrm{At}}}{\mathcal{M}_{\mathrm{t}}} \mathbf{t}_0 \qquad \mathbf{t}_0 \parallel \boldsymbol{\mathfrak{e}}_{0\mathrm{A}} \, .$$

A system of three orthogonal test sources is clearly able to probe the complete vector field produced by A over the space external to V_{A}.

This concept is basic to the measurement of the vector field scattered or emitted from the terrestrial environment, either by multi-polarization or by polarimetric techniques.

3.2.2 Equivalence

Introducing sources that are equivalent to any actual originator of electromagnetic field turns out particularly useful in many instances. Reciprocity and test sources provide the frame for defining the *equivalent sources*.

According to (3.49), the reaction I_{At} of the source A onto a unit electric test source ($\mathcal{M} = 1$ [A m]) with versor $\mathbf{t}_0$, yields the component along $\mathbf{t}_0$ of the electric field $\boldsymbol{E}_{\mathrm{A}}$ produced by A:

$$\boldsymbol{E}_{\mathrm{A}} \cdot \mathbf{t}_0 = I_{\mathrm{At}} \, .$$

Let us implement the reciprocity theorem (3.45) for the region of space V_{t} indicated in Fig. 3.12, consisting of the whole space deprived of an *arbitrary* volume V_{eA} contoured by surface S_{eA}, containing the source A. Equation (3.47) applies, so that

$$\oiint_{S_{\mathrm{eA}}} (\boldsymbol{E}_{\mathrm{A}} \times \boldsymbol{H}_{\mathrm{t}} - \boldsymbol{E}_{\mathrm{t}} \times \boldsymbol{H}_{\mathrm{A}}) \cdot (-\mathbf{n}_0) \, \mathrm{d}S = -I_{\mathrm{tA}} \, .$$

Since reciprocity is assumed to hold, $I_{\mathrm{tA}} = I_{\mathrm{At}}$ and

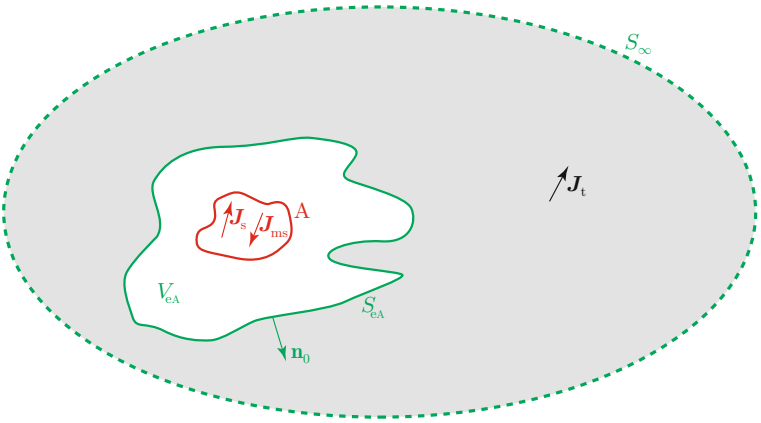

Fig. 3.12 Equivalence allows replacing the volumic currents in the source A by the areic equivalent currents smeared over any surface S_{eA} enclosing A

$$\oiint_{S_{eA}} (\boldsymbol{E}_A \times \boldsymbol{H}_t - \boldsymbol{E}_t \times \boldsymbol{H}_A) \cdot \mathbf{n}_0 \, dS = I_{At} = \boldsymbol{E}_A \cdot \mathbf{t}_0 \, . \tag{3.50}$$

According to the property of the mixed double product reported in Sect. A.1.2.4, Eq. (3.50) becomes

$$\boldsymbol{E}_A \cdot \mathbf{t}_0 = \oiint_{S_{eA}} [(\mathbf{n}_0 \times \boldsymbol{E}_A) \cdot \boldsymbol{H}_t - \boldsymbol{E}_t \cdot (\boldsymbol{H}_A \times \mathbf{n}_0)] \, dS \, , \tag{3.51}$$

where the fields in the integral are obviously those that the source A produces on the surface S_{eA}. In the following, these fields are denoted by $\boldsymbol{E}_{eA}$ and $\boldsymbol{H}_{eA}$, respectively, to avoid possible misunderstanding. By defining the *equivalent* electric *and* magnetic *surface* currents

$$\boldsymbol{J}_{eA} := \mathbf{n}_0 \times \boldsymbol{H}_{eA} \, ; \tag{3.52}$$

$$\boldsymbol{J}_{meA} := -\mathbf{n}_0 \times \boldsymbol{E}_{eA} \, , \tag{3.53}$$

the field (3.51) produced by A *outside* the arbitrary surface S_{eA} is expressed in terms of the equivalent currents by

$$\boldsymbol{E}_A \cdot \mathbf{t}_0 = \oiint_{S_{eA}} (\boldsymbol{J}_{eA} \cdot \boldsymbol{E}_t - \boldsymbol{J}_{meA} \cdot \boldsymbol{H}_t) \, dS \, . \tag{3.54}$$

Equation (3.54) demonstrates that the component along $\mathbf{t}_0$ of the electric field produced by the source A coincides with that produced by the surface currents $\boldsymbol{J}_{eA}$ and $\boldsymbol{J}_{meA}$, laying on S_{eA}. The currents are given by the electric and magnetic fields that the original source A creates in the points of S_{eA}.

The result is of great conceptual and practical importance, since it allows the replacement of any three-dimensional "physical" source, usually difficult to localize and to model (e.g., a scattering object or a radar transmitter), by a system of two-dimensional currents, the intensity and phase of which are provided by a-priori information. The *closed* surface over which the equivalent currents are distributed can be chosen suitably around the source. It is just the freedom in choosing the wrapping surface that provides a quite powerful tool for optimizing the efficiency of the method.

Note that *both* electric and magnetic currents are always required to represent any source. To this end, the previous results worked out for electric sources can be readily extended by duality to sources modeled by magnetic currents.

3.2.2.1 Field of Equivalent Sources

The previous section shows that the field of any actual source is the same as the field produced by the equivalent source composed of electric and magnetic surface currents, which both contribute to the field. The far field contributed by the equivalent electric current[15] $\boldsymbol{\mathcal{J}}_\mathrm{e}$ spread on the surface S_e is directly obtained from (3.31) and (3.32):

$$\boldsymbol{H}_\infty(\boldsymbol{r}) = -\mathrm{j}\kappa \frac{\mathrm{e}^{-\mathrm{j}\kappa r}}{4\pi r} \mathbf{r}_0 \times \oiint_{S_\mathrm{e}} \boldsymbol{\mathcal{J}}_\mathrm{e}(\boldsymbol{r}\,') \, \mathrm{e}^{\mathrm{j}\kappa \boldsymbol{r}\,' \cdot \mathbf{r}_0} \, \mathrm{d}V' \, ;$$

$$\boldsymbol{E}_\infty(\boldsymbol{r}) = \mathrm{j}\omega\mu_0 \frac{\mathrm{e}^{-\mathrm{j}\kappa r}}{4\pi r} \, \mathbf{r}_0 \times \left[\mathbf{r}_0 \times \oiint_{S_\mathrm{e}} \boldsymbol{\mathcal{J}}_\mathrm{e}(\boldsymbol{r}\,') \, \mathrm{e}^{\mathrm{j}\kappa \boldsymbol{r}\,' \cdot \mathbf{r}_0} \, \mathrm{d}V' \right] .$$

Duality (1.8) transforms the magnetic field (3.31) contributed by the electric current into the electric field contributed by the magnetic current $\boldsymbol{J}_\mathrm{me}$. Then the complete far electric field is obtained by superposing the contributions of the electric current (3.32) and of the magnetic current obtained by duality. The result is

$$\begin{aligned} \boldsymbol{E}_\infty(\boldsymbol{r}) = {} & \mathrm{j}\kappa \frac{\mathrm{e}^{-\mathrm{j}\kappa r}}{4\pi r} \mathbf{r}_0 \times \oiint_{S_\mathrm{e}} \boldsymbol{\mathcal{J}}_\mathrm{me}(\boldsymbol{r}\,') \mathrm{e}^{\mathrm{j}\kappa \boldsymbol{r}\,' \cdot \mathbf{r}_0} \, \mathrm{d}S \\ & + \mathrm{j}\omega\mu_0 \frac{\mathrm{e}^{-\mathrm{j}\kappa r}}{4\pi r} \mathbf{r}_0 \times \left[\mathbf{r}_0 \times \oiint_{S_\mathrm{e}} \boldsymbol{\mathcal{J}}_\mathrm{e}(\boldsymbol{r}\,') \mathrm{e}^{\mathrm{j}\kappa \boldsymbol{r}\,' \cdot \mathbf{r}_0} \, \mathrm{d}S \right] . \end{aligned}$$

The equivalent surface currents in (3.56) are given by

$$\boldsymbol{\mathcal{J}}_\mathrm{me}(\boldsymbol{r}\,') = -\mathbf{n}_0 \times \boldsymbol{E}(\boldsymbol{r}\,'); \qquad \boldsymbol{\mathcal{J}}_\mathrm{e}(\boldsymbol{r}\,') = \mathbf{n}_0 \times \boldsymbol{H}(\boldsymbol{r}\,') \tag{3.55}$$

[15] The notations are henceforth simplified by replacing the subscript $\mathrm{e_A}$ with e.

as functions of the fields $\boldsymbol{E}(\boldsymbol{r}')$ and $\boldsymbol{H}(\boldsymbol{r}')$ created by the original source in the points $\boldsymbol{r}'$ of the closed surface S_e chosen to envelop the source.

In several instances, as for the case considered in Sect. 11.1, the field produced by the original source differs appreciably from zero only on a portion S_g of S_e. Then the far electric field is obtained in terms of the electric and magnetic fields created by the original source on S_g, called *geometric aperture* and denoted by A_g:

$$\boldsymbol{E}_\infty(\boldsymbol{r}) \simeq \mathrm{j}\kappa \frac{\mathrm{e}^{-\mathrm{j}\kappa r}}{4\pi r} \mathbf{r}_0 \times \left[\iint_{A_g} -\mathbf{n}_0 \times \boldsymbol{E}(\boldsymbol{r}') \, \mathrm{e}^{\mathrm{j}\kappa \boldsymbol{r}' \cdot \mathbf{r}_0} \, \mathrm{d}S \right.$$
$$\left. + \eta \, \mathbf{r}_0 \times \iint_{A_g} \mathbf{n}_0 \times \boldsymbol{H}(\boldsymbol{r}') \, \mathrm{e}^{\mathrm{j}\kappa \boldsymbol{r}' \cdot \mathbf{r}_0} \, \mathrm{d}S \right], \tag{3.56}$$

where $\mathbf{n}_0$ is the local normal to A_g *on the outer side* with respect to the source.

Once determined the complete far electric field (3.56), the radiation parameters of the original source that were introduced in Sect. 3.1.4.3 are readily obtained in terms of the system of surface currents (3.55) equivalent to the source. This approach is followed extensively throughout Chap. 11 to describe the radiative and receiving features of antennas and apertures.

We Meet the Electromagnetic Radiation

Since the beginning of the section introducing the radiation, the electromagnetic formalism has resumed tormenting us. The impulse response of space continues our affliction, until at last our perseverance gets rewarded: we meet the wave. Finally the symbols start having the air of tangible quantities and we can appreciate the concreteness of more or less customary concepts such as wavelength, direction and velocity of propagation, and Doppler shift.

Examining wave interference demands turning to the complex number formalism, which carries the phase information in a quite direct way. We see that the spatial pattern of the field radiated by a source is shaped effectively and plainly by simple sums of the complex quantities representing the contributions from the source elements, which pile up or vanish according their relative phases.

The simplest field is the one radiated by the elementary point source. We learn that frequency, distance and direction all play crucial roles in determining the amplitude of the field. We realize that at far distance from the source, the electric field fully characterizes the properties of the radiation, and, in particular, the power that crosses the unit surface. Still more interesting is the fact that the field radiated by large sources, such as the antennas and telescope apertures we know are used in the real world, behaves like the field of the elementary source at large distance. The concept of directional pattern is then introduced to represent the way the source spreads the radiated power in the various directions.

Reciprocity concludes the discussion on the radiation. We face again a number of abstract concepts and of likely unfamiliar mathematical expressions. We take note of the formal results and expect that the envisioned applications to ensuing concrete instances of Earth observation will clarify their meaning and convince us of their value.

References

1. Carson JR (1929) Reciprocal theorems in radio communication. Proc Inst Radio Eng 17(6):952–956. doi:10 1109/JRPROC.1929.221772
2. Cloude S (1995) An introduction to electromagnetic wave propagation and antennas. Taylor & Francis. ISBN:9781857282412
3. Electromagnetic Wave Propagation. Amanogawa Digital Maestro. http://www.amanogawa.com/archive/PlaneWave/PlaneWave-2.html. Visited on 14 May 2014
4. Electromagnetic Wave Propagation. YouTube. http://www.youtube.com/watch?v=9VpDO2iYpRU. Visited on 14 May 2014
5. Eom HJ (2004) Electromagnetic wave theory for boundary-value problems: an advanced course on analytical methods. Springer. ISBN:9783540212669
6. Goubau G (1960) A reciprocity theorem for nonperiodic fields. IRE Trans Antennas Propag 8(3):339–342. doi:10.1109/TAP.1960.1144847
7. Harrison DM. Downloadable flash animations from David M. Harrison. University of Toronto Department of Physics. http://www.cabrillo.edu/~jmccullough/Applets/Flash.html. Visited on 11 Mar 2015
8. Hecht E (2002) Optics. Addison-Wesley Longman. ISBN:9780805385663
9. Maxwell2D: animations of electromagnetic waves. University of Reading Department of Meteorology The Clouds Group. http://www.met.reading.ac.uk/clouds/maxwell/. Visited on 10 Sept 2014
10. Orfanidis SJ (2002) Electromagnetic waves and antennas. Rutgers University. ISBN:0130938556
11. Rumsey VH (1954) Reaction concept in electromagnetic theory. Phys Rev 94(6):1483–1491. doi:10.1103/PhysRev.94.1483
12. Some Educational Java Applets. http://www.falstad.com/mathphysics.html. Visited on 10 Sept 2014
13. Staelin DH, Morgenthaler AW, Kong JA (1994) Electromagnetic waves. Prentice Hall. ISBN:9780132258715
14. Tai CT (1994) Dyadic Green functions in electromagnetic theory. IEEE Press. ISBN:9780780304499
15. Welch W (1960) Reciprocity theorems for electromagnetic fields whose time dependence is arbitrary. IRE Trans Antennas Propag 8(1)::68–73. doi:10.1109/TAP.1960.1144806

Chapter 4
Waves and Fields

In a homogeneous lossless material at far distance from the source and in a limited angular range such that $\mathcal{F}(\vartheta, \varphi)$ in (3.33) is almost constant, the field is regarded as a function of distance r only, of the form

$$\boldsymbol{E}_{\infty}(\boldsymbol{r}) = C \, \frac{\mathrm{e}^{-\mathrm{j}\kappa r}}{r} \, \boldsymbol{\mathfrak{e}}_{0\infty} \, ,$$

where the factor C includes the amplitude information, and the unit vector $\boldsymbol{\mathfrak{e}}_{0\infty}$ accounts for the polarization. In Earth observation, the distance r between the source (Sun, satellite, scattering object) and the region where the field is considered is generally quite large with respect to the dimension of the region itself. For instance, the distance from the Sun is large compared with the dimension of the elementary portion of the Earth's surface being imaged by a space-based optical sensor. Analogously, the dimension of the antenna receiving the power scattered from the surface is much smaller than the distance between the observed surface and the platform on which the antenna is based. Therefore, within such limited angular ranges, the spherical wave surface $\Phi = \kappa \, r$ does not differ appreciably from a plane surface, neither the angular pattern changes. Again, this features apply to the solar radiation illuminating the scene instantaneously observed by a spectrometer, to the field *locally* created on the earth surface by a space-based radar, or to the wave reflected from an area of the surface and collected by the aperture of a satellite sensor. In such limited regions of space, in practice, the radial unit vector $\mathbf{r}_0$ is regarded as constant.

D. Solimini, *Understanding Earth Observation*, Remote Sensing and Digital Image Processing 23, DOI 10.1007/978-3-319-25633-7_4

4.1 Plane Wave Approximation

The spherical phase surfaces Φ, which Sect. 3.1.4.2 has shown to be perpendicular to the radial direction $\mathbf{r}_0$, are then locally approximated by

$$\Phi(r) = \kappa\, r \simeq k_x\, x + k_y\, y + k_z\, z\ . \tag{4.1}$$

Equation (4.1) indicates that the phase Φ is constant on the planes $k_x x + k_y y + k_z z = const$ perpendicular to the reference local radial direction $\mathbf{r}_0$: according to Sect. 3.1.1.2, the local field is a *plane wave*. Given the large distance from the source, also the amplitude of the field is almost constant in the considered limited region, thus the far field is represented by

$$\boldsymbol{E}_\infty(\boldsymbol{r}) = C\,\frac{\mathrm{e}^{-\mathrm{j}\kappa r}}{r}\,\boldsymbol{\mathfrak{e}}_{0\infty} \simeq \boldsymbol{E}_0\mathbf{E}_0\,\mathrm{e}^{-\mathrm{j}(k_x x + k_y y + k_z z)}\ . \tag{4.2}$$

The constant vector $\boldsymbol{E}_0$ expresses the amplitude and polarization of the field that the source produces in the far region of interest, while the exponential yields its approximate space-dependent phase.

The *propagation vector* $\boldsymbol{k}$ is then introduced so that the plane wave (4.2) is written in the compact form[1]

$$\boldsymbol{E}(\boldsymbol{r}) = \boldsymbol{E}_0\,\mathrm{e}^{-\mathrm{j}\boldsymbol{k}\cdot\boldsymbol{r}}\ . \tag{4.3}$$

Vector $\boldsymbol{k}$ is determined not only by the direction $\mathbf{r}_0$, but also by the constraints set by the relations the field must satisfy. Indeed, from the spectral Maxwell's equations

$$\nabla\times\boldsymbol{E} = -\mathrm{j}\omega\mu_0\boldsymbol{H}\ ; \tag{4.4}$$

$$\nabla\times\boldsymbol{H} = \mathrm{j}\omega\epsilon\boldsymbol{E}\ , \tag{4.5}$$

by substitution of

$$\boldsymbol{H} = \frac{\nabla\times\boldsymbol{E}}{-\mathrm{j}\omega\mu_0}$$

into (4.5), the relation

$$\nabla\times(\nabla\times\boldsymbol{E}) = -\mathrm{j}\omega\mu_0\ \mathrm{j}\omega\epsilon\,\boldsymbol{E} = \kappa^2\boldsymbol{E}$$

[1] From now on the subscript $_\infty$ is dropped in the expression of the plane wave.

is obtained, which, taking into account (A.41) and the absence of unbalanced charge density[2] which implies $\rho_s = \rho \equiv 0$, becomes the *homogeneous Helmholtz equation* [15, Chap. 11]

$$\nabla^2 \boldsymbol{E} + \kappa^2 \boldsymbol{E} = 0 \,. \tag{4.6}$$

The propagation vector in (4.3) must be such that the plane-wave field (4.3) satisfies (4.6).

4.1.1 The Propagation Vector

By inserting the plane wave expression into the Helmholtz equation, since $\boldsymbol{E}_0$ is independent of coordinates,

$$\boldsymbol{E}_0 \left[\left(\frac{\partial^2}{\partial x^2} + \frac{\partial^2}{\partial y^2} + \frac{\partial^2}{\partial z^2} \right) \mathrm{e}^{-\mathrm{j}(k_x x + k_y y + k_z z)} + \kappa^2 \mathrm{e}^{-\mathrm{j}\boldsymbol{k}\cdot\boldsymbol{r}} \right] = 0 \,.$$

It follows

$$\boldsymbol{E}_0 \left[-(k_x^2 + k_y^2 + k_z^2) + \kappa^2 \right] = 0 \,,$$

which implies

$$k_x^2 + k_y^2 + k_z^2 = \boldsymbol{k} \cdot \boldsymbol{k} = \kappa^2 = \omega^2 \mu_0 \epsilon \,. \tag{4.7}$$

Therefore, the modulus of the propagation vector of the plane wave coincides with the propagation constant (3.6) that was introduced in Sect. 3.1.1, and

$$\boldsymbol{k} = \kappa \, \mathbf{k}_0 \,. \tag{4.8}$$

4.1.2 Phase and Amplitude

The assumption of lossless materials, that throughout Chap. 3 was instrumental to a smoother understanding of the electromagnetic radiation and of the radiating properties of sources, is now relaxed, for a more realistic modeling of the terrestrial environment. Real materials are dissipative, in that they transform electromagnetic energy into heat. This happens through the mechanisms discussed in Sects. 2.1.1, 2.1.2 and 2.1.3, leading to complex values of permittivity ϵ.

[2] The density of free charge vanishes everywhere in a source-free neutral material.

As a consequence, because of (4.7), $\boldsymbol{k}$ is a complex vector, with generally complex components. As discussed in Sect. 1.3.1, a complex vector is formed by a pair of real vectors, which combine through the imaginary unit. Therefore, in general, the propagation vector is

$$\boldsymbol{k} = \boldsymbol{\beta} - \mathrm{j}\boldsymbol{\alpha}$$

and the expression of the plane wave[3] becomes

$$\boldsymbol{E}(\boldsymbol{r}) = \boldsymbol{E}_0\, \mathrm{e}^{-\mathrm{j}\boldsymbol{k}\cdot\boldsymbol{r}} = \boldsymbol{E}_0\, \mathrm{e}^{-\mathrm{j}(\boldsymbol{\beta}-\mathrm{j}\boldsymbol{\alpha})\cdot\boldsymbol{r}} = \boldsymbol{E}_0\, \mathrm{e}^{-\boldsymbol{\alpha}\cdot\boldsymbol{r}}\, \mathrm{e}^{-\mathrm{j}\boldsymbol{\beta}\cdot\boldsymbol{r}}\,, \tag{4.9}$$

in which the real *amplitude factor* $\mathrm{e}^{-\boldsymbol{\alpha}\cdot\boldsymbol{r}}$ and the complex *phase factor* $\mathrm{e}^{-\mathrm{j}\boldsymbol{\beta}\cdot\boldsymbol{r}}$ are identified. Given the dependence (4.9) of the plane wave on the point of space,

- $\boldsymbol{\alpha} = \alpha\,\boldsymbol{\alpha}_0$, which affects the amplitude of the field, is named *attenuation vector*: the amplitude of the field is constant on the equal-amplitude planes $\boldsymbol{\alpha}\cdot\boldsymbol{r} = const$, perpendicular to $\boldsymbol{\alpha}$;
- $\boldsymbol{\beta} = \beta\,\boldsymbol{\beta}_0$, which affects the phase of the field, is the *phase vector*: the phase of the field is constant on the equiphase planes $\Phi = \boldsymbol{\beta}\cdot\boldsymbol{r} = const$, perpendicular to $\boldsymbol{\beta}$ (Fig. 4.1). This latter is parallel to $\mathbf{r}_0$ in the limited region in which the plane wave approximates the field (4.2).

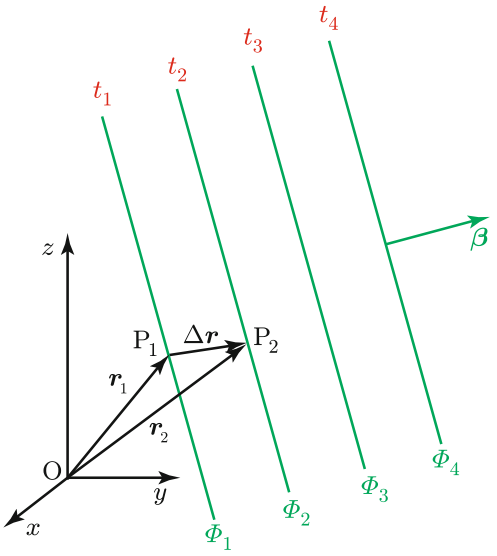

Fig. 4.1 Traces of plane equiphase surfaces Φ_i, $i = 1, 2, 3, \ldots$, at different times t_i, and displacement $\Delta\boldsymbol{r}$ between point P_1 where the wave has phase Φ_1 and P_2 with phase Φ_2

[3]The magnetic field has clearly the same expression as the electric field.

Note that the vectors $\boldsymbol{\alpha}$ and $\boldsymbol{\beta}$ are not necessarily parallel, since they depend not only on the complex permittivity, but, in a different way, also on the position of the source relative to possible boundaries between piecewise homogeneous media. However, the losses of the material set basic constraints on the attenuation and phase vectors.

Since

$$\boldsymbol{k} \cdot \boldsymbol{k} = (\boldsymbol{\beta} - \mathrm{j}\boldsymbol{\alpha}) \cdot (\boldsymbol{\beta} - \mathrm{j}\boldsymbol{\alpha}) = \beta^2 - \alpha^2 - 2\mathrm{j}\boldsymbol{\alpha} \cdot \boldsymbol{\beta} \ , \tag{4.10}$$

- in a lossless material,

$$\boldsymbol{k} \cdot \boldsymbol{k} = \omega^2 \mu_0 \epsilon \quad \text{is real,} \quad \text{hence} \ \ \boldsymbol{\alpha} \cdot \boldsymbol{\beta} = 0 \ ,$$

  which requires

  - either $\boldsymbol{\alpha} = 0$, which means that the field is not attenuated,
  - or $\boldsymbol{\alpha} \perp \boldsymbol{\beta}$, i.e., the field has equal-amplitude planes perpendicular to equiphase planes[4];

- in a lossy medium (i.e., with complex permittivity)

$$\boldsymbol{k} \cdot \boldsymbol{k} = \omega^2 \mu_0 \epsilon \quad \text{is complex,} \quad \text{hence} \ \ \boldsymbol{\alpha} \cdot \boldsymbol{\beta} \neq 0 \ ;$$

  the requirement is now $\boldsymbol{\alpha} \neq 0, \ \boldsymbol{\alpha} \not\perp \boldsymbol{\beta}$.

Waves usually encountered in Earth observation have $\boldsymbol{\alpha} \parallel \boldsymbol{\beta}$, i.e., $\boldsymbol{\alpha}_0 = \boldsymbol{\beta}_0 \equiv \mathbf{k}_0$: in this case the wave is named *homogeneous wave*. Instances in which $\boldsymbol{\alpha} \nparallel \boldsymbol{\beta}$ (*inhomogeneous waves*) are also encountered, due to the effects of the interfaces between different materials.[5]

In a lossless material, (4.10) yields

$$\boldsymbol{k} \cdot \boldsymbol{k} = \beta^2 - \alpha^2 = \omega^2 \mu_0 \epsilon = \omega^2 \mu_0 \epsilon_0 \tilde{\epsilon} = \kappa_0^2 \tilde{\epsilon} \ ,$$

where $\kappa_0 = \omega \sqrt{\mu_0 \epsilon_0}$ is the propagation constant *in vacuo*, i.e., relative to vacuum. The *phase constant* β of a homogeneous wave, which has $\alpha = 0$, is

$$\beta = \kappa_0 \sqrt{\tilde{\epsilon}} \ ,$$

while

$$\beta = \sqrt{\omega^2 \mu \epsilon + \alpha^2}$$

[4] Section 6.4 discusses this relevant case.

[5] An examples is given in Sect. 6.3.

holds for an inhomogeneous wave, which has $\alpha \neq 0$. Therefore, for given frequency, in a lossless material the phase constant of an inhomogeneous plane wave is larger than that of a homogeneous one and, because of (3.16), the velocity of propagation is lower. This property is essential for understanding the totally reflected waves considered in Sect. 6.4.

On its side, in a lossy material, (4.10) results in[6]

$$\beta^2 - \alpha^2 - 2\mathrm{j}\alpha\beta = \omega^2\mu_0\epsilon_0(\tilde{\epsilon}_\mathrm{r} + \mathrm{j}\tilde{\epsilon}_\mathrm{j}) \; . \tag{4.11}$$

The complex-coefficients Eq. (4.11) splits into

$$\begin{cases} \beta^2 - \alpha^2 = \kappa_0 \, \tilde{\epsilon}_\mathrm{r} \; ; \\ \alpha \, \beta \quad\quad = -\dfrac{\kappa_0 \, \tilde{\epsilon}_\mathrm{j}}{2} \; , \end{cases}$$

which readily yield the phase and attenuation[7] constants:

$$\beta = \frac{\kappa_0 \sqrt{\tilde{\epsilon}_\mathrm{r}}}{\sqrt{2}} \left[1 + \sqrt{1 + \left(\frac{\tilde{\epsilon}_\mathrm{j}}{\tilde{\epsilon}_\mathrm{r}} \right)^2} \right]^{\frac{1}{2}} \; ; \tag{4.12}$$

$$\alpha = \frac{\kappa_0 \, |\tilde{\epsilon}_\mathrm{j}|}{\sqrt{2 \, \tilde{\epsilon}_\mathrm{r}}} \left[1 + \sqrt{1 + \left(\frac{\tilde{\epsilon}_\mathrm{j}}{\tilde{\epsilon}_\mathrm{r}} \right)^2} \right]^{-\frac{1}{2}} \; . \tag{4.13}$$

The relations (4.12) and (4.13) indicate that both the phase and the attenuation constants of the plane wave depend on the relative permittivity of the material. It is worth observing that, in particular, β is generally larger than the propagation constant κ_0 in vacuo, while α is directly related to $\tilde{\epsilon}_\mathrm{j}$. A material in which the dielectric polarization process were, ideally, "frictionless", hence for which $\tilde{\epsilon}_\mathrm{j} = 0$, would have $\alpha = 0$.

The imaginary part of permittivity has been shown in Sect. 2.1 to originate from the damping of the motion of the charges contributing the induced dielectric dipole. The damped motion finally results in the absorption of electromagnetic energy by the lossy material. This aspect was considered in Sect. 2.1.4 within the general frame of the impact of complex permittivity on the electromagnetic power budget. Given the origin of the wave attenuation in the assumed homogeneous material, α is also named *absorption constant*. Chapter 9 shows that the field can likewise be attenuated by dielectric inhomogeneities of the material even if this latter is lossless. In this case the term *extinction* is used.

[6] A homogeneous wave is assumed.

[7] The attenuation constant $\alpha \geq 0$ since $\tilde{\epsilon}_\mathrm{j} \leq 0$ (Sect. 2.1).

Of particular interest in Earth observation is the case $|\tilde{\epsilon}_\mathrm{j}| \ll \tilde{\epsilon}_\mathrm{r}$ that occurs in *weakly lossy media*, such as the air. Then, successive approximations of (4.12) and (4.13) are

$$\beta \simeq \kappa_0 \sqrt{\tilde{\epsilon}_\mathrm{r}} \left[1 + \frac{1}{8} \left(\frac{\tilde{\epsilon}_\mathrm{j}}{\tilde{\epsilon}_\mathrm{r}} \right) \right] \simeq \kappa_0 \sqrt{\tilde{\epsilon}_\mathrm{r}} \, ; \tag{4.14}$$

$$\alpha \simeq \frac{\kappa_0 \, |\tilde{\epsilon}_\mathrm{j}|}{\sqrt{2\,\tilde{\epsilon}_\mathrm{r}}} \left[1 - \frac{1}{8} \left(\frac{\tilde{\epsilon}_\mathrm{j}}{\tilde{\epsilon}_\mathrm{r}} \right) \right] \simeq \frac{\kappa_0 \, |\tilde{\epsilon}_\mathrm{j}|}{\sqrt{2\,\tilde{\epsilon}_\mathrm{r}}} \cdot \tag{4.15}$$

The approximate relations (4.14) and (4.15) now show that

- the phase constant in a weakly dissipative material is directly proportional to the parameter

$$n = \sqrt{\tilde{\epsilon}_\mathrm{r}} \, , \tag{4.16}$$

  which is named *refractive index* (or index of refraction);
- the absorption constant depends directly on $\tilde{\epsilon}_\mathrm{j}$.

Note that $n \geq 1$, since, apart from peculiar materials in some ranges of frequencies, $\tilde{\epsilon}_\mathrm{r} \geq 1$. It is also worth mentioning the formal definition of complex refractive index

$$n = \sqrt{\tilde{\epsilon}} = \sqrt{\tilde{\epsilon}_\mathrm{r} + \mathrm{j}\,\tilde{\epsilon}_\mathrm{j}} = n_\mathrm{r} + \mathrm{j}\, n_\mathrm{j} \, , \tag{4.17}$$

which introduces real (n_r) and imaginary (n_j) parts of the latter for lossy materials.

As mentioned in Sect. 2.1.3.1, in some fields of Earth observation it is still customary to use conductivity g as distinct from the part of permittivity $\epsilon_0 \, \tilde{\epsilon}_\mathrm{do}$ contributed by deformation and orientation. When conductivity is used, the phase and absorption constants are expressed in terms of g and $\tilde{\epsilon}_\mathrm{do}$ by[8]

$$\beta = \omega \sqrt{\frac{\mu_0 \epsilon_0 \tilde{\epsilon}_\mathrm{do}}{2} \left[\sqrt{1 + \left(\frac{g}{\omega \epsilon_0 \tilde{\epsilon}_\mathrm{do}} \right)^2} + 1 \right]} \, ; \tag{4.18}$$

$$\alpha = \omega \sqrt{\frac{\mu_0 \epsilon_0 \tilde{\epsilon}_\mathrm{do}}{2} \left[\sqrt{1 + \left(\frac{g}{\omega \epsilon_0 \tilde{\epsilon}_\mathrm{do}} \right)^2} - 1 \right]} \, . \tag{4.19}$$

The expressions (4.18) and (4.19) of the constants are suitably approximated according to the wave frequency.

[8] The expressions hold for frequencies far from resonance and relaxation.

At "low" frequencies, such that $g/(\omega\epsilon_0\tilde{\epsilon}_{\rm do}) \gg 1$, phase and absorption constants approximately coincide:

$$\beta \simeq \alpha \simeq \sqrt{\frac{\omega\mu_0 g}{2}} \,.$$

For many terrestrial materials, this approximation typically holds in the lower microwave range, that is at frequencies which are small with respect to the lowest resonance or Debye relaxation frequency.

Instead, at relatively high frequencies, such that $g/(\omega\epsilon) \ll 1$, the constants are approximated by

$$\beta \simeq \omega\sqrt{\mu_0\epsilon_0\tilde{\epsilon}_{\rm do}}\,; \qquad \alpha \simeq \frac{g}{2}\sqrt{\frac{\mu_0}{\epsilon_0\tilde{\epsilon}_{\rm do}}} \,.$$

The phase and attenuation constants clearly affect the observed field. The space-time field of a plane wave is obtained by (1.25):

$$\boldsymbol{E}(\boldsymbol{r},t) = \Re\left[\boldsymbol{E}(\boldsymbol{r})\mathrm{e}^{\mathrm{j}\omega t}\right] = \Re\left[\boldsymbol{E}_0\,\mathrm{e}^{-\boldsymbol{\alpha}\,\cdot\,\boldsymbol{r}}\,\mathrm{e}^{-\mathrm{j}(\boldsymbol{\beta}\,\cdot\,\boldsymbol{r}\,-\,\omega t)}\right] \,. \tag{4.20}$$

The amplitude of the field of a homogeneous wave varies with distance in the direction $\mathbf{k}_0 \equiv \boldsymbol{\beta}_0 = \boldsymbol{\alpha}_0$ of the propagation vector (i.e., for $\boldsymbol{r} = r\mathbf{r}_0 \equiv r\mathbf{k}_0$) according to the exponential real factor

$$\tilde{E}(r) = E_0\,\mathrm{e}^{-\alpha\, r} \,. \tag{4.21}$$

Equation (4.21) indicates that the field decays exponentially[9] with distance: the wave is *attenuated*, with rate of decay given by the absorption constant α, which, according to (4.15), is directly proportional to $\kappa_0\left|\tilde{\epsilon}_{\rm j}\right|$ in case of low losses. Note that the effect of $\tilde{\epsilon}_{\rm j}$ on attenuation is amplified by κ_0, so that, coarsely speaking, higher frequencies are more affected by the material losses. Because of the effect of frequency, even low values of $\tilde{\epsilon}_{\rm j}$ may correspond to high attenuation.

The *attenuation* $\mathcal{A}$ undergone by the field when traveling from $r = 0$ to r is defined as the ratio between the field amplitudes at distance r and at $r = 0$

$$\mathcal{A}(r,0) := \frac{E(r)}{E_0} = \mathrm{e}^{-\alpha\, r} \,. \tag{4.22}$$

Attenuation is usually expressed in dB by

$$\mathcal{A}(r,0) = -20\log_{10}\frac{E(r)}{E_0} = -20\log_{10}(\mathrm{e}^{-\alpha\, r}) = 20\,\alpha\, r\,\log_{10}(\mathrm{e}) \quad [\mathrm{dB}] \,. \tag{4.23}$$

[9] Exponential decay of the field is subject to the homogeneity of the propagation medium.

Equation (4.23) indicates that the attenuation expressed in dB is a linear[10] function of distance r. Thanks to this feature, the attenuation α per unit path length can be defined, usually expressed in dB km^{-1} or, alternatively, in Np m^{-1}.

4.1.2.1 Wavelength

The space-time complex exponential factor in (4.20),

$$\mathrm{e}^{-\mathrm{j}(\boldsymbol{\beta}\cdot\boldsymbol{r}-\omega t)}\ , \tag{4.24}$$

determines the periodicity of the field, the phase of which in the direction $\mathbf{k}_0$ of the propagation vector is

$$\Phi(r,t) = -\beta r + \omega t + \Phi_0\ , \tag{4.25}$$

where the constant Φ_0 accounts for the phase of $\boldsymbol{E}_0$. The wavelength, introduced by (3.14) in Sect. 3.1.1.2, provides the spatial periodicity of the plane wave: according to (4.14), in a weakly lossy material[11]

$$\lambda = \frac{2\pi}{\beta} \simeq \frac{2\pi}{\kappa_0\sqrt{\tilde{\epsilon}_\mathrm{r}}} = \frac{\lambda_0}{n}\ , \tag{4.26}$$

where

$$\lambda_0 = \frac{2\pi}{\kappa_0} = \frac{2\pi}{\omega\sqrt{\mu_0\epsilon_0}} = \frac{c_0}{f} \tag{4.27}$$

denotes the wavelength *in vacuo*, clearly the same as that (3.15) found for the spherical wave. As said, especially in the optical range, λ_0 is commonly used in place of frequency, given its biunivocal correspondence with this latter through the "speed of light" *in vacuo* $c_0 \approx 3\cdot 10^8\,\mathrm{m\,s^{-1}}$! Equation (4.26) points out that the wavelength is reduced by a factor equal to the refractive index of the material. In the atmosphere, which, being a *tenuous* dielectric material, has $\tilde{\epsilon}_\mathrm{r} \approx 1$ (Sect. 2.2.1), $\lambda \approx \lambda_0$. From this point of view, the atmosphere is usually regarded as the vacuum.[12] On their side, some *dense* media, such as aqueous dielectrics (Sect. 2.2.2.3), at the low microwave frequencies have λ considerably smaller than λ_0. In general, the wavelength inside a material, for which $\tilde{\epsilon}_\mathrm{r} \geq 1$, is smaller than that in the vacuum.

[10] Since the material is assumed homogeneous, α is constant.

[11] Weak losses clearly include the lossless case.

[12] It is understood that the deviations of λ from λ_0, however small, cannot be neglected in certain applications, as, for instance, radar interferometry (cf. Sect. 12.3.2.1).

4.1.2.2 Velocity of Propagation

The form of the exponential (4.24) hints at a first extension of the concepts introduced in Sect. 3.1.1.2 to describe the propagation of the wave. Figure 4.1 depicts the equiphase planes that translate with time in the direction of $\boldsymbol{\beta}$: it is easily realized that the phase Φ_1 of the field at any point P_1 on an equiphase plane differs from the phase Φ_2 at any point P_2 on another equiphase plane by the same quantity $\Phi_2 - \Phi_1$, irrespective of the distance $\Delta\boldsymbol{r}$ between the points P_1 and P_2. This observation implies that the *phase velocity*, that is the velocity with which a point has to move to keep unchanged its phase, depends on the direction in which the translation is being considered. The sketch in Fig. 4.1 shows that the phase velocity is minimum in the direction of $\boldsymbol{\beta}$: this minimum value, which is the velocity at which the equiphase planes move, is the *velocity of propagation* u of the plane wave. As for (3.16), the value of the velocity is derived by imposing $\mathrm{d}\Phi|_{\beta_0} = 0$ to (4.25), thus obtaining

$$u = \frac{\omega}{\beta} \,. \tag{4.28}$$

Given the dependence of the velocity on the phase constant β, the waves propagate at different velocities according to their nature. With reference to a lossless medium, according to the results obtained in Sect. 4.1.2, the velocity of propagation u_h of the homogeneous wave, which has $\beta = \kappa$, is

$$u_\mathrm{h} = \frac{\omega}{\omega\sqrt{\mu_0\epsilon}} = \frac{1}{\sqrt{\mu_0\epsilon_0}\sqrt{\tilde{\epsilon}}} = \frac{c_0}{n} \,.$$

The relative permittivity of the material lowers the velocity in vacuo by the factor n^{-1}, hence the velocity of propagation decreases with increasing refractive index. On its turn, the inhomogeneous wave propagates at velocity

$$u_\mathrm{i} = \frac{\omega}{\sqrt{\omega^2\mu_0\epsilon + \alpha^2}} \leq u_\mathrm{h} \,. \tag{4.29}$$

An inhomogeneous wave is *slower* than a homogeneous one in the same material. This feature makes inhomogeneous waves to arise when total reflection occurs (Sect. 6.4).

4.1.2.3 Interrelation Among Fields and Propagation Vector

Amplitudes and directions of the vectors $\boldsymbol{E}_0$, $\boldsymbol{H}_0$ and $\boldsymbol{k}$ of plane waves are not independent, but are related by the constraints posed by Maxwell's equations.

By substitution for $\boldsymbol{E}$ in the first Maxwell's equation,

$$\nabla \times \boldsymbol{E} = \nabla \times \boldsymbol{E}_0 \, \mathrm{e}^{-\mathrm{j}\boldsymbol{k}\cdot\boldsymbol{r}} = -\mathrm{j}\boldsymbol{k} \times \boldsymbol{E}_0 \, \mathrm{e}^{-\mathrm{j}\boldsymbol{k}\cdot\boldsymbol{r}} = -\mathrm{j}\omega\mu_0 \boldsymbol{H}_0 \, \mathrm{e}^{-\mathrm{j}\boldsymbol{k}\cdot\boldsymbol{r}} \, .$$

By similarly substituting for $\boldsymbol{H}$ in the second Maxwell's equation, an additional relation is obtained, so that

$$\boldsymbol{k} \times \boldsymbol{E}_0 = \omega\mu_0 \boldsymbol{H}_0; \qquad -\boldsymbol{k} \times \boldsymbol{H}_0 = \omega\epsilon \boldsymbol{E}_0 \, .$$

Therefore, $\boldsymbol{E}_0$ and $\boldsymbol{H}_0$ are mutually related through the propagation vector $\boldsymbol{k} = \boldsymbol{\beta} - \mathrm{j}\boldsymbol{\alpha}$ by

$$\boldsymbol{H}_0 = \frac{\boldsymbol{k} \times \boldsymbol{E}_0}{\omega\mu_0}; \qquad \boldsymbol{E}_0 = \frac{-\boldsymbol{k} \times \boldsymbol{H}_0}{\omega\epsilon} \, . \tag{4.30}$$

Since for a homogeneous wave[13]

$$\boldsymbol{k} = (\beta - \mathrm{j}\alpha)\, \mathbf{k}_0 \, ,$$

the following relations generally hold:

$$\boldsymbol{H}_0 = \frac{\kappa\, \mathbf{k}_0 \times \boldsymbol{E}_0}{\omega\mu_0} = \frac{\omega\sqrt{\mu_0\epsilon}}{\omega\mu_0} \mathbf{k}_0 \times \boldsymbol{E}_0 = \frac{\mathbf{k}_0 \times \boldsymbol{E}_0}{\eta} \, ; \tag{4.31}$$

$$\boldsymbol{E}_0 = -\eta\, \mathbf{k}_0 \times \boldsymbol{H}_0 \, . \tag{4.32}$$

The coupled pair of cross products in (4.31) and (4.32) indicate that components of $\boldsymbol{E}_0$ of a homogeneous plane wave are orthogonal to those of $\boldsymbol{H}_0$ and that each component of $\boldsymbol{E}_0$ and $\boldsymbol{H}_0$ is orthogonal to the propagation vector $\boldsymbol{k}$. The result implies that both $\boldsymbol{E}_0$ and $\boldsymbol{H}_0$ lie on a plane perpendicular to $\boldsymbol{k}$. In case the fields $\boldsymbol{E}_0 = E_0 \boldsymbol{\mathfrak{e}}_0$ and $\boldsymbol{H}_0 = H_0 \boldsymbol{\mathfrak{h}}_0$ are linearly polarized, the versors $\boldsymbol{\mathfrak{e}}_0$ and $\boldsymbol{\mathfrak{h}}_0$ are perpendicular to each other and to $\mathbf{k}_0$:

$$\boldsymbol{\mathfrak{e}}_0 \times \boldsymbol{\mathfrak{h}}_0 = \mathbf{k}_0 \, .$$

Moreover, (4.31) indicates that the moduli of the fields of the homogeneous plane wave are related by the intrinsic impedance (3.25):

$$\frac{|\boldsymbol{E}_0|}{|\boldsymbol{H}_0|} = \sqrt{\frac{\mu_0}{|\epsilon|}} = |\eta| \, . \tag{4.33}$$

[13] In a lossless medium, $\boldsymbol{\alpha} = 0$, so that $\boldsymbol{k} \equiv \boldsymbol{\beta}$.

Equation (4.33), clearly consistent with (3.34), confirms that electric and magnetic fields of the plane wave behave like the fields radiated by a general source at far distance. After all, Sect. 4.1 has introduced the plane wave as a local approximation of the general radiation field.

The intrinsic impedance is suitably expressed by

$$\eta = \sqrt{\frac{\mu_0}{\epsilon}} = \sqrt{\frac{\mu_0}{\epsilon_0 \tilde{\epsilon}}} = \frac{\eta_0}{\sqrt{\tilde{\epsilon}}} = \frac{\eta_0}{n} \cdot \tag{4.34}$$

where the quantity

$$\eta_0 = \frac{\mu_0}{\epsilon_0} \tag{4.35}$$

is recognized to be the intrinsic impedance of the vacuum. Equation (4.34) points out that the intrinsic impedance of the material is inversely proportional to its refractive index. Chapter 6 shows how this feature plays a crucial role in determining the amount of reflection from the terrestrial materials.

4.1.2.4 Power Density

Because of the interrelations among $\boldsymbol{E}_0$, $\boldsymbol{H}_0$ and $\mathbf{k}_0$, the Poynting vector of the homogeneous plane wave becomes[14]

$$\boldsymbol{\mathcal{P}}(r) = \frac{1}{2}\boldsymbol{E} \times \boldsymbol{H}^* = \frac{1}{2}\boldsymbol{E}_0 \, \mathrm{e}^{-\alpha\, r} \times \frac{\mathbf{k}_0 \times \boldsymbol{E}_0^*}{\eta} \, \mathrm{e}^{-\alpha\, r} \, .$$

By expanding the double cross product according to (A.5) and taking account of the orthogonality between $\boldsymbol{E}_0$ and $\mathbf{k}_0$,

$$\boldsymbol{\mathcal{P}}(r) = \frac{\boldsymbol{E}_0 \cdot \boldsymbol{E}_0^*}{2\eta} \, \mathrm{e}^{-2\,\alpha r} \, \mathbf{k}_0 = \mathcal{P}(0) \, \mathrm{e}^{-2\,\alpha r} \, \mathbf{k}_0 \, . \tag{4.36}$$

Equation (4.36) indicates that

- the homogeneous plane wave carries the power in the direction $\mathbf{k}_0$ of the propagation vector;
- the areic power decays as $\mathrm{e}^{-2\alpha r}$, i.e., at an exponential rate that is *twice* the one given by (4.22) for the field.

[14] The variation with distance r is understood to be in the direction $\mathbf{k}_0$ of the propagation vector.

For this reason, the power attenuation in dB is defined as

$$\mathcal{A}(r,0) := -10\log_{10}\frac{\mathcal{P}(r)}{\mathcal{P}(0)}\,,$$

so that its value coincides with the one yielded by (4.23) for the field. Use of this formalism makes attenuation as well as the attenuation constant invariant with respect to the quantity, field or power, which it refers to.

4.1.2.5 Refraction and Absorption in the Atmosphere

It is now worthwhile to anchor the previous definitions and theoretical considerations to some specific Earth observation issues that can offer the opportunity of better grasping meaning and relevance of the analytical results obtained so far, as well as of the data presented in Chap. 2. In particular, the index of refraction and the attenuation introduced in Sect. 4.1.2 are suitably linked to the dielectric properties of the air sketched in Sect. 2.2.1 to determine some features of wave propagation in the terrestrial atmosphere.

As a matter of fact, the atmosphere is expected to play a considerable role in observing the Earth's surface from elevated platforms, since the electromagnetic field has to cross it along more or less extended paths both in the downward and in the upward directions in optical and radar observations, or in a single direction when the thermal emission is measured. Air is a tenuous weakly lossy material, the permittivity of which is close to that of vacuum, as suggested by Fig. 2.7. Nevertheless, both $\tilde{\epsilon}_\mathrm{r} \neq 1$ and $\tilde{\epsilon}_\mathrm{j} \neq 0$ can impact Earth observation considerably, as discussed, in particular, in Chaps. 10 and 12.

4.1.2.5.1 Atmospheric Refractivity

The index of refraction is cast in the form

$$n = 1 + \delta n\,,$$

where δn is the *excess* refractive index,[15] that is the deviation of n from one. In the low-loss approximation (4.14), the refractive index (4.16) depends on the real part of permittivity (2.34). Therefore, the line shapes $\mathscr{F}_i{}'(\omega)$ of the more abundant and active atmospheric constituents determine the main trend of δn, but the effect of carbon dioxide cannot be neglected, at least in the optical range of the electromagnetic spectrum. The dependence of the permittivity on the densities of the molecular species and on the respective line shapes makes the index of refraction a

[15] In optics, the excess refractive index $\delta n = n - 1$ is usually called refractivity.

function of the air pressure, temperature humidity and composition,[16] as well as of frequency or wavelength [2, 13].

Because of the low numerical value of the excess refractive index, it is customary to introduce the quantity

$$N = 10^6 \, \delta n \, ,$$

which is called *refractivity* in the microwave, or, in general, in the radio frequency jargon [8].

4.1.2.5.2 Atmospheric Absorption

The damping of the field caused by the air determines the performance of the observing systems, by affecting the signal-to-noise ratio, which is a basic specification to meet in EO. This section summarizes only the effects of absorption by the gaseous constituents, postponing the analysis of the effects of hydrometeors and aerosols, to Chaps. 9 and 10 and to Sect. 14.3.

The imaginary part of atmospheric permittivity of the gaseous atmosphere is strongly dependent on frequency f, given the nature of the field-molecule interaction processes discussed in Sects. 2.1.1 and 2.1.2. Frequency is then expected to play a crucial role in the atmospheric attenuation, which the results of the preceding Sect. 4.1.2 show directly related to $\left|\tilde{\epsilon}_{\mathrm{j}}\right|$.

As displayed by the diagram of $\tilde{\epsilon}_{\mathrm{j}}(f)$ in Fig. 2.7, the imaginary part of the overall permittivity of the atmosphere is quite low in the microwave range, up to $f \approx 10\,\mathrm{GHz}$, at which the Earth observing radar systems typically operate, but has a generally increasing trend, with peaks at the resonance frequencies of water vapor and oxygen [21, Chap. 5]. Given (4.15), the atmospheric permittivity pattern of Fig. 2.7 reflects largely in the absorption coefficient of Fig. 4.2, which depicts the microwave attenuation caused by the atmospheric gaseous absorption at sea level ($h = 0$) and at height $h = 4\,\mathrm{km}$ above sea level. The diagram refers to *standard* clear air, that means absence of hydrometeors and reference values for pressure, temperature and humidity.

It is worth pointing out that, on a large scale, the atmospheric complex permittivity decreases with altitude due to the decreasing air density (cf. Sect. 5.2.1), so that the atmosphere is not a homogeneous medium in a strict sense. However, the spatial variations of permittivity are so smooth that the air can be considered a *locally* homogeneous material and the plane wave approximation applied, with corresponding consideration of a height-dependent absorption constant.[17] Note the quite high values of α in correspondence of the major absorption peaks, in spite of

[16] The effects of CO_2, which are generally small, are taken into account when enhanced accuracy is required.

[17] The correct concept of specific absorption is introduced in Sect. 5.3.2.2.

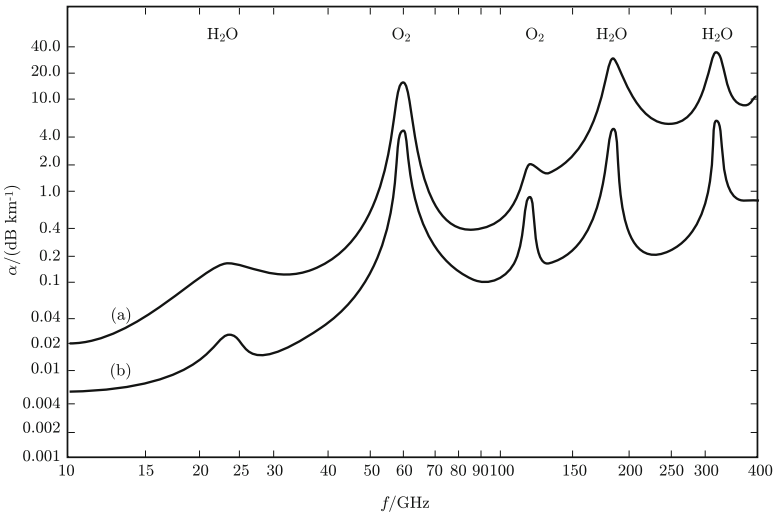

Fig. 4.2 Trend of the absorption coefficient α of the clear atmosphere vs. microwave frequency f: (**a**), at "sea level" (total pressure $p_t = 1013\,\text{hPa}$, $T = 20\,^\circ\text{C}$, water vapor density $\rho_{wv} = 7.5\,\text{g}\,\text{m}^{-3}$); (**b**), at height $h = 4\,\text{km}$ above sea level ($T = 0\,^\circ\text{C}$, water vapor density $\rho_{wv} = 1\,\text{g}\,\text{m}^{-3}$). The constituents ($H_2O$ and O_2) responsible for the respective absorption peaks are indicated (Curves interpolate data from [1])

the apparently low numerical values of $\tilde{\epsilon}_j$ displayed in the diagram of Fig. 2.7. The strong absorption is also related to the high values of κ_0 which depend on frequency according to (4.15). The generally increasing trend of $\alpha(f)$ is apparent: indeed, $\tilde{\epsilon}_j$ and in turn α exalt in the THz range, the spectral region in which, as outlined in Sect. 2.2.1, a number of rotational and vibrational resonances of atmospheric species [19] occur. In this frequency range the atmosphere becomes practically *opaque*, except that for relatively short paths and/or in specific narrow frequency windows. Low absorption is found again in the visible, which, together with the microwaves, is the main *transparent* band at which the Earth observing systems operate from space. Chapter 10 discusses these issues in more detail.

Outside the microwave frequency range, it is customary to use *transmission*, or *direct transmittance*

$$\mathcal{T} = \frac{\mathcal{P}(r)}{\mathcal{P}(0)}$$

in place of attenuation $\mathcal{A}$ and to express it in linear instead that logarithmic scale. The linear scale representation has the disadvantage of making indiscernible the values of $\mathcal{T}$ in the absorbed bands for long atmospheric paths, what makes diagrams of this kind of little use for atmospheric characterization in case of observation from space in the frequency range, say, between $f \approx 300\,\text{GHz}$ and $f \approx 300\,\text{THz}$ (cf. Fig. 10.8).

Given the correspondence (3.15) or (4.27) between f and λ_0 determined in Sects. 3.1.1.2 and 4.1.2.1, the transmission $\mathcal{T}$ in the optical range is customarily expressed as a function of wavelength. Section 10.1.2 details the effects of the constituents gases on the atmospheric transmission and the corresponding impact on the performance of Earth observing systems operating in this range of the electromagnetic spectrum.

4.2 Vector-Field Representations of Plane Waves

Representing the electric field $\boldsymbol{E}_0$ of the plane wave (4.9) through the complex vector formalism introduced in Sect. 1.3.1.1 provides complete information on the polarimetric features of the wave. Two types of formalism are more commonly adopted in Earth observation to describe the polarization state of $\boldsymbol{E}_0$.

4.2.1 Jones Representation

Section 4.1.2.3 shows that the complex vector $\boldsymbol{E}_0$ forming the plane wave

$$\boldsymbol{E}(\boldsymbol{r}) = \boldsymbol{E}_0 \, \mathrm{e}^{-\mathrm{j}\boldsymbol{k}\cdot\boldsymbol{r}}$$

lies on the plane perpendicular to the propagation vector $\boldsymbol{k}$ when the wave is homogeneous, as frequently occurs in Earth observation. The vector

$$\boldsymbol{E}_0 = E_{0\mathrm{V}}\mathbf{v}_0 + E_{0\mathrm{h}}\,\mathrm{e}^{\mathrm{j}\Phi_{\mathrm{hv}}}\mathbf{h}_0 \tag{4.37}$$

represents any field polarization, provided $\mathbf{v}_0$ and $\mathbf{h}_0$ are mutually orthogonal versors, which orderly form the right-handed triplet with $\mathbf{k}_0$ sketched in Fig. 4.3. Given the

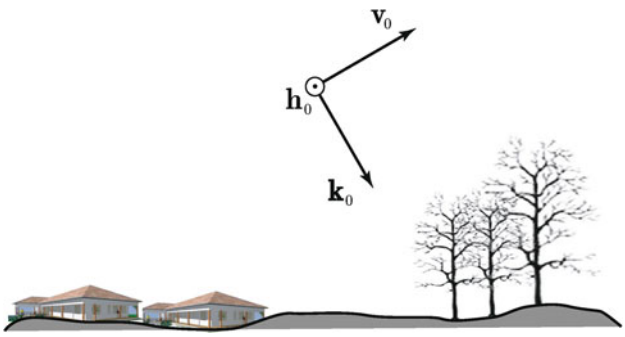

Fig. 4.3 Jones field representation: the vertical plane on which $\mathbf{v}_0$ lies and the horizontal direction $\mathbf{h}_0$ are referred to the locally plane surface of the Earth

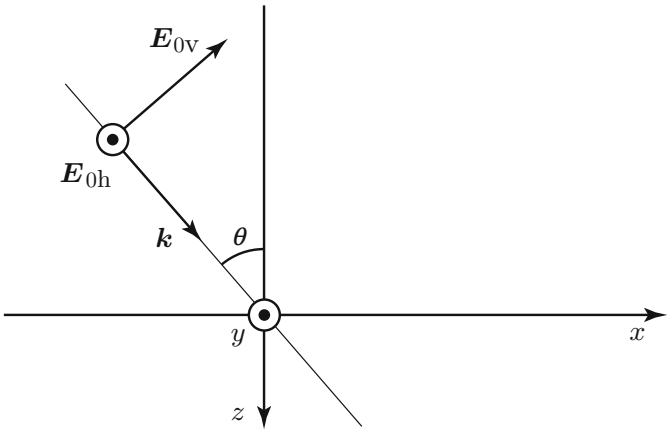

Fig. 4.4 Mutually orthogonal field components $\boldsymbol{E}_{0p}$, $(p = \mathrm{h}, \mathrm{v})$, and propagation vector $\boldsymbol{k}$ of a wave traveling at angle θ with respect to a reference direction z, typically perpendicular to the $(x\,y)$-plane representing the local earth surface

arbitrariness of the absolute phase, the *vertical* component $E_{0\mathrm{v}}$ and the *horizontal* one $E_{0\mathrm{h}}$ are taken real, while all the meaningful phase information is included into the difference $\Phi_{\mathrm{hv}} = \Phi_{\mathrm{h}} - \Phi_{\mathrm{v}}$ between the phases of horizontal and vertical components.

The propagation vector $\boldsymbol{k}$ provides information on the dependence of the field on space, for instance, on the Cartesian coordinates x, y, z, as in (4.2). A homogeneous wave propagating in the *vertical* $(x\,z)$-plane, forming an angle θ with the vertical direction $\mathbf{z}_0$ (Fig. 4.4) is

$$\boldsymbol{E}(\boldsymbol{r}) = \boldsymbol{E}_0\,\mathrm{e}^{-\mathrm{j}(k_x x + k_z z)} = \boldsymbol{E}_0\,\mathrm{e}^{-\mathrm{j}\kappa(x\sin\theta + z\cos\theta)}\ .$$

The vector $\boldsymbol{E}_0$ must satisfy the orthogonality conditions with $\boldsymbol{k}$. Therefore,

$$\mathbf{v}_0 = \mathbf{x}_0\cos\theta + \mathbf{z}_0\sin\theta\ ; \qquad \mathbf{h}_0 \equiv \mathbf{y}_0\ , \tag{4.38}$$

so that

$$\boldsymbol{E}(\boldsymbol{r}) = \left[E_{0\mathrm{v}}(\mathbf{x}_0\cos\theta + \mathbf{z}_0\sin\theta) + E_{0\mathrm{h}}\,\mathbf{y}_0\,\mathrm{e}^{\mathrm{j}\Phi_{\mathrm{hv}}}\right]\mathrm{e}^{-\mathrm{j}\kappa(x\sin\theta + z\cos\theta)} \tag{4.39}$$

represents the field at any polarization, according to the relative amplitudes $E_{0\mathrm{v}}$ and $E_{0\mathrm{h}}$ of the components and to their phase difference Φ_{hv}. In particular, consistently with the results of Sect. 1.3.1.1:

- the polarization of $\boldsymbol{E}$ is linear if $\Phi_{\mathrm{hv}} = 0$, or $\Phi_{\mathrm{hv}} = \pi$ for any values of $E_{0\mathrm{v}}$ and $E_{0\mathrm{h}}$, or when
  - either $E_{0\mathrm{v}} = 0$: in this case the wave is *horizontally polarized*,
  - or $E_{0\mathrm{h}} = 0$: then the wave is *vertically polarized*,

for any Φ_{hv};

- circular polarization is expressed by $E_{0\mathrm{V}} = E_{0\mathrm{h}}$ and $\Phi_{\mathrm{hv}} = \pm\frac{\pi}{2}$, i.e.,

$$\boldsymbol{E}(\boldsymbol{r}) = E_0[(\mathbf{x}_0 \cos\theta + \mathbf{z}_0 \sin\theta) \pm \mathrm{j}\,\mathbf{y}_0]\mathrm{e}^{-\mathrm{j}\kappa(x\sin\theta + z\cos\theta)} ,$$

- otherwise, polarization is elliptical.

The *Jones formalism* (4.37) is frequently adopted in polarimetric radar applications [9, Chap. 2], [4] that exploit the full polarization features of the field. A drawback of the formalism is represented by the need of handling complex quantities, which requires specific processing tools.

4.2.2 Stokes Representation

The amplitude and polarization features of a plane wave are alternatively represented by the *Stokes vector* [5]

$$\boldsymbol{S} := \begin{bmatrix} S_0 \\ S_1 \\ S_2 \\ S_3 \end{bmatrix} = \begin{bmatrix} E_{\mathrm{h}}^2 + E_{\mathrm{v}}^2 \\ E_{\mathrm{h}}^2 - E_{\mathrm{v}}^2 \\ 2E_{\mathrm{h}}E_{\mathrm{v}}\cos\Phi_{\mathrm{hv}} \\ 2E_{\mathrm{h}}E_{\mathrm{v}}\sin\Phi_{\mathrm{hv}} \end{bmatrix} . \tag{4.40}$$

The *Stokes parameters* S_i, $i = 0, .., 3$, are able to represent any state of polarization and, being *real* quantities, do not need computational environments in the complex domain. Moreover, the Stokes vector is in a straightforward relation with the second-order moments of the field (Sect. 1.3.4), which turn out useful in the frequently encountered case of quasi-monochromaticity. Indeed, S_0 is proportional to the areic power carried by the wave, S_1 measures the power unbalance between horizontal and vertical components, while S_2 and S_3 provide information on their phase difference. Note that the Stokes vector has only three independent components, since

$$S_0^2 = S_1^2 + S_2^2 + S_3^2 .$$

The Stokes parameters can be expressed in terms of the polarization parameters ψ and χ introduced in Sect. 1.3.1.2, by

$$\begin{aligned} S_1 &= S_0 \cos 2\psi \cos 2\chi \ ; \\ S_2 &= S_0 \sin 2\psi \cos 2\chi \ ; \\ S_3 &= S_0 \sin 2\chi \ , \end{aligned}$$

so that the wave can be alternatively represented by the *normalized Stokes vector*

$$\boldsymbol{Y} = S_0 \begin{bmatrix} 1 \\ \cos(2\psi)\cos(2\chi) \\ \sin(2\psi)\cos(2\chi) \\ \sin(2\chi) \end{bmatrix}.$$

It should be also taken into consideration a further representation of the quasi-monochromatic field through the *modified Stokes vector* $\boldsymbol{Y}_{\mathrm{m}}$, defined by [10]

$$\boldsymbol{Y}_{\mathrm{m}} := S_0 \begin{bmatrix} \frac{1}{2}\left[1 + \cos(2\psi)\cos(2\chi)\right] \\ \frac{1}{2}\left[1 - \cos(2\psi)\cos(2\chi)\right] \\ \sin(2\psi)\cos(2\chi) \\ \sin(2\chi) \end{bmatrix}. \tag{4.41}$$

4.2.2.1 The Poincaré Sphere

Given the above relations of S_0 to S_1, S_2 and S_3, these three latter parameters can be regarded as a Cartesian coordinate triplet identifying a point on the sphere of radius S_0 named *Poincaré sphere* [7, Chap. 7] and represented in Fig. 4.5. A point P on the Poincaré sphere identified by colatitude 2 χ and longitude 2 ψ, corresponds to a polarization state of the field:

- The points on the equator, for which $\chi = 0$, i.e., $\Phi_{\mathrm{hv}} = 0$, correspond to linear polarization, with inclination angle changing with longitude:

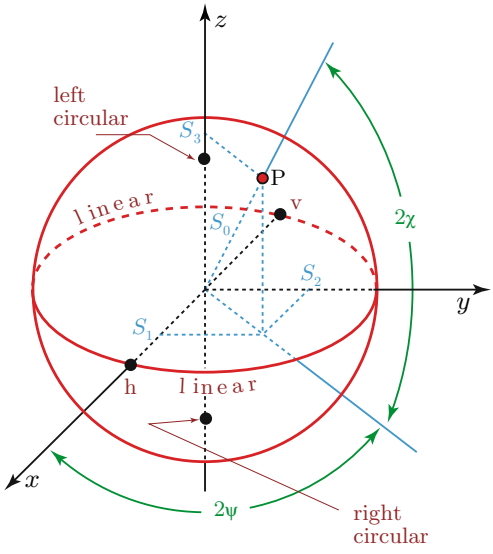

Fig. 4.5 Sketch of the Poincaré sphere with indicated the locations of relevant field polarizations

  - the intersection point with the positive x semi-axis having coordinates $(S_0, 0, 0)$ and identified by h on the figure, corresponds to horizontal polarization ($\psi = 0$);
  - the opposite point v$(-S_0, 0, 0)$, intersection with the negative x semi-axis, corresponds to vertical polarization ($\psi = \pi/2$).
- The poles, where $\chi = \pi/4$, identify circular polarizations,
  - left (clockwise with respect to $\mathbf{k}_0$) at the upper (north) pole, where $\Phi_{\text{hv}} = \pi/2$;
  - right (counterclockwise with respect to $\mathbf{k}_0$) at the lower (south) pole, where $\Phi_{\text{hv}} = -\pi/2$.
- Points on the upper emisphere correspond to elliptical left polarization, while points on the lower emisphere correspond to elliptical right polarization.

Starting from a pole and moving along a meridian ($\psi = const$), polarization changes from circular to elliptical of decreasing ellipticity, until it becomes linear on the equator, where the ellipticity angle vanishes. The trend with the colatitude and the sense of rotation revert when keeping moving beyond the equator.

4.3 Interference of Plane Waves

Section 3.1.2 shows that the values of the electromagnetic field undergo substantial variations when waves interfere. The information on the phase differences between the waves which is contained in the interference pattern turns out quite useful in radar Earth observation. Given the large distances from the source and the limited areas that are observed, the plane-wave approximation is generally acceptable, as mentioned in Sect. 4.1. Therefore, the interference of plane waves is a simple yet useful model yielding the basic features of radar interferometry, which is considered in more detail in Chap. 12.

Consider two monochromatic horizontally polarized homogeneous plane waves, having the same amplitude, which propagate in the vertical $(x\,z)$-plane in different directions, i.e., with the propagation vectors lying in the $(x\,z)$-plane and forming different angles, θ_1, θ_2, with $\mathbf{z}_0$:

$$\boldsymbol{E}_1(\boldsymbol{r}) = E_0\,\mathbf{y}_0\,\mathrm{e}^{-\mathrm{j}\kappa(x\sin\theta_1 + z\cos\theta_1)}\;; \tag{4.42}$$

$$\boldsymbol{E}_2(\boldsymbol{r}) = E_0\,\mathbf{y}_0\,\mathrm{e}^{-\mathrm{j}\kappa(x\sin\theta_2 + z\cos\theta_2)}\;. \tag{4.43}$$

The electric field $\boldsymbol{E}_{\text{tot}}$ at point $\boldsymbol{r}$ is the sum of the fields of the two coherent waves

$$\begin{aligned}\boldsymbol{E}_{\text{tot}}(\boldsymbol{r}) &= \boldsymbol{E}_1(\boldsymbol{r}) + \boldsymbol{E}_2(\boldsymbol{r}) \\ &= E_0\,\mathbf{y}_0\left[\mathrm{e}^{-\mathrm{j}\kappa(x\sin\theta_1 + z\cos\theta_1)} + \mathrm{e}^{-\mathrm{j}\kappa(x\sin\theta_2 + z\cos\theta_2)}\right]\;.\end{aligned} \tag{4.44}$$

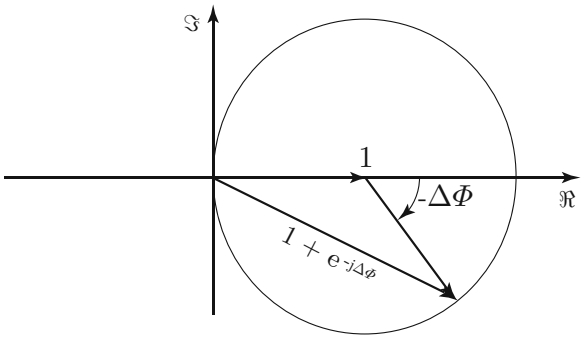

Fig. 4.6 Phasor representation in the $\{\Re\ \Im\}$ complex plane of: 1, $e^{-j\Delta\Phi}$, and $1 + e^{-j\Delta\Phi}$

Then, on the *horizontal plane* $z = 0$, $\boldsymbol{E}_{\text{tot}}$ is given by

$$\begin{aligned}\boldsymbol{E}_{\text{tot}}(x) &= E_0\,\mathbf{y}_0\left[e^{-j\kappa x\sin\theta_1} + e^{-j\kappa x\sin\theta_2}\right] \\ &= E_0\,\mathbf{y}_0 e^{-j\kappa x\sin\theta_1}\left[1 + e^{-j\kappa x(\sin\theta_2 - \sin\theta_1)}\right]\end{aligned}$$

and has modulus

$$|\boldsymbol{E}_{\text{tot}}(x)| = |E_0|\left|1 + e^{-j\kappa x(\sin\theta_2 - \sin\theta_1)}\right| .$$

With the position

$$\Delta\Phi := \kappa x(\sin\theta_2 - \sin\theta_1)$$

and with reference to the representation in the $\{\Re\ \Im\}$ complex plane of Fig. 4.6,

$$\left|1 + e^{-j\Delta\Phi}\right| = 2[1 - \cos(\Delta\Phi)] .$$

Therefore, $|\boldsymbol{E}_{\text{tot}}|$ is readily obtained as

$$|\boldsymbol{E}_{\text{tot}}(x)| = 2|E_0|\{1 - \cos[\kappa\, x\,(\sin\theta_2 - \sin\theta_1)]\} . \tag{4.45}$$

The modulus of the total field resulting from the two waves propagating in different directions exhibits periodic minima and maxima over the horizontal plane: the pattern is named *interference fringes*.[18] The fringes derive from the *coherent* addition of the fields, carried out analytically by adding the complex quantities representing the respective field amplitudes and phases [3, Chap. 7].

[18]The intensity interference fringes are considered here, while the phase fringes are specifically considered in Sect. 12.3.1.

The distance from consecutive amplitude minima or maxima identifies the *fringe spatial period*. The minima[19] of $|\boldsymbol{E}_{\text{tot}}(x)|$ on the horizontal ($z = 0$)-plane occur for

$$\Delta\Phi = \frac{2\pi}{\lambda} x(\sin\theta_2 - \sin\theta_1) = 2m\,\pi, \qquad m = 0, 1, 2, \dots \ .$$

In earth surface interferometry, $\lambda \approx \lambda_0$, since the interfering waves propagate in the atmosphere. If the origin of the coordinates is assumed as reference, the horizontal distances x_{min} at which the minima of field amplitude occur are

$$x_{\text{min}} = \frac{m\lambda}{\sin\theta_2 - \sin\theta_1}\,, \qquad m = 1, 2, 3, \dots \ ,$$

with the corresponding fringe period

$$\Lambda_{\text{F}} = \frac{\lambda}{\sin\theta_2 - \sin\theta_1}\,.$$

The inverse of the period is the *fringe spatial frequency*

$$\Upsilon_{\text{F}} = \frac{\sin\theta_2 - \sin\theta_1}{\lambda}\,,$$

which depends on the wavelength of the electromagnetic field and on the relative directions of propagation.[20] It stands out that in the present context the term "frequency" is akin to "wavelength".

In radar interferometry the directions of propagation of the two waves are very close. Therefore, by posing $\theta_1 \equiv \theta$ and

$$\theta_2 = \theta + \Delta\theta\,,$$

since $\Delta\theta \ll \pi$,

$$\sin\theta_2 = \sin(\theta + \Delta\theta) = \sin\theta\cos\Delta\theta + \cos\theta\sin\Delta\theta \simeq \sin\theta + \Delta\theta\cos\theta\,,$$

whence

$$\sin(\theta + \Delta\theta) - \sin\theta \simeq \Delta\theta\cos\theta\,.$$

[19] Here the minimum value is $|\boldsymbol{E}_{\text{tot}}(x)| = 0$, since the waves are assumed of the same amplitude.

[20] SAR interferometry requires a somewhat different approach [6], although the concepts are analogous.

For close directions of propagation, the fringe frequency tends to be linearly dependent on the angular difference $\Delta\theta$ between the two propagation vectors:

$$\Upsilon_{\mathrm{F}} \simeq \frac{\Delta\theta \cos\theta}{\lambda} \,. \tag{4.46}$$

4.3.1 Effect of Height

The position of the fringes depends on the *height* z of the horizontal plane over which they are considered. From the general expression (4.44) of the total field

$$\begin{aligned} \boldsymbol{E}_{\mathrm{tot}}(x,z) = E_0\,\mathbf{y}_0 \;\; & \mathrm{e}^{-\mathrm{j}\kappa(x\sin\theta_1 + z\cos\theta_1)} \\ & \times \;\; \left\{1 + \mathrm{e}^{-\mathrm{j}\kappa[x(\sin\theta_2 - \sin\theta_1) + z(\cos\theta_2 - \cos\theta_1)]}\right\} \,, \end{aligned}$$

the modulus of the total field is obtained like in (4.45)

$$|\boldsymbol{E}_{\mathrm{tot}}(x)| = 2|E_0|\,[1 - \cos(\Delta\Phi_x + \Delta\Phi_z)] \,,$$

where

$$\Delta\Phi_x = \frac{2\pi}{\lambda} x(\sin\theta_2 - \sin\theta_1); \qquad \Delta\Phi_z = \frac{2\pi}{\lambda} z(\cos\theta_2 - \cos\theta_1) \,.$$

It is important to note that both height z and horizontal distance x affect the interference pattern. Minima now form when

$$\Delta\Phi_x + \Delta\Phi_z = 2m\,\pi, \qquad m = 0, 1, 2, \dots \,,$$

that is, at distances from the origin

$$x_{\min} = \frac{m\lambda - z(\cos\theta_2 - \cos\theta_1)}{\sin\theta_2 - \sin\theta_1} \,, \qquad m = 1, 2, 3, \dots \,,$$

that depend on z: over horizontal planes at heights z, the fringes translate as z changes. When, as before, $\theta_2 = \theta + \Delta\theta$ with $\Delta\theta \ll \pi$, then

$$\cos(\theta + \Delta\theta) \simeq \cos\theta - \Delta\theta \sin\theta$$

and

$$x_{\min} \simeq \frac{m\lambda}{\Delta\theta} \sec\theta + z\tan\theta, \qquad m = 1, 2, 3, \dots \,. \tag{4.47}$$

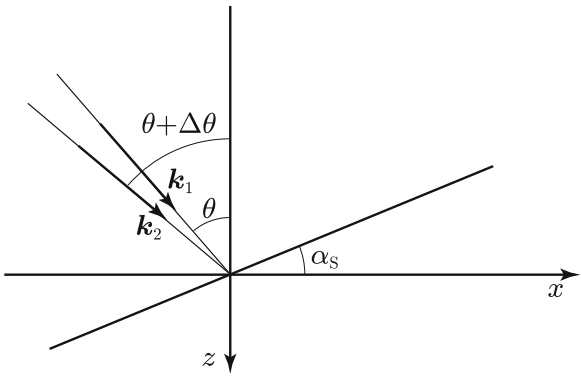

Fig. 4.7 Geometry of interference of two waves on a slant plane

4.3.1.1 Interference Fringes on a Slant Plane

Because of the dependence of the position of the fringes on height, the interferometric patterns on slant planes differ from the ones on horizontal planes. According to (4.47) and with reference to Fig. 4.7, the minima of the field modulus on the plane

$$z = -x \tan \alpha_s$$

occur at distances that satisfy the relation

$$x_{\min} \simeq \frac{m\lambda}{\Delta\theta} \sec\theta - x_{\min} \tan\alpha_s \tan\theta, \qquad m = 0, 1, 2, \ldots . \tag{4.48}$$

Equation (4.48) implies that the fringe frequency

$$\Upsilon_F \simeq \frac{\Delta\theta}{\lambda} \cos\theta (1 + \tan\alpha_s \tan\theta)$$

varies with the slope angle α_s: the interferometric pattern contains information on the slope or on the height of the surface on which the fringes are measured. Figure 4.8 shows an example of the interferometric *phase* pattern[21] observed on a surface, the slope of which varies: the local spatial frequency of the fringes increases following the increasing slope of the surface from the relatively flat area of Rome on the left side, to the Colli Albani hills on the right. Each color cycle represents a $\Delta\Phi_x = 2\pi$ interferometric phase variation, corresponding to a height difference $\Delta z \approx 150\,\text{m}$.

[21]The intensity fringes are determined by the phase pattern of the interfering waves and replicate this latter, which, however, can be directly measured and displayed, as detailed in Sect. 12.3.1.

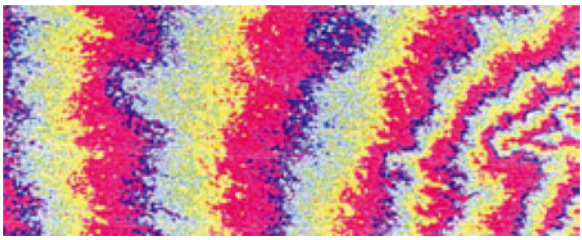

Fig. 4.8 Interferometric phase fringes over the area south east of Rome, Italy. The fringe frequency increases from left to right following the raising slope of the surface (ERS data credit: ESA; processing, Mirko Albani.)

4.3.2 Interference and Coherence

Section 1.3.2 hints at the non-monochromaticity of the fields generally encountered in Earth observation. Therefore, the previous analysis of interference must be extended to include fields that are not purely deterministic [3, Chap. 10].

Assume that the interfering waves are modeled, instead that by the deterministic (4.42) and (4.43), by the more realistic analytic signals introduced in Sect. 1.3.2

$$\boldsymbol{E}_1(\boldsymbol{r},t) = E_{01}(\boldsymbol{r},t)\,\mathbf{y}_0\,\mathrm{e}^{\mathrm{j}\Phi_1(\boldsymbol{r},t)}\,\mathrm{e}^{-\mathrm{j}\kappa(x\sin\theta_1 + z\cos\theta_1)}\;; \tag{4.49}$$

$$\boldsymbol{E}_2(\boldsymbol{r},t) = E_{02}(\boldsymbol{r},t)\,\mathbf{y}_0\,\mathrm{e}^{\mathrm{j}\Phi_2(\boldsymbol{r},t)}\,\mathrm{e}^{-\mathrm{j}\kappa(x\sin\theta_2 + z\cos\theta_2)}\;. \tag{4.50}$$

The *real* random quantities E_{01} and E_{02} represent the wave amplitudes, which vary "slowly" both in time (with appreciable variations over time intervals $\Delta t \gg T$) and in space, where they change significantly only over distances $\Delta r \gg \lambda$. The phases Φ_1 and Φ_2 are correspondingly space-time random functions, also varying slowly with respect to T and λ. The statistical properties of the fields modeled by (4.49) and (4.50) are determined by E_{0i} and Φ_i, $i = 1, 2$, while the wave propagation factor contributes a deterministic phase term.

The total scalar field on the $(z = 0)$-plane,

$$E_{\mathrm{tot}}(x,t) = E_1(x,t) + E_2(x,t)\;,$$

is a space-time random function. Its instantaneous values have little meaning and its average value vanishes, given the $0 - 2\pi$ uniform distribution of Φ_1 and Φ_2 that is encountered in real cases. Then, the properties of E_{tot} must be described by its higher-order moments, and, in particular, by the second-order moment (Sect. 1.3.4). A particularly significant moment is the power density, which, for $\theta_1 \approx \theta_2$, is proportional to the coherence (1.41) of E_{tot} for coincident space and time:

$$\Gamma(x) = \left\langle E_{\mathrm{tot}}(x,t)\,E^*_{\mathrm{tot}}(x,t)\right\rangle = \left\langle [E_1(x,t) + E_2(x,t)]\,[E_1(x,t) + E_2(x,t)]^*\right\rangle\;.$$

Expanding the product within the angular brackets yields

$$\left\langle E_{\text{tot}}(x,t)\, E_{\text{tot}}^{*}(x,t)\right\rangle = \left\langle |E_1(x,t)|^2\right\rangle + \left\langle |E_2(x,t)|^2\right\rangle + 2\,\Re\left[\left\langle E_1(x,t)\, E_2^{*}(x,t)\right\rangle\right] .$$

By recalling (1.38), the coherence of the total field is expressed by the total intensity

$$\mathcal{I}_{\text{tot}} = \frac{\left\langle E_{\text{tot}}\, E_{\text{tot}}^{*}\right\rangle}{2}$$

and put into relation with the intensities

$$\mathcal{I}_1 = \frac{\left\langle E_{01}^2\right\rangle}{2}, \qquad \mathcal{I}_2 = \frac{\left\langle E_{02}^2\right\rangle}{2}$$

of the interfering waves:

$$\mathcal{I}_{\text{tot}}(x) = \mathcal{I}_1 + \mathcal{I}_2 + \Re\left[\left\langle E_1(x,t)\, E_2^{*}(x,t)\right\rangle\right] .$$

Assuming space-time field stationariness, as is often suitable in practice, the intensities $\mathcal{I}_1$ and $\mathcal{I}_2$ are independent of position x. Then the intensity of the field created by the interference of the two waves is composed of a pedestal given by the sum of the intensities of the interfering waves plus a term that is proportional to the coherence function $\left\langle E_1\, E_2^{*}\right\rangle$. Taking account of (4.49) and (4.50), this latter is given by

$$\left\langle E_1\, E_2^{*}\right\rangle = \left\langle E_{01}\, E_{02}\, \mathrm{e}^{-\mathrm{j}(\Phi_1 - \Phi_2)}\right\rangle \mathrm{e}^{-\mathrm{j}\kappa x(\sin\theta_1 - \sin\theta_2)} .$$

The quantity

$$\Gamma_{12} := \left\langle E_{01}\, E_{02} \mathrm{e}^{-\mathrm{j}(\Phi_1 - \Phi_2)}\right\rangle$$

represents the *mutual coherence of the interfering waves*, which is determined by the properties of the respective sources (Chaps. 7 and 8) or by the transformations the waves may have undergone during their propagation (Chaps. 5 and 9). The intensity $\mathcal{I}_{\text{tot}}$ of the field produced by the interference is then expressed by

$$\mathcal{I}_{\text{tot}}(x) = \mathcal{I}_1 + \mathcal{I}_2 + \Re\left[\Gamma_{12}\, \mathrm{e}^{-\mathrm{j}\kappa x(\sin\theta_1 - \sin\theta_2)}\right] .$$

A suitable normalization like in (1.43) and (1.44) leads to the definition of the *degree of mutual coherence* γ_{12} of the interfering waves

$$\gamma_{12} := \frac{\Gamma_{12}}{\sqrt{\langle |E_1|^2\rangle}\sqrt{\langle |E_2)|^2\rangle}} = \frac{\left\langle E_{01}\, E_{02}\, \mathrm{e}^{-\mathrm{j}(\Phi_1 - \Phi_2)}\right\rangle}{\sqrt{\left\langle E_{01}^2\right\rangle}\sqrt{\left\langle E_{02}^2\right\rangle}} = |\gamma_{12}|\, \mathrm{e}^{\mathrm{j}\Phi_\gamma} . \tag{4.51}$$

The total intensity distribution, which forms the *interference pattern* on the $(z = 0)$-plane is then given by

$$\begin{aligned}\mathcal{I}_{\text{tot}}(x) &= \mathcal{I}_1 + \mathcal{I}_2 + 2\sqrt{\mathcal{I}_1}\sqrt{\mathcal{I}_2}\,\Re\left[\gamma_{12}\mathrm{e}^{-\mathrm{j}\kappa x(\sin\theta_1 - \sin\theta_2)}\right] \\ &= \mathcal{I}_1 + \mathcal{I}_2 + 2\sqrt{\mathcal{I}_1}\sqrt{\mathcal{I}_2}\;|\gamma_{12}|\cos\left[(\kappa x(\sin\theta_1 - \sin\theta_2) + \Phi_\gamma\right] \quad (4.52)\end{aligned}$$

in terms of the correlation between the interfering waves. The intensity pattern consists of a uniform background $\mathcal{I}_1 + \mathcal{I}_2$ on which a sinusoidal variation, the amplitude of which depends on $|\gamma_{12}|$, superimposes. Intensity maxima $\mathcal{I}_\mathrm{M}$ alternate with minima $\mathcal{I}_\mathrm{m}$, forming the interference fringes. The *fringe visibility*

$$\mathcal{V} := \frac{\mathcal{I}_\mathrm{M} - \mathcal{I}_\mathrm{m}}{\mathcal{I}_\mathrm{M} + \mathcal{I}_\mathrm{m}}$$

depends on the correlation between the interfering waves expressed by their degree of mutual coherence. Visibility is maximum when the waves are fully correlated ($|\gamma_{12}| = 1$), hence they interfere coherently, whereas it vanishes when the waves interfere incoherently ($|\gamma_{12}| = 0$). Figure 4.9 shows the interference pattern for the two mentioned limiting cases and for an intermediate value of $|\gamma_{12}|$, in case the waves carry the same average power density. No interference pattern is discerned when $|\gamma_{12}| = 0$.

Although the degree of coherence depends on both amplitude and phase fluctuations, these latter are crucial in determining the wave correlation. Assume that the phases of the interfering waves fluctuate randomly, while the wave amplitudes do not vary and are equal, so that (4.51) simplifies in

$$\gamma_{12} = \left\langle \mathrm{e}^{\mathrm{j}(\Phi_1 - \Phi_2)} \right\rangle = \langle\cos(\Phi_1 - \Phi_2)\rangle - \mathrm{j}\,\langle\sin(\Phi_1 - \Phi_2)\rangle\ . \quad (4.53)$$

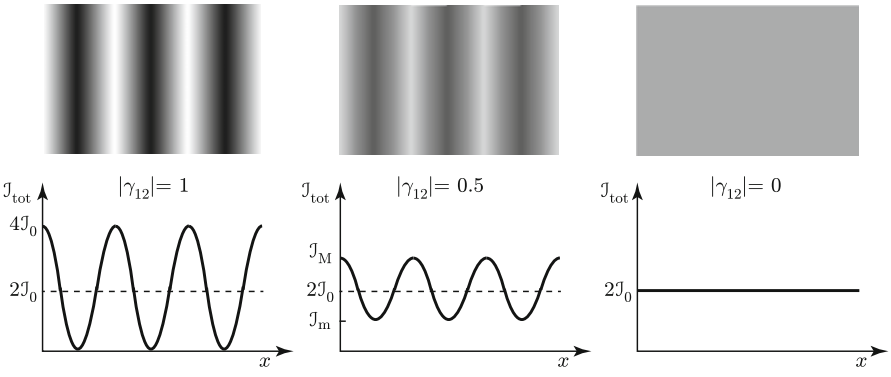

Fig. 4.9 Intensity interference pattern generated by waves of the same intensity $\mathcal{I}_0$ and different mutual coherence γ_{12}

If, as is often the case, the phase fluctuations are normally distributed and have zero mean, i.e.

$$\langle \Phi_1 \rangle = \langle \Phi_2 \rangle = 0 \,,$$

then [16, Chap. 2]

$$\langle \cos(\Phi_1 - \Phi_2) \rangle = \mathrm{e}^{-\frac{1}{2}\left\langle (\Phi_1 - \Phi_2)^2 \right\rangle}; \qquad \langle \sin(\Phi_1 - \Phi_2) \rangle = 0 \,. \tag{4.54}$$

The exponent

$$\left\langle (\Phi_1 - \Phi_2)^2 \right\rangle = \left\langle \Phi_1^2 \right\rangle + \left\langle \Phi_2^2 \right\rangle - 2 \left\langle \Phi_1 \Phi_2 \right\rangle$$

contains the variance

$$\left\langle \Phi_1^2 \right\rangle = \left\langle \Phi_2^2 \right\rangle = \sigma_\phi^2$$

and the cross-correlation of the phase fluctuations. A common assumption for this latter is

$$\langle \Phi_1 \Phi_2 \rangle = \sigma_\phi^2 \, \mathcal{B}_\phi \,, \tag{4.55}$$

where $\mathcal{B}_\phi \leq 1$ is the correlation coefficient of the fluctuations.[22] Then the degree of coherence (4.53), taking (4.54) and (4.55) into account, becomes an exponential function of the phase variance

$$\gamma_{12} = \mathrm{e}^{-\sigma_\phi^2 \left(1 - \mathcal{B}_\phi\right)} \,. \tag{4.56}$$

Expression (4.56) provides a suggestive insight into the effect of the phase random fluctuations of the waves that create the interference pattern:

– When the phases of the interfering waves are completely correlated, so that $\mathcal{B}_\phi = 1$, the degree of coherence is unitary and $\mathcal{I}_\mathrm{M} = 4\,\mathcal{I}_0$, while $\mathcal{I}_\mathrm{m} = 0$. Then, the visibility of the fringes is $\mathcal{V} = 1$ for any value of σ_ϕ^2. The fields of the interfering waves, which have a fixed phase relation, add as in (4.44): the maximum value of the total field is twice that of the single wave and, correspondingly, the total power density is four times that carried by the single wave. This case is shown in the left diagram of Fig. 4.9.

[22] $\mathcal{B}_\phi$ is a function of time when the individual interfering waves exist at different times, as it occurs for repeat-pass interferometry (Sect. 12.3.3.1).

– Uncorrelated phase fluctuations, such that $\mathcal{B}_\phi = 0$, are characterized by a degree of coherence that depends on the magnitude of the phase fluctuations[23]: the larger the variance σ_ϕ^2, the smaller is $|\gamma_{12}|$ and, correspondingly, the lower is the fringe visibility. When $|\gamma_{12}| \to 0$, there is no addition *of the fields*, given their random phase relation, rather the waves *add in power*: the power density is everywhere just twice that carried by the single wave (right diagram of Fig. 4.9).
– Interference patterns of partially correlated waves fall in between the limiting cases and are characterized by intermediate values $0 < \mathcal{V} < 1$ of the fringe visibility.

Chapter 12 includes a more detailed analysis of the coherence effects on the *phase fringes* generated by interferometric pairs of radar images.

Surfing Fields and Waves

The plane wave is a quite intuitive model of traveling electromagnetic field. Its mathematical expression has the form of an exponential function, the exponent of which is characterized by the propagation vector, which controls how phase and amplitude change with the traveled distance. The underlying analitical relations put the motion and the decay of the wave into relation with the dielectric properties of the material in which the wave propagates. The real part of the permittivity mainly affects wavelength and velocity of propagation, while the attenuation is determined essentially by the imaginary part. We learn that increasing the permittivity slows down the wave and that a high value of $\tilde{\epsilon}_j$ produces a rapid decay of the field. Then we come across refractive index and attenuation, which are both expected to play a key role in many aspects of Earth observation. As a first step approaching the characterization of the terrestrial environment, the refractive and the transmission properties of the atmosphere are surveyed. Two different ways of representing the electric field of a plane wave in its various polarization state are also reported.

The important issue of what happens when a pair of plane waves superpose is investigated. Constructive and destructive interferences are modeled quite effectively by the complex formalism, which is able to handle the information on the phase of the waves in compact and significant way. We learn about the formation of the interference fringes and how their properties are affected by height and slope of the surfaces on which they form. If we are not yet used to stochastic models, our mind boggles at the thought that the nature of the real world is essentially random and that in fact the phase of the field is particularly subject to fluctuations. To model correctly the interference of fields the relative phase of which is not deterministic,

[23]The normal distribution assumption is significant and useful, but, given the $\mathrm{mod}(\Phi, 2\pi)$ phase feature, may possibly lead to inconsistent results.

we have to introduce randomness into the expressions of the waves. The mutual coherence of the interfering waves is then defined to take account of the phase fluctuations. We realize that the fringes fade out as the coherence decreases, until their visibility vanishes when waves with uncorrelated phase fluctuations interfere. Clearly the analysis is preliminary to the understanding of the features of the radar interferometry, a major tool in earth surface observation.

References

1. Attenuation by Atmospheric Gases (1990) Technical report CCIR Doc. Rep. 719–3, International Telecommunications Union – ITU
2. Bean BR, Thayer GD (1959) Models of the atmospheric radio refractive index. Proc IRE 47(5):740–755. doi:10.1109/JRPROC.1959.287242
3. Born M, Wolf E, Bhatia AB (2002) Principles of optics: electromagnetic theory of propagation, interference and diffraction of light. Cambridge University Press. ISBN:9781139643405
4. Börner W-M. Basic concepts in radar polarimetry. In: PolSARpro V 3.0 – Lecture Notes (ESA). http://earth.eo.esa.int/polsarpro/Manuals/LN_Basic_Concepts.pdf. Visited on 04 Nov 2014
5. Collett E (2005) Field guide to polarization. SPIE field guide series. International Society for Optical Engineering. ISBN:9780819458681
6. Gatelli F, Monti Guarnieri A, Parizzi F, Pasquali P, Prati C, Rocca F (1994) The wavenumber shift in SAR interferometry. IEEE Trans Geosci Remote Sens 32(4):855–865. doi:10.1109/36.298013
7. Iizuka K (2002) Elements of photonics. In: Free space and special media, vol I. Wiley. ISBN:9780471221074, doi:10.1002/0471221074.ch7
8. ITU Radiocommunication Sector (2012) The radio refractive index: its formula and refractivity data. Technical report Rec. ITU-R pp 453–10. International Telecommunications Union P Series – Radiowave Propagation
9. Lee JS, Pottier E (2009) Polarimetric radar imaging: from basics to applications. Taylor & Francis. ISBN:9781420054989
10. Le Vine DM, Utku C (2009) Comment on modified Stokes parameters. IEEE Trans Geosci Remote Sens 47(8):2707–2713. doi:10.1109/TGRS.2009.2015875
11. McMaster WH (1961) Matrix representation of polarization. Rev Mod Phys 33(1):8–28. doi:http://dx.doi.org/10.1103/RevModPhys.33.8
12. Meggers WF, Peters CG (1919) Measurements on the index of refraction of air for wavelengths from 2218 A to 9000 A. Astrophys J 56–71. doi:10.1086/142481
13. Owens JC (1967) Optical refractive index of air: dependence on pressure, temperature and composition. Appl Opt 6(1):51–59. doi:10.1364/AO.6.000051
14. Refractive index database. Refractive Index.Info. http://refractiveindex.info/legacy/?group=LIQUIDS&material=Water; http://refractiveindexinfo/legacy/?group=CRYSTALS&material=H20-ice. Visited on 12 Sept 2014
15. Riley KF, Hobson P (2011) Essential mathematical methods for the physical sciences. Cambridge University Press. ISBN:9781139492942
16. Rytov SM, Kravtsov YuA, Tatarskii VI (1988) Principles of statistical radiophysics 2: correlation theory of random processes. Springer. ISBN:9780387161860
17. Salvail JZ, Agnew M, Johnson AS, Bolduc E, Leach J, Boyd RW (2013/04) Full characterization of polarization states of light via direct measurement. Nat Photonics 7(4):316–321. doi:10.1038/nphoton.2013.24
18. Schott JR (ed) (2009) Fundamentals of polarimetric remote sensing. SPIE. ISBN:9780819478764

19. Slocum DM, Slingerland EJ, Giles RH, Goyette TM (2013) Atmospheric absorption of terahertz radiation and water vapor continuum effects. J Quant Spectrosc Radiat Transf. http://dx.doi.org/10.1016/j.jqsrt.2013.04.022
20. Tervo J, Setälä T, Friberg AT (2003) Degree of coherence for electromagnetic fields. Opt Exp 11(10):1137–1143. doi:10.1364/OE.11.001137
21. Ulaby FT, Moore RK, Fung AK (1981) Microwave remote sensing: active and passive. Volume 1, microwave remote sensing fundamentals and radiometry. Addison-Wesley. ISBN:9780890061909

Chapter 5
Propagation

The electromagnetic energy, which provides the basic substance to satellite Earth observation, always transfer through parts of the terrestrial environment. The traversed medium consists of the atmosphere and of the layers of other materials that the wave has to cross along the path between source of radiation, target under observation, and observing platform. Wave propagation affects the performance of the EO systems not only because it changes the amplitude of the field, but also because it modifies the phase, which carries its own peculiar information. The effect of absorption on the wave amplitude has already been considered from different points of view in Sects. 2.1.4 and 4.1.2. However, the inhomogeneities of the materials change the field magnitude also through mechanisms which are independent of absorption. The large-scale[1] spatial variations of permittivity heighten or weaken the field, essentially through the modifications they induce in the shape of the phase. Moreover, the changes of phase that the permittivity structure produces at a given point of space may have an equally substantial impact on the performance of the observation techniques that exploit the phase information (Chap. 12). Analyzing the effect that the wave propagation has on the phase obviously requires a coherent approach. In this frame, a model that considers the propagation environment as a continuous medium able to preserve the phase relations, is clearly needed. It should be clear that the continuous medium is intended to be a *reference* space-time *average* environment. Actually, the space-time fluctuations of the physical parameters of a *real* terrestrial material involve also abrupt variations. The analysis of the effects of discontinuities and inhomogeneities is postponed to the next chapters 6, 7 and 9.

[1]The effect of scattering by small-scale inhomogeneities on the wave amplitude is specifically discussed in Chap. 9.

D. Solimini, *Understanding Earth Observation*, Remote Sensing
and Digital Image Processing 23, DOI 10.1007/978-3-319-25633-7_5

5.1 Field in Weakly Inhomogeneous Materials

Spherical and plane waves which can exist in homogeneous materials display numerous fundamental features of the actual electromagnetic field and form a basic reference, crucial to understand the information content of remote measurements. However, the materials that form the terrestrial environment are essentially inhomogeneous and can induce modifications or add new features to the properties the field. Relaxing the assumption of homogeneity under which the results discussed in the previous Chap. 4 have been obtained, is then needed. Such a generalization improves the understanding of the characteristics of the field that can exist in the actual environment and that interacts with the real terrestrial materials.

5.1.1 The Geometrical Optics Model

The starting point for determining the features of the field is the same as the one in Sect. 4.1: by substituting for $\boldsymbol{H}$ in the second spectral Maxwell's equations, the electric field vector is found to satisfy the usual relation

$$\nabla\nabla\cdot\boldsymbol{E}-\nabla^2\boldsymbol{E}=\kappa^2\boldsymbol{E}\ .$$

The innovation consists in considering the permittivity a function of space, having now relaxed the assumption of homogeneity.[2] The third Maxwell's equation (1.34) in a neutral[3] inhomogeneous material, yields

$$\nabla\cdot\boldsymbol{D}=\nabla\cdot[\epsilon(\boldsymbol{r})\boldsymbol{E}]=\boldsymbol{E}\cdot\nabla\epsilon+\epsilon\nabla\cdot\boldsymbol{E}=\rho=0\ ,$$

whence

$$\nabla\cdot\boldsymbol{E}=-\frac{1}{\epsilon}\boldsymbol{E}\cdot\nabla\epsilon\ .$$

By substituting for the divergence,

$$\nabla\nabla\cdot\boldsymbol{E}=-\nabla\Big(\frac{1}{\epsilon}\boldsymbol{E}\cdot\nabla\epsilon\Big)$$

and the equation satisfied by the electric field becomes

$$\nabla^2\boldsymbol{E}+\kappa^2\boldsymbol{E}+\nabla\Big(\boldsymbol{E}\cdot\frac{\nabla\epsilon}{\epsilon}\Big)=0\ . \tag{5.1}$$

[2] For the time being, the materials are assumed lossless, so that permittivity is a real quantity.

[3] The assumption that no unbalanced charge density exists implies $\rho=0$.

The relation (5.1) is recognized to be the Helmholtz equation (4.6) encountered in Sect. 4.1, but with an additional term containing the gradient of permittivity. Clearly, when the rate of variation of ϵ with space is small, this new term is negligible. However, it is important to realize that the gradient term is negligible not only when the permittivity of the material varies little with the coordinates, but also when the propagation constant κ is relatively large: indeed, when $\kappa^2 \to \infty$, Eq. (5.1) is approximated by

$$\nabla^2 \boldsymbol{E} + \kappa^2 \boldsymbol{E} \simeq 0 \,. \tag{5.2}$$

Since in a continuous medium this approximation holds for the extremely high frequencies of light waves, it is named *optics approximation* [26, 29]. But, in spite of its denomination, the approach is quite serviceable in Earth observation not only at optical wavelengths, but very often also at microwaves. Its accuracy depends on the *relative* values of the terms in (5.1), irrespective of frequency, permittivity, and its variations. In general, neglecting the gradient term is a suitable approximation

- on one side, for propagation in *weakly inhomogeneous* [16, Chap. 2] materials, such as the gaseous atmosphere, the permittivity of which changes so little with distance that $|\nabla\epsilon|$ has negligible values;
- on the other, in the propagation of waves the frequencies of which make κ^2 to attain extremely high values, hence to dominate over the term contributed by the dielectric inhomogeneities, even if this latter has not negligible absolute values.

In practice, for given inhomogeneity, the accuracy of the optical approximation increases with frequency.

It is important to bear in mind that the assumption of weak inhomogeneities is instrumental to determine the relevant features of coherent propagation in the large-scale continuous model of the terrestrial materials. The assumption is obviously removed in Chaps. 6 and 7, where the focus is just on the role of inhomogeneities in affecting the field through reflection and scattering mechanisms.

Equation (5.2), which provides the "optical" field in a weakly inhomogeneous medium,

$$\nabla^2 \boldsymbol{E} + \kappa_0^2 \, n^2(\boldsymbol{r}) \boldsymbol{E} = 0 \tag{5.3}$$

is the Helmholtz equation with a non-constant coefficient which depends on the spatial dielectric structure of the material. The propagation parameter κ has been cast in the form introduced in Sect. 4.1.2,

$$\kappa(\boldsymbol{r}) = \omega \sqrt{\mu_0 \epsilon_0} \, n(\boldsymbol{r}) = \kappa_0 \, n(\boldsymbol{r}) \,,$$

where κ_0 is the propagation constant for vacuum and $n(\boldsymbol{r}) = \sqrt{\tilde{\epsilon}(\boldsymbol{r})}$ is the refractive index, which now depends on the point of space. Based on a generalization of the field (3.23) produced by the point source described in Sect. 3.1.3, the *Luneburg-Kline expansion* [7, Chap. 6], [25, 30], is assumed to represent the electric field in the inhomogeneous material:

$$\boldsymbol{E}(\boldsymbol{r}) = e^{-\mathrm{j}\kappa_0\phi(\boldsymbol{r})} \sum_{m=0}^{\infty} \frac{\boldsymbol{E}_m(\boldsymbol{r})}{(\mathrm{j}\kappa_0)^m} \,. \tag{5.4}$$

Now the function ϕ represents the phase Φ of the field normalized to the vacuum propagation constant κ_0, i.e., $\Phi = \kappa_0\phi$. The general form (5.4) of the field, by specializing the phase term, is able to represent both the spherical and the plane waves previously considered. Obviously, a field with the form (5.4) can really exist only if both the normalized phase and the field vectors satisfy the Helmoltz equation. Therefore, the quantities in (5.4) are subject to specific conditions.

First of all, by substituting (5.4) for the field in (5.3), some algebraic manipulations lead to the relation

$$n^2 - |\nabla\phi|^2 = 0 \,. \tag{5.5}$$

Condition (5.5), named *eikonal equation*, constrains the space-dependent *eikonal function* $\phi(\boldsymbol{r})$ to be consistent with the spatial structure of $n(\boldsymbol{r})$. In several instances the three-dimensional pattern of the eikonal function is close to the spatial structure of the phase of the field. Therefore the *eikonal surfaces* $\phi = const$ are called *phase surfaces* or *wave surfaces*. The phase surfaces adapt to the local value of the refractive index through (5.5), which relates the rate of variation of ϕ to n. The higher n the larger is $|\nabla\phi|$, that is, for given frequency, the spatial variation of phase.

Condition (5.5) is not the only constraint that the Helmoltz equation poses on the field (5.4). In fact, an additional condition is expressed by

$$\left(\nabla^2\phi\right)\boldsymbol{E}_0(\boldsymbol{r}) + 2\,(\nabla\phi)\cdot[\nabla\boldsymbol{E}_0(\boldsymbol{r})] = 0 \,, \tag{5.6}$$

known as the *transport equation*, which yields the space variations of the *dominant term* $\boldsymbol{E}_0(\boldsymbol{r})$ which are compatible with the dielectric structure of the material.[4] While the eikonal equation relates the *phase* of the wave to the dielectric structure, the transport equation puts this latter into relation with the *amplitude* of the field.

5.1.1.1 Dielectric Structure and Propagation Features

Around a given point, the direction $\mathbf{s}_0$ of $\nabla\phi$, perpendicular to the eikonal surface ϕ is the direction of maximum phase variation. The elementary change of the eikonal function in the verse of $\mathbf{s}_0$ is obtained from (5.5):

$$\mathrm{d}\phi = n\,\mathrm{d}r \,, \tag{5.7}$$

[4] In practice, the dominant term closely models the field, since in many instances a satisfactory approximation does not require including the higher-order terms $\boldsymbol{E}_m$, $m \neq 0$.

where $\mathrm{d}r$ is the elementary displacement. By integrating $\mathrm{d}\phi$ along the path from abscissa r_1 to r_2, the phase Φ of the field is obtained as

$$\Phi(r_2) = \kappa_0 \int_{r_1}^{r_2} n(r)\,\mathrm{d}r \; + \Phi(r_1) \; , \tag{5.8}$$

where $\Phi(r_1)$ is the initial phase. In case of homogeneous medium, the relative phase of the field that travels a path of length $r_2 - r_1$ reduces to

$$\Phi(r_2) - \Phi(r_1) = \kappa_0 n\,(r_2 - r_1) = \beta\,(r_2 - r_1) \; ,$$

the same as in Sect. 4.1.2. Indeed, the spectral field in the weakly inhomogeneous material has substantially the form found in Chaps. 3 and 4 respectively for spherical and plane waves in homogeneous media, with suitable modifications. In fact, the general expression (5.4)

$$\boldsymbol{E}(\boldsymbol{r}) = \boldsymbol{E}_{\mathrm{LK}}(\boldsymbol{r})\,\mathrm{e}^{-\mathrm{j}\kappa_0\phi(\boldsymbol{r})} \tag{5.9}$$

is the product of

- the vector factor $\boldsymbol{E}_{\mathrm{LK}}$, which contains the information on amplitude and polarization of the field and in general varies *slowly*[5] with space;
- the phase factor $\mathrm{e}^{-\mathrm{j}\kappa_0\phi(\boldsymbol{r})}$, that changes with space according to $\phi(\boldsymbol{r})$, which adapts itself to the dielectric structure.

The space-time field (1.25)

$$\boldsymbol{E}(\boldsymbol{r},t) = \Re\left[\boldsymbol{E}(\boldsymbol{r})\,\mathrm{e}^{\,\mathrm{j}\omega t}\right] = \Re\left[\boldsymbol{E}_{\mathrm{LK}}(\boldsymbol{r})\mathrm{e}^{-\mathrm{j}[\kappa_0\phi(\boldsymbol{r})\,-\,\omega t]}\right]$$

is derived from a complex quantity that contains the space-dependent vector $\boldsymbol{E}_{\mathrm{LK}}(\boldsymbol{r})$ multiplied by the complex exponential

$$\mathrm{e}^{-\mathrm{j}[\kappa_0\phi(\boldsymbol{r})\,-\,\omega t]} \; ,$$

which adds a space-time dependence. The dependence of the field on time is, obviously, the same everywhere as for the homogeneous medium, whereas the dielectric inhomogeneity of the material changes, albeit slightly, its space dependence, in the sense that near a point $\boldsymbol{r}$, the p-component of the field (1.23) varies with abscissa r according to

$$E_p(r,t) = E_{\mathrm{LK}p}\cos[\omega t - \kappa_0\phi(r)] \; ; \qquad p = x, y, z \; ,$$

[5] Remember that the field is considered in a weakly inhomogeneous medium.

which is not precisely a harmonic function of r. However, in a neighbourhood of $\boldsymbol{r}$ within which $n \approx const$, (5.7) yields a nearly linear function of displacement

$$\phi \simeq nr + \phi_{\mathrm{C}} \ ,$$

where ϕ_{C} is the *initial* value of the eikonal, that is the normalized space-time phase value Φ_{C}, in $\boldsymbol{r}$. Therefore, in the surroundings of a given point, E_p varies nearly harmonically with r:

$$E_p(r,t) \simeq E_{\mathrm{LK}p} \cos(\omega t - \kappa_0 nr + \Phi_{\mathrm{C}}) \ ; \qquad p = x, y, z \ .$$

The *local* wavelength

$$\lambda(\boldsymbol{r}) = \frac{2\pi}{\kappa_0 \, n(\boldsymbol{r})} \tag{5.10}$$

measures the spatial periodicity of the field in the direction perpendicular to the eikonal surface. Given its space-time dependence, the *local* sinusoid representing a component of the field moves according to the results of Sect. 3.1.1.2. The *wave surface* $\Phi(\boldsymbol{r}) = const$ translates in the 3-D space, as sketched in Fig. 5.1, which shows the traces of the surfaces at various times. Consider that the lines in the figure can be regarded to represent the traces of the space-time phase $\Phi(\boldsymbol{r}, t_i)$ at different times t_i, $(i = 1, 2, 3, \ldots)$, as well as of the space-dependent phase $\Phi(\boldsymbol{r})$ at a given time, or likewise of the eikonal lines ϕ. By generalizing the approach of Sect. 4.1.2.2, from the condition of invariance of the p-component of the field:

$$E_p(\boldsymbol{r}, t) = const \qquad \text{if} \ \ \omega t - \kappa_0 \phi(\boldsymbol{r}) = const \ ,$$

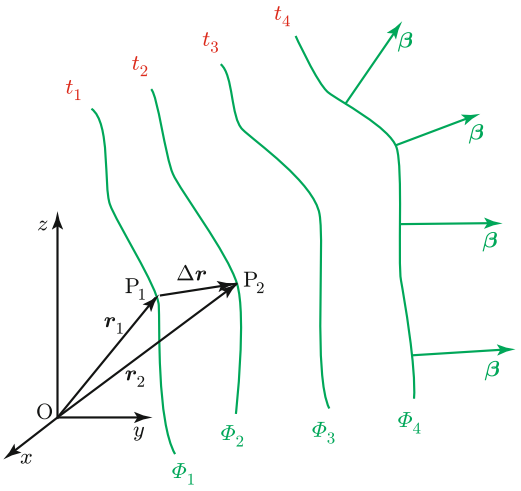

Fig. 5.1 Traces of the phase surfaces $\Phi_i = const$ at different times t_i in an inhomogeneous material; the figure represents a generalization of the plane wave case shown in Fig. 4.1. The phase vector $\boldsymbol{\beta}$ now depends on the point of space

the elementary displacement $\mathrm{d}r$ in a given direction $\mathbf{r}_0$ which cancels the total differential of the phase in that direction is given by

$$\omega\,\mathrm{d}t - \kappa_0(\nabla\phi\cdot\mathbf{r}_0)\,\mathrm{d}r = 0\ ,$$

from which the *phase velocity* along $\mathbf{r}_0$ is derived:

$$\left.\frac{\mathrm{d}r}{\mathrm{d}t}\right|_{\mathbf{r}_0} = \frac{\omega}{\kappa_0\nabla\phi\cdot\mathbf{r}_0} = u|_{\mathbf{r}_0}\ .$$

When the change of the phase is considered in the direction perpendicular to the wave surface, i.e., when $\mathbf{r}_0 \parallel \nabla\phi$, the *local velocity of propagation* u is obtained

$$u(\boldsymbol{r}) = \frac{\omega}{\kappa_0|\nabla\phi(\boldsymbol{r})|} = \frac{\omega}{\kappa_0 n(\boldsymbol{r})} = \frac{c_0}{n(\boldsymbol{r})}\ . \tag{5.11}$$

The velocity of propagation is the one in the vacuum, reduced by the local refractive index. It changes smoothly from point to point, following the change of refraction index of the weakly inhomogeneous material.

Wavelength and propagation velocity are the same everywhere when the inhomogeneity vanishes. In case the eikonal surfaces are plane,

$$\Phi(\boldsymbol{r}) = \kappa_0\phi(\boldsymbol{r}) = \boldsymbol{\beta}\cdot\boldsymbol{r}$$

is a linear function of the coordinates, with

$$\kappa_0\nabla\phi = \boldsymbol{\beta}\ .$$

Then (5.10) and (5.11) reduce to the wavelength and velocity of propagation of a homogeneous plane wave determined in Sects. 4.1.2.1 and 4.1.2.2.

5.1.1.2 The Direction of Propagation

As mentioned, in many practical cases the electric field is suitably approximated by the dominant term $\mathbf{E}_0$ of the Luneburg-Kline expansion,[6] so that electric and magnetic fields are expressed by

$$\boldsymbol{E}(\boldsymbol{r}) = \boldsymbol{E}_0(\boldsymbol{r})\,\mathrm{e}^{-\mathrm{j}\kappa_0\phi(\boldsymbol{r})}\ ;$$

$$\boldsymbol{H}(\boldsymbol{r}) = \boldsymbol{H}_0(\boldsymbol{r})\,\mathrm{e}^{-\mathrm{j}\kappa_0\phi(\boldsymbol{r})}\ .$$

[6]This implies far distance from the source, as, indeed, it generally occurs in EO.

Then the first spectral Maxwell's equation (1.32)

$$\nabla \times \left[\boldsymbol{E}_0(\boldsymbol{r})\, \mathrm{e}^{-\mathrm{j}\kappa_0 \phi(\boldsymbol{r})} \right] = -\mathrm{j}\omega\mu_0 \boldsymbol{H}_0(\boldsymbol{r})\, \mathrm{e}^{-\mathrm{j}\kappa_0 \phi(\boldsymbol{r})}$$

yields

$$\nabla\phi(\boldsymbol{r}) \times \boldsymbol{E}_0(\boldsymbol{r}) - \sqrt{\frac{\mu_0}{\epsilon_0}}\, \boldsymbol{H}_0(\boldsymbol{r}) = \frac{\nabla \times \boldsymbol{E}_0(\boldsymbol{r})}{\mathrm{j}\kappa_0} \,. \tag{5.12}$$

On its turn, the second Maxwell's equation (1.33) gives

$$\nabla\phi(\boldsymbol{r}) \times \boldsymbol{H}_0(\boldsymbol{r}) + \frac{\epsilon\, \boldsymbol{E}_0(\boldsymbol{r})}{\sqrt{\mu_0\epsilon_0}} = \frac{\nabla \times \boldsymbol{H}_0(\boldsymbol{r})}{\mathrm{j}\kappa_0} \,. \tag{5.13}$$

Taking into account that $|\nabla\phi| = n > 1$ and that $\mathbf{E}_0$ varies slowly with space in the weakly inhomogeneous medium, at sufficiently high frequency, (5.12) and (5.13) are approximated by

$$\nabla\phi(\boldsymbol{r}) \times \boldsymbol{E}_0(\boldsymbol{r}) - \eta_0 \boldsymbol{H}_0(\boldsymbol{r}) \simeq 0 \,; \tag{5.14}$$

$$\nabla\phi(\boldsymbol{r}) \times \boldsymbol{H}_0(\boldsymbol{r}) + \frac{\epsilon(\boldsymbol{r}) \boldsymbol{E}_0(\boldsymbol{r})}{\sqrt{\mu_0\epsilon_0}} \simeq 0 \,. \tag{5.15}$$

By defining the *local* intrinsic impedance

$$\eta(\boldsymbol{r}) = \sqrt{\frac{\mu_0}{\epsilon(\boldsymbol{r})}} = \frac{\eta_0}{n(\boldsymbol{r})} \,,$$

and by denoting with $\mathbf{s}_0$ the versor of $\nabla\phi$, (5.14) and (5.15) yield

$$\boldsymbol{H}_0(\boldsymbol{r}) = \frac{\nabla\phi(\boldsymbol{r}) \times \boldsymbol{E}_0(\boldsymbol{r})}{\eta_0} = \frac{\sqrt{\tilde{\epsilon}(\boldsymbol{r})}\, \mathbf{s}_0 \times \boldsymbol{E}_0(\boldsymbol{r})}{\eta_0} = \frac{1}{\eta(\boldsymbol{r})}\, \mathbf{s}_0 \times \boldsymbol{E}_0(\boldsymbol{r}) \,; \tag{5.16}$$

$$\boldsymbol{E}_0(\boldsymbol{r}) = -\eta(\boldsymbol{r})\, \mathbf{s}_0 \times \boldsymbol{H}_0(\boldsymbol{r}) \,. \tag{5.17}$$

The relations (5.16) and (5.17) relating $\boldsymbol{E}_0$, $\boldsymbol{H}_0$ and $\mathbf{s}_0$ are analogous to (4.31) and (4.32) for the homogeneous plane wave, with the space-dependent $\mathbf{s}_0$ in place of the invariant $\mathbf{k}_0$, the versor of the propagation vector. Some important conclusions can be drawn:

- both the in-phase and quadrature components of $\boldsymbol{E}_0$ and $\boldsymbol{H}_0$ are mutually perpendicular;
- the ratio between electric and magnetic amplitudes is equal to the (local) intrinsic impedance of the medium;

– the components form right-handed terns of reciprocally orthogonal vectors with the unit vector $\mathbf{s}_0$, which points in the direction of $\nabla\phi$, that is in the direction along which the rate of variation of the phase is maximum.

The direction $\mathbf{s}_0$, like $\mathbf{k}_0$ for the plane wave, is the *direction of propagation*, but, unlike $\mathbf{k}_0$ in the homogeneous medium, $\mathbf{s}_0$ generally changes from point to point, according to the spatial structure of the refractive index: $\mathbf{s}_0$ is then the *local* direction of propagation. However, given the assumed weak inhomogeneity of the material, the spatial variations of $\mathbf{s}_0$ are slow, so that the direction of propagation is approximately constant over limited regions of space, within which the plane-wave reference model holds.

5.2 Electromagnetic Rays

Given the mutual orientation of $\boldsymbol{E}_0$, $\boldsymbol{H}_0$ and $\mathbf{s}_0$, the Poynting vector

$$\mathcal{P} = \frac{1}{2}\boldsymbol{E} \times \boldsymbol{H}^* = \frac{1}{2}\boldsymbol{E}_0 \times \boldsymbol{H}_0^* = \frac{1}{2}\boldsymbol{E}_0 \times \frac{\mathbf{s}_0 \times \boldsymbol{E}_0^*}{\eta} = \frac{\boldsymbol{E}_0 \cdot \boldsymbol{E}_0^*}{2\eta}\,\mathbf{s}_0$$

has the same direction as $\mathbf{s}_0$, which is perpendicular to the eikonal surfaces[7] $\phi(\boldsymbol{r}) = const$. It means that the transport of electromagnetic power occurs in the directions locally perpendicular to $\phi(\boldsymbol{r}) = const$. The curves orthogonal to the wave surfaces are trajectories of the electromagnetic energy: the curves are named *electromagnetic rays*. They describe how the electromagnetic energy is transported by the field in the *geometrical optics* model. The rays depend on the spatial structure of the refractive index $n(\boldsymbol{r})$, on the position of the source, and on the initial direction of propagation, related to the directional properties of the source (for instance, to the instantaneous pointing direction of a radar antenna). Figure 5.2 depicts rays along which the electromagnetic wave carries the energy. The Poynting vector has the direction of $\mathbf{s}_0$, tangent to the ray and perpendicular to the equiphase $\Phi = const$ surfaces. On their side, the electric and magnetic fields are tangent to the wave surfaces. This result is clearly consistent with the homogeneous plane wave model discussed in Sect. 4.1. Coarsely speaking, the field associated with a ray can be regarded as a portion of homogeneous plane wave in a limited region of space. The plane wave in a homogeneous material corresponds to a bundle of parallel rays, the direction $\mathbf{s}_0$ of which coincides with the direction of propagation $\mathbf{k}_0$ of the wave, which is clearly the same everywhere. Consistently with (4.36), the energy is carried along the single direction $\mathbf{s}_0 \equiv \mathbf{k}_0$ in the extended region of space in which the plane wave approximation holds.

[7] Remember that the wave surface Φ is a scaled replica of the eikonal ϕ.

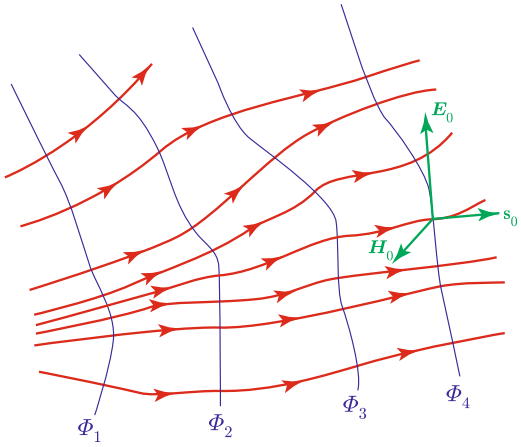

Fig. 5.2 Rays, wave surfaces $\Phi_i = const$, and fields in an inhomogeneous medium

The eikonal equation (5.5) provides the means to relate the trajectories of the electromagnetic energy to the dielectric structure of the material. From the general relation

$$\nabla\phi(\boldsymbol{r}) = n(\boldsymbol{r})\,\mathbf{s}_0 \;,$$

the lineic variation of the eikonal function along a ray is immediately obtained as the local value of the refractive index

$$\frac{\mathrm{d}\phi(\boldsymbol{r})}{\mathrm{d}s} = n(\boldsymbol{r}) \;.$$

Taking now the gradient of both members,

$$\frac{\mathrm{d}}{\mathrm{d}s}(n\mathbf{s}_0) = \nabla n \;, \tag{5.18}$$

which yields

$$\frac{\mathrm{d}n}{\mathrm{d}s}\mathbf{s}_0 + n\frac{\mathrm{d}\mathbf{s}_0}{\mathrm{d}s} = \nabla n \;,$$

whence the variation of direction of the ray is related to the dielectric structure by

$$\frac{\mathrm{d}\mathbf{s}_0}{\mathrm{d}s} = \frac{\nabla n}{n} - \frac{\mathbf{s}_0}{n}\frac{\mathrm{d}n}{\mathrm{d}s} \;. \tag{5.19}$$

Equation (5.19) represents an important result: the spatial variation of permittivity modifies the direction $\mathbf{s}_0$ along which the electromagnetic energy travels.[8] The

[8] Clearly excepted that $\mathbf{s}_0 \parallel \nabla n$.

variation of direction occurs in the plane of ∇n and $\mathbf{s}_0$. The *curvature* of the ray, that is the inverse of the *radius of curvature* ϱ, depends both on the magnitude of the refractive index variation and on the direction of propagation, since, by definition,

$$\frac{\mathbf{v}_0}{\varrho} := \frac{\mathrm{d}\mathbf{s}_0}{\mathrm{d}s} ,$$

where $\mathbf{v}_0 \perp \mathbf{s}_0$ denotes the *principal normal* to the ray. The curvature is then obtained from (5.19):

$$\frac{1}{\varrho} = \mathbf{v}_0 \cdot \frac{\mathrm{d}\mathbf{s}_0}{\mathrm{d}s} = \mathbf{v}_0 \cdot \left(\frac{\nabla n}{n} - \frac{\mathbf{s}_0}{n} \frac{\mathrm{d}n}{\mathrm{d}s} \right) = \mathbf{v}_0 \cdot \frac{\nabla n}{n} \cdot \tag{5.20}$$

The relation (5.20) indicates that, for given n and direction, the curvature increases with increasing $|\nabla n|$. The concavity, corresponding to $\varrho > 0$, is towards the region with increasing refractive index: the electromagnetic energy pattern bends towards regions of higher permittivity. As said, in a homogeneous medium the ray is straight everywhere.

5.2.1 Rays in Layered Media

Layered structures, representing materials the refractive index of which varies continuously only along one direction, are of particular relevance to Earth observation.

5.2.1.1 Spherical Layering

The large-scale decrease of air density, hence of the number of molecules per unit volume is the prevailing phenomenon that causes the corresponding decrease with height of the *average* refractive index of the terrestrial atmosphere,[9] given the relation between permittivity and the electric charge density contributing the dielectric polarization seen in Sect. 2.1. Therefore, the Earth's atmosphere is coarsely regarded as a radially symmetric medium, with a large-scale average index of refraction [35–38] varying along the radial direction $\mathbf{r}_0$ only:

$$n(\boldsymbol{r}) \equiv n(r) = 1 + \delta n(r) ,$$

[9] Small-scale deviations from the average trend caused by particular spatial distributions of air constituents and/or of temperature are considered in Sect. 5.2.3.

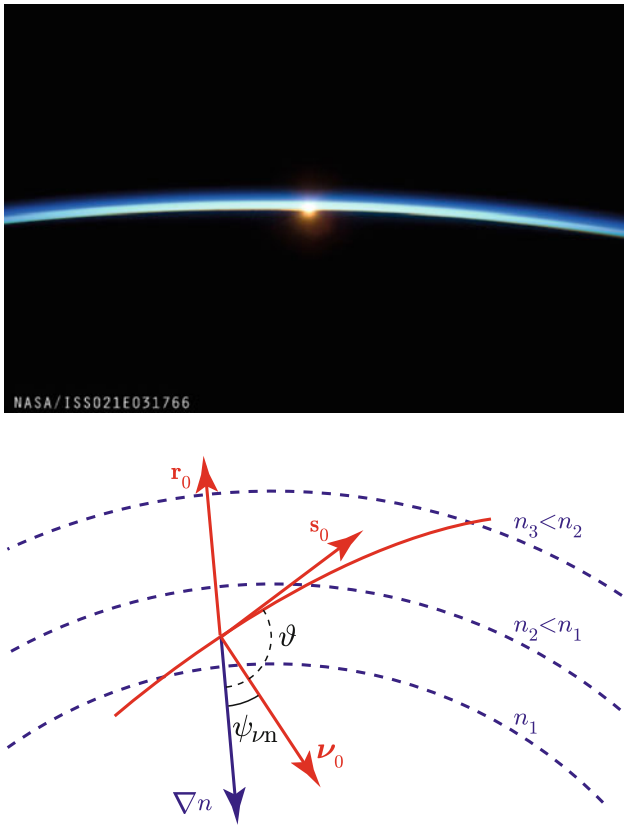

Fig. 5.3 At large scale the Earth's atmosphere is regarded as a spherically layered material with refraction index decreasing with height (*Upper image* credit: NASA)

where $\delta n(r)$ is the excess refractive index introduced in Sect. 4.1.2.5.1. The refractivity gradient is correspondingly a radial vector field (Fig. 5.3) oriented in the local *nadir* direction:

$$\nabla n = -|\nabla n|\mathbf{r}_0 \, .$$

Since the ray bending given by (5.19) is

$$\frac{\mathrm{d}\mathbf{s}_0}{\mathrm{d}s} = -\frac{|\nabla n|}{n}\mathbf{r}_0 - \frac{\mathbf{s}_0}{n}\frac{\mathrm{d}n}{\mathrm{d}s} \, ,$$

the ray is confined in the radial (i.e., vertical) plane containing $\mathbf{s}_0$ and bends *towards the surface*, with curvature (5.20)

$$\frac{1}{\varrho} = \mathbf{v}_0 \cdot \frac{\nabla n}{n} = \frac{|\nabla n|}{n} \cos \psi_{\nu \mathrm{n}} = \frac{|\nabla n|}{n} \sin \vartheta \ .$$

essentially depending on the local gradient of refractivity and on the *off-nadir angle* ϑ.

As suggested by Fig. 5.3, an air or space platform appears at higher elevation than its geometric one from a point on the surface that is not at nadir. The bending of the direction of propagation in the atmosphere [18] introduces corresponding errors into the localization of a target [13, 20, 21, 34, 41] observed by both optical and microwave systems, according to the respective refractivity gradients. The effect increases with decreasing elevation of the observing platform.[10]

5.2.1.1.1 Reference Refractivity

The microwave, or, in general, the radio frequency excess refractive index is modeled at a first approximation by an exponential function [3] decreasing with height $h = r - r_{\mathrm{E}}$ above Earth's surface:

$$\delta n(h) = \delta n_{\mathrm{S}} \, \mathrm{e}^{-h/h_0} \ . \tag{5.21}$$

In the model (5.21), δn_{S} is the value of δn on the surface of the Earth, assumed at the distance $r = r_{\mathrm{E}}$ from the center, and h_0 is a characteristic height.[11] Both δn_{S} and h_0 depend on climatology. Reference values for mid-latitudes are $\delta n_{\mathrm{S}} \approx 3.15 \cdot 10^{-4}$ and $h_0 \approx 8\,\mathrm{km}$.

The altitude dependence of the average optical refractivity [43] is essentially controlled by the mean atmospheric temperature profile, which shows a typical mid-latitude lapse rate $|\nabla T| \approx -6\,\mathrm{K\,km^{-1}}$.

It is worth to point out that the reference or "standard" average structure of the atmospheric refractivity is eventually modified by local and transitory fluctuations of the spatial distribution of temperature and of water vapor density, which affect ∇n. In some geographic areas and/or in peculiar meteorological conditions, ∇n close to the surface, where moisture and temperature deviations occur more frequently, can vanish or even change sign, giving rise to anomalous changes of the direction of propagation of the wave. Following the dielectric polarization mechanisms discussed in Sect. 2.2.1, water vapor mainly impacts refractivity at microwaves, while temperature affects n mainly at optical wavelengths.

[10] Nadir observation corresponds to off-nadir angle $\vartheta = 0$ or $\vartheta = \pi$, according to the downward or upward direction of propagation $\mathbf{s}_0$ considered in the geometry of Fig. 5.3.

[11] At "low" height, such that $h/h_0 \ll 1$, the decreasing exponential is often approximated by the linear relation $\delta n(h) \simeq \delta n_{\mathrm{S}} \, (1 - h/h_0)$.

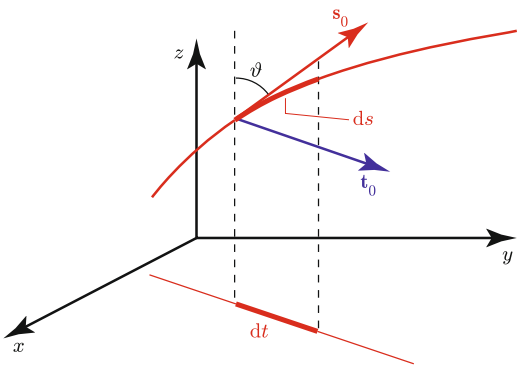

Fig. 5.4 Plane layering is assumed for limited horizontal portions of the atmosphere; $\mathbf{t}_0$ is the horizontal component of versor $\mathbf{s}_0$, while dt denotes the projection of ds onto the horizontal plane (*Upper image* credit: NASA)

5.2.1.2 Plane Layering

On a limited horizontal scale, at which the sphericity of the Earth can be neglected, the atmospheric refractive index is approximated by an average planar structure [14]. The values of n decrease with the altitude $h \equiv z$ above the plane $z = 0$ that locally approximates the earth surface (Fig. 5.4). In this case the gradient of n is vertical:

$$\nabla n = -|\nabla n|\, \mathbf{z}_0 \, .$$

The ray bending (5.19) is now

$$\frac{\mathrm{d}\mathbf{s}_0}{\mathrm{d}s} = -\frac{|\nabla n|}{n}\mathbf{z}_0 - \frac{\mathbf{s}_0}{n}\frac{\mathrm{d}n}{\mathrm{d}s} \, .$$

Analogously to the spherical layering, also in this case the ray lies in the vertical plane containing $\mathbf{s}_0$ and bends towards the surface. The local reference refractivity closely follows the one seen in Sect. 5.2.1.1.1.

5.2.2 Rays and Path Length

Representing the field through rays allows the transfer of electromagnetic energy from the source to a point of interest to be determined along a single curve, irrespective of the distribution of the radiation in the various directions. Use can be made of relatively simple geometric relations and basic properties to implement effective computational tools. Rays also provide intuitive envisioning of complicated wave phenomena, by resorting to common optical experience.

5.2.2.1 Ray Tracing

The electromagnetic ray [27, Chap. 5] is *traced* by the position vector $\boldsymbol{r}(s)$ as a function of the distance the electromagnetic energy travels from the source, as measured by the curvilinear abscissa s. Equation (5.18) and the definition of the unit vector $\mathbf{s}_0$ tangent to the curve,

$$\mathbf{s}_0 := \frac{\mathrm{d}\boldsymbol{r}}{\mathrm{d}s} ,$$

yield the relation

$$\frac{\mathrm{d}}{\mathrm{d}s}\left[n(\boldsymbol{r})\frac{\mathrm{d}\boldsymbol{r}}{\mathrm{d}s}\right] = \nabla n , \tag{5.22}$$

which provides the ray, taking account of the refractive index and of its gradient. The position vector $\boldsymbol{r}$ sweeps the ray as the arc length s traveled by the electromagnetic energy increases. Any point on the curve at distance s from the initial position[12] is localized in space according to (5.22). Figure 5.5 represents the ray described by the end of the position vector $\boldsymbol{r}$, which changes following the dielectric spatial structure to which the eikonal function ϕ likewise adapt. Given the positions of the initial (source) and end (observation or target) points, $\mathrm{P_s}$ and P, respectively, (5.22) determines the curve along which the electromagnetic energy travels.

[12] Provided the condition of far field is met.

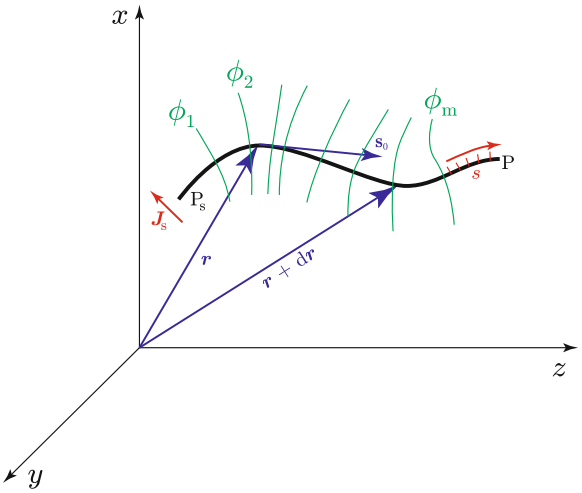

Fig. 5.5 A ray is described by the evolving end of the position vector $\boldsymbol{r}(s)$ from the point P_s where the source $\boldsymbol{J}_s$ is located to point P where the field is considered; traces of eikonal surfaces ϕ_m, $m = 1, 2, \ldots$, and curvilinear abscissa s along the ray are indicated

5.2.2.2 Fermat Principle

Besides the analytical relation (5.22), which provides the foundation of numerical ray-tracing tools, a basic property of the electromagnetic trajectory turns out useful in wave propagation. The *Fermat principle* [19] states that the electromagnetic ray passing through two points P_1 and P_2 satisfies the condition that its *electromagnetic path length*

$$\mathcal{L} := \int_{P_1}^{P_2} n(\boldsymbol{r})\, \mathrm{d}s \,, \tag{5.23}$$

functional of the trajectory between P_1 and P_2, is stationary. The consequence is that among the curves connecting the two points, the ones (possibly a single one) that make stationary (usually minimum) the value of the line integral of the refraction index are trajectories of the electromagnetic energy, hence identify the ray. With reference to Fig. 5.6, the path lengths $\mathcal{L}_{c'}$ along generic curve segments c' between P_1 and P_2 exceed $\mathcal{L}_c$ along the ray c. The Fermat principle provides an alternative and effective numerical technique to trace the rays [45], that is to identify the electromagnetic trajectories, especially when reflections (Chap. 6) are involved. For instance, in the case of the plane mirror sketched in Fig. 5.7 and homogeneous media, the straight segment c_{dr} has the shortest among the paths between P_1 and P_2 that do not hit the mirror, while $c_{\mathrm{rr}} = \overline{P_1\,Q\,P_2}$ is the shortest among the broken

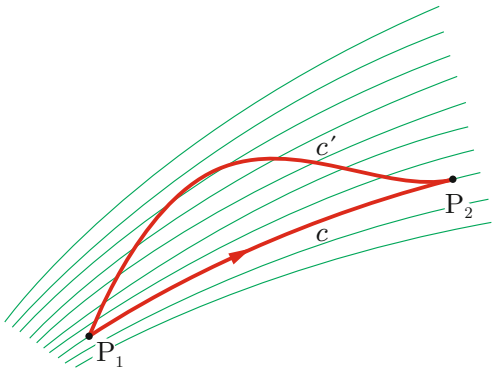

Fig. 5.6 The ray is the trajectory c that minimizes the electromagnetic path length between P_1 and P_2

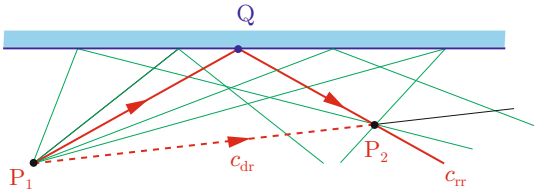

Fig. 5.7 The direct ($c_{dr} \equiv P_1 P_2$) and reflected ($c_{rr} \equiv P_1 Q P_2$) rays minimize the path lengths between P_1 and P_2 respectively among the direct trajectories and among those passing through a point of the reflecting surface

lines touching it.[13] The trajectories c_{dr} and c_{rr} that correspond to the *local minima* of length, respectively identify the *direct* and the *reflected* rays linking P_1 and P_2.

5.2.2.3 Electromagnetic Path Length and Distance

The path length $\mathcal{L}$ defined by (5.23) has major importance in Earth observation, since it is directly related to two measurable quantities, i.e.,

- the time τ the electromagnetic energy takes to travel between two points P_1 and P_2, for instance where source and receiver are located;
- the relative phase Φ of the field between the two locations.

Given the velocity of propagation (5.11), an elementary arc of length ds along a ray in an inhomogeneous medium is traveled in an elementary time[14]

[13] Here the electromagnetic path length is simply proportional to the geometric length, since the material is assumed homogeneous.

[14] Actually, the *group velocity* rather than the phase velocity determines the travel time of wave pulses [1, 48, 49]. The two velocities have close values when the refractive index is a weak function of the wavenumber κ.

$$\mathrm{d}t = \frac{\mathrm{d}s}{u(s)} = \frac{n(s)\,\mathrm{d}s}{c_0}\,,$$

hence the wave travels from the abscissa s_1 at point P_1 to s_2 at P_2 in the time

$$\Delta t \equiv \tau = \frac{1}{c_0}\int_{s_1}^{s_2} n(s)\,\mathrm{d}s = \frac{\mathcal{L}}{c_0}\,. \tag{5.24}$$

Equation (5.24) relating time to distance implies that measuring Δt yields the electromagnetic path length and, in turn, the distance between the points, provided the ray and $n(s)$ along it are known. Likewise, the relation (5.8) between phase and path length is the basis of highly sensitive distance measurements, albeit also subject to knowledge of the refractive index along the measurement path.

The exploitation of the link of both travel time and phase difference to distance has allowed tremendous advances in systems and methods crucial to geoscience and its applications. The following are worth mentioning.

5.2.2.3.1 The GPS

The three coordinates which identify the position of a receiver are provided by measuring the traveling times from (at least) three space-based suitably positioned transmitters. The **G**lobal **P**ositioning **S**ystem (GPS), or, in general, the **G**lobal **N**avigation **S**atellite **S**ystem (GNSS) [23, 33], yields a horizontal localization open accuracy which typically varies from some tens of meters down to a few meters. The **d**ifferential **G**lobal **P**ositioning **S**ystem (DGPS) technique is able to enhance the relative positioning accuracy to decimeters, or, locally, to centimeters [42]. It is important pointing out that the L-band GNSS signals not only provide position and navigation tools, but also find a number of relevant applications in Earth observation [5, 22].

5.2.2.3.2 The Radar

A **ra**dio **d**etection **a**nd **r**anging (radar) system [40] determines the distance of the observed target (be it aircraft, ship, or portion of the earth surface) from the lag between the time at which the electromagnetic energy is transmitted and the time at which the echo, that is the energy that is sent back from the object, is received. The basics of radar observations are summarized in Sects. 10.2.4 and 11.4.3, while, in particular, the foundations of radar imaging and of the SAR systems are outlined in Sect. 10.2.4.1, as well as in 11.4.3.4.

Analogous sensors operating at optical wavelengths are the **li**ght **d**etection **a**nd **r**anging (lidar) systems [15], on which Sect. 10.2.5 gives some details.

5.2.2.3.3 Radar Interferometry

The **s**ynthetic **a**perture **r**adar **in**terferometry (InSAR) [12] exploits the interference between two waves propagating in different directions discussed in Sect. 4.3, to map the height-dependent (Sect. 4.3.1) phase difference. This kind of measurement, as outlined in Sect. 12.2, leads to the generation of the **d**igital **e**levation **m**odel (DEM) for global topographic mapping. Multiple *relative* measurements enhance the distance sensitivity to a fraction of wavelength, down to a few millimeters. Such tiny vertical displacements of points on the earth surface are measured as functions of time through the **d**ifferential **SAR in**terferometry (DinSAR) technique [39].

5.2.3 Atmospheric Path Delay

The end of Sect. 5.2.2.3 calls attention to the effect of the refractive index on the quantitative relation existing between time or phase and distance. Indeed, the accuracy in measuring distance is affected by the incomplete knowledge of the profile $n(s)$ of the refractive index[15] along the propagation path. Models and a-priori information on $n(s)$ provide suitable links of the path length $\mathcal{L}$ to the geometric distance. However, the variations of n caused by random space-time fluctuations of the parameters affecting refractivity [31, 44, 46] generate unavoidable measurement noise.

The path length is related to the permittivity profile $\tilde{\epsilon}(s)$ by

$$\mathcal{L} = \int_{P_1}^{P_2} n(s)\,\mathrm{d}s = \int_{P_1}^{P_2} \sqrt{1 + \delta\tilde{\epsilon}(s)}\,\mathrm{d}s\ ,$$

where $\delta\tilde{\epsilon}$ depends on the local physical characteristics of the material crossed by the ray. In the air, $\delta\tilde{\epsilon} \ll 1$, so

$$n \simeq 1 + \frac{\delta\tilde{\epsilon}}{2}\ .$$

In this approximation, the path length becomes

$$\mathcal{L} \simeq \overline{P_1\,P_2} + \frac{1}{2}\int_{P_1}^{P_2} \delta\tilde{\epsilon}(s)\mathrm{d}s\ . \tag{5.25}$$

The relation (5.25) indicates that the electromagnetic path length exceeds the *geometric length of the ray* between P_1 and P_2 by a quantity which depends on the

[15] As mentioned, enhanced accuracy requires considering the *group refractive index* [9, Chap. 4], [32].

values along the ray[16] of the aerological parameters that affect the air refractivity [11]. Therefore, the electromagnetic energy travels from P_1 to P_2 in the time

$$\tau \simeq \frac{\overline{P_1\,P_2}}{c_0} + \frac{1}{2\,c_0}\int_{P_1}^{P_2} \delta\tilde{\epsilon}(s)\,\mathrm{d}s = \tau_0 + \delta\tau\ ,$$

which exceeds the time in vacuo τ_0 by a *delay* $\delta\tau$.

The formula (2.36) yields the tropospheric path length at microwave frequencies[17] in terms of the routinely measurable meteorological parameters p_t, p_w and T (Sect. 2.2.1.1)[18]:

$$\mathcal{L} \simeq \overline{P_1\,P_2} + 7.76\cdot 10^{-5}\int_{P_1}^{P_2}\frac{p_t(s)}{T(s)}\,\mathrm{d}s + 0.37\int_{P_1}^{P_2}\frac{p_w(s)}{T(s)^2}\,\mathrm{d}s\ . \tag{5.26}$$

Therefore, the path length $\mathcal{L}$ is larger than the geometric length $\mathcal{L}_0 = \overline{P_1\,P_2}$ of the ray arc by a quantity

$$\mathcal{L}_a = \mathcal{L}_d + \mathcal{L}_w$$

that depends, as the air refractivity, on pressure, temperature and humidity. Based on the model introduced in Sect. 2.2.1, relevant features of the excess length terms are:

- the *dry excess path length* $\mathcal{L}_d$ is higher, but more stable and predictable from weather observations and climatic modeling;
- the *wet excess path length* $\mathcal{L}_w$ has lower values, but, as p_w, is more variable and less predictable: it is the main responsible of the measurement errors, as shown glaringly by Fig. 12.25.

The discussion on the effects of the atmospheric excess path length, as well as examples of its statistical distributions are postponed to Sect. 12.3.2.1.

Note that, in discussing the atmospheric delay, no reference has been made to the ionosphere, which, indeed, can also affect the path length, when observations are carried out at the lower microwave frequencies [47], as mentioned in Sect. 2.2.5.

[16]The random variations of $\delta\tilde{\epsilon}$ actually affect also the trajectory of the electromagnetic energy. However, the effect of the air fluctuations on the ray geometry is neglected here.

[17]The dependence of the refractivity on the appropriate aerological parameters, such as p_t and T in (2.37), has to be considered if the phase information was needed at optical wavelengths.

[18]Regarding the numerical coefficients in (5.26), see Footnote 14 of Sect. 2.2.1.1.

5.3 Properties of the Field

The results obtained in the previous sections are now assembled together with the outcome of the transport equation. Indications on the general features of amplitude, phase and polarization of the field propagating in weakly inhomogeneous materials are drawn according to the geometrical optics model. The case of lossless media is treated separately from that of dissipative materials.

5.3.1 Field in Lossless Media

Although the energy of the field remains unchanged during propagation, its amplitude generally changes following the refractivity structure of the lossless material. The transport equation (5.6) provides the relation between dielectric structure and amplitude of the field.

5.3.1.1 Flux Tubes and Field Amplitude

The geometric trajectories of the electromagnetic energy (rays) have been identified on the basis of (5.5) and of the derived relations, as well as by exploiting the Fermat principle. The field[19] along the ray varies according to (5.6):

$$\boldsymbol{E}_0(\boldsymbol{r})\nabla^2\phi(\boldsymbol{r}) + 2\left[\nabla\phi(\boldsymbol{r})\cdot\nabla\right]\boldsymbol{E}_0(\boldsymbol{r}) = 0\,. \tag{5.27}$$

To obtain the field amplitude from (5.27), the flux tube depicted in Fig. 5.8 is considered around a ray. Expanding the Laplacian of the eikonal function, using the definition of divergence and realizing that the flux is only trough the tube sections

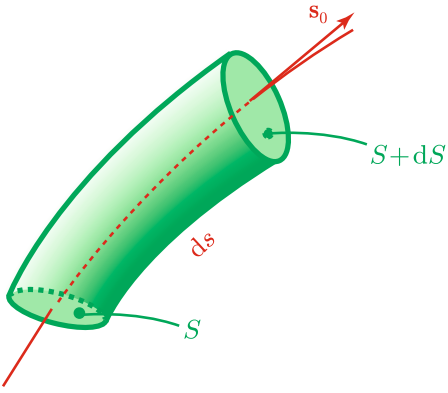

Fig. 5.8 An elementary-length segment of divergent flux tube around a ray

[19] As said, the field is approximated by the dominant term $\boldsymbol{E}_0$ of the Luneburg-Kline expansion, which is assumed real.

S and $S + dS$, while the one through the lateral wall vanishes, some algebraic manipulation of (5.27) leads to

$$E_0^2 \left(\frac{\partial n}{\partial s} + \frac{n}{S} \frac{\partial S}{\partial s} \right) + n \frac{\partial E_0^2}{\partial s} = 0 \, . \tag{5.28}$$

Equation (5.28) expresses the balance between a term proportional to the power density and one relative to the variation that the power density undergoes along the ray. Both terms take account of the dielectric structure of the material and, through the section S and its variation, of the divergence or convergence of the rays[20] in the neighborhood of the considered position. Further manipulation of (5.28) readily yields the invariance of the product of wave intensity, refractive index and flux tube section:

$$E_0^2(s)\, n(s)\, S(s) = const \, , \tag{5.29}$$

for any value of abscissa s along the ray. Therefore, if $E_{0\mathrm{i}}^2$, n_i and S_in are the respective initial values at a reference initial abscissa s_i, the relation (5.29) provides the amplitude of the field at a subsequent abscissa s along the ray:

$$E_0(s) = E_{0\mathrm{i}} \sqrt{\frac{n_\mathrm{i}}{n(s)}} \sqrt{\frac{S_\mathrm{in}}{S(s)}} \, . \tag{5.30}$$

As expected, (5.30) is consistent with the energy conservation in a lossless medium, requiring that the field amplitude respectively decreases or increases according to the expansion or shrinking of the sections of the flux tubes. It should also be noted the likewise consistent inverse dependence of the electric field amplitude on $\sqrt{n}$. For given initial conditions of the wave, the variations undergone by the sections of the flux tubes depend on the trajectories of the electromagnetic energy, which are ultimately related to the dielectric spatial structure of the material according to the results of Sect. 5.2.

5.3.1.2 Phase

The phase of the field, consistent with the coherent approach, is provided by (5.8). Therefore, the complete expression of the complex field, joining both phase and amplitude information is

$$E(s) = E_{0\mathrm{i}} \sqrt{\frac{n_\mathrm{i}\, S_\mathrm{in}}{n(s)\, S(s)}} \, \mathrm{e}^{-\mathrm{j}\kappa_0 \int_{s_\mathrm{i}}^{s} n(s)\, \mathrm{d}s} \, , \tag{5.31}$$

[20] The shape of the flux tube is affected both by the dielectric structure and by the nature of the source.

where the initial phase $\Phi(s_\mathrm{i})$ is taken as reference. Equation (5.31) is also known as the **W**entzel-**K**ramers-**B**rillouin (WKB) field approximation.

The expression of the field clearly contains the electromagnetic path length between the initial abscissa taken as reference and the abscissa s along the wave trajectory:

$$E(s) = E_{0\mathrm{i}} \sqrt{\frac{n_\mathrm{i}\, S_\mathrm{in}}{n(s)\, S(s)}}\, \mathrm{e}^{-\mathrm{j}\kappa_0 \mathcal{L}(s)} \ . \tag{5.32}$$

Equation (5.32) provides a tool for measuring distance that accompanies the one based on the travel time considered in Sect. 5.2.2.3. Indeed, measuring the relative phase of the field in s allows the *electromagnetic* distance $\mathcal{L}$ between s_i and s to be determined. The retrieval of the *geometric* distance $s - s_\mathrm{i}$ from $\mathcal{L}$ obviously suffers from the same drawbacks discussed in Sect. 5.2.3 and further detailed in Sect. 12.3.2.1.

5.3.1.3 Polarization

Each component of the vector field obeys the same scalar relation derived from (5.3) in an isotropic weakly inhomogeneous medium, given the independence of the refractive index from the field direction. The electromagnetic path length $\mathcal{L}$ is correspondingly independent of the component and, since the relative phase between components remains unchanged along the ray, the type of polarization does not change during propagation. Rather, the constraint (5.17), that is, $\mathfrak{e}_0 \perp \mathbf{s}_0$, may change the field orientation, following the variations (5.19) of $\mathbf{s}_0$ caused by the dielectric structure. As already mentioned, the assumption of isotropy, which is straightforward for the troposphere, may fail at the lower microwave frequencies in the ionosphere (cf. Sect. 2.2.5).

5.3.2 Field in Lossy Media

The presence of dissipations in the actual terrestrial materials demands that the basic field definition (5.4) be modified. In fact, the approach of Sect. 5.1.1 leads to a *complex* eikonal equation

$$\nabla\phi \cdot \nabla\phi = \tilde{\epsilon}_\mathrm{r} + \mathrm{j}\tilde{\epsilon}_\mathrm{j}$$

that the real eikonal function $\phi(\boldsymbol{r})$ can no longer satisfy. Therefore, a *complex* function $\Psi(\boldsymbol{r})$ is now required to appear in the field (5.9):

$$\boldsymbol{E}(\boldsymbol{r}) = \boldsymbol{E}_\mathrm{LK}(\boldsymbol{r})\, \mathrm{e}^{-\mathrm{j}\kappa_0 \Psi(\boldsymbol{r})} \ .$$

The complex function $\Psi(\boldsymbol{r})$, formed by the combination of two real functions,

$$\Psi(\boldsymbol{r}) = \phi(\boldsymbol{r}) - \mathrm{j}\alpha(\boldsymbol{r}) \ ,$$

leads to a complex relation which replaces (5.5):

$$(\nabla\phi - \mathrm{j}\nabla\alpha) \cdot (\nabla\phi - \mathrm{j}\nabla\alpha) - \tilde{\epsilon}_\mathrm{r} - \mathrm{j}\tilde{\epsilon}_\mathrm{j} = 0 \ ,$$

or

$$\nabla\phi \cdot \nabla\phi - \nabla\alpha \cdot \nabla\alpha - 2\mathrm{j}\nabla\phi \cdot \nabla\alpha - \tilde{\epsilon}_\mathrm{r} - \mathrm{j}\tilde{\epsilon}_\mathrm{j} = 0 \ . \tag{5.33}$$

The equation with complex coefficients (5.33) splits into

$$\begin{cases} |\nabla\phi|^2 - |\nabla\alpha|^2 = \tilde{\epsilon}_\mathrm{r} \ ; \\ \nabla\phi \cdot \nabla\alpha \qquad\quad = -\dfrac{\tilde{\epsilon}_\mathrm{j}}{2} \ , \end{cases} \tag{5.34}$$

from which, at least in principle, the eikonal function $\phi(\boldsymbol{r})$ and the *absorption function* $\alpha(\boldsymbol{r})$ are determined in terms of $\tilde{\epsilon}_\mathrm{r}(\boldsymbol{r})$ and $\tilde{\epsilon}_\mathrm{j}(\boldsymbol{r})$. The resulting field is then

$$\boldsymbol{E}(\boldsymbol{r}) = \boldsymbol{E}_\mathrm{LK}(\boldsymbol{r}) \, \mathrm{e}^{-\kappa_0 \alpha(\boldsymbol{r})} \, \mathrm{e}^{-\mathrm{j}\kappa_0 \phi(\boldsymbol{r})} \ . \tag{5.35}$$

The losses result in the introduction of a real exponential which causes an additional variation of the field amplitude, which combines with that produced by the inhomogeneities, considered in Sect. 5.3.1.1. The surfaces $\alpha(\boldsymbol{r}) = const$ are the *amplitude surfaces* and $\nabla\alpha$ identifies the direction of maximum rate of amplitude variation. The close similarity with the structure of plane waves in homogeneous media introduced in Sect. 4.1.2 is readily realized. After all, homogeneous medium and plane wave are just particular cases of the more general situation of inhomogeneity and waves of general configuration. In particular, correspondingly to the relation between $\nabla\phi$ and $\boldsymbol{\beta}$ noted in Sect. 5.1.1, a plane wave in a homogeneous medium has

$$\kappa_0 \nabla\alpha \equiv \boldsymbol{\alpha} \ ,$$

that is, the gradient of the absorption function α reduces to the attenuation vector $\boldsymbol{\alpha}$ introduced in Sect. 4.1.2, scaled by the vacuum angular wavenumber κ_0.

5.3.2.1 Weakly Lossy Materials

The various examples discussed in Sect. 2.2 suggest that several terrestrial materials have $\left|\tilde{\epsilon}_\mathrm{j}\right| \ll \tilde{\epsilon}_\mathrm{r}$. The pair of relations (5.34) then indicates that

$$|\nabla\alpha| \ll |\nabla\phi| \ .$$

Therefore, the imaginary part of permittivity does not affect appreciably the electromagnetic trajectories, which are essentially determined by the spatial distribution of $\tilde{\epsilon}_\mathrm{r}$. The results found for the lossless medium remain almost unchanged, and, since the field decay depends on the distance traveled along a ray,

$$\nabla\phi \parallel \nabla\alpha \parallel \mathbf{s}_0 \, .$$

As a consequence, the dot product in (5.34) is approximated by the product of the moduli of the gradients and

$$\nabla\phi \simeq \sqrt{\tilde{\epsilon}_\mathrm{r}}\left[1 + \frac{1}{8}\left(\frac{\tilde{\epsilon}_\mathrm{j}}{\tilde{\epsilon}_\mathrm{r}}\right)^2\right]\mathbf{s}_0 \simeq \sqrt{\tilde{\epsilon}_\mathrm{r}}\,\mathbf{s}_0 = n\,\mathbf{s}_0 \, ; \tag{5.36}$$

$$\nabla\alpha \simeq \frac{-\tilde{\epsilon}_\mathrm{j}}{\sqrt{2\,\tilde{\epsilon}_\mathrm{r}}}\left[1 - \frac{1}{8}\left(\frac{\tilde{\epsilon}_\mathrm{j}}{\tilde{\epsilon}_\mathrm{r}}\right)^2\right]\mathbf{s}_0 \simeq \frac{|\tilde{\epsilon}_\mathrm{j}|}{\sqrt{2\,\tilde{\epsilon}_\mathrm{r}}}\,\mathbf{s}_0 \, . \tag{5.37}$$

Equations (5.36) and (5.37), which clearly correspond to (4.14) and (4.15), provide quite useful approximate expressions of the phase progression and of the decay rate of the field traveling along a ray in a weakly inhomogeneous and weakly lossy material such as the gaseous atmosphere. The gradient of the eikonal function, from which the wavelength and the propagation velocity are obtained, is essentially determined by the local value of the refractive index, with, if required, a possible correction which takes the ratio $\tilde{\epsilon}_\mathrm{j}/\tilde{\epsilon}_\mathrm{r}$ into account. On its turn, the decay caused by absorption is proportional to the imaginary part of the relative permittivity. It should be reminded that the values of $\nabla\phi$ and $\nabla\alpha$ are *local* values, given the inhomogeneity of the material. The values are also normalized to the propagation constant for the vacuum, which can have quite high values when the observing systems operate in the upper range of frequencies.

5.3.2.2 The Attenuated Field

The superposition of the effects of inhomogeneities and of absorption in modifying the amplitude of the field is taken into account by the transport equation. This latter is only slightly modified under the assumption of weak losses, so that the field is regarded as the field (5.31) relative to the material with $\tilde{\epsilon} = \tilde{\epsilon}_\mathrm{r}$, suitably attenuated by a factor which depends on $\tilde{\epsilon}_\mathrm{j}$.

The complete expression of the attenuated field including the amplitude and phase factors in terms of real and imaginary parts of relative permittivity is suitably written as

$$E(s) \simeq E_{0\mathrm{i}}\sqrt{\frac{n_\mathrm{i}\,S_\mathrm{in}}{n(s)\,S(s)}}\;\mathrm{e}^{-\kappa_0\int_{s_\mathrm{i}}^{s}\frac{|\tilde{\epsilon}_\mathrm{j}(s')|}{\sqrt{2\,\tilde{\epsilon}_\mathrm{r}(s')}}\,\mathrm{d}s'}\;\mathrm{e}^{-\mathrm{j}\kappa_0\left[s - s_\mathrm{i} + \int_{s_\mathrm{i}}^{s}\delta\tilde{\epsilon}_\mathrm{r}(s')\,\mathrm{d}s'\right]} \, . \tag{5.38}$$

Given its relevance, the path length in (5.38) has been split into the vacuum component $\kappa_0(s - s_\mathrm{i})$ and the excess component $\kappa_0 \int_{s_\mathrm{i}}^{s} \delta\tilde{\epsilon}_\mathrm{r}(s')\,\mathrm{d}s'$. This latter can be further expanded in terms of the meteorological parameters following Sect. 5.2.3, if propagation in the troposphere is being considered.

The real exponential in (5.38) depends on the quantity

$$\mathfrak{a}(s') = \frac{\kappa_0\,|\tilde{\epsilon}_\mathrm{j}(s')|}{\sqrt{2\,\tilde{\epsilon}_\mathrm{r}(s')}} \tag{5.39}$$

integrated along the path. The parameter $\mathfrak{a} \geq 0$ is the *specific absorption* of the medium at abscissa s'. The value of the exponential

$$\mathrm{e}^{-\kappa_0 \int_{s_\mathrm{i}}^{s} \mathfrak{a}(s')\,\mathrm{d}s'}$$

decreases with increasing traveled distance s, thus attenuating the field, as already considered in Sect. 4.1.2 for the plane waves in homogeneous media. The *attenuation* $A(s_\mathrm{i}, s)$ the field undergoes because of absorption from s_i to s is obviously the same as (4.22) for plane waves:

$$A(s_\mathrm{i}, s) = \left| \frac{E(s)}{E(s_\mathrm{i})} \right| .$$

As usual, it is expressed in dB by

$$A(s, s_\mathrm{i}) = -20 \log_{10} \left| \frac{E(s)}{E(s_\mathrm{i})} \right| \equiv -10 \log_{10} \frac{\mathcal{P}(s)}{\mathcal{P}(s_\mathrm{i})} \quad \mathrm{dB}\ , \tag{5.40}$$

so that the values of field attenuation and power attenuation coincide.

Note that, given the spatial variations of $\tilde{\epsilon}_\mathrm{r}$ and $\tilde{\epsilon}_\mathrm{j}$, the exponentials in (5.38) are not exponential functions of s: the amplitude of the field does not decrease exponentially with distance. This behavior clearly differs from that of the plane waves in a homogeneous medium, for which the specific attenuation coincides with the absorption constant and the attenuation factor is the decreasing exponential function of distance (4.23). In that case, the attenuation constant yields the decrease of the field per unit distance, typically expressed in $\mathrm{dB\,km^{-1}}$, which is the same everywhere. In the present case, the specific absorption can likewise be expressed in $\mathrm{dB\,km^{-1}}$, but with the precaution of bearing in mind its spatial variability. In particular, care must be exerted when evaluating the atmospheric attenuation on a satellite to ground path or vice-versa, since $\tilde{\epsilon}_\mathrm{j}$, and consequently $\mathfrak{a}$, decrease with height and in practice vanish beyond a certain altitude, outside the atmosphere.

Waves in a Smooth Environment

After learning the rudiment of wave propagation, necessarily circumscribed to the simplest case of homogeneous media, we have now to consider materials the dielectric properties of which vary from point to point, as it occurs in the real Earth's environment. Describing waves in inhomogeneous media hardly augurs an easy task, so the assumption of smoothly varying refractive index is invoked. Going through the by now usual analytical burden leads us to find more general waves, the propagation of which is directly governed by the spatial distribution of the permittivity. Wave surfaces, wavelength and velocity adapt to the local value of the index of refraction. A further quite interesting feature is that the conformation of the wave in the smoothly varying material is analogous to the one of the field we observe far from the source in a homogeneous medium.

The approach introduces the concept of ray as the trajectory along which the electromagnetic energy travels. We see that the energy does not move along straight lines, but follows the spatial variations of the refractive index. Only when the latter is constant, the rays are rectilinear. The direction of propagation bends toward the regions where n is higher, so that focusing and dispersion of the electromagnetic power density are observed locally in inhomogeneous materials. We are especially informed of the features of the rays in the atmosphere, given its relevance to Earth observation. The Fermat principle introduces us to the electromagnetic path length and path delay, concepts of vital importance for distance measurements in crucial applications like the Global Navigation Satellite System, as well as radar, and SAR interferometry.

How the magnitude of the field evolves in a weakly inhomogeneous environment is investigated through the notion of flux tube, while the way the phase of the field progresses is linked to the propagation constant and the profile of the refractive index. The features of the waves are then examined when the material is lossy. An absorption function that accounts for the conversion of electromagnetic energy into heat is introduced. A result the conscientious reader may expect is that the wave attenuation is directly related to the imaginary part of the permittivity of the material.

References

1. Abshire JB, Gardner CS (1985) Atmospheric refractivity corrections in satellite laser ranging. IEEE Trans Geosci Remote Sens GE-23(4):414–425. doi:10.1109/TGRS.1985.289431
2. Bean BR, Dutton EJ (1966) Radio meteorology, U.S. Government Printing Office. ISBN:9780486618890
3. Bean BR, Thayer GD (1959) Central radio propagation laboratory exponential reference atmosphere. J Res Nat Bur Stand-D Radio Propag 63D(3):315–317. doi:10.6028/jres.063D.031
4. Bertoni HL (1999) Radio propagation for modern wireless systems. Prentice-Hall. ISBN:9780132441964

5. Bevis M, Businger S, Herring TA, Rocken C, Anthes RA, Ware RH (1992) GPS meteorology: remote sensing of atmospheric water vapor using the global positioning system. J Geophys Res Atmos 97(D14):15787–15801. doi:10.1029/92JD01517
6. Choudhary S, Felsen L (1973) Asymptotic theory for inhomogeneous waves. IEEE Trans Antennas Propag 21(6):827–842. doi:10.1109/TAP.1973.1140598
7. Courant R, Hilbert D (2008) Methods of mathematical physics, vol 1. Wiley. ISBN:9783527617227
8. Denny M (2000) Refracted propagation effects for airborne radar. In: Radar Conference, 2000. The Record of the IEEE 2000 International, pp 554–559. doi:10.1109/RADAR.2000.851894
9. Ditchburn RW (1991) Light. Dover. ISBN:9780486666679
10. Dominek A, Peters L, Burnside WD (1987) An additional physical interpretation in the Luneburg-Kline expansion. IEEE Trans Antennas Propag 35(4):406–411. doi:10.1109/TAP.1987.1144128
11. Elgered G (1993) Tropospheric radio-path delay from ground-based microwave radiometry. In: Janssen MA (ed) Atmospheric remote sensing by microwave radiometry. Wiley. ISBN:9780471628910
12. Ferretti A, Monti-Guarnieri A, Prati C, Rocca F, Massonnet D (2007) InSAR principles: guidelines for SAR interferometry processing and interpretation. ESA. ISBN:9789290922339
13. Fortunati S, Gini F, Greco M, Farina A, Graziano A, Giompapa S, Castella FR (2013) Correction of refracted propagation effects for airborne radar tracking. IEEE Trans Aerosp Electron Syst 49(1):20–41. doi:10.1109/TAES.2013.6404089
14. Freehafer JE, Fishback WT, Furry WH, Kerr DE (1951) Theory of propagation in a horizontally stratified atmosphere. In: Kerr DE (ed) Propagation of short radio waves, Chap. 2. McGraw-Hill. ISBN:9780863410994
15. Fujii T, Fukuchi T (2005) Laser remote sensing. Taylor & Francis. ISBN:9781420030754
16. Fuki AA, Kravtsov YA, Naida ON (1998) Geometrical optics of weakly anisotropic media. Gordon & Breach. ISBN:9789056990367
17. Gleason S, Gebre-Egziabher D (eds) (2009) GNSS applications and methods. Artech House. ISBN:9781596933309
18. Hohenkerk CY, Sinclair AT (1985) The computation of angular atmospheric refraction at large zenith angles. Technical report, Nautical Almanac Office TN 63. Royal Greenwich Observatory
19. Holm DD (2012) Fermat's principle and the geometric mechanics of ray optics. Summer School Lectures, Fields Institute, Toronto. https://www.fields.utoronto.ca/programs/scientific/12-13/Marsden/FieldsSS2-FinalSlidesJuly2012.pdf (visited on 14 June 2014)
20. Hulley G, Pavlis EC, Mendes VB (2007) Validation of improved atmospheric refraction models for satellite laser ranging (SLR). In: Tregoning P, Rizos C (eds) Dynamic planet. International association of geodesy symposia, vol 130. Springer, pp 844–852. ISBN:978-3-540-49349-5. doi:10.1007/978-3-540-49350-1_119
21. Jiang C, Wang B (2001) Atmospheric refraction corrections of radiowave propagation for airborne and satellite-borne radars. Sci China Ser E Technol Sci 44(3):280–290. doi:10.1007/BF02916705
22. Jin S, Komjathy A (2010) GNSS reflectometry and remote sensing: new objectives and results. Adv Space Res 46(2):111–117. doi:10.1016/j.asr.2010.01.014
23. Kaplan ED, Hegarty CJ (eds) (2005) Understanding GPS: principles and applications. Artech House. ISBN:9781580538954
24. Keller JB, Lewis RM (1995) Asymptotic methods for partial differential equations: the reduced wave equation and Maxwell's equations. In: Keller JB, McLaughlin DW, Papanicolaou GC (eds) Surveys in applied mathematics, vol 1. Plenum. ISBN:9781489904386
25. Kline M (1951) An asymptotic solution of Maxwell's equations. Commun Pure Appl Math 4(2–3):225–262. doi:10.1002/cpa.3160040203
26. Kline M, Kay IW (1965) Electromagnetic theory and geometrical optics. Interscience. ISBN:9780470491195
27. Levy M (2000) Parabolic equation methods for electromagnetic wave propagation. Institution of Electrical Engineers. ISBN:9780852967645

28. Ling H, Chou R-C, Lee S-W (1989) Shooting and bouncing rays: calculating the RCS of an arbitrarily shaped cavity. IEEE Trans Antennas Propag 37(2):194–205. doi:10.1109/8.18706
29. Luneburg RK (1964) Mathematical theory of optics. University of California Press. ISBN:9780520007802
30. Luneburg RK (1948) Propagation of electromagnetic waves. Mimeographed lecture notes. New York University, New York
31. Meyer-Arendt JR, Emmanuel CB (1965) Optical scintillation: a survey of the literature. National Bureau of standards NBS technical note, vol 225. U.S. G.P.O., Washington, DC
32. Owens JC (1967) Optical refractive index of air: dependence on pressure, temperature and composition. Appl Opt 6(1):51–59. doi:10.1364/AO.6.000051
33. Parkinson BW, Spilker JJ (eds) (1996) Global positioning system: theory and applications, vol 1. American Institute of Aeronautics and Astronautics. ISBN:9781600864193
34. Saastamoinen J (1972) Atmospheric correction for the troposphere and stratosphere in radio ranging satellites. In: The use of artificial satellites for geodesy. Geophys Monogr Ser 15:247–251. doi:10.1029/GM015p0247
35. Saastamoinen J (1972) Contributions to the theory of atmospheric refraction – part I. Astronomical refraction. Bull Gaeodésique 105:279–298. doi:10.1007/BF02521844
36. Saastamoinen J (1973) Contributions to the theory of atmospheric refraction – part II. Refraction corrections in satellite geodesy. Bull Gaeodésique 107(1):13–34. doi:10.1007/BF02522083
37. Saastamoinen J (1972) Introduction to practical computation of astronomical refraction. Bull Gaeodésique 106(1):383–397. doi:10.1007/BF02522047
38. Schulkin M (1952) Average radio-ray refraction in the lower atmosphere. Proc IRE 40(5):554–561. doi:10.1109/JRPROC.1952.273820
39. Simonetto E, Follin J-M (2012) An overview on lnterferometric SAR software and a comparison between DORIS and SARSCAPE packages. In: Bocher E, Neteler M (eds) Geospatial free and open source software in the 21st century: proceedings of the first open source geospatial research symposium, OGRS 2009, Chap. 7. Lecture notes in geoinformation and cartography. Springer. ISBN:9783642105951
40. Skolnik MI (2003) Introduction to radar systems. McGraw Hill. ISBN:9780070445338.
41. Sweezy WB, Bean BR (1963) Correction of atmospheric refraction errors in radio height finding. J Res Nat Bur Stand-D Radio Propag 67D(2):139–151. doi:10.6028/jres.067D.017
42. The Global Differential GPS (GDGPS) System. NASA/Caltech JPL. http://www.gdgps.net/ (visited on 06 Jan 2014)
43. Thomas ME, Joseph RI (1996) Astronomical refraction. Johns Hopkins APL Tech Dig 17(3):279–284
44. VanZandt TE, Green JL, Gage KS, Clark WL (1978) Vertical profiles of refractivity turbulence structure constant: comparison of observations by the Sunset radar with a new theoretical model. Radio Sci 13(5):819–829. doi:10.1029/RS013i005p00819
45. Waltham DA (1988) Two-point ray tracing using Fermat's principle. Geophys J 93(3):575–582. doi:10.1111/j.1365-246X.1988.tb03883.x
46. Wyngaard JC, Seaman N, Kimmel SJ, Otte M, Di X, Gilbert KE (2001) Concepts, observations, and simulation of refractive index turbulence in the lower atmosphere. Radio Sci 36(4):643–669. doi:10.1029/2000RS002380
47. Xu Z, Wu J, Wu Z (2004) A survey of ionospheric effects on space-based radar. Waves Random Media 14(2):S189–S273. doi:10.1088/0959-7174/14/2/008
48. Yan H, Wang G (1999) New consideration of atmospheric refraction in laser ranging data. Mon Not R Astron Soc 307(3):605–610. doi:10.1046/j.1365-8711.1999.02618.x
49. Yunck TP (2013) Coping with the atmosphere and ionosphere in precise satellite and ground positioning. In: Environmental effects on spacecraft positioning and trajectories. American Geophysical Union. ISBN:9781118666548. doi:10.1029/GM073p0001

Chapter 6
Reflection

A space- or air-borne sensor acquires information on the terrestrial environment by measuring the relevant features of the electromagnetic wave that, after interacting in a large sense with the materials present on the Earth, travels upward to the sensor. With the exception of observations of thermal emission,[1] the wave may have been originated either by the sensor itself, as in case of radar sensing, or by the Sun, in passive optical measurements. In both cases, when it reaches a target on the surface of the Earth, the wave which travels downward in the air, encounters a solid or liquid boundary of a natural or man-made material. The propagation constant κ and the intrinsic impedance η, which in the air are quite close to those of vacuum, undergo a sudden transition to the values determined by the permittivity of the encountered material. Therefore, the field cannot have the simple form considered in the previous Chaps. 3 and 4 because now the space is filled with different matters. However, since the field propagates in piecewise approximately homogeneous albeit different materials, spherical and plane waves can still be used in each portion of nearly homogeneous medium, provided the field is constrained to satisfy the conditions seen in Sect. 1.1.4 at the boundaries of the materials. Given the generally small dimensions of the region of interest with respect to the distances from the sources, the arguments put forward in Sects. 4.1 and 5.2 justify the plane wave as suitable approximation to the form of the field. Moreover, the interface between air and the earth material, for the time being is assumed locally smooth, so that a *plane of discontinuity* is considered. In general, the results apply to plane boundaries between any pair of different materials, such as, for instance, between water and rocky sea bottom.

[1] In this case, the wave-matter interaction consists of the emission process itself.

D. Solimini, *Understanding Earth Observation*, Remote Sensing and Digital Image Processing 23, DOI 10.1007/978-3-319-25633-7_6

6.1 Reflection for Normal Incidence

Consider the two lossless isotropic media, M_1 and M_2 shown in Fig. 6.1, with $\epsilon = \epsilon_1$, and $\epsilon = \epsilon_2$, respectively, representing, for instance, air and a solid or liquid terrestrial material; both have $\mu = \mu_0$, as said. A homogeneous plane wave, representing, for instance, solar radiation or the field sent by a radar, impinges normally from M_1 (air) onto the plane boundary of material M_2. The *incident wave* characterized by the phase vector $\boldsymbol{\beta}$ gives origin to a *refracted wave*, characterized by the phase vector $\boldsymbol{\beta}'$, carrying power into material M_2, hence propagating in the same direction as the incident wave. Since $\epsilon_2 \neq \epsilon_1$, the intrinsic impedance (4.34) η_2 of M_2 differs from that, η_1, of M_1. Therefore, the incident and refracted waves alone are not able to satisfy the boundary conditions: the required continuity of the tangential components of *both* electric and magnetic[2] fields (Sect. 1.1.4.2) demands that a third wave, the *reflected wave*, propagating in M_1, in the direction opposite to that of the incident wave, originates from the plane interface between M_1 and M_2. Three plane waves are thus present in the inhomogeneous structure, with phase vectors

$$\boldsymbol{\beta} = \omega\sqrt{\mu_1\epsilon_1}\,\mathbf{z}_0 \qquad \text{(incident wave)};$$

$$\boldsymbol{\beta}' = \omega\sqrt{\mu_2\epsilon_2}\,\mathbf{z}_0 \qquad \text{(refracted wave)};$$

$$\boldsymbol{\beta}'' = -\omega\sqrt{\mu_1\epsilon_1}\,\mathbf{z}_0 = -\boldsymbol{\beta} \qquad \text{(reflected wave)}.$$

The basic quantity of interest in Earth observation is the amount of incident wave that is reflected from the terrestrial material. To find the amount of reflection, the fields $\boldsymbol{E}_0'', \boldsymbol{H}_0''$ of the reflected wave must be determined. To this end, the continuity conditions (1.12) and (1.11) that the overall field must satisfy *at the separation surface* $z = 0$ are exploited:

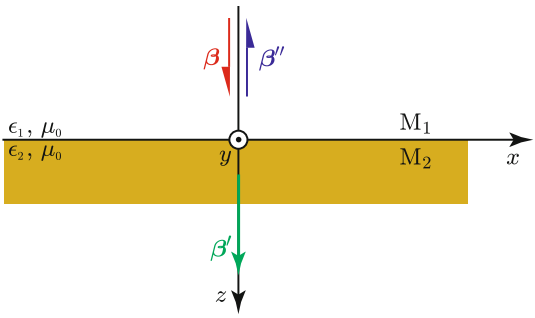

Fig. 6.1 A plane wave impinging normally onto the plane of separation between materials M_1 and M_2 gets refracted into M_2 and reflected back into M_1

[2]The tangential magnetic field is also continuous because no areic current can flow on the boundary of material M_2.

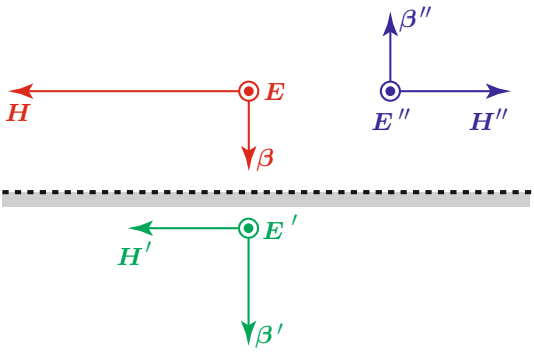

Fig. 6.2 A-priori orientation of electric and magnetic fields of incident, refracted and reflected waves

$$\boldsymbol{E}_0 + \mathbf{E}_0'' = \mathbf{E}_0' \; ; \tag{6.1}$$

$$\boldsymbol{H}_0 + \boldsymbol{H}_0'' = \boldsymbol{H}_0' \; . \tag{6.2}$$

Given their vector character, the boundary conditions indicate that, if the incident field is

$$\boldsymbol{E}_0 = E_0 \, e_0; \qquad \boldsymbol{H}_0 = H_0 \, \hbar_0 \; ,$$

the unitary vectors of both reflected and refracted fields have the same respective directions as those of the incident ones, but, their orientation is constrained by the relations between fields and propagation vector found in Sect. 4.1.2.3. Therefore, with reference to Fig. 6.2, the reflected field is

$$\boldsymbol{E}_0'' = E_0'' \, \mathbf{e}_0; \qquad \boldsymbol{H}_0'' = -H_0'' \, \mathbf{h}_0 \; . \tag{6.3}$$

The refracted field is simultaneously obtained by Eqs. (6.1) and (6.2):

$$\boldsymbol{E}_0' = E_0' \, \mathbf{e}_0; \qquad \boldsymbol{H}_0' = H_0' \, \mathbf{h}_0 \; . \tag{6.4}$$

6.1.1 Field Reflection and Transmission

The reflected and refracted electric fields are readily obtained from (6.3) and (6.4), taking the constraints (4.31) and (4.32) into account. The continuity conditions

$$E_0 + E_0'' = E_0' \; ;$$

$$\frac{E_0}{\eta_1} - \frac{E_0''}{\eta_1} = \frac{E_0'}{\eta_2} \; ,$$

yield

$$E_0''(\eta_2 + \eta_1) = E_0(\eta_2 - \eta_1) \ ,$$

which relates the reflected field to the incident one by

$$E_0'' = \frac{\eta_2 - \eta_1}{\eta_2 + \eta_1} E_0 \ .$$

The proportionality factor q_{E} between reflected and incident field is named *reflection coefficient* of the electric field. In the present case of normal incidence,

$$q_{\mathrm{E}} = \frac{E_0''}{E_0} = \frac{\eta_2 - \eta_1}{\eta_2 + \eta_1} = \frac{1 - \eta_1/\eta_2}{1 + \eta_1/\eta_2} \ .$$

Of course, $q_{\mathrm{E}} = 0$ when $\eta_1 = \eta_2$. When the medium M_1 is air, which is a tenuous medium with $\epsilon_1 \approx \epsilon_0$, q_{E} is obtained in terms of the refractive index (4.16) of the material

$$q_{\mathrm{E}} = \frac{1 - n}{1 + n} \ . \tag{6.5}$$

Since for the terrestrial materials at the frequencies of interest in Earth observation $n > 1$, the reflection coefficient is negative: $q_{\mathrm{E}} < 0$ means that the reflected electric field is *opposite* to the incident one, whereas the magnetic field keeps the same orientation, as shown in Fig. 6.3. Moreover, the larger the refractive index, the stronger is the reflection. Given the dielectric features discussed in Sect. 2.2, the materials with high moisture content are expected to be highly reflecting at the lower microwave frequencies.

The field that penetrates the material is proportional to the *transmission coefficient* t_{E} of the electric field, given by

$$t_{\mathrm{E}} = \frac{E_{0i}'}{E_{0i}} = 1 + \frac{\eta_2 - \eta_1}{\eta_2 + \eta_1} = \frac{2\eta_2}{\eta_2 + \eta_1} = \frac{2}{1 + n} \ , \tag{6.6}$$

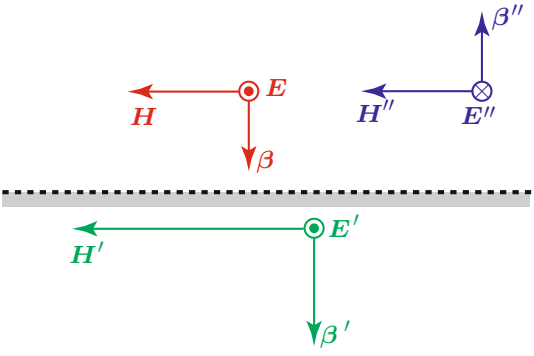

Fig. 6.3 Actual orientation of electric and magnetic fields of incident, reflected and refracted waves

in case of air-material interface. As expected, the larger is the refractive index, less field penetrates into the terrestrial material.

6.1.2 Power Reflection and Transmission

The power that is reflected back into the atmosphere from the unit area of earth surface is represented by the Poynting vector $\mathcal{P}''$ of the reflected wave

$$\mathcal{P}'' = \frac{\boldsymbol{E}'' \cdot \boldsymbol{E}''^*}{2\eta_0}\,\boldsymbol{\beta}'' = q_{\mathrm{E}}^2\,\frac{\boldsymbol{E}\cdot\boldsymbol{E}^*}{2\eta_0}\,\boldsymbol{\beta}'' = -q_{\mathrm{E}}^2\,\mathcal{P} = -\mathcal{R}\,\mathcal{P}\,,$$

where the *power reflection coefficient*

$$\mathcal{R} := q_{\mathrm{E}}^2 \tag{6.7}$$

has been introduced. The power transmitted into the subsurface unit area is analogously related to the power incident from the air by the *power transmission coefficient* $\mathcal{T} := n\,t_{\mathrm{E}}^2$

$$\mathcal{P}' = \frac{\boldsymbol{E}' \cdot \boldsymbol{E}'^*}{2\eta_2}\,\boldsymbol{\beta}' = \frac{\sqrt{\tilde{\epsilon}}}{2\eta_0}\,t_{\mathrm{E}}^2\,\boldsymbol{E}\cdot\boldsymbol{E}^*\,\boldsymbol{\beta} = \sqrt{\tilde{\epsilon}}\,t_{\mathrm{E}}^2\,\mathcal{P} = \mathcal{T}\,\mathcal{P}\,.$$

The affinity between the power transmission coefficient $\mathcal{T}$ and the transmittance $\mathcal{T}$ introduced in Sect. 4.1.2.5.2 is worth noting.

6.1.2.1 Lossy Materials

The results obtained in the limiting case of lossless materials provide a quite useful reference to the reflecting behavior of actual materials. In case the lossless condition is not adequate to model the actual material M_2, the procedure to obtain the reflection coefficient of the air-material interface remains the same and yields

$$q_{\mathrm{E}} = \frac{1-\sqrt{\tilde{\epsilon}}}{1+\sqrt{\tilde{\epsilon}}}\,. \tag{6.8}$$

The field reflection coefficient is now a complex quantity: this implies that the reflected electric field has a phase difference $\Delta\Phi \neq \pi$ with respect to the incident one.

6.1.2.2 Power Absorption

The power $\mathcal{P}^{(\mathrm{a})}$ absorbed by a lossy material through the unit area of its interface differs from $\mathcal{T}\,\mathcal{P}$, since $\mathcal{T}$ is now complex, hence both real and what is called reactive power are present. Rather, the power irreversibly transferred into the material is

$$\mathcal{P}^{(\mathrm{a})} = \Re\left[\mathcal{P}'\right] = \Re\left[\sqrt{\tilde{\epsilon}}\right]|t_{\mathrm{E}}|^2\,\mathcal{P} = \frac{4\Re\left[\sqrt{\tilde{\epsilon}}\right]}{\left|1+\sqrt{\tilde{\epsilon}}\right|^2}\mathcal{P} = \mathscr{A}\;\mathcal{P}\;,$$

where the *absorption coefficient* $\mathscr{A}$ has been introduced. Note that the absorption coefficient is related to the reflection coefficient q_{E} by

$$\mathscr{A} = 1 - q_{\mathrm{E}}\,q_{\mathrm{E}}^{*} = 1 - \mathcal{R}\;. \tag{6.9}$$

The relation (6.9) expresses the conservation of energy, as can be readily obtained by applying the Poynting's theorem to a layer across the M_1–M_2 interface, thin enough to have negligible power dissipated in it. Figure 6.4 shows a thin slice of the boundary between the air M_1 and the lossy material M_2 and the incident Poynting vector $\boldsymbol{\mathcal{P}}$ together with those of the reflected ($\boldsymbol{\mathcal{P}}''$) and transmitted ($\boldsymbol{\mathcal{P}}'$) waves. Specializing (1.20) to the volume of boundary slice within the dashed lines having unit area on the $(x\,y)$-plane and sufficiently thin to have negligible the power dissipated in it, readily leads to (6.9).

6.1.3 The Stationary Field

Section 2.2 mentions that several terrestrial materials have high permittivity at frequencies relevant to EO, such that $|\tilde{\epsilon}| \gg 1$. The modulus of the reflection coefficient (6.8) is then $|q_{\mathrm{E}}| \approx 1$ and correspondingly $t_{\mathrm{E}} \approx 0$. The incident wave is (almost) completely reflected and the power entering the high-permittivity material

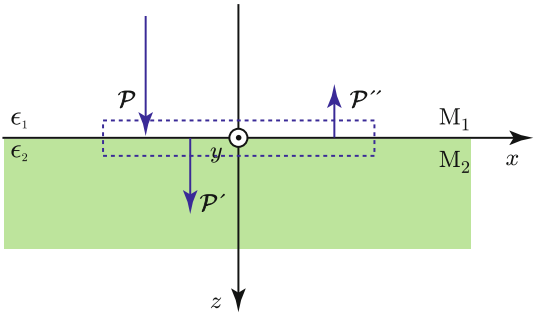

Fig. 6.4 Balance of incident, refracted and reflected areic power in a thin slice of air-material boundary for normal incidence

is low. The power penetrated in M_2 decays exponentially with the distance below the surface, according to the attenuation constant (4.13), or (4.15) in the weakly dissipative case. On its side, the field in the air results from the superposition of the one of the incident wave and that of the reflected wave. Assume that the reflection coefficient (6.8) $q_E \approx -1$ in case $\tilde{\epsilon}_j \ll \tilde{\epsilon}_r$, as it often occurs. Then the total electric field in the air, given by the superposition of that of the incident wave and of the reflected one, is

$$\boldsymbol{E}_{tot} = \boldsymbol{E}_0 \, e^{-j\beta z} + \boldsymbol{E}_0'' \, e^{j\beta z} \simeq \boldsymbol{E}_0 \left(e^{-j\beta z} - e^{j\beta z} \right) = -2j \, \boldsymbol{E}_0 \sin(\beta z) \; .$$

The total magnetic field is found in a straightforward manner from the electric fields of incident and reflected waves, making use of the relation (4.31):

$$\boldsymbol{H}_{tot} = \boldsymbol{H}_0 e^{-j\beta z} + \boldsymbol{H}_0'' e^{j\beta z} \simeq \boldsymbol{H}_0 \left(e^{-j\beta z} + e^{j\beta z} \right) = 2\boldsymbol{H}_0 \cos(\beta z) \; .$$

Figure 6.5 shows the electric and magnetic field magnitude patterns near the boundary of a high-permittivity material. Because of the normal incidence, the fields are tangential to the boundary. Therefore, the electric field has a quite low value in correspondence of the surface, since it must be continuous, across the boundary, with the low field inside, consistently with the results of Sect. 1.1.4.2. The variation of the total field with space and time provides an interesting insight into the structure of the field near the boundaries of high-dielectric materials. The space-time total electric field is

$$\boldsymbol{E}_{tot}(z,t) \simeq \Re \left[-2jE_0 \, \sin(\beta z) \, e^{j\omega t} \right] = E_0 \, \sin(\beta z) \, \sin(\omega t) \; . \tag{6.10}$$

Equation (6.10) indicates that the phase of the total field does not have the *coupled* dependence on both space and time, that, according to Sect. 3.1.1.2, is required to have the propagation of the wave. This means that E_{tot} does not propagate: the field is said to be *stationary*.

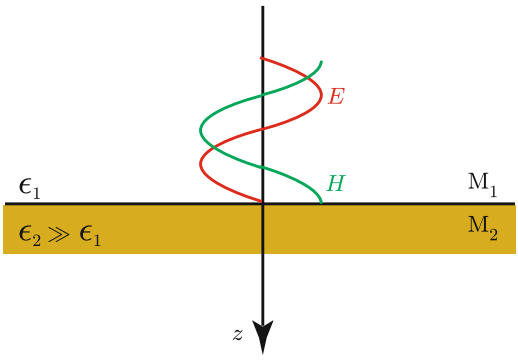

Fig. 6.5 Patterns of electric and magnetic field amplitudes near the boundary of a high-permittivity material (cf. Fig. 1.2) for normal incidence

The Poynting vector of the total field

$$\boldsymbol{\mathcal{P}}_{\text{tot}} = -2\text{j}\frac{|E_0|^2}{\eta}\sin(\beta z)\cos(\beta z)\,\mathbf{z}_0 = -\text{j}\frac{|E_0|^2}{\eta}\sin(2\beta z)\,\mathbf{z}_0 \tag{6.11}$$

varies with a spatial periodicity which is twice that of the stationary field. Since $\boldsymbol{\mathcal{P}}_{\text{tot}}$ in (6.11) is imaginary, the stationary field does not carry power. It means that all the power carried downward by the incident wave is bounced in the backward direction by the high-permittivity material.

6.2 Oblique Incidence, Lossless Materials

Consider now the more common case of oblique incidence, that is of a wave arriving at the surface of the material with an *incidence angle* $\theta \neq 0$ off the normal direction,[3] as shown in Fig. 6.6. As before, the boundary conditions cannot be satisfied by the incident and refracted waves alone, but require a reflected wave originating from the plane of separation between the two media. The electric and magnetic fields of each wave have the following expressions:

- incident wave

$$\boldsymbol{E} = \boldsymbol{E}_0\,\text{e}^{-\text{j}(\beta_x x + \beta_z z)}\ ;$$
$$\boldsymbol{H} = \boldsymbol{H}_0\,\text{e}^{-\text{j}(\beta_x x + \beta_z z)}\ ,$$

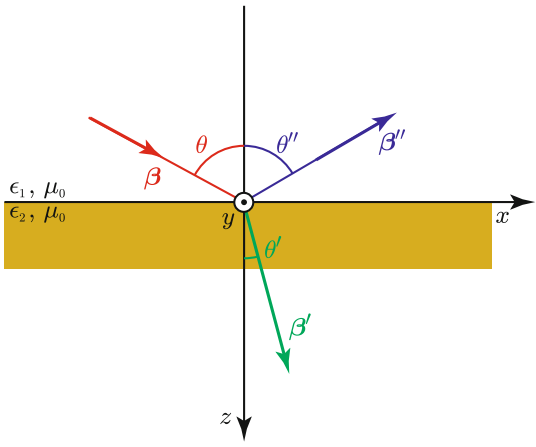

Fig. 6.6 Phase vectors of incident, refracted and reflected waves in oblique incidence

[3]The angle of incidence θ is generally different from the off-nadir angle ϑ introduced in Sect. 5.2.1.1 because of the local slope of the surface with respect to the geodetic reference, as well as of the atmospheric refractivity effects considered in Sect. 5.2.1.

- refracted wave

$$\boldsymbol{E}' = \boldsymbol{E}'_0 \, \mathrm{e}^{-\mathrm{j}(\beta'_x x + \beta''_z z)} \; ;$$
$$\boldsymbol{H}' = \boldsymbol{H}'_0 \, \mathrm{e}^{-\mathrm{j}(\beta'_x x + \beta''_z z)} \; ,$$

- reflected wave

$$\boldsymbol{E}'' = \boldsymbol{E}''_0 \, \mathrm{e}^{-\mathrm{j}(\beta''_x x + \beta''_z z)} \; ;$$
$$\boldsymbol{H}'' = \boldsymbol{H}''_0 \, \mathrm{e}^{-\mathrm{j}(\beta''_x x + \beta''_z z)} \; .$$

The above fields must satisfy the continuity conditions determined in Sect. 1.1.4 on the air-material interface.

6.2.1 Angles of Reflection and Refraction

The tangential components of the fields, $\boldsymbol{E}_\mathrm{t}$ and $\boldsymbol{H}_\mathrm{t}$, in the adjacent materials must be the same for $z = 0$ and for any x and y. The field in the air is the superposition of the fields of the incident and reflected waves, while in the material the field is that of the refracted wave. Therefore, the continuity conditions are

$$\boldsymbol{E}_{0\mathrm{t}} \, \mathrm{e}^{-\mathrm{j}\beta_x x} + \boldsymbol{E}''_{0\mathrm{t}} \, \mathrm{e}^{-\mathrm{j}\beta''_x x} = \boldsymbol{E}'_{0\mathrm{t}} \, \mathrm{e}^{-\mathrm{j}\beta'_x x} \; . \tag{6.12}$$

To satisfy (6.12) it is necessary that

$$\mathrm{e}^{-\mathrm{j}\beta_x x} = \mathrm{e}^{-\mathrm{j}\beta''_x x} = \mathrm{e}^{-\mathrm{j}\beta'_x x} \; ,$$

whence the tangential components of the propagation vectors are the same

$$\beta_x = \beta''_x = \beta'_x; \qquad \beta_y = 0 = \beta''_y = \beta'_y \; . \tag{6.13}$$

Equation (6.13) implies that the propagation vectors of the reflected and refracted waves lie in the *plane of incidence*, formed by the propagation vector and the normal to the surface, the $(x\,z)$-plane in this case. Moreover, the angles of reflection and refraction must satisfy the relations

$$\theta'' = \theta \; , \tag{6.14}$$

which is known as the *Hero of Alexandria law*, and

$$\frac{\sin\theta}{\sin\theta'} = \frac{\beta'}{\beta} \; , \tag{6.15}$$

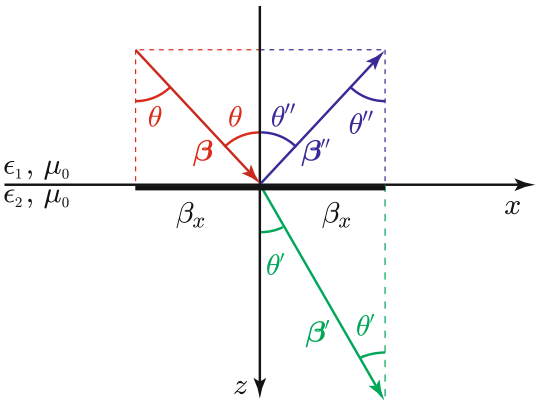

Fig. 6.7 The equal tangential component β_x of the propagation vectors determines the angles of reflection and refraction

named *Snell's law* (Fig. 6.7). The relations express the physical requirement that the velocity of propagation of the three waves be the same everywhere over the boundary in order to satisfy the continuity of the tangential field. It is worth mentioning that the velocity of propagation u_x along the x-direction, *is not* the x-component of the velocity of propagation, but is the *phase velocity* along x, which depends inversely on the x-component of the phase vector

$$u_x = \frac{\omega}{\beta_x} = \frac{\omega}{\beta \sin\theta} \cdot \tag{6.16}$$

Basic consequences of the continuity are then:

- the reflection angle equals the incidence angle;
- the phase vector bends toward the normal[4] according to

$$\sin\theta' = \frac{\sin\theta}{n} \cdot$$

6.2.2 *Reflection Coefficients and Wave Polarization*

The velocity of the three waves must necessarily be the same along the air-material boundary to ensure the required continuity of the tangential field. This condition is satisfied by (6.14) and (6.15) which make equal the exponential functions ruling the propagation of the waves for $z = 0$. As in the previous Sect. 6.1.1, the further constraints

[4]The wave is assumed to arrive from the air.

$$\boldsymbol{E}_{0\mathrm{t}} + \boldsymbol{E}''_{0\mathrm{t}} = \boldsymbol{E}'_{0\mathrm{t}} \; ;$$
$$\boldsymbol{H}_{0\mathrm{t}} + \boldsymbol{H}''_{0\mathrm{t}} = \boldsymbol{H}'_{0\mathrm{t}} \; ,$$

on the tangential components of the vector fields are now needed. According to the Jones formalism and taking (4.38) into account,

$$\boldsymbol{E}_0 = \boldsymbol{E}_{0\mathrm{h}} + \boldsymbol{E}_{0\mathrm{v}} = E_{0y}\,\mathbf{y}_0 + E_{0\mathrm{v}}\mathbf{v}_0 \; ;$$
$$\boldsymbol{H}_0 = \frac{\boldsymbol{\beta}_0 \times \boldsymbol{E}_0}{\eta_1} = -\frac{E_{0y}}{\eta_1}\,\mathbf{v}_0 + \frac{E_{0\mathrm{v}}}{\eta_1}\,\mathbf{y}_0 \; .$$

Analogous expressions hold for the reflected wave

$$\boldsymbol{E}''_0 = \boldsymbol{E}''_{0\mathrm{h}} + \boldsymbol{E}''_{0\mathrm{v}} = E''_{0y}\,\mathbf{y}_0 + E''_{0\mathrm{v}}\,\mathbf{v}''_0 \; ;$$
$$\boldsymbol{H}''_0 = \frac{\boldsymbol{\beta}''_0 \times \boldsymbol{E}''_0}{\eta_1} = -\frac{E''_{0y}}{\eta_1}\,\mathbf{v}''_0 + \frac{E''_{0\mathrm{v}}}{\eta_1}\,\mathbf{y}_0 \; ,$$

where $\mathbf{v}''_0 = -\mathbf{x}_0 \cos\theta - \mathbf{z}_0 \sin\theta$, and for the refracted wave

$$\boldsymbol{E}'_0 = \boldsymbol{E}'_{0\mathrm{h}} + \boldsymbol{E}'_{0\mathrm{v}} = E'_{0y}\,\mathbf{y}_0 + E'_{0\mathrm{v}}\mathbf{v}'_0 \; ;$$
$$\boldsymbol{H}'_0 = \frac{\boldsymbol{\beta}'_0 \times \boldsymbol{E}'_0}{\eta_2} = -\frac{E'_{0y}}{\eta_2}\,\mathbf{v}'_0 + \frac{E'_{0\mathrm{v}}}{\eta_2}\,\mathbf{y}_0 \; ,$$

where $\mathbf{v}'_0 = \mathbf{x}_0 \cos\theta' - \mathbf{z}_0 \sin\theta'$. Angles and field components of the three waves are detailed in Fig. 6.8. The boundary conditions, which are relative to the components parallel to the $(x\,y)$-plane, require projecting the electric and magnetic field vectors onto the x and y axes and imposing the continuity of the respective components:

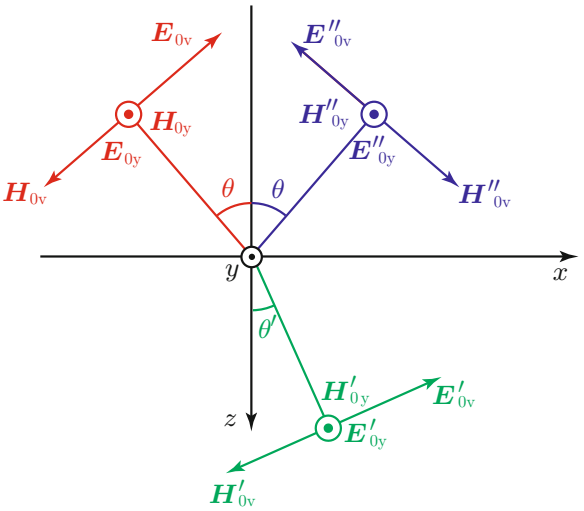

Fig. 6.8 A-priori directions of horizontal and vertical components of electric and magnetic fields of incident, reflected and refracted waves

$$E_{0y} + E''_{0y} = E'_{0y} \; ; \tag{6.17}$$

$$E_{0\mathrm{V}} \cos\theta - E''_{0\mathrm{V}} \cos\theta = E'_{0\mathrm{V}} \cos\theta' \; ; \tag{6.18}$$

$$-\frac{E_{0y}}{\eta_1} \cos\theta + \frac{E''_{0y}}{\eta_1} \cos\theta = -\frac{E'_{0y}}{\eta_2} \cos\theta' \; ; \tag{6.19}$$

$$\frac{E_{0\mathrm{V}}}{\eta_1} + \frac{E''_{0\mathrm{V}}}{\eta_1} = \frac{E'_{0\mathrm{V}}}{\eta_2} \; . \tag{6.20}$$

The Jones representation based on $\mathbf{E}_{0\mathrm{h}}$ and $\mathbf{E}_{0\mathrm{V}}$ allows the four-unknowns four-equations system (6.17)–(6.20) to be split into the pair of two-unknowns two-equations *independent* systems, (6.17) (6.19) for the horizontal component of the electric field and (6.18) (6.20) for the vertical component. This result is quite significant from the physical point of view: $\mathbf{E}_{0\mathrm{h}}$ and $\mathbf{E}_{0\mathrm{V}}$ are reflected and refracted in *independent modes*, hence they represent the *principal polarizations* of the field.

The continuity conditions (6.17) and (6.19) involving the *horizontal component* of the electric field yield

$$\frac{\cos\theta}{\eta_1}(E''_{0y} - E_{0y}) = -\frac{E_{0y} + E''_{0y}}{\eta_2} \cos\theta' \; ,$$

which provides the *reflection coefficient*[5] q_{h} for *horizontal polarization*

$$q_{\mathrm{h}} = \frac{E''_{0y}}{E_{0y}} = \frac{\eta_2 \cos\theta - \eta_1 \cos\theta'}{\eta_2 \cos\theta + \eta_1 \cos\theta'} \; .$$

By use of the Snell's law (6.15)

$$q_{\mathrm{h}} \simeq \frac{\cos\theta - \sqrt{n^2 - \sin^2\theta}}{\cos\theta + \sqrt{n^2 - \sin^2\theta}} \leq 0 \; ,$$

for the wave incident from the air onto a material with refractive index n. Since in practice $n \geq 1$, the modulus of the reflection coefficient for horizontal polarization $|q_{\mathrm{h}}|$ increases monotonically with increasing incidence angle θ from the normal incidence value (6.5) up to 1, which is approached in the limiting case $\theta \to \pi/2$.

In turn, (6.18) and (6.20) lead to the relation involving the *vertical component* of the electric field:

$$\eta_1(E_{0\mathrm{V}} \cos\theta - E''_{0\mathrm{V}} \cos\theta) = \eta_2(E_{0\mathrm{V}} \cos\theta' - E''_{0\mathrm{V}} \cos\theta') \; ,$$

[5] Also called *Fresnel* reflection coefficient.

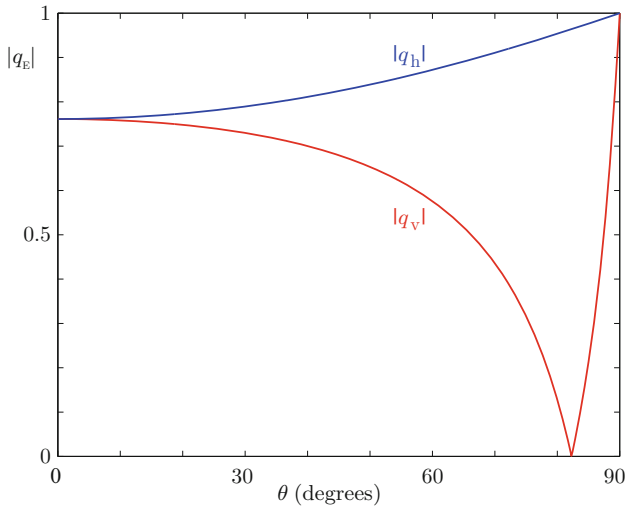

Fig. 6.9 Moduli of horizontal ($|q_h|$) and vertical ($|q_v|$) reflection coefficients for a smooth interface between air and a high-permittivity ($\tilde{\epsilon} = 60$) lossless material vs. incidence angle θ; q_v changes sign beyond the Brewster angle

which provides the *reflection coefficient* q_v for *vertical polarization*

$$q_v = \frac{E''_{0V}}{E_{0V}} = \frac{\eta_1 \cos\theta - \eta_2 \cos\theta'}{\eta_1 \cos\theta + \eta_2 \cos\theta'} \,.$$

When the wave comes from the air,

$$q_v \simeq \frac{n^2 \cos\theta - \sqrt{n^2 - \sin^2\theta}}{n^2 \cos\theta + \sqrt{n^2 - \sin^2\theta}} \,.$$

The behavior of the vertical-polarization reflection coefficient with the incidence angle is substantially different from that for the horizontal polarization. In fact, the modulus $|q_v|$ is not monotonic with the incidence angle θ, but it first decreases from the value is has at normal incidence, vanishes at the angle $\theta = \theta_B$, then it subsequently increases to approach 1 for $\theta \to \pi/2$. Figure 6.9 shows the moduli of the reflection coefficients $|q_v|$ and $|q_h|$ as functions of the incidence angle for a plane wave incident from the air onto the plane surface of a material having $\tilde{\epsilon}_2 = 60$. Note the dramatic changes of $|q_v|$ contrasting with the smooth monotonic behavior of $|q_h|$.

The incidence angle $\theta = \theta_B$ at which $q_v = 0$ is named *Brewster angle*, given, for incidence from air, by

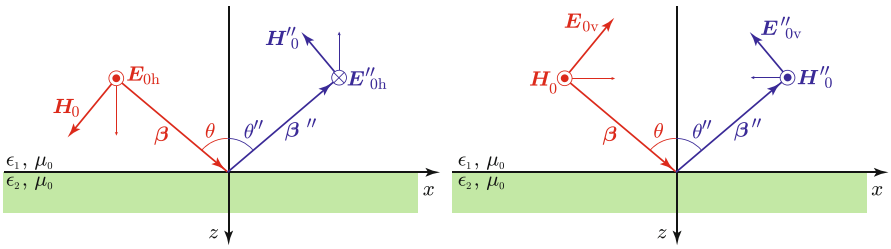

Fig. 6.10 Actual orientation of horizontal and vertical electric and magnetic field components of incident and reflected waves at oblique incidence

$$\sin\theta_B = \sqrt{\frac{\epsilon_2}{\epsilon_1 + \epsilon_2}} = \sqrt{\frac{n^2}{1 + n^2}}\,. \tag{6.21}$$

Equation (6.21) indicates that the Brewster angle $\theta_B > \pi/4$ and increases with increasing refractive index. Materials with high permittivity, such as aqueous dielectrics at microwave frequency,[6] are expected to have θ_B beyond the commonly used observation angles, although the *local* incidence angle may exceed θ_B for particular geometries of the Earth's environment (Sect. 6.6.1). Note that $q_v < 0$ for $\theta < \theta_B$ and $q_v > 0$ for $\theta > \theta_B$. This change of sign translates into a π change of phase of the reflection coefficient for vertical polarization. Given the different behavior of the respective reflection coefficients, the reflected fraction of vertical field is lower than that of the horizontal component, clearly excepted that for $\theta = 0$. This behavior has an important impact on the choice of the polarization at which both active and passive microwave Earth observation is carried out, as well as on the interpretation of acquired data. Moreover, the diverse manner with which reflection occurs suggests that the reflected horizontal and vertical components may carry independent pieces of information on the observed terrestrial targets.

Finally, it worth mentioning that, given the sign of the reflection coefficients for $\theta < \theta_B$ and the orientation of the vectors, the horizontal component of the reflected electric field is opposite to the incident one, while $\boldsymbol{E}''_v$ maintains its z-component and inverts the one along x (Fig. 6.10). This feature has an important bearing on the phase behavior of the reflection from the dihedral or trihedral composite structures considered in the following Sects. 6.6.1 and 6.6.2.

[6]The Brewster angle actually refers to lossless substances, however, lossy terrestrial materials behave in a fairly close manner, as discussed in Sect. 6.3.2.

6.3 Oblique Incidence, Lossy Materials

The preceding results, which have been obtained under the lossless assumption, provide a quite useful reference for the reflecting behavior of the actual materials in the terrestrial environment, which, however, are lossy, characterized by the complex permittivity $\epsilon_2 = \epsilon_0(\tilde{\epsilon}_{r_2} + j\tilde{\epsilon}_{j_2})$, consistently with the findings of Chap. 2.

The fields in the approximately lossless air, that is, the incident and reflected ones characterized by their respective phase vectors, are, as before,

$$\begin{aligned} \boldsymbol{E} &= \boldsymbol{E}_0\, e^{-j(\beta_x x + \beta_z z)} \; ; \\ \boldsymbol{H} &= \boldsymbol{H}_0\, e^{-j(\beta_x x + \beta_z z)} \; ; \\ \boldsymbol{E}'' &= \boldsymbol{E}''_0\, e^{-j(\beta_x x - \beta_z z)} \; ; \\ \boldsymbol{H}'' &= \boldsymbol{H}''_0\, e^{-j(\beta_x x - \beta_z z)} \; , \end{aligned}$$

whereas, the results of Sect. 4.1.2 indicate that the propagation vector $\boldsymbol{k}' = \boldsymbol{\beta}' - j\boldsymbol{\alpha}'$ of the wave refracted into the terrestrial material (terrain, water, ...) must now be complex and include an attenuation vector $\boldsymbol{\alpha}' \nparallel \boldsymbol{\beta}'$, given the complex permittivity of the material. Therefore,

$$\begin{aligned} \boldsymbol{E}' &= \boldsymbol{E}'_0\, e^{-\boldsymbol{\alpha}'\cdot\boldsymbol{r} - j\boldsymbol{\beta}'\cdot\boldsymbol{r}} \; ; \\ \boldsymbol{H}' &= \boldsymbol{H}'_0\, e^{-\boldsymbol{\alpha}'\cdot\boldsymbol{r} - j\boldsymbol{\beta}'\cdot\boldsymbol{r}} \; . \end{aligned} \tag{6.22}$$

The continuity (6.12) of the tangential components of the fields requires that on the boundary

$$e^{-j\boldsymbol{k}\cdot\boldsymbol{r}} = e^{-j\boldsymbol{k}'\cdot\boldsymbol{r}} \; ,$$

or, since the condition holds for $z = 0$,

$$e^{-j\beta_x x} = e^{-(\alpha'_x x + j\beta'_x x)} \qquad \forall x \; . \tag{6.23}$$

Equation (6.23) implies the following condition on the coefficients of the exponent

$$-j\beta_x = -\alpha'_x - j\beta'_x \; ,$$

whence

$$\alpha'_x = 0; \qquad \beta'_x = \beta_x \; .$$

It follows that

$$\boldsymbol{\alpha}' = \alpha' \mathbf{z}_0; \qquad \beta'_x = \beta' \sin\theta' = \beta \sin\theta \ .$$

As expected, the phase vector satisfies the same relation as for the lossless case, while the attenuation vector is perpendicular to the boundary. The first condition corresponds to the requirement that incident, refracted and reflected waves travel along the boundary with the same phase velocity. The second derives from the independence of the amplitude of the incident field from the points on the boundary, which implies that the amplitude of the reflected and refracted waves cannot even vary with x.

The general expression of the refracted electric field is then

$$\boldsymbol{E}' = \boldsymbol{E}'_0 \, \mathrm{e}^{-\alpha z - \mathrm{j}(\beta'_x x + \beta''_z z)} \ . \tag{6.24}$$

6.3.1 The Refracted Wave

The wave excited in the lossy material by the plane wave incident at an angle $\theta \neq 0$ is non-homogeneous since $\boldsymbol{\alpha}' \nparallel \boldsymbol{\beta}'$. Then the approach followed in Sect. 6.2.2 fails: the refraction angle θ' cannot be obtained from Snell's law in terms of refractive index, nor $\boldsymbol{\beta}'$ neither, in turn, $\boldsymbol{\alpha}'$, are obtainable from the boundary conditions alone, since θ' is unknown.

Then, starting from the complex (4.10), that is

$$\begin{aligned} \boldsymbol{k}' \cdot \boldsymbol{k}' &= (\boldsymbol{\beta}' - \mathrm{j}\boldsymbol{\alpha}') \cdot (\boldsymbol{\beta}' - \mathrm{j}\boldsymbol{\alpha}') = \beta'^2 - \alpha'^2 - 2\mathrm{j}\, \boldsymbol{\alpha}' \cdot \boldsymbol{\beta}' \\ &= \omega^2 \mu_0 \epsilon_2 = \omega^2 \mu_0 \epsilon_0 \left(\tilde{\epsilon}_{\mathrm{r}2} + \mathrm{j}\tilde{\epsilon}_{\mathrm{j}2}\right) \ , \end{aligned}$$

two relations are obtained:

$$\begin{aligned} \beta'^2 - \alpha'^2 &= \omega^2 \mu_0 \epsilon_0 \tilde{\epsilon}_{\mathrm{r}2} = \kappa_0^2 \tilde{\epsilon}_{\mathrm{r}2} \ ; \\ 2\, \boldsymbol{\alpha}' \cdot \boldsymbol{\beta}' &= 2\, \alpha' \beta' \sqrt{1 - \sin^2\theta'} = \omega^2 \mu_0 \epsilon_0 |\tilde{\epsilon}_{\mathrm{j}2}| = \kappa_0^2 |\tilde{\epsilon}_{\mathrm{j}2}| \ , \end{aligned}$$

from which the attenuation and phase vectors of the refracted wave are determined by some tedious algebra, taking into account that $\beta'_x = \beta_x$. The refracted field shows some particularly significant features for materials that, *at a given frequency*, have either low or high losses.

When dissipation is low such that $\tilde{\epsilon}_{\mathrm{j}2} \ll \tilde{\epsilon}_{\mathrm{r}2}$,

$$\beta' \simeq \kappa_0 \sqrt{\tilde{\epsilon}_{\mathrm{r}2}} = \kappa_0 n \ ; \qquad \sin\theta' \simeq \frac{\sin\theta}{\sqrt{\tilde{\epsilon}_{\mathrm{r}2}}} = \frac{\sin\theta}{n} \ .$$

Both modulus and direction of $\boldsymbol{\beta}'$ are the same as for a lossless medium with refracive index $n = \sqrt{\tilde{\epsilon}_{\mathrm{r}2}}$, while

$$\alpha' \simeq \frac{\kappa_0 \left|\tilde{\epsilon}_{\mathrm{j}2}\right|}{2\sqrt{n - \sin^2\theta}} = \frac{\omega \left|\tilde{\epsilon}_{\mathrm{j}2}\right|}{2c_0\sqrt{n - \sin^2\theta}} \,. \tag{6.25}$$

As expected, the modulus α' of the attenuation vector is directly proportional to the frequency and to the imaginary part of the permittivity. Also, α' increases with increasing incidence angle. On the other side, for high-losses (i.e., $\left|\tilde{\epsilon}_{\mathrm{j}2}\right| \gg \tilde{\epsilon}_{\mathrm{r}2}$),

$$\alpha' \simeq \beta' \simeq \omega\sqrt{\frac{\mu_0\epsilon_0 \left|\tilde{\epsilon}_{\mathrm{j}2}\right|}{2}} = \frac{\omega}{c_0}\sqrt{\frac{\left|\tilde{\epsilon}_{\mathrm{j}2}\right|}{2}} \,,$$

as found in Sect. 4.1.2 for a homogeneous wave. Then, since generally $\tilde{\epsilon}_{\mathrm{r}2} \geq 1$, Snell's law yields

$$\sin\theta' \simeq \sqrt{\frac{2}{\left|\tilde{\epsilon}_{\mathrm{j}2}\right|}}\sin\theta \ll \sin\theta \,.$$

Therefore, the refracted wave propagates in a direction nearly orthogonal to the air-material interface shown in Fig. 6.11, so that

$$\boldsymbol{\beta}' \simeq \beta'\mathbf{z}_0 \parallel \boldsymbol{\alpha}' \,.$$

The refracted wave is nearly homogeneous in case of high dissipation. This is the so-called *Leontovich condition*. Note that the field has features analogous to those for "dense" lossless materials, that is, those for which $n \gg 1$. In conclusion, the field at frequencies or wavelengths at which the material is highly dissipative is

$$\boldsymbol{E}' \simeq \boldsymbol{E}'_0 \mathrm{e}^{-\alpha' z - \mathrm{j}\beta' z} \,;$$
$$\boldsymbol{H}' \simeq \boldsymbol{H}'_0 \mathrm{e}^{-\alpha' z - \mathrm{j}\beta' z} \,,$$

and behaves like a homogeneous wave, with

$$\boldsymbol{E}'_0 \perp \boldsymbol{H}'_0 \perp \mathbf{z}_0 \,; \qquad \boldsymbol{E}'_0 = -\eta_2 \, \mathbf{z}_0 \times \boldsymbol{H}'_0 \,,$$

where

$$\eta_2 \simeq \frac{\omega\mu_0}{\beta' - \mathrm{j}\alpha'} = \frac{1+\mathrm{j}}{\sqrt{2}}\sqrt{\frac{\mu_0}{\epsilon_0 \left|\tilde{\epsilon}_{\mathrm{j}2}\right|}} = \frac{1+\mathrm{j}}{\sqrt{2}}\frac{\eta_0}{\sqrt{\left|\tilde{\epsilon}_{\mathrm{j}2}\right|}} \,.$$

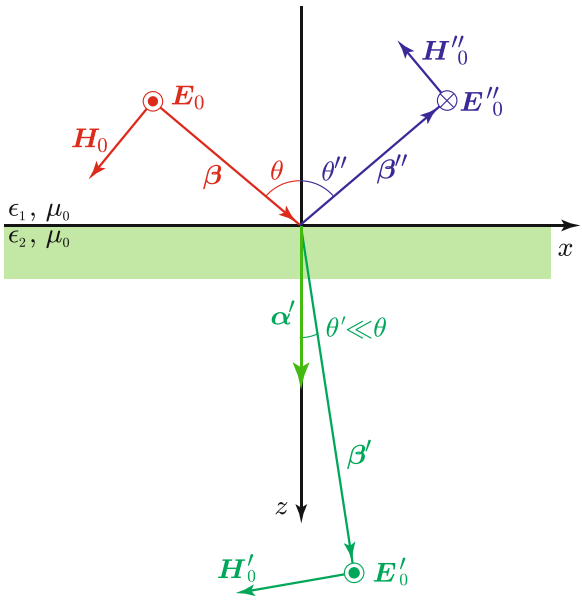

Fig. 6.11 Attenuation and phase vectors of refracted quasi-homogeneous wave in high-loss material

6.3.1.1 Penetration Depth

The depth $z = \ell$ at which the refracted field amplitude reduces to $1/\mathrm{e}$ of its initial value is named *penetration depth*:

$$\ell := \frac{1}{\alpha'} \cdot \tag{6.26}$$

The expression of ℓ depends on the spectral features of the permittivity of the material. When the low-loss approximation (6.25) holds,

$$\ell \simeq \frac{2c_0\sqrt{n - \sin^2\theta}}{\omega\,|\tilde{\epsilon}_{\mathrm{j}2}|} = \lambda_0 \frac{\sqrt{n - \sin^2\theta}}{\pi\,|\tilde{\epsilon}_{\mathrm{j}2}|} \cdot$$

Instead, in case of high dissipation,

$$\ell = \frac{\sqrt{2}}{\omega\sqrt{\mu_0\epsilon_0\,|\tilde{\epsilon}_{\mathrm{j}2}|}} = \frac{c_0}{\omega}\frac{\sqrt{2}}{\sqrt{|\tilde{\epsilon}_{\mathrm{j}2}|}} = \frac{\lambda_0}{\sqrt{2}\pi\sqrt{|\tilde{\epsilon}_{\mathrm{j}2}|}} \cdot \tag{6.27}$$

The penetration depth increases with wavelength and decreases with increasing imaginary part of permittivity[7]: in particular, ℓ is a rather small fraction of the wavelength *in vacuo* in case $\left|\tilde{\epsilon}_{\mathrm{j}2}\right| \gg 1$.

The penetration depth is an important parameter to consider in Earth observation, since it is related to the depth below the surface down to which an observing system is able to gain information. At microwave frequencies, that is, at centimeter to decimeter wavelengths, the high values of $\left|\tilde{\epsilon}_{\mathrm{j}2}\right|$ limit the penetration depth in aqueous dielectrics to millimeters or few centimeters at most [4, 11, 20], whereas the low $\left|\tilde{\epsilon}_{\mathrm{j}2}\right|$ of dry loose materials allows sub-surface penetration down to meters [7, 10]. In the optical range, the wavelength of the order of micrometers allows to extract information only from the skin layer of the materials [6, 18], apart from clear water, where the penetration can reach several meters [8].

6.3.2 *Reflection Coefficient of Lossy Media*

Assume for simplicity of notations that the incident field is horizontally polarized, that is $\boldsymbol{E} = E_0 \mathbf{y}_0$. The tangential field continuity requires

$$E_0 - E_0'' = E_0' \; ;$$
$$H_{0x} + H_{0x}'' = H_{0x}' \; .$$

Since incident and reflected waves are homogeneous, the magnetic field is immediately related to the electric field by

$$H_{0x} = -\frac{E_0}{\eta_1} \cos\theta \; ; \qquad H_{0x}'' = -\frac{E_0''}{\eta_1} \cos\theta \; .$$

Instead, the refracted wave, which is inhomogeneous, has $\boldsymbol{E}_0'$ and $\boldsymbol{H}_0'$ related by (4.30), hence

$$\begin{aligned} \boldsymbol{H}_0' &= \frac{\mathrm{j}\boldsymbol{k}' \times \boldsymbol{E}_0'}{\mathrm{j}\omega\mu_0} = \frac{\alpha' \mathbf{z}_0 + \mathrm{j}\boldsymbol{\beta}'}{\mathrm{j}\omega\mu_0} \times E_0' \mathbf{y}_0 \\ &= \frac{1}{\mathrm{j}\omega\mu_0} (-\alpha' E_0' \mathbf{x}_0 - \mathrm{j}\beta' \cos\theta' E_0' \mathbf{x}_0 + \mathrm{j}\beta' \sin\theta' E_0' \mathbf{z}_0) \; . \end{aligned}$$

Some manipulation leads to the reflection coefficient

$$q_{\mathrm{h}} = \frac{\eta_0 - \eta_{\mathrm{S}2} \cos\theta}{\eta_0 + \eta_{\mathrm{S}2} \cos\theta} \; . \tag{6.28}$$

[7] It is worth recalling that the values of $\tilde{\epsilon}_{\mathrm{j}}$ and $\tilde{\epsilon}_{\mathrm{r}}$ are related.

Equation (6.28) contains the so-called *surface impedance* η_{S2} for material M_2, defined as

$$\eta_{S2} = \frac{j\,\omega\mu_0}{\alpha' + j\beta'\cos\theta'}\,.$$

When dissipation is low, $\alpha' \ll \beta'$ and the field behaves like in the lossless case, while

$$q_h \simeq \frac{\eta_0 - \eta_2\cos\theta}{\eta_0 + \eta_2\cos\theta}$$

for high losses. Coarsely speaking, in this latter case $\left|\tilde{\epsilon}_{j2}\right|$ is high, the intrinsic impedance is low and, in the limit $(\eta_2/\eta_0) \to 0$, the reflection coefficient $q_h \to 1$. As already observed, the reflecting behavior in case of high losses is similar to that of the high-permittivity lossless case.[8]

Analogous and more tedious computations lead to determining the behavior of the reflection coefficient q_v for vertical polarization, which retains the features it has in the lossless case, but with a major difference: since the intrinsic impedance of lossy materials is complex, no incidence angle can satisfy the two independent equations into which the complex condition $q_v = 0$ splits, hence no Brewster angle exists for lossy materials. As the incidence angle varies, the reflection coefficient for vertical polarization decreases from its value (6.8) for normal incidence to a non-zero minimum, which is reached at the *pseudo-Brewster angle* θ_{pB}, then it goes up towards 1, as in the lossless case. Correspondingly, the phase Φ_{qv} of q_v shows a continuous decrease from the value (which is frequently $\Phi_{qv} \approx \pi$) it has at normal incidence to $\Phi_{qv} = 0$ for grazing incidence.

Figures 6.12, 6.13, and 6.14 show some relevant examples of the trend with the incidence angle of the reflection coefficients of lossy media for both horizontal and vertical polarizations. Figure 6.12 refers to $|q_h|$ and $|q_v|$ computed at $f = 1$ GHz for a material having a high real part of permittivity and two different imaginary parts. The diagrams are indicative of the reflecting behavior of the smooth interface between air and an aqueous material at L-band. The reflection for vertical polarization reproduces the trend of the lossless case, especially for the lower value of $\left|\tilde{\epsilon}_j\right|$. The pseudo-Brewster angle exceeds 80°, given the quite high permittivity, which leads to an elevated overall power reflection coefficient for $\theta \lesssim 50°$. A comparison among the reflecting behavior that an aqueous material could exhibit at three microwave frequencies of particular interest for radar Earth observation is reported in Fig. 6.13. The effect of frequency, the increase of which causes a decrease of permittivity, is shown by the slight modification of the trends, which, after all, remain relatively stable. Finally, Fig. 6.14 shows the reflecting

[8] Note that the suitable choice of the direction of the reflected electric field indicated in Fig. 6.11 is opposite to the one in Sect. 6.2.2, with a corresponding reversal of the sign of q_h in the limiting lossless case.

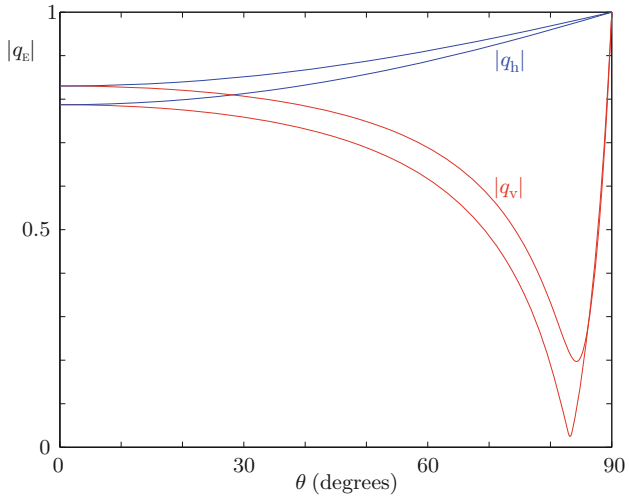

Fig. 6.12 Moduli of reflection coefficients q_h and q_v at frequency $f = 1$ GHz vs. incidence angle θ of the smooth interface between air and a simulated aqueous material with $\tilde{\epsilon} = 70 - j70$ (*upper pair of curves*) and $\tilde{\epsilon} = 70 - j7$ (*lower curves*) (Diagrams, courtesy G. Schiavon)

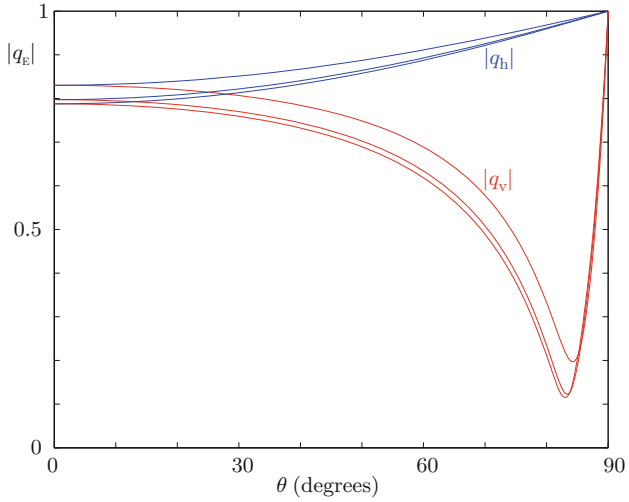

Fig. 6.13 Moduli of reflection coefficients q_h and q_v at L- (*top pair of curves*), C- (*middle*) and X-band (*bottom*) vs. incidence angle θ of the smooth interface between air and a simulated aqueous material with permittivity $\tilde{\epsilon} = 70 - j70$ at L-band, $\tilde{\epsilon} = 65 - j35$ at C-band, $\tilde{\epsilon} = 60 - j30$ at X-band (Diagrams, courtesy G. Schiavon)

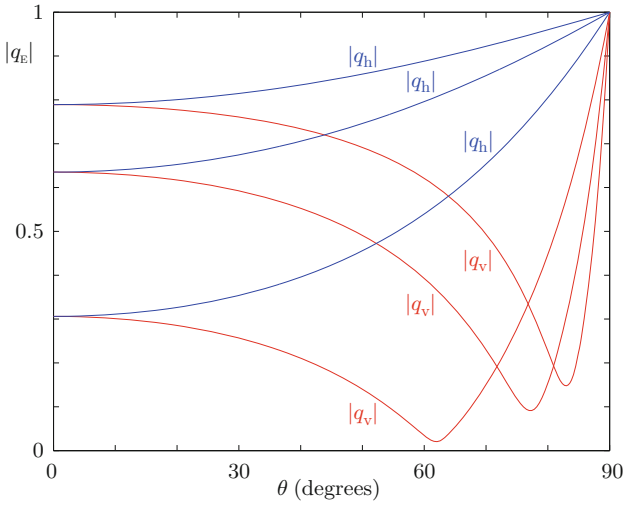

Fig. 6.14 Moduli of reflection coefficients q_h and q_v at X-band vs. incidence angle θ of the smooth interface between air and simulated terrain, for: wet ($\tilde{\epsilon} = 54.4 - j36.8$, *top pair of curves*); humid ($\tilde{\epsilon} = 17.9 - j7.2$, *middle*); dry ($\tilde{\epsilon} = 3.5 - j0.4\epsilon_0$, *bottom*) soil conditions (Diagrams, courtesy G. Schiavon)

behavior that could be expected at X-band for soil with different moisture contents. The simulations indicate the considerable effect of humidity, given the change of permittivity it entails. The dry terrain shows a fairly low reflection coefficient on both polarizations, with the pseudo-Brewster angle $\theta_B \approx 60°$, whereas the behavior of the wet soil approaches that of water.

As already observed, comparing the reflection from the dissipative materials considered in the previous examples with the results displayed in Fig. 6.9 suggests that the reflecting behavior in the lossy case does not differ substantially from to the one in absence of dissipations.

6.3.2.1 Power Absorption

As for the normal incidence case considered in Sect. 6.1.2.2, indications on the fraction of electromagnetic power crossing the interface between air and a lossy material are obtained by the Poynting's theorem applied to the unit-area slice of the M_1–M_2 boundary shown in Fig. 6.15, thin enough that the power dissipated in it is negligible. The power $\mathcal{P}'$ entering the material through the unit area of its boundary derives from the incident power $\mathcal{P}$ deprived of the power $\mathcal{P}''$ carried back by the reflected wave

$$-\mathcal{P}\cos\theta + \mathcal{P}''\cos\theta + \mathcal{P}' = 0\,. \tag{6.29}$$

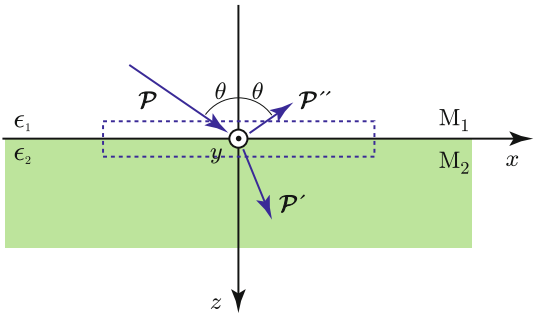

Fig. 6.15 Balance of incident, refracted and reflected areic power in a thin slice of air-material boundary (in the *dashed contour*) for oblique incidence

By relating $\mathcal{P}''$ to $\mathcal{P}$ and taking (6.9) into account, (6.29) yields

$$\begin{aligned}\mathcal{P}^{(\mathrm{a})} &= (\mathcal{P} - \mathcal{P}'')\cos\theta = (1 - |q_{\mathrm{E}}|^2)\cos\theta\,\mathcal{P} = (1 - \mathcal{R})\cos\theta\,\mathcal{P} \\ &= \mathscr{A}\cos\theta\,\mathcal{P} = \mathcal{A}\,\mathcal{P}\,,\end{aligned}$$

where q_{E} represents either q_{h} or q_{v} according to the polarization of the incident field. The *absorptivity*

$$\mathcal{A} := \mathscr{A}\cos\theta$$

is introduced to account for the combined effect of both $\cos\theta$ and $q_{\mathrm{E}}(\theta)$. Absorptivity represents the fraction of the incident areic power that is delivered to the material through the unit area of its boundary. Therefore, independently from the reflection coefficient, $\mathcal{A}$ depends on the angle the surface forms with the direction of incidence: as θ increases, $\mathcal{A}$ decreases. When also the behavior of the reflection coefficients is taken into account, a maximum of absorption of a vertically polarized wave is expected about the pseudo-Brewster angle, while absorption of horizontally polarized waves is lower and decreases monotonically with increasing incidence angle.

6.4 Total Reflection

Part of the wave coming from the external source, that is, the Sun, a radar transmitter or a laser, is refracted into the encountered material and propagates in it. Given the possible sub-surface inhomogeneities and the finite dimensions of natural or man-made objects, part of the refracted power is sent back by inner reflection or scattering (Chap. 7), hence it re-emerges from the material and is transmitted into the air following the reversed propagation path. With reference to Fig. 6.16, this process can be modeled as the incidence of the wave from M_1, which is now a *denser* material, onto the air, which is now a tenuous medium M_2. Denser material means that M_1 is such that

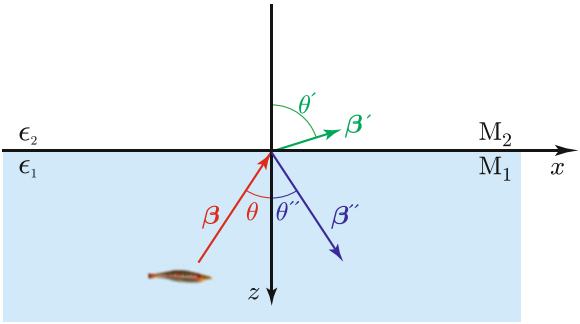

Fig. 6.16 The wave emerging from a denser material propagates in a direction away from the normal

$$\sqrt{\mu_0\epsilon_1} > \sqrt{\mu_0\epsilon_2} \approx \sqrt{\mu_0\epsilon_0} \ . \tag{6.30}$$

For the sake of simplicity, materials M_1 and M_2 are both assumed lossless.

The continuity (6.12) of the tangential components of the fields that leads to Snell's law (6.15) yields

$$\sin\theta' = \sqrt{\frac{\mu_0\epsilon_1}{\mu_0\epsilon_2}}\sin\theta \ . \tag{6.31}$$

Since (6.30) holds, now $\theta' > \theta$, i.e., the direction of propagation of the emerging wave divaricates from the normal to the boundary plane, as sketched in Fig. 6.16, to be compared with Fig. 6.6. As the incidence angle θ increases, the direction of $\boldsymbol{\beta}'$ approaches $\mathbf{x}_0$. At the angle $\theta = \theta_\mathrm{L}$, named *limit angle*, and such that

$$\sin\theta_\mathrm{L} = \sqrt{\frac{\mu_0\epsilon_2}{\mu_0\epsilon_1}} \ ,$$

$\sin\theta' = 1$: for incidence angle $\theta = \theta_\mathrm{L}$, the emerging wave propagates along the boundary. This implies that for further increase of the incidence angle, that is for $\theta > \theta_\mathrm{L}$, no (real) refraction angle can satisfy the continuity of the tangential components of the field, thus the system of waves considered in Sect. 6.3 breaks down. From the physical point of view, beyond the limit angle, the phase velocity (6.16) along x of the wave coming from the denser material M_1 (e.g., water, terrain, etc.) is lower than the *minimum* velocity (4.28) that a homogeneous plane wave can have in the thinner material M_2 (air, in the case at hand), i.e.

$$\frac{\omega}{\beta\sin\theta} < \frac{\omega}{\beta'} \qquad \forall\theta > \theta_\mathrm{L} \ .$$

This consideration suggests that a *slower* plane wave must exist in the thinner medium to satisfy continuity. Section 4.1.2.2 demonstrates that an *inhomogeneous*

wave propagates at a velocity (4.29) lower than that of the corresponding homogeneous wave, and therefore it is able to guarantee the tangential field continuity. In particular, the velocity of propagation u' of the inhomogeneous refracted wave must be

$$u' = \frac{\omega}{\beta'} = \frac{\omega}{\sqrt{\alpha'^2 + k'^2}} < \frac{1}{\sqrt{\mu_0 \epsilon_2}} \qquad \forall \theta > \theta_{\mathrm{L}} \, . \tag{6.32}$$

The condition (6.32) is satisfied, because, as the phase velocity along x of the incident wave decreases with increasing θ, the attenuation constant α' increases to correspondingly lower the velocity of the refracted wave. The generation of the inhomogeneous wave thus guarantees the field continuity.

Since air is suitably modeled as a lossless medium, $\boldsymbol{\alpha}' \perp \boldsymbol{\beta}'$, hence the refracted wave is expressed by

$$\boldsymbol{E}' = \boldsymbol{E}'_0 \, \mathrm{e}^{\alpha' z - \mathrm{j}\beta' x} \qquad (z < 0) \, . \tag{6.33}$$

Equation (6.33) shows that the field of the refracted wave travels along the boundary while its amplitude decreases with the distance from the boundary. The phase and attenuation vectors of incident, reflected and refracted waves are shown in Fig. 6.17.

The values of the phase and attenuation constants of the refracted wave are obtained from the continuity condition

$$\beta' = \sqrt{\alpha'^2 + \omega^2 \mu_0 \epsilon_2} = \omega \sqrt{\mu_0 \epsilon_1} \sin \theta \, ,$$

and, correspondingly,

$$\alpha' = \omega \sqrt{\mu_0 \epsilon_1} \sqrt{\sin^2 \theta - \frac{\epsilon_2}{\epsilon_1}} \, .$$

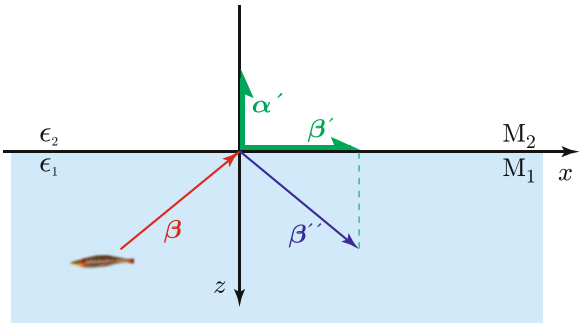

Fig. 6.17 Perpendicular phase and attenuation vectors of totally reflected wave

For some further insight into the physics of total reflection, assume a horizontally polarized wave emerging from the material M_1. The field continuity requires horizontal polarization also for the wave in the air, so that

$$\boldsymbol{E}'_0 = E'_0\,\mathbf{y}_0\ ;$$
$$\boldsymbol{H}'_0 = \frac{\beta' E'_0}{\omega\mu_0}\,\mathbf{z}_0 + \mathrm{j}\frac{\alpha' E'_0}{\omega\mu_0}\,\mathbf{x}_0\ .$$

Then the Poynting vector of the refracted wave[9] is

$$\boldsymbol{\mathcal{P}}' = \frac{1}{2}E'_0\,\mathbf{y}_0\,\mathrm{e}^{\alpha' z - \mathrm{j}\beta' x} \times \left[\frac{\beta' E'_0}{\omega\mu_0}\mathbf{z}_0 - \mathrm{j}\frac{\alpha' E'_0}{\omega\mu_0}\,\mathbf{x}_0\right]\mathrm{e}^{\alpha' z - \mathrm{j}\beta' x}$$
$$= \mathrm{j}\,\frac{\left|E'_0\right|^2}{2}\,\frac{\alpha'}{\omega\mu_0}\,\mathrm{e}^{2\alpha' z}\mathbf{z}_0 + \frac{\left|E'_0\right|^2}{2}\,\frac{\beta'}{\omega\mu_0}\,\mathrm{e}^{2\alpha' z}\mathbf{x}_0\ .$$

The Poynting vector emerging from a denser material for incidence beyond the limit angle is complex:

$$\boldsymbol{\mathcal{P}}' = \mathcal{P}'_{\mathrm{r}}\,\mathbf{x}_0 + \mathrm{j}\mathcal{P}'_{\mathrm{j}}\,\mathbf{z}_0\ .$$

The x-direction of the real component indicates that the emerging power is transported along the interface, hence no power is transferred from the denser material to the thinner one. In fact, the component of $\boldsymbol{\mathcal{P}}'$ perpendicular to the boundary is imaginary and, according to the results of Sect. 1.2.5, does not correspond to any transfer of power. Therefore, the power reflected or scattered inside the denser material is invisible to the external sensor when total reflection occurs.

6.5 Reflection from Layered Materials

The models that have been worked out in the preceding sections to evaluate the basic reflecting features of a target surface assume infinite thickness of the materials. This assumption is sufficiently realistic in several instances, such as off-shore waters or deep rock-beds. However, also structures formed by more or less thick layers of different kinds of matter are found in the terrestrial environment.

To obtain information on the reflecting behavior of layered structures [3, 19], consider now the three media, M_0, M_1, and M_2 shown in Fig. 6.18, separated by plane parallel interfaces. Media M_0 and M_2 are assumed of infinite vertical extent, eventually of the same material, M_1 is a layer of finite thickness d_1. The upper medium M_0 may be air and M_1 and M_2 materials found on the Earth's surface, such as snow over terrain, soil over bedrock, or wax cuticle over leaf epidermis. The slab

[9] Remember that the refracted wave exists for $z < 0$.

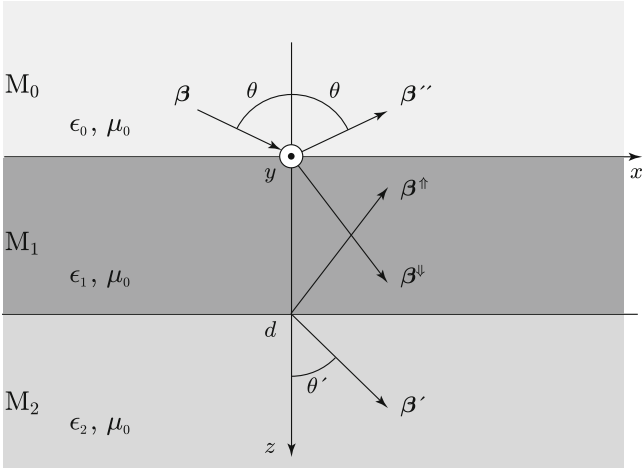

Fig. 6.18 Three-layer plane model of a stratified structure with downward (denoted by the $\Downarrow$ superscript) and upward (denoted by the $\Uparrow$ superscript) obliquely propagating waves

M_1 can also represent a planar leaf or a building wall, in which case M_0 and M_2 are both air. It is understood that the respective permittivities and the incidence angles are such that no total reflection occurs at any of the boundaries.[10]

6.5.1 Lossless Materials

When the homogeneous plane wave originated by a radar or by the Sun, impinges onto the M_0–M_1 interface at $z = 0$, part of the incident power enters M_1 and travels *downward* with propagation vector $\boldsymbol{\beta}^{\Downarrow}$. The M_1–M_2 dielectric discontinuity at the bottom $z = d$ of the M_1 layer reflects the downward wave, thus originating an *upward* wave traveling with propagation vector $\boldsymbol{\beta}^{\Uparrow}$. The upward wave is in turn reflected by the upper M_1–M_0 interface, and adds to the downward wave, and so on. Such a *multiple reflection* process is taken into account by one single downward *global* wave and one upward global wave.

Following the approach of Sect. 6.2.2, two sets of continuity conditions are now needed to match the tangential field vectors of the waves in the three homogeneous media:

- At the $z = 0$ upper boundary

$$\boldsymbol{E}_{0\mathrm{t}} + \boldsymbol{E}''_{0\mathrm{t}} = \boldsymbol{E}^{\Downarrow}_{0\mathrm{t}} + \boldsymbol{E}^{\Uparrow}_{0\mathrm{t}} \; ;$$

[10] Following the discussion in Sect. 6.3.2 for the Brewster angle, the lossless case is indicative also of the total-reflection behavior of actual dissipative materials.

$$\boldsymbol{H}_{0\mathrm{t}} + \boldsymbol{H}''_{0\mathrm{t}} = \boldsymbol{H}^{\Downarrow}_{0\mathrm{t}} + \boldsymbol{H}^{\Uparrow}_{0\mathrm{t}} \,.$$

- At the $z = d$ bottom boundary[11]

$$\boldsymbol{E}^{\Downarrow}_{0\mathrm{t}} \mathrm{e}^{-\mathrm{j}\beta^{\Downarrow}_z d} + \boldsymbol{E}^{\Uparrow}_{0\mathrm{t}} \mathrm{e}^{\mathrm{j}\beta^{\Uparrow}_z d} = \boldsymbol{E}'_{0t} \,;$$
$$\boldsymbol{H}^{\Downarrow}_{0\mathrm{t}} \mathrm{e}^{-\mathrm{j}\beta^{\Downarrow}_z d} + \boldsymbol{H}^{\Uparrow}_{0\mathrm{t}} \mathrm{e}^{\mathrm{j}\beta^{\Uparrow}_z d} = \boldsymbol{H}'_{0\mathrm{t}} \,.$$

A total of 16 unknown tangential (scalar) components of the electric and magnetic fields are now present in the system of equations originated by the required continuity. Given the homogeneity of the waves, the relations (4.31) and (4.32) hold between $\boldsymbol{E}$ and $\boldsymbol{H}$, thus halving the number of unknowns. Moreover, the 8 – equation system splits into two independent systems of four equations in the four unknown corresponding to the principal polarization components, vertical and horizontal, like in Sect. 6.2.2. The reflection (backward into M_0) and transmission (forward into M_2) coefficients depend not only on the electromagnetic parameters of the materials and on the incidence angle as for the half-space, but also on the thickness d of the slab of material M_1, which affects the phases of the upward and downward waves, according to the wavelength in it. Indeed, given the $\mathrm{mod}(\Phi, 2\pi)$ property, periodicity with $\beta^{\Downarrow}_z d = \beta^{\Uparrow}_z d$ is expected.

6.5.1.1 The Reflection Coefficient

To avoid cumbersome algebra, an incident wave traveling along z is now considered, with moderate loss of generality.

When $\boldsymbol{\beta} = \beta\,\mathbf{z}_0$, all waves propagate along z, hence $\beta_z \equiv \beta$. Assume linear polarization and the y-axis along the electric field: the boundary conditions at the bottom $z = d$ of the M_1 slab are

$$E^{\Downarrow}_0 \mathrm{e}^{-\mathrm{j}\Phi_\mathrm{d}} + E^{\Uparrow}_0 \mathrm{e}^{\mathrm{j}\Phi_\mathrm{d}} = E'_0 \,; \tag{6.34}$$
$$-H^{\Downarrow}_0 \mathrm{e}^{-\mathrm{j}\Phi_\mathrm{d}} + H^{\Uparrow}_0 \mathrm{e}^{\mathrm{j}\Phi_\mathrm{d}} = -H'_0 \,, \tag{6.35}$$

where Φ_d denotes the phase shift due to the slab of thickness d and permittivity ϵ_1:

$$\Phi_\mathrm{d} = \beta^{\Downarrow} d = \beta^{\Uparrow} d = \omega\sqrt{\mu_0 \epsilon_1}\, d \,.$$

Expressing the magnetic fields in terms of the electric fields through the intrinsic impedances η_1 of material M_1 and η_2 of material M_2 yields

[11] The phase of the wave transmitted into M_2 has been suitably referred to the $(z = d)$-plane, so that the z-dependent phase factor of the transmitted field is $\mathrm{e}^{-\mathrm{j}\beta''_z (z-d)}$ instead of $\mathrm{e}^{-\mathrm{j}\beta''_z z}$.

$$-\frac{E_0^{\Downarrow}}{\eta_1}\mathrm{e}^{-\mathrm{j}\Phi_\mathrm{d}} + \frac{E_0^{\Uparrow}}{\eta_1}\mathrm{e}^{\mathrm{j}\Phi_\mathrm{d}} = \frac{E_0'}{\eta_2} .$$

By substituting for E_0',

$$E_0^{\Downarrow}\mathrm{e}^{-\mathrm{j}\Phi_\mathrm{d}} + E_0^{\Uparrow}\mathrm{e}^{\mathrm{j}\Phi_\mathrm{d}} = \frac{\eta_2}{\eta_1}E_0^{\Downarrow}\mathrm{e}^{-\mathrm{j}\Phi_\mathrm{d}} - \frac{\eta_2}{\eta_1}E_0^{\Uparrow}\mathrm{e}^{\mathrm{j}\Phi_\mathrm{d}} ,$$

so that

$$E_0^{\Uparrow} = \frac{\eta_2 - \eta_1}{\eta_2 + \eta_1}E_0^{\Downarrow}\mathrm{e}^{-\mathrm{j}2\Phi_\mathrm{d}} = q_\mathrm{E}^{(12)}E_0^{\Downarrow}\mathrm{e}^{-\mathrm{j}2\beta_1 d} . \tag{6.36}$$

Equation (6.36) shows that the field $E_0^{\Uparrow}$ of the upward traveling wave arriving at the M_1–M_0 interface is the downward traveling field $E_0^{\Downarrow}$ reflected by the M_1–M_2 interface and shifted in phase by $2\Phi_\mathrm{d} = 2\beta_1 d$ because of the up and down double path in M_1. Then, the field E_0' exiting the slab M_1 and entering the infinitely thick M_2 material is

$$E_0' = E_0^{\Downarrow}\mathrm{e}^{-\mathrm{j}\Phi_\mathrm{d}} + q_\mathrm{E}^{(12)}E_0^{\Downarrow}\,\mathrm{e}^{-\mathrm{j}2\Phi_\mathrm{d}}\,\mathrm{e}^{\mathrm{j}\Phi_\mathrm{d}} = (1 + q_\mathrm{E}^{(12)})\,E_0^{\Downarrow}\,\mathrm{e}^{-\mathrm{j}\beta_1 d} . \tag{6.37}$$

The relation (6.37) indicates that the field that emerges from the bottom of M_1 into M_2 is the field that entered M_1 with amplitude modified by the reflection from the M_1–M_2 interface and with the phase shift produced by the path in M_1. The field E_0'' globally reflected by the layered structure, which is the field that is ultimately measurable by a remote sensor, is obtained from the boundary conditions at the M_0–M_1 interface

$$E_0 + E_0'' = E_0^{\Downarrow} + E_0^{\Uparrow} ; \tag{6.38}$$

$$-H_0 + H_0'' = -H_0^{\Downarrow} + H_0^{\Uparrow} . \tag{6.39}$$

Using (6.37), Eqs. (6.38) and (6.39) become

$$E_0 + E_0'' = (1 + q_\mathrm{E}^{(12)}\mathrm{e}^{-\mathrm{j}2\Phi_\mathrm{d}})\,E_0^{\Downarrow} ;$$

$$-\frac{E_0}{\eta_0} + \frac{E_0''}{\eta_0} = \frac{1}{\eta_1}(-1 + q_\mathrm{E}^{(12)}\mathrm{e}^{-\mathrm{j}2\Phi_\mathrm{d}})\,E_0^{\Downarrow} ,$$

from which the reflection coefficient $q_\mathrm{ES}^{(01)}$ of the layered structure is finally obtained as

$$q_\mathrm{ES}^{(01)} = \frac{E_0''}{E_0} = \frac{\eta_1(q_\mathrm{E}^{(12)}\mathrm{e}^{-\mathrm{j}2\beta_1 d} + 1) + \eta_0(q_\mathrm{E}^{(12)}\mathrm{e}^{-\mathrm{j}2\beta_1 d} - 1)}{\eta_1(q_\mathrm{E}^{(12)}\mathrm{e}^{-\mathrm{j}2\beta_1 d} + 1) + \eta_0(q_\mathrm{E}^{(12)}\mathrm{e}^{-\mathrm{j}2\beta_1 d} + 1)} , \tag{6.40}$$

where the reflection coefficient $q_{\mathrm{E}}^{(12)}$ at the M_1–M_2 interface is found in (6.36). The reflection coefficient $q_{\mathrm{Es}}^{(01)}$ of the layered structure obviously reduces to the value

$$q_{\mathrm{Es}}^{(01)} = q_{\mathrm{E}}^{(01)} = \frac{\eta_1 - \eta_0}{\eta_1 + \eta_0} ,$$

if no reflection occurs at the M_1–M_2 interface.

It is worth to point out that, as expected, the phase shift $2\beta_1 d = 4\pi(d/\lambda_1)$ introduces a periodicity into the reflection coefficient: this implies that the amplitude of the reflected field varies periodically with both wave frequency and thickness of the slab M_1, for given ϵ_1. Note that, in case of oblique incidence, the periodicity of the reflecting behavior depends also on the angle of incidence.

In essence, the periodic behavior of the reflection coefficient of the layered structure is due to the interference between the downward and the upward waves. When the two waves at the M_0–M_1 interface are in phase, the reflection coefficient has a maximum, whereas it is minimum for waves out of phase. The phase difference depends on a number of parameters, that is, on the thickness of slab M_1, on permittivities of the materials, on angle of incidence and on wave frequency. In case the incident radiation is not monochromatic, but composed of many wavelengths, the occurrence of constructive or destructive interference depends on wavelength, for given values of the other parameters. The reflected radiation has maxima at the wavelengths at which constructive interference happens, i.e., at wavelengths at which (6.40) has maxima. Figure 6.19 depicts the combined effect of the thickness d of the slab M_1 and of the wavelength λ_1 in originating constructive or destructive interference. The variable thickness d of the oil film (material M_1 in the considered model) over water (material M_2) results in the appearance of *color fringes*. The "color" is given by the wavelength λ_1 at which the local thickness d yields constructive interference between the waves traveling downward and upward in the oil film. In essence, the *color fringes* represents a map of the thickness of the oil film.

For the periodic variation of reflection to be actually observable, the assumed plane parallel boundary must be a sufficiently approximate representation of the real surface structure. Since the deviation from planarity must be small with respect to wavelength, in the optical wavelength range such a model is seldom realistic for many layered terrestrial materials, although, as seen above, it can be representative of fluid structures, such as a thin oil slick over water, that are indeed quite relevant to environmental monitoring. Rather, the model can be serviceable at microwaves, especially in the lower frequency range, where, for instance, the effect is observed on ice sheets over liquid water [17].

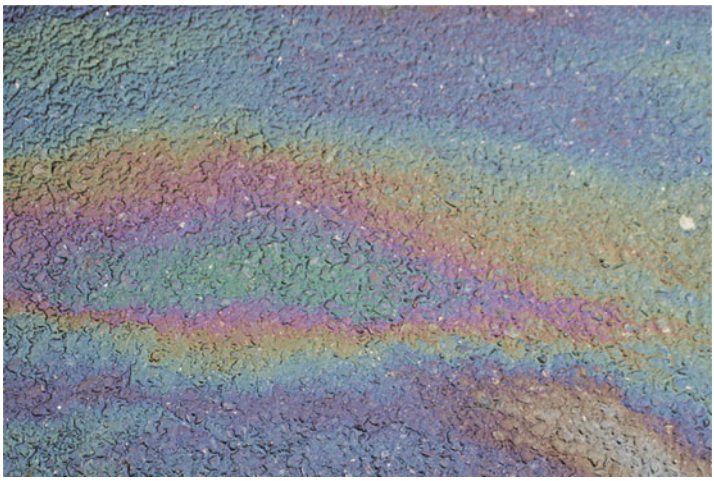

Fig. 6.19 The color fringes on an oil film are modeled by wavelength-selective interference between upward and downward waves in a three-layer structure as in Fig. 6.18

6.5.2 Lossy Materials

The essential information on the reflecting behavior of layered structures has been readily obtained under the assumption of lossless ideal materials. Further insight into the reflection mechanisms is gained by extending the analysis to the more realistic lossy media. In such a case, the waves in M_1 and M_2 are obviously attenuated. The model is complicated when incidence is oblique, since, according to the results of Sect. 6.3, the phase vector $\boldsymbol{\beta} = \beta_x \mathbf{x}_0 + \beta_z \mathbf{z}_0$ is not parallel to the attenuation vector $\boldsymbol{\alpha} = \alpha \mathbf{z}_0$. Therefore, to avoid cumbersome algebra, normal incidence (i.e., $\beta_x = 0$) is considered again here. After all, the results of Sect. 6.3.1 indicate that this assumption well approximates the behavior of the field penetrating into various "humid" terrestrial materials. In this introductory approach, the continuous vertical inhomogeneities (cf. Sect. 7.3.3) that are encountered in several actual instances, such as in soil [2], snow [16], or sea foam [1] layers, are also disregarded.

The fields to include into the continuity relations (6.34) and (6.35) on the $z = d$ boundary now have to account for the attenuation[12] $\mathcal{A}_1$ (Sect. 4.22) undergone in M_1, i.e.,

$$\mathcal{A}_1 = \mathrm{e}^{-\alpha^{\Downarrow} d} = \mathrm{e}^{-\alpha^{\Uparrow} d} \equiv \mathrm{e}^{-\alpha_1 d} \,.$$

[12]The attenuation caused by M_1 is clearly the same for both downward and upward waves.

Correspondingly, the continuity conditions are now

$$E_0^{\Downarrow}\mathcal{A}_1 \mathrm{e}^{-\mathrm{j}\Phi_\mathrm{d}} + \frac{E_0^{\Uparrow}}{\mathcal{A}_1}\mathrm{e}^{\mathrm{j}\Phi_\mathrm{d}} = E_0' \,; \tag{6.41}$$

$$-H_0^{\Downarrow}\mathcal{A}_1 \mathrm{e}^{-\mathrm{j}\Phi_\mathrm{d}} + \frac{H_0^{\Uparrow}}{\mathcal{A}_1}\mathrm{e}^{\mathrm{j}\Phi_\mathrm{d}} = -H_0' \,. \tag{6.42}$$

By relating H_0 to E_0 through the complex intrinsic impedances η_1 and η_2 and taking (6.41) into account, (6.42) becomes

$$-\mathcal{A}_1 \frac{E_0^{\Downarrow}}{\eta_1}\mathrm{e}^{-\mathrm{j}\Phi_\mathrm{d}} + \frac{E_0^{\Uparrow}}{\mathcal{A}_1\,\eta_1}\mathrm{e}^{\mathrm{j}\Phi_\mathrm{d}} = -\mathcal{A}_1 \frac{E_0^{\Downarrow}}{\eta_2}\mathrm{e}^{-\mathrm{j}\Phi_\mathrm{d}} - \frac{E_0^{\Uparrow}}{\mathcal{A}_1\,\eta_2}\mathrm{e}^{\mathrm{j}\Phi_\mathrm{d}} \,,$$

whence the upward traveling field $E_0^{\Uparrow}$ is finally

$$E_0^{\Uparrow} = \frac{\eta_2 - \eta_1}{\eta_2 + \eta_1}\,\mathrm{e}^{-2\alpha_1 d}\,\mathrm{e}^{-\mathrm{j}2\beta_1 d}\,E_0^{\Downarrow} = q_\mathrm{E}^{(12)}\,\mathrm{e}^{-2\alpha_1 d}\,\mathrm{e}^{-\mathrm{j}2\beta_1 d}\,E_0^{\Downarrow} \,,$$

which indicates that the field of the upward wave arriving at the M_1–M_0 interface is the field $E_0^{\Downarrow}$ that entered M_1, reflected by the M_1–M_2 interface and attenuated by the round trip within M_1.

The field E_0' transmitted into M_2 is

$$E_0' = \left(1 + q_\mathrm{E}^{(12)}\right)\mathrm{e}^{-\alpha_1 d}\,\mathrm{e}^{-\mathrm{j}\beta_1 d}\,E_0^{\Downarrow} \,,$$

that is, the field entering M_2 is the one that entered M_1, shifted in phase and attenuated by the path in the M_1 slab, and refracted through the M_1–M_2 interface. For given $E_0^{\Downarrow}$, the transmitted field decreases with increasing attenuation, i.e., in particular, with increasing imaginary part $|\tilde{\epsilon}_{\mathrm{j}1}|$ of the permittivity of material M_1, which affects the penetration depth (6.26) in the layer.

6.5.2.1 The Reflection Coefficient

The field E_0'' globally reflected at the interface $z = 0$ between air and layered structure is

$$E_0'' = \frac{\eta_1 + \eta_0\,\mathcal{C}_s}{\eta_1 - \eta_0\,\mathcal{C}_\mathrm{s}}E_0 = q_\mathrm{ES}^{(12)}\,E_0 \,,$$

having defined the *slab factor*

$$\mathcal{C}_\mathrm{s} = \frac{q_\mathrm{E}^{(12)}\mathrm{e}^{-2\alpha_1 d}\,\mathrm{e}^{-\mathrm{j}2\beta_1 d} - 1}{q_\mathrm{E}^{(12)}\mathrm{e}^{-2\alpha_1 d}\,\mathrm{e}^{-\mathrm{j}2\beta_1 d} + 1} \,.$$

The slab factor is a complicated function of the complex permittivities of materials M_1 and M_2, of frequency, and of the thickness of the M_1 slab. The presence of the phase factors suggests an essentially periodic behavior, like in the lossless case of Sect. 6.5.1.1, but now damped by attenuation. The analysis of particular cases provides some further insight into the reflecting behavior of the layered structure.

If the material M_1 is tenuous,[13] such that $\eta_1 \simeq \eta_0$

$$E_0'' \simeq q_{\mathrm{E}}^{(12)} \mathrm{e}^{-\mathrm{j}2\beta_1 d} E_0 \,,$$

i.e., the field reflected from the layered structure reduces to the one reflected from the M_1–M_2 transition, modified by the appropriate phase factor. Analogously, if $\eta_2 \simeq \eta_1$, $q_{\mathrm{E}}^{(12)} \simeq 0$ and

$$E_0'' \simeq \frac{\eta_1 - \eta_0}{\eta_1 + \eta_0} E_0$$

approximates the field reflected by the single M_0–M_1 discontinuity. When the M_1 slab contains a high-loss material and/or its thickness d is large with respect to the penetration depth (6.26) so that $\mathrm{e}^{-2\alpha_1 d} \approx 0$,

$$E_0'' \simeq \frac{\eta_1 - \eta_0}{\eta_1 + \eta_0} E_0$$

is again the field reflected when the M_1–M_2 discontinuity vanishes: little effect of the underlying material M_2 is observed when the covering layer M_1 has sufficiently high losses or is sufficiently thick compared with the penetration depth ℓ. In practice, this condition tends to be more frequently met at the higher microwave frequencies and/or for a layer of moist material with thickness at least of the order of the free-space (vacuum) wavelength. At optical wavelengths, the effects both of the peaks of $|\tilde{\epsilon}_{\mathrm{j}1}|$ in correspondence of the resonances and of the extremely high frequency, make many natural and man-made materials[14] of non-negligible thickness opaque, so that the underlying materials are typically not observable.

As another significant reference, consider now the case of a slab of material M_1 for which $2\beta_1 d = 2m\,\pi$ ($m = 1, 2, 3, \ldots$), so that

$$\mathcal{C}_s = \frac{q_{\mathrm{E}}^{(12)} \mathrm{e}^{-2\alpha_1 d} - 1}{q_{\mathrm{E}}^{(12)} \mathrm{e}^{-2\alpha_1 d} + 1} \,.$$

When attenuation is high, $\mathrm{e}^{-2\alpha_1 d} \approx 0$ and the reflection coefficient of the layered structure is again

[13] This happens, for instance, in thin vegetation, dry snow, or sea foam at the lower microwave frequencies.

[14] "Clean" water, is a notable exception.

$$q_{\mathrm{Es}}^{(01)} \simeq \frac{\eta_1 - \eta_0}{\eta_1 + \eta_0} = q_{\mathrm{E}}^{(01)} \,.$$

Instead, when attenuation is low, $\mathrm{e}^{-2\alpha_1 d} \approx 1$ and the slab factor becomes

$$\mathcal{C}_{\mathrm{s}} \simeq \frac{q_{\mathrm{E}}^{(12)} - 1}{q_{\mathrm{E}}^{(12)} + 1} \,.$$

Then, in case the bottom M_1–M_2 interface is highly reflecting, $\left|q_{\mathrm{Es}}^{(01)}\right| \approx 1$. The above results indicate that the reflection coefficient of a slab of material M_1 overlying a material M_2 having high permittivity, such as an aqueous dielectric at microwaves, ranges between $\left|q_{\mathrm{Es}}^{(01)}\right| \approx 1$ when M_1 is transparent, and considerably lower values at frequencies at which M_1 absorbs. The effect of absorption adds to the wave interference considered in Sect. 6.5.1 to make color patterns to appear when polychromatic radiation impinges onto the surface of layered structures. Coarsely speaking, a maximum of reflection takes place at less absorbed wavelengths, thus enhancing the corresponding color, while low reflection occurs at the absorbed ones. It important to bear in mind that this mechanism has little relation with the effect of permittivity on the reflection coefficient considered in Sect. 6.3.2. The effect of absorption in coloring the reflected radiation is also clearly different from that of interference outlined in Sect. 6.5.1.1.

6.5.2.2 The Transmission Coefficient

The field E_0' entering M_2 depends on the parameters of the layered structure according to

$$E_0' = \frac{2\eta_1 \left(1 + q_{\mathrm{E}}^{(12)}\right) \mathrm{e}^{-\alpha_1 d}\, \mathrm{e}^{-\mathrm{j}\beta_1 d}}{\eta_1 \left(q_{\mathrm{E}}^{(12)} \mathrm{e}^{-2\alpha_1 d}\, \mathrm{e}^{-\mathrm{j}2\beta_1 d} + 1\right) - \eta_0 \left(q_{\mathrm{E}}^{(12)} \mathrm{e}^{-2\alpha_1 d}\, \mathrm{e}^{-\mathrm{j}2\beta_1 d} - 1\right)} E_0 = t_{\mathrm{Es}}^{(01)}\, E_0 \,.$$

The transmission coefficient $t_{\mathrm{Es}}^{(01)}$ is a complicated function of the involved parameters, essentially because of the interference between the upward and downward waves at the M_0–M_1 interface. If the round trip attenuation in M_1 is sufficiently high, $E_0^{\Uparrow} \ll E_0^{\Downarrow}$, the upward traveling wave interfering with the downward wave tends to vanish and the periodicities in reflection and transmission tend correspondingly to disappear. When

$$\left|q_{\mathrm{E}}^{(12)}\right| \mathrm{e}^{-2\alpha_1 d} \ll 1 \,,$$

the transmission coefficient simplifies in

Fig. 6.20 The white solar light appears green when transmitted through a leaf since it is depleted of the radiation at the wavelengths more absorbed by the vegetal matter

$$t_{\mathrm{ES}}^{(01)} \simeq \frac{2\eta_1}{\eta_0+\eta_1}\frac{2\eta_2}{\eta_1+\eta_2}\,\mathrm{e}^{-\alpha_1 d}\,\mathrm{e}^{-\mathrm{j}\beta_1 d}\,. \tag{6.43}$$

Equation (6.43) shows that the transmission of the field through the total structure depends on the transmissions at the M_0–M_1 and M_1–M_2 interfaces, taking account of the attenuation and phase shift caused by the lossy propagation path in the slab M_1.

A particularly relevant case is when M_2 is the same as M_0: this happens, for instance, for a planar leaf surrounded by air. The transmission coefficient of the leaf, modeled by the slab M_1, is then

$$t_{\mathrm{ES}}^{(01)} = 4\frac{\eta_0\,\eta_1}{(\eta_0+\eta_1)^2}\,\mathrm{e}^{-\alpha_1 d}\,\mathrm{e}^{-\mathrm{j}\beta_1 d}\,.$$

It is important to recall that the absorption coefficient α_1 depends on the imaginary part of permittivity $\tilde{\epsilon}_{\mathrm{j}1}$ of the leaf material M_1 according to (4.13). Therefore, given the results of Sect. 2.2.3, the transmission through the slab M_1 is a function of wavelength. When the polychromatic solar radiation impinges onto the leaf surface, the radiation transmitted beyond the leaf is depleted of the bands absorbed by the vegetal matter, for which $e^{-\alpha_1(\lambda)d} \ll 1$. This crucial effect is detailed in Sect. 14.1.1.2. An example of leaf transmission is shown in Fig. 6.20.

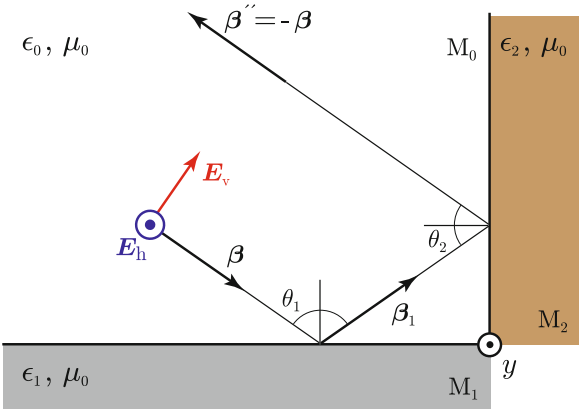

Fig. 6.21 Double reflection in a dihedral corner structure; the waves concurrently follow the path in the reverse directions

6.6 Reflection from Composite Planar Structures

The plane structures considered in the previous sections, in spite of their extreme simplicity, provide quite useful indications on the reflecting behavior of many terrestrial environments. But the plane model misses a basic feature observed in the reflection from some actual structures. Indeed, (6.14) indicates that the reflected wave travels in the specular direction, thus ruling out the possibility that the field is conveyed back in the same direction of incidence when $\theta \neq 0$. In fact, this actually happens when combined planar structures, typically found in urban environments, produce multiple reflections.

6.6.1 Reflection from Dihedrons

Some structures, mainly man-made, are *dihedral*, that is, they ideally consist of two orthogonal half-planes delimiting materials as asphalt (the horizontal plane) and wall plaster (the vertical plane). Apart from a limited area in the neighborhood of the edge, each half-plane reflects the incident field essentially according to the rules seen in Sect. 6.2.2 for plane waves. With reference to Fig. 6.21, the electric field $\boldsymbol{E}_1''$ reflected from the horizontal plane,[15] in the Jones notation has the form

$$\boldsymbol{E}_1'' = (q_{\mathrm{h}1}\, E_{0\mathrm{h}}\, \mathbf{h}_{01} + q_{\mathrm{v}1}\, E_{0\mathrm{V}}\, \mathbf{v}_{01})\ \mathrm{e}^{-\mathrm{j}\boldsymbol{\beta}_1 \cdot \boldsymbol{r}}\ , \tag{6.44}$$

[15]Given the symmetry, reflection from the vertical plane is concurrent to that from the horizontal one, so the order of reflection is irrelevant.

where q_{p1}, (p = h, v), denotes the reflection coefficient for polarization p at the interface between M_0 (air) and material M_1 (e.g., pavement). The field (6.44) reflected by the horizontal plane and traveling in the direction specular to the incident one, impinges onto the vertical plane boundary of material M_2. When the phase vector of the incident wave is perpendicular to the edge of the dihedron, i.e., $\boldsymbol{\beta} \perp \mathbf{y}_0$, the horizontal and vertical components of $\boldsymbol{E}_1''$ are horizontal and vertical components, respectively, also for the vertical plane. The field reflected by this latter has then the form (cf. Sect. 12.1.2.5)

$$\boldsymbol{E}'' = \left[q_{\mathrm{h2}}\, q_{\mathrm{h1}}\, E_{0\mathrm{h}}\, \mathbf{h}_0'' + q_{\mathrm{v2}}\, q_{\mathrm{v1}}\, E_{0\mathrm{v}}\, \mathbf{v}_0''\right] \mathrm{e}^{-\mathrm{j}\boldsymbol{\beta}''\cdot\boldsymbol{r}} \,. \tag{6.45}$$

Simple geometric considerations show that the wave reflected by this *double-bounce* mechanism has $\boldsymbol{\beta}'' = -\boldsymbol{\beta}$, thus it propagates in the verse opposite to that of the incident wave, like for normal incidence.

6.6.1.1 Phase Shift Between Polarizations

However, the polarization of the field reflected by a dihedral structure behaves differently from that discussed in Sect. 6.1.1. Figure 6.3 shows that the components of the field reflected in case of normal incidence are both opposite to the incident ones, i.e., $\mathbf{h}_0'' = -\mathbf{h}_0$ and $\mathbf{v}_0'' = -\mathbf{v}_0$. Instead, Fig. 6.22 indicates that the double-bounce inverts the vertical component, while it leaves the verse of the horizontal one unchanged, i.e.,

$$\mathbf{h}_0'' = \mathbf{h}_0 \,; \qquad \mathbf{v}_0'' = -\mathbf{v}_0 \,. \tag{6.46}$$

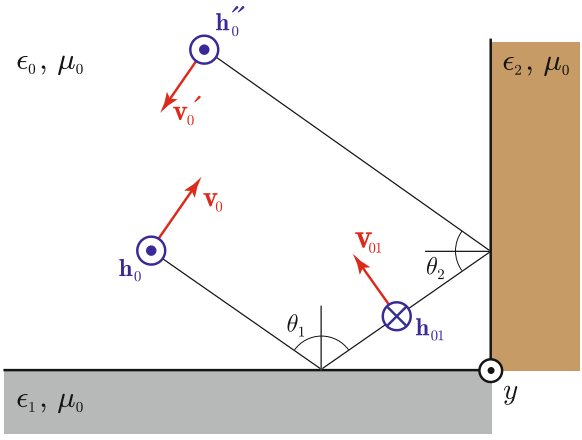

Fig. 6.22 Versors of horizontal and vertical electric field components in double-bounce mechanism

The relations (6.46) translate into a π-change[16] of the phase difference Φ_{hv} between the horizontal and vertical components of the field (4.39) in the Jones representation. For an incident wave

$$\boldsymbol{E} = \left[E_{0\mathrm{V}}\, \mathbf{v}_0 + E_{0\mathrm{h}}\, \mathrm{e}^{\mathrm{j}\Phi_{\mathrm{hv}}}\, \mathbf{h}_0 \right] \mathrm{e}^{-\mathrm{j}\boldsymbol{\beta}\cdot\boldsymbol{r}} ,$$

the field (6.45) reflected by the lossless dihedral corner reflector[17] is

$$\boldsymbol{E}'' = \left[q_{\mathrm{v}2}\, q_{\mathrm{v}1}\, E_{0\mathrm{V}}\, \mathbf{v}_0 + q_{\mathrm{h}2}\, q_{\mathrm{h}1}\, E_{0\mathrm{h}}\, \mathrm{e}^{\mathrm{j}(\Phi_{\mathrm{hv}} + \pi)}\, \mathbf{h}_0 \right] \mathrm{e}^{\mathrm{j}\boldsymbol{\beta}\cdot\boldsymbol{r}} . \tag{6.47}$$

The expression (6.47) shows that the relative phase of the horizontal component reflected through the double-bounce mechanism is $\Phi''_{\mathrm{hv}} = \Phi_{\mathrm{hv}} + \pi$, while the field reflected for normal incidence clearly has $\Phi''_{\mathrm{hv}} = \Phi_{\mathrm{hv}}$.

In conclusion, provided the angles of incidence *on both* horizontal and vertical half-planes are lower than the respective Brewster angles given by (6.21),

- the *relative* phase of the horizontal component of the electric field undergoes two changes of π rad, hence is left unchanged by the double bounce;
- the relative phase of the vertical component, which changes direction at each reflection, at the end is shifted by π rad.

This phase behavior, which is peculiar of the double-bounce reflection mechanism [13, Chap. 3] [9, Chap. 5], allows to discriminate the reflection from dihedral corner reflectors against the one for normal incidence. Figure 6.23 reports the map of the phase difference between horizontal and vertical field components for an urban scenario where the density of dihedral corner reflectors is relatively high. Figure 6.24, which refers to an agricultural area with a low density of dihedrons, is shown for suitable comparison.[18] The difference between the relative phase $\Phi''_{\mathrm{hv}} = \Phi_{\mathrm{hv}} + \pi$ of the reflected components and that, Φ_{hv}, of the incident ones is color-coded, with red denoting values $\Phi''_{\mathrm{hv}} - \Phi_{\mathrm{hv}} \approx \pi$ and blue relative to $\Phi''_{\mathrm{hv}} - \Phi_{\mathrm{hv}} \approx 0$. The urban zone shows an elevated number of double-bounce occurrences per unit area, in contrast with the quite low density exhibited by the agricultural landscape. Indeed, double reflections between horizontal street pavement and vertical building walls are expected to occur frequently in the town but only occasionally in the area that mainly includes cultivated or natural surfaces and a few sparse building. The results suggest that the phase behavior is only slightly modified when the involved materials are lossy, given the substantial similarity of the reflection features with those in the lossless case discussed in Sect. 6.3.2.

[16] For lossless materials.

[17] Apart from an absolute phase term.

[18] The white and light blue patches refer to areas of the hilly surface where nearly normal local incidence with correspondingly high backscattering occurs.

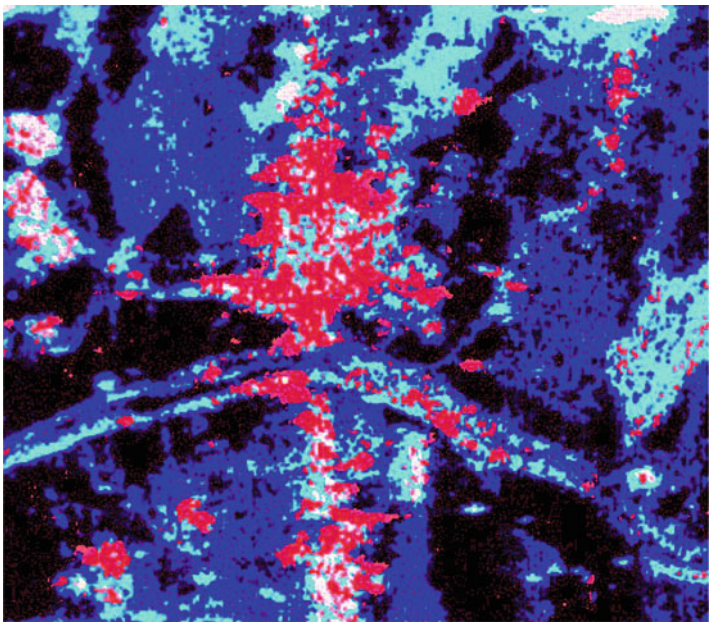

Fig. 6.23 Observed phase difference $\Delta\Phi_{\mathrm{hv}}$ between horizontal and vertical co-polarized components of the field backscattered at P-band by an urban area; spots with $|\Delta\Phi_{\mathrm{hv}}| \gtrsim \frac{2}{3}\pi$ are in *red*; light color denotes high backscattering, dark represents low backscattering. Data acquired during MAC 91 [5]

6.6.2 *Reflection from Trihedrons*

Several man-made structures are composed of three mutually orthogonal planes, as further discussed in Sect. 14.1.2.2. These geometric arrangements are quite common not only inside buildings, but also at their exterior, where, for instance, the horizontal surface of the roof or of a terrace forms trihedrons with pairs of orthogonal walls at its corners (Fig. 6.25). An electromagnetic wave approximately undergoes specular reflections from the surfaces of which the corner reflector is composed [14]. After bouncing on each of the three sides, the wave is sent back in the same direction of arrival, ideally irrespective of the angle this latter forms with the edges. Since the number of bounces in the trihedral reflection is odd, the relative phase of the components remains unchanged,[19] like for normal incidence. Note that the horizontal and vertical unit vectors are referred to the horizontal surface, that is, to the xy-plane in Fig. 6.26. A field that is horizontally or vertically polarized with respect to this latter may not have the same polarizations with respect to

[19]The requirement that the angle of incidence be below the Brewster angle for each face of the trihedron holds as for the dihedral reflection.

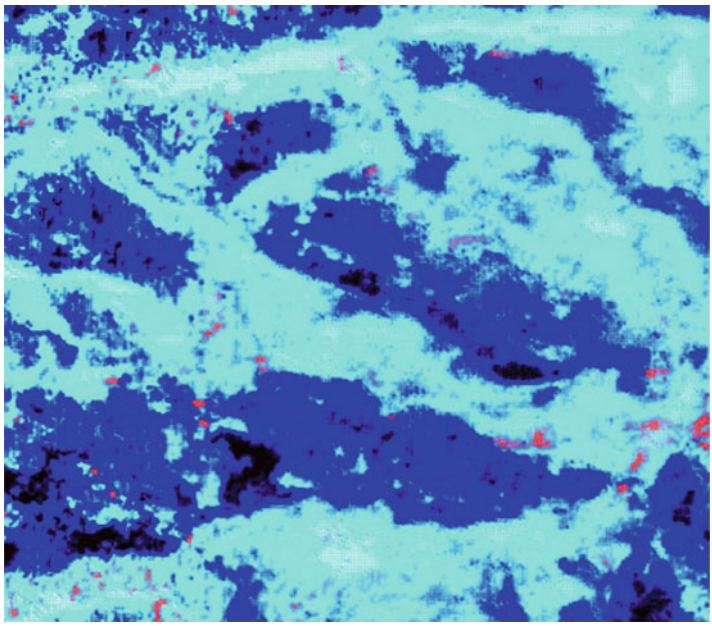

Fig. 6.24 Observed phase difference between horizontal and vertical field components backscattered at P-band by an agricultural area; spots with $\Delta\Phi_{\mathrm{hv}} \gtrsim \frac{2}{3}\pi$ are in *red*. Data acquired during MAC 91 [5]

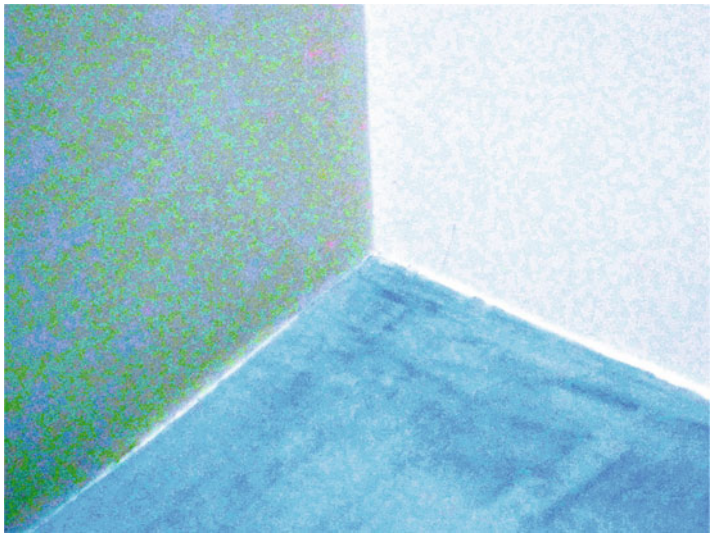

Fig. 6.25 Actual trihedral corner reflector formed by floor and walls

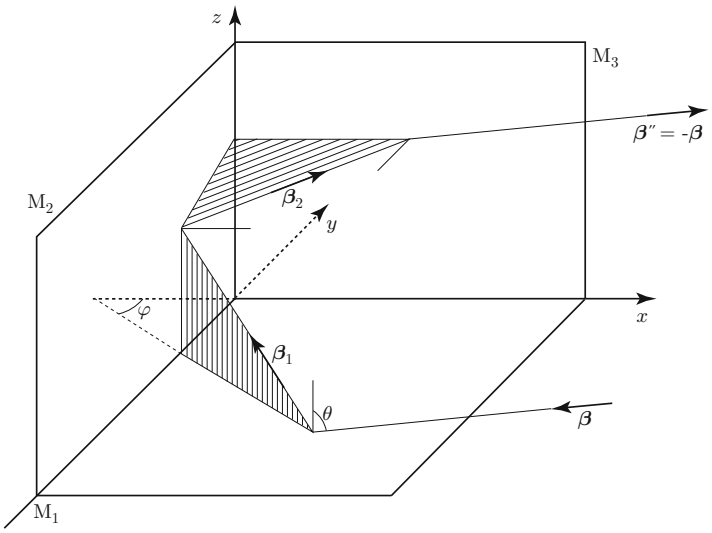

Fig. 6.26 The triple bounce in a trihedron reflects the wave back in the same direction of incidence

the vertical surfaces.[20] This implies mixing the reflection coefficients into three generally different combinations.

Bounced Waves

The familiar concept that an object is bounced back from the surface of a material on which it impinges is interpreted to understand which parameter is effective when we deal with electromagnetic waves. If we recall the field continuity we learnt just at the beginning, we are easily convinced that the key quantity is the intrinsic impedance. Any change of η encountered by the wave makes a fraction of the latter to revert the direction of propagation, giving rise to the reflected wave. This clearly occurs when the radiation coming from the Sun or from a space- or air-based platform hits a solid or liquid target. The larger the change of impedance, the stronger is the reflection and less power is able to penetrate into the material.

To determine the reflecting properties, we resort extensively to field continuity, field representation and plane wave features. A result is straightforward, the law of reflection from mirrors, known for centuries, before the nature of the electromagnetic field was understood. A little mathematical effort provides us with other well established properties of reflection and refraction, the most interesting of

[20]The axonometric representation of the 3-D geometry alters the appearance of the angles in Fig. 6.26.

which is perhaps the substantial dependence of reflection on the wave polarization. We begin to get used to the idea that the vertical component of the field is reflected less, even considerably, than the horizontal one, according to the incidence angle. How far the arriving wave is able to travel below the surface of lossy materials is of considerable interest to assess the amount of information that Earth observing systems can draw from sub-surface targets. We find that the penetration depth is proportional to wavelength and decreases as the imaginary part of the permittivity increases, i.e., with raising absorption of the material.

Boring algebra is demanded by modeling reflection from layered materials, as indeed are encountered on Earth. A striking feature is the periodicity with thickness or, equivalently, with wavelength, displayed by the reflection coefficient, which we learn to be caused by the constructive or destructive interference of waves bouncing back and forth between top and bottom boundaries of a horizontal slab. Moreover, the dependence of the reflection and transmission coefficients on wavelength-selective absorption hints at the origin of the color of the objects under natural illumination.

A class of structures we especially see in the urban landscape consists of pairs or triplets of orthogonal plane surfaces. Simple ray tracing shows that such geometries may be able to send the incident wave back in the same direction of arrival, like a single plane orthogonal to the direction of incidence. It is the difference of phase between horizontal and vertical field components that reveals the diverse origin of the reflection.

References

1. Anguelova MD, Gaiser PW (2013) Microwave emissivity of sea foam layers with vertically inhomogeneous dielectric properties. Remote Sens Environ 139:81–96. doi:10.1016/j.rse.2013.07.017
2. Behari J (2006) Microwave dielectric behaviour of wet soils. Springer. ISBN:9781402032882
3. Brekhovskikh LM (1980) Waves in layered media. Academic. ISBN:9780121305604
4. Bruckler L, Witono H, Stengel P (1988) Near surface soil moisture estimation from microwave measurements. Remote Sens Environ 26(2):101–121. doi:http://dx.doi.org/10.1016/00344257(88)90091-0
5. Canuti P, d'Auria G, Pampaloni P, Solimini D (1992) MAC 91 on Montespertoli: an experiment for agro-hydrology. In: International Geoscience and Remote Sensing Symposium (IGARSS'92), May 1992, vol 2, pp 1744–1746. doi:10.1109/IGARSS.1992.578869
6. Ciani A, Goss K-U, Schwarzenbach RP (2005) Light penetration in soil and particulate minerals. Eur J Soil Sci 56(5):561–574. doi:10.1111/j.1365-2389.2005.00688.x
7. Farr TG, Elachi C, Hartl P, Chowdhury K (1986) Microwave penetration and attenuation in desert soil: a field experiment with the shuttle imaging radar. IEEE Trans Geosci Remote Sens GE-24(4):590–594. doi:10.1109/TGRS.1986.289675
8. Gordon HR, McCluney WR (1975) Estimation of the depth of sunlight penetration in the sea for remote sensing. Appl Opt 14(2):413–416. doi:10.1364/AO.14.000413
9. Massonnet D, Souyris JC (2008) Imaging with synthetic aperture radar. EPFL. ISBN:9781439808139

10. McCauley JF, Schaber GG, Breed CS, Grolier MJ, Haynes CV, Issawi B, Elachi C, Blom R (1982) Subsurface valleys and geoarcheology of the Eastern Sahara revealed by shuttle radar. Science 218(4576):1004–1020. doi:10.1126/science.218.4576.1004
11. Nolan M, Fatland DR (2003) Penetration depth as a DInSAR observable and proxy for soil moisture. IEEE Trans Geosci Remote Sens 41(3):532–537. doi:10.1109/TGRS.2003.809931
12. Parcak SH (2009) Satellite remote sensing for archaeology. Taylor & Francis. ISBN:9780203881460
13. Richards JA (2009) Remote sensing with imaging radar. Springer. ISBN:9783642020209
14. Robertson SD (1947) Targets for microwave radar navigation. Bell Syst Tech J 26(4):852–869. doi:10.1002/j.1538-7305.1947.tb01325.x
15. Santeford HS, Smith JLR (eds) (1974) Advanced concepts and techniques in the study of snow and ice resources: an interdisciplinary symposium. National Academy of Sciences, Washington, DC. ISBN:9780309022354
16. Song K, Zhou X, Fan Y (2012) Electromagnetic scattering from a multi-layered surface with lossy inhomogeneous dielectric profiles for remote sensing of snow. Progress Electromagn Res M 25:197–209. doi:10.2528/PIERM12063004
17. Swift CT, St. Germain K, Jezek KC, Gogineni SP, Gow AJ, Perovich DK, Grenfell TC, Onstott RG (1992) Laboratory investigations of the electromagnetic properties of artificial sea ice. In: Carsey FD (ed) Microwave remote sensing of sea ice. American Geophysical Union, pp 177–200. ISBN:9781118663950
18. Vogelmann CT (1989) Penetration of light into plants. Photochem Photobiol 50(6):895–902. doi:10.1111/j.1751-1097.1989.tb02919.x
19. Wait JR (1995) Electromagnetic waves in stratified media. IEEE. ISBN:9780780311244
20. Zribi M, Gorrab A, Baghdadi N, Lili-Chabaane Z, Mougenot B (2014) Influence of radar frequency on the relationship between bare surface soil moisture vertical profile and radar backscatter. IEEE Geosci Remote Sens Lett 11(4):848–852. doi:10.1109/LGRS.2013.2279893

Chapter 7
Scattering

Earth observation relies heavily on the scattering of electromagnetic waves from the terrestrial environment. The passive measurements in the optical band exploit the fraction of solar radiation scattered by the matter it encounters on the surface or in the atmosphere. The active techniques, lidar and radar, are by themselves intrinsically based on scattering. On their side, the observations that take advantage of thermal emission are tightly related to the reflection and scattering mechanisms through reciprocity, as shown in the subsequent Chap. 8. This preamble suggests that understanding the salient properties of scattering plays a crucial role in interpreting remote sensing images and data, as well as in devising efficient tools for their exploitation.

Electromagnetic scattering is a complicated process that requires considerable modeling effort, especially when natural media are involved. Given the multi-sided nature of the terrestrial environment, drastic simplifying assumptions are needed if the salient features of images of scattering have to be readily understood and effectively utilized. However, after all, the results that are obtained even from elementary models prove quite useful, since often they are fairly representative of the behavior that can be expected in actual instances.

The presentation that follows is limited to *macroscopic* scattering, on which the interpretation of largely used optical and radar images of the Earth's surface are based. Radiation-matter interaction involving molecular or atomic *microscopic* mechanisms, such as Raman scattering [7, 39, 65] and fluorescence [5, 42, 61], which also find applications in remote sensing [23, 51, 64], here is not explicitly considered.

D. Solimini, *Understanding Earth Observation*, Remote Sensing and Digital Image Processing 23, DOI 10.1007/978-3-319-25633-7_7

7.1 Scatter Modeling

The characteristics of the electromagnetic field in an inhomogeneous material have been determined in Sect. 5.1 under the assumption of weak inhomogeneities, which leads to smoothly varying waves *progressing* along the rays. The properties of the progressive wave are readily obtained by the sourceless formula (5.2). Such an approach neglects that the spatial variations of permittivity represented by the third term in (5.1) act as secondary sources of the electromagnetic field. On the other side, the effect of steep changes of permittivity in re-directing part of a progressive wave in directions different from that of arrival has been considered in Chap. 6 for the reference case of plane boundaries between different piecewise homogeneous materials. The properties of the wave reflection have been obtained directly from the boundary conditions without involving the mentioned dielectric secondary sources.

In fact, most Earth observation techniques are essentially based just on the behavior of the environmental inhomogeneities that act as secondary sources. This implies that the weak inhomogeneity assumption has to be removed to progress further in understanding the information content of the remote sensing images.

7.1.1 Scattering Source

The field created by the primary source (Sun or radar antenna) represented in Fig. 7.1 by the impressed current $\boldsymbol{J}_\mathrm{s}$ satisfies the spectral Maxwell's equations

$$\nabla \times \boldsymbol{E} = -\mathrm{j}\omega\mu_0 \boldsymbol{H} \; ; \tag{7.1}$$

$$\nabla \times \boldsymbol{H} = \mathrm{j}\omega\epsilon(\boldsymbol{r})\boldsymbol{E} + \boldsymbol{J}_\mathrm{s} \; . \tag{7.2}$$

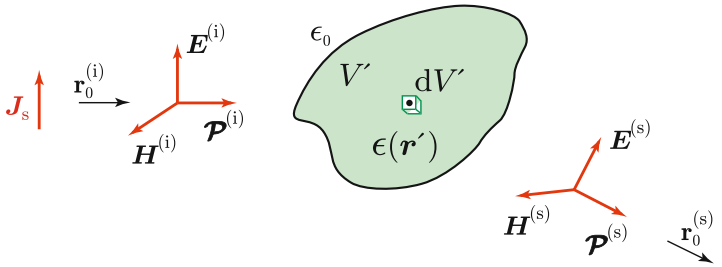

Fig. 7.1 The wave incident from the direction $\boldsymbol{r}_0^{(\mathrm{i})}$ onto the object $\epsilon(\boldsymbol{r}')$ in V' is scattered into the various directions $\boldsymbol{r}_0^{(\mathrm{s})}$; $\mathrm{d}V'$ denotes the elementary scattering volume

Assume that the wave created by $\boldsymbol{J}_\mathrm{s}$ propagates in the Earth's atmosphere and that it encounters an "object", be it a rain drop, a tree, or a building, intended to be the *target* of the observation. Figure 7.1 represents the wave arriving from the direction $\mathbf{r}_0^{(\mathrm{i})}$ by the electric, $\boldsymbol{E}^{(\mathrm{i})}$, and magnetic, $\boldsymbol{H}^{(\mathrm{i})}$, fields and by the corresponding incident areic power $\boldsymbol{\mathcal{P}}^{(\mathrm{i})}$. From the electromagnetic point of view, the object is nothing else but the region of space schematized by V' the complex permittivity $\epsilon(\boldsymbol{r}')$ of which differs from that of the *background*. Since the latter is air,[1] to a first approximation assimilated to vacuum,

$$\epsilon(\boldsymbol{r}') = \epsilon_0[\tilde{\epsilon}_\mathrm{r}(\boldsymbol{r}') + \mathrm{j}\tilde{\epsilon}_\mathrm{j}(\boldsymbol{r}')] \neq \epsilon_0, \qquad \boldsymbol{r}' \in V' .$$

If permittivity is written

$$\epsilon = \epsilon_0 + \epsilon - \epsilon_0 ,$$

the second Maxwell's equation (7.2) becomes

$$\nabla \times \boldsymbol{H} = \mathrm{j}\omega\epsilon_0 \boldsymbol{E} + \mathrm{j}\omega[\epsilon(\boldsymbol{r}') - \epsilon_0]\boldsymbol{E} + \boldsymbol{J}_\mathrm{s} . \tag{7.3}$$

The term containing the deviation of the permittivity from that of vacuum is now regarded as a spatially distributed current density $\boldsymbol{J}_\mathrm{ob}$ representing the effect of the object [26, Chap. 10]:

$$\boldsymbol{J}_\mathrm{ob}(\boldsymbol{r}') := \mathrm{j}\omega[\epsilon(\boldsymbol{r}') - \epsilon_0]\boldsymbol{E} \qquad \boldsymbol{r}' \in V' , \tag{7.4}$$

so that (7.3) is written

$$\nabla \times \boldsymbol{H} = \mathrm{j}\omega\epsilon_0 \boldsymbol{E} + \boldsymbol{J}_\mathrm{ob} + \boldsymbol{J}_\mathrm{s} .$$

The current $\boldsymbol{J}_\mathrm{ob}$, which differs from zero only inside the volume V' of the object, behaves as a *re-radiating* source current, which produces the *scattered* field $\boldsymbol{E}^{(\mathrm{s})}$ and $\boldsymbol{H}^{(\mathrm{s})}$ outside V', according to

$$\nabla \times \boldsymbol{H}^{(\mathrm{s})}(\boldsymbol{r}) = \mathrm{j}\omega\epsilon_0 \boldsymbol{E}^{(\mathrm{s})}(\boldsymbol{r}) + \boldsymbol{J}_\mathrm{ob}(\boldsymbol{r}') \qquad \boldsymbol{r} \ni V' .$$

The scattered field superposes to the *incident field* $\boldsymbol{E}^{(\mathrm{i})}$ and $\boldsymbol{H}^{(\mathrm{i})}$, which is the field in absence of the object and that satisfies

$$\nabla \times \boldsymbol{H}^{(\mathrm{i})} = \mathrm{j}\omega\epsilon_0 \boldsymbol{E}^{(\mathrm{i})} + \boldsymbol{J}_\mathrm{s} ,$$

[1] The approach holds as well for particular cases in which the background is not air.

to compose the *total field*

$$\begin{aligned} \boldsymbol{E}(\boldsymbol{r}) &= \boldsymbol{E}^{(\mathrm{i})}(\boldsymbol{r}) + \boldsymbol{E}^{(\mathrm{s})}(\boldsymbol{r}) \; ; \\ \boldsymbol{H}(\boldsymbol{r}) &= \boldsymbol{H}^{(\mathrm{i})}(\boldsymbol{r}) + \boldsymbol{H}^{(\mathrm{s})}(\boldsymbol{r}) \; , \end{aligned} \qquad \boldsymbol{r} \ni V' \; . \tag{7.5}$$

The total field is the field that is actually created by the *primary source* $\boldsymbol{J}_{\mathrm{s}}$ in presence of the object, hence satisfying the original Eqs. (7.1) and (7.2) for the inhomogeneous medium.

It is important to bear in mind that, according to this model,

- the scattered field produced by $\boldsymbol{J}_{\mathrm{ob}}$ is meaningful only *outside* the object, and so does the total field (7.5);
- the secondary source current $\boldsymbol{J}_{\mathrm{ob}}$ defined by (7.4) is proportional to the local deviation of permittivity from the background multiplied by the *internal* electric field at the same location $\boldsymbol{r}'$;
- the field inside the scatterer yielding $\boldsymbol{J}_{\mathrm{ob}}$ *is not* the incident field, but derives from this latter taking account of the *inwards* effect of the object.

In the following, even if $\epsilon \neq \epsilon_0$ in V', the propagation constant inside the object is eventually assumed to differ little from the one in the vacuum, under the assumption of tenuous material. Finally, note that, based on the equivalence introduced in Sect. 3.2.2, the volume V' filled with the re-radiating current $\boldsymbol{J}_{\mathrm{ob}}$ can be replaced by a surface wrapping V' with the equivalent scattering source surface currents (3.52) and (3.53) smeared on it.

7.1.2 Scattered Field

Section 3.1 shows that the radiated electromagnetic field is conveniently related to the source current by means of the vector potential. The current is now $\boldsymbol{J}_{\mathrm{ob}}$, which acts as source of the vector potential $\mathfrak{A}^{(\mathrm{s})}$ from which the fields scattered by the target[2] are obtained:

$$\begin{aligned} \boldsymbol{H}^{(\mathrm{s})}(\boldsymbol{r}) &= \nabla \times \mathfrak{A}^{(\mathrm{s})}(\boldsymbol{r}) \; ; \\ \boldsymbol{E}^{(\mathrm{s})}(\boldsymbol{r}) &= \frac{1}{\mathrm{j}\omega\epsilon_0} \nabla \times \nabla \times \mathfrak{A}^{(\mathrm{s})}(\boldsymbol{r}) \; , \end{aligned} \qquad \boldsymbol{r} \ni V' \; . \tag{7.6}$$

[2] As stated, the scattered field is meaningful out of the target body, i.e., for $\boldsymbol{r} \neq \boldsymbol{r}'$.

The vector potential $\mathfrak{A}^{(\mathrm{s})}$ in (7.6) is given by (3.9) in terms of the secondary source current (7.4):

$$\begin{aligned}\mathfrak{A}^{(\mathrm{s})}(\boldsymbol{r}) &= \iiint_{V'} \frac{\mathrm{e}^{-\mathrm{j}\kappa_0(|\boldsymbol{r}-\boldsymbol{r}'|)}}{4\pi(|\boldsymbol{r}-\boldsymbol{r}'|)} \boldsymbol{J}_{\mathrm{ob}}(\boldsymbol{r}')\,\mathrm{d}V' \\ &= \mathrm{j}\omega\epsilon_0 \iiint_{V'} \frac{\mathrm{e}^{-\mathrm{j}\kappa_0(|\boldsymbol{r}-\boldsymbol{r}'|)}}{4\pi(|\boldsymbol{r}-\boldsymbol{r}'|)} [\tilde{\epsilon}_{\mathrm{r}}(\boldsymbol{r}') + \mathrm{j}\tilde{\epsilon}_{\mathrm{j}}(\boldsymbol{r}') - 1]\,\boldsymbol{E}(\boldsymbol{r}')\,\mathrm{d}V' \\ &= \mathrm{j}\omega\epsilon_0 \iiint_{V'} \frac{\mathrm{e}^{-\mathrm{j}\kappa_0(|\boldsymbol{r}-\boldsymbol{r}'|)}}{4\pi(|\boldsymbol{r}-\boldsymbol{r}'|)} [\Delta\epsilon(\boldsymbol{r}')]\,\boldsymbol{E}(\boldsymbol{r}')\,\mathrm{d}V' \,.\end{aligned}$$

In turn, the fields re-radiated in the vacuum by the target at far distance R in direction $\mathbf{r}_0^{(\mathrm{s})}$ are given by (3.31) and (3.32), with the re-radiating current $\boldsymbol{J}_{\mathrm{ob}}$ in place of the primary source current $\boldsymbol{J}_{\mathrm{s}}$:

$$\boldsymbol{H}_{\infty}^{(\mathrm{s})}(\boldsymbol{r}) \simeq -\mathrm{j}\kappa_0 \frac{\mathrm{e}^{-\mathrm{j}\kappa_0 R}}{4\pi R} \iiint_{V'} \mathbf{r}_0^{(\mathrm{s})} \times \boldsymbol{J}_{\mathrm{ob}}(\boldsymbol{r}')\,\mathrm{e}^{\mathrm{j}\kappa_0 \boldsymbol{r}'\cdot\mathbf{r}_0^{(\mathrm{s})}}\,\mathrm{d}V' \,; \tag{7.7}$$

$$\boldsymbol{E}_{\infty}^{(\mathrm{s})}(\boldsymbol{r}) \simeq \mathrm{j}\omega\mu_0 \frac{\mathrm{e}^{-\mathrm{j}\kappa_0 R}}{4\pi R} \iiint_{V'} \mathbf{r}_0^{(\mathrm{s})} \times \left[\mathbf{r}_0^{(\mathrm{s})} \times \boldsymbol{J}_{\mathrm{ob}}(\boldsymbol{r}')\right] \mathrm{e}^{\mathrm{j}\kappa_0 \boldsymbol{r}'\cdot\mathbf{r}_0^{(\mathrm{s})}}\,\mathrm{d}V' \,. \tag{7.8}$$

It is worth pointing out that while $\boldsymbol{J}_{\mathrm{s}}$ is determined by the process of energy conversion (Sect. 1.1.3) taking place in the primary source (e.g., in a radar transmitter), now the secondary-source current density $\boldsymbol{J}_{\mathrm{ob}}$ depends on the field incident on the target and on the dielectric properties of this latter.

In Earth observation, the target is usually located at a distance far from the primary source such that the incident wave is approximately plane, with propagation vector

$$\mathbf{k}^{(\mathrm{i})} \simeq \boldsymbol{\beta}^{(\mathrm{i})} \simeq \kappa_0 \mathbf{r}_0^{(\mathrm{i})} \,.$$

The secondary-source current density $\boldsymbol{J}_{\mathrm{ob}}$, which is a function of the field induced into the object by the incident wave, depends on $\mathbf{r}_0^{(\mathrm{i})}$, i.e., on the direction in which the primary source is located *with respect to the target*. Consequently, the scattered field is a function of both $\mathbf{r}_0^{(\mathrm{i})}$ and $\mathbf{r}_0^{(\mathrm{s})}$. The far electric field is written in the compact form (3.33) as

$$\boldsymbol{E}_{\infty}^{(\mathrm{s})}(\boldsymbol{r}) = \frac{\mathrm{e}^{-\mathrm{j}\kappa_0 R}}{R} \mathcal{F}_0(\mathbf{r}_0^{(\mathrm{i})}, \mathbf{r}_0^{(\mathrm{s})}) \,,$$

where the free-space *scattering function*

$$\mathcal{F}_0(\mathbf{r}_0^{(\mathrm{i})}, \mathbf{r}_0^{(\mathrm{s})}) \equiv \mathcal{F}(\theta^{(\mathrm{i})}, \varphi^{(\mathrm{i})}; \theta^{(\mathrm{s})}, \varphi^{(\mathrm{s})})$$

clearly corresponds to the radiation function (3.35). The angular coordinates $\theta^{(\mathrm{i})}$, $\varphi^{(\mathrm{i})}$ and $\theta^{(\mathrm{s})}$, $\varphi^{(\mathrm{s})}$ identify the incidence and scattering directions respectively.

By expanding the double cross product in (7.8), the scattering function is directly related to the secondary-source current:

$$\mathcal{F}_0(\mathbf{r}_0^{(\mathrm{i})}, \mathbf{r}_0^{(\mathrm{s})}) = \mathrm{j}\omega\mu_0 \iiint_{V'} \left\{ \boldsymbol{J}_{\mathrm{ob}}(\boldsymbol{r}') - \mathbf{r}_0^{(\mathrm{s})} \left[\mathbf{r}_0^{(\mathrm{s})} \cdot \boldsymbol{J}_{\mathrm{ob}}(\boldsymbol{r}') \right] \right\} \mathrm{e}^{\mathrm{j}\kappa_0 \boldsymbol{r}' \cdot \mathbf{r}_0^{(\mathrm{s})}} \, \mathrm{d}V' \,, \tag{7.9}$$

in which the implicit dependence of $\boldsymbol{J}_{\mathrm{ob}}$ on $\mathbf{r}_0^{(\mathrm{i})}$ must be always born in mind.

Formula (7.9) highlights that the scattering function is contributed only by the component of the secondary-source current $\boldsymbol{J}_{\mathrm{ob}}$ perpendicular to the scattering direction, consistently with the result found in Sect. 3.1.4.1 for the far field. Since $\boldsymbol{J}_{\mathrm{ob}}$ is proportional to the internal field[3] $\boldsymbol{E}(\boldsymbol{r}')$, only the component of the latter perpendicular to $\mathbf{r}_0^{(\mathrm{s})}$

$$\boldsymbol{E}_{\perp}(\mathbf{r}_0^{(\mathrm{i})}, \mathbf{r}_0^{(\mathrm{s})}, \boldsymbol{r}') = \boldsymbol{E}(\boldsymbol{r}') - \mathbf{r}_0^{(\mathrm{s})} \left[\mathbf{r}_0^{(\mathrm{s})} \cdot \boldsymbol{E}(\boldsymbol{r}') \right]$$

contributes to scattering in direction $\mathbf{r}_0^{(\mathrm{s})}$. Therefore,

$$\mathcal{F}_0(\mathbf{r}_0^{(\mathrm{i})}, \mathbf{r}_0^{(\mathrm{s})}) = -\frac{\pi}{\lambda_0^2} \iiint_{V'} \boldsymbol{E}_{\perp}(\mathbf{r}_0^{(\mathrm{i})}, \mathbf{r}_0^{(\mathrm{s})}, \boldsymbol{r}') \, \Delta\tilde{\epsilon}(\boldsymbol{r}') \, \mathrm{e}^{\mathrm{j}\kappa_0 \boldsymbol{r}' \cdot \mathbf{r}_0^{(\mathrm{s})}} \, \mathrm{d}V' \,. \tag{7.10}$$

The scattering function $\mathcal{F}_0$ yields amplitude, phase and polarization of the far field scattered in direction $\mathbf{r}_0^{(\mathrm{s})}$ by a body occupying the volume V' hit by a plane wave propagating in direction $\mathbf{r}_0^{(\mathrm{i})}$.

Equation (7.10) provides some first useful hints on the behavior of scattering. The scattered field *tends to* depend inversely on the square of free-space wavelength and directly on the dimension of V'. Therefore, "small" (with respect to λ_0) bodies are expected to scatter less than large ones, and vice-versa. This is a coarse trend which may possibly deviate from the one actually observed. In fact, $\boldsymbol{J}_{\mathrm{ob}}$, which depends both on permittivity and on inner field, has a generally complicated dependence on frequency, because, first, permittivity changes with frequency as seen throughout Chap. 2, and, second, the internal field may also change with frequency. Indeed, this latter affects the spatial variations of the internal field according to the object shape, orientation, dimensions, homogeneity, and permittivity. The determination or even the estimation of the internal field proves difficult in many real cases. In practice, without drastic assumptions, only small scatterers [2, 75] allow simplifications that make the task less arduous.

[3] The materials are assumed dielectrically isotropic.

The field inside a scattering body is proportional[4] to the incident field, albeit with generally different local direction and polarization [24]. Therefore, the internal field at a given point $\boldsymbol{r}'$ is linked to the incident one by the formal relation

$$\boldsymbol{E}(\mathbf{r}_0^{(\mathrm{i})}, \boldsymbol{r}') = \mathbb{Q} \cdot \mathbf{E}_0^{(\mathrm{i})} \ .$$

Tensor $\mathbb{Q}$, with components $Q_{pq}(\mathbf{r}_0^{(\mathrm{i})}, \boldsymbol{r}')$, $p, q = x, y, z$, transforms the incident field $\boldsymbol{E}^{(\mathrm{i})} = E_0^{(\mathrm{i})} \boldsymbol{\epsilon}_0^{(\mathrm{i})}$ into the *local* internal field. In matrix notation, the scattering function is then related to the incident field by[5]

$$\mathcal{F}_0(\mathbf{r}_0^{(\mathrm{i})}, \mathbf{r}_0^{(\mathrm{s})}) = \frac{\pi}{\lambda_0^2} \iiint_{V'} [\mathbf{Q}_\perp] \boldsymbol{E}_0^{(\mathrm{i})} \, \Delta\tilde{\epsilon}(\boldsymbol{r}') \, \mathrm{e}^{\mathrm{j}\kappa_0 \boldsymbol{r}' \cdot \mathbf{r}_0^{(\mathrm{s})}} \, \mathrm{d}V' \ . \tag{7.11}$$

Matrix $[\mathbf{Q}_\perp]$, with elements $Q_{\perp pq}(\mathbf{r}_0^{(\mathrm{i})}, \mathbf{r}_0^{(\mathrm{s})}, \boldsymbol{r}')$, now operates the transformation of the incident field into the internal field component perpendicular to $\mathbf{r}_0^{(\mathrm{s})}$, which is the only component that contributes scattering in that direction. The field scattered at far distance, like the scattering function, is thus formally put into relation with the incident field:

$$\boldsymbol{E}_\infty^{(\mathrm{s})}(\boldsymbol{r}) = \frac{\pi}{\lambda_0^2} \frac{\mathrm{e}^{-\mathrm{j}\kappa_0 R}}{R} \iiint_{V'} [\mathbf{Q}_\perp] \boldsymbol{E}_0^{(\mathrm{i})} \, \Delta\tilde{\epsilon}(\boldsymbol{r}') \, \mathrm{e}^{\mathrm{j}\kappa_0 \boldsymbol{r}' \cdot \mathbf{r}_0^{(\mathrm{s})}} \, \mathrm{d}V' \ . \tag{7.12}$$

Ultimately, the target transforms the vector field $\boldsymbol{E}^{(\mathrm{i})}$ impinging on it into the scattered one[6] $\boldsymbol{E}^{(\mathrm{s})}$. This linear transformation is expressed by the *scattering matrix* $[\mathbf{S}]$:

$$\boldsymbol{E}^{(\mathrm{s})} = \frac{\mathrm{e}^{-\mathrm{j}\kappa_0 R}}{R} [\mathbf{S}] \boldsymbol{E}^{(\mathrm{i})} \ . \tag{7.13}$$

Matrix $[\mathbf{S}]$ is obtained by equating (7.13) to (7.12).

7.1.2.1 Scattering Matrix

For given frequency and orientation with respect to the incidence and scattering directions, the elements of $[\mathbf{S}]$ depend on the volume integral in (7.13), hence on geometric and physical characteristics of the scatterer, including shape, dimensions, and complex permittivity. It means that information on the features of the observed terrestrial environment is contained in the elements of the scattering matrix,

[4] Possible but uncommon nonlinearities are disregarded.

[5] The inessential negative sign is hereinafter disregarded.

[6] The subscript ∞ is dropped from now on.

which are obtainable by measuring the scattered vector field [29, 76]. Different pieces of information useful to the characterization of the scatterer are expected from measurements at different frequencies, field polarizations, and incidence and scattering directions.

By representing scattered and incident fields according to the Jones formalism (4.37) of Sect. 4.2.1, the relation (7.13) becomes

$$\begin{bmatrix} E_{0\mathrm{v}}^{(\mathrm{s})} \\ E_{0\mathrm{h}}^{(\mathrm{s})} \end{bmatrix} = \frac{\mathrm{e}^{-\mathrm{j}\kappa_0 R}}{R} [\mathbf{S}] \begin{bmatrix} E_{0\mathrm{v}}^{(\mathrm{i})} \\ E_{0\mathrm{h}}^{(\mathrm{i})} \end{bmatrix} = \frac{\mathrm{e}^{-\mathrm{j}k_0 R}}{R} \begin{bmatrix} S_{\mathrm{vv}} & S_{\mathrm{vh}} \\ S_{\mathrm{hv}} & S_{\mathrm{hh}} \end{bmatrix} \begin{bmatrix} E_{0\mathrm{v}}^{(\mathrm{i})} \\ E_{0\mathrm{h}}^{(\mathrm{i})} \end{bmatrix} . \tag{7.14}$$

The scattering matrix[7] $[\mathbf{S}]$ relates vertical (as usual denoted by subscript v) and horizontal (denoted by h) components of the scattered field to the ones of the incident field. The elements

$$S_{pq} = S_{pq}(f;\, \theta^{(\mathrm{i})},\, \varphi^{(\mathrm{i})};\, \theta^{(\mathrm{s})},\, \varphi^{(\mathrm{s})};\, \mathfrak{P}), \qquad p, q \equiv \mathrm{v}, \mathrm{h}$$

of $[\mathbf{S}]$ are tightly related to the components of the vector scattering function $\mathcal{F}_0$ given by (7.11), hence they are complex functions of frequency f, of the angles $\theta^{(\mathrm{i})}, \varphi^{(\mathrm{i})}$ of incidence and $\theta^{(\mathrm{s})}, \varphi^{(\mathrm{s})}$ of scattering, and of the morphological and physical parameters of the scattering object, formally dumped into the vector of parameters $\mathfrak{P}$. The elements S_{vv} and S_{hh} link the *co-polar* components of the scattered field to those of the incident one, while S_{vh} and S_{hv} are the *cross-polar* elements. The elements of the scattering matrix are complex: it means that they contain information not only on the amplitudes but also on the phases of the field components. The scattering matrix is thus able to represent the *full polarimetric* scattering behavior of the observed terrestrial environment.

7.1.2.2 Müller Matrix

Section 4.2.2 introduces the Stokes vector (4.40) as a useful tool in representing quasi-monochromatic fields, as are frequently encountered in Earth observation. The scattering process transforming the Stokes vector of the incident field into the scattered one is described by the Müller matrix[8] $[\mathbf{M}]$. With reference to (4.41), the modified Stokes vector of the scattered field, $\boldsymbol{Y}_{\mathrm{m}}^{(\mathrm{s})}$, is related to the incident $\boldsymbol{Y}_{\mathrm{m}}^{(\mathrm{i})}$ by

$$\boldsymbol{Y}_{\mathrm{m}}^{(\mathrm{s})} = \frac{1}{R^2} [\mathbf{M}]\, \boldsymbol{Y}_{\mathrm{m}}^{(\mathrm{i})} . \tag{7.15}$$

[7] The scattering matrix is also frequently named Sinclair matrix [1, 46].

[8] The denomination Kennaugh matrix [47] is also used, especially for backscattering.

Like the scattering matrix, the Müller matrix [**M**] too is able to represent the polarimetric scattering behavior of the object, being its 4×4 real elements M_{ij}, $i,j = 1,\ldots,4$, related to the amplitudes and phases of the components of the vector scattering function (7.11). As in the scattering matrix, the elements M_{ij} depend on the bio-geo-physical and morphological parameters $\mathfrak{P}$ characterizing the observed target, as well as on the remote sensing system parameters and observing geometry.

7.1.3 Scattered Power

Both the scattering and the Müller matrices describe how a given target transforms each component of the incident field into each component of the scattered one. Measuring the elements of the matrices requires sophisticated specifications of the observing system, which has to measure the field coherently (i.e., preserving the phase) on the different polarizations. After all, an amount of information adequate to a first observational approach is contained in the scattered power, which, for instance, leads to mapping the scattering intensity originating from different parts of the observed scenario. If only power is measured, the complexity of the sensor is reduced and the image processing requirements are correspondingly relaxed.

Section 3.1.4.2 shows that at far distance from the scattering source the field consists of two components transverse to the direction $\mathbf{r}_0^{(s)}$ in which scattering is observed. The properties of the wave with such a configuration are fully described by the elements of the coherency matrix introduced in Sect. 1.3.4.2. A particular case of such quadratic quantities is power, which, although deprived of phase knowledge, carries a substantial amount of information on the target.

The wave is scattered into the direction $\mathbf{r}_0^{(s)}$ of the observing platform by the various portions of the terrestrial environment according to the local scattering directional properties. The scattered field reaches the sensor, which captures some of the arriving energy in the way outlined in Sect. 11.2 and transforms it into the *signal*. The signal is then attributed[9] to each discernible element of the observed scenario, the scattering properties of which are typically represented in two dimensions[10] by an *image*. The spatial patterns of several bio-geo-physical properties of the observed terrestrial environments are contained in the scattered power images, acquired either at optical wavelengths or at microwaves.

[9]It is worth calling attention onto the correspondence discussed in Chap. 12 between direction of observation, related to $\mathbf{r}_0^{(s)}$, and location of the scattering source on the Earth's surface.

[10]The third dimension is added by sounding systems having distance discrimination capability (Sect. 11.4.3), possibly also through profile retrieval processing.

7.1.3.1 Transverse Sections

An effective way of characterizing the interaction of the targets with the waves in terms of power is through the *transverse sections*. Three of them deal directly with the scattering process.

- The *bistatic scattering cross-section* $\sigma(\mathbf{r}_0^{(\mathrm{i})}, \mathbf{r}_0^{(\mathrm{s})})$ is defined as the angular power $\mathcal{P}^{(\mathrm{s})}$ scattered by the target normalized to the areic power $\mathcal{P}^{(\mathrm{i})}$ of the incident wave:

$$\sigma(\mathbf{r}_0^{(\mathrm{i})}, \mathbf{r}_0^{(\mathrm{s})}) := 4\pi \, \frac{\mathcal{P}^{(\mathrm{s})}(\mathbf{r}_0^{(\mathrm{i})}, \mathbf{r}_0^{(\mathrm{s})})}{\mathcal{P}^{(\mathrm{i})}(\mathbf{r}_0^{(\mathrm{i})})} \, . \tag{7.16}$$

  The bistatic cross-section σ provides information on how an object spreads into the various directions $\mathbf{r}_0^{(\mathrm{s})}$ the power incident onto it from a given direction $\mathbf{r}_0^{(\mathrm{i})}$.
- The *monostatic* scattering cross-section, or *radar cross-section* $\sigma_{\mathbf{b}}$, is the value of σ for $\mathbf{r}_0^{(\mathrm{s})} = -\mathbf{r}_0^{(\mathrm{i})}$:

$$\sigma_{\mathbf{b}}(\mathbf{r}_0^{(\mathrm{i})}) := \sigma(\mathbf{r}_0^{(\mathrm{i})}, -\mathbf{r}_0^{(\mathrm{i})}) \, . \tag{7.17}$$

  Earth observing radars in monostatic or quasi-monostatic configurations exploit *backscatter*, i.e., scattering only in the backward (or nearly backward) direction.
- The *scattering cross-section* σ_{s} is the power W_{sc} globally scattered by the target, normalized to the incident surface power density $\mathcal{P}^{(\mathrm{i})}$:

$$\sigma_{\mathrm{s}}(\mathbf{r}_0^{(\mathrm{i})}) := \frac{1}{4\pi} \iint\limits_{4\pi} \sigma(\mathbf{r}_0^{(\mathrm{i})}, \mathbf{r}_0^{(\mathrm{s})}) \, \mathrm{d}\Omega = \frac{W_{\mathrm{sc}}}{\mathcal{P}^{(\mathrm{i})}} \, . \tag{7.18}$$

  The scattering cross-section, which depends only on the direction of arrival of the incident wave, is a measure of the global scattering property of the target.

Two further cross-sections are defined, that do not refer uniquely to the scattering process, but take account also of the losses within the object onto which the wave impinges.

- To account for the fraction of incident power that is dissipated inside a lossy target, the *absorption cross-section* σ_{a} is defined as the dissipated power W_{d} given by (2.32) normalized to $\mathcal{P}^{(\mathrm{i})}$:

$$\sigma_{\mathrm{a}}(\mathbf{r}_0^{(\mathrm{i})}) := \frac{W_{\mathrm{d}}}{\mathcal{P}^{(\mathrm{i})}} = \frac{\omega \epsilon_0 \iiint_{V'} \left| \tilde{\epsilon}_{\mathrm{j}} \right| \boldsymbol{E} \cdot \boldsymbol{E}^* \, \mathrm{d}V'}{2\mathcal{P}^{(\mathrm{i})}} \, , \tag{7.19}$$

  where $\boldsymbol{E}$ is the field inside the volume V' of the body. The absorption cross-section expresses the property of the lossy target in transforming part of the arriving electromagnetic energy into heat.

- Both the dissipation process inside the body and its scattering subtract power to the incident wave, the amplitude of which globally lessens past the target.[11] The *extinction cross-section* σ_e is the sum of scattering and absorption cross-sections:

$$\sigma_e(\mathbf{r}_0^{(i)}) := \sigma_s(\mathbf{r}_0^{(i)}) + \sigma_a(\mathbf{r}_0^{(i)}) \,. \tag{7.20}$$

  The extinction cross-section characterizes the effectiveness of a body in subtracting power from a wave incoming from direction $\mathbf{r}_0^{(i)}$. It is a crucial parameter in determining the radiative transfer properties of the terrestrial environments. Details on this important issue are given in Chap. 9.

Finally, a parameter derived from both scattering and extinction is defined.

- The *albedo* $\mathcal{A}$ is the ratio between scattered and extinguished (i.e., scattered plus absorbed) power:

$$\mathcal{A}(\mathbf{r}_0^{(i)}) = \frac{\sigma_s(\mathbf{r}_0^{(i)})}{\sigma_e(\mathbf{r}_0^{(i)})} \,. \tag{7.21}$$

  The albedo provides information on the effectiveness of a body in globally rejecting the power arriving from direction $\mathbf{r}_0^{(i)}$. Among other, $\mathcal{A}$ is a crucial parameter in modeling the Earth's climate dynamics [52, 63, 80].

7.1.3.2 The Backscattering Coefficient

Observation of the Earth by optical or radar sensors is essentially based on the power or on the field that originate from the observed volume of terrestrial material and reach the observing platform. Since the field reaching the sensor depends on the dimensions of the re-radiating target according to (7.12), while the main interest is in the properties of the latter, a quantity independent of the extent of the probed volume is clearly desirable. To this end, with particular reference to radar observations of the earth surface, the *backscattering coefficient* σ^0, defined as the backscattering cross-section $\Delta\sigma_b$ of a given portion of terrestrial environment normalized to the area[12] ΔA of the surface delimiting[13] the observed target, is commonly used:

$$\sigma^0 := \frac{\Delta\sigma_b}{\Delta A} \,. \tag{7.22}$$

The backscattering coefficient is measured in $m^2 \times m^{-2}$ and usually expressed in dB.

[11] Assumed isolated in space.

[12] With the caveat of Sect. 7.4.7.1.

[13] On a suitable reference.

It is worth adding that, when suitable, the previously defined transverse sections can be reduced to corresponding coefficients by normalizing them in a similar way. Other normalized parameters are also defined to get rid of the dependence of the observed quantities on the dimensions of the targets. Reflectivity (8.19) and reflectance in (8.26), linked to the reflection parameters introduced in Chap. 6, are meaningful examples.

7.2 Coherent and Incoherent Scattering

Section 7.1.3 anticipates that the basic signal provided by a remote sensor is function of the areic power $\mathcal{P}^{(\mathrm{s})}$ reaching the observing platform. The details are postponed to Sect. 11.2. Definition (3.37) relates $\mathcal{P}^{(\mathrm{s})}$, hence the acquired signal, to the scattering function $\mathcal{F}_0$ of the target volume V':

$$\mathcal{P}^{(\mathrm{s})}(\mathbf{r}_0^{(\mathrm{s})}) = \frac{1}{2\eta_0}\boldsymbol{E}^{(\mathrm{s})}(\mathbf{r}_0^{(\mathrm{s})}) \cdot \left[\boldsymbol{E}^{(\mathrm{s})}(\mathbf{r}_0^{(\mathrm{s})})\right]^* = \frac{\mathcal{F}_0(\mathbf{r}_0^{(\mathrm{s})}) \cdot \left[\mathcal{F}_0(\mathbf{r}_0^{(\mathrm{s})})\right]^*}{2\eta_0 R^2} \cdot \tag{7.23}$$

The environments observed on Earth are exceedingly varied. They range from man-made or natural surfaces, such as a parking lot or grassland, to individual bodies as isolated trees or buildings, to ensembles of bodies forming dense urban areas, forests, crop canopies, rain cells, aerosol layers. A large variety of scattering properties ensues, which correspondingly demands considerable multiplicity and complexity of models and leads to intricate interpretation processes.

From a basic and general point of view, Earth observation is not concerned as much with *individual* more or less simple targets[14] that are known and can be described exactly, but rather with often compound environments the parameters of which are generally space-time random functions. Just a few suggestive examples:

- a wind-rippled water surface, exhibiting superimposed periodic and random mobile height variations;
- a plot of dry terrain, with surface and subsurface mixtures of compact and granular inhomogeneous mineral materials;
- a parcel of humid soil, the moisture content of which varies in space and changes with time;
- a vegetation canopy, formed by plant elements which are different, randomly distributed, and moved by wind.

[14]This kind of objects is associated with the concept of *permanent* or *persistent* scatterer [15] (cf. Sect. 12.3.3).

A direct consequence of such an intrinsic randomness of the environmental materials is that the permittivity and the internal field are stochastic functions of space and time. The scattered field, which is a deterministic function of random variables, is in turn a random quantity.

Keeping the above considerations in mind, consider the volume V' of a terrestrial material. At a given point $\boldsymbol{r}'$ and at a given time t, the deviation of permittivity $\Delta\tilde{\epsilon}$ acting in the source current (7.4) that originates scattering according to (7.10), is the superposition of two terms:

$$\Delta\tilde{\epsilon} = \overline{\Delta\tilde{\epsilon}} + \Delta\tilde{\epsilon}\,' = \langle\Delta\tilde{\epsilon}\rangle + \Delta\tilde{\epsilon}\,' \,. \tag{7.24}$$

The quantity $\overline{\Delta\tilde{\epsilon}}$ is the deviation of relative permittivity averaged over the ensemble of realizations of the given material, while $\Delta\tilde{\epsilon}\,'$ denotes the zero-mean random deviation from the average value. The scattering-effective (perpendicular to $\mathbf{r}_0^{(\mathrm{s})}$) component of the inner field is composed of two analogous terms[15]:

$$\boldsymbol{E}_\perp = \overline{\boldsymbol{E}_\perp} + \boldsymbol{E}'_\perp \,, \tag{7.25}$$

with the same meaning of notations.

The scattering function (7.10), which, apart from the spherical wave factor, coincides with the scattered far field, depends directly on the statistical properties of the scattering source. For an individual realization of the material in the observed volume V' and for a given direction of incidence $\mathbf{r}_0^{(\mathrm{i})}$, the scattering function[16]

$$\mathcal{F}_0(\mathbf{r}_0^{(\mathrm{s})}) = \frac{\pi}{\lambda_0^2} \iiint_{V'} \left(\overline{\boldsymbol{E}_\perp} + \boldsymbol{E}'_\perp\right) \left(\overline{\Delta\tilde{\epsilon}} + \Delta\tilde{\epsilon}\,'\right) \mathrm{e}^{\mathrm{j}\kappa_0 \boldsymbol{r}'\cdot\mathbf{r}_0^{(\mathrm{s})}} \,\mathrm{d}V' \tag{7.26}$$

is approximated by

$$\begin{aligned}\mathcal{F}_0(\mathbf{r}_0^{(\mathrm{s})}) &\simeq \frac{\pi}{\lambda_0^2} \left[\iiint_{V'} \overline{\boldsymbol{E}_\perp}\,\overline{\Delta\tilde{\epsilon}}\, \mathrm{e}^{\mathrm{j}\kappa_0 \boldsymbol{r}'\cdot\mathbf{r}_0^{(\mathrm{s})}} \,\mathrm{d}V' + \iiint_{V'} \overline{\boldsymbol{E}_\perp}\,\Delta\tilde{\epsilon}\,' \mathrm{e}^{\mathrm{j}\kappa_0 \boldsymbol{r}'\cdot\mathbf{r}_0^{(\mathrm{s})}} \,\mathrm{d}V' \right] \\ &= \mathcal{F}_{0\mathrm{c}} + \mathcal{F}'_0 \,,\end{aligned} \tag{7.27}$$

provided the fluctuations of the inner field are small with respect to its average, as indeed is frequently the case. Within this approximation, the scattering function of the individual volume V' of material is composed of two parts, $\mathcal{F}_{0\mathrm{c}}$ and $\mathcal{F}'_0$:

- The term $\mathcal{F}_{0\mathrm{c}}$ relates to the average values of internal field and permittivity which characterize the given volume of material or the selected ensemble of volumes

[15]Note that $\overline{\boldsymbol{E}_\perp} \neq 0$ when the incident field is deterministic, as it can occur for observing systems employing coherent radars.

[16]The dependence of $\mathcal{F}_0$ and of $\boldsymbol{E}_\perp$ on $\mathbf{r}_0^{(\mathrm{i})}$ is now omitted to lighten the notations.

and, in principle, are known quantities. Amplitude, phase and polarization of the scattered field are as those of a deterministic source (Sect. 3.1.4.1): they derive from the coherent superposition, that is with their respective phases, of the contributions from the elements $\mathrm{d}V'$ of V'. This *deterministic* part is the *coherently diffracted* scattering function, affected by the diffraction phase factor $\exp(\mathrm{j}\kappa_0 \boldsymbol{r}' \cdot \mathbf{r}_0^{(\mathrm{s})})$. At least in principle, $\mathcal{F}_{0\mathrm{c}}$ can be interpreted by referring to suitable models of the average properties of the material originating the scattering.

- The second contribution, $\mathcal{F}_0'$, which is a function of the zero-mean random fluctuations $\Delta\tilde{\epsilon}'$, adds a random component to the scattering function of V'. The value of $\mathcal{F}_0'$ changes from one realization of the scatterer to the other, a single value is meaningless and scattering must be characterized on a statistical basis.

If the dielectric structure of the material of a particular target is exactly known for any image acquisition, as in case of a *stable, simple* man-made or natural structure such as a basic building element or an exposed plain rock, the ensemble reduces to that single member. Then $\Delta\tilde{\epsilon}' = 0$ and $\mathcal{F}_{0\mathrm{c}}$ fully describes the scattering, which becomes a deterministic process. However, the preceding conditions are clearly not satisfied by a majority of terrestrial environments, therefore a statistical approach is in general needed to interpret the features of the scattering images. Since the scattered field has zero average value because of the uniform $0 - 2\pi$ phase distribution (Sect. 1.3.4), the first-order moment is meaningless, hence the observed scattering must be characterized by the second-order moments (1.36) of the field.

Given (7.23), the amount of scattered power captured by the sensor depends on $\mathcal{F}(\theta^{(\mathrm{s})}, \varphi^{(\mathrm{s})})$, the behavior of which is thus crucial for understanding the information content of the images and for retrieving the environmental parameters. Equation (7.27) yields the scattered angular power density, to which the signal is related,

$$\mathcal{P}^{(\mathrm{s})} = \frac{1}{2\eta_0}\left[\left(\mathcal{F}_{0\mathrm{c}} + \mathcal{F}_0'\right)\cdot\left(\mathcal{F}_{0\mathrm{c}}^{*} + \mathcal{F}_0'^{*}\right)\right] = \mathcal{P}_{\mathrm{c}}^{(\mathrm{s})} + \mathcal{P}'^{(\mathrm{s})}\,, \tag{7.28}$$

in terms of

- the coherent component $\mathcal{P}_{\mathrm{c}}^{(\mathrm{s})}$ *diffracted* by the average permittivity structure of the target,
- the random component $\mathcal{P}'^{(\mathrm{s})}$ contributed by the permittivity fluctuations, possibly causing *speckle* [50].

Interpreting optical and radar power images requires understanding how $\mathcal{P}_{\mathrm{c}}^{(\mathrm{s})}$ and $\mathcal{P}'^{(\mathrm{s})}$ relate to the bio-geo-physical and geometric properties of the imaged terrestrial environment. It has to be cautioned that relating the observed scattering features to the properties of the imaged objects is a usually arduous task, because of the difficulties that are encountered in modeling the field inside man-made, and, especially, natural bodies, as well as in evaluating the effect of the generally complicated geometry of the scattering objects.

7.2.1 General Features of Scattering

The severe difficulties that so often hamper understanding the full scattering behavior of the terrestrial environment call for simplifications and assumptions. These are essentially based on the geometric and dielectric properties of the observed objects in relation to the observational parameters. In particular, the crucial quantities are the size of the scatterers, the permittivity of the materials and the wavelength at which the observation is carried out. Note that the effects of geometric and dielectric features of the scatterers and of the sensor parameters are substantially interrelated, what sometimes makes difficult to draw conclusions that are widely applicable.

In the following, some general features of scattering intensity and angular distribution, as well as of polarization characteristics are summarized, in anticipation of some more detailed and specific analysis presented mainly in Chaps. 10 and 14. The discussion is drastically simplified and abridged, with the main purpose of giving a first suggestive albeit coarse idea of the scattering behavior of terrestrial materials and targets more relevant to Earth observation. It should be born in mind that the conclusions that are drawn under the various assumptions have intrinsically limited ranges of validity, even in case of deterministic scattering by simple bodies.

7.2.1.1 Intensity

Intensity of scattering is a complicate function of dimensions, wavelength and permittivity of the target. In fact, the power that is re-radiated in a given direction depends on the internal field according to (7.27). The internal field is subject to *inner interference*, i.e., it derives from the interference among waves multiply reflected and redirected by the inner boundaries and inhomogeneities of the scatterer, as discussed in Chap. 6 (Sect. 6.5, in particular) and in Chap. 5. On its side, the field scattered in a given direction is subject to *outer interference*, i.e., it results from the contributions by the different portions of the target interfering in that direction according to the mechanism described in Sect. 3.1.2.

Inside *small bodies*, for which all dimensions are small with respect to wavelength, the *relative* phases of the inner multiply reflected interfering waves are small everywhere. The internal field has little phase and amplitude spatial variations and tends to be independent of the direction of the incident wave. Therefore, as a reference behavior,

- the power scattered by small objects has a weak dependence on both shape and orientation of the scatterer;
- given (7.28) and (7.27), the scattered power tends to simply depend on λ_0^{-4}: this scattering regime is named *Rayleigh scattering*.

The effect of Rayleigh scattering is well evidenced by the blue color of the clear sky: since the intensity of scattering of the polychromatic sunlight from the "small"

Fig. 7.2 Bistatic ($\mathbf{r}_0^{(s)} \neq -\mathbf{r}_0^{(i)}$) scattering of low-elevation solar light from air molecules (*bluish-grey*) and water particles (*rose*); the dark region denotes high attenuation by the cloud

air molecules increases with decreasing wavelength, the power diffused by the sky in Fig. 7.2 is higher at the lower wavelengths and the color is bluish. Instead, the intensity of the Mie [2, 66] scattering from the ensemble of larger water droplets of the cloud is relatively independent of wavelength,[17] hence the power they diffuse tends to reproduce the spectral characteristics of the light from the Sun. Since this latter is low over the horizon, the radiation incident on the cloud has been depleted of the low-wavelength components by the Rayleigh extinction along the lengthy atmospheric path, so that the scattered light appears reddish. Note that the high extinction (Chap. 7.1.3.1) by the cloud droplets that attenuates the scattered power (Chapter 9) makes the cloud bulk dark.

7.2.1.2 Angular Dependence

Many of the concepts at the basis of the behavior of the scattering intensity can be extended to understand the dependence of the scattered power on the scattering direction. Like the intensity, also the angular dependence of the scattered power is a complicate function of shape, dimensions and permittivity of the target, of its orientation with respect to $\mathbf{r}_0^{(i)}$, and of the polarization and frequency of the incident field. Again, the angular dependence of scattering from bodies the dimensions of which are small with respect to wavelength is relatively simple. In fact, analogously to the inner waves, the relative phases of the field contributions originated by

[17] The statistical distribution of particle dimensions D_i tends to smooth out the resonant behavior of the scattering for $\lambda_0 \simeq D_i$.

Fig. 7.3 Bistatic ($\mathbf{r}_0^{(s)} \neq -\mathbf{r}_0^{(i)}$) scattering of solar light from dust particles

different portions of the small scattering object are close to zero and almost independent of the scattering direction $\mathbf{r}_0^{(s)}$. Therefore, given the quenching of both inner and outer interferences, and apart from polarization effects, the scattering from small objects tends to vary smoothly with the scattering direction. Figure 7.3 shows the bistatic scattering of solar light from dust particles: the *average* intensity appears fairly independent of the angular position of the scattering particles with respect to the observing point.

7.2.1.3 Polarization

The polarization of the scattered field is related to that of the internal field by (7.27). For a given direction of incidence, the polarization of the inner field generally follows that of the incident field, although with some change from point to point. However, since scattering is contributed only by the component $\overline{\boldsymbol{E}_\perp}$ orthogonal to the scattering direction, the polarization of the scattered field is expected to depend on the direction in which scattering is observed. This effect is enhanced in case of low-symmetry bodies, for which the components of tensor $\mathbb{Q}_\perp$ depend considerably on $\mathbf{r}_0^{(s)}$. Section 7.3.4 gives some details on this issue.

It should be considered that the additional combined effects of the geometric and dielectric parameters make usually difficult the detailed interpretation of the polarization features of the field scattered by bodies of general geometry and structure. A way of comprehensively representing the polarization behavior of scattering from complex objects through their polarimetric signatures is outlined in Sect. 14.1.2.1.

7.3 Coherent Scattering

Coherent scattering indicates the scattering from a target of given permittivity structure, with a correspondingly known inner field.

The scattering features represented by the coherent (*deterministic*) components in (7.28) are in some instances fairly representative of the real individual environments and terrestrial materials being observed. In other cases, a deterministic body is able to represent the *average* properties of an ensemble of individual scatterers. Therefore, its behavior provides significant information on the typical scattering behavior that can be expected from a member of the ensemble, and is often regarded as a quite useful reference for interpreting scattering images.

In the following outline of coherent scattering, the deterministic targets are assumed to be characterized by their average permittivity $\overline{\epsilon}$, with the corresponding scattering-effective internal field $\overline{\boldsymbol{E}_\perp}$. As said, the complexity of actual structures and the basic intricacy of the mathematical formalism call for drastically simplified representations of the reality.

7.3.1 Scattering from Plane Homogeneous Targets

A frequently encountered class of scatterers is modeled by *large* objects having locally *smooth* boundaries and composed of lossy materials with *weak* dielectric inhomogeneities. The transverse dimensions large with respect to the wavelength of the incident field and the air-matter interface which differs from a plane by a quantity small with respect to the wavelength[18] suggest a plane parallel structure. The object is thus modeled as the lossy homogeneous parallelepiped plate sketched in Fig. 7.4. Its $a \times b$ upper rectangular boundary lies in the $(x'\, y')$ transverse plane and its thickness d is measured along the longitudinal coordinate z'. Within the range of validity of the model, the field entering the object is a plane wave having the approximate general form (6.24). When the thickness is large *with respect to the penetration depth* defined in Sect. 6.3.1, i.e., $d \gg \ell$, multiple reflections involving the lower boundary are negligible, as noted in Sect. 6.1.2.1. Therefore, the inner field behaves locally like the single wave refracted through the planar air-material interface and traveling downward in the weakly inhomogeneous material. The expression (5.35) of the field, assumed to be scarcely affected by ray bending, is further simplified into

$$\overline{\boldsymbol{E}} \simeq \overline{\boldsymbol{E}_0}\, \mathrm{e}^{-a(z')} \mathrm{e}^{-\mathrm{j}\kappa_0[\phi_\mathrm{t}(x',y') + \phi_\mathrm{z}(z')]}\,, \tag{7.29}$$

[18] A quantitative approach to this issue is summarized in Sect. 13.1.1.1.

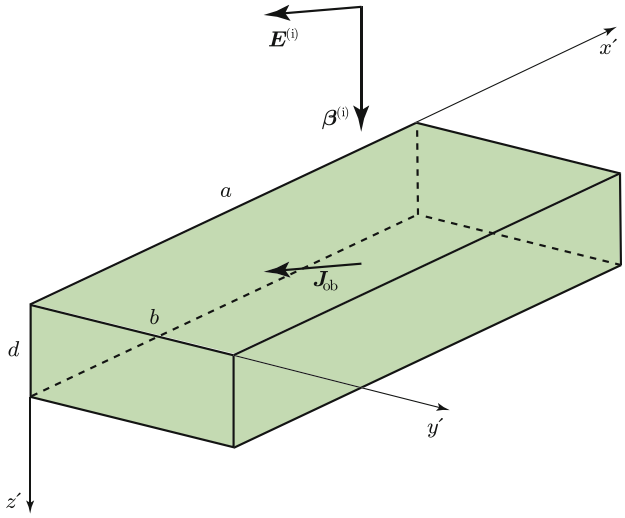

Fig. 7.4 Dielectric parallelepiped into which the normally incident plane wave induces the secondary current density $\boldsymbol{J}_{ob}$ that originates scattering

by assuming the specific attenuation (5.39) independent of the transverse position (x', y'), so that the *electromagnetic thickness*[19] a, which conveys the attenuation undergone by the wave, is a function only of depth z'. Note the factorization of the eikonal function in (7.29) into its *lateral* factor $\phi_t(x', y')$ and *longitudinal* factor $\phi_z(z')$. It is understood that a and ϕ are relative to the average scatterer at hand.

7.3.1.1 Coherently Scattered Field

The first feature of interest is the scattering intensity and how it relates to the dielectric properties of the material and to the dimension of the scatterer.

To arrive at a particularly simple expression of the coherently scattered field, a further simplification considers the incident wave impinging normally on the boundary of the parallelepiped of quasi-homogeneous material, so that the inner field (7.29) is a plane wave propagating along z'. The incident field is assumed linearly polarized, as sketched in Fig. 7.4. The field is re-radiated by the average secondary-source current (7.4)

[19]The radiative transfer incoherent approach of Sect. 9.2.2 leads to the introduction of a closely related parameter.

$$\overline{J_{\mathrm{ob}}} \simeq \mathrm{j}\omega\epsilon_0 \left(\overline{\tilde{\epsilon}} - 1\right) t_{\mathrm{E}}\, E_0\, \mathrm{e}^{-\mathrm{j}\beta' z'} ,$$

which is linked to the incident field E_0 by the air-to-material transmission coefficient t_{E}, defined in Sect. 6.1.1, for the average permittivity of the scatterer. Analogously, the phase constant β' of the wave penetrating the body refers to the average $\overline{\tilde{\epsilon}}$. The field backscattered coherently by the parallelepiped of transverse section $a \times b$ is then obtained by the first term of (7.27) as

$$E_{\mathrm{c}}^{(\mathrm{s})} \simeq -2\omega^2\mu_0\epsilon_0 \left(\sqrt{\overline{\tilde{\epsilon}}} - 1\right) E_0 \frac{\mathrm{e}^{-\mathrm{j}\kappa_0 R}}{4\pi R} \frac{a\,b}{\mathrm{j}(\beta' + \kappa_0)} ,$$

which is readily expressed through the air-matter reflection coefficient (6.8):

$$E^{(\mathrm{s})} \simeq -\mathrm{j}\frac{a\,b}{\lambda_0} \frac{\mathrm{e}^{-\mathrm{j}\kappa_0 R}}{4\pi R} q_{\mathrm{E}}\, E_0 \cdot \tag{7.30}$$

Equation (7.30) indicates that the field backscattered by a *large and thick* plate of lossy quasi-homogeneous material is proportional to the *reflection coefficient* q_{E} of the air-plate interface. Indeed, the assumption of quasi-homogeneity of the material, with an inner field coincident with the downward wave (7.29), restricts the origin of scattering to the air-material interface: this mechanism is named *surface scattering* (cf. Sect. 7.4.7). The factor $(a\,b)/\lambda_0$ points out that objects with nearly plane surfaces the dimensions of which are large with respect to the wavelength scatter with quite high intensity. This is typically the case of the building walls that often behave as smooth surfaces at microwaves, as outlined in Sect. 6.6.1.

The polarization of the scattered field is clearly the same as that of the incident wave for the considered case of normal incidence.

The previous result can be extended to oblique incidence, for which the dependence of the reflection coefficients on polarization seen in Sect. 6.2.2 has clearly to be taken into account. It is worth again emphasizing the crucial role that reflection plays in scattering from large targets.

7.3.1.2 Angular Dependence of Coherent Scattering

A main feature of the dependence of the scattered field on the direction $\mathbf{r}_0^{(\mathrm{s})}$ in which it is observed, derives from the properties of the exponential functions in the first term of (7.27).

To this end, the propagation vector of the incident plane wave is split into its components, tangential, $\boldsymbol{\beta}_{\mathrm{t}}^{(\mathrm{i})}$, and normal, $\boldsymbol{\beta}_{\mathrm{z}}^{(\mathrm{i})}$, to the locally plane air-material boundary,[20] consistently with the general eikonal in (7.29):

[20] Tangential and normal may respectively correspond to lateral and longitudinal in the general case.

$$\boldsymbol{\beta}^{(\mathrm{i})} = \kappa_0 \, \mathbf{r}_0^{(\mathrm{i})} = \boldsymbol{\beta}_{\mathrm{t}}^{(\mathrm{i})} + \boldsymbol{\beta}_{\mathrm{z}}^{(\mathrm{i})} = \kappa_0 (\mathbf{r}_{0\mathrm{t}}^{(\mathrm{i})} + \mathbf{r}_{0\mathrm{z}}^{(\mathrm{i})}) \; .$$

The continuity of incident and refracted field on the boundary, resulting in the equality (6.13) of the tangential components of the respective propagation vectors, yields a scattering-effective average internal field of the form

$$\overline{\boldsymbol{E}_\perp}(\boldsymbol{r}\,') \simeq \overline{\boldsymbol{E}_\perp}(z') \, \mathrm{e}^{-\mathrm{j}\kappa_0 \mathbf{r}_{0\mathrm{t}}^{(\mathrm{i})} \cdot \boldsymbol{r}\,'} \; , \tag{7.31}$$

where $\overline{\boldsymbol{E}_\perp}(z')$ takes into account the variation with depth of both amplitude and phase of the inner field. By analogously splitting the propagation vector of the scattered field,

$$\boldsymbol{\beta}^{(\mathrm{s})} = \kappa_0 \big(\mathbf{r}_{0\mathrm{t}}^{(\mathrm{s})} + \mathbf{r}_{0\mathrm{z}}^{(\mathrm{s})} \big) \; ,$$

the coherent component $\mathcal{F}_{0c}$ of the scattering function is given by

$$\mathcal{F}_{0\mathrm{c}} \simeq \frac{\pi}{\lambda_0^2} \int_0^d \overline{\boldsymbol{E}_\perp} \, \overline{\Delta\epsilon} \, \mathrm{e}^{\mathrm{j}\kappa_0 r_{0\mathrm{z}}^{(\mathrm{s})} z'} \, \mathrm{d}z' \iint_{S'} \mathrm{e}^{-\mathrm{j}\kappa_0 (\mathbf{r}_{0\mathrm{t}}^{(\mathrm{i})} - \mathbf{r}_{0\mathrm{t}}^{(\mathrm{s})}) \cdot \boldsymbol{r}\,'} \, \mathrm{d}x' \, \mathrm{d}y' \; , \tag{7.32}$$

where S' is the approximately plane surface of the body and d its thickness. The surface integral in (7.32) peaks for $\mathbf{r}_{0\mathrm{t}}^{(\mathrm{s})} = \mathbf{r}_{0\mathrm{t}}^{(\mathrm{i})}$, independently of the possible variation of permittivity with depth. This property indicates that the coherent scattering has two maxima in the directions shown in Fig. 7.5 by the propagation vectors $\boldsymbol{\beta}_{\mathrm{s}}^{(\mathrm{s})}$ and $\boldsymbol{\beta}_{\mathrm{f}}^{(\mathrm{s})}$:

- one in the *specular* direction

$$\mathbf{r}_{0\mathrm{s}}^{(\mathrm{s})} = \mathbf{r}_{0\mathrm{t}}^{(\mathrm{i})} - \mathbf{r}_{0\mathrm{z}}^{(\mathrm{i})} \, \mathbf{z}_0$$

- and the other in the *forward* direction

$$\mathbf{r}_{0\mathrm{f}}^{(\mathrm{s})} = \mathbf{r}_{0\mathrm{t}}^{(\mathrm{i})} + \mathbf{r}_{0\mathrm{z}}^{(\mathrm{i})} \, \mathbf{z}_0 \; .$$

Only the specular (or, in general, the *backward*) scattering from a target on the Earth's surface is directly measured by a sensor on airborne or space platforms, while the forward scattering produces *shadowing* [72] past the object. As observed for the case of normal incidence, the scattering intensity in the specular direction attains quite high values when the dimensions of the surface S' are large with respect to the wavelength λ_0.

The dependence of $\mathcal{F}_{0\mathrm{c}}$ on the scattering direction is essentially determined by shape and dimensions of S', which strongly affect the surface integral in (7.32). The possible change of the scattering-effective component $\overline{\boldsymbol{E}_\perp}$ of the inner field, which, being perpendicular to the scattering direction depends geometrically on this latter, also contributes an angular dependence. However, as discussed in Sect. 11.3.1,

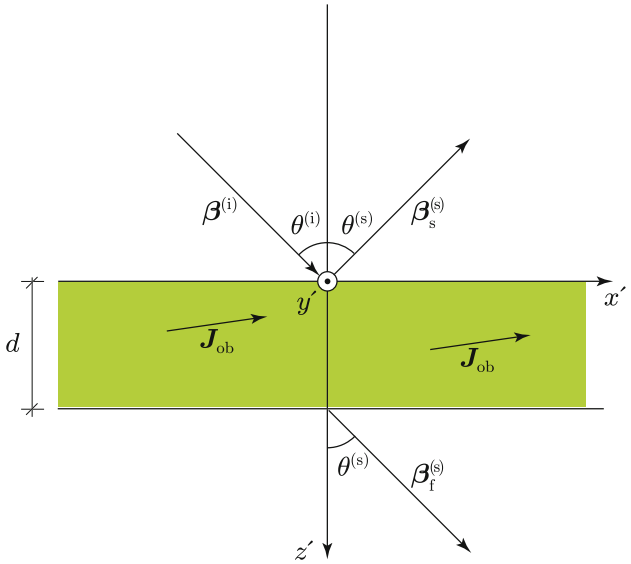

Fig. 7.5 Intensity of scattering from a slab has maxima in the specular and forward directions, for which $\theta^{(\mathrm{s})} = \theta^{(\mathrm{i})}$

this geometric effect turns out relatively smooth for the large nearly plane objects considered here. A further moderate variation with the scattering angle is expected when permittivity changes with depth, because of the ray bending considered in Sect. 5.2.

Note that the change of the complex vector $\overline{\boldsymbol{E}_{\perp}}$, hence of the source current $\boldsymbol{J}_{\mathrm{ob}}$ with $\mathbf{r}_{0\mathrm{s}}^{(\mathrm{s})}$ clearly affects the polarization of the scattered field. For instance, in the case of scattering in the vertical plane to which Fig. 7.6 refers, the scattering-effective component $\boldsymbol{J}_{\mathrm{ob}\perp}$ of the vertical source current $\boldsymbol{J}_{\mathrm{obv}}$ varies with the scattering angle $\theta^{(\mathrm{s})}$, whereas the horizontal component, which remains perpendicular to any $\mathbf{r}_0^{(\mathrm{s})}$, is left unchanged.

7.3.2 *Scattering from Curved Homogeneous Targets*

It is intuitive that a curved surface with "large" radius of curvature can be approximated by an envelope of locally tangent planes.[21] The validity of this approach to scattering, leading to the **P**hysical **O**ptics (PO) approximation, is subordinated to the admissible phase difference that is introduced by replacing the actual curved surface

[21] Section 13.1.1.2 elaborates on this concept.

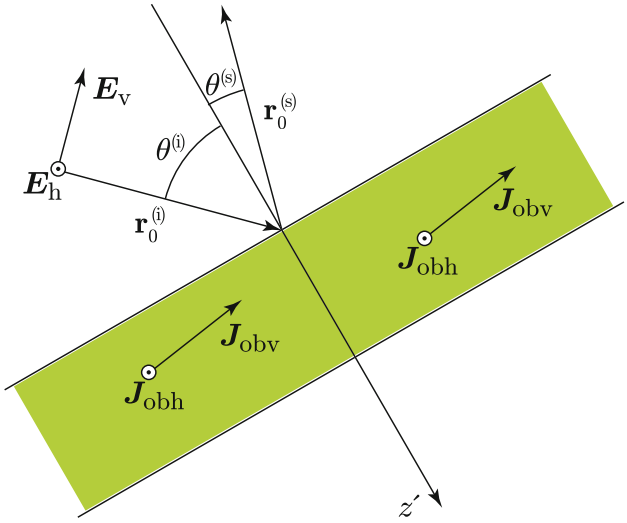

Fig. 7.6 The scattering-effective component of the vertically polarized secondary current $\boldsymbol{J}_{\text{obv}}$ varies with $\theta^{(s)}$, whereas the horizontal one remains unchanged

with the tangent plane. Since the phase depends inversely on wavelength, the plane approximation holds provided the local radius of curvature ϱ of the air-material interface is *large with respect to the wavelength* λ_0 of the wave. A degradation of the PO approximation is clearly expected as the actual surface departs from a flat one.[22] Based on the result of Sect. 7.3.3, such a model allows interpretation of scattering from quasi-homogeneous bodies with non-planar contours according to the behavior of the local reflection coefficient. In particular, the approach yields useful information on the scattered field especially in the neighborhood of the specular direction, around which the re-radiation is concentrated. Given (7.32), "bright" high-scattering areas are identified on the curved boundary of the body where the elementary contributions to the surface integral interfere constructively, with almost the same phase, so that the scattering function peaks. These highly reflecting areas are centered on the *flash points* [32], around which specific local portions of the object surface contribute most of scattering in a given direction. Figure 7.7 shows a suggestive early representation of bistatic flash points at optical wavelengths. As the integration elements in (7.32) depart from a flash point, the exponent in the surface scattering integral changes, thus introducing contributions with varying phases, as discussed in Sect. 3.1.2. The value of the integral lowers with increasing distance of the area element from the flash point because of intervening destructive interference. The phase variations enhance with decreasing wavelength

[22] Some approximate approaches to surface scattering are mentioned in Sect. 13.1.1.2.1, where the range of validity of the approximations is also outlined.

Fig. 7.7 Flash points seen by Caravaggio at the end of the sixteenth century. Note that the daylight radiation of the flash points is not colored (cf. Sect. 10.3.2). Pinacoteca Ambrosiana, Milano, Italy

and, correspondingly for a given frequency, the more curved the surface, the smaller is the area contributing elementary fields with almost the same phase. Since for scattering in the backward direction the local normal to the surface in a flash point is parallel to the direction of incidence, no appreciable depolarization[23] occurs in backscattering from this kind of targets.

Interpreting coherent scattering from real targets requires identification and modeling of their large-scale shape. Reference is usually made to canonical geometries, for which the relevant features of scattering are known [3, 56]: cylinders, cones, spheroids, dihedrons, trihedrons are commonly considered. Figure 7.8 strives to suggest the variety of man-made large geometric structures with which Earth observation deals. On their side, the larger elements of natural vegetation are essentially the cylindrical tree boles shown in Fig. 7.9. However, although a tree trunk is coarsely regarded as a cylinder at the lower microwave frequencies, often its surface is not smooth, being the bark shaped quite irregularly, as Fig. 7.10 suggests.

[23]Care must be exerted in identifying the horizontal and vertical field components and the angle of incidence, since they refer to the *local* tangent plane, which varies from point to point on the target's surface.

Fig. 7.8 Plane, cylindrical, conical and spheroidal large-scale shapes are often identified in man-made objects. *Top*: Delos (Greece), *left*, and Carcassonne (France), *right*; *bottom*: Trani (Italy), *left*, and Roma (Italy), *right*

Fig. 7.9 The cylindrical shape characterizes the large vegetation elements

Fig. 7.10 Many tree trunks, both of broad leaf (*left*) and conifer (*right*) trees, look like large cylinders with rough surface

7.3.3 Coherent Scattering from Rough Targets

Natural objects and man-made structures have almost always[24] *rough* surfaces. Figure 7.11 shows examples of the boundaries of natural materials such as water, snow, or terrain, and of a man-made object like a daubed wall. The boundary of a material is the ensemble of points where the permittivity jumps from the value ϵ_0 it has in the air to that $\epsilon_\mathrm{b} = \epsilon_0 \tilde{\epsilon}_\mathrm{b}$ of the material.[25] The jump occurs in correspondence of the height z' with respect to a reference plane. "Rough" means that the height is a random function $z' = \mathfrak{z}(x', y')$ of the *horizontal* coordinates x', y' (Fig. 7.12a). Given its stochastic character, an individual function $\tilde{\epsilon}(x', y')$ has little value in characterizing the boundary, since $\tilde{\epsilon}(x', y')$ changes randomly with the horizontal coordinates from one sample to another of the ensemble of surfaces. Rather, moments [57, Chap. 4], such as the average $\langle \tilde{\epsilon}(x', y') \rangle$, are suitable. By

[24] Roughness is understood relative to wavelength, as clarified hereinafter.

[25] The material is now assumed lossless to avoid unessential formal complexity.

Fig. 7.11 Water body (*top left*), snow cover (*top right*), terrain (*bottom left*) and daubed wall (*bottom right*) are examples of natural and man-made rough surfaces

averaging over the ensemble of rough surface realizations,[26] the permittivity is expected to increase continuously from ϵ_0 in the air to $\epsilon_0\tilde{\epsilon}_\mathrm{b}$ in the bulk material. The basic way of describing the variation is through a linear dependence of $\langle\epsilon(z')\rangle$ on the height z' with respect to the reference $(x'y')$-plane.

The individual object is regarded as a homogeneous half-space of material having bulk permittivity ϵ_b with rough boundary, while the average ensemble of air-objects assemblies is modeled as sketched in Fig. 7.12b: two homogeneous half-spaces are interfaced through a locally plane transition region of thickness d across which the average permittivity $\langle\epsilon(z')\rangle$ varies linearly with z' from ϵ_0 to $\epsilon_0\,\tilde{\epsilon}_\mathrm{b}$, that is, according to

$$\left\langle\tilde{\epsilon}_\mathrm{r}(z')\right\rangle = \frac{1+\tilde{\epsilon}_\mathrm{b}}{2} + \triangle_\epsilon\, z' \qquad \text{for} \quad -\frac{d}{2} \le z' \le \frac{d}{2}\,. \tag{7.33}$$

In Eq. (7.33),

$$\triangle_\epsilon := \frac{\tilde{\epsilon}_\mathrm{b} - 1}{d}$$

[26] In practice, the average can be frequently carried out over a portion of the surface large enough to satisfy spatial ergodicity [57, Chap. 4].

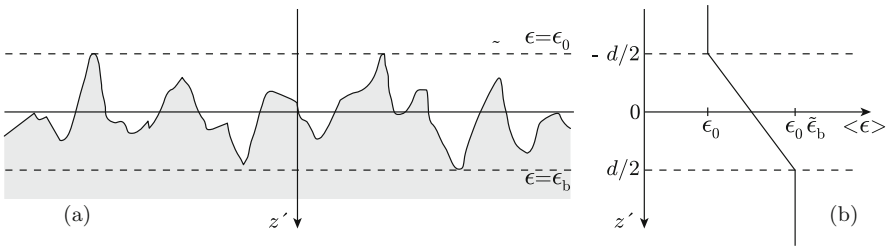

Fig. 7.12 Profile of a rough surface, (**a**), and linear model of the variation of average permittivity $\langle\epsilon\rangle$ with height z', (**b**); the thickness of the transition layer from air ($\epsilon = \epsilon_0$) to bulk matter ($\epsilon = \epsilon_0\,\tilde{\epsilon}_\mathrm{b}$) is d

measures the gradient of the average relative permittivity. For a given material, the gradient increases with decreasing roughness, $\langle\epsilon(z')\rangle$ tending to a step function when the surface is smooth.

For horizontal polarization, the reflection coefficient of such a structure is known [74, Chap. 2] to depend on $\tilde{\epsilon}_\mathrm{b}$ and incidence angle θ according to

$$q_\mathrm{h}(\theta) \simeq \frac{-\triangle_\epsilon}{\mathrm{j}8\kappa_0 \cos^3\theta} = \mathrm{j}\frac{\tilde{\epsilon}_\mathrm{b} - 1}{16\pi\,\cos^3\theta}\,\frac{\lambda_0}{d}\,, \tag{7.34}$$

provided the thickness d of the transition region is large[27] with respect to λ_0. Equation (7.34) indicates that $q_\mathrm{h} \to 0$ when $\lambda_0/d \to 0$: this result implies that the coherent component of scattering from a rough surface decreases as roughness, represented in this case by the thickness d, increases with respect to λ_0. Therefore, for given roughness, the coherent component decreases with increasing frequency: coherent scattering is not present in the optical observations of a large majority of natural (with the exception of calm water) and man-made (with the exceptions of *polished* glass, plastic and metal) surfaces. At microwaves, the coherent component increases with decreasing frequency, hence, for instance, it is expected to be higher at L-band than at X-band, apart from the effect of the permittivity changes.

The reflection coefficient at vertical polarization, which is hard to obtain in closed form [4], is expected to be lower [77] than the one at horizontal polarization, consistently with the results of Sect. 6.2.2.

[27] The constraint clearly rules out the applicability of (7.34) to perfectly smooth surfaces.

7.3.4 Scattering from Small Bodies

Section 7.2.1 remarks that the dimensions of a target with respect to wavelength play a crucial role in determining the scattering behavior. The intensity of scattering from large bodies is strongly affected by the local reflection coefficient, i.e., by the reflecting properties of the almost plane area about the point that originates re-radiation in the specular direction. This concept becomes clearly meaningless when the scatterers are small, because the scattered field is originated globally by the whole body and is contributed by the various parts of the latter with almost the same relative phase, as outlined in Sects. 7.2.1.1 and 7.2.1.2.

Consider a reference scatterer characterized by the ensemble averages $\overline{\mathbb{Q}_\perp}$ and $\overline{\mathbb{Q}}$ of the respective field transformation tensors introduced in Sect. 7.1.2. When the dimensions are small with respect to the wavelength in vacuo, the exponential in the first scattering integral of (7.27) tends to one because $\kappa_0 r'_{\max} \ll 1$, thus denoting absence of outer interference. In this case the scattering function[28] has the simplified expression

$$\mathcal{F}_{0\mathrm{C}}(\mathbf{r}_0^{(\mathrm{i})}, \mathbf{r}_0^{(\mathrm{s})}) \simeq \frac{\pi}{\lambda_0^2} \iiint_{V'} \overline{\mathbb{Q}_\perp} \cdot \boldsymbol{E}_0^{(\mathrm{i})}\, \Delta\tilde{\epsilon}(\boldsymbol{r}')\, \mathrm{d}V' = \frac{\pi}{\lambda_0^2}\, \mathbf{r}_0^{(\mathrm{s})} \times \left[\mathbf{r}_0^{(\mathrm{s})} \times \iiint_{V'} \overline{\mathbb{Q}} \cdot \boldsymbol{E}_0^{(\mathrm{i})}\, \Delta\tilde{\epsilon}(\boldsymbol{r}')\, \mathrm{d}V'\right] . \tag{7.35}$$

When the material of the body has low losses and, as it occurs especially at microwaves, is weakly inhomogeneous with dimensions small also with respect to the inner wavelength, $\overline{\mathbb{Q}_\perp}$ is almost independent of the location $\boldsymbol{r}'$ inside the scatterer. Then the scattering function can be directly related to amplitude and polarization of the incident field by

$$\mathcal{F}_{0\mathrm{C}}(\mathbf{r}_0^{(\mathrm{i})}, \mathbf{r}_0^{(\mathrm{s})}) \simeq \frac{\pi}{\lambda_0^2}\, E_0^{(\mathrm{i})}\, \mathbf{r}_0^{(\mathrm{s})} \times \left[\mathbf{r}_0^{(\mathrm{s})} \times \overline{\mathbb{P}} \cdot \mathbf{e}_0^{(\mathrm{i})}\right] V' ,$$

where the average effective *polarizability tensor* $\overline{\mathbb{P}}$ that globally characterizes the scatterer is defined by

$$\overline{\mathbb{P}} := \Delta\tilde{\epsilon}\, \overline{\mathbb{Q}} . \tag{7.36}$$

The introduction of the polarizability tensor allows amplitude and polarization of the field scattered by small bodies to be directly related to amplitude and polarization of the incident field:

$$E^{(\mathrm{s})}\mathbf{e}_0^{(\mathrm{s})} = \frac{\pi}{\lambda_0^2} \frac{\mathrm{e}^{-\mathrm{j}\kappa_0 R}}{R}\, \mathbf{r}_0^{(\mathrm{s})} \times \left[\mathbf{r}_0^{(\mathrm{s})} \times [\overline{\mathbf{P}}]\mathbf{e}_0^{(\mathrm{i})}\right] E_0^{(\mathrm{i})} V' . \tag{7.37}$$

[28] The scattering function is regarded as $\mathcal{F}_{0\mathrm{C}}$ because it is relative to the average scatterer.

Fig. 7.13 Prolate and oblate spheroids model common fruit geometry

The elements of matrix $\left[\overline{\mathbf{P}}\right]$ depend on the permittivity of the scattering object, on the frequency and on shape and orientation of the body with respect to the direction of incidence. Matrix $\left[\overline{\mathbf{P}}\right]$ transforms the polarization of the incident field expressed by $\boldsymbol{\epsilon}_0^{(\mathrm{i})}$ into the polarization of the inner field. Then the double cross product with $\mathbf{r}_0^{(\mathrm{s})}$ in (7.37) yields the polarization of the scattered field. The intensity of scattering in a given direction depends on frequency through the combined effect of both $\overline{\mathbb{P}}$ and λ_0^{-2}.

The structure of the polarizability tensor[29] is essentially determined by the shape of the scatterer: symmetrical lossless bodies have real diagonal $[\mathbf{P}]$. Among this class of scatterers, the spheroidal geometry is known to allow analytical models [13] that can be used to obtain the components of the tensor. Spheroids are particularly interesting because they approximate the shape of fairly common botanical fruits (including culinary vegetables), as Fig. 7.13 suggests, as well as of hydrometeors [49]. But, more important, spheroids with extreme aspect ratios [43, Chap. 10] are suitable to represent several types of scatterers often encountered in the terrestrial

[29]The scattering bodies are considered deterministic for now; therefore, in the following, the notation omits the overline.

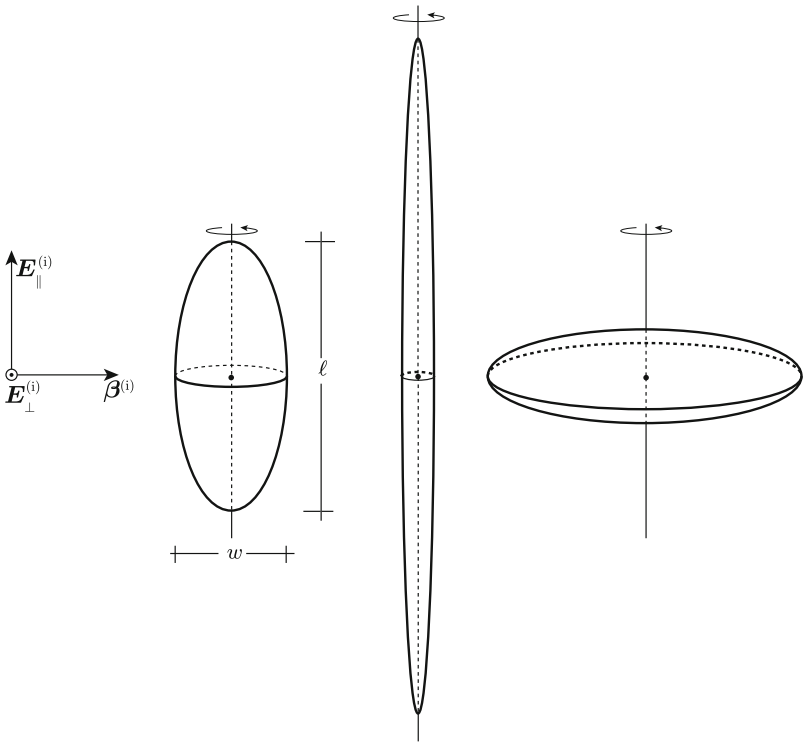

Fig. 7.14 Generic spheroid (*left*) of length ℓ and width w, rods or needles (*middle*), and disks (*right*) are reference shapes quite useful to interpret scattering from vegetation and hydrometeors

environment. In fact, consider the spheroids having length (i.e., the dimension along the axis) ℓ and width (orthogonal to the axis) w, sketched in Fig. 7.14:

- length-to-width ratio $\ell/w \to \infty$, limiting case of the long thin ellipsoid shown in the middle of Fig. 7.14, approximates a *rod* or a *needle*, a shape suitable to model scattering bodies such as single ice crystals and elongated elements of plants as thin branches, twigs, or needle-shaped leaves;
- the condition $\ell/w \approx 1$ yields an approximately spherical shape, such as water drops, hailstones, round fruits;
- on the other side, $\ell/w \to 0$, limiting case of the short wide ellipsoid shown on the right of Fig. 7.14 yields a disk, a shape quite useful to represent planar leaves.

Given the symmetry, only two independent elements characterize the polarizability matrix $[\mathbf{P}]$ of a spheroid, i.e., $P_{\parallel}$, relative to the electric field component along the symmetry axis and $P_{\perp}$, for the orthogonal component.

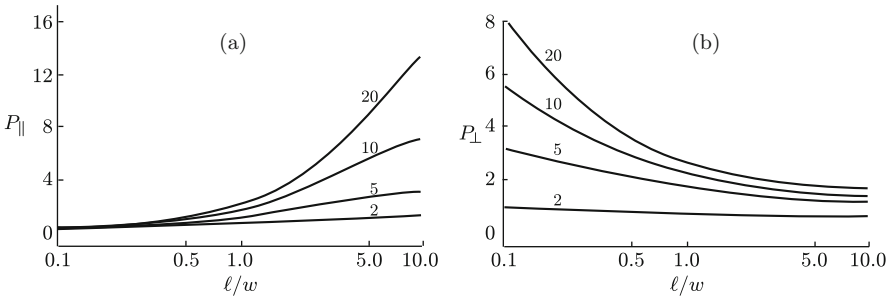

Fig. 7.15 Components $P_\parallel$, (**a**), and $P_\perp$, (**b**), of the polarizability tensor of a lossless spheroid vs. length-to-width ratio ℓ/w for different values of $\tilde{\epsilon}$ between 2 and 20 (Curves interpolate data from [73])

The geometry of the incident wave, with its electric field components parallel $\boldsymbol{E}_\parallel^{(\mathrm{i})}$ and perpendicular $\boldsymbol{E}_\perp^{(\mathrm{i})}$ to the axis of the spheroid is also shown in Fig. 7.14. The electric field induced inside the spheroidal body has a component along its axis which is proportional to the element $P_\parallel$, while the component perpendicular to the axis is correspondingly proportional to $P_\perp$. When the body is not spherical, clearly $P_\parallel \neq P_\perp$, hence the polarization or the orientation of the inner field generally differ from those of the incident wave, according to the relative values of the components of the polarizability tensor. Figure 7.15a, b show $P_\parallel$ and $P_\perp$ as functions of the length-to-width ratio ℓ/w. The curves in Fig. 7.15a indicate that the inner field component along the symmetry axis is low in a flat spheroid for which the ratio $\ell/w \ll 1$ and increases with increasing ratio. The inner field component orthogonal to the axis is correspondingly high for such a plate and shows the opposite trend with ℓ/w shown by Fig. 7.15b. By decomposing a linearly polarized incident field $\boldsymbol{E}_0^{(\mathrm{i})}$ in its components $\boldsymbol{E}_\parallel^{(\mathrm{i})} = E_0^{(\mathrm{i})}\boldsymbol{e}_{0\parallel}$ and $\boldsymbol{E}_\perp^{(\mathrm{i})} = E_0^{(\mathrm{i})}\boldsymbol{e}_{0\perp}$, the internal field $\boldsymbol{E}$ is given by

$$\boldsymbol{E} = \mathbb{P}\cdot\boldsymbol{E}_0^{(\mathrm{i})} = E_0^{(\mathrm{i})}\,\mathbb{P}\cdot(\boldsymbol{e}_{0\perp}+\boldsymbol{e}_{0\parallel}) = E_0^{(\mathrm{i})}\,(P_\perp\boldsymbol{e}_{0\perp}+P_\parallel\,\boldsymbol{e}_{0\parallel})\ . \tag{7.38}$$

Equation (7.38) indicates that the inner field is polarized like the incident one when $P_\perp \approx P_\parallel$, which occurs in small scatterers of approximately spherical shape, whereas

- in disk-like scatterers, being $P_\perp > P_\parallel$, the internal electric field tends to lay in the plane of the plate;
- in a rod or needle, $P_\perp < P_\parallel$ and the internal field tends to be oriented longwise.

In both cases, the vector features of the scattering source, hence of the scattered field, generally differ from those of the incident wave. Expressions of the polarizability tensor components in terms of the relative permittivity are available for spheres and for the limiting cases of disks and rods. Table 7.1 reports the corresponding expressions.

Table 7.1 Parallel, $P_{\parallel}$, and perpendicular, $P_{\perp}$, elements of polarizability matrix vs. $\tilde{\epsilon}$ for disk, sphere and rod [73]

Shape/element	$P_{\parallel}$	$P_{\perp}$
Disk	$\frac{\tilde{\epsilon}-1}{\tilde{\epsilon}}$	$\tilde{\epsilon}-1$
Sphere	$3\frac{\tilde{\epsilon}-1}{\tilde{\epsilon}+2}$	$3\frac{\tilde{\epsilon}-1}{\tilde{\epsilon}+2}$
Rod	$\tilde{\epsilon}-1$	$2\frac{\tilde{\epsilon}-1}{\tilde{\epsilon}+1}$

The effect of the above inner field features on the intensity and polarization of scattering from small bodies can be summarized as follows. The scattering intensity increases with increasing permittivity, since the source current increases with $\tilde{\epsilon}$, irrespective of the direction of the incident field. The expected behavior of polarization can be deduced from (7.38), which provides general indications, clearly apart from the effect of the scattering direction mentioned in Sect. 7.1.2. In essence, the polarization of the field scattered by a body the shape of which is similar to a sphere is the same as that of the incident field for any direction of incidence: *co-polar scattering* characterizes bodies with central symmetry. Also the polarization of the field scattered by a disk-like object is the same, but only for normal incidence, although it remains related to that of the incident field as the incidence direction varies. Instead, in case of an elongated body such as a rod or a needle, since the scattering source current is oriented along the axis for almost any polarization of the incident field, the polarization of the scattered field tends to be linear and to lie in a plane containing the axis of the scatterer, consistently with the results of Sect. 3.1.3. This effect, generally implying change of polarization type and/or direction, is at the origin of *cross-polar* scattering. As examples, the crown of a deciduous broad-leaf tree is expected to be mainly characterized by co-polar backscattering at *high* microwave frequency, whereas a conifer tree with its needle-shaped leaves yields a more de-polarized scattering. Analogous effects are clearly observed in microwave and optical scattering from atmospheric particles, as discussed in Sect. 14.3.

Examples of microwave scattering from single bodies representing both planar and needle-shaped leaves are reported in the next sections. The Jones formalism is adopted and reference is made to frequencies at which the Earth observing SAR systems commonly operate. These numerical results contribute an introductory tangible understanding of the salient features of the radar images of vegetation, or, with suitable modification of parameters, of the optical scattering from atmospheric particles. The deterministic scattering by individual bodies is subsequently combined in a statistical fashion to gain further information on the behavior of examples of canopies of random vegetation elements which are encountered in real terrestrial environments. This step marks the transition from the coherent approach to the incoherent formulation of scattering outlined in Sect. 7.4.

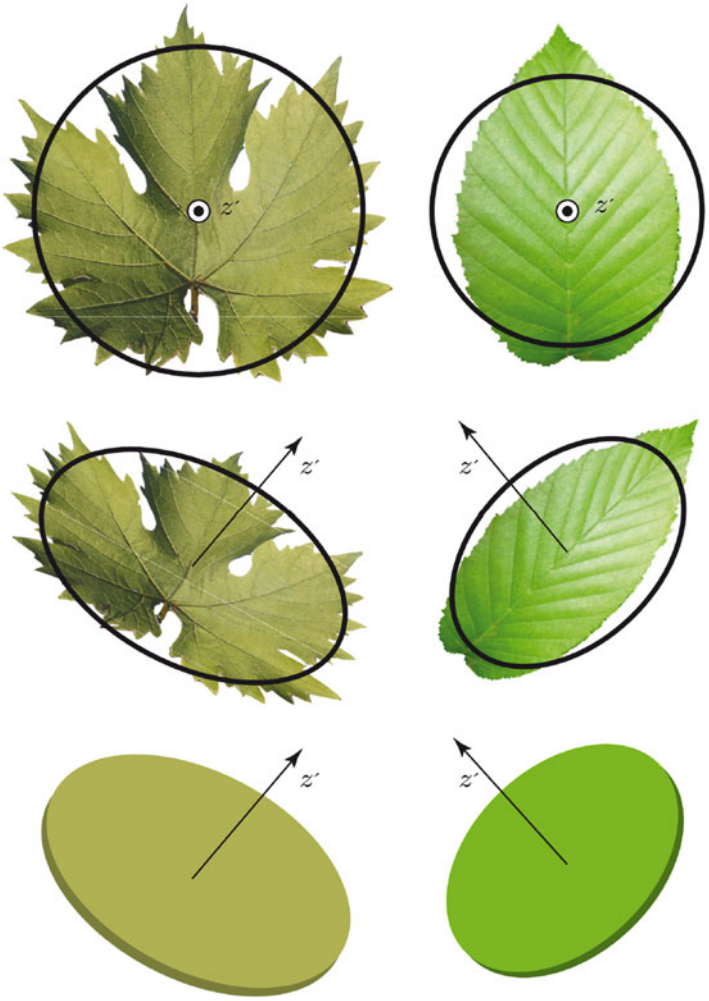

Fig. 7.16 A circular plate – or flat ellipsoid – of vegetal matter is an effective geometric model to interpret scattering from planar leaves. Axis z' is perpendicular to the plane of the leaf

7.3.4.1 Scattering from Disks

The planar leaves[30] are effectively modeled as the circular plates with symmetry axis z' depicted in Fig. 7.16, which behave substantially like the short and wide ellipsoid considered as one limiting case in Sect. 7.3.4. The permittivity of the vegetal matter forming the disks, related to the plant water content as discussed in Sect. 2.2.3, changes with the frequency at which scattering is considered.

[30] Analogous modeling is suitable for flat atmospheric particles, such as ice plates, for which polygonal shapes are also used [78].

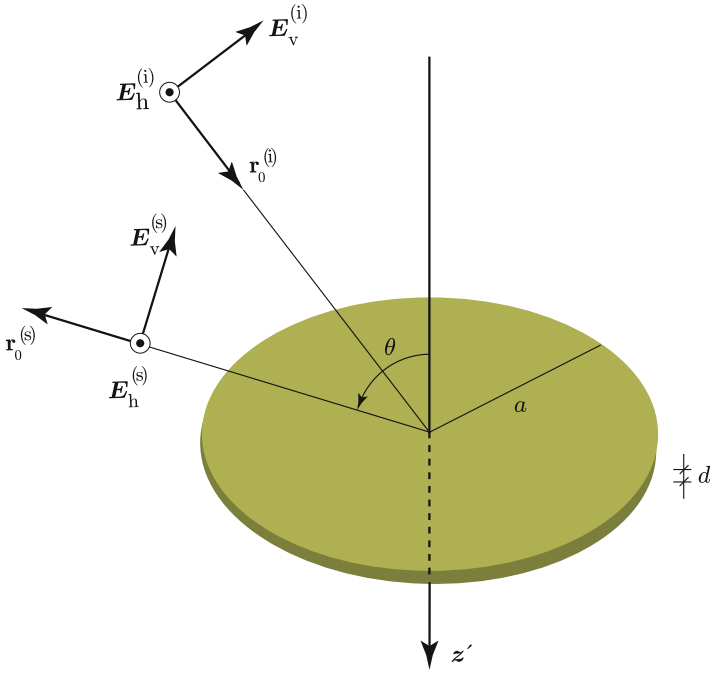

Fig. 7.17 Geometry of bistatic scattering from a circular disk of radius $a = 2\,\mathrm{cm}$ and characteristic thickness $d = 0.02\,\mathrm{cm}$ simulating a planar leaf. The elevation angles θ are measured with respect to the axis z', the azimuth angles in Fig. 7.18 refer to the plane orthogonal to z'. The relative permittivity of the material composing the disk has the values $\tilde{\epsilon} = 34.6 - \mathrm{j}8$ at frequency $f = 1.2\,\mathrm{GHz}$ (L-band, $\lambda_0 = 25.0\,\mathrm{cm}$), $\tilde{\epsilon} = 32.3 - \mathrm{j}8$ at $f = 5.3\,\mathrm{GHz}$ (C-band, $\lambda_0 = 5.7\,\mathrm{cm}$), $\tilde{\epsilon} = 27.3 - \mathrm{j}11$ at $f = 10\,\mathrm{GHz}$ (X-band, $\lambda_0 = 3.0\,\mathrm{cm}$)

In the geometry sketched in Fig. 7.17, the incident wave impinges at a fixed angle onto a disk of radius a and thickness d representative of the dimensions of some common broad-leaf trees. The normalized power density scattered by the disk is reported as a function of the scattering angle $\theta^{(\mathrm{s})}$ in the plane of incidence,[31] that is the plane formed by the versor of incidence $\mathbf{r}_0^{(\mathrm{i})}$ and the normal $\mathbf{z}_0$ along z'. The numerical values of the normalized scattered power density correspond to the co-polar scattering cross-section (7.16) of the disk at the horizontal polarization identified by the shown geometry. The polar diagrams of the bistatic scattering cross-section reported in Fig. 7.18 provide a visual representation of some of the relevant properties outlined in the preceding sections. The intensity of scattering is low at L-band, at which the scatterer appears small with respect to wavelength, and it increases with increasing frequency, in spite of the decreasing permittivity. The angular pattern, which is almost uniform at the lowest frequency and fairly similar in the azimuth plane to that of the point source current considered in Sect. 3.1.3,

[31] The scattering direction is also identified by the condition $\varphi^{(\mathrm{s})} = \pm\varphi^{(\mathrm{i})}$ on the azimuth angle.

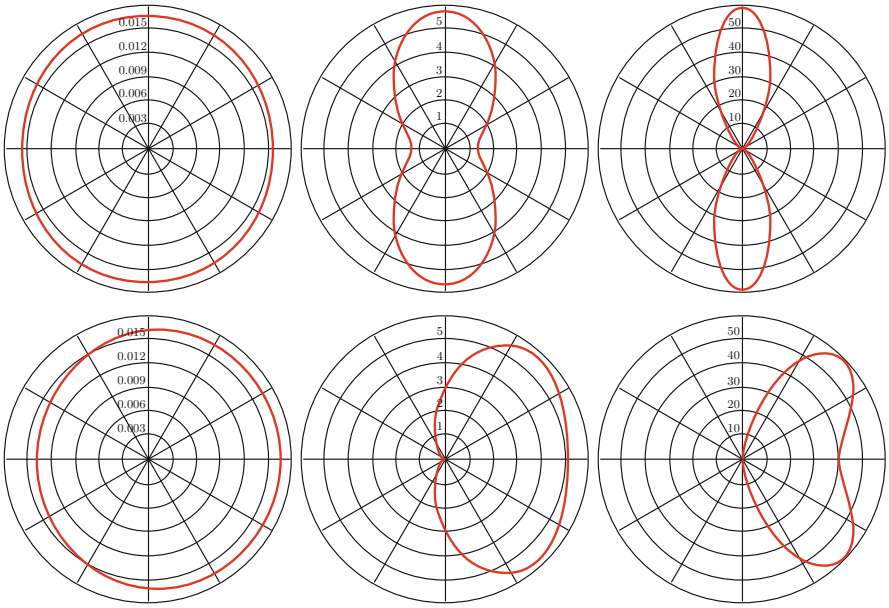

Fig. 7.18 Bistatic scattering cross-sections $\sigma_{\mathrm{hh}}\left(\theta^{(\mathrm{i})}, \varphi^{(\mathrm{i})}; \theta^{(\mathrm{s})}, \varphi^{(\mathrm{s})}\right)$ of disk simulating a planar leaf as functions of scattering angle $\theta^{(\mathrm{s})}$ for $\varphi^{(\mathrm{s})} = \pm\varphi^{(\mathrm{i})}$ and: $\theta^{(\mathrm{i})} = 0°$ (normal incidence, *top*) and $\theta^{(\mathrm{i})} = 45°$ (oblique incidence, *bottom*). The values are in cm^2 for the disk dimensions indicated in Fig. 7.17. Both incident and scattered fields are orthogonal to the incidence $(\mathbf{r}_0^{(\mathrm{i})}\,\mathbf{z}_0')$-plane (co-polar horizontal scattering). Frequencies are: L-band (*left*), C-band (*middle*), and X-band (*right*) (Data, courtesy Leila Guerriero)

sharpens as the wavelength decreases and a/λ_0 correspondingly increases.[32] The diagrams for the oblique incidence show also the progressive formation of the scattering maxima in the specular and forward directions discussed in Sect. 7.3.1.2. Note that the considered co-polar scattering at horizontal polarization is not affected by the double cross product in (7.8) involving the scattering direction, since, as Fig. 7.6 suggests, the re-radiating current $\boldsymbol{J}_{\mathrm{obh}}$ is orthogonal to any $\mathbf{r}_0^{(\mathrm{s})}$.

7.3.4.2 Scattering from Needles

The elongated leaves[33] shown in Fig. 7.19, are *needles*, the long and thin approximate ellipsoids considered as the other limiting case in Sect. 7.3.4, which behave

[32] Actually, a leaf with the assumed dimension is no more a *small* scatterer at X-band.

[33] As the planar leaves, also the elongated ones have their corresponding counterpart among the needle-shaped atmospheric particles [81].

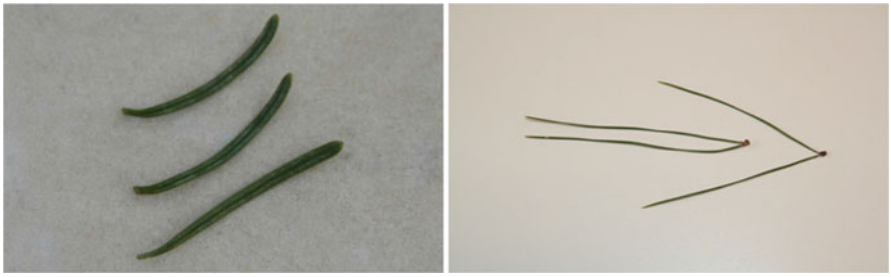

Fig. 7.19 Needle-shaped leaves of conifers

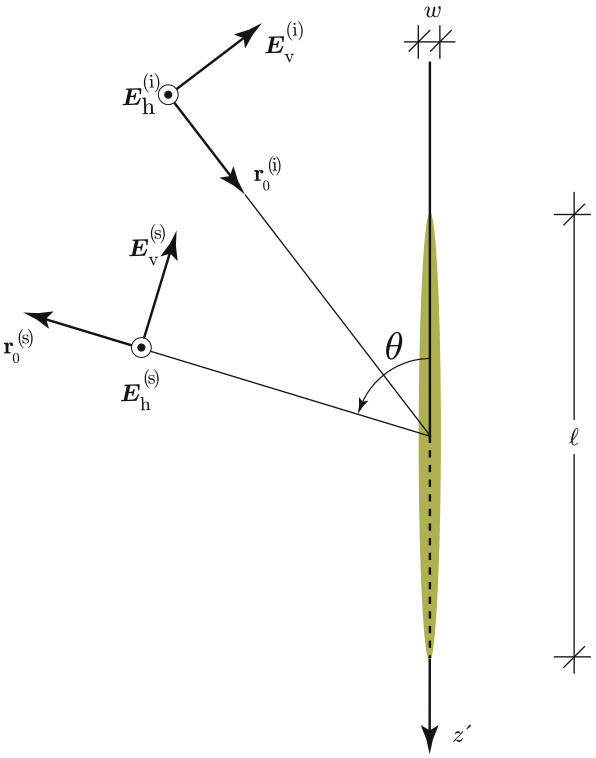

Fig. 7.20 Geometry of bistatic scattering from a needle of length $\ell = 7\,\mathrm{cm}$ and characteristic width $w = 0.03\,\mathrm{cm}$ simulating a conifer leaf. The elevation angles θ are measured with respect to the axis z', the azimuth angles in Fig. 7.21 refer to the plane orthogonal to z'. The relative permittivity of the material composing the needle is the same as for the disks, i.e., $\tilde{\epsilon} = 34.6 - \mathrm{j}8$ at frequency $f = 1.2\,\mathrm{GHz}$ (L-band, $\lambda_0 = 25.0\,\mathrm{cm}$), $\tilde{\epsilon} = 32.3 - \mathrm{j}8$ at $f = 5.3\,\mathrm{GHz}$ (C-band, $\lambda_0 = 5.7\,\mathrm{cm}$), $\tilde{\epsilon} = 27.3 - \mathrm{j}11$ at $f = 10\,\mathrm{GHz}$ (X-band, $\lambda_0 = 3.0\,\mathrm{cm}$)

as slim cylinders. The geometry is now detailed in Fig. 7.20. The incident wave impinges at a fixed angle $\theta^{(\mathrm{i})} = 45°$ onto a needle of length ℓ and with section of characteristic width w, representative of the dimensions of some common conifer leaves. As in the preceding section, the normalized power density scattered by the needle is reported as a function of the scattering angle $\theta^{(\mathrm{s})}$ in the plane of incidence, that is the plane formed by the propagation versor $\mathbf{r}_0^{(\mathrm{i})}$ of the incident wave and the axis z' of the needle. The numerical values of the normalized scattered power

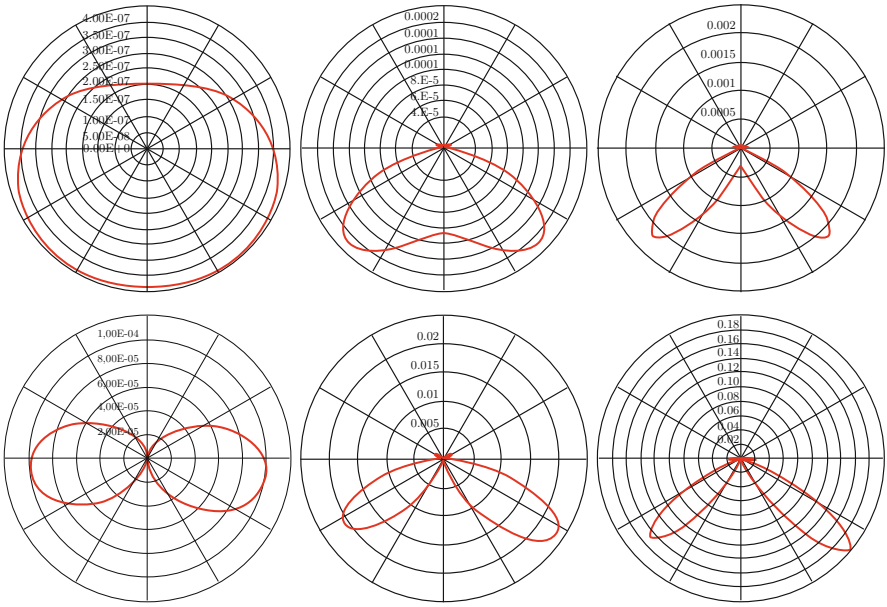

Fig. 7.21 Bistatic scattering cross-sections $\sigma_{\mathrm{hh}}\left(\theta^{(\mathrm{i})}, \varphi^{(\mathrm{i})}; \theta^{(\mathrm{s})}, \varphi^{(\mathrm{s})}\right)$ (*top*) and $\sigma_{\mathrm{vv}}\left(\theta^{(\mathrm{i})}, \varphi^{(\mathrm{i})}; \theta^{(\mathrm{s})}, \varphi^{(\mathrm{s})}\right)$ (*bottom*) of a needle simulating a conifer leaf as functions of scattering angle $\theta^{(\mathrm{s})}$ for $\varphi^{(\mathrm{s})} = \varphi^{(\mathrm{i})}$ and $\theta^{(\mathrm{i})} = 45°$ (oblique incidence with respect to the axis of the needle). The values are in cm^2 for the needle dimensions indicated in Fig. 7.20. The upper diagrams refer to incident and scattered fields orthogonal to the incidence $(\mathbf{r}_0^{(\mathrm{i})}\,\mathbf{z}_0')$-plane (co-polar horizontal scattering), while the lower diagrams refer to incident and scattered fields in the incidence $(\mathbf{r}_0^{(\mathrm{i})}\,\mathbf{z}_0')$-plane (co-polar vertical scattering). Frequencies are at: L-band (*left*), C-band (*middle*), and X-band (*right*) (Data, courtesy Leila Guerriero)

density correspond to the scattering cross-section (7.16) of the needle at the two co-polarization, horizontal and vertical, identified by the geometry shown in the figure.

As for the disks, the polar diagrams of the bistatic scattering cross-section reported in Fig. 7.21 provide a visual representation of some of the relevant properties of scattering. The intensity of scattering is low at L-band, at which the scatterer appears small with respect to wavelength, and, again, it increases with increasing frequency, from left to right. It is worth pointing out the extremely low values of the scattering cross-section at horizontal polarization (i.e., for electric field perpendicular to the needle), due to the unbalance $P_\perp \ll P_\parallel$ between the polarizability matrix elements that was mentioned in Sect. 7.3.4 and shown by the curves in Fig. 7.15. The ensuing differences by orders of magnitude between the cross-sections at horizontal (upper diagrams) and vertical (lower diagrams) suggest the de-polarizing effect of elongated bodies.

The result of the incidence obliquity appears in the scattering patterns, which exhibit the progressive sharpening of the angular distribution of the scattered power around the specular and the forward direction at both horizontal and vertical

polarizations. Note however that the L-band scattering cross-section at vertical polarization behaves differently, since it exhibits maxima around $\theta^{(s)} \approx \pi/2$ for $\varphi^{(s)} = \pm\varphi^{(i)}$. This is due to the fact that the direction of the re-radiating current $\boldsymbol{J}_{ob} \approx J_{ob}\,\mathbf{z}_0$ and the small length of the source, make this latter similar to the point source of Sect. 3.1.3, the far field (3.24) of which has its maximum[34] in the plane perpendicular to $\mathbf{z}_0$. As the wavelength decreases, the phase change over the length ℓ becomes appreciable, the scatterer looses its point-source character and the pattern tilts toward the specular and forward directions. A final observation is that, given the direction of $\boldsymbol{J}_{ob}$ for vertical polarization, the scattering-effective current $\boldsymbol{J}_{ob\perp}$ now depends on $\mathbf{r}_0^{(s)}$ and the angular pattern is affected by the double cross product in (7.8).

7.4 Incoherent Scattering

The planar or needle-shaped objects previously assumed to represent the scattering behavior of leaves or hydrometeors are not isolated in the real terrestrial environment. Rather, they are arranged in composite clusters to form vegetation canopies, or clouds and precipitation. The complexity of the canopies that may be encountered [55] is suggested by the example of vegetation shown in Fig. 7.22. A remote sensing system clearly does not image a single small scatterer, rather the ensemble of bodies that fall within the field of view (or, better, within the resolution

Fig. 7.22 Complex vegetation canopy in a tropical environment

[34] This issue is further discussed in Sect. 7.4.7.2.

cell) of the instrument (cf. Sect. 11.4.3.2). It means that the field reaching the sensor results from the scattering contributed collectively by the set of elements being observed [38]. The natural arrangement of bodies, be it in a tree crown or crop canopy, as well as in the hazy air or in rain cells, is essentially random, hence the fields contributed by the individual elements [31] arrive at the sensor with a random distribution of relative phases. The power captured by the sensor, which implies spatial and/or temporal averaging, then derives from the *incoherent* superposition of the elementary contributions, as mentioned in Sect. 4.3.2 for the basic case of two plane waves. It was shown that, when the phase fluctuations are uncorrelated, the waves add in power.

7.4.1 Scattering from Ensembles of Discrete Elements

On this basis, the discrete approach to incoherent scattering considers the *addition of the power* originating from *many* single scatterers to obtain the power scattered by the observed ensemble, without reference to the individual fields. The cross-sections of the individual elements reported in the preceding sections can then be combined to model the collective scattering from ensembles of bodies, such as disks and needles simulating the leaves composing canopies, as well as bundles of hydrometeors. Some significant features of the scattering behavior that is generally expected from this kind of targets are illustrated by the following simple examples.

7.4.1.1 Scattering from a Canopy of Random Disks

The broad-leaf canopy of Fig. 7.23a is schematized as an ensemble of randomly oriented disks with the same dimensions and frequency-dependent permittivity as those of the single disk reported in Fig. 7.17. The geometry is detailed in Fig. 7.23b. The model can be similarly extended, say, to a volume of precipitating snow flakes. The incident wave impinges onto a half-space filled with the random disks, at a fixed angle $\theta^{(\mathrm{i})} = 45°$ with respect to the direction $\mathbf{z}_0$ of the axis z' perpendicular to the plane delimiting the canopy. The scattered power density is normalized with respect to the area and to the surface density of the disks, so that it can be regarded as a scattering coefficient (Sect. 7.1.3.2). The co-polar horizontal bistatic scattering cross-section $\langle\sigma_{\mathrm{hh}}\rangle$ and the cross-polar $\langle\sigma_{\mathrm{hv}}\rangle$ are now considered, as identified by the geometry of the figure. Only single scattering is included into the results. Details on this issue are reported in Sect. 9.1.

The cross-sections $\langle\sigma_{\mathrm{hh}}\rangle$ and $\langle\sigma_{\mathrm{hv}}\rangle$ per unit element and unit area of the canopy are reported in Fig.7.24 as functions of the scattering angle $\theta^{(\mathrm{s})}$ in the plane of incidence, that is the plane formed by the propagation versor $\mathbf{r}_0^{(\mathrm{i})}$ of the incident wave with the axis z'. As expected from the behavior of the single element analyzed in Sect. 7.3.4.1, the intensity of scattering increases with increasing

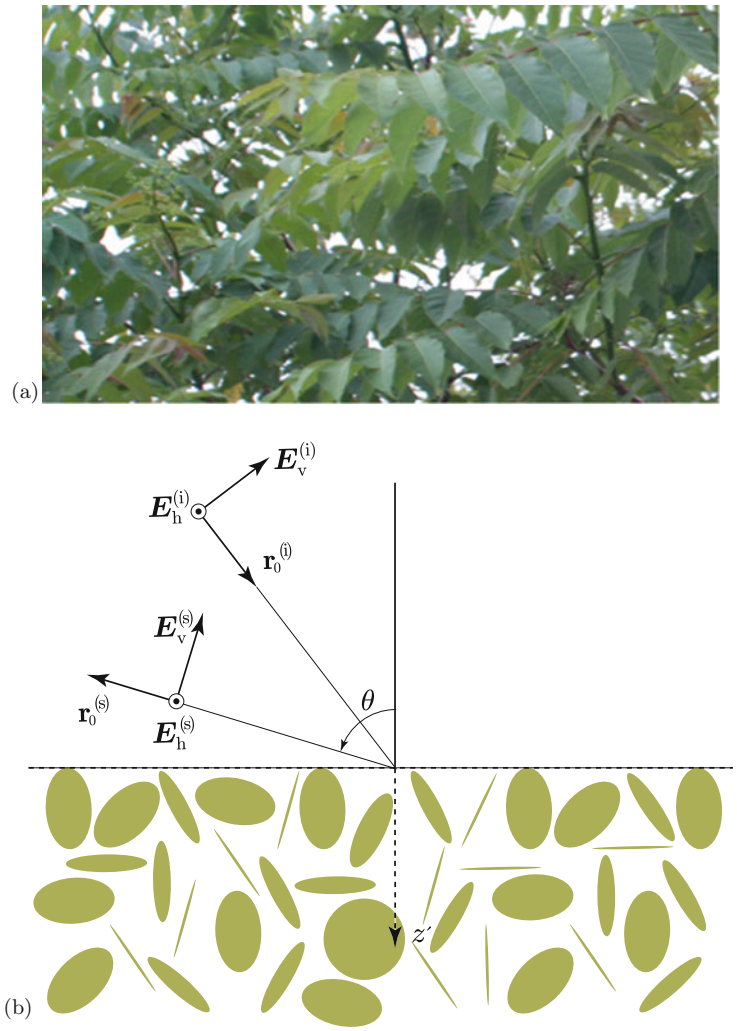

Fig. 7.23 Canopy of a broad-leaf tree crown, (**a**), and corresponding model of randomly oriented disks representing the leaves as in Fig. 7.16, (**b**); the elevation angle θ is measured with respect to the normal to the plane layer of disks, in which the azimuth angle of Fig. 7.24 is defined

frequency. The cross-polar intensity is lower by about one order of magnitude than the co-polar one. The angular pattern peaks around the forward direction for both pairs of polarizations, with directionality increasing with frequency. It is important to note the quite low value of scattering at cross-polarization for the higher frequencies, especially in the backward direction. Indeed, backscattering is dominated by the specular scattering from the fraction of disks that are oriented almost perpendicularly to the incident wave and, as seen in Sect. 6.2.2, this geometry of reflection does not de-polarize the field.

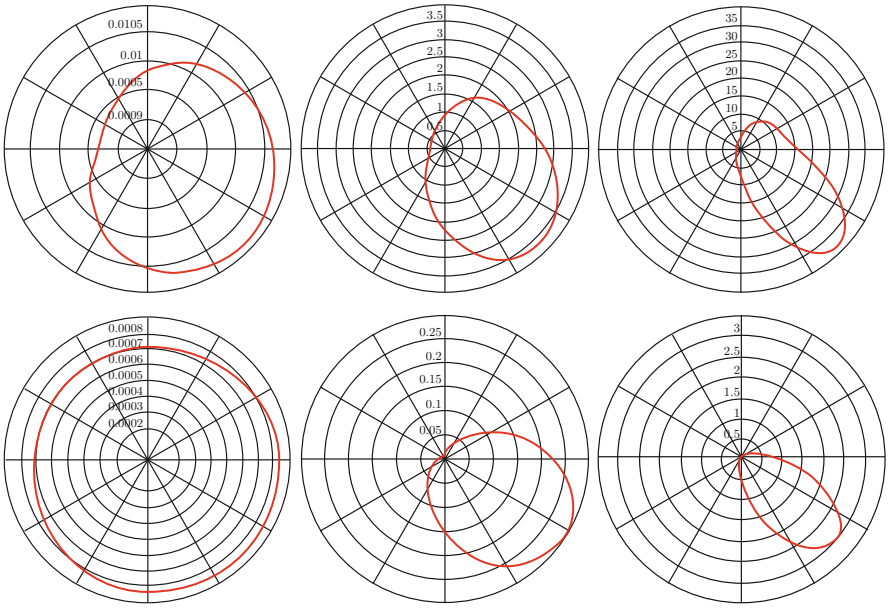

Fig. 7.24 Normalized bistatic scattering cross-sections $\langle \sigma_{hh} \rangle \left(\theta^{(i)}, \varphi^{(i)}; \theta^{(s)}, \varphi^{(s)}\right)$ (*top*) and $\langle \sigma_{hv} \rangle \left(\theta^{(i)}, \varphi^{(i)}; \theta^{(s)}, \varphi^{(s)}\right)$ (*bottom*) of a canopy of disks simulating planar leaves as functions of scattering angle $\theta^{(s)}$ for $\varphi^{(s)} = \varphi^{(i)}$ and $\theta^{(i)} = 45°$ (oblique incidence with respect to the normal to the canopy boundary). The values in cm^2 refer to a randomly oriented disk per unit area, with the dimensions indicated in Fig. 7.17. The upper diagrams are relative to incident and scattered fields orthogonal to the incidence $(\mathbf{r}_0^{(i)}\, \mathbf{z}_0')$-plane (co-polar horizontal scattering), while the lower diagrams refer to incident field $\boldsymbol{E}^{(i)} = E^{(i)}\mathbf{v}_0$ in the incidence $(\mathbf{r}_0^{(i)}\, \mathbf{z}_0')$-plane and scattered field $\boldsymbol{E}^{(s)} = E^{(s)}\mathbf{h}_0$ perpendicular to it (cross-polar scattering). Frequencies are at: L-band (*left*), C-band (*middle*), and X-band (*right*) (Data, courtesy Leila Guerriero)

7.4.1.2 Scattering from a Canopy of Random Needles

As before for the broad-leaf, the conifer canopy of Fig. 7.25a (or, again, with suitable scaling, a cirrus cloud) is schematized as an ensemble of randomly oriented needles with the same dimensions and frequency-dependent permittivity as those of the single needle reported in Fig. 7.20. The geometry is detailed in Fig. 7.25b. The incident wave impinges onto a half-space filled with the random needles, at a fixed angle $\theta^{(i)} = 45°$ with respect to the direction z' perpendicular to the plane delimiting the canopy. The scattered power density is normalized with respect to the area and to the surface density of the needles, so that, as before, it can be regarded as a scattering coefficient. No multiple scattering is considered. The co-polar horizontal bistatic scattering cross-section $\langle \sigma_{hh} \rangle$ and the cross-polar $\langle \sigma_{hv} \rangle$ are again considered, as identified by the geometry of the figure.

The cross-sections $\langle \sigma_{hh} \rangle$ and $\langle \sigma_{hv} \rangle$ per unit element and unit area of the canopy are reported in Fig. 7.26 as functions of the scattering angle $\theta^{(s)}$ in the plane of

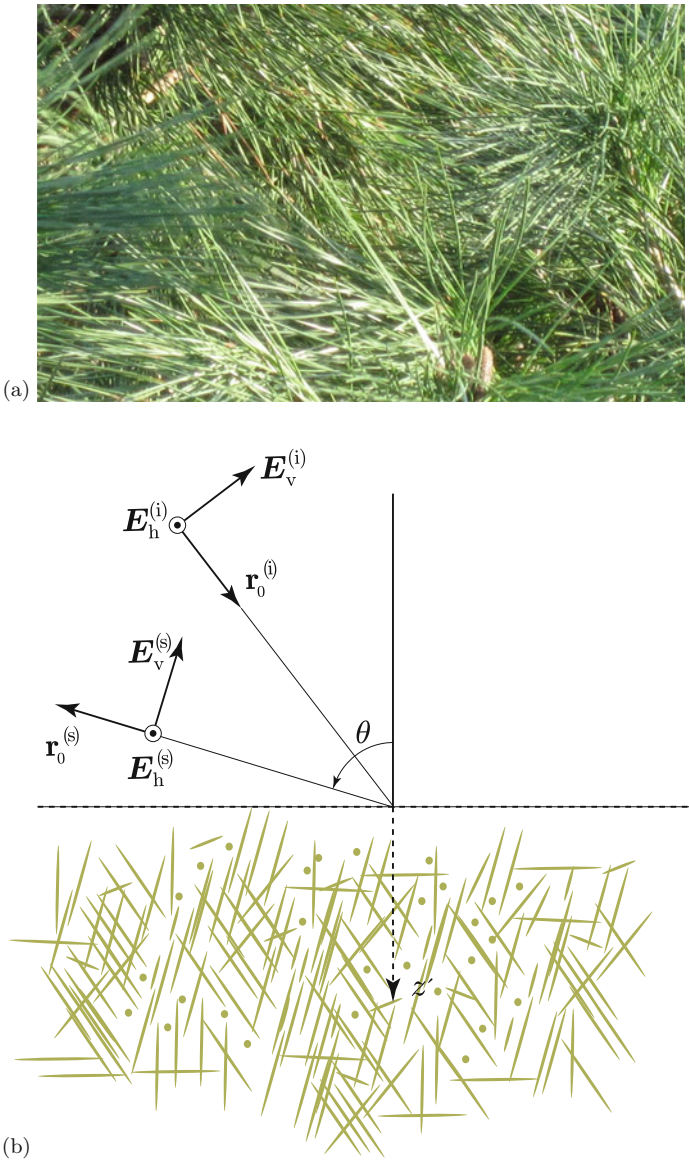

Fig. 7.25 Canopy of conifer tree crown, (**a**), and corresponding model of randomly oriented needles, as in Fig. 7.21, (**b**); the elevation angle θ is measured with respect to the normal to the plane layer of needles, in which the azimuth angle of Fig. 7.26 is defined

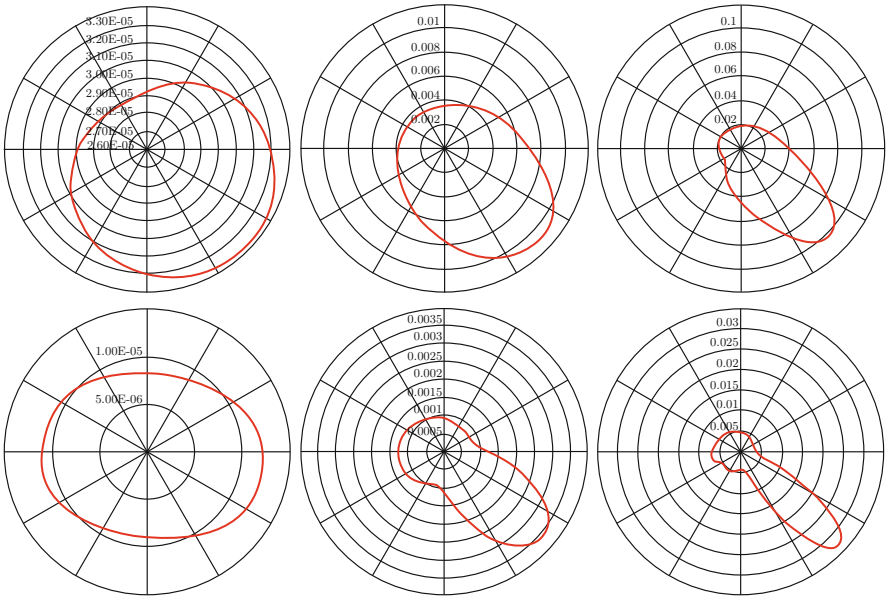

Fig. 7.26 Normalized bistatic scattering cross-sections $\langle \sigma_{hh} \rangle \left(\theta^{(i)}, \varphi^{(i)}; \theta^{(s)}, \varphi^{(s)}\right)$ (*top*) and $\langle \sigma_{hv} \rangle \left(\theta^{(i)}, \varphi^{(i)}; \theta^{(s)}, \varphi^{(s)}\right)$ (*bottom*) of a canopy of needles simulating conifer leaves as functions of scattering angle $\theta^{(s)}$ for $\varphi^{(s)} = \varphi^{(i)}$ and $\theta^{(i)} = 45°$ (oblique incidence with respect to the normal to the canopy boundary). The values in cm^2 refer to a randomly oriented needle per unit area, with the dimensions indicated in Fig. 7.20. The upper diagrams are relative to incident and scattered fields orthogonal to the incidence $(\mathbf{r}_0^{(i)}\, \mathbf{z}_0')$-plane (co-polar horizontal scattering), while the lower diagrams refer to incident field $\boldsymbol{E}^{(i)} = E^{(i)}\mathbf{h}_0$ in the incidence $(\mathbf{r}_0^{(i)}\, \mathbf{z}_0')$-plane and scattered field $\boldsymbol{E}^{(s)} = E^{(s)}\mathbf{v}_0$ perpendicular to it (cross-polar scattering). Frequencies are at: L-band (*left*), C-band (*middle*), and X-band (*right*) (Data, courtesy Leila Guerriero)

incidence, which, as before, is the plane formed by the propagation versor $\mathbf{r}_0^{(i)}$ of the incident wave and z'. The main characteristics of the intensity and angular pattern of scattering from the disk canopy are found again in Fig. 7.26. However, a significant difference appears in the polarization behavior of scattering in the backward direction: the cross-polarized backscattering from the needle canopy not only is of the same order of magnitude as the co-polarized one, but it exceeds that from the disk canopy. This observation confirms the de-polarizing effects of asymmetric bodies, and, in particular, of those with one prevailing dimension.

The analysis carried out for the needles can be suitably adapted to derive analogous properties of the scattering from ensembles of cylindrical woody elements of vegetation, such as the trunks and branches[35] of Fig. 7.9, and, especially, like the intricate shrub and twig canopies in Fig. 7.27.

[35]Provided the diameter is not large with respect to wavelength.

Fig. 7.27 Intricate canopies of cylindrical elements in low and high vegetation

It has been emphasized that the evaluation of scattering from the random canopies has followed the *incoherent* approach. The coherent approach would have been based on the interference of the fields originating from the single elements of a possibly *known* canopy. But then, beside the assumption being unrealistic, the coherent scattering from the single *individual* canopy would have been of unknown representativeness of the general behavior expected by this *class* of scatterers in the real world. In this context, the only valuable information obtainable from the coherent scattering would be the (specular) reflection from the boundary of the half-space having the average permittivity of the canopy, i.e., the average of the permittivity of the air and of the scattering elements weighted by the volume fraction of these latter. Then an approach analogous to the one followed in Sect. 7.3.3 for the rough surface could provide some useful hint. Apart from this kind of information, interpreting scattering images of canopies, and, in particular, their backscattering, in practice uses the incoherent[36] approach.

7.4.2 Continuous Approach to Incoherent Scattering

The preceding analysis has been carried out by assembling the power contributions from single deterministic elements of known behavior, subject to the prior introduction of some *collective* statistical features able to model the random character of the observed target. The probabilistic combination of deterministic individual elements is one of the approaches that can be followed to characterize the scattering from the terrestrial environment. An alternative approach, able to yield further significant insight into the bio-geo-physical information contained in the scattering images, is based on continuous stochastic models rather than on random assemblies of

[36]Coherent models are clearly needed when the phase is of interest, as in radar interferometric measurements (cf. Sect. 12.3).

discrete elements. The two approaches use different points of view of the same scenario, hence they are expected to yield consistent results, provided the respective characterizing parameters are suitably selected.

The continuous approach to incoherent scattering starts from the consideration that the electromagnetic power received by an Earth observing sensor generally originates from a region of space characterized by a complicated and a-priori unknown spatial distribution of permittivity. Equation (7.28) points out that the power density $\mathcal{P}^{(\mathrm{s})}$ scattered into the unit solid angle by the portion of terrestrial environment observed by the sensor presents a random component $\mathcal{P}'^{(\mathrm{s})}$ originated by the fluctuations of permittivity about the average dielectric structure. To obtain meaningful information, and consistently with the previous discussion, the approach needs to be statistical, based on ensemble averages, as done for the canopies of disks and needles. The average of $\mathcal{P}'^{(\mathrm{s})}$ over the ensemble of realizations of the considered class of scatterers, within the approximation (7.27), is

$$\begin{aligned}\left\langle \mathcal{P}'^{(\mathrm{s})} \right\rangle &= \frac{\left\langle \mathcal{F}' \cdot \mathcal{F}'^{*} \right\rangle}{2\,\eta_0} \\ &\simeq \frac{\kappa_0^4}{32\,\pi^2\,\eta_0} \left\langle \left[\iiint_{V'} \left(\overline{\boldsymbol{E}_\perp} \Delta\tilde{\epsilon}' \right) \mathrm{e}^{\,\mathrm{j}\kappa_0 \boldsymbol{r}' \cdot \mathbf{r}_0^{(\mathrm{s})}} \,\mathrm{d}V' \right] \left[\iiint_{V'} \left(\overline{\boldsymbol{E}_\perp^{*}} \Delta\tilde{\epsilon}'^{*} \right) \mathrm{e}^{-\mathrm{j}\kappa_0 \boldsymbol{r}' \cdot \mathbf{r}_0^{(\mathrm{s})}} \,\mathrm{d}V' \right] \right\rangle .\end{aligned} \tag{7.39}$$

The product of the integrals in (7.39) is put under the form of a unique integral by distinguishing the integration point $\boldsymbol{r}_1$ in V_1' from $\boldsymbol{r}_2$ in V_2':

$$\begin{aligned}&\left\langle \mathcal{P}'^{(\mathrm{s})} \right\rangle \simeq \\ &\quad \frac{\kappa_0^4}{32\pi^2\eta_0} \iiint_{V'} \iiint_{V'} \overline{\boldsymbol{E}_\perp}(\boldsymbol{r}_1') \cdot \overline{\boldsymbol{E}_\perp^{*}}(\boldsymbol{r}_2') \left\langle \Delta\tilde{\epsilon}'(\boldsymbol{r}_1')\, \Delta\tilde{\epsilon}'^{*}(\boldsymbol{r}_2') \right\rangle e^{\mathrm{j}\kappa_0 \mathbf{r}_0^{(\mathrm{s})} \cdot (\boldsymbol{r}_1' - \boldsymbol{r}_2')} \mathrm{d}V_2' \,\mathrm{d}V_1' \,.\end{aligned} \tag{7.40}$$

The average is intended over the relevant ensemble of realizations of the scattering source of volume V', which is typically identified by the *resolution cell* of the remote sensing system. The ensemble can be spanned by observations of the same volume carried out at different times, or by the ensemble of image elements with homogeneous statistical characteristics contained in single acquisitions, such as, for instance, ensembles of portions of cloud volumes, of bare soil plots, or of forest stands.

Note that if the resolution cell V' contains permittivity fluctuations which span the ensemble of realizations, the power scattered by the cell tends to the ensemble average value, as indicated by the mentioned space ergodicity. An example is a closed thick stable plant canopy of given plant species: the structure of the permittivity in the resolution cell is close to the structure that would be found in an infinite number of cells of the same type of canopy. The probability that the

cell includes all realizations of the ensemble clearly increases with increasing cell's dimensions. The theoretical requirement $V' \to \infty$ translates in *large* resolution cells. As an example, it is known that the fluctuations of the backscattering coefficient in a SAR image decrease with the increasing dimensions of the resolution cell obtained by *multi-look* [21, 53].[37] Instead, as the spatial resolution increases (i.e., as the dimensions of the cell decrease), less samples of the random elements are present in V' and the more the individual power deviates from the ensemble average. In practice, few large scattering elements in a cell make the fluctuations of the scattered power to become a substantial fraction of its statistical mean and the measurement ceases to be representative of the expected value.

7.4.3 Incoherent Scattering from Inhomogeneous Targets

The large object the scattering from which was discussed in Sect. 7.3.1 is again considered, but now the material is randomly inhomogeneous. The deviation of permittivity $\Delta\tilde{\epsilon}'(\boldsymbol{r}')$ in (7.40) is assumed to be a zero-mean random function of both lateral coordinates x', y' and of the longitudinal coordinate z' delineated in Fig. 7.28. The parallelepiped represents the volume from which the power received by the

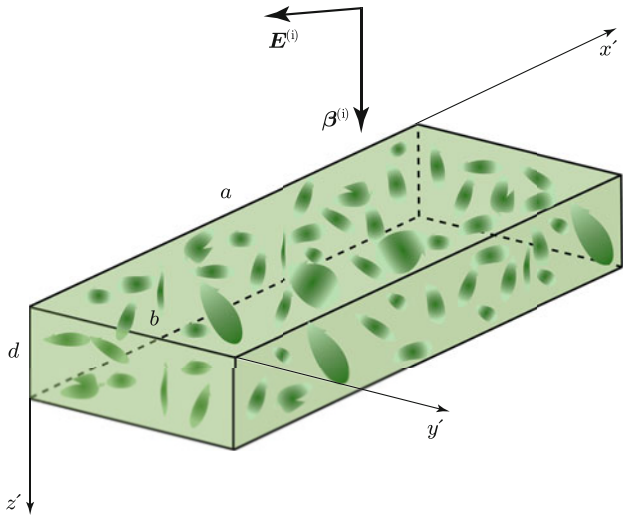

Fig. 7.28 Volume of randomly inhomogeneous material onto the surface of which a plane wave impinges normally; the *shades of green* denote the values of permittivity: light indicates lower; dark, higher; the uniform *pale green* represents the spatial average

[37]Examples of multi-looked image generation are found at https://earth.esa.int/web/guest/software-tools/best-basic-envisat-sar-toolbox/best-examples/generating-a-multi-look-image.

sensor originates, therefore it models a resolution cell of the observed terrestrial environment, such as terrain, forest, water, atmosphere.

The source-effective electric field $\overline{\boldsymbol{E}_{\perp}}$ in (7.40) depends on the field that penetrates into the assumed homogeneous[38] volume with average permittivity. Following the approach of Sect. 7.3.1, the inner field (7.31) is assumed to be that of the refracted[39] plane wave (6.22)

$$\overline{\boldsymbol{E}} \equiv \overline{\boldsymbol{E}'} = \overline{\boldsymbol{E}'_0}\, \mathrm{e}^{-\mathrm{j}\boldsymbol{k}'\cdot\boldsymbol{r}'} \ .$$

With the notations of Sect. 6.3, the propagation vector $\boldsymbol{k}' = \boldsymbol{\beta}' - \mathrm{j}\alpha'\mathbf{z}_0$ in the volume V' filled with the average material is written as

$$\boldsymbol{k}' = \boldsymbol{\beta}'^{(\mathrm{i})}_{\mathrm{t}} + \beta'_z\, \mathbf{z}_0 - \mathrm{j}\alpha'\, \mathbf{z}_0 \ ,$$

since the transverse component $\boldsymbol{\beta}'_{\mathrm{t}} = \beta'_x\mathbf{x}_0 + \beta'_y\mathbf{y}_0$ of the phase vector of the refracted wave is the same as that of the incident wave because of the field continuity (6.13) on the air-material interface. Then the field inside the average-permittivity scattering volume is approximated by

$$\overline{\boldsymbol{E}'} = \overline{\boldsymbol{E}'_0}\, \mathrm{e}^{-\alpha' z'}\, \mathrm{e}^{-\mathrm{j}\boldsymbol{\beta}'^{(\mathrm{i})}_{\mathrm{t}}\cdot\boldsymbol{r}'_{\mathrm{t}}}\, \mathrm{e}^{-\mathrm{j}\beta'_z z'} \ , \tag{7.41}$$

where $\boldsymbol{r}'_{\mathrm{t}} = x'\mathbf{x}_0 + y'\mathbf{y}_0$ is the position vector in the transverse plane. Both the attenuation and the longitudinal phase constants in (7.41) depend on the average complex permittivity of the material. With reference to earth surface observation, the transverse plane may be the locally horizontal one, while the longitudinal coordinate z' represents depth.

The dielectric inhomogeneities originate a scattered field which propagates in V'. Under the assumption of horizontal *statistical homogeneity* [59, Chap. 1], the amplitude of this scattered internal plane wave depends only on depth, so that the propagation vector $\boldsymbol{k}''$ of the scattered field in the volume V' filled with the average material is

$$\boldsymbol{k}'' = \boldsymbol{\beta}''_{\mathrm{t}} + \beta''_z\mathbf{z}_0 + \mathrm{j}\alpha''\mathbf{z}_0 = \boldsymbol{\beta}^{(\mathrm{s})}_{\mathrm{t}} + \beta''_z\mathbf{z}_0 + \mathrm{j}\alpha''\mathbf{z}_0 \ . \tag{7.42}$$

Note that the field continuity on the air-material interface holds not only for incident and refracted waves, but, clearly, also for the inner and outer scattered waves. Therefore, in (7.42) the transverse component of the phase vector $\boldsymbol{\beta}''$ of the internal scattered wave is equal to that of the external scattered field, i.e., $\boldsymbol{\beta}''_{\mathrm{t}} = \boldsymbol{\beta}^{(\mathrm{s})}_{\mathrm{t}}$.

[38] Here "homogeneous" clearly refers to the average material.

[39] The superscript $'$ may denote either fluctuating or refracted quantities: the reader should carefully identify the meaning of the notation according to the peculiar context in which it appears.

To proceed further, the requirement that no total reflection (cf. Sect. 6.4) occurs, must be satisfied.

By now removing the assumption of average tenuous material[40] and introducing the plane-wave expressions (7.41) into Eq. (7.40), the average value of the random scattered angular power density is obtained as

$$\left\langle \mathcal{P}'^{(\mathrm{s})} \right\rangle \simeq \frac{\kappa_0^4}{16\pi^2} \frac{\overline{\boldsymbol{E}'_{0\perp}} \cdot \overline{\boldsymbol{E}'_{0\perp}}^{*}}{2\eta} \iiint_{V'} \iiint_{V'} \left\langle \Delta\tilde{\epsilon}\,'(\boldsymbol{r}'_{\mathrm{t}1}, z'_1)\, \Delta\tilde{\epsilon}\,'^{*}(\boldsymbol{r}'_{\mathrm{t}2}, z'_2) \right\rangle$$
$$\times\, \mathrm{e}^{-\alpha'(z'_1 + z'_2)}\, \mathrm{e}^{-\mathrm{j}\beta'_z (z'_1 - z'_2)}\, \mathrm{e}^{-\mathrm{j}\boldsymbol{\beta}_{\mathrm{t}}^{(\mathrm{i})} \cdot (\boldsymbol{r}'_{\mathrm{t}1} - \boldsymbol{r}'_{\mathrm{t}2})} \tag{7.43}$$
$$\times\, \mathrm{e}^{-\alpha''(z'_1 + z'_2)}\, \mathrm{e}^{\mathrm{j}\beta''_z (z'_1 - z'_2)}\, \mathrm{e}^{\mathrm{j}\boldsymbol{\beta}_{\mathrm{t}}^{(\mathrm{s})} \cdot (\boldsymbol{r}'_{\mathrm{t}1} - \boldsymbol{r}'_{\mathrm{t}2})}\, \mathrm{d}V'_2\, \mathrm{d}V'_1 \,.$$

The substantial feature in (7.43) is the presence of the *autocovariance function* [58, Chap. 1] of permittivity fluctuations

$$\left\langle \Delta\tilde{\epsilon}\,'(\boldsymbol{r}'_{\mathrm{t}1}, z'_1)\, \Delta\tilde{\epsilon}\,'^{*}(\boldsymbol{r}'_{\mathrm{t}2}, z'_2) \right\rangle = \sigma_\epsilon^2(\boldsymbol{r}'_{\mathrm{t}1}, z'_1; \boldsymbol{r}'_{\mathrm{t}2}, z'_2)\, \mathcal{B}_\epsilon(\boldsymbol{r}'_{\mathrm{t}1}, z'_1; \boldsymbol{r}'_{\mathrm{t}2}, z'_2) \,.$$

To simplify the notations, two assumptions, after all frequently admissible, are put forward. The first, horizontal statistical homogeneity, yields a permittivity covariance independent of the horizontal position

$$\sigma_\epsilon^2(\boldsymbol{r}'_{\mathrm{t}1}, z'_1; \boldsymbol{r}'_{\mathrm{t}2}, z'_2) = \sigma_\epsilon^2(z'_1, z'_2) \,. \tag{7.44}$$

The assumption (7.44) means that a horizontal layer of the material has the same magnitude of dielectric inhomogeneities everywhere.

The second, horizontal *isotropy*, makes the normalized autocorrelation function to depend only on the horizontal distance $\left|\boldsymbol{r}'_{\mathrm{t}1} - \boldsymbol{r}'_{\mathrm{t}2}\right|$

$$\mathcal{B}_\epsilon\left(\left|\boldsymbol{r}'_{\mathrm{t}1} - \boldsymbol{r}'_{\mathrm{t}2}\right|; z'_1, z'_2\right) = \mathcal{B}_{\epsilon\mathrm{t}}\left(\left|\boldsymbol{r}'_{\mathrm{t}1} - \boldsymbol{r}'_{\mathrm{t}2}\right|\right)\, \mathcal{B}_{\epsilon\mathrm{Z}}\left(z'_1, z'_2\right) \,.$$

The assumption of *local quasi-homogeneity* of the permittivity fluctuations, with smooth variations in the vertical direction, is a further serviceable approximation in many cases regarding plant canopies, atmospheric or water layers and soil. Moreover, in several instances, the characteristics of the observed target make acceptable the factorization of the normalized autocorrelation function into horizontal (lateral) $\mathcal{B}_{\epsilon\mathrm{t}}$ and vertical (longitudinal) $\mathcal{B}_{\epsilon\mathrm{Z}}$ functions:

$$\mathcal{B}_\epsilon\left(\left|\boldsymbol{r}'_{\mathrm{t}1} - \boldsymbol{r}'_{\mathrm{t}2}\right|; z'_1, z'_2\right) = \mathcal{B}_{\epsilon\mathrm{t}}\left(\left|\boldsymbol{r}'_{\mathrm{t}1} - \boldsymbol{r}'_{\mathrm{t}2}\right|\right)\, \mathcal{B}_{\epsilon\mathrm{Z}}\left(z'_1, z'_2\right) \,. \tag{7.45}$$

[40] This means that the initial hypothesis that the propagation constant of the scattered field within V' is the same as that in the vacuum is now removed from (7.40).

The average of the fluctuating angular power scattered by a target for which the previous assumptions are admissible is

$$\left\langle \mathcal{P}'^{(\mathrm{s})} \right\rangle \simeq \frac{\kappa_0^4}{16\pi^2}\,\overline{\mathcal{P}'_{\mathrm{o}}} \iiint_{V'}\iiint_{V'} \sigma_\epsilon^2(z'_1, z'_2)\, \mathcal{B}_{\epsilon\mathrm{t}}(|\boldsymbol{r}'_{\mathrm{t}1} - \boldsymbol{r}'_{\mathrm{t}2}|)\mathcal{B}_{\epsilon\mathrm{z}}(z'_1, z'_2)$$
$$\times\, \mathrm{e}^{-(\alpha'+\alpha'')(z'_1+z'_2)}\mathrm{e}^{-\mathrm{j}(\beta'_z - \beta''_z)(z'_1 - z'_2)}\, \mathrm{e}^{-\mathrm{j}(\boldsymbol{\beta}_{\mathrm{t}}^{(\mathrm{i})} - \boldsymbol{\beta}_{\mathrm{t}}^{(\mathrm{s})})\cdot(\boldsymbol{r}_{\mathrm{t}1}' - \boldsymbol{r}_{\mathrm{t}2}')}\, \mathrm{d}V'_2\, \mathrm{d}V'_1 \,. \tag{7.46}$$

The areic power $\overline{\mathcal{P}'_{\mathrm{o}}}$ entering the average observed volume,[41]

$$\overline{\mathcal{P}'_{\mathrm{o}}} = \frac{\overline{\boldsymbol{E}'_{0\perp}} \cdot \overline{\boldsymbol{E}'^{*}_{0\perp}}}{2\eta} \,,$$

has been suitably introduced into (7.46). If $S' = a\,b$ is the transverse section and d the thickness of the resolution cell V' shown in Fig. 7.28, manipulation of (7.46) yields[42]

$$\left\langle \mathcal{P}'^{(\mathrm{s})} \right\rangle \simeq \frac{\kappa_0^4}{16\pi^2}\,\overline{\mathcal{P}'_{\mathrm{o}}}$$
$$\times \int_0^d \mathrm{d}z'_1 \int_0^d \mathrm{d}z'_2\, \sigma_\epsilon^2(z'_1, z'_2)\, \mathcal{B}_{\epsilon\mathrm{z}}(z'_1, z'_2)\, \mathrm{e}^{-(\alpha' + \alpha'')(z'_1 + z'_2)}\, \mathrm{e}^{-\mathrm{j}(\beta'_z - \beta''_z)(z'_1 - z'_2)}$$
$$\times \iint_{S'} \mathrm{d}S'_1 \iint_{S'} \mathcal{B}_{\epsilon\mathrm{t}}(|\boldsymbol{r}'_{\mathrm{t}1} - \boldsymbol{r}'_{\mathrm{t}2}|)\mathrm{e}^{-\mathrm{j}(\boldsymbol{\beta}_{\mathrm{t}}^{(\mathrm{i})} - \boldsymbol{\beta}_{\mathrm{t}}^{(\mathrm{s})})\cdot(\boldsymbol{r}'_{\mathrm{t}1} - \boldsymbol{r}'_{\mathrm{t}2})}\, \mathrm{d}S'_2 \,. \tag{7.47}$$

The *lateral* (horizontal in the present case) coordinates are transformed according to

$$\boldsymbol{r} = \boldsymbol{r}'_{\mathrm{t}1} - \boldsymbol{r}'_{\mathrm{t}2}, \qquad \boldsymbol{\mathfrak{r}} = \frac{\boldsymbol{r}'_{\mathrm{t}1} + \boldsymbol{r}'_{\mathrm{t}2}}{2} \,, \tag{7.48}$$

which lead to the more compact notation

$$\left\langle \mathcal{P}'^{(\mathrm{s})} \right\rangle \simeq \frac{\kappa_0^4}{16\pi^2}\,\overline{\mathcal{P}'_{\mathrm{o}}}\, Z_{\mathcal{P}} \iint_{S'_{\boldsymbol{\mathfrak{r}}}} \mathrm{d}\boldsymbol{\mathfrak{r}} \iint_{S'_r} \mathcal{B}_{\epsilon\mathrm{t}}(r)\, \mathrm{e}^{-\mathrm{j}(\boldsymbol{\beta}_{\mathrm{t}}^{(\mathrm{i})} - \boldsymbol{\beta}_{\mathrm{t}}^{(\mathrm{s})})\cdot\boldsymbol{r}}\, \mathrm{d}\boldsymbol{r} \,. \tag{7.49}$$

The factor $Z_{\mathcal{P}}$ in (7.49) representing the double integral over the longitudinal dimension, takes into account the effect of the vertical structure of permittivity,

[41] Here the symbol $\overline{\boldsymbol{E}_0}$ denotes the primary field inside the scattering volume.

[42] The reader should have noticed that the superscript $'$ in $\mathcal{P}'^{(\mathrm{s})}$ denotes *fluctuation*, whereas $'$ in $\overline{\mathcal{P}'_{\mathrm{o}}}$ indicates *refracted*.

also reckoning the attenuation, which, as shown in Sect. 6.3, acts in the vertical direction. The integration domains $S'_{\mathfrak{r}}$ and S'_r are the ones respectively corresponding to the transformations (7.48). The domain $S'_{\mathfrak{r}}$ spans the values of the horizontal (lateral) mean position $\mathfrak{r}$ of a pair of points inside the scattering volume, while S'_r is generated by the horizontal distance r between any pairs of points in V'. Note that, for a general scattering direction, $\alpha' \neq \alpha''$, since the attenuation depends on the angle the direction of propagation forms with z', as detailed in Sect. 6.3.1. However, $\alpha' = \alpha''$ for backscattering, because $\boldsymbol{\beta}' = -\boldsymbol{\beta}''$, hence the angles are the same.

Equation (7.49) points out that the scattered angular power density is affected by both horizontal and vertical inhomogeneities of permittivity. It is important to note that the dielectric structure is not described by the *discrete model* of Sect. 7.4.1 considering a random ensemble of bodies, rather it is now represented according to a *continuous approach*, based on the correlation function of permittivity. It means that the scattering intensity depends on the amount of correlation between the fluctuation of permittivity in one point of the scattering volume and the fluctuation in another point. The dielectric structure of a random ensemble of discrete bodies can be expressed by the corresponding three-dimensional autocorrelation function of the permittivity and the two approaches are clearly expected to lead to consistent results.

7.4.4 Dependence of Scattering on Target Structure

Given the statistical homogeneity (7.44), the lateral autocorrelation function $\mathcal{B}_{\epsilon \mathfrak{t}}$ of the permittivity fluctuations depends only on the horizontal distance r between a pair of points and is independent of the position $\mathfrak{r}$ of the middle point in the horizontal plane, so that (7.49) yields

$$\left\langle \mathcal{P}'^{(\mathrm{s})} \right\rangle \simeq \frac{\kappa_0^4}{16\,\pi^2}\,\overline{\mathcal{P}'_{\mathrm{o}}}\,Z_{\mathcal{P}}\,A_{\mathrm{S}} \iint_{S'_r} \mathcal{B}_{\epsilon \mathfrak{t}}(r) \mathrm{e}^{-\mathrm{j}(\boldsymbol{\beta}_{\mathfrak{t}}^{(\mathrm{i})} - \boldsymbol{\beta}_{\mathfrak{t}}^{(\mathrm{s})}) \cdot \boldsymbol{r}}\,\mathrm{d}\boldsymbol{r}\,. \tag{7.50}$$

Here A_{S} is the area of the transverse (horizontal) surface binding the scattering volume. Coarsely speaking, A_{S} is the area of the elementary area (*pixel*) of the map (*image*) representing the local scattering from the terrestrial surface (cf. Sect. 10.2). The correlation $\mathcal{B}_{\epsilon \mathfrak{t}}$ generally decreases with distance. When the scattering volume contains a high number of random objects as sketched in Fig. 7.29, the horizontal *correlation distance* (or correlation *radius*) r_ϵ of permittivity fluctuations, that is the distance beyond which the autocorrelation function decays to negligible values, is much smaller than the transverse dimension D of the scattering volume. The dimension D corresponds to the linear spatial resolution at which the image of the earth surface is acquired. Indeed, this is frequently the case both at macroscopic

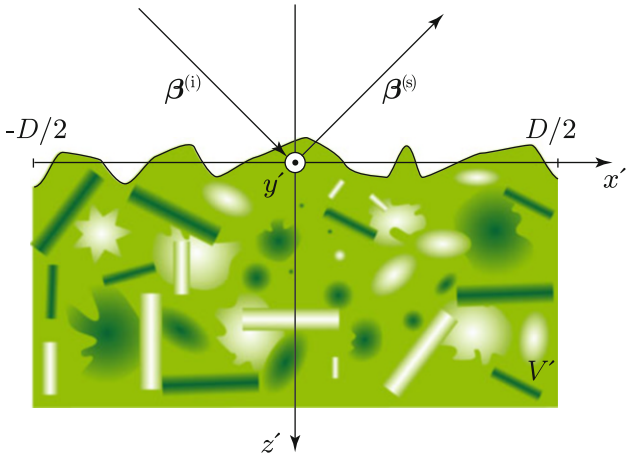

Fig. 7.29 The volume V' of a resolution cell of dimension D generally contains a high number of dielectric inhomogeneities, represented by the *shades of green*

and microscopic scales. As a few examples of *macroscopic* inhomogeneities, it is readily realized that within the resolution cell of many Earth observing systems:

- the volume of a forest stand contains numerous leaves, twigs and thin branches;
- the rippled surface of a water body is formed by many random undulations;
- bare terrain consists of a quite large number of inhomogeneities corresponding to granular material, embedded small stones and fragments of remaining vegetation;
- a volume of turbid air contains many water droplets or aerosol particles.

On the other side, at *microscopic* scales, i.e., at scales comparable to optical wavelengths, most surfaces are rough and almost any natural material is inhomogeneous. Therefore, given the decay of the autocorrelation function over distances corresponding to the dimensions of the inhomogeneities, the condition $r_\epsilon \ll D$ is frequently met both in optical and microwave observations.

In practice, the decreasing shape of the autocorrelation function implies that negligible contribution to the scattered power comes from pairs of scattering elements which are located beyond a threshold mutual distance, so that S'_r in (7.50) can be extended to infinity without appreciably changing the value of the angular power density:

$$\left\langle \mathcal{P}'^{(\mathrm{s})} \right\rangle \simeq \frac{\kappa_0^4}{16\,\pi^2}\,\overline{\mathcal{P}'_{\mathrm{o}}}\,Z_{\mathcal{P}}\,A_{\mathrm{S}} \int_{-\infty}^{\infty}\int_{-\infty}^{\infty} \mathcal{B}_{\epsilon\mathrm{t}}(r)\,\mathrm{e}^{-\mathrm{j}(\boldsymbol{\beta}_{\mathrm{t}}^{(\mathrm{i})} - \boldsymbol{\beta}_{\mathrm{t}}^{(\mathrm{s})})\cdot \boldsymbol{r}}\,\mathrm{d}r_y\,\mathrm{d}r_x\,. \tag{7.51}$$

Considering the resolution cell of infinite dimension leads to a quite important result, as far as scattering is concerned: the incoherently scattered power is proportional to the two-dimensional Fourier transform of the horizontal spatial correlation function of the permittivity fluctuations.

It is known that the Fourier transform of the correlation function $\mathcal{B}$ of a random variable yields the *spectral density* Ξ of this latter, in general defined in the bi-dimensional domain by

$$\Xi(\boldsymbol{\varkappa}) := \int_{-\infty}^{\infty}\int_{-\infty}^{\infty} \mathcal{B}(\boldsymbol{q})\mathrm{e}^{-\mathrm{j}\,\boldsymbol{\varkappa}\cdot\boldsymbol{q}}\,\mathrm{d}q_2\,\mathrm{d}q_1\ , \tag{7.52}$$

where $\boldsymbol{\varkappa}$ and $\boldsymbol{q}$ denote the pair of conjugate vector variables. By specializing definition (7.52) to Eq. (7.51), the incoherent scattered power is found to be proportional to the horizontal spatial spectral density $\mathcal{S}_{\epsilon\mathrm{t}}$ of the permittivity fluctuations [60, Chap.4]

$$\mathcal{S}_{\epsilon\mathrm{t}}(\boldsymbol{\kappa}_\mathrm{t}) = \int_{-\infty}^{\infty}\int_{-\infty}^{\infty} \mathcal{B}_{\epsilon\mathrm{t}}(\boldsymbol{r})\mathrm{e}^{-\mathrm{j}\,\boldsymbol{\kappa}_\mathrm{t}\cdot\boldsymbol{r}}\,\mathrm{d}r_y\,\mathrm{d}r_x \tag{7.53}$$

corresponding to the lateral component $\boldsymbol{\kappa}_\mathrm{t} = \boldsymbol{\beta}_\mathrm{t}^{(\mathrm{i})} - \boldsymbol{\beta}_\mathrm{t}^{(\mathrm{s})}$ of the *scattering vector* delineated in Fig. 7.30. In the considered model of scattering volume, the lateral component results from the difference between the horizontal component $\boldsymbol{\beta}_\mathrm{t}^{(\mathrm{i})}$ of the phase vector of the wave "refracted" into the average random medium[43] and the horizontal component $\boldsymbol{\beta}_\mathrm{t}^{(\mathrm{s})}$ of the phase vector in the scattering direction

$$\boldsymbol{\kappa}_\mathrm{t} = \boldsymbol{\beta}_\mathrm{t}^{(\mathrm{i})} - \boldsymbol{\beta}_\mathrm{t}^{(\mathrm{s})} = \kappa_0\left(\boldsymbol{r}_{0\mathrm{t}}^{(\mathrm{i})} - \boldsymbol{r}_{0\mathrm{t}}^{(\mathrm{s})}\right) = \kappa_0\left(\sin\theta^{(\mathrm{i})} - \sin\theta^{(\mathrm{s})}\right)\boldsymbol{r}_{0\mathrm{t}}^{(\mathrm{i})}\ .$$

Therefore,

- $\boldsymbol{\kappa}_\mathrm{t} = 0$ for scattering in the specular direction, since $\theta^{(\mathrm{s})} = \theta^{(\mathrm{i})}$;
- $\boldsymbol{\kappa}_\mathrm{t} = 2\kappa_0 \sin\theta^{(\mathrm{i})}\,\boldsymbol{r}_{0\mathrm{t}}^{(\mathrm{i})}$ for backscattering, because $\theta^{(\mathrm{s})} = \theta^{(\mathrm{i})}$; $\varphi^{(\mathrm{s})} = \varphi^{(\mathrm{i})} \pm \pi$.

Note that the factorization (7.45) of the autocorrelation function implies that the horizontal spectrum of the dielectric fluctuations is independent of depth.

The average angular power density scattered incoherently by a volume with random inhomogeneities of the dielectric constant is obtained by (7.51) in terms of the dielectric spectral density $\mathcal{S}_{\epsilon\mathrm{t}}$:

[43] As said, the results of Sect. 1.1.4.2 constrain the horizontal component of the refracted phase vector to be equal to that of the incident one.

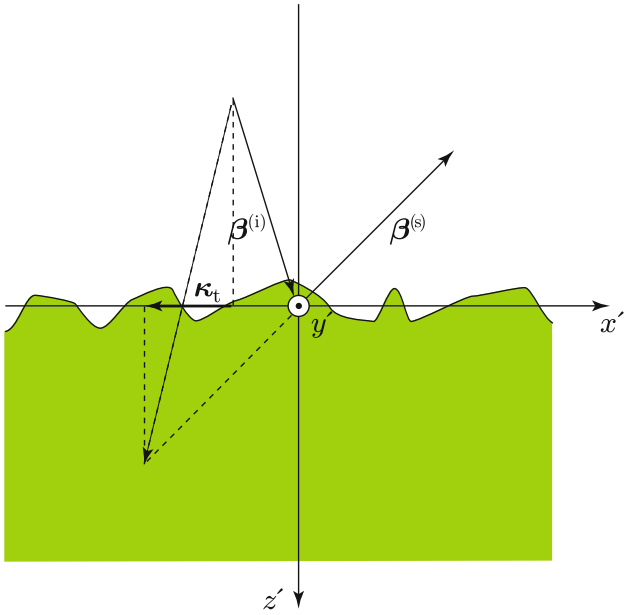

Fig. 7.30 The horizontal component of the scattering vector $\boldsymbol{\kappa}_{\mathrm{t}}$ derives from the difference $\boldsymbol{\beta}^{(\mathrm{i})} - \boldsymbol{\beta}^{(\mathrm{s})}$ of the phase vectors of incident and scattered waves

$$\left\langle \mathcal{P}'^{(\mathrm{s})} \right\rangle = \left(\frac{\pi}{\lambda_0^2} \right)^2 \overline{\mathcal{P}'_{\mathrm{o}}}\, Z_{\mathcal{P}}\, A_{\mathrm{S}}\, \mathcal{S}_{\epsilon \mathrm{t}}(\boldsymbol{\kappa}_{\mathrm{t}}) \ . \tag{7.54}$$

The basic relation (7.54) indicates that the scattering intensity is proportional to the horizontal spectral component of the dielectric fluctuations corresponding to $\boldsymbol{\kappa}_{\mathrm{t}}$. It means that the average scattered power originates from the spatial inhomogeneities having the periodicity corresponding to the difference between the horizontal components of the incident and scattered wave vectors. The frequency and the incidence and scattering directions select the appropriate spatial period of the random permittivity variations which originates the scattered power. This latter is proportional to the magnitude of the variations that occur, on average, at that particular horizontal periodicity. In case the inhomogeneities result from discrete objects, the magnitude of the selected spectral component depends on the characteristic dimension of the scatterers, as well as on their spatial arrangement, in particular on their horizontal distance.

The effect of the spatial periodicity is consistent with the mechanisms affecting the radiation from extended sources. In fact, the contributions from the re-radiating source currents (7.4) associated with the spatial variations of permittivity add in phase statistically when the path lengths satisfy the conditions for constructive interference discussed in Sect. 3.1.2. These conditions take also into account the phase of $\boldsymbol{J}_{\mathrm{ob}}$, which is determined by the phase of the inner field in correspondence

of the spatial structure of the random permittivity. However, it is important to note a substantial difference between the coherent and the incoherent scattered power. The intensity of coherent scattering is proportional to the *square* of the modulus of the scattering function given by (7.32) in terms of the *known* $\overline{\Delta\tilde{\epsilon}}$ and of the scattering volume, taking due account of the phase of the inner field. Instead, the incoherent intensity (7.50) is proportional to the autocorrelation of the *random* $\Delta\tilde{\epsilon}'$ and to the scattering volume, in place, coarsely speaking, of the *square* of this latter. Because of this feature, coherent scattering from large objects is expected to exceed their incoherent scattering. It is also realized that the phase of the inner field is destroyed by the incoherent scattering mechanism expressed by (7.43) and does not affect the scattered power, clearly apart from the underlying randomly constructive interference mentioned above.

In the considered case of isotropic random inhomogeneities, the lateral spectrum $\mathcal{S}_{\epsilon t}$ of the horizontal permittivity fluctuations

$$\mathcal{S}_{\epsilon t}(\varkappa) = \int_{-\infty}^{\infty}\int_{-\infty}^{\infty} \mathcal{B}_{\epsilon t}(r)\, \mathrm{e}^{-\mathrm{j}(\varkappa_x r_x + \varkappa_y r_y)}\, \mathrm{d}r_y\, \mathrm{d}r_x$$

depends only on the magnitude of the angular wavenumber $\varkappa = (2\pi)/\Lambda$ corresponding to the spatial period Λ of the harmonic of the horizontal dielectric fluctuations. The autocorrelation functions characterizing the random permittivity of natural media are frequently represented by exponential or Gaussian[44] functions: in case the normalized horizontal (lateral) covariance is Gaussian,

$$\mathcal{B}_{\epsilon t}(r) = \mathrm{e}^{-(r/r_\epsilon)^2}\,. \tag{7.55}$$

The parameter r_ϵ is the previously introduced horizontal *correlation radius*, that measures the horizontal (or lateral) distance beyond which the dielectric fluctuations become uncorrelated. The spectral density of the inhomogeneities yielded by the one-dimensional Fourier transform of the Gaussian [8, Chap.8] autocorrelation function (7.55) is

$$\mathcal{S}_{\epsilon t}(\varkappa) = \sqrt{\pi}\, r_\epsilon\, \mathrm{e}^{-(\varkappa r_\epsilon/2)^2}\,. \tag{7.56}$$

The spectral density is in turn Gaussian, with the magnitude of the spectral components which decreases with increasing spatial angular wavenumber $\varkappa$. Figure 7.31 shows examples of two pairs of autocorrelation functions and corresponding spectra. The *width of the spectrum*, conventionally set by the *cut-off angular wavenumber* $\varkappa_\epsilon = 2/r_\epsilon$, is a measure of the range of harmonic components contained in the permittivity fluctuations: in this case, the harmonics having $\varkappa < \varkappa_\epsilon$, i.e., having

[44]Further details on the relation between dimension of scatterers and permittivity spectrum are outlined in Sect. 9.1.

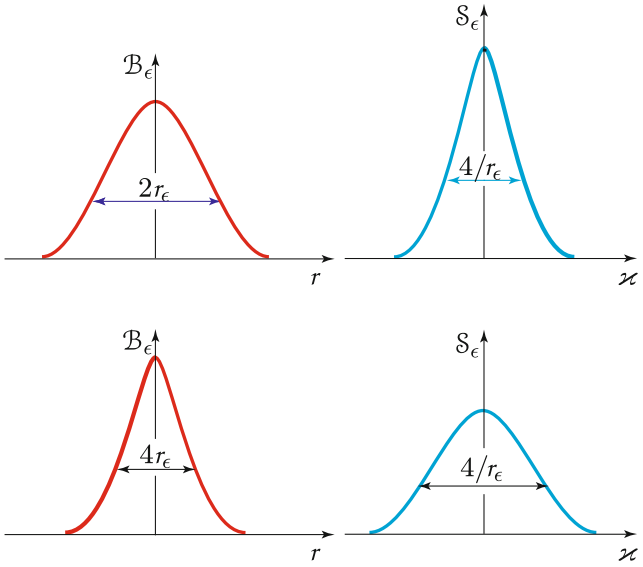

Fig. 7.31 Gaussian autocorrelation functions $\mathcal{B}_\epsilon(r)$ (*left*) and corresponding spectra $\mathcal{S}_\epsilon(\varkappa)$ (*right*). The parameters of the Gaussian curves demonstrate the inverse relation between width of autocorrelation and width of spectrum: the wider autocorrelation function (*top left*) corresponds to a narrower and higher spectrum, and vice-versa (*bottom*), as found for the discrete scatterers in Fig. 7.32

spatial period $\Lambda > \pi r_\epsilon$, mainly determine the dielectric structure. Note also that the amplitude of the spectrum is proportional to r_ϵ, which corresponds to the characteristic dimension of the dielectric inhomogeneities.

To clarify the relation between the discrete approach such as the one followed in Sect. 7.4.1 to characterize the scattering from canopies of random scatterers and the present continuous model expressed by (7.43), consider the line of dielectric elements in Fig. 7.32a.

The corresponding diagram of the random deviation $\Delta\tilde{\epsilon}'$ of the relative permittivity from its average $\overline{\Delta\tilde{\epsilon}}$ is shown in Fig. 7.32b. It is known [35, Chap. 2] that the autocorrelation function of such a rectangular random pulse train [70], satisfying suitable constraints,[45] is the triangular function of Fig. 7.32c, and that the power spectrum is the (sinc^2)-function represented in Fig. 7.32d. The shape of the autocorrelation $\mathcal{B}_\epsilon(r)$ indicates that the variations of permittivity are decorrelated at distances r larger than the dimension D of the scatterers, or, rather, that appreciable correlation exists only within a correlation distance[46] r_ϵ that is a fraction

[45] In particular, the dielectric elements should be sparse, rather than closely packed as, because of the layout requirements, they are represented in Fig. 7.32.

[46] The choice of r_ϵ is clearly subject to some degree of arbitrariness.

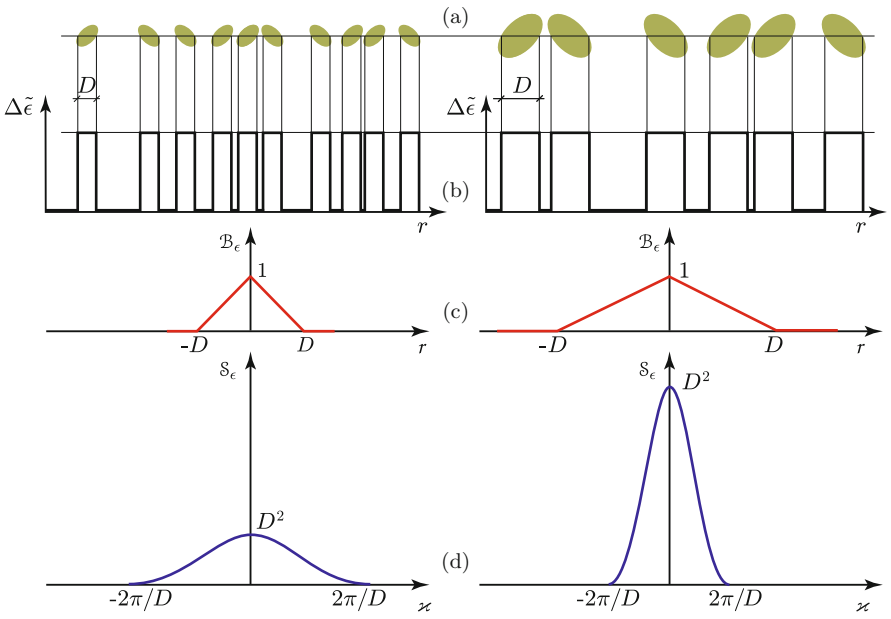

Fig. 7.32 Row of randomly located discrete scatterers (**a**), spatial distribution of permittivity (**b**), autocorrelation function (**c**), and spectrum (**d**); the same quantities are displayed for equal discrete scatterers with two different dimensions. The diagrams suggest the inverse relation between scatterer dimension D and width of spectrum: the wider autocorrelation function of the larger elements corresponds to the narrower and higher spectrum, and vice-versa. Note the similarity of the shape of the spectrum, expressed in this case by the (sinc^2)-function (cf. Sect. 11.3.1.2), to a Gaussian (Fig. 7.31) in the neighborhood of the origin of $\varkappa$

of D. In turn, the shape of the spectrum $\mathcal{S}_\epsilon$, decreasing with the wavenumber $\varkappa$, can be characterized by a width $\varkappa_\epsilon$ which is inversely proportional to the dimension D of the scatterers. Figure 7.32 depicts the same quantities for two different D: comparing the left with the right part of the figure makes apparent how the increased correlation distance is accompanied by the corresponding narrowing of the spectrum, i.e., by the decrease of the minimum spatial period of the harmonics present in the dielectric structure.

The assembly of scatterers to which the results schematized in Fig. 7.32 refer is obviously unrealistic, since a variety of dimensions and of permittivity values, possibly mixed with continuous variations, are expected in an actual terrestrial scenario [79]. However, the basic concepts and trends of the involved relations hold in general [16]. Moreover, the Gaussian model introduced previously for the autocorrelation function and spectral density is a suitable approximation frequently adopted to represent the three-dimensional dielectric structure of real environments.

The conclusions that are drawn from (7.55) and (7.56) and that, after all, are suitable for a first understanding of the scattering process,[47] are the following.

- For a given variance of permittivity fluctuations, the wider are the inhomogeneities, the larger is the magnitude of the spectrum.
- The inverse relation between the correlation radius and the cut-off wavenumber indicates that:
  - fine-scale irregularities, hence with small correlation lengths, have wide spectra, with large cut-off wavenumbers;
  - instead, irregularities with large dimensions, hence with large correlation lengths, have narrow spectra, with small cut-off wavenumbers.

In the scattering process described by (7.53), the condition

$$\varkappa = \kappa_{\mathrm{t}} \,.$$

means that the combinations of electromagnetic wavelength and of incidence and scattering angles, which determine κ_{t}, select the corresponding spatial wavenumber $\varkappa$ of the permittivity spectrum. This implies that the incoherently scattered power originates essentially from the inhomogeneities having the dimensions selected by the observational parameters (frequency and geometry). In particular, the angular power density (7.54) is expressed in terms of incidence and scattering angles[48] by

$$\left\langle \mathcal{P}'^{(\mathrm{s})}\left(\theta^{(\mathrm{i})},\, \theta^{(\mathrm{s})}\right)\right\rangle = \left(\frac{\pi}{\lambda_0^2}\right)^2 \overline{\mathcal{P}'_{\mathrm{o}}}\, Z_{\mathcal{P}}\, A_{\mathrm{S}}\, \mathcal{S}_{\epsilon\mathrm{t}} \left[\frac{2\pi}{\lambda_0}\left(\sin\theta^{(\mathrm{i})} - \sin\theta^{(\mathrm{s})}\right)\right] \cdot \tag{7.57}$$

The general trends of the incoherent scattering intensity are then summarized taking account of (7.57) and of the preceding considerations:

- scattering decreases with decreasing size of dielectric inhomogeneities, since the amplitude of the spectrum depends directly on τ_ϵ;
- small irregularities, with wide spectrum, spread the scattered power broadly in angle;
- large irregularities, with narrow spectrum, tend to concentrate scattering in the neighborhood of the specular direction;
- scattering at relatively large electromagnetic wavelengths is contributed by correspondingly large irregularities,
- whereas small irregularities contribute to scattering at small wavelengths.

[47] From the physical point of view, the re-radiating current (7.4) exists only in limited regions of space in case of discrete scatterers (e.g., leaves, rain drops), while it is distributed in the scattering volume in case of continuous material (e.g., terrain with moisture inhomogeneities). The unified approach based on the correlation function has the advantage of modeling in a simple fashion some qualitative features of scattering that both cases have in common.

[48] Here scattering is considered in the incidence $(x\,z)$-plane.

The relations between magnitude of scattering and dimensions of dielectric inhomogeneities allow some broad final conclusions on the role of the particular range of electromagnetic spectrum at which the scattering images are acquired:

- microscopic irregularities do not scatter at microwaves;
- rather, they are responsible for scattering in the optical spectral range;
- irregularities of centimeter or decimeter size are responsible for incoherent scattering at microwaves;
- at these frequencies, larger inhomogeneities tend to behave like single scatterers when the dimension of the resolution cell decreases, so that their scattering features can be interpreted on a deterministic basis (cf. Sect. 7.3).

Some qualitative consideration can be finally added relative to the consistency of the spectral approach with the one followed in Sect. 7.3.3 to relate the roughness of a surface to its reflection. Decreasing the thickness d of the rough boundary layer increases the low-spatial frequency components of the spectrum, thus enhances the specular reflection, for which $\boldsymbol{\kappa}_t = 0$. The decrease of the power scattered in the backward (for oblique incidence) direction correspondingly accompanies the depletion of the higher-wavenumber portion of the spectrum. More interpretive details on this issue are provided in Sect. 13.1.1.

7.4.5 *Scattering from Periodic Structures*

Although randomness prevails in several terrestrial environment, it is ordinary experience that spatial periodicity is not uncommon in some of them. Figure 7.33 suggests that this is generally the case of water surfaces, but that it is also frequently encountered in agricultural scenarios. An ensemble of dielectric structures which are periodic in the horizontal plane, such as sea waves or rows of agricultural crops, has harmonic components the magnitude of which peaks at the horizontal wavenumbers corresponding to the spatial periods of the dielectric variations. Indeed, the one-dimensional autocorrelation function of dielectric random fluctuations with embedded periodicity is suitably modeled by the periodic function enveloped by the Gaussian (7.55) shown in Fig. 7.34 and given by

$$\mathcal{B}_{\epsilon t}(r) = \mathrm{e}^{-(r/r_\epsilon)^2} \cos(K_0 r) \ . \tag{7.58}$$

The parameter $K_0 = (2\pi)/\Lambda_0$ in (7.58) is the angular wavenumber corresponding to the spatial period Λ_0 of the dielectric variations, e.g., of the water waves or of the crop rows. The spectral density corresponding to the autocorrelation (7.58) is known to be

$$\mathcal{S}_{\epsilon t}(\varkappa) = \sqrt{\pi}\, r_\epsilon \left\{ \mathrm{e}^{-[(\varkappa - K_0)\, r_\epsilon/2]^2} + \mathrm{e}^{-[(\varkappa + K_0)\, r_\epsilon/2]^2} \right\} . \tag{7.59}$$

Fig. 7.33 Water surfaces (*top*) and cultivated fields frequently show periodic patterns (Image of vineyard in the Tor Vergata – Frascati test area, courtesy A. Burini)

As sketched in Fig. 7.35, the spectrum (7.59) peaks at the angular wavenumbers

$$\varkappa = \pm K_0 = \pm \frac{2\pi}{\Lambda_0} \cdot$$

Correspondingly, the scattered power is expected to peak when the frequency of the electromagnetic wave and the observation geometry are such that the lateral component of the scattering vector matches the spatial periodicity of the dielectric structure, that is, with reference to the elevation angles and in the local incidence plane,

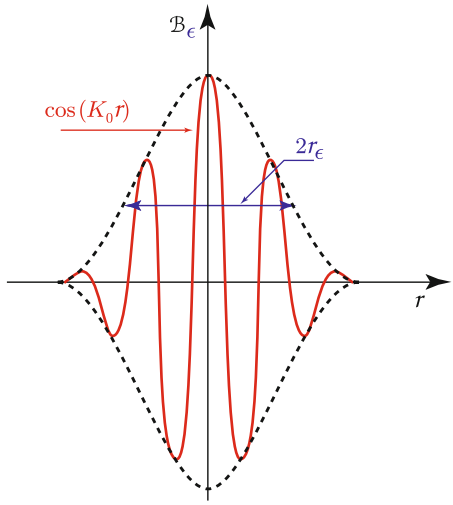

Fig. 7.34 The auto-correlation function of random fluctuations with embedded periodicity is suitably modeled by a circular function enveloped by a Gaussian

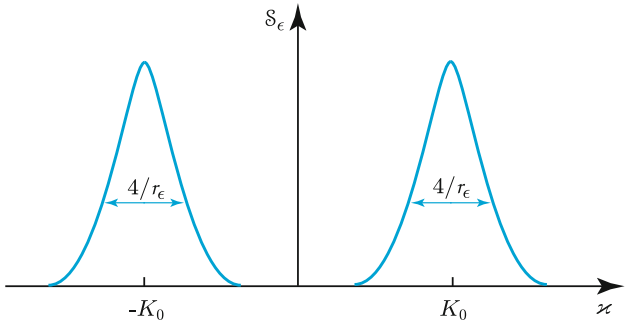

Fig. 7.35 The spectrum of a partially coherent periodic function with Gaussian-envelop auto-correlation such as in Fig. 7.34, is composed of two portions, peaked on the wavenumbers $\varkappa = \pm K_0 = \pm 2\pi/\Lambda_0$ and having width determined by the distance r_ϵ over which the periodic component keeps its coherence

$$\kappa_t = \frac{2\pi}{\lambda_0}\left(\sin\theta^{(i)} - \sin\theta^{(s)}\right) = \pm K_0 = \pm\frac{2\pi}{\Lambda_0}\,. \tag{7.60}$$

Equation (7.60) translates into the condition[49]

$$\sin\theta^{(s)} = \sin\theta^{(i)} \pm \frac{\lambda_0}{\Lambda_0}\,.$$

[49]Wavelength and spatial periodicity are such that $\left|\sin\theta^{(s)}\right| \leq 1$.

Therefore, peaks of intensity occur in the backward and forward directions, provided the observation is carried out at wavelength λ_0 and incidence angle $\theta^{(\mathrm{i})}$ compatible with the spatial periodicity of the surface. In particular, the peak of backscattered power occurs when the *Bragg condition*[50]

$$\sin\theta^{(\mathrm{i})} = \frac{\lambda_0}{2\Lambda_0}$$

is satisfied.[51] Note that the electromagnetic wavelength yielding the peak of backscattering is of the order of the spatial periodicity of the observed surface, for instance, in case of water, of the gravity-capillary waves. This implies that, for an incidence angle $\theta^{(\mathrm{i})} \approx 30°$, $\lambda_0 \approx \Lambda_0$, which means that the radar must operate in the centimeter to decimeter wavelength range to effectively observe the backscattering from these waves, as detailed in Sect. 14.2.2.

7.4.6 *Effect of Sub-surface Structure*

The effect of the vertical structure of the dielectric inhomogeneities on scattering is expressed by the factor $Z_{\mathcal{P}}$ in (7.49), representing the sub-surface[52] contributions in (7.47):

$$Z_{\mathcal{P}} = \int_0^d \mathrm{d}z_1' \int_0^d \mathrm{d}z_2'\, \sigma_\epsilon^2(z_1', z_2')\, \mathcal{B}_{\epsilon z}(z_1', z_2')\, \mathrm{e}^{-(\alpha'+\alpha'')(z_1'+z_2')}\, \mathrm{e}^{-\mathrm{j}(\beta_z' - \beta_z'')(z_1' - z_2')} .$$

The vertical dielectric structure affects the incoherent scattering intensity according to

- the magnitude of the permittivity fluctuations, expressed by the covariance σ_ϵ^2, function of depth
- and the vertical spatial distribution of inhomogeneities, described by the autocorrelation function $\mathcal{B}_{\epsilon z}$.

Given the assumed factorized form (7.45) of the autocovariance function of $\tilde{\epsilon}'$ and consistently with the assumptions for the horizontal factor $\mathcal{B}_{\boldsymbol{\epsilon t}}$, the intensity σ_ϵ^2 of the permittivity fluctuations is reasonably assumed to depend on the average depth, i.e.

$$\sigma_\epsilon^2(z_1', z_2') = \sigma_\epsilon^2\left(\frac{z_1' + z_2'}{2}\right) ,$$

[50] Further discussion on this issue is postponed to Sect. 13.1.1.2.2.

[51] The direction of backscattering is identified by $\theta^{(\mathrm{s})} = -\theta^{(\mathrm{i})}$, since in the plane of incidence reference is made to the elevation angle only.

[52] Here "sub-surface" indicates the region $z' > 0$ of Fig. 7.28: according to the location of the reference ($z' = 0$)-plane, it may correspond to the terrain below the average soil surface, or to the vegetation below its top canopy level (cf. Fig. 14.4), etc.

while the vertical correlation $\mathcal{B}_{\epsilon Z}$ depends on the vertical distance between pairs of points

$$\mathcal{B}_{\epsilon z}(z_1', z_2') = \mathcal{B}_{\epsilon z}(|z_1' - z_2'|) \, .$$

Both σ_ϵ^2 and $\mathcal{B}_{\epsilon Z}$ clearly affect the scattered angular power, since (7.57) contains the factor

$$\begin{aligned} Z_{\mathcal{P}} \; &= \int_0^d \int_0^d \sigma_\epsilon^2 \left(\frac{z_1' + z_2'}{2} \right) \mathcal{B}_{\epsilon z}(|z_1' - z_2'|) \, \mathrm{e}^{-(\alpha' + \alpha'')(z_1' + z_2')} \\ &\quad \times \mathrm{e}^{-\mathrm{j}(\beta_z' - \beta_z'')(z_1' - z_2')} \, \mathrm{d}z_2' \, \mathrm{d}z_1' \, . \end{aligned}$$

A suitable transformation of vertical coordinates [59, Chap. 4],

$$\varsigma_{12} = z_1' - z_2'; \qquad z_{12} = \frac{z_1' + z_2'}{2} \, ,$$

transforms the z_1', z_2' domain of integration into the rhombus of Fig. 7.36 in the $(\varsigma_{12}\, z_{12})$-plane. Then, some algebra yields:

$$\begin{aligned} Z_{\mathcal{P}} = &\int_{-d}^{0} \int_{-\frac{\varsigma_{12}}{2}}^{d+\frac{\varsigma_{12}}{2}} \sigma_\epsilon^2(z_{12}) \, \mathrm{e}^{-2(\alpha' + \alpha'')z_{12}} \, \mathcal{B}_{\epsilon z}(|\varsigma_{12}|) \, \mathrm{e}^{-\mathrm{j}(\beta_z' - \beta_z'')\varsigma_{12}} \, \mathrm{d}z_{12} \, \mathrm{d}\varsigma_{12} \\ + &\int_{0}^{d} \int_{\frac{\varsigma_{12}}{2}}^{d-\frac{\varsigma_{12}}{2}} \sigma_\epsilon^2(z_{12}) \, \mathrm{e}^{-2(\alpha' + \alpha'')z_{12}} \, \mathcal{B}_{\epsilon z}(|\varsigma_{12}|) \, \mathrm{e}^{-\mathrm{j}(\beta_z' - \beta_z'')\varsigma_{12}} \, \mathrm{d}z_{12} \, \mathrm{d}\varsigma_{12} \, . \end{aligned} \tag{7.61}$$

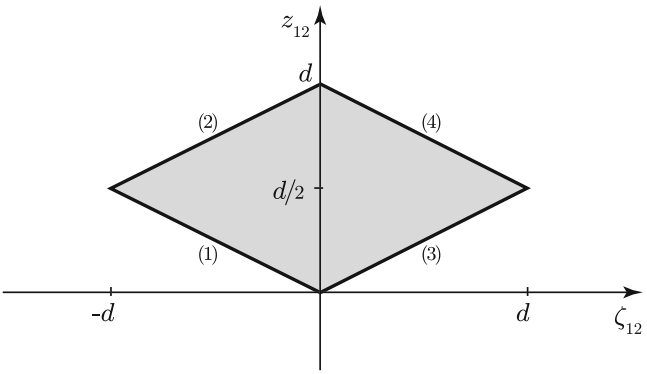

Fig. 7.36 The *gray area* represents the domain of double integration in the vertical direction; d is the thickness of the scattering volume sketched in Fig. 7.28

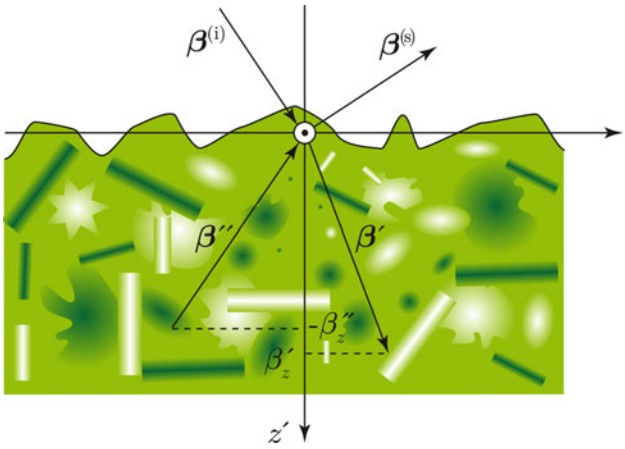

Fig. 7.37 The wave incident with phase vector $\boldsymbol{\beta}^{(i)}$ is refracted into the average-permittivity volume and travels downward with phase vector $\boldsymbol{\beta}'$; the wave originating from the inhomogeneities travels upward with phase vector $\boldsymbol{\beta}''$ and gives origin to the scattered wave with phase vector $\boldsymbol{\beta}^{(s)}$ towards the sensor. No total reflection is assumed to occur

In Eq. (7.61) β_z' and β_z'' are the vertical components of the phase vectors of the downward (refracted) and upward scattered wave, as sketched in Fig. 7.37. The corresponding attenuation constants are α' and α'' respectively. When the material has a dielectric structure that is statistically homogeneous in the vertical direction, σ_ϵ^2 is independent of depth and (7.61) simplifies into

$$
\begin{aligned}
Z_{\mathcal{P}} = \frac{\sigma_\epsilon^2}{\alpha' + \alpha''} \Bigg\{ & \int_0^d \mathcal{B}_{\epsilon z}(\varsigma_{12})\, \mathrm{e}^{-2(\alpha' + \alpha'')\varsigma_{12}} \cos\left[\left(\beta_z' - \beta_z''\right)\varsigma_{12}\right] \mathrm{d}\varsigma_{12} \\
& - \int_0^d \mathcal{B}_{\epsilon z}(\varsigma_{12})\, \mathrm{e}^{-2(\alpha' + \alpha'')(d - \varsigma_{12})} \cos\left[\left(\beta_z' - \beta_z''\right)\varsigma_{12}\right] \mathrm{d}\varsigma_{12} \Bigg\} \qquad (7.62) \\
= \sigma_\epsilon^2 \frac{1 - \mathrm{e}^{-2(\alpha' + \alpha'')d}}{\alpha' + \alpha''} & \int_0^d \mathcal{B}_{\epsilon z}(\varsigma_{12}) \mathrm{e}^{-2(\alpha' + \alpha'')\varsigma_{12}} \cos\left[\left(\beta_z' - \beta_z''\right)\varsigma_{12}\right] \mathrm{d}\varsigma_{12} \,.
\end{aligned}
$$

The *vertical* factor $Z_{\mathcal{P}}$ that affects (7.57), which represents the intensity maps produced by monostatic imaging radars,[53] is readily obtained by setting

$$
\beta_z'' = -\beta_z' \equiv \beta_z; \qquad \alpha' = \alpha'' \equiv \alpha \,,
$$

[53] Apart from possible flash-point reflections.

so that (7.62) becomes

$$Z_{\mathcal{P}}\left(\theta^{(\mathrm{i})}, -\theta^{(\mathrm{i})}\right) = \sigma_{\epsilon}^{2}\,\frac{1-\mathrm{e}^{-4\alpha d}}{2\alpha}\int_{0}^{d}\mathcal{B}_{\epsilon z}(\varsigma_{12})\,\mathrm{e}^{-4\alpha\varsigma_{12}}\,\cos(2\beta_{z}\varsigma_{12})\,\mathrm{d}\varsigma_{12}\,. \tag{7.63}$$

Note that this result holds also for *quasi-monostatic* measurements, i.e., when

$$\beta_{z}'' \approx -\beta_{z}'; \qquad \alpha' \approx \alpha''\,,$$

as is the case for SAR missions of the type **T**erraSAR-X **a**dd-o**n** for **D**igital **E**levation **M**easurement (TanDEM) [67], which utilize platforms at very close observing locations.

Expression (7.63) highlights the effect of the vertical dielectric structure and of the observation parameters on the incoherently scattered power. In short summary, the backscattering intensity

- is proportional to the magnitude of the dielectric fluctuations, expressed by the variance σ_{ϵ}^{2};
- depends on the attenuation of the incident and scattered inner waves caused by the material;
- is affected by vertical dimensions of the inhomogeneities expressed by the autocovariance $\mathcal{B}_{\epsilon z}$, as previously discussed;
- depends on wavelength and local incidence angle, which affect the vertical component of the phase constant β_{z}.

It has to be mentioned that the effects of the various parameters are interrelated and difficult to single out, although some trends can be identified to facilitate the interpretation of the backscattering images.

7.4.7 Surface and Volume Scattering

The expected angular power density scattered by the observed portion of the Earth's environment is obtained by averaging (7.28):

$$\left\langle \mathcal{P}^{(\mathrm{s})}\right\rangle = \mathcal{P}_{\mathrm{c}}^{(\mathrm{s})} + \left\langle \mathcal{P}'^{(\mathrm{s})}\right\rangle .$$

The coherent component derives from the diffraction, often tied with reflection, by the average dielectric structure of the volume corresponding to the resolution cell, as discussed in Sect. 7.3. Since the coherent power density typically peaks in the specular direction (cf. Sect. 7.3.1.2), it does not contribute appreciably to monostatic or quasi-monostatic observations that are carried out at definitely *oblique* incidence, except that for particular geometries of the target, such as the corner reflectors considered in Sect. 6.6.

The incoherent component, given by (7.54), depends both on the horizontal and on the vertical structure of the fluctuations of permittivity about its average value. The results obtained by the model outlined in the previous sections apply, clearly provided the observed inhomogeneous material satisfies the relevant assumptions. It is worth pointing out that the quantities that affect scattering, i.e., magnitude and autocorrelation function of the dielectric inhomogeneities, as well as attenuation and phase constants, often have distinct characteristics at different depths inside V', according to the nature of the observed scenario. Therefore, to approach the local character of approximately horizontal statistical homogeneity, V' is suitably modeled by layers composed of the same materials and with similar structure.

In the simple case of a bare natural surface, two regions are readily identified: the surface layer and the bulk.[54] The contributions to backscattering for oblique observation are separated according to the depth of the region from which they originate:

$$\left\langle \mathcal{P}'^{(\mathrm{s})}\left(\theta^{(\mathrm{i})}, -\theta^{(\mathrm{i})}\right)\right\rangle \simeq \left\langle \mathcal{P}'^{(\mathrm{s})}\right\rangle = \left\langle \mathcal{P}_{\mathrm{s}}'^{(\mathrm{s})}\right\rangle + \left\langle \mathcal{P}_{\mathrm{b}}'^{(\mathrm{s})}\right\rangle ,$$

where $\left\langle \mathcal{P}_{\mathrm{s}}'^{(\mathrm{s})}\right\rangle$ is the contribution from the surface layer, that is, from the air-to-material transition layer, while $\left\langle \mathcal{P}_{\mathrm{b}}'^{(\mathrm{s})}\right\rangle$ originates from the bulk, i.e., from the sub-surface region. This model results in subdividing the domain of integration over the vertical (or longitudinal) coordinate z' into the two sub-domains indicated in Fig. 7.38. The first extends from the highest level at which the volume V' begins, assumed as the reference $z' = 0$, to the depth $z' = d_{\mathrm{s}}$ at which the bulk material

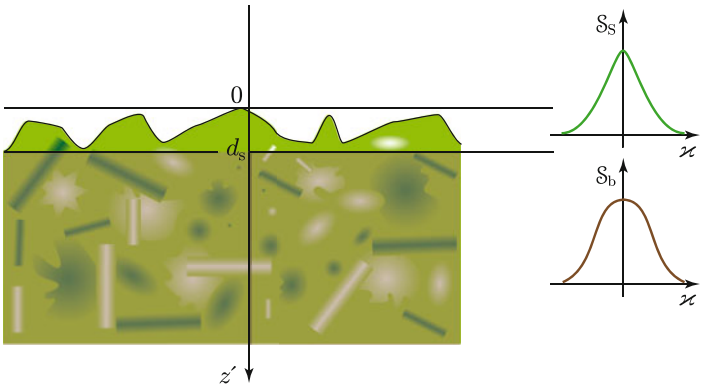

Fig. 7.38 The scattering volume is subdivided vertically into the surface layer, extending over the depth interval $0 < z' < d_{\mathrm{s}}$ (cf. Fig. 7.12), and the bulk for $z' > d_{\mathrm{s}}$. The lateral spectrum of dielectric inhomogeneities in the surface layer ($\mathcal{S}_{\mathrm{s}}$, *top right*) is generally different from the one in the bulk ($\mathcal{S}_{\mathrm{b}}$, *bottom right*)

[54] The model is consistent with the one introduced in Sect. 7.3.3.

begins, the second from $z' = d_\mathrm{S}$ to the total thickness d of the scattering volume, which possibly extends to infinity.[55] The backscattered power is contributed by the two terms that are derived from (7.57) after splitting the integral of (7.62) and relating the inner power to the incident one

$$\left\langle \mathcal{P}^{(\mathrm{s})}\left(\theta^{(\mathrm{i})}, -\theta^{(\mathrm{i})}\right)\right\rangle \simeq \left(\frac{\pi}{\lambda_0^2}\right)^2 \cos\theta^{(\mathrm{i})} \left[Z_{\mathcal{P}\mathrm{S}}\, \mathcal{S}_{\epsilon\mathrm{ts}}\left(\frac{4\pi}{\lambda_0}\sin\theta^{(\mathrm{i})}\right) + \mathrm{e}^{-2\alpha_\mathrm{S} d_\mathrm{S}}\, Z_{\mathcal{P}\mathrm{b}} \mathcal{S}_{\epsilon\mathrm{tb}}\left(\frac{4\pi}{\lambda_0}\sin\theta^{(\mathrm{i})}\right)\right] A_\mathrm{S}\,(1-\mathcal{R}_\mathrm{c})\,\mathcal{P}^{(\mathrm{i})}\,, \tag{7.64}$$

where $\mathcal{R}_\mathrm{c}$ is the (coherent) local power reflection coefficient for the average dielectric structure of V'. Note how the second term, which expresses the backscattering intensity contributed by the bulk, is reduced by the power transmission coefficient $1-\mathcal{R}_\mathrm{c}$ of the interface between air and average material. This factor takes account of the power reflected in the specular direction, hence unavailable to the backward scattering from the sub-surface material.

Inspection of (7.64) indicates that the contribution to the backscattering originating from the surface layer is proportional to the lateral spectrum of permittivity $\mathcal{S}_{\epsilon\mathrm{ts}}$ characterizing the surface roughness[56] features, weighted by the vertical factor $Z_{\mathcal{P}\mathrm{S}}$ for the surface layer, given by

$$Z_{\mathcal{P}\mathrm{S}} = \sigma_{\epsilon\mathrm{S}}^2\, \frac{1-\mathrm{e}^{-4\alpha_\mathrm{S} d_\mathrm{S}}}{2\alpha_\mathrm{S}} \int_0^{d_\mathrm{S}} \mathcal{B}_{\epsilon z\mathrm{S}}(\varsigma_{12})\, \mathrm{e}^{-4\alpha_\mathrm{S}\varsigma_{12}}\, \cos(2\beta_{z\mathrm{S}}\,\varsigma_{12})\, \mathrm{d}\varsigma_{12}\,,$$

in which the subscript $_\mathrm{S}$ denotes the quantities relative to the surface layer. The weight $Z_{\mathcal{P}\mathrm{S}}$ that controls the intensity of the backscattering from the surface layer

- is proportional to the variance of permittivity $\sigma_{\epsilon\mathrm{S}}^2$, hence, for given spatial structure of inhomogeneities, it is expected to increase with increasing overall permittivity;
- for given $\sigma_{\epsilon\mathrm{S}}^2$, it increases with thickness d_S, hence with surface roughness;
- decreases with increasing attenuation, which quenches the deeper source currents.

In turn, the power contributed by the sub-surface material is proportional to the lateral spectrum $\mathcal{S}_{\epsilon\mathrm{tb}}$ of permittivity weighted by the bulk vertical factor $Z_{\mathcal{P}\mathrm{b}}$ as for

[55] More than two layers may be required by more complex scenarios, such as, for instance terrain covered with vegetation or snow. Chapter 14 outlines some relevant examples.

[56] In case of vegetation cover, $\mathcal{S}_{\epsilon\mathrm{ts}}$ can be regarded as the lateral spectrum of the permittivity fluctuations in the plant canopy. Then, the re-definition of the bulk material is clearly needed.

the surface layer, but with a major difference. In fact, it is reduced by the attenuation factor $\mathrm{e}^{-2\alpha_\mathrm{s} d_\mathrm{s}}$ introduced by the overlying surface layer. The bulk vertical factor is given by

$$Z_{\mathcal{P}\mathrm{b}} = \frac{\sigma^2_{\epsilon\mathrm{b}}}{2\alpha_\mathrm{b}} \int_{d_\mathrm{s}}^{\infty} \mathcal{B}_{\epsilon\mathrm{zb}}(\zeta_{12})\, \mathrm{e}^{-4\alpha_\mathrm{b}\zeta_{12}}\, \cos(2\beta_{\mathrm{zb}}\,\zeta_{12})\, \mathrm{d}\zeta_{12}\ ,$$

where now the subscript $_\mathrm{b}$ denotes the quantities relative to the bulk material.

The two terms contributing the total backscattering intensity (7.64) respectively represent the *surface scattering* and the *volume scattering* discussed in more detail in Sect. 13.1. Both are generally present and add incoherently, but either one or the other may prevail when observing a given target, according to the observational parameters. In case the bulk material is sufficiently homogeneous so that

$$\sigma^2_{\epsilon\mathrm{b}}\, \mathcal{S}_{\epsilon\mathrm{tb}} \ll \sigma^2_{\epsilon\mathrm{s}}\, \mathcal{S}_{\epsilon\mathrm{ts}}\ ,$$

scattering from the rough surface prevails. This is often the case of water or of uniform terrain, at microwaves. Then the model introduced in Sect. 7.3.3, which localizes the source of scattering only to the random air-matter interface, can be extended to incoherent scattering. The second term in (7.64) vanishes and the lateral spectrum of permittivity $\mathcal{S}_{\epsilon\mathrm{ts}}$ is directly related to the spectrum of roughness $\mathcal{S}_\mathfrak{z}$ of the surface. Surface scattering also prevails when, for comparable permittivity structures, attenuation and thickness of the surface layer are such that $\mathrm{e}^{-2\alpha_\mathrm{s} d_\mathrm{s}} \ll 1$. Coarsely speaking, given the analogous trend with attenuation of both surface and volume scattering, increasing attenuation decreases the depth from which the scattered power originates, thus making the contribution from the shallower layers to predominate.

On the contrary, for comparable variances and lateral spectra of permittivity, when the attenuation α_s is moderate and/or the surface layer is sufficiently thin so that $\alpha_\mathrm{s}\, d_\mathrm{s} \ll 1$, backscattering is mainly contributed by the bulk material. Vegetation canopies typically originate volume scattering since, on one side the dielectric inhomogeneities enhance with z' and, on the other, the air-material transition layer, located in the upper part of the canopy, has a sparse and relatively thin dielectric structure, with correspondingly low $Z_{\mathcal{P}\mathrm{S}}$.

As a general trend, volume backscattering is lower at more attenuated wavelengths. Indeed, increasing attenuation decreases the backscattered power because the incident internal field, hence the source of scattering, decreases with depth. Moreover, the amplitude of the internal scattered waves decreases while traveling upward. In optical observations, which exploit the scattering of the polychromatic solar radiation, samples of the spectrum of the scattered radiation are measured. The spectrum contains the imprinting by the material in the form of alternating strongly and weakly absorbed wavelength ranges, according to the features outlined in Sect. 2.2. The scattered power density is lower at the more absorbed wavelengths and has peaks at the less attenuated ones, thus originating

the *color* of the targets, as already observed in Sect. 6.5.2 for reflection. It can be anticipated that multi-spectral measurements of scattered solar radiation carry information on the dielectric spectrum, hence on the nature of the materials present in the scattering volume. This issue is detailed in Chap. 14 for relevant terrestrial environments.

7.4.7.1 Modeling the Backscattering Coefficient

By inserting the expression of the angular density of backscattered power into (7.17) and recalling definition (7.22), the backscattering coefficient σ^0 is finally obtained as a function of the material and observation parameters

$$\sigma^0 \simeq \pi \left(\frac{2\pi}{\lambda_0^2}\right)^2 (1-\mathcal{R}_c)\cos\theta^{(i)} \left[\sigma_{\epsilon s}^2 \frac{1-e^{-4\alpha_s d_s}}{2\alpha_s} \mathcal{S}_{\epsilon ts}\left(\frac{4\pi}{\lambda_0}\sin\theta^{(i)}\right) \right.$$
$$\int_0^{d_S} \mathcal{B}_{\epsilon zs}(\varsigma_{12})\, e^{-4\alpha_s \varsigma_{12}} \cos(2\beta_{zs}\,\varsigma_{12})\, d\varsigma_{12} + \sigma_{\epsilon b}^2 \frac{e^{-2\alpha_s d_s}}{2\alpha_b} \mathcal{S}_{\epsilon tb}\left(\frac{4\pi}{\lambda_0}\sin\theta^{(i)}\right)$$
$$\left. \int_{d_S}^{\infty} \mathcal{B}_{\epsilon zb}(\varsigma_{12})\, e^{-4\alpha_b \varsigma_{12}} \cos(2\beta_{zb}\,\varsigma_{12}) d\varsigma_{12} \right] . \tag{7.65}$$

It has to be pointed out that the backscattering coefficient defined by (7.22) as the cross-section per unit area is meaningful provided the power originated from the observed volume V' is mainly contributed by the incoherent mechanism described in Sect. 7.4.3. When this model holds, the power is proportional to the lateral area A_S of V', as given by (7.50). But, if a source of relatively high coherent backscattering is present in the resolution cell, $\mathcal{P}^{(s)}$ *is not proportional* to A_S and the concept underlying the definition itself fails.

Given the essential randomness of many natural materials at microscopic scale, coherent scattering does not occur at optical wavelengths with the exception of calm water surfaces, or particular man-made surfaces. The normalization of the scattered power with respect to the observed area is thus generally meaningful. Anyway, the definition of backscattering coefficient is limited to radar observation, although lidar measurements are based on analogous quantities.

7.4.7.2 Effect of Polarization

The polarization of the incident field affects several of the quantities in (7.65) on which the backscattered field depends [71, Chap. 3]. In particular, the scattering source current (7.4) is proportional to the field that penetrates into the average object. Since the reflection coefficient depends on polarization and, at least in

the geometrical optics approach, the results of Sect. 6.2.2 show that a horizontally polarized wave is reflected more than a vertically polarized one, i.e.,

$$\mathcal{R}_{\mathrm{ch}} > \mathcal{R}_{\mathrm{cv}} \ ,$$

the fraction of incident power density that interacts with the material is larger at vertical polarization than at horizontal. This implies that the incoherent scattering from a rough surface at vertical polarization is larger than at horizontal, as it is actually observed (cf. Sects. 13.1.1.2.1 and 14.1.2.1). The power scattered by the sub-surface dielectric inhomogeneities is correspondingly higher at vertical polarization, clearly provided that the permittivity structure is isotropic.

A second effect derives directly from the polarization of the inner field, which depends on the structure of the scatterer through the field transformation matrix $\langle[\mathbf{Q}]\rangle$ introduced in Sect. 7.1.2 and extended to the randomly inhomogeneous material. In the Jones formalism, the elements of

$$[\mathbf{Q}] = \begin{bmatrix} Q_{\mathrm{vv}} & Q_{\mathrm{vh}} \\ Q_{\mathrm{hv}} & Q_{\mathrm{hh}} \end{bmatrix}$$

depend on the geometry of the dielectric structure. In case of highly symmetric random inhomogeneities, for instance with nearly spherical patterns, the co-polar elements are close, whereas the cross-polar ones are relatively low, that is

$$Q_{\mathrm{vv}} \approx Q_{\mathrm{hh}}; \qquad Q_{\mathrm{hv}} = Q_{\mathrm{vh}} \ll Q_{\mathrm{vv}} \approx Q_{\mathrm{hh}} \ .$$

Then the scattering-source current tends to be parallel[57] to the incident field, hence co-polar scattering dominates. On the other side, increasing asymmetry of the dielectric structure enhances the cross-polar elements. As a result, cross-polarized scattering from the surface layer is low when the boundary is relatively smooth and increases with increasing roughness. Analogously, a lopsided random permittivity structure in the bulk material produces cross-polarization, as observed for the canopy of needles of Sect. 7.4.1.2.

Dielectric structures with preferential orientation behave differently according to the field polarization. Indeed, (7.10) indicates that only the component of $\boldsymbol{J}_{\mathrm{ob}}$ orthogonal to the direction of observation radiates effectively. Therefore, the dependence of the backscattering intensity on the direction is related to the magnitude of $\boldsymbol{E}_{\perp}$ that the incident field is able to create in the material, hence to the directional features of the dielectric structure characterizing the resolution cell. As usual, the discussion is limited to scattering in the $(x\,z)$-plane of incidence, i.e., for $\varphi^{(\mathrm{s})} = \varphi^{(\mathrm{i})}$ or $\varphi^{(\mathrm{s})} = \varphi^{(\mathrm{i})} + \pi$. The re-radiation from a horizontally polarized current $\boldsymbol{J}_{\mathrm{ob}} = J_{\mathrm{ob}}\,\mathbf{y}_0$ has no additional dependence on the scattering angle, being $\boldsymbol{J}_{\mathrm{ob}} \perp \mathbf{r}_0^{(\mathrm{s})}$ for any $\theta^{(\mathrm{s})}$.

[57] Apart from the possible effect of the refraction angle on the vertical polarization.

Instead, the field scattered by a vertically polarized secondary source has a further dependence on $\theta^{(s)}$, since, for given $\theta^{(i)}$, the matrix elements $Q_{vv\perp}$ and $Q_{vh\perp}$ are functions of the scattering direction. In particular, Sect. 3.1.4.1 indicates that the scattered field vanishes when the direction of the upward scattered wave is parallel to the re-radiating current, the direction of which is determined by the structure (shape and prevailing orientation) of the dielectric inhomogeneities. Taking into account the refraction relative to the average material, the condition of parallelism

$$\mathbf{r}_0'' \parallel \boldsymbol{J}_{ob}$$

implies that the vertically polarized scattered field vanishes at the scattering angle such that

$$\sin\theta^{(s)} = n_{ev}\sin\theta_{ob} \ ,$$

where n_{ev} is the effective refractive index of the material for vertical polarization[58] and θ_{ob} is the angle formed by $\boldsymbol{J}_{ob}$ with the vertical direction. When the medium is tenuous, such as a thin vegetation canopy [69] at the lower microwave frequencies, $\theta' \approx \theta^{(i)}$ and $\theta'' \approx \theta^{(s)}$, hence the vertically polarized backscattered field tends to vanish when $\boldsymbol{J}_{ob} \parallel \mathbf{r}_0^{(i)}$. Figure 7.39 suggests how the backscattering from a material

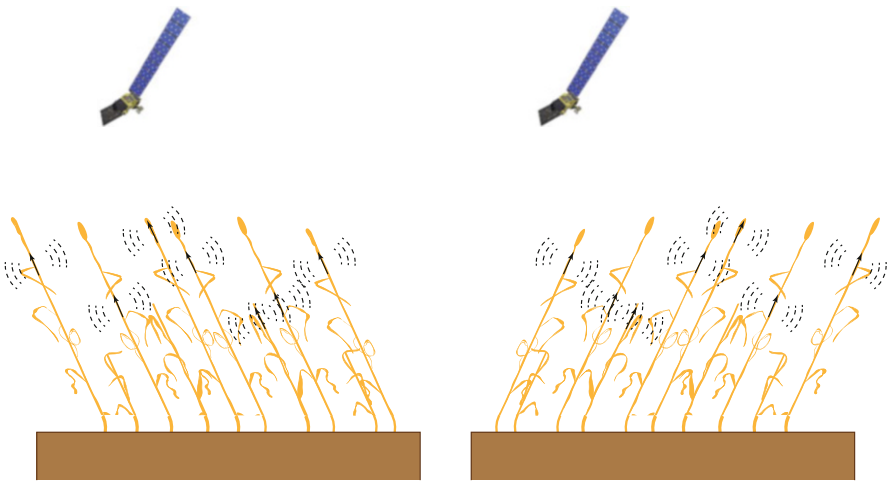

Fig. 7.39 The power radiated by the scattering source current $\boldsymbol{J}_{ob}$ represented by the *arrows* along the stems, concentrates about the plane perpendicular to the latter, according to (3.26); therefore, the direct backscattering from the canopy tends to vanish when the angle of scattering is close to the tilt angle of the stems (*left*)

[58] A material with oriented dielectric structure behaves as an anisotropic medium, in which the propagation constant depends on the wave polarization.

characterized by an elongated dielectric structure, as is a canopy of thin stalks, changes according to the orientation of these latter with respect to the observing direction.

Note that the [**Q**] matrix for the surface layer generally differs from the one for the bulk, hence the polarization properties of the surface scattering may differ from those of the volume scattering.

Scattered Waves

The assumption of plane boundaries between air and terrestrial materials has allowed us to gain valued information on the properties of reflection, which, if we think about it, is the first kind of wave-matter direct interaction we encounter. Now we have to take into account that many real targets are not planar. The idea is to introduce secondary source currents able to represent the effects of the material objects onto which the waves impinge. The approach, based on an ingenuous algebraic artifice, allows us to re-use the analytical frame that was set up for the radiation, to determine the re-radiation from the targets. The procedure delivers tools that we can use to relate the re-radiated field to the one that hits the target. The connection between scattered and incident field is just what we need to sense the scattering target. Various indicators are established, from the scattering and Müller matrices to a number of transverse sections, to the backscattering coefficient.

Given the nature of the terrestrial environment, the secondary source current is composed of a stable term and of a fluctuating component. The deterministic current is responsible for coherent scattering, the features of which are obtained from the radiation formulas tailored to the specific geometries at hand. A first intuitive result is that, under suitable assumptions, the scattered field is proportional to the reflection coefficient. The concept of directional pattern is readily adapted to represent the angular dependence of the scattered field. Targets that are large with respect to wavelength present enhanced scattering around the local direction of specular reflection, whereas small objects tend to spread power all around. Moreover, scattering from small objects increases strongly with decreasing wavelength. Hence we realize the crucial role taken on by the latter compared with the size of the scatterer or with some dimension characterizing its rough surface. We also become aware of the effort that is demanded to identify those canonical shapes that make more or less workable the scattering formulas for the exceedingly various geometries of terrestrial scenarios.

At this stage, the dreaded hurdle brought about by the stochastic nature of the Earth's landscape comes into play: how can we cope with the random field originating from the fluctuating environment? We are presented with two ways for approaching incoherent scattering. One is based on averaging the scattering from the individual elements over the ensemble of scatterers, taken the statistical distribution of their properties into account. The cross-sections of canopies of disks and of needles are examples quite suggestive of the directional and polarization behavior

we expect from random assemblies of elements. The other approach introduces randomness into the spatial distribution of permittivity, the statistical properties of which are characterized by corresponding features of the covariance function. A simple model strives to convince us of the equivalence between the discrete and the continuous approaches. A considerable portion of eccentric mathematics leads to expressing the incoherent angular power in terms of target dielectric spectral density and of scattering vector. We have to acknowledge that the result is effective, as correlation functions and spectra are apt to represent the dielectric structure of a variety of materials and configurations. For instance, the presence of periodic components in the scattering source, as it occurs on water surfaces, is handled quite adequately.

The analysis is extended to the scattering from sub-surface materials through another clump of unwatchable mathematical formalism. Anyhow, the result is instructive, as it clarifies how scattering is affected by the bulk properties of the target. Therefore, we can get an idea of the kind of information the interacting wave is able to mine, for given wavelength and incidence angle. High scattering denotes large permittivity and/or the presence of inhomogeneities with dimensions of the order of the wavelength. As expected, the depth from which the information is extracted decreases with growing attenuation. The formulation is such that the scattered power can be split into the contribution from the surface layer and the one by the underlying bulk material. So we have the opportunity for interpreting the images in terms of relative magnitudes of surface and volume scattering, taking also the polarization of the field into account.

References

1. Boerner WM (2007) Introduction to synthetic aperture radar (SAR) polarimetry. Wexford College Press. ISBN:9781934939062
2. Bohren CF, Huffman DR (2008) Absorption and scattering of light by small particles. Wiley. ISBN:9783527618163
3. Bowman JJ, Senior TBA, Uslenghi PLE (1969) Electromagnetic and acoustic scattering by simple shapes. North-Holland. ISBN:9780891166726
4. Burman R (1964) Some approximate formulas concerning the reflection of electromagnetic waves from a stratified semiinfinite medium. RADIO Sci J Res NBS/USNC-URSI 68D(11):1215–1218. doi:10.6028/jres.068D.122
5. Chappelle EW, Kim MS, Mulchi CL, Daughtry CST, McMurtrey J, Corp L (1998) Laser induced fluorescence (LIF) as a remote sensing tool: a review. Technical report 19990036474. NASA Goddard Space Flight Center
6. Chappelle EW, Williams DL (1987) Laser-induced fluorescence (LIF) from plant foliage. IEEE Trans Geosci Remote Sens GE-25(6):726–736. doi:10.1109/TGRS.1987.289742
7. Das RS, Agrawal YK (2011) Raman spectroscopy: recent advancements, techniques and applications. Vib Spectrosc 57(2):163–176. doi:http://dx.doi.org/10.1016/j.vibspec.2011.08.003
8. Davenport WB, Root WL (1958) An introduction to the theory of random signals and noise. McGraw-Hill. ISBN:9780879422356

9. Edwards HGM, Chalmers JM (eds) (2005) Raman spectroscopy in archaeology and art history. R Soc Chem. ISBN:9780854045228
10. Efremov EV, Ariese F, Gooijer C (2008) Achievements in resonance Raman spectroscopy: review of a technique with a distinct analytical chemistry potential. Anal Chimica Acta 606(2):119–134. doi:10.1016/j.aca.2007.11.006
11. Engman ET, Chauhan N (1995) Status of microwave soil moisture measurements with remote sensing. Remote Sens Environ 51(1):189–198. doi:10.1016/0034-4257(94)00074-W
12. Evans RM (1948) An introduction to color. Wiley. ISBN:9780471247838
13. Farafonov V (2013) Application of non-orthogonal bases in the theory of light scattering by spheroidal particles. In: Kokhanovsky AA (ed) Radiative transfer and light scattering. Light scattering reviews, vol 8. Springer. ISBN:9783642321054
14. Felsen LB, Marcuvitz N (1972) Radiation and scattering of waves. Prentice-Hall. ISBN:9780137503643
15. Ferretti A, Prati C, Rocca F (2001) Permanent scatterers in SAR interferometry. IEEE Trans Geosci Remote Sens 39(1):8–20. doi:10.1109/36.898661
16. Gabor D (1946) Theory of communication. Part 1: the analysis of information. J Inst Electr Eng Part III Radio Commun Eng 93(26):429–441. doi:10.1049/ji-3-2.1946.0074
17. Garbacz RJ, Moffatt DL (1961) An experimental study of bistatic scattering from some small, absorber-coated, metal shapes. Proc IRE 49(7):1184–1192. doi:10.1109/JRPROC.1961.287862
18. Gaskill JD (1978) Linear systems, Fourier transforms, and optics. Wiley. ISBN: 9780471292883
19. Generating a Multi Look Image From an SLC Product. European Space Agency, ESA Earth Online. https://earth.esa.int/web/guest/software-tools/best-basic-envisat-sar-toolbox/best-examples/generating-a-multi-look-image (visited on 01/20/2014).
20. Gonzalez RC, Woods RE (2008) Digital image processing. Pearson/Prentice Hall. ISBN:9780131687288
21. Goodman JW (1976) Some fundamental properties of speckle. J Opt Soc Am 66(11):1145–1150. doi:10.1364/JOSA.66.001145
22. Gorbe E, Calatayud A (2012) Applications of chlorophyll fluorescence imaging technique in horticultural research: a review. Sci Hortic 138:24–35. doi:http://dx.doi.org/10.1016/j.scienta.2012.02.002
23. Guanter L, Frankenberg C, Dudhia A, Lewis PE, Gómez-Dans J, Kuze A, Suto H, Grainger RG (2012) Retrieval and global assessment of terrestrial chlorophyll fluorescence from GOSAT space measurements. Remote Sens Env 121:236–251. doi:http://dx.doi.org/10.1016/j.rse.2012.02.006
24. Harl J (2008) The linear response function in density functional theory. PhD dissertation. Fakultät für Physik, University of Vienna, 31 Oct 2008
25. Hobro AJ, Lendl B (2009) Stand-off Raman spectroscopy. TrAC Trends Anal Chem 28(11):1235–1242. doi:http://dx.doi.org/10.1016/j.trac.2009.08.008. http://www.sciencedirect.com/science/article/pii/S0165993609002064
26. Ishimaru A (1991) Electromagnetic wave propagation, radiation, and scattering. Prentice-Hall. ISBN:9780132490535
27. Jensen JR (2005) Introductory digital image processing: a remote sensing perspective. Prentice Hall. ISBN:9780131453616
28. Jin YQ (1993) Electromagnetic scattering modelling for quantitative remote sensing. World Scientific. ISBN:9789810216481
29. Jin YQ (2006) Theory and approach of information retrievals from electromagnetic scattering and remote sensing. Springer. ISBN:9781402040306
30. Jones DS (1964) The theory of electromagnetism. Pergamon, Macmillan. ISBN:9780080136868
31. Karam MA, Fung AK, Antar YMM (1988) Electromagnetic wave scattering from some vegetation samples. IEEE Trans Geosci Remote Sens 26(6):799–808. doi:10.1109/36.7711

32. Knott EF (2008) Radar cross section. In: Skolnik MI (ed) Radar handbook. McGraw-Hill. ISBN:9780071485470
33. Knott EF, Shaeffer J, Tuley M (2004) Radar cross section, 2nd edn. SciTech. ISBN:9781891121258
34. Kozlov AI, Ligthart LP, Logvin AI (2001) Mathematical and physical modelling of microwave scattering and polarimetric remote sensing: monitoring the Earth's environment using polarimetric radar: formulation and potential applications. Springer. ISBN:9781402001222
35. Kraniauskas P (1992) Transforms in signals and systems. Addison-Wesley. ISBN:9780201196948
36. Kudelski A (2008) Analytical applications of Raman spectroscopy. Talanta 76(1):1–8. doi:http://dx.doi.org/10.1016/j.talanta.2008.02.042
37. Kumke MU, Löhmannsröben H-G, Roch Th (1995) Fluorescence spectroscopy of polynuclear aromatic compounds in environmental monitoring. J Fluoresc 5(2):139–152. doi:10.1007/BF00727531
38. Lang RH, Sidhu JS (1983) Electromagnetic backscattering from a layer of vegetation: a discrete approach. IEEE Trans Geosci Remote Sens GE-21(1):62–71. doi:10.1109/TGRS.1983.350531
39. Long DA (1977) Raman spectroscopy. McGraw-Hill. ISBN:9780070386754
40. Louis J, Ounis A, Ducruet J-M, Evain S, Laurila T, Thum T, Aurela M, Wingsle G, Alonso L, Pedros R, Moya I (2005) Remote sensing of sunlight-induced chlorophyll fluorescence and reflectance of Scots pine in the boreal forest during spring recovery. Remote Sens Environ 96(1):37–48 doi:http://dx.doi.org/10.1016/j.rse.2005.01.013
41. Maurel A (2010) Reflection and transmission by a slab with randomly distributed isotropic point scatterers. J Comput Appl Math 234(6):1842–1850. doi:http://dx.doi.org/10.1016/j.cam.2009.08.35
42. Meroni M, Rossini M, Guanter L, Alonso L, Rascher U, Colombo R, Moreno J (2009) Remote sensing of solar-induced chlorophyll fluorescence: review of methods and applications. Remote Sens Environ 113(10):2037–2051. doi:http://dx.doi.org/10.1016/j.rse.2009.05.003
43. Mishchenko MI, Travis LD, Lacis AA (2002) Scattering, absorption, and emission of light by small particles. Cambridge University Press. ISBN:9780521782524
44. Mishchenko MI, Travis LD, Mackowski DW (1996) T-matrix computations of light scattering by nonspherical particles: a review. J Quant Spectrosc Radiat Transf 55(5):535–575. doi:10.1016/0022-4073(96)00002-7
45. Mogilevsky G, Borland L, Brickhouse M, Fountain III AW (2012) Raman spectroscopy for homeland security applications. Int J Spectrosc 2012. doi:10.1155/2012/808079
46. Moreira A, Prats-Iraola P, Younis M, Krieger G, Hajnsek I, Papathanassiou KP (2013) A tutorial on synthetic aperture radar. IEEE Geosci Remote Sens Mag 6–43. doi:10.1109/MGRS.2013. 2248301
47. Mott H (2007) Remote sensing with polarimetric radar. Wiley. ISBN:9780470074763
48. Moya I, Camenen L, Evain S, Goulas Y, Cerovic ZG, Latouche G, Flexas J, Ounis A (2004) A new instrument for passive remote sensing: 1. Measurements of sunlight-induced chlorophyll fluorescence. Remote Sens Environ 91(2):186–197. doi:http://dx.doi.org/10.1016/j.rse.2004.02.012
49. Oguchi T (1983) Electromagnetic wave propagation and scattering in rain and other hydrometeors. Proc IEEE 71(9):1029–1078. doi:10.1109/PROC.1983.12724
50. Oliver C, Quegan S (2004) Understanding synthetic aperture radar images. SciTech. ISBN:9781891121319
51. Philbrick CR, Brown DM, Willitsford AH, Edwards PS, Wyant AM, Liu ZZ, Chadwick CT, Hallen H (2009) Remote sensing of chemical species in the atmosphere. In: Fourth Symposium on Lidar Atmospheric Applications, Phoenix, 11–15 Jan 2009. https://ams.confex.com/ams/89annual/techprogram/programexpanded_515.htm (visited on 08/31/2014)
52. Pierrehumbert RT (2010) Principles of planetary climate. Cambridge University Press. ISBN:9781139495066

53. Porcello LJ, Massey NG, Innes RB, Marks JM (1976) Speckle reduction in synthetic-aperture radars. J Opt Soc Am 66(11):1305–1311. doi:10.1364/JOSA.66.001305
54. Resta R (1994) Macroscopic polarization in crystalline dielectrics: the geometric phase approach. Rev Modern Phys 66:899–915. doi:10.1103/RevModPhys.66.899
55. Ross J (ed) (1981) The radiation regime and architecture of plant stands. Kluwer. ISBN:9789061936077
56. Ruck GT, Barrick DE, Stuart WD, Krichbaum CK (1970) Radar cross-section handbook, vols 1 and 2. Plenum. ISBN:9780306303432
57. Rytov SM, Kravtsov YuA, Tatarskii VI (1987) Principles of statistical radiophysics 1: elements of random process theory. Springer. ISBN:9780387125626
58. Rytov SM, Kravtsov YuA, Tatarskii VI (1988) Principles of statistical radiophysics 2: correlation theory of random processes. Springer. ISBN:9780387161860
59. Rytov SM, Kravtsov YuA, Tatarskii VI (1989) Principles of statistical radiophysics 3: elements of random fields. Springer. ISBN:9783540178293
60. Rytov SM, Kravtsov YuA, Tatarskii VI (1989) Principles of statistical radiophysics 4: wave propagation through random media. Springer. ISBN:9783540178286
61. Sauer M, Hofkens J, Enderlein J (2010) Handbook of fluorescence spectroscopy and imaging: from ensemble to single molecules. Wiley. ISBN:9783527633524
62. Schulz H, Baranska M (2007) Identification and quantification of valuable plant substances by IR and Raman spectroscopy. Vib Spectrosc 43(1):13–25. doi:http://dx.doi.org/10.1016/j.vibspec.2006.06.001
63. Sellers WD (1969) A global climatic model based on the energy balance of the earth-atmosphere system. J Appl Meteorol 8(3):392–400. doi:10.1175/1520-0450(1969)008(0392:AGCMBO)2.0.CO;2
64. Sharma SK, Lucey PG, Ghosh M, Hubble HW, Horton KA (2003) Stand-off Raman spectroscopic detection of minerals on planetary surfaces. Spectr Acta Part A 59(10):2391–2407. doi:10.1016/S1386-1425(03)00080-5
65. Smith E, Dent G (2013) Modern Raman spectroscopy: a practical approach. Wiley. ISBN:9780470011829
66. Stratton JA, Adams SJ (2007) Electromagnetic theory. McGraw-Hill. ISBN:9781406765472
67. TanDEM-X – A New High Resolution Interferometric SAR Mission. DLR Institut für Hochfrequenztechnik und Radarsysteme. http://www.dlr.de/hr/desktopdefault.aspx/tabid-2317/3669_read-5488/ (visited on 06/18/2014)
68. Tarcea N, Harz M, Rösch P, Frosch T, Schmitt M, Thiele H, Hochleitner R, Popp J (2007) UV Raman spectroscopy – a technique for biological and mineralogical *in situ* planetary studies. Spectr Acta Part A Mol Biomol Spectrosc 68(4):1029–1035; Seventh International Conference on Raman Spectroscopy Applied to the Earth and Planetary Sciences GeoRaman 2006. doi:http://dx.doi.org/10.1016/j.saa.2007.06.051
69. Tsang L, Kong J-A (1981) Application of strong fluctuation random medium theory to scattering from vegetation-like half space. IEEE Trans Geosci Remote Sens GE-19(1):62–69. doi:10.1109/ TGRS.1981.350329
70. Tsang L, Kong J-A, Newton RW (1982) Application of strong fluctuation random medium theory to scattering of electromagnetic waves from a half-space of dielectric mixture. IEEE Trans Antennas Propag 30(2):292–302. doi:10.1109/TAP.1982.1142774
71. Tsang L, Kong JA, Shin RT (1985) Theory of microwave remote sensing. Wiley. ISBN:9780471888604
72. Ufimtsev PY (2007) Fundamentals of the physical theory of diffraction. Wiley. ISBN:9780470109007
73. Ulaby FT, Elachi C (eds) (1990) Radar polarimetry for geoscience applications. Artech House. ISBN:9780890064061
74. Ulaby FT, Moore RK, Fung AK (1981) Microwave remote sensing: active and passive. Microwave remote sensing fundamentals and radiometry, vol 1. Addison-Wesley. ISBN:9780890061909
75. van de Hulst HC (2012) Light scattering by small particles. Dover. ISBN:9780486139753

76. vanZyl JJ, Zebker HA, Elachi C (1987) Imaging radar polarization signatures: theory and observation. Radio Sci 22(4):529–543. doi:10.1029/RS022i004p00529
77. Wait JR, Walters LC (1963) Reflection of VLF radio waves from an inhomogeneous ionosphere. Part 1. Exponentially varying isotropic model. J Res Nat Bureau Stand D Radio Propag 67D(3):361–367. doi:10.6028/jres.067D.075
78. Westbrook CD (2013) Rayleigh scattering by hexagonal ice crystals and the interpretation of dual-polarisation radar measurements. Q J R Meteorol Soc. doi:10.1002/qj.2262
79. Wigneron JP (1994) Retrieval of geophysical parameters from multifrequency passive microwave measurements over a soybean canopy. In: Choudhury BJ, Kerr YH, Njoku EG, Pampaloni P (eds) Passive Microwave Remote Sensing of Land-Atmosphere Interactions ESA/NASA International Workshop, Saint Lary, 11–15 Jan 1993. VSP, pp 403–422. ISBN:9789067641883
80. Winton M (2006) Surface albedo feedback estimates for the AR4 climate models. J Clim 19(3):359–365. doi:10.1175/JCLI3624.1
81. Wyser K, Yang P (1998) Average ice crystal size and bulk short-wave single-scattering properties of cirrus clouds. Atmos Res 4:315–335. doi:10.1016/S0169-8095(98)00083-0
82. Yamashita E (ed) (1996) Analysis methods for electromagnetic wave problems, vol 2. Artech House. ISBN:9780890067468
83. Zarco-Tejada PJ, Berni JAJ, Suárez L, Sepulcre-Cantó G, Morales F, Miller JR (2009) Imaging chlorophyll fluorescence with an airborne narrow-band mul-tispectral camera for vegetation stress detection. Remote Sens Environ 113(6):1262–1275. doi:http://dx.doi.org/10.1016/j.rse.2009.02.016
84. Zarco-Tejada PJ, González-Dugo V, Berni JAJ (2012) Fluorescence, temperature and narrow-band indices acquired from a UAV platform for water stress detection using a micro-hyperspectral imager and a thermal camera. Remote Sens Environ 117:322–337. doi:http://dx.doi.org/10.1016/j.rse.2011.10.007

Chapter 8
Thermal Emission

Charged particles in matter, being in an accelerated motion caused by collisions, can originate electromagnetic radiation. The emission process is reciprocal of absorption. As outlined in Sect. 2.1, this latter consists in the conversion of electromagnetic energy into thermal energy through particle collision. In the reverse sense, a charge accelerated by a collision converts part of its (thermal) kinetic energy into electromagnetic energy giving rise to *spontaneous radiation*.

8.1 Spontaneous Radiation

The electromagnetic field forming the spontaneous radiation is basically ruled by Maxwell's equations (1.6) and (1.7) containing macroscopic source terms which account for the collective radiating action of the charges. This model regards the electromagnetic sources as local time-varying elementary impressed currents the momentum (Sect. 3.1.3) of which is suitable to account for the transfer of energy from the thermal system to the radiation field. The motion of the particles is chaotic, hence the sources consist of *space-time fluctuating currents*, which radiate a random field.

The Fourier-transformed radiation field is related to the thermal source currents $\boldsymbol{J}_{\mathrm{eT}}$ and $\boldsymbol{J}_{\mathrm{mT}}$ in the spectral domain by (1.32) and (1.33):

$$\nabla \times \boldsymbol{E} = -\mathrm{j}\omega \boldsymbol{B} - \boldsymbol{J}_{\mathrm{eT}} \; ; \tag{8.1}$$

$$\nabla \times \boldsymbol{H} = \quad \mathrm{j}\omega \boldsymbol{D} + \boldsymbol{J}_{\mathrm{mT}} \; , \tag{8.2}$$

where $\boldsymbol{J}_{\mathrm{eT}}$ and $\boldsymbol{J}_{\mathrm{mT}}$ are the electric and magnetic current densities, respectively modeling the corresponding sources of thermal radiation. The vectors are spectral

D. Solimini, *Understanding Earth Observation*, Remote Sensing and Digital Image Processing 23, DOI 10.1007/978-3-319-25633-7_8

quantities referring to the angular frequency $\omega = 2\pi f$. The dielectric equation (2.6) in an isotropic generally inhomogeneous material gives the electric displacement

$$\boldsymbol{D}(\omega, \boldsymbol{r}) = \epsilon(\omega, \boldsymbol{r})\, \boldsymbol{E}(\omega, \boldsymbol{r}) \ , \tag{8.3}$$

where, as usual, permittivity takes into account all the sources of dielectric polarization considered in Sect. 2.1, including free charges. In absence of ferromagnetic materials, $\boldsymbol{B} \simeq \mu_0 \boldsymbol{H}$.

Since the source currents are random quantities, (8.1) and (8.2) are called stochastic Maxwell's equations [11, Chap. 3]. The currents $\boldsymbol{J}_{\mathrm{eT}}$ and $\boldsymbol{J}_{\mathrm{mT}}$ need a stochastic characterization based on moments, as discussed in Sect. 1.3.4. The random thermal field is likewise described by moments, which are linearly related to the moments of the source currents because of the linearity of Maxwell's equations.

According to the Nyquist theory of thermal fluctuations in electric networks [5, Chap. XIII], the **F**luctuation-**D**issipation **T**heorem (FDT) for continuos media in **l**ocal **t**hermodynamic **e**quilibrium (LTE) yields the covariances of the thermal source currents as functions of the thermodynamic temperature of a body, of its losses, and of frequency. The spatial covariance of the p-component of the spectral thermal electric source current density $\boldsymbol{J}_{\mathrm{eT}}$ in an *isotropic* material is given by

$$\left\langle J_{\mathrm{eT}p}(\boldsymbol{r})\, J^{*}_{\mathrm{eT}p}(\boldsymbol{r}\,')\right\rangle_f = \Theta(f,T)\, \epsilon_0 \left|\tilde{\epsilon}_{\mathrm{j}}\right| f\, \delta(\boldsymbol{r}-\boldsymbol{r}\,') \qquad (p = 1,2,3) \ , \tag{8.4}$$

where average is over the equilibrium ensemble of the thermal random sources at frequency f and the function Θ is the mean energy of the quantum oscillator, given by

$$\Theta(f,T) = \frac{\hbar f}{2} \coth\left(\frac{\hbar f}{2 k T}\right) \cdot \tag{8.5}$$

The quantities in Eq. (8.5) are: Planck's constant $\hbar = 6.63 \cdot 10^{-34}$ J s, Boltzmann's constant $k = 1.38 \cdot 10^{-23}$ J K^{-1}, temperature T and frequency f.

The basic result (8.4) of the FDT points out that the intensity of the thermal radiation source is proportional to the imaginary part $\tilde{\epsilon}_{\mathrm{j}}$ of the permittivity, i.e., depends on the dissipation of the material. Therefore, in absence of absorption, the source current vanishes: this means that a lossless material does not give origin to thermal radiation. For this reason, the assumption $\mu = \mu_0$ implies that no magnetic thermal current is present and the only acting thermal source is the electric one, henceforth denoted by $\boldsymbol{J}_{\mathrm{TH}}$. The spatial impulse function $\delta(\boldsymbol{r}-\boldsymbol{r}\,')$ in (8.4) indicates that the thermal source currents are spatially uncorrelated. Indeed, the actual sources act independently at a microscopic level, over distances of the order of interatomic spacing, hence the correlation distance of $\boldsymbol{J}_{\mathrm{TH}}$ vanishes in the macroscopic continuos approach.

8.1.1 The Thermal-Emission Field

The electromagnetic field produced by the thermal sources can be effectively obtained by use of the reciprocity worked out in Sect. 3.2.1. To this end, consider the electric test source $\boldsymbol{J}_\mathrm{t}$ introduced in Sect. 3.2.1.2, having momentum $\mathcal{M}_\mathrm{t}$ and located at a point $\boldsymbol{r}_\mathrm{t}$ clearly outside the volume of the thermal source:

$$\boldsymbol{J}_\mathrm{t} = \mathcal{M}_\mathrm{t}\,\delta(\boldsymbol{r}-\boldsymbol{r}_\mathrm{t})\,\mathbf{t}_0\ .$$

Section 3.2.1.2 shows that the reaction I_{tT} of the thermal source on the test source gives the component along $\mathbf{t}_0$ of the electric field $\boldsymbol{E}_{\mathrm{TH}}(\boldsymbol{r}_\mathrm{t})$ created in $\boldsymbol{r}_\mathrm{t}$ by the thermal source:

$$\boldsymbol{E}_{\mathrm{TH}}(\boldsymbol{r}_\mathrm{t})\cdot\mathbf{t}_0 = \frac{I_{\mathrm{tT}}}{\mathcal{M}_\mathrm{t}}\ .$$

By the equality of reactions,

$$I_{\mathrm{tT}} = I_{\mathrm{Tt}}\ ,$$

derived in Sect. 3.2.1.1, the emitted electric field is obtained as a function of the field $\boldsymbol{E}_\mathrm{t}(\boldsymbol{r}'_\mathrm{T},\boldsymbol{r}_\mathrm{t},\mathbf{t}_0)$ that the test source produces at a point $\boldsymbol{r}'_\mathrm{T}$ inside the body of volume V'_T where the thermal source current $\boldsymbol{J}_{\mathrm{TH}}$ acts.[1] Figure 8.1 depicts the current $\boldsymbol{J}_{\mathrm{TH}}$ in the material and the location of the test source $\boldsymbol{J}_\mathrm{t}$. By expressing the dot product in the reaction integral in terms of the components of $\boldsymbol{J}_{\mathrm{TH}}$ and $\boldsymbol{E}_\mathrm{t}$,

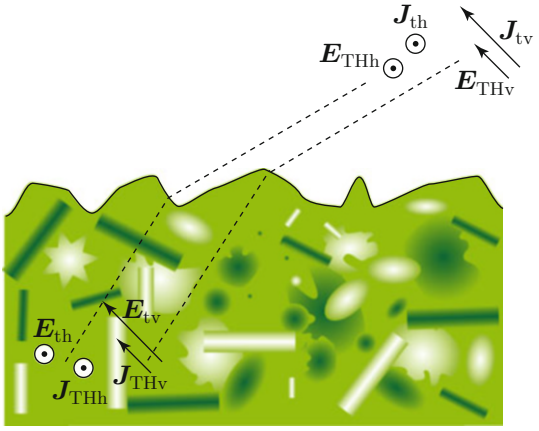

Fig. 8.1 The emitted thermal field $\boldsymbol{E}_{\mathrm{TH}p}$ ($p = \mathrm{h}, \mathrm{v}$) is determined by means of reciprocity through the field $\boldsymbol{E}_{\mathrm{t}p}$ that is created inside the emitting material by the test source $\boldsymbol{J}_{\mathrm{t}p}$ placed where the thermal electromagnetic field is observed; horizontal and vertical components of the emitting thermal current $\boldsymbol{J}_{\mathrm{TH}p}$ are indicated

[1] Volume V'_T may include more than one body.

$$\boldsymbol{E}_{\mathrm{TH}}(\boldsymbol{r}_{\mathrm{t}})\cdot\mathbf{t}_0=\frac{\iiint_{V'_{\mathrm{T}}}\boldsymbol{J}_{\mathrm{TH}}(\boldsymbol{r}'_{\mathrm{T}})\cdot\boldsymbol{E}_{\mathrm{t}}(\boldsymbol{r}'_{\mathrm{T}},\boldsymbol{r}_{\mathrm{t}},\mathbf{t}_0)\,\mathrm{d}V'}{\mathcal{M}_{\mathrm{t}}}=\frac{\iiint_{V'_{\mathrm{T}}}\sum_p J_{\mathrm{TH}p}(\boldsymbol{r}'_{\mathrm{T}})E_{\mathrm{t}p}(\boldsymbol{r}'_{\mathrm{T}},\boldsymbol{r}_{\mathrm{t}},\mathbf{t}_0)\,\mathrm{d}V'}{\mathcal{M}_{\mathrm{t}}}\,, \tag{8.6}$$

where V'_{T} is the volume of the bodies contributing the thermal radiation and p denotes the field components.[2] To simplify the notations, a unit momentum ($\mathcal{M}_{\mathrm{t}}=1$) is assumed in the following, without loss of generality.

It is important to bear in mind that the concept of test source is an expedient that is put to use for characterizing the behavior of the thermal radiation source: the test field is a *virtual* quantity that does not exist physically, rather it performs the task of establishing the relevant analytical relations between thermal radiation and parameters of the emitting body.

The emitted field, being a random quantity, as said, must be characterized by the moments introduced in Sect. 1.3.4. The second moment of the components E_{THt1}, E_{THt2} of $\boldsymbol{E}_{\mathrm{TH}}$ along two directions $\mathbf{t}_{01}$, $\mathbf{t}_{02}$, at two points $\boldsymbol{r}_1$, $\boldsymbol{r}_2$, is obtained from (8.6) as

$$\begin{aligned}
&\left\langle E_{\mathrm{THt1}}(\boldsymbol{r}_1)\,E^*_{\mathrm{THt2}}(\boldsymbol{r}_2)\right\rangle\\
&=\left\langle\iiint_{V'_{\mathrm{T}}}\boldsymbol{J}_{\mathrm{TH}}(\boldsymbol{r}'_{\mathrm{T}})\cdot\boldsymbol{E}_{\mathrm{t1}}(\boldsymbol{r}'_{\mathrm{T}},\boldsymbol{r}_1,\mathbf{t}_{01})\,\mathrm{d}V'\left[\iiint_{V'_{\mathrm{T}}}\boldsymbol{J}_{\mathrm{TH}}(\boldsymbol{r}'_{\mathrm{T}})\cdot\boldsymbol{E}_{\mathrm{t2}}(\boldsymbol{r}'_{\mathrm{T}},\boldsymbol{r}_2,\mathbf{t}_{02})\,\mathrm{d}V'\right]^*\right\rangle\\
&=\iiint_{V'_{\mathrm{T}}}\iiint_{V'_{\mathrm{T}}}\left\langle\boldsymbol{J}_{\mathrm{TH}}(\boldsymbol{r}'_{\mathrm{T}})\cdot\boldsymbol{E}_{\mathrm{t1}}(\boldsymbol{r}'_{\mathrm{T}},\boldsymbol{r}_1,\mathbf{t}_{01})\left[\boldsymbol{J}_{\mathrm{TH}}(\boldsymbol{r}_{\mathrm{T}})\cdot\boldsymbol{E}_{\mathrm{t2}}(\boldsymbol{r}_{\mathrm{T}},\boldsymbol{r}_2,\mathbf{t}_{02})\right]^*\right\rangle\mathrm{d}V\,\mathrm{d}V' \qquad (8.7)\\
&=\iiint_{V'_{\mathrm{T}}}\iiint_{V'_{\mathrm{T}}}\sum_p\sum_q\left\langle J_{\mathrm{TH}p}(\boldsymbol{r}'_{\mathrm{T}})J^*_{\mathrm{TH}q}(\boldsymbol{r}_{\mathrm{T}})\right\rangle E_{\mathrm{t}p}(\boldsymbol{r}'_{\mathrm{T}},\boldsymbol{r}_1,\mathbf{t}_{01})E^*_{\mathrm{t}q}(\boldsymbol{r}_{\mathrm{T}},\boldsymbol{r}_2,\mathbf{t}_{02})\,\mathrm{d}V\,\mathrm{d}V'\,.
\end{aligned}$$

Equation (8.7) has been obtained by placing a unitary-momentum test source in each of the two points $\boldsymbol{r}_1$ and $\boldsymbol{r}_2$ to which the second-order moment refers, according to the geometry schematized in Fig. 8.1. The field components are denoted by p and q, with $p,\ q=x,y,z$ in Cartesian notation. Since the emitting materials are assumed isotropic, different components of the thermal source currents are uncorrelated, so that the mixed products ($p\neq q$) in (8.7) vanish and

$$\begin{aligned}
&\left\langle E_{\mathrm{THt1}}(\boldsymbol{r}_1)\,E^*_{\mathrm{THt2}}(\boldsymbol{r}_2)\right\rangle\\
&\quad=\iiint_{V'_{\mathrm{T}}}\iiint_{V'_{\mathrm{T}}}\sum_p\left\langle J_{\mathrm{TH}p}(\boldsymbol{r}'_{\mathrm{T}})J^*_{\mathrm{TH}p}(\boldsymbol{r}_{\mathrm{T}})\right\rangle E_{\mathrm{t}p}(\boldsymbol{r}'_{\mathrm{T}},\boldsymbol{r}_1,\mathbf{t}_{01})E^*_{\mathrm{t}p}(\boldsymbol{r}_{\mathrm{T}},\boldsymbol{r}_2,\mathbf{t}_{02})\,\mathrm{d}V\,\mathrm{d}V'\,.
\end{aligned}$$

[2] As said, no thermal magnetic currents are considered, because of the assumed absence of magnetic losses. In case thermal magnetic emission be present, a magnetic test source would be added in a straightforward fashion.

By relating the covariance of the thermal source current to the dielectric ($\tilde{\epsilon}_\mathrm{j}$) and thermodynamic ($T$) properties of the emitting body through (8.4), the moment of the field is expressed by

$$\begin{aligned}&\left\langle E_{\mathrm{THt1}}(\boldsymbol{r}_1)\, E^*_{\mathrm{THt2}}(\boldsymbol{r}_2)\right\rangle \\ &\quad = \epsilon_0 f \iiint_{V'_\mathrm{T}} \iiint_{V'_\mathrm{T}} \Theta(f,T)\, \tilde{\epsilon}_\mathrm{j}\, \delta(\boldsymbol{r}_\mathrm{T}-\boldsymbol{r}'_\mathrm{T}) \sum_p E_{\mathrm{t}p}(\boldsymbol{r}'_\mathrm{T},\boldsymbol{r}_1,\mathbf{t}_{01}) E^*_{\mathrm{t}p}(\boldsymbol{r}_\mathrm{T},\boldsymbol{r}_2,\mathbf{t}_{02})\, \mathrm{d}V\, \mathrm{d}V' \,.\end{aligned} \tag{8.8}$$

The impulse function $\delta(\boldsymbol{r}_\mathrm{T}-\boldsymbol{r}'_\mathrm{T})$ indicates that the covariance of the thermal source current vanishes for $\boldsymbol{r}_\mathrm{T} \neq \boldsymbol{r}'_\mathrm{T}$, therefore (8.8) yields immediately

$$\begin{aligned}&\left\langle E_{\mathrm{THt1}}(\boldsymbol{r}_1)\, E^*_{\mathrm{THt2}}(\boldsymbol{r}_2)\right\rangle \\ &\quad = \epsilon_0 f \iiint_{V'_\mathrm{T}} \Theta[f, T(\boldsymbol{r}'_\mathrm{T})]\, \tilde{\epsilon}_\mathrm{j}(\boldsymbol{r}'_\mathrm{T})\, \boldsymbol{E}_\mathrm{t}(\boldsymbol{r}'_\mathrm{T},\boldsymbol{r}_1,\mathbf{t}_{01}) \cdot \boldsymbol{E}^*_\mathrm{t}(\boldsymbol{r}_\mathrm{T},\boldsymbol{r}_2,\mathbf{t}_{02})\, \mathrm{d}V' \,.\end{aligned} \tag{8.9}$$

The dependence of both temperature T and permittivity[3] $\tilde{\epsilon}$ on the position $\boldsymbol{r}'_\mathrm{T}$ inside the emitting body has been indicated explicitly in (8.9). Indeed, the thermal and dielectric inhomogeneities of the terrestrial environment are often a major issue in passive observation of Earth. The emission from materials with dielectric and thermal inhomogeneities is outlined in Sect. 8.1.4.

In summary, the covariance matrix elements of the electric field $\boldsymbol{E}_\mathrm{TH}$ originated by the thermal emission from the lossy bodies occupying the observed volume V'_T are obtained, thanks to electromagnetic reciprocity, by means of the electric field $\boldsymbol{E}_\mathrm{t}$ that the test currents *virtually* produce inside the bodies. The pair of test sources are placed at the points $\boldsymbol{r}_1$, $\boldsymbol{r}_2$ where the thermal field is observed, and are oriented along the directions $\mathbf{t}_{01}$, $\mathbf{t}_{02}$ of the thermal field components that are measured. The intensity of the thermal emission depends on the temperature distribution and on the imaginary part of permittivity, which is also a function of frequency. The volume V'_T contributing the emission is understood to be the resolution cell of the observing (*radiometric*) system. As said, more than one emitting body are possibly identified within the volume V'_T.

Consider now the simple case of a single body at uniform temperature T occupying the whole V'_T. The mean-square value of a component p (e.g., $p = \mathrm{h}$, v in Jones' notations) of the thermal field emitted by the body is obtained by setting $\boldsymbol{r}_1 = \boldsymbol{r}_2$ and $\mathbf{t}_{01} = \mathbf{t}_{02}$ in (8.9):

$$\left\langle \left| E_{\mathrm{TH}p}(\boldsymbol{r}) \right|^2 \right\rangle = \frac{\Theta\, \omega\, \epsilon_0}{2\pi} \iiint_{V'_\mathrm{T}} \tilde{\epsilon}_\mathrm{j}\, \boldsymbol{E}_{\mathrm{t}p} \cdot \boldsymbol{E}^*_{\mathrm{t}p}\, \mathrm{d}V' = \frac{\Theta}{\pi} W_{\mathrm{td}p} \,. \tag{8.10}$$

[3]The dependence of the dielectric properties of the emitting body on temperature has been disregarded to somewhat lighten the notations.

The expression (2.32) of the dissipated power $\overline{W_\mathrm{d}}$ obtained in Sect. 2.1.4 is immediately recognized in (8.10), where, to be more precise, $W_{\mathrm{td}p}$ is the power dissipated in the body when a unitary test source in direction of the p component is placed at $\boldsymbol{r}$. This result, which ultimately stems from the electromagnetic reciprocity, allows the intensity of the thermal emission from the body to be put into straight relation with the power it absorbs. Again, it is stressed that the absorption here is a virtual process.

Equation (8.10) is named *generalized Kirchhoff's law*, or Kirchhoff form of the Fluctuation Dissipation Theorem. Obviously it confirms that a lossless material, in which $\tilde{\epsilon}_\mathrm{j} = 0$, has no thermal emission.

8.1.2 Thermal Emission at Far Distance

The electromagnetic field created by thermal emission has a complicated dependence on the distance R from the emitting body.[4] However, at a sufficiently large distance, the dependence of the emitted field on R tends to smooth out, the magnetic field becomes proportional to the electric one, and electric field, magnetic field and radial direction are mutually orthogonal, as shown in Sect. 3.1.4.2. The properties of the far field allow the Poynting vector $\boldsymbol{\mathcal{P}}_\mathrm{TH}$ of the thermal radiation to be readily obtained at far distance in the direction $\mathbf{r}_\mathrm{oe}$ for p polarization[5]

$$\langle \boldsymbol{\mathcal{P}}_{\mathrm{TH}p} \rangle = \frac{\left\langle \left| E_{\mathrm{TH}p}(\boldsymbol{r}) \right|^2 \right\rangle}{2\eta_0} \mathbf{r}_\mathrm{oe} = \frac{\Theta}{2\pi\eta_0} \frac{W_{\mathrm{td}p}}{|\mathcal{M}_p|^2} \mathbf{r}_\mathrm{oe} \,. \tag{8.11}$$

Here $W_{\mathrm{td}p}$ is the power virtually dissipated in the body when a test source of momentum $\boldsymbol{\mathcal{M}}_p \perp \mathbf{r}_\mathrm{oe}$ is present in the direction $\mathbf{r}_\mathrm{oe}$ at far distance from the body. This latter is assumed of finite dimensions and at a uniform temperature. Given its proportionality to $W_{\mathrm{td}p}$, the power density of the emitted thermal radiation depends on shape, dimensions, and permittivity of the body, on its orientation with respect to $\mathbf{r}_\mathrm{oe}$, and on polarization p, in addition, of course, to temperature and frequency. The dependence of $\langle \boldsymbol{\mathcal{P}}_{\mathrm{TH}p} \rangle$ on polarization originates from the dependence of the internal field, hence of $W_{\mathrm{td}p}$, on the polarization of the test source and hence on the complex momentum $\boldsymbol{\mathcal{M}}_p$. If the body has rotational symmetry about $\mathbf{r}_\mathrm{oe}$, the emitted power density is the same over any pair of orthogonal polarizations, consistently with the dissipated power.

[4] Note that a source of thermal radiation behaves differently from the electromagnetic sources considered in Chap. 3, given its incoherent nature, which modifies the wave interference mechanism discussed in Sect. 3.1.2.

[5] To avoid unnecessary formal complexity, the emitting body is assumed to be surrounded by a lossless medium, e.g., vacuum approximating air.

Definition (7.19) of *absorption cross-section* at p-polarization σ_{ap} allows to express the power dissipated in a body as

$$W_{tdp} = \sigma_{ap}\, \mathcal{P}_{tp} \ , \tag{8.12}$$

where $\mathcal{P}_{tp}$ is the areic power that the *far* test source sends onto the body at p-polarization. Therefore, the thermal power emitted by the body is put into direct relation with its absorption cross-section by

$$\langle \boldsymbol{\mathcal{P}}_{THp} \rangle = \frac{\Theta}{2\pi\eta_0} \frac{\mathcal{P}_{tp}}{|\mathcal{M}_p|^2}\, \sigma_{ap}\, \mathbf{r}_{oe} \tag{8.13}$$

If an extended area A_{gt} transverse to $\mathbf{r}_{oe}$ can be identified, such that

$$W_{tg} = A_{gt}\, \mathcal{P}_t$$

is the power coming from the test source located in the direction $\mathbf{r}_{oe}$ *geometrically incident* on the body, or *intercepted* by it, then

$$W_{tdp} \leq W_{tg} \ ,$$

since a fraction[6] of the intercepted power W_{tg} is scattered and, clearly, not absorbed. This observation implies that

$$\sigma_{ap} \leq A_{gt} \ .$$

A completely absorbing body dissipates all the power its transverse area intercepts, that is, $W_{td} = W_{tg}$ at any polarization. In this case

$$\sigma_a = A_{gt} \ . \tag{8.14}$$

The *ideal* body for which (8.14) holds is named *black body*.

The power density (3.26) created at far distance R by the test source[7] is given by

$$\mathcal{P}_{tp} = \frac{\eta_0\, |\mathcal{M}_p|^2}{8\, \lambda_0^2 R^2} \ ,$$

which, once inserted into (8.13), provides the power density vector of the thermal radiation

[6]The scattered fraction of power clearly depends on the polarization of the field and on the direction $-\mathbf{r}_{oe}$ of incidence, according to the findings of Chap. 7.

[7]The orientation of $\boldsymbol{J}_t$, parallel to the far electric field emitted on p-polarization by the body, is chosen such that $\vartheta = \pi/2$ in (3.26).

$$\langle \boldsymbol{\mathcal{P}}_{\mathrm{TH}p} \rangle = \frac{\Theta}{16\pi} \frac{\sigma_{\mathrm{a}p}}{\lambda_0^2 R^2} \mathbf{r}_{\mathrm{oe}} \ . \tag{8.15}$$

The power density (8.15) emitted in the direction of observation $-\mathbf{r}_{\mathrm{oe}}$ is finally put into relation with the transverse area A_{gt} that the body presents in that direction:

$$\langle \boldsymbol{\mathcal{P}}_{\mathrm{TH}p} \rangle = \frac{\Theta}{16\pi} \frac{e_p \, A_{\mathrm{gt}}}{\lambda_0^2 R^2} \mathbf{r}_{\mathrm{oe}} \ . \tag{8.16}$$

Equation (8.16) introduces the *emissivity* e_p of the body at p-polarization as

$$e_p(\mathbf{r}_{\mathrm{oe}}) := \frac{W_{\mathrm{td}p}}{\mathcal{P}_{tp} \, A_{\mathrm{gt}}} \leq 1 \ .$$

The emissivity of the body in the direction $\mathbf{r}_{\mathrm{oe}}$ coincides with the fraction of the geometrically incident power coming from the direction $-\mathbf{r}_{\mathrm{oe}}$ that is able to enter the body and gets dissipated in it.

The emitted power density vector can be expressed in terms of the solid angle $\Delta\Omega$, represented in Fig. 8.2, under which the body is seen from the *large*[8] distance R

$$\langle \boldsymbol{\mathcal{P}}_{\mathrm{TH}p} \rangle = \frac{e_p \, \Theta}{16\pi\lambda_0^2} \Delta\Omega \ \mathbf{r}_{\mathrm{oe}} \ .$$

The solid angle $\Delta\Omega$ and hence $\mathcal{P}_{\mathrm{TH}}$, decrease with the square of distance R, whereas the ratio

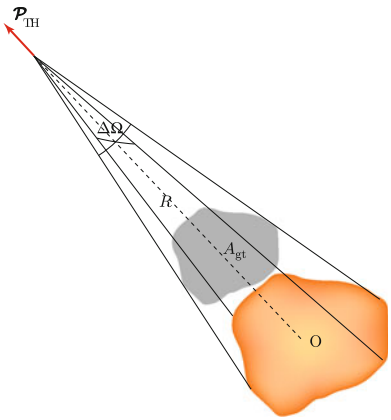

Fig. 8.2 The thermal power density vector $\boldsymbol{\mathcal{P}}_{\mathrm{TH}}$ at distance R from the emitting body in a given direction depends on the solid angle $\Delta\Omega$ under which the body, of transverse geometric area A_{gt}, is seen in that direction

[8] Note that "large" here means that the far-field conditions are satisfied for the observed portion V'_{T} of the body, determined by the spatial resolution of the radiometric observation, and may not refer to the whole scenario (e.g., the entire portion of the earth surface visible from the observing platform).

$$\mathcal{I}(\mathbf{r}_{\rm oe}) := \frac{\langle \mathcal{P}_{\rm TH} \rangle}{\Delta\Omega} = e\,\frac{\Theta}{16\pi\,\lambda_0^2} \tag{8.17}$$

is independent of distance in a lossless medium such as, in practice, the air can be assumed at little attenuated wavelengths. The quantity $\mathcal{I}$ is named *radiance* and is widely used to characterize the electromagnetic radiation. For given body, polarization and direction of observation, the variation with wavelength of the emitted radiance is affected both by the thermal function Θ and by the body emissivity, related by reciprocity to its absorption cross section.

8.1.3 Thermal Emission from Body with Plane Boundary

The far-distance thermal power emitted by a lossy body bound by a plane surface is effectively obtained from (8.11) by determining the power virtually absorbed by the body when a test source is placed at a correspondingly large distance.[9] According to reciprocity, the test current complex vector selects the polarization. As schematized in Fig. 8.1, a momentum $\boldsymbol{\mathcal{M}} = \mathcal{M}\mathbf{h}_0$ perpendicular to the plane $(\mathbf{r}_{\rm oe}\,\mathbf{z}_0)$ is required to determine the power emitted on horizontal polarization, while vertical polarization corresponds to $\boldsymbol{\mathcal{M}} = \mathcal{M}\mathbf{v}_0$ in the $(\mathbf{r}_{\rm oe}\,\mathbf{z}_0)$-plane.

The power dissipated in a portion $V'_{\rm T}$ of a "thick" body is approximated by the power W_{tp} that the p-polarized test wave traveling along $-\mathbf{r}_{\rm oe}$ carries across the corresponding portion $\Delta S'_{\rm T}$ of the $(x'y')$-plane delimiting the half-space[10] representing the body schematized in Fig. 8.3:

$$W_{{\rm td}p} \simeq W'_{tp} = \boldsymbol{\mathcal{P}}'_{\rm t}\cdot\mathbf{z}_0\,\Delta S'_{\rm T} = (\boldsymbol{\mathcal{P}}_{\rm t} - \boldsymbol{\mathcal{P}}''_{\rm t})\cdot\mathbf{z}_0\,\Delta S'_{\rm T} \simeq (1-\mathcal{R}_p)\boldsymbol{\mathcal{P}}_{\rm t}\cdot\mathbf{z}_0\,\Delta S'_{\rm T}\,, \tag{8.18}$$

where $\boldsymbol{\mathcal{P}}_{\rm t}$, $\boldsymbol{\mathcal{P}}'_{\rm t}$ and $\boldsymbol{\mathcal{P}}''_{\rm t}$ are the Poynting vectors of the incident, refracted and reflected waves, respectively, in the locally plane wave approximation with the notations of Chap. 6. Equation (8.18) makes use of the *reflectivity*, which, in the considered case of plane boundary, is the power reflection coefficient $\mathcal{R}_p$ at p-polarization determined in Sect. 6.2.2 for the half-space:

$$\mathcal{R}_p = |q_p|^2, \qquad (p = {\rm h},\ {\rm v})\,. \tag{8.19}$$

By inserting W'_{tp} given by (8.18) into (8.15) and taking account of (8.12), the far-distance thermal power originated by the portion of surface $\Delta S'_{\rm T}$ is related to the reflectivity $\mathcal{R}_p$ that this latter presents at p-polarization:

[9] The large distance allows the assumption that the wave produced on the surface of the body by the test source is a plane wave.

[10] The volume $V'_{\rm T}$ can be considered to correspond to the resolution cell of a radiometric observation and its surface $\Delta S'_{\rm T}$ to the elementary area (pixel) of a thermal emission image (cf. Sect. 10.2).

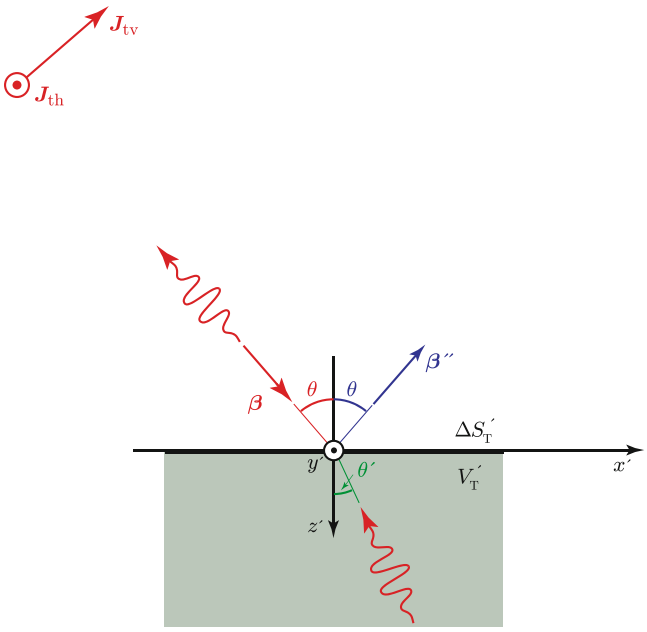

Fig. 8.3 The p-polarized emission at angle θ from the body of volume $V_{\rm T}'$ with plane boundary $\Delta S_{\rm T}'$ is obtained from the fraction of the power radiated by the test source current $\boldsymbol{J}_{tp}$ ($p = \mathrm{h}, \mathrm{v}$), and incident at the angle θ, absorbed by the body

$$\langle \boldsymbol{\mathcal{P}}_{{\rm TH}p} \rangle \simeq \frac{\Theta}{16\pi\,\lambda_0^2}\,(1-\mathcal{R}_p)\frac{\Delta S_{\rm T}'\cos\theta}{R^2}\,\mathbf{r}_{\rm oe}\ .$$

Note that, as the direction $\mathbf{r}_{\rm oe}$ changes, $\mathcal{P}_{\rm TH}(\mathbf{r}_{\rm oe})$ does not vary like $\cos\theta$, since it depends also on the reflection coefficient q_p, which, in turn, varies with θ. The deviation can be dramatic especially at vertical polarization, at which the pseudo-Brewster angle effect seen in Sect. 6.3.2 occurs. In case a plane boundary cannot be identified, the reflectivity differs from (8.19), but the underlying concepts, based on reciprocity, are clearly still applicable.

With reference to the solid angle

$$\Delta\Omega = \frac{\Delta S_{\rm T}'\cos\theta}{R^2}$$

under which the surface $\Delta S_{\rm T}'$ is seen from the direction $\mathbf{r}_{\rm oe}$,

$$\langle \boldsymbol{\mathcal{P}}_{{\rm TH}p} \rangle \simeq \frac{\Theta}{16\pi\,\lambda_0^2}\,(1-\mathcal{R}_p)\,\Delta\Omega\ \mathbf{r}_{\rm oe}\ .$$

As observed in Sect. 8.1.2, the thermal power density emitted through $\Delta S'_{\mathrm{T}}$, measured at the far distance R is proportional to $\Delta\Omega$. Therefore, the areic thermal power flowing in directions confined within the solid angle $\Delta\Omega$ and normalized to $\Delta\Omega$ itself is independent of distance, consistently with the conservation of energy in a lossless medium and, of course, with (8.17). The radiance at p-polarization is then

$$\mathcal{I}_p = \frac{\langle \mathcal{P}_{\mathrm{TH}p} \rangle}{\Delta\Omega} = \frac{1 - \mathcal{R}_p}{16\pi} \frac{\Theta}{\lambda_0^2} \cdot$$

At given body temperature and wavelength, the maximum emitted power corresponds to $\mathcal{R} = 0$, i.e., to a totally absorbing (*black*) body, the radiance of which is[11]

$$\mathcal{I}_{\mathrm{b}} = \frac{\Theta}{16\pi\,\lambda_0^2} \cdot \tag{8.20}$$

The radiance of any other (real) body is lower:

$$\mathcal{I} = (1 - \mathcal{R})\,\mathcal{I}_{\mathrm{b}} = e\,\mathcal{I}_{\mathrm{b}} \leq \mathcal{I}_{\mathrm{b}} \,, \tag{8.21}$$

according to the complementarity $e = 1 - \mathcal{R}$ of emissivity and reflectivity[12] at a given polarization.

Emissivity is the parameter that characterizes the ability of a body to originate electromagnetic radiation by spontaneous emission; it provides important information on the observed terrestrial environment, as the following examples suggest.

The figures from 8.4 to 8.6 display the expected microwave emissivities of water and of homogeneous terrain with ideally smooth surfaces at vertical and horizontal polarizations. All diagrams highlight the divarication of the emissivities at the two polarizations as the observation direction departs from the normal to the surface. This is a consequence of the diverse trends of the reflection coefficients with the incidence angle discussed in Sects. 6.2.2 and 6.3.2. Figure 8.4 shows that little variations of the emissivity of a smooth water surface can be expected with microwave frequency, at least in the range from L- to X-band. Rather, wind-induced roughness can affect emissivity through the different frequency-dependent mechanism outlined in Sect. 14.2.4. The following figures refer to simulated soil with different moisture contents. Figure 8.5 shows how the C-band emissivity decreases with increasing soil moisture content. The pseudo-Brewster angle, at which the emissivity on vertical polarization is almost unitary, is identified. The angle displaces towards higher values as the moisture content, and hence the permittivity, increase, as indicated by (6.21) for lossless materials and by the diagrams in Sect. 6.3.2 for the lossy

[11] The body is assumed black at any polarization.

[12] Clearly in this case of plane boundary.

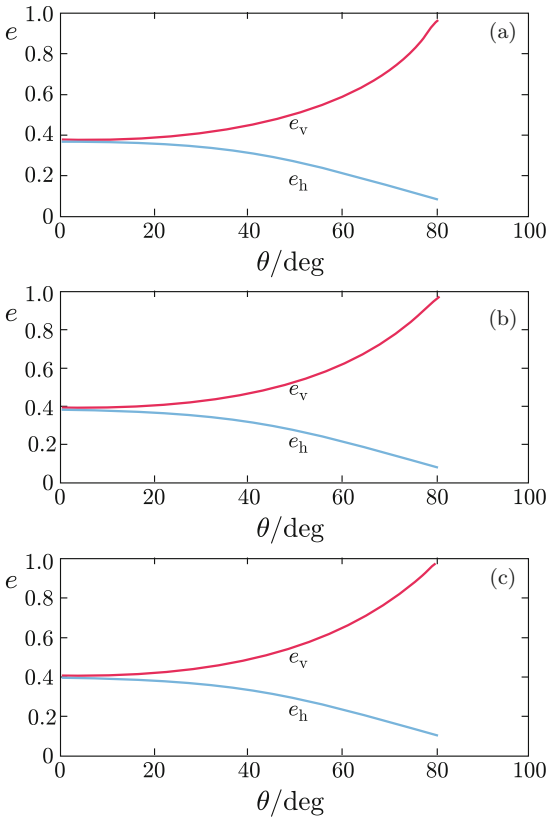

Fig. 8.4 Modeled microwave emissivity e of fresh water with flat surface vs. observation angle θ for L (**a**), C (**b**) and X (**c**) bands at vertical (e_v) and horizontal (e_h) polarizations

case. The decrease of the L-band emissivity with increasing soil moisture shown by the diagrams of Fig. 8.6 is more observable than at C-band, because of the slightly larger sensitivity of the permittivity to the amount of water indicated by Fig. 2.20. The displacement of the pseudo-Brewster angle is also apparent, as well as the discernible decrease of the maximum emissivity below one for the wettest terrain. The trend of $e_p(\theta)$ is consistent with that of the reflection coefficient shown, for instance, in Fig. 6.14, given, in this case, the complementarity between emissivity and reflectivity.

8.1.4 Thermal Emission from Plane-Layered Body

The simplifications brought by the assumption of dielectric and thermal homogeneity have lead to the preceding results, which are a quite useful reference for understanding the coarse characteristics of the thermal emission. To start gaining a finer insight into the behavior of some real terrestrial environment, the basic relation (8.9) is the natural starting point. Once relaxed the homogeneity conditions,

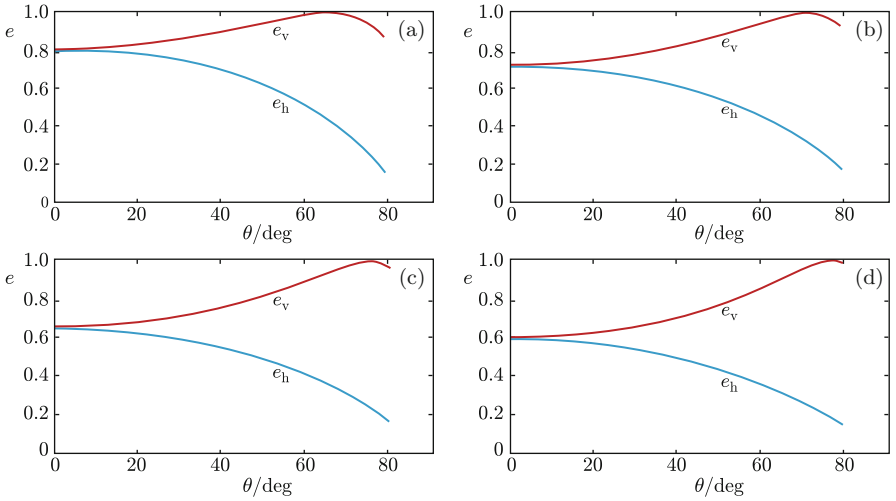

Fig. 8.5 Modeled C-band emissivity e of ideal flat-surface homogeneous terrain vs. observation angle θ: (**a**), dry ($m_v = 12\,\%$); (**b**), moist ($m_v = 21\,\%$); (**c**), wet ($m_v = 31\,\%$); (**d**), very wet ($m_v = 35\,\%$). Curves e_v refer to vertical polarization, e_h to horizontal polarization

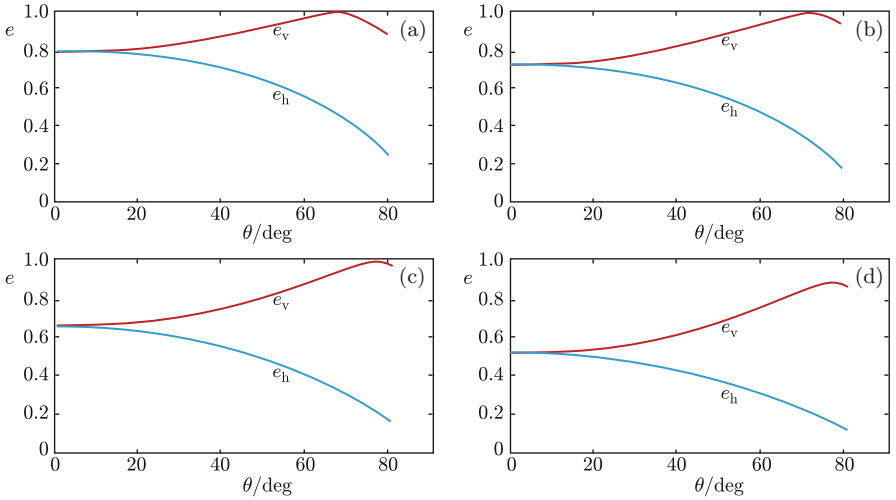

Fig. 8.6 Modeled L-band emissivity e of ideal flat-surface homogeneous terrain vs. observation angle θ: (**a**), dry ($m_v = 12\,\%$); (**b**), moist ($m_v = 21\,\%$); (**c**), wet ($m_v = 31\,\%$); (**d**), very wet ($m_v = 35\,\%$). Curves e_v refer to vertical polarization, e_h to horizontal polarization. Note that $e_v < 1$ at the pseudo-Brewster angle for the wettest soil (**d**)

the areic power $\mathcal{P}_{\text{TH}}$ carried at far distance by the thermal radiation originated by the inhomogeneous volume V'_{T} with non-uniform temperature distribution, but in LTE, is

$$\langle \mathcal{P}_{\text{TH}} \rangle = \frac{\omega\, \epsilon_0}{4\pi\, \eta_0\, |\mathcal{M}|^2} \iiint_{V'_{\text{T}}} \Theta\, \tilde{\epsilon}_{\text{j}}\, \boldsymbol{E}_{\text{t}} \cdot \boldsymbol{E}_{\text{t}}{}^{*}\, \text{d}V' \ .$$

The permittivity of the material is now assumed not to vary appreciably on the horizontal plane and, moreover, the dielectric vertical variations are supposed sufficiently smooth that the virtual internal field $\boldsymbol{E}_{\text{t}}$ can be locally approximated by the plane wave (6.24) refracted into a homogeneous lossy half-space:

$$\boldsymbol{E}_{\text{t}}(\boldsymbol{r}'_{\text{T}}) = \boldsymbol{E}'_{\text{t0}}\, e^{-\alpha' z' - j(\beta'_x x' + \beta'_z z')} \ .$$

Then,

$$\langle \mathcal{P}_{\text{TH}} \rangle = \frac{f\epsilon_0}{2\pi}\, \frac{\boldsymbol{E}'_{\text{t0}} \cdot \boldsymbol{E}'^{*}_{\text{t0}}}{2\eta_0\, |\mathcal{M}|^2} \iiint_{V'_{\text{T}}} \Theta\, \tilde{\epsilon}_{\text{j}}\, e^{-2\alpha' z'}\, \text{d}V' \ .$$

If neither the temperature varies appreciably on the horizontal plane,

$$\langle \mathcal{P}_{\text{TH}} \rangle = f\epsilon_0\, \frac{\mathcal{P}'_{\text{t}}(0)}{|\mathcal{M}|^2} A'_{\text{T}} \int_0^{\infty} \Theta(z')\, \tilde{\epsilon}_{\text{j}}(z')\, e^{-2\alpha' z'}\, \text{d}z' \ ,$$

where A'_{T} is the area of the surface $\Delta S'_{\text{T}}$ delimiting the emitting volume V'_{T}. The refracted test power density $\mathcal{P}'_{\text{t}}(0)$ is the part of virtual incident power that crosses the unit area of the body boundary:

$$\mathcal{P}'_{\text{t}}(0) = \boldsymbol{\mathcal{P}}_{\text{t}} \cdot \mathbf{z}_0 = \mathcal{P}_{\text{t}} |\mathbf{r}_{\text{oe}} \cdot \mathbf{z}_0| = \left(1 - |q_p|^2\right) \mathcal{P}_{\text{t}} \cos\theta \ ,$$

where $\mathcal{P}_{\text{t}}$ is the modulus of the Poynting vector that the test source sends onto the surface A'_{T} of the body and θ the incidence angle, corresponding to the direction $-\mathbf{r}_{\text{oe}}$ of observation. Note that the reflection coefficient q_p takes into account the variation of permittivity in the vertical direction, as considered in Sect. 7.3.3. Finally, the thermal power density radiated at p-polarization by the body through its surface A'_{T} is

$$\langle \mathcal{P}_{\text{TH}} \rangle = f\epsilon_0\, (1 - \mathcal{R}_p)\, \frac{\mathcal{P}_{\text{t}}}{|\mathcal{M}|^2} A'_{\text{T}} \cos\theta \int_0^{\infty} \Theta(z')\, \tilde{\epsilon}_{\text{j}}(z')\, e^{-2\alpha' z'}\, \text{d}z' \ . \tag{8.22}$$

The relation (3.26) between the power density $\mathcal{P}_{\text{t}}$ that the test source virtually sends onto the surface of the body and the momentum $\mathcal{M}$ of the test source allows (8.22) to be written

$$\langle \mathcal{P}_{\text{TH}} \rangle = \frac{1 - \mathcal{R}_p}{8\,\lambda_0^3}\,\Delta\Omega \int_0^\infty \Theta(z')\,\tilde{\epsilon}_{\text{j}}(z')\,e^{-2\alpha' z'}\,\text{d}z' \ ,$$

where use has been made of the solid angle $\Delta\Omega$ under which A'_{T} is seen from the location where $\mathcal{P}_{\text{TH}}$ is measured. The integral over depth z' points out that the effect of the thermodynamic temperature distribution in the body expressed by $\Theta(z')$ is weighted by the product of $\tilde{\epsilon}_{\text{j}}$ times the attenuation:

$$\langle \mathcal{P}_{\text{TH}} \rangle = \frac{1 - \mathcal{R}_p}{8\,\lambda_0^3}\,\Delta\Omega \int_0^\infty \mathcal{W}(z')\,\Theta(z')\,\text{d}z' \ .$$

The *weighting function*, defined here by[13]

$$\mathcal{W}(z') := \tilde{\epsilon}_{\text{j}}(z')\,e^{-2\alpha' z'} \ , \tag{8.23}$$

assumes considerable importance in the radiometric observation of the Earth's atmosphere [1, 9]. However, the concept of weighting function is quite general and can form the basis for retrieving the profiles of a number of bio-geo-physical parameters from both passive and active remote observations [7, 10]. The variation of $\mathcal{W}$ with the depth[14] z' depends crucially on the *profile* of $\tilde{\epsilon}_{\text{j}}$, which affects the absorption coefficient α', as discussed in Sect. 6.3.1. In particular,

- if $\tilde{\epsilon}_{\text{j}}$ is constant, $\mathcal{W}$ is an exponential function decreasing with z';
- similarly, if $\tilde{\epsilon}_{\text{j}}$ is a decreasing function of depth, $\mathcal{W}$ decreas monotonically;
- if, on the other side, $\tilde{\epsilon}_{\text{j}}$ increases with depth, a maximum of $\mathcal{W}$ forms at a given z'.

In the last case, since in general $\tilde{\epsilon}_{\text{j}}(z')$ is a function of frequency, the maximum of $\mathcal{W}(z')$ at different frequencies may occur at different depths: the higher $\tilde{\epsilon}_{\text{j}}(z')$, at shallower depths the maximum of the weighting function forms. Coarsely speaking, thermal emission is contributed by the bulk of the body for materials presenting weak attenuation, whereas only the layers close to the surface contribute when attenuation is high. From another point of view, the radiation originating from the deeper layers gets partially absorbed before being able to emerge from the surface $z' = 0$: the higher the attenuation, the shallower the layers from which an appreciable fraction of the radiation able to cross the surface originates. Figure 8.7 shows the two coarse trends of the weighting functions, the monotonically decreasing $\mathcal{W}$ and the peaked one.

[13] The present weighting function is relative to temperature: functions relative to other parameters are outlined in Sect. 9.4 for the atmosphere.

[14] In general, z' denotes the longitudinal coordinate.

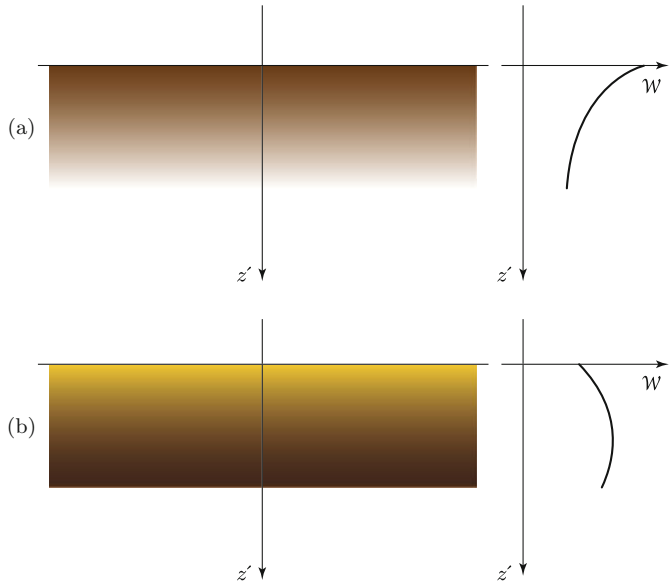

Fig. 8.7 Typical profiles of the imaginary part of permittivity and of the corresponding weighting function: the shades of color denote the value of $|\tilde{\epsilon}_j|$ (light corresponds to low values, dark to high values); constant or decreasing $|\tilde{\epsilon}_j(z')|$ yields a monotonically decreasing $\mathcal{W}(z')$, (**a**), while $|\tilde{\epsilon}_j|$ increasing with z' leads to a peak in the weighting function, (**b**)

8.1.5 Thermal Emission from Randomly Inhomogeneous Bodies

If the material is randomly inhomogeneous and the volume is bound by a rough surface, its thermal emission also depends on the bulk dielectric structure and on the surface roughness. The electromagnetic reciprocity, which clearly holds for any kind of inhomogeneity, provides the basic means of evaluating the thermal emission. In fact, the emissivity is derived from the fraction of the geometrically incident power virtually arriving from the test source that enters into the body and is dissipated inside it:

$$e_p = \frac{W_{\mathrm{td}p}}{\mathcal{P}_{\mathrm{t}p}\, A_{\mathrm{gt}}\, \cos\theta} ,$$

in which $W_{\mathrm{td}p}$ is the power dissipated in the material when the areic power $\mathcal{P}_{\mathrm{t}p}$ carried by the test wave at polarization p virtually impinges from the direction of observation $-\mathbf{r}_{\mathrm{oe}}$ opposite to that of emission.[15] The rough surface of the body is

[15] As before, the direction of emission is assumed to be the direction in which the observing platform is seen from the observed target.

assumed plane on average within the resolution cell of area ΔA_g, and θ is the angle between $\mathbf{r}_\mathrm{oe}$ and the normal to the surface.

This power virtually entering the body is the power $W_{tp}^{(\mathrm{i})}$ incident onto ΔA_g deprived of the fractions that are coherently reflected and incoherently scattered both from the surface layer and from the bulk of the inhomogeneous material, according to the approach of Sect. 7.2:

$$W_{\mathrm{td}p} = W_{tp}^{(\mathrm{i})}(1 - \mathcal{R}_{cp}) - W_{tp}^{(\mathrm{s})} \,. \tag{8.24}$$

In Eq. (8.24), $\mathcal{R}_{cp}$ denotes the coherent reflectivity linked to the reflection coefficient, while $W_{tp}^{(\mathrm{s})}$ is the total scattered power. This latter is the power scattered over the entire solid angle[16] by the incoherent mechanism discussed in Sect. 7.4:

$$W_{tp}^{(\mathrm{s})} = \int_0^{2\pi}\int_0^{\pi} \left\langle \mathcal{P}_\mathrm{t}^{\prime(\mathrm{s})} \right\rangle \mathrm{d}\varphi \, \mathrm{d}\theta \,. \tag{8.25}$$

The incoherently scattered power is related to the incident one by the incoherent reflectivity $\mathcal{R}_{ip}$

$$W_{tp}^{(\mathrm{s})} = \mathcal{R}_{ip} W_{tp}^{(\mathrm{i})} \,, \tag{8.26}$$

so that the power virtually entering the body and being absorbed is

$$W_{\mathrm{td}p} = (1 - \mathcal{R}_{cp} - \mathcal{R}_{ip})\, W_{tp}^{(\mathrm{i})} = (1 - \mathcal{R}_p)\, W_{tp}^{(\mathrm{i})} \,, \tag{8.27}$$

where the *reflectance* at p-polarization $\mathcal{R}_p := \mathcal{R}_{cp} + \mathcal{R}_{ip}$ has been introduced to take account of the power that is *globally* rejected by the body. The reflectance now replaces the reflectivity used in (8.21) for the particular case of plane boundaries.

When the emitting volume is a portion of a water body or of solid land, which in practice are half-spaces of infinite thickness,[17] all the net power that is virtually delivered to the body through ΔA_g gets dissipated. In this case the power is globally scattered only into the "upper" half-space, which means that the elevation angle θ in (8.25) and shown in Fig. 8.8 varies between $\theta = 0$ and $\theta = \pi/2$. The power scattered by a randomly inhomogeneous material depends on its spatial permittivity structure and, in particular, Sect. 7.4.4 shows that it is related to the spatial spectrum $\mathcal{S}_{\epsilon\mathrm{t}}(\boldsymbol{\kappa}_\mathrm{t})$ of its transverse dielectric inhomogeneities by (7.54). The spectral approach can be readily extended to the three-dimensional case. According to (8.25), the *total* power scattered into the upper half-space is then obtained by integrating the *three-dimensional* spatial spectrum with respect to azimuth and elevation angles.

[16] For the time being, the emitting body is assumed of finite dimensions.

[17] A finite-thickness body also behaves like a half-space when *electromagnetically thick*.

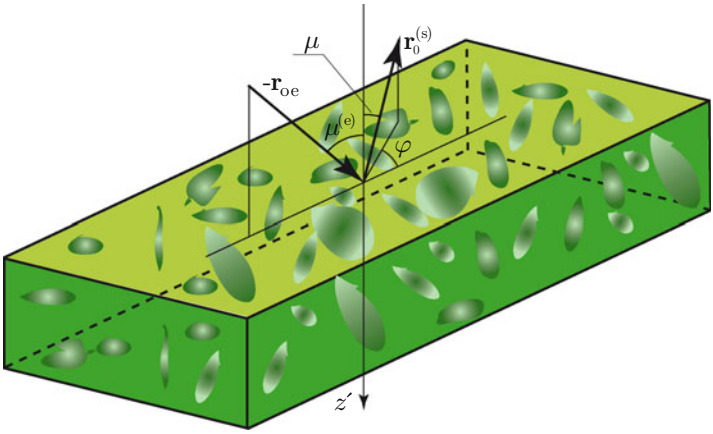

Fig. 8.8 Geometry of emission from a randomly inhomogeneous body: $\mathbf{r}_{oe}$, at the elevation angle $\theta^{(e)}$, is the direction in which emission is observed; φ and θ are the variable azimuth and elevation angles in (8.25)

As discussed in Sect. 7.4.4, a suitable reference inhomogeneous medium is statistically homogeneous and isotropic, with real[18] Gaussian autocovariance function of the permittivity fluctuations

$$\left\langle \Delta\tilde{\epsilon}'(\boldsymbol{r}_{1'})\,\Delta\tilde{\epsilon}'^{*}(\boldsymbol{r}_{2'})\right\rangle \simeq \sigma_\epsilon^2\,\mathrm{e}^{-\left[\left(|\boldsymbol{r}_{1'}-\boldsymbol{r}_{2'}|\right)/r_\epsilon\right]^2} = \sigma_\epsilon^2\,\mathrm{e}^{-\left(r/r_\epsilon\right)^2}\,, \tag{8.28}$$

the three-dimensional spatial spectrum[19] of which is [11, Chap. 4]

$$\mathcal{S}_\epsilon(\varkappa) = \frac{\sigma_\epsilon^2\, r_\epsilon^{\,3}}{8\,\pi^{3/2}}\,\mathrm{e}^{-\left(\varkappa\, r_\epsilon/2\right)^2}\,. \tag{8.29}$$

The power virtually scattered by the volume $V' = \Delta A_\mathrm{g} \times d$ of such a low-loss material into the upper half-space is obtained by relating the angular power density $\left\langle \mathcal{P}_\mathrm{t}'^{(s)}\right\rangle$ to the three-dimensional dielectric spatial spectrum (8.29) and using (8.25). For a unitary geometrically incident test power, and taking account of the fraction removed by reflection through the coefficient $\mathcal{R}_p$, the incoherently scattered power is[20]

[18] The condition $\tilde{\epsilon}_\mathrm{r} \gg \tilde{\epsilon}_\mathrm{j}$ if frequently satisfied in natural materials.

[19] The spatial spectral density (8.29) is recognized to be the three-dimensional generalization of (7.56).

[20] The dependence of the wavenumber $\varkappa$ on both azimuth and elevation angles has to be considered.

$$W_{tp}^{(s)} = (1 - \mathcal{R}_p) \frac{1}{16\sqrt{\pi}} \frac{r_\epsilon \, d}{\lambda_0^2} \frac{\sigma_\epsilon^2}{\langle \tilde{\epsilon} \rangle} \left[1 - \mathrm{e}^{-\left(2\pi \frac{r_\epsilon}{\lambda_0} \right)^2} \right] . \tag{8.30}$$

To arrive at (8.30), a simplified approach ignoring attenuation has been followed. However, the results of Sect. 6.3.1 point out that the amplitude of the test wave that virtually penetrates into an actual material does decrease with depth. If the field decay is taken into account by simply replacing the thickness d with the penetration depth ℓ obtained by (6.27), the emissivity is finally obtained as[21]

$$e_p \simeq (1 - \mathcal{R}_p) \left\{ 1 - \frac{1}{16\sqrt{\pi}} \frac{r_\epsilon \, \ell}{\lambda_0^2} \frac{\sigma_\epsilon^2}{\langle \tilde{\epsilon} \rangle} \left[1 - \mathrm{e}^{-\left(2\pi \frac{r_\epsilon}{\lambda_0} \right)^2} \right] \right\} . \tag{8.31}$$

Some useful indications on the effect of the structure of the terrestrial environment on the emissivity behavior can be drawn from (8.31).

8.1.5.1 Connection of Emission with Reflection

The coherent reflectivity $\mathcal{R}_p$ of the air-to-material transition, modeled, for instance, as the layer with linearly increasing average permittivity considered in Sect. 7.3.3, decreases as roughness increases. This property has two important consequences:

- for given permittivity structure and frequency (or wavelength), the emissivity increases with increasing surface roughness, which also implies that, due to microstructure, emissivity tends to be higher in the thermal infrared than at microwaves, with slight effect of polarization[22];
- the emissivity at vertical polarization is expected to be larger than that at the horizontal one.

Note that the coherent reflectivity is relative to the direction $-\mathbf{r}_{\mathrm{oe}}$ of incidence of the test wave, which corresponds to the direction of observation. This implies a decrease of emissivity with increasing the elevation angle $\theta^{(\mathrm{e})}$ indicated in Fig. 8.8.

8.1.5.2 Effect of Structure

The dielectric structure of the material affects its emission through both magnitude and dimensions of the permittivity fluctuations.

[21] In case the emissivity of a slab is considered, it must be assumed sufficiently thick compared with the penetration depth, so that no appreciable test power leaks from its bottom boundary.

[22] The effects of the surface macroscopic roughness [3] should also be accounted for.

Emissivity decreases with increasing scattering from the inhomogeneous material, that is, given (8.30), with increasing magnitude σ_ϵ^2 of the dielectric inhomogeneities. Given the relatively low values that the permittivity of many natural and man-made materials have in the infrared, as outlined in Sect. 2.2, the emissivity in this wavelength range is generally higher that at microwaves. Moreover, a material with strong inhomogeneities tends to emit less than the same homogeneous material, clearly apart from the aforementioned effect of the surface reflection.

The correlation radius of the dielectric inhomogeneities, which Sect. 7.4.4 shows to be a measure of their characteristic dimension, plays a crucial role in determining the emissivity of the inhomogeneous material. Dielectric irregularities that are small with respect to wavelength raise the value of the exponential in (8.30) and produce little scattering,[23] thus favoring emission. For example, vegetation canopies with relatively small plant elements, such as wheat, rice, or rape-seed, produce little scattering at microwave frequencies and, if sufficiently thick, they tend to have large emissivity. In the atmosphere, non-precipitating clouds behave analogously and satellite or ground-based radiometric observations at microwaves (and up to the thermal infrared) can be interpreted on the basis of a *non-scattering atmosphere*, that is, of a medium in which the effect of absorption predominates over that of scattering (Sect. 9.2).

8.1.5.3 Effect of Absorption

Absorption determines the penetration depth ℓ, which, in combination with the correlation radius and the wavelength, affects the emissivity according to (8.31). For given values of the various parameters, emissivity is higher for lower ℓ, i.e., at more absorbed wavelengths. This effect is relevant to material identification.

Section 2.2 reports examples of $\tilde{\epsilon}_\mathrm{j}$ of the terrestrial materials of main interest. The values of $\tilde{\epsilon}_\mathrm{j}(\lambda_0)$ correspond to the penetration depths $\ell(\lambda_0)$ and, in turn, to the emissivity $e(\lambda_0)$. This implies that the measure of $e(\lambda_0)$ carries information on the spectrum of $\tilde{\epsilon}_\mathrm{j}$: at least in principle, the emissivity is higher at the wavelengths at which $\tilde{\epsilon}_\mathrm{j}$ peaks[24] and the material is more opaque. Therefore, information on the nature of the materials is contained in the spectrum of emissivity, although, in practice, the effects of other physical and observational parameters often act to entangle the interpretation of the measured spectral features of thermal emission.

[23] This issue is discussed further in Sect. 9.1.

[24] Provided the reflectivity is not appreciably affected by the wavelength-dependent $\tilde{\epsilon}_\mathrm{r}$.

8.2 Features of Thermal Radiation

As mentioned previously, the electromagnetic field originated by thermal emission is random, therefore, only second (and, when needed, higher) moments are meaningful. Power is the second-order moment that is commonly measured. Quantities directly derived from the power measurements are then frequently used to characterize the thermal radiation.

It has to be pointed out that, on one side, the technology of man-made (typically, antennas, radar) radiation and, on the other, the studies on natural radiation were developed in diverse disciplinary fields. The separated cultural environments, unfortunately, have led to *different names* possibly given to the *same electromagnetic quantities*. For analogous reasons, the names of some quantities in the *optical* (ultraviolet, visible, infrared) range may differ from those of the same quantities at *microwaves*. We need, at this point, to stress that the comprehension of Earth observation on a unified basis would benefit from keeping uniformity of nomenclature. Nevertheless, making reference to the usual terminology was deemed appropriate, both to avoid possible misunderstanding and to mitigate the hurdle in drawing on different sources of information.

Keeping in mind this preliminary remark, some relevant parameters characterizing the thermal radiation are now listed and sketched out.

8.2.1 Thermal Radiation Parameters

Coming back to the measurement of emitted power, we mention that, in the thermal infrared practice, the time-average areic power, that is the Poynting vector average modulus $\langle \mathcal{P}_{\mathrm{T}} \rangle$, is named *radiant flux* or, also, *irradiance*. Since the thermal radiation is not monochromatic, spectral quantities are needed: therefore, reference is made to the power per unit area and unit wavelength $\langle \mathcal{P}_{\mathrm{TH}\lambda} \rangle$ carried by the thermal radiation in the neighborhood of a given λ_0

$$\langle \mathcal{P}_{\mathrm{TH}\lambda}(\lambda_0) \rangle := \left. \frac{\mathrm{d}\langle \mathcal{P}_{\mathrm{TH}}(\lambda) \rangle}{\mathrm{d}\lambda} \right|_{\lambda_0} , \tag{8.32}$$

which is named *spectral radiant flux*. Given the optical origin of the definition, reference is made to the wavelength, typically measured in micrometers.

Antennas or man-made scatterers are of limited dimensions, so that from a given location at far distance they appear as point sources and the *coherent* electromagnetic radiation they originate travels in one given (radial) direction. The earth surface or the atmosphere are instead extended thermal sources of *incoherent* radiation and are not seen as point objects by the observing systems. Rather, at a given point, the thermal radiation travels in different directions and its spatial variation can differ from that of a spherical wave. Therefore, differential quantities

involving angular dimensions and orientation are suitably demanded that, in general, do not have their counterpart in radar wave propagation. Consistently with the quantity previously defined by (8.17) for the emission from a body, the thermal radiation field is characterized by the *radiance* $\mathcal{I}(\mathbf{r}_0)$ in direction[25] $\mathbf{r}_0$, defined as the power traveling within the unit solid angle in the considered direction that crosses the oriented unit area:

$$\mathcal{I}(\mathbf{r}_0) := \frac{\mathrm{d}W}{\mathrm{d}A\,\cos\gamma\,\mathrm{d}\Omega} = \frac{\mathrm{d}\mathcal{P}(\mathbf{r}_0)}{\mathrm{d}\Omega}\,. \tag{8.33}$$

In Eq. (8.33) γ is the angle between the considered direction $\mathbf{r}_0$ and the normal to the elementary surface $\mathrm{d}A$, while $\mathrm{d}\Omega$ is the elementary solid angle about $\mathbf{r}_0$, and $\mathrm{d}\mathcal{P}$ is the modulus of the (average) Poynting vector associated with the thermal field traveling along $\mathbf{r}_0$. The definition of radiance looks analogous to the power radiation pattern introduced in Sect. 3.1.4.3. Actually, the angular power density (3.40) originated by a coherent point source is a *finite* quantity,[26] while the corresponding spectral radiance (8.33) diverges. Thermal radiation is substantially different: the angular power emitted by an element of the extended incoherent source characterized by (8.4) is infinitesimal and the radiance

$$\mathcal{I}(\mathbf{r}_0) = \frac{\mathrm{d}\mathcal{P}(\mathbf{r}_0)}{\mathrm{d}A\,\cos\gamma}\,, \tag{8.34}$$

is finite. To take in due account the non-monochromaticity of thermal fields, the *spectral radiance* $\mathcal{I}_\lambda$ denoting the radiance per unit wavelength is defined, analogously to (8.32):

$$\mathcal{I}_\lambda(\lambda, \mathbf{r}_0) := \frac{\mathrm{d}\mathcal{I}(\lambda, \mathbf{r}_0)}{\mathrm{d}\lambda}\,. \tag{8.35}$$

Multi-spectral measurements, consisting of the values of $\mathcal{I}_\lambda$ of the emitted radiation at different wavelengths, allow the spectral characterization of the emitting source.

At microwaves, the name *brightness*, denoted by $\mathcal{I}_f$, is used in place of spectral radiance. Since in this range of the electromagnetic spectrum (cf. Sect. 10.1.1) frequency is often used in place of wavelength, brightness refers to the power density per unit frequency. The relation between brightness $\mathcal{I}_f(f)$ and spectral radiance $\mathcal{I}_\lambda(\lambda)$ is based essentially on the spectral energy conservation, which is expressed by

[25] From now on, the direction of observation $\mathbf{r}_{oe}$ will be simply denoted by $\mathbf{r}_0$. With further regard to the notations, power and derived thermal quantities are understood to be averages, hence neither the sharp bracket symbol nor subscript $_{TH}$ will appear in the following, unless necessary.

[26] The point source current in Sect. 3.1.1 is described by an impulsive function.

$$\mathcal{I}_f(f) = \left|\frac{\mathrm{d}\lambda}{\mathrm{d}f}\right| \mathcal{I}_\lambda(\lambda) \ . \tag{8.36}$$

8.2.2 Black-Body Radiation

Given the definition (8.20) and the dependence (8.5) of Θ on temperature and wavelength stemming from the FDT, the spectral radiance $\mathcal{I}_{\lambda\mathrm{b}}$ of the black body, also denoted by $\mathcal{B}_\lambda$, is

$$\mathcal{B}_\lambda(\lambda_0, T) = 2\hbar c_0^2 \left\{\lambda_0^5 \left[\mathrm{e}^{(\hbar c)/(\lambda_0 k T)} - 1\right]\right\}^{-1} \ . \tag{8.37}$$

The value given by (8.37) is the power density per unit surface, unit solid angle and unit wavelength leaving the surface of a black body at temperature T in the neighborhood of wavelength λ_0. Consistently with (8.21), the function $\mathcal{B}_\lambda$ sets the upper limit to the spectral radiance emitted around λ_0 by any body at temperature T:

$$\mathcal{I}_\lambda(\lambda_0, T, \mathbf{r}_0) \le \mathcal{B}(\lambda_0, T) \ .$$

Equation (8.37) is known as *Planck's radiation law* [2, Chap. 2] and the function $\mathcal{B}_\lambda$ is the *Planck function*. The *spectral emissivity* e_λ is correspondingly introduced following (8.21) as

$$\mathcal{I}_\lambda(\lambda_0, T, \mathbf{r}_0) = e_\lambda(\lambda_0, \mathbf{r}_0)\, \mathcal{B}(\lambda_0, T) \ . \tag{8.38}$$

The Planck's law shows that the spectral radiance of a black body at temperature T has its maximum at a wavelength λ_M that depends on T according to *Wien's law*:

$$\lambda_\mathrm{M} = \frac{2898}{T} \quad [\mu\mathrm{m}] \ ,$$

where the wavelength is expressed in micrometers. As an example, the "effective" temperature of Sun $T_\odot \approx 5800\,\mathrm{K}$ yields a maximum of spectral radiance at $\lambda_\mathrm{M} \approx 500\,\mathrm{nm}$. At temperatures commonly encountered in the terrestrial environment (say between 240 and 320 K), the maximum of the Planck function falls in the wavelength range $9\,\mu\mathrm{m} \lesssim \lambda_0 \lesssim 12\,\mu\mathrm{m}$ and the power is mainly emitted in the spectral region between $\lambda_0 \approx 4\,\mu\mathrm{m}$ and $\lambda_0 \approx 20\,\mu\mathrm{m}$, which, for this reason, is named **t**hermal **i**nfra**r**ed (TIR).

The temperature of the body, on which the covariance of the source current depends according to (8.4) and (8.5), also directly affects the total emitted power: the *Stefan-Boltzmann law* states that the black-body radiance depends strongly on temperature according to

$$\mathcal{I}(T) = \int_0^\infty \mathcal{B}(\lambda_0, T)\, \mathrm{d}\lambda_0 = \frac{\sigma}{\pi} T^4 ,$$

in which $\sigma = 5.67 \cdot 10^{-8}\,\mathrm{W\,m^{-2}\,K^{-4}}$ is the Stefan-Boltzmann constant.

8.2.2.1 Black-Body Radiation at Microwave Frequencies

At the relatively long microwave wavelengths and at the temperatures of the terrestrial environment, the exponent at the denominator of the Planck function is such that

$$\frac{hc_0}{\lambda_0 k T} \ll 1 .$$

The exponential can then be replaced by its first-order Taylor polynomial, which reduces the Planck function to

$$\mathcal{B}(\lambda_0, T) \simeq \frac{2c_0 k T}{\lambda_0^4} . \tag{8.39}$$

Equation (8.39) is the *Rayleigh-Jeans approximation* of the Planck's law. In its regime of validity, the Rayleigh-Jeans' law offers the advantage of setting a linear relation between emitted power and temperature.

The microwave black-body brightness (8.39) is expressed as a function of frequency f according to (8.36) by

$$\mathcal{B}(f, T) = \left|\frac{\mathrm{d}\lambda}{\mathrm{d}f}\right| \mathcal{B}(\lambda, T) = \frac{2k T f^2}{c_0^2} .$$

The linear relation between power and temperature allows the quick introduction of the *brightness temperature* T_B of a source of thermal radiation characterized by the spectral radiance $\mathcal{I}_f$

$$T_\mathrm{B}(f, T, \mathbf{r}_0) = \frac{\mathcal{I}_f(f, T, \mathbf{r}_0)\, c_0^2}{2k f^2} . \tag{8.40}$$

The brightness temperature corresponds to the temperature of a black body yielding the same microwave brightness as the observed body in direction $\mathbf{r}_0$ at a given polarization. Temperature T_B is usually used in place of brightness $\mathcal{I}$.

If the thermodynamic temperature T of the body can be identified, the microwave emissivity e_f at frequency f, corresponding to the spectral emissivity (8.38), is the ratio

$$e_f(f, \mathbf{r}_0) = \frac{T_\mathrm{B}(f, T, \mathbf{r}_0)}{T} \tag{8.41}$$

and is clearly related by (8.27) to the reflectance[27] $\mathcal{R}_p$ of the emitting body at frequency f and polarization p

$$e_{fp}(f, \mathbf{r}_0) = 1 - \mathcal{R}_p(f, \mathbf{r}_0) \ . \tag{8.42}$$

It is understood that the brightness temperature (8.40) generally varies with the polarization, just as reflectance and emissivity.

Emitted Waves Carry Information

We know that charges in the matter get accelerated by the electric field, from which they draw energy. The energy is eventually transferred to heat the material through collisions. We reasonably envision the reciprocal path: collisions between charges in thermal agitation transfer energy to the field. We also know that the electromagnetic radiation originated by the thermal mechanism is obtained from Maxwell's equations containing the appropriate thermal source current. Given the obviously random nature of the process, source currents and radiated field are not deterministic, hence they must be described by moments. The key indication is that the magnitude of the source is proportional to the imaginary part of permittivity and depends on frequency and, as expected, on temperature.

At this point, the reader peculiarly interested in theoretic aspects will perceive the strength of the so far kept aside reciprocity theorem, which, through a carefully sustained conceptual effort, now succeeds in establishing the relation between thermal radiation and reflection. Finding how straight is the otherwise unpredicted relation between emission features and the parameters that affect the reflecting properties is amazing. Apart from the notional aspect, we realize that the thermal emission process, which can be reasonably deemed a form of wave-matter inner interaction, is able to generate remote information not only on the thermal state of the target, but also on its dielectric and geometric features. The conclusion holds for both homogeneous and inhomogeneous materials. In the latter case, the relevant scattering properties affect the emission behavior in the reciprocal mode.

The somewhat debated terminology for radiative notations is presented and selected. We encounter several quantities, including black body, emissivity, and radiance, which are basic to EO. The concept of weighting function also comes across. The more or less familiar fundamental laws that rule thermal emission are finally introduced and the convenient Rayleigh-Jeans microwave approximation is outlined.

[27] In case the thick body is homogeneous and a plane boundary is identified, the reflectivity $\mathcal{R}$ in (8.21) coincides with the reflectance $\mathcal{R}$ in (8.27).

References

1. Eyre JR Inversion methods for satellite sounding data. European Centre for Medium-Range Weather Forecasts (ECMWF). http://www.ecmwf.int/newsevents/training/rcourse_notes/DATA_ASSIMILATION/INVERSION_METHODS/Inversion_methods2.html. Visited on 22 Jan 2014
2. Goody RM, Yung YL (1995) Atmospheric radiation: theoretical basis. Oxford University Press. ISBN:9780195356106
3. Henderson BG, Theiler J, Villeneuve P (2003) The polarized emissivity of a wind-roughened sea surface: a Monte Carlo model. Remote Sens Environ 88(4):453–467. ISSN:0034-4257, doi:http://dx.doi.org/10.1016/j.rse.2003.09.003
4. Kelly FJ (1965) On Kirchhoff's law and its generalized application to absorption and emission by cavities. J Res Natl Bur Stand–B Math Math Phys 69B:165–171. doi:10.6028/jres.069B.019
5. Landau LD, Lifshitz EM (1960) Electrodynamics of continuous media. Pergamon. ISBN:9780080302751
6. Long MW, Rivers WK (1961) Submillimeter wave radiometry. Proc IRE 49(6):1024–1027. doi:10.1109/JRPROC.1961.287885
7. Menke W (1989) Geophysical data analysis: discrete inverse theory. Elsevier. ISBN:9780080507323
8. Nicoll GR (1957) The measurement of thermal and similar radiations at millimetre wavelengths. Proc IEE B: Radio Electron Eng 104(17):519–527. doi:10.1049/pi-b-1.1957.0199
9. Rodgers CD (1976) Retrieval of atmospheric temperature and composition from remote measurements of thermal radiation. Rev Geophys 14(4):609–624. doi:10.1029/RG014i004p00609
10. Rodgers CD (1990) Characterization and error analysis of profiles retrieved from remote sounding measurements. J Geophys Res 95(D5):5587–5595. doi:10.1029/JD095iD05p05587
11. Rytov SM, Kravtsov YA, Tatarskii VI (1989) Principles of statistical radio-physics 3: elements of random fields. Springer. ISBN:9783540178293

Chapter 9
Radiative Transfer and Passive Sensing

Chapter 7 highlights that most materials found in the Earth's environment are randomly inhomogeneous in space and time. Their dielectric structure is then characterized by permittivity values that fluctuate about the local average. By using a notation analogous to (7.24), permittivity is written

$$\epsilon(\boldsymbol{r},t)=\epsilon_0\left[\overline{\tilde{\epsilon}}(\boldsymbol{r})+\tilde{\epsilon}'(\boldsymbol{r},t)\right]\,, \tag{9.1}$$

where $\overline{\tilde{\epsilon}}$ is the value of $\tilde{\epsilon}$ averaged over the ensemble of realizations of the medium and $\tilde{\epsilon}'$ denotes its *slowly* fluctuating part.[1] The electromagnetic field produced by a source modeled by its impressed electric current $\boldsymbol{J}_{\rm s}$ satisfies the spectral Maxwell's equations (2.1)–(2.2):

$$\nabla\times\boldsymbol{E}=-\mathrm{j}\omega\mu_0\boldsymbol{H}\,; \tag{9.2}$$

$$\nabla\times\boldsymbol{H}=\mathrm{j}\omega\epsilon_0\left[\overline{\tilde{\epsilon}}(\boldsymbol{r})+\tilde{\epsilon}'(\boldsymbol{r},t)\right]\boldsymbol{E}+\boldsymbol{J}_{\rm s}\,, \tag{9.3}$$

which, given the presence of the fluctuations of permittivity which introduce a random parameter into (9.3), are *stochastic Maxwell's equations*, even if, unlike the thermal currents in (8.1) and (8.2), now the source is deterministic. The equations yield the quasi-monochromatic field in the random medium characterized by (9.1).

The field is obtained according to the procedure of Sect. 3.1 utilizing the Green's function taking due account of the dielectric inhomogeneities. Chapter 7 shows that these latter originate scattering, which redirects the wave coming from the source into different directions. It stands to reason that, in turn, the scattered waves undergo repeated scattering from the further inhomogeneities they encounter. Such

[1] The commonly encountered variations of $\tilde{\epsilon}'$ are slow as to preserve the quasi-monochromaticity (Sect. 1.3.2) of the field. Statistical homogeneity and isotropy are also suitable assumptions.

D. Solimini, *Understanding Earth Observation*, Remote Sensing and Digital Image Processing 23, DOI 10.1007/978-3-319-25633-7_9

a *multiple scattering* process increasingly perturbs the field with respect to the configuration it has in the homogeneous medium. Therefore, waves in random media are clearly rather complicate to model and considerably involved analytical tools are required.

The following section presents a quite coarse outline of multiple scattering[2] in random media, essentially based on [64, Chap. 4], in the attempt of making some of the basic conceptual aspects to seep through the burden of the mathematical formalism. The follow-up brings about the subsequent radiative transfer approach to Earth observation, in which some outcome of the theoretical analysis finds important practical use, especially in passive remote sensing.

9.1 Radiation in Random Medium

The characteristics of the field are determined by extending to the randomly inhomogeneous medium the analysis of the radiation developed in Chap. 3 for the vacuum. The Green's function, introduced in that deterministic context by (3.8), becomes now the *random Green's function*, satisfying the random wave equation for a unit point source current located in $\boldsymbol{r}_\mathrm{s}$:

$$\nabla^2 \mathcal{G}(\boldsymbol{r}, \boldsymbol{r}_\mathrm{s}) + \kappa_0^2 \left[\overline{\overline{\epsilon}}(\boldsymbol{r}) + \tilde{\epsilon}\,'(\boldsymbol{r}, t) \right] \mathcal{G}(\boldsymbol{r}, \boldsymbol{r}_\mathrm{s}) = -\delta(\boldsymbol{r} - \boldsymbol{r}_\mathrm{s}) \ .$$

By taking the average permittivity as suitable deterministic reference, $\mathcal{G}$ is written as

$$\mathcal{G}(\boldsymbol{r}, \boldsymbol{r}_\mathrm{s}) = \mathcal{G}_0(\boldsymbol{r}, \boldsymbol{r}_\mathrm{s}) + \mathcal{G}'(\boldsymbol{r}, \boldsymbol{r}_\mathrm{s}) \ , \tag{9.4}$$

where $\mathcal{G}_0$ is the *primary* Green's function, produced by the unit source in the average spatial distribution of permittivity. Under the weak inhomogeneity hypothesis, $\mathcal{G}_0$ satisfies the deterministic wave equation corresponding to (5.3):

$$\nabla^2 \mathcal{G}_0(\boldsymbol{r}, \boldsymbol{r}_\mathrm{s}) + \kappa_0^2 \, \overline{\overline{\epsilon}}(\boldsymbol{r}) \ \mathcal{G}_0(\boldsymbol{r}, \boldsymbol{r}_\mathrm{s}) = -\delta(\boldsymbol{r} - \boldsymbol{r}_\mathrm{s}) \ , \tag{9.5}$$

while $\mathcal{G}'$ is the random component that accounts for the effect of the dielectric fluctuations $\tilde{\epsilon}\,'$. The primary Green's function represents a coherent wave, in the sense that the phase of $\mathcal{G}_0$ can be determined from the dielectric structure $\overline{\overline{\epsilon}}(\boldsymbol{r})$ of the material in which it propagates, by following, for instance, the "optical" approach of Chap. 5. Instead, $\mathcal{G}'$ corresponds to an incoherent wave, since it originates from a random source and therefore its phase cannot be established.

[2] Only scalar waves are considered.

Substitution for $\mathcal{G}$ yields the equation for the Green's function random component

$$\nabla^2 \mathcal{G}' + \kappa_0^2 \, \overline{\tilde{\epsilon}}(\boldsymbol{r}) \, \mathcal{G}' = -\kappa_0^2 \, \tilde{\epsilon}'(\mathcal{G}_0 + \mathcal{G}') \; .$$

A *secondary source* $\boldsymbol{J}_{\epsilon' 1}$ is now introduced, consistently with the conceptual frame set forth in Sect. 7.2:

$$\boldsymbol{J}_{\epsilon' 1}(\boldsymbol{r}_1, \boldsymbol{r}_\mathrm{s}) := \kappa_0^2 \, \tilde{\epsilon}' \left[\mathcal{G}_0(\boldsymbol{r}_1, \boldsymbol{r}_\mathrm{s}) + \mathcal{G}'(\boldsymbol{r}_1, \boldsymbol{r}_\mathrm{s}) \right] = \kappa_0^2 \, \tilde{\epsilon}' \, \mathcal{G}(\boldsymbol{r}_1, \boldsymbol{r}_\mathrm{s}) \; . \tag{9.6}$$

The equivalent current density (9.6) is a random source created by the primary elementary source $\delta(\boldsymbol{r} - \boldsymbol{r}_\mathrm{s})$ in the points $\boldsymbol{r}_1$ of volume V' where the fluctuations $\tilde{\epsilon}'(\boldsymbol{r}_1)$ of permittivity occur. By this definition, the random component $\mathcal{G}'$ formally still obeys the wave equation

$$\nabla^2 \mathcal{G}'(\boldsymbol{r}, \boldsymbol{r}_\mathrm{s}) + \kappa_0^2 \, \overline{\tilde{\epsilon}}(\boldsymbol{r}) \, \mathcal{G}'(\boldsymbol{r}, \boldsymbol{r}_\mathrm{s}) = -\boldsymbol{J}_{\epsilon' 1}(\boldsymbol{r}_1, \boldsymbol{r}_\mathrm{s}) \; . \tag{9.7}$$

Equation (9.7) indicates that the random component of the Green's function is produced by the secondary source located in $\boldsymbol{r}_1$ which radiates into the *average permittivity* $\overline{\tilde{\epsilon}}$. Therefore, the expressions worked out in Sect. 3.1.1 hold[3] and $\mathcal{G}'$ is formally obtained by (3.20):

$$\mathcal{G}'(\boldsymbol{r}, \boldsymbol{r}_\mathrm{s}) = \iiint_{V'} \mathcal{G}_0(\boldsymbol{r}, \boldsymbol{r}_1) \, \boldsymbol{J}_{\epsilon' 1}(\boldsymbol{r}_1, \boldsymbol{r}_\mathrm{s}) \, \mathrm{d}V_1 \; . \tag{9.8}$$

By substituting (9.6) for the secondary source,

$$\begin{aligned} \mathcal{G}'(\boldsymbol{r}, \boldsymbol{r}_\mathrm{s}) &= \kappa_0^2 \left[\iiint_{V'} \mathcal{G}_0(\boldsymbol{r}, \boldsymbol{r}_1) \, \tilde{\epsilon}'(\boldsymbol{r}_1) \, \mathcal{G}_0(\boldsymbol{r}_1, \boldsymbol{r}_\mathrm{s}) \, \mathrm{d}V_1 \right. \\ &\qquad \left. + \iiint_{V'} \mathcal{G}_0(\boldsymbol{r}, \boldsymbol{r}_1) \, \tilde{\epsilon}'(\boldsymbol{r}_1) \, \mathcal{G}'(\boldsymbol{r}_1, \boldsymbol{r}_\mathrm{s}) \, \mathrm{d}V_1 \right] \\ &= \mathcal{G}^{\Rightarrow \circ \rightsquigarrow} + \kappa_0^2 \iiint_{V'} \mathcal{G}_0(\boldsymbol{r}, \boldsymbol{r}_1) \, \tilde{\epsilon}'(\boldsymbol{r}_1) \, \mathcal{G}'(\boldsymbol{r}_1, \boldsymbol{r}_\mathrm{s}) \, \mathrm{d}V_1 \; . \end{aligned} \tag{9.9}$$

The *first-order* random Green's function $\mathcal{G}^{\Rightarrow \circ \rightsquigarrow}$ is produced at the position $\boldsymbol{r}$ by the random permittivity fluctuation $\tilde{\epsilon}'(\boldsymbol{r}_1)$ occurring at the position $\boldsymbol{r}_1$ coupled with the deterministic (coherent) Green's function $\mathcal{G}_0$ created in the same point $\boldsymbol{r}_1$ by the primary source located in $\boldsymbol{r}_\mathrm{s}$. In principle, being relative to the average permittivity structure, the amplitude and phase of $\mathcal{G}_0$ are obtained from (9.5) for all pairs of points $\boldsymbol{r}_1$, $\boldsymbol{r}_\mathrm{s}$. Therefore $\mathcal{G}^{\Rightarrow \circ \rightsquigarrow}$ is obtained in terms of the dielectric fluctuations by

[3] The procedure is simplified from now on by assuming a homogeneous average permittivity structure. If suitable, the case of weakly inhomogeneous average medium can be approached as done in Chap. 5.

$$\mathcal{G}^{\Rightarrow\circ\rightsquigarrow} = \kappa_0^2 \iiint_{V'} \mathcal{G}_0(\boldsymbol{r}, \boldsymbol{r}_1)\, \tilde{\epsilon}\,'(\boldsymbol{r}_1)\, \mathcal{G}_0(\boldsymbol{r}_1, \boldsymbol{r}_\mathrm{s})\, \mathrm{d}V_1 \,.$$

Unfortunately, $\mathcal{G}^{\Rightarrow\circ\rightsquigarrow}$ is only part of the random Green's function $\mathcal{G}'$, because the second term in (9.9) is unknown, since it contains $\mathcal{G}'$ itself. However, the procedure that leads to (9.9) can be iterated by introducing a further secondary-source term as in (9.6):

$$\boldsymbol{J}_{\epsilon' 2}(\boldsymbol{r}_2, \boldsymbol{r}_\mathrm{s}) := \kappa_0^2\, \tilde{\epsilon}\,'\, \mathcal{G}(\boldsymbol{r}_2, \boldsymbol{r}_\mathrm{s}) \,. \tag{9.10}$$

The random Green's function in the second term of (9.9) is then obtained like (9.8) for the average permittivity structure. It is crucial to realize that $\mathcal{G}'$ now is produced at point $\boldsymbol{r}_1$ by the dielectric fluctuations $\tilde{\epsilon}\,'(\boldsymbol{r}_2)$ occurring in other points $\boldsymbol{r}_2$ of volume V', as expressed by the new secondary source $\boldsymbol{J}_{\epsilon' 2}$ in (9.10). This concept is expressed by

$$\begin{aligned} \mathcal{G}'(\boldsymbol{r}_1, \boldsymbol{r}_\mathrm{s}) &= \iiint_{V'} \mathcal{G}_0(\boldsymbol{r}_1, \boldsymbol{r}_2) \boldsymbol{J}_{\epsilon' 2}(\boldsymbol{r}_2, \boldsymbol{r}_\mathrm{s})\, \mathrm{d}V_2 \\ &= \kappa_0^2 \iiint_{V'} \mathcal{G}_0(\boldsymbol{r}_1, \boldsymbol{r}_2)\, \tilde{\epsilon}\,'(\boldsymbol{r}_2) \left[\mathcal{G}_0(\boldsymbol{r}_2, \boldsymbol{r}_\mathrm{s}) + \mathcal{G}'(\boldsymbol{r}_2, \boldsymbol{r}_\mathrm{s}) \right] \mathrm{d}V_2 \,. \end{aligned} \tag{9.11}$$

The second term of (9.9) is modified by (9.11) to finally yield the augmented expression of the random component $\mathcal{G}'(\boldsymbol{r}, \boldsymbol{r}_\mathrm{s})$ created in $\boldsymbol{r}$ by the primary source acting in $\boldsymbol{r}_\mathrm{s}$:

$$\begin{aligned} \mathcal{G}'(\boldsymbol{r}, \boldsymbol{r}_\mathrm{s}) &= \kappa_0^2 \iiint_{V'} \mathcal{G}_0(\boldsymbol{r}, \boldsymbol{r}_1)\, \tilde{\epsilon}\,'(\boldsymbol{r}_1)\, \mathcal{G}_0(\boldsymbol{r}_1, \boldsymbol{r}_\mathrm{s})\, \mathrm{d}V_1 \\ &\quad + \kappa_0^4 \iiint_{V'} \mathcal{G}_0(\boldsymbol{r}, \boldsymbol{r}_1)\, \tilde{\epsilon}\,'(\boldsymbol{r}_1) \iiint_{V'} \mathcal{G}_0(\boldsymbol{r}_1, \boldsymbol{r}_2)\, \tilde{\epsilon}\,'(\boldsymbol{r}_2)\, \mathcal{G}_0(\boldsymbol{r}_1, \boldsymbol{r}_2)\, \mathrm{d}V_2\, \mathrm{d}V_1 \\ &\quad + \kappa_0^4 \iiint_{V'} \mathcal{G}_0(\boldsymbol{r}, \boldsymbol{r}_1)\, \tilde{\epsilon}\,'(\boldsymbol{r}_1) \iiint_{V'} \mathcal{G}_0(\boldsymbol{r}_1, \boldsymbol{r}_2)\, \tilde{\epsilon}\,'(\boldsymbol{r}_2)\, \mathcal{G}'(\boldsymbol{r}_2, \boldsymbol{r}_\mathrm{s})\, \mathrm{d}V_2\, \mathrm{d}V_1 \\ &= \mathcal{G}^{\Rightarrow\circ\rightsquigarrow} + \mathcal{G}^{\Rightarrow\circ\rightsquigarrow\circ\rightsquigarrow} + \kappa_0^4 \iiint_{V'} \mathcal{G}_0(\boldsymbol{r}, \boldsymbol{r}_1)\, \tilde{\epsilon}\,'(\boldsymbol{r}_1) \\ &\qquad \iiint_{V'} \mathcal{G}_0(\boldsymbol{r}_1, \boldsymbol{r}_2)\, \tilde{\epsilon}\,'(\boldsymbol{r}_2)\, \mathcal{G}'(\boldsymbol{r}_2, \boldsymbol{r}_\mathrm{s})\, \mathrm{d}V_2\, \mathrm{d}V_1 \,. \end{aligned} \tag{9.12}$$

The procedure has added the new component $\mathcal{G}^{\Rightarrow\circ\rightsquigarrow\circ\rightsquigarrow}$ to the random Green's function, although the unknown quantity $\mathcal{G}'(\boldsymbol{r}_2, \boldsymbol{r}_\mathrm{s})$ still remains in (9.13). But also $\mathcal{G}'(\boldsymbol{r}_2, \boldsymbol{r}_\mathrm{s})$ is cast in terms of its respective source by an expression analogous to (9.11) for $\mathcal{G}'(\boldsymbol{r}_1, \boldsymbol{r}_\mathrm{s})$, and so on. With this multiple-scattering approach [2, 24], a series of

"perturbation" terms is generated iteratively for the random part of the Green's function. The terms add to the deterministic part $\mathcal{G}_0$ satisfying (9.5) to form the Green's function for the random medium. The series

$$\mathcal{G} = \mathcal{G}_0 + \mathcal{G}^{\Rightarrow\circ\rightsquigarrow} + \mathcal{G}^{\Rightarrow\circ\rightsquigarrow\circ\rightsquigarrow} + \cdots$$

is known as the *Rayleigh-Born expansion*.

It is important to look at the physical meaning of the terms of the expansion:

- the first term $\mathcal{G}_0$ corresponds to the *primary field*, that is the coherent one created by the source in the average permittivity structure;
- the second, $\mathcal{G}^{\Rightarrow\circ\rightsquigarrow}$, describes the incoherent *single-scattered field*, produced directly by the primary field because of the permittivity fluctuations;
- the third, $\mathcal{G}^{\Rightarrow\circ\rightsquigarrow\circ\rightsquigarrow}$, corresponds to the *double-scattered field*, caused by the single-scattered field and not directly by the primary one;
- in turn, the double-scattered field produces the triple-scattered field, and so on.

It can be recognized that the simple approach followed in Sect. 7.4 takes only single scattering into consideration.

Because of the random nature of the medium, the Green's function contains a fluctuating component and has to be characterized by the moments introduced in Sect. 1.3.4. The $\mathcal{G}_0$ term in the Rayleigh-Born expansion is deterministic, while $\tilde{\epsilon}'$ is a zero-mean random field. Inspection of (9.13) shows that $\langle \mathcal{G}^{\Rightarrow\circ\rightsquigarrow} \rangle = 0$, whereas $\langle \mathcal{G}^{\Rightarrow\circ\rightsquigarrow\circ\rightsquigarrow} \rangle \neq 0$, since it contains the second-order moment of $\tilde{\epsilon}'$. By extending the analysis to higher-order terms of the expansion, one clearly realizes that the average Green's function contains only terms with even moments of $\tilde{\epsilon}'$:

$$\begin{aligned}
&\langle \mathcal{G}(\boldsymbol{r}, \boldsymbol{r}_\mathrm{s}) \rangle \equiv \overline{\mathcal{G}}(\boldsymbol{r}, \boldsymbol{r}_\mathrm{s}) \\
= \;& \mathcal{G}_0(\boldsymbol{r}, \boldsymbol{r}_\mathrm{s}) \\
&+ \kappa_0^4 \iiint_{V'} \iiint_{V'} \mathcal{G}_0(\boldsymbol{r}, \boldsymbol{r}_1)\, \mathcal{G}_0(\boldsymbol{r}_1, \boldsymbol{r}_2)\, \mathcal{G}_0(\boldsymbol{r}_2, \boldsymbol{r}_\mathrm{s}) \left\langle \tilde{\epsilon}'(\boldsymbol{r}_1) \tilde{\epsilon}'(\boldsymbol{r}_2) \right\rangle \mathrm{d}V_2\, \mathrm{d}V_1 \\
&+ \kappa_0^8 \iiint_{V'} \iiint_{V'} \iiint_{V'} \iiint_{V'} \mathcal{G}_0(\boldsymbol{r}, \boldsymbol{r}_1)\, \mathcal{G}_0(\boldsymbol{r}_1, \boldsymbol{r}_2)\, \mathcal{G}_0(\boldsymbol{r}_2, \boldsymbol{r}_3)\, \mathcal{G}_0(\boldsymbol{r}_3, \boldsymbol{r}_4)\, \mathcal{G}_0(\boldsymbol{r}_4, \boldsymbol{r}_\mathrm{s}) \\
&\times \left[\left\langle \tilde{\epsilon}'(\boldsymbol{r}_1) \tilde{\epsilon}'(\boldsymbol{r}_2) \right\rangle \left\langle \tilde{\epsilon}'(\boldsymbol{r}_3) \tilde{\epsilon}'(\boldsymbol{r}_4) \right\rangle + \left\langle \tilde{\epsilon}'(\boldsymbol{r}_1) \tilde{\epsilon}'(\boldsymbol{r}_3) \right\rangle \left\langle \tilde{\epsilon}'(\boldsymbol{r}_2) \tilde{\epsilon}'(\boldsymbol{r}_4) \right\rangle \right. \\
&\left. + \left\langle \tilde{\epsilon}'(\boldsymbol{r}_1) \tilde{\epsilon}'(\boldsymbol{r}_4) \right\rangle \left\langle \tilde{\epsilon}'(\boldsymbol{r}_2) \tilde{\epsilon}'(\boldsymbol{r}_3) \right\rangle \right] \mathrm{d}V_4\, \mathrm{d}V_3\, \mathrm{d}V_2\, \mathrm{d}V_1 \\
&+ \cdots .
\end{aligned}$$

The average Green's function satisfies the *Dyson equation* [71]

$$\overline{\mathcal{G}}(\boldsymbol{r}, \boldsymbol{r}_\mathrm{s}) = \mathcal{G}_0(\boldsymbol{r}, \boldsymbol{r}_\mathrm{s}) + \iiint_{V'} \iiint_{V'} \mathcal{G}_0(\boldsymbol{r}, \boldsymbol{r}_m) Q(\boldsymbol{r}_m, \boldsymbol{r}_n) \overline{\mathcal{G}}(\boldsymbol{r}_n, \boldsymbol{r}_\mathrm{s})\, \mathrm{d}V_n\, \mathrm{d}V_m \;,$$

where the kernel Q denotes the series of terms containing moments of even order of $\tilde{\epsilon}'$:

$$\begin{aligned} & Q(\boldsymbol{r}_m, \boldsymbol{r}_n) \\ & = \kappa_0^4 \, \mathcal{G}_0(\boldsymbol{r}_m, \boldsymbol{r}_n) \left\langle \tilde{\epsilon}'(\boldsymbol{r}_m) \tilde{\epsilon}'(\boldsymbol{r}_n) \right\rangle \\ & \quad + \kappa_0^8 \iiint_{V'} \iiint_{V'} \mathcal{G}_0(\boldsymbol{r}_m, \boldsymbol{r}_1) \, \mathcal{G}_0(\boldsymbol{r}_1, \boldsymbol{r}_2) \, \mathcal{G}_0(\boldsymbol{r}_2, \boldsymbol{r}_n) \left\langle \tilde{\epsilon}'(\boldsymbol{r}_m) \tilde{\epsilon}'(\boldsymbol{r}_2) \right\rangle \left\langle \tilde{\epsilon}'(\boldsymbol{r}_1) \tilde{\epsilon}'(\boldsymbol{r}_n) \right\rangle \mathrm{d}V_2 \, \mathrm{d}V_1 \\ & \quad + \cdots . \end{aligned}$$

The series Q takes into account the scattering of various order from the dielectric inhomogeneities and includes the permittivity covariances for any pairs of points $\boldsymbol{r}_i$, $\boldsymbol{r}_j$,

$$\left\langle \tilde{\epsilon}'(\boldsymbol{r}_i) \tilde{\epsilon}'(\boldsymbol{r}_j) \right\rangle = \sigma_\epsilon^2 \, \mathcal{B}_\epsilon(\boldsymbol{r}_i, \boldsymbol{r}_j) \ ,$$

as well as their products of corresponding multiplicity. In case Q is known, the Dyson equation is a linear integral equation that, in principle, yields the average Green's function $\overline{\mathcal{G}}$ in the random medium.

In practice, the expansion Q is approximated by the lower-order terms only, since the terms progressively decline with increasing order of scattering. In particular, the *Bourret approximation* [13, 14] truncates the expansion to its first-order term, by considering only double scattering:

$$Q \simeq Q_1 = \kappa_0^4 \, \mathcal{G}_0(\boldsymbol{r}_1, \boldsymbol{r}_2) \left\langle \tilde{\epsilon}'(\boldsymbol{r}_1) \tilde{\epsilon}'(\boldsymbol{r}_2) \right\rangle \ .$$

This approximate kernel, which acts like a secondary source, is directly proportional to the covariance of the dielectric fluctuations and depends inversely on the fourth power of wavelength, as found in Sect. 7.4 for the incoherently scattered power.

Under the Bourret approximation, the average Green's function in a random material which is *lossless* and *statistically* homogeneous, formally has the same expression as (3.17):

$$\overline{\mathcal{G}}(\boldsymbol{r}, \boldsymbol{r}_\mathrm{s}) = \overline{\mathcal{G}}(|\boldsymbol{r} - \boldsymbol{r}_\mathrm{s}|) \simeq \frac{\mathrm{e}^{-\mathrm{j}\kappa_1 R}}{4\pi R} \ , \tag{9.13}$$

but with a propagation constant κ_1 which now is *complex*:

$$\kappa_1 = \beta_1 - \mathrm{j}\alpha_1 \ .$$

The phase constant β_1 is found to be larger than the one, β, relative to the homogeneous medium having permittivity equal to the average value $\overline{\epsilon}$, i.e.,

$$\beta_1 > \beta = \kappa_0 \sqrt{\overline{\epsilon}} = \kappa_0 \, \overline{n} \ ,$$

where $\overline{n}$ is the refractive index (4.16) of the average material. Indeed, the scattering from the random inhomogeneities, on one side subtracts power from the wave, thus attenuating it, and, on the other, increases its electromagnetic path length also through multiple bouncing [40]. It is important to note that the attenuation, more suitably named *extinction*, is caused by scattering and not by absorption by the material, which, as said, is lossless.[4] Both the extinction and the excess path length depend on magnitude and dimensions of the permittivity fluctuations.[5]

The phase constant β_1 is obtained from the dielectric structure by

$$\beta_1 = \beta\left[1 + \frac{(\pi\sigma_\epsilon)^2}{2\lambda_0}\int_0^\infty \ln\left(\frac{2\beta+\varkappa}{2\beta-\varkappa}\right)^2 \mathcal{S}_\epsilon(\varkappa)\varkappa\, d\varkappa\right]. \tag{9.14}$$

Equation (9.14) indicates that β_1 depends on the entire three-dimensional spatial spectrum[6] $\mathcal{S}_\epsilon(\varkappa)$ (cf. Sect. 7.4.4) of the permittivity, i.e., on the total intensity and spatial structure of the dielectric fluctuations. Clearly, $\beta_1 \to \beta$ when scatter is negligible, i.e., when $\sigma_\epsilon^2 \to 0$. On its side, the extinction constant is given by

$$\alpha_1 = \left(\frac{\pi^2\sigma_\epsilon}{\lambda}\right)^2 \int_0^{2\beta} \mathcal{S}_\epsilon(\varkappa)\varkappa\, d\varkappa\ . \tag{9.15}$$

This expression shows that the attenuation of the field in the random medium increases with the magnitude σ_ϵ^2 of the dielectric inhomogeneities, which pump power out of the progressing wave by spreading its energy. The growth of extinction with frequency, indicated by the λ^{-2} factor, is consistent with the features of scattering discussed throughout Chap. 7. Further insight into the extinction process is provided by the integral in (9.15). Indeed, given the limits of integration, α_1 is more affected by the larger dielectric inhomogeneities and grows with the frequency also because the upper limit 2β increases.

As said, the dielectric structure of many terrestrial environments is suitably approximated by a Gaussian covariance of permittivity fluctuations under the mentioned assumption of statistical homogeneity and isotropy. This kind of structure is consistent with the one to which the results of Sects. 7.4.4 and 8.1.5 refer and, after all, it is a quite useful simple reference.[7]

[4]The extinction in a *lossy* randomly inhomogeneous material depends in a *coupled* way [22] both on the absorbing and on the scattering properties of the inhomogeneities.

[5]Multiple scattering in random media can be based on the discrete or continuous inhomogeneity approaches [39, 43, 75] discussed in Sect. 7.4.4.

[6]Defined by extending (7.52) to three dimensions.

[7]Real scenarios of textured random media are approached by more complex anisotropic models [49].

The three-dimensional permittivity spectrum corresponding to the autocovariance (8.28) is given by (8.29), i.e.,

$$\mathcal{S}_\epsilon(\varkappa) = \frac{\sigma_\epsilon^2\, r_\epsilon^3}{8\,\pi^{3/2}}\, \mathrm{e}^{-(\varkappa r_\epsilon/2)^2}\ , \tag{9.16}$$

and the extinction constant obtained by inserting (9.16) into (9.15) is then[8]

$$\alpha_1 = \left(\frac{\sigma_\epsilon}{\lambda_0}\right)^2 \frac{(\pi r_\epsilon)^3}{8\sqrt{\pi}} \int_0^{2\beta} \mathrm{e}^{-(\varkappa r_\epsilon/2)^2}\, \varkappa\, \mathrm{d}\varkappa\ ,$$

whence

$$\alpha_1 = \frac{\sigma_\epsilon^2}{\langle\tilde{\epsilon}\rangle}\, \frac{\pi^{5/2}}{\lambda_0}\, \frac{r_\epsilon}{\lambda_0} \left[1 - \mathrm{e}^{-(2\pi r_\epsilon/\lambda_0)^2}\right]\ . \tag{9.17}$$

The expression (9.17) shows quantitatively how the extinction constant of a randomly inhomogeneous lossless (i.e., with no or negligible absorption) medium

- is proportional to the magnitude of the dielectric fluctuations expressed by σ_ϵ^2;
- increases with decreasing wavelength;
- increases considerably with increasing dimensions of the inhomogeneities, represented by the correlation radius r_ϵ, with respect to the wavelength.

Summarizing, the wave propagating in a randomly inhomogeneous lossless medium undergoes multiple scattering that modifies its propagation characteristics. The phase constant, hence the path length, is increased by the bouncing of energy among regions where dielectric inhomogeneities occur. The wave is also attenuated by scattering, which re-directs the electromagnetic energy into directions different from the one along which the unperturbed wave propagates. This scattering mechanism originates attenuation of the primary[9] wave. The attenuation caused by scattering has to be kept distinct from absorption and clearly occurs also in lossless materials. In case of lossy randomly inhomogeneous material, as a first approximation,[10] absorption adds to scattering to yield the total wave extinction. According to (9.17), absorption prevails over scattering in case of *small* lossy inhomogeneities, whereas attenuation is essentially determined by scattering in a material with *large* inhomogeneities.

[8] A background approximating vacuum ($\lambda \approx \lambda_0$) is assumed.

[9] The primary wave is the one arriving directly from the source.

[10] Cf. footnote 4.

9.1.1 Radiation from Extended Sources

The field produced in a random medium by an extended deterministic source J_s is obtained by convolving the source current density with the Green's function, according to the procedure that led to (3.11). If the polarization effects are disregarded, that is, only scalar quantities are considered, the electric field is

$$E(\boldsymbol{r}) = \mathrm{C} \iiint_{V'} \mathcal{G}(\boldsymbol{r}, \boldsymbol{r}') J_s(\boldsymbol{r}') \, \mathrm{d}V' \, . \tag{9.18}$$

Its average value $\overline{E}(\boldsymbol{r})$ relates to the average Green's function (9.13) determined previously for the random medium

$$\overline{E}(\boldsymbol{r}) \simeq \mathrm{C} \iiint_{V'} \frac{\mathrm{e}^{-(\alpha_1 + \mathrm{j}\beta_1)|\boldsymbol{r} - \boldsymbol{r}'|}}{4\pi |\boldsymbol{r} - \boldsymbol{r}'|} J_s(\boldsymbol{r}') \, \mathrm{d}V' \, .$$

Since ϵ' is a zero-mean random function, the average Green's function is contributed under the Bourret approximation by the double scattering and not by the single one. Rather, this latter affects the second-order moment of the Green's function, related in general to the field coherence (1.41) and, in particular, to the power density considered in Sect. 7.2. Measurements of coherence carry information on the characteristics of the extended source[11] that originates the radiation, as well as on the medium through which the radiation travels. Given (9.18), the field coherence function Γ is related to the correlation of the Green's functions

$$\Gamma_{\mathcal{G}}(\boldsymbol{r}_m, \boldsymbol{r}_n; \boldsymbol{r}_{si}, \boldsymbol{r}_{sj}) = \left\langle \mathcal{G}(\boldsymbol{r}_m, \boldsymbol{r}_{si}) \, \mathcal{G}^*(\boldsymbol{r}_n, \boldsymbol{r}_{sj}) \right\rangle$$

produced in two points $\boldsymbol{r}_m$ and $\boldsymbol{r}_n$ by two source elements in $\boldsymbol{r}_{si}$ and $\boldsymbol{r}_{sj}$, respectively. Following (9.4), $\Gamma_{\mathcal{G}}$ is found to satisfy the *Bethe-Salpeter equation* [74, Chap. 5]

$$\begin{aligned} \Gamma_{\mathcal{G}} \; (\boldsymbol{r}_m, \boldsymbol{r}_n; \boldsymbol{r}_{si}, \boldsymbol{r}_{sj}) &= \overline{\mathcal{G}}(\boldsymbol{r}_m, \boldsymbol{r}_{si}) \, \overline{\mathcal{G}}^*(\boldsymbol{r}_n, \boldsymbol{r}_{sj}) \\ &+ \iiint_{V'} \cdots \iiint_{V'} \overline{\mathcal{G}}(\boldsymbol{r}_m, \boldsymbol{r}_1) \overline{\mathcal{G}}^*(\boldsymbol{r}_n, \boldsymbol{r}_2) \mathcal{K}(\boldsymbol{r}_1, \boldsymbol{r}_2; \boldsymbol{r}_3, \boldsymbol{r}_4) \Gamma(\boldsymbol{r}_3, \boldsymbol{r}_4; \boldsymbol{r}_{si}, \boldsymbol{r}_{sj}) \, \mathrm{d}V_4 \cdots \mathrm{d}V_1 \, . \end{aligned}$$

The quantity $\mathcal{K}$, named *kernel of intensity operator*, takes account of the spatial correlation of the permittivity fluctuations. In case $\boldsymbol{r}_{si} = \boldsymbol{r}_{sj} \equiv \boldsymbol{r}_s$, the function $\Gamma_{\mathcal{G}}$ is the correlation of the radiation originating from a (single) point source in the random medium considered in the previous section. On the other hand, if $\boldsymbol{r}_{sm} = \boldsymbol{r}_{sn} \equiv \boldsymbol{r}$, then $\Gamma_{\mathcal{G}}$ is related to the power density produced in the point $\boldsymbol{r}$ of the random medium.

[11] The source may be an observed target.

The coherence Γ of the electric field produced by an extended source, again apart from polarization effects, is

$$\begin{aligned}\Gamma(\boldsymbol{r}_m,\boldsymbol{r}_n) &= \langle E(\boldsymbol{r}_m)\,E^*(\boldsymbol{r}_n)\rangle \\ &= |\mathrm{C}|^2\Big\langle \iiint_{V'} \mathcal{G}(\boldsymbol{r}_m,\boldsymbol{r}')J_\mathrm{s}(\boldsymbol{r}')\,\mathrm{d}V' \iiint_{V'} \mathcal{G}^*(\boldsymbol{r}_n,\boldsymbol{r}')J_\mathrm{s}^*(\boldsymbol{r}')\,\mathrm{d}V'\Big\rangle \\ &= |\mathrm{C}|^2 \iiint_{V'}\iiint_{V'} \big\langle \mathcal{G}(\boldsymbol{r}_m,\boldsymbol{r}_1')\,\mathcal{G}^*(\boldsymbol{r}_n,\boldsymbol{r}_2')\big\rangle J_\mathrm{s}(\boldsymbol{r}_1')J_\mathrm{s}^*(\boldsymbol{r}_2')\,\mathrm{d}V_2'\,\mathrm{d}V_1' \\ &= |\mathrm{C}|^2 \iiint_{V'}\iiint_{V'} \Gamma_\mathcal{G}(\boldsymbol{r}_m,\boldsymbol{r}_n;\boldsymbol{r}_1',\boldsymbol{r}_2')J_\mathrm{s}(\boldsymbol{r}_1')J_\mathrm{s}^*(\boldsymbol{r}_2')\,\mathrm{d}V_2'\,\mathrm{d}V_1'\ .\end{aligned}$$

Given the Bethe-Salpeter equation, the coherence of the scalar electric field radiated by an extended source in the random medium is

$$\begin{aligned}\Gamma(\boldsymbol{r}_m,\boldsymbol{r}_n) &\simeq \overline{E}(\boldsymbol{r}_m)\overline{E}^*(\boldsymbol{r}_n) \\ &\quad + \iiint_{V'}\cdots\iiint_{V'} \overline{\mathcal{G}}(\boldsymbol{r}_m,\boldsymbol{r}_1)\,\overline{\mathcal{G}}^*(\boldsymbol{r}_n,\boldsymbol{r}_2)\mathcal{K}(\boldsymbol{r}_1,\boldsymbol{r}_2;\boldsymbol{r}_3,\boldsymbol{r}_4)\Gamma(\boldsymbol{r}_3,\boldsymbol{r}_4)\,\mathrm{d}V_4\cdots\mathrm{d}V_1\ .\end{aligned}$$

The coherence for coincident points $\boldsymbol{r}_m = \boldsymbol{r}_n$ is proportional to the power density, which, as mentioned several times, is the primary quantity in Earth observation, also given the practical difficulties in measuring Γ. Indeed, power and related quantities are commonly measured by passive (radiometric) systems to gain information on the observed target from the characteristics of the radiation field it originates.

The above theoretical frame, although of moderate practical outcome in the present introductory approach to EO, is quite useful for contextualizing the phenomenology of power transfer in randomly inhomogeneous materials, as are commonly found in the terrestrial environment. Moreover, the wave-based Bethe-Salpeter equation can be manipulated under suitable assumptions to yield the basic relation that is going to be obtained through a phenomenological approach, governing the transfer of radiation in a statistically inhomogeneous medium.

9.2 Radiative Transfer

Chapter 5 regards the Earth's environment as a lossy electromagnetic medium that is weakly inhomogeneous on its ensemble average. Afterwards, Sect. 7.2 introduces the inhomogeneities of the terrestrial materials that do perturb the smoothly varying average background permittivity. The consequence is that the wave coming from the target, traveling through the atmosphere or another terrestrial material in a given direction, is modified by absorption and refraction, but also by direct scattering. The latter reduces the wave amplitude by spreading part of the power into directions different from the propagation one, following the results of Sect. 9.1.

On the other hand, the Earth's environment is traversed by plenty of radiation traveling in a multiplicity of directions, given the variety of man-made and natural simultaneous electromagnetic sources, as well as the ubiquity of scattering centers. The dielectric inhomogeneities, which are responsible for the extinction of the wave progressing in one direction, act reciprocally by scattering power traveling in the various directions into the direction in which the wave propagates. Moreover, Chap. 8 shows that, by reciprocity of absorption, the medium in which the propagation of the wave takes place is by itself source of thermal radiation, which also adds to the power carried by the wave.

Earth observing systems gain information on the terrestrial environment by measuring the field parameters or the power of the wave that, after interacting with the target, travels in the direction of observation. The field parameters and the power that carry the imprinting by the target, form the *signal*. The radiation that the traversed medium adds to the interacting wave through scattering and emission represents *noise*. Extinction caused by absorption and direct scattering reduces the signal, while emission and reverse scattering increase the noise. The latter may have the form of phase disturbance in case a coherent wave is used to probe the target, or of polarization distortion in polarimetric observations. The role of the atmosphere in reducing the signal-to-noise ratio is clearly of paramount importance in Earth observation.

The wave-based analytical method previously adopted for characterizing the field radiated in random media is now replaced by a simpler phenomenological approach that disregards the phase of the radiation. This type of analysis is clearly appropriate to observations that exploit thermal sources, as the Sun or the Earth itself.

9.2.1 Incoherent Radiation

Given its stochastic nature, the radiation originated by spontaneous emission must be characterized by moments such as the coherency dyadic introduced in Sect. 1.3.4.2. Also the incoherent part of an originally coherent wave which is made *partially coherent* by emission and/or random scattering, must be treated on the basis of moments. For the sake of simplicity, a linearly polarized field is assumed, for which the coherency matrix reduces to the single non-zero element (1.41). This second-order moment for coincident space points and times is proportional to the time-average power density, hence is readily measured by Earth observing systems.

The non-monochromaticity of the radiation, as well as the spatially distributed nature of sources and of the interaction mechanisms, are taken into account by the spectral radiance, following the definition (8.35). The location of the sources and the absorbing and scattering characteristics of the medium, which generally vary in space, determine the direction of flow of the incoherent average power density, related to the spectral radiance by (8.33):

$$\frac{\langle \mathrm{d}\boldsymbol{\mathcal{P}} \rangle}{\mathrm{d}\lambda} = \mathcal{I}_\lambda(\mathbf{s}_0)\,\mathrm{d}\Omega\ \mathbf{s}_0\ . \tag{9.19}$$

The direction along which the power is transported is now denoted with $\mathbf{s}_0$, to be consistent with the notations of Sect. 5.3. The average power $\langle W \rangle$ that *geometrically* crosses the surface S, which, for instance, may correspond to the collecting area of a telescope (Fig. 11.2), is

$$\langle W \rangle = \int_{\lambda_1}^{\lambda_2} \mathrm{d}\lambda \int_{\Omega} \mathrm{d}\Omega \iint_{S} \mathcal{I}_\lambda(\lambda, \boldsymbol{r}, \mathbf{s}_0)\, \mathbf{s}_0 \cdot \mathbf{n}_0 \, \mathrm{d}S \,, \tag{9.20}$$

where λ_1 and λ_2 are the limit wavelengths of the considered instrumental spectral band,[12] Ω is the solid angle within which the radiation is flowing and $\mathbf{n}_0$ is the local normal to S. Equation (9.20) points out that the spectral radiance is the quantity that characterizes the transport of energy (*radiative transfer*) [15, 47, 54] by the incoherent electromagnetic radiation. For given sources, the space dependence of $\mathcal{I}$ is affected by the absorbing, emitting and scattering features of the medium traversed by the radiation.

9.2.2 The Radiative Transfer Equation

The concepts outlined at the beginning of Sect. 9.2 are now cast in analytical form with reference to the geometrical optics model considered in Sect. 5.3 and extended to the randomly inhomogeneous material sketched in Fig. 9.1. The direction of $\mathbf{s}_0$ is the direction of interest, along which, for instance, the radiation moves from the

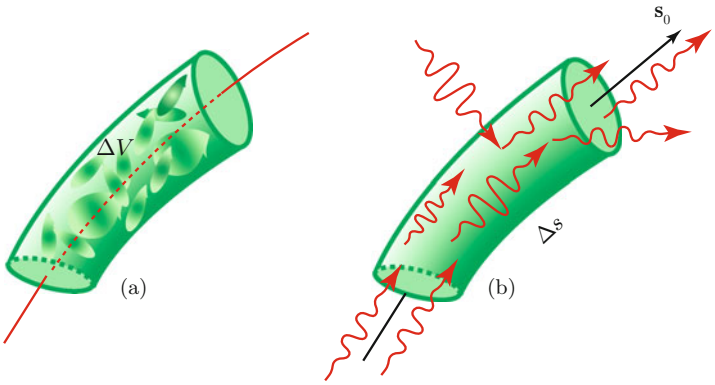

Fig. 9.1 Flux tube segment of length Δs (cf. Fig. 5.8) enclosing the volume ΔV of random inhomogeneous material (**a**), and representation of absorption, emission and scattering in ΔV that affect the spectral radiance in direction $\mathbf{s}_0$ (**b**)

[12] Details are given in Sect. 11.4.2.2.

target towards an observing instrument. The intensity of radiation traveling along $\mathbf{s}_0$ that enters a finite-length segment of a flux tube through its input cross-section

- is reduced by
  - the dissipation mechanisms of the background material,
  - the absorption by the lossy inhomogeneities embedded in the background,
  - the removal of radiation from the direction $\mathbf{s}_0$ by the (destructive) scattering into different directions caused by the inhomogeneities in the volume ΔV;
- on the other side, it is increased by
  - the thermal emission from the background medium,
  - the thermal emission from the embedded inhomogeneities,
  - the bistatic (constructive) scattering into $\mathbf{s}_0$ of radiation traveling in different directions, caused by the inhomogeneities in ΔV.

It is worth saying again that the dielectric structure of the flux tube is assumed to be a weakly inhomogeneous background medium in which random fluctuations are embedded. The background medium is characterized by the average permittivity of the material, while the fluctuations correspond to the deviation of the local permittivity from the average value, possibly due to different materials. An example is found in the turbid atmosphere, where the permittivity of the air (the weakly inhomogeneous background medium) is randomly perturbed by that of the water droplets or dust particles. Another relevant case is a vegetation canopy [16], for which the background dielectric structure is a weighted average between the permittivity of the air and the one of the vegetal matter, while the random local fluctuations correspond to the plant element (leaves, stems, etc.). It is understood that the flux tube in Fig. 9.1 refers to the average dielectric structure, as in Fig. 5.8.

In summary, the radiation traveling in a given direction through an inhomogeneous lossy medium lowers because of absorption and scattering. The Beer-Lambert's law, which is readily obtained from the spectral Poynting's theorem (2.28), states that the variation $\Delta\mathcal{I}_\lambda$ of spectral radiance undergone by the radiation after traveling over the incremental distance Δs along $\mathbf{s}_0$ is proportional to $\mathcal{I}_\lambda$:

$$\Delta\mathcal{I}_\lambda = -\alpha_\mathrm{e}\,\mathcal{I}_\lambda\,\Delta s\,. \tag{9.21}$$

The decrease $\Delta\mathcal{I}_\lambda$ depends on the local *extinction coefficient* α_e, which, under the assumption of linearity, is defined as the sum of the three coefficients corresponding to the three mechanisms mentioned previously:

$$\alpha_\mathrm{e} := \alpha_\mathrm{eb} + \alpha_\mathrm{ea} + \alpha_\mathrm{es}\,, \tag{9.22}$$

where

- α_{eb} accounts for the absorption of the weakly inhomogeneous lossy background medium (for instance, the gaseous atmosphere),
- α_{ea} accounts for the absorption from the lossy inhomogeneities (e.g., cloud water droplets) embedded in the background,
- α_{es} accounts for the removal of radiation by scattering by the inhomogeneities (droplets) present in ΔV from the direction $\mathbf{s}_0$ into directions $\mathbf{r}_0^{(\mathrm{s})} \neq \mathbf{s}_0$.

But, as said, the radiation traveling in a given direction is concurrently augmented by the mechanisms reciprocal of those causing extinction, i.e., both by emission and by constructive[13] scattering. The gain in spectral radiance is cast in the form

$$\Delta \mathcal{I}_\lambda = (e_{\mathrm{b}}\, \mathcal{J}_{\mathrm{b}} + e_{\mathrm{a}}\, \mathcal{J}_{\mathrm{a}} + \kappa_{\mathrm{s}}\, \mathcal{J}_{\mathrm{s}})\, \Delta s\ . \tag{9.23}$$

The model expressed by (9.23) attributes the increment of radiation to the three *source functions* $\mathcal{J}$, corresponding to the above three extinction mechanisms:

- $\mathcal{J}_{\mathrm{b}}$ is the thermal source of the background material,
- $\mathcal{J}_{\mathrm{a}}$ is the thermal source of the scatterers present in ΔV,
- $\mathcal{J}_{\mathrm{s}}$ accounts for the emitting and scattering environment that surrounds ΔV.

The thermal and scattering sources affect the spectral radiance according to the respective emission coefficients e_{b} and e_{a}, and scattering coefficient κ_{s}. The emission coefficients both of the background and of the inhomogeneities coincide with the respective absorption coefficients, given the electromagnetic reciprocity expressed by the Kirchhoff's law (8.10):

$$\alpha_{\mathrm{ea}} = e_{\mathrm{a}}; \qquad \alpha_{\mathrm{eb}} = e_{\mathrm{b}}\ . \tag{9.24}$$

The thermal source functions $\mathcal{J}_{\mathrm{b}}$ and $\mathcal{J}_{\mathrm{a}}$ are given by the Planck's radiation law (8.37). Since *local thermodynamic equilibrium* generally holds, $\mathcal{J}_{\mathrm{b}} = \mathcal{J}_{\mathrm{a}}$, so that a single *thermal source* function $\mathcal{J}_{\mathrm{T}}$ is introduced:

$$\mathcal{J}_{\mathrm{b}} = \mathcal{J}_{\mathrm{a}} \equiv \mathcal{J}_{\mathrm{T}}\ . \tag{9.25}$$

A single emission coefficient e_{T} is then sufficient to characterize the inhomogeneous medium

$$e_{\mathrm{T}} := e_{\mathrm{b}} + e_{\mathrm{a}}\ . \tag{9.26}$$

The *scattering source function* $\mathcal{J}_{\mathrm{s}}$ describes the effects of the dielectric inhomogeneities present in ΔV in constructively re-directing the radiation incident from different directions $\mathbf{r}_0^{(\mathrm{i})}$ into the scattering direction $\mathbf{r}_0^{(\mathrm{s})} = \mathbf{s}_0$, i.e.,

[13] That is, into the direction $\mathbf{s}_0$.

$$\mathcal{J}_s(\mathbf{s}_0) = \frac{1}{4\pi} \iint_{4\pi} \mathcal{S}(\mathbf{s}_0, \mathbf{r}_0^{(i)})\, \mathcal{I}_\lambda(\mathbf{r}_0^{(i)})\, \mathrm{d}\Omega \ .$$

The *volume scattering phase function* $\mathcal{S}$, which depends on the re-directing properties of the random material, is directly proportional to the bistatic scattering cross-section $\sigma(\mathbf{r}_0^{(i)}, \mathbf{r}_0^{(s)})$ defined by (7.16) averaged over the ensemble of scatterers contained in ΔV (*discrete approach*). Alternatively, $\mathcal{S}$ can be related to the three-dimensional spectrum of the dielectric fluctuations (Sect. 9.1) by extending the procedure followed in Sect. 7.4 that leads to (7.57) (*continuous approach*). The scattering source coefficient κ_s in (9.23), which expresses the contribution of the scattering to the increment of radiance, coincides with the scattering extinction coefficient α_{es} in (9.22) because of reciprocity. The results obtained in Sect. 9.1 suggest that the effect of the scattering in attenuating or in enhancing the radiance is related to the characteristic dimensions of the dielectric inhomogeneities with respect to the wavelength.

In the discrete approach to radiative transfer, the scattering source coefficient is defined as the local value of the volumic scattering cross-section (7.18):

$$\kappa_s := \lim_{\Delta V \to 0} \frac{\langle \sigma_s \rangle}{\Delta V} \ . \tag{9.27}$$

Correspondingly, the phase function

$$\mathcal{S} = \frac{\langle \sigma \rangle}{\langle \sigma_s \rangle} \tag{9.28}$$

is the bistatic cross-section normalized to the total one. The definitions (9.27) and (9.28) point out that κ_s takes the magnitude of the scattering into account, while $\mathcal{S}$ represents its directional features. The source term expressing the contribution to $\Delta\mathcal{I}_\lambda$ that comes from the environment surrounding ΔV has then the form

$$\kappa_s\, \mathcal{J}_s = \frac{1}{4\pi} \frac{\langle \sigma_s \rangle}{\Delta V} \iint_{4\pi} \frac{\left\langle \sigma(\mathbf{s}_0, \mathbf{r}_0^{(i)}) \right\rangle}{\langle \sigma_s \rangle}\, \mathcal{I}_\lambda(\mathbf{r}_0^{(i)})\, \mathrm{d}\Omega \ . \tag{9.29}$$

This scattering source adds to the thermal source in (9.23) to form the source of energy acting globally in the volume ΔV.

To simplify the approach, a homogeneous background medium is assumed from now on, so that refraction effects are absent; moreover, the embedded inhomogeneities are supposed uniformly distributed.

By suitably identifying the terms in the power balance (2.28) accounting for the aforementioned sinks and sources of radiation, the power budget for the volume ΔV of the cylindrical flux tube[14] with axis parallel to $\mathbf{s}_0$ represented in Fig. 9.2, is expressed by

[14]This model is consistent with the assumed homogeneous background material.

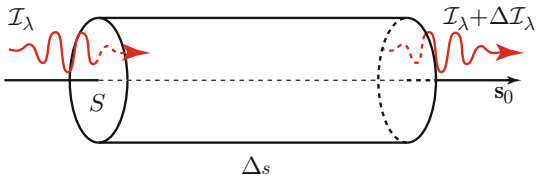

Fig. 9.2 The spectral radiance $\mathcal{I}_\lambda$ varies by $\Delta\mathcal{I}_\lambda$ according to the sources and the sinks acting in the cylindrical volume of length Δs and section S

$$\iiint_{\Delta V} (e_\mathrm{T}\,\mathcal{J}_\mathrm{T} + \kappa_\mathrm{s}\,\mathcal{J}_\mathrm{s})\,\mathrm{d}V - \iiint_{\Delta V} \alpha_\mathrm{e}\,\mathcal{I}_\lambda\,\mathrm{d}V = \oiint_S \mathcal{I}_\lambda\,\mathbf{s}_0\cdot\mathbf{n}_0\,\mathrm{d}S\,, \tag{9.30}$$

where only the radiation traveling along $\mathbf{s}_0$, i.e., in the direction from target to observing platform, is now of interest. Over short distances Δs, Eq. (9.30) yields

$$(e_\mathrm{T}\,\mathcal{J}_\mathrm{T} + \kappa_\mathrm{s}\,\mathcal{J}_\mathrm{s})\,S\Delta s - \alpha_\mathrm{e}\,\mathcal{I}_\lambda S\Delta s = (-\mathcal{I}_\lambda + \mathcal{I}_\lambda + \Delta\mathcal{I}_\lambda)S\,.$$

Then, considering an infinitesimal-length slice $\mathrm{d}V = S\,\mathrm{d}s$ of the flux tube, the **r**adiative **t**ransfer **e**quation (RTE) is obtained for the radiation traveling along $\mathbf{s}_0$:

$$\frac{\mathrm{d}\mathcal{I}_\lambda}{\mathrm{d}s} + \alpha_\mathrm{e}\,\mathcal{I}_\lambda = e_\mathrm{T}\,\mathcal{J}_\mathrm{T} + \kappa_\mathrm{s}\,\mathcal{J}_\mathrm{s}\,. \tag{9.31}$$

Equation (9.31) is transformed by introducing an *effective total source function*

$$\mathcal{J}_\mathrm{e} := \frac{e_\mathrm{T}}{\alpha_\mathrm{e}}\,\mathcal{J}_\mathrm{T} + \frac{\kappa_\mathrm{s}}{\alpha_\mathrm{e}}\,\mathcal{J}_\mathrm{s}\,, \tag{9.32}$$

so that it becomes

$$\frac{\mathrm{d}\mathcal{I}_\lambda}{\mathrm{d}s} + \alpha_\mathrm{e}\,\mathcal{I}_\lambda = \alpha_\mathrm{e}\,\mathcal{J}_\mathrm{e}\,. \tag{9.33}$$

The effective source is meaningfully expressed in terms of the *single-scattering albedo* $\mathcal{A}_\mathrm{s}$ introduced by (7.21),

$$\mathcal{A}_\mathrm{s} = \frac{\kappa_\mathrm{s}}{\alpha_\mathrm{e}}\,, \tag{9.34}$$

so that, taking account of (9.22) and of the Kirchhoff's law, the emission coefficient e_T normalized to the extinction coefficient is given by

$$\frac{e_\mathrm{T}}{\alpha_\mathrm{e}} = 1 - \mathcal{A}_\mathrm{s}\,.$$

The effective source (9.32) is then directly related to the single-scattering albedo:

$$\mathcal{J}_\mathrm{e} = (1 - \mathcal{A}_\mathrm{s})\mathcal{J}_\mathrm{T} + \mathcal{A}_\mathrm{s}\,\mathcal{J}_\mathrm{s}\,. \tag{9.35}$$

Equation (9.35) points out the role that the albedo has in setting the balance between thermal emission and scattering in the source of radiation: coarsely speaking, thermal emission predominates when scattering is low compared to absorption, whereas radiation is essentially contributed by scattering in strongly inhomogeneous weakly dissipative materials.

In radiative transfer applications, it is customary to define the local elementary *optical thickness* [15]

$$\mathrm{d}\tau_\mathrm{o} := \alpha_\mathrm{e}\,\mathrm{d}s\ , \tag{9.36}$$

in order to write the RTE as

$$\frac{\mathrm{d}\mathcal{I}_\lambda}{\mathrm{d}\tau_\mathrm{o}} + \mathcal{I}_\lambda = \mathcal{J}_\mathrm{e}\ . \tag{9.37}$$

All quantities in (9.37) are understood to be functions of space points, while the spectral radiance refers to the flux of power along the specified direction $\mathbf{s}_0$. Note that, given the definition of the elementary quantity (9.36), the optical thickness of the medium traversed by the radiation between abscissas s_1 and s_2 along the trajectory of the radiation, for instance along an electromagnetic ray as determined in Sect. 5.2, is

$$\tau_\mathrm{o}(s_1, s_2) = \int_{s_1}^{s_2} \alpha_\mathrm{e}\,\mathrm{d}s\ . \tag{9.38}$$

The optical thickness clearly depends on both absorption and scattering. The traditionally used adjective "optical" does not limit the approach to the optical range of the electromagnetic spectrum, rather, as discussed in Sect. 5.1, the results hold widely for frequencies and materials that satisfy possible specific "high-frequency" constraints.

The variety of boundary conditions and of features of the traversed materials affect the variation of the spectral radiance along the radiation path. The dependence of $\mathcal{I}_\lambda$ on the traveled distance s is now determined with reference to the geometry and to the notations[16] displayed in Fig. 9.3. Consider the radiative transfer equation (9.37) at a generic abscissa s' along $\mathbf{s}_0$ and multiply its terms by the optical thickness (9.38) of the path between the initial abscissa $s' = 0$ and s':

[15] The terms *optical depth* or *opacity* are also used. Note that τ_o is dimensionless, in spite of the name "thickness".

[16] Given the involvement of the Earth's surface, the off-nadir angle is now denoted by θ to keep consistency with the geometries considered in Chaps. 6, 7 and 8 implicating the local orientation of the target boundaries.

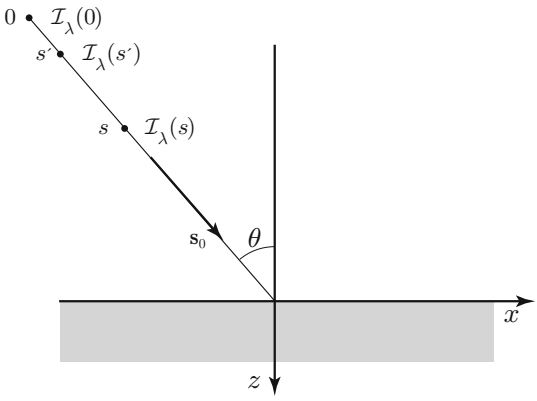

Fig. 9.3 The spectral radiance $\mathcal{I}_\lambda$ of radiation traveling in a semi-infinite medium along $\mathbf{s}_0$ at angle θ with the vertical, depends on the abscissa s

$$\frac{\mathrm{d}\mathcal{I}_\lambda(s')}{\mathrm{d}\tau_\mathrm{o}}\mathrm{e}^{\tau_\mathrm{o}(0,\,s')} + \mathcal{I}_\lambda(s')\mathrm{e}^{\tau_\mathrm{o}(0,\,s')} = \frac{\mathrm{d}}{\mathrm{d}\tau_\mathrm{o}}\left[\mathcal{I}_\lambda(s')\mathrm{e}^{\tau_\mathrm{o}(0,\,s')}\right] = \mathcal{J}_\mathrm{e}(s')\mathrm{e}^{\tau_\mathrm{o}(0,\,s')} \,. \tag{9.39}$$

Integration of (9.39) between the initial optical thickness $\tau_\mathrm{o} = 0$ and the final one $\tau_\mathrm{o} = \tau_\mathrm{o}(0, s)$ gives

$$\mathcal{I}_\lambda(s')\mathrm{e}^{\tau_\mathrm{o}(0,\,s')}\Big|_0^{\tau_\mathrm{o}(0,s)} = \int_0^{\tau_\mathrm{o}(0,s)} \mathcal{J}_\mathrm{e}(s')\,\mathrm{e}^{\tau_\mathrm{o}(0,\,s')}\mathrm{d}\tau_\mathrm{o} \,.$$

Therefore, the spectral radiance at the abscissa s, using the definition (9.36), is

$$\mathcal{I}_\lambda(s) = \mathcal{I}_\lambda(0)\mathrm{e}^{-\tau_\mathrm{o}(0,\,s)} + \int_0^s \alpha_\mathrm{e}(s')\mathcal{J}_\mathrm{e}(s')\mathrm{e}^{-\tau_\mathrm{o}(s',\,s)}\mathrm{d}s' \,. \tag{9.40}$$

The two terms composing the spectral radiance suggest that the radiation in s traveling in a given direction is the superposition of:

- the radiation $\mathcal{I}_\lambda(0)$ that originates or enters the medium at the initial point $s = 0$, attenuated by the extinction between 0 and s;
- the contribution by emission and scattering distributed along the path between 0 and s, attenuated by the extinction between the intermediate source position s' and the final abscissa s.

It is worth pointing out that the extinction coefficient α_e appears in the second term of (9.40), which describes an increase of radiation. This is not surprising, since the electromagnetic reciprocity ensures that the emitting and constructive-scattering behavior is the same as the absorbing and destructive-scattering one, as specified by (9.24). Therefore α_e in (9.40) now stands in for a source coefficient and is by no means related to a sink of radiation, in spite of the notation.

The actual usefulness of the formal relation (9.40) is limited mainly by the difficulties in evaluating $\mathcal{J}_\mathrm{e}$ in the general case [7, 50, 63]. The formula expresses the concept that the spectral radiance at every point of the radiative path depends on absorption and scattering at every other point. Moreover, the source function

is affected by the radiative environment as a whole and its determination requires evaluating the radiative contribution from the various directions over the entire solid angle. However, the spectral range in which the observation is carried out may allow some corresponding simplification. For instance, given the findings of Sect. 9.1 and the properties outlined in Sect. 2.2.1 and further discussed in Sect. 10.1.2, the atmosphere is a generally scattering and absorbing medium in the optical spectral range, while at the lower microwave frequencies scattering may become sufficiently small to allow crucial simplifications in modeling the radiative transfer. In particular, when scattering is negligible, given (9.34), $\kappa_s = \mathcal{A}_s \approx 0$, and $\alpha_e \simeq e_T$ because of (9.22), (9.24) and (9.26). Then (9.40) simplifies into

$$\mathcal{I}_\lambda(s) \simeq \mathcal{I}_\lambda(0)\mathrm{e}^{-\tau_o(0,s)} + \int_0^s \alpha_e(s')\mathcal{J}_T(s')\mathrm{e}^{-\tau_o(s',s)}\mathrm{d}s' \,. \tag{9.41}$$

The "optical" thickness now depends only on absorption, i.e.,

$$\tau_o(s',s) \simeq \int_{s'}^{s} (\alpha_{ea} + \alpha_{eb})\,\mathrm{d}s \,.$$

The *scatter-free* expression (9.41) turns out quite useful in a variety of Earth observation applications.

As a final remark, it is important to recall that in Earth observation the information is retrieved from the power of the observed radiation or from amplitude and phase[17] of the electromagnetic wave. Exploiting phase is only possible when the source is coherent and the field coherence is not destroyed by the traversed medium through the multiple scattering discussed in Sect. 9.1. In case of predominantly coherent wave propagation, reference can be suitably made to (5.38) to determine the quantities of interest. When the source is incoherent or the highly random materials make incoherent propagation mechanisms to dominate insomuch as the phase information is extinguished, only power is measured and wave expressions such as (5.38), which contain the phase term, are of scarce significance. Indeed, the observed electromagnetic power is *transported* (cf. Sect. 5.3.1.1) rather than propagates, so that relations such as the previous ones based on the RTE become appropriate.

9.3 Passive Sensing of the Earth's Surface

It was mentioned previously that the features of the radiative transfer vary widely according to the values of the parameters that affect the transport of radiation. As expected, the frequency at which the Earth observing system operates is a primary

[17] Statistical properties such as coherency are also exploited.

cause of variation of the behavior, given the dependence of scattering, absorption, and emission on the wavelength.

9.3.1 *Optical Sensing of the Surface and Atmospheric Correction*

The spectral radiance of the thermal emission varies with the wavelength according to the Planck function (8.37). The shape of this latter indicates that the thermal source function (9.25) in the terrestrial environment[18] is negligible at wavelengths falling in the optical range (cf. Sect. 10.1.1). The only natural source that can be widely exploited by Earth observation in the optical spectral region is the solar radiation [4]. Lidars are effective man-made sources of optical radiation, but of somewhat restricted use [26, 45, 61, 82]. Once the radiation emitted by the terrestrial materials is neglected, the spectral radiance at the location of an airborne or satellite-based downward-looking sensor is the spectral radiance of the radiation leaving the earth surface attenuated by the extinction along the atmospheric path, with the addition of the interfering radiation scattered by the atmospheric inhomogeneities. The radiation leaving the surface originates from the electromagnetic interaction between the materials at the surface and the solar radiation that reaches the ground attenuated and spectrally modified by interaction with the atmospheric constituents. Figure 9.4 shows the geometry[19] relevant to optical observation of the earth surface from space. Gases, particulate matter aerosols, liquid water droplets and ice particles scatter and absorb both the direct (i.e., reaching the ground) and the "reflected" (reaching the elevated sensor) solar radiation through spatially variable and wavelength-dependent mechanisms: the spectral and spatial distributions of the radiation are altered, with corresponding decrease of the accuracy of the *spectrometric* measurements. An *atmospheric correction* [69] is then required to counteract the artifacts of the atmosphere.

Given the absence of thermal sources in (9.32), for optical observations,

$$\alpha_e \, \mathcal{J}_e = \kappa_s \, \mathcal{J}_s \; .$$

The spectral radiance $\mathcal{I}_\lambda(s, \mathbf{s}_0)$ varies along the path according to (9.40), which is now specialized by considering only scattering, as well as by using (9.35) and the phase function:

[18] With the exception of incandescent materials, such as burning wood or fluid lava.

[19] Actually, the sensors observe the upwelling radiation generally from the same side of the Sun with respect to the nadir direction, to reduce the unwanted effects of specular reflection. The mutual position of Sun and platform has been changed in the figure for better clarity.

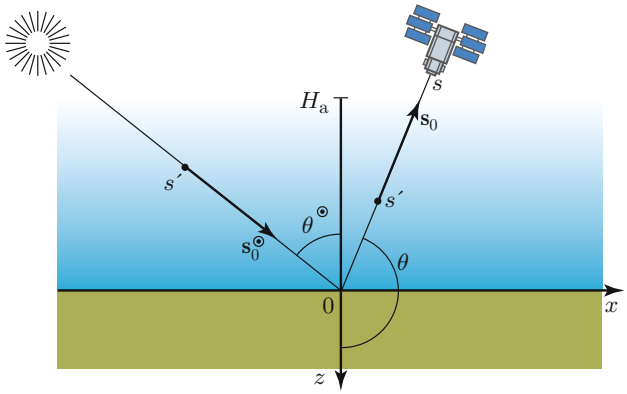

Fig. 9.4 Reference geometry of optical observation of the surface (cf. Fig. 9.3) from a space-based platform; H_a denotes the height at the "top of the atmosphere"

$$\mathcal{I}_\lambda(s, \mathbf{s}_0) = \mathcal{I}_\lambda(0, \mathbf{s}_0)\mathrm{e}^{-\tau_o(0,\, s)} + \frac{1}{4\pi}\int_0^s \iint_{4\pi} \mathcal{A}_s(s')\, \mathcal{S}(s', \mathbf{s}_0, \mathbf{r}_0^{(i)})\, \mathcal{I}_\lambda(s', \mathbf{r}_0^{(i)})\mathrm{e}^{-\tau_o(s',\, s)}\mathrm{d}\Omega\, \mathrm{d}s' \,. \tag{9.42}$$

Equation (9.42) provides $\mathcal{I}_\lambda(s, \mathbf{s}_0)$ in the direction $\mathbf{s}_0$ at the distance s from the conventional origin $s = 0$ where the radiation originates or enters the path. The spectral radiance (9.42), which is the quantity measured by the observing systems, is composed of the term $\mathcal{I}_\lambda(0, \mathbf{s}_0)$ at $s = 0$ attenuated by the extinction described by the optical thickness $\tau_o(0, s)$, and of the interfering term caused by scattering. This term results from the product of three factors:

- the albedo $\mathcal{A}_s(s')$, expressing the intensity of the scattering taking place at the abscissa s',
- the phase function $\mathcal{S}(s', \mathbf{s}_0, \mathbf{r}_0^{(i)})$, representing the re-directing characteristics of the material in s',
- the radiation $\mathcal{I}_\lambda(s', \mathbf{r}_0^{(i)})$ reaching s' from the various directions $\mathbf{r}_0^{(i)}$.

It is important to bear in mind that the phase function is relative to the fixed direction $\mathbf{s}_0$ of the sensor platform into which the radiation is scattered and to the variable direction $\mathbf{r}_0^{(i)}$ from which the radiation arrives and that spans the entire solid angle around the point at the abscissa s'. Consistently with the concept expressed by (9.32), the interfering radiation originated in s' arrives at the observing platform attenuated by the extinction between s' and the sensor located at distance s from the origin of the path. It is realized that the spectral radiance cannot be readily obtained from (9.32), since the radiation field $\mathcal{I}_\lambda(\mathbf{r}_0^{(i)})$ is not known unless some suitable assumption[20] is put forward. The *single-scattering approximation*, already

[20]Equation (9.32) is actually regarded as an integral equation in the unknown spectral radiance.

exploited throughout Sect. 7.4, provides the means for obtaining useful results in several cases frequently encountered when observing the earth surface.

Going back to the observation procedure, the sought information on the surface has to be extracted from the measured spectral radiance (9.42). The information is clearly contained in the spectral radiance $\mathcal{I}_\lambda(0, \mathbf{s}_0)$, which is originated by scattering or by reflection of the solar radiation from the surface, as sketched in Fig. 9.5. The radiation leaving the surface target in the direction $\mathbf{s}_0$ towards the observing platform,

$$\mathcal{I}_\lambda(s_g, \mathbf{s}_0) = \mathcal{R}_\lambda(\mathbf{s}_0, \mathbf{s}_0^\odot)\, \mathcal{I}_\lambda^\odot(s_H)\, \mathrm{e}^{-\tau_o^\odot(s_H,\, s_g)} \,, \tag{9.43}$$

is given by the product of two factors[21]:

- the first factor, $\mathcal{R}_\lambda$, is the *spectral reflectivity* of the surface for the pair $(\mathbf{s}_0,\ \mathbf{s}_0^\odot)$ of observation and solar directions (for this reason, $\mathcal{R}_\lambda$ is also called *bi-directional spectral reflectivity* [62, 68]);
- the second factor is the solar radiation downwelling through the atmosphere, that reaches the surface attenuated by the optical thickness $\tau_o^\odot(s_H,\, s_g)$ from the top of the atmosphere located at $s = s_H$ to the ground at $s = s_g$ in the direction $\mathbf{s}_0^\odot$ of the Sun.[22]

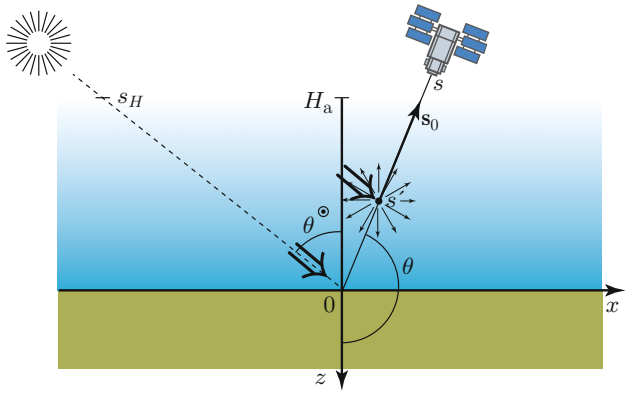

Fig. 9.5 Reference geometry for evaluating the interfering term in the optical observation of the surface; s_H denotes the abscissa at the "top of the atmosphere" along $\mathbf{s}_0^\odot$

[21]The origin of the ascending path is now suitably located at the abscissa $s = s_g$ corresponding to the local ground level with respect to a geodetic reference. This allows the altimetry of the earth surface to be taken into due account.

[22]The corresponding geometric length of the descending radiative path is $|s_H - s_g|$ along $\mathbf{s}_0^\odot$ (cf. Sect. 5.2.1).

The second term in the measured quantity (9.42) represents the interfering radiation. In the single-scattering approximation, as sketched in Fig. 9.5, this latter is assumed to originate uniquely from the *direct* downwelling solar radiation,[23] the radiance of which is expressed by

$$\mathcal{I}_\lambda(s', \mathbf{r}_0^{(\mathrm{i})}) = \mathcal{I}_\lambda^{\odot}(s_H, \mathbf{s}_0^{\odot})\, \mathrm{e}^{-\tau_\mathrm{o}^{\odot}(s_H, s')} \delta(\mathbf{r}_0^{(\mathrm{i})} - \mathbf{s}_0^{\odot}) \,. \tag{9.44}$$

In Eq. (9.44):

- $\mathcal{I}_\lambda(s', \mathbf{r}_0^{(\mathrm{i})})$, which is the originator of the interfering source, is the spectral radiance of the solar radiation in s';
- $\mathrm{e}^{-\tau_\mathrm{o}^{\odot}(s_H, s')}$ takes account of the attenuation undergone by the solar radiation over the path *along* $\mathbf{s}_0^{\odot}$ from the top of the atmosphere to the abscissa s' where the interfering radiation originates;
- the impulse function $\delta(\mathbf{r}_0^{(\mathrm{i})} - \mathbf{s}_0^{\odot})$ formally expresses the concept that the radiation arriving from the environment surrounding s' and described by the function $\mathcal{I}_\lambda(s', \mathbf{r}_0^{(\mathrm{i})})$ in (9.42) actually comes from the single direction $\mathbf{r}_0^{(\mathrm{i})} \equiv \mathbf{s}_0^{\odot}$ along which the downwelling direct solar radiation $\mathcal{I}_\lambda^{\odot}$ travels.[24]

The solar radiation scattered by the atmosphere into the direction $\mathbf{s}_0$ towards the observing platform and represented by (9.44) adds along the path to the radiation originated from the surface to yield the spectral radiance measured by the sensor at the generic location s:

$$\begin{aligned}\mathcal{I}_\lambda(s, \mathbf{s}_0) = {} & \mathcal{I}_\lambda(s_\mathrm{g}, \mathbf{s}_0)\, \mathrm{e}^{-\tau_\mathrm{o}(s_\mathrm{g}, s)} \\ & + \frac{\mathcal{I}_\lambda^{\odot}(s_H)}{4\pi} \int_{s_\mathrm{g}}^{s} \mathcal{A}_\mathrm{s}(s')\, \mathcal{S}(s', \mathbf{s}_0, \mathbf{s}_0^{\odot})\, \mathrm{e}^{-\tau_\mathrm{o}^{\odot}(s_H,\, s')} \mathrm{e}^{-\tau_\mathrm{o}(s',\, s)}\, \mathrm{d}s' \,.\end{aligned} \tag{9.45}$$

9.3.1.1 Optical Sensing from Space Platforms

The radiance seen by a space-borne sensor looking downward in direction $-\mathbf{s}_0$ is readily obtained from (9.45), taking account of (9.43):

$$\begin{aligned}\mathcal{I}_\lambda(\mathbf{s}_0) = {} & \mathcal{R}_\lambda(\mathbf{s}_0, \mathbf{s}_0^{\odot})\, \mathcal{I}_\lambda^{\odot}(s_H)\, \mathrm{e}^{-\tau_\mathrm{o}^{\odot}(s_H,\, s_\mathrm{g})}\, \mathrm{e}^{-\tau_\mathrm{o}(s_\mathrm{g},\, s_H)} \\ & + \frac{\mathcal{I}_\lambda^{\odot}(s_H)}{4\pi} \int_{s_\mathrm{g}}^{s_H} \mathcal{A}_\mathrm{s}(s)\, \mathcal{S}(s, \mathbf{s}_0, \mathbf{s}_0^{\odot})\, \mathrm{e}^{-\tau_\mathrm{o}^{\odot}(s_H,\, s)} \mathrm{e}^{-\tau_\mathrm{o}(s,\, s_H)}\, \mathrm{d}s \,.\end{aligned} \tag{9.46}$$

[23] This implies that the radiation arriving from the environment (atmosphere and surface) surrounding s' is negligible.

[24] This approach neglects both the angular dimension of the Sun and the refraction effects of the atmosphere (Sect. 5.2.1).

Equation (9.46) puts into evidence that the spectral reflectivity $\mathcal{R}_\lambda$ from which the useful information on the Earth's surface has to be extracted is just one of the several quantities which affect the measured radiance. At this time, it is worth to clarify the meaning of some of the symbols by recalling that:

- the length of the atmospheric path affecting $\mathcal{I}_\lambda^\odot$ depends on $s^\odot = s_\mathrm{g} - s_H$, where s_g denotes the abscissa *along* $\mathbf{s}_0^\odot$ at which the downwelling solar radiation encounters the earth surface;
- the upwelling radiation originated by scattering or reflection from the surface is attenuated over the path along $\mathbf{s}_0$ from s_g to the top of the atmosphere[25] s_H; since generally $\mathbf{s}_0 \neq \mathbf{s}_0^\odot$, the attenuation undergone by the radiation coming from the surface differs from that of the solar radiation, i.e., $\tau_\mathrm{o}(s_\mathrm{g}, s_H) \neq \tau_\mathrm{o}^\odot(s_H, s_\mathrm{g})$;
- the interfering radiation originates from any portion ds of the path around $s_\mathrm{g} < s < s_H$ between the ground ($s = s_\mathrm{g}$) and the top of the atmosphere ($s = s_H$): the primary source is the solar radiation, which arrives at s attenuated by the optical thickness between s_H and s along $\mathbf{s}_0^\odot$.

A useful reference model is a horizontally stratified atmosphere, hence neglecting sphericity; moreover, by also disregarding the refractive effects, the trajectories of the radiation are straight lines,[26] as sketched in Figs. 9.4 and 9.5. Then the radiative path lengths are simply related to the height z above the geodetic reference[27] and to the off-nadir angles θ and $\theta^\odot$ in Fig. 9.5 by

$$\Delta s = \Delta z \sec\theta \quad \text{along } \mathbf{s}_0; \qquad \Delta s = \Delta z \sec\theta^\odot \quad \text{along } \mathbf{s}_0^\odot$$

and the involved optical thicknesses between the generic abscissas s_1 and s_2 are, correspondingly,

$$\tau_\mathrm{o}(s_1, s_2) = \int_{z_1 \sec\theta}^{z_2 \sec\theta} \alpha_\mathrm{e}(z)\,\mathrm{d}z; \qquad \tau_\mathrm{o}^\odot(s_1, s_2) = \int_{z_1 \sec\theta^\odot}^{z_2 \sec\theta^\odot} \alpha_\mathrm{e}(z)\,\mathrm{d}z\,. \tag{9.47}$$

It is worth noting that $\sec\theta < 0$, while $\sec\theta^\odot > 0$.

Following the model, the upwelling spectral radiance emerging in the direction $\mathbf{s}_0$ from such a horizontally stratified atmosphere[28] is

[25] Since a space platform is beyond the top of the atmosphere, the path contributing attenuation has the upper limit $s = s_H$.

[26] Within these assumptions, off-nadir angle and incidence angle coincide.

[27] The vertical coordinate axis is oriented downward to be consistent with the notations of the basic Chaps. 6 and 7, therefore increasing heights correspond to decreasing z.

[28] As said, the height of the ground is denoted by $z = z_\mathrm{g}$, while the top of the atmosphere is at height $z = H_\mathrm{a}$, as in Fig. 9.5.

$$\mathcal{I}_\lambda(\mathbf{s}_0) \simeq \mathcal{R}_\lambda(\mathbf{s}_0, \mathbf{s}_0^\odot)\, \mathcal{I}_\lambda^\odot(s_H)\, \mathrm{e}^{-(\tau_\mathrm{a}^\odot + \tau_\mathrm{a})} + \frac{\mathcal{A}_\mathrm{s}}{4\pi}\, \mathcal{S}(\mathbf{s}_0, \mathbf{s}_0^\odot)\, \mathcal{I}_\lambda^\odot(s_H) \int_{z_\mathrm{g} \sec\theta}^{H_\mathrm{a} \sec\theta} \mathrm{e}^{-[\tau_\mathrm{o}(H_\mathrm{a} \sec\theta^\odot,\, z \sec\theta^\odot) - \tau_\mathrm{o}(z \sec\theta,\, H_\mathrm{a} \sec\theta)]} \sec\theta \, \mathrm{d}z \,, \tag{9.48}$$

provided both $\mathcal{A}_\mathrm{s}$ and $\mathcal{S}$ are little dependent on s. The optical thickness $\tau_\mathrm{a}^\odot$ in the sun direction and τ_a in the observation direction have been defined for the entire atmosphere to make more compact the expression of the surface term in (9.48):

$$\tau_\mathrm{a}^\odot = \int_{H_\mathrm{a} \sec\theta^\odot}^{z_g \sec\theta^\odot} \alpha_\mathrm{e}(z)\, \mathrm{d}z; \qquad \tau_\mathrm{a} = \int_{z_\mathrm{g} \sec\theta}^{H_\mathrm{a} \sec\theta} \alpha_\mathrm{e}(z)\, \mathrm{d}z \,. \tag{9.49}$$

Equation (9.48) is the basic relation between the spectral radiance $\mathcal{I}_\lambda$ that is measured by the space-based optical spectrometer and the spectral reflectivity $\mathcal{R}_\lambda$ which contains the information sought on the observed area of the earth surface. As already observed, the quantity of interest $\mathcal{R}_\lambda$ appears in the first of the two terms, attenuated by the atmospheric extinction, while the solar radiation scattered by the atmosphere forms the second term, which adds to the measurement. The map of the measured radiance $\mathcal{I}_\lambda$ is a corrupted replica of the image of $\mathcal{R}_\lambda$, which actually represents the properties of the surface. Therefore, an atmospheric correction is clearly needed to reduce the noxious effect of the attenuation and of the interfering term, hence to approximate the true surface reflectivity.

The contamination of the reflectivity image by both atmospheric extinction and scattering of sunlight depends on wavelength, varies in space and time, and, when multiple scattering [20] is not negligible, is also affected by the spatial structure of the surface reflectivity. In a few words, the atmospheric impact varies according to the sensor features and the kind of measurements that are carried out. Therefore, apart from an initial wide-purpose coarse procedure, the steps for a fine correction of the data are driven by the envisaged application. The successful outcome of the processing relies on the accuracy with which the relevant atmospheric parameters are known. The effect of the permanent gases can be generally modeled and reduced by suitably choosing the spectral channels in which the radiance is measured. Instead, the aerosols exhibit high space-time variations [46], hence their effects are less predictable. The aerosol optical thickness is usually a key quantity for image correction, although an adequate estimate of albedo and of the scattering function may be also required when enhanced accuracy is demanded. General information on the optical properties of the atmosphere is derived from regional and seasonal climatology, while specific local information is derived from the images themselves, also exploiting a-priori information on the surface reflectivity of selected portions of the images and in significant wavelength bands. It is also worth mentioning that

the vertical profiles of the relevant atmospheric quantities are important for the successful correction of **v**ery **h**igh-**r**esolution (VHR)[29] images [37].

9.3.1.2 Optical Sensing from Aerial Platforms

The spectral radiance measured by sensors installed on an aircraft or on an RPAP, also named **u**nmanned **a**erial **v**ehicle (UAV) or **r**emotely **p**iloted **v**ehicle (RPV) [51], is still given by (9.45), which remains obviously unchanged with respect to the abscissa s where the observation is performed. The only need is replacing in two terms of (9.46) the abscissa s_H of the top of the atmosphere with the abscissa s_p where the platform is located, i.e.,

$$\begin{aligned}\mathcal{I}_\lambda(\mathbf{s}_0) = {} & \mathcal{R}_\lambda(\mathbf{s}_0, \mathbf{s}_0^\odot)\, \mathcal{I}_\lambda^\odot(s_H)\, \mathrm{e}^{-\tau_\mathrm{o}^\odot(s_H,\, s_\mathrm{g})}\, \mathrm{e}^{-\tau_\mathrm{o}(s_\mathrm{g},\, s_\mathrm{p})} \\ & + \frac{\mathcal{I}_\lambda^\odot(s_H)}{4\pi} \int_{s_\mathrm{g}}^{s_\mathrm{p}} \mathcal{A}_\mathrm{s}(s)\, \mathcal{S}(s, \mathbf{s}_0, \mathbf{s}_0^\odot)\, \mathrm{e}^{-\tau_\mathrm{o}^\odot(s_H,\, s)} \mathrm{e}^{-\tau_\mathrm{o}(s,\, s_\mathrm{p})}\, \mathrm{d}s\,. \end{aligned} \tag{9.50}$$

Through corresponding straightforward substitutions, the horizontally stratified model yields the upwelling spectral radiance

$$\begin{aligned}\mathcal{I}_\lambda(\mathbf{s}_0) = {} & \mathcal{R}_\lambda(\mathbf{s}_0, \mathbf{s}_0^\odot)\, \mathcal{I}_\lambda^\odot(s_H)\, \mathrm{e}^{-(\tau_\mathrm{a}^\odot + \tau_\mathrm{ap})} \\ & + \frac{\mathcal{A}_\mathrm{s}}{4\pi}\, \mathcal{S}(\mathbf{s}_0, \mathbf{s}_0^\odot)\, \mathcal{I}_\lambda^\odot(s_H) \\ & \int_{z_\mathrm{g} \sec\theta}^{z_\mathrm{p} \sec\theta} \mathrm{e}^{-[\tau_\mathrm{o}(H_\mathrm{a} \sec\theta^\odot,\, z \sec\theta^\odot) - \tau_\mathrm{o}(z \sec\theta,\, z_\mathrm{p} \sec\theta)]} \sec\theta\, dz\,, \end{aligned}$$

where the atmospheric optical thickness τ_ap in the observation direction is defined analogously to τ_a in (9.49) as[30]

$$\tau_\mathrm{ap} = \int_{z_\mathrm{g} \sec\theta}^{z_\mathrm{p} \sec\theta} \alpha_\mathrm{e}(z)\, dz\,. \tag{9.51}$$

with reference to the altitude z_p of the observing aerial platform.

The previous discussion on the contamination of the reflectivity of a ground-based target by atmospheric effects still holds, but the relatively short length of the path allows relaxing some of the conclusions. While the extinction undergone by the solar radiation reaching the ground level is clearly independent of the altitude of the sensor, the radiation scattered by the observed object is attenuated according to the length of the path from the target to the sensor. RPAPs can operate

[29] Typically metric, or, if available, sub-metric resolution.

[30] As previously noted, $\sec\theta < 0$.

at relatively low heights, thus substantially reducing the optical thickness of the interposed atmospheric layers, even in opaque[31] wavelength ranges. Therefore, the spectral limitations posed by the atmosphere can be mitigated and, at least in principle, the whole optical spectrum[32] can be exploited. Moreover, the interfering radiation originating along the atmospheric path lessens correspondingly. These effects concur to yield observations which are radiometrically more accurate than those from space and require lighter, if any, atmospheric corrections.

9.3.2 *Sensing the Surface in the Thermal Infrared*

Section 8.2.2 mentions that the Planck function for the Sun's temperature decreases substantially with increasing wavelength in the thermal infrared. Together, the scattering and absorption mechanisms prevailing in this spectral range lower the reflectivity of the Earth's surface (cf. Sect. 10.2.2.1). The two effects combine to make the solar radiation scattered by the Earth generally small with respect to the radiation this latter emits spontaneously. As a result, the radiation leaving the surface in the TIR is mainly originated by thermal emission[33] and hence the spectral radiance $\mathcal{I}_\lambda(0)$ in (9.40) now depends on the spectral emissivity $e_{\lambda\mathrm{S}}$ introduced by (8.38) and on the *skin* [58] temperature T_S of the surface.[34] For analogous reasons, the environmental spectral radiance $\mathcal{I}_\lambda(\mathbf{r}_0^{(\mathrm{i})})$ contributing the scattering source (9.29) along the atmospheric path is expressed only by the thermal source $\mathcal{J}_{T_\mathrm{env}}$ relative to an effective environmental temperature T_env suitably defined through the same (9.29). The measurable spectral radiance is then given by

$$\mathcal{I}_\lambda(s) \simeq e_{\lambda\mathrm{S}}\,\mathcal{B}_\lambda(T_\mathrm{S})\,\mathrm{e}^{-\tau_\mathrm{o}(s_\mathrm{g},\,s)} + \int_{s_\mathrm{g}}^{s} \alpha_\mathrm{e}[(1-\mathcal{A}_\mathrm{s})\mathcal{J}_T + \mathcal{A}_\mathrm{s}\,\mathcal{J}_{T_\mathrm{env}}]\,\mathrm{e}^{-\tau_\mathrm{o}(s',\,s)}\mathrm{d}s' \tag{9.52}$$

and consists of the contribution from the surface carrying the useful information and of the contribution from the atmosphere. The interfering source distributed along the path from ground, identified by $s = s_\mathrm{g}$, to sensor at abscissa s, is composed of the local emission from the crossed atmosphere taken into account by $\mathcal{J}_T$ and of the thermal radiation from the environment $\mathcal{J}_{T_\mathrm{env}}$ which is locally scattered into the direction of observation and that is expressed in terms of the effective temperature T_env.

The presence of scattering limits the usefulness of (9.52), since evaluating the effect of the thermal environment is quite difficult in general conditions. On the

[31] The effect of the instrument's spectral resolution on the optical thickness has also to be accounted for.

[32] At the resolution of common spectrometric channels.

[33] The possible occurrence of specular reflection of the sun radiation is kept out.

[34] In practice, the temperature varies within the emitting volume, hence T_S should be regarded as an effective temperature [87].

other hand, because of the dependence of scattering on wavelength discussed in Sect. 9.1, the TIR albedo $\mathcal{A}_s$ in the *clear*[35] atmosphere is low, given the typical dimensions of the suspended particles with respect to the TIR wavelengths, so that the scattering term in (9.35) becomes negligible with respect to the thermal source. In this *scatter-free* atmosphere, the extinction is correspondingly caused by absorption rather than by scattering. The radiation emitted by the earth surface is then attenuated by the absorbing atmospheric constituents and interfered only by the *thermal* source along the radiation path.

9.3.2.1 TIR Sensing from Space Platforms

The spectral radiance emerging in the direction $\mathbf{s}_0$ from the top of a non-scattering stratified[36] atmosphere is given in terms of the vertical coordinate z by

$$\mathcal{I}_\lambda(\mathbf{s}_0) \simeq e_{\lambda S}\, \mathcal{B}_\lambda(T_S)\, \mathrm{e}^{-\tau_a} + \int_{z_g \sec\theta}^{H \sec\theta} e_T(z)\, \mathcal{B}_\lambda[T(z)]\, \mathrm{e}^{-\tau_o(z \sec\theta,\, H_a \sec\theta)} \sec\theta\, dz\,, \tag{9.53}$$

where the "optical" thickness of the atmosphere τ_a is defined by (9.49). The interfering term in the approximation (9.53) depends on the *vertical profile* $e_T(z)$ of the emission coefficient (9.26) and on that of the thermodynamic temperature $T(z)$ of the atmosphere. In the thermal infrared, consistently with the scatter-free assumption, the optical thickness τ_o of the layer $z_1 < z < z_2$ depends only on the absorption by the air gases (expressed by the background coefficient α_{eb}) and by the suspended particles (expressed by α_{ea}), according to (9.21) and (9.22)

$$\tau_o(z_1, z_2, \theta) = \int_{z_1 \sec\theta}^{z_2 \sec\theta} [\alpha_{ea}(z) + \alpha_{eb}(z)]\, dz\,.$$

In absence of haze, fog or clouds, $\alpha_{ea} \approx 0$ and absorption is caused by the background atmospheric constituent gases, essentially the water vapor. Processing of TIR data for reducing the atmospheric interfering term requires information on the local radiative environment [55], in particular through the knowledge or estimate of the profiles of moisture and temperature. It is worth mentioning that independent radiative data collected by operational space platforms are also assimilated into the atmospheric correction schemes for the TIR.

[35] Clear here indicates the absence of dense clouds and precipitation.

[36] Atmospheric refraction is neglected.

9.3.2.2 TIR Sensing from Aerial Platforms

The TIR spectral radiance observed from an RPAP [9, 31] is obtained by (9.53) suitably modified to account for the altitude z_p of the sensor, as done in Sect. 9.3.1.2:

$$\mathcal{I}_\lambda(\mathbf{s}_0) \simeq e_{\lambda S}\, \mathcal{B}_\lambda(T_S)\, \mathrm{e}^{-\tau_{ap}} + \int_{z_g \sec\theta}^{z_p \sec\theta} e_T(z)\, \mathcal{B}_\lambda[T(z)]\, \mathrm{e}^{-\tau_o(z \sec\theta,\, z_p \sec\theta)} \sec\theta\, dz\,, \tag{9.54}$$

The optical depth τ_{ap} of the atmospheric layer interposed between the ground-based target and the sensor,

$$\tau_{ap} = \int_{z_g \sec\theta}^{z_p \sec\theta} [\alpha_{ea}(z) + \alpha_{\mathbf{b}}(z)]\, dz\,,$$

depends on the altitude of the platform and can be possibly reduced by lowering the height of acquisition. The reduction of the target-to-sensor distance concurrently decreases the interfering thermal emission distributed along the atmospheric path, as discussed in Sect. 9.3.1.2, and enhances the overall radiometric accuracy of the observations.

9.3.3 Passive Sensing of the Surface at Microwaves

As in the thermal infrared, also at microwaves the density of solar radiation scattered by the land surface is generally small with respect to the emitted thermal radiation. Therefore, the radiance $\mathcal{I}(0)$ in (9.40) depends on the microwave emissivity and on the temperature of the surface materials. Section 8.2.2.1 introduces the concept of brightness temperature, which is suitably used in place of the radiance. With this approach, the basic expression (9.40) can be transformed into the corresponding relation involving the temperatures of the surface and of the atmosphere. Regarding this latter, under the assumption that the Rayleigh-Jeans approximation (8.39) holds, the atmospheric thermal source in local thermodynamic equilibrium conditions is

$$\mathcal{J}_T(s) = \frac{2k}{\lambda^2}\, \Delta f\; T(s)\,,$$

if $T(s)$ is the thermodynamic temperature of the atmosphere at the abscissa s along the considered path. The other term in (9.35), is proportional to the scattering source $\mathcal{J}_s$ which clearly does not correspond to a thermodynamic temperature. However, on the same grounds of proportionality between radiation intensity and temperature, $\mathcal{J}_s$ is expressed in terms of an *effective scattered temperature* T_{es} for the ground-to-satellite direction $\mathbf{s}_0$:

$$\mathcal{J}_s(s) = \frac{2k}{\lambda^2}\,\Delta f\, T_{es}(s)\ .$$

The temperature $T_{es}(s)$ takes account of the amount of microwave radiation that arrives at s from the various directions $\mathbf{r}_0^{(i)}$ and that gets re-directed into $\mathbf{s}_0$ by the scattering mechanism acting in s, according to (9.29). Consistently with the Rayleigh-Jeans approximation, the angular distribution of radiation contributing scattering into the direction of interest $\mathbf{s}_0$ is represented by an *environment effective microwave temperature* T_{me}, so that

$$T_{es}(\mathbf{s}_0) := \frac{1}{4\pi}\iint_{4\pi} \mathcal{S}(\mathbf{s}_0, \mathbf{r}_0^{(i)})\, T_{me}(\mathbf{r}_0^{(i)})\, \mathrm{d}\Omega\ , \tag{9.55}$$

where $\mathcal{S}$ is the phase function (9.28). All the quantities in (9.55) are understood to depend on the abscissa s. With the above positions, the source functions in (9.35) are expressed in terms of temperatures by

$$[(1-\mathcal{A}_s)\mathcal{J}_T + \mathcal{A}_s\,\mathcal{J}_s] = [(1-\mathcal{A}_s)T(s) + \mathcal{A}_s\,T_{es}(\mathbf{s}_0)]\frac{2k}{\lambda^2}\,\Delta f\ .$$

The microwave spectral radiance is in turn transformed into the brightness temperature (8.40), so that, ultimately, the radiation field filling the space is converted into a temperature field, clearly with reference to the direction in which the radiation is considered. The transformed radiative transfer equation provides the brightness temperature T_B in the direction $\mathbf{s}_0$ as a function of the abscissa s

$$T_B(s) = T_B(s_g)\,\mathrm{e}^{-\tau_o(0,\,s)} + \int_{s_g}^{s} \alpha_e(s')[(1-\mathcal{A}_s)T(s') + \mathcal{A}_s\,T_{es}(s', \mathbf{s}_0)]\mathrm{e}^{-\tau_o(s',\,s)}\mathrm{d}s'\ . \tag{9.56}$$

The relation (9.56) is readily recognized to correspond to (9.40), with an equivalent interpretation of the two terms. Although (9.56) is simpler than (9.40), the usefulness of the expression is still limited in the general case by its complexity and by computational difficulties arising, as for (9.52), from the scattering term.

If scattering is negligible, given (9.34), $\kappa_s = \mathcal{A}_s \approx 0$, and $\alpha_e \simeq e_T$ because of (9.22), (9.24) and (9.26). This physical condition reduces (9.56) to the more manageable expression

$$T_B(s) \simeq T_B(s_g)\,\mathrm{e}^{-\tau_o(s_g,\,s)} + \int_{s_g}^{s} e_T(s')T(s')\,\mathrm{e}^{-\tau_o(s',\,s)}\mathrm{d}s'\ . \tag{9.57}$$

The "optical", or, as it should be named more appropriately in this microwave context, the *electromagnetic thickness*, now depends only on the absorption by the background and by the possibly present inhomogenities:

$$\tau_{\mathrm{o}}(s', s) \simeq \int_{s'}^{s} (\alpha_{\mathrm{ea}} + \alpha_{\mathrm{eb}})\, \mathrm{d}s \,. \tag{9.58}$$

If microwave radiative transfer takes place in the atmosphere, this latter is free from scattering for most weather conditions. Indeed, only thick clouds, formed by droplets of liquid water having diameters up to a few tens of micrometers, and especially rain, with diameters of drops up to a few millimeters, produce appreciable scattering, the intensity of which we know to depend on the dimensions of the drops with respect to the observation wavelength. In practice, scattering is negligible for observations at frequencies below the X-band, except that for extreme precipitation phenomena, as detailed in Sect. 10.1.2, while non-precipitating clouds are usually assumed free of scattering up to the $\mathrm{K_a}$-band.[37] This effect of frequency implies that the microwave radiometric observations of the earth surface can be interpreted in most cases on the basis of scatter-free radiative transfer.

The relatively short paths make microwave radiometric observations from aerial platforms generally little subject to atmospheric contamination, since extinction and concurrent interference are reduced, at least for operations outside the more intense absorption bands shown in Fig. 4.2. Therefore, as a first approximation, the brightness temperature observed by the airborne sensor is the same as that of the target.

9.4 Passive Sensing of the Earth's Atmosphere

The atmosphere [29] is the terrestrial environment for which satellite observations have first reached their operational maturity [19, 33, 42]. It is worth mentioning that the down-looking synoptic observations from space platforms have been joined by up-looking ground-based [78, 79] local measurements. As opposite to the observation of the surface, the quantity of interest in atmospheric sensing is the radiation emitted or scattered by the atmosphere, that is the quantity previously regarded as a noxious term, whereas the radiation originated by the surface is now the interfering term.[38] The radiation leaving the surface is actually a source of considerable overall uncertainty, given the variability of covers and, for passive observations in the TIR or at microwaves, of surface temperatures [57].

The need to keep the uncertain contribution from the surface as low as possible with respect to the atmospheric one suggests the useof sufficiently absorbed

[37] The designation of the microwave bands is given in Sect. 10.1.1.

[38] In the case of ground-based measurements, the noise originates from the *cosmic background*, which corresponds to a black body at temperature $T_{\mathrm{C}} \approx 2.7\,\mathrm{K}$, the power of which peaks at $f \approx 160\,\mathrm{GHz}$, corresponding to $\lambda_0 \approx 1.9\,\mathrm{mm}$.

frequencies. Moreover, since the emission by the thermal source is proportional to the absorption coefficient, a strongly absorbed wavelength corresponds to a highly emitting source, hence to a high signal drawn from the atmosphere. On the other side, high emission is accompanied by high attenuation in the source-to-sensor atmospheric path, so that the atmospheric layers closer to the sensor contribute the larger fraction of power, hence, the highest layers of the atmosphere are effectively observed by a space platform, while, correspondingly, ground-based systems are fit to sense the lowest layers.

The fraction of power reaching the sensor, emitted by a thermal source at a given position in the atmosphere, is described by the *weighting functions* $\mathcal{W}$, introduced in Sect. 8.1.4: the decrease of atmospheric density with height changes the effect of absorption, hence the shapes of the weighting functions.[39] The selection of the radiometric channels considers a suitable balance between source strength and attenuation to avoid the loss of information ensuing from a low signal-to-noise ratio for the atmospheric layers of interest.

9.4.1 Thermal Sensing of the Non-scattering Atmosphere

Section 9.2.2 shows that negligible scattering allows simplification of the radiative transfer formalism leading to the reduced expression (9.41) of the spectral radiance. The basic relation has to be specialized according to the direction from which the atmosphere is observed, that is from above or from below.

9.4.1.1 Satellite-Based Sounding of the Atmosphere

The spectral radiance or the brightness temperature of the *non-scattering* atmosphere sensed by a nadir-looking radiometer operating at TIR or microwave wavelengths are provided by (9.53) or (9.57), respectively. The measured quantity contains the attenuated contribution of the surface, which now acts as a noise term, and the contribution of the atmosphere, which carries the information on its temperature profile $T(z)$ and on the density profiles of the *absorbing* constituents, such as water vapor and liquid water, that affect the emission coefficient $e_{\mathrm{T}}(z)$, and, correspondingly, the optical thickness τ_{o} (9.58). The product

$$\mathcal{W}_T(z, z') = e_{\mathrm{T}}(z')\, \mathrm{e}^{-\tau_{\mathrm{o}}(z', z)} \ , \tag{9.59}$$

[39] The shape of $\mathcal{W}$ is drastically linked to the direction, upward or downward, of observation.

consistently with the definition (8.23), forms the *temperature weighting function*[40] for observation of a plane-layered atmosphere from the altitude z. The temperature weighting functions peak at different heights z' according to the imaginary part of atmospheric permittivity (Sect. 2.2.1), which determines the dependence of the optical thickness on height:

- more absorbed frequencies yield weighting functions peaking at higher altitudes, so that the received power mainly originates from the upper part of the atmosphere;
- frequencies at which the atmosphere is more transparent allow the power emitted also by the lower layers to reach the space platform, according to weighting functions which are flatter and peak at lower altitudes.

The off-nadir angle[41] ϑ at which the observations are carried out affects the height at which the weighting functions peak, given the dependence of the optical thickness (9.47) on ϑ: increasing ϑ clearly lifts up the height of the atmospheric layers the contribution of which is larger.[42] Sounding observations are frequently carried out by nadir-looking satellite sensors.

Note that the weighting functions are defined not only for temperature, but also for the absorbing atmospheric constituents, such as water vapor or cloud liquid density. Although the conceptual basis is the same, the more general notions of brightness temperature response and of averaging kernel are introduced in view of the retrieval [11, 60, 76] of the atmospheric quantity of interest from the radiometric measurements. In particular, the straightforward definition (8.23) has to be suitably modified and adapted to the parameter under consideration. Figure 9.6 shows examples of weighting functions relative to atmospheric temperature and water vapor. Coarsely speaking, the value of $\mathcal{W}_T(h)$ represents the fraction of power reaching the sensor from an emitting layer around the height h above the reference (e.g., sea) level. A multi-frequency radiometer, receiving the power in channels centered on different frequencies, exploits the difference of absorption to sound the atmosphere, that is, to discriminate the contributions from layers at different heights [1] in terms of their temperature. The retrieval scheme can be extended to the emission coefficient by assuming a known temperature profile. The density of the atmospheric constituent, for instance water vapor, which emits at the frequencies of operation, is estimated from the height-discriminated emission, taking account of the dependence of the optical depth τ_o on the sought quantity. Then the weighting

[40] It is worth recalling that the relation between TIR spectral radiance and thermodynamic temperature set by Planck's law (8.37) is non linear, whereas the microwave brightness temperature is related linearly to the temperature thanks to the Rayleigh-Jeans approximation (8.39). This implies that (9.59) is the temperature weighting function in a strict sense only for microwave observations.

[41] Off-nadir angle is generally denoted by ϑ when the surface is not directly involved in the observation.

[42] Limb-sounding observations (cf. Sect. 14.3.4) are not being considered here.

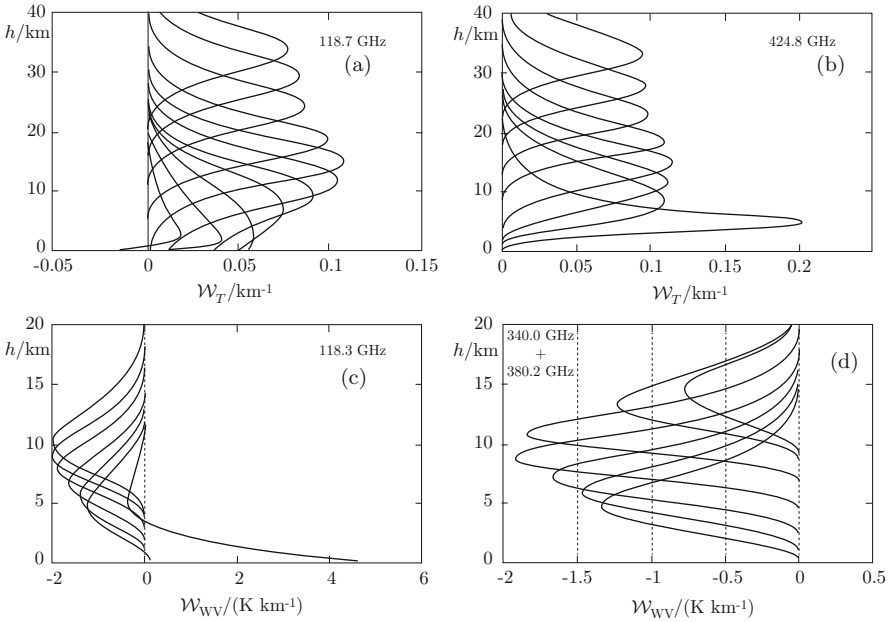

Fig. 9.6 Examples of nadir-looking weighting functions $\mathcal{W}$ at mm- and sub-mm wavelengths vs. height h above sea level: $\mathcal{W}_T$ for temperature, (**a**), (**b**); $\mathcal{W}_{WV}$ for water vapor (**c**), (**d**). Changing the observation frequency in the neighborhood of the indicated frequency changes the atmospheric specific absorption, hence the height at which the weighting functions peak (cf. Sect. 8.1.4) (Curves interpolate data from [65])

function takes the meaning of sensitivity of the sensor response to the deviation of the considered atmospheric variable from a *first-guess* (climatic average, for instance) profile.

In presence of scattering (9.57) fails, with ensuing decrease of overall retrieval accuracy and need of sophisticated procedures for successfully inverting possibly hyperspectral [10] brightness measurements.

9.4.1.2 Ground-Based Sounding of the Atmosphere

It is interesting to compare the weighting functions of Fig. 9.6 for satellite observation with those displayed in Fig. 9.7, which refer to ground-based measurements [36, 78]. The brightness temperature[43] sensed by a zenith-looking radiometer located at the ground level z_g is obtained from (9.57), with the modifications required to account for the upward direction of observation:

[43]The TIR spectral radiance is readily obtained in an analogous way.

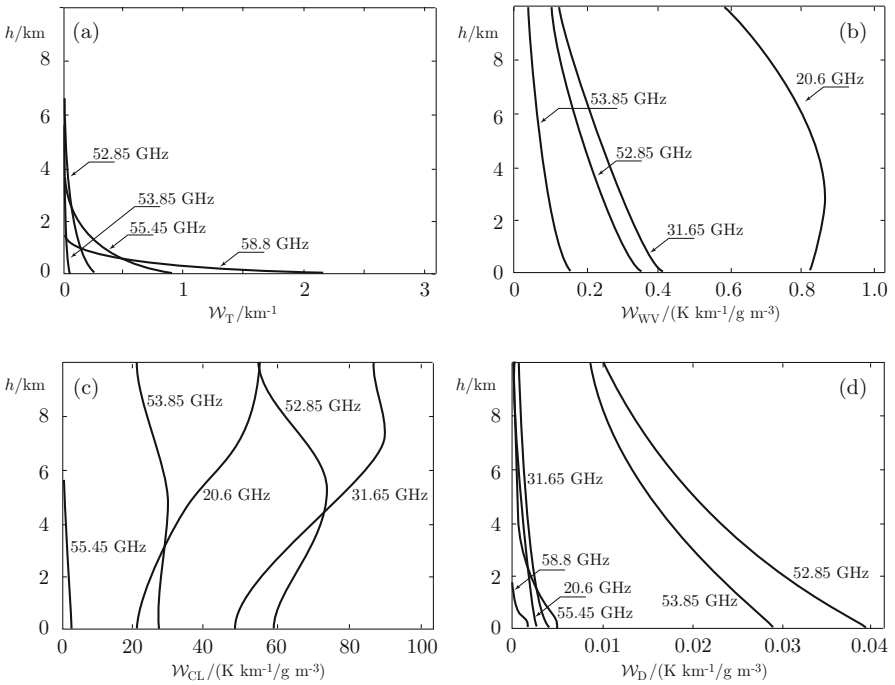

Fig. 9.7 Zenith-looking ground-based microwave *brightness temperature response* vs. height h AGL: (**a**), $\mathcal{W}_T$ for temperature; (**b**), $\mathcal{W}_{WV}$ for water vapor; (**c**), $\mathcal{W}_{CL}$ for cloud liquid; (**d**), $\mathcal{W}_D$ for dry air density. The monotonic trend of $\mathcal{W}_T$ derives from the frequency-dependent specific absorption (cf. Fig. 2.7) of air decreasing with height, as sketched in Fig. 8.7 (Curves interpolate data from [78])

$$T_B(z_g) = \int_{H_a}^{z_g} e_T(z)\, T(z)\, e^{-\tau_o(z,\, z_g)} dz + T_C\, e^{-\tau_o(H_a,\, z_g)} \ .$$

As discussed previously, the first term is the *useful* one, expressing the atmospheric contribution that carries the explicit information on the *profile* of temperature $T(z)$ and, implicitly, on the atmospheric constituents which affect e_T and τ_o. The diagrams in Fig. 9.7 are useful to concretely appreciate the different behavior of the weighting functions, according to the trends of the emissivity coefficient already discussed in Sect. 8.1.4. Since the air density decreases monotonically with height, power is largely received from the lower part of the atmosphere. Therefore, the ground-based weighting functions for temperature and for dry air, which mainly depend on the density of the stable gases, are also essentially monotonic decreasing functions of height, consistently with the trend sketched in Fig. 8.7a. On their side, the weighting functions for constituents such as water vapor [35] and cloud liquid, the densities of which do not decrease monotonically with height, may show peaks at heights dependent on frequency and climatology, as Fig. 8.7b suggests, albeit for a different physical mechanism.

As a final remark, the interfering term now derives from the brightness temperature T_C of the cosmic background,[44] which, differently from the term originated by the surface in (9.53) and (9.57), is stable and low [81].

Managing Multiple Scattering and Radiation Transfer

It is understandable that the waves cannot be expressed in a simple way when they happen to be in a random medium. Consider that the primary wave is scattered by the inhomogeneity it encounters, then the scattered fraction of wave is scattered again by another inhomogeneity. This doubly scattered wave hits further inhomogeneities, thus undergoing multiple scattering. The field resulting from this chaotic process has intricate properties and its quantitative representation is problematic. We are guided through some terrible formalisms to establishing the dependence of the main wave on the properties of the random environment with which it interacts. We learn that the field decays with an extinction constant that grows with increasing permittivity fluctuations and with decreasing wavelength, and that attenuation is particularly sensitive to large inhomogeneities. We get also informed that the phase constant is increased by the bouncing of electromagnetic energy among the randomly distributed scatterers. The dependence of both attenuation and phase constants on the inhomogeneity of the material is clearly a major conceptual addition to the idea that wave propagation is affected by absorption and refractive index.

Refractive, dissipative and scattering overlapping effects rule the transfer of electromagnetic energy in the chaotic terrestrial environment. We learn that the radiative transfer formalism is able to provide us with quantitative information on the evolution of the intensity of the radiation that travels between the Earth's surface and an elevated platform on which the observing system is located. Simplifying assumptions make the general expressions more manageable, according to the wavelength at which the observing systems operate. In optical observations we can profit from the exiguity of emission and consider only atmospheric scattering, while in the thermal infrared and at microwaves, the disturbing effects of the atmosphere are prevailingly attributed to absorption and emissions. Of course, we must look at the state of the portion of atmosphere traversed by the wave coming from the target to decide on the suitability of a facilitating hypothesis.

Observing the atmosphere deserves a separate discussion. The physics involved in the radiative transfer is clearly the same, but we have to reverse the roles of the term expressing the signal carrying the information and of the one accounting for interference. We have also to distinguish between space-based and ground-based observation, because not only the background against which the atmosphere is sounded changes drastically, but also the sounding specifications, revealed by the shape of the weighting functions, modify.

[44] The radiometer does not aim at the Sun.

References

1. Aqua Project Science. NASA. http://www.aqua.nasa.gov/about/instrument_amsu.php (visited on 26 Jan 2014)
2. Aristégui C, Angel YC (2002) New results for isotropic point scatterers: Foldy revisited. Wave Motion 36(4):383–399. doi:http://dx.doi.org/10.1016/S0165-2125(02)00031-8
3. Askne JIH, Westwater ER (1986) A review of ground-based remote sensing of temperature and moisture by passive microwave radiometers. IEEE Trans Geosci Remote Sens GE-24(3):340–352. doi:10.1109/TGRS.1986.289591
4. Asrar G (ed) (1989) Theory and applications of optical remote sensing. Wiley. ISBN:9780471628958
5. Barabanenkov YN (1968) Application of the smooth-perturbation method to the solution of general equations of multiple wave-scattering theory. Sov Phys JETP 27(6):954–959. http://jetp.ac.ru/cgi-bin/dn/e_027_06_0954.pdf (visited on 05 Nov 2014)
6. Barabanenkov YN, Ozrin VD (1991) Asymptotic solution of the Bethe-Salpeter equation and the Green-Kubo formula for the diffusion constant for wave propagation in random media. Phys Lett A 154(1–2):38–42. doi:http://dx.doi.org/10.1016/0375-9601(91)90425-8
7. Battaglia A, Simmer C, Crewell S, Czekala H, Emde C, Marzano F, Mishchenko M, Pardo J, Prigent C (2006) Emission and scattering by clouds and precipitation. In: Mätzler C (ed) Thermal microwave radiation: applications for remote sensing. Institution of Engineering and Technology. ISBN:9780863415739
8. Berginc G, Bourrely C (2010) Light scattering from 3-D nanoscale disordered media. PIERS online 6(8):730–734. doi:10.2529/PIERS091218110418
9. Berni J, Zarco-Tejada PJ, Suarez L, Fereres E (2009) Thermal and narrowband multispectral remote sensing for vegetation monitoring from an unmanned aerial vehicle. IEEE Trans Geosci Remote Sens 47(3):722–738. doi:10.1109/TGRS.2008.2010457
10. Blackwell WJ, Bickmeier LJ, Leslie RV, Pieper ML, Samra JE, Surussavadee C, Upham CA (2011) Hyperspectral microwave atmospheric sounding. IEEE Trans Geosci Remote Sens 49(1):128–142. doi:10.1109/TGRS.2010.2052260
11. Blackwell WJ, Chen FW (2009) Neural networks in atmospheric remote sensing. Artech House. ISBN:9781596933736
12. Bobeth M, Diener G (1983) Electromagnetic wave propagation and radiative transfer in strongly heterogeneous random media. Phys A: Stat Mech Appl 117(2–3):427–444. doi:10.1016/0378-4371(83)90125-5
13. Bourret RC (1962) Propagation of randomly perturbed fields. Can J Phys 40(6):782–790. doi:10.1139/p62-084
14. Bourret RC (1962) Stochastically perturbed fields, with applications to wave propagation in random media. Il Nuovo Cim Ser 10 26(1):1–31. doi:10.1007/BF02754339
15. Chandrasekhar S (1960) Radiative transfer. Dover. ISBN:9780486605906
16. Chukhlantsev AA (2006) Microwave radiometry of vegetation canopies. Springer. ISBN:9781402046827
17. Clough SA, Shephard MW, Mlawer EJ, Delamere JS, Iacono MJ, Cady-Pereira K, Boukabara S, Brown PD (2005) Atmospheric radiative transfer modeling: a summary of the *AER* codes. J Quant Spectrosc Radiat Transf 91(2):233–244. doi:http://dx.doi.org/10.1016/j.jqsrt.2004.05.058
18. Cogan J, Meaure E, Wolfe D (1997) Atmospheric soundings in near-real time from combined satellite and ground-based remotely sensed data. J Atmos Ocean Technol 14(5):1127–1138. doi:10.1175/1520-0426(1997)014(1127:ASINRT)2.0.CO;2
19. Collard A, Hilton F, Forsythe M, Candy B (2011) From observations to forecasts – part 8: the use of satellite observations in numerical weather prediction. Weather 66(2):31–36. doi:10.1002/wea.736
20. Deirmendjian D, Sekera Z (1954) Global radiation resulting from multiple scattering in a Rayleigh atmosphere. Tellus 6(4):382–398. doi:10.1111/j.2153-3490.1954.tb01132.x

21. Dinnat EP, Le Vine DM, Abraham S, Floury N (2010) Map of sky background brightness temperature at L-band. NASA GSFC. http://oceancolor.gsfc.nasa.gov/AQUARIUS/DinnatEtAl2010/ (visited on 05 Feb 2014)
22. Durant S, Greffet J-J, Calvo-Perez O, Vukadinovic N (2007) Extinction coefficient in absorbing media: a theoretical and numerical study. In: Tenth conference on electromagnetic and light scattering, Bodrum, 17–22 June 2007, pp 33–36. doi:10.1615/ICHMT.2007.ConfElectromagLigScat.110
23. Finkel'berg VM (1968) Wave propagation in a random medium. The correlation group method. Sov Phys JETP 26(1):268–277. http://www.jetp.ac.ru/cgi-bin/dn/e026010268.pdf (visited on 05 Nov 2014)
24. Foldy LL (1945) The multiple scattering of waves. I. General theory of isotropic scattering by randomly distributed scatterers. Phys Rev 67(3–4):107–119. doi:10.1103/PhysRev.67.107
25. Frisch U (1968) Wave propagation in random media. In: Bharucha-Reid AT (ed) Probabilistic methods in applied mathematics, vol 1. Academic. ISBN:9780120957026
26. Glennie CL, Carter WE, Shrestha RL, Dietrich WE (2013) Geodetic imaging with airborne LiDAR: the Earth's surface revealed. Rep Prog Phys 76(8). doi:10.1088/0034-4885/76/8/086801
27. Grody NC (1976) Remote sensing of atmospheric water content from satellites using microwave radiometry. IEEE Trans Antennas Propag 24(2):155–162. doi:10.1109/TAP.1976.1141324
28. Hogg DC (1989) Rain, radiometry, and radar. IEEE Trans Geosci Remote Sens 27(5):576–585. doi:10.1109/TGRS.1989.35940
29. Houghton JT (1977) The physics of atmospheres. Cambridge University Press. ISBN:9780521214438
30. Houweling S, Hartmann W, Aben I, Schrijver H, Skidmore J, Roelofs G-J, Breon F-M (2005) Evidence of systematic errors in SCIAMACHY-observed CO_2 due to aerosols. Atmos Chem Phys 5:3003–3013. doi:10.5194/acp-5-3003-2005
31. Hu S, Chao H, Coopmans C, Han J, McKee M, Chen Y-Q (2010) Low-cost UAV-based thermal infrared remote sensing: platform, calibration and applications. In: 2010 IEEE/ASME international conference on mechatronics and embedded systems and applications (MESA), July 2010, pp 38–43. doi:10.1109/MESA.2010.5552031
32. Ishimaru A (1991) Wave propagation and scattering in random media and rough surfaces. Proc IEEE 79(10):1359–1366. doi:10.1109/5.104210
33. Janssen MA (ed) (1993) Atmospheric remote sensing by microwave radiometry. Wiley. ISBN:9780471628910
34. Jensen AM, Neilson BT, McKee M, Chen Y-Q (2012) Thermal remote sensing with an autonomous unmanned aerial remote sensing platform for surface stream temperatures. In: 2012 IEEE international Geoscience and remote sensing symposium (IGARSS), July 2012, pp 5049–5052. doi:10.1109/IGARSS.2012.6352476
35. Kämpfer N (2012) Monitoring atmospheric water vapour: ground-based remote sensing and in-situ methods. Springer. ISBN:9781461439097
36. Karmakar PK (2013) Ground-based microwave radiometry and remote sensing: methods and applications. Taylor & Francis. ISBN:9781466516311
37. Kaufman YJ, NASA GFSC (1989) The atmospheric effect on remote sensing and its correction. In: Asrar G (ed) Theory and applications of optical remote sensing. Wiley. ISBN:9780471628958
38. Keller JB (1964) Stochastic equations and wave propagation in random media. In: Bellman R (ed) Stochastic processes in mathematical physics and engineering, vol XVI. American Mathematical Society. ISBN:9780821867273
39. Keller JB (1960) Wave propagation in random media. Technical report AFCRL-TN-60-1 149. U.S. Air Force Cambridge Research Laboratories
40. Keller JB, Karal FC (1966) Effective dielectric constant, permeability, and conductivity of a random medium and the velocity and attenuation coefficient of coherent waves. J Math Phys 7(4):661–670. doi:http://dx.doi.org/10.1063/1.1704979

41. Kidd C (2010) From observations to forecasts – part 3. Key principles and recent developments in satellite observations. Weather 65(1):3–9. doi:10.1002/wea.388
42. Kidder SQ, Vonder Haar TH (1995) Satellite meteorology: an introduction. Academic. ISBN:9780124064300
43. Klusch D, Pflug Th, Thielheim KO (1993) Wave propagation in isotropic random media with nondiscrete spherical perturbations. Phys Rev B Condens Matter 47(14):8539–8546. doi:10.1103/PhysRevB.47.8539
44. Korn M (1993) Seismic waves in random media. J Appl Geophys 29(3–4):247–269. doi:http://dx.doi.org/10.1016/0926-9851(93)90007-L
45. Lefsky MA, Cohen WB, Parker GG, Harding DJ (2002) Lidar remote sensing for ecosystem studies. Bioscience 52(1):19–30. doi:10.1641/0006-3568(2002)052[0019:LRSFES]2.0.CO;2
46. Li J, Carlson BE, Lacis AA (2013) Application of spectral analysis techniques in the inter-comparison of aerosol data part III: using combined PCA to compare spatio-temporal variability of MODIS, MISR and OMI aerosol optical depth. J Geophys Res: Atmos. ISSN:2169-8996. doi:10.1002/2013JD020538
47. Liou KN (2002) An introduction to atmospheric radiation. Academic. ISBN:9780124514515
48. Maignan F, Bréon F-M, Lacaze R (2004) Bidirectional reflectance of Earth targets: evaluation of analytical models using a large set of spaceborne measurements with emphasis on the Hot Spot. Remote Sens Environ 90(2):210–220. doi:10.1016/j.rse.2003.12.006
49. Margerin L (2006) Attenuation, transport and diffusion of scalar waves in textured random media. Tectonophysics 416(1–4):229–244. doi:10.1016/j.tecto.2005.11.011
50. Marshak A, Davis, A (eds) (2006) 3D radiative transfer in cloudy atmospheres. Springer. ISBN:9783540285199
51. Martinsanz GP (ed) (2012) Unmanned aerial vehicles (UAVs) based remote sensing. Special issue of Remote Sensing. ISSN:2072-4292. http://www.mdpi.com/journal/remotesensing/specialissues/uav (visited on 27 June 2014)
52. Mätzler C, Rosenkranz PW (2007) Dependence of microwave brightness temperature on bistatic surface scattering: model functions and application to AMSU-A. IEEE Trans Geosci Remote Sens 45(7):2130–2138. doi:10.1109/TGRS.2007.898089
53. Mobley CD (1994) Light and water: radiative transfer in natural waters. Academic. ISBN:9780125027502
54. Modest MF (2013) Radiative heat transfer. Elsevier. ISBN:9780123869906
55. Monteith J, Unsworth M (2007) Principles of environmental physics. Elsevier. ISBN:9780080924793
56. Norouzi H, Rossow W, Temimi M, Prigent C, Azarderakhsh M, Boukabara S, Khanbilvardi R (2012) Using microwave brightness temperature diurnal cycle to improve emissivity retrievals over land. Remote Sens Environ 123:470–482. doi:10.1016/j.rse.2012.04.015
57. Plokhenko Y, Menzel WP (2000) The effects of surface reflection on estimating the vertical temperature-humidity distribution from spectral infrared measurements. J Appl Meteorol 39(1):3–14. doi:10.1175/1520-0450(2000)039(0003:TEOSRO)2.0.CO;2
58. Prigent C, Aires F, Rossow WB (2003) Land surface skin temperatures from a combined analysis of microwave and infrared satellite observations for an all-weather evaluation of the differences between air and skin temperatures. J Geophys Res 108(D10). doi:0.1029/2002JD002301, 2003
59. Prigent C, Jaumouille E, Chevallier F, Aires F (2008) A parameterization of the microwave land surface emissivity between 19 and 100 GHz, anchored to satellite-derived estimates. IEEE Trans Geosci Remote Sens 46(2):344–352. doi:10.1109/TGRS.2007.908881
60. Rodgers CD (2000) Inverse methods for atmospheric sounding: theory and practice. World Scientific. ISBN:9789810227401
61. Rosette J, Suárez J, Nelson R, Los S, Cook B, North P (2012) Lidar remote sensing for biomass assessment. In: Fatoyinbo L (ed) Remote sensing of biomass – principles and applications. InTech. ISBN:9789535103134
62. Roujean J-L, Leroy M, Deschamps P-Y (1992) A bidirectional reflectance model of the Earth's surface for the correction of remote sensing data. J Geophys Res 97(D18):20455–20468. doi:10.1029/92JD01411

63. Rutily B, Chevallier L (2005) Why is it so difficult to solve the radiative transfer equation? In: Stee Ph (ed) Transfert Radiatif et Exploitation des TGE, Third GRETA meeting, Fréjus, 11–13 May 2005, pp 1–23
64. Rytov SM, Kravtsov YA, Tatarskii VI (1989) Principles of statistical radiophysics 4: wave propagation through random media. Springer. ISBN:9783540178286
65. Schiavon G, Del Frate F, Iapaolo MF, Solimini D (2004) Neural network inversion algorithms for satellite temperature and humidity profiling. In: Microwave radiometry and remote sensing applications – MicroRad'04, Roma, 24–27 Feb 2004
66. Schneebeli M, Mätzler C (2011) A radiative transfer model for an idealized and non-scattering atmosphere and its application for ground-based remote sensing. J Quant Spectrosc Radiat Transf 112(5):883–892. doi:10.1016/j.jqsrt.2010.10.018
67. Sharkov EA (2003) Passive microwave remote sensing of the Earth: physical foundations. Springer. ISBN:9783540439462
68. Snyder WC, Wan Z (1998) BRDF models to predict spectral reflectance and emissivity in the thermal infrared. IEEE Trans Geosci Remote Sens 36(1):214–225. doi:10.1109/36.655331
69. Song C, Woodcock CE, Seto KC, Lenney MP, Macomber SA (2001) Classification and change detection using Landsat TM data: when and how to correct atmospheric effects? Remote Sens Environ 75(2):230–244. doi:10.1016/S0034-4257(00)00169-3
70. Tikhonov AN, Arsenin VIA (1977) Solutions of ill-posed problems. Winston. ISBN:9780470991244
71. Tsang L (1992) Dense media radiative transfer theory for dense discrete random media with particles of multiple sizes and permittivities. In: Priou A (ed) Progress in electromagnetic research PIER 6 – dielectric properties of heterogeneous materials. Elsevier. ISBN:9780444016461
72. Tsang L, Chen C-T, Chang ATC, Guo J, Ding K-H (2000) Dense media radiative transfer theory based on quasicrystalline approximation with applications to passive microwave remote sensing of snow. Radio Sci 35(3):731–749. doi:10.1029/1999RS002270
73. Tsang L, Jin P, Ding L, Li Z, Cline DW, Tan Y (2007) Modeling active microwave remote sensing of snow using dense media radiative transfer (DMRT) theory with multiple-scattering effects. IEEE Trans Geosci Remote Sens 45(4):990–1004. doi:10.1109/TGRS.2006.888854
74. Tsang L, Kong JA, Shin RT (1985) Theory of microwave remote sensing. Wiley. ISBN:9780471888604
75. Twersky V (1962) On scattering of waves by random distributions. I. Free-space scatterer formalism. J Math Phys 3(4):700–715. doi:http://dx.doi.org/10.1063/1.1724272
76. Twomey S (2002) Introduction to the mathematics of inversion in remote sensing and indirect measurements. Dover. ISBN:9780486495170
77. Weng F, Zhao L, Ferraro R, Poe G, Li X, Grody N (2003) Advanced microwave sounding unit cloud and precipitation algorithms. Radio Sci 38(4):8086–8096. doi:10.1029/2002RS002679
78. Westwater ER (1993) Ground-based microwave remote sensing of meteorological variables. In: Janssen MA (ed) Atmospheric remote sensing by microwave radiometry. Wiley. ISBN:9780471628910
79. Westwater ER, Crewell S, Mätzler C (2004) A review of surface-based microwave and millimeter wave radiometric remote sensing of the troposphere. Radio Sci Bull URSI RSB-310:59–80. ISSN:1024–4530
80. Westwater ER, Wang Z, Grody NC, McMillin LM (1985) Remote sensing of temperature profiles from a combination of observations from satellite-based microwave sounding unit and the ground-based Profiler. J Atmos Ocean Technol 2(2):97–102. doi:10.1175/1520-0426(1985)002(0097:RSOTPF)2.0.CO;2
81. Wilson RW, Penzias AA (1967) Isotropy of cosmic background radiation at 4080 Megahertz. Science 156(3778):1100–1101. doi:10.1126/science. 156.3778.1100
82. Winker DM, Pelon JR, McCormick MP The CALIPSO mission: spaceborne lidar for observation of aerosols and clouds. In: Itabe Z-S, Liu UN, Singh T (eds) Lidar remote sensing for industry and environment monitoring III, Hangzhou, 23 Oct 2002. Proceeding of SPIE 4893. doi:10.1117/12.466539

83. Wright HS, Levine JS, Croom MA, Edwards WC, Qualls GD, Gasbarre JF (2004) Measurements from an aerial vehicle: a new tool for planetary exploration. Technical report NTIS N20040171491. National Aeronautics and Space Administration
84. Wu R-S (1982) Mean field attenuation and amplitude attenuation due to wave scattering. Wave Motion 4(3):305–316. doi:10.1016/0165-2125(82)90026-9
85. Wu X, Smith WL (1997) Emissivity of rough sea surface for 8–13 μm: modeling and verification. Appl Opt 36(12):2609–2619. doi:10.1364/AO.36.002609
86. Young LA, Pisanich G, Ippolito C, Alena R (2005) Aerial vehicle surveys of other planetary atmospheres and surfaces: imaging, remote-sensing, and autonomy technology requirements. Technical report Army Aviation and Missile Command, Army/NASA Rotorcraft Division, Jan 2005
87. Zwally HJ (1977) Microwave emissivity and accumulation rate of Polar Firn. J Glaciol 18(79):195–215. http://www.igsoc.org:8080/journal/18/79/igs_journal_vol18_issue079_pg195-215.pdf (visited on 05 Nov 2014)

Chapter 10
Electromagnetic Spectrum and Remote Information

It should be clear by now that the electromagnetic waves are originator and carrier of information in Earth observation. The information content of the products delivered by a given type of sensor is essentially related to the parameters, mainly frequency (or wavelength) and polarization, characterizing the observing system, including the geometry at which data are acquired. Therefore, the specifications of an EO system, which include the type of sensor, the band of operation, the observation angle, etc., depend on the kind of information the system has to provide, as well as on the required reliability of operation and quality of products. Correspondingly, the interpretation of the data, preliminary to the retrieval and corresponding put into use of information, must refer to the interaction features of the electromagnetic wave with the observed environment. But, since the waves originating and carrying the information must cross at least once all or part of the atmosphere interposed between the target and the sensor, accounting for the atmospheric interaction is also crucial both in system specification and in data interpretation.

10.1 Selection of Frequency/Wavelength

The frequency or wavelength of operation is constrained by

- kind, intensity and effectiveness of the wave interaction with the material and structure to observe;
- transmission of the atmosphere interposed between the sensor and the sensed target.

The basic mechanisms of interaction between waves and materials differ according to the frequency range. At a microscopic level, the dielectric polarization mechanisms depend crucially on the frequency of the wave, while at the macroscopic level are essentially the dimensions of the objects with respect to the wavelength

D. Solimini, *Understanding Earth Observation*, Remote Sensing and Digital Image Processing 23, DOI 10.1007/978-3-319-25633-7_10

that determine the result of the interaction. Coarsely speaking, each mechanism produces effects which are mainly related to a particular parameter of the target. Moreover, the acquisition of information and the transfer process are degraded by atmospheric absorption, scattering, and emission, all depending on wavelength.

Given the variety of the terrestrial environments to observe, the waves interact with substantially different kinds of materials, including natural and man-made solid, liquid and gaseous targets. Because of the variety of the information that can be obtained and the numerous atmospheric windows (cf. Sect. 10.1.2.1) that can be exploited, the portion of the electromagnetic spectrum over which the various Earth observation missions[1] operate is quite wide, spanning from the low microwave frequencies to the ultraviolet wavelengths. The nature of the processes controlling both the generation of information and its transport is expected to change drastically over such a broad interval of frequency. The users choose the kind of sensor, the frequency band of operation and the type of product essentially according to

- the targets to observe,
- the parameters to retrieve.

Advised selection and effective utilization of the measurements among the host of available space-based observations require basic comprehension of their information content over the whole portion of the electromagnetic spectrum, spanning, as said, from the microwaves up to the visible (and even to the ultraviolet).

10.1.1 The Electromagnetic Spectrum

The spectrum of electromagnetic radiation is subdivided into wavelength bands the definitions and names of which may possibly differ among different organizations. A partition frequently used in Earth observation refers to the conventional wavelength limits listed in Table 10.1.

The infrared band can be found subdivided into alternative sections, e.g.,

- NIR (near IR or IR-A) for $0.75\,\mu\text{m} < \lambda_0 < 1.4\,\mu\text{m}$ ($214\,\text{THz} < f < 400\,\text{THz}$);

Table 10.1 Denomination of the intervals of electromagnetic spectrum according to wavelength range

Band	Wavelength range
ultra**v**iolet (UV)	10 nm to 400 nm
visible (VIS)	0.4 μm to 0.7 μm
near **i**nfra**r**ed (NIR)	0.7 μm to 2 μm
thermal infrared (TIR)	4 μm to 20 μm
far **i**nfra**r**ed (FIR)	20 μm to 300 μm
sub-millimeter waves	300 μm to 1 mm
microwaves	1 mm to 1 m

[1] Missions that are based on different physical mechanisms, such as GOCE [30], are not considered.

Table 10.2 Denomination of the microwave bands, based on IEEE Standard 521-1984 [43], according to their frequency range

Band	Frequency range (GHz)
P (UHF)	0.3 – 1.0
L	1.0 – 2.0
S	2.0 – 4.0
C	4.0 – 8.0
X	8.0 – 12.0
K_u	12.0 – 18.0
K	18.0 – 27.0
K_a	27.0 – 40.0
V	40.0 – 75.0
W	75.0 – 110.0

- SWIR (short-wavelength IR or IR-B) for $1.4\,\mu\text{m} < \lambda_0 < 3.0\,\mu\text{m}$ ($100\,\text{THz} < f < 214\,\text{THz}$);
- MWIR (mid-wavelength IR or IR-C) for $3\,\mu\text{m} < \lambda_0 < 8\,\mu\text{m}$ ($37\,\text{THz} < f < 100\,\text{THz}$);
- LWIR (long-wavelendth IR or IR-C) for $8\,\mu\text{m} < \lambda_0 < 15\,\mu\text{m}$ ($20\,\text{THz} < f < 37\,\text{THz}$);
- FIR (far IR) for $15\,\mu\text{m} < \lambda_0 < 1000\,\mu\text{m}$ ($0.3\,\text{THz} < f < 20\,\text{THz}$),

while the "microwaves" spectral interval is often split into the sub-intervals

- *millimeter waves*, for wavelength between $\lambda_0 = 1\,\text{mm}$ ($f = 300\,\text{GHz}$) and $\lambda_0 = 2.7\,\text{mm}$ ($f = 110\,\text{GHz}$);
- *microwaves*, with frequency limits between $f = 300\,\text{MHz}$ ($\lambda_0 = 1\,\text{m}$) and $f = 110\,\text{GHz}$.

This latter frequency range is further subdivided into bands denoted by the letters[2] shown in Table 10.2. The reader is warned that diverse letter designation and additional ranges may be found.

10.1.2 Role of the Atmosphere in Surface Observation from Space

Observing the surface of the Earth or the lower atmospheric layers from space platforms clearly implies that the electromagnetic radiation has to cross the whole atmosphere, twice if the observation exploits the Sun or an active (radar or lidar) system as source, and once in case a TIR or microwave radiometer is employed. This basic consideration points out that the atmosphere interferes with the observing process by making the target at ground or at low elevation more or less visible to the sensor. The extinction, caused both by absorption and by scattering [113, Chap. 5], is the key factor in determining the magnitude of atmospheric detrimental

[2]The designation *Q-band* for the 33–50 GHz frequency range is also encountered.

interference. The excess path length introduced in Sect. 5.2.3 has to be added as the relevant adverse factor in SAR interferometry (cf. Sect. 12.3.2.1).

Absorption by the more abundant atmospheric gases is relatively stable and determines the essential spectral features of extinction, according to the trend of the molecular resonances outlined in Sect. 2.2.1. A crucial issue to bear in mind is that *pressure broadening* [64] strongly affects the atmospheric absorption spectra, which are thus dependent on the varying altitude of the layers traversed by the observation path. Close to ground, the roto-vibrational lines tend to overlap and to form a smoothly-varying wide band with a more or less pronounced ripple in correspondence of the individual resonances. Observing targets on the ground implies crossing denser atmospheric layers, what can make relatively opaque the inter-line wavelength intervals that are otherwise transparent at higher altitudes [93].

The interaction of the electromagnetic waves with the particles present in the air superimposes to the gaseous absorption. As a general feature, the effect of the particles increases with frequency and, in particular:

- the scattering by the particles increases considerably with frequency, as seen in Sects. 7.3.4 and 9.1 and is expected to have major effects in the visible;
- the absorption by the particles behaves smoothly, since it tends to increase linearly[3] with the frequency, as suggested, for instance, by (7.19).

Coarsely speaking, in spectral ranges in which the gaseous atmosphere is relatively transparent, scattering generally predominates over absorption as the observation wavelength decreases, and vice-versa. However, it has to be considered that scattering is highly variable in space and time, given the strong diversity of nature and density of the atmospheric particles. In any case, the dramatic change of absorption with wavelength in correspondence of the resonant lines, as compared with the relatively smooth behavior of scattering, should not be overlooked.

10.1.2.1 Air Transmissivity

The absorption by the atmospheric gases is the basic delimiter of the wavelength ranges in which the earth-surface observing systems are allowed to operate from space or from high altitude.

10.1.2.1.1 Absorption by the Gaseous Atmosphere

Figure 10.1 shows examples of direct transmittance[4] of the entire *gaseous* atmosphere at low spectral resolution[5] as a function of UV, VIS and NIR wavelengths for two directions of observation, one nadir-looking and the other along a $\vartheta = 70°$

[3] In circumscribed frequency range.

[4] The re-directed radiation is not considered.

[5] Estimates of the atmospheric transmissivity at higher spectral resolution can be obtained, for instance, by the code MODTRAN5 [9].

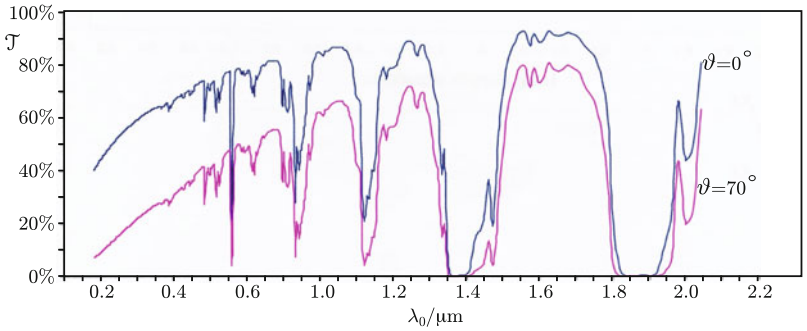

Fig. 10.1 Example of total atmospheric transmissivity $\mathcal{T}$ at low spectral resolution vs. vacuum-wavelength λ_0 for nadir ($\vartheta = 0°$) and $\vartheta = 70°$ slant path directions (Data simulated by LOWTRAN-7 [51] for cloud-free conditions and without aerosol)

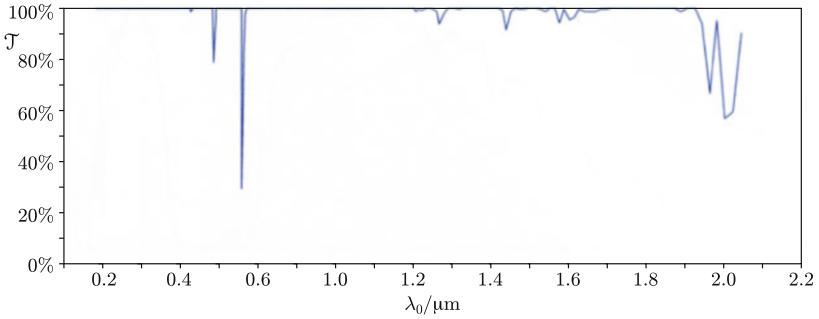

Fig. 10.2 Example of carbon dioxide total zenith atmospheric transmissivity $\mathcal{T}$ vs. wavelength λ_0 simulated at low spectral resolution by LOWTRAN-7 [51] for cloud-free conditions and without aerosol in the visible and near infrared

off-nadir rectilinear slant path. The decrease of transparency caused by the elongated slant path with respect to that at nadir is apparent.

The diagram shows the strong wavelength dependence of the absorption caused by the ensemble of the constituent gases. Indeed, the molecular roto-vibrational transitions of ozone, methane, carbon dioxide, and, especially, water vapor are particularly active in absorbing radiation in the visible and infrared bands. Figures 10.2 and 10.3 display the direct transmittance for the last two individual constituents. It can be remarked how the transparency of the air is mainly affected by the interaction with the water vapor molecules, which suggests a considerable influence of climatology. A fairly transparent spectral interval, relatively wide in terms of wavelength, occurs in the thermal infrared, as shown by Fig. 10.4. In this spectral region, of high impact on the climate of the Earth, ozone, carbon dioxide and, again, water vapor are the more active atmospheric constituents. Their respective contributions to the atmospheric transmissivity are displayed in Figs. 10.5, 10.6 and 10.7. The long-term apparently increasing trend of the CO_2 [89] and tropospheric H_2O [23] concentration in the air has to be born in mind.

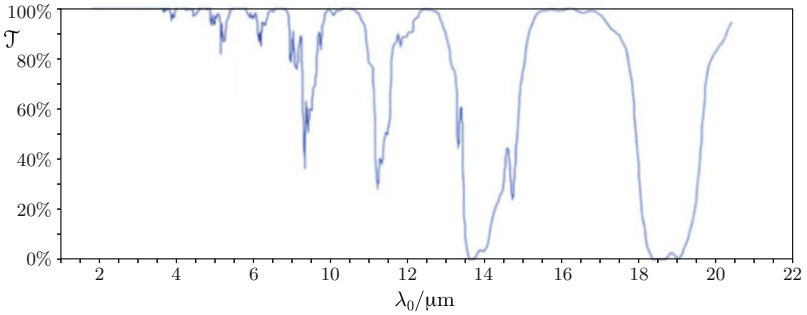

Fig. 10.3 Example of water vapor total zenith atmospheric transmissivity $\mathcal{T}$ vs.wavelength λ_0 simulated at low spectral resolution by LOWTRAN-7 [51] for cloud-free conditions and without aerosol in the visible and near infrared

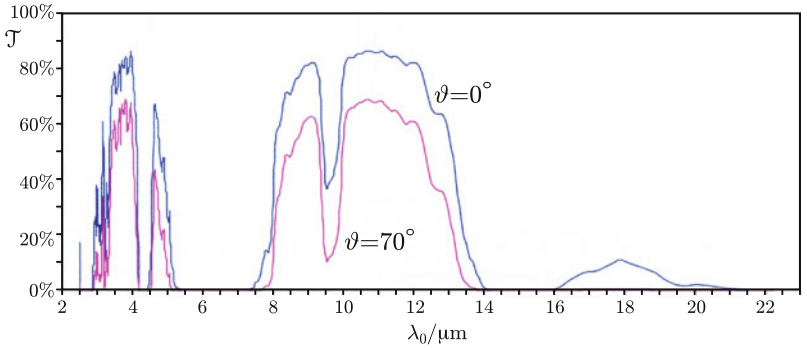

Fig. 10.4 Example of transmissivity $\mathcal{T}$ of the total atmosphere vs. infrared wavelength λ_0 simulated at low spectral resolution by LOWTRAN-7 [51] for cloud-free conditions and without aerosol over vertical ($\vartheta = 0$) and slant ($\vartheta = 70°$) paths

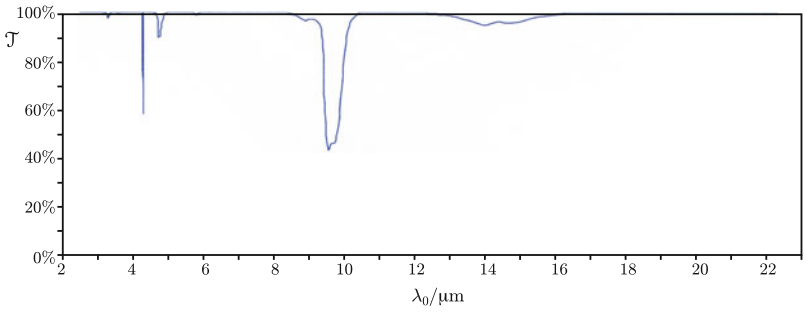

Fig. 10.5 Example of total zenith atmospheric ozone transmissivity $\mathcal{T}$ vs. infrared wavelength λ_0 simulated by LOWTRAN-7 [51] for cloud-free conditions and without aerosol

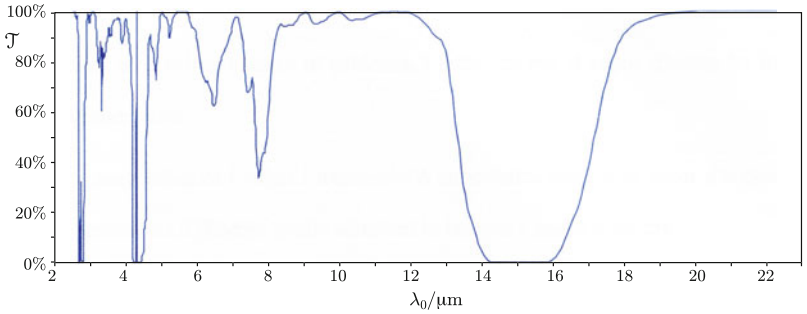

Fig. 10.6 Example of total zenith atmospheric carbon dioxide transmissivity $\mathcal{T}$ vs. infrared wavelength λ_0 simulated by LOWTRAN-7 [51] for cloud-free conditions and without aerosol

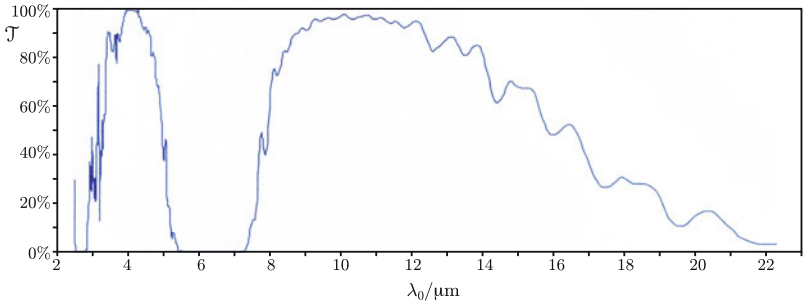

Fig. 10.7 Example of total zenith atmospheric water vapor transmissivity $\mathcal{T}$ vs. infrared wavelength λ_0 simulated by LOWTRAN-7 [51] for cloud-free conditions and without aerosol

The mechanisms of interaction of the water vapor are active over the whole far infrared, sub-millimeter and millimeter spectral range down to the microwaves, where a different spin-related effect in the oxygen molecules joins to absorb the electromagnetic radiation [107, 115]. Figure 10.8 shows the atmospheric transmission $\mathcal{T}$ over the millimeter-wave range.

Indeed, in the wavelength range from $\lambda_0 \approx 30\,\mu m$ to $\lambda_0 \approx 300\,\mu m$, a myriad of vibrational, rotational and composite modes of the water vapor molecules intensively absorb the electromagnetic energy, so that the gaseous atmosphere forms an opaque screen. Joining the trend of the transmission depicted by Fig. 10.1 with that of Fig. 10.8 suggests that this spectral region has to be avoided for effective observation of the surface from space.[6] The resonances of the main gaseous constituents rarefy with increasing wavelength. As a consequence, the atmosphere

[6]Particular high-altitude [109] (or/and high-latitude [55]) geographic locations, where the amount of precipitable water vapor is relatively low [110], are possibly less affected, provided the observations are carried out from low-flying platforms and at sufficiently high spectral resolution to exploit *microwindows* between water vapor lines.

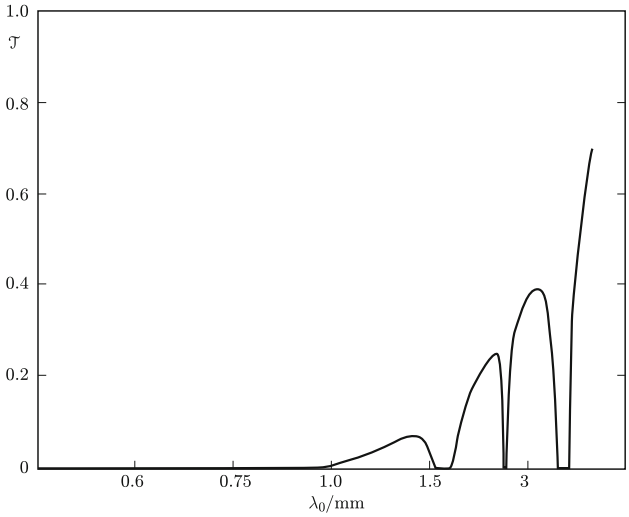

Fig. 10.8 Example of transmission $\mathcal{T}$ of the absorbing atmosphere for an Earth-space vertical path vs. millimeter wavelength λ_0 (Data simulated by H. Liebe et al.'s MPM [59], diagram courtesy G. Schiavon)

presents wavelength *windows* within which it is rather transparent, interspersed with spectral ranges at which it is opaque, as displayed by the trend of $\mathcal{T}$ at the longer wavelength in the diagram of Fig. 10.8.

The disadvantage of the linear scale representation, hinted at in Sect. 4.1.2.5.2, clearly appears from the indiscernible values of $\mathcal{T}$ in the absorbed bands, what makes diagrams of this kind of little use for atmospheric characterization at wavelengths below $\lambda_0 \approx 1$ mm. Moreover, as noted in Sect. 8.2.1, frequency is preferred to wavelength at microwave and radio frequencies. Figure 10.9 reports the attenuation[7] in dB caused by the atmospheric absorbing gases on a vertical path from sea level ($z_g = h = 0$) to a point at the height above sea level $h = H_a$, top of the atmosphere, above which, for instance, a nadir-observing satellite is located. The diagram is derived by vertical integration of the specific absorption represented in Fig. 4.2, of which it clearly reproduces the trend. However, note the jagged appearance of the 60-GHz attenuation peak values due to the high-altitude splitting of the pressure-broadened lines forming the oxygen absorption complex.

It is worth mentioning that, consistently with the radiative transfer features discussed in Sect. 9.4.1.1, measurements are required in the opaque intervals when information has to be gained on meteorological parameters, such as temperature

[7]Section 4.1.2.5 mentions that the gaseous atmosphere is an inhomogeneous medium, but the variations of its permittivity are so smooth that it can be considered locally homogeneous and the geometrical optics approximation (5.38), to which the definition of absorption coefficient refers, can be applied.

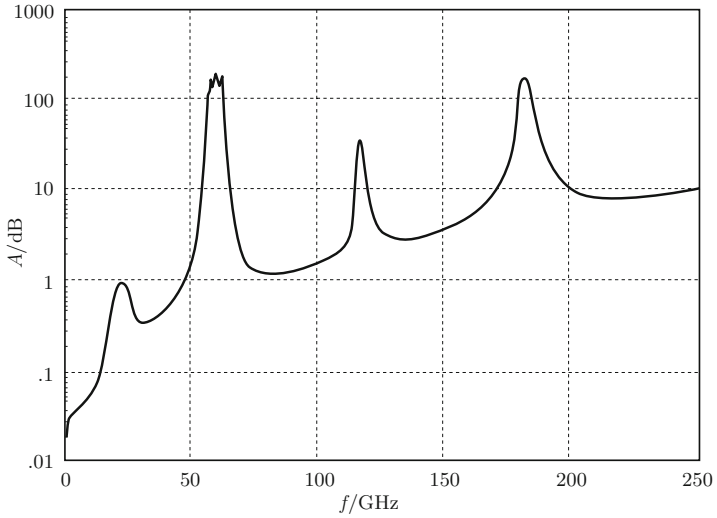

Fig. 10.9 Example of Earth-space one-way zenith attenuation A caused by the absorbing gaseous atmosphere vs. microwave frequency f (Curves interpolate data from [58])

and humidity profiles of the atmosphere. Observations are typically carried out at wavelengths from $\lambda_0 \approx 4\,\mu\text{m}$ to $\lambda_0 \approx 8\,\mu\text{m}$ of the TIR and from $\lambda_0 \approx 14\,\mu\text{m}$ to $\lambda_0 \approx 100\,\mu\text{m}$ of the far and **ex**treme **i**nfra**r**ed (XIR), as well as at frequencies within the water vapor [92] and oxygen [108] millimeter-wave and microwave absorption peaks.

Finally, apart from the low-moisture cases, the limits set by extinction are relaxed when the sensor is carried by low-altitude **r**emotely **p**iloted **a**erial **p**latform (RPAP)s [125], with consequent shortening of the length of the atmospheric path. In this case, observation at enhanced spectral resolution is needed to steer clear of the individual resonant absorption lines [22].

10.1.2.1.2 Extinction by Aerosols

The diagrams shown in the preceding Figs. 10.1–10.9 refer to the purely absorbing atmosphere, so that only the absorption coefficient α_b contributes to the specific extinction (9.22). Scattering is indeed always present, although it may either prevail or be negligible according to the wavelength at which the observations are performed and to the atmospheric conditions.

First of all, Rayleigh scattering from the air molecules is ubiquitous [14, 85]. Given the "dimensions" of the particles, it increases the extinction appreciably at the shortest visible wavelengths, while it becomes negligible in the red. The increase, which is of the order of 20 % in the blue, is expected to enhance with the decreasing wavelength in the ultraviolet range.

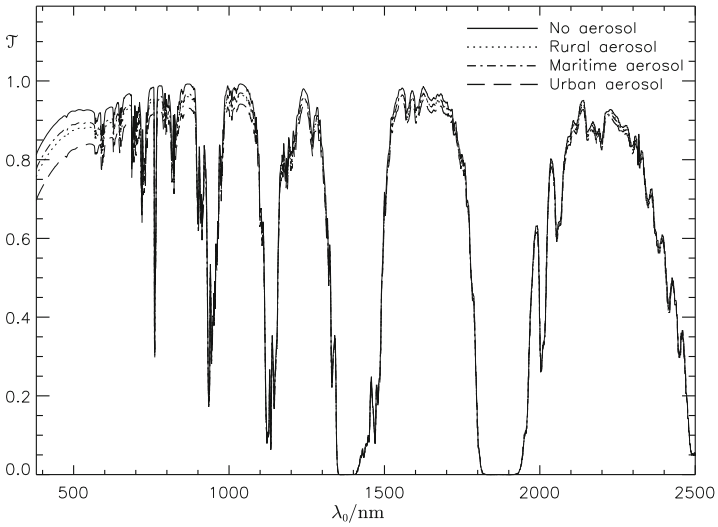

Fig. 10.10 Example of total atmospheric transmissivity $\mathcal{T}$ vs. wavelength λ_0 simulated by LOWTRAN-7 [51] in the visible and near infrared taking account of model aerosols of different kinds (Diagram, courtesy A. Di Noia)

The presence of solid (ice, mineral dust, soot-like particulates) small (their size generally lies between $D \approx 10^{-2}\mu$m and $D \approx 10^{2}\mu$m) inhomogeneities suspended in air causes additional extinction, contributed by both absorption and scattering [15, 16]. Air molecules essentially scatter according to the inverse fourth power of wavelength (Sect. 7.2.1.1), while, given their wide size distribution, the effect of the particles is relatively independent of frequency. The atmospheric windows in the visible and infrared bands are made less transparent, depending on the particle nature and density. Figures 10.10 and 10.11 suggest the effect of the aerosols on the atmospheric transmittance. As expected, the aerosol extinction increases with decreasing wavelength and, given the dimensions of the particles, it affects the transmittance mainly in the visible, while the effect of the particulate tends to disappear already in the near infrared. Only relatively high concentrations of particles of urban origin extend their aftermath to longer wavelengths. The effect of the aerosols can be summarized by saying that the turbid atmosphere is expected to be less transparent in the visible windows than in the infrared ones, although the consequence of the frequency-dependent permittivity of the atmospheric particles and of their dimension-to-wavelength ratio can occasionally modify this coarse trend.[8] The atmospheric transmissivity in the TIR is essentially controlled by the constituent gases, so that only the spectral intervals from $\lambda_0 \approx 3.5\,\mu$m to $\lambda_0 \approx$

[8]Reversing the perspective, the aerosols themselves are clearly object of remote measurement [7], given their global and local impact on the atmospheric environment.

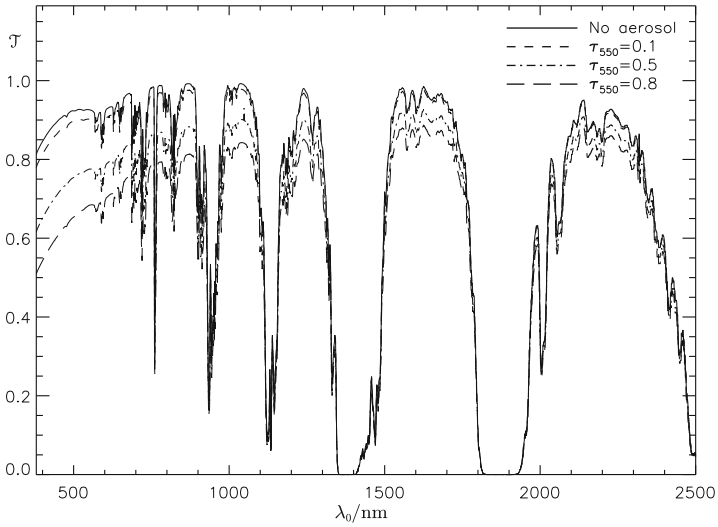

Fig. 10.11 Example of total atmospheric transmissivity $\mathcal{T}$ vs. wavelength λ_0 simulated by LOWTRAN-7 [51] in the visible and near infrared taking account of different concentrations of model urban aerosol (Diagram, courtesy A. Di Noia)

4 μm and from $\lambda_0 \approx 8\,\mu$m to $\lambda_0 \approx 12\,\mu$m (clearly excepted the ozone absorption region) are of interest for observing the earth surface from space.

10.1.2.1.3 Extinction by Hydrometeors

The transmission properties of the atmosphere are substantially modified in presence of mist, fog or non-precipitating clouds. These hydrometeors are forms of aerosol, consisting of water droplets the dimensions D of which, as said, are distributed in the range $10^{-2}\mu\text{m} \lesssim D \lesssim 10^{2}\mu\text{m}$. Their effect is clearly strong at optical wavelengths and decreases throughout the infrared and sub-millimeter ranges, until it becomes negligible at microwaves. The imaginary part of water permittivity is sufficiently low at VIS and NIR wavelengths that extinction is essentially determined by scattering, while absorption is the main cause of attenuation from the FIR onward, when the wavelength becomes large with respect to the dimension of a large fraction of the particles. The volume density of the water particles in thick fog and dense clouds can reach relatively high values, corresponding to specific attenuation up to the order of hundred dB km^{-1}, thus hampering observation at wavelengths through the sub-millimeter range even from low-flying (provided operation is feasible) platforms. Note that the spatial and temporal variability of density and size distribution of the droplets makes atmospheric attenuation a random quantity difficult to estimate and predict.

On their side, precipitating clouds ordinarily contain also drops with dimensions up to a few millimeters [8, 84, 87], which typically make opaque the atmosphere for $\lambda_0 \lesssim 1.5$ cm. The magnitude of the effect depends on the precipitation rate. In

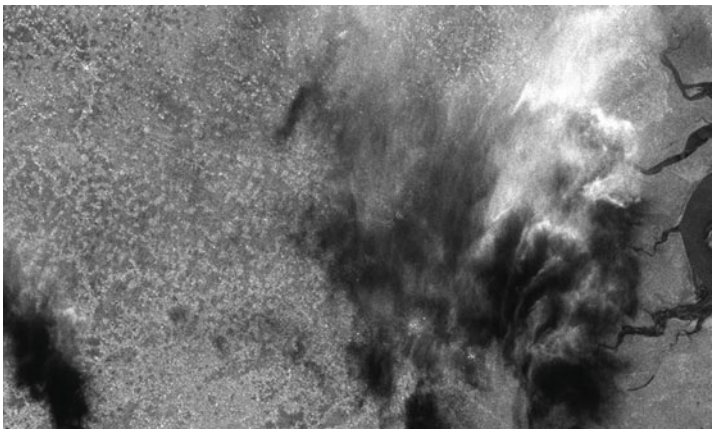

Fig. 10.12 Radar image taken at X-band by TerraSAR-X showing enhanced scattering (*brighter*) from the convective cell facing the radar and decreased backscattering (*darker*) from the Earth's surface past the cloud [120]

case of particularly intense precipitations, microwave observations can be affected at frequencies down to X-band [65, 66], as the SAR image of Fig. 10.12 puts forward. The sketch in Fig. 10.13 suggests that strong scatter may originate from parts of very dense precipitating clouds facing the radar, which are formed by a high number of large particles per unit volume, whereas the scattering from the surface past the clouds may appear weak due to the two-way high extinction expressed by (9.17), in which r_ϵ is of the order of the particle dimension (Sect. 7.4.4). This effect diminishes the ability of space-based or high-flying systems to gain information on the surface [33], the scattering from which reaches the sensor weakened by extinction and interfered by scattering from the convective cell. At frequencies lower than X–band, rain, however heavy, has negligible effect on the Earth observing systems. Only in exceptional events, some effect, mainly of the mixed liquid-ice phase, can be experienced by systems even at frequencies down to C-band [45, 72, 73]. Figure 10.14 seems to confirm this hypothesis.

The radar image of dense clouds of Fig. 10.12 puts into visual evidence that the information carried through the atmosphere not only fades because of the extinction, but is also interfered by unwanted power originated by scattering along the atmospheric path. This effect is predicted analytically by the relation (9.41), which clearly applies to the radiative transfer in general, irrespective of frequency. The optical radiation carrying information on the surface is attenuated by extinction and concurrently interfered by the solar radiation scattered along the atmospheric path (Sect. 9.3.1). On their side, radiometric TIR observations of the surface are diminished by atmospheric absorption and, because of reciprocity, concurrently contaminated by thermal emission as described by (9.52) and (9.56) or (9.57). Attenuation and interference become less intense as absorption and scattering decrease. Apart from the cases mentioned above relative to fairly uncommon meteorological phenomena, the atmospheric interference weakens at microwaves, especially at the lower frequencies.

Fig. 10.13 Sketch of radar observation of the surface through clouds, with representation of scattering from convective cells (COSMO-SkyMed, © ASI; artwork by A. Perrone)

In summary, taking account of the joint effect of extinction and emission, the performance of observing systems operating in the visible and infrared windows is substantially degraded by clouds and dense fog, while microwave measurements are almost always able to gain remote information on the earth surface, with a possible exception only when the observation occurs through very heavy precipitation.

Correspondingly to the use of absorbed bands mentioned in Sect. 10.1.2.1.1 for thermal and moisture sounding of the atmosphere, systems dedicated to the observation of clouds and precipitation operate at wavelengths that are substantially subject to absorption and scattering from the hydrometeors [50]. Some details are found in Sect. 14.3.

10.1.3 Wavelength and Information

The information that an observing system is able to acquire depends on which kind of electromagnetic interaction with the environment of interest originates the wave captured by the sensor. Each frequency or wavelength band corresponds to a main type of interaction. In short:

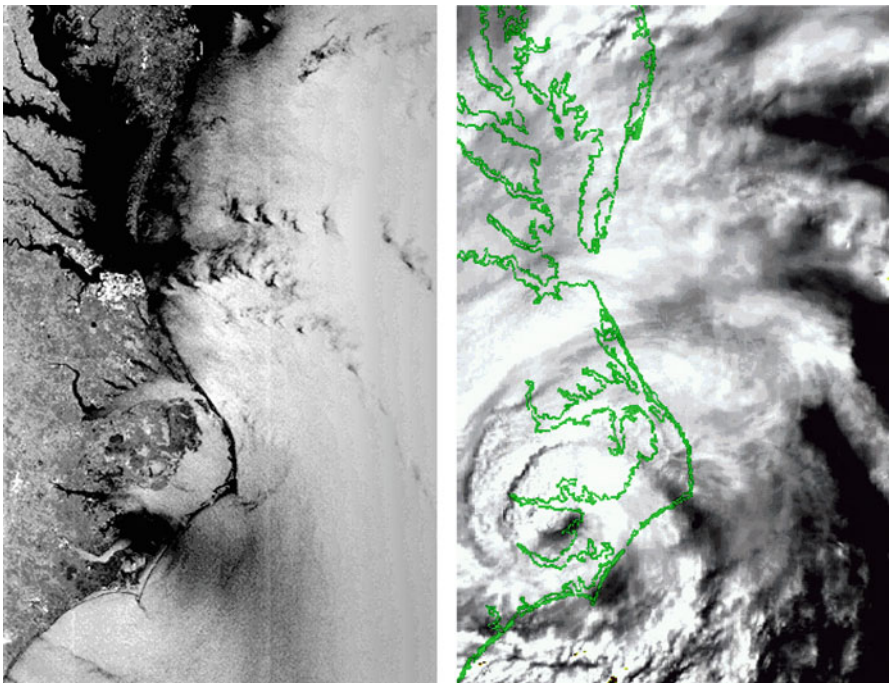

Fig. 10.14 C-band radar image (ASAR, *left*) and optical image acquired simultaneously by MERIS (*right*) of the U.S.A. east coast affected by the hurricane Irene: in the SAR image high backscattering (*brighter*) appears in the outer spiral branches on the side of the towering clouds facing the radar, while low backscattering (*darker*) originates from the opposite shadowed side, similarly to Fig. 10.12. Note how the shore line delineated in *green* in the *right image* is recognized through the thick clouds by the C-band radar, whereas it is not visible to the optical sensor (Credit: data, ESA; processing, courtesy C. Solimini, M. Picchiani)

– in the ultraviolet, visible and near infrared, the interaction mainly consists of scattering of the waves radiated by the Sun, or, for particular purposes, by active (lidar) [31] systems;
– scattering and reflection are also exploited by microwave active (radar) systems;
– instead, emission is the basic interaction mechanism for passive (radiometric) systems operating in the thermal infrared and at microwaves.

Actually, *reflection* in a strict sense is the coherent re-radiation in the specular direction by the average air-material interface. This latter can be often visualized as the plane surface of discontinuity considered throughout Chap. 6, or as the smooth thin layer of permittivity variation introduced in Sect. 7.3.3. On its side, *scattering* is the re-radiation, spread in angle, by non-ordered ensembles of individual elements (Sect. 7.4.1) or by a randomly inhomogeneous dielectric structure, modeling rough surfaces of targets or continuous bulk inhomogeneities (Sect. 7.4).

Further particular observing systems, such as limb sounders [36, 119] or transmissiometers [38], exploit extinction, that is, measure the fraction of power originated by natural (typically the Sun) or artificial sources that is absorbed and/or scattered, to gain information on the matter present in the region crossed by the electromagnetic path.

It is worth adding that the reflected or scattered field generally has the same wavelength as the incident wave. However, possibly virtual, interlinked absorption-emission processes can result in re-radiation also at frequencies different from that of the incident wave (*Raman scattering* [32], *fluorescence* [34, 80]). The wavelength-shifted re-radiation may contain useful information on the scattering material, so that observing systems exist, although of more limited use, based on these kinds of non-linear interaction.

The inmost mechanisms at the basis of scattering, reflection, absorption and emission depend on the wavelength band, since they are ultimately related to the energy exchanges between the electromagnetic wave and the material, be it gas, liquid, or solid, under observation:

- at the higher frequencies (ultraviolet, visible, infrared), and/or for elementary structures (mainly gases), the process is modeled as absorption and re-emission of photons, at wavelengths corresponding to the energy level transitions induced in the microscopic systems (molecules, atoms) composing the observed medium;
- at lower frequencies (microwaves), for composite materials (e.g., soil, vegetation), macroscopic collective mechanisms intervene, which are described classically by electric charge mobility, and dielectric polarization and relaxation.

One major consequence is the marked interaction of optical[9] radiation with the materials almost only in correspondence of the absorption lines or bands related to electronic, vibrational, roto-vibrational and rotational transitions: strong variations with wavelength are expected, especially for "simple" materials, as observed for the atmosphere [102] in Sects. 2.2.1 and 4.1.2.5.2, as well as Sect. 10.1.2.1. At microwaves, Figs. 10.9 and 10.8 suggest that the spectral selectivity is still present in the atmosphere, mainly due to rotational transitions of the gas molecules, whereas much less marked variations with frequency are shown by the liquid and solid heterogeneous natural materials of the earth surface and of man-made objects, the behavior of which is substantially affected by the dielectric relaxation of liquid water and by dissolved salts, as outlined in Sects. 2.2.2.3, 2.2.3 and 2.2.4.

Such a variable nature of the interaction mechanisms makes each frequency band suitable to extract information on particular properties of the observed target. Operating at wavelengths at which the interaction occurs through electronic or molecular processes is mainly apt to gain information on the microstructure, such as chemical composition or some biological properties, while the use of frequencies at which the radiation interacts through collective processes is suitable to sense physical properties, such as soil moisture, and morphology, such as, for instance, sea

[9] As usual, optical designates ultraviolet, visible and infrared.

Table 10.3 Short summary of spectral bands, prevailing interaction mechanisms and main sensed quantities

Bands	Basic mechanisms of interaction	Main sensed parameters	
		surface	atmosphere
UV, VIS NIR	electronic/vibrational processes	chemical composition vegetation, land cover	constituents aerosols
TIR	roto-vibrational processes thermal emission	temperature thermal capacity	constituents temperature profiles
FIR	rotational processes thermal emission	temperature	constituents temperature profiles
mm-waves		water content	precipitation
Microwaves	scattering reflection	moisture, biomass morphology	precipitation

surface roughness. Table 10.3 summarizes the interaction mechanisms prevailing in each spectral band together with the main parameters both of the surface and of the atmosphere that are correspondingly sensed.

10.2 Basic Measurements

The basic quantities to which a sensor directly responds and from which the information is derived are the amplitude and phase of the electromagnetic field. A straightforward alternative to the field amplitude is the power density, which is indeed the most commonly measured quantity, or even the only one when the incoherence of the radiation makes meaningless the measures of phase. The output of the sensor, created by the field that is scattered, reflected, emitted, or absorbed by the portion of the terrestrial environment being observed, represents the signal. Suitable *calibration* allows this latter to correspond directly to the power or to the amplitude and phase of the field arriving at the sensor. Since the field relates to the properties of the observed environment, the signal contains information on the scattering, reflecting or emission properties of the target. Subsequent processing of the signal pursues the *retrieval* – in a wide sense – of the environmental parameters of interest to users. Intermediate *products* of various levels are customarily derived from the power or from the field, according to the spectral band and to the measurement technique. The products generally form the *primary* quantities for specific applications.

The measured quantities, or, in general, the products relative to the Earth's surface, are assigned to an individual area and are suitably normalized and organized in two-dimensional matrix form, presented as *images*, for example of the types, microwave and optical, shown in Fig. 10.14. An individual area is a *picture element (pixel)* of the image. The images are generally *geo-located*, i.e., the position of the center of an individual area corresponds to a set of geographic coordinates.

Fig. 10.15 Image taken by the LANDSAT multi-spectral scanner over New Jersey, U.S.A., on October 10, 1972 (*left*) compared with a WorldView-2 over Rome, Italy, on December 10, 2009 (*right*) (WV2 image, © DigitalGlobe, 2009)

Figure 10.15 makes a comparison suggestive of the progress between an early optical image of the first **Land** Remote-Sensing **Sat**ellite (LANDSAT) with that acquired about 40 years later by an enhanced sensor (WordView2).

It can be added that in atmospheric sensing the measurements and derived quantities can be assigned either to a volume or to a height interval, frequently in form of *profiles*.

10.2.1 Passive Measurements in Ultraviolet, Visible, Near Infrared

In this wavelength range, which is generically named *optical*, thermal emission from the terrestrial materials at the environmental temperatures is negligible.[10] Therefore the optical spectrometric systems exploit Sun as source of the very-wide band (*polychromatic*) electromagnetic power, which probes the environment, extracts the information and carries it to the observing platform.

[10]With the exception of burning matter (e.g., forest fires [2]) and of some active volcanic areas [123].

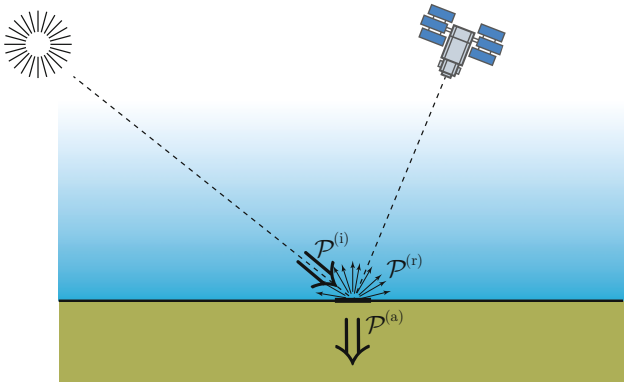

Fig. 10.16 The solar radiation incident onto the earth surface carries the areic power $\mathcal{P}^{(i)}$, which splits into the "reflected" $\mathcal{P}^{(r)}$ and absorbed $\mathcal{P}^{(a)}$

10.2.1.1 Optical Observation of the Surface

Section 10.1.2 points out that to obtain remote information either on targets at ground level or on the lowest atmospheric layers, space-based and high-flying sensors must operate in *atmospheric windows*, where the atmosphere is sufficiently transparent to guarantee an exploitable signal-to-noise ratio. The solar polychromatic radiation transmitted within the transparent atmospheric windows that reaches a target located on or close to the earth surface is partly absorbed and partly re-radiated by the target. From the basic electromagnetic point of view, a fraction of the incident irradiance $\mathcal{P}^{(i)}$ defined in Sect. 8.2.1 is concurrently absorbed and the remaining part reflected and scattered, as sketched in Fig. 10.16:

$$\mathcal{P}^{(i)} = \mathcal{P}^{(a)} + \mathcal{P}^{(r)} \ .$$

The re-radiated radiation is customarily named "reflected", though, actually, is not only reflected through the mechanisms considered in Sects. 7.3.1 or 7.3.3, but mainly scattered according to Sect. 7.4. Measuring the "reflected" irradiance, that is the power density $\mathcal{P}^{(r)}$ globally re-radiated by the unit area of the target yields the albedo $\mathcal{A}$ introduced by (7.21) in Sect. 7.1.3.1 or also by (9.34).

While the albedo describes the *global* reflecting properties of the observed terrestrial environment over the *entire spectrum* of the incident radiation, detailed information on how the reflecting properties change with wavelength is provided by the *spectral reflectance* $\mathcal{R}_\lambda$, defined as the ratio of the reflected (in the above wide sense) spectral radiant flux $\mathcal{P}_\lambda^{(r)}$ at a given wavelength to the incident one $\mathcal{P}_\lambda^{(i)}$:

$$\mathcal{R}_\lambda := \mathcal{P}_\lambda^{(r)} / \mathcal{P}_\lambda^{(i)} \ .$$

It has to be born in mind that $\mathcal{R}_\lambda$ is an integral quantity referring to the *hemisphere*, whereas a single sensor captures instantaneously the spectral radiance in a given direction. To take this concept into account, the bi-directional spectral reflectivity $\mathcal{R}_\lambda$, introduced in Sect. 9.3.1 must be used for the considered pair of solar and observation angles. In case the hemispherical spectral reflectance $\mathcal{R}_\lambda$ is the quantity of interest, $\mathcal{R}_\lambda$ data from multiple acquisitions at different observation angles may be combined, provided the image processing includes correction for the space-time varying atmospheric and radiative effects discussed in Sect. 9.3.1.

An additional derived quantity that is found useful in characterizing the Earth's surface environment, is the *spectral absorbance* $\mathcal{A}_\lambda$, defined by

$$\mathcal{A}_\lambda := \mathcal{P}_\lambda^{(\mathrm{a})} / \mathcal{P}_\lambda^{(\mathrm{i})} = 1 - \mathcal{R}_\lambda \ .$$

Both $\mathcal{R}_\lambda$ and $\mathcal{A}_\lambda$ refer to the "central" wavelength of a given channel of the spectrometric instrument. Instead, the *absorbance* $\mathcal{A}$, just like the *reflectance* $\mathcal{R}$, is relative to the global quantities. Global now means integral with respect to λ, that is, over the whole observed spectrum.

The basic quantity that is directly measured by space-based spectrometric systems is the upward spectral radiance $\mathcal{I}_\lambda^{\Uparrow}$ of the radiation originated by the earth surface or lower atmospheric layers, which reaches the sensor, attenuated and contaminated by the atmosphere as outlined in Sect. 9.3.1. The surface spectral reflectivity $\mathcal{R}_\lambda$, which contains the information on the parameters of users' interest, is derived from the observed upward spectral radiance $\mathcal{I}_\lambda^{\Uparrow}(s_H)$ (9.46) or $\mathcal{I}_\lambda^{\Uparrow}(s_\mathrm{p})$ (9.50) once the radiance measured from the space or air platform is reduced to that, $\mathcal{I}_\lambda^{\Uparrow}(s_\mathrm{g})$, at the bottom of the atmosphere and the solar spectral radiance $\mathcal{I}_\lambda^{\odot\Downarrow}(s_\mathrm{g})$ incident onto the surface is estimated. The solar spectral radiance at ground depends on the seasonal and diurnal angular position of the Sun and varies according to the meteorological conditions, which affect the atmospheric transmittance, especially through aerosol and water vapor extinction. In practice, as anticipated in Sect. 9.3.1, atmospheric corrections are applied. It is worth reminding that the spectral characteristics of the source exploited in optical spectrometric observations are constrained by the features of the solar radiation and by the transmission properties of the atmosphere. Figure 10.17 shows a typical pattern of the spectral radiance of the Sun at sea level. The shape of the Planck function is recognized, distorted by the atmospheric absorption bands outlined in Sect. 10.1.2.1.

10.2.2 Measurements in the Thermal Infrared

Apart from peculiar applications of CO_2 lidars [86, 88], sensing in the thermal infrared is essentially passive, exploiting spontaneous emission from the terrestrial environment. According to the Fluctuation-Dissipation Theorem mentioned in Sect. 8.1, any electromagnetically lossy material at thermodynamic temperature

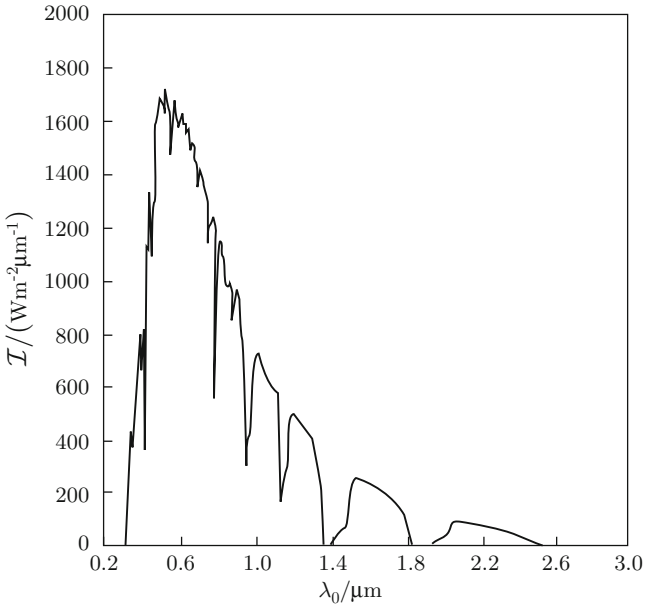

Fig. 10.17 Example of spectral radiance $\mathcal{I}_\lambda$ of solar radiation at the bottom of the atmosphere as a function of wavelength λ_0 in the UV-NIR range (Curves interpolate data from [49])

$T \neq 0$ K spontaneously radiates (*emits*) spread-spectrum electromagnetic power. The emitted power is distributed over the whole spectrum, according to the frequency behaviors both of the Planck function $\mathcal{B}$ (8.37) and of the spectral emissivity e_λ introduced by (8.38). Therefore, for given λ_0, direction of observation, field polarization and thermodynamic temperature, the spectral radiance depends on the geometric and physical characteristics of the body, as well as on the energy fluxes surrounding it.

It was mentioned in Sect. 9.3.2 that only about one tenth of the spectral radiance of a black body at $T = 5800$ K simulating the solar radiation is generally scattered from the earth environment. Figure 10.18 compares the spectral radiances of black bodies at four typical terrestrial temperatures with the expected radiance of the solar radiation scattered by the Earth. Measurements taken at night are clearly not affected by the solar radiation, whereas day-time observation of the thermal emission from the earth environment are interfered by the scattered solar radiation according to Sect. 9.3.2. Given the relative intensities of the radiation arriving from the Sun and of that emitted by the Earth, Fig. 10.18 indicates that the solar spectral radiance diffused by the terrestrial environment, characterized by the reference value $\mathcal{R}_\lambda \approx 0.1$, generally exceeds the emitted one at wavelengths below $\lambda_0 \approx 3\,\mu$m, whereas for wavelengths $\lambda_0 \gtrsim 7\,\mu$m, emission exceeds diffusion by at least one order of magnitude.

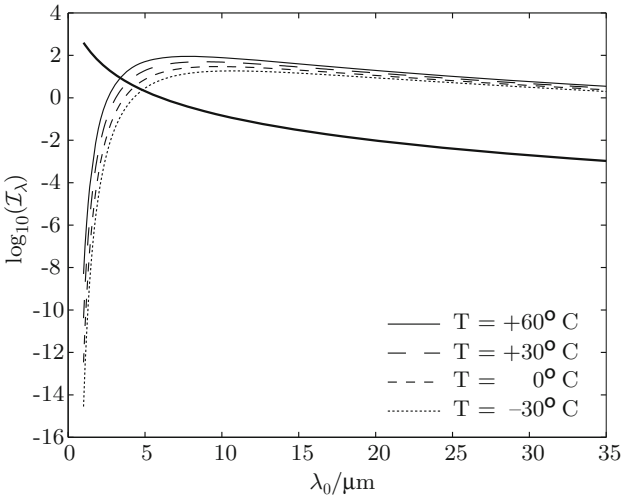

Fig. 10.18 Spectral radiance of scattered solar radiation (*decreasing curve*) compared with black-body emission relative to the indicated environmental temperatures $-30^\circ\,\mathrm{C} \le T \le 60^\circ\,\mathrm{C}$; $\mathcal{I}_\lambda$ is in logarithmic scale

10.2.2.1 TIR Observation of the Surface

Taken into account the atmospheric transmissivity shown in Fig. 10.4, two spectral windows are in practice exploitable in the TIR sensing of the surface from space or high-altitude platforms, the one about $\lambda_0 \approx 3.7\,\mu$m and the wide $8\,\mu\mathrm{m} \lesssim \lambda_0 \lesssim 14\,\mu$m window. This latter is split into two sub-bands by the ozone absorption peak around $\lambda_0 \approx 9.7\,\mu$m for observation from space. The contribution by the solar radiation "reflected" by the earth surface is comparable with that of the emitted radiation in the $3.7\,\mu$m window, with corresponding uncertainty in interpreting the data taken during daylight hours. Instead, the solar radiation diffused by the surface in the 10–12 μm maximum-transmittance window is often negligible with respect to that emitted by the terrestrial materials.[11] Indeed, given the relatively low values of permittivity (Sect. 2.2) and high roughness of surfaces,[12] the TIR reflectivity of terrestrial materials is generally low and their emissivity correspondingly large. For instance, generally, $0.8 \lesssim e_\lambda \lesssim 0.99$ in the wavelength range 10–14 μm.

Since the thermal emission of a body depends jointly on its temperature and emissivity according to the definition (8.38), both quantities are jumbled up in the radiance measurements and must be separated. Coarselyspeaking, if the emissivity

[11] This conclusion does not apply to *sunglint*, i.e., to *specular reflection* of solar radiation.

[12] Remember that the effect of roughness is commensurate to wavelength.

of the body is known, measuring the outgoing spectral radiance allows estimating its temperature [116], while if the temperature of the emitting body can be estimated a-priori, the measure allows determining its spectral emissivity, thus, in turn, obtaining information on the parameters that affect this latter.[13] It is worth pointing out that an uncertainty in the spectral emissivity value of the order of 1 % yields an error in temperature estimate of the order of 1 K. The TIR surface observation methods typically exploit measurements taken at different wavelengths to concurrently estimate both emissivity and temperature [100]. The **t**emperature **e**missivity **s**eparation (TES) algorithm [42] is expected to provide estimates with typical accuracies within 0.015 for emissivity and 1.5 K for temperature.

The signal delivered by a linear-response radiometer is proportional to the power W captured by the instrument, hence to the observed spectral radiance $\mathcal{I}_\lambda$ of the emitting body in the neighborhood of the "center" wavelength of the radiometric channel:

$$W(\lambda, T) \simeq \mathrm{C}\,\mathcal{I}_\lambda(T) = \mathrm{C}\,e_\lambda\,\mathcal{B}(\lambda, T)\ .$$

In the thermal infrared, the magnitude and spectral dependence of the emissivity e_λ of sea, of particular land regions with appropriate bio-geo-physical characteristics, and of the atmosphere are known with serviceable approximation. Therefore, the temperature of the observed areas can be retrieved with the needed accuracy, for instance, better than 1 K for sea. The **s**ea **s**urface **t**emperature (SST), that is the water temperature close to the ocean's surface, is indeed a quite important environmental parameter being measured routinely from space. Figure 10.19 shows an SST map of a portion of the Mediterranean Sea. In other cases, the temperature is reasonably known, thus the measurements can be utilized to gain information on the emissivity that is, in turn, on the physical or morphological properties of the observed target (e.g., Sect. 14.1.3).

The ability to gain information on the surface is conditional upon the interference by the atmosphere discussed in Sect. 9.3.2 being sufficiently low or known. Figure 10.4 shows that the clear atmosphere has reasonably transparent windows in the thermal infrared; however, if enhanced accuracy of the retrieved surface parameters is demanded, the interfering atmospheric effects need to be considered. Water vapor contributes to absorption in the 10–14 μm wavelength range (Fig. 10.7), in addition to ozone (Fig. 10.5). Air moisture can change both the radiation field at the surface and the radiances measured from an elevated platform. Since the effects vary with the atmospheric conditions, meteorological observations and models are the basis for fine data correction. Multi-wavelength sophisticated data processing is also applied to attain particularly high accuracies in surface temperature retrieval.

[13] The approach assumes linearity, i.e., independence of emissivity from temperature.

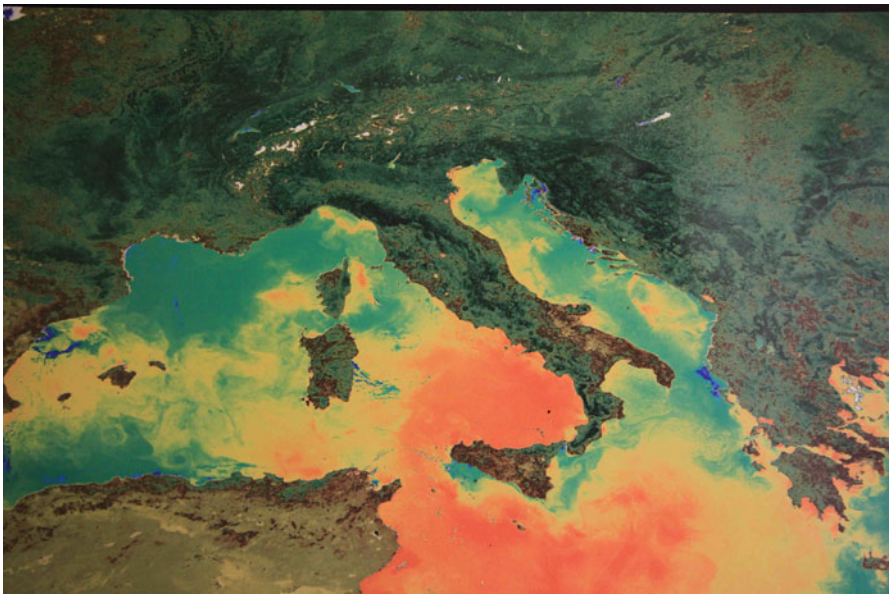

Fig. 10.19 Color-coded surface temperature of sea facing Italy in summer 1996, retrieved from ERS-2 ATSR measurements; land temperature cannot be retrieved with sufficient accuracy, since the local nature and state of surface modifies its emissivity (Image credit: ESA)

10.2.2.2 TIR Observation of the Atmosphere

The emission coefficient of an air mass and, correspondingly, its electromagnetic thickness τ_o are adequately known at the wavelengths at which stable constituent gases interact, that is, their absorption lines occur. Measurements of the spectral radiance taken by the operational meteorological satellites in the 15 μm CO_2 absorption band (Fig. 10.6) provide information on temperature. The observed atmospheric target is the air itself, or the clouds. Temperature sounding, that is the retrieval of temperature profiles from multi-wavelength measurements is based on the relation (9.53) in which $T(z)$ is the unknown quantity. The retrieval exploits the change of the weighting functions with the wavelength, similar to the one shown in Fig. 9.6, to create an *averaging kernel* [5, 6] which sweeps the atmosphere vertically. The temperature of the cloud top is estimated together with its height from the first term of (9.53) once the vertical distribution of the thermal source $e_T \mathcal{B}_\lambda$ is known (cf. Sect. 14.3.3.1). Cloud measurements at wavelengths at which the gaseous atmosphere is particularly transparent are obviously scarcely interfered by the latter.

Sounding of the atmospheric constituents is essentially based on the retrieval of the profile $e_T(z)$ of the emission coefficient, which is related to the density of the absorbing species. Estimating the abundance of the constituents,among which water

vapor is clearly of the utmost importance, requires the serviceable knowledge of the temperature profile. Information on the densities of water droplets and ice particles in low-density clouds can analogously be gained from this kind of measurements.

10.2.3 Passive Measurements at Microwaves

At microwaves, where the Rayleigh-Jeans approximation (8.39) holds, the thermodynamic temperature T of a body can be linearly related to the measured brightness temperature T_B, once the emissivity (8.41) is known. Clearly this is not possible in the thermal infrared, given the non-linear relation (8.37) between emitted power and body temperature.

The basic relation for interpreting the images taken by a microwave radiometer is Eq. (9.56), or, when scattering is negligible, (9.57). The observations at the lower microwave frequency (below X-band) are little affected by the atmosphere, because absorption by this latter is quite low, transmittance almost unitary and the interfering term negligible. Increasing the frequency at which the microwave thermal images are acquired makes the atmosphere less transparent and its interference more important. Finally, measurements at absorbed frequencies are mainly affected by atmospheric emission and respond essentially to the gases and to the clouds.

In summary, the satellite radiometric images taken at the lower microwave frequencies exhibit the emissivity and thermal features of the surface of the Earth, while those acquired at the higher microwave frequencies carry the imprinting by both the surface and the atmospheric characteristics, provided the atmosphere is not substantially opaque.

Microwave radiometric images acquired from relatively low altitudes by RPAP are clearly less or not at all affected by atmospheric interferences.

10.2.3.1 Microwave Observation of the Surface

A striking feature displayed by maps of the microwave brightness temperature of the Earth's surface is that the measured T_B can be much lower than the surface thermodynamic temperature T. Values $T_B \ll T$ can be interpreted on the basis of reciprocity, as discussed in Sect. 8.1. For a given T, the brightness temperature of the surface in the first term of (9.57) is proportional to the microwave emissivity. This latter is low when the surface is smooth, its permittivity is large and observation is carried out at horizontal polarization. These three features, which, as repeatedly discussed (for instance, in Sects. 8.1.3 and 8.1.5) concur to enhance the reflectivity, hence to decrease the emissivity, are typical characteristics of the water surfaces. Figures 10.20 and 10.21 show global images of the brightness temperature at two microwave frequencies [98].

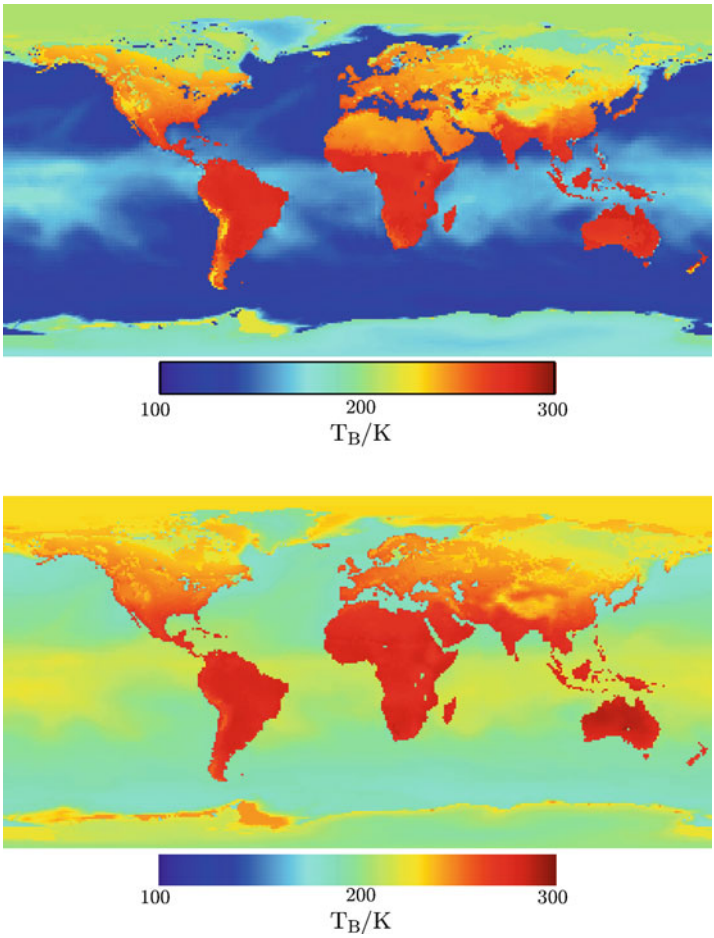

Fig. 10.20 Global distribution of boreal winter microwave brightness temperature T_B at frequency $f = 19$ GHz: *top*, horizontal polarization; *bottom*, vertical polarization (Image: Tor Vergata Earth Observation Laboratory)

Values of T_B much lower than the environmental temperatures are noted on the ocean at both polarizations. The sea images show values substantially higher at vertical polarization than at the horizontal one, consistently with the analysis of Sect. 8.1.3, while the difference is reduced over land, where the randomness of the surface environment (mainly due to the vegetation cover) tends to bring the emissivities closer. Section 2.2 points out that the permittivity of water, moist soil and vegetal matter is lower at 37 GHz than at 19 GHz. This feature concurs to explain the generally higher values of T_B at the higher frequency. Finally, it is important to observe the increasing interference by the atmosphere in the areas where the weather systems are more active, like, especially, in the inter-tropical

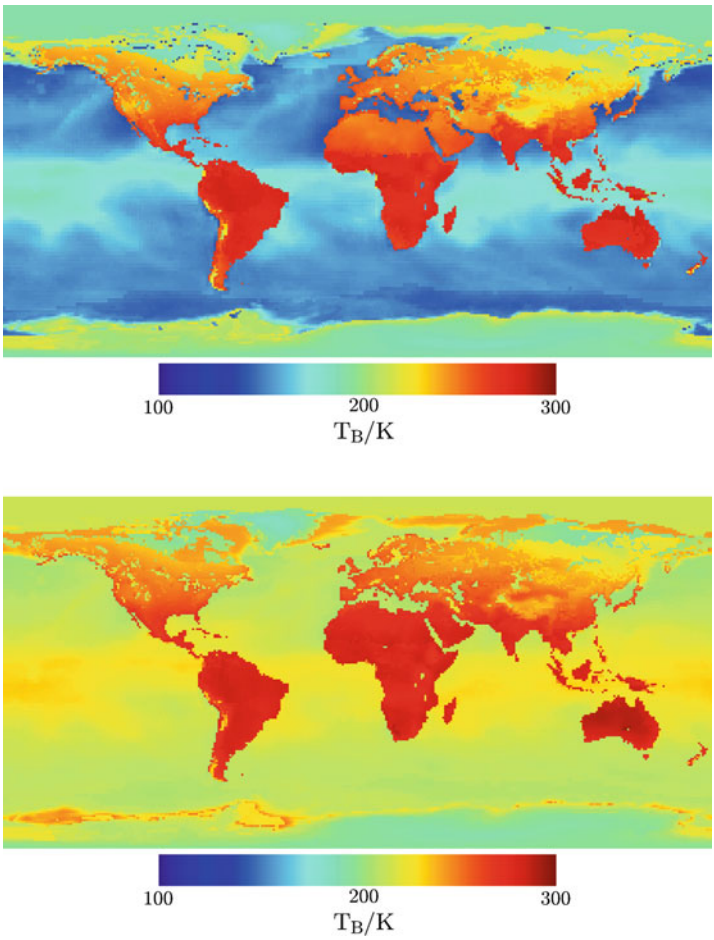

Fig. 10.21 Global distribution of boreal winter microwave brightness temperature T_B at frequency $f = 37$ GHz: *top*, horizontal polarization; *bottom*, vertical polarization (Image: Tor Vergata Earth Observation Laboratory)

convergence zone. The emission from the liquid water in clouds and precipitation adds to the term originated by the surface in (9.57) and has the overall effect of increasing the brightness temperature over the sea. As the frequency of observation is further increased, a decrease of T_B caused by the "cold" tops of the clouds at high altitude is expected, as it occurs in the thermal infrared (cf. Sect. 14.3).

By exploiting additional or a priori temperature information, the measure of T_B yields the microwave emissivity, from which information can be retrieved on the bio-geo-physical and morphological properties of land (forinstance, vegetation

cover and soil moisture content), or sea (e.g., wind speed and salinity). More details on this type of observations are given in Chap. 14.

10.2.3.2 Microwave Observation of the Atmosphere

The concepts outlined in Sect. 10.2.2.2 for the thermal infrared apply also to microwave passive sensing. Oxygen is the only gas interacting at these frequencies which is stable, i.e., it has a known relative density, expressed by the *mixing ratio*. Therefore, the atmospheric emission coefficients in correspondence of the 60 GHz oxygen resonant complex and of the 118 line are adequately known from the total pressure, so that information on temperature is retrievable. This forms the basis of the microwave *radiometric sounder* [1, 20, 69, 105, 122].

At other interaction frequencies, the brightness temperature carries information on the interacting constituents, once the temperature profile is reasonably known. In particular, atmospheric water vapor is retrieved from measurements in the 22.2 GHz [104] and 183.3 GHz [97] resonance bands[14] [83] mentioned in Sect. 2.2.1. On their side, bands at which the air is transparent (as an example, at $f \approx 37$ GHz), but where the absorbing properties of water particles mainly affect emission, allow gaining information on liquid drops or ice crystals in non-precipitating (and non-scattering) clouds [39]. Multi-channel passive instruments extending their operating wavelengths from conventional microwaves into the millimeter range offer potential for jointly profiling water vapor, mapping precipitation and measuring nonprecipitating cloud parameters [35].

10.2.3.3 Radiometric Measurements and Polarimetry

Microwave radiometers, similarly to radars, readily capture the electromagnetic power separately on orthogonal polarizations, e.g., horizontal and vertical. As shown by Figs. 10.20 and 10.21, emissivity has dramatically different values for different polarizations, according to the nature of the emitting surface. The differences between the brightness temperatures at different polarizations are exploited to obtain information on the properties of the terrestrial environment, especially on vegetation cover (cf. Sect. 14.1.4.2) [81, 82].

More in general, the Stokes vector (4.41) of the thermal radiation, which is measurable by polarimetric microwave radiometers [103] receiving coherently on two orthogonal polarizations, can carry significant content of information on the *anisotropy* of the observed target [19], such as the directional features of the sea surface associated with the waves [126].

[14] Observations in opaque channels near the 183 GHz water vapor rotational resonance are also effective for estimating precipitation over land [106].

10.2.4 Radar Measurements

Section 5.2.2.3.2 mentions the detection and ranging capability of this observing system which exploits scattering. Section 7.1.3.2 introduces the coefficient (7.22) expressing the local backscattering properties of the target. Such properties are related to the macroscopic physical and geometric features of the observed environment discussed in Sect. 7.2 and following paragraphs of Chap. 7. It is then apparent that measuring microwave scattering provides a valuable source of information on the terrestrial environment, be it the Earth's surface or atmosphere. It is worth adding that the abundance of observation techniques offered by the possibility of measuring not only power, but also amplitude and phase of the field makes the radar a quite attractive instrument in Earth observation. Its attractiveness is obviously enhanced by the capability of operating also in absence of solar radiation and with scarce interference by the atmosphere even in adverse weather conditions (Sect. 10.1.2.1).

A radar captures the power that is scattered, commonly in the backward direction, by the observed target. The receiving system translates power into *raw data* that are processed by dedicated tools to yield a variety of user products. The basic quantity commonly delivered by simple single-polarization monostatic (Sect. 7.1.3.1) systems after calibration is the backscattering coefficient [54] σ^0 defined by (7.22). Multi-polarization SARs provide σ^0 at different field polarizations, including hv cross-polarization (Sect. 7.1.2.1). The received backscattered power is further processed to yield scattering cross-sections or other normalized quantities. Polarimetric systems keep track of the phase of the field received at different polarizations, thereby providing elements of the scattering matrix (7.14) and of the Müller matrix in (7.15). The quantities of interest are generally organized and presented in *images*. Maps of the phase of the scattered field obtained by coherently combining pairs of images are also generated when required by applications, as detailed in Sect. 12.3.1.

10.2.4.1 Radar Images of the Earth's Surface

A SAR *intensity image* is the visual representation of the power received from each spatial resolution cell belonging to the observed geographic area, suitably normalized to correspond to the local backscattering coefficient. The *digital numbers* through which σ^0 is expressed are organized in a two-dimensional matrix and displayed as a grid of picture elements. The map of the backscattering coefficient shows the quantity (7.22),

$$\sigma^0 = \frac{\sigma(\theta, \varphi;\ \theta, \varphi + \pi)}{\Delta A}\ , \tag{10.1}$$

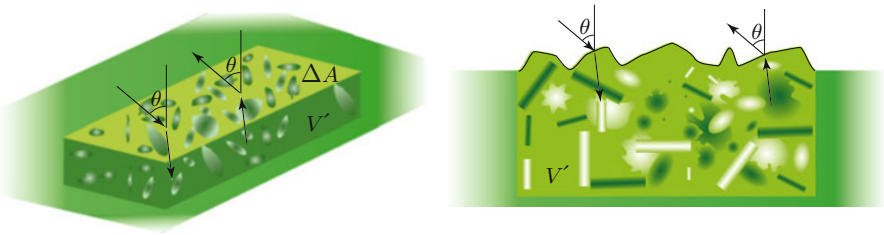

Fig. 10.22 The backscattering coefficient σ^0 is the backscattering cross-section σ of the resolution cell V' normalized to the area ΔA of the horizontal surface delimiting V', i.e., to the area of the rectangular pixel; the *upper arrows* denote incidence and backscattering directions, the *lower arrows* downward (refracted) and upward sub-surface waves

which is suitably *georeferenced*, that means assigned to the geographic coordinates of the center of the corresponding pixel. The area ΔA in (10.1) is the area of the reference surface delimiting the resolution cell for the radar observation. As is customary, the backward direction has been denoted by the same elevation angle as the one of the direction of incidence ($\theta^{(s)} = \theta^{(i)} \equiv \theta$) and by the opposite azimuth angle ($\varphi^{(s)} = \varphi^{(i)} + \pi \equiv \varphi + \pi$). Figure 10.22a is a schematic representation of the three-dimensional resolution cell, having pixel area ΔA, originating the backscattered power captured by the radar, while the corresponding transect is sketched in Fig. 10.22b.

Maps of the backscattering coefficient observed at two different spatial resolutions are shown in Figs. 10.23 and 10.24. While postponing more detailed interpretation to Chaps. 13 and 14, some useful hints can be based on the general visual appearance of these figures. The images show that the backscattering coefficient carries information on the type of land cover and on the orography:

- high values of σ^0 are peculiar of urbanized areas, where large smooth surfaces contribute high power scattered in the *backward* direction mainly through the double or triple coherent scattering (reflection) mechanisms considered in Sects. 6.6.1 and 6.6.2;
- high σ^0 is also peculiar of surfaces oriented almost perpendicularly to the direction of incidence, so that the received power is contributed by coherent specular reflection from large areas,
- instead, σ^0 is low for surfaces where the incidence angle is large, since backscattering diminishes at grazing direction and tends to vanish in the *shadowed* areas considered in Sect. 12.1.2.4.

The effects of the orientation of the surfaces make the radar image suggestive of the large-scale morphology of the area, hence of its orography: the dense drainage grid spread over almost the whole area is plainly delineated in Fig. 10.23.

Low backscattering is also peculiar of smooth horizontal surfaces, such as airport runways and small water bodies hidden from wind, such as the meandering Tiber river and the crater lakes, which mainly reflect in the specular direction, with very

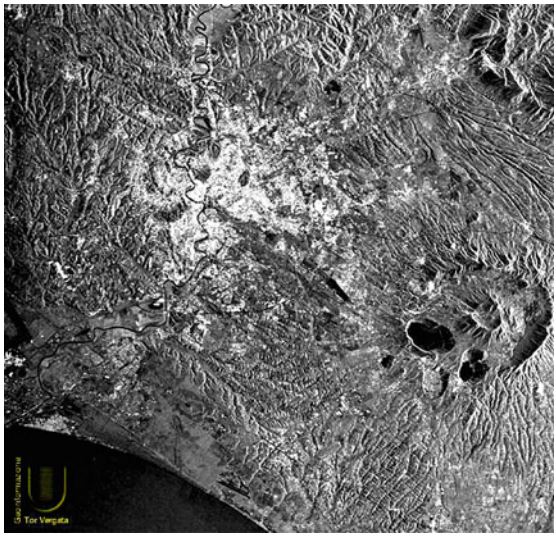

Fig. 10.23 Single-polarization (σ^0_{vv}) decametric-resolution ERS image of the Rome, Italy, extended area; *light grey* corresponds to high values of σ^0, dark to low (Credit: data, ESA; processing, Tor Vergata Earth Observation Laboratory)

Fig. 10.24 Single-polarization (σ^0_{hh}) metric-resolution COSMO-SkyMed image of part of Tor Vergata University campus, Rome, Italy; *light grey* corresponds to high values of σ^0, dark to low (Credit: data, © ASI, 2010; processing, C. Pratola, Tor Vergata Earth Observation Laboratory)

low return in the backward direction. The roughness of the surface of the open sea depends on the wind, hence σ^0 is highly variable in space and time: the low wind at the time the image in Fig. 10.23 was acquired makes the sea in the south west area to appear dark (cf. Fig. 14.52). Intermediate values of σ^0 characterize natural land surfaces, that is, bare or vegetated soil. Backscattering from this kind of environment results from wave interaction either with the vegetation canopy elements considered in Sect. 7.4.1, or with the rough surface of the terrain, as well as from combined vegetation-soil effects (Sect. 14.1.2.4). Plant type, development stage and water content, soil roughness and moisture affect the measured backscattered power,

which can vary considerably with space and time, according to the mentioned parameters.

10.2.4.1.1 Multi-temporal Imaging

Images acquired on different dates provide information on the temporal evolution of the backscattering features[15] of the observed areas. Color-composite images readily visualize the dynamic features of the types of surface which undergo changes in their bio-geo-physical and/or geometric parameters: whitish pixels correspond to little changed areas, for which the backscatter intensity remains nearly the same, whereas colored pixels denote corresponding increase or decrease of σ^0 from one date to the other. This kind of representation is particularly suggestive of the local modification of backscattering due to variations of the roughness of water surfaces (Fig. 10.25) and of the progressive change caused by development or decay of vegetation, or associated with rain events which change the soil moisture (Fig. 10.26). On their side, Fig. 10.27 demonstrates that very-high resolution images are able to sharply represent the considerable transformations of buildings in the course of their construction.

10.2.4.1.2 Multi-polarization Imaging

Multi-polarization or polarimetric SAR systems yield images acquired at different co-polarizations (e.g., for a linear basis, σ^0_{vv}, σ^0_{hh}) and at cross-polarization (σ^0_{hv}). Given the dependence of the scattering mechanisms and magnitude on the polarization both of the incident and of the scattered field discussed throughout Chap. 7, the image at each polarization carries pieces of information on the observed surface.[16] The color-composite images now visually display the different values of the polarization-dependent backscattering coefficients, which are particularly affected by the geometry of the target, as, for instance, it was observed in Sect. 7.4.1 with regards to the behavior of canopies. Figure 10.28 suggests the capabilities of the multi-polarization data in discriminating among the various environments encountered in a complex scenario in which developed zones coexist with widespread agriculture and extended natural areas, including pasture, forest and rocky slopes.

[15] On their side, multi-temporal optical images clearly provide the evolution with time of spectral reflectance and derived quantities [114].

[16] Although considerably reduced with respect to microwaves because of the effect of roughness, also optical images show the effect of polarization [61, 111] when reflection is involved.

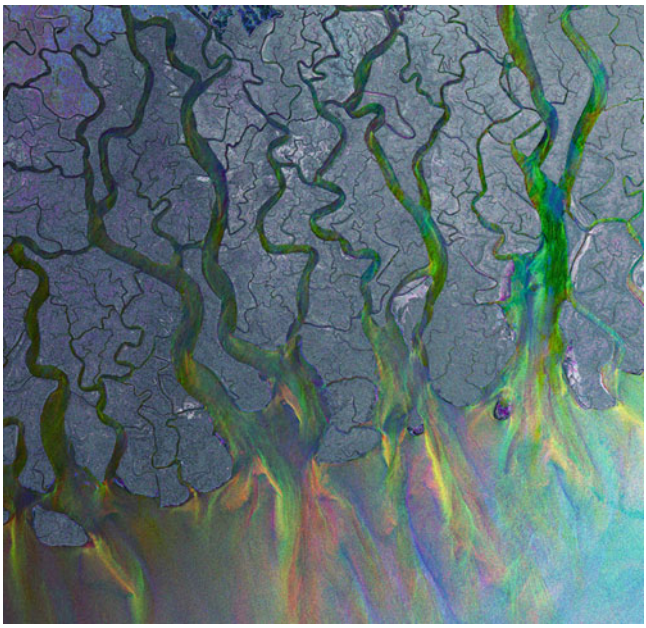

Fig. 10.25 Multi-temporal ENVISAT ASAR C-band σ^0_{vv} image of the Ganges Delta in the Bay of Bengal; RGB: 20 Jan., 24 Feb., 31 Mar. 2009 (Credit: data, ESA; processing, C. Solimini)

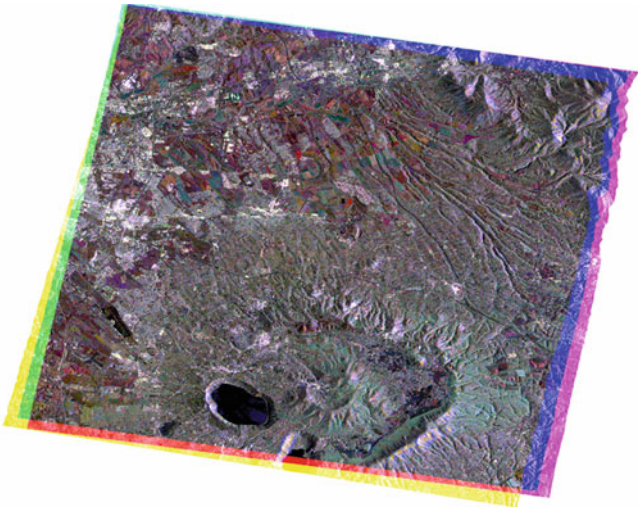

Fig. 10.26 Multi-temporal CSA/MDA RADARSAT-2 C-band σ^0_{hh} georeferenced image of the Tor Vergata Frascati test site; RGB: 13 Dec., 9 Oct., 25 Aug., 2008 (Credit: data, SOAR Project 1488; processing, courtesy C. Solimini)

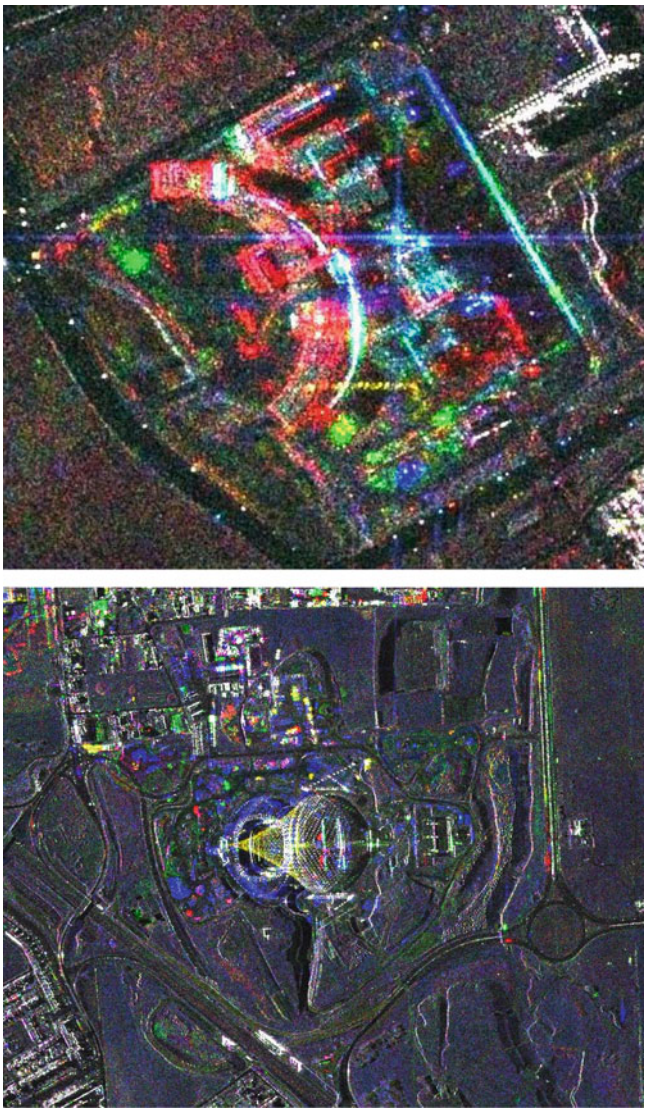

Fig. 10.27 Multi-temporal COSMO-SkyMed 1 m-resolution X-band σ^0_{hh} details of the Tor Vergata University campus including the Italian Space Agency complex (*top*) and the sport center (*bottom*) both during their construction; RGB: 2008, 2011, 2012 (*top*), 2010, 2011, 2012 (*bottom*). Note that the multi-temporal backscattering image of the unchanged buildings is *white* (Credit: data, © ASI 2008–2012; processing, courtesy C. Solimini)

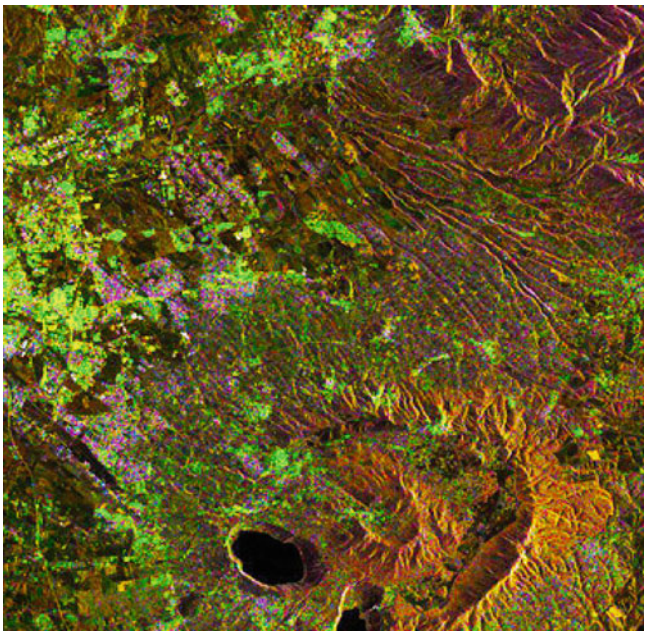

Fig. 10.28 Multi-polarization RADARSAT-2 C-band image of the Tor Vergata Frascati test site; October 8 2008, RGB: σ^0_{vv}, σ^0_{hh}, σ^0_{hv} (Credit: data, SOAR Project 1488; processing, Tor Vergata Earth Observation Laboratory)

10.2.4.2 Microwave Backscattering vs. Emission

The relation (8.42) between emissivity e and reflectance $\mathcal{R}$ sets a basic link between passive (radiometric) and active (radar) microwave measurements. Coarsely speaking, terrestrial environments which reflect and/or scatter strongly have low emission. However, careful attention must be paid to the fact that the emissivity, which is actually measured by a radiometer, relates to a quantity that *is not measurable* by a monostatic radar. In fact, according to (8.27), (8.26) and (8.25), the reflectance represents the fraction of incident power that is *globally* (i.e., in all directions)[17] reflected and scattered by the target, whereas radars measure only the scattering in the single backward direction. Therefore, when comparing passive with active measurements, it should be taken into careful account that emissivity is not necessarily related to backscattering, which represents only a single angular sample of the reflecting properties of the target.

[17]The solid angle in (8.25) is limited to the upper hemisphere when the target is the surface of the Earth.

10.2.5 Lidar Measurements

The basic principle of operation of lidars is the same as that of radars. A lidar provides the range between the sensor and the target by measuring the round-trip time of the optical pulse[18] that is backscattered by the natural or man-made object being observed and, as in the radar-altimeter processing, relevant features are extracted from the echo waveform to gain information on the geometric and microphysical properties of the scattering volume [56, 63, 77]. Lidar multi-polarization [95] and multi-spectral [74] imaging is also feasible to observe the optical polarimetric or spectral signatures of surface and atmospheric targets and corresponding spatial variations. It is worth adding that the remote sensing potential of lidar systems is enhanced by the availability of broadband laser sources, which allows acquiring hyperspectral[19] reflectivity data [40].

10.3 Interpreting Observations of the Earth's Surface

Postponing a detailed discussion to Chap. 14, the remote observation of the terrestrial environment in different ranges of the electromagnetic spectrum must account for two fundamental effects:

- increasing the observation frequency from the lower microwave band onward, generally implies interaction with materials with decreasing permittivity, and, in particular, at optical wavelengths the crucial librational contribution of the liquid water (Sect. 2.1.2) is totally quenched;
- at the same time, shorter λ imply increase of the dimension-to-wavelength ratio, which substantially affects scattering from objects, which may *appear small* at microwaves and *large* in the visible; analogously, diminishing λ increases the effect of the surface roughness, so that the same surface may behave as *smooth* at microwaves and as *rough* in the visible.

Given the lower permittivity and rising roughness, reflectivity, which results from both coherent reflection and incoherent scattering, tends to decrease with increasing frequency. Therefore, coarsely speaking, more power crosses the air-to-material interface at shorter wavelengths. In turn, the amplitude of the wave penetrating below the surface decreases with depth because of extinction, and more attenuation is expected at higher frequencies. Indeed, given the concurrent effects of frequency in enhancing absorption (5.39) and scattering (9.17), the amplitude of the penetrating wave decays more rapidly as frequency increases.

[18] Continuous-wave radar systems exploit the phase difference between returned and transmitted coherent waves.

[19] Hyperspectral imaging has been defined as the acquisition of images in many contiguous spectral bands such that for each picture element a "complete" reflectance spectrum is derived [37].

10.3.1 Interpreting Microwave Data

The results of Sects. 2.2.3 and 2.2.4 point out that the microwave complex permittivity of land materials is essentially controlled by their water content. Therefore, both reflection and scattering of compact materials are expected to increase with their moisture, concurrently with attenuation. For a given type of material and surface roughness, backscattering follows a correspondingly increasing trend with increasing moisture: scattering of moist materials essentially originates from the shallow layers, whichever the deeper inhomogeneities, because little power crosses the interface and attenuation with depth is high. It can be concluded that microwave scattering carries information on the near-surface moisture content of compact *humid* materials.

Given the increasing trend of reflectance, microwave emissivity correspondingly decreases with increasing moisture content, following the result of Sect. 8.2.2.1.

Dry terrestrial materials have relatively low reflectivity and extinction, so that a high fraction of incident power crosses the interface and undergoes moderate attenuation in the bulk. The inner field forming the scattering source (7.4) keeps appreciable values below the surface and a significant amount of the power scattered from the sub-surface inhomogeneities is able to emerge. This mechanism gives rise to comparable values of the components of the scattering originating from the surface and from the volume considered in Sect. 7.4.7. Therefore, microwave scattering contains information also on sub-surface layers of *dry* materials [26, 68]. The depth that can be probed is clearly determined by the wave extinction. Since waves at higher frequencies undergo higher attenuation, the layers contributing scattering become shallower as λ decreases: low microwave frequencies (for instance, L- or, especially, P-band) are better suited for sub-surface sensing of *dry* materials.[20] Loose materials tend to behave like the dry ones, even if the moisture in the sparse matter is high. Vegetation canopies are a particularly relevant environment of this kind [44].

On its turn, the microwave emissivity increases with decreasing moisture content and, correspondingly, more thermal power originates from deeper layers of relatively dry and/or loose materials [78, 101]. The combined effect of the imaginary part of average permittivity and of the attenuation results in flatter weighting functions, consistently with the definition (8.23).

The variety of object dimensions and of roughness scales, often comparable with wavelength, makes the information carried by microwave observations to depend considerably on frequency. Special care is then required in data interpretation. With reference to two frequencies representative of the lower and upper ends of the microwave range at which observations are frequently carried out, in a nutshell:

[20] Sensing of moist materials is in practice limited to depths of the order of a fraction of wavelength.

- at L-band ($\lambda_0 \approx 0.2\,\text{m}$)
  - some natural targets such as sub-surface moisture inhomogeneities, cobbles, leaves, woody plant elements as short branches, may be small compared to the wavelength, so that low scattering may be observed,
  - but low backscattering from an area observed at oblique incidence may also correspond to a *relatively* smooth surface reflecting in the specular direction rather than scattering backward;
- instead at X-band ($\lambda_0 \approx 0.03\,\text{m}$)
  - the *same* targets may be large with respect to λ or have comparable dimensions, so relatively high scattering is observed,
  - moreover, the surfaces appearing smooth at L-band may now behave as rough and exhibit enhanced backscattering.

A word of caution is clearly needed, in that the interpretation of backscattering and emission data based on the above tangled coarse behavior is expected to be further compounded by the dependence of permittivity on frequency.

10.3.2 Interpreting Optical Data

At optical wavelengths, that means of the order of micrometers, the permittivity of many natural (vegetation elements, granular matter such as terrain, etc.) and man-made (plaster, concrete, etc.) materials containing water is considerably lower than at microwaves, so that the air-matter discontinuity is moderate from the electromagnetic point of view. In addition, most surfaces present random irregularities that are quite large with respect to the wavelength. Given the resulting low reflectivity, a relatively large fraction of the solar radiation penetrates into the bulk matter. Here the embedded inhomogeneities behave as strong scatterers, since their dimensions are usually large with respect to λ, or comparable. Multiple scattering (Sect. 9.1) occurs that, also according to the micro-structure of the material, re-directs the refracted radiation into a broad range of directions inside the material, following the radiative transfer mechanisms discussed in Sect. 9.2. A fraction of the radiation multiply scattered in the bulk randomly inhomogeneous medium emerges from its surface and goes away in the various directions of the upper hemisphere. Since the absorption caused by the resonances of the material is wavelength-selective (Sect. 2.1.1), the radiation emerging from the surface through the *volume scattering* mechanism has become *colored*, i.e., the wide-band solar spectrum has been deprived of the power in the bands corresponding to the resonant absorption, as already hinted at in Sect. 7.4.7. The radiation emerging from the bulk adds to that, relatively weak and broadly distributed in angle, which is scattered by the rough

surface layer, as well as to the one coherently reflected around the specular direction, which is strong when the surface is optically smooth.[21]

The radiation in the specular direction generally keeps unaltered an important fraction of the spectrum of the incident solar radiation, since the coherent reflection, mainly affected by $\tilde{\epsilon}_r$ (Sect. 6.3.2), is weakly dependent on wavelength in the optical range, according to the model considered in Sect. 2.1.1.2. This feature is clearly suggested by Fig. 7.7. On its side, the scattering in non-specular directions is mainly contributed by the combined extinction-scattering process occurring in the bulk matter. Consequently, the spectrum of the radiation reaching the optical sensor in a direction non-specular with respect to the Sun contains the imprinting of the resonance patterns of the material, i.e., carries information on its chemical nature and microstructure. Note that, given the usually high extinction coefficient of land materials or of turbid water, the probed volume is limited to layers close to the surface. However, in case of "clear" water, the scattered radiation carries biological and chemical information also from deeper layers, giving rise to the *Ocean Color* [13, 79] data, which may contain information also on the ecosystem at the bottom of relatively shallow ocean waters [124].

Some kinds of surfaces (relatively calm water, ice, polished metals, glass), present areas which are flat over distances of many optical wavelengths. Strong reflection can then occur giving rise to the *sun glint*, which may alter the information content of the measurements were these be taken in the direction specular to the Sun. This effect advises against the acquisition of optical[22] data from such a direction.

10.3.3 Interpreting Thermal Emission Data

Measurements of the thermal emission possess peculiar characteristics, since, differently from the radar and optical observations, the physical temperature T of the observed target directly affects the data. The thermal nature of the source may complicate the data interpretation in terms of bio-geo-physical properties, clearly excepted that in regards of the temperature T itself. On the other side, observations in the thermal infrared in principle contain a wealth of information on the target. In fact, many absorption bands, corresponding to specific molecular bonds, fall in this wavelength range. The corresponding complex permittivity, which affects both the emissivity and, through the imaginary part, the intensity of the thermal source, changes sharply with wavelength and so does the emitted power. Therefore, multi-spectral data taken in the TIR contain information on the dielectric spectral patterns, and are thus expected to have considerable potential in the identification of

[21] Apart from the effect of the roughness, the optical incoherent scattering from the surface layer is generally weaker than at microwaves, because, as said, of the lower value of the permittivity.

[22] Apart from particular applications, the specular direction is generally avoided [62] at all wavelengths, including microwaves.

terrestrial materials. It is worth adding that the refractive index of many materials reaches values $n \approx 1$ in neighborhoods of the resonances. The corresponding high emissivity, which is observed especially in the 10–14 μm wavelength range, leads to large emitted power. This feature, discussed in Sect. 9.3.2, may be noxious yet, given the relatively low spectral contrast that characterizes the measurements throughout the TIR range (cf. Sect. 14.1.3).

A final remark is that the source of the measured radiation is distributed internally to the observed target, so the atmosphere is crossed only once by the information-carrying wave.

A Panorama on Spectral Bands and Techniques for EO

After the long prologue intended to fill analytical and conceptual gaps, let us now get to the heart of remote sensing.

The first issue regards the selection of the wavelength at which to carry out the observations. Two main aspects have to be considered. One regards the transparency of the atmosphere, the other the extent and quality of interaction. We are informed on the variation of the air transmissivity with wavelength from the ultraviolet to microwaves, so we are able to understand one of the reasons for choosing the bands at which EO systems operate. The discussion regards not only gaseous absorption but also the extinction caused by aerosols and hydrometeors. Given the broad range of dimensions of the particles in the atmosphere, the interference originated by scattering can be expected to affect the whole spectrum to a greater or lesser extent, in any case subject to climatic or meteorological conditions. The kind of information that we seek on the target is the other main driver in the choice both of the spectral band and of the technique of observation. From an alternative point of view, we must be inspired by wavelength and type of instrument when interpreting a remote image or measurement we procured as users. The physical mechanisms previously overviewed should have instructed us on the nature of the information that each frequency band is able to gain, therefore we should have got some preliminary idea of the specifications and of the performance of the systems.

Our awareness of Earth observation is expected to be enhanced by detailing the basic measurements that passive and active systems take at the various frequencies. Starting from passive sensing, we overview the nature of the measurements at optical wavelengths and in the thermal infrared, then we discuss relevant features of the observations at microwave frequencies. The review concerns both the surface and the atmosphere. Radars are considered next from multiple points of view, including the influence of spatial resolution and polarization on the details revealed by the images of certain classes of targets.

The previous considerations are preparatory to a more systematic discussion that aims at providing the prospective users with a first key to interpret the appearance of the EO products. Some suggestions regarding the retrieval of target parameters are correspondingly expected to ensue. The basic issues involving the coupled effects of

permittivity and wavelength are recalled when presenting the many factors affecting the observation both of the surface and of the atmosphere. Numerical values and selected features presented in practice by data at microwaves are overviewed, together with examples of optical and TIR measurements. The physical rationale underlying the encountered figures is regularly recalled to provide the users with a consistent guide to better understanding the information content of the products they may have at hand.

References

1. Ali ADS, Rosenkranz PW, Staelin DH (1980) Atmospheric sounding near 118 GHz. J Appl Meteorol 19(10):1234–1238. doi:10.1175/1520-0450(1980)019⟨1234:ASNG⟩2.0.CO;2
2. Alkhatib AAA (2014) A review on forest fire detection techniques. Int J Distrib Sens Netw. Article ID 597368. doi:10.1155/2014/597368
3. Alpers W, Melsheimer C (2004) Rainfall. In: Jackson CR, Apel JR (eds) Synthetic aperture radar marine user's manual, chapter 17. NOAA/NESDIS Office of Research and Applications. ISBN:9780160732140. http://www.sarusersmanual.com/ (visited on 10 Oct 2014)
4. Anding D, Kauth R (1970) Estimation of sea surface temperature from space. Remote Sens Environ 1(4):217–220. doi:10.1016/S0034-4257(70)80002-5
5. Backus GE, Gilbert F (1968) The resolving power of gross Earth data. Geophys J R Astron Soc 16(2):169–205. doi:10.1111/j.1365-246X.1968.tb00216.x
6. Backus GE, Gilbert F (1970) Uniqueness in the inversion of inaccurate gross Earth data. Philos Trans R Soc Lond A 266:123–192. doi:10.1098/rsta.1970.0005
7. Baron PA, Willeke K (2001) Aerosol measurement: principles, techniques, and applications. Wiley. ISBN:9780471356363
8. Beard KV (1976) Terminal velocity and shape of cloud and precipitation drops aloft. J Atmos Sci 33(5):851–864. doi:10.1175/1520-0469(1976)033(0851:TVASOC)2.0.CO;2
9. Berk A, Anderson GP, Acharya PK, Bernstein LS, Muratov L, Lee J, Fox MJ, Adler-Golden SM, Chetwynd JH, Hoke ML, Lockwood RB, Cooley TW, Gardner JA (2005) MODTRAN5: a reformulated atmospheric band model with auxiliary species and practical multiple scattering options. Proc SPIE 5655:88–95. doi:10.1117/12.578758
10. Berkner LV (1962) Geoscience and geoengineering. Geosci Electron Spec Issue Proc IRE 50(11):2180–2182. doi:10.1109/JRPROC.1962.288329
11. Bertero M, De Mol C, Pike ER (1985) Linear inverse problems with discrete data. I: general formulation and singular system analysis. Inverse Probl 1(4):301–330. doi:10.1088/0266-5611/1/4/004
12. Bertero M, De Mol C, Pike ER (1988) Linear inverse problems with discrete data. II: stability and regularisation. Inverse Probl 4(3):573–594. doi:10.1088/0266-5611/4/3/004
13. Blondeau-Patissier D, Gower JFR, Dekker AG, Phinn SR, Brando VE (2014) A review of ocean color remote sensing methods and statistical techniques for the detection, mapping and analysis of phytoplankton blooms in coastal and open oceans. Prog Oceanogr 123:123–144. doi:10.1016/j.pocean.2013.12.008
14. Bodhaine BA, Wood NB, Dutton EG, Slusser JR (1999) On Rayleigh optical depth calculations. J Atmos Ocean Technol 16(11):1854–1861. doi:10.1175/1520-0426(1999)016⟨1854:ORODC⟩2.0.CO;2
15. Bohren CF, Huffman DR (2008) Absorption and scattering of light by small particles. Wiley. ISBN:9783527618163
16. Boucher O, Randall D, Artaxo P, Bretherton C, Feingold G, Forster P, Kerminen V-M, Kondo Y, Liao H, Lohmann U, Rasch P, Satheesh SK, Sherwood S, Stevens B, Zhan XY (2013)

Clouds and aerosols. In: Stocker TF, Qin D, Plattner G-K, Tignor M, Allen SK, Boschung J, Nauels A, Xia Y, Bex V, Midgley PM (2013) Climate change 2013: the physical science basis. Contribution of working group I to the fifth assessment report of the intergovernmental panel on climate change. Cambridge University Press. ISBN:9781107661820
17. Chahine MT (1968) Determination of the temperature profile in the atmosphere from its outgoing radiance. J Opt Soc Am 58(12):1634–1637. doi:10.1364/JOSA.58.001634
18. Chen X-X, Vierling L (2006) Spectral mixture analyses of hyperspectral data acquired using a tethered balloon. Remote Sens Environ 103(3):338–350. doi:10.1016/j.rse.2005.05.023
19. Coppo P, Johnson JT, Guerriero L, Kong JA, Macelloni G, Marzano F, Pampaloni P, Pierdicca N, Solimini D, Susini C, Tofani G, Zhang Y (1996) Polarimetry for passive remote sensing. ESA contract 1146/95/NL/NB final report. European Space Agency
20. Croom DL (1971) The 2.53 mm molecular rotation line of atmospheric O_2. Planet Space Sci 19(7):777–789. doi:10.1016/0032-0633(71)90035-3
21. Deepak A (ed) (2012) Inversion methods in atmospheric remote sounding. Elsevier. ISBN:9780323144148
22. Denny SP, Suen JY, Lubin PM (2013) Fundamental limits of detection in the far infrared. New Astron 25:114–129. doi:10.1016/j.newast.2013.04.008
23. Dessler AE, Davis SM (2010) Trends in tropospheric humidity from reanalysis systems. J Geophys Res 115(D19127). doi:10.1029/2010JD014192
24. Egan WG (1985) Photometry and polarization in remote sensing. Elsevier. ISBN:9780444008923
25. Ehret G, Kiemle C, Wirth M, Amediek A, Fix A, Houweling S (2008) Spaceborne remote sensing of CO_2, CH_4, and N_2O by integrated path differential absorption lidar: a sensitivity analysis. Appl Phys B B90:593–608. doi:10.1007/s00340-007-2892-3
26. Elachi C, Roth LE, Schaber GG (1984) Spaceborne radar subsurface imaging in hyperarid regions. IEEE Trans Geosci Remote Sens GE-22(4):383–388. doi:10.1109/TGRS.1984.350641
27. Elsasser WM (1938) Far infrared absorption of atmospheric water vapor. Astrophys J 87(5):497–507. doi:0.1086/143940
28. Erlick C, Frederick JE (1998) Effects of aerosols on the wavelength dependence of atmospheric transmission in the ultraviolet and visible: 2. Continental and urban aerosols in clear skies. J Geophys Res 103(D18):23275–23285. doi:10.1029/98JD02119
29. Erlick C, Frederick JE, Saxena VK, Wenny BN (1998) Atmospheric transmission in the ultraviolet and visible: aerosols in cloudy atmospheres. J Geophys Res 103(D24):31541–31556. doi:10.1029/1998JD200053
30. ESA's Gravity Mission GOCE. ESA. http://www.esa.int/OurActivities/Observing_the_Earth/TheLiving_Planet_Programme/EarthExplorers/GOCE (visited on 09 Dec 2014)
31. Fernandez Diaz J-C, Carter WE, Shrestha RL, Glennie CL (2013) Lidar remote sensing. In: Pelton JN, Madry S, Camacho-Lara S (eds) Handbook of satellite applications. Springer, New York, pp 757–808. ISBN:978-1-4419-7670-3. doi:10.1007/978-1-4419-7671-0_44
32. Ferraro JR, Nakamoto K, Brown CW (2003) Introductory Raman spectroscopy. Elsevier. ISBN:9780080509129
33. Ferrazzoli P, Schiavon G (1987) Rain-induced modification of SAR performance. Adv Space Res 7(11):269–272. doi:http://dx.doi.org/10.1016/0273-1177(87)90323-1
34. Frankenberg C, O'Dell C, Guanter L, McDuffie J (2012) Chlorophyll fluorescence remote sensing from space in scattering atmospheres: implications for its retrieval and interferences with atmospheric CO_2 retrievals. Atmos Meas Tech Discuss 5:2487–2527. doi:10.5194/amtd-5-2487-2012
35. Gasiewski AJ (1992) Numerical sensitivity analysis of passive EHF and SMMW channels to tropospheric water vapor, clouds, and precipitation. IEEE Trans Geosci Remote Sens 30(5):859–870. doi:10.1109/36.175320
36. Gille JC, House FB (1971) On the inversion of limb radiance measurements I: temperature and thickness. J Atmos Sci 28(8):1427–1442. doi:10.1175/1520-0469(1971)028⟨1427:OTIOLR⟩2.0.CO;2

37. Goetz AFH, Vane G, Solomon JE, Rock BN (1985) Imaging spectrometry for Earth remote sensing. Science 228(4704):1147–1153. doi:10.1126/science.228.4704.1147
38. Grant WB, Kagann RH, McClenny WA (1992) Optical remote measurement of toxic gases. J Air Waste Manag Assoc 42(1):18–30. doi:10.1080/10473289.1992.1046696
39. Greenwald TJ, Stephen GL, Vonder Haar TH, Jackson DL (1993) A physical retrieval of cloud liquid water over the global oceans using special sensor microwave/imager (SSM/I) observation. J Geophys Res 98(D10):18471–18488. doi:10.1029/93JD00339
40. Hakala T, Suomalainen J, Kaasalainen S, Chen Y (2012) Full waveform hyperspectral LiDAR for terrestrial laser scanning. Opt Expr 20(7):7119–7127. doi:10.1364/OE.20.007119
41. Houghton JT, Taylor FW, Rodgers CD (1984) Remote sounding of atmospheres. Cambridge University Press. ISBN:9780521310659
42. Hulley G, Hook S (2011) HyspIRI level-2 thermal infrared (TIR) land surface temperature and emissivity algorithm theoretical basis document. JPL Publication 11-5. NASA JPL, May 2011
43. IEEE Standard Letter Designations for Radar-Frequency Bands (1984). IEEE Std 521-1984. doi:10.1109/IEEESTD.1984.81588
44. Imhoff M, Story M, Vermillion C, Khan F, Polcyn F (1986) Forest canopy characterization and vegetation penetration assessment with space-borne radar. IEEE Trans Geosci Remote Sens GE-24(4):535–542. doi:10.1109/TGRS.1986.289668
45. Jameson AR, Li FK, Durden SL, Haddad ZS, Holt B, Fogarty T, Im E, Moore RK (1997) SIR-C/X-SAR observations of rain storms. Remote Sens Environ 59(2):267–279. doi:10.1016/S0034-4257(96)00159-9
46. Jensen JR (2007) Remote sensing of the environment: an Earth resource perspective. Pearson Prentice Hall. ISBN:9780131889507
47. Kaplan LD (1959) Inference of atmospheric structures from satellite remote radiation measurements. J Opt Soc Am 49(10):1004–1006. doi:10.1364/JOSA.49.001004
48. Kaufman I (1959) The band between microwave and infrared regions. Proc IRE 47(3):381–396. doi:10.1109/JRPROC.1959.287174
49. Kaufman YJ, NASA GFSC (1989) The atmospheric effect on remote sensing and its correction. In: Asrar G (ed) Theory and applications of optical remote sensing. Wiley. ISBN:9780471628958
50. King MD, Menzel WP, Kaufman YJ, Tanré D, Gao B-C, Platnick S, Ackerman SA, Remer LA, Pincus R, Hubanks PA (2003) Cloud and aerosol properties, precipitable water, and profiles of temperature and water vapor from MODIS. IEEE Trans Geosci Remote Sens 41(2):442–458. doi:10.1109/TGRS.2002.808226
51. Kneizys FX, Shettle EP, Abreu LW, Chetwynd JH, Anderson GP, Gallery WO, Selby JEA, Clough SA (1988) Users guide to LOWTRAN7. Technical report AFGL-TR-88-0177. Air Force Geophysics Laboratory, Hanscom AFB
52. Kobayashi T (2007) Significant differences in the cloud droplet effective radius between nonprecipitating and precipitating clouds. Geophys Res Lett 34:L15811. doi:10.1029/2007GL029606
53. Kramer HJ (2002) Observation of the Earth and its environment: survey of missions and sensors. Springer. ISBN:9783540423881
54. Laur H, Bally P, Meadows P, Sanchez J, Schaettler B, Lopinto E, Esteban D (2004) Derivation of the backscattering coefficient σ^0 in ESA ERS SAR PRI products. Document no. ES-TN-RS-PM-HL09. European Space Agency
55. Lawrence JS (2004) Infrared and submillimeter atmospheric characteristics of high Antarctic Plateau sites. Publ Astron Soc Pac 116(819):482–492. doi:10.1086/420757
56. Lee S, Ni-Meister W, Yang W, Chen Q (2011) Physically based vertical vegetation structure retrieval from ICESat data: validation using LVIS in White Mountain national forest, New Hampshire, USA. Remote Sens Environ 115(11):2776–2785. doi:10.1016/j.rse.2010.08.026
57. Liang S, Li X, Wang J (eds) (2012) Advanced remote sensing: terrestrial information extraction and applications. Elsevier. ISBN:9780123859556

58. Liebe HJ (1983) An atmospheric millimeter wave propagation model. Technical report NTIA Report 83–137. U.S. Department of Commerce
59. Liebe HJ, Hufford GA, Cotton MG (1993) Propagation modeling of moist air and suspended water/ice particles at frequencies below 1000 GHz. In: NATO/AGARD wave propagation panel, 52nd meeting atmospheric propagation effects through natural and man-made obscurants for visible to MM-wave radiation, Palma de Mallorca, 17–20 May 1993. AGARD-CP-542. ISBN:9283507274
60. MacDonald JS, Ustin SL, Schaepman ME (2009) The contributions of Dr. Alexander F.H. Goetz to imaging spectrometry. Remote Sens Environ 113(Supplement 1. Imaging Spectroscopy Special Issue):S2–S4. doi:http://dx.doi.org/10.1016/j.rse.2008.10.017
61. Maignan F, Bréon F-M, Fédèle E, Bouvier M (2009) Polarized reflectances of natural surfaces: spaceborne measurements and analytical modeling. Remote Sens Environ 113(12):2642–2650. doi:10.1016/j.rse.2009.07.022
62. Mailhe LM, Schiff C, Stadler JH (2004) CALIPSO's mission design: sun-glint avoidance strategies. NASA Technical Documents AAS 04-114. https://archive.org/details/nasa\techdoc\20040081137 (visited on 18 Feb 2014)
63. Mallet C, Bretar F (2009) Full-waveform topographic lidar: state-of-the-art. ISPRS J Photogramm Remote Sens 64(1):1–16. doi:http://dx.doi.org/10.1016/j.isprsjprs.2008.09.007
64. Margenau H, Watson WW (1936) Pressure effects on spectral lines. Rev Modern Phys 8(1):22–53. doi:10.1103/RevModPhys.8.22
65. Marzano FS, Mori S, Weinman JA (2010) Evidence of rainfall signatures on X-band synthetic aperture radar imagery over land. IEEE Trans Geosci Remote Sens 48(2):950–964. doi:10.1109/TGRS.2009.2034843
66. Marzano FS, Mori S, Weinman JA, Montopoli M (2012) Modeling polarimetric response of spaceborne synthetic aperture radar due to precipitating clouds from X- to Ka-band. IEEE Trans Geosci Remote Sens 50(3):687–703. doi:10.1109/TGRS.2011.2163942
67. Marzano FS, Visconti G (eds) (2003) Remote sensing of atmosphere and ocean from space: models, instruments and techniques. Springer. ISBN:9781402009433
68. McCauley JF, Schaber GG, Breed CS, Grolier MJ, Haynes CV, Issawi B, Elachi C, Blom R (1982) Subsurface valleys and geoarcheology of the Eastern Sahara revealed by shuttle radar. Science 218(4576):1004–1020. doi:10.1126/science.218.4576.1004
69. Meeks ML, Lilley AE (1963) The microwave spectrum of oxygen in the Earth's atmosphere. J Geophys Res 68(6):1683–1703. doi:10.1029/JZ068i006p01683
70. Milton EJ, Schaepman ME, Anderson K, Kneubühler M, Fox N (2009) Progress in field spectroscopy. Remote Sens Environ 113(suppl 1):S92–S109. doi:10.1016/j.rse.2007.08.001
71. Hartmann J-M, Flaud J-M (eds) (2005) Molecular spectroscopy and planetary atmospheres. C R Phys 6(8). doi:http://dx.doi.org/10.1016/S1631-0705(05)00155-6
72. Moore RK, Mogili A, Fang Y, Beh B, Ahamad A (1996) Rain measurement with SIR-C/X-SAR. In: IGARSS'96, international geoscience and remote sensing symposium, vol 2, pp 1266–1269. doi:10.1109/IGARSS.1996.516633
73. Moore RK, Mogili A, Fang Y, Beh B, Ahamad A (1997) Rain measurement with SIR-C/X-SAR. Remote Sens Environ 59(2):280–293. doi:10.1016/S0034-4257(96)00147-2
74. Morsdorf F, Nichol C, Malthus T, Woodhouse IH (2009) Assessing forest structural and physiological information content of multi-spectral LiDAR waveforms by radiative transfer modelling. Remote Sens Environ 113(10):2152–2163. doi:10.1016/j.rse.2009.05.019
75. Muttiah RS (2002) From laboratory spectroscopy to remotely sensed spectra of terrestrial ecosystems. Springer. ISBN:9781402007538
76. Nelson R, Krabill W, Tonelli J (1988) Estimating forest biomass and volume using airborne laser data. Remote Sens Environ 24(2):247–267. doi:10.1016/0034-4257(88)90028-4
77. Nilsson M (1996) Estimation of tree heights and stand volume using an airborne lidar system. Remote Sens Environ 56(1):1–7. doi:10.1016/0034-4257(95)00224-3
78. Njoku EG, Kong J-A (1977) Theory for passive microwave remote sensing of near-surface soil moisture. J Geophys Res 82(20):3108–3118. doi:10.1029/JB082i020p03108

79. OceanColor WEB, NASA GSFC (2013). http://http://oceancolor.gsfc.nasa.gov/ (visited on 18 Feb 2014)
80. Palombi L, Alderighi D, Cecchi G, Raimondi V, Toci G, Lognoli D (2013) A fluorescence LIDAR sensor for hyper-spectral time-resolved remote sensing and mapping. Opt Expr 21(12):14736–14746. doi:10.1364/ OE.21.014736
81. Paloscia S, Pampaloni P (1985) Experimental relationships between microwave emission and vegetation features. Int J Remote Sens 6(2):315–323. doi:10.1080/01431168508948446
82. Paloscia S, Pampaloni P (1988) Microwave polarization index for monitoring vegetation growth. IEEE Trans Geosci Remote Sens 26(5):617–621. doi:10.1109/36.7687
83. Payne VH, Delamere JS, Cady-Pereira KE, Gamache RR, Moncet J-L, Mlawer EJ, Clough SA (2008) Air-broadened half-widths of the 22- and 183-GHz water-vapor lines. IEEE Trans Geosci Remote Sens 46(11):3601–3617. doi:10.1109/TGRS.2008.2002435
84. Penide G, Kumar VV, Protat A, May PT (2013) Statistics of drop size distribution parameters and rain rates for stratiform and convective precipitation during the North Australian wet season. Mon Weather Rev 141:3222–3237. doi:10.1175/MWR-D-12-00262.1
85. Penndorf R (1957) Tables of the refractive index for standard air and the Rayleigh scattering coefficient for the spectral region between 0.2 and 20.0 μ and their application to atmospheric optics. J Opt Soc Am 47(2):176–182. doi:10.1364/JOSA.47.000176
86. Petrin RR, Foy BR, MacKerrow EP, McVey BD, Nemzek RJ, Quick CR, Tiee JJ (2000) Using active TIR imaging for ground cover identification and mapping. In: Proceedings of the geoscience and remote sensing international symposium 2000, vol 3. ISBN:0780363590. doi:10.1109/IGARSS.2000.857994
87. Pruppacher HR, Pitter RL (1971) A semi-empirical determination of the shape of cloud and rain drops. J Atmos Sci 28(1):86–94. doi:10.1175/1520-0469(1971)028⟨0086:ASEDOT⟨2.0.CO;2
88. Quagliano JR, Stoutland PO, Petrin RR, Sander RK, Romero RJ, Whitehead MC, Quick CR, Tiee JJ, Jolin LJ (1997) Quantitative chemical identification of four gases in remote infrared (9–11 μm) differential absorption lidar experiments. Appl Opt 36(9):1915–1927. doi:10.1364/AO.36.001915
89. Le Quéré C, Raupach MR, Canadell JG, Marland G et al (2009) Trends in the sources and sinks of carbon dioxide. Nat Geosci–Adv Online Publ (2009). doi:10.1038/NGEO689. www.nature.com/naturegeoscience (visited on 29 Jan 2014)
90. Rees G (1999) The remote sensing data book. Cambridge University Press. ISBN:9780521480406
91. Rees WG (2012) Physical principles of remote sensing. Cambridge University Press. ISBN:9780521181167
92. Ricaud P, Gabard B, Derrien S, Chaboureau J-P, Rose T, Mombauer A, Czekala H (2010) HAMSTRAD-Tropo, A 183-GHz radiometer dedicated to sound tropospheric water vapor over Concordia Station, Antarctica. IEEE Trans Geosci Remote Sens 48(3):1365–1380. doi:10.1109/TGRS.2009.2029345
93. Rothman LS, Gordon IE, Babikov Y, Barbe A, Chris Benner D, Bernath PF, Birk M, Bizzocchi L, Boudon V, Brown LR, Campargue A, Chance K, Cohen EA, Coudert LH, Devi VM, Drouin BJ, Fayt A, Flaud J-M, Gamache RR, Harrison JJ, Hartmann J-M, Hill C, Hodges JT, Jacquemart D, Jolly A, Lamouroux J, Le Roy RJ, Li G, Long DA, Lyulin OM, Mackie CJ, Massie ST, Mikhailenko S, Müller HSP, Naumenko OV, Nikitin AV, Orphal J, Perevalov V, Perrin A, Polovtseva ER, Richard C, Smith MAH, Starikova E, Sung K, Tashkun S, Tennyson J, Toon GC, Tyuterev VlG, Wagner G (2013) The HITRAN12 molecular spectroscopic database. J Quant Spectrosc Radiat Transf 130:4–50. doi:http://dx.doi.org/10.1016/j.jqsrt.2013.07.002
94. Ryerson RA, Rencz AN (eds) (1999) Manual of remote sensing: remote sensing for the Earth sciences. Wiley. ISBN:9780471294054
95. Sassen K (2005) Polarization in lidar. In: Weitkamp C (ed) Lidar. Springer, pp 19–42. ISBN:9780387400754. doi:10.1007/0-387-25101-4_2

96. Schaepman ME, Ustin SL, Plaza AJ, Painter TH, Verrelst J, Liang S (2009) Earth system science related imaging spectroscopy – an assessment. Remote Sens Environ 113(suppl 1):S123–S137. doi:10.1016/j.rse.2009.03.001
97. Schaerer G, Wilheit TT (1979) A passive microwave technique for profiling of atmospheric water vapor. Radio Sci 14(3):371–375. doi:10.1029/RS014i003p00371
98. Schiavon G, Ferrazzoli P, Solimini D, de Maagt P, Poiares Baptista JPV (1998) A global high-resolution microwave emission model for the Earth. Radio Sci 33(3):753–766. doi:10.1029/97RS02304
99. Schlüssel P, Shin H-Y, Emery WJ, Grassl H (1987) Comparison of satellite-derived sea surface temperatures with in situ skin measurements. J Geophys Res Oceans 92(C3):2859–2874. doi:10.1029/JC092iC03p02859
100. Schmugge T, French A, Ritchie JC, Rango A, Pelgrum H (2002) Temperature and emissivity separation from multispectral thermal infrared observations. Remote Sens Environ 79(2–3):189–198. doi:http://dx.doi.org/10.1016/S0034-4257(01)00272-3
101. Schmugge TJ, Choudhury BJ (1981) A comparison of radiative transfer models for predicting the microwave emission from soils. Radio Sci 16(5):927–938. doi:10.1029/RS016i005p00927
102. Sigrist MW (ed) (1994) Air monitoring by spectroscopic techniques. Wiley. ISBN:9780471558750
103. Skou N (1989) Microwave radiometer systems: design and analysis. Artech House. ISBN:9780890063682
104. Solheim F, Godwin JR, Westwater ER, Han Y, Keihm SJ, Marsh K, Ware RH (1998) Radiometric profiling of temperature, water vapor and cloud liquid water using various inversion methods. Radio Sci 33(2):393–404. doi:10.1029/97RS03656
105. Staelin DH, Barrett AH, Waters JW, Barath FT, Johnston EJ, Rosenkranz PW, Gaut NE, Lenoir WB (1973) Microwave spectrometer on the Nimbus 5 satellite: meteorological and geophysical data. Science 182(4119):1339–1341. doi:10.1126/science.182.4119.1339
106. Staelin DH, Chen FW (2000) Precipitation observations near 54 and 183 GHz using the NOAA-15 Satellite. IEEE Trans Geosci Remote Sens 38(5):2322–2232. doi:10.1109/36.868889
107. Strandberg MWP, Meng CY, Ingersoll JG (1949) The microwave absorption spectrum of oxygen. Phys Rev 75(10):1524–1528. doi:10.1103/PhysRev.75.1524
108. Troitsky AV, Gajkovich KP, Gromov VD, Kadygrov EN (1993) Thermal sounding of the atmospheric boundary layer in the oxygen absorption band center at 60 GHz. IEEE Trans Geosci Remote Sens 31(1):116–120. doi:10.1109/36.210451
109. Turner DD, Mlawer EJ (2010) The radiative heating in underexplored bands campaigns. Bull Am Meteorol Soc 91(7):911–923. doi:10.1175/2010BAMS2904.1
110. Turner DD, Mlawer EJ, Bianchini G, Cadeddu MP, Crewell S, Delamere JS, Knuteson RO, Maschwitz G, Mlynzcak M, Paine S, Palchetti L, Tobin DC (2012) Ground-based high spectral resolution observations of the entire terrestrial spectrum under extremely dry conditions. Geophys Res Lett L10801. doi:10.1029/2012GL051542
111. Tyo JS, Goldstein DL, Chenault DB, Shaw JA (2006) Review of passive imaging polarimetry for remote sensing applications. Appl Opt 45(22):5453–5469. doi:10.1364/AO.45.005453
112. Ulaby FT, Long DG (eds) (2014) Microwave radar and radiometric remote sensing. University of Michigan Press. ISBN:9780472119356
113. Ulaby FT, Moore RK, Fung AK (1981) Microwave remote sensing: active and passive. In: Microwave remote sensing fundamentals and radiometry, vol 1. Addison-Wesley. ISBN:9780890061909
114. Verbesselt J, Hyndman R, Newnham G, Culvenor D (2010) Detecting trend and seasonal changes in satellite image time series. Remote Sens Environ 114(1):106–115. doi:10.1016/j.rse.2009.08.014
115. van Vleck JH (1947) The absorption of microwaves by oxygen. Phys Rev 71(7):413–424. doi:10.1103/PhysRev.71.413

116. Wan Z, Dozier J (1989) Land-surface temperature measurement from space: physical principles and inverse modeling. IEEE Trans Geosci Remote Sens GE-27(3):268–278. doi:10.1109/36.17668
117. Wark DO, Fleming HE (1966) Indirect measurements of atmospheric temperature profiles from satellites: I. Introduction. Mon Weather Rev 94(6):351–362. doi:10.1175/1520-0493(1966)094⟨0351:IMOATP⟩2.3.CO;2
118. Wark DQ, Hilleary DT (1969) Atmospheric temperature: a successful test of remote probing. Science 165(3899):1256–1258. doi:10.1126/science.165.3899.1256
119. Waters JW, Froidevaux L, Harwood RS, Jarnot RF, Pickett HM, Read WG, Siegel PH, Cofield RE, Filipiak MJ, Flower DA, Holden JR, Lau GK, Livesey NJ, Manney GL, Pumphrey HC, Santee ML, Wu DL, Cuddy DT, Lay RR, Loo MS, Perun VS, Schwartz MJ, Stek PC, Thurstans RP, Boyles MA, Chandra KM, Chavez MC, Chen G-S, Chudasama BV, Dodge R, Fuller RA, Girard MA, Jiang JH, Jiang Y, Knosp BW, LaBelle RC, Lam JC, Lee KA, Miller D, Oswald JE, Patel NC, Pukala DM, Quintero O, Scaff DM, Van Snyder W, Tope MC, Wagner PA, Walch MJ (2006) The Earth observing system microwave limb sounder (EOS MLS) on the Aura satellite. IEEE Trans Geosci Remote Sens 44(5):1075–1092. doi:10.1109/TGRS.2006.873771
120. Weinman JA, Marzano FS, Plant WJ, Mugnai A, Pierdicca N (2009) Rainfall observation from X-band, space-borne, synthetic aperture radar. Nat Hazards Earth Syst Sci 9:77–84. doi:10.5194/nhess-9-77-2009
121. Weng Q (2009) Thermal infrared remote sensing for urban climate and environmental studies: methods, applications, and trends. ISPRS J Photogramm Remote Sens 64(4):335–344. doi:10.1016/j.isprsjprs.2009.03.007
122. Westwater ER (1972) Ground-based determination of low altitude temperature profiles by microwaves. Mon Weather Rev 100(1):15–28. doi:10.1175/1520-0493(1972)100(0015:GDOLAT)2.3.CO;2
123. Wooster MJ, Rothery DA (2000) A review of volcano surveillance applications using the ATSR instrument series. Adv Environ Monit Model 1(1):3–35. http://www.kcl.ac.uk/advances
124. Xu J, Zhao D (2014) Review of coral reef ecosystem remote sensing. Acta Ecologica Sinica 34(1):19–25. doi:10.1016/j.chnaes.2013.11.003
125. Yan L, Gou Z-Y, Duan Y-N (2009) A UAV remote sensing system: design and test. In: Li D-R, Shan J, Gong J-Y (eds) Geospatial technology for earth observation. Springer. ISBN:9781441900500
126. Yueh SH, Wilson WJ, Li FK, Nghiem SV, Ricketts WB (1995) Polarimetric measurements of sea surface brightness temperatures using an aircraft K-band radiometer. IEEE Trans Geosci Remote Sens 33(1):85–92. doi:10.1109/36.368219

Chapter 11
Antennas and Apertures in Earth Observation

Antennas [95, Chap. 3] and apertures [46] cover the dual role of receiving the wave carrying information on the observed target, as well as of acting as a source in case they are part of active systems.[1] Passive instruments pick up either the solar radiation at ultraviolet, visible and near infrared wavelengths "reflected" in the sense seen in Sects. 9.3.1 and 10.2.1.1 by the observed portion of the Earth, or the thermal radiation which is spontaneously emitted by this latter in the infrared (Sect. 9.3.2) or at microwaves (Sect. 9.3.3). On their side, the active systems (Sect. 10.2.4) intercept a fraction of the power they have transmitted and that is carried back by the wave after interaction with the target.

Mirrors and lenses, assembled, e.g., in a telescope, are commonly employed at optical wavelengths, while parabolic dishes [4] or planar arrays [44] are mainly used at microwaves. In all cases, a physical aperture is identified which the electromagnetic wave has to cross traveling towards the outer space when the system transmits, or in the opposite direction in reception. In the transmitting mode, the metallic or dielectric structure transforms the wave produced by a concentrated or distributed *internal* source and adapts it to the outer space according to the pattern that satisfies the specified performance of the system. In the receiving mode, the structure acts to collect the incoming wave and to transfer the captured field to the *receiver* or to the *detector*. Although the transmit and receive channels must be kept separated, active systems employ essentially the same structure both in transmission and in reception.

Emphasis is now going to be put on the way antennas and apertures radiate the electromagnetic power. The reason is that, apart from the obvious need of determining the properties of the radiating element to characterize an active system, the receiving behavior of both active and passive instruments is effectively

[1] Earth observing active systems include lidars and radars in various forms, named after their peculiar function, such as: profiling, imaging, altimeter, scatterometer.

D. Solimini, *Understanding Earth Observation*, Remote Sensing
and Digital Image Processing 23, DOI 10.1007/978-3-319-25633-7_11

understood from the transmitting features on the basis of the reciprocity[2] introduced in Sect. 3.2.1 [27]. The receiving properties are determined by making use of a *virtually radiated* field, which is able to comprehensively describe the geometric and electrical structure at hand. After all, the reciprocal approach of Sect. 8.1.1, based on the concept of virtual sources, proved quite effective in describing thermal emission.

To figure out how microwave and optical antenna behave, let us have a tour inside the electromagnetic segment of Earth observing systems and try to grasp information on what happens when the systems transmit or receive.

11.1 Radiating Antennas

In the transmit mode, the system is fed by the internal power source[3] and the antenna radiates the electromagnetic field into the outer space. In summary, the power is delivered by the source to an *internal field* which is guided towards the outer antenna structure either by a physical *line*,[4] or by an arrangement of optical mirrors and lenses. Figure 11.1 shows the conventional scheme of a reflector antenna [82] employed by microwave systems, while Fig. 11.2 represents an optical telescope

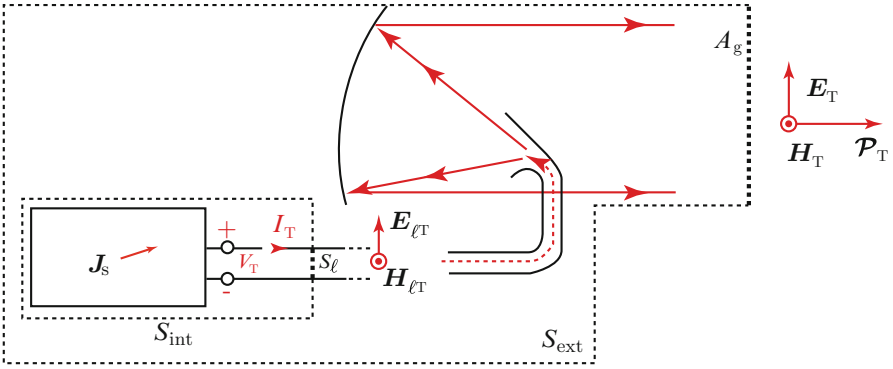

Fig. 11.1 Schematic representation of a microwave reflector antenna in transmitting mode: the power delivered by the internal source $\boldsymbol{J}_s$ is guided by an RF line towards the reflector, which re-directs the transmitted field $\boldsymbol{E}_T$, $\boldsymbol{H}_T$ outward through the geometric aperture A_g

[2]Reciprocity relations can be used in general, since they have been established for electromagnetic fields with arbitrary time dependence [22, 91].

[3]The source current $\boldsymbol{J}_s$ denotes any source of electromagnetic radiation, independently of its origin (be it natural or man-made), wavelength (optical or microwave) and nature, i.e., physically present or virtual.

[4]The line represents a radio-frequency guiding structure such as waveguide, strip-line, or coaxial cable.

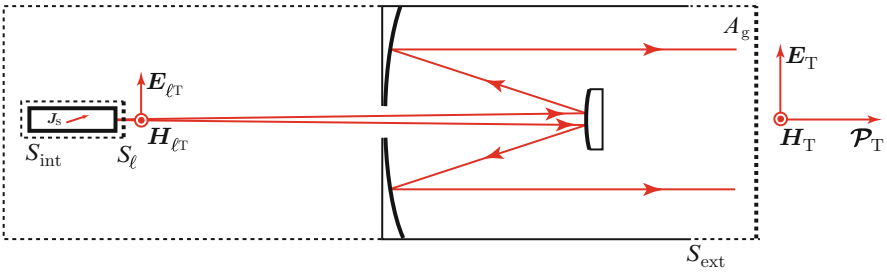

Fig. 11.2 Schematic representation of an optical telescope: the power delivered by the internal source $\boldsymbol{J}_s$ travels towards the double-reflector system that sends it outward through the geometric aperture A_g

[11]. The sketches, which refer to the transmit mode, suggest the similarity of the radiant behavior of microwave antennas and diffraction-limited[5] optical apertures.

It is worth mentioning that microwave technology exploits the high flexibility of *arrays* [7, 30, 51, 59, 100, 102] to build radar antennas with enhanced imaging capabilities. Figure 11.3 represents the Italian Space Agency's COSMO-SkyMed X-band SAR satellite, highlighting its planar-array antenna [18]. For a better insight into the radiating (and, by reciprocity, receiving) features of this kind of antenna, Fig. 11.4 shows an exploded view of a planar array of small linear structures each of which behaves like the point source considered in Sect. 3.1.3. The radiated electric field (3.24) was found to be co-planar with the source current: it means that the antenna in Fig. 11.4 radiates (and, by reciprocity, receives) a horizontally[6] polarized field.

To understand the basic principles of antennas, with particular reference to polarimetric observations, reference is made to the structures and symbols shown in the Figs. 11.1, 11.2, 11.3 and 11.4. Particular attention is called to the geometric antenna aperture A_g: it separates the *internal* space[7] from the *external* space, that is the outer space into which the antenna sends the transmitted wave or from which the wave comes.

In all the displayed antenna systems, optical or microwave, the source is represented by the impressed current density $\boldsymbol{J}_S$ introduced in Sect. 1.1.3. The power W_T that the source $\boldsymbol{J}_s$ delivers to the *internal* field satisfies the Poynting's theorem (1.20) relative to the *internal* surface S_{int} enveloping any volume which includes the source:

[5]The basically different features of incoherent-detection optical systems are outlined in Sect. 11.4.2.2.

[6]Being arbitrary, here the "horizontal" direction is assumed parallel to the linear elements of Fig. 11.4.

[7]"Internal" here denotes the space inside the system between the transmitter (or the receiver considered in Sect. 11.2) and A_g.

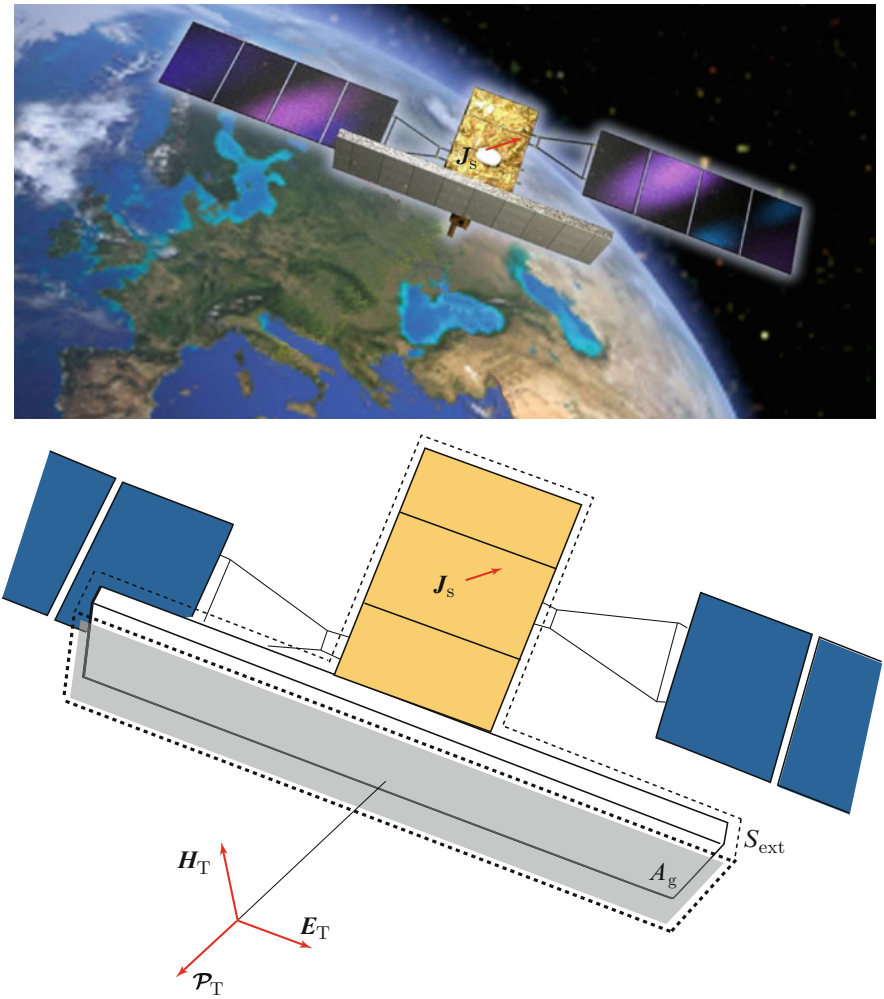

Fig. 11.3 Schematic representation of the planar radiating structure on the Italian Space Agency's (ASI) COSMO-SkyMed X-band SAR satellite: the geometric aperture A_g through which the power carried by the transmitted $\boldsymbol{E}_\mathrm{T}$, $\boldsymbol{H}_\mathrm{T}$ field flows is represented by the *grey rectangle* (Credit: image source, ASI; artwork by A. Perrone, Tor Vergata University Earth Observation Laboratory)

$$W_\mathrm{T} = \oiint_{S_\mathrm{int}} \boldsymbol{\mathcal{P}} \cdot \mathbf{n}_0 \, \mathrm{d}S = \frac{1}{2} \oiint_{S_\mathrm{int}} \Re\left[\boldsymbol{E} \times \boldsymbol{H}^*\right] \cdot \mathbf{n}_0 \, \mathrm{d}S \,, \tag{11.1}$$

where $\boldsymbol{E}$ is the field on S_int and the ideal lossless case is assumed. The field necessarily differs appreciably from zero only on the limited portion S_ℓ of S_int corresponding to the source-line coupling section, where the general field $\boldsymbol{E}$ in (11.1)

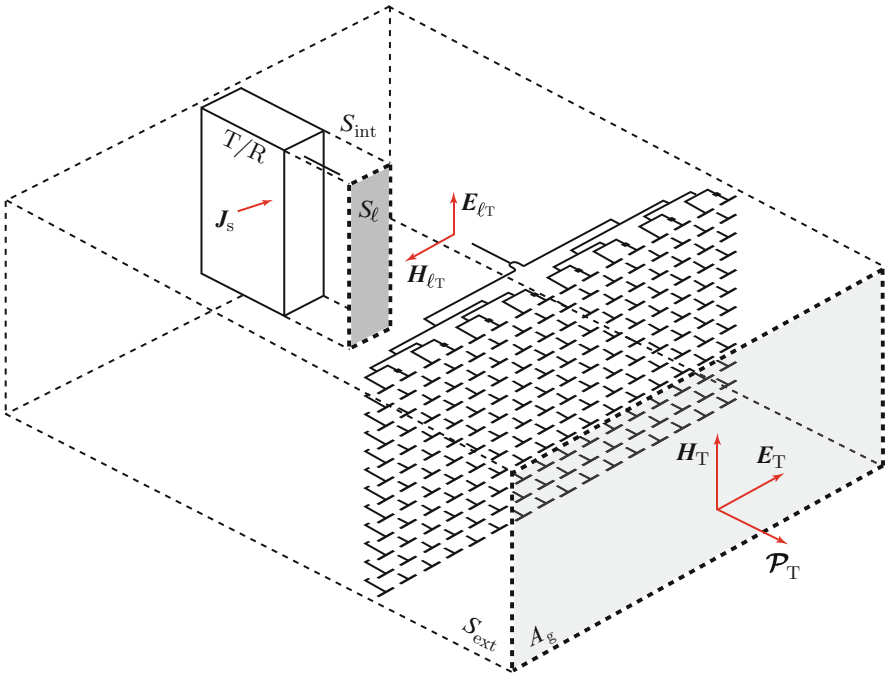

Fig. 11.4 Schematic representation of a planar array of elements transmitting a "horizontally" polarized field $\boldsymbol{E}_T$ (cf. Sect. 3.1.3); the geometric aperture A_g is represented by the *grey rectangle* in the forefront

takes the specific form $\boldsymbol{E}_{\ell T}$ of the field in the guiding [6] structure.[8] The power delivered by the source to the antenna is clearly the one that crosses the section S_ℓ:

$$W_T = \frac{1}{2\eta_\ell} \iint_{S_\ell} \boldsymbol{E}_{\ell T} \cdot \boldsymbol{E}^*_{\ell T} \, dS \, . \tag{11.2}$$

According to the type of system, the surface S_ℓ may be the section of the guiding structure shown in Figs. 11.1 and 11.4, or the surface limited by an *aperture stop* in the optical free-space case of Fig. 11.2. In the expression (11.2) η_ℓ is the *wave impedance*[9] for the considered lossless structure. It is known [63] that the internal field $\boldsymbol{E}_{0\ell T}$ can be factorized into a parameter V_T, depending on the field amplitude,

[8] For instance, in a microwave system, $\boldsymbol{E}_{\ell T}$ can be the field carried by the dominant mode of a waveguide.

[9] In the microwave case to which Fig. 11.1 refers, $\eta_\ell \equiv \eta_z$, that is, it coincides with the wave impedance of the dominant mode in the guiding structure, while $\eta_\ell \equiv \eta_0$, the intrinsic impedance of vacuum (4.35), for the free-space propagation inside the telescope optics of Fig. 11.2.

times a vector $\mathfrak{e}_{\ell\mathrm{T}}$, function of the transverse coordinates on the section of the radio-frequency line or of the optical system:

$$\boldsymbol{E}_{0\ell\mathrm{T}} = V_{\mathrm{T}}\,\mathfrak{e}_{\ell\mathrm{T}}\ .$$

After substitution for $\boldsymbol{E}_{\ell\mathrm{T}}$ into (11.2), given the properties of the wave propagation modes, the power delivered to the antenna is expressed by

$$W_{\mathrm{T}} = \frac{|V_{\mathrm{T}}|^2}{2\eta_\ell}\iint_{S_\ell}\mathfrak{e}_{\ell\mathrm{T}}\cdot\mathfrak{e}_{\ell\mathrm{T}}\,\mathrm{d}S = \frac{1}{2}\frac{|V_{\mathrm{T}}|^2}{\eta_\ell}\ , \tag{11.3}$$

since the functions $\mathfrak{e}_{\ell\mathrm{T}}$ form an ortho-normal set [21, 23, 74] on the section of the line.

At this point, we can readily realize that the *internal* field is invisible to an observer in the external space, which, rather, is reached by the *external* field. Therefore, it is the whole radiating structure that the exterior environment perceives as the actual source of electromagnetic field. To model the radiating properties of the antenna system we can resort to the results of Sect. 3.2.2. The approach makes use of the equivalent surface currents (3.52), $\boldsymbol{\mathcal{J}}_{\mathrm{eA}}$, and (3.53), $\boldsymbol{\mathcal{J}}_{\mathrm{meA}}$, laying on the arbitrary geometrical surface[10] indicated in Figs. 11.1–11.4 by S_{ext}, which wraps the antenna.

According to the results of Sect. 3.2.2.1, the field radiation pattern $\mathcal{F}$, defined by (3.36), is

$$\mathcal{F}(\vartheta,\varphi) = \frac{\mathrm{j}\kappa_0}{4\pi}\oiint_{S_{\mathrm{ext}}}\mathbf{r}_0\times\left[\boldsymbol{\mathcal{J}}_{\mathrm{meA}}(\boldsymbol{r}\,') + \eta_0\,\mathbf{r}_0\times\boldsymbol{\mathcal{J}}_{\mathrm{eA}}(\boldsymbol{r}\,')\right]\mathrm{e}^{\mathrm{j}\kappa_0\,\boldsymbol{r}\,'\cdot\,\mathbf{r}_0}\,\mathrm{d}S\ ,$$

where angles ϑ and φ are relative to the antenna reference frame. The key point is that the external fields $\boldsymbol{E}_{\mathrm{T}}$ and $\boldsymbol{H}_{\mathrm{T}}$ that compose the equivalent currents on S_{ext},

$$\boldsymbol{\mathcal{J}}_{\mathrm{meA}} = -\mathbf{n}_0\times\boldsymbol{E}_{\mathrm{T}};\qquad \boldsymbol{\mathcal{J}}_{\mathrm{eA}} = \mathbf{n}_0\times\boldsymbol{H}_{\mathrm{T}}\ ,$$

differ appreciably from zero only within the *geometric antenna aperture* A_{g}, identified as the portion of plane contoured by the rim of the reflector, mirror, or planar array[11] sketched in Figs. 11.1–11.4. Hence, the field radiation pattern is approximated by

[10] Alternatively, but less effectively in the present context, the currents could be those actually flowing on the physical structure, for instance those on the reflecting parabolic conducting surface of Fig. 11.1 or on the array elements of Fig. 11.4.

[11] In practice, the accuracy of this serviceable assumption depends on the kind of system and on the band of operation.

$$\mathcal{F}(\vartheta,\varphi) \simeq \frac{\mathrm{j}}{2\lambda_0} \iint_{A_\mathrm{g}} \mathbf{r}_0 \times [-\mathbf{n}_0 \times \boldsymbol{E}_\mathrm{T} + \eta_0\, \mathbf{r}_0 \times (\mathbf{n}_0 \times \boldsymbol{H}_\mathrm{T})]\, \mathrm{e}^{\mathrm{j}\kappa_0 \boldsymbol{r}' \cdot \mathbf{r}_0}\, \mathrm{d}S\,. \tag{11.4}$$

Equation (11.4) indicates that the radiation pattern is uniquely determined by the external fields $\boldsymbol{E}_\mathrm{T}(\boldsymbol{r}')$, $\boldsymbol{H}_\mathrm{T}(\boldsymbol{r}')$ that the internal transmitting source excites on the points $\boldsymbol{r}'$ of the antenna aperture A_g, as well as by shape and dimension of this latter and by the wavelength of operation.

In many cases, the external field has the form (4.3) of a quasi-homogeneous plane wave propagating perpendicularly to the aperture,[12] so that, by calling $\mathfrak{e}_{0\mathrm{T}}$ the unit vector of the electric field and using (4.31),

$$\boldsymbol{H}_{0\mathrm{T}} = \frac{\mathbf{n}_0 \times \boldsymbol{E}_{0\mathrm{T}}}{\eta_0} = \frac{E_{0\mathrm{T}}}{\eta_0}\, \mathbf{n}_0 \times \mathfrak{e}_{0\mathrm{T}}\,.$$

Substitution into (11.4) allows one to express the radiation pattern as a function of the electric field only:

$$\begin{aligned}\mathcal{F}(\vartheta,\varphi) \simeq{}& \frac{\mathrm{j}}{2\lambda_0} \{(\mathbf{n}_0 \cdot \mathbf{r}_0)\,(1 + \mathbf{n}_0 \cdot \mathbf{r}_0)\, \mathfrak{e}_{0\mathrm{T}} + (\mathbf{r}_0 \times \mathbf{n}_0)\,[\mathbf{n}_0 \cdot (\mathfrak{e}_{0\mathrm{T}} \times \mathbf{r}_0)]\} \\ &\times \iint_{A_\mathrm{g}} E_{0\mathrm{T}}(\boldsymbol{r}')\, \mathrm{e}^{\mathrm{j}\kappa_0 \boldsymbol{r}' \cdot \mathbf{r}_0}\, \mathrm{d}S\,.\end{aligned} \tag{11.5}$$

For simplicity, Eq. (11.5) assumes that the external field $\boldsymbol{E}_{0\mathrm{T}} = E_{0\mathrm{T}}\, \mathfrak{e}_{0\mathrm{T}}$ has the same polarization over the whole aperture A_g.

The radiation pattern (11.5) depends on the direction $\mathbf{r}_0$ in which the field is conveyed, therefore, its angular dependence is contributed both by the products $\mathbf{n}_0 \cdot \mathbf{r}_0$ and $\mathbf{r}_0 \times \mathbf{n}_0$ and by the surface integral, which contains $\boldsymbol{r}' \cdot \mathbf{r}_0$. The expression is considerably simplified if interest is in the radiation pattern in *paraxial* directions, i.e., for $\mathbf{r}_0 \sim \mathbf{n}_0 \equiv \mathbf{z}_0$. Then, close to the aperture axis,

$$\mathcal{F}(\vartheta,\varphi) \simeq \frac{\mathrm{j}}{\lambda_0}\, \mathfrak{e}_{0\mathrm{T}} \iint_{A_\mathrm{g}} E_{0\mathrm{T}}(\boldsymbol{r}')\, \mathrm{e}^{\mathrm{j}\,\kappa_0 \boldsymbol{r}' \cdot \mathbf{r}_0}\, \mathrm{d}S\,. \tag{11.6}$$

In the paraxial approximation, the vector radiation pattern (11.6) is simply composed of the unit vector $\mathfrak{e}_{0\mathrm{T}}$ times the scalar radiation pattern. Within these assumptions, the electric far field has the same polarization as the electric field on the aperture: it is parallel to this latter in the particular case of linear polarization.

[12] Actually, the external field propagates perpendicularly to the equiphase plane in correspondence of A_g; for simplicity, here the plane of A_g is assumed equiphase.

Given (11.6), the power radiation pattern

$$\mathcal{P}(\vartheta, \varphi) = \frac{1}{2\eta_0} |\mathcal{F}(\vartheta, \varphi)|^2 \tag{11.7}$$

depends on $E_{0\mathrm{T}}$, hence on the power delivered by the source. Since an antenna has characteristics that are clearly independent of the power it radiates,[13] the *directivity pattern* $\mathcal{D}$ is introduced by normalizing the power radiation pattern to the average power density $W_\mathrm{T}/4\pi$ radiated per unit solid angle:

$$\mathcal{D}(\vartheta, \varphi) := \frac{\mathcal{P}(\vartheta, \varphi)}{W_\mathrm{T}/4\pi} \cdot \tag{11.8}$$

The directivity $\mathcal{D}$ defined by (11.8) is obviously independent of W_T. Because of (11.7) and (11.5) or (11.6), the directivity pattern depends on shape and dimensions of the antenna aperture A_g, as well as on the vector field $E_{0\mathrm{T}}$ on it and on wavelength. As said, the angles ϑ and φ are defined with respect to the chosen antenna reference, sketched in Fig. 11.5. The directivity angular

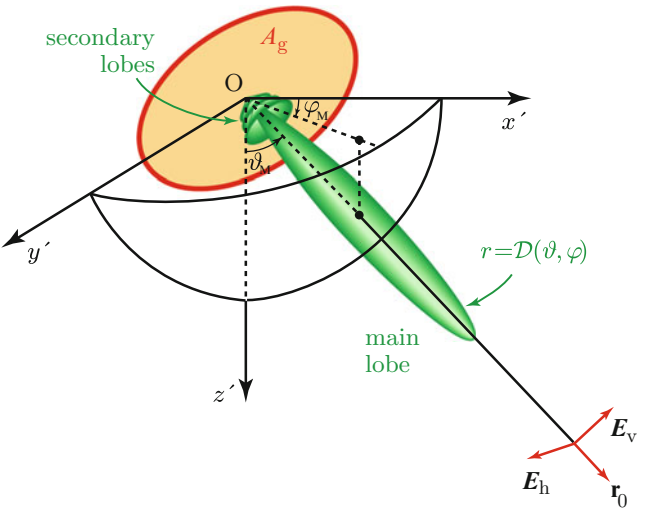

Fig. 11.5 Sketch of the directivity pattern of an aperture antenna of geometric area A_g lying on the $(x'\,y')$-source plane: the value of the directivity in the direction $\mathbf{r}_0(\vartheta, \varphi)$ is proportional to the length of the segment between the origin O and the surface $r = \mathcal{D}(\vartheta, \varphi)$; the direction of maximum directivity is denoted by $\vartheta = \vartheta_\mathrm{M}, \varphi = \varphi_\mathrm{M}$. Horizontal and vertical components $\boldsymbol{E}_p$, $p = \mathrm{h}, \mathrm{v}$, of the field are indicative, since they are often meaningless without reference to the observed target (e.g., the Earth's surface)

[13] The power radiated by the antenna coincides with the power delivered by the source when the structure is lossless.

pattern is commonly represented in spherical coordinates by the normalized surface $r = \mathcal{D}(\vartheta, \varphi)$ with the origin on the antenna position.[14] Note that the term *antenna gain* is used to denote the maximum value $\mathcal{D}_\mathrm{M}$ of the directivity pattern. It can be observed that the modulus of the radiation pattern (11.6) is maximum when $\boldsymbol{r}' \perp \mathbf{r}_0$, i.e., in the direction perpendicular to the aperture, in case the latter is an equiphase surface of $E_{0\mathrm{T}}$. The direction in which $\mathcal{D}(\vartheta, \varphi) = \mathcal{D}_\mathrm{M}$ is the boresight, which, as a reference,[15] is perpendicular to the aperture and identifies the pointing direction of the radiating system (cf. Sect. 11.3.1.1).

11.1.1 Directivity and Reaction

Reasons that will appear clear in the following suggest to apply a result of reciprocity (cf. Sect. 3.2.1) to express the directivity in terms of the reaction integral introduced in Sect. 3.2.1.1.

Consider the antenna A characterized by a distribution of equivalent currents $\boldsymbol{\mathcal{J}}_{\mathrm{meA}}$, $\boldsymbol{\mathcal{J}}_{\mathrm{eA}}$ on its geometric aperture A_g. Given the reciprocity with the test source considered in Sect. 3.2.1.2, the far electric field $\boldsymbol{E}_\infty$ radiated by A is obtained by (3.49) from the reaction I_{tA} of A onto a test source of momentum $\boldsymbol{\mathcal{M}} = \mathcal{M}\,\mathfrak{e}_0$ located at far distance r from the antenna and parallel[16] to $\boldsymbol{E}_\infty$ (Fig. 11.6):

$$\boldsymbol{E}_\infty = \frac{I_{\mathrm{tA}}}{\mathcal{M}}\,\mathfrak{e}_0 \,.$$

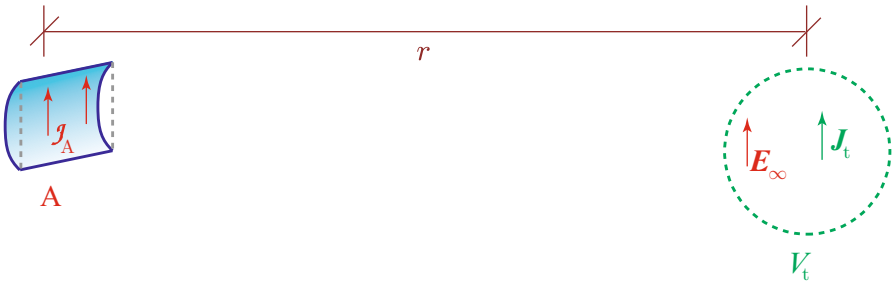

Fig. 11.6 Reaction of antenna A onto the test source $\boldsymbol{J}_\mathrm{t} \parallel \boldsymbol{E}_\infty$; $\boldsymbol{\mathcal{J}}_\mathrm{A}$ denotes a generic antenna equivalent current

[14] The present radial coordinate r in the antenna reference system should not be confused with the distance from the antenna; similarly, the polar angle ϑ must be kept distinct from the off-nadir angle.

[15] Systems are frequently encountered that steer the beam (electronically or mechanically), i.e., vary the aperture boresight by tilting the equiphase surface of $E_{0\mathrm{T}}$.

[16] Linear polarization is assumed; complex $\mathfrak{e}_0$ are needed for circular or elliptical polarizations.

Then the power radiation pattern (3.37) of the antenna is readily obtained from the reaction integral

$$\mathcal{P}(\vartheta,\varphi) = r^2 \frac{1}{2} \frac{|E_\infty|^2}{\eta_0} = \frac{r^2}{2\eta_0} \frac{|I_{\mathrm{tA}}|^2}{\mathcal{M}^2} ,$$

whence

$$\mathcal{D}(\vartheta,\varphi) = \frac{2\pi\, r^2\, |I_{\mathrm{tA}}|^2}{\eta_0\, W_{\mathrm{T}}\, \mathcal{M}^2} \cdot \tag{11.9}$$

Suitable selection of the unit vector $\mathfrak{e}_0$ of the test source and of its orientation yields the radiation pattern of A for different polarizations of the far field. Particular attention is called to the dependence of the directivity on the reaction integral.

11.2 Receiving Antennas

The antenna in the receive mode acts in a fashion reciprocal to transmission: the wave incident from the external space, denoted by the superscript $^{(\mathrm{i})}$ in Fig. 11.7, crosses the geometric aperture A_{g} and excites currents on the reflecting surface, which act as a secondary source to focus the field into the entrance (the *feed*) of the antenna-to-receiver line. The internal field created by the re-radiation from the reflector travels inward, either along the guiding structure of the microwave receiving channel or going through the mirrors and lenses of the optical receiving system. Then the internal wave delivers the power W_{r} to the microwave receiver or to the optical *point* detector located at the end of the receiving path. The

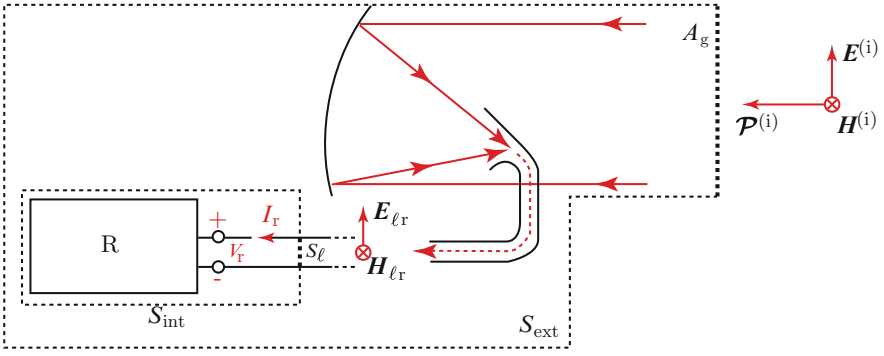

Fig. 11.7 Schematic representation of a microwave reflector antenna in receive mode: careful comparison with Fig. 11.1 highlights several noticeable issues, among which the orientation of the fields; the received power, carried by the incident wave $\boldsymbol{E}^{(\mathrm{i})}, \boldsymbol{H}^{(\mathrm{i})}$ enters the system through the geometric aperture A_{g}

receiving process scheme depicted in Fig. 11.7 for a radio-frequency system is readily extended to the optical telescope shown in Fig. 11.2 by reversing directions and by straightforward substitutions.

The formalism for modeling the receiving process is quite analogous to the one used in the previous Sect. 11.1 for analyzing the transmitting behavior. The received power is given by an expression corresponding to (11.2):

$$W_\mathrm{r} = \frac{1}{2\eta_\ell} \iint_{S_\ell} \boldsymbol{E}_{\ell\mathrm{r}} \cdot \boldsymbol{E}^*_{\ell\mathrm{r}} \, \mathrm{d}S \, ,$$

where the incident and received fields, shown in Fig. 11.7, are recognized to correspond to the transmitted ones in Fig. 11.1 and in Eq. (11.2). Since the receiving channel is assumed the same as the transmitting one, the internal received field $\boldsymbol{E}_{\ell\mathrm{r}}$ differs appreciably from zero only on the section S_ℓ of the line or of the optical system, and the impedances $\eta_\ell \equiv \eta_z$ or $\eta_\ell \equiv \eta_0$ according to the case at hand, are also the same. As in Sect. 11.1, the internal field is factorized into a complex parameter V_r, which depends on amplitude and phase of the received field, times a vector $\boldsymbol{e}_{\ell\mathrm{r}}$, function of the transverse line coordinates:

$$\boldsymbol{E}_{0\ell\mathrm{r}} = V_\mathrm{r} \, \boldsymbol{e}_{\ell\mathrm{r}} \, ,$$

so that the received power is given by the expression corresponding to (11.3),

$$W_\mathrm{r} = \frac{|V_\mathrm{r}|^2}{2\eta_\ell} \iint_{S_\ell} \boldsymbol{e}_{\ell\mathrm{r}} \cdot \boldsymbol{e}_{\ell\mathrm{r}} \, \mathrm{d}S = \frac{1}{2} \frac{|V_\mathrm{r}|^2}{\eta_\ell} \, , \tag{11.10}$$

because of the orthonormality of the $\boldsymbol{e}_{\ell\mathrm{r}}$ set.

11.2.1 Reception and Reaction

Two distinct modes of operation have been discussed in the previous paragraphs:

- transmit mode, with the *internal source* feeding the antenna, which radiates into the external space;
- receive mode, with a source in the *external space* creating the incident field captured by the antenna, which feeds the receiver.

Tight connection between receive and transmit properties of antennas was anticipated. Reciprocity provides the bridging module.

The approach followed in Sect. 3.2.1 highlights that the reciprocity relations stem directly from the spectral Maxwell's equations, which are theoretical relations separately satisfied by the fields of each source. Therefore, the results of reciprocity hold for the fields, transmitted and received, and to the currents of the respective

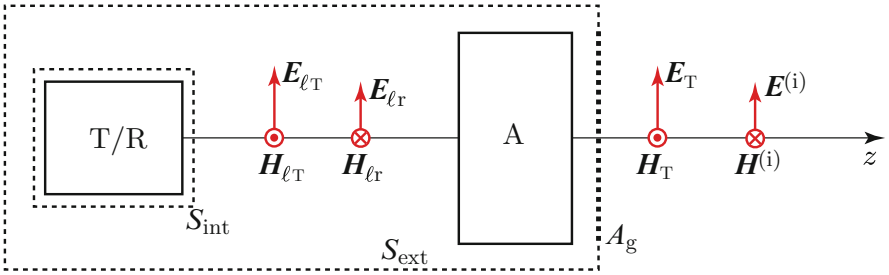

Fig. 11.8 Schematic representation of a transmitting/receiving system, with indication of the transmit/receive (T/R) and antenna (A) blocks, internal S_{int} and external S_{ext} surfaces and of the geometric aperture A_{g}; the transmitted ($\boldsymbol{E}_{\text{T}}$, $\boldsymbol{H}_{\text{T}}$) and incident ($\boldsymbol{E}^{(\text{i})}$, $\boldsymbol{H}^{(\text{i})}$) fields in the outer space and in the line connecting the T/R block with the antenna A are also represented with their respective directions

sources also when the transmit and receive processes are *virtual*, in the sense discussed in Sect. 8.1. Further advantage is taken from the arbitrariness of S of Fig. 3.10 by choosing S_{int} in such a way that it includes internal source and receiver, and excludes the elementary (test) source (Sect. 3.2.1.2) at the far location in the external space, from which, for the time being, the incident field is assumed to originate.

With reference to the schematic representation of Fig. 11.8, Eq. (3.46) is specified to the *virtually* transmitted ($\boldsymbol{E}_1, \boldsymbol{H}_1 \equiv \boldsymbol{E}_{\text{T}}, \boldsymbol{H}_{\text{T}}$) and *actually* received ($\boldsymbol{E}_2, \boldsymbol{H}_2 \equiv \boldsymbol{E}_{\text{r}}, \boldsymbol{H}_{\text{r}}$) fields:

$$I_{\text{At}} = \oiint_{S_{\text{int}}} (\boldsymbol{E}_{\text{T}} \times \boldsymbol{H}_{\text{r}} - \boldsymbol{E}_{\text{r}} \times \boldsymbol{H}_{\text{T}}) \cdot \mathbf{n}_0 \, \mathrm{d}S = \iint_{S_\ell} (\boldsymbol{E}_{\ell\text{T}} \times \boldsymbol{H}_{\ell\text{r}} - \boldsymbol{E}_{\ell\text{r}} \times \boldsymbol{H}_{\ell\text{T}}) \cdot (-\mathbf{z}_0) \, \mathrm{d}S \, . \tag{11.11}$$

Given the modal properties, which are clearly the same for both transmission and reception through the same line,[17]

$$I_{\text{At}} = \iint_{S_\ell} \left[\boldsymbol{E}_{0\ell\text{T}} \cdot \left(-\frac{\boldsymbol{E}_{0\ell\text{r}}}{\eta_\ell} \right) - \boldsymbol{E}_{0\ell\text{r}} \cdot \frac{\boldsymbol{E}_{0\ell\text{T}}}{\eta_\ell} \right] \mathrm{d}S = -2 \frac{V_{\text{T}} V_{\text{r}}}{\eta_\ell} \iint_{S_\ell} \mathfrak{e}_{\ell\text{T}} \cdot \mathfrak{e}_{\ell r} \, \mathrm{d}S = -2 \frac{V_{\text{T}} \, V_{\text{r}}}{\eta_\ell} \, \cdot$$

The purpose of the above sequence of steps is to express the received field factor V_{r} in terms of the reaction of the test source onto the antenna

$$V_{\text{r}} = -\frac{\eta_\ell \, I_{\text{At}}}{2 V_{\text{T}}} \, \cdot \tag{11.12}$$

[17] The neglected phase factor here is inessential.

Then, the received power (11.10) is obtained thanks to (11.12) and taken (11.3) into account:

$$W_{\mathrm{r}} = \frac{1}{2}\,\frac{\eta_\ell^2\,|I_{\mathrm{At}}|^2}{\eta_\ell\,4\,|V_{\mathrm{T}}|^2} = \frac{|I_{\mathrm{At}}|^2}{16\,W_{\mathrm{T}}}\,. \tag{11.13}$$

It is important to realize that the geometrical (e.g., dimensions, shape, structure) and electromagnetic features of the antenna are implicitly and completely included in I_{At} which depends on the field $\boldsymbol{E}_{\mathrm{T}}$ that the antenna transmits.

At first sight, the relation (11.13) between received power and transmitted power may not make sense. But, again, when an antenna is only receiving, as in passive systems or in receive mode for active systems, the transmitted field must be considered as *virtual*, that is, the receiver must *be thought* to be replaced by a virtual transmitter, taking care of leaving the whole structure unchanged.[18] The surprising presence of the *virtually* transmitted power at the denominator of (11.13) has just the role of making W_{r} independent of the transmitted quantities, since W_{T} cancels out the same quantities which are present in $|I_{\mathrm{At}}|^2$ at the numerator of (11.13). This issue is further considered in Sects. 11.2.2.1 and 11.2.3.

The reader should have noticed that the procedure is the same as the one followed throughout Chap. 8 to arrive at the basic relations for the thermal emission. These latter that, after all, pertain to the transmitting process, have been obtained by considering a virtual *incident* field, whereas now, reciprocally, in the receiving process it is the *transmitted* field that is considered virtual.

Clearly, the electromagnetic reciprocity establishes the tight link between receiving and transmitting properties of the antennas at any frequency/wavelength they operate. As a word of caution, some care must be exerted, since, as mentioned in Sect. 3.2.1, exploitation of reciprocity is subject to the condition that the whole system at hand does not include anisotropic nor nonlinear materials.

11.2.2 Polarization-Selective Antennas

The essential concepts derived from reciprocity are that the receiving antenna is fully represented by the field it virtually transmits and that the received power is directly related to the reaction between incoming and virtually transmitted fields. This approach has the crucial advantage of the arbitrariness of the surface over which the reaction (3.46) is evaluated, with the only constraint of including the source of the virtually transmitted field and the receiving device. The internal surface S_{int} has been instrumental to obtain W_{r} in terms of I_{At}, but the external

[18] It means that the direction of propagation of the arriving field must be reversed, making it to propagate back from the point where the receiver or the detector is located towards the external space, through any microwave component or optical element actually traversed by the incident field.

surface S_{ext} can be used as well. This latter wraps the antenna system, includes the receiver/virtual transmitter, and leans on the antenna aperture A_{g}. With this choice, the reaction integral in (11.13) which yields the received power W_{r} is

$$I_{\text{At}} = \oiint_{S_{\text{ext}}} \left(\boldsymbol{E}_{\text{T}} \times \boldsymbol{H}^{(\text{i})} - \boldsymbol{E}^{(\text{i})} \times \boldsymbol{H}_{\text{T}}\right) \cdot \mathbf{n}_0 \, \mathrm{d}S \simeq \iint_{A_{\text{g}}} \left(\boldsymbol{E}_{\text{T}} \times \boldsymbol{H}^{(\text{i})} - \boldsymbol{E}^{(\text{i})} \times \boldsymbol{H}_{\text{T}}\right) \cdot \mathbf{n}_0 \, \mathrm{d}S \,, \tag{11.14}$$

under the reasonable assumption that the virtually transmitted field differs appreciably from zero only within the rim of the antenna aperture A_{g}. While (11.11) refers to the internal quantities, the flexibility brought about by the reciprocity theorem has allowed (11.14) to be expressed in terms of the external ones, and in particular of the incident field $\boldsymbol{E}^{(\text{i})}$, $\boldsymbol{H}^{(\text{i})}$. This latter is reasonably assumed associated with a homogeneous plane wave arriving perpendicularly onto the aperture, taken to lie on the $(z = 0)$-plane. The virtually transmitted external field $\boldsymbol{E}_{\text{T}}$, $\boldsymbol{H}_{\text{T}}$ is also assumed as that of a quasi-homogeneous plane wave propagating along z, clearly in the direction opposite to that of the incident one. Taking account for the opposite propagation directions of virtually transmitted and incident waves, the reaction becomes

$$\begin{aligned} I_{\text{At}} &= \iint_{A_{\text{g}}} \left(\boldsymbol{E}_{\text{T}} \cdot \boldsymbol{H}^{(\text{i})} \times \mathbf{z}_0 - \boldsymbol{E}^{(\text{i})} \cdot \boldsymbol{H}_{\text{T}} \times \mathbf{z}_0\right) \mathrm{d}S \\ &= \iint_{A_{\text{g}}} \left[\boldsymbol{E}_{0\text{T}} \cdot \left(-\frac{1}{\eta_0} \mathbf{z}_0 \times \boldsymbol{E}_0^{(\text{i})}\right) \times \mathbf{z}_0 - \boldsymbol{E}_0^{(\text{i})} \cdot \left(\frac{1}{\eta_0} \mathbf{z}_0 \times \boldsymbol{E}_{0\text{T}}\right) \times \mathbf{z}_0\right] \mathrm{d}S \\ &= -\frac{2}{\eta_0} \iint_{A_{\text{g}}} \boldsymbol{E}_{0\text{T}} \cdot \boldsymbol{E}_0^{(\text{i})} \, \mathrm{d}S \,. \end{aligned}$$

Substitution into (11.13) yields the received power

$$W_{\text{r}} = \frac{\left| \iint_{A_{\text{g}}} \boldsymbol{E}_{0\text{T}} \cdot \boldsymbol{E}_0^{(\text{i})} \, \mathrm{d}S \right|^2}{4 \, \eta_0^2 \, W_{\text{T}}} \,. \tag{11.15}$$

The inner product

$$\boldsymbol{E}_{0\text{T}} \cdot \boldsymbol{E}_0^{(\text{i})} = E_{0\text{T}} \, E_0^{(\text{i})} \, \boldsymbol{\mathfrak{e}}_{0\text{T}} \cdot \boldsymbol{\mathfrak{e}}_0^{(\text{i})}$$

in the reaction integral, reveals the essential impact that polarization has on the received power [99]:

– when the polarization of the virtually transmitted wave is *matched* to that of the incident one (*co-polarized* waves), that means $\boldsymbol{\mathfrak{e}}_{0\text{T}} = \boldsymbol{\mathfrak{e}}_0^{(\text{i})*}$, then the dot product $\boldsymbol{\mathfrak{e}}_{0\text{T}} \cdot \boldsymbol{\mathfrak{e}}_0^{(\text{i})} = 1$ and the power carried by the incoming wave is fully received;

– when the polarization of the virtually transmitted wave is *orthogonal* to that of the incident one (*cross-polarized* waves), the dot product vanishes and no power is received.

Note that, given the opposite directions of propagation of transmitted and incident waves, cross-polarization [62] of the waves does not necessarily imply orthogonality of the fields in the sense discussed in Sect. 1.3.1.1.1. The result holds for any polarization, be it linear, circular or elliptic. Two orthogonal linear polarizations, for instance horizontal and vertical in the Jones' formalism, are commonly used to synthesize [39] any polarization.

Summarizing, the polarization at which power is received is selected by the polarization of the virtually transmitted field: for instance, if the virtually transmitted field is horizontally polarized, only power carried by a horizontally polarized incident wave is received. It is important to realize that in active systems such as SARs, the transmit and receive modes use partially separated channels, hence the polarization at which power is *actually* radiated is independent from that of the *virtually* transmitted field that controls reception. Given the time lag between transmission and reception, the system may radiate, e.g., horizontal polarization, and afterwards receive on both horizontal and vertical polarizations [77]. In practice, the polarization selection is set by the receiving channel, which includes polarization-sensitive devices, as array elements, or reflector feeds.

Multi-polarization systems receive on two orthogonally polarized, for instance horizontal and vertical, independent channels, which are not combined. *Polarimetric* systems use coherent reception and the two channels can be combined to synthetically produce any polarization. Active systems have different configurations [31, 69, 70, 75, 92] according to specifications: the antenna can transmit on a single polarization and receive on two cross-polarized channels or both transmit and receive on two orthogonal channels, with suitable time division. Anyway, the importance of keeping separated the concepts of actually and virtually transmitted field cannot be overemphasized.

11.2.2.1 Optical Systems

Optical systems using direct detection are generally not polarization-selective and, in absence of polarizing devices, the receiving channels, including detectors, equally respond to any polarization of the incident field. Therefore, the virtually transmitted field is co-polarized to any incident wave, and, being both waves homogeneous, the integral in (11.15) simplifies into

$$\iint_{A_g} \boldsymbol{E}_{0T} \cdot \mathbf{E}_0^{(i)} \, \mathrm{d}S = E_{0T} E_0^{(i)} A_g \, ,$$

so that the received power is proportional to the total incident power density $\langle \mathcal{P}^{(\mathrm{i})} \rangle$:

$$\langle W_\mathrm{r} \rangle = \frac{\left\langle \left| E_0^{(\mathrm{i})} \right|^2 \right\rangle |E_{0\mathrm{T}}|^2 A_\mathrm{g}^2}{4\,\eta_0^2\,W_\mathrm{T}} = \frac{|E_{0\mathrm{T}}|^2 A_\mathrm{g}^2}{2\,\eta_0\,W_\mathrm{T}} \left\langle \mathcal{P}^{(\mathrm{i})} \right\rangle . \tag{11.16}$$

The virtually transmitted power W_T is the flux of the Poynting vector through the aperture A_g, i.e.,

$$W_\mathrm{T} = \frac{|E_{0\mathrm{T}}|^2}{2\eta_0} A_\mathrm{g} .$$

Then (11.16) becomes

$$\langle W_\mathrm{r} \rangle = \langle \mathcal{P}^{(i)} \rangle A_\mathrm{g} . \tag{11.17}$$

The average power received by the optical system, independent of polarization, is simply given by the power per unit area carried by the incident radiation times the geometric area A_g of the optical aperture. The normalizing role of W_T, that is its role in making the received power independent of the virtually transmitted one, is now apparent.

The intuitive result (11.17) has been obtained under the assumption of homogeneous virtually transmitted wave, as is common in optical systems, in which the field is approximately constant over A_g. On the contrary, both theoretical and technical reasons prevent the transmitted wave from being homogeneous over a microwave antenna aperture.

11.2.3 Aperture Efficiency and Effective Area

At microwaves, the dependence of $\boldsymbol{E}_{0\mathrm{T}}$ on the point on the antenna aperture must be taken into account. A frequently used position is

$$\boldsymbol{E}_{0\mathrm{T}} = E_{0\mathrm{T}}\, \mathcal{E}_\mathrm{T}(x', y')\, \mathfrak{e}_{0\mathrm{T}} , \tag{11.18}$$

where $E_{0\mathrm{T}}$ is a magnitude factor independent of coordinates, the function $\mathcal{E}_\mathrm{T}(x', y')$ describes the distribution of the virtually transmitted field on the aperture, and $\mathfrak{e}_{0\mathrm{T}}$ yields its polarization, assumed constant on A_g. With the position (11.18), the received power (11.15) *for matched polarization* becomes[19]

[19]Once again, attention is called onto the normalizing effect of the denominator of (11.19), which makes the received power independent of the magnitude of the virtually transmitted field.

$$W_\mathrm{r} = \frac{\left|E_0^{(\mathrm{i})}\right|^2 |E_{0\mathrm{T}}|^2 \left| \iint_{A_\mathrm{g}} \mathcal{E}_\mathrm{T}\, \mathrm{d}S \right|^2}{4\eta_0^2 \dfrac{|E_{0\mathrm{T}}|^2}{2\eta_0} \iint_{A_\mathrm{g}} |\mathcal{E}_\mathrm{T}|^2\, \mathrm{d}S} = \frac{\left| \iint_{A_\mathrm{g}} \mathcal{E}_\mathrm{T}\, \mathrm{d}S \right|^2}{A_\mathrm{g} \iint_{A_\mathrm{g}} |\mathcal{E}_\mathrm{T}|^2\, \mathrm{d}S} A_\mathrm{g} \mathcal{P}^{(\mathrm{i})} = \eta_\mathrm{A} A_\mathrm{g} \mathcal{P}^{(\mathrm{i})} \,. \tag{11.19}$$

The coefficient η_A, named *aperture efficiency* of the antenna is defined as

$$\eta_\mathrm{A} := \frac{\left| \iint_{A_\mathrm{g}} \mathcal{E}_\mathrm{T}\, \mathrm{d}S \right|^2}{A_\mathrm{g} \iint_{A_\mathrm{g}} |\mathcal{E}_\mathrm{T}|^2\, \mathrm{d}S} \,.$$

Recalling Schwarz's inequality,

$$\eta_\mathrm{A} \leq 1 \,, \tag{11.20}$$

where equality holds when $\mathcal{E}_\mathrm{T}(x', y') = \text{const}$ is independent of point on A_g.

The antenna *effective area* A_e is defined as

$$A_\mathrm{e} := \eta_\mathrm{A} A_\mathrm{g} \leq A_\mathrm{g} \tag{11.21}$$

so that the received power (11.19) is given by

$$W_\mathrm{r} = A_\mathrm{e}\, \mathcal{P}^{(\mathrm{i})} \,. \tag{11.22}$$

The effective area determines the received power, which is tightly related to the useful signal considered in Sect. 11.4.2. Therefore, both geometric area and aperture efficiency are crucial parameters in the specification of Earth observing systems, especially of radars (cf. the basic radar Eq. (11.41) of Sect. 11.4.3.1). Given (11.20), the effective area of an aperture antenna is a fraction of its geometric area. Only if a structure able to produce a virtually transmitted field uniform on the aperture was feasible, the effective area would coincide with the geometric one. In practice, a reference value is $\eta_\mathrm{A} \approx 0.8$ for microwave antennas, while generally $\eta_\mathrm{A} \approx 1$ in optical systems. It can be added that, because of the relatively high value of η_A, denoting nearly uniform fields, the relations (4.31) and (4.32) between electric and magnetic fields are frequently satisfactory assumptions.

11.2.4 Reception vs. Transmission

The properties of receiving systems have been found to be closely related to the field they (virtually) transmit, hence a tight quantitative link is expected between radiating and receiving parameters of antennas. To establish the significant relation,

assume that the field $\boldsymbol{E}^{(\mathrm{i})}$ impinging onto the antenna system A in receiving mode is originated by a far-range test source (Sect. 3.2.1.2) of momentum $\mathcal{M}$ and with current density $\boldsymbol{J}_{\mathrm{t}}$ oriented along the electric field virtually radiated by the antenna, as described in Sect. 11.1.1 and as sketched in Fig. 11.6. Equation (11.9) points out that the reaction integral I_{tA} yields the directivity of the antenna and, on its side, (11.13) shows that the effective area of the antenna depends on the reaction integral I_{At}. Since under the assumption of reciprocal media, generally satisfied in Earth observation,[20]

$$I_{\mathrm{tA}} = I_{\mathrm{At}} \,,$$

the effective area A_{e} is directly related to the directivity by combining (11.9) with (11.13):

$$A_{\mathrm{e}} = \frac{\eta_0 \, W_{\mathrm{T}} \, \mathcal{M}^2 \, \mathcal{D}}{2\pi \, r^2 \, 16 W_{\mathrm{T}} \, \mathcal{P}^{(\mathrm{i})}} \,.$$

The far field Poynting vector $\mathcal{P}^{(\mathrm{i})}$ that the suitably oriented test source at distance r produces onto A is obtained by (3.26):

$$\mathcal{P}^{(\mathrm{i})} = \frac{1}{2\eta_0} \left| E^{(\mathrm{i})} \right|^2 = \frac{\eta_0 \, \mathcal{M}^2}{8 \lambda_0^2 \, r^2} \,,$$

whence

$$A_{\mathrm{e}} = \frac{\lambda_0^2}{4\pi} \, \mathcal{D} \,. \tag{11.23}$$

In the present context, the simplifying assumption made in Sect. 11.2.2 that the incident wave arrives from a direction perpendicular to the aperture plane $z' = 0$ can be relaxed. The relation (11.23) is then extended to any direction identified by the angles ϑ and φ shown in Fig. 11.5:

$$A_{\mathrm{e}}(\vartheta, \varphi) = \frac{\lambda_0^2}{4\pi} \, \mathcal{D}(\vartheta, \varphi) \,. \tag{11.24}$$

It is understood that the general relation (11.24) holds for any polarization of the incident field provided that the wave arrives from directions at small obliquity with respect to the z-axis (cf. Sect. 11.1).

Equation (11.24) expresses the basic property that the effective area of a receiving system is proportional to its directivity. Therefore, the directivity pattern shown in Fig. 11.5 represents also the effective area pattern of the receiving antenna.

[20] An exception is represented by the ionosphere at the lower microwave frequencies.

Reciprocally, the directivity of a transmitting system is proportional to its effective area, hence, given (11.21), to its geometric area A_g. For given aperture dimensions and efficiency, the directivity increases with the square of frequency. Therefore, when high directivity is required, aperture dimensions large with respect to wavelength are needed.

11.3 Directional Properties of Apertures

An Earth observing system generally *maps* the parameters of interest, that is, associates them with a geographic location. Geo-location requires that the system has a spatial discrimination capability, i.e., it is able to separate the information carried by waves coming from individual targets located in different geographic locations within the observed portion of terrestrial environment. Antennas and apertures are the interface between the system and the observed scenery. The dependence on the direction of observation of their radiating/receiving properties, expressed by the directivity function (11.8) or by the effective area (11.24), is the means to obtain *angular* discrimination.

Taking account of (11.24), the aperture sketched in Fig. 11.5 is able to collect power (11.22) mainly from a narrow solid angle around the *boresight* direction $\vartheta = \vartheta_M, \varphi = \varphi_M$ at which the directivity is maximum. It can be repeated that reciprocity relates the angular discrimination properties of receiving antennas to shape and width of their *virtual* radiation pattern. In active systems, the directional properties of apertures typically act twice, i.e., both in transmission, by concentrating the actually radiated power around the antenna boresight, and in reception, by capturing power mainly coming back from the boresight direction.

It is anticipated that angular discrimination can be physically performed by *real apertures* [96, Chap. 8], or can result from suitable processing of the received field, as in *synthetic apertures* [96, Chap. 9]. The synthesis technique, commonly employed in space[21] radar systems, since NASA's **Sea Sat**ellite (SEASAT) (1978, Fig. 11.9) [13], NASA's **S**huttle **I**maging **R**adar (SIR)-A (1982) [33] and ERS-1 (1991, Fig. 11.10) [94], has been extended to microwave passive interferometric sensors such as the ESA's **S**oil **M**oisture and **O**cean **S**alinity **M**ission (SMOS) (Fig. 11.11) [87].

[21] Airborne SARs have notoriously operated since several decades and systems are also in use on RPAPs.

Fig. 11.9 SeaSat, first open satellite SAR system: the *grey rectangular panel* in the forefront is the observing array-SAR antenna (cf. Fig. 11.4) (Credit: NASA/JPL)

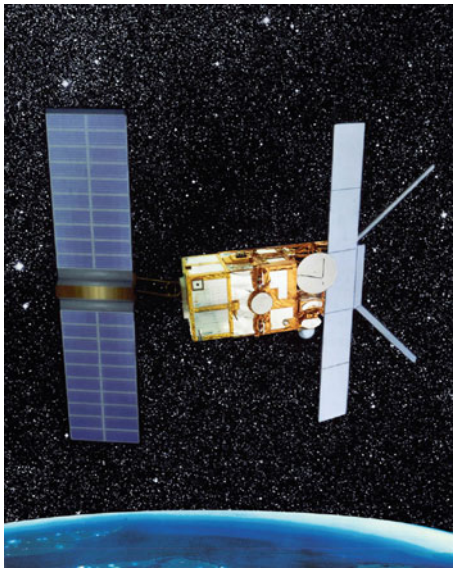

Fig. 11.10 ERS-1, first European Earth observing satellite carrying a SAR system; the *large grey panel* on the center-right of the image is the SAR antenna, while the smaller panels are antennas dedicated to scatterometric measurements (Credit: image, ESA; artwork, A. perrone, Tor Vergata University Earth Observation Laboratory)

Fig. 11.11 SMOS, European space borne interferometric-antenna L-band radiometer; the three elongated panels form the two-dimensional array interferometer (Credit: satellite image, ESA; artwork, A. Perrone, Tor Vergata University Earth Observation Laboratory)

11.3.1 Radiating/Receiving Angular Pattern

It is now clear that the radiating or receiving system, whatever its operating wavelength and internal structure, is fully characterized by the *external* field $\boldsymbol{E}_{\mathrm{T}} = E_{\mathrm{T}}\,\mathfrak{e}_{0\mathrm{T}}$ that the actual or virtual source creates on a surface which wraps the system itself. Since the external field is close to zero outside the geometric aperture A_{g} through which the radiated or captured wave has to pass, the main radiating/receiving features are determined by the field localized only over A_{g}. The relation of proportionality between directivity and effective area makes the angular features of the antenna indifferent to the function, transmitting or receiving, of the latter. It is understood that the radiating (and receiving) properties are still analyzed in the paraxial angular region.

The phase vector $\boldsymbol{\beta}$ of the wave radiated at far distance by the system through the aperture A_{g} is expanded in terms of its cartesian components by utilizing (A.10) with reference to Fig. A.3:

$$\boldsymbol{\beta} = \kappa_0 \mathbf{r}_0 = \kappa_0 (\sin\vartheta\cos\varphi\ \mathbf{x}_0 + \sin\vartheta\sin\varphi\ \mathbf{y}_0)\ ,$$

whence the radiation pattern (11.6) becomes

$$\begin{aligned}\mathcal{F}(\vartheta,\varphi) &= \frac{\mathrm{j}}{\lambda_0}\,\mathfrak{e}_{0\mathrm{T}} \iint_{A_\mathrm{g}} E_\mathrm{T}(\boldsymbol{r}')\,\mathrm{e}^{\mathrm{j}\kappa_0 \boldsymbol{r}'\cdot\mathbf{r}_0}\,\mathrm{d}S \\ &= \frac{\mathrm{j}}{\lambda_0}\,\mathfrak{e}_{0\mathrm{T}} \iint_{A_\mathrm{g}} E_\mathrm{T}(\boldsymbol{r}')\,\mathrm{e}^{\mathrm{j}\kappa_0(\sin\vartheta\cos\varphi\,x' + \sin\vartheta\sin\varphi\,y')}\mathrm{d}x'\,\mathrm{d}y' \,.\end{aligned} \tag{11.25}$$

It is worth pointing out that $\mathbf{r}_0$ indicates the direction toward which the antenna radiates, but, reciprocally, $-\mathbf{r}_0$ is also the direction from which the wave arrives when the system receives.

The reader should have been convinced that the mapping effectiveness of an Earth observing system is substantially affected by its angular discrimination capability, hence by the directional properties of the aperture it utilizes. The radiation pattern depends on shape and dimensions of A_g. Common aperture configurations are now examined with the intent of outlining their radiating/receiving characteristics, as well as of highlighting the role of the wavelength. To simplify the notations, the scalar case is considered.[22]

11.3.1.1 Angular Pattern of Circular Apertures

Circular apertures are employed by most optical sensors,[23] as well as by microwave radiometers that do not need asymmetric angular performances. The relevant geometry is reported in Fig. 11.12.

The antenna pattern (11.25) of a circular aperture of radius a in its scalar form is

$$\mathcal{F}(\vartheta,\varphi) = \frac{1}{\lambda_0}\int_0^a \int_0^{2\pi} E_\mathrm{T}(r',\psi')\,\mathrm{e}^{\mathrm{j}\boldsymbol{\beta}\cdot\boldsymbol{r}'}\,r'\,\mathrm{d}r'\,\mathrm{d}\psi' \,.$$

The field E_T on the aperture is usually independent of the angular position ψ', so that

$$\begin{aligned}&\mathcal{F}(\vartheta,\ \varphi) \\ &\quad= \frac{1}{\lambda_0}\int_0^a \int_0^{2\pi} E_\mathrm{T}(r')\,\mathrm{e}^{\mathrm{j}\kappa_0(\sin\vartheta\cos\varphi\ r'\cos\psi' + \sin\vartheta\sin\varphi\ r'\sin\psi')}\,r'\,\mathrm{d}r'\,\mathrm{d}\psi' \\ &\quad= \frac{1}{\lambda_0}\int_0^a \int_0^{2\pi} E_\mathrm{T}(r')\,\mathrm{e}^{\mathrm{j}\kappa_0 r'\sin\vartheta\ \cos(\varphi-\psi')}\,r'\,\mathrm{d}r'\,\mathrm{d}\psi' \,.\end{aligned}$$

[22] The imaginary unit factor in (11.25), which refers to the absolute phase of the field, is also disregarded.

[23] For the time being, receiving systems called *diffraction-limited* are considered; Sect. 11.4.2.2 looks at optical sensors with alternative properties.

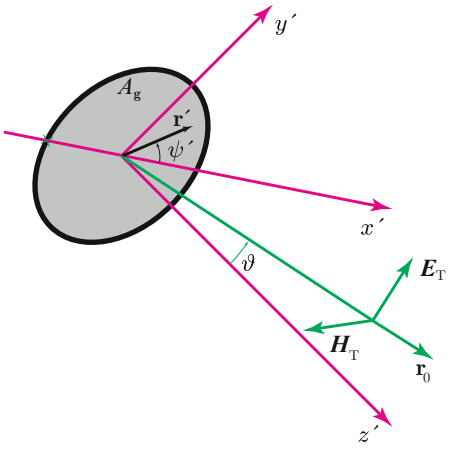

Fig. 11.12 Geometry of a circular aperture antenna transmitting the field $\boldsymbol{E}_T$, $\boldsymbol{H}_T$, assumed linearly polarized: the polar coordinates r', ψ' identify point $\boldsymbol{r}'$ in A_g

A result of the Bessel functions theory [1] is

$$\int_0^{2\pi} \mathrm{e}^{\mathrm{j}\kappa_0 r' \sin\vartheta \cos(\varphi - \psi')}\, \mathrm{d}\psi' = 2\pi\, \mathrm{J}_0(\kappa_0 r' \sin\vartheta)\ ,$$

where $\mathrm{J}_0(t)$ is the zero-order Bessel function of the first kind of argument t; therefore, the scalar radiation pattern is given by

$$\mathcal{F}(\vartheta,\varphi) \equiv \mathcal{F}(\vartheta) = \frac{2\pi}{\lambda_0} \int_0^a E_T(r')\, \mathrm{J}_0(\kappa_0 r' \sin\vartheta)\, r'\, \mathrm{d}r'\ .$$

As already done in Sect. 7.4.4, since the virtually transmitted field approximately vanishes outside the aperture, i.e., for $r' > a$, the limits of integration can be extended to infinity, by truncating E_T through multiplication by the rectangle function $\sqcap_a(r')$:

$$\mathcal{F}(\vartheta) \simeq \frac{2\pi}{\lambda_0} \int_0^\infty E_T(r')\ \sqcap_a(r')\, \mathrm{J}_0(\kappa_0 r' \sin\vartheta)\, r'\, \mathrm{d}r'\ . \tag{11.26}$$

Using a known transform result of Fourier optics [42], the transmitting/receiving pattern of a circular aperture is then proportional to the zero-order Hankel transform of the (truncated) field on the aperture. In the simple albeit important case the aperture has *uniform illumination*, E_T is constant and

$$\mathcal{F}(\vartheta) = \frac{\pi a^2}{\lambda_0} \frac{2\,\mathrm{J}_1(\kappa_0 a \sin\vartheta)}{\kappa_0 a \sin\vartheta} E_T\ .$$

The directivity function (11.8) of the circular aperture is then

$$\mathcal{D}(\vartheta) = \left[\kappa_0 a \frac{2\,\mathrm{J}_1(\kappa_0 a \sin\vartheta)}{\kappa_0 a \sin\vartheta}\right]^2 .$$

The function $\mathrm{Bs}(t) = 2\mathrm{J}_1(t)/t$ is known as the Besinc function: it has unit value for $t \equiv \kappa_0 a \sin\vartheta = 0$ and interposes nulls and secondary maxima which decrease with increasing argument t, i.e., with increasing angle ϑ between the direction $\mathbf{r}_0$ and the aperture axis $\mathbf{z}_0'$, clearly within the limits of validity of the paraxial approximation. Figure 11.13 shows the Besinc function squared, which is directly proportional to the directivity function of the circular aperture.

The corresponding effective area of the uniformly illuminated circular aperture in the paraxial region[24] given by (11.23) is

$$A_\mathrm{e} = \pi a^2 [\mathrm{Bs}(\kappa_0 a \sin\vartheta)]^2 .$$

The paraxial effective area of an axially symmetric system with circular aperture is symmetric around the aperture axis, that is, the power received from a given direction depends only on the angle between the considered direction and that of the aperture axis, regarded as the *pointing direction*. The diagram of Fig. 11.13 shows that a large fraction of the power is received within the *main lobe* of the directivity pattern, i.e., when the waves come from angles ϑ from the pointing direction such that[25]

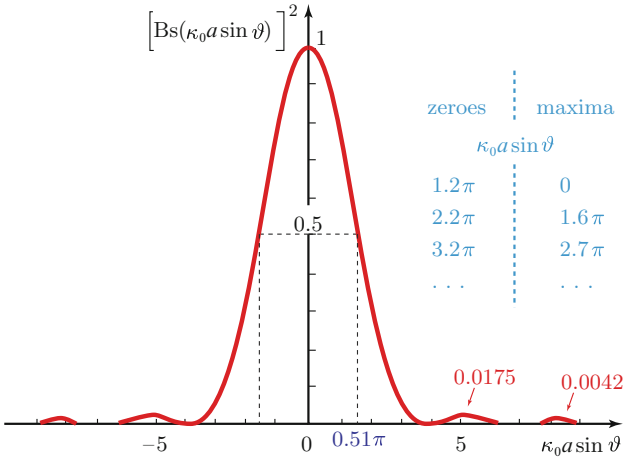

Fig. 11.13 Besinc function squared $[\mathrm{Bs}(t)]^2$, proportional to the effective area of a circular aperture, vs. argument $t \equiv \kappa_0 a \sin\vartheta$; the values of t corresponding to the first zeroes and maxima of the Besinc are reported, together with the value of t for which $[\mathrm{Bs}(t)]^2 = 0.5$ (half-power)

[24] This means that the incident waves arrive from a narrow angular range about the axis of the aperture.

[25] Note that different conventions can be adopted.

$$\sin|\vartheta| < \frac{0.51\pi}{\kappa_0 a} \approx 0.5\,\frac{\lambda_0}{2a}\,.$$

Observing systems use apertures that are large with respect to wavelength, i.e., $\lambda_0 \ll a$. Then $\sin|\vartheta| \approx |\vartheta|$ and the received power is considered to arrive indistinctly from directions contained within an angle of width $\Delta\vartheta \approx \lambda_0/(2a)$ around the pointing direction $\vartheta = 0$. Consequently, when the system observes the earth surface from distance R, a transverse dimension D_g of the order of

$$D_\mathrm{g} \approx R\,\frac{\lambda_0}{2a} \tag{11.27}$$

is attributed to the portion of surface altogether contributing the instantaneous received power. The dimension D_g is the width of the *footprint* of the antenna, that is, of the intersection of its main lobe with the earth surface. Equation (11.27) points out that, for a given distance, the dimension of the footprint is determined by the ratio of the wavelength to the aperture diameter.[26] Short wavelengths and large apertures are required to obtain small footprints. The relative power received from different directions by a circular aperture is visualized by the central bright circle and weaker concentric rings shown in Fig. 11.14.

The transverse dimension of the observed area on Earth is of paramount importance inasmuch D_g determines the *spatial resolution* of the observingsystem.

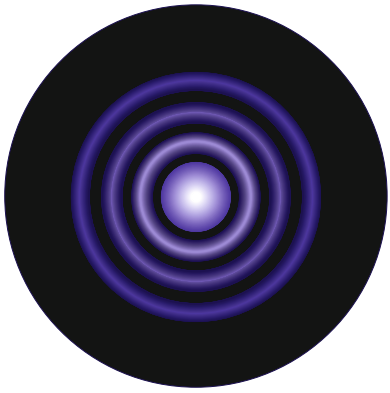

Fig. 11.14 Visualization of power received from different directions by a diffraction-limited circular aperture: the *inner bright circle* corresponds to the antenna footprint on a plane surface perpendicular to the axis; compression of central brightness was necessary to handle the high dynamics (cf. Fig. 11.13) (From [14])

[26] As said, in case of optical sensors the result holds for diffraction-limited systems.

It means that the volume originating, through scattering or emission, the power received by the sensor is delimited by a transverse surface the dimension of which is D_g. This concept was introduced in Sect. 7.4.4 and is visualised by Fig. 7.28. The spatial resolution (11.27) depends on the width of the main lobe, i.e., on the antenna *angular resolution*[27]

$$\vartheta_{dl} := \frac{\lambda_0}{2a} \tag{11.28}$$

of the diffraction-limited sensor[28] and on the distance R from which it is observing the extended surface. As an example, an aperture diameter of the order $2a \approx 1\,\text{m}$, yields an order of magnitude $\vartheta_{dl} \approx 10^{-6}\,\text{rad}$ of the angular resolution at "optical" wavelengths (say $\lambda_0 \approx 1\,\mu\text{m}$). If the sensor is observing the Earth from a distance $R \approx 10^6\,\text{m}$, the linear spatial resolution is of the order $D_g \approx 1\,\text{m}$. Instead, the order of magnitude of the spatial resolution would be $D_g \approx 10\,\text{km}$ at microwaves (say $\lambda_0 = 10^{-2}\,\text{m}$).

Note that the shape of the footprint is not circular, even for a flat surface, when observations are carried out on locally slant directions.

11.3.1.1.1 Angular Pattern of Elliptic Apertures

The radiation pattern of elliptic apertures is axially asymmetric, which may meet particular requirements in slant observations. The pattern $\mathcal{F}_{ell}$ of a uniformly illuminated elliptic aperture of semiaxes having lengths a and b, along x' and y' respectively, and such that $a = C\,b$, is obtained by integration over the elliptic domain A_{ell}

$$\mathcal{F}_{ell}(\vartheta, \varphi) = \frac{E_T}{\lambda_0} \iint_{A_{ell}} e^{j(\beta_x x' + \beta_y y')}\, dx'\, dy' .$$

The transformation of the x-coordinate into $\xi = (1/C)\,x'$ transforms the elliptic integration domain into a circle of radius b. The radiation pattern is then simply obtained by integration with respect to the transformed variables over the circular domain A_{cir}

$$\mathcal{F}_{ell}(\vartheta, \varphi) = \frac{E_T}{\lambda_0} \iint_{A_{cir}} e^{j[\beta_x (C\xi) + \beta_y y']}\, d(C\xi)\, dy' ,$$

[27] Also called *antenna beam width*.

[28] The subscript $_{dl}$ is suitable to distinguish the diffraction-limited angular resolution considered here from the optics-limited field of view outlined in Sect. 11.4.2.2.

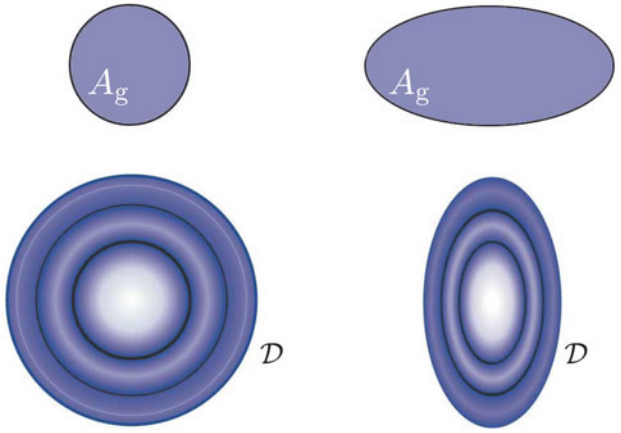

Fig. 11.15 Comparison between angular patterns $\mathcal{D}$ of diffraction-limited circular and elliptic apertures; note the inverse relation between aperture dimension (*top*) and pattern width (*bottom*) (From [14])

whence the paraxial antenna pattern is such that

$$\mathcal{F}_{\text{ell}}(\vartheta, \varphi) \equiv \mathcal{F}_{\text{ell}}(\beta_x, \beta_y) = C\, \mathcal{F}_{\text{cir}}[(C\, \beta_x), \beta_y] \; . \tag{11.29}$$

Equation (11.29) points out that when a circular aperture is uniformly stretched or shrank with ratio $C : 1$ in a given direction, the radiation pattern respectively shrinks or stretches in the same direction with ratio $1 : C$. The sketches of Fig. 11.15 visualize the inverse relation between angular width of the radiation pattern and width of the radiating aperture. As usual, the results hold both for reception and for transmission.

11.3.1.2 Angular Pattern of Rectangular Apertures

Given their peculiar system specifications, synthetic aperture radar antennas have different dimensions in two perpendicular directions, for instance, in the horizontal and vertical planes. Indeed, the array technology makes relatively straightforward the assembly of planar antennas with rectangular shape, as shown in Fig. 11.4. Reference is made to Fig. 11.16 for the analysis of the angular pattern of a rectangular aperture.

The scalar antenna pattern derived from (11.25) is now

$$\mathcal{F}(\vartheta, \varphi) = \frac{1}{\lambda_0} \int_{-a}^{a} \int_{-b}^{b} E_{\text{T}}(x', y') \; \mathrm{e}^{\mathrm{j}(\beta_x x' \, + \, \beta_y y')} \; \mathrm{d}y' \, \mathrm{d}x' \; .$$

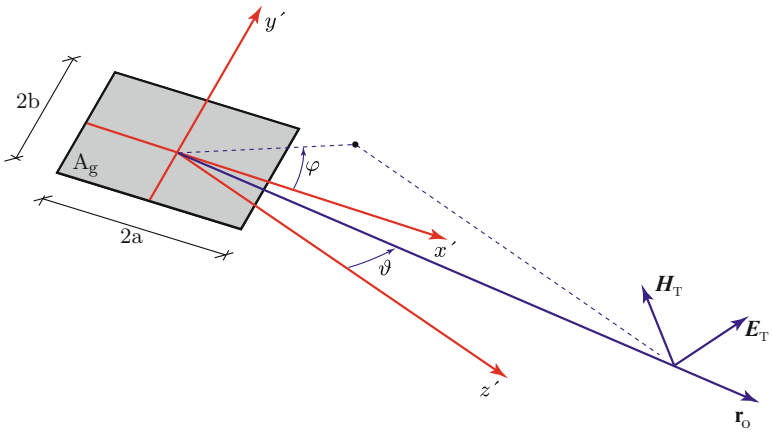

Fig. 11.16 Rectangular antenna aperture of dimensions $2a \times 2b$ on the $(x'y')$-plane, coordinate systems and external field $\boldsymbol{E}_\mathrm{T}$, $\boldsymbol{H}_\mathrm{T}$, assumed linearly polarized, transmitted in the direction $\mathbf{r}_0(\vartheta, \varphi)$

Noting again that the transmitted field almost vanishes outside the aperture, the limits of integration can be extended to infinity, provided E_T is truncated by multiplying it by the two-dimensional separable rectangle function $\square_{a,b}$ [17]

$$E_\mathrm{T}^{\square}(x', y') = E_\mathrm{T}(x', y') \times \square_{a,b}(x', y') = E_\mathrm{T}(x', y') \times \sqcap_a(x') \times \sqcap_b(y') \,,$$

so that

$$\mathcal{F}(\vartheta, \varphi) \simeq \frac{1}{\lambda_0} \int_{-\infty}^{\infty} \int_{-\infty}^{\infty} E_\mathrm{T}(x', y') \sqcap_a(x') \sqcap_b(y') \, \mathrm{e}^{\mathrm{j}(\beta_x x' + \beta_y y')} \, \mathrm{d}y' \, \mathrm{d}x' \,. \tag{11.30}$$

Equation (11.30) indicates that the angular antenna pattern is proportional to the inverse two-dimensional Fourier transform of the product of the field E_T on the aperture by the rectangle truncation functions. This implies that the pattern is linearly related to the convolution of the inverse Fourier transforms, denoted by $\mathcal{F}^{-1}$, of field and rectangle functions. An external field E_T separable in the spatial domain over the aperture allows separability also in the angular domain. In the simple reference case of constant E_T, the antenna pattern is

$$\begin{aligned} \mathcal{F}(\vartheta, \varphi) &= \frac{E_\mathrm{T}}{\lambda_0} \mathcal{F}^{-1}[\square_{a,b}(x', y')] = \frac{E_\mathrm{T}}{\lambda_0} \mathcal{F}^{-1}[\sqcap_a(x') \sqcap_b(y')] \\ &= \frac{E_\mathrm{T}}{\lambda_0} \, 2a \, \mathrm{sinc}(t_x) \, 2b \, \mathrm{sinc}(t_y) \,, \end{aligned}$$

where the conjugate angular variables ($t_x \leftrightarrow x'$) in the "horizontal" and ($t_y \leftrightarrow y'$) in the "vertical" direction[29] are defined by

$$t_x := \kappa_0 a \sin\vartheta \cos\varphi; \qquad t_y := \kappa_0 b \sin\vartheta \sin\varphi$$

and the sinc function is known to be

$$\mathrm{sinc}(t) = (\sin t)/t \,.$$

The features of the separable antenna pattern are readily and effectively analyzed in the two *principal planes*, horizontal ($x'z'$) and vertical ($y'z'$). Apart from the factor $[(4ab)/\lambda_0]E_T$, the horizontal factor $\mathcal{F}_h$ of the paraxial pattern on the horizontal half-planes defined by $\varphi = 0, \varphi = \pi$, is

$$\mathcal{F}_h(\vartheta) = \frac{\sin(t_x)}{t_x} = \frac{\sin\left(\dfrac{2\pi a}{\lambda_0}\sin\vartheta\right)}{\dfrac{2\pi a}{\lambda_0}\sin\vartheta} = \mathrm{sinc}(t_x) \,.$$

The sinc function for the rectangular aperture, shown in Fig. 11.17, corresponds to the Besinc function previously found for the circular aperture and the square of which is represented in Fig. 11.13. Analogously to the circular aperture, the horizontal factor of the antenna pattern has an absolute maximum in the direction of the aperture axis ($\vartheta = 0$) and a series of nulls alternated with relative maxima, which decrease with increasing ϑ. The *main lobe* of the antenna pattern, within which a large part of the power is radiated or received,

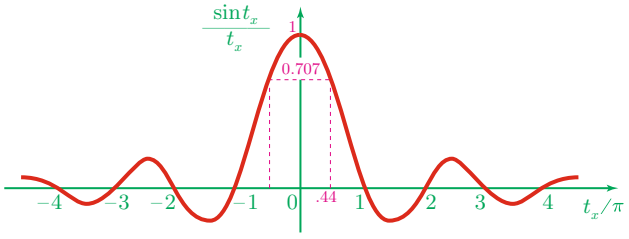

Fig. 11.17 The sinc function describes the field pattern of a uniformly illuminated rectangular antenna in a principal plane; the value of t_x for which $\mathrm{sinc}(t_x) = 0.707$ ("half power") is indicated

[29] As observed, identifying horizontal and vertical directions presupposes a target (e.g., Earth) reference.

is also bound by the angle at which the field pattern reduces to $1/\sqrt{2} \approx 0.707$ of the value in the axial direction, that is

$$\sin|\vartheta| < \frac{0.44\,\pi}{\kappa_0\, a} = 0.22\,\frac{\lambda_0}{a}\,.$$

Given the large dimensions of a satellite SAR antenna (say $2a \approx 10\,\mathrm{m}$), the wavelength $\lambda_0 \ll a$, so that $\sin|\vartheta| \approx |\vartheta|$. Then the transmitted or received power is considered to be concentrated within an angle of width

$$\Delta\vartheta \simeq \frac{0.88\,\lambda_0}{2a}$$

around the pointing direction $\vartheta = 0$ in the horizontal plane. Since suitable tapering of the transmitted field is demanded by secondary lobe reduction, with ensuing broadening of the pattern,[30] the width of the main lobe is commonly assumed to be

$$\vartheta_\mathrm{h} \simeq \frac{\lambda_0}{2a}\,, \tag{11.31}$$

as for the circular aperture. The width of the footprint in the horizontal plane is also clearly the same as (11.27), apart from the effect of the local incidence angle.

The behavior of the pattern in the vertical half-planes, identified by $\varphi = \pi/2$ and $\varphi = (3/2)\pi$, is analogous. The vertical factor is

$$\mathcal{F}_\mathrm{v}(\vartheta) = \frac{\sin(t_\mathrm{y})}{t_\mathrm{y}} = \frac{\sin\left(\dfrac{2\pi b}{\lambda_0}\sin\vartheta\right)}{\dfrac{2\pi b}{\lambda_0}\sin\vartheta} = \mathrm{sinc}(t_\mathrm{y})\,.$$

The vertical dimension b of the rectangular aperture now replaces the horizontal one a. Therefore, in particular, the beamwidth ϑ_v in the vertical plane is

$$\vartheta_\mathrm{v} \simeq \lambda_0/(2b)\,.$$

The field *diffraction pattern* of a uniformly illuminated rectangular aperture antenna of geometric area $A_\mathrm{g} = 2a \times 2b$ is finally obtained by combining the horizontal and vertical factors:

$$\mathcal{F}(\vartheta,\varphi) = \frac{A_\mathrm{g}}{\lambda_0}\,E_\mathrm{T}\,\frac{\sin(\kappa_0 a\ \sin\vartheta\cos\varphi)}{\kappa_0 a\ \sin\vartheta\cos\varphi}\,\frac{\sin(\kappa_0 b\ \sin\vartheta\sin\varphi)}{\kappa_0 b\ \sin\vartheta\sin\varphi}\,. \tag{11.32}$$

[30] Aperture field tapering entails $\eta_\mathrm{A} < 1$.

The power diffraction pattern of a rectangular aperture is visualized in Fig. 11.18. The diffraction pattern characteristic of rectangular apertures is actually observed in SAR images when the scene includes a small target having backscattering exceedingly high with respect to the scenery. Then also the footprints of the secondary lobes of the synthetic antenna angular pattern become visible against the low background. Figures 11.19 and 11.20 show examples of such occurrences.

The previous results highlight that the dimension of an aperture antenna with respect to the wavelength determines the angular beam width of the antenna and, consequently, the spatial discrimination capability of the observing system. High directivity, hence narrow beam width, which is crucial in Earth observation, demands large apertures and high frequencies. Rectangular apertures with *separable*

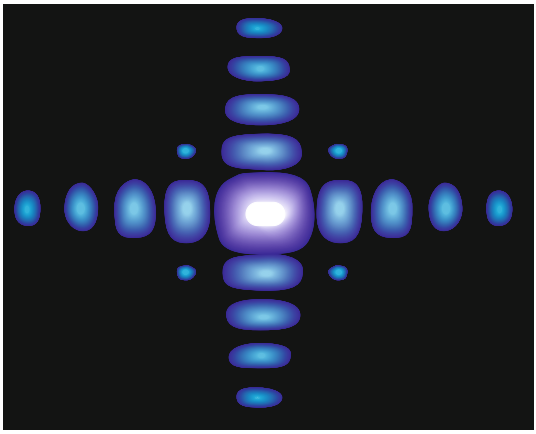

Fig. 11.18 Visualization of the power diffraction pattern of a rectangular aperture; the pattern compares with the one of the circular aperture of Fig. 11.14 (From [14])

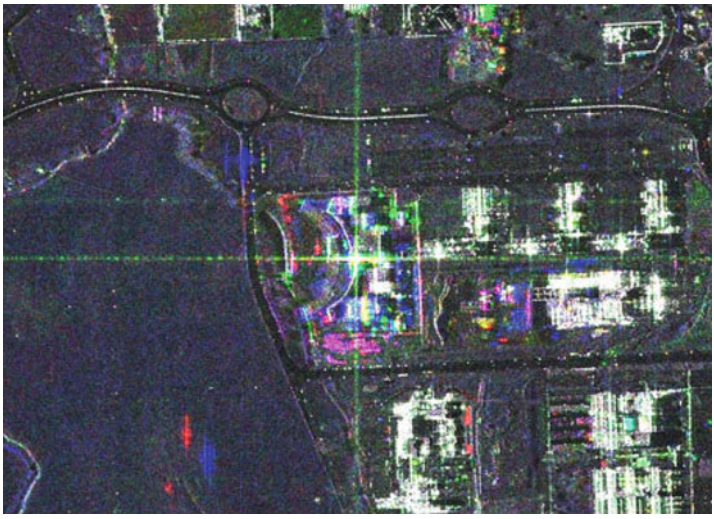

Fig. 11.19 Strong *flash-point* (Sect. 7.3.2) spread pattern in COSMO-SkyMed image of Tor Vergata University campus (Credit: data, ©ASI; multi-temporal processing, courtesy C. Solimini)

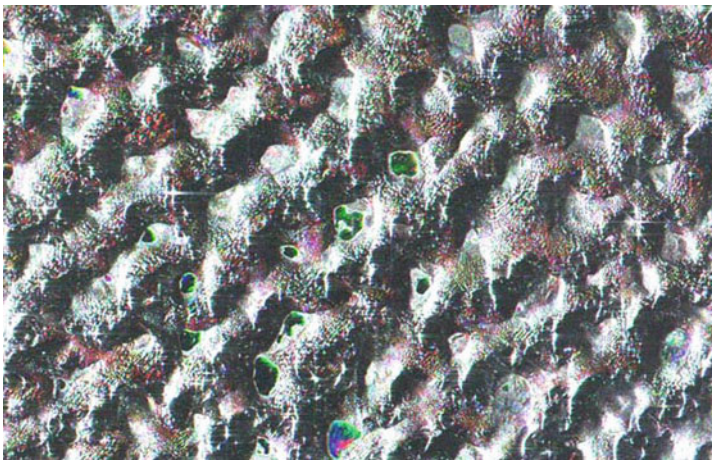

Fig. 11.20 Careful visual inspection reveals the presence of several small natural-surface point spread patterns in this ENVISAT ASAR image of Gobi Desert (Credit: data, ESA; multi-temporal processing, courtesy C. Solimini)

external field, have different beam widths controlled by the corresponding dimensions in two orthogonal planes, e.g., horizontal and vertical, and are suitable to meet the specifications of SAR systems.

11.4 The Role of Antennas and Apertures in Earth Observation

Antennas and apertures are crucial components of the remote sensing systems inasmuch their properties determine the observing capability in terms not only of the already discussed spatial discrimination, but also of exploitable signal.

11.4.1 Antennas and Surface Spatial Resolution

An image of the Earth's surface has been defined as a 2-dimensional representation, hence a *map*, of the scattering or emitting features of an actually 3-dimensional scenario. Passive systems distinguish each portion of the surface from the surrounding ones by exploiting the beam width of the receiving antenna, or the instantaneous field of view of the optical telescope, as outlined in Sect. 11.4.2.2. Correspondingly, the size of an element of the image, introduced in Sect. 10.2 as picture element or pixel, for space-borne instruments vary from tens of km (e.g., for the SMOS L-band radiometer) to hectometers as for MERIS or for the NASA's **Mod**erate-Resolution **I**magine Spectrometer (MODIS) [67], decameters

(LANDSAT) [61], and down to meters or less as is the case of DigitalGlobe Inc.'s **Q**uick**B**ird (QB) and WorldView [29].[31]

The spatial resolution is obviously enhanced when observations are carried out from aerial platforms [36, 105]. Indeed, the basic relation (11.27), together with (11.28) and (11.31), highlights that the pixel size[32] varies according to the height of the platform, wavelength of operation and, in particular, to the size of the system aperture. The contributions from portions of a pixel clearly cannot be singled out nor identified from a unique value of the received power, since the whole volume of the resolution cell (cf. Fig. 10.22) contributes W_r collectively. Figure 11.21 shows some of the geometric elements relevant to the observation of the surface from a circular-aperture system on a moving elevated platform, postponing further details to Fig. 11.27 and to Sect. 12.1.

When observing the surface, the power received at a given time is attributed to the volume V' located in the direction of the system boresight at that time. With particular reference to microwave or coherent-detection optical systems and to the

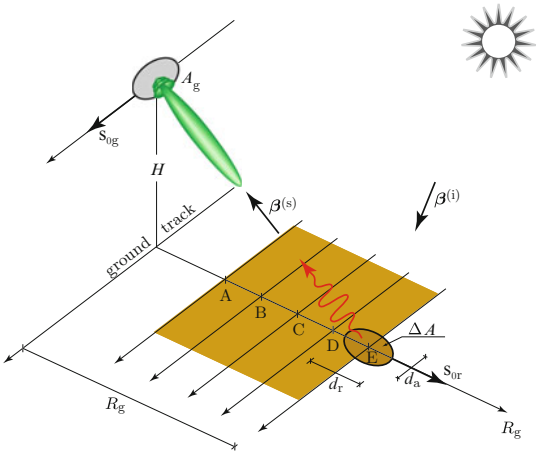

Fig. 11.21 A circular aperture A_g on a platform at height H collects the power scattered or emitted by the portion of earth environment identified by the footprint centered on point E; as the platform moves, the footprint travels in direction $\mathbf{s}_{0g}$ parallel to the ground track; a scanning system or a detector array allows to cover the *swath* A–E in the horizontal direction $s_{0r} \perp s_{0g}$, along which the ground distance R_g is measured. The instantaneous received power originates mainly from volume V' (cf. Fig. 10.22) delimited on the reference surface (e.g., horizontal plane) by ΔA

[31] Different (and possibly inconsistent) terms are found denoting spatial resolution. Just as an example, [108] use "coarse resolution" for pixels larger than 100 m, "medium" for dimensions between 10 and 100 m, and "high" for a resolution equal to or finer than 10 m, while [43] introduce the following nomenclature for TIR pixel size: "ultra-fine" resolution for pixel sizes of less than 1 m, "very fine" fo sizes of 1–5 m, "fine" for 5–15 m, "medium" for 15–100 m, and "coarse resolution" for pixel sizes greater than 100 m.

[32] **G**round-**R**esolved **D**istance (GRD) is an alternative parameter frequently used.

results of Sect. 11.3.1.1, the dimensions of the area ΔA bordering V' (cf. Fig. 11.27) are:

- *along the track*, $d_a = \vartheta_{dl} R$, as in (11.27), if R is the distance of the platform from the earth surface in the direction of observation $-\mathbf{s}_0$ and ϑ_{dl} is the diffraction-limited beamwidth (11.28) of the aperture;
- in the *ground range* across the track, the transverse dimension d_r of the volume in the direction $\mathbf{s}_{0r} \perp \mathbf{s}_{0g}$ in the horizontal plane depends not only on the beamwidth ϑ_{dl}, but also on the angle between $-\mathbf{s}_0$ and the *local vertical* direction $\mathbf{z}_0$.

Section 11.4.2.2 shows that analogous relations hold for incoherent-detection systems, with the beamwidth replaced by the IFOV angle ϑ_{if}. The extension to apertures having different beamwidths in the horizontal and vertical planes is straightforward.

11.4.2 The Received Signal

It is now appropriate to focus onto the quantities that contain the target information and to highlight how the latter is affected by the radiating properties of the observing system.

We know that both the magnitude and the phase of the field that is received by the sensor when the axis z' of its aperture[33] is oriented along $-\mathbf{s}_0$ represent *signals*, inasmuch they carry information on the portion V' of the terrestrial environment observed in that direction. The elementary power dW_r captured by an aperture having effective area A_e is given by (11.22):

$$dW_r = A_e \, d\mathcal{P}^{(i)} ,$$

where $d\mathcal{P}^{(i)}$ is the elementary areic power[34] incoming from the direction $-\mathbf{s}_0$ of the target in the geometry adopted in Sect. 9.3.1, and the effective area refers to that direction. The power density $d\mathcal{P}^{(i)}$ reaching the sensor follows from the interaction of the electromagnetic field with the materials present in the volume V' of the observed target, hence, as outlined in Sect. 10.1.3, it is originated by

- a scattering[35] process, in case the Sun or a radar transmitter are utilized as *primary* source,
- or an emission process when spontaneous thermal radiation is measured.

[33] The aperture axis is understood to coincide with the pointing direction of the beam.

[34] To simplify the notations, average is not indicated, but it is implied when measuring solar radiation or the Earth's thermal emission.

[35] Reflection can be considered a particular (coherent) case of scattering.

The *oriented* elementary surface power density of a quasi-monochromatic wave traveling in direction $\mathbf{s}_0$ from V' towards the sensor is expressed in terms of the spectral radiance by (9.19)

$$\mathrm{d}\boldsymbol{\mathcal{P}}(\mathbf{s}_0) = \mathcal{I}_\lambda(\mathbf{s}_0)\,\mathrm{d}\Omega\,\mathrm{d}\lambda\;\mathbf{s}_0\;.$$

The elementary power captured by the antenna pointing in the direction $-\boldsymbol{s}_o$ is then proportional to the spectral radiance in the direction $\mathbf{s}_0$:

$$\mathrm{d}W_\mathrm{r}(-\mathbf{s}_0) = A_\mathrm{e}(\lambda, -\mathbf{s}_0)\,\mathrm{d}\mathcal{P}(\mathbf{s}_0) = A_\mathrm{e}(-\mathbf{s}_0)\mathcal{I}_\lambda(\mathbf{s}_0)\,\mathrm{d}\Omega\,\mathrm{d}\lambda\;.$$

The total power received by the observing system derives from the contributions from the various directions, taking into account the bandwidth of the receiving channel and, especially at microwaves, the field polarization (cf. Sect. 11.2.2).

Within this general frame, the features of the signal are peculiar to the kinds of sensors and of observation techniques.

11.4.2.1 Signal in Passive Microwave Observation of the Surface

Observation of thermal emission is characterized by *incoherency* between fields arriving from different directions $-\mathbf{s}_0(\vartheta, \varphi)$ and in different spectral intervals. Therefore, the power received by a radiometric channel of bandwidth $\Delta\lambda = \lambda_2 - \lambda_1$ is

$$W_\mathrm{r} = \int_{\lambda_1}^{\lambda_2}\iint_\Omega A_\mathrm{e}(\lambda, -\mathbf{s}_0)\,\mathcal{I}_\lambda(\mathbf{s}_0)\,\mathrm{d}\Omega\;\mathrm{d}\lambda\;. \tag{11.33}$$

In case no contribution comes from outside the terrestrial environment, the angular integration is limited to the solid angle $\Omega = \Omega_\mathrm{E}$ under which the Earth is seen from the sensor.

The area ΔA of the portion of the Earth's surface observable at a given time (Fig. 11.21) is determined by the dimension (11.27) of the antenna footprint. To attain the required spatial resolution and signal-to-noise ratio, radiometric antennas need high values of their directivity pattern in a narrow angular range around the boresight direction $\vartheta = 0$ and low values at wider angles. With reference to the circular aperture diffraction-limited pattern modeled in Sect. 11.3.1.1, a common assumption is

$$A_\mathrm{e}(\vartheta) = A_\mathrm{M} \quad \text{for } \vartheta < \frac{\vartheta_\mathrm{dl}}{2}; \qquad A_\mathrm{e}(\vartheta) = 0 \quad \text{for } \vartheta > \frac{\vartheta_\mathrm{dl}}{2}\,. \tag{11.34}$$

In the narrow angular range $0 \le \vartheta < \vartheta_\mathrm{dl}/2$, the spectral radiance is reasonably assumed independent of direction, i.e.,

$$\mathcal{I}_\lambda(\vartheta, \varphi) \approx \mathcal{I}_{\lambda\mathrm{M}}\;,$$

so that the power W_r captured by the circular radiometric antenna per unit bandwidth is

$$W_\mathrm{r} \simeq 2\pi A_\mathrm{M} \mathcal{I}_{\lambda\mathrm{M}} \int_0^{\vartheta_\mathrm{dl}/2} \sin\vartheta \, \mathrm{d}\vartheta = 2\pi A_\mathrm{M} \mathcal{I}_{\lambda\mathrm{M}} \left[1 - \cos(\vartheta_\mathrm{dl}/2)\right] .$$

The narrow beam width allows $\cos(\vartheta_\mathrm{dl})$ to be approximated by its truncated McLaurin expansion

$$\cos(\vartheta_\mathrm{dl}) \simeq 1 - \frac{\vartheta_\mathrm{dl}^2}{8} ,$$

so that

$$W_\mathrm{r} \simeq \frac{\pi}{4} A_\mathrm{M} \mathcal{I}_{\lambda\mathrm{M}} \vartheta_\mathrm{dl}^2 ,$$

or, by expressing the boresight effective area A_M in terms of the antenna gain $\mathcal{D}_\mathrm{M}$,

$$W_\mathrm{r} \simeq \frac{C_p}{16} \lambda_0^2 \mathcal{D}_\mathrm{M} \mathcal{I}_{\lambda\mathrm{M}} \vartheta_\mathrm{dl}^2 .$$

The factor C_p accounts for the polarization response of the radiometric system. Given the commonly used approximate relation between gain and beam width (in radians) of high-directivity antennas,

$$\mathcal{D}_\mathrm{M} \vartheta_\mathrm{dl}^2 \approx 16 ,$$

the received power is suitably given by

$$W_\mathrm{r} \simeq C_p \lambda_0^2 \mathcal{I}_{\lambda\mathrm{M}} . \tag{11.35}$$

Equation (11.35) expresses the expected and quite useful result that the captured power is proportional though the square of the wavelength to the spectral radiance in the direction of the antenna boresight. The radiance at the sensor location is related to the radiance upwelling at the surface level by the basic relation (9.40):

$$\mathcal{I}_{\lambda\mathrm{M}} = \mathcal{I}_{\lambda\mathrm{M}}(0) \, \mathrm{e}^{-\tau_\mathrm{a}} + \mathcal{I}_{\lambda\mathrm{Ma}} , \tag{11.36}$$

where $\mathcal{I}_{\lambda\mathrm{M}}(0)$ is the spectral radiance at the surface level containing the information on the observed spatial resolution cell, $\mathrm{e}^{-\tau_\mathrm{a}} \equiv \mathcal{T}_\mathrm{a}$ is the atmospheric transmissivity and $\mathcal{I}_{\lambda\mathrm{Ma}}$ is the spectral radiance added by emission and scattering from the interfering atmosphere in the direction of observation $\mathbf{s}_{0\mathrm{M}}$, which coincides with the antenna boresight. Therefore, within the approximation (11.34), the received power (11.36),

$$W_{\mathrm{r}} \simeq C_p\,\lambda_0^2\,[\mathcal{I}_{\lambda\mathrm{M}}(0) + \mathcal{A}_{\mathrm{a}}\,\mathcal{I}_{\lambda\mathrm{Ma}}]\,\mathcal{T}_{\mathrm{a}} = W_{\mathrm{rs}} + W_{\mathrm{ra}} \tag{11.37}$$

consists of the power W_{rs} arriving from the resolution cell observed on the surface of the Earth and of the contribution W_{ra} coming from the crossed atmosphere. The information on the surface is contained in $\mathcal{I}_{\lambda\mathrm{M}}(0)$, the measurement of which is corrupted by the atmospheric radiance $\mathcal{I}_{\lambda\mathrm{Ma}}$ amplified by the the attenuation $\mathcal{A}_{\mathrm{a}} \geq 1$ of the atmosphere interposed between the ground and the sensor. Equation (11.37) confirms that the observation of the surface is hampered by the atmosphere, the noxious effect of which is clearly enhanced by increasing attenuation.

Moreover, albeit small, $A_{\mathrm{e}}(\vartheta) \neq 0$ for $\vartheta > \vartheta_{\mathrm{dl}}/2$. Consequently, *stray-radiation* power W_{sl} is received also through the side lobes, hence coming from zones of the surface outside the resolution cell at which the antenna aims its boresight. The power W_{sl}, which depends on the *antenna beam efficiency* $\eta_{\mathrm{B}} < 1$ [95, Chap. 4], adds as noise, just like W_{ra}. Further noise power W_{N}, including thermal noise, is expected to originate from the system hardware itself and by the processing chain.

To sum up, the power W_{rs} which carries the useful information on the observed portion of surface, i.e., the signal, is given comprehensively by

$$W_{\mathrm{rs}} = W_{\mathrm{r}} - W_{\mathrm{ra}} - W_{\mathrm{sl}} - W_{\mathrm{N}}\ .$$

The stray-radiation power and the system noise add to the atmospheric interference in increasing the overall noise, while, given (11.37), the attenuation, which, because of reciprocity (cf. Sect. 9.2) is in general correlated positively with the radiance of atmospheric origin, plays a crucial role in reducing the measurement signal-to-noise ratio.

The spectral radiance $\mathcal{I}_{\lambda\mathrm{M}}(0)$ of the surface resolution cell singled out by the pointing direction of the radiometer antenna depends on the emissivity e_{S} and temperature T_{S} of the surface[36] according to (8.38) and (8.39):

$$\mathcal{I}_{\lambda\mathrm{M}}(0) = e_{\mathrm{S}}\,\mathcal{B}(\lambda, T_{\mathrm{S}}) \simeq e_{\mathrm{S}}\,\frac{2c_0 k\,T_{\mathrm{S}}}{\lambda_0^4}\ ,$$

whence the radiometric signal is

$$W_{\mathrm{rs}}(\lambda) \simeq C_p\,e_{\mathrm{S}}\,\frac{2c_0 k\,T_{\mathrm{S}}}{\lambda_0^2}\,\mathcal{T}_{\mathrm{a}}\ .$$

In terms of frequency (cf. Sect. 8.2.2.1),

$$W_{\mathrm{rs}}(f) \simeq 2C_p\,e_{\mathrm{S}}\,k\,T_{\mathrm{S}}\,\mathcal{T}_{\mathrm{a}}\ .$$

[36] It should be remembered that the emissivity depends on polarization according to the basic results throughout Chap. 8, and that usually T_{S} is an equivalent temperature.

It is customary to refer the received power to the *antenna temperature* T_A introduced by

$$W_r := \Delta f \, k \, T_A \, ,$$

where Δf if the frequency bandwidth of the receiving channel. The *signal temperature* T_{AS} expresses the contribution per unit bandwidth from the surface at temperature T_S:

$$T_{AS} := e_S \, T_S \, \mathcal{T}_a \, .$$

In the ideal case of unit emissivity and no atmospheric extinction,

$$T_{AS} \equiv T_S \, ,$$

i.e., the signal antenna temperature coincides with the temperature of the observed element of surface. The contributions to the received power are frequently expressed in terms of brightness temperature (8.40) in place of spectral radiance:

- the interfering power contributed by the atmosphere is expressed in terms of the *atmospheric brightness temperature* T_{Ba};
- the power received through the antenna side lobes is expressed in terms of the *off-boresight brightness temperature* T_{Bsl};
- analogously, the noise power is expressed though a *noise temperature* T_N.

The signal temperature T_{AS} is then derived from the measured antenna temperature T_A by

$$T_{AS} = e_S \, T_S \, \mathcal{T}_a = T_A - T_{Ba} - T_{Bsl} - T_N \, . \tag{11.38}$$

Equation (11.38) once again points out the need to account for the detrimental effects of atmospheric extinction, beam efficiency and system noise when interpreting the radiometric data.

11.4.2.2 Signal in Passive Optical Observation

Apart from particular systems with interferometric configuration such as SMOS, the field incident onto the *elements of the aperture* of a microwave antenna adds in phase in the focal point to form the total field that is then detected to yield the received signal. In common optical systems, the detector that converts the arriving radiation into the electric signal has a distributed structure and, if the system does not include coherent (heterodyne) detection [85], the *elements of the detector* act independently in converting the field collected by the aperture into elementary signals that add *irrespective of their phase* to yield the total received signal. With reference to the reciprocity-based approach of Sect. 11.2, the external field $\boldsymbol{E}_T$ in microwave

antennas is originated by a single virtual *point source* located in the *focal point* of the system, whereas, in optical systems the external field must be regarded as the superposition of the fields contributed *incoherently* by the elements of a virtual *extended source* distributed in the *focal plane*.[37]

This substantial structural difference constrains the microwave systems to operate in a *diffraction-limited* mode, so that their receiving pattern is determined by the radiating properties of the antenna aperture, in particular, by the wavelength-to-dimension ratio. Instead, the receiving properties of incoherent-detection optical systems are affected by the size of the individual detecting element and by the system focal length, the ratio of which limits[38] the **i**nstantaneous **f**ield **o**f **v**iew (IFOV), defined as the angle through which the individual detector is sensitive to radiation [79, Chap. 4]. As a consequence, the effective area of an *optics-limited* system is independent of the attainable spatial resolution: for given spectral radiance, the received power can be varied by varying the aperture dimension, irrespective of the angular resolution, which is set by the *linear* IFOV angle ϑ_{if}, determined by the optics. As outlined in Sect. 11.2.2.1, the effective area of an optical telescope is close to that of a uniformly illuminated circular aperture and, if the system does not include heterodyne detection or polarizing components, it is independent of polarization.

The basic expression (11.33) of the incoherent power captured by an aperture

$$W_{\mathrm{r}} = \int_{\lambda_1}^{\lambda_2} \int_0^{\frac{\pi}{2}} \int_0^{2\pi} A_{\mathrm{e}}(\lambda, \vartheta, \varphi)\, \mathcal{I}_{\lambda}(\lambda, \vartheta, \varphi)\, \sin\vartheta \, \mathrm{d}\varphi \, \mathrm{d}\vartheta \, \mathrm{d}\lambda$$

is simplified, as in the previous Sect. 11.4.2.1, under the assumption that

$$A_{\mathrm{e}}(\lambda, \vartheta, \varphi) \equiv A_{\mathrm{e}}(\lambda, \vartheta) = \mathcal{T}(\lambda) A_{\mathrm{g}} \quad \text{for } \vartheta < \frac{\vartheta_{\mathrm{if}}}{2}; \quad A_{\mathrm{e}}(\lambda, \vartheta) = 0 \quad \text{for } \vartheta > \frac{\vartheta_{\mathrm{if}}}{2},$$

where $A_{\mathrm{g}} = \pi a^2$ is the geometric area of the circular aperture of radius a and $\mathcal{T}(\lambda)$ accounts for the instrument spectral response. By assuming the constant spectral radiance $\mathcal{I}_{\lambda \mathrm{M}}$ in the boresight direction, i.e., in the narrow angular range $0 \leq \vartheta < \vartheta_{\mathrm{if}}/2$, the power reaching the individual sensor in a given spectral channel is

$$W_{\mathrm{r}} \simeq \pi A_{\mathrm{g}}\, \mathcal{T}(\lambda_{\mathrm{c}})\, \mathcal{I}_{\lambda \mathrm{M}}(\lambda_{\mathrm{c}})\, \vartheta_{\mathrm{if}}^2 \,, \tag{11.39}$$

where $\mathcal{T}(\lambda_{\mathrm{c}})$ is the channel spectral response[39] referred to a suitable "central" wavelength λ_{c}. The presence of the geometric aperture area A_{g} in (11.39) sets the

[37] The reciprocity approach replaces receiving devices with virtually transmitting ones, keeping phase features.

[38] In practice, the IFOV angle is generally determined by the *field stops* forming the instrument optics.

[39] The effective area A_{e} includes the spectral response for each instrument channel "centred" on λ_{c}.

difference of receiving behavior between the present optics-limited systems and the diffraction-limited ones, which capture power according to (11.35).

11.4.2.2.1 Observation in the Visible/NIR

The basic relation (9.40) and its outcome (11.36) clearly hold for the spectral radiance $\mathcal{I}_{\lambda\mathrm{M}}$ at the sensor location in the wavelength range from visible to near infrared. According to (9.48), the information is now embedded in the solar radiance "reflected" by the surface

$$\mathcal{I}_{\lambda\mathrm{M}}(0) = \mathcal{R}_\lambda \, \mathcal{I}_\lambda^{\odot}(0) \; ,$$

which is interfered by the radiance $\mathcal{I}_{\lambda\mathrm{Ma}}$ originated by the atmospheric scattering of the solar radiation into the aperture boresight[40] direction. The power (11.39) received in the spectral channel centered about λ_c,

$$W_\mathrm{r} = \pi \, A_\mathrm{g} \, \mathcal{T}(\lambda_\mathrm{c}) \, \vartheta_\mathrm{if}^2 \, \mathcal{R}_\lambda \, \mathcal{I}_\lambda^{\odot}(0) \, \mathcal{T}_\mathrm{a} + W_\mathrm{N} = W_\mathrm{rs} + W_\mathrm{N} \; ,$$

consists of the signal power W_rs carrying information on the spectral reflectivity $\mathcal{R}_\lambda$ of the resolution cell singled out by the *solid-angle* IFOV of the optics, and of a noise term W_N including interfering scattered solar radiation and overall system noise. The received power must by cleared of the noise to exploit the useful signal W_rs.

11.4.2.2.2 Observation in the TIR

Following Sect. 9.3.2, the boresight spectral radiance $\mathcal{I}_{\lambda\mathrm{M}}$ at the sensor location is now related to the spectral emissivity $e_{\lambda\mathrm{S}}$ (8.38) and temperature T_S of the surface by

$$\mathcal{I}_{\lambda\mathrm{M}} = e_{\lambda\mathrm{S}} \, \mathcal{B}_\mathrm{S}(T_\mathrm{S}) \, \mathcal{T}_\mathrm{a} + \mathcal{I}_{\lambda\mathrm{Ma}} \; .$$

The transmissivity $\mathcal{T}_\mathrm{a}$ in the frequently encountered non-scattering case depends on the absorption by the atmospheric constituent gases and suspended *small* particles, while the interfering radiance $\mathcal{I}_{\lambda\mathrm{Ma}}$ is reciprocally contributed by the thermal emission along the atmospheric path (cf. Sect. 9.3.2). Therefore, the part of received power which carries information on the features of the surface observed in a TIR channel centered on λ_c is given by

$$W_\mathrm{rs} = \pi \, A_\mathrm{g} \, \mathcal{T}(\lambda_\mathrm{c}) \, \vartheta_\mathrm{if}^2 \, e_{\lambda\mathrm{S}} \, \mathcal{B}_\mathrm{S}(T_\mathrm{S}) \, \mathcal{T}_\mathrm{a} = W_\mathrm{r} - W_\mathrm{N} \; .$$

[40] As usual, the aperture boresight is assumed to be the system pointing direction.

11.4.3 Radar Observation

Radars were originally devised to *detect* objects [41, 104] of *limited* dimensions, typically aircrafts and ships, and to obtain some information on them, by capturing the part of scattered electromagnetic power forming the *echo*. The measured quantities regarded essentially distance, obtained from the time interval between the transmission of the signal and the arrival of the echo, and radial velocity, estimated from the Doppler frequency shift (3.19). The radar operation soon reached out *mapping* [3] of *large* targets. Discrimination between scattering from different portions of the observed scenario, attained by jointly exploiting time of arrival and Doppler features, led to SAR systems [54], for which relative *radial* motion between platform and elements of extended objects is needed.

It is the peculiar capability of measuring distance that adds crucial value to active systems inasmuch they reckon with the third dimension of the terrestrial environment. Mapping targets in 3-D is directly based on comparing the returned wave against the transmitted one in the time domain. Moreover, information on the third dimension can be retrieved effectively from the relations of phase of the field sampled in different radar positions, i.e., in the space domain. SAR interferometry [9] is based on this feature.

11.4.3.1 Basic Radar Operation

For a first understanding of basic radar operation [89, 90], reference is made to Fig. 11.22. The wave radiated by the radar that impinges on the far object is locally plane and carries an areic power given by (3.37), taking definition (11.8) into account:

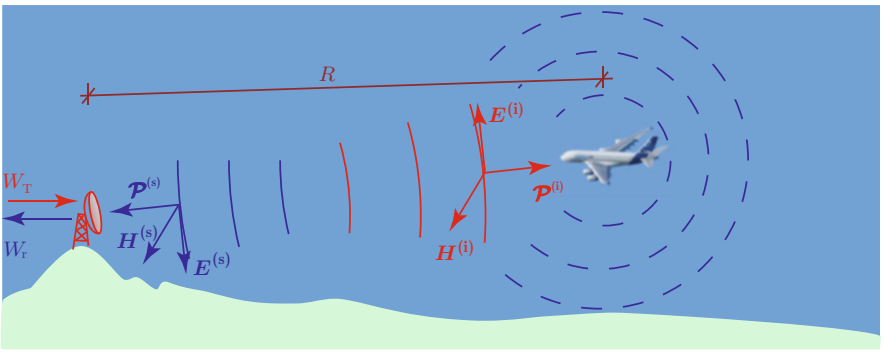

Fig. 11.22 In common ground-based radar applications, e.g., air traffic control, the system transmits the power W_T. The radiated wave travels in the atmosphere and hits an object (the aircraft) at distance R; the wave returned by scattering from the target originates the *echo*, characterized by the received power W_r

$$\mathcal{P}^{(\mathrm{i})} = \frac{\mathcal{D}_{\mathrm{M}}\, W_{\mathrm{T}}}{4\pi R^2}\, \mathrm{e}^{\,-2\int_0^R \alpha_{\mathrm{e}}(f,s)\, ds} \,. \tag{11.40}$$

The power density (11.40) is expressed in terms of the radar antenna gain[41] $\mathcal{D}_{\mathrm{M}}$ defined in Sect. 11.1, of the transmitted power W_{T} and of the distance R of the target from the radar, taking also account of the atmospheric extinction α_{e} introduced in Sect. 9.2. Negligible atmospheric scattering allows use of absorption (5.39) in place of extinction. Scattering from the materials forming the object occurs according to the properties of the bistatic scattering cross-section $\sigma(\mathbf{r}_0^{(\mathrm{i})}, \mathbf{r}_0^{(\mathrm{s})})$ outlined in Sect. 7.2. In particular, the angular power density $\mathcal{P}^{(\mathrm{s})}$ leaving the target in the backward direction is obtained by definition (7.17):

$$\mathcal{P}^{(\mathrm{s})}(\mathbf{r}_0^{(\mathrm{i})}, -\mathbf{r}_0^{(\mathrm{i})}) = \frac{\sigma_{\mathrm{b}}(\mathbf{r}_0^{(\mathrm{i})})\mathcal{P}^{(\mathrm{i})}}{4\pi} \,.$$

The backscattered wave coming back to the radar antenna carries a surface power density

$$\mathcal{P}^{(\mathrm{s})} = \frac{\sigma_{\mathrm{b}}(\mathbf{r}_0^{(\mathrm{i})})\, \mathcal{P}^{(\mathrm{i})}}{4\pi R^2}\, \mathrm{e}^{\,-2\int_0^R \alpha_{\mathrm{e}}(\lambda_0,s)\, ds} \,,$$

which, by substituting (11.40) for $\mathcal{P}^{(\mathrm{i})}$, is

$$\mathcal{P}^{(\mathrm{s})} = \frac{\mathcal{D}_{\mathrm{M}}\, W_{\mathrm{T}}\, \sigma_{\mathrm{b}}}{(4\pi R^2)^2}\, \mathrm{e}^{\,-4\int_0^R \alpha_{\mathrm{e}}(\lambda_0,s)\, ds} \,.$$

The basic model of radar signal assumes that the backscattered wave is monochromatic and comes from a single direction, the one in which the target is being observed by the system. This assumption translates into modeling the spectral radiance as an impulse function[42] both in angle and in frequency, so that (11.33) reduces to (11.22). Then the radar antenna in receive mode captures the power

$$W_{\mathrm{r}} = A_{\mathrm{e}}\mathcal{P}^{(\mathrm{s})} = \frac{A_{\mathrm{e}}\, \mathcal{D}_{\mathrm{M}}\, \sigma_{\mathrm{b}}}{(4\pi R^2)^2}\, W_{\mathrm{T}}\, \mathrm{e}^{\,-4\int_0^R \alpha_{\mathrm{e}}(\lambda_0,s)\, ds} \,.$$

Use of the relation (11.23) between gain and effective area yields the alternative expression

[41] The target is assumed to be in the direction of the antenna boresight.

[42] Accurate analysis actually requires considering the *point spreead function* [12, 34] of the system.

$$W_{\mathrm{r}} = \frac{\eta_{\mathrm{A}}^2 A_{\mathrm{g}}^2 \sigma_{\mathrm{b}}}{4\pi \lambda_0^2 R^4} W_{\mathrm{T}} \, \mathrm{e}^{-4\int_0^R \alpha_{\mathrm{e}}(\lambda_0, s)\, ds}, \tag{11.41}$$

which highlights the role of the antenna dimensions and of the wavelength.

The received power W_{r} forms the echo of the target, the backscattering properties of which are represented by its cross-section σ_{b}. Equation (11.41) is the *basic radar equation*. It points out the heavy effects of the distance and of the atmospheric attenuation on the received power: the *signal* received by far, say at $R \approx 10^2$ km, scatterers is quite low, hence, measuring σ_{b} with adequate signal-to-noise ratio calls for operation in atmospheric windows, high peak power, large and efficient antennas, advanced receivers and sophisticated signal processing.

The radio-frequency source is replaced by an optical one in lidar observations [47, 83, 103], without formal modification of the radar equation.

11.4.3.2 Radar Mapping

When the target is an *extended object*, purpose of the observation is clearly not the measure of the backscattering cross-section it presents globally, rather, the determination of its *local* scattering features, from which information on its detailed structure can be retrieved. A suggestive example of target mapping is the radar image of the orbiting ENVISAT satellite shown in Fig. 11.23.

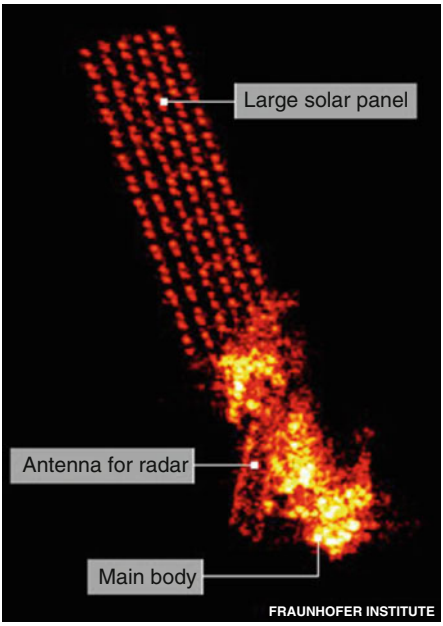

Fig. 11.23 Radar image of the orbiting ENVISAT satellite (Image credit: Fraunhofer Institute)

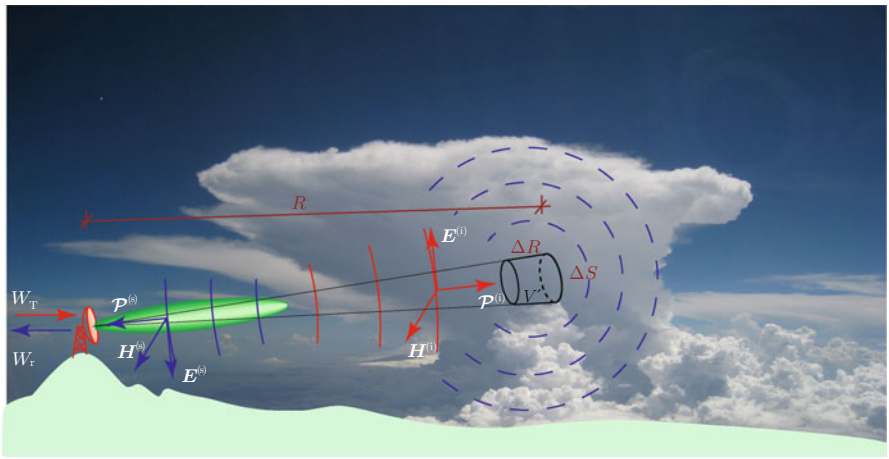

Fig. 11.24 A meteorological radar observing a precipitating cloud: the system identifies the resolution cell V' from which the received power W_r originates

To further clarify radar imaging and to extend the concept to the three-dimensional case, reference is made to a meteorological radar [2] that *maps* the precipitating cloud of Fig. 11.24 by sampling its local scattering. Differently from the conventional radar detection of a single isolated object such as an aircraft, mapping requires that the power scattered by a portion of the target be discriminated in the three dimensions against that coming from adjacent portions. Space discrimination is accomplished in 3-D by

- *angular localization* associated both with the pointing direction of the antenna and with its beam width ϑ_A (11.28);
- *range localization* based on the time of arrival Δt of the echo and on the radar *pulse duration* τ_p.

The *angular positions* of two cloud portions appear distinct[43] if the scattered fields which reach the radar antenna come from directions at an angular distance $\vartheta_2 - \vartheta_1$ such that

$$\vartheta_2 - \vartheta_1 > \vartheta_A \simeq \frac{\lambda_0}{D_A} ,$$

where D_A is the dimension of the antenna aperture. In turn, the locations of two cloud portions appear *distinct in range* if the times Δt_1 and Δt_2 at which two echoes arrive are such that

[43] Different angular discrimination criteria may be found.

$$\Delta t_2 - \Delta t_1 > \frac{\tau_p}{2} \cdot$$

The sample at time t_0 of the incoming scattered power is attributed to the cloud volume $V' = \Delta S \, \Delta R$ having:

- transverse section of area

$$\Delta S \simeq \frac{\pi}{4} \vartheta_A^2 R^2$$

  around the time-varying *known*[44] direction $\mathbf{r}_0 \, [\vartheta(t_0), \, \varphi(t_0)]$ of the steered antenna beam axis;
- range interval

$$\Delta R = \frac{c_0 \, \tau_p}{2}$$

  around the distance

$$R = \frac{c_0 \, \Delta t}{2} \, , \tag{11.42}$$

  where the time of arrival Δt of the sampled echo power is counted from the time, say t_0, at which the pulse was transmitted.

All water or ice particles[45] present in the scattering cloud volume V' contribute indiscriminately to the received power, hence the positions of individual scatterers in V' cannot be singled out.

11.4.3.3 Radar Observation of Earth

Some space-based radar missions are dedicated to meteorological observations like in the previous example and as further discussed in Sect. 14.1.2, but the Earth's surface is the target for which radar mapping finds wide and numerous applications [50, 96, 97]. Satellite altimetry [10, 40, 72] maps the height of the Earth's surface with respect to the reference ellipsoid by estimating distance (11.42) from the measure of satellite-to-surface round-trip time. The basic topographic parameter is just one example of the wealth of information that a radar is able to gain, as outlined later in Sects. 14.1.2 and 14.2.2. To this end, the features of backscattering must be addressed.

[44] The radar system scans the region of atmosphere to be monitored by changing the direction of the antenna boresight with time, either mechanically or electrically, in a known fashion.

[45] Also aerosol particles in lidar observation.

When interest is in the *local* behavior of scattering, following the general approach of Sect. 7.1, the power scattered by the volume V' corresponding to a portion of the *reference* surface (e.g., cf. Fig. 10.22) must be discriminated against that coming from the volumes underneath adjacent areas. Discrimination is based on the antenna features and on the pulse duration just as before, with the suitable modification required by the two-dimensional nature of the surface. The received power is attributed to a volume delimited along the track (Fig. 11.21) by the horizontal width of the antenna main lobe, and longitudinally by the ground range set either by the main lobe or by the pulse duration and by the angle of incidence. The footprint is centered about the point of intersection of the antenna boresight with the earth surface. Figure 11.25 shows the relevant parameters involved in the surface observation from a space-based radar. The along-track dimension d_a of the ground resolution cell is[46]

$$d_\mathrm{a} \simeq \frac{\lambda_0}{2a} R \,, \tag{11.43}$$

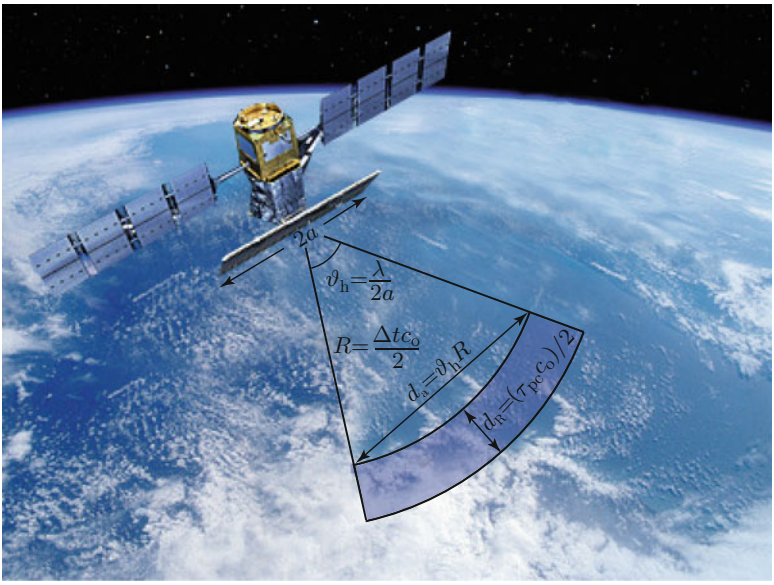

Fig. 11.25 Geometry of space-based radar observation of the surface with indication of the instantaneous footprint (*shaded area*) (Credit: satellite image, ASI; artwork by A. Perrone, Tor Vergata University Earth Observation Laboratory)

[46] Substantially analogous alternative definitions can be found.

while, given the antenna size and the distance, the dimension d_r in the *ground-range*[47] direction is related to the pulse duration τ_p by

$$d_r = \frac{c_0 \tau_p}{2 \sin \theta^{(i)}} \cdot$$

The available *pulse compression* techniques allow to achieve very short pulse durations, so that *ground range resolution* $d_r \lesssim 1\,\text{m}$ can be attained for usual incidence angles $\theta^{(i)}$. Instead, the obviously constrained dimensions of a space-borne antenna set a substantial limit to the along-track or *azimuth resolution*, typically $d_a \gtrsim 10\,\text{km}$ for observation from space,[48] as mentioned in Sect. 11.3.1.1.

Since decametric or even metric spatial resolution is needed by a majority of current environmental applications, an antenna that can be actually installed on a space platform is not able to meet the specifications. However, the *synthetic aperture* technology [25] provides the means of extending the width $2a$ of the *real antenna* far beyond its physical dimension by suitable processing. The synthesis is essentially modeled by the numerical integration of the received complex field[49] over a sufficiently long portion of orbit, so that the aperture A_g in (11.25) is streched in the horizontal direction. For instance, integration over an orbital segment a few kilometers long yields an along-track spatial resolution of the order of 1 m. Based on this technique, depicted in Fig. 11.26, space-based Synthetic Aperture Radars are able, at least in principle, to attain decimeter resolution.[50] Aperture synthesis overcomes the limit to the azimuth resolution set by the mechanical dimension of the real antenna and, together with pulse-compression technology, allows attaining dimensions of the pixel that are of the same order both in azimuth and in ground range. Figure 11.27 provides a further schematic view of the observation geometry together with indication of relevant parameters and of the used nomenclature.

11.4.3.4 SAR Observation of the Surface

The length L_S of the synthetic antenna is determined from (11.43) once the desired azimuth resolution d_a is specified [26]:

$$L_s = R \frac{\lambda_0}{d_a} \cdot$$

[47] The difference between ground range, that is along the reference earth surface, and slant range, i.e., along the satellite-to ground path, should be well kept in mind.

[48] The limitation in spatial resolution set by the distance R in (11.43) is clearly mitigated when the observations are carried out from aerial platforms.

[49] Practical reasons related to the processing time lead to a synthesis technique exploiting the Doppler frequency shift of the received scattered field.

[50] Enhanced spatial resolution may require particular observing techniques, such as the *spotlight* mode.

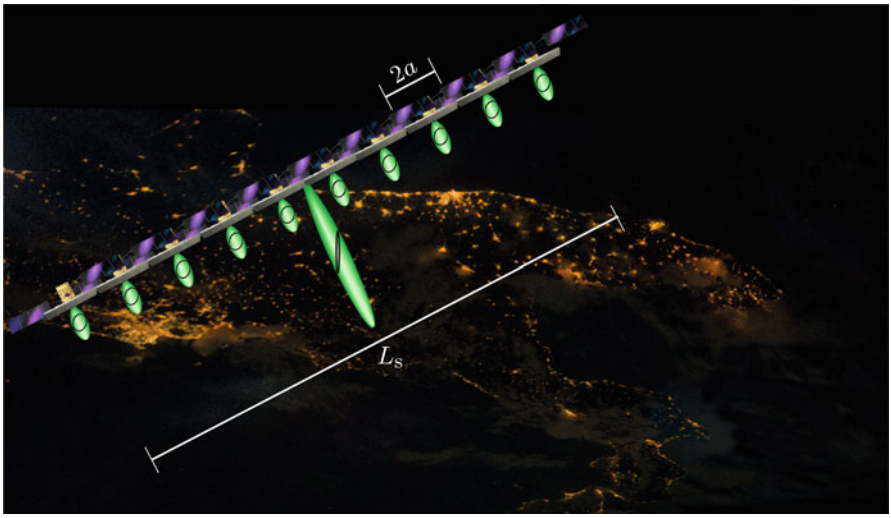

Fig. 11.26 Antenna azimuth synthesis exploiting the motion of the radar platform, here represented at sequential times, yields enhanced azimuth angular resolution, as suggested by the resulting *synthesized* radiation pattern (in the center) narrower in the horizontal plane than the individual antenna beams; $2a$ is the horizontal dimension of the real antenna, L_S is the length of the synthetic antenna (Credits: COSMO-SkyMed satellite, ASI; South Italy night image, NASA; artwork, A. Perrone, Tor Vergata University Earth Observation Laboratory)

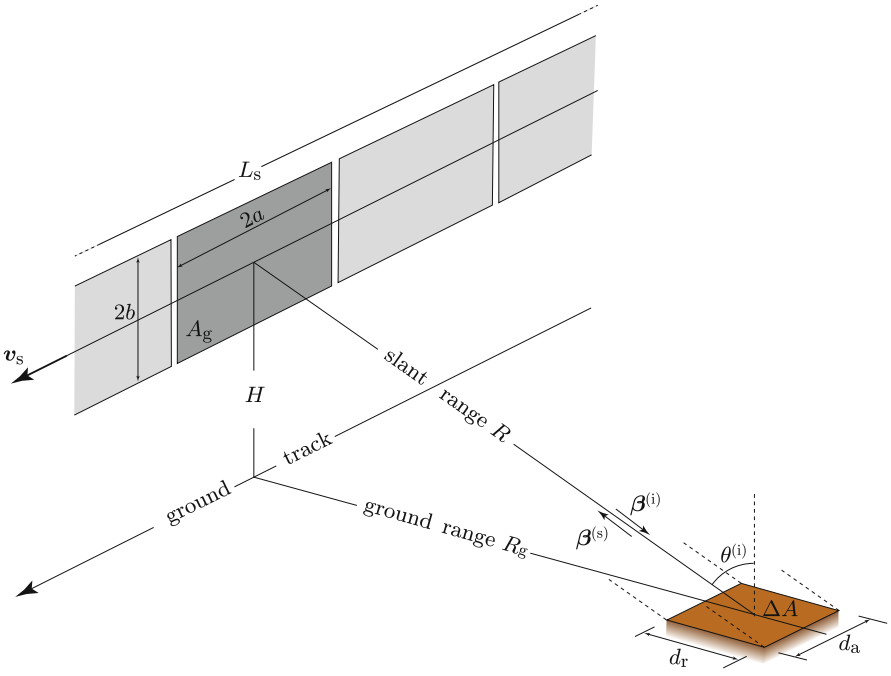

Fig. 11.27 SAR acquisition geometry, nomenclature, and scattering cell V' corresponding to a surface pixel S' of area ΔA (cf. Fig. 10.22) with horizontal dimensions in *azimuth* (d_a) and in *ground range* (d_r) determined by synthetic aperture length L_s and compressed pulse duration τ_{pc}, respectively

The satellite[51] traveling at speed v_s covers the orbit segment of length L_S in the *synthetic antenna time*

$$\Delta t_s = \frac{L_s}{v_s} \cdot$$

In this time, the radar operating at a **p**ulse **r**epetition **f**requency (PRF) f_{pr} transmits N_S pulses, where N_S is given by

$$N_s = f_{pr}\, \Delta t_s = f_{pr}\, \frac{L_s}{v_s} = f_{pr}\, \frac{\lambda_0}{d_a}\, \frac{R}{v_s} \cdot$$

By adding over N_S pulses the energy received from a given resolution cell for each transmitted pulse, an antenna of length L_S is *synthesized*, provided the system keeps track of the phase of the received field from pulse to pulse. Therefore, the primary output of the SAR processing chain consists of the synthesized power[52]

$$W_{rs} = N_s\, W_r = N_s\, \frac{\eta_A^2 A_g^2}{4\pi\, \lambda_0^2 R^4}\ \sigma_b\, W_T\ ,$$

where $\eta_A A_g = A_e$ is the effective area of the *real* satellite antenna and W_T is the power delivered by the radar transmitter. Thanks to the synthesis processing and pulse compression, the horizontal dimensions of the resolution cell originating the synthesized power W_{rs} are reduced to

$$d_a = \frac{\lambda_0}{L_s} R; \qquad d_r = \frac{c_0\, \tau_{pc}}{2} \csc \theta^{(i)}\ ,$$

where τ_{pc} is the duration of the compressed pulse. Note that, by decreasing the duration of the pulse, compression not only enhances the range resolution, but also increases the instantaneous radiated power

$$W_{Tc} = \frac{\tau_p}{\tau_{pc}}\, W_T\ ,$$

thus improving the signal-to-noise ratio. By substituting for N_S and accounting for the pulse compression, the synthesized received power becomes

$$W_{rs} = \frac{A_e^2}{4\pi\, \lambda_0\, R^3\, v_s\, \tau_{pc}\, d_a}\ \sigma_b\, \overline{W}_T\ ,$$

[51] The formalism is readily extended to airborne platforms.

[52] Atmospheric extinction is neglected here.

where $\overline{W}_{\mathrm{T}}$ denotes the power transmitted by the radar averaged over the synthetic aperture time. The backscattering cross-section σ_{b} of the observed resolution cell is related to its backscattering coefficient σ^0 by (7.22), so that the power received by the synthetic antenna is

$$W_{\mathrm{rs}} = \frac{A_{\mathrm{e}}^2 f}{8\pi R^3 v_{\mathrm{s}}} \csc\theta^{(\mathrm{i})}\, \sigma^0\, \overline{W}_{\mathrm{T}} \,. \tag{11.44}$$

Equation (11.44) refers to a surface pixel observed at local incidence angle $\theta^{(\mathrm{i})}$ by a SAR operating at frequency f. The increase of W_{rs} with decreasing incidence angle can be noted. The independence of the received power from the dimension of the pixel is only apparent, since $\overline{W}_{\mathrm{T}}$ is proportional to τ_{pc}, hence to d_{r} and, moreover, v_{s}^{-1} is proportional to L_{S}^{-1}, hence to d_{a}.

The SAR equation (11.44) relates the received signal to the backscattering properties of the terrestrial environment through a relation which differs from the "static" radar equation (11.41). Indeed, quantities that are peculiar to the aperture synthesis are involved, such as the motion of the radar platform, the speed of the latter, and the average power over the synthesis time.

Thanks to SAR, decametric-resolution radar images are commonly made available by public and commercial providers. *Spotlight* [19, 49] images are also commercially available down to 1 m resolution[53] and are possibly doomed to reach decimeters, as the security regulations are relaxed. From this point of view, the radar images are competitive to the optical images, which are publicly available at metric resolution, or even finer, especially in the panchromatic mode [29].

On their side, real-aperture microwave radiometric systems are not able to attain analogous performances regarding spatial resolution, given the feasible wavelength-to-dimension ratio, after all like real-aperture radars. The antenna synthesis [64, 65, 71, 81], is a key issue to boost the resolution of passive observations.

11.4.3.4.1 Antenna Elevation Synthesis

The motion of the radar platform along its orbit or flight path allows to synthesize the antenna in the *horizontal* direction, with corresponding enhancement of the *angular resolution in azimuth*. The satellite orbits being not exactly the same, repeated passes of the platform over a given area occur at slightly different heights. This feature offers the means of synthesizing the antenna in the *vertical* plane, to create enhanced *angular resolution in elevation* [76]. The antenna *elevation synthesis*, clearly less direct than the azimuth synthesis which is carried out over a single pass, is achieved by utilizing acquisitions at the times of the different passes. Figure 11.28 shows a sketch of the synthesis in elevation.

[53] The theoretical limit $d_{\mathrm{a}} = a$ (Fig. 11.27) is overcome by suitable synthesis processing.

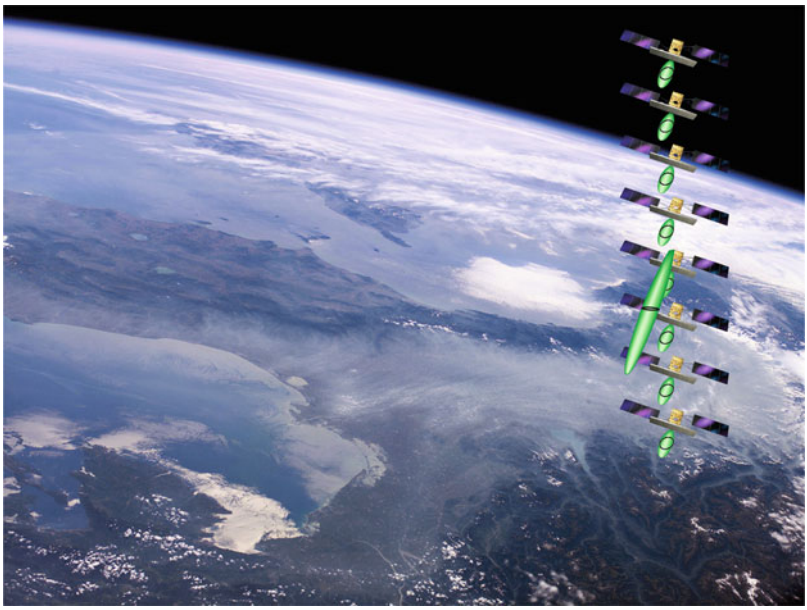

Fig. 11.28 Sketch of antenna elevation synthesis exploiting radar acquisitions by passes of the platform at different heights (Credits: COSMO satellite, ASI; northern and central Italy image, NASA; artwork, A. Perrone, Tor Vergata University Earth Observation Laboratory)

11.4.4 Lidar Observation

As noted in Sect. 10.2.5, remote sensing laser systems [66, 86] operate like radars in observing targets on the surface of the Earth [83, 106], in its atmosphere [48, 107] or in sea shallow waters [103]. They primarily measure the distance between the sensor and a reference location within the illuminated volume on land, water body or in the air. In surface observation, the output of the receiving chain provides maps of elevation, especially required in urban areas. By processing the amplitude of the echo waveform, range (e.g., vertical) profiles of backscattering intensity are also reconstructed, from which the mutual position and scattering properties of multiple objects are inferred. The structure of vegetation canopies and the profiles of atmospheric aerosols are suggestive examples of the information that is embedded in the *full-waveform* data of lidar returns. Lidar fluorescence spectra prove also useful in sensing parameters of interest of land, marine and atmospheric diverse environments [5, 20, 55], as outlined in Chap. 14.

Getting to the Heart of Observing Systems

A smattering of remote sensing systems helps us understanding many features of the Earth observation products a user may be dealing with. Indeed, issues like the spatial resolution at which the images are acquired or the change of their appearance at different polarizations are explained by resorting to the structure of the instrument, and, in particular, of its radiant element. So, matters like antennas and apertures, which only occasionally are part of the education of EO users, are introduced, even if just enough.

When radiation comes into play, the electromagnetic formalism pops out. We use transmission line concepts to express both the transmitted and the received power. Equivalence reduces the system to a diffracting aperture the radiating properties of which are described by the directivity function. Reciprocity provides us with a further powerful tool that relates the power captured by the system to its inner structure. Directivity function, gain and effective area are thus defined and related to a unique physical quantity, which, besides, explains the polarization-selective performance of polarimetric systems. We realize that it is not only the operation of active systems that is characterized by the radiating properties of the aperture, but also the receive-only passive systems behave according to their virtual radiant features. Therefore, the knowledge of the directional properties of the apertures is a key element for the comprehension of the EO products.

Active and passive systems are commonly equipped with circular or rectangular apertures. Specifying the radiation formalism to two-dimensional sources leads to the angular pattern for the shape at hand. Some analytical effort involving special functions reveals that circular diffraction-limited systems capture the power arriving within an angular range about the pointing direction. The angle beyond which the system loses sensitivity is directly proportional to the wavelength and inversely to the diameter of the aperture. The crucial aspect is that the angular discrimination determines the spatial resolution at which the system is able to observe the target from a given distance. We find that the rectangular apertures behave in an analogous fashion, with the dimensions of the sides in place of the diameter.

The role of antennas and apertures is then outlined, especially with regard to the spatial resolution attainable by the observing system. We are reminded that an image is the mapping of the result of an electromagnetic interaction with the terrestrial environment. The picture element is identified by the along-the-track and ground range coordinates, with the corresponding resolutions determined by the beam width of the real apertures in the horizontal and vertical planes. The directional properties of the radiating systems affect the signal-to-noise ratio of the measurement as well, both for microwave and for optical observations. We realize that aperture dimensions large with respect to wavelengths are ordinarily demanded by EO systems.

Radar sensing is worth a separate discussion. The particularity resides in the third dimension that active systems obtain directly by measuring time delays. The localization of the target is complete, since the angular localization, identified by

pointing direction and beam width of the antenna, is accompanied by the range localization, based on the measurement of the time at which the echo of the transmitted pulse arrives and on the duration of the latter. The phase-preserving capability of radar systems allows a further crucial advance: the angular resolution is enhanced through the implementation of synthetic antennas. Actually, it has to be added that some peculiar problems arise in mapping the Earth's surface by radar, not only because the effect of the pulse duration combines with the one of the incidence angle, but also because orography and range mix up in the measurements.

References

1. Abramowitz M, Stegun IA (2012) Handbook of mathematical functions: with formulas, graphs, and mathematical tables. Dover. ISBN:9780486158242
2. Atlas D (ed) (1990) Radar in meteorology. American Meteorological Society. ISBN:9780933876866
3. Ausherman DA, Kozma A, Walker JL, Jones HM, Poggio EC (1984) Developments in radar imaging. IEEE Trans Aerosp Electron Syst 20(4):363–400. doi:10.1109/TAES.1984.4502060
4. Baars JWM (2007) The paraboloidal reflector antenna in radio astronomy and communication: theory and practice. Springer. ISBN:9780387697345
5. Babichenko S, Poryvkina L, Arikese V, Kaitala S, Kuosa H (1993) Remote sensing of phytoplankton using laser-induced fluorescence. Remote Sens Environ 45(1):43–50. doi:10.1016/0034-4257(93)90080-H
6. Bakshi AV, Bakshi UA (2008) Transmission lines and waveguides. Technical Publications. ISBN:9788184314298
7. Balanis CA (2007) Antenna theory: analysis and design. Wiley. ISBN:9788126513932
8. Baltsavias EP (1999) Airborne laser scanning: basic relations and formulas. ISPRS J Photogramm Remote Sens 54(2–3):199–214. doi:http://dx.doi.org/10.1016/S0924-2716(99)00015-5
9. Bamler R, Hartl P (1998) Synthetic aperture radar interferometry. Inverse Probl 14(4):R1–R54. doi:10.1088/0266-5611/14/4/001
10. Basic Radar Altimetry Toolbox (BRAT). ESA. https://earth.esa.int/web/guest/software-tools/content/-/article/basic-radar-altimetry-toolbox-brat-5040. Visited on 31 Aug 2014
11. Bely PY (2003) The design and construction of large optical telescopes. Springer. ISBN:9780387955124
12. Bertero M, Boccacci P (1998) Introduction to inverse problems in imaging. CRC. ISBN:9781439822067
13. Born GH, Dunne JA, Lame DB (1979) Seasat mission overview. Science 204(4400):1405–1406. doi:10.1126/science.204.4400.1405
14. Born M, Wolf E, Bhatia AB (2002) Principles of optics: electromagnetic theory of propagation, interference and diffraction of light. Cambridge University Press. ISBN:9781139643405
15. Bracewell RN (1995) Two-dimensional imaging. Prentice Hall. ISBN:9780130626219
16. Bracewell RN (2000) The Fourier transform and its applications. McGraw-Hill. ISBN:9780073039381
17. Bracewell R (2003) Fourier analysis and imaging. Springer. ISBN:9780306481871
18. Capece P (2009) Active SAR antennas: design, development, and current programs. Int J Antennas Propag. Article ID 796064. doi:10.1155/2009/796064
19. Carrara WG, Goodman RS, Majewski RM (1995) Spotlight synthetic aperture radar: signal processing algorithms. Artech House. ISBN:9780890067284

20. Cecchi G, Pantani L, Raimondi V, Tomaselli L, Lamenti G, Tiano P, Chiari R (2000) Fluorescence lidar technique for the remote sensing of stone monuments. J Cult Herit 1(1):29–36. doi:10.1016/S1296-2074(99)00120-X
21. Chen CL (2006) Foundations for guided-wave optics. Wiley. ISBN:9780470042212
22. Cheo B (1965) A reciprocity theorem for electromagnetic fields with general time dependence. IEEE Trans Antennas Propag 13(2):278–284. doi:10.1109/TAP.1965.1138400
23. Collin RE (1991) Field theory of guided waves. IEEE. ISBN:9780198592136
24. Collin RE, Zucker FJ (1969) Antenna theory, Parts 1–2. McGraw-Hill. ISBN:9780070117990
25. Curlander JC, McDonough RN (1991) Synthetic aperture radar: systems and signal processing. Wiley. ISBN:9780471857709
26. Cutrona LJ (1970) Synthetic aperture radar. In: Skolnik MI (ed) Radar handbook. McGraw-Hill. ISBN:9780071485470
27. De Hoop AT (1968) A reciprocity relation between the transmitting and the receiving properties of an antenna. Appl Sci Res 19(1):90–96. doi:10.1007/BF00383914
28. de Hoop AT, de Jong G (1974) Power reciprocity in antenna theory. Proc Inst Electr Eng 121(10):1051–1056. doi:10.1049/piee.1974.0247
29. DigitalGlobe. http://www.digitalglobe.com/about-us/content-collection#overview;-https://www.digitalglobe.com/30cm/. Visited on 20 May 2015
30. Drabowitch S, Papiernik A, Griffiths H, Encinas J, Smith BL (2005) Modern antennas. Springer. ISBN:9781402032165
31. Dubois-Fernandez PC, Souyris J-C, Angelliaume S, Garestier F (2008) The compact polarimetry alternative for spaceborne SAR at low frequency. IEEE Trans Geosci Remote Sens 46(10):3208–3222. doi:10.1109/TGRS.2008.919143
32. Elachi C (1987) Spaceborne radar remote sensing: applications and techniques. IEEE. ISBN:9780879422417
33. Elachi C, Brown WE, Cimino JB, Dixon T, Evans DL, Ford JP, Saunders RS, Breed C, Masursky H, McCauley JF, Schaber G, Dellwig L, England A, MacDonald H, Martin-Kaye P, Sabins F (1982) Shuttle imaging radar experiment. Science 218(4576):996–1003. doi:10.1126/science. 218.4576.996
34. Ender JHG (2011) Introduction to radar – Part I. Ruhr-Universität Bochum, Scriptum of a Lecture. http://www.ei.rub.de/media/ei/lehrmaterialien/39/a715b063167d904ec4a9a5cea2a1a54d4defc115/RuhrUniScriptum.pdf. Visited on 04 July 2014
35. Estes JE (ed) (1983) Interpretation and applications, vol 2 of Manual of remote sensing Colwell RN (ed). American Society of Photogrammetry. ISBN:9780937294420
36. Everaerts J (2008) The use of unmanned aerial vehicles (UAVS) for remote sensing and mapping. In: The international archives of the photogrammetry, remote sensing and spatial information sciences, Beijing, vol XXXVII, pp 1187–1191
37. Fiorani L, Colao F (eds) (2008) Laser applications in environmental monitoring. Nova. ISBN:9781604562491
38. Fornaro G, Pascazio V (2013) SAR interferometry and tomography: theory and applications. In: Chellappa R, Theodoridis S (eds) Communications and radar signal processing. Academic press library in signal processing, vol 2. Academic. ISBN:9780123972248
39. Freeman A (1992) SAR calibration: an overview. IEEE Trans Geosci Remote Sens 30(6):1107–1121. doi:10.1109/36.193786
40. Fu LL, Cazenave A (2000) Satellite altimetry and Earth sciences: a handbook of techniques and applications. Elsevier. ISBN:9780080516585
41. Galati G (2015) 100 years of radar. Springer. ISBN:9783319005836
42. Goodman JW (2005) Introduction to Fourier optics. McGraw-Hill. ISBN:9780974707723
43. Handcock RN, Torgersen CE, Cherkauer KA, Gillespie AR, Tockner K, Faux RN, Tan J (2012) Thermal infrared remote sensing of water temperature in riverine landscapes. In: Carbonneau P, Piégay H (eds) Fluvial remote sensing for science and management. Wiley. ISBN:9781119940784
44. Hansen RC (2009) Phased array antennas. Wiley. ISBN:9780470529171

45. Harra LK, Mason KO (eds) (2004) Space science. Imperial College Press. ISBN:9781860943614
46. Hemmati H (ed) (2006) Deep space optical communications. Wiley. ISBN:9780470042403
47. Heritage G, Large A (2009) Laser scanning for the environmental sciences. Wiley. ISBN:9781444311945
48. Hinkley ED (1976) Laser monitoring of the atmosphere. Springer. ISBN:9783540077435
49. Jakowatz C Jr, Wahl D, Eichel P, Ghiglia D, Thompson P (1996) Spotlight-mode synthetic aperture radar: a signal processing approach. Kluwer. ISBN:9780792396772
50. Jin YQ, Xu F (2013) Polarimetric scattering and SAR information retrieval. Wiley. ISBN:9781118188163
51. Johnson RC, Jasik H (1993) Antenna engineering handbook. McGraw-Hill. ISBN:9780070323810
52. Kalmykov AI, Velichko SA, Tsymbal VN, Kuleshov Yu A, Weinman JA, Jurkevich I (1993) Observations of the marine environment from spaceborne side-looking real aperture radars. Remote Sens Environ 45(2):193–208. doi:10.1016/0034-4257(93)90042-V
53. Kerr Y, Waldteufel P, Wigneron J-P, Cabot F, Boutin J, Escorihuela M-J, Font J, Reul N, Gruhier C, Juglea S, Delwart S, Drinkwater M, Hahne A, Martin-Neira M, Mecklenburg S (2010) The SMOS mission: new tool for monitoring key elements of the global water cycle. Proc IEEE 98(5):666–687. doi:10.1109/JPROC.2010.2043032
54. Keydel W (2004) Present and future airborne and space-borne systems. NATO lecture series on radar polarimetry and interferometry RTO-EN-SET-081
55. Killinger DK, Menyuk N (1987) Laser remote sensing of the atmosphere. Science 235(4784):37–45. doi:10.1126/science.235.4784.37
56. Kingsley S, Quegan S (1999) Understanding radar systems. SciTech. ISBN:9781891121050
57. Ko HC (1962) On the reception of quasi-monochromatic, partially polarized radio waves. Proc IRE 50(9):1950–1957. doi:10.1109/JRPROC.1962.288174
58. Kovaly JJ (1976) Synthetic aperture radar. Artech House. ISBN:9780890060568
59. Kraus JD, Marhefka RJ (2002) Antennas for all applications. McGraw-Hill. ISBN:9780072321036
60. Kraus JD, Marhefka RJ, Khan AS (2006) Antennas and wave propagation. McGraw-Hill. ISBN:9780070671553
61. Landsat Science. NASA. http://landsat.gsfc.nasa.gov/. Visited on 07 Mar 2014
62. Ludwig A (1973) The definition of cross polarization. IEEE Trans Antennas Propag 21(1):116–119. doi:10.1109/TAP.1973.1140406
63. Marcuvitz N (1951) Waveguide handbook. McGraw-Hill. ISBN:9780863410581
64. Martín-Neira M, Goutoule JM (1997) A two-dimensional aperture-synthesis radiometer for soil moisture and ocean salinity observations. ESA Bull 92:95–104
65. Martín-Neira M, Menard Y, Goutoule J, Kraft U (1994) MIRAS, a two-dimensional aperture synthesis radiometer. In: Geoscience and remote sensing symposium, IGARSS'94. Surface and atmospheric remote sensing: technologies, data analysis and interpretation, international, vol 3, pp 1323–1325. doi:10.1109/IGARSS.1994.399429
66. Measures RM (1984) Laser remote sensing: fundamentals and applications. Wiley. ISBN:9780471081937
67. MODIS Web. NASA. http://modis.gsfc.nasa.gov/. Visited on 07 Mar 2014
68. Neiman MS (1943) The principle of reciprocity in antenna theory. Proc IRE 31(12):666–671. doi:10.1109/JRPROC.1943.233683
69. Nest – Next ESA SAR toolbox. ESA. https://earth.esa.int/web/nest/downloads. Visited on 14 Sept 2014
70. Nord ME, Ainsworth TL, Lee J-S, Stacy NJS (2009) Comparison of compact polarimetric synthetic aperture radar modes. IEEE Trans Geosci Remote Sens 47(1):174–188. doi:10.1109/TGRS.2008.2000925
71. Park H, Kim Y-H (2009) Microwave motion-induced synthetic aperture radiometer using sparse array. Radio Sci 44(3). doi:10.1029/2008RS003998

72. Radar Altimetry Tutorial. ESA. http://earth.eo.esa.int/brat/html/alti/welcome_en.html. Visited on 31 Aug 2014
73. Raimondi V, Cecchi G, Lognoli D, Palombi L, Grönlund R, Johansson A, Svanberg S, Barup K, Hällström J (2009) The fluorescence lidar technique for the remote sensing of photoautotrophic biodeteriogens in the outdoor cultural heritage: a decade of in situ experiments. Int Biodeterior Biodegrad 63(7):823–835. doi:10.1016/j.ibiod.2009.03.006
74. Ramo S, Whinnery JR, Van Duzer T (1965) Fields and waves in communication electronics. Wiley. ISBN:9780471585510
75. Raney RK (2007) Hybrid-polarity SAR architecture. IEEE Trans Geosci Remote Sens 45(11):3397–3404. doi:10.1109/TGRS.2007.895883
76. Reigber A, Moreira A (2000) First demonstration of airborne SAR tomography using multibaseline L-band data. IEEE Trans Geosci Remote Sens 38(5):2142–2152. doi:10.1109/36.868873
77. Richards JA (2009) Remote sensing with imaging radar. Springer. ISBN:9783642020209
78. Richards MA, Scheer JA, Holm WA (eds) (2010) Principles of modern radar: basic principles, vol 1. SciTech. ISBN:9781891121524
79. Robinson IS (2004) Measuring the oceans from space: the principles and methods of satellite oceanography. Springer. ISBN:9783540426479
80. Robinson JA, Amsbury DL, Liddle DA, Evans CA (2002) Astronaut-acquired orbital photographs as digital data for remote sensing: spatial resolution. Int J Remote Sens 23(20):4403–4438. doi:10.1080/01431160412331317775
81. Ruf CS, Swift CT, Tanner AB, Le Vine DM (1988) Interferometric synthetic aperture microwave radiometry for the remote sensing of the Earth. IEEE Trans Geosci Remote Sens 26(5):597–611. doi:10.1109/36.7685
82. Rusch WVT, Potter PD (1970) Analysis of reflector antennas. Academic. ISBN:9780126034509
83. Shan J, Toth CK (eds) (2008) Topographic laser ranging and scanning: principles and processing. Taylor & Francis. ISBN:9781420051438
84. Siegman AE (1967) A maximum-signal theorem for the spatially coherent detection of scattered radiation. IEEE Trans Antennas Propag 15(1):192–194. doi:10.1109/TAP.1967.1138845
85. Siegman AE (1966) The antenna properties of optical heterodyne receivers. Appl Opt 1(5):1588–1594. doi:10.1364/AO.5.001588
86. Siegman AE (1986) Lasers. University Science Books. ISBN:9780935702118
87. Silvestrin P, Berger M, Kerr YH, Font J (2001) ESA's second Earth explorer opportunity mission: the soil moisture and ocean salinity mission – SMOS. IEEE Geosci Remote Sens Soc Newsl 118. ISSN:0161–7869
88. Simonett DS, Colwell RN (eds) (1983) Manual of remote sensing, vol 1: theory, instruments and techniques. American Society of Photogrammetry. ISBN:9780937294413
89. Skolnik MI (2003) Introduction to radar systems. McGraw Hill. ISBN:9780070445338
90. Skolnik M (ed) (2008) Radar handbook. McGraw-Hill. ISBN:9780071485470
91. Smith GS (2004) A direct derivation of a single-antenna reciprocity relation for the time domain. IEEE Trans Antennas Propag 52(6):1568–1577. doi:10.1109/TAP.2004.830257
92. Souissi B, Ouarzeddine M, Belhadj-Aissa A (2012) Investigation of the capability of the compact polarimetry mode to reconstruct full polarimetry mode using RADARSAT2 data. Adv Electromagn 1(1). doi:10.7716/aem.v1i1.12
93. Steinberg BD (1976) Principles of aperture and array system design: including random and adaptive arrays. Wiley. ISBN:9780471821021
94. The ERS Satellites. Delft University of Technology, DEOS. http://www.deos.tudelft.nl/ers/ers1info.html. Visited on 06 Mar 2014
95. Ulaby FT, Moore RK, Fung AK (1981) Microwave remote sensing fundamentals and radiometry. Microwave remote sensing: active and passive, vol 1. Addison-Wesley. ISBN:9780890061909

96. Ulaby FT, Moore RK, Fung AK (1982) Radar remote sensing and surface scattering and emission theory. Microwave remote sensing: active and passive, vol 2. Addison-Wesley. ISBN:9780890061916
97. Ulaby FT, Moore RK, Fung AK (1986) From theory to applications. Microwave remote sensing: active and passive, vol 3. Artech House. ISBN:9780890061923
98. Urkowitz H, Hauer CA, Koval JF (1962) Generalized resolution in radar systems. Proc IRE 50(10):2093–2105. doi:10.1109/JRPROC.1962.288247
99. van Zyl JJ (2011) Synthetic aperture radar polarimetry. Wiley. ISBN:9781118116098
100. Visser HJ (2006) Array and phased array antenna basics. Wiley. ISBN:9780470871188
101. Waite AH, Schmidt SJ (1962) Gross errors in height indication from pulsed radar altimeters operating over thick ice or snow. Proc IRE 50(6):1515–1520. doi:10.1109/JRPROC.1962.288195
102. Wang CW, Keech T (2012) Antenna models for electromagnetic compatibility analyses. NTIA Technical Memorandum NTIA TM-13-489. http://www.ntia.doc.gov/files/ntia/publications/antenna_models_report_tm-13-489.pdf. Visited on 19 Feb 2014
103. Wang C-K, Philpot WD (2007) Using airborne bathymetric lidar to detect bottom type variation in shallow waters. Remote Sens Environ 106(1):123–135. doi:10.1016/j.rse.2006.08.003
104. Watson RC Jr (2009) Radar origins worldwide: history of its evolution in 13 nations through World War II. Trafford Publishing, UK. ISBN:9781426921117
105. Watts AC, Ambrosia VG, Hinkley EA (2012) Unmanned aircraft systems in remote sensing and scientific research: classification and considerations of use. Remote Sens 4(6):1671–1692. doi:10.3390/rs4061671, http://www.mdpi.com/2072-4292/4/6/1671
106. Wehr A, Lohr U (1999) Airborne laser scanning – an introduction and overview. ISPRS J Photogramm Remote Sens 54(2):68–82. doi:doi:10.1016/S0924-2716(99)00011-8
107. Weitkamp C (ed) (2005) Lidar: range-resolved optical remote sensing of the atmosphere. Springer. ISBN:9780387400754
108. Weng Q, Gamba P, Mountrakis G, Pesaresi M, Lu L, Kemper T, Heinzel J, Xian G, Jin H, Miyazaki H, Xu B, Quresh S, Keramitsoglou I, Ban Y, Esch T, Roth A, Elvidge CD (2014) Urban observing sensors. In: Weng Q (ed) Global urban monitoring and assessment through earth observation. CRC. ISBN:9781466564497
109. Wolff C (1996) Radartutorial.eu. http://www.radartutorial.eu/index.en.html. Visited on 10 Sept 2014

Chapter 12
Earth Surface Rendering from Images

It has been mentioned that an image of the surface of the Earth is a two-dimensional representation, i.e., a *map*, of a three-dimensional object. Each elementary portion (pixel) of the surface in the image is distinguished from the surrounding ones and is located, according to the features of the Earth observing system that produces the image.

Optical passive systems, which deliver maps of the scattered solar radiation, single out the pixels according to their IFOV (Sect. 11.4.2.2) and locate them in the direction at which the optics boresight aims at each acquisition time. Images from microwave radiometers, which exploit the radiation emitted by the terrestrial environment and operate on a diffraction-limited mode (Sect. 11.3.1.1), are produced in a generally analogous fashion, with spatial resolution related to the antenna beamwidth and pixel position identified by the direction of the boresight.

The images produced by the radar systems differ from those of the passive sensors. The spatial resolution in azimuth[1] still depends on the antenna beam width in the horizontal plane, but with the peculiar possibility of being enhanced by the aperture synthesis (Sect. 11.4.3.3). Instead, the difference is substantial in the ground range direction. In this direction the resolution is generally independent of the beam width in the vertical plane, because it is controlled by the duration of the radar pulse,[2] which can be made very short by the compression technique. But what especially distinguishes active system images from the passive ones is the modality of pixel identification and positioning in range. In fact, the position of a target is essentially related to the time of arrival of the echo, i.e., to the distance between platform and source of scattering, rather than to the instantaneous direction of the

[1]The azimuth direction is parallel to the line of flight indicated in Fig. 11.27.

[2]The antenna elevation synthesis mentioned in Sect. 11.4.3.4.1 is disregarded.

D. Solimini, *Understanding Earth Observation*, Remote Sensing
and Digital Image Processing 23, DOI 10.1007/978-3-319-25633-7_12

antenna boresight.[3] This feature makes the appearance of SAR images substantially different from that of the optical ones.

Analyzing the mechanisms that govern the generation of the images is necessary to understand the underlying features of the observed targets, as well as to counteract the noxious artifacts that the sensing system may possibly introduce into the representation of the various scenarios.

12.1 Range Positioning in Images of the Earth's Surface

Given the difference in the mechanisms yielding the geometric features of the images, the range positioning characteristics of passive systems are to be compared against those of the active ones. Special attention must be devoted to how the third dimension, i.e., the elevation, affects the position in range of pixels located at different heights with respect to the geodetic reference surface.

12.1.1 Range Positioning by Passive Systems

A passive system locates the center of a pixel at the intersection of the geodetic reference surface with the direction of observation $\mathbf{r}_0 = -\mathbf{s}_0 = -\boldsymbol{\beta}_0^{(s)}$, identified as that of the boresight of the optical system, under the assumption of negligible refractive effects in the atmosphere (cf. Figs. 9.4 and 11.21).

12.1.1.1 Flat Surface

In case of the flat surface depicted in Fig. 12.1, the centers of the pixels A, B, ..., E, corresponding to the points A', B', ..., E' on the topographic map, are imaged by a passive sensor, operating, for instance, at optical wavelengths, in the points A_i, B_i, ..., E_i coincident with A', B', ..., E'. Therefore, the relative topographic range positions R_g of the pixel centers are reproduced in the image.

12.1.1.2 Surface with Elevation

The relative positions of the points in the image of the surface with an elevated area shown in Fig. 12.2 differ from those of the flat surface. Indeed, the range R_g of the intersection C_i of the geodetic reference surface with the observing direction passing through the elevated point C deviates from the range of its topographic location C' according to the height z of C and to the angle of observation θ. Consequently,

[3] In case of synthetic aperture radar observation, the absolute location of a pixel *on the reference geoid* is derived from the SAR platform position through the Doppler image forming algorithm [9].

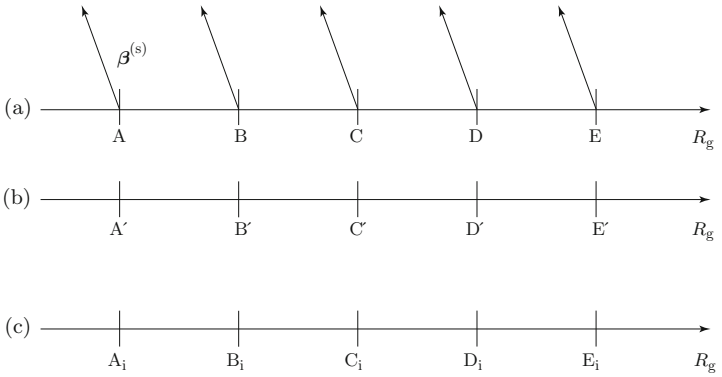

Fig. 12.1 Range positioning by a passive optical system of pixels on flat surface: (**a**), pixel centers A, B, C, . . . ; (**b**), topographic projection of pixel centers A', B', C', . . .; (**c**), images of pixel centers A_i, B_i, C_i . . . . The pixel images are co-located with the topographic projections

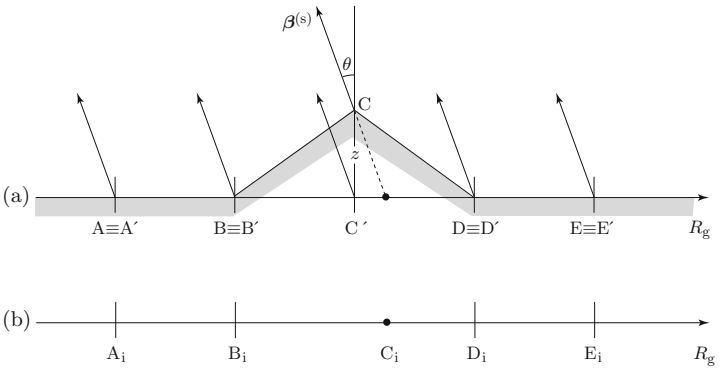

Fig. 12.2 Range positioning by a passive optical system of the pixels on a surface with elevation: (**a**), pixel centers and ground-range projection of pixel centers; (**b**), images of pixel centers. The image C_i of the elevated pixel center C is located at a ground distance R_g larger the topographic one C'; the position of C_i has to be compared with the corresponding one of Fig. 12.5

higher pixels are located at *larger distances* from the ground track of the observing platform. The optical image of Manhattan taken on 12 September 2001 and shown in Fig. 12.3 points out the dramatic effect of elevation on the positioning of tall objects, particularly evident for the almost vertical smoke plume, the image of which is widely spread in range. Based on purely geometric considerations, the center of pixel C at height z is imaged in C_i, displaced by $\Delta R_g = \overline{C'C_i} = z \tan\theta$ from its topographic range location. Therefore, the distance between the images of points on the slopes differs from that on the geodetic surface. In particular, with reference to Fig. 12.2,

$$\overline{B_iC_i} = \overline{B'C'} + z \tan\theta; \qquad \overline{C_iD_i} = \overline{C'D'} - z \tan\theta \ .$$

Fig. 12.3 Optical image of Manhattan taken on 12 September 2001: the effect of the elevation in moving the high pixels away from the satellite ground track is dramatically highlighted especially by the taller buildings and by the smoke plume (Credit: Space Imaging)

Elevated pixels, as those of the roofs or of the front walls of the buildings, are imaged at ranges which are larger than those of their topographic positions. For the same reason, the dimension in range of the pixels laying on the slopes facing the satellite are stretched, whereas those on the opposite slopes are shrunk.

12.1.2 Range Positioning by Active Systems

An active (radar or lidar) imaging system attributes the value of the echo (power or complex field) sampled at time Δt to a pixel centered on the range R given by (11.42). It is important to note that the distance R is in *slant range*, that is, along the electromagnetic trajectory from the space platform to the observed terrestrial object, as indicated in Fig. 11.27. As a matter of fact, applications often require distances in a geodetic reference grid. The slant distance R must then be converted (*re-projected*) into the *ground range* R_g on the geodetic surface, that is, into the distance of the observed target from the reference origin.

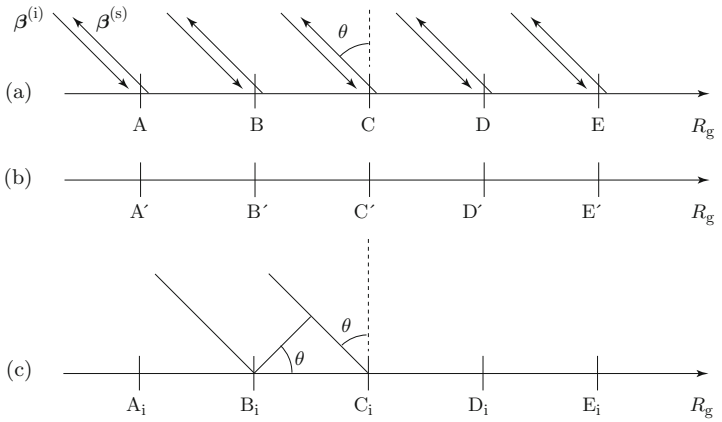

Fig. 12.4 Range positioning by an active system of the pixels on flat surface: (**a**), pixel centers; (**b**), ground-range projection of pixel centers; (**c**), images of pixel centers. Note that the image points are co-located with the ground-range projections, as in the passive case (Fig. 12.1)

12.1.2.1 Flat Surface

Figure 12.4 shows a sequence of pixels on a flat surface, with the corresponding topographic locations and radar images. As said, the active systems basically locate the pixels at the ground ranges R_g identified by the times of arrival of the echoes. Since the angle of observation θ is locally (almost) the same for all pixels on the flat surface, the correspondence between ground range and time of arrival is biunivocal for the given angle,[4] i.e., the conversion factor from slant to ground range is independent of the pixel center position on the surface. Therefore, both the absolute and the relative range positions of the pixel centers are reproduced in the radar image of the horizontal flat surface. The absolute and relative distances in slant range of two contiguous pixels, for instance those centered on B and C, derived from the times of arrival Δt of the respective echoes, are

$$R_B = \frac{c_0 \Delta t_B}{2}; \quad R_C = \frac{c_0 \Delta t_C}{2};$$

$$R_{BC} \equiv R_C - R_B = \frac{c_0}{2}(\Delta t_C - \Delta t_B).$$

The distance R in slant range is then transformed into ground distance R_g through the incidence angle[5] θ. The relative distance on the geodetic reference flat surface of the images B_i and C_i of the pixels B and C is

[4] Recall that the refractive effects of the atmosphere are neglected.

[5] To simplify the notation, the incidence angle denoted by $\theta^{(i)}$ in Fig. 11.27 is now θ.

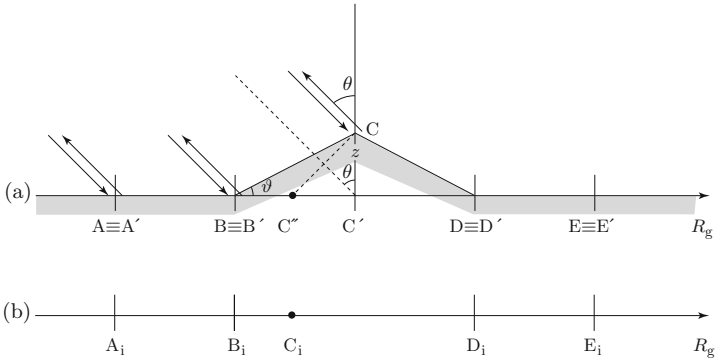

Fig. 12.5 Range positioning by an active system of the pixels on a surface with elevation: (**a**), pixel centers and ground-range projection of pixel centers; (**b**), images of pixel centers. Note that the image C_i of the elevated pixel center C is located at a ground distance smaller than the topographic one C'; the position of C_i has to be compared with the corresponding one of Fig. 12.2

$$\overline{B_iC_i} \equiv R_{gBC} = R_{BC} \csc\theta = \frac{c_0}{2}(\Delta t_C - \Delta t_B) \csc\theta \ . \tag{12.1}$$

The resolution in ground range d_r is correspondingly related to the resolution in slant range d_R through the incidence angle by

$$d_r = d_R \csc\theta = \frac{c_0 \tau_c}{2} \csc\theta \ . \tag{12.2}$$

12.1.2.2 Surface with Elevation

When the area imaged by a radar is not flat, substantial differences with passive imaging arise. Differently from the passive ones, active systems derive the ground range R_g of the target from the time of arrival of its echo, time which depends on the slant range R, that is the electromagnetic path length between space platform and scatterer. The slant range R clearly depends on the elevation[6] z of the target: with reference to the elevated pixel C in Fig. 12.5, the distance R_C between platform and C is

$$R_C = R_{C'} - z\cos\theta \ , \tag{12.3}$$

where C' is the pixel C reduced to $z = 0$, i.e., lowered onto the flat surface. Given the relation (12.1) between ground and slant ranges, (12.3) indicates that the image C_i of C is displaced towards the radar ground track with respect to its topographic

[6]Height above the reference surface is denoted by the variable z from now on.

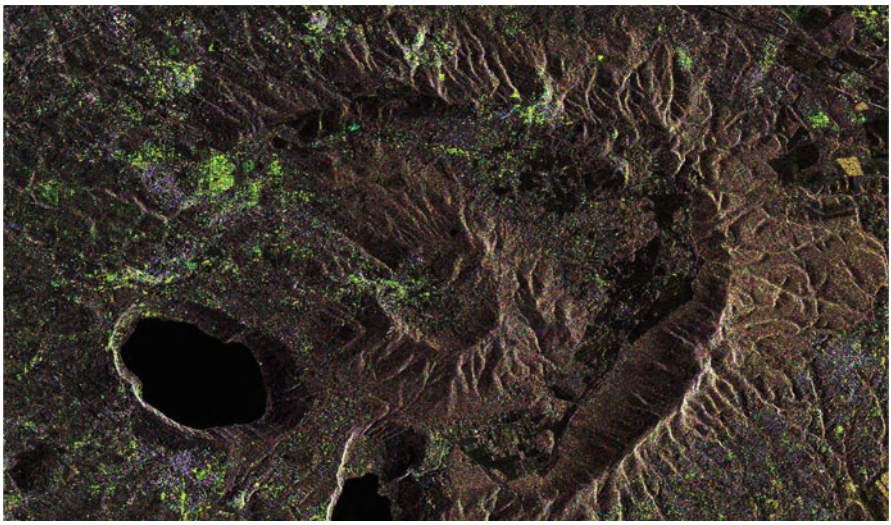

Fig. 12.6 West-looking RadarSat-2 image of the Albani hills volcanic area, near Rome, Italy: eastward slopes are shrunk, westward slopes are stretched (Credit: data, CSA/CCRS SOAR Project 1488; processing by Tor Vergata University Earth Observation Laboratory)

position C'. In particular, the distance between the image of the elevated pixel C and that of one, say B, on the flat surface, is obtained by combining[7] (12.1) with (12.3):

$$\overline{\mathrm{B_i C_i}} \equiv R_{\mathrm{gBC}} = (R_{\mathrm{C'}} - R_{\mathrm{B}}) \csc\theta - z \cot\theta \ . \tag{12.4}$$

Equation (12.4) points out that the distance in ground range between images of pixels on a slope facing the radar is shorter[8] than their topographic relative distance: the image of the *facing slope is shrunk*, yielding the so-called *foreshortening*. Instead, for a pixel D on the opposite slope,

$$R_{\mathrm{D}} = R_{\mathrm{C'}} + z\cos\theta, \qquad \overline{\mathrm{C_i D_i}} \equiv R_{\mathrm{gCD}} = (R_{\mathrm{D}} - R_{\mathrm{C'}}) \csc\theta + z \cot\theta \ ,$$

which shows that the image of the *opposite slope is stretched*. Figure 12.6 gives an example of actual foreshortening and related effects in a SAR image of a hilly area. Note how the foreshortened slopes generally show high backscattering, since:

– the backscattering coefficient actually augments, because the incidence and scattering directions approach the specular direction, following the outline of Sect. 7.3;

[7] Atmospheric refraction effects are still neglected.

[8] Once the radar-measured slant distance is turned into ground distance, taking account of the acquisition parameters.

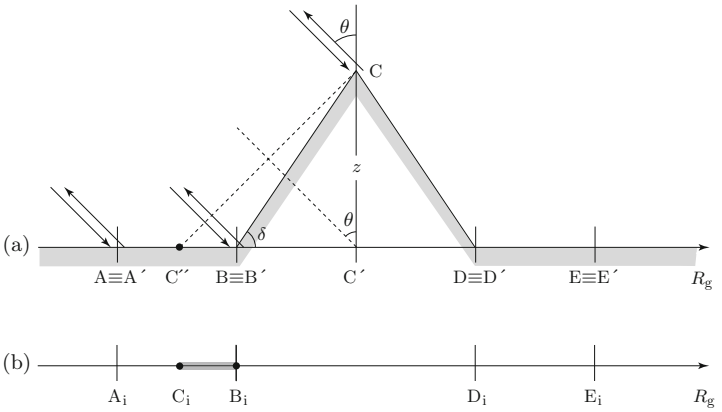

Fig. 12.7 Schematic range positioning by a radar system of the pixels on a surface with a high slope, (**a**): the image C_i the elevated pixel center C is located at a ground distance smaller than that of B_i, image of B, (**b**); the image C_iB_i (note the inversion of the pixel order) of the sloping segment BC *lays over* the image of the segment C"B at the foot of the slope

– but the dimension in ground range of the surface on the slopes facing the radar is also shrunk, given the effect of the incidence angle sketched in Fig. 11.27; therefore, the geometric area of a pixel in the image corresponds to an actual larger area and in turn to a larger scattering volume.[9]

As expected, the slopes opposite to the satellite show a contrary behavior for the corresponding reasons.

12.1.2.3 Lay-Over

The positioning in range of the targets, based on their distance from the radar platform, originates peculiar features which are observed in the SAR images. Reference is made to Fig. 12.7 for a better understanding. When the slope of the portion of surface is such that $z\cos\theta > \overline{BC'}$, the pixel centered on C is imaged closer to the radar than the pixel in B; therefore, the ground distances of the images of the pixels are such that

$$\overline{B_iC_i} \equiv R_{gBC} = (R_{C'} - R_B)\sec\theta - z\cot\theta < 0\ . \tag{12.5}$$

Equation (12.5) indicates that the image C_i of the elevated pixel C is positioned a ground range shorter than that of the image B_i of the pixel B and, moreover, that the images of the pixels on the sloping face BC are superimposed to those along

[9]This latter artifact is corrected by simply modifying the backscattering intensity on the basis of geometric considerations.

the segment C"B of the flat surface before the slope. This effect of superposition is named *lay-over*.

With reference to the surface height profile in the range direction shown in Fig. 12.7, the backscattering from the pixels on the rising slope BC adds to the one from the pixels located on the foregoing horizontal area between C" and B when the slope angle δ is larger than the incidence angle θ, i.e., satisfies the relation

$$\delta = \arctan \frac{z}{\overline{\mathrm{BC}'}} > \theta \ . \tag{12.6}$$

Note that in altimetrically rough areas, lay-over is often accompanied by *shadowing* of the pixels downslope to the radar, which are not in geometric visibility with it. Since there is no directly incident wave, the re-radiating current (7.4), which is proportional to the incident field, has quite low values,[10] so that the received scattered power may fall below the noise level of the system.

12.1.2.4 Images of Vertical Objects

The images of natural or man-made *vertical* objects[11] such as trees, poles or common buildings, are affected both by lay-over and by the corresponding shadowing, since this kind of radar imaging is always[12] performed at slant angles. Some features of a tree image acquired from a space radar are first discussed for a better understanding of SAR images, then the analysis is extended to the somewhat more complicated case of buildings.

12.1.2.4.1 Images of Trees

The backscattering that originates from an area including a tree is typically contributed by

- the crown of the plant, which can be modeled by the canopy of disc- or needle-shaped leaves seen in Sect. 7.4.1, and of cylinders of various dimensions representing twigs and branches;
- the trunk, which is regarded as a large rough (Fig. 7.10) cylinder;
- the underlying soil, a generally plane rough (Fig. 7.11) surface, the scattering behavior of which is outlined in Sects. 7.3.3 and 7.4.

[10] The value of the field incident onto areas which are in geometric shadow is low but not zero, since it is created anyplace by diffraction.

[11] Vertical means perpendicular to the plane locally approximating the geodetic reference surface.

[12] The ground-range resolution (12.2) would tend to blow-up at nadir ($\theta \approx 0$) observations, neither the antenna synthesis (Sect. 11.4.3.4) would be feasible in practice.

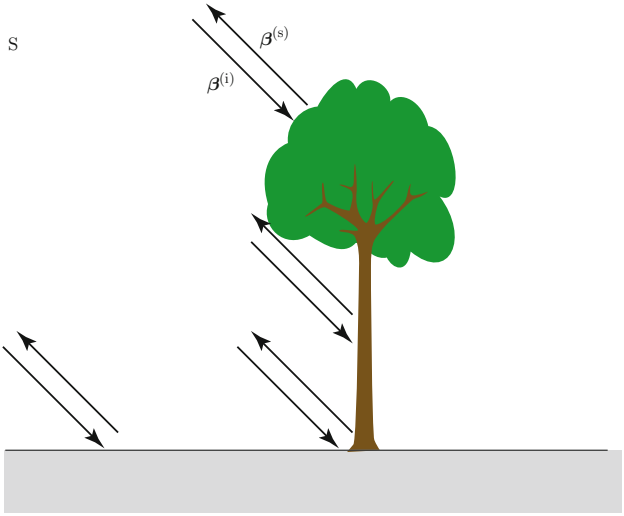

Fig. 12.8 The sources of backscattering from an area including a tree are located in the crown (*leaves* and *branches*), rough trunk and terrain; S indicates the direction of the *far* radar platform

The various sources of backscattering, indicated in Fig. 12.8, are clearly located at different heights and at generally different distances from the platform. The radar image of the tree is created as sketched in Fig. 12.9 according to the distance between the radar and the parts of the plant from which the backscattering originates. The point P_c of the crown at height h is imaged in P_{ci}, located at a distance from the reference O of the ground range such that the distance R_{SPci} between the space platform S and the image P_c of the crown point P_c is equal to the distance R_{SPci} between S and the latter. Turning the slant distance into ground distance by (12.4) yields the location of the tree crown point in the image:

$$\overline{OP_{ci}} \equiv R_{gPc} = \overline{OP_b} - h \cot\theta \ .$$

The same concept holds for a point P_t of the trunk at height $z < h$, which is imaged in P_{ti} at the ground range

$$\overline{OP_{ti}} \equiv R_{gPt} = \overline{OP_b} - z \cot\theta > R_{gPc} \ .$$

The image of the tree base P_b, which clearly is at $z = 0$, is not displaced. In conclusion, the tree crown is imaged[13] before the trunk, which foreruns the base, i.e., the topographic location, towards the ground track of the radar platform.

[13]Note that the first point P_{ci} encountered in ground range needs not to be the highest point, but the closest to the radar platform, hence its location in the image of a given tree depends on θ.

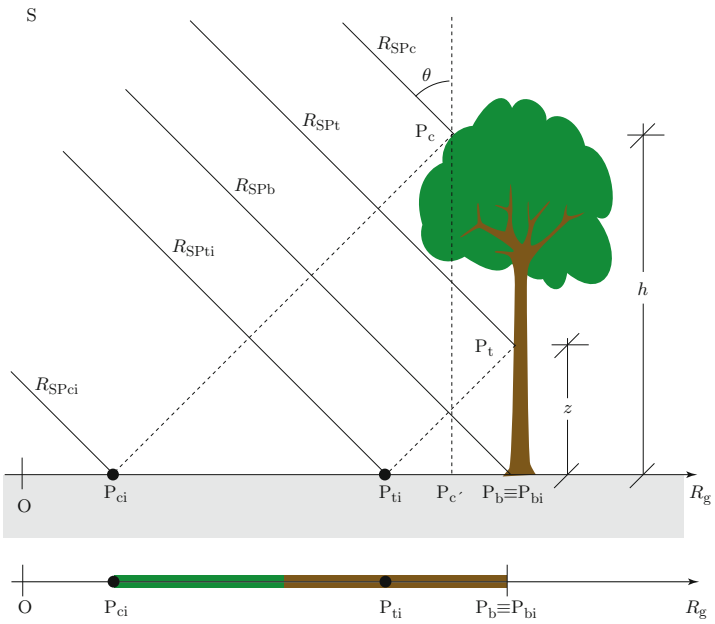

Fig. 12.9 The radar image of a tree is created according to the distances of the sources of backscattering from the sensor platform S: the *bottom diagram* shows that the image P_{bi} of the base of the plant coincides with its actual position P_b, whereas the elevated parts, which are closer to the space platform, are imaged at ground distances correspondingly closer to the radar ground track, according to height and incidence angle; this implies that the image of the tree *lays over* the segment $P_{ci}P_b$ of the rough flat terrain at the foot of the plant, as suggested by the *green* (crown) and *brown* (trunk) segment in the *bottom diagram*

In an image, such as the one in Fig. 12.10, the trees appear to lean against the radar ground track. The ground-range migration of the elevated scatterers increases with decreasing incidence angle θ.

12.1.2.4.2 Images of Buildings

Like trees, buildings are frequently characterized by vertical structures. Their radar images are similarly created according to the relative distances of the sources of scattering from the sensor platform. With reference to the notations in Fig. 12.11, the image P_{rli} of the front pixel P_{rl} on the roof at height h falls at a ground distance

$$\overline{P_{rli}P_{bli}} = -h\cot\theta$$

Fig. 12.10 The trees, which are actually located on the *left* of the country road, in this radar image appear to lean against the satellite ground track, which here is on the *right*; note the shadow past the crown, due to extinction, as outlined in Sect. 9.2 (Credit: COSMO-SkyMed data, ASI; processing by Tor Vergata Earth Observation Laboratory)

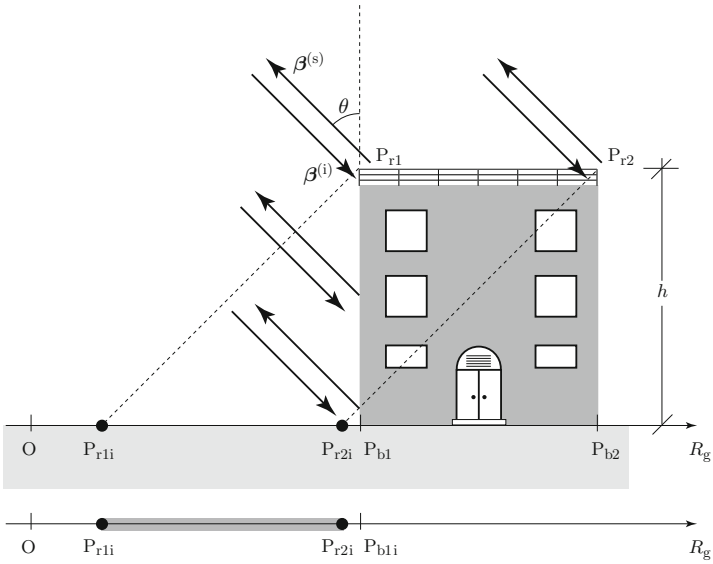

Fig. 12.11 The radar image of a vertical building is created according to the distances of the sources of backscattering from the radar platform: the *bottom diagram* shows that the image P_{b1i} of the base P_{b1} coincides with the actual position, whereas the elevated parts are imaged at ground distances closer to the radar, according to height h and incidence angle θ; note that the roof image $P_{r1i}P_{r2i}$ here is entirely located outside the topographic projection $P_{b1}P_{b2}$

Fig. 12.12 A high-scattering metallic banister

from the actual position P_{b1} of the vertical building wall facing the radar. The higher the building, the larger is the displacement of the roof image *towards the ground track*, hence in the direction *opposite* to the one displayed by the passive optical image in Fig. 12.3. Structures at intermediate heights, such as windows, are displaced analogously. Note that structures (e.g., eaves, banisters or parapets, also arranged in trihedral configuration) producing high backscattering are often present on the roof of buildings; an example of this kind of strong scatterers is shown in Fig. 12.12.

12.1.2.5 The Double Bounce Effect

Backscattering re-directs a fraction of the incident power into the direction of the transmit-receive radar platform. Since large flat surfaces mainly reflect in the specular direction, their radar image is characterized by low backscattering unless they are almost perpendicular to the propagation direction $\boldsymbol{\beta}_0^{(\mathrm{i})}$ of the incident wave. However, when several scatterers are present, multiple scattering among bodies can occur that re-direct power in the backscattering direction, even if a single object does not scatter in the backward direction. As discussed in Sect. 9.1, the multiple-scattering adds to the single scattering from the individual bodies. Figure 12.13 visualizes how the specular scattering from two targets combine to contribute backscattering even if each single object does not reflect directly in the backward direction. Indeed, in addition to the possible direct contributions from the single bodies, backscattering is originated by a *double bounce* mechanism: this occurs when, in the physical optics model, a pair of locally tangent planes form an orthogonal dihedron schematized in Fig. 12.13 by the orthogonal dashed lines with vertex in P_v. Substantially, backscattering by double-bounce is a generalization of the reflection from dihedrons outlined in Sect. 6.6.1 to which the reader is referred for further details. Simple geometric considerations show that the path lengths are such that

$$\overline{\mathrm{S\,A_1A_2S}} \equiv \overline{\mathrm{S\,A_2A_1S}} = 2\,\overline{\mathrm{S\,A_v}}\,,$$

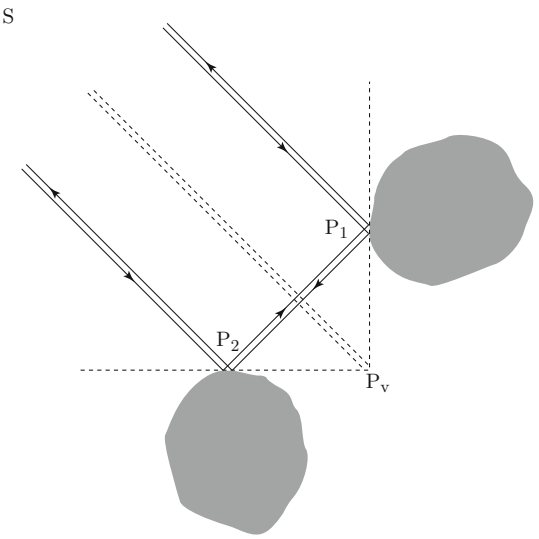

Fig. 12.13 Specular scattering from each body combines to yield backscattering in direction of the sensor platform S: the *double-bounce* return originated by the points P_1 and P_2 appears to come from the vertex P_v

where S denotes the position of the platform, as usual. Given the positioning mechanisms in radar images, the echo reaching the radar through the double bounce mechanism appears to originate from the vertex point P_v.

Many targets in the terrestrial environment produce double bounce in combination with the ubiquitous Earth's surface. The double bounce produced by tree trunks (mainly at lower microwave frequencies) and, especially, by building walls, can be particularly large, since strong coherent scattering occurs in the specular direction. Moreover, incoherent scattering from dielectric structures with large horizontal or vertical correlation distances r_ϵ also peaks around the specular direction, given the prevailing low components in the spatial frequency spectrum (cf. Sects. 7.4.4 and 7.4.6). The field reflected and scattered in the specular direction from the vertical targets is in turn specularly scattered by the average soil surface into the backward direction and adds to the concurrent incoherent backscattering through the soil-to-target reciprocal path. As before, trees and buildings are examples worth of consideration to understand how the double-bounce affects the radar images.

12.1.2.5.1 Double Bounce from Individual Trees

Figures 12.13 and 12.14 suggest that the whole source of backscattering through the double-bounce paths trunk-to-soil and soil-to-trunk is located at the base P_b of the tree,[14] because $\overline{SP_tP_{ti}S} \equiv \overline{SP_{ti}P_tS} = 2\overline{SP_b}$ irrespective of the height of P_t. Therefore, the double-bounce mechanism differs substantially from the layover previously considered, which resulted in a displacement of the ground-range

[14]The tree is regarded as a vertical cylinder over a horizontal plane.

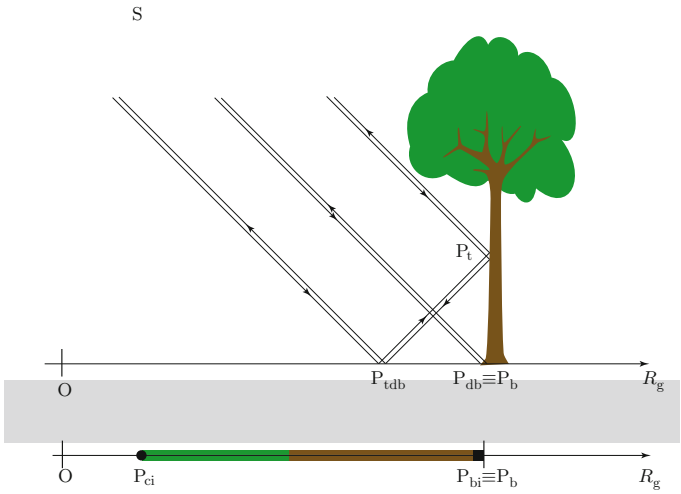

Fig. 12.14 The back-and-forth path lengths between the radar platform S, the points P_t on the *vertical* trunk and the points P_{tdb} of corresponding specular reflection (and vice-versa) on the *horizontal* surface are the same as the double path from S to the tree base P_b: the image of the tree consists of the lay-over segment $P_{ci}P_b$ including the double-bounce pixel $P_{db} \equiv P_b$

dependent on the height of the scatterer. Now the backscattering from all the vertical structure in *concentrated* in the pixel located *at the base* of the latter. The diagram at the bottom of Fig. 12.14 schematizes the line of lay-over (cf. Fig. 12.9) ending with the double-bounce pixel at the base P_b of the tree.

12.1.2.5.2 Double Bounce from Individual Building Walls

A vertical wall standing on a horizontal surface forms a rectangular dihedral structure which reflects in the backward direction[15] by the double reflection mechanism outlined in Sect. 6.6.1. Because of the geometric properties of the double-bounce paths, the radar assigns the power originated by the dihedron to the pixels along the wedge, located at the base of the wall, as just seen for the tree. The corresponding intensity of backscatter can be quite high, given the usually large and relatively flat surfaces which are involved in the reflection, which enhance the diffraction pattern (11.32) especially at the shorter wavelengths. Moreover, (6.45) points out that the backscatter originated by this mechanism involving a double reflection is particularly high at horizontal polarization, since $q_h > q_v$ for both the wall and the ground surfaces.

[15]The edge of the dihedron is assumed perpendicular to the incidence plane, i.e., along the azimuth direction.

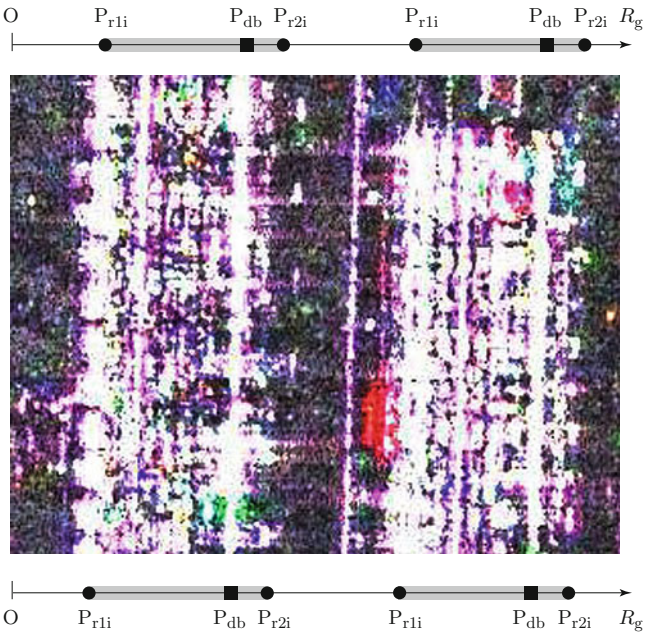

Fig. 12.15 Metric-resolution σ^0_{hh} COSMO-SkyMed image of two buildings near the Tor Vergata University campus, Rome, Italy, with front wall almost perpendicular to the incidence plane and a street in between; the positions of the double-bounce lines P_{db} and of the lay-over areas $P_{r1i}P_{db}$ towards the satellite ground track, which here is on the *left*, are schematically indicated in the *top* and *bottom* diagrams by the notations of Figs. 12.11 and 12.16; the images of the roofs extend from P_{r1i} to P_{r2i} (Data, © ASI, 2010, 2011, 2012; processing, courtesy C. Solimini)

Figure 12.15 shows the radar image of an urban scenario including two similar buildings, in which lay-over and double bounce combine. The noteworthy features of the image can be interpreted with the help of Fig. 12.16, also with reference to Fig. 12.11:

- lines of high-intensity pixels (on the right side of the image of each building) P_{db} correspond to the street-wall main double bounce and are located at the edge of the dihedrons, that is, with reference to the scheme in Fig. 12.16, at the base P_b of the front walls;
- aligned patches of relatively high-intensity pixels correspond to the direct scattering from structures on the near edges of the roofs P_{r1} (cf. Fig. 12.11); they are positioned at the beginning of the respective lay-over regions *towards the ground track* on the left, at distance $\Delta R_g = h \cot\theta$ from their topographic ground range;
- stripes of higher-intensity pixels alternating in ground range with lower-intensity ones, located in the lay-over regions $P_{r1i}P_{db}$, correspond todirect scattering

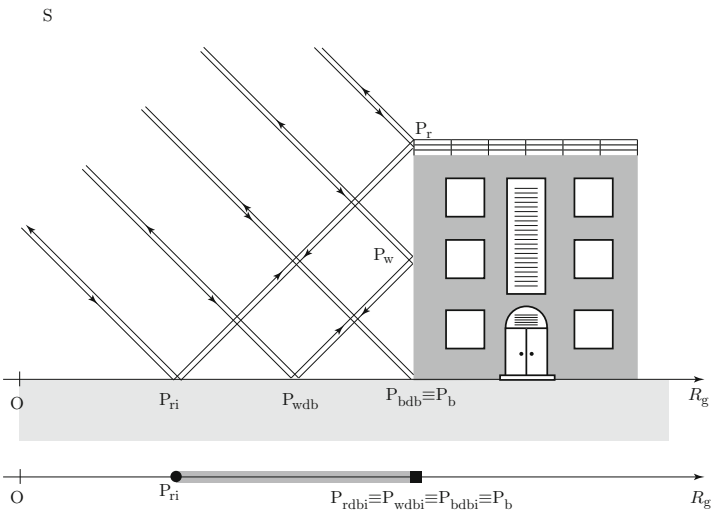

Fig. 12.16 The equal length of the paths between the radar location S, the points P_w on the vertical wall and the corresponding reflection points P_{wdb} on the *flat horizontal surface* concentrate the *double-bounce reflection* into a single pixel P_{bdb} located at the base P_b of the building; the *direct scattering* from the wall is located in the lay-over segment $P_{ri}P_b$ (cf. Fig. 12.11)

architectural elements, such as jutting ledges and windows; the distances $\Delta R_g = z \cot\theta < h \cot\theta$ from their topographic ground range typically correspond to the heights of the various floors; their backscattering is superimposed to that from the targets on the street;

– pixels at the far side P_{r2} of the roofs correspond to structures, which, consistently with angle of incidence, roof width and building height, are imaged on the right, in this case beyond the double-bounce lines, i.e., beyond the base of the buildings.

Summarizing, the radar image of a building with vertical walls is generally composed of a lay-over area where three *direct scattering* contributions, from the ground, from the front wall and from the roof, superimpose, and of a double-bounce line[16] of high-backscattering produced by pairs of street-wall coherent reflections. The double-bounce line coincide with the base of the building and can lie either within or past the roof lay-over area, according to the angle of incidence, the height of the building and the width of the roof in ground range. Images of buildings with complex structures clearly exhibit more complicated patterns and may be quite difficult to interpret, especially when the walls are oblique to the incidence plane.

[16] In practice, the line is a stripe.

12.2 3-D Information in EO Images

Sections 12.1.1.2 and 12.1.2.2 show that the height of the target affects the position of its image in the map produced by the observing system. This feature suggests that the images do contain information on the earth surface relief. Substantial differences in how the altitude information is contained in the images is expected between those produced by passive sensors and those by active systems, given the diverse mechanisms of acquisition. The difference clearly results in separate methods of interpretation and of elevation retrieval. Once retrieved, the important 3-D information on the observed landscape can be transformed into a DEM [40], essentially consisting of the set of heights corresponding to each element of the geographic grid of the area.

12.2.1 3-D Rendering from Passive Images

Altimetric restitution from optical images is essentially based on the previously discussed variation with the observation angle of the ground range of pixels at given elevations. Coarsely speaking, both terrain relief and height of buildings are estimated by pairs of stereoscopic images [39], which are acquired nearly simultaneously from different positions along the track of agile imaging sensors. Cross-track images also contain stereoscopic information and are used similarly for altimetric representation of terrestrial landscapes. The technique is standard for landscapes with relatively smooth variations of height, while particular procedures may be required to generate 3-D models of complex urban geometries [4, 6], especially where parts of the objects (mainly buildings) may be optically hidden by other parts. It can be added that high-spatial resolution observations from low-flying platforms allow 3-D characterization of tree canopies or urban structures, thanks to photogrammetric computer-vision algorithms [10, 31].

12.2.2 3-D Rendering from Radar Images

Let us carry on the discussion initiated in Sect. 12.1.2.2 on what geometrically differentiates passive optical imaging from radar mapping. It was observed that the distance from the radar replaces the angle of arrival of the scattered solar radiation, identified by the pointing direction of the optical aperture in the vertical plane. Therefore, distance is the key quantity in radar mapping that tracks down the range from which the backscattered field originates.

Recalling (7.26), the field forming the radar echo originated by the target, that is, by the volume V' in which inhomogeneities $\Delta\tilde{\epsilon}$ of permittivity are present, has the basic expression

$$\boldsymbol{E}^{(\mathrm{s})} = \frac{\mathrm{e}^{-\mathrm{j}\kappa_0 R}}{R} \frac{\kappa_0^2}{4\pi} \iiint_{V'} \left(\overline{\boldsymbol{E}_\perp} + \boldsymbol{E}'_\perp\right) \left(\overline{\Delta\epsilon} + \Delta\epsilon'\right) \mathrm{e}^{\mathrm{j}\kappa_0 \boldsymbol{r}' \cdot \mathbf{r}_0^{(\mathrm{s})}} \, \mathrm{d}V' \, . \tag{12.7}$$

In Eq. (12.7) R is the distance between the "phase center" [2, 21] of the SAR antenna [3] and the one of V' [36]. The scattering volume V' identifies the resolution cell from which the scattered field returns to the radar at time Δt after the signal[17] is transmitted. Section 11.4.3.4 shows that for an extended target such as the Earth's environment, the transverse dimension (width) of the resolution cell V' depends on the synthetic antenna beam width, while its longitudinal dimension (length) depends on the duration of the compressed pulse. The vertical dimension (depth) of the resolution cell, which is often relevant to image understanding, depends on the penetration of the incident wave, hence on frequency, angle of incidence and permittivity features of the terrestrial materials in V', as discussed in Sect. 7.4.7.

The scattered field returning to the radar is a modified replica of the transmitted field E_T, delayed by the time Δt the electromagnetic energy takes on the antenna-to-scatterer round trip:

$$E^{(\mathrm{s})}(t) = E^{(\mathrm{s})}\big(E_\mathrm{T}(t - \Delta t)\big) \simeq C\, E_\mathrm{T}(t - \Delta t) \, ,$$

assuming for simplicity that the scattered field is linearly related to the transmitted one by the proportionality factor C. The radar system associates the target with a distance proportional to the time Δt at which the echo is sampled by the receiver, consistently with Sect. 11.4.3.2. Indeed, by taking account of the speed of electromagnetic energy, the system attributes the scattered field that is sampled at time Δt after transmission to a round trip between radar and target of length (11.42):

$$2R \approx \frac{\Delta t}{c_0} \, .$$

12.2.2.1 Height-Ground Range Ambiguity

Section 11.4.3.3 mentions that the resolution cell on the Earth's surface is identified by a pixel, represented in Fig. 11.27 by the portion of geodetic reference surface S' of dimensions $d_\mathrm{a} \times d_\mathrm{r}$ bounding V'. Constructing the map of the surface requires that pairs of azimuth and ground-range coordinates be assigned to the center of each pixel. The antenna synthesis process identifies the azimuth of S' univocally, but the identification of the range of the pixel on the reference surface is not univocal because *ground range* R_g and *height* z are mixed together in the *slant range* R, which is the only quantity that is measurable through the time of arrival of the echo Δt. Figure 12.17 points out the ground-range ambiguity that can occur

[17] A pulse is a common reference signal.

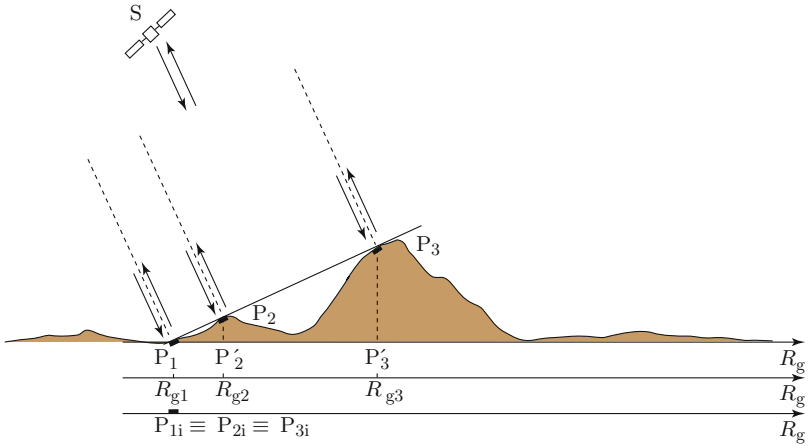

Fig. 12.17 "Centers" P_1, P_2, P_3 of pixels at different ground ranges R_{g1}, R_{g2}, R_{g3} and heights such that $\overline{SP_1} = \overline{SP_2} = \overline{SP_3}$, are located at the same ground range $R_g = R_{g1}$, i.e., the radar images of pixels P_1, P_2, P_3 collapse into a unique image $P_{1i} \equiv P_{2i} \equiv P_{3i}$

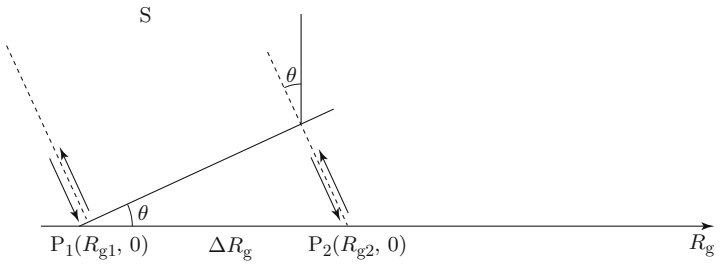

Fig. 12.18 Two pixels $[P_i(R_g = R_{gi},\ z_i = 0)\ i = 1, 2]$ at ground distance ΔR_g on a flat $(z = 0)$ surface

when observing a variable-elevation landscape by an active sensor: as outlined in Sect. 12.1.2.3, the images of pixels at different ground ranges and altitudes are superimposed because the times of arrival of the respective echoes happen to be the same.

Resorting to the phase of the arriving scattered field meets with further obstacles. The phases[18] of the received waves originated by the two pixels P_1 and P_2 laying on the ideal horizontal surface ($z_1 = z_2 = 0$) shown in Fig. 12.18 are

$$\Phi_1 = \frac{2\pi}{\lambda_0} 2\,\overline{SP_1} + \Phi_{\mathcal{F}1}; \qquad \Phi_2 = \frac{2\pi}{\lambda_0} 2\,\overline{SP_2} + \Phi_{\mathcal{F}2}\ , \tag{12.8}$$

where $\Phi_{\mathcal{F}i}$ is the phase of the scattering function of the i-th resolution cell ($i = 1, 2$) for the considered polarization. Equation (12.8) points out that the measured phases

[18] It is understood that the phase of the received wave is relative to that of the transmitted one.

Φ_1 and Φ_2 depend on $\Phi_{\mathcal{F}1}$ and $\Phi_{\mathcal{F}2}$, which are often badly known. But, even if serviceable estimates of the complex scattering functions were available, after all the phase Φ_i of the scattered field is related to the distance $\overline{\mathrm{SP}_i}$ of the i-th target, just like the time delay: if the distances are the same, the phases are obviously the same.

Let us now examine the information contained in the difference of phase of the fields scattered by the two pixels P_1 and P_2. The phase difference is related to the pixel ground-range separation ΔR_g by

$$\Phi_2 - \Phi_1 = \frac{4\pi}{\lambda_0}\left(\overline{\mathrm{SP}_2} - \overline{\mathrm{SP}_1}\right) = \frac{4\pi}{\lambda_0}\Delta R_\mathrm{g} \sin\theta \ ,$$

provided the scattering functions $\Phi_{\mathcal{F}1}$ and $\Phi_{\mathcal{F}2}$ have the *same phase*.[19] But the phase difference $\Delta\Phi = \Phi_2 - \Phi_1$ suffers from the $\mathrm{mod}(\Delta\Phi, 2\pi)$ property. Only if

$$\frac{\Delta R_\mathrm{g} \sin\theta}{\lambda_0} < \frac{1}{4} \ , \tag{12.9}$$

the phase difference can be recovered from the $\mathrm{mod}(\Delta\Phi, 2\pi)$ measured value. In fact, in this case the difference of phase of the received fields would be in a biunivocal correspondence with the difference of the ground ranges of P_1 and P_2. When the above condition is satisfied,

$$\Delta R_\mathrm{g} = \frac{\lambda_0}{4\pi}\frac{\Phi_2 - \Phi_1}{\sin\theta}$$

would provide the *relative* measurement of R_g. Satisfying (12.9) requires that, for a given angle of incidence, the difference in ground range ΔR_g of the centers of the two pixels be

$$\Delta R_\mathrm{g} < \frac{\lambda_0}{2} \ ,$$

a condition clearly unrealistic, since, at microwaves, generally $\Delta R_\mathrm{g} > \lambda_0$. Therefore, the phase difference between the field scattered by two pixels, even if they are identical (i.e., for which $\Phi_\mathcal{F}$ is the same) and even when they lie on a flat surface, is not univocally related to their separation. Rather, being the range dimension of the pixels not multiple of wavelength, in practice the phase has a random-like behavior for a generic incidence angle.

The conclusion is that values cannot be assigned to height and ground range of a target neither from measurements of the time of arrival of the echo, nor from the phase of the field measured at a given position. This feature deteriorates the performance of synthetic aperture radars in imaging the uneven Earth's surface (Fig. 12.6).

[19] Atmospheric refraction is still neglected.

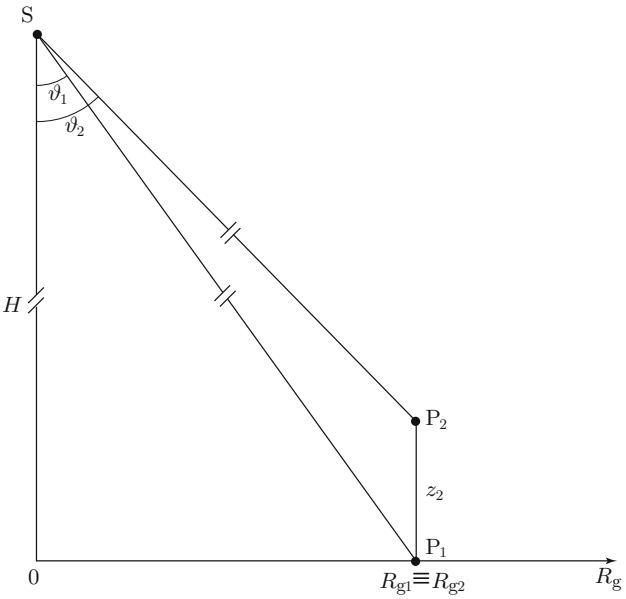

Fig. 12.19 The off-nadir angle ϑ_i depends on the altitude z_i of the target P_i at a given ground range

12.2.2.2 Disentangling Height from Ground Range

Measurements of different kind are needed, possibly following schemes suggested by the stereoscopic technique used in optical observations. Radargrammetry [20, 24, 41], like photogrammetry (Sect. 12.2.1), exploits observations from two different positions (stereo pairs). SAR interferometry [5, 17, 35, 43] is a widely used technique which exploits the difference of phase measured from different locations of the radar platform to retrieve the height of a target located at a given ground range.

Figure 12.19 shows that the height z_i of the scattering resolution cell P_i located at the ground range R_{gi} determines the corresponding off-nadir angle ϑ_i according to

$$\vartheta_i \simeq \arctan\left(\frac{R_{gi}}{H - z_i}\right) , \tag{12.10}$$

where H is the height of the radar platform and the refractive effects of the atmosphere are assumed negligible.[20] The knowledge of ϑ_i, i.e., of the angle of arrival of the echo, would allow the determination of the height z_i of the target that scatters from the ground range R_{gi}. Stereoscopy suggests to pursue this goal by using a pair of images acquired from two positions of the radar platform. Figure 12.20

[20]The assumption implies that $\vartheta_i \simeq \theta_i$ for a locally horizontal reference surface.

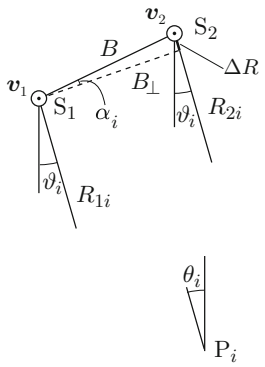

Fig. 12.20 Basic geometry of interferometric acquisition for the target P_i: the positions S_1 and S_2 of the platform are separated by the baseline B; the component of B perpendicular to the direction of observation at the off-nadir angle ϑ_i is the perpendicular baseline $B_\perp$; the orbital velocity is $\boldsymbol{v}_i$ and the local angle of incidence on the reference flat earth surface is $\theta_i \simeq \vartheta_i$ when the refractive effects of the atmosphere are neglected

schematizes the SAR antenna[21] in the platform position S_1 observing the pixel centered on P_i at ground range R_{gi}, $(i = 1, \ldots, N_r)$, and the same antenna in the different position S_2 in the vertical plane containing S_1 and P_i.

The distances R_{1i} and R_{2i} between pixel P_i and platform positions S_1 and S_2 where the field is sampled, are related by

$$R_{2i} \simeq R_{1i} + B \sin \alpha_i \ ,$$

where $B = \overline{S_1\, S_2}$ is the *baseline*, laying on the plane orthogonal to the trajectory of the platform, that is, to its local velocity $\boldsymbol{v}$. If observation from space is considered, $\boldsymbol{v}$ is the satellite orbital velocity. The angle of arrival of the echo $\theta_i \simeq \vartheta_i$ is immediately related to α_i by

$$\theta_i \simeq \gamma - \alpha_i \ , \tag{12.11}$$

where γ, shown in Fig. 12.21, is known from the platform motion data. The angle α_i depends on the difference of distance $\Delta R_i = R_{2i} - R_{1i}$ just like the difference of the phases of the fields in S_1 and S_2 does. Measuring the latter is thus expected to yield the unknown off-nadir angle. Indeed, the difference of phase $\Delta\Phi$ of the field in S_2 and S_1 backscattered from the i-th pixel P_i is related to the difference of path length ΔR_i, hence to the angle θ_i, by

$$\Delta\Phi_i = \Phi_{2i} - \Phi_{1i} = \frac{4\pi}{\lambda_0}\Delta R_i \simeq \frac{4\pi}{\lambda_0} B \sin(\gamma - \theta_i) \ . \tag{12.12}$$

[21]The antenna is intended collapsed in the point S corresponding to its electric center, further identified as the platform position.

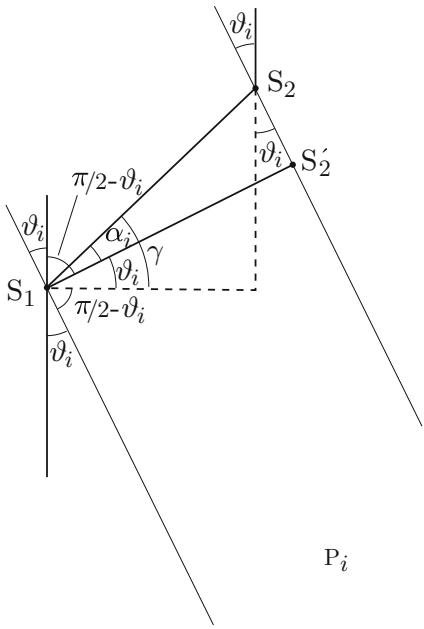

Fig. 12.21 Baseline $\overline{S_1S_2}$, perpendicular baseline $\overline{S_1S_2'}$, and off-nadir angle ϑ_i relative to the target P_i

In reality, (12.12) is unproductive. As a matter of fact,

$$4\pi\,\Delta R_i \gg \lambda_0$$

while $\Delta\Phi_i$ is limited by the mod$(\Delta\Phi, 2\pi)$ property. This basic feature prevents the retrieval of θ_i from $\Delta\Phi_i$. To surmount the obstacle, a differential approach is pursued. Another pixel P_j is considered, for which

$$\Delta\Phi_j = \Phi_{2j} - \Phi_{1j} = \frac{4\pi}{\lambda_0}\Delta R_j \simeq \frac{4\pi}{\lambda_0} B \sin\alpha_j \ .$$

The angles α_j and α_i are quite close because, in practice, $\vartheta_j \simeq \vartheta_i$. Therefore, if $\alpha_j = \alpha_i + \Delta\alpha_{ij}$, the difference $\Delta\alpha_{ij} \ll \pi$, so that

$$\sin\alpha_j \simeq \sin\alpha_i + \cos\alpha_i \ \sin\Delta\alpha_{ij} \ .$$

The *second difference* of phase

$$\Delta\Phi_{ij} \simeq 4\pi\frac{B\cos\alpha_i}{\lambda_0} \ \sin\Delta\alpha_{ij} = 4\pi\frac{B_{\perp i}}{\lambda_0} \ \sin\Delta\alpha_{ij} \simeq 4\pi\frac{B_{\perp i}}{\lambda_0}\Delta\alpha_{ij}$$

is then linearly related to $\Delta\alpha_{ij}$ and to the component $B_{\perp i} \equiv B_\perp$ of the *baseline perpendicular* to the observation direction at the off-nadir angle $\vartheta_j \approx \vartheta_i \equiv \vartheta$

indicated in Fig. 12.21. Combining (12.11) and (12.10) yields the second difference of phase $\Delta\Phi_{ij}$ as a linear function of the difference of the off-nadir angles, relating it to the ground ranges and heights of the two pixels:

$$\Delta\Phi_{ij} \simeq 4\pi\frac{B_\perp}{\lambda_0}\left(\theta_j - \theta_i\right) = 4\pi\frac{B_\perp}{\lambda_0}\left(\arctan\frac{R_{gj}}{H - z_j} - \arctan\frac{R_{gi}}{H - z_i}\right). \tag{12.13}$$

The phase difference $\Delta\Phi_{ij}$, proportional to the small difference $\theta_j - \theta_i$, can now fall within the $0-2\pi$ range when the pixels are sufficiently close, as, for instance, when they are adjacent, say a few meters, or less, apart. It is important to consider that, on one side the closeness of the angles of arrival is able to keep $\Delta\Phi_{ij}$ within the $0-2\pi$ interval, while, on the other, even small variations of the pixel positions can result in measurable changes of the relative phase (12.13), because $B \gg \lambda_0$.

Equation (12.13) indicates that the height z_j of the j-th pixel, obviously related to that of the initial one by $z_j = z_i + \Delta z_{ij}$, can be retrieved by measuring the difference of phase $\Delta\Phi_{ij}$ of the scattered field corresponding to the ground ranges R_{gj} and R_{gi}. When the local altitude of the surface is small with respect to the height of the radar platform[22] H, the following approximation holds

$$\frac{R_{gj}}{H - z_j} \simeq \frac{R_{gj}}{H}\left(1 + \frac{\Delta z_{ij}}{H}\right).$$

Given the properties of the arctan function, when the maximum value of $|R_{gj} - R_{gi}|$ is also small with respect to H,

$$\begin{aligned}\Delta\Phi_{ij} &\simeq 4\pi\frac{B_\perp}{\lambda_0}\arctan\left[\frac{R_{gi} - R_{gj} - \dfrac{R_{gj}\Delta z_{ij}}{H}}{H + \dfrac{R_{gi}R_{gj}}{H}\left(1 + \dfrac{\Delta z_{ij}}{H}\right)}\right] \\ &\simeq \Delta\Phi_{ijf} - 4\pi\frac{B_\perp}{\lambda_0}\frac{R_{gj}\Delta z_{ij}}{H^2 + R_{gi}R_{gj}}.\end{aligned} \tag{12.14}$$

In Eq. (12.14), the quantity $\Delta\Phi_{ijf}$ is the second phase difference for $\Delta z_{ij} = 0$, that is the variation of phase caused only by the change of ground range $R_{gj} - R_{gi}$ on the reference geodetic *smooth* surface considered in Sect. 4.3. The height difference Δz_{ij} between the pixel at range R_{gj} and the one at R_{gi} is obtained from the second phase difference $\Delta\Phi_{ij}$ once this latter is corrected for the ground-range contribution:

$$\Delta z_{ij} = z_j - z_i \simeq -\frac{\lambda_0}{B_{\perp i}}\frac{H^2 + R_{gi}R_{gj}}{R_{gj}}\frac{\Delta\Phi_{ij} - \Delta\Phi_{ijf}}{4\pi}. \tag{12.15}$$

The elevation z_j of the scatterers at a given azimuth angle are given by (12.15) with respect to the known height z_i of a reference pixel.

[22] The requirement is clearly satisfied for a space-based platform.

12.3 SAR Interferometry

Equation (12.15) indicates that three-dimensional information on the surface of the Earth can be obtained by measuring differences of phase of the scattered field. The waves are those traveling back and forth between the radar platform[23] in the positions S_1 and S_2 and the scatterers located on the surface of the Earth. Section 4.3 shows that the differential phase is delineated by interfering waves. The *interferometric phase*, that is the phase difference $\Delta\Phi_{ij}$ as a function of the ground ranges of consecutive pixels for each azimuth, forms the interferometric *phase* fringes. Since the underlying physical phenomenon is the same, the phase fringes clearly correspond to the *intensity* fringes over a plane surface, which Sect. 4.3 showed to be sensitive to height. This feature suggests that mapping the terrain elevation can be carried out by combining pairs of SAR *complex* interferometric images, i.e., including information on both amplitude and phase of the field, taken from different platform positions.

Equation (12.14) points out that the interferometric fringes have a "flat-earth" contribution superimposed to the component originated by the topographic elevation. The flat-earth phase difference computed as a function of range must be cancelled to retrieve height. Such a *de-ranging* operation is commonly named *flattening*. The relative height is derived as a function of ground range for each azimuth from the de-ranged fringes. The relative altitudes derived for each pair of azimuth and ground range coordinates yield the 3-D representation of the imaged area, that is its DEM [26]. Figure 12.22 shows the rough interferometric phase pattern produced by the combined effects of range and altitude and the de-ranged pattern, from which the topography of the area is readily visualized, to details down to the minor rills and combes.

12.3.1 The Interferogram

The map of interferometric phase represents the values of the difference of phase for each pair of azimuth and range coordinates. It is called *interferometric image*, or *interferogram* and features the altitude information. In case of linearly co-polarized fields, the interferogram $\mathfrak{I}$ is obtained by the pixel-by-pixel dot product $\mathfrak{I}_{ij}$ of the scattered field measured at point S_m times the conjugate of the field measured at a different point S_s, similarly[24] to the interferometric product of Sect. 4.3.2

[23] The approach holds for pairs of platforms as well.

[24] The interferogram, which now refers to the scattered field measured at two different points, is actually a kind of generalization of the approach of Sect. 4.3.2.

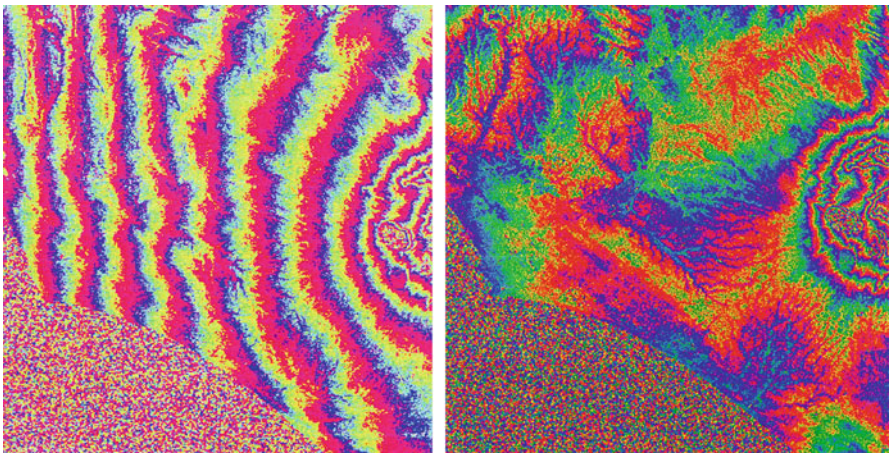

Fig. 12.22 Interferometric phase of the Rome, Italy, area, showing the combined effects of both range and topography (*left*) and interferometric phase of the same acquisition after de-ranging (i.e., after subtracting the phase difference relative to the variation of ground range), highlighting the topographic features of the area (*right*) (Credit: ERS C-band SAR data, ESA; processing, Mirko Albani)

$$\mathfrak{I}_{ij} := \boldsymbol{E}^{(\mathrm{s})}_{ij\,\mathrm{m}} \cdot \boldsymbol{E}^{(\mathrm{s})*}_{ij\,\mathrm{s}} \ . \tag{12.16}$$

It is important to realize the present meaning of the subscripts in (12.16): now $\boldsymbol{E}^{(\mathrm{s})}_{ijk}$ is the field received by the SAR at position S_k ($k = \mathrm{m}, \mathrm{s}$) from the scattering pixel P_{ij} located at the azimuth position i ($i = 1, \ldots, N_\mathrm{a}$) and the range position j ($j = 1, \ldots, N_\mathrm{r}$), of an image formed by $N_\mathrm{a} \times N_\mathrm{r}$ pixels. The point S_m is the position[25] of the platform from which the so-called *master* image is acquired, while S_s denotes the point of acquisition of the *slave* image.

The complex quantity represented by the interferogram has modulus equal to the product of the amplitudes and argument equal to the difference of the phases of the field at the two measurement points:

$$\mathfrak{I}_{ij} = \left|\mathfrak{I}_{ij}\right| e^{-\mathrm{j}(\Phi_{ij\,\mathrm{m}} - \Phi_{ij\,\mathrm{s}})} \qquad (i = 1, \ldots, N_\mathrm{a};\ \ j = 1, \ldots, N_\mathrm{r}) \ .$$

Section 12.2.2 shows that the phase difference $\Phi_{ij\,\mathrm{m}} - \Phi_{i\ell\,\mathrm{s}}$ (with $\ell \neq j$) for a given surface slope, depends on the ratio $B_\perp/\lambda_0$, which increases or decreases the

[25] Related to the electric center of the antenna.

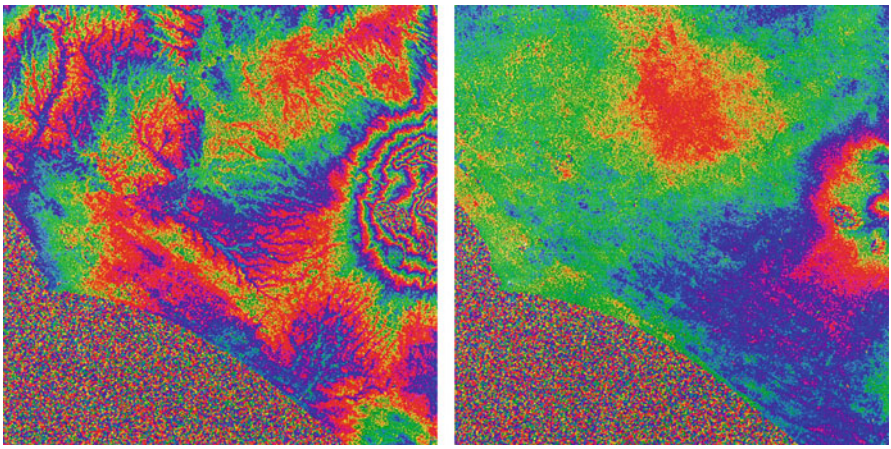

Fig. 12.23 De-ranged interferometric fringes with perpendicular baselines $B_\perp = 99\,\text{m}$ (*left*) and $B_\perp = 20\,\text{m}$ (*right*) on the Rome, Italy, area: in the Colli Albani volcanic complex ($z_{\max} \approx 950\,\text{m}$) on the *right* of the images, the number of fringes for $B_\perp = 99\,\text{m}$ is about five times the one for $B_\perp = 20\,\text{m}$. The *left* image is the same as in Fig. 12.22, repeated here to ease the comparison (Credit: ERS C-band data, ESA; processing, Mirko Albani)

number of fringes per unit ground range interval, that is the fringe spatial frequency introduced in Sect. 4.3. According to (12.14),

$$|\Delta\Phi_\text{d}| \simeq C\,\frac{B_\perp}{R\,\lambda_0}\,|\Delta z|\ ,$$

where $\Delta\Phi_\text{d}$ is the de-ranged interferometric phase difference, R the distance in slant range and the proportionality factor C depends on the angle[26] of incidence θ. For a given height difference between two pixels, a larger baseline increases the number of fringes between the two pixels, whereas a lower baseline decreases their number, in analogy with (4.46). Therefore, at a given radar frequency, the sensitivity to the height differences increases with increasing perpendicular baseline and, correspondingly, for a given baseline, the sensitivity increases with decreasing wavelength. The effect of the baseline on the fringe frequency can be appreciated by comparing the interferometric phase images acquired on the same area with different baselines shown in Fig. 12.23. Given the $\text{mod}(\Delta\Phi, 2\pi)$ feature, the interferometric phase fringes are *wrapped* into the 0 to 2π range and must be *unwrapped* [15, 16, 22, 38], that is, the phase must be transformed into a single-valued function of R_g, before the altitude structure of the surface can be retrieved. Unwrapping requires proceeding continuously from one pixel to the adjacent ones, so that

[26]Both distance R and angle θ are intended to be mean quantities for the interval of ground range to which the altitude difference Δz refers.

the variation of z with R_g is tracked. If the perpendicular baseline is such that $\Delta\Phi_{ij+1} - \Delta\Phi_{ij} \geq 2\pi$, there is no deterministic relation between the interferometric phases of two pixels adjacent in ground range. The perpendicular baseline $B_{\perp C}$ for which $\Delta\Phi_{ij+1} - \Delta\Phi_{ij} = 2\pi$ is the *critical baseline*: at a given incidence angle, $B_{\perp C} \propto \lambda_0/d_r$, i.e., it is larger for finer ground-range resolution d_r. Typical system parameters and common earth surface features yield $B_{\perp C}$ of the order of 1 km. When $B_\perp \gtrsim B_{\perp C}$, the topographic information becomes buried in noise and the height information cannot be retrieved. It should be considered that, in practice, the irregularities in the unwrapped phase, hence in the retrieved height, tend to blow up already when $B_\perp$ approaches $B_{\perp C}$.

12.3.2 Accuracy of Interferometric Measurements

The phase irregularities in the interferometric image, and especially the discontinuities, may hamper the unwrapping procedure and prevent recovery of the total phase, hence the retrieval of height. A number of effects are present in an actual scenario which adversely affect the interferometric performance. The phase irregularities mainly derive from atmospheric propagation, labile nature of surface, low field amplitude, while singularities may be caused by lay-over, double bounce, shadowing and system noise. Moreover, a limit in the accuracy of the phase measurement is set by the baseline and is inherent to the interferometric technique.

12.3.2.1 Effect of the Atmosphere

As discussed in Sects. 2.2.1 and 5.2.3, the atmosphere has refractive index $n \neq 1$, hence the incident and scattered waves do not propagate in vacuo, as assumed in the initial approach based only on geometric considerations. The basic expression (12.7) of the scattered field producing the monostatic radar echo has to be modified accordingly, to take into account both the phase shift and the possible attenuation caused by the one-way propagation in the atmosphere:

$$\boldsymbol{E}^{(s)} = \frac{\mathcal{F}\left(\mathbf{r}_0^{(i)}, \mathbf{r}_0^{(s)}\right)}{R} \, e^{-\int_0^R \alpha_e(s)ds} \, e^{-j\kappa_0 \int_0^R n(s)ds} . \tag{12.17}$$

Equation (12.17), of the form (5.38), is a convenient expression highlighting the roles of the scattering function $\mathcal{F}$ (by definition relative to vacuum), of the extinction $\alpha_e(s)$, which is caused by absorption in the non-scattering case,[27] and of the refractive index $n(s)$ of the air along the path of geometric length R. The effect

[27] If needed, the specific extinction α_e can include scattering according to (9.15).

of the refractivity on the amplitude, described by the transport equation outlined in Sect. 5.3, is now neglected.

For a given target, the phase of the scattered field received by the radar depends not only on the geometric distance between the platform and the scatterer, but also on the atmospheric parameters that affect the electromagnetic path length. Since along the platform-to-surface round trip path $n \geq 1$, the wave velocity and correspondingly the wavelength are smaller than those in vacuo (cf. Sects. 4.1.2.1 and 4.1.2.2), the "arrival" of the echo field looks "delayed" and the distance of the scatterer appears larger than its geometric one. In particular, the phase of the scattered field[28] exceeds the phase relative to the geometric distance because the atmospheric path length in (12.17) is larger than that in the vacuum. The difference $\mathcal{L}_\mathrm{a}$ between the electromagnetic length of the path in the atmosphere and that of vacuum $\mathcal{L}_0$ is the *excess path length*[29] introduced in Sect. 5.2.3,

$$\mathcal{L}_\mathrm{a} = \int_0^R n(s)\, ds - \int_0^R ds = \int_0^R [n(s) - 1]\, ds \; .$$

Sections 2.2.1 and 5.2.3 point out that $\mathcal{L}_\mathrm{a}$ depends on climatology, that is, on the atmospheric parameters p_t, T, and, mainly, p_w, according to (2.36) and (5.26). The typical excess path length in temperate climates has values of a few meters and undergoes seasonal changes of tens of centimeters. Figure 12.24 shows an example of the distribution of $\mathcal{L}_\mathrm{a}$ and of its seasonal variations. The field $\boldsymbol{E}_\mathrm{m}^{(\mathrm{s})}$ originated by a given resolution cell and received by the SAR antenna located in the position S_m of the master acquisition at time t_m, is expressed in compact form by

$$\boldsymbol{E}_\mathrm{m}^{(\mathrm{s})} = \frac{\mathrm{e}^{-\mathrm{j}\kappa_0 \mathcal{L}_\mathrm{m}}}{R_\mathrm{m}} \mathcal{A}_\mathrm{m}\, \mathcal{F}_\mathrm{m} \; . \tag{12.18}$$

Equation (12.18) contains the electromagnetic length $\mathcal{L}_\mathrm{m}$ of the path from the target to the SAR in the master position S_m, as well as the geometric distance R_m, the corresponding attenuation $\mathcal{A}_\mathrm{m}$, and the free-space scattering function $\mathcal{F}_\mathrm{m}$ (7.10) at the time[30] t_m at which the master image is acquired. With analogous notations, the field backscattered by the same resolution cell and received by the sensor in the position S_s of the slave acquisition at time t_s is

$$\boldsymbol{E}_\mathrm{s}^{(\mathrm{s})} = \frac{\mathrm{e}^{-\mathrm{j}\kappa_0 \mathcal{L}_\mathrm{s}}}{R_\mathrm{s}} \mathcal{A}_\mathrm{s}\, \mathcal{F}_\mathrm{s} \; . \tag{12.19}$$

[28] The phase of the incident field, which behaves analogously, must be also accounted for.

[29] The excess path length is sometimes improperly called atmospheric path *"delay"*.

[30] Temporal changes of the bio-geo-physical parameters of the target modify its dielectric structure, hence the scattering function (cf. Sect. 12.3.2.2).

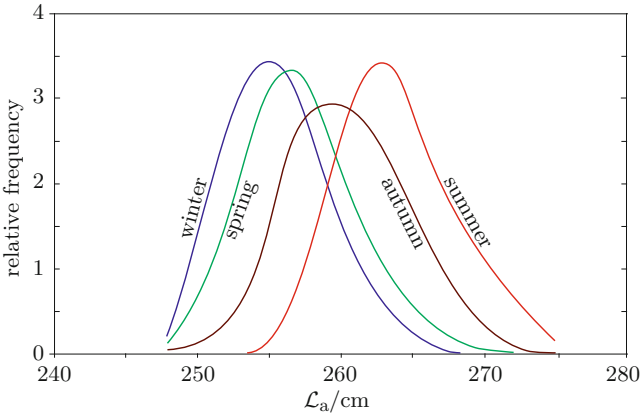

Fig. 12.24 Example of seasonal statistical distribution of excess path length $\mathcal{L}_a$ caused by the atmosphere in correspondence of De Bilt, The Netherlands, computed from meteorological data; the higher the climatological atmospheric water vapor content (autumn, summer), the larger the wet path delay and, in general, the expected fluctuations

The dyadic interferometric product $\mathbb{I}$ formed by the vector field received at the two space locations and times is

$$\mathbb{I} = \frac{\mathrm{e}^{-\mathrm{j}\kappa_0(\mathcal{L}_\mathrm{m} - \mathcal{L}_\mathrm{s})}}{R_\mathrm{m} R_\mathrm{s}} \mathcal{A}_\mathrm{m} \mathcal{A}_\mathrm{s} \ \mathcal{F}_\mathrm{m} \mathcal{F}_\mathrm{s}^* \ . \tag{12.20}$$

For given free-space scattering functions,[31] the phase of the interferometric product elements is affected by the difference $\mathcal{L}_\mathrm{m} - \mathcal{L}_\mathrm{s}$ between path lengths, hence by the atmospheric propagation conditions[32] existing along each path at the respective times of the radar measurements. The phase contributed by the atmosphere depends on the difference between the patterns $n_\mathrm{m}(s)$ and $n_\mathrm{s}(s)$ of the air refractive index along the master and slave paths, since the electromagnetic lengths (5.23) are

$$\mathcal{L}_\mathrm{m} = \int_0^{R_\mathrm{m}} n_\mathrm{m}(s)\, ds; \qquad \mathcal{L}_\mathrm{s} = \int_0^{R_\mathrm{s}} n_\mathrm{s}(s)\, ds \ .$$

It has been observed that the microwave refractive index $n(s)$ (2.36) of the air is considerably affected by the density of water vapor, which is less abundant than the main atmospheric constituents, but has high polarizability. Given the turbulent dynamics of the atmosphere [30], the air parameters exhibit space-time

[31] Remember that the scattering function (7.10) contains the internal field created by the wave incident onto the target.

[32] Differences between geometric path lengths are assumed to be known.

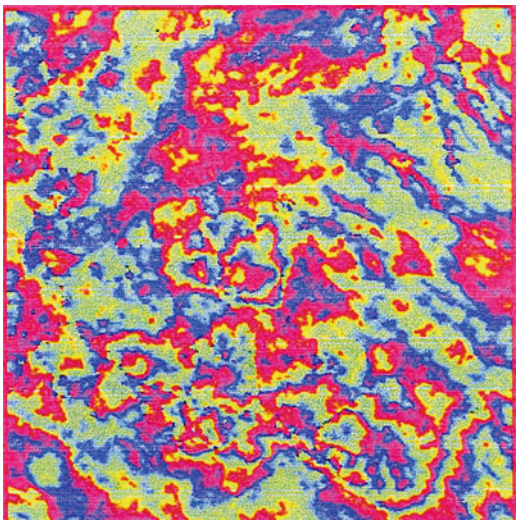

Fig. 12.25 Example of interferometric phase random patterns caused by space-time fluctuations of excess path length caused by the atmospheric refractive turbulence on the fairly flat Tor Vergata area, Rome, Italy

random fluctuations: the pressure has large scale (typically of the order of tens of kilometers) and slow (of the order of tens of minutes) variations and its pattern is usually monitored and forecasted with adequate accuracy; instead, water vapor has additional small-scale space-time fluctuations which are hard to determine. Therefore, the atmospheric refractive index may vary appreciably over hundreds of meters and over tens of seconds because of the water vapor turbulence, neither its detailed space-time structure can be modeled in a deterministic fashion with serviceable accuracy. Figure 12.25 shows the dramatic effect of the water vapor turbulence on the interferometric phase pattern, which, in this case, loses connection with the topography of the imaged area.

The random fluctuations of the atmospheric water vapor density induce fluctuations $\mathcal{L}'$ of the path length $\mathcal{L}$ around its average value $\overline{\mathcal{L}}$:

$$\mathcal{L} = \overline{\mathcal{L}} + \mathcal{L}' \ .$$

Taking now into account the platform-to-target round trip, the interferometric phase factor that the atmosphere contributes to the interferometric product is given by

$$\mathrm{e}^{-\mathrm{j}2\kappa_0(\mathcal{L}_\mathrm{m} - \mathcal{L}_\mathrm{s})} = \mathrm{e}^{-\mathrm{j}2\kappa_0(\overline{\mathcal{L}_\mathrm{m}} + \mathcal{L}'_\mathrm{m} - \overline{\mathcal{L}_\mathrm{s}} - \mathcal{L}'_\mathrm{s})} \ .$$

The atmospheric refractive index is close to that of vacuum and, moreover, the interferometric measurements are taken from close locations of the radar platform; therefore, the mean electromagnetic path lengths are almost the same and their difference can be assumed proportional to the difference between the geometric distances:

$$\mathrm{e}^{-\mathrm{j}2\kappa_0(\overline{\mathcal{L}_\mathrm{m}} - \overline{\mathcal{L}_\mathrm{s}})} \simeq \mathrm{e}^{-\mathrm{j}2\kappa_0 \overline{n}\,(R_\mathrm{m} - R_\mathrm{s})} \ ,$$

where $\overline{n}$ is an effective refractive index dependent on the local climatology and which, to some extent, can be estimated. Instead, the unremovable random parts of the path lengths cause the stochastic fluctuations of the field phase factors

$$\mathrm{e}^{-\mathrm{j}2\kappa_0(\mathcal{L}'_\mathrm{m} - \mathcal{L}'_\mathrm{s})} = \mathrm{e}^{-\mathrm{j}\Delta\Phi'_\mathrm{ms}} \ ,$$

which adversely affect the correspondence between interferometric phase and height on which many applications of SAR interferometry [23, 27] are based. The random component that the atmosphere introduces into the difference of interferometric phase for the pixels P_{ij} and $\mathrm{P}_{i\ell}$ at the two different ground ranges[33] identified by the subscripts $_j$ and $_\ell$ is

$$\Delta\Phi'_{j\ell} = \frac{4\pi}{\lambda_0}\left[(\mathcal{L}'_{ij\,\mathrm{m}} - \mathcal{L}'_{ij\,\mathrm{s}})\right] - (\mathcal{L}'_{i\ell\,\mathrm{m}} - \mathcal{L}'_{i\ell\,\mathrm{s}})\right] \ .$$

This phase fluctuation causes errors in the retrieval of both the relative height of the pixels and of its temporal variation, which is the quantity of interest in DinSAR applications [28].

Repeat-pass satellite interferometry uses pairs of images acquired at different passes over the area of interest, with typical time intervals between interferometric acquisitions from one day to a few tens of days. The parameters of the atmosphere, hence the electromagnetic path lengths, may change dramatically between the master and the slave acquisitions, especially due to possible changes of air mass, which are accompanied by changes of pressure, temperature and, particularly, of water vapor. As said, large-scale variations produce effects that can be mitigated, especially over flat areas, but the small-scale fluctuations of air moisture, which combine over the two image acquisitions, can strongly affect the interferograms and corrupt the altitude retrieval. When dynamical phenomena such as, for instance, rapid crustal deformation are not being observed, the fluctuations can clearly be smoothed out by averaging over a sufficiently large set of interferometric pairs.

The effects of the random fluctuations of the excess path lengths tend to vanish when $\mathcal{L}'_\mathrm{m} \approx \mathcal{L}'_\mathrm{s}$. Given the relative closeness of S_m to S_s and of P_{ij} to $P_{i\ell}$, hence the proximity of the master and slave propagation paths in the troposphere, this condition is approached if the pair of interferometric images is acquired at the same time, so that the crossed air mass is almost the same. Taking measurements from two different positions at the same time with a single platform is made difficult by the needed baselines, obviously contrasting with the physical dimensions of usual payloads. Regarding space-based platforms, an experiment was carried out in 2000 from the NASA's Space Shuttle Endeavour,

[33] Subscript $_i$ identifies the azimuth position and, for the time being, is fixed.

Fig. 12.26 The extended interferometric radar antenna on the SRTM shuttle (Credit: NASA/JPL-Caltech, Ball Aerospace & Technologies Corp.)

which was put in orbit with a payload outfitted with two radar antennas: one antenna was located in the shuttle's payload bay, the other on the end of a 60-m mast that extended once the shuttle was in orbit, as sketched in Fig. 12.26. The experimental NASA's **S**huttle **R**adar **T**opography **M**ission (SRTM) was able to systematically collect data with reduced atmospheric interference over most of the land surfaces that lay between 60° north and 54° south latitude, that is about 80 % of all the land on Earth. An extensive topographic data base was generated and made available, although at relatively low horizontal and vertical resolutions.

Contemporary acquisitions from multiple operational platforms are able to substantially reduce the inaccuracy in fine surface topographic mapping caused by tropospheric (and also ionospheric [25, 32, 33]) refractivity turbulence, with altitude retrieval accurate to a few meters. The TanDEM system has been providing data of this kind since the end of 2010 (Fig. 12.27).

12.3.2.2 Effect of the Structure of the Target

The interferometric product for a given pixel imaged by two radar acquisitions carried out from positions S_k at times t_k ($k = \mathrm{m},\ \mathrm{s}$), contains the scattering functions $\mathcal{F}_k$ relative to the pertinent directions of incidence $\mathbf{r}_{0k}^{(\mathrm{i})}$ and scattering $\mathbf{r}_{0k}^{(\mathrm{s})}$ and to the time t_k. Attenuation is usually negligible, at least for systems operating at C- or L-band (cf. Sect. 10.1.2.1), therefore $\mathcal{A}_k \approx 1$. The k-th *free-space* scattering function (7.10) is

Fig. 12.27 The TanDEM-X Mission, which has operated since 12 October 2010, acquires interferometric image pairs simultaneously from two satellites in quasi-monostatic configuration (Credit: ©2010 DLR)

$$\mathcal{F}_k\left(\mathbf{r}_{0k}^{(\mathrm{i})}, \mathbf{r}_{0k}^{(\mathrm{s})}\right) = \frac{\kappa_0^2}{4\pi} \iiint_{V_k'} \boldsymbol{E}_{\perp k}\, \Delta\tilde{\epsilon}_k\, \mathrm{e}^{\mathrm{j}\kappa_0 \boldsymbol{r}'\cdot \mathbf{r}_{0k}^{(\mathrm{s})}}\, \mathrm{d}V' \,.$$

As usual, the volume V_k' denotes the resolution cell, bound horizontally by the element of reference surface corresponding to the pixel, which originates the scattered field received in the k-th acquisition. Each component $\mathcal{F}_{pk}$ of $\mathcal{F}_k$ is expressed by

$$\mathcal{F}_{pk} = \left|\mathcal{F}_{pk}\right| \mathrm{e}^{\mathrm{j}\Phi_{\mathcal{F}pk}} = \frac{\kappa_0^2}{4\pi} \iiint_{V_k'} E_{\perp pk}\, \Delta\tilde{\epsilon}_k\, \mathrm{e}^{\mathrm{j}\kappa_0 \boldsymbol{r}'\cdot \mathbf{r}_{0k}^{(\mathrm{s})}}\, \mathrm{d}V', \qquad p = x, y, z \,. \tag{12.21}$$

The phase $\Phi_{\mathcal{F}p\,k}$ of the *free-space* scattering function of a given pixel depends on the k-th acquisition for several reasons. First of all, if the interferometric images are not acquired simultaneously, the bio-geo-physical parameters of the observed terrestrial environment generally differ between the acquisitions, hence the spatial distribution of the relative permittivity $\Delta\tilde{\epsilon}_k(\boldsymbol{r}')$ depends on k. The internal field $\boldsymbol{E}_{\perp k}$ also depends on k, because, in addition to its dependence on the varying permittivity structure, the incidence direction $\mathbf{r}_{0k}^{(\mathrm{i})}$ changes. Finally, the volume V_k' of the scattering resolution cell corresponding to a given pixel is affected by the change of permittivity of

the terrestrial materials and by the incidence angle. The pixel-dependent change of phase of the scattering function between acquisitions perturbs the interferogram, thus corrupting the topographic or differential height information it contains.

The permittivity at each point $\boldsymbol{r}'$ of the resolution cell fluctuates about its mean value according to (7.24):

$$\Delta\tilde{\epsilon}_k = \overline{\Delta\tilde{\epsilon}} + \Delta\tilde{\epsilon}'_k \, .$$

The average $\overline{\Delta\tilde{\epsilon}} = \langle \Delta\tilde{\epsilon}_k(\boldsymbol{r}') \rangle$ is over the ensemble of interferometric acquisitions for the same target, while the zero-mean fluctuation $\Delta\tilde{\epsilon}'_k$ is relative to the k-th acquisition. The internal transverse electric field $\boldsymbol{E}_\perp$ at each point $\boldsymbol{r}'$ of the resolution cell is analogously written as in (7.25):

$$\boldsymbol{E}_{\perp k} = \boldsymbol{E}_{\perp \overline{\epsilon} k} + \boldsymbol{E}_{\perp \epsilon' k} \, ,$$

with $\boldsymbol{E}_{\perp \overline{\epsilon} k}$ denoting the field in the *average permittivity* resolution cell for the incidence angle relative to the k-th acquisition and $\boldsymbol{E}_{\perp \epsilon' k}$ is the field deviation corresponding to the permittivity structure relative to the same k-th acquisition. The free-space scattering function relative to the k-th acquisition is correspondingly given by (7.26):

$$\mathcal{F}_k \left(\mathbf{r}_{0k}^{(\mathrm{i})}, \mathbf{r}_{0k}^{(\mathrm{s})} \right) = \frac{\kappa_0^2}{4\pi} \iiint_{V'_k} (\boldsymbol{E}_{\perp \overline{\epsilon} k} + \boldsymbol{E}_{\perp \epsilon' k}) \left(\overline{\Delta\tilde{\epsilon}} + \Delta\tilde{\epsilon}'_k \right) \mathrm{e}^{\mathrm{j}\kappa_0 \boldsymbol{r}' \cdot \mathbf{r}_{0k}^{(\mathrm{s})}} \, \mathrm{d}V' \, .$$

The assumption leading to (7.27), i.e., that the deviation of the inner field caused by the fluctuating part of the permittivity is small with respect to the field in the average-permittivity resolution cell, is maintained, so that

$$\mathcal{F}_k \left(\mathbf{r}_{0k}^{(\mathrm{i})}, \mathbf{r}_{0k}^{(\mathrm{s})} \right) \simeq \frac{\kappa_0^2}{4\pi} \iiint_{V'_k} \boldsymbol{E}_{\perp \overline{\epsilon} k} \left(\overline{\Delta\tilde{\epsilon}} + \Delta\tilde{\epsilon}'_k \right) \mathrm{e}^{\mathrm{j}\kappa_0 \boldsymbol{r}' \cdot \mathbf{r}_{0k}^{(\mathrm{s})}} \, \mathrm{d}V' := \mathcal{F}_{\overline{\epsilon} k} + \mathcal{F}_{\epsilon' k} \, . \tag{12.22}$$

It is worth pointing out that the part $\mathcal{F}_{\overline{\epsilon} k}$ of the scattering function relative to the deterministic permittivity structure varies with the acquisition, since both the complex field $\boldsymbol{E}_{\perp \overline{\epsilon} k}$ inside the average-permittivity resolution cell and the diffraction phase factor $\exp\left(\mathrm{j}\kappa_0 \boldsymbol{r}' \cdot \mathbf{r}_{0k}^{(\mathrm{s})}\right)$ in (12.22) depend on the particular incidence and scattering directions relative to the k-th acquisition.

The free-space interferometric scattering dyadic $\mathbb{I}_0$ contains mixed products of components $\mathcal{F}_{\overline{\epsilon} k}$ and $\mathcal{F}_{\epsilon' k}$ of the scattering functions corresponding to the pair ($k = \mathrm{m}, \mathrm{s}$) of acquisitions:

$$\mathbb{I}_0 := \mathcal{F}_\mathrm{m} \mathcal{F}_\mathrm{s}^* = \mathcal{F}_{\overline{\epsilon}\mathrm{m}} \mathcal{F}_{\overline{\epsilon}\mathrm{s}}^* + \mathcal{F}_{\overline{\epsilon}\mathrm{m}} \mathcal{F}_{\epsilon'\mathrm{s}}^* + \mathcal{F}_{\overline{\epsilon}\mathrm{s}}^* \mathcal{F}_{\epsilon'\mathrm{m}} + \mathcal{F}_{\epsilon'\mathrm{m}} \mathcal{F}_{\epsilon'\mathrm{s}}^* = \mathbb{I}_{0\overline{\epsilon}} + \mathbb{I}_{0\epsilon'} \, . \tag{12.23}$$

Therefore, the dyadic $\mathbb{I}_0$ consists of a term $\mathbb{I}_{0\overline{\epsilon}}$ relative to the average (deterministic) permittivity $\overline{\epsilon}$ plus the term $\mathbb{I}_{0\epsilon'}$ including dyadics relative to the fluctuations ϵ' of $\Delta\tilde{\epsilon}$. Each element of $\mathbb{I}_0$, which contributes to the interferogram for a given pair

of components of the received electric field vector, introduces a perturbation into the relation between interferometric phase and distance of the target. As said, the phase of the scattered field is altered not only because the permittivity structure and consequently the inner field vary between non-simultaneous acquisitions, but also because the field inside the stable structure of the resolution cell and the diffraction phase factor change with the incidence angle.

12.3.2.2.1 Effect of Permanent Structure

The part of scattering dyadic relative to the deterministic permittivity structure is

$$\mathcal{F}_{\overline{\epsilon}\mathrm{m}}\,\mathcal{F}^{*}_{\overline{\epsilon}\mathrm{s}} \simeq \frac{\kappa_0^4}{(4\pi)^2} \iiint_{V'_{\mathrm{m}}} \boldsymbol{E}_{\perp\overline{\epsilon}\mathrm{m}}\,\overline{\Delta\epsilon}\;\mathrm{e}^{\mathrm{j}\kappa_0 \boldsymbol{r}'\cdot\mathbf{r}^{(\mathrm{s})}_{0\mathrm{m}}}\,\mathrm{d}V' \iiint_{V'_{\mathrm{s}}} \boldsymbol{E}^{*}_{\perp\overline{\epsilon}\mathrm{s}}\,\overline{\Delta\epsilon}^{\,*}\;e^{-j\kappa_0 \boldsymbol{r}'\cdot\mathbf{r}^{(\mathrm{s})}_{0\mathrm{s}}}\,\mathrm{d}V' \,. \tag{12.24}$$

In Eq. (12.24), $\overline{\Delta\tilde{\epsilon}}(x', y', z')$, independent of the k-th acquisition, describes a *permanent target*, which remains unchanged with respect to the acquisition. In spite of the invariant dielectric structure, the change of the incidence[34] angle causes a variation in the phase of the first element of the scattering dyadic (12.23). Resolution cells the dielectric structure of which has symmetry such that both $\boldsymbol{E}_{\perp\overline{\epsilon}k}$ and V'_k are invariant with respect to the incidence direction $\mathbf{r}^{(\mathrm{i})}_{0k}$ are clearly exception. This occurs when an ideal target has, for instance, spherical symmetry. With the notation[35] (12.21), the mean-permittivity part of the scattering function adds a term

$$\Phi_{\overline{\epsilon}\mathrm{ms}} = \Phi_{\overline{\epsilon}\mathrm{m}} - \Phi_{\overline{\epsilon}\mathrm{s}} \tag{12.25}$$

to the interferometric phase relative to a given pixel imaged at p polarization.

Figure 12.28 refers to the simple model already considered in Sect. 7.4 to interpret the behavior of scattering. The resolution cell V' is bound by the $(x'y')$-horizontal plane, with $\mathbf{x}_0$ in the range direction and $\mathbf{y}_0$ along the azimuth (Fig. 11.27). As in Sect. 7.4, the scattering-effective[36] field internal to the deterministic part of the target is regarded as a plane wave "refracted" (Sect. 6.3.1) into the average-permittivity volume V':

$$\boldsymbol{E}_{\overline{\epsilon}k} = \boldsymbol{E}_{0\overline{\epsilon}k}\,\mathrm{e}^{-\alpha'_k z'}\,\mathrm{e}^{-\mathrm{j}\boldsymbol{\beta}'_{\mathrm{t}k}\cdot\boldsymbol{r}'_{\mathrm{t}}}\,\mathrm{e}^{-\mathrm{j}\beta'_{zk}z'} = \boldsymbol{E}_{0\overline{\epsilon}k}\,\mathrm{e}^{-\alpha'_k z'}\,\mathrm{e}^{-\mathrm{j}\beta'_{xk}x'}\,\mathrm{e}^{-\mathrm{j}\beta'_{zk}z'} \,. \tag{12.26}$$

[34] Obviously, also the backscattering direction $\mathbf{r}^{(\mathrm{s})}_{0k} = -\mathbf{r}^{(\mathrm{i})}_{0k}$ changes, being opposite to the incidence one.

[35] The subscripts $_{\mathcal{F}}$ and $_p$ have been dropped to lighten the notation.

[36] Also the subscript $_{\perp}$ is omitted to simplify the notation.

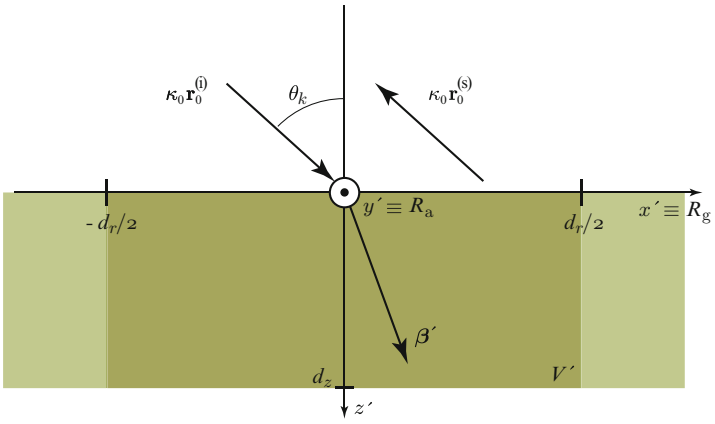

Fig. 12.28 Geometry of backscattering in the incidence vertical plane: x' coincides with the ground-range coordinate R_g, y' with the azimuth coordinate R_a, z' is the depth; the ground-range width of the resolution cell V' is d_r (cf. Fig. 7.28)

The propagation vector $\boldsymbol{k}'_k = \boldsymbol{\beta}'_k - \mathrm{j}\boldsymbol{\alpha}'_k$ of the refracted wave may depend on the polarization of the field according to the possible anisotropy[37] of the average structure of the background material in the scattering volume V'_k. The deterministic-permittivity component of the scattering function (12.22) is then given by

$$\mathcal{F}_{\overline{\epsilon}k} \simeq \frac{\kappa_0^2}{4\pi} \boldsymbol{E}_{0\overline{\epsilon}k} \int_0^{d_z} \iint_{S'} \overline{\Delta\tilde{\epsilon}}\, \mathrm{e}^{-\alpha'_k z'} \mathrm{e}^{-\mathrm{j}\beta'_{xk} x'}\, \mathrm{e}^{-\mathrm{j}\beta'_{zk} z'} \mathrm{e}^{\mathrm{j}\boldsymbol{k}''_k \cdot \boldsymbol{r}'}\, \mathrm{d}S'\, \mathrm{d}z' \,,$$

where S', having area $\Delta A = d_a \times d_r$, is the surface of the pixel sketched in Fig. 11.27, and d_z is the vertical extension of the resolution cell,[38] assumed independent of k, i.e., of the master or slave image acquisition (Fig. 12.20).

Inside the volume of the target, the propagation vector $\boldsymbol{k}''_k$ of the backscattered wave is opposite to the one of the refracted wave:

$$\boldsymbol{k}''_k = -\beta'_{xk}\, \mathbf{x}_0 - (\beta'_{zk} - j\alpha'_k)\, \mathbf{z}_0 \,, \tag{12.27}$$

so that

$$\mathcal{F}_{\overline{\epsilon}k} \simeq \frac{\kappa_0^2}{4\pi} \boldsymbol{E}_{0\overline{\epsilon}k} \int_0^{d_z} \iint_{S'} \overline{\Delta\tilde{\epsilon}}\, \mathrm{e}^{-2\alpha'_k z'} \mathrm{e}^{-\mathrm{j}2\beta'_{zk} z'}\, \mathrm{e}^{-\mathrm{j}2\beta'_{xk} x'}\, \mathrm{d}S'\, \mathrm{d}z' \,. \tag{12.28}$$

Similarly to the approach followed in Sect. 7.4.3, the average permittivity structure in the object is conveniently factorized by

[37] Anisotropy can occur, for instance, in a canopy of oriented elements such as prevailingly vertical vegetation stems.

[38] Often the thickness $d_z \to \infty$ when the observed target is solid land or sea.

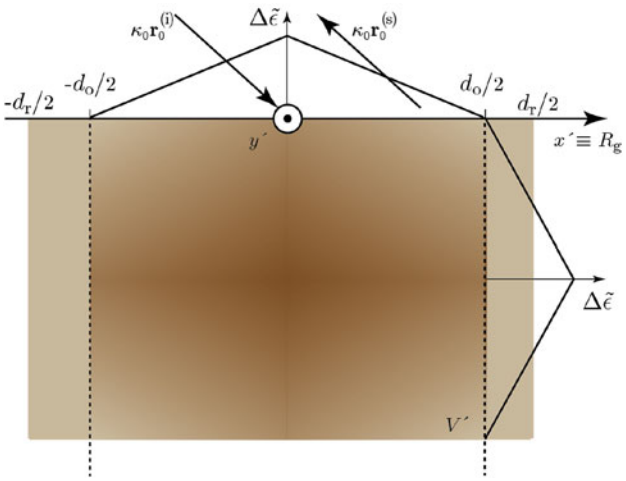

Fig. 12.29 Phase vectors of incident and backscattered waves in the $(x'z')$-vertical plane; the ground range width of the resolution cell is d_r, while that of the scattering object, the permittivity of which $\overline{\Delta\tilde{\epsilon}}(x', z') = \Delta\tilde{\epsilon}(x') \times \Delta\tilde{\epsilon}(z')$ is assumed separable, is $d_o \leq d_r$. *Darker color* denotes higher permittivity

$$\overline{\Delta\tilde{\epsilon}} = \tilde{\varepsilon}_o \, \varepsilon_x(x') \, \varepsilon_z(z') \, , \tag{12.29}$$

where $\tilde{\varepsilon}_o$ is a magnitude factor, and ε_x and ε_z describe the dielectric variations in the range direction[39] and with depth, respectively. The scattering geometry and the permittivity structure are sketched in Fig. 12.29 for the simple case of linear trends of ε_x and ε_z. Introducing (12.29) into (12.28) yields

$$\begin{aligned} \mathcal{F}_{\overline{\epsilon}k} &\simeq \frac{\kappa_0^2}{4\pi} \boldsymbol{E}_{0\overline{\epsilon}k} \, \tilde{\varepsilon}_o \, d_a \int_0^{d_z} \varepsilon_z(z') \, \mathrm{e}^{-2\alpha'_k z'} \, \mathrm{e}^{-\mathrm{j}2\beta'_{zk} z'} \, \mathrm{d}z' \int_{-d_r/2}^{d_r/2} \varepsilon_x(x') \, \mathrm{e}^{-\mathrm{j}2\beta'_{xk} x'} \, \mathrm{d}x' \\ &= \frac{\kappa_0^2}{4\pi} \boldsymbol{E}_{0\overline{\epsilon}k} \, \tilde{\varepsilon}_o \, d_a \, \mathcal{X}_{\varepsilon k} \, \mathcal{Z}_{\varepsilon k} \, , \end{aligned} \tag{12.30}$$

where d_a is the resolution in azimuth, while $\mathcal{X}$ and $\mathcal{Z}$ denote the vertical and horizontal factors, respectively. The scattering object in V'_k has dimension in ground range $d_o \leq d_r$ and it is assumed centered on the pixel, to simplify the notations. The horizontal permittivity function is truncated by multiplying it by the rectangle function, as done in Sects. 11.3.1.1 and 11.3.1.2 for the field on apertures:

$$\varepsilon_x^T(x') = \varepsilon_x(x') \, \sqcap_{do}(x') \, .$$

[39]The permittivity is assumed independent of azimuth and with proportional real and imaginary parts.

The truncation allows one to obtain the horizontal factor $\mathcal{X}_{\varepsilon k}$ as the Fourier transform $\mathcal{F}$ of the truncated *average* permittivity structure in the range direction

$$\mathcal{X}_{\varepsilon k} = \int_{-\infty}^{\infty} \varepsilon_{\mathrm{x}}(x') \sqcap_{d\mathrm{o}}(x') \, \mathrm{e}^{-\mathrm{j}\kappa_{xk} x'} \, \mathrm{d}x' = \mathcal{F}\left[\varepsilon_{\mathrm{x}} \sqcap_{d\mathrm{o}}\right] \, . \tag{12.31}$$

The transform of the product is known to be the convolution of the transforms [7, 37]:

$$\mathcal{X}_{\varepsilon k} = \sqrt{2\pi} \, d_{\mathrm{o}} \, \mathcal{E}_{\mathrm{x}}(\kappa_{xk}) * \mathrm{sinc}\left(\frac{d_{\mathrm{o}}}{2}\kappa_{xk}\right) \cdot \tag{12.32}$$

Equation (12.32) contains the Fourier transform $\mathcal{E}_{\mathrm{x}} = |\mathcal{E}_{\mathrm{x}}| \, e^{\mathrm{j}\Phi_{\varepsilon \mathrm{x}}}$ of the permanent permittivity in the range direction and the sinc function, which is the transform of the rectangle. The angular wavenumber κ_{xk} that appears in the arguments of the transforms is the ground-range component of the scattering vector introduced in Sect. 7.4.4, which is equal to twice the lateral component of the phase vector of the incident wave

$$\kappa_{xk} = 2\beta'_{xk} \, ,$$

because backscattering is being considered. In an actual environment, the object that mainly contributes to scattering is generally not centered on the pixel, but at a distance d_{d} from the local origin of coordinates. Given the translation property of the Fourier transform, the shift of position results in a phase term linearly dependent on d_{d}:

$$\mathcal{X}_{\varepsilon k} = \sqrt{2\pi} \, d_{\mathrm{o}} \, |\mathcal{E}_{\mathrm{x}}(\kappa_{xk})| \, \mathrm{e}^{\mathrm{j}\Phi_{\varepsilon \mathrm{x}}(\kappa_{xk})} * \mathrm{sinc}\left(\frac{d_{\mathrm{o}}}{2}\kappa_{xk}\right) \mathrm{e}^{-\mathrm{j}\kappa_{xk} d_{\mathrm{d}}} \, .$$

The horizontal factor is then the complex quantity

$$\mathcal{X}_{\varepsilon k} = |\mathcal{X}_{\varepsilon}(\kappa_{xk})| \, \mathrm{e}^{\mathrm{j}\Phi_{\overline{\epsilon}\mathrm{x}}(\kappa_{xk})} \, ,$$

while, in turn, the vertical factor in (12.30) is

$$\mathcal{Z}_{\varepsilon k} = \int_0^{d_z} \varepsilon_{\mathrm{z}}(z') \, \mathrm{e}^{-2\alpha'_k z'} \, \mathrm{e}^{-\mathrm{j}2\beta'_{zk} z'} \, \mathrm{d}z' = |\mathcal{Z}_{\varepsilon}(\kappa_{zk})| \, \mathrm{e}^{\mathrm{j}\Phi_{\overline{\epsilon}\mathrm{z}}(\kappa_{zk})} \, . \tag{12.33}$$

When the solid or liquid surface of the Earth is observed, or, in general, for large values of the optical thickness, in practice $d_z \to \infty$ and the factor $\mathcal{Z}$ tends to become the Laplace transform [11] $\mathrm{L}_{\overline{\epsilon}\mathrm{z}}(\xi_k)$ of the vertical structure ε_{z} of the permanent permittivity, relative to the complex vertical scattering wavenumber $\xi_k = \kappa_{zk} =$

$2(\alpha'_k + j\beta'_{zk})$ corresponding to the k-th acquisition. On the other side, $\mathcal{Z}_\varepsilon$ tends to the Fourier transform of the truncated ε_z in case of low[40] attenuation.

By combining the effects of the horizontal and vertical permanent dielectric structures, the scattering function of the stable target is expressed by[41]

$$\begin{aligned}\mathcal{F}_{\overline{\epsilon}k} &\simeq \frac{\kappa_0^2}{4\pi^2}\boldsymbol{E}_{0\overline{\epsilon}k}\,\tilde{\varepsilon}_{\mathrm{o}}\,d_{\mathrm{a}}\,|\mathcal{X}_\varepsilon(\kappa_{xk})|\,|\mathcal{Z}_\varepsilon(\kappa_{zk})|\,\mathrm{e}^{\mathrm{j}[\Phi_{\overline{\epsilon}\mathrm{x}}(\kappa_{xk})+\Phi_{\overline{\epsilon}\mathrm{z}}(\kappa_{zk})]}\\ &\simeq |\mathcal{F}_{\overline{\epsilon}k}|\,\mathrm{e}^{\mathrm{j}[\Phi_{\overline{\epsilon}\mathrm{x}}(\kappa_{xk})+\Phi_{\overline{\epsilon}\mathrm{z}}(\kappa_{zk})]} = |\mathcal{F}_{\overline{\epsilon}k}|\,\mathrm{e}^{\mathrm{j}\Phi_{\overline{\epsilon}k}}\,,\end{aligned} \tag{12.34}$$

in case of low-loss materials, that is under the assumption $\tilde{\varepsilon}_{\mathrm{oj}} \ll \tilde{\varepsilon}_{\mathrm{or}}$. The interferometric phase (12.25) contributed by the scattering function of the permanent target is then

$$\overline{\Phi}_{\overline{\epsilon}\mathrm{ms}} = \Phi_{\overline{\epsilon}\mathrm{x}}(\kappa_{x\mathrm{m}}) + \Phi_{\overline{\epsilon}\mathrm{z}}(\kappa_{z\mathrm{m}}) - [\Phi_{\overline{\epsilon}\mathrm{x}}(\kappa_{x\mathrm{s}}) + \Phi_{\overline{\epsilon}\mathrm{z}}(\kappa_{z\mathrm{s}})]\,. \tag{12.35}$$

Both the horizontal backscattering wavenumber

$$\kappa_{xk} = 2\beta'_{xk} = \frac{4\pi}{\lambda_0}\sin\theta_k^{(\mathrm{i})}, \qquad k = \mathrm{m},\,\mathrm{s} \tag{12.36}$$

and the vertical one κ_{zk} depend on the angle of incidence, which does vary between the master and the slave interferometric acquisitions. Therefore the interferometric phase term (12.35) is related not only to the position (ground-range and elevation) of the considered pixel, but depends also on the *permanent* dielectric structure of the target. This means that the features (dimensions, shape, permittivity) of the sources of scattering present in the resolution cell perturb the interferometric phase, even if they do not change between pairs of acquisitions. The issue is further analyzed in Sect. 12.3.3.2.

12.3.2.2.2 Effect of Temporal Changes

So far, only the contribution to the interferometric product by the permanent permittivity of the scattering cell has been examined. In fact, (12.23) contains also terms relative to the variations $\mathcal{F}_{\epsilon' k}$ of the free-space scattering function (12.22) caused by the changes of the dielectric structure,[42] that is, from the zero-mean[43]

[40] Vanishing, in the limiting case.

[41] The dependence of the moduli and phases on the polarization is still omitted to simplify the notations.

[42] Note that the possible dependence of the scattering volume V' on the acquisition may also account for the fluctuations of the scattering function.

[43] As said, the average is intended over the ensemble of interferometric acquisitions.

deviation $\Delta\tilde{\epsilon}'$ of the permittivity in correspondence of the k-th acquisition from its *permanent* value $\overline{\Delta\tilde{\epsilon}}$.

The fluctuation of the permittivity affects the interferometric dyadic through the three terms in (12.23):

$$\mathbb{I}_{0\epsilon'} = \mathcal{F}_{\overline{\epsilon}\mathrm{m}}\,\mathcal{F}^{*}_{\epsilon'\mathrm{s}} + \mathcal{F}^{*}_{\overline{\epsilon}\mathrm{s}}\,\mathcal{F}_{\epsilon'\mathrm{m}} + \mathcal{F}_{\epsilon'\mathrm{m}}\,\mathcal{F}^{*}_{\epsilon'\mathrm{s}}\,. \tag{12.37}$$

Given the definition (12.22),

$$\mathcal{F}_{\epsilon' k} \simeq \frac{\kappa_0^2}{4\pi} \iiint_{V'_k} \boldsymbol{E}_{\perp\overline{\epsilon}k}\,\Delta\tilde{\epsilon}'_k\,\mathrm{e}^{\mathrm{j}\kappa_0 \boldsymbol{r}'\cdot\mathbf{r}^{(\mathrm{s})}_{0k}}\,\mathrm{d}V', \qquad k = \mathrm{m},\,\mathrm{s}\,,$$

the first two terms of (12.37) produce fluctuations of the interferometric products[44] which depend both on the average dielectric structure $\overline{\Delta\tilde{\epsilon}}$ and on that, $\Delta\tilde{\epsilon}'$, in correspondence of the individual acquisitions, while the third term takes account of the permittivity changes for both individual acquisitions. To simplify the approach, the scattering-effective internal field is assumed to be the plane wave (12.26) in the permanent target, as before:

$$\boldsymbol{E}_{\perp k} = \boldsymbol{E}_{0\overline{\epsilon}k}\,\mathrm{e}^{-\alpha'_k z'}\mathrm{e}^{-\mathrm{j}\beta'_{xk}x'}\,\mathrm{e}^{-\mathrm{j}\beta'_{zk}z'}\,, \qquad k = \mathrm{m},\,\mathrm{s}\,.$$

The ensuing component of the backscattering function is

$$\mathcal{F}_{\epsilon' k} \simeq \frac{\kappa_0^2}{4\pi}\boldsymbol{E}_{0\overline{\epsilon}k} \iiint_{V'_k} \Delta\tilde{\epsilon}'_k\,\mathrm{e}^{-\alpha'_k z'}\mathrm{e}^{-\mathrm{j}\beta'_{xk}x'}\,\mathrm{e}^{-\mathrm{j}\beta'_{zk}z'}\mathrm{e}^{\mathrm{j}\boldsymbol{k}''_k\cdot\boldsymbol{r}'}\,\mathrm{d}V'\,, \qquad k = \mathrm{m},\,\mathrm{s}\,.$$

Since (12.27) holds for the inner propagation vector $\boldsymbol{k}''$, which refers to backscattering,

$$\mathcal{F}_{\epsilon' k} \simeq \frac{\kappa_0^2}{4\pi}\boldsymbol{E}_{0\overline{\epsilon}k} \iiint_{V'_k} \Delta\tilde{\epsilon}'_k\,\mathrm{e}^{-2\alpha'_k z'}\mathrm{e}^{-\mathrm{j}2\beta'_{xk}x'}\,\mathrm{e}^{-\mathrm{j}2\beta'_{zk}z'}\,\mathrm{d}V'\,, \qquad k = \mathrm{m},\,\mathrm{s}\,. \tag{12.38}$$

The perturbation (12.38) of the backscattering function caused by the changes of the dielectric structure is clearly a complex quantity, expressed, analogously to (12.34) for the stable target, by

$$\mathcal{F}_{\epsilon' k} = |\mathcal{F}_{\epsilon' k}|\,\mathrm{e}^{\mathrm{j}\Phi_{\epsilon' k}}\,, \qquad k = \mathrm{m},\,\mathrm{s}\,.$$

where modulus and phase of $\mathcal{F}$ depend not only on the permittivity fluctuations, but also on the horizontal and vertical components of the scattering vector.

[44] A general polarization of the field is considered.

Equation (12.37) indicates that the change of permittivity between the master and slave acquisitions perturbs the interferometric phase relative to a given pixel through the three terms

$$\Phi_{\overline{\epsilon}\mathrm{m}} - \Phi_{\epsilon'\mathrm{s}} \ , \qquad \Phi_{\epsilon'\mathrm{m}} - \Phi_{\overline{\epsilon}\mathrm{s}} \ , \qquad \Phi_{\epsilon'\mathrm{m}} - \Phi_{\epsilon'\mathrm{s}} \ ,$$

the weights of which depend on the mixed products of the moduli $|\mathcal{F}_{\overline{\epsilon}k}|$ and $|\mathcal{F}_{\epsilon'k}|$. For a given permittivity change, the phase perturbation depends on the field polarization,[45] as well as on the scattering vector, which affects (12.38). The sensitivity to the wavelength brought about jointly both by the factor κ_0^2 and by the phase constant β' should be noticed.

To evaluate the magnitude of the phase perturbation induced by the permittivity changes, a statistical characterization over the ensemble of pairs (m,s) of interferometric acquisitions is suitable. A reasonable assumption is that the first two terms of (12.37) approximately have zero mean,[46] which suggests that they *do show* their effect in a *single pair* of interferometric acquisitions, but the perturbation they produce tends to vanish when a large number of interferograms is averaged. The average of the third term

$$\mathcal{F}_{\epsilon'\mathrm{m}}\,\mathcal{F}^*_{\epsilon'\mathrm{s}} \simeq \frac{\kappa_0^4}{(4\pi)^2} \iiint_{V'_\mathrm{m}} \boldsymbol{E}_{\perp\overline{\epsilon}\mathrm{m}}\ \Delta\tilde{\epsilon}'_\mathrm{m}\ \mathrm{e}^{\mathrm{j}\kappa_0 \boldsymbol{r}'\cdot\mathbf{r}^{(\mathrm{s})}_{0\mathrm{m}}}\,\mathrm{d}V' \iiint_{V'_\mathrm{s}} \boldsymbol{E}^*_{\perp\overline{\epsilon}\mathrm{s}}\ \Delta\tilde{\epsilon}'^*_\mathrm{s}\ \mathrm{e}^{-\mathrm{j}\kappa_0 \boldsymbol{r}'\cdot\mathbf{r}^{(\mathrm{s})}_{0\mathrm{s}}}\,\mathrm{d}V' \ ,$$

containing the product of the permittivity fluctuations for the master and slave acquisitions, does not vanish. Its statistical characterization is conveniently based on the second-order moment of the co-polar backscattering function. In case of single-polarization field,

$$\mathcal{F}_{\epsilon'\mathrm{m}}\cdot\mathcal{F}^*_{\epsilon'\mathrm{s}} \simeq \frac{\kappa_0^4}{(4\pi)^2}\,\boldsymbol{E}_{\perp\overline{\epsilon}\mathrm{m}}\cdot\boldsymbol{E}^*_{\perp\overline{\epsilon}\mathrm{s}} \times \Big\langle \iiint_{V'_\mathrm{m}} \Delta\tilde{\epsilon}'_\mathrm{m}\ \mathrm{e}^{-2\alpha'_\mathrm{m}z'}\,\mathrm{e}^{-\mathrm{j}2\beta'_{x\mathrm{m}}x'}\,\mathrm{e}^{-\mathrm{j}2\beta'_{z\mathrm{m}}z'}\,\mathrm{d}V' \iiint_{V'_\mathrm{s}} \Delta\tilde{\epsilon}'^*_\mathrm{s}\,\mathrm{e}^{-2\alpha'_\mathrm{s}z'}\,\mathrm{e}^{\mathrm{j}2\beta'_{x\mathrm{s}}x'}\,\mathrm{e}^{\mathrm{j}2\beta'_{z\mathrm{s}}z'}\,\mathrm{d}V' \Big\rangle \ ,$$

where the average is on the ensemble of pairs ($k = \mathrm{m}, \mathrm{s}$) of interferometric acquisitions. The angles of incidence (and scattering) are very close for the master and slave interferometric acquisitions, therefore, the reasonable[47] assumptions

[45] Starting from (12.25) the subscript $_p$ has been dropped.

[46] The permittivity deviation $\Delta\tilde{\epsilon}'_k$ is by definition a zero-mean quantity.

[47] Remember that the inner field is assumed to refer to the average dielectric structure $\overline{\Delta\tilde{\epsilon}}$.

$$\boldsymbol{E}_{0\overline{\epsilon}\mathrm{m}} \simeq \boldsymbol{E}_{0\overline{\epsilon}\mathrm{s}} \equiv \boldsymbol{E}_{0\overline{\epsilon}}\,; \quad \alpha'_{\mathrm{m}} \simeq \alpha'_{\mathrm{s}}; \quad \beta'_{z\mathrm{m}} \simeq \beta'_{z\mathrm{s}}; \quad \beta'_{x\mathrm{m}} \simeq \beta'_{x\mathrm{s}}; \quad \mathbf{r}^{(\mathrm{s})}_{0\mathrm{m}} \simeq \mathbf{r}^{(\mathrm{s})}_{0\mathrm{s}}; \quad V'_{\mathrm{m}} \simeq V'_{\mathrm{s}}$$

for the refracted wave, are instrumental, *for the time being*,[48] to highlight the effects of the changes of permittivity.

As in Sect. 7.4, the product of integrals is reduced to an augmented-dimension integral by singling out the integration variables $\boldsymbol{r}'_1$ and $\boldsymbol{r}'_2$:

$$\left\langle \mathcal{F}_{\epsilon'\mathrm{m}} \cdot \mathcal{F}^*_{\epsilon'\mathrm{s}} \right\rangle \simeq \frac{\kappa_0^4}{(4\pi)^2} \; |\boldsymbol{E}_{0\overline{\epsilon}}|^2 \iiint\limits_{V'} \iiint\limits_{V'} \left\langle \Delta\tilde{\epsilon}'_{\mathrm{m}}(\boldsymbol{r}'_1) \; \Delta\tilde{\epsilon}'^*_{\mathrm{s}}(\boldsymbol{r}'_2) \right\rangle \times \mathrm{e}^{-2\alpha'(z'_1 + z'_2)} \; \mathrm{e}^{-\mathrm{j}2\beta'_z(z'_1 - z'_2)} \; \mathrm{e}^{-\mathrm{j}2\beta'_x(x'_1 - x'_2)} \, \mathrm{d}V'_2 \, \mathrm{d}V'_1 \,. \tag{12.39}$$

The expression (12.39) shows how the second-order moment of the random-permittivity term of the interferometric product of the scattering function depends on the space-time covariance of permittivity in the volume V' of the scattering resolution cell, consistently with the theoretical results[49] of Sect. 9.1. Then the formal approach of Sect. 7.4.3 can be followed by setting

$$\left\langle \Delta\tilde{\epsilon}'_{\mathrm{m}}(\boldsymbol{r}'_1) \; \Delta\tilde{\epsilon}'^*_{\mathrm{s}}(\boldsymbol{r}'_2) \right\rangle = \sigma_\epsilon^2 \, \mathcal{B}_\epsilon(\boldsymbol{r}'_1, t_{\mathrm{m}};\; \boldsymbol{r}'_2, t_{\mathrm{s}}) \,,$$

where t_{m} and t_{s} are the times of the master (m) and slave (s) acquisitions, respectively. Statistical homogeneity is assumed in V' for the random process $\Delta\tilde{\epsilon}'$, considered also independent of the azimuth coordinate y.

To make easier the interpretation of the results, first the permittivity covariance is factorized, extending (7.45) to include the temporal factor $\mathcal{B}_{\epsilon t}$

$$\mathcal{B}_\epsilon(\boldsymbol{r}'_1, t_{\mathrm{m}};\; \boldsymbol{r}'_2, t_{\mathrm{s}}) = \mathcal{B}_\epsilon(x'_1, z'_1, t_{\mathrm{m}};\; x'_2, z'_2, t_{\mathrm{s}}) = \mathcal{B}_{\epsilon\mathrm{x}}(x'_1, x'_2) \, \mathcal{B}_{\epsilon\mathrm{z}}(z'_1, z'_2) \, \mathcal{B}_{\epsilon t}(t_{\mathrm{m}}, t_{\mathrm{s}}) \,.$$

Then some statistical properties are assumed for the factors, still following the approach of Sect. 7.4.3. In particular, the dielectric fluctuations are considered to be characterized by

- horizontal statistical isotropy, which implies that $\mathcal{B}_{\epsilon\mathrm{x}}$ depends on the horizontal distance $|x'_1 - x'_2|$ only,
- vertical statistical stationarity, i.e., $\mathcal{B}_{\epsilon\mathrm{z}}$ depends, analogously, on vertical distance $|z'_1 - z'_2|$, irrespective of depth,
- temporal stationarity, so that $\mathcal{B}_{\epsilon t}$ is a decreasing[50] function of the time interval $\Delta t = |t_{\mathrm{m}} - t_{\mathrm{s}}|$ between master and slave acquisitions.

[48] This assumption implies neglecting the variation of the scattering function of the stable target between master and slave acquisitions.

[49] As a matter of fact, single scattering is implicitly assumed.

[50] For instance, $|\mathcal{B}_{\epsilon t}|$ decreases, while $\arg \mathcal{B}_{\epsilon t}$ does not vary appreciably.

The above assumptions allow the moment of the $\mathcal{F}_{\epsilon'}$-part of the backscattering function to be expressed by

$$\left\langle \mathcal{F}_{\epsilon' \mathrm{m}} \cdot \mathcal{F}^*_{\epsilon' \mathrm{s}} \right\rangle \simeq \frac{\kappa_0^4}{(4\pi)^2} \, |\boldsymbol{E}_{0\bar{\epsilon}}|^2 \, \sigma_\epsilon^2 \, \mathcal{B}_{\epsilon t}(\Delta t) \iiint\limits_{V'} \iiint\limits_{V'} \mathcal{B}_{\epsilon \mathrm{z}}(|z'_1 - z'_2|) \, \mathcal{B}_{\epsilon \mathrm{x}}(|x'_1 - x'_2|)$$
$$\times \, \mathrm{e}^{-2\alpha'(z'_1 + z'_2)} \, \mathrm{e}^{-\mathrm{j}2\beta'_z(z'_1 - z'_2)} \, \mathrm{e}^{-\mathrm{j}2\beta'_x(z'_1 - z'_2)} \, \mathrm{d}V'_2 \, \mathrm{d}V'_1 \, .$$

The appropriate transformations of coordinates lead to a final result analogous to that obtained in Sects. 7.4.4 and 7.4.6:

$$\left\langle \mathcal{F}_{\epsilon' \mathrm{m}} \cdot \mathcal{F}^*_{\epsilon' \mathrm{s}} \right\rangle \simeq \frac{\kappa_0^4}{(4\pi)^2} \, |\boldsymbol{E}_{0\bar{\epsilon}}|^2 \, d_\mathrm{a}^2 \, \sigma_\epsilon^2 \, \mathcal{S}_{\epsilon \mathrm{x}}(\kappa_x) \, \mathcal{Z}_\epsilon(\kappa_z) \, \mathcal{B}_{\epsilon t}(\Delta t) \, . \tag{12.40}$$

Equation (12.40) indicates that the moment[51] of the part of the backscattering function relative to the random changes $\Delta\tilde{\epsilon}'$ of permittivity is proportional to the spectral density $\mathcal{S}_{\epsilon \mathrm{x}}(\kappa_x)$ of the permittivity fluctuations[52] in the ground-range direction to which (7.53) reduces in the one-dimensional case. The spectral component which contributes the moment is selected by the range-wavenumber κ_x determined by the incidence angle and the wavelength, as discussed in Sect. 7.4.4. The vertical factor $\mathcal{Z}_\epsilon(\kappa_z)$ tends to the Laplace transform of the z-dependent permittivity fluctuations at the complex vertical wavenumber κ_z, also determined by wavelength and incidence angle, in the often encountered case $d_\mathrm{z} \to \infty$. For vanishing extinction, $\mathcal{Z}_\epsilon$ tends to be proportional to the spectral density $\mathcal{S}_{\epsilon \mathrm{z}}$ of the vertical dielectric fluctuations.

The temporal decorrelation of the permittivity expressed by the decreasing trend of $\mathcal{B}_{\epsilon t}(\Delta t)$ reduces the magnitude of the moment as the time interval between master and slave acquisitions increases. This feature does not mean that the fluctuating-permittivity part $\mathcal{F}_{\epsilon' \mathrm{m}} \cdot \mathcal{F}^*_{\epsilon' \mathrm{s}}$ of the *individual* interferometric product decreases with increasing master-slave time lapse,[53] rather it indicates that the randomness, growing with time, reduces the magnitude of the *average* value $\left\langle \mathcal{F}_{\epsilon' \mathrm{m}} \cdot \mathcal{F}^*_{\epsilon' \mathrm{s}} \right\rangle$ of the complex[54] terms of the interferometric pairs.

[51] Coarsely speaking, the magnitude of variation.

[52] It is important to keep in mind that the statistical ensemble is now the one of the pairs master/slave acquisitions of a *given* target; in particular, the dielectric fluctuations result from the space-time variability of the target between the dates or times of the data takes pairs.

[53] Besides, increasing the time lapse clearly enhances the variable part of permittivity, thus increasing the variance σ_ϵ^2 in (12.40).

[54] The average of the complex terms tends to vanish because the individual samples add with randomly distributed phases.

12.3.3 Coherence of the Scattered Field

A stable target, for which $\Delta\tilde{\epsilon}' = 0$, obviously does not suffer from permittivity changes. However, the dielectric invariance does not imply that the phase of the interferometric product is stable, since Sect. 12.3.2.2 reminds us that the changes of phase (12.35) are inherent to the interferometric observation technique and cannot be neglected, not even for invariant targets. Indeed, the effect of the permanent dielectric structure considered in Sect. 12.3.2.2.1 just combines with that of the permittivity change (Sect. 12.3.2.2.2) in globally affecting the phase of the product $\mathcal{F}_{\mathrm{m}}\mathcal{F}_{\mathrm{s}}^{*}$ of the free-space scattering functions. Such an essentially random behavior of the phase of the scattered field tends to distort the relation between interferometric phase and target position on which the 3-D rendering is obtained from SAR images. Therefore, the interferograms must be characterized from the point of view of the phase stability to assess their suitability for retrieving the altimetric information on the observed targets.

The space-time statistical characteristics of the electromagnetic field are expressed by the moments introduced in Sect. 1.3.4 and, in particular, by the coherency dyadic (1.39). Information on the interferometric phase stability of a given target is contained in the second-order moment of the scattered field acquired from the master and the slave positions. Therefore, the relevant measurable statistical quantity is the coherency dyadic

$$\mathbb{\Gamma}(\boldsymbol{r}_{\mathrm{m}}, \boldsymbol{r}_{\mathrm{s}}; t_{\mathrm{m}}, t_{\mathrm{s}}) = \left\langle \boldsymbol{E}_{\mathrm{m}}^{(\mathrm{s})} \left(\boldsymbol{E}_{\mathrm{s}}^{(\mathrm{s})}\right)^{\mathrm{H}} \right\rangle \Big|_{\mathrm{ms}} ,$$

where, as indicated by the subscripts, average is over the ensemble of samples of the field scattered[55] by the considered target and taken from the master ($\boldsymbol{r}_{\mathrm{m}}$) and slave ($\boldsymbol{r}_{\mathrm{s}}$) platform positions at the respective times t_{m} and t_{s}. Superscript $^{\mathrm{H}}$ is the Hermitian notation, alternative to * used in (1.36), to indicate conjugate transpose. The elements of the coherency matrix $[\boldsymbol{\Gamma}]$ (1.40) contain the products of the co- and cross-polar scattering functions averaged over the ensemble of master/slave pairs (m, s) of acquisitions. With reference to the simple case of single-component co-polar scattering involving scalar quantities, and *disregarding the changing atmospheric phase terms*,[56] the space-time normalized coherence, that is the *degree of coherence* comprehensive of (1.43) and (1.44), is related to the statistical properties of the scattering function $\mathcal{F}$ through (12.18) and (12.19) by

[55] Superscript $^{(\mathrm{s})}$ denotes "scattered" and should not be confused with "slave", denoted by subscript $_{\mathrm{s}}$.

[56] The possible variations of the atmospheric path lengths are considered in Sect. 12.3.4.

$$\gamma(\boldsymbol{r}_{\mathrm{m}},\boldsymbol{r}_{\mathrm{s}};t_{\mathrm{m}},t_{\mathrm{s}})=\frac{\Gamma(\boldsymbol{r}_{\mathrm{m}},\boldsymbol{r}_{\mathrm{s}};t_{\mathrm{m}},t_{\mathrm{s}})}{\sqrt{\Gamma(\boldsymbol{r}_{\mathrm{m}},\boldsymbol{r}_{\mathrm{m}};t_{\mathrm{m}},t_{\mathrm{m}})}\sqrt{\Gamma(\boldsymbol{r}_{\mathrm{s}},\boldsymbol{r}_{\mathrm{s}};t_{\mathrm{s}},t_{\mathrm{s}})}}\propto\frac{\left\langle\mathcal{F}_{\mathrm{m}}\,\mathcal{F}_{\mathrm{s}}^{*}\right\rangle}{\sqrt{\left\langle|\mathcal{F}_{\mathrm{m}}|^{2}\right\rangle}\sqrt{\left\langle|\mathcal{F}_{\mathrm{s}}|^{2}\right\rangle}}=\gamma_{\mathcal{F}}\ . \tag{12.41}$$

Equation (12.41) indicates that the degree of coherence γ is proportional[57] to the normalized moment $\gamma_{\mathcal{F}}$ of the scattering functions of the considered resolution cell, relative to the master and slave positions at the corresponding times. The attenuation as well as the inessential phase factor due to the difference of geometric distances are not considered.
By extending the definition (12.22),

$$\mathcal{F}_{k}:=\overline{\mathcal{F}}+\mathcal{F}'_{k},\qquad k=\mathrm{m},\,\mathrm{s}\ , \tag{12.42}$$

where $\overline{\mathcal{F}}$ is the permanent part of the scattering function[58] and $\mathcal{F}'$ its zero-mean fluctuation, which accounts for the variations caused both by the stable part of the dielectric structure and by the changes of the latter. Therefore, the moment of $\mathcal{F}$ is

$$\left\langle\mathcal{F}_{\mathrm{m}}\,\mathcal{F}_{\mathrm{s}}^{*}\right\rangle=\overline{\mathcal{F}_{\mathrm{m}}}\,\overline{\mathcal{F}_{\mathrm{s}}}^{*}+\left\langle\mathcal{F}'_{\mathrm{m}}\,\mathcal{F}'^{*}_{\mathrm{s}}\right\rangle\ ,$$

and, realizing that

$$\overline{\mathcal{F}}_{\mathrm{m}}=\overline{\mathcal{F}}_{\mathrm{s}}\equiv\overline{\mathcal{F}};\qquad\left\langle\left|\mathcal{F}'_{\mathrm{m}}\right|^{2}\right\rangle=\left\langle\left|\mathcal{F}'_{\mathrm{s}}\right|^{2}\right\rangle\equiv\left\langle\left|\mathcal{F}'\right|^{2}\right\rangle,$$

the normalized moment $\gamma_{\mathcal{F}}$ of the free-space scattering function $\mathcal{F}$ to which the coherence of the target is proportional, is expressed by

$$\gamma_{\mathcal{F}}=\frac{1+\left\langle\mathcal{F}'_{\mathrm{m}}\,\mathcal{F}'^{*}_{\mathrm{s}}\right\rangle\left|\overline{\mathcal{F}}\right|^{-2}}{\sqrt{1+\left\langle|\mathcal{F}'_{\mathrm{m}}|^{2}\right\rangle\left|\overline{\mathcal{F}}\right|^{-2}}\sqrt{1+\left\langle\left|\mathcal{F}'_{\mathrm{s}}\right|^{2}\right\rangle\left|\overline{\mathcal{F}}\right|^{-2}}}=\frac{1+\left\langle\mathcal{F}'_{\mathrm{m}}\,\mathcal{F}'^{*}_{\mathrm{s}}\right\rangle\left|\overline{\mathcal{F}}\right|^{-2}}{1+\left\langle|\mathcal{F}'|^{2}\right\rangle\left|\overline{\mathcal{F}}\right|^{-2}}\ . \tag{12.43}$$

Equation (12.43) shows that the interferometric degree of coherence of the target depends both on the magnitude of the fluctuating parts $\mathcal{F}'_{k}$, $(k=\mathrm{m},\mathrm{s})$, with respect to the permanent part $\overline{\mathcal{F}}$ of the scattering function, and on how much the fluctuations $\mathcal{F}'_{\mathrm{s}}$ for the slave acquisitions are correlated to the fluctuations $\mathcal{F}'_{\mathrm{m}}$ for the master acquisitions.

In case the scattering function of the observed resolution cell has little variations among the various interferometric acquisitions, $\mathcal{F}'_{k}\to 0$ and $\gamma_{\mathcal{F}}\to 1$. Instead, when

[57] The scattering function is reasonably independent of the wave propagation parameters in the atmosphere.

[58] The conceptual difference between permanent part of the scattering function and permanent (i.e., dielectrically invariant) target should be clearly born in mind.

the permanent part of the scattering function is relatively low, or, in the limiting case, $\overline{\mathcal{F}} \to 0$, then

$$\gamma_{\mathcal{F}} \to \frac{\left\langle \mathcal{F}'_{\mathrm{m}}\, \mathcal{F}'^{*}_{\mathrm{s}} \right\rangle}{\left\langle |\mathcal{F}'|^2 \right\rangle} \,.$$

If the effect of the atmosphere is negligible, in case $\mathcal{F}' \to 0$, the modulus of the degree of interferometric coherence $|\gamma| \to 1$, while, when $\overline{\mathcal{F}} \to 0$, $|\gamma|$ tends to the master-slave correlation coefficient[59] of the fluctuating part of the scattering function of the target. The previous expressions confirm formally that not only the changes of permittivity but also the permanent dielectric structure of the resolution cell affect the coherence of the field it scatters, as discussed in Sects. 12.3.2.2.1 and 12.3.2.2.2.

12.3.3.1 Effect of Changes and Temporal Coherence

The effects on the normalized moment (12.43) of the dielectric changes between interferometric acquisitions are highlighted under the reasonable assumption that the average scattering function $\overline{\mathcal{F}}$ approximates the mean scattering function for the average permittivity $\overline{\mathcal{F}}_{\overline{\epsilon}k}$ at the incidence angle[60] appropriate to the considered set of interferometric data takes. Equation (12.30) yields

$$\left|\overline{\mathcal{F}}\right|^2 \simeq \overline{\mathcal{F}}_{\overline{\epsilon}k} \simeq C_1\, |\tilde{\epsilon}_{\mathrm{o}}|^2\, |\mathcal{X}_\epsilon|^2\, |\mathcal{Z}_\epsilon|^2 \,, \tag{12.44}$$

where $\mathcal{X}_\epsilon$ and $\mathcal{Z}_\epsilon$ are respectively the average-permittivity horizontal and vertical factors introduced in Sect. 12.3.2.2.1, and the factor C_1 accounts for spatial resolution and wavelength. In turn, (12.40) provides the moment of the random component of the scattering function

$$\left\langle \mathcal{F}_{\epsilon' \mathrm{m}}\, \mathcal{F}^{*}_{\epsilon' \mathrm{s}} \right\rangle \simeq C_2\, \sigma_\epsilon^2\, \mathcal{S}_{\epsilon \mathrm{x}}\, \mathcal{Z}_\epsilon\, \mathcal{B}_{\epsilon t}(\Delta t) \,, \tag{12.45}$$

while the magnitude of the fluctuations, clearly independent of the acquisition when the process is stationary, is

$$\left\langle |\mathcal{F}'|^2 \right\rangle \simeq C_2\, \sigma_\epsilon^2\, \mathcal{S}_{\epsilon \mathrm{x}}\, \mathcal{Z}_\epsilon \,. \tag{12.46}$$

[59] In several instances $\gamma_{\mathcal{F}}$ is a real quantity.

[60] Given the relatively short baselines, the incidence angles for master and slave acquisitions are very close; this assumption clearly leaves out the effect of the baseline.

By inserting (12.44), (12.45) and (12.46) into (12.43), the free-space degree of coherence is related to the dielectric changes occurring in the scattering resolution cell and to their temporal decorrelation described by $\mathcal{B}_{\epsilon t}$. In compact form,

$$\gamma \simeq \frac{1 + Q\,\sigma_\epsilon^2\ |\tilde{\epsilon}_o|^{-2}\ \mathcal{B}_{\epsilon t}(\Delta t)}{1 + Q\,\sigma_\epsilon^2\ |\tilde{\epsilon}_o|^{-2}}\ , \tag{12.47}$$

with the assumed real factor $Q \leq 1$.

The simple model represented by (12.47) highlights the dependence of the degree of coherence of the scattered field on the time interval Δt between interferometric acquisitions and to the magnitude of the relative dielectric changes $\sigma_\epsilon^2 / |\tilde{\epsilon}_o|^2$ occurring in the imaged target. This latter is then characterized by its *temporal coherency*, which depends not only on the temporal covariance of the permittivity, but also on the relative dielectric variation. When the dielectric structure of the scattering volume has little changes, in the sense that $\sigma_\epsilon^2 \ll |\tilde{\epsilon}_o|^2$, the degree of coherence keeps high values. If strong variations of permittivity occur, such that $Q\,\sigma_\epsilon^2 \gg |\tilde{\epsilon}_o|^2$, the temporal degree of coherence is simply approximated by

$$\gamma \simeq \mathcal{B}_{\epsilon t}(\Delta t)$$

and decreases with time because of the random variations of permittivity, according to the time autocorrelation function $B_{\epsilon t}$ of this latter.

12.3.3.2 Effect of Baseline

Section 12.3.2.2.1 points out that changes of the scattering function occur even if no dielectric change intervenes in the target. This effect was found to originate from the change of the angle of incidence, hence also of the angle of scattering, due to the different positions of the radar platform. Both horizontal and vertical scattering wavenumbers κ_{xk} and κ_{zk}, ($k = \mathrm{m}, \mathrm{s}$), vary, with consequent variations of amplitude and phase between the scattered field sampled at the master and slave positions. This aspect was neglected when discussing the effect of dielectric changes in the previous Sect. 12.3.3.1, where, for simplicity, the scattering function for the average permittivity was considered invariant.

How the angle of incidence affects amplitude and phase of the scattered field is directly obtained from the expression of the part of the scattering function involving both the Fourier transform (12.31) of the stable dielectric structure in the range direction and the corresponding vertical factor (12.33), which tends to the Laplace transform of the permittivity profile when the target is electromagnetically thick.

The field scattered by complicated structures, such as many that are encountered in the terrestrial environment, exhibits considerable phase variation with the incidence/scattering angle. Therefore, even the slightly different positions of the sensor required by the interferometric technique can result in appreciable changes of the phase pattern, which corrupts the relation between phase and altitude. The diagram in Fig. 12.30 suggests the dramatic changes of phase with incidence angle

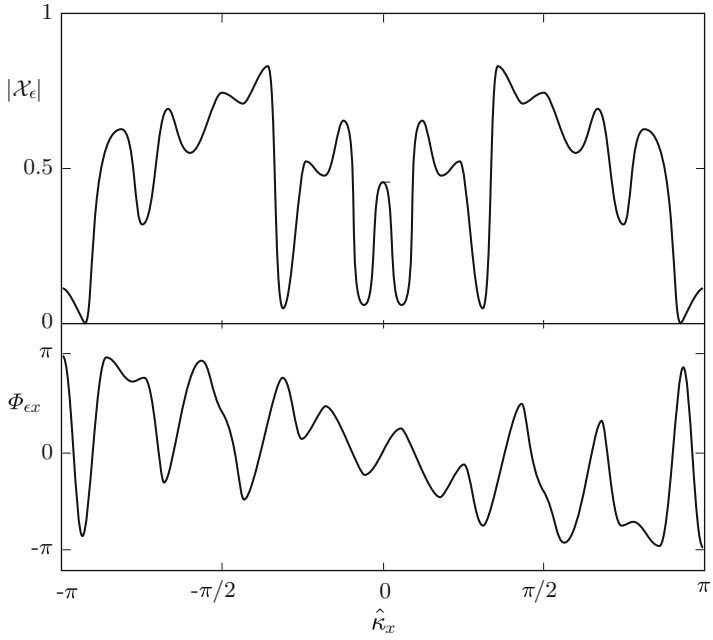

Fig. 12.30 Amplitude $|\mathcal{X}_\epsilon|$ and phase $\Phi_{\epsilon x}$ of the fourier transform of a symmetric off-set irregular function simulating the horizontal permittivity random variation with ground range, vs. normalized range wavenumber $\hat{\kappa}_x = \kappa_x d_r$; note the dramatic changes of phase with $\hat{\kappa}_x$ (Curves interpolate data from [18])

that are expected when a complicated target with random-like dielectric structure is observed. Although related to average, i.e., permanent, dielectric structures, the phase changes are essentially random in practice, given the variety of the parameters involved in actual terrestrial scenarios.

The feature is inherent to the interferometric technique and sets an essential practical limit to the baseline. The limit depends on frequency, which affects the propagation vectors and, correspondingly, the horizontal and vertical wavenumbers κ_x and κ_z. For given parameters, higher frequencies are more affected, since the same angular variation causes a larger change of the wavenumbers. The spatial resolution, which is related to the radar system bandwidth, also affects the limit baseline. A higher spatial resolution tends to quench the effect, since it decreases the size of the scattering volume, thus both making less complex the scattering sources corresponding to a given pixel, and smoothing the phase variations.

The phase may tend to remain constant with the change of incidence angle only in the simplest and relatively rare case of a horizontally symmetric source centered on the considered range, although the vertical structure may contribute a more or less significant phase variation. Some man-made scatterers and peculiar natural objects exhibit a relatively stable phase behavior, especially if scattering mainly originates from the shallow surface layers only (cf. Sect. 7.4.7).

12.3.3.3 Permanent Scatterers

As said, the variation of interferometric phase related to the permanent dielectric structure of the scattering volume adds to the variation of phase caused by the possible changes of its dielectric structure.[61] In case the target is sufficiently *simple in space and stable in time*, neither the amplitude of its scattering function nor the interferometric phase change appreciably within the ensemble of acquisitions. A resolution cell the backscattering of which exhibits these characteristics is named *permanent* or *persistent* scatterer [13]. Emphasis is again on the conceptual distinction between permanent scattering function and permanent dielectric structure, as well as on the prerequisite of symmetry and simplicity of the permittivity pattern.

The interferometric phase of a permanent scatterer tends to be related essentially to its position, hence these targets are quite useful geometric reference points on the earth surface. To be permanent, scatterers must possess both spatial and temporal phase invariance features: given the generally restricted number of realizations of the stochastic process of field sampling, the empirical approach for identifying stable scatterers uses the field amplitude together with the phase information [13].

12.3.4 Interferometric Coherence

The considered outcome of the interferometric technique is the production of maps of altitude or of differential height. To this end, the exploitability of pairs of radar acquisitions has to be evaluated by suitably characterizing the phase stability of the scattering from the area or sub-area of interest. Since collective properties are now involved, the measurements do not regard a given single resolution cell, rather ensembles of pixels belonging to the area of interest. This implies that the statistical ensemble over which the moments are computed is not that of the field scattered by a single resolution cell sampled at different points of space and time, which, as discussed before, is instrumental to the characterization of the features of a given target. Rather, the second-order moment of the scattered field, sampled at two points and times, needs to be computed over the ensemble of pixels belonging to the area to characterize, formed by N_a pixels in the azimuth direction and by N_r pixels in ground range. Therefore, a single element of the ensemble is the dyadic interferometric product (12.20) relative to the pixel P_{ij} and to the pair of observations (m, s):

[61] The geometric changes can be regarded as modification of the dielectric structure.

$$\mathbb{I}_{ij\,\mathrm{ms}} = \boldsymbol{E}^{(\mathrm{s})}_{ij\mathrm{m}} \left(\boldsymbol{E}^{(\mathrm{s})}_{ij\mathrm{s}}\right)^{\mathrm{H}} = \frac{\mathrm{e}^{-\mathrm{j}2\kappa_0(\mathcal{L}_{ij\mathrm{m}} - \mathcal{L}_{ij\mathrm{s}})}}{R_{ij\mathrm{m}} R_{ij\mathrm{s}}} \mathcal{A}_{ij\mathrm{m}} \mathcal{A}_{ij\mathrm{s}} \ \mathcal{F}_{ij\mathrm{m}} \mathcal{F}^*_{ij\mathrm{s}}$$
$$i = 1, \ldots, N_{\mathrm{a}}; \quad j = 1, \ldots, N_{\mathrm{r}} \,. \tag{12.48}$$

The interferometric product (12.48) is obtained from the values $\boldsymbol{E}^{(\mathrm{s})}_{ij\mathrm{m}}$ and $\boldsymbol{E}^{(\mathrm{s})}_{ij\mathrm{s}}$ of the field backscattered by P_{ij} measured at the master and slave platform positions m and s, taking account of the corresponding atmospheric path length $\mathcal{L}$ and attenuation $\mathcal{A}$. The phase stability of the considered area is measured by the dyadic *interferometric coherence* $\mathbb{\Gamma}$, which is the average of $\mathbb{I}$ over the ensemble of $N_{\mathrm{a}} \times N_{\mathrm{r}}$ pixels belonging to the area or class of environment to be characterized:

$$\mathbb{\Gamma}_{\mathrm{ms}} = \left\langle \mathbb{I}_{ij\,\mathrm{ms}} \right\rangle\big|_{ij} = \frac{1}{N_{\mathrm{a}} N_{\mathrm{r}}} \sum_{i=1}^{N_{\mathrm{a}}} \sum_{j=1}^{N_{\mathrm{r}}} \boldsymbol{E}^{(\mathrm{s})}_{ij\mathrm{m}} \left(\boldsymbol{E}^{(\mathrm{s})}_{ij\mathrm{s}}\right)^{\mathrm{H}} .$$

The number of pixels N_{a} and N_{r} are set by the dimensions in azimuth and in ground range of the area of interest[62] and by the respective spatial resolutions. From the theoretical point of point of view, to obtain a stable meaningful result, the ensemble should include all the realizations of the stochastic process relative to the considered area, that is, in principle, infinite pixels, with obvious loss of spatial resolution. In practice, to follow the contours of the areas of interest, the estimates are carried out over relatively small boxes including a limited number of pixels, with ensuing instability of estimates, hence limited, albeit instrumental, accuracy of results. It should also be considered that the estimate of $\mathbb{\Gamma}$ from actual data is affected by the atmosphere.

To single out the effect of the kind of terrestrial environment on the interferometric coherence, the atmosphere is left apart as before, and the effect of distance on magnitude and phase is not considered. Then the approach of Sect. 12.3.2.2 indicates that the interferometric coherence is proportional to the product of pairs of scattering functions. With reference to single-component co-polar backscattering, for the pair (m, s) of radar image acquisitions, (12.42) is written

$$\mathcal{F}_{ijk} = \overline{\mathcal{F}}_{ij} + \mathcal{F}'_{ijk}, \qquad k = \mathrm{m}, \mathrm{s} \,, \tag{12.49}$$

i.e., the scattering function of pixel P_{ij} is decomposed into the part $\overline{\mathcal{F}}_{ij}$ invariant[63] with respect to the acquisition k, and the deviation $\mathcal{F}'$ from $\overline{\mathcal{F}}_{ij}$ for the single k-th data take. Position (12.49) yields the average of the product of the scattering functions *over the ensemble of pixels* P_{ij} forming the area of interest:

$$\left\langle \mathcal{F}_{ij\mathrm{m}} \mathcal{F}^*_{ij\mathrm{s}} \right\rangle\big|_{ij} = \left\langle \left(\overline{\mathcal{F}}_{ij} + \mathcal{F}'_{ij\mathrm{m}}\right) \left(\overline{\mathcal{F}}_{ij} + \mathcal{F}'_{ij\mathrm{s}}\right)^* \right\rangle\big|_{ij} \,. \tag{12.50}$$

[62] The target corresponding to a single pixel considered in Sect. 12.3.3 clearly $N_{\mathrm{a}} = N_{\mathrm{r}} = 1$.

[63] Within the ensemble of master-slave acquisitions pairs.

When the mean of the deviations of the scattering function tends to vanish *over the ensemble of pixels*, (12.50) reduces to

$$\left\langle \mathcal{F}_{ijm}\, \mathcal{F}_{ijs}^{*} \right\rangle\big|_{ij} \simeq \left\langle \left|\overline{\mathcal{F}}_{ij}\right|^2 \right\rangle\big|_{ij} + \left\langle \mathcal{F}'_{ijm}\, \mathcal{F}'^{*}_{ijs} \right\rangle\big|_{ij}$$

and the degree of interferometric coherence (12.41) for the area of interest and relative to the considered pair (m, s) of acquisitions is

$$\begin{aligned} \gamma_{ms} &\propto \frac{\left\langle \mathcal{F}_{ijm}\, \mathcal{F}_{ijs}^{*} \right\rangle}{\sqrt{\left\langle \left|\mathcal{F}_{ijm}\right|^2 \right\rangle}\, \sqrt{\left\langle \left|\mathcal{F}_{ijs}\right|^2 \right\rangle}} \\ &\simeq \frac{1 + \left\langle \mathcal{F}'_{ijm}\, \mathcal{F}'^{*}_{ijs} \right\rangle / \left\langle \left|\overline{\mathcal{F}}_{ij}\right|^2 \right\rangle}{\sqrt{1 + \left\langle \left|\mathcal{F}'_{ijm}\right|^2 \right\rangle / \left\langle \left|\overline{\mathcal{F}}_{ij}\right|^2 \right\rangle}\, \sqrt{1 + \left\langle \left|\mathcal{F}'_{ijs}\right|^2 \right\rangle / \left\langle \left|\overline{\mathcal{F}}_{ij}\right|^2 \right\rangle}} \,. \end{aligned} \tag{12.51}$$

It can be realized that the expression for the degree of interferometric coherence (12.51) for an area including several pixels is formally analogous to that (12.43) relative to a single scatterer. The substantial difference is that, when the single scatterer has to be characterized, average is carried out over the ensemble of acquisitions, whereas now, for extended target connotation, average is over the pixels forming the region.

Apart from the random fluctuations of the electromagnetic path lengths caused by the atmosphere, it is the inter-pixel stability of the scattering functions with respect to the acquisition that determines the degree of interferometric coherence. In case the variations of the scattering functions of the pixels composing the observed area are small with respect to their permanent parts for the considered pair of master-slave acquisitions, that is

$$\left|\mathcal{F}'_{ijk}\right| \ll \left|\overline{\mathcal{F}}_{ij}\right|, \qquad k = \mathrm{m}, \mathrm{s} \,,$$

then

$$|\gamma_{ms}| \to 1 \,.$$

Consistently with the results of Sect. 12.3.3, this is the case of pairs of images acquired with short baselines over areas containing dominant small scatterers with simple dielectric structure and the permittivity of which does not undergo appreciable variation between the two data takes. On the opposite side, for labile areas such that

$$\left|\mathcal{F}'_{ijk}\right| \gg \left|\overline{\mathcal{F}}_{ij}\right|, \qquad k = \mathrm{m}, \mathrm{s} \,,$$

the degree of interferometric coherence becomes

$$\gamma_{\rm ms} \propto \frac{\langle \mathcal{F}'_{ijm}\, \mathcal{F}'^{*}_{ijs} \rangle}{\sqrt{\langle |\mathcal{F}'_{ijm}|^2 \rangle}\, \sqrt{\langle |\mathcal{F}'_{ijs}|^2 \rangle}} \,. \tag{12.52}$$

Since the average is over the ensemble of pixels P_{ij} belonging to the area of interest, (12.52) means that the interferometric coherence depends on how much the variation $\mathcal{F}'$ of the scattering function of one pixel in the master acquisition is correlated with the variation $\mathcal{F}'$ of another pixel in the slave acquisition. For instance, when the scattering functions undergo similar inter-pixel variations over the considered area, such that

$$\mathcal{F}'_{ijk} \approx C_k\, \overline{\mathcal{F}}_{ij}, \qquad k = \mathrm{m}, \mathrm{s}\,,$$

with the complex factor C_k generally randomly dependent on the acquisition k but independent of pixel, then

$$\gamma_{\rm ms} \simeq \frac{C^*_{\rm ms}}{|C_{\rm ms}|}\,,$$

whence $|\gamma_{\rm ms}| \approx 1$. The conclusion is that the scatter from the observed area shows *high coherence* when the scattering functions undergo variations that are highly correlated among the pixels.

Coming back to the general expression (12.48), by considering the effects of the atmosphere reasonably[64] uncorrelated with those of the scatterers, the degree of coherence of an area of interest for the (m, s) acquisition pair is

$$\gamma_{\rm ms} \propto \frac{1 + \langle \mathcal{F}'_{ijm}\, \mathcal{F}'^{*}_{ijs} \rangle / \langle |\overline{\mathcal{F}}_{ij}|^2 \rangle}{\sqrt{1 + \langle |\mathcal{F}'_{ijm}|^2 \rangle / \langle |\overline{\mathcal{F}}_{ij}|^2 \rangle}\, \sqrt{1 + \langle |\mathcal{F}'_{ijs}|^2 \rangle / \langle |\overline{\mathcal{F}}_{ij}|^2 \rangle}} \times \left\langle \mathrm{e}^{-\mathrm{j}2\kappa_0 \left(\mathcal{L}'_{ijm} - \mathcal{L}'_{ijs}\right)} \right\rangle , \tag{12.53}$$

where the averages are always intended to be carried out over the ensemble of pixels P_{ij} forming the considered region. Since the modulus of the average exponential function decreases with increasing differences between the random path lengths $\mathcal{L}'$, the atmospheric propagation lowers $|\gamma|$. This was outlined in Sect. 12.3.2.1, where it was also anticipated that the effects of the atmosphere become generally negligible in case the master and slave acquisitions are taken simultaneously so that $\mathcal{L}'_{ijm} \approx \mathcal{L}'_{ijs}$. What is important is that, when imaging is simultaneous, clearly no dielectric changes occur that lower the target coherence (12.47) because of

[64] However, in some occurrences the state of the surface (e.g., the moisture) could be correlated with the meteorological parameters.

the temporal decorrelation introduced in Sect. 12.3.2.2.2. Therefore, the single-pass interferometric coherence of a given area is higher than that for repeat-pass acquisitions. The higher value of $|\gamma|$ suggests that single-pass interferometry is expected to reduce the errors caused by the overall time-dependent irregularities of the interferometric phase.

12.3.4.1 Decorrelation Factors

The fluctuations of the backscattering functions are jointly caused by the change of angles of incidence and scattering (Sect. 12.3.2.2.1), combined with the variation of permittivity between interferometric acquisitions mentioned in Sect. 12.3.2.2.2 [45]. Modeling the effects of the baseline separately from those of the dielectric changes is quite arduous in many real scenarios. Nevertheless, the factorization[65] of the degree of coherence (12.53), i.e.,

$$\gamma \propto \gamma_{\mathrm{a}}\, \gamma_{\mathrm{B}}\, \gamma_{\epsilon}\ , \tag{12.54}$$

is useful to put into evidence the roles

- of the turbulence of the atmospheric refractivity, expressed by the "atmospheric decorrelation" γ_{a},
- of the baseline, through the "geometric decorrelation" γ_{B},
- and of the dielectric stability of the targets, described by the "temporal decorrelation" γ_{ϵ}.

When the effect of the atmosphere is negligible, that means $\mathcal{L}' \approx 0$ or $\mathcal{L}'_{\mathrm{m}} \approx \mathcal{L}'_{\mathrm{s}}$,

$$\gamma_{\mathrm{a}} = \left\langle \mathrm{e}^{-\mathrm{j}2\kappa_0 \left(\mathcal{L}'_{ij\mathrm{m}} - \mathcal{L}'_{ij\mathrm{s}}\right)} \right\rangle \approx 1$$

and the interferometric coherence (12.53) carries information prevailingly on the variable and stable parts of the scattering functions $\mathcal{F}$, hence on the nature of the observed areas. Indeed, several types of terrestrial environments show peculiar phase and amplitude stochastic behavior of the backscattered field. Therefore, the interferometric measurements, which have been previously characterized mainly from the point of view of the stability of scattering and of the ensuing accuracy of altitude retrieval, also provide means of discriminating among various kinds of targets, as well as of estimating some of their relevant features. Figure 12.31 shows the considerable difference of interferometric coherence that is usually observed in areas including different types of terrestrial environments. Section 14.1.2 hints at the coherence properties of some classes of terrestrial targets.

[65] Additional factors, often included into the degree of coherence, are outside the scope of this outline.

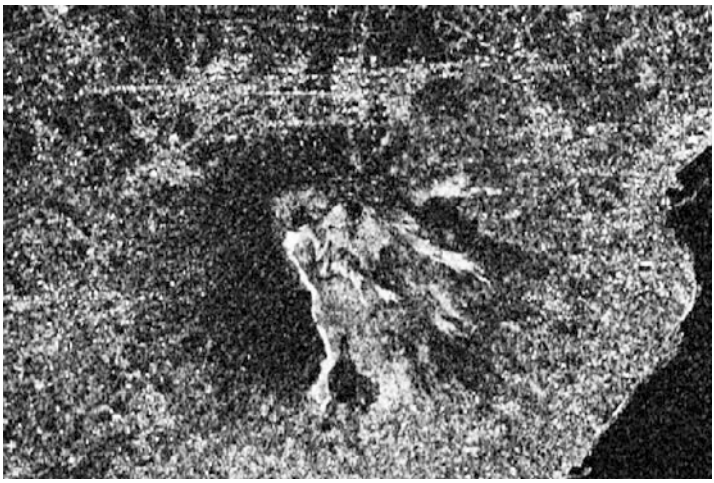

Fig. 12.31 The multi-pass interferometric degree of coherence is high (*clear gray*) over stable areas, such as buildings and exposed rocks, and is low (*dark gray*) over labile areas, such as water (*lower right*) and thick vegetation (Credit: ESA Earthnet Online [34])

Retrieving Height Information is Not a Simple Task

Transforming a two-dimensional map into a three-dimensional scenario is a clearly ill-posed process, because both horizontal and vertical positions of the target concur to determine the location of its image. Stereoscopy is a well-established technique that is used for the altimetric restitution of terrain relief or of buildings from pairs of passive optical images. 3-D rendering from radar acquisitions needs a different processing approach, given the peculiar mechanism of image formation by active systems. For the moment, we have to get used to the typical appearance of the radar maps, which are affected in a reverse manner by the slopes. We also learn about specific features, ascribed to lay-over and double bounce, especially observable when vertical objects such as buildings are imaged.

Understanding the rationale behind the retrieval of the altimetric information is facilitated by addressing the mechanisms that bunch up height and ground range into single measurements of slant distance. Extending the concept of stereoscopy to the coherent radar observations leads to the idea that the phase differences of the field sampled at a master and at a slave locations are related to the height of the target. SAR interferometry is thus introduced. Definitions and features of interferogram, baseline, and phase fringes and unwrapping are presented.

The complexity of the procedure for retrieving height information from interferograms advises us to assess the accuracy of the obtainable digital elevation models, if not even their feasibility. The quantitative approach to estimate the errors, necessarily involving the phase of the scattered field, demands resorting to the electromagnetic theory. First of all, we realize how the path delays undergone by

the waves propagating in the atmosphere may degrade the relation between phase and distance, hence height. Then we have to pay specific attention to the target. The formulas relative both to coherent and to incoherent scattering are recalled to estimate the interferometric phase stability of the observed object. The changes with time of the permittivity is not the only source of uncertainty, since we recognize that the dielectric structure itself, even if stable, may introduce unpredictable variations of the phase of the scattered field. The random nature of the process requires a stochastic characterization based on the second-order moments. Therefore, we put into place basic quantities, such as the coherency dyadic of the scattered field, to describe the phase stability at different polarizations. We have to endure the thorough electromagnetic approach to grasp the concept of permanent scatterer and to understand the rationale for using the interferometric coherence in the identification of classes of terrestrial surfaces.

References

1. Ackermann F (1983) High precision digital image correlation. In: 39-th Photogrammetric Week, Stuttgart, pp 231–243. http://www.ifp.uni-stuttgart.de/publications/phowo.en.html (Visited on 01/12/2014)
2. Appel-Hansen L (1982) Centers of structures in electromagnetism – A critical analysis. IEEE Trans Antennas Propag AP-30(4):606–610. doi:10.1109/TAP.1982.1142861
3. Bachmann M, Schwerdt M, Alfonzo GC, Schrank D (2013) Phase pattern calibration for interferometric applications in spaceborne SAR systems. Int J Antennas Propag. doi:10.1155/2013/284698
4. Baillard C, Maître H (1999) 3-D reconstruction of urban scenes from aerial stereo imagery: a focusing strategy. Comput Vis Image Underst 76(3):244–258. doi:10.1006/cviu.1999.0793
5. Bamler R, Hartl P (1998) Synthetic aperture radar interferometry. Inverse Probl 14(4):R1–R54. doi:10.1088/0266-5611/14/4/001
6. Berthod M, Gabet L, Giraudon G, Lotti JL (1995) High-resolution stereo for the detection of buildings. In: Grün A, Kübler P, Aguris P (eds) Automatic extraction of man-made objects from aerial and space images. Birkhäuser, pp 135–144. ISBN:9783034892421
7. Bracewell RN (2000) The Fourier transform and its applications. McGraw-Hill. ISBN:9780073039381
8. Brodrick D, Kennedy T, Tingay S, Brooke D, Fringe dwellers. http://fringes.org/ (Visited on 02/02/2015)
9. Curlander JC (1982) Location of spaceborne SAR imagery. IEEE Trans Geosci Remote Sens GE-20(3):359–364. doi:10.1109/TGRS.1982.350455
10. Dandois JP, Ellis EC (2013) High spatial resolution three-dimensional mapping of vegetation spectral dynamics using computer vision. Remote Sens Environ 136:259–276. doi:10.1016/j.rse.2013.04.005
11. Dyke PPG (1999) An introduction to Laplace transforms and Fourier series. Springer. ISBN:9781852330156
12. Ferretti A (2014) Satellite InSAR data: reservoir monitoring from space. EAGE. ISBN:9789073834712
13. Ferretti A, Prati C, Rocca F (2001) Permanent scatterers in SAR interferometry. IEEE Trans Geosci Remote Sens 39(1):8–20. doi:10.1109/36.898661
14. Friden J, Kristensson G (2013) Calculation of antenna radiation center using angular momentum. In: 7th European Conference on Antennas and Propagation (EuCAP 2013), Gothenburg, pp 1531–1535

15. Ghiglia DC, Pritt MD (1998) Two-dimensional phase unwrapping: theory, algorithms, and software. Wiley. ISBN:9780471249351
16. Goldstein RM, Zebker HA, Werner CL (1988) Satellite radar interferometry: two-dimensional phase unwrapping. Radio Sci 23(4):713–720. doi:10.1029/RS023i004p00713
17. Graham LC (1974) Synthetic interferometer radar for topographic mapping. Proc IEEE 62(6):763–768. doi:10.1109/PROC.1974.9516
18. Gray RM, Goodman JW (1996) Fourier transforms: an introduction for engineers. Kluwer Academic. ISBN:9789810078522
19. Hein A (2004) Processing of SAR data: fundamentals, signal processing, interferometry. Springer. ISBN:9783540050438
20. Hensley S, Shaffer S (1994) Automatic DEM generation using Magellan stereo data. In: International Geoscience and Remote Sensing Symposium (IGARSS'94). Surface and Atmospheric Remote Sensing: Technologies, Data Analysis and Interpretation, vol 3, pp 1470–1472. doi:10.1109/IGARSS.1994.399472
21. IEEE Standard Definitions of Terms for Antennas. In: IEEE Std 145-1993 (Apr 2013), pp 1–32. doi:10.1109/IEEESTD.2013.6507364
22. Itoh K (1982) Analysis of the phase unwrapping algorithm. Appl Opt 21(14):2470–2470. doi:10.1364/AO.21.002470
23. Keydel W (2007) Normal and differential SAR interferometry. In: Radar polarimetry and interferometry. RTO Educational Notes EN-SET-081bis. NATO Science and Technology Organization. ISBN:9789283700661
24. Leberl FW (1990) Radargrammetric image processing. Artech House. ISBN:9780890062739
25. Liu H-L, Wang W, Richmond AD, Roble RG (2010) Ionospheric variability due to planetary waves and tides for solar minimum conditions. J Geophys Res Space Phys 115(A6). ISSN:2156–2202. doi:10.1029/2009JA015188
26. Li Z, Zhu C, Gold C (2010) Digital terrain modeling: principles and methodology. Taylor & Francis. ISBN:9780203486740
27. Madsen S, Zebker H (1998) Imaging radar interferometry. In: Henderson FM, Lewis AJ (eds) Principles and applications of imaging radar. Manual of remote sensing, vol 2. Wiley. ISBN:9780471294061
28. Massonnet D, Feigl KL (1998) Radar interferometry and its application to changes in the Earth's surface. Rev Geophys 36(4):441–500. doi:10.1029/97RG03139
29. Mikhail EM, Bethel JS, McGlone JC (2001) Introduction to modern photogrammetry. Wiley. ISBN:9780471309246
30. Monin AS, Yaglom AM (2007) Statistical fluid mechanics: mechanics of turbulence, vols 1 and 2. Dover. ISBN:9780486458830, 9780486458915
31. Nex F, Remondino F (2014) UAV for 3D mapping applications: a review. Appl Geomat 6(1):1–15. doi:10.1007/s12518-013-0120-x
32. Rishbeth H (2006) F-region links with the lower atmosphere? J Atmos Sol-Terr Phys 68(3–5):469–478. doi:10.1016/j.jastp.2005.03.017
33. Rishbeth H, Mendillo M (2001) Patterns of F2-layer variability. J Atmos Sol-Terr Phys 63(15):1661–1680. doi:10.1016/S13646826(01)00036-0
34. Rocca F, Prati C, Ferretti A. An overview of SAR interferometry. ESA Earthnet Online. http://earth.esa.int/workshops/ers97/program-details/speeches/rocca-et-al/ (visited on 10/13/2014)
35. Rosen PA, Hensley S, Joughin IR, Li FK, Madsen SN, Rodríguez E, Goldstein RM (2000) Synthetic aperture radar interferometry. Proc IEEE 88(3):333–382. doi:10.1109/5.838084
36. Sarabandi K, Lin Y-C (2000) Simulation of interferometric SAR response for characterizing the scattering phase center statistics of forest canopies. IEEE Trans Geosci Remote Sens 38(1):115–125. doi:10.1109/36.823906
37. Sneddon IN (1995) Fourier transforms. Dover. ISBN:9780486685229
38. Spagnolini U (1995) 2-D phase unwrapping and instantaneous frequency estimation. IEEE Trans Geosci Remote Sens 33(3):579–589. doi:10.1109/36.387574

39. Stereoscopy (2014) The Pennsylvania State University. https://www.e-education.psu.edu/natureofgeoinfo/c6_p13.html (Visited on 03/12/2014)
40. Topographic Data and Images NOAA. http://www.ngdc.noaa.gov/mgg/topo/topo.html (Visited on 03/12/2014)
41. Toutin T, Gray L (2000) State-of-the-art of elevation extraction from satellite SAR data. ISPRS J Photogramm Remote Sens 55(1):13–33. doi:10.1016/S0924-2716(99)00039-8
42. Trouvé E, Nicolas J-M, Maitre H (1998) Improving phase unwrapping techniques by the use of local frequency estimates. IEEE Trans Geosci Remote Sens 36(6):1963–1972. doi:10.1109/36.729368
43. Zebker HA, Goldstein RM (1986) Topographic mapping from interferometric synthetic aperture radar observations. J Geophys Res Solid Earth 91(B5):4993–4999. doi:10.1029/JB091iB05p04993
44. Zebker HA, Lu Y (1998) Phase unwrapping algorithms for radar interferometry: residue-cut, least-squares, and synthesis algorithms. J Opt Soc Am A 15(3):586–598. doi:10.1364/JOSAA.15. 000586
45. Zebker HA, Villasenor J (1992) Decorrelation in interferometric radar echoes. IEEE Trans Geosci Remote Sens 30(5):950–959. doi:10.1109/36.175330

Chapter 13
Sensing Surface and Underneath Features

It is now clear that both passive and active remote observing systems gain information on the Earth's environment by essentially capturing the power carried by the electromagnetic waves[1] that interacted with the terrestrial materials in the sense outlined in Sect. 10.1.3. It should be added that the phase of the waves, measurable by coherent radar observations, provides supplemental pieces of knowledge. The information brought by the directly measured wave quantities (power and/or phase) resides in the imprinting that the observed target exerts on the interacting electromagnetic field. A few examples were occasionally met in previous chapters, including the effect of moisture content on the fraction of microwave power reflected by smooth terrain (Sect. 6.3.2), or of the sea surface state on the intensity of backscattering (Sect. 7.4.5), the bearing of the temperature profile upon the thermal power emitted by the atmosphere (Sect. 9.4.1.1), the spectral changes of optical radiance related to vegetation (Fig. 10.15), or the effect of urban features on the interferometric coherence (Fig. 12.31). The reader also knows that the electromagnetic waves that interacted with the target always carry the drawn information across all or part of the atmosphere. The extinction and radiative contribution of the latter alter the information conveyed to the sensor. But the role of the wave interaction with the atmosphere as itself source of meteorological and climatological information cannot be even overlooked. Section 10.1.3 mentions that these either noxious or productive interactions of the probing and carrier waves with natural and man-made targets depend in a crucial way on the frequency (or wavelength) bands at which the systems operate.

Regarding the targets of interest, three wide classes of terrestrial environment are considered: solid land, water bodies and atmosphere. Solid land coarsely consists of a more or less inhomogeneous bulk material bound by a surface with irregular height fluctuations, over which substantially different materials possibly lie. The land

[1] Systems exploiting low-frequency or quasi-static fields are not considered.

D. Solimini, *Understanding Earth Observation*, Remote Sensing and Digital Image Processing 23, DOI 10.1007/978-3-319-25633-7_13

environment includes a large variety of frequently time-varying local structures, met both in natural areas and in managed or developed zones. The structure of water bodies is less varied, since it generally consists of a half-space of relatively homogeneous bulk material with a rough boundary, the geometrical features of which are related to the local or remote wind field. Water is covered by layers of foam in high-wind areas, by permanent or seasonal ice, possibly with overlaying snow, in cold regions, and by films of oil or of other slick-forming organic matter on particular occurrences. Finally, the atmosphere is a coarsely homogeneous layer of gaseous material with embedded solid or liquid inhomogeneities, representing dust and aerosol particles, rain drops and ice particles.

Various physical and analytical elementary models have been introduced to represent the basic interaction of electromagnetic waves and matter in its various states of aggregation. Thereby, a first understanding of the primary origin of the remote information has been gained. Nevertheless, the considered schemes are sometimes far from the intricate nature of many real terrestrial environments and of the wave interaction mechanisms. This is especially true if the models are supposed to explain the actual behavior with respect to extended ranges both of observation parameters and of bio-geo-physical features. Models that are still manageable, but more comprehensive than some of the basic ones, are then attractive.

This further modeling effort regards the scattering and reflecting behavior of the targets, because scatter and reflection are at the source of the optical and radar data. On the other side, Chap. 8 clarifies that the other main data source, thermal emission, is intimately related to reflection and scattering by the electromagnetic reciprocity seen in Sect. 3.2.1.

13.1 Macroscopic Scattering Mechanisms

The variety of terrestrial targets, of observation techniques and of parameters to monitor demands clever identification of the models best suited to understand the information content of actual data and images. The analysis carried out in the previous chapters suggests that the choice of a model is based not only on the nature of the target and of the observables, but also on the frequency range at which the observation is carried out. Nevertheless, the two comprehensive mechanisms of wave-environment interaction introduced in Sect. 7.4.7 and described quantitatively by (7.64), i.e.,

– interaction with surfaces separating different materials,
– interaction with inhomogeneous volumetric structures,

are suitable to substantially categorize and drive the interpretation of the data, as well as to provide the basis of parameter retrieval. Reflection and scattering from the surface and volume scattering are then the basic constituent models of macroscopic wave interaction, which, together with wave propagation, are able to lead to the essential comprehension of the radar and optical Earth observation data. Reciprocity

suggests that they are also instrumental to understanding the radiometric passive observations at microwaves and TIR. On these grounds, the following formulation disregards thermal emission.

Both reflection and scattering are components of essentially the same general re-radiation process of the incident power, neither their respective contributions to the remote measures can be separated in a straightforward fashion. This consideration advises using the term "scattering" in the broad sense[2] of Chap. 7 to include "reflection", being understood the convenience of analyzing the reflecting properties of a target separately from its *pure* scattering.

It is important to bear in mind that the strong dependence on frequency both of the dielectric properties of the terrestrial materials and of the scattering features changes the relative importance of the surface and volume scattering mechanisms expressed by the two terms in (7.64) between microwave and visible or IR observations. As an example, Sect. 9.1 shows that a target with bulk inhomogeneities of given characteristic dimension D tends to behave as homogeneous at sensing wavelengths markedly longer than D. Coarsely speaking, data collected in the microwave spectral range on a land or sea target are then expected to be shaped mainly by surface scattering. On the other side, the volume scattering mechanism becomes essential to understand the measurements taken on the *same* target in the optical range.

How the various factors in (7.64) are affected by the observing parameters and target features can be scrutinized to examine in depth the expected behavior of surface and volume scattering, as well as their relative weight in the image formation. Nevertheless, the simply qualitative description that follows, together with the examples presented in Chap. 14, can help the reader to get a sense of the images that are produced by the Earth observing systems, even without delving deeper into the bulky details of scattering models.

13.1.1 Surface Scattering

Air-material interfaces are ubiquitous components of the generally composite environments on the surface of Earth. Moreover, exposed *bare surfaces* are frequently found both in natural and in developed areas. Typical examples are

- exposed rocks,
- soil in arid areas or, seasonally, in temperate regions,
- sea or lakes outside high-wind regions,
- man-made structures, such as streets, parking lots, building walls and roofs.

[2]Indeed, as already noted, it is not even uncommon to find the term "reflection" denoting scattering.

Bare surface denotes the physical boundary between air and a natural or man-made material, the bulk of which can be regarded more or less homogeneous according to the frequency at which it is sensed. As mentioned, many materials tend to behave as uniform media at microwaves, at which frequencies the high reflectivity caused by the generally large[3] permittivity (cf. Sect. 2.2) keeps low the sub-surface field. For these concurrent reasons, little scattering originates from the volume below the surface: re-radiation mainly originates from the secondary source defined by (7.4) located in correspondence of the air-matter transition layer, according to the dielectric and geometric features of the latter. Scattering by these surface-type sources occur through both coherent and incoherent mechanisms, according to the approach of Sects. 7.2 and 7.4.7. Thus, the re-radiated wave is the superposition of a *coherent* component *reflected*[4] by the possibly plane *average* surface transition layer (Sect. 7.3.3) and of a *stochastic* component *diffused* by the *random height* irregularities. The coherent component evidently characterizes the directional reflecting behavior of the target, while the incoherent component yields its diffused scattering properties. It should be also considered that the periodic components which are usually embedded in the surface roughness of water or of agricultural plots enhance re-radiation at particular incidence and scattering angles, which depend on the frequency of observation according to the results of Sect. 7.4.5.

13.1.1.1 Reflection from the Surface Layer

The model presented in Sect. 7.3.3 relates the *coherent* reflecting behavior of the air-matter interface to the transition layer thickness corresponding to the surface roughness, for given permittivity of the material, wave frequency, polarization, and incidence angle. The factor λ_0/d in the expression (7.34) indicates that, at a given wavelength, the reflection coefficient increases with decreasing d. This means that the wave is increasingly reflected around the specular direction as the surface roughness decreases, and, correspondingly, that reflection especially occurs at the lower microwave range. Such a behavior is consistent with the spectral approach of Sect. 7.4.4, since scattering about the specular direction, corresponding to $\boldsymbol{\kappa}_\mathrm{t} = 0$, is mainly contributed by the lowest spatial frequencies, the amplitude of which enhance with decreasing roughness.

The encountered bare surfaces are often locally plane *on average*, with random deviations of height characterized by the *roughness parameters* [23], which affect the reflecting behavior. However, for a practical quick approach, a traditional geometric parameter indicating how reflecting is a rough surface which on average is plane, refers to the phase difference $\Delta\Phi$ between rays (Sect. 5.3.1.2) evaluated over a plane perpendicular to the specular direction $\boldsymbol{\beta}_0''$ (Fig. 13.1). The phase difference

[3] Extremely dry scenarios are disregarded.

[4] Given the finite dimension of the coherent source, the term *diffracted* could be more appropriate.

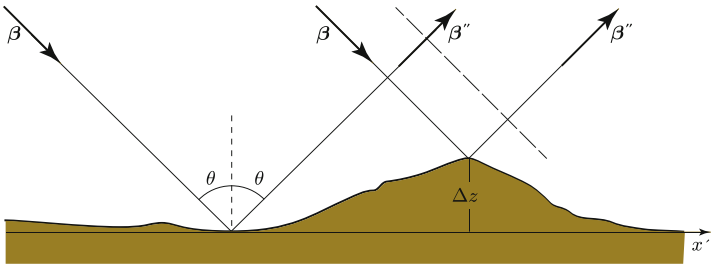

Fig. 13.1 The Rayleigh criterion refers to the geometrical optics model in relating the height deviation Δz of the random surface $z = \mathfrak{z}(x', y')$ to the phase of the reflected wave over the plane perpendicular to the specular direction $\boldsymbol{\beta}_0''$, the trace of which is represented by the oblique *dashed line*

$\Delta\Phi$ of a pair of rays in the $(x\,z)$-plane of incidence depends on the vertical path difference according to

$$\Delta\Phi = 2\kappa_0\,\Delta z\,\cos\theta = 4\pi\,\frac{\Delta z}{\lambda_0}\cos\theta\ . \tag{13.1}$$

Equation (13.1) shows that $\Delta\Phi$ is proportional to the difference of height Δz between two reflecting facets for given wavelength and angle of incidence. When the phase difference between specular rays originating from any reflecting facet is below the *Rayleigh limit*[5]

$$\Delta\Phi_{\mathrm{R}} = \frac{\pi}{16}\ ,$$

the surface is assumed to re-radiate an approximately plane wave in the specular direction. In turn, taking account of the total path, the phase threshold $\Delta\Phi_{\mathrm{R}}$ corresponds to a threshold $\sigma_{z\mathrm{R}}$ for the height standard deviation σ_z characterizing the random function $z' = \mathfrak{z}(x', y')$ which describes the rough surface:

$$\sigma_{z\mathrm{R}} = \frac{\lambda_0}{8\,\cos\theta}\ .$$

The surface is conventionally assumed to reflect like a smooth plane one if its height standard deviation σ_z is below the threshold $\sigma_{z\mathrm{R}}$. This condition on the roughness is known as the *Rayleigh criterion* [11], [20, Chap. 5]. It should be noted that the standard deviation σ_z of height $\mathfrak{z}$, for given roughness statistics, is directly related to the mentioned thickness d of the transition layer introduced in Sect. 7.3.3 (Fig. 7.12).

The coherent reflectivity (8.19) decreases with increasing roughness (Fig. 13.2a–13.2c), according to the simplified expression

[5]The more restrictive Fraunhofer criterium [22, Chap. 11] can be also adopted.

Fig. 13.2 Examples of bare soil with different geometrical roughness: relatively smooth (**a**), rough (**b**), very rough (**c**). Ground data acquired during MAC 91 [4]

$$\mathcal{R}_p \simeq \left|q_p\right|^2 \mathrm{e}^{-4\,\kappa_z^2\,\sigma_z^2}\ ; \qquad p = \mathrm{h}, \mathrm{v}\ , \tag{13.2}$$

where subscript $p = \mathrm{h}, \mathrm{v}$ denotes *locally* horizontal or vertical polarization and

$$\kappa_z = \frac{2\pi}{\lambda_0}\cos\theta$$

is the wavenumber in the direction perpendicular to the average surface, that is the vertical wavenumber when the surface is horizontal. Equation (13.2) indicates that, at a given wavelength,

- the specular reflectivity of a smooth surface tends to the modulus square of the reflection coefficients introduced in Sect. 6.1.2;
- the specular reflectivity of a very rough surface tends to zero, thus denoting the vanishing of the coherent component: re-radiation occurs almost exclusively in the form of *diffused field*, consistently with the results of Sects. 7.3.3 and 7.4.7.1.

As expected, the coherent reflectivity for oblique incidence at horizontal and vertical polarizations depends on the material permittivity,[6] which affects the reflection coefficients q_p according to the results of Sect. 6.3.2. Given the tight relation between water content and microwave permittivity, this means that, for given roughness, wavelength and incidence angle, the amount of *microwave* specular reflection contains the imprinting by the moisture content [8, 15] of the material, typically of the soil (Sect. 2.2.4). It is worth recalling that the angular dependence of

[6]The reflection coefficients can be alternatively expressed in terms of refractive index.

reflectivity (13.2) for the two polarizations differs substantially, with the vertical one reflected less than the horizontal and presenting a marked minimum at the pseudo-Brewster angle. Increasing moisture, hence complex permittivity, increases reflection at all angles, included at the pseudo-Brewster one in case of vertical polarization, as illustrated by the examples in Fig. 6.14.

Since the reflectivity at both polarizations decreases with increasing product $\kappa_z \sigma_z$,

- at optical wavelength, only polished materials (e.g., glass or metal) or relatively calm water tend to behave as reflecting surfaces, yielding the *sun glint*, whereas the other kinds of surfaces, generally having $\sigma_z \gg \lambda_0$, produce diffuse scattering;
- at microwaves, the encountered reflecting properties are varied, since, on one side, the surfaces may have quite different roughness[7] and, on the other, common observing systems operate at wavelengths λ_0 in the range from a few to tens of centimeters, often comparable with σ_z.

In operational applications, the systems observing the Earth in the optical range generally avoid the sun glint, rather they exploit the incoherent bistatic scattering of the solar radiation, actually originated by interaction with the skin layer of the bulk material. On their side, neither the common side-looking radar systems exploit specular reflection,[8] because they operate in monostatic or quasi-monostatic (Sect. 7.1.3.1) configuration, in the sense that they sample the scattered field only in the neighborhood of the *backscattering wavenumber* (12.36). Sophisticated multi-platform SARs [24, 25] on one side, and parasitic systems [16] based on "illuminators of opportunity" on the other, can measure the surface reflection by taking advantage of their actual bistatic observation geometry. Conspicuous potential is anticipated in various applications [12].

13.1.1.2 Scattering from the Surface Layer

We know that surface scattering is the interaction mechanism that mainly affects the radar echo, expressed by the backscattering coefficient (7.65), from the boundary of a target the internal homogeneity of which makes negligible the scattering from its bulk.[9] Moreover, the results obtained in Sect. 7.4 indicate that

- the essentially random height deviation $z' = \mathfrak{z}(x', y')$ of the air-material interface (Sect. 7.3.3) originates a *scattered* field that adds to the one *coherently reflected* in the local specular direction by the average structure;

[7] The degree of roughness can be consequence of natural processes, as well as of agricultural practices [28].

[8] Clearly apart from targets the surface of which has peculiar orientations, or which include corner reflectors.

[9] As said, the second term in (7.65) is further reduced by the effect of the permittivity-dependent attenuation in the surface layer.

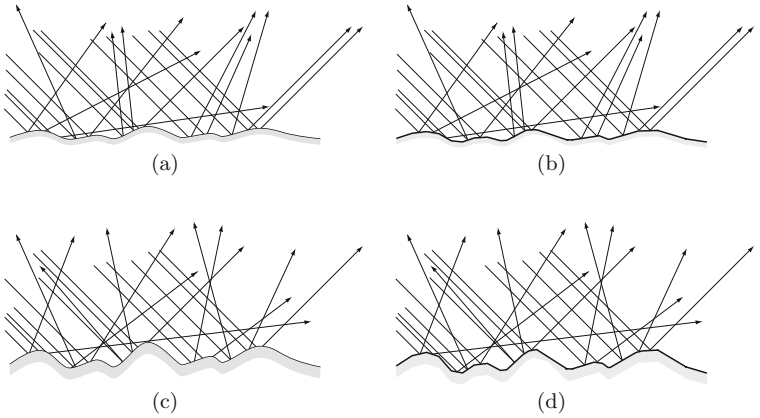

Fig. 13.3 The facet model, which approximates the rough surfaces (**a**) and (**c**) with ensembles of portions of tangent planes (**b**) and (**d**), explains intuitively how the angular spread of the scattered power increases with increasing surface roughness (**c**) and (**d**), i.e., with rising facet slopes

– the spatial spectrum of roughness S_ζ affects the scattering intensity for given wavelength and incidence and scattering directions.

A further model helps one to interpret scattering measurements on somewhat more intuitive grounds. It regards the scattered field as a superposition of elementary contributions *diffracted* by ensembles of plane elements, named *facets*, locally tangent to the rough surface, again assumed plane on average. Figure 13.3 sketches such a representation of surface scattering. The *facet model* suggests in a quite simple way the relation between bistatic scattering pattern and roughness features of the surface, consistently with the proportionality between scattering intensity and spatial spectrum discussed in Sect. 7.4.4.

Backscattering from a generally-oriented bare-surface pixel has been found composed of a reflected component and a diffused one. The effect of roughness on the relative contribution of reflection and scattering to the backward radar[10] return differs substantially according to the incidence angle, determined by the local orientation of the mean rough surface within the pixel. The field coherently reflected from the surface is strong for normal incidence, that is when the plane mean surface is locally perpendicular to the observation direction, and decreases with increasing roughness because, roughly speaking, the number of perpendicular facets contained in the unit area decreases. Instead, the trend is opposite for oblique observation: consistently with the spectral approach of Sect. 7.4.4, backscatter, which is negligible for a smooth surface, increases with increasing roughness, given the augmenting number of oblique facets. This feature is depicted in Fig. 13.4 in one dimension.

[10]Lidar returns behave analogously.

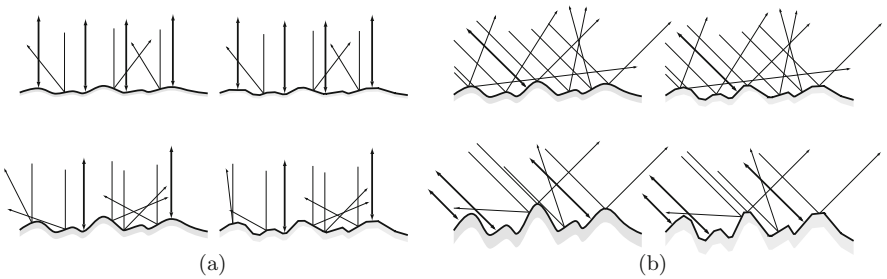

Fig. 13.4 The left part of the figure (**a**) suggests that increasing roughness, hence the local slopes in the facet model, spreads the scattered power in angle, hence decreases the scattering in the specular direction when incidence is normal; the right part of the figure (**b**) shows that, on the contrary, the increasing angular spread of scattered power caused by increasing roughness, enhances backscattering when incidence is oblique (cf. Fig. 13.5)

More precisely, if each facet is regarded as a re-radiating plane source diffracting the field, the results of Sects. 7.3.1.2 and 11.1 point out that the maximum of re-radiation occurs in the neighborhood of the direction specular to that of local incidence and that the angular distribution of the diffracted power broadens as the source dimension shrinks (Sect. 11.3.1). Therefore, the field scattered by the bare surface depends on the dimensions and distributions of slopes of the facets: increasing the areic number of facets with non-zero slopes and correspondingly decreasing their dimensions increase the angular spread of scattering. The consequence is that the field returning in the backward direction increases with roughness when the average surface of the pixel is oblique to the direction of propagation of the incident wave, whereas it decreases for perpendicular orientation of the pixel. Figure 13.5 complements Fig. 13.4 in visualizing the ambivalent effect of roughness.

It is worth adding that, in principle, measurements of bistatic scattering patterns contain full information on the surface geometry, should this latter be of interest; however, multi-angle observations of this kind [6] are substantially complicated, while backscattering, i.e., the field returning in the backward direction, is readily measured.[11]

13.1.1.2.1 Backscattering from Rough Surfaces

A quantitative approach relates the slopes of the facets both to the surface height standard deviation σ_z and to the *correlation distance* ℓ_c of height, which represents the characteristic horizontal dimension of facets, in case the usual Gaussian surface

[11] It is again pointed out that the multi-platform systems such as TanDEM, although named *bistatic*, actually do not perform this kind of measurements, which should be carried out over an angular range sufficiently wide to observe the complete features of bistatic "scattering", including specular reflection.

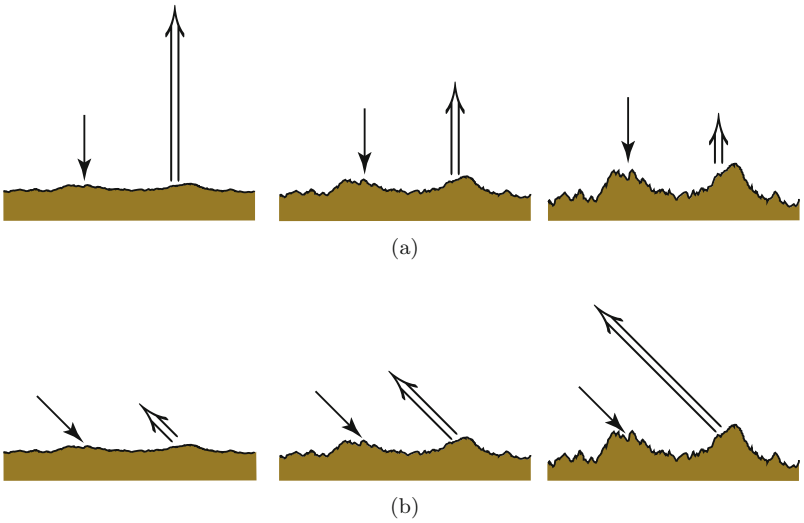

Fig. 13.5 Increasing roughness lowers backscattering at normal incidence, (**a**), while enhances it at oblique incidence, (**b**)

approximation holds [3, 7, 19]. The relevant parameter combining the two quantities is the *slope standard deviation* $\mathfrak{m}$, defined as

$$\mathfrak{m} := \sqrt{2}\,\sigma_z/\ell_c \ ,$$

which is used to describe the roughness of the surface. The effect of the material permittivity is taken into account by the power reflection coefficient (6.7) for normal incidence $\mathcal{R}(0) = |q(0)|^2$. The co-polar backscattering coefficient $\sigma^0_{pp}(\theta)$ for incidence angle θ is then approximated, in the **g**eometrical **o**ptics (GO) model introduced in Sect. 5.1.1, by

$$\sigma^0_{\rm hh}(\theta) = \sigma^0_{\rm vv}(\theta) \simeq \frac{\mathcal{R}(0)}{2\mathfrak{m}^2}\ \mathrm{e}^{-[\tan^2\theta/(2\mathfrak{m}^2)]}\,(\cos\theta)^{-2}\ .$$

It is important to note that the geometrical optics model yields σ^0 independent of frequency.[12] Moreover, the assumption of optically diffracting plane facets does not allow one to interpret possible differences between horizontal and vertical polarizations, neither cross-polarization measurements. In fact, differences of backscattering from rough surfaces do exist between vertical and horizontal polarization. However, it is observed that the difference decreases with increasing roughness, so that, when the surface is sufficiently rough (or the frequency is high enough) to satisfy the condition $\sigma_z\,\kappa_0\,\cos\theta > 1$, the difference tends to vanish and the facet model yields

[12] Clearly apart from the effect of the frequency-dependent permittivity on $\mathcal{R}$.

an acceptable accuracy in interpreting co-polar backscattering from rough surfaces at any polarization in terms of roughness and material permittivity.

In practice, backscattering from natural rough surfaces such as bare soil shows little difference between polarizations when measured at frequencies above C-band, typically at X-band and higher. For frequencies and/or roughness sufficiently low to satisfy the condition $\sigma_z \kappa_0 < 0.3$ (for common natural surfaces, this occurs at L-band frequencies and below), a *higher value* of the backscattering coefficient is measured at *vertical polarization*. This observation implies that a different model is needed to interpret low-frequency radar images.

A model frequently used to relate the co-polar backscattering coefficients measured at low microwave frequency to roughness and permittivity is based on the **S**mall **P**erturbation **M**ethod (SPM) [22, Ch. 12], [5], which yields the approximate expression

$$\sigma^0_{pp}(\theta) = 2\,\mathrm{m}^2 \kappa_0^4 \cos^4\theta \;\left|\mathrm{q}_{pp}(\theta)\right|^2 \mathrm{e}^{(\kappa_0 \ell_\mathrm{c} \sin\theta)^2} \;; \qquad p = \mathrm{h}, \mathrm{v}\,. \tag{13.3}$$

The *reflection parameter* q_{pp} in (13.3) depends on polarization according to

$$\begin{aligned} \mathrm{q}_{\mathrm{hh}}(\theta) &\equiv q_\mathrm{h}(\theta)\;; \\ \mathrm{q}_{\mathrm{vv}}(\theta) &= (\tilde{\epsilon} - 1) \frac{\sin^2\theta - \tilde{\epsilon}(1 + \sin^2\theta)}{\left(\tilde{\epsilon}\,\cos\theta + \sqrt{\tilde{\epsilon} - \sin^2\theta}\right)^2}\,, \end{aligned}$$

where $\tilde{\epsilon}$ is the complex relative permittivity of the sub-surface material, assumed homogeneous within the pixel area. It is worth pointing out that the roughness of the surface tends to quench the pseudo-Brewster angle effect for the vertical polarization.

Given the limitations of the models, care must be exerted in interpreting and exploiting data at C-band, since the scattering from frequently encountered bare surfaces behaves differently from that both at low (L-band) and high (X-band) microwave frequencies. To this end, the C-band image interpretation can take advantage of analytical expressions derived by the **I**ntegral **E**quation **M**ethod (IEM) [1, 9, 10], which is an effective, though rather bulky, approach to scattering estimation, less subject to wavelength or roughness constraints.

13.1.1.2.2 Backscattering from Periodic Surfaces

Section 7.4.5 mentions that surfaces with spatial periodicity are frequently encountered in the terrestrial environment, typically on the sea surface. Given the rather regular spatial arrangement of the surface scattering sources, a field-based deterministic approach is suitable.

The scattered scalar field $E^{(\mathrm{s})}$ is regarded as the superposition in amplitude and phase of the specular contributions from the individual facets contained in the pixel:

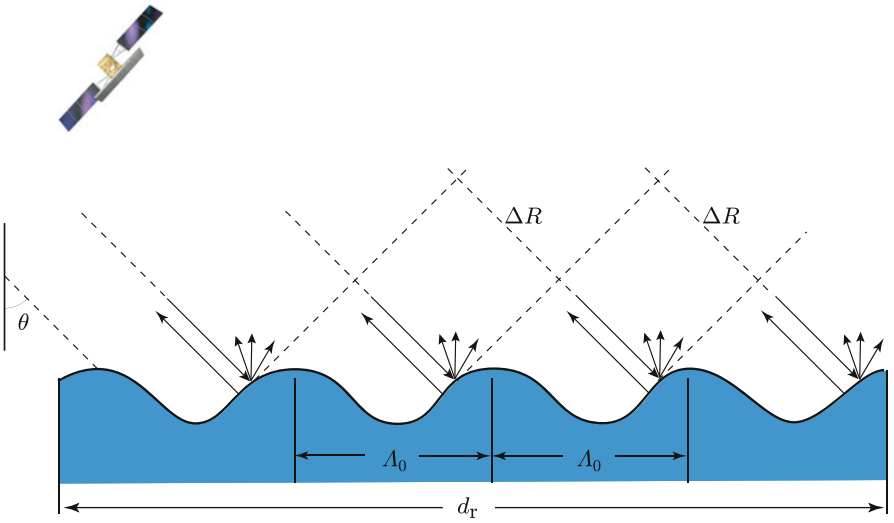

Fig. 13.6 Backscattering of periodic surfaces is affected by the interference of the field contributions originating from regularly located facets: for given electromagnetic wavelength and spatial period Λ_0, enhanced backscattering is observed at the angle of incidence θ that satisfies the Bragg condition (13.6)

$$E^{(\mathrm{s})} = \sum_{m=0}^{M-1} q\, E_0^{(\mathrm{i})} \mathrm{e}^{-\mathrm{j}\, 2\kappa_0 R_0}\, \mathrm{e}^{-\mathrm{j}\, 2m\, \kappa_0 \Delta R}\,. \tag{13.4}$$

The field $E^{(\mathrm{s})}$ given by (13.4) for the one-dimensional geometrical-optics backscattering model sketched in Fig. 13.6, depends on the number M of spatial periods of the surface contained in the pixel and on the coefficient q modeling the local reflection. The phase factors in (13.4) are determined by the distance R_0 from the radar antenna[13] to a reference point in the pixel (e.g., its center), and by the difference ΔR of the path lengths between facets located in adjacent spatial periods. The expression of $E^{(\mathrm{s})}$ contains the sum of a geometrical progression, which yields

$$E^{(\mathrm{s})} = q E_0^{(\mathrm{i})}\, \frac{\sin[\kappa_0 (M+1)\Delta R]}{\sin(\kappa_0 \Delta R)}\, \mathrm{e}^{-\mathrm{j}\, 2\kappa_0 R_0}\,. \tag{13.5}$$

Equation (13.5) indicates that the amplitude of $E^{(\mathrm{s})}$ varies with the radar frequency and with the single-path length difference $\Delta R = \Lambda_0 \sin\theta$, which depends on the spatial period Λ_0 of the surface and on the incidence angle. The backscattered field peaks to the value

[13] As usual, the antenna is assumed collapsed in its phase center.

$$\left|E^{(\mathrm{s})}\right| = M\, q \left|E_0^{(\mathrm{i})}\right| ,$$

when the *Bragg resonance condition*

$$\kappa_0 \Delta R = \frac{2\pi}{\lambda_0} \Lambda_0 \sin\theta = n\pi \; ; \qquad (n = 0, 1, 2, \ldots) \tag{13.6}$$

is satisfied. This corresponds to the condition that the difference of total path length for adjacent scattering facets be a multiple integer of the wavelength, so that the M individual field contributions add in phase. In case the dimension d_r in range of the pixel is large with respect to the spatial period of the surface undulation, so that M is a large number, the peak value of $\left|E^{(\mathrm{s})}\right|$ is quite high. Therefore, even if the surface spectral component which satisfies the Bragg condition has a moderate value, the field backscattered by that component prevails over the field backscattered by the other spectral components, which, although possibly larger, do not satisfy the Bragg resonance condition. It is worth observing that the deterministic model considered here yields a result which is qualitatively consistent with the incoherent approach followed in Sect. 7.4.5, relating the scattered power to the amplitude of the spectral component of the dielectric inhomogeneities corresponding to the horizontal scattering wavenumber set by electromagnetic wavelength and incidence angle.

13.1.2 Volume Scattering

The second basic interaction mechanism has a volumetric character in the sense that the re-radiating sources are distributed in a three-dimensional region of space. A scattering source of this type arises when the incident wave interacts with an inhomogeneous dielectric structure over a significantly long path. A variety of environments are customarily[14] characterized by volume scattering, like, for instance,

- vegetation canopies permanently or seasonally present in non-arid regions;
- the terrain, which contains rock fragments, decomposed vegetation, water inclusions and air cavities;
- snow covers, formed by inhomogeneous mixtures of ice aggregates and air;
- sea surf, a mixture of salty water and air;
- the turbid atmosphere.

In several instances of land and marine environment, the inhomogeneous material in which the three-dimensional source is located forms a layer overlying a thick region of space of different relatively homogeneous matter.

[14] Clearly according to the frequency of the interacting wave.

The electromagnetic wave originated by the external primary source (radar transmitter, laser, or Sun) enters the inhomogeneous material in which it induces the secondary sources (7.4) originating the volume scattering. In some instances the scattering sources are located within actual dielectric objects in air, like leaves, twigs and branches of a plant canopy; in other cases they rather represent a more or less smooth re-radiating current distribution associated with the deviation of permittivity from the dielectric background. For instance, this occurs for the mainly continuous distribution of air or water in the solid matrix of moist terrain.

The ensemble of dielectric elements forms a medium which, according to the frequency of observation, may be either *sparse* or *dense* from the electromagnetic point of view. When the elements are located at a mutual distance sufficiently large with respect to the wavelength, scattering and absorption are essentially affected by the characteristics of the single constituents, otherwise, interaction among elements must be considered [27], given their short mutual distances. Because of the generally random spatial arrangement of the dielectric inhomogeneities, the electromagnetic fields scattered by the single elements in a sparse medium [13] superpose incoherently, i.e., with random phase. Then, the general approach followed in Chap. 9 basically applies.

13.1.2.1 Volume Scattering Source Function

The areic power density $\mathcal{P}$ sent in a given direction by scattering from the 3-D inhomogeneities distributed in the observed volume is ruled by the radiative transfer equation (9.33):

$$\frac{\mathrm{d}\mathcal{P}}{\mathrm{d}s} + \alpha_\mathrm{e}\mathcal{P} = \kappa_\mathrm{s}\,\mathfrak{J}\ . \tag{13.7}$$

The scalar[15] source term $\mathfrak{J}$, which in absence of thermal emission corresponds to $\mathcal{J}_\mathrm{s}$ in (9.31), expresses the collective contribution to the scattered power by the inhomogeneity elements. In the single-scattering approximation of Sect. 7.4, $\mathfrak{J}$ is proportional to the power density $\mathcal{P}'$ of the "refracted" wave that, originated by a man-made source or by the Sun, crosses the air-material interface and propagates in the inhomogeneous medium, i.e.,

$$\mathfrak{J}(\lambda_0, s) = \mathcal{S}(\lambda_0, s)\,\mathcal{P}'(\lambda_0, s)\ , \tag{13.8}$$

where $\mathcal{S}$ is the volume scattering phase function introduced by (9.28). The relations (13.7) and (13.8) refer to narrow bandwidths around λ_0. Their validity is limited to radar observations, but hold also for optical sensing when thermal emission is negligible with respect to the scattered solar or laser radiation.

[15] The present simplified approach does not account for polarization.

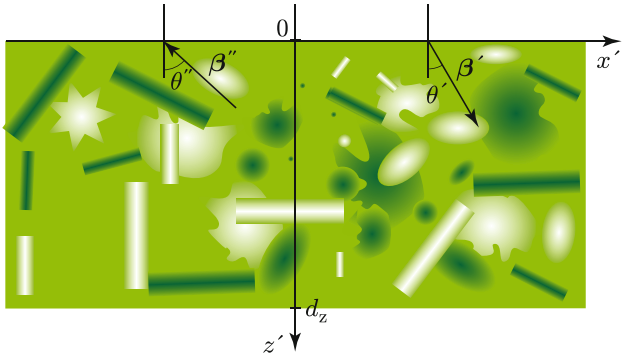

Fig. 13.7 Phase vector $\boldsymbol{\beta}'$ of "refracted" (*downward*) wave and phase vector $\boldsymbol{\beta}''$ of scattered (*upward*) wave inside an inhomogeneous layer of thickness d_z (cf. Fig. 7.37)

For discrete scatterers, based on definitions (7.16) and (9.28), the *volume scattering source function* $\kappa_s \mathfrak{J}$ is expressed through the bistatic scattering cross-section $\langle\sigma\rangle$ of the inhomogeneities, averaged over their ensemble

$$k_s \mathfrak{J} = \langle\sigma\rangle \mathcal{P}' \,. \tag{13.9}$$

In case of monostatic or quasi-monostatic radar observation, $\kappa_s \mathfrak{J}$ reduces to the volume *backscattering* source function and correspondingly depends on the average backscattering cross-section $\langle\sigma_b\rangle$ of the dielectric inhomogeneities in the unit volume. Because of the loss of power caused by the combined effect of absorption (Sect. 5.3.2.2) and scattering (Sect. 9.1), the primary wave is attenuated, hence its power density decays with the traveled path s as

$$\mathcal{P}'(\lambda_0, s) = \mathcal{P}'(0)\, \mathrm{e}^{-\int_0^s \alpha_e(\lambda_0, s')\, \mathrm{d}s'} \,, \tag{13.10}$$

where α_e represents the *specific extinction* in the inhomogeneous lossy material. With reference to the plane-parallel layer of earth-surface material with random dielectric inhomogeneities depicted in Fig. 13.7, the power density $\mathcal{P}(0)$ of the field scattered in the direction θ'' reaching the top ($z' = 0$) of the slab is obtained from the radiative transfer relation (13.7) by inserting the power density $\mathcal{P}'$ given by (13.10) of the primary field into the scattering source function (13.9):

$$\mathcal{P}(0) = \mathcal{P}'(0) \int_0^{d_z} \langle\sigma\rangle\, \mathrm{e}^{-\alpha_e\,(\sec\theta' + \sec\theta'')\, z}\, \mathrm{d}z \;+\; \mathcal{P}''(d_z)\, \mathrm{e}^{-\int_0^{d_z} \alpha_e\, \sec\theta''\, z\, \mathrm{d}z} \,, \tag{13.11}$$

where $\mathcal{P}''(d_z)$ is the power density originated in direction θ'' from the bottom $z = d_z$ of the layer, $\langle\sigma\rangle$ is the volumic bistatic (or *bi-directional*) scattering cross-section (7.16) for the pair of angles θ' and θ'', which are, respectively, the angles that the directions of propagation of the primary field and of the scattered one form with the local perpendicular to the slab boundaries. For monostatic radar observation, $\theta'' = \theta'$ and $\langle\sigma\rangle \equiv \langle\sigma_b\rangle$. The correspondence of (13.11) and (9.40) is readily recognized.

The upward power density $\mathcal{P}''(d_z)$ at the bottom of the inhomogeneous layer takes into account the effect of the different material over which the layer possibly lies, for instance:

- in observing a vegetation canopy, $\mathcal{P}''$ represents the power scattered from the terrain in the direction $\theta = \theta''$,
- when observing high seas, $\mathcal{P}''$ is the power scattered by the rough surface of the ocean water entering an overlying foam layer,
- or, when sensing the atmosphere from space, $\mathcal{P}''$ takes account of the contribution by the earth surface, consistently with the general approach of Sect. 9.3.

The power emerging from the layer where volume scattering occurs is thus composed of the power originating from the scattering elements in the layer itself and of the one contributed by the environment below[16] it. The two contributions superimpose with relative weights determined by the scattering and extinction features of the inhomogeneities distributed in the random layer, as well as by the average transmission properties of this latter [2].

In case the material is *statistically homogeneous* [17, Chap. 1], α_e becomes the *extinction constant*, independent of s. Then the power density of the primary field simply decays exponentially as it progresses in the volume with random dielectric fluctuations, according to

$$\mathcal{P}'(\lambda_0, s) = \mathcal{P}'(\lambda_0, 0)\, \mathrm{e}^{-\alpha_e(\lambda_0)\, s} \ .$$

The scattered power (13.11) at $z = 0$ correspondingly simplifies in

$$\mathcal{P}(0) = \frac{\langle\sigma\rangle}{\langle\sigma_e\rangle}\, \mathcal{P}'(0)\, \frac{1 - \mathrm{e}^{-\alpha_e\, (\sec\theta' + \sec\theta'')\, d}}{\sec\theta' + \sec\theta''} + \mathcal{P}''(d_z)\, \mathrm{e}^{-\alpha_e\, d\, \sec\theta''} \ ,$$

where $\langle\sigma_e\rangle$ is the volumic average extinction cross-section (7.20). In the frequently encountered case of statistically isotropic scattering, the emerging power[17] is expressed in terms of the albedo (7.21) and of the electromagnetic thickness (9.38) by

[16] In ground-based observations, the contribution comes from the environment *above* the observed layer.

[17] The upward scattered wave is assumed to emerge almost entirely: this implies that the inner field has negligible stationary component and that total reflection (Sect. 6.4) does not occur.

$$\mathcal{P}(0) = \mathcal{A}\,\mathcal{P}'(0)\,\frac{1 - \mathrm{e}^{-(\tau_\mathrm{o}' + \tau_\mathrm{o}'')}}{\sec\theta' + \sec\theta''} + \mathcal{P}''(d_\mathrm{z})\,\mathrm{e}^{-\tau_\mathrm{o}''}\,. \tag{13.12}$$

For bistatic observation, ordinarily carried out in the optical spectral range, the electromagnetic thickness for the primary wave differs from that of the scattered wave, since τ_o depends on θ:

$$\tau_\mathrm{o}' = \alpha_\mathrm{e}\,d\,\sec\theta'; \qquad \tau_\mathrm{o}'' = \alpha_\mathrm{e}\,d\,\sec\theta''\,.$$

In case of monostatic or quasi-monostatic radar observation, $\theta'' \approx \theta' \equiv \theta$, $\tau_\mathrm{o}'' \approx \tau_\mathrm{o}' \equiv \tau_\mathrm{o}$ and the power density at the top of the scattering volume is

$$\mathcal{P}(0) \simeq \mathcal{A}\,\mathcal{P}'(0)\,\frac{1 - \mathrm{e}^{-2\tau_\mathrm{o}}}{2\,\sec\theta} + \mathcal{P}''(d_\mathrm{z})\,\mathrm{e}^{-\tau_\mathrm{o}}\,.$$

For given $\mathcal{P}'$ and $\mathcal{P}''$, the spectral features of the radiation scattered by a volume of dielectric inhomogeneities are essentially determined by the extinction, which affects the electromagnetic thickness τ_o and, especially at optical wavelengths, the albedo $\mathcal{A}$ in (13.12). The extinction constant depends on the physical and, to a lesser extent, on the geometric characteristics of the materials forming the inhomogeneous volume. Section 5.3.2 shows that the absorption constant is directly related to the imaginary part of the permittivity of the material, while Sect. 9.1 relates the extinction caused by scattering to the geometry of the dielectric inhomogeneities. Therefore, due both to scattering effects and, especially, to wavelength-selective absorption, the extinction constant, hence, in turn, albedo and optical thickness, can vary dramatically with the wavelength. The corresponding variations with λ of the observed power (13.12) form the already mentioned spectral signature of the material. From an extended point of view, the effect may also explain the substantially different behavior between the power originated by volume scattering at microwaves and the one at optical wavelengths.

It is worth pointing out that the dependence both of α_e and of $\langle\sigma\rangle$ on the wave polarization has to be taken into account when the scatterers are not symmetrical, neither isotropically arranged.

Analogous concepts hold for passive observation at microwaves and in the TIR: to a first-order approximation, the power emerging from the layer is assumed to originate uniquely by thermal emission from both this latter and the bottom material. Equation (13.11) is easily converted into the analogous of (9.53) by recognizing that $\mathcal{P}''(d_z)$ is spontaneously emitted by the bottom bulk material and by replacing the scattering term (13.8) with the thermal source, clearly still including scattering into the extinction coefficient. The balance between emission and extinction affects the global emitting features of the layer-over-bulk structure (cf. Sect. 14.1.4.2).

13.1.3 General Features of Volume Scattering

The angle and the frequency at which a layer of inhomogeneous material overlying a different one is observed affect the type of information carried by the measurements.

First of all, the angle at which the scattered power is measured changes the relative balance between the contribution $\mathcal{P}''(d_z)$ from the bottom of the layer and that from this latter. Increasing θ'' increases the length of the path in the material and consequently raises the electromagnetic thickness τ_o'', thus quenching the amount of power originated from the bottom that reaches the top: when $\tau_o'' \gg 1$, the emerging power is approximated by

$$\mathcal{P}(0) \simeq \frac{\mathcal{A}\,\mathcal{P}'(0)}{\sec\theta' + \sec\theta''} \,. \tag{13.13}$$

The expression (13.13) indicates that the emerging power tends to carry information mainly on the albedo of the material forming the inhomogeneous layer. Instead, at low angles such that the electromagnetic thickness tends to vanish,[18]

$$\mathcal{P}(0) \simeq \mathcal{P}''(d_z) \,.$$

The emerging power now provides information essentially on structure and nature of the material underlying ($z' > d_z$) the layer.

The role of frequency is variegated, since it affects both electromagnetic thickness and albedo through diverse physical mechanisms. At wavelengths falling in absorbed bands of the material, the electromagnetic thickness is high, hence the underlaying structure is not visible and the measured power originates almost uniquely from the layer. At these wavelengths the volume scattering source is correspondingly low, since both the albedo and the primary wave power density decrease with increasing absorption.

Frequency has the further effect previously hinted at. The results obtained in Sect. 9.1 indicate that scattering increases considerably with increasing dimensions of the inhomogeneities with respect to the wavelength, thus enhancing the albedo. Coarsely speaking, volume scattering is expected to be relatively low at microwaves, at which frequencies the dielectric inhomogeneities of several materials have spatial scales short compared to wavelength, and to be relatively large in the optical range. Moreover, since the permittivity of moist materials has a trend generally decreasing with frequency, reflection tends to be relatively high at microwaves, thus lowering the volume source function. This trend is further strengthened by the behavior of many air-material transition surfaces, which, as observed in Sect. 13.1.1.1, behave like smooth at microwaves and quite rough in the optical range.

In practice, many natural and man-made (e.g., asphalt, concrete, plaster, painted wood), materials are inhomogeneous at a micrometer scale, hence, essentially over

[18] For sufficiently low extinction.

all the optical range, while only inhomogeneities at centimeter or decimeter spatial scale are effective at microwave frequencies. Optical observations are then expected to contain the imprinting almost exclusively of the volume scattering, whereas only some kinds of earth cover, typically the vegetation canopies, contribute to radar measurements through prevailing volume scatter. However, it should be born in mind that, given the diverse extinction, the microwave and optical penetration depths differ by orders of magnitude: optical observations are generally able to gain information on very shallow layers, of the order of micrometers, while radar measurements typically observe backscattering down to a few centimeters in moderately moist and mildly compact materials and to several tens of centimeters, or more, in loose dry matter (cf. Sect. 6.3.1.1).

13.1.4 Surface and Volume Scattering in Image Features

Many features of images acquired in different ranges of the electromagnetic spectrum can be interpreted by resorting to the behavior of surface and volume scattering, clearly bearing in mind their interdependence.

In a few words, radar images of essentially "bare" targets, i.e., excluding composite environments such as vegetation, snow covers or sea foam, tend to display the local backscattering features of the geometric surface, while optical images carry the imprinting by the volume scattering originating from a more or less shallow (depth of the order of wavelength, at most) layer of sub-surface bulk material.

A surface the height standard deviation σ_z of which is above the Rayleigh limit σ_{zR}, behaves as rough: the coherent reflection is relatively low, while the power scattered into the various directions is enhanced by the considerable amplitudes of the spectral components (7.52) of the random height. The rough area is then visualized by a cluster of relatively bright[19] pixels in a backscattering power image. Vice-versa, when $\sigma_z < \sigma_{zR}$, reflection is high and backscattering low, given the trend of the roughness spectrum, which peaks at $\kappa_t \approx 0$ and rapidly decays with increasing modulus of the lateral scattering vector. Since reflection occurs in the specular direction, a smooth area returns little or no echo[20] to an observing monostatic, or quasi-monostatic (cf. Sect. 12.3.2.1) radar,[21] and is thus characterized by a region of dark pixels in the power image.

[19] Strong fluctuations of scattering intensity about high values are observed because of speckle (Sect. 7.2).

[20] The relatively smooth surface of oil-covered water in the slick area considered in Sect. 14.2.2.3 is a typical target yielding reduced *backscattered* power.

[21] Except that when the mean surface is perpendicular to the direction of observation, or when its shape corresponds to the dihedral or trihedral configurations considered in Sect. 6.6.

On its side, the main mechanism on which the passive optical observations are based is the sub-surface[22] diffuse (bistatic) scattering of solar radiation outlined in Sect. 9.3.1. Because of the absorption bands, this feature results in "coloring" the observed target. Sufficiently smooth natural surfaces can affect the measurements through specular reflection originating the nearly "white" *sun glint*[23] only for particular mutual positions of the sensor platform and of the Sun with respect to the observed marine or lacustrine calm water area. Apart from such peculiar geometries, the observed radiation is relatively independent of the macroscopic roughness of the surface and, if anything, is affected by the orientation of the mean surface with respect to Sun[24] and to the sensor.

13.1.5 Scattering Mechanisms and Interferometric Coherence

The interferometric coherence has been analyzed in Sect. 12.3.4 from the point of view of the impact it may have on the production of altitude maps or on monitoring height variations. In fact, the phase stability of the scattered field carries information on the kind of terrestrial environment and on its features, so that the measured coherence is in itself useful in Earth observation. An example is shown in Fig. 12.31. The two previously considered scattering mechanisms, of surface and of volume origin, are characterized by essentially different magnitudes of interferometric coherence. This latter depends on the dielectric structure of the observed target as well as on its time stability, at least for repeat-pass interferometry.

13.1.5.1 Coherence in Surface Scattering

When surface scattering prevails, the scattering function is clearly determined by the dielectric features only of the surface of the material. In case the surface has no or little macroscopic variations with time, as is typically the case of exposed rocks and man-made structures, the factor $|\gamma_\epsilon|$ in (12.54) is high. Analogous is the behavior of a homogeneous terrain when the acquisitions are carried out simultaneously or at a sufficiently short time interval. It can be added that the two-dimensional scattering source of the surface has a relatively simple structure and is expected to be characterized by a scattering function moderately sensitive to the incidence angle and weakly dependent on the interferometric baseline, so that also $|\gamma_B|$ is high. Therefore, the modulus of the degree of coherence $|\gamma|$ is expected to show relatively large values in cases in which surface scattering is dominant.

[22] Clearly, down to the penetration depth (say, a few micrometers) of the optical radiation.

[23] Application details are given in Sect. 14.2.1.1.

[24] Especially at grazing angles.

It is worth observing that increasing wavelength selects larger spectral components (7.53) of the dielectric fluctuations. Since the larger structures change less with time, the repeat-pass coherence is expected to be generally higher at the lower microwave frequencies.[25]

13.1.5.2 Coherence in Volume Scattering

Fluctuating and stable parts of the scattering function are affected not only by the dielectric structure of the surface but also, and sometimes in a prevailing way, by the permittivity in the bulk volume of the resolution cell. The scattering function of a random-like three-dimensional dielectric structure, such as that of a natural environment, is clearly more complex than that of a two-dimensional one, thus it is expected to be quite sensitive to the incidence angle, hence to the baseline. The relatively low value of $|\gamma_B|$ contributes to keep low the interferometric coherence. Moreover, appreciable changes of the spatial structure of terrestrial environments characterized by significant volume scattering occur frequently. For instance, the plant canopies undergo ceaseless seasonal variations (cf. Fig. 14.26), but also the terrain is subject to changes mainly of its vertical permittivity structure, caused by rain or, oppositely, by evaporation. The fluctuating part of the scattering function in (12.51) can then be a considerable fraction of the average one, with corresponding reduction of $|\gamma_\epsilon|$.

As a result, the magnitude of the degree of coherence $|\gamma|$ is expected to be moderate or low when volume scattering prevails.

Further Steps Toward Interpreting Images

By now we understand the primary information that the basic products delivered by the remote sensing systems are expected to contain. We also suspect that the models worked out to represent the sensing process may not be able to approach the reality, given the physical complexity of many targets and the analytical intricacy of the electromagnetic interaction. To progress further, the scattering mechanism, which we know is at the basis of many types of observation, is rationalized in the two broad classes of surface and volume interactions. We get hints that information originates essentially from a volume mechanism at optical wavelengths, while microwave systems probe the targets through both surface and volume interactions.

We can grasp a qualitative understanding of the reflecting and scattering behavior of rough surfaces by using the concept of facet and by adopting the geometrical optics model. Establishing the link between the geometric structure of the surface and the predicted reflection and backscattering coefficients is approached quantita-

[25] This concept should be kept distinct from that of permanent scatterer outlined in Sect. 12.3.3.3.

tively by introducing roughness parameters such as correlation distance and height and slope standard deviations. We realize that tractable formulas have limited ranges of validity, so that we must chose our computational scheme watchfully according to the wavelength of operation. Periodic surfaces demand a separate approach, considering the coherent superposition of elementary contributions from equidistant facets.

Volumetric scattering is a complicate process, especially if we realize that the sparse or dense layer of random elements frequently lays over the rough surface of another material. We must resort to the radiative transfer formalism, subject to prior identification of the volume scattering source function, as well as of the contribution from the material underlaying the layer. The analysis shows us that long microwave wavelengths and low observation angles allow observing the bottom material, whereas data acquired at higher frequencies and angles carry the imprinting by the covering layer.

The relative amount of signal contributed by the surface or by the bulk affects the interferometric coherence characterizing the target. Coherence is relatively high when surface scattering prevails, while low values are typically expected for targets that scatter mainly through a volumetric mechanism.

References

1. Alvarez-Perez JL (2009) The Extended Integral Equation Model IEM2M for topographically modulated rough surfaces. In: Ho P-GP (ed) Geoscience and remote sensing. InTech, pp 497–529. ISBN:9789533070032. doi:10.5772/ 8297
2. Attema EPW, Ulaby FT (1978) Vegetation modeled as a water cloud. Radio Sci 13(2):357–364. doi:10.1029/RS013i002p00357
3. Beckman P, Spizzichino A (1987) The scattering of electromagnetic waves from rough surfaces. Artech House. ISBN:9780890062388
4. Canuti P, d'Auria G, Pampaloni P, Solimini D (1992) MAC 91 on Montespertoli: an experiment for agro-hydrology. In: International geoscience and remote sensing symposium (IGARSS '92), vol 2, pp 1744–1746. doi:10.1109/IGARSS.1992.578869
5. Chen MF, Fung AK (1988) A numerical study of the regions of validity of the Kirchhoff and small-perturbation rough surface scattering models. Radio Sci 23(2):163–170. doi:10.1029/RS023i002p00163
6. Cherniakov M (ed) (2008) Bistatic radars: emerging technology. Wiley. ISBN:9780470985748
7. Davidson M, Le Toan T, Mattia F, Satalino G, Manninen T, Borgeaud M (2000) On the characterization of agricultural soil roughness for radar remote sensing studies. IEEE Trans Geosci Remote Sens 38(2):630–640. doi:10.1109/36.841993
8. De Roo RD, Ulaby FT (1994) Bistatic specular scattering from rough dielectric surfaces. IEEE Trans Antennas Propag 42(2):220–231. doi:10.1109/8.277216
9. Eftimiu C (1986) Scattering by rough surfaces: a simple model. IEEE Trans Antennas Propag 34(5):626–630. doi:10.1109/TAP.1986.1143873.
10. Fung AK, Pan GW (1987) A scattering model for perfectly conducting random surfaces I. Model development. Int J Remote Sens 8(11):1579–1593. doi:10.1080/01431168708954800
11. Ishimaru A (1978) Wave propagation and scattering in random media. Academic. ISBN:9780123747020
12. Krieger G, Moreira A (2006) Spaceborne bi- and multistatic SAR: potential and challenges. IEE Proc Radar Sonar Navig 153(3). doi:10.1049/iprsn:20045111

13. Lang RH (1981) Electromagnetic backscattering from a sparse distribution of lossy dielectric scatterers. Radio Sci 16(1):15–30. doi:10.1029/RS016i001p00015
14. Ogilvy JA (1991) Theory of wave scattering from random rough surfaces. Taylor & Francis. ISBN:9780750300636
15. Prakash R, Singh D, Singh KP (2013) Analysis and retrieval of soil parameters with specular scattering data at different incidence angle. In: 2013 IEEE international geoscience and remote sensing symposium (IGARSS), Video TU4.T03.2. pp 755–758. doi:10.1109/IGARSS20136721267. http://www.igarss2013.org/ShowRecording.asp?C=E34B7C42 (visited on 19 Mar 2014)
16. Prati C, Rocca F, Giancola D, Monti Guarnieri A (1998) Passive geosynchronous SAR system reusing backscattered digital audio broadcasting signals. IEEE Trans Geosci Remote Sens 36(6):1973–1976. doi:10.1109/36.729370
17. Rytov SM, Kravtsov YuA, Tatarskii VI (1989) Principles of statistical radiophysics 3: elements of random fields. Springer. ISBN:9783540178293
18. Schooley AH (1962) Upwind-downwind ratio of radar return calculated from facet size statistics of a wind-disturbed water surface. Proc IRE 50(4):456–461. doi:10.1109/JRPROC.1962.288043
19. Shepard MK, Campbell BA, Bulmer MH, Farr TG, Gaddis LR, Plaut JJ (2001) The roughness of natural terrain: a planetary and remote sensing perspective. J Geophys Res Planets 106(E12):32777–32795. doi:10.1029/2000JE001429
20. Träger F (ed) (2012) Springer handbook of lasers and optics. Springer. ISBN:9783642194092
21. Ulaby FT, Dobson C (1989) Handbook of radar scattering: statistics for terrain. Artech House. ISBN:9780890063361
22. Ulaby FT, Moore RK, Fung AK (1982) Microwave remote sensing: active and passive. Radar remote sensing and surface scattering and emission theory, vol. 2. Addison-Wesley. ISBN:9780890061916
23. Verhoest N, Lievens H, Wagner W, Alvarez-Mozos J, Moran MS, Mattia F (2008) On the soil roughness parameterization problem in soil moisture retrieval of bare surfaces from synthetic aperture radar. Sensors 8(7):4213–4248. doi:10.3390/s8074213
24. Willis NJ (2005) Bistatic radar. SciTech. ISBN:9781891121456
25. Willis NJ, Griffiths H (eds) (2007) Advances in bistatic radar. SciTech. ISBN:9781891121487
26. Woodhouse IH (2005) Introduction to microwave remote sensing. CRC. ISBN: 9780203646526
27. Yueh SH, Kong JA, Jao JK, Shin RT, Le Toan T (1992) Branching model for vegetation. IEEE Trans Geosci Remote Sens 30(2):390–402. doi:10.1109/36.134088
28. Zheng B, Campbell JB, Serbin G, Galbraith JM (2014) Remote sensing of crop residue and tillage practices: present capabilities and future prospects. Soil Tillage Res 138:26–34. doi:10.1016/j.still.2013.12.009

Chapter 14
Wave Interaction with Land, Water and Air

Much of the matter presented in the previous parts of this book aims at providing a unified rationale within which the interaction of the electromagnetic waves with natural and man-made materials and structures can be framed for the frequency/wavelength bands at which common Earth observing systems operate. The frame facilitates the understanding of the mechanisms through which the observed terrestrial environment confers the bio-geo-physical information to the probing wave and how this latter carries it to the sensor across the interfering atmosphere. The interpretation of the images and of the data the more common Earth observing systems acquire can be guided by the theoretical and empirical models that were outlined and by the examples occasionally presented to anchor the abstract theory to the complicated real world. This concluding chapter intends to provide a systematic overview of the kind of information that the various remote observation techniques are expected to gain on the three basic terrestrial environments, solid land, water bodies and atmosphere. Several examples are reported, based both on numerical simulations and on actual observations. The presented results are discussed on the basis of the relevant electromagnetic models and interaction mechanisms, with the intent of mitigating the feeling of fortuity or of inexplicable occurrence that a possible inextricable and apparently inconsistent behavior of the observations may sometimes raise in absence of a comprehensive rationale.

For each class of Earth's environment, the theoretical or experimental results are gathered according to the observation technique they refer to: the target imprinting onto the scattered solar radiation is discussed first, followed by the radar response[1] and then by the features of spontaneous emission in the thermal infrared and at microwaves. Each method of observation includes examples relative to the more relevant kinds of terrestrial targets, for instance, relative to bare soil, urban areas, vegetation and snow, just to mention the solid-land environment class.

[1] Selected applications of lidar systems are mentioned when appropriate.

D. Solimini, *Understanding Earth Observation*, Remote Sensing and Digital Image Processing 23, DOI 10.1007/978-3-319-25633-7_14

14.1 Interaction with Land

The solid land presents a wide variety of scenarios, the observation of which is carried out by almost all the available observation techniques and exploiting the whole applicable electromagnetic spectrum. Understanding the relevant features of the land images often requires a balanced consideration of the prevailing interaction mechanisms, which may depend critically on the sensor parameters and on the acquisition geometry. The reader is cautioned that the variability with time and geographic location of the land environment is a further source of hurdle in interpreting and exploiting the remote observations.

14.1.1 Passive Observation of Land in the Optical Spectral Range

Sections 2.2.3 and 2.2.4 point out that at optical[2] wavelengths the permittivity both of moist and of dry organic and mineral matter has generally moderate and close values because the dielectric polarization loses the librational contribution by the permanent dipoles. Moreover, with the exception of polished materials and calm water, the typical surface height standard deviation is large with respect to wavelength. These dielectric and geometric features make reflection and direct scattering of sunlight from the surfaces of many kinds of materials relatively low. As a consequence, a large fraction of the incident radiation penetrates into the matter below the geometric boundary.

Common natural and man-made materials are aggregates of substances having different local properties and density, resulting in dielectric inhomogeneities. For instance, soil [359, Chap. 1] contains tiny fragments of rocks and residuals of vegetal matter, air cavities, unequal moisture distribution; asphalted road pavements are mixtures of aggregate mineral particles, with sand, fly ash, bitumen, air and water [226, 382]; leaves [7, 135] basically consist of upper and lower epidermises, parenchyma layers rich of chlorophyll, loosely arranged spongy mesophyll and vascular bundles. Given the short wavelengths, multiple scattering (cf. Sect. 9.1) by the subsurface inhomogeneities in the three-dimensional matter is substantial, so that part of the downwelling solar power is redirected back into the atmosphere. The path traveled inside the material attenuates the wave according to the specific extinction, essentially caused by absorption, which is a function of wavelength[3] characteristic of the subsurface materials. The consequence is the modification of the spectrum of the solar radiation that arrives at ground level (Sect. 10.2.1.1),

[2] Remind that the "optical" wavelength range includes ultraviolet, visible and near infrared.

[3] Scattering, which also contributes to extinction, is generally much less wavelength-selective than absorption.

penetrates below the boundaries of the bodies (soil, asphalt, leaves, etc.) present in the observed area, and is finally scattered. The radiation that is sent upward into the atmosphere by the subsurface volume-scattering process contains the imprinting by the resonances of the matter composing the skin layer of the target: the returned radiation has been *colored* (Sect. 10.3.2) by the material.

In essence, the upward solar radiation is composed of a generally low[4] direct contribution by scattering (including reflection) from the surface and of a substantial contribution from the skin sub-surface matter through the *volume scattering* mechanism discussed in Sect. 13.1.2.1. The spectrum of the upward polychromatic radiation that reaches the sensor, apart from possible atmospheric interference, is basically affected (colored) by the material present in the region of interest at which the sensor aims (Fig. 11.21). The power captured by the receiving aperture is sampled in wavelength by the channels of the spectrometric system and transformed into values of the spectral reflectance $\mathcal{R}_\lambda$ defined in Sect. 10.2.1.1, which are assigned to the "central" wavelength λ_{0i} of the i-th channel of the instrument. The pattern $\mathcal{R}(\lambda_{0i})$ forms the spectral signature of the observed material, carried by the scattered[5] solar radiation. In the receiving process, the values $\mathcal{R}(\lambda_{0i})$ are transformed into digital signals, which, in practice, provide information on nature and state of the observed target and form the basis for substance identification, land cover inventory, vegetation monitoring, just to cite a few common applications of optical passive observation.

14.1.1.1 Optical Observation of Bare Surfaces

Bare surfaces, which include terrain and rocks, are always more or less discernible on the solid earth surface, with the exception of areas seasonally or permanently covered by snow. The soil features also affect the spectral reflectance of vegetated areas, especially where vegetation is sparse or senescent. The terrain is the upper part of the layer of unconsolidated material overlaying a rock bed, is exposed to atmosphere and solar radiation and undergoes physical, chemical and biological alterations. The terrain contains inorganic solid particles (most common are sand, silt and clay) deriving from rock erosion, organic matter (remaining of plants and living organisms), air, and water, which fill the cavities with time-variable relative concentrations. Therefore, the downwelling solar radiation interacts with an inhomogeneous, sometimes granular, material, with highly rough boundary (Fig. 7.11). The global interaction features depend on the properties of the geometric surface of the soil [27] and, mainly, of the underlying shallow (skin) layer. The scattering from the surface is affected by its porosity and micro-roughness caused by emerging fragments, agglomerates, and cleavages, as well as by the overall fraction of exposed structure, while the volume scattering depends on the chemical nature

[4] No sun glint is assumed.

[5] As said, sometimes called "reflected".

and concentration of the subsurface composing substances and on the crystalline structure and dimension distribution of the inorganic particles, that is, on the terrain *micro-texture*. It has to be considered that roughness, composition and overall structure are substantially affected by the climatic conditions, which strongly modify the water and air content of the soil, with further modifications caused by erosion and by growth and senescence of plants.

The results of Sect. 13.1.2.1 show that the spectrum of the scattered solar radiation differs from the incident one because the albedo of the traversed thin subsurface layer depends on wavelength, essentially due to selective absorption. The absorption mechanisms introduced in Sect. 2.1 primarily involve vibrational and electronic transitions, since, in the optical range, molecular translations and rotations are quenched in most soil materials. The *transitions between vibrational states* mainly affect the infrared: in particular, liquid water has three strong absorption bands in the range 2.5–7 μm, associated with fundamental vibrational modes of the polar molecules, together with two weaker bands around 1.45 and 1.95 μm. On their side, the *electronic transitions* determine the absorption bands in the visible and ultraviolet.

The commonly encountered mineral substances, formed prevailingly by silicon, aluminum and oxygen atoms, do not present energy levels that allow transitions involving visible or near-infrared photons, rather, their presence affects the reflectance spectra through electron transitions in the impurity centers, or through vibrational transitions of the hydroxyl. Moreover, it should be considered that many types of terrain contain iron ions which strongly absorb the shorter visible wavelengths. On its side, even a moderate quantity of organic matter has a strong influence on reflectance, given its water retentivity. Indeed, in presence of precipitation or of irrigation, water takes the place of the air in the terrain, whereas the opposite happens during drying out. Fairly common patterns of the spectral reflectance of bare soil [346] show minima in correspondence of the wide water absorption bands centered on 1.4 and 1.9 μm. Lower reflectance of the soil with higher organic matter content is also observed, as Fig. 14.1 shows. Indeed, the water film that usually adheres to the solid particles of both organic and mineral origin, traps the radiation through a total reflection mechanism (Sect. 6.4) and dissipates it, thus lowering the scattered power over the whole band [32]. In general, for a given kind of soil, the higher the moisture content, the lower is the spectral reflectance, as clearly displayed by Fig. 14.2.

The soil is widespread and in many cases it overlays consolidated rock structures, which, therefore, are not optically visible. However, the granular material which is present in the terrain partly derives from erosion and alteration of rocks. Given the soil formation process, its reflectance may contain various spectral components of the underlying minerals, mixed with other spectral features, mainly those of vegetal matter and of water. The spectra of pure rocky materials are usually less complex than those of the soil, since they depend essentially on the interaction of radiation with the relatively simple mineral lattice. Each type of mineral generally shows a characteristic pattern of its spectral reflectance, which, at least in principle, allows identification of the material [319]. As an example, olivine has a minimum

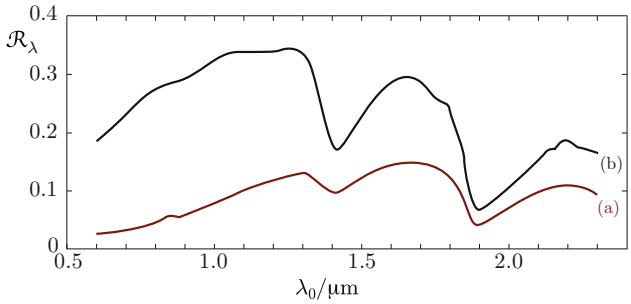

Fig. 14.1 Qualitative spectral reflectance of fine-texture terrain with high, (a), and low, (b), organic matter content vs. wavelength λ_0 in the visible and near infrared (Curves interpolate data from [169])

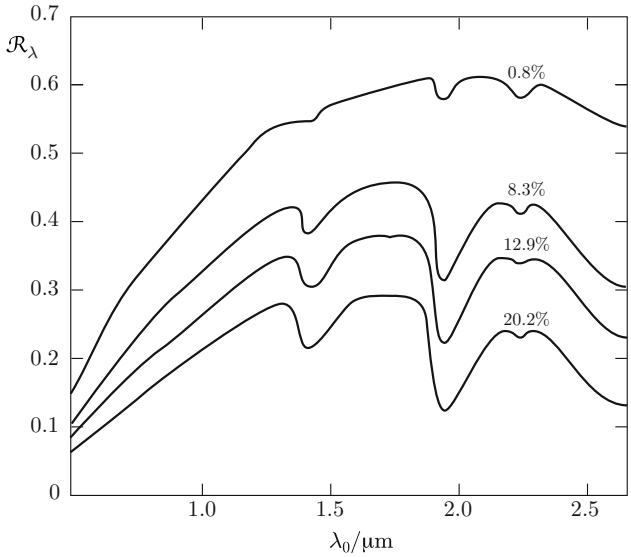

Fig. 14.2 Typical spectral reflectance of soil with diverse moisture contents (in percent) vs. wavelength λ_0 in the visible and near infrared (Curves interpolate data from [169])

of spectral reflectance near $\lambda_0 = 1\,\mu m$, caused by absorption by the Fe^{2+} ion, while carbonates show strong oscillations in the 1.4–2.5 μm range, associated with the absorption bands of the CO_3 ion. Other types of rocks show patters of spectral reflectance which obey analogous general rules, i.e., the observed spectral reflectance $\mathcal{R}_\lambda$ contains the imprinting of the absorption spectrum of the materials. The maxima of $\mathcal{R}_\lambda$ clearly correspond to maxima of the albedo $\mathcal{A}$ and minima to absorbed wavelengths. Figure 14.3 shows a few examples of the spectral reflectance of rock-forming minerals.

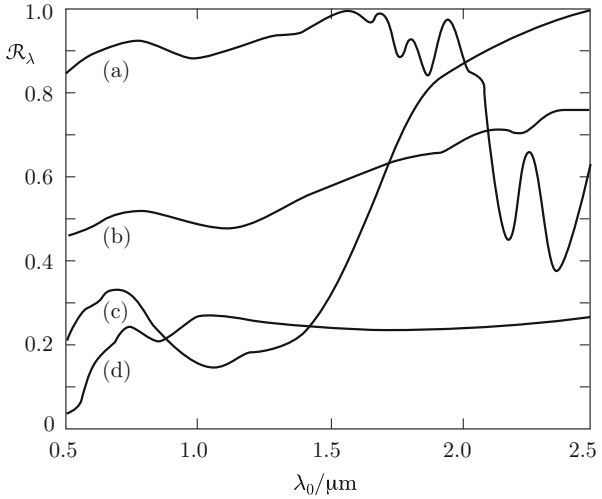

Fig. 14.3 Typical non-specular spectral reflectance of minerals vs. wavelength λ_0 in the visible and near infrared: (a), Dolomite; (b), Obsidian; (c), Fayalite; (d), Hematite (Curves interpolate data from [2])

It is worth adding that a considerable fraction of irrigated land is affected by the presence of salts at the surface of the terrain, with corresponding degradation of agricultural productivity [239]. Salinity modifies the spectral reflectance of the soil surface according to its mineralogy and moisture content, thus allowing mapping of affected areas and salt identification.

14.1.1.2 Optical Observation of Vegetation

The vegetation elements are typically arranged in canopies. In temperate and polar climatic regions, the leaves of deciduous plant canopies form its largest fraction of light-intercepting surface especially in summer, whereas the perennial wood elements are exposed in winter. Being generally sparse [15], a canopy has negligible specular reflection and scattering from its average upper boundary, while the three-dimensional structure originates volume scattering, with multiple bouncing [160, 175], as sketched in Fig. 14.4.

Leaves are composed of cellulose, lignin, proteins, carbohydrates, and, mainly, water, which represents between 40 % and 80 % of the weight of green matter. The amount of cellulose, which is a polysaccharide deriving from glucose chains, varies between 10 % and 35 %, while pectin contributes to form the cell walls. Clearly, green leaves also contain chlorophyll. The surface of an individual leaf is *optically rough*, hence a considerable fraction of the incident light penetrates below

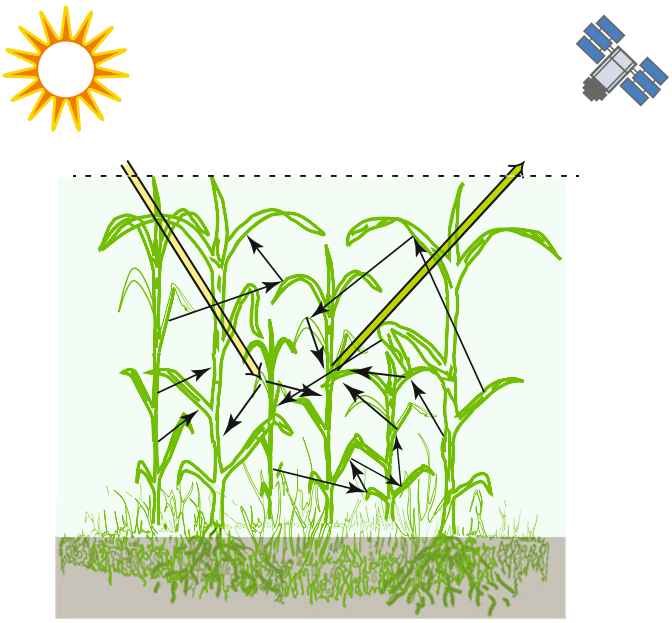

Fig. 14.4 Multiple scattering in a vegetation canopy. The *dashed line* denotes the upper boundary of the average air-canopy transition layer; the *light green* background hints at the mean permittivity in the vegetation layer (cf. Sect. 7.2), the *brown* one represents soil

the epidermis.[6] The substances present in the vegetal matter cause wavelength-selective absorption, essentially related to vibrational transitions in the water and in the pigments, mainly the chlorophyll [88] of the palisade mesophyll. The internal structure of a leaf, and in particular the spongy mesophyll, is inhomogeneous at spatial scales comparable to wavelength, so that considerable multiple scattering occurs [116]. The spectrum of the radiation that emerges from the leaf after multiple inner refraction and volume scattering has a spectrum which differs from that of the incident one according to the absorption and the albedo, the wavelength dependence of which are peculiar of the plant and of its state [40, Chap. 17].

Three characteristic spectral regions [381] can be identified in the typical reflectance of a "green" leaf sketched in Fig. 14.5:

– $\mathcal{R}_\lambda$ is relatively low at visible wavelengths, given the wide-band photosynthetic absorption by chlorophyll, which peaks at $\lambda_0 \approx 0.4\,\mu\text{m}$ (blue) and $\lambda_0 \approx 0.7\,\mu\text{m}$ (red): the moderate maximum of reflectance in the green gives visual indication on the chlorophyll content;
– starting from the *red edge* and increasing λ_0, absorption by chlorophyll declines, more incident radiation can reach the inner inhomogeneous cellular structure, a

[6] Reflection by the waxy cuticle can possibly lower the fraction of penetrating radiation.

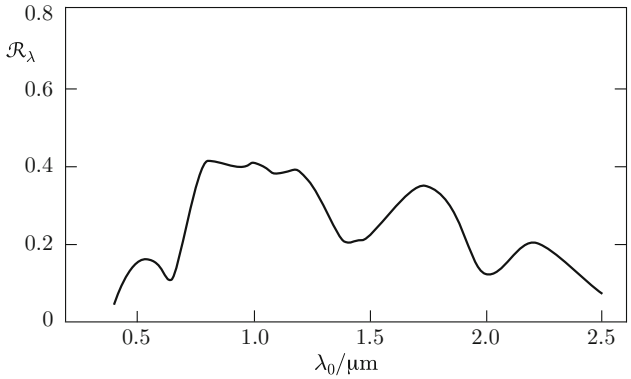

Fig. 14.5 Typical trend of spectral reflectance of *green* vegetation vs. wavelength λ_0 in the visible and near infrared (The curve interpolate data from [172, 284])

larger fraction of the scattering by this latter[7] emerges from the vegetal matter and consequently the reflectance raises significantly, up to the plateau value in the 0.8–1.2 μm wavelength range: the relative NIR reflectance is an effective indicator of vegetal matter, as specified by (14.1);
– at longer wavelengths, water absorption prevails and the reflectance drops: its pattern yields information on possible plant water stress.

The vegetation elements usually do not cover entirely the observed area, so that part of the solar radiation is able to reach the underlying terrain, the scattering of which superimposes to that of the plants, yielding a soil-vegetation composite reflectance. Therefore, $\mathcal{R}_\lambda$ of a vegetated area generally depends on the relative fractions [121] of vegetation and of exposed soil: growing crops show the characteristic temporal trend of their spectral reflectance, displaying the transition from $\mathcal{R}_\lambda$ of bare soil to that of *closed* vegetation displayed in Fig.14.6. The main effects of the growth of the plants are:

– a small relative maximum of $\mathcal{R}_\lambda$ appears in the green because of the plant chlorophyll absorption at the lower and higher ends of the visible wavelength range;
– in the $0.8\,\mu\text{m} < \lambda_0 < 1.2\,\mu\text{m}$ interval, $\mathcal{R}_\lambda$ considerably increases with increasing phytomass density, which enhances the overall spectral reflectance;
– at longer wavelengths, the minima in correspondence of the water absorption deepen, since the absorbing moisture in the plants is generally higher than that in the soil.

[7] Scattering from the dielectric inhomogeneities is also enhanced by the relatively high values of the permittivity of the vegetal matter in this wavelength range.

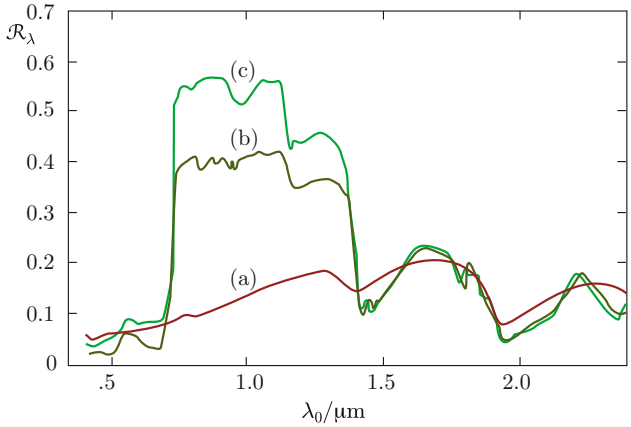

Fig. 14.6 Typical temporal variation of the spectral reflectance of a crop at different development stages vs. wavelength λ_0 in the visible and near infrared: (a), bare soil; (b), intermediate plant growth; (c) fully developed vegetation (Curves (b) and (c) interpolate vegetation data from [71])

The relative value that the spectral reflectance has in the relatively flat 0.8–1.2 μm plateau is an effective indicator of the global phytomass and is useful to monitor *crop growth*. The **n**ormalized **d**ifference **v**egetation **i**ndex (NDVI) [286, 367], based on this observation, is a widely used simple parameter.[8] It is defined by

$$NDVI := \frac{\mathcal{R}_{\lambda\text{nir}} - \mathcal{R}_{\lambda\text{vis}}}{\mathcal{R}_{\lambda\text{nir}} + \mathcal{R}_{\lambda\text{vis}}} \cdot \tag{14.1}$$

in which $\mathcal{R}_{\lambda\text{nir}}$ denotes the spectral reflectance in the near infrared, where the green vegetal matter scatters more, and $\mathcal{R}_{\lambda\text{vis}}$ is its value in the visible.

Given the sensitivity to microstructure and pigments [337], reflectance measurements in this spectral interval are also effective[9] in *plant discrimination* [117, 264, 411]. Indeed, the spectral reflectance of different kinds of vegetation differs scarcely in the visible, where the "green color" predominates for all plants, whereas it differentiates significantly beyond $\lambda_0 \approx 0.75\,\mu m$ (Fig. 14.7).

Data acquired by visible and near infrared[10] spectrometric channels also yield information on possible *plant diseases* [46, 325], which cause loss of water and a resulting increase of reflectivity, especially in correspondence of the absorbed wavelengths. The curves in Fig. 14.8 suggest that a severe stress, implying a

[8] Methods such as the **s**pectral **m**ixture **a**nalysis (SMA) [3] may yield results more accurate than NDVI [93] for particular conditions of vegetation and soil [342, 402].

[9] The sensitivity of reflectance to several environmental parameters combined with the similarity between spectra of different vegetation species [294] may hamper the discrimination capability of spectroscopic techniques.

[10] In particular, the range between $\lambda_0 \approx 500\,nm$ and $\lambda_0 \approx 850\,nm$ is generally exploited.

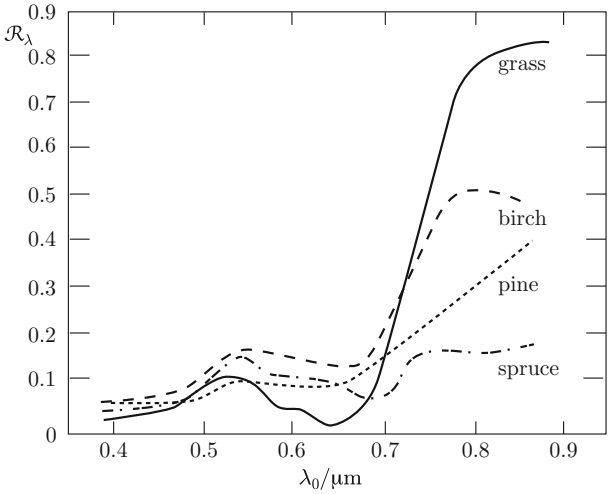

Fig. 14.7 The trend of the spectral reflectance with wavelength λ_0 differs at the red edge according to the type of plant (Curves interpolate data from [256, Chap. 3])

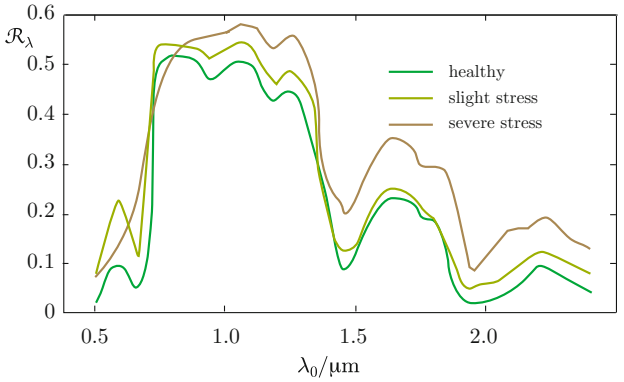

Fig. 14.8 Effect of vegetation health on the spectral reflectance pattern vs. wavelength λ_0 in the visible and near infrared (Curves interpolate data from [376])

substantial decrease of photosynthesis, also quenches the tiny reflectance peak in the green. It is worth adding that the red and far-red spectral features of the fluorescence induced by solar radiation are indicative of the photosynthesis state of plants and provide means of detecting vegetation stress [249].

Finally, note that some plants have the capability of uptaking and accumulating traces of chemical elements or inorganic compounds present in the terrain. As a consequence, the high-spectral resolution reflectance of the leaves can exhibit peculiar and indicative deviations from the typical shape, useful to identify the *elements in the soil* [42, 53, 155], also when this latter is concealed by an overlying closed canopy.

14.1.1.3 Optical Observation of Snow

Snow is an aggregate of ice particles and air, which at temperatures $T \approx 0\,^{\circ}\mathrm{C}$ may contain a significant fraction of liquid water. Its visible and near infrared reflecting properties are determined by the physical characteristics and morphology of the ice granules, by the liquid water inclusions, and by the eventual impurities, such as dust and combustion residues, which are possibly present. Following the properties outlined in Sect. 2.2.2.2, ice is rather transparent in the visible, with an absorption minimum around $\lambda_0 = 0.5\,\mu\mathrm{m}$, and becomes opaque in the infrared. The real part of its refractive index is relatively flat over the optical wavelength band. The dielectric properties of ice in the visible and near infrared are detailed in Fig. 14.9, with a suitable comparison with liquid water.

Given the granular structure of the snow cover, its interaction with the solar radiation is through a volume scattering mechanism. Therefore, the spectral reflectance of pure snow depends essentially on the distribution of dimensions of the granules, as the diagrams of Fig. 14.10 indicate. Liquid water has little effect in this wavelength range, since its refractive index is not far from that of ice. In the visible, where ice is fairly transparent, the spectral reflectance $\mathcal{R}_\lambda$ of snow does not vary appreciably with the characteristic dimension D of the granules, while the effect of absorption becomes important at wavelengths beyond $\lambda_0 \approx 0.75\,\mu\mathrm{m}$. It is worth noting that $\mathcal{R}_\lambda$ is fairly high up to $\lambda_0 \approx 1\,\mu\mathrm{m}$: this feature allows discrimination between

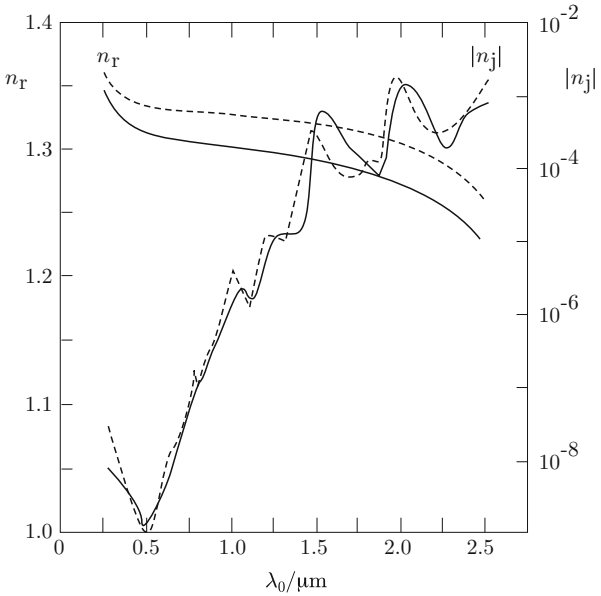

Fig. 14.9 Real (n_r) and imaginary (n_j) parts of ice refractive index vs. wavelength λ_0 (*continuous line*) compared with those of liquid water (*dashed*) in the visible and near infrared (Curves interpolate data from [86])

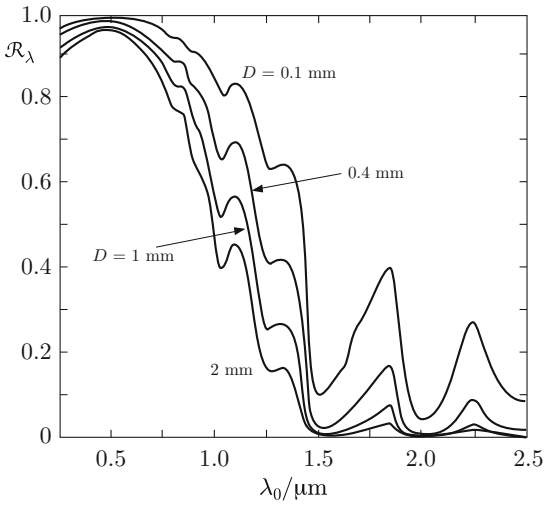

Fig. 14.10 Spectral reflectance $\mathcal{R}_\lambda$ of snow vs. wavelength λ_0 in the visible and near infrared for various characteristic dimensions D of ice particles (Curves interpolate data from [86])

snow and other earth surface materials, which have relatively low reflectance, so that snow cover maps are effectively derived from observations in the visible.[11] The reflectance in the near infrared becomes sensitive both to the snow age, since the dimensions of the granules are increased by the melting-refreezing process, and to the liquid water in the wet snow matrix. Moderate thickness of the snow layer makes it partially transparent and $\mathcal{R}_\lambda$ dependent on thickness, hence on its **s**now **w**ater **e**quivalent (SWE), which represents a quantity of considerable interest to users. Figure 14.12 shows the spectral reflectance of layers of snow having different water equivalents.

14.1.2 Radar Observation of Land

The microwave dielectric properties of natural and man-made materials differ substantially from those in the visible and infrared wavelength range, mainly because of the high values of the permittivity of liquid water, which is very often present in the temperate terrestrial environment. Moreover, given the wavelengths of the microwave radiation, which are larger than the optical ones by several orders of magnitude, a crucial factor is now the macrostructure of the target. Basically, the geometric properties of the air-material interface and the sub-surface dielectric features affect both amplitude and phase of the backscattered field, according to the respective spatial spectrum of inhomogeneities discussed in Sect. 7.4.7. The

[11] However, ice clouds, the spectral reflectivity of which is similar to that of snow, may hamper snow mapping, as shown in Fig. 14.11.

Fig. 14.11 Snow cover is readily discriminated against land and sea surface, but the analogous spectral reflectance of ice clouds is a possible major source of ambiguity (MERIS image of Italy credit: data, ESA; processing, courtesy C. Solimini)

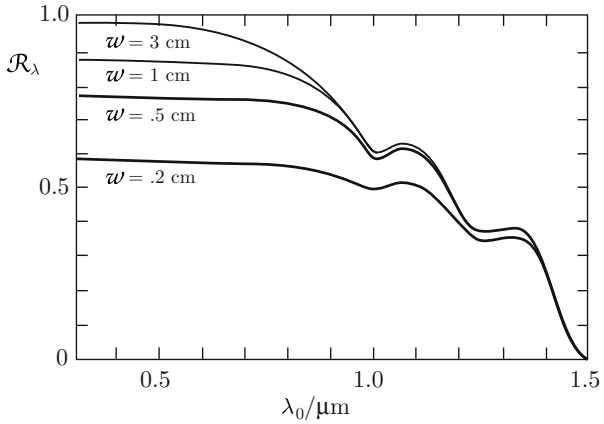

Fig. 14.12 Spectral reflectance $\mathcal{R}_\lambda$ of snow layers with different water equivalent w vs. wavelength λ_0 in the visible and near infrared (Curves interpolate data from [86])

effect on the extinction of the random variations of permittivity outlined in Sect. 9.1 combines with that of the absorption in setting the depth below the surface down to which a radar at a given frequency is able to gain information.

14.1.2.1 Radar Observation of Bare Soil

Given the high values of microwave permittivity of moist terrain and the usually rough nature of its interface, the backscattering images of pixels of bare soil, assumed of homogeneous material, contain shuffled information on both moisture

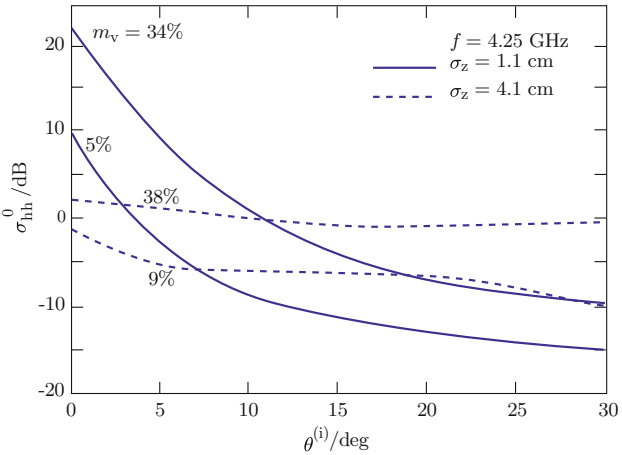

Fig. 14.13 Horizontal co-polar backscattering coefficient σ^0_{hh} vs. incidence angle $\theta^{(i)}$ for two different soil moisture content m_v [m^3 m^{-3}] and random surface standard deviation σ_z (Curves interpolate data from [368])

and roughness. In general, increasing soil moisture content m_v increases the backscattering coefficient σ^0 at all incidence angles θ for given surface roughness σ_z. The effect of this latter depends on θ, as seen in Sect. 13.1.1.2.1: at low incidence angles, typically for $\theta \lesssim 15°$, increasing σ_z reduces the reflected component, thus decreasing backscattering[12]; the opposite occurs for $\theta \gtrsim 15°$, where the backscattered incoherent component is enhanced by increasing values of the spatial spectral density that characterizes the surface roughness. Figure 14.13 shows typical trends of the backscattering coefficient with the incidence angle. Backscattering decreases monotonically with increasing incidence angle: the decrease is steeper for smoother surfaces, for which coherent scattering, which peaks sharply at low[13] wavenumbers, dominates, while the curves flatten for high roughness, since the spectral components maintain relatively high values over an extended range of lateral wavenumbers (Sect. 7.4.4). Note that the value of the backscattering coefficient in the neighborhood of the incidence angles (coarsely, between 15° and 25°) at which the curves cross, is weakly dependent on roughness, hence it is expected to be indicative of soil moisture. In the angular region in which the incoherent scattering dominates, typically $\theta \gtrsim 15°$, increasing frequency increases σ^0, whereas at angles at which coherent reflection prevails, an increase of frequency reduces σ^0. However, it is important to bear in mind that the permittivity does depend on frequency, hence when comparing σ^0 at substantially different frequencies, inconsistencies with the above conclusion might be observed.

[12] Actually, the definition of σ^0 is based on the incoherent scattering component.

[13] Ideally, for $\kappa_t \to 0$.

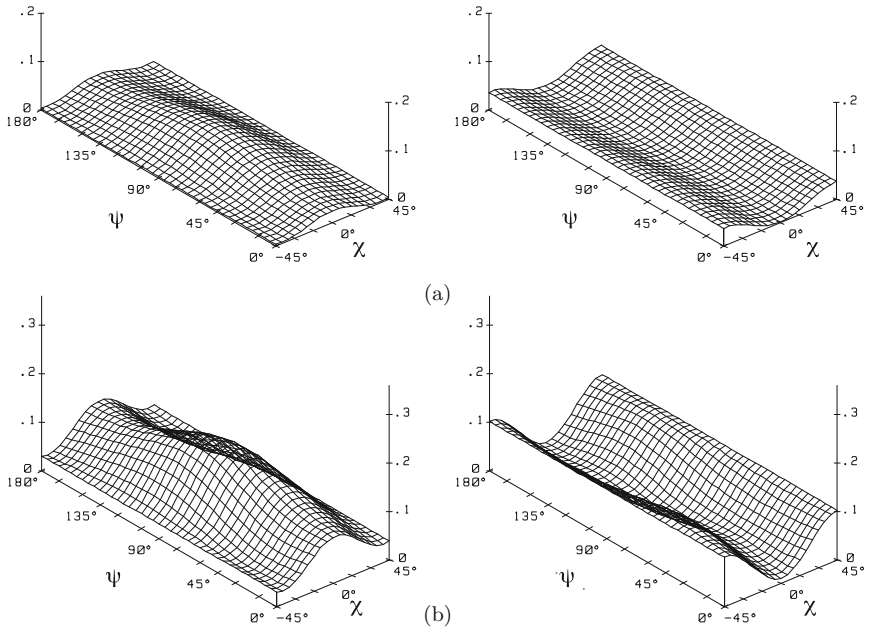

Fig. 14.14 L-band co-polar (*left*) and cross-polar (*right*) experimental signatures of bare soil: (a), low surface roughness; (b), high roughness. The polarization parameters ψ and χ are defined in Sect. 1.3.1.2

The electromagnetic interaction with bare soil clearly depends on polarization, as mentioned in Sect. 13.1.1.2.1. For low roughness, or, equivalently, for large wavelengths, and at angles at which scattering predominates on backward reflection, $\sigma^0_{hh} < \sigma^0_{vv}$, while $\sigma^0_{hh} \to \sigma^0_{vv}$ as σ_z (or the frequency) increases. On its side, cross-polar backscattering is lower than the co-polar one, so that σ^0_{hv} remains always below both σ^0_{hh} and σ^0_{vv}, and can be quite low when the observed surface is smooth. A comprehensive representation of the backscattering behavior for variable polarizations is provided by the *polarimetric signatures*, an example of which is shown in Fig. 14.14. The maxima of the co-polarized σ^0, which occur in correspondence of the ellipticity angle $\chi = 0$ (linear polarization) and inclination angle $\psi \approx 90°$ (vertical direction), highlight that $\sigma^0_{vv} > \sigma^0_{hh}$ for rough surface backscattering. The *pedestal*, that is the values of σ^0 in correspondence of $\chi = \pi/4$, represents the backscattering for circular polarization. At this polarization it is prevailingly cross-polar, consistently with the surface scattering mechanism and the definitions of co- and cross-polar components for circular polarization. In fact, the propagation vector of the backscattered field is opposite to the that of the incident one, hence the *relative* direction of rotation reverses.

As far as the phase difference between the field scattered at co-polarization is concerned, the values of $\Delta\Phi_{hv} = \Phi_{hh} - \Phi_{vv}$ for surface scattering remain low, consistently with the results given by the applicable models outlined in Sect. 13.1.1.2.1.

14.1.2.1.1 The Interferometric Coherence of Bare Soil

The interferometric degree of coherence shown by bare soil areas depends both on the random fluctuations of permittivity *within the individual radar resolution cells* and on the roughness parameters of the soil surface. The effect of roughness is negligible when the soil moisture content m_V is fairly uniform, whereas high dielectric variations in the single scattering volumes enhance the random phase fluctuations, hence decrease the coherence [216] according to the roughness of the surface, consistently with the results of Sect. 12.3.3.2. In general, $|\gamma| \approx 1$ for small variability of soil moisture content in the resolution cells, irrespective of the variations the moisture undergoes globally between the multi-temporal acquisitions.[14]

It can be added that separate information on moisture and roughness is not readily obtainable from interferometric images of bare soil.

14.1.2.2 Radar Observation of Urban Areas

Backscattering from built-up structures can be much higher than that of natural terrestrial environments. Indeed, as already observed in Sect. 12.1.2.5, man-made structures are often characterized by smooth large plane surfaces forming dihedral or trihedral configurations in combination with the horizontal surface. Then the multiple-bounce mechanism involving coherent scattering yields a large angular density of retroreflected power. Moreover, smooth curved surfaces and metallic structures are generally characterized by flash points (Sect. 7.3.2). A pixel within which such a large reflected power density originates is attributed a high backscattering coefficient. Images of dense urban areas at decametric resolution are generally characterized by a rather uniform distribution of σ^0, given the high probability that a corner reflector or a flash point falls within each pixel. For this reason, the images of dense urban areas acquired at such a spatial resolution appear characterized by fairly uniform high backscattering, such as the city of Rome, Italy, shown in Fig. 14.15. This feature makes decametric-resolution acquisitions suitable to delineate large-scale urban environments with simple processing, or even by visual inspection.

On the contrary, images of dense urban areas taken at metric spatial resolution are typically characterized by "bright" pixels, within which the high-intensity backscattering sources associated with the above effects fall, commixed with low-signal pixels, where shadowing and forward specular reflection occur. The metric-resolution images have then the potential of differentiating buildings or aggregates of buildings within the urban area and of singling out individual structures. However, the peculiar geometric effects introduced by the radar data takes call for particular care in image interpretation and information retrieval. As example of the difficulties that are encountered, Fig. 14.16 shows the tangled appearance of the

[14] The collective change of permittivity induces a corresponding phase shift [261].

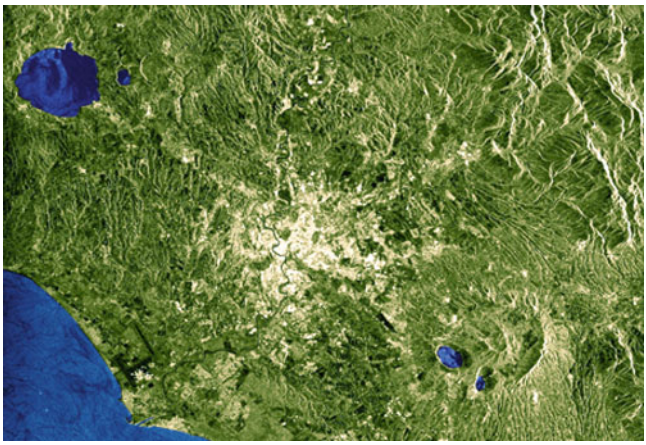

Fig. 14.15 Decametric-resolution SAR image of the Rome, Italy, extended area. This was the last image taken by the ERS-2 SAR over Rome before its dysfunction (Credits: data, ESA, 2011; processing, courtesy C. Solimini, and Tor Vergata University Earth Observation Laboratory)

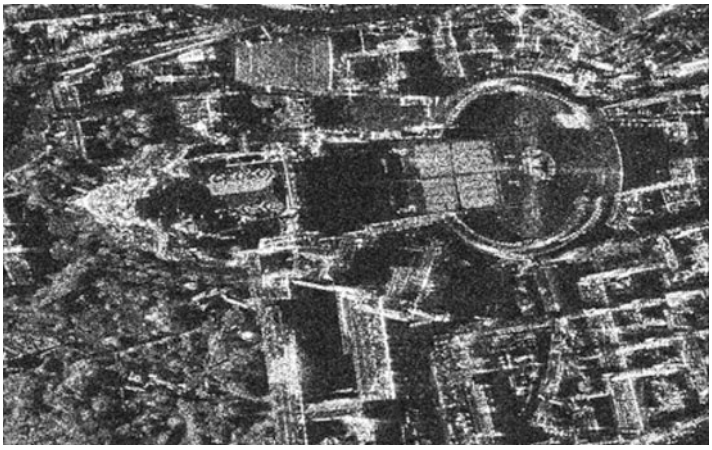

Fig. 14.16 Metric-resolution images highlight minute details of the urban environment, here around the St. Peter's church, Vatican City and Rome, Italy; ground track is on the left (Credits: COSMO-SkyMed data, ©ASI, 2011; image processing, courtesy A. Giardino, Tor Vergata University Earth Observation Laboratory)

historic area surrounding the St. Peter's church in Rome. The dramatic distortion of the actual scenario, caused both by the radar location mechanism discussed in Sect. 12.2.2 and by the mixture of flash points and low-backscattering areas, is quite apparent and makes fairly hard the identification of objects and shapes. Some further peculiar features of SAR very-high resolution images of buildings are displayed in Fig. 14.17. A striking characteristic is now represented by the rows of

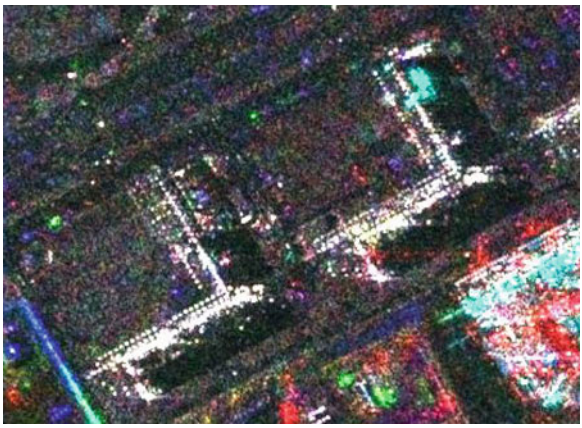

Fig. 14.17 Metric-resolution σ^0_{hh} COSMO-SkyMed image of two Engineering L-shaped buildings of Tor Vergata University, Rome, Italy, oblique to the incidence plane. Ground track is on the left. Note the sharp shadowing right of the buildings and the rows of high-backscattering pixels corresponding to the window trihedrons in Fig. 14.18 (Credits: COSMO-SkyMed data, © ASI, 2008, 2011, 2012; multi-temporal processing, courtesy C. Solimini)

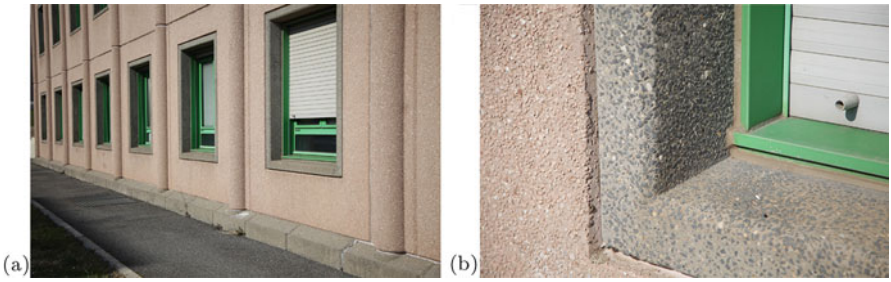

Fig. 14.18 (a) Windows imaged by the rows of bright pixels of Fig. 14.17 and (b), a window trihedral corner reflector originating the high backscattering

high-backscattering pixels corresponding to the rows of windows of Fig. 14.18a and originated by the trihedral corner reflectors formed by sill, wall and metallic frame shown in Fig. 14.18b.

The high backscattering originated by built-up structures is analogous to the one of bare surfaces oriented almost perpendicularly to the incidence direction. However, amplitude and phase of the field carry pieces of nearly independent information on the scattering source: in particular, the phase difference $\Delta\Phi_{hv}$ between the scattered fields for hh and vv co-polarizations provides means to discriminate between the two kinds of scattering environments. Section 6.6.1.1 shows that $\Delta\Phi_{hv} = \pi$ when the echo is originated by a double-bounce mechanism,[15]

[15]Provided the incidence angle is below θ_B *for each surface* of approximately lossless materials.

whereas no phase difference originates from rough-surface scattering. Indeed, images of urban areas, such as the one in Fig. 6.23, show a relatively frequent occurrence of pixels for which $\Delta\Phi_{hv} \approx \pi$. Nevertheless, pixels with $\Delta\Phi_{hv} \approx 0$ are also observed, because the built-up environment contains areas the return of which is dominated by scattering from trihedral structures, which, as observed in Sect. 6.6.2, behave like bare surfaces as far as $\Delta\Phi_{hv}$ is concerned. The decametric-resolution images clearly exhibit a phase behavior smoother than the very-high resolution ones, for the reasons previously mentioned for the intensity.

It can be added that the tightly packed heterogeneous structures that characterize the urban environment make lidars preferable to radars for generating the 3-D city models required by infrastructure planning, and, in general, competitive for ultrahigh-spatial resolution mapping of developed areas.

14.1.2.3 The Interferometric Coherence on Urban Areas

The majority of pixels of urban areas contain man-made structures or part of them, which are relatively simple and stable scatterers. Therefore, a generally high (up to $|\gamma| \approx 0.8$) long-term degree of interferometric coherence is shown by ordered built-up environments, at least for small baselines. However, the presence of green areas, the dimensions and density of which vary according to the geographic area and to the section of the cities, introduces low-coherence patches into the urban interferometric images. Moreover, buildings tightly packed in geometrically heterogeneous and irregular arrangements also exhibit low-coherence spots, especially where meandrous narrow alleys originate electromagnetic canyons. The spatial resolution has impact on the interferometric coherence for the reasons mentioned above, especially because the definition of γ involves spatial averaging. Ultimately, taken also account of their geographic heterogeneity, the coherence values of the urban environments are expected to span a wide range, say $0.1 \lesssim |\gamma| \lesssim 0.9$, according to the baseline (cf. Sect. 12.3.3.2), with the 0.3–0.6 range more frequently observed [130].

14.1.2.4 Radar Observation of Vegetation

Vegetation essentially introduces a volume scattering component, which interacts with the surface scattering from the ubiquitous soil. Both the vegetation parameters and those of the underlying terrain affect the backscattering coefficient. From the user point of view, particularly relevant are:

- the morphological parameters, water content and biomass of crops [252, 330];

- the above-ground wood volume (related to the biomass density) [166, 207] of arboreal vegetation.[16]

14.1.2.4.1 Backscattering from Crops

The variations with frequency undergone by the backscattering coefficients at a given incidence angle are quite significant, mainly because the extinction and, correspondingly, the penetration depth in the plant canopy change considerably. The behavior depends essentially on morphology and density of vegetation, and on the plant water content. Coarsely speaking, in case of herbaceous plants, such as field crops or pasture, backscattering at shorter wavelengths (C-band and, especially, X-band) mainly originates from the top of the canopy, that is from leaves, petioles and twigs, while the underlying stalks and soil add a generally considerable contribution at the less extinguished L-band. Indeed, given the typical dimensions of the leaves, their scattering follows the general increasing trend with the radar frequency that has been mentioned, for instance, in Sect. 7.3.4.1. The contribution from the stems, which is low at the large P-band wavelengths, typically increases at L-band, but subsequently decreases at C-band, when the lower part of the plants is shielded by the leaves in the upper part of the canopy. Soil has a similar behavior, since its contribution to backscattering is low both at P-band, at which it generally behaves like a specular smooth surface, and at C-band, when the shielding by the vegetation canopy becomes high. The diagrams of Fig. 14.19 suggest the trends with frequency of the expected scattering contributions.[17]

The incidence angle affects backscattering, mainly because it modifies the contribution from the underlying rough soil, according to the general features of volume scattering discussed in Sect. 13.1.2.1.

At low incidence angles, especially at the longer wavelengths, the radar return from the soil frequently dominates over the direct backscattering from the vegetation canopy, which essentially behaves as an attenuating layer. For typical terrain roughness, plants with higher biomass density, as, for instance, sugar-beet, show a lower σ^0, since their dense succulent structure produces an extinction of the power backscattered by the soil which is considerably larger than that of crops with small leaves and tenuous structure such as alfalfa. A comparison between the observed backscattering behavior of examples of the two kinds of crops is provided by Fig. 14.20, while Fig. 14.21 helps visualizing the corresponding dimensions of the vegetation elements.

[16]Global quantitative mapping of woods from space-based observations is beneficial to climate dynamics modeling, given the uncertainty of estimate of the amount of carbon [157, 285] stored in the world's forests.

[17]The reader is warned to regard the numerical values in this and in the following analogous diagrams as purely indicative. In fact, the numbers are the output of theoretical models that, no matter how clever, have intrinsic limits in representing the electromagnetic behavior of complicated real structures such as those shown in Figs. 14.21 or 14.26.

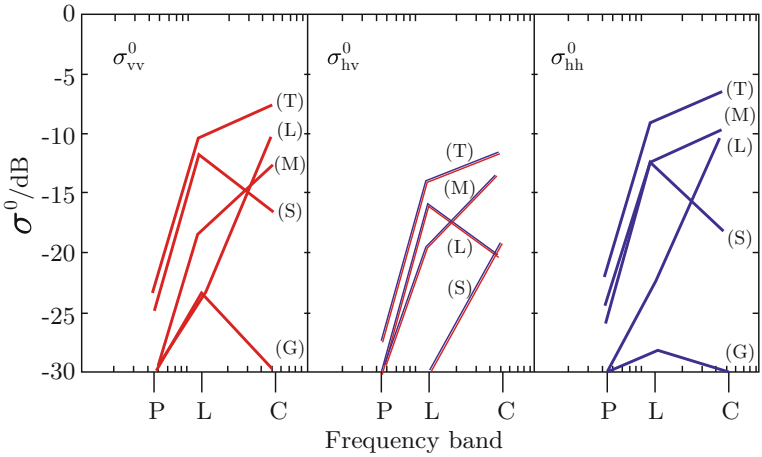

Fig. 14.19 Model backscattering coefficients at vertical (σ^0_{vv}) and horizontal (σ^0_{hh}) co-polarization and at cross-polarization (σ^0_{hv}) of a simulated potato field linearly interpolated for different frequency bands: (T), total σ^0, with contributions from leaves (L), vegetation-soil multiple scattering (M), direct scattering from stems (S), direct scattering from soil (G) (Data, courtesy P. Ferrazzoli)

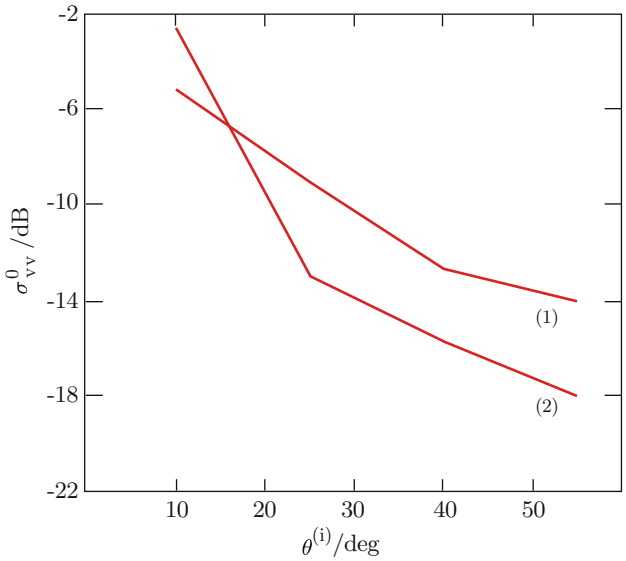

Fig. 14.20 Example of L-band backscattering coefficient σ^0_{vv} of two crop fields from linearly interpolated measurements at various incidence angles $\theta^{(i)}$ on vertical co-polarization: (1), sugar-beet field; (2), alfalfa field (Data, courtesy P. Ferrazzoli)

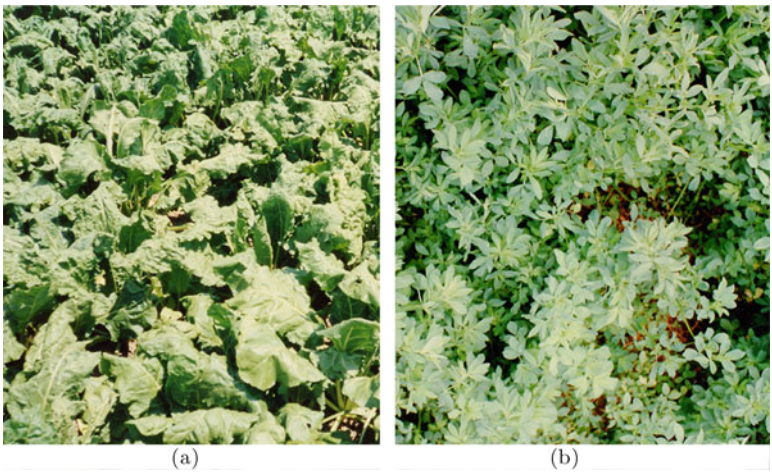

Fig. 14.21 The upper vegetation elements of sugar-beet, (a), are relatively large with respect to those of alfalfa, (b). Ground data acquired during MAC 91 [43]

As the incidence angle increases, two conflicting trends compete: on one side, the extinction by the longer path in the canopy reduces the contribution from the soil, while, on the other, the direct scattering from the plants grows, given the enhanced interaction along the lengthening path. The resulting generally observed trend is the decrease of σ^0 with increasing θ. It can be added that, once the contribution from the soil has fallen off substantially, backscattering from high-density wide-leaf crops is higher than the one by low-density small-leaf plants.

For a given morphology, the magnitude of backscattering from herbaceous plants depends on the surface density of the vegetal matter, hence essentially on the mass of water w_S stored in the vegetal matter present over the unit area of observed surface. It is worth mentioning that the co-polarized backscattering has trends with the plant water content opposite to the cross-polar one. For given canopy density, at moderate incidence angles, σ^0_{vv} and σ^0_{hh} tend to decrease with increasing w_S, whereas σ^0_{hv} increases. Indeed, the backscattering contribution from the terrain is almost exclusively co-polar at linear polarization. The extinction by an overlying increasingly moister canopy reduces the soil backscattering, thus counterbalancing the augmenting direct co-polar backscattering from the plants. Instead, the linearly cross-polarized backscattering originates almost solely from the randomly oriented elements of the plants, hence it keeps increasing with the areic water content of the canopy. The trend of σ^0_{hv}, which is expected to tend to a saturation value resulting from the balance between backscattering and extinction, is illustrated by the diagrams of Fig. 14.22.

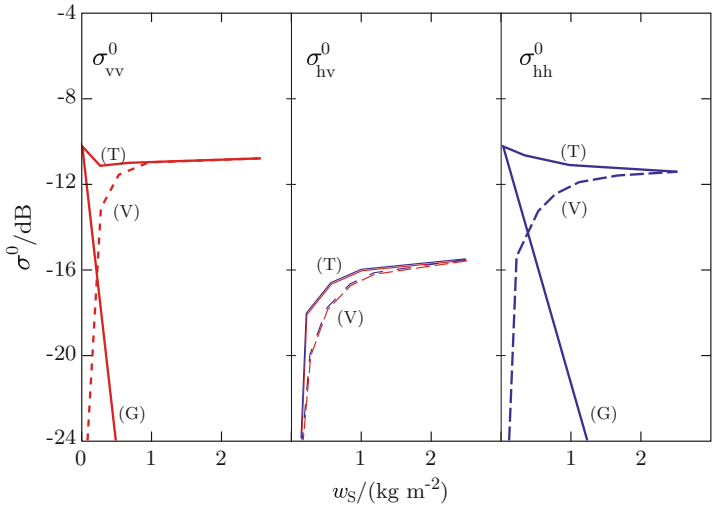

Fig. 14.22 Simulated co- and cross-polar backscattering coefficients of a model alfalfa field computed as linearly interpolated functions of the areic plant water content w_S, representative of the fresh biomass surface density, at X-band and $\theta = 45°$: (T), total backscattering; (V) contribution from vegetation; (G), contribution from soil (Data, courtesy P. Ferrazzoli)

14.1.2.4.2 Backscattering from Trees

The backscattering image of an area with arboreal vegetation also displays the result of the combination of the volume-scattering contribution from the plants and of the surface-scattering from the underlying soil. However, the structure of trees, substantially different from that of herbs, calls for suitable adjustments of the wave-vegetation interaction model and of the data interpretation criteria. In arboreal vegetation, the electromagnetic field at X- or C-band interacts with the upper part of the crown, composed of leaves, twigs and secondary branches, while at L-band the field penetrates deeper into the canopy and interacts mainly with the principal branches. At P-band the penetration is maximum[18] and the electromagnetic field interacts with almost all the tree structure, with significant reflection from the boles, mainly through the trunk-terrain double bounce introduced in Sect. 12.1.2.5.1. The main electromagnetic interaction mechanisms with arboreal vegetations are sketched in Fig. 14.23.

The backscattering from a tree stand is essentially contributed by three mechanisms, which show different trends according to frequency and polarization:

- the volume-scattering contribution by the crown, originates essentially from the branches and increases with frequency;

[18]Clearly within the microwave band (cf. Table 10.2).

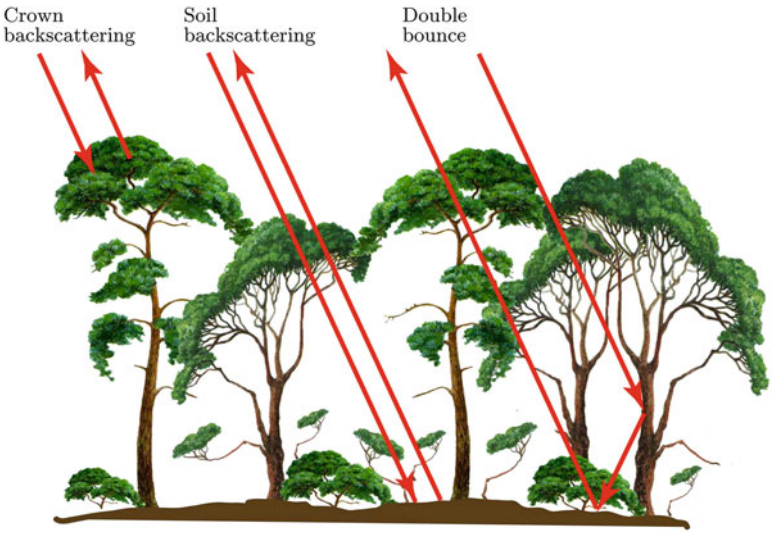

Fig. 14.23 Main mechanisms of interaction between electromagnetic waves and tree stand

- the surface backscattering from the rough soil, including the vegetation-terrain multiple scattering, increases from P-band to L-band, then tends to remain constant or to decrease because of the shielding by the crown;
- the bole-ground double bounce reflection gives its main contribution at horizontal polarization and low frequencies, while the values at vertical polarization are quenched by the trend of the reflection coefficient with θ discussed in Sect. 6.3.2.

Note that the double bounce does not contribute appreciable cross-polarized scattering. Figure 14.24 overviews the trends with frequency that are expected for the co- and cross-polar backscattering of a tree stand.

The trend of the measured backscattering with the variation of the areic above-ground biomass $\mathfrak{B}_S$ or of the wood volume surface density[19] V_S is of particular interest to the user community [83, 410]. Although each tree species may have its peculiar backscattering pattern at a given frequency, general trends can be identified. Figure 14.25 shows an example of co- and cross-polar σ^0 against the above-ground volume of wood; the diagrams refer to simulations at L-band, which, all included, appears to be an effective frequency for arboreal vegetation monitoring. The conclusions that can be drawn from simulated and experimental results are basically the following:

[19]The surface density of above-ground tree biomass $\mathfrak{B}_S$ [kg m^{-2}] in temperate climates is indicatively related to the areic wood volume V_S [m^3 ha^{-1}] by $\mathfrak{B}_S \approx 0.04\, V_S$.

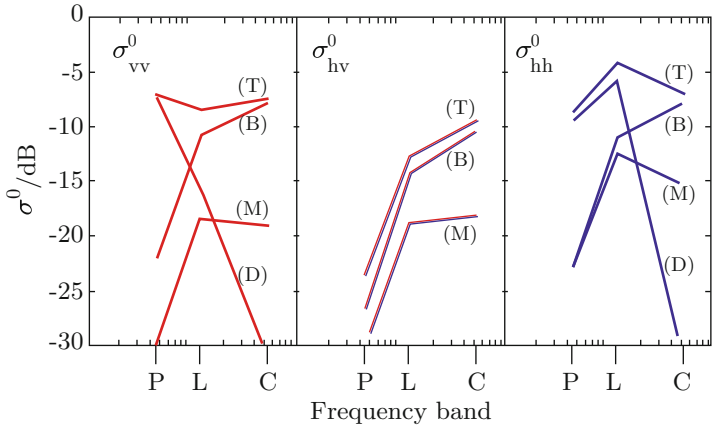

Fig. 14.24 Linearly interpolated backscattering coefficients σ^0_{vv}, σ^0_{hh} and σ^0_{hv} of model arboreal vegetation (simulated young maple) computed at different frequencies: (T), total σ^0, with contributions from branches (B), crown-soil multiple scattering (M), trunk-soil double bounce (D) (Data, courtesy P. Ferrazzoli)

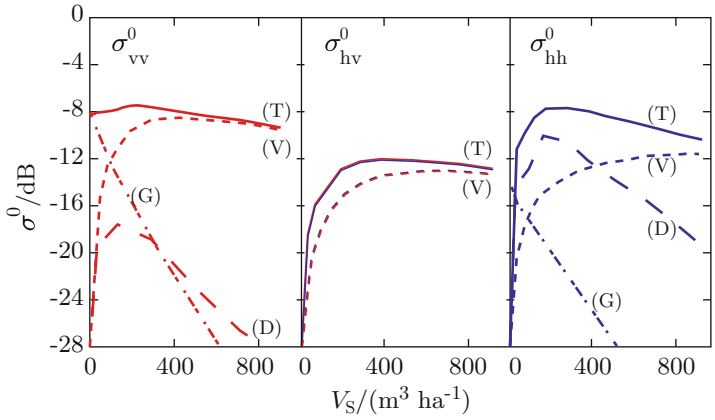

Fig. 14.25 Linearly interpolated backscattering coefficients of modeled deciduous arboreal vegetation computed as functions of areic above-ground wood volume V_S at L-band, $\theta = 45°$: (T), total backscattering coefficient, with contributions from tree crown (V), soil (G), trunk-ground double bounce (D) (Data, courtesy P. Ferrazzoli)

– the volume-scattering contribution by the crown generally increases with increasing spatial density of the vegetation elements, although a moderate decrease is sometimes observed at vertical polarization, according to the tree geometry;
– co-polar backscattering from the rough terrain keeps decreasing as the enlarging tree crowns shield the soil;
– the co-polar bole-ground double bounce reflection reaches a maximum, typically between P- and L-band, above which the increasing extinction by the upper vegetation elements prevails over the effect of the growing bole diameter.

The general saturation of backscattering with increasing biomass density of the tree stand is apparent. Rather, a decreasing trend [44] is also observed, since the increase of co-polar scattering from the larger and more numerous branches in the crown is counterbalanced by the decrease of the trunk-soil double bounce reflection caused by the crown extinction. Indeed, direct measurements of dense forest stands [77], say with biomass density higher that about $20\,\mathrm{kg\,m^{-2}}$, are difficult to perform by monostatic techniques [97] even at the lower microwave frequencies, since the electromagnetic wave is not able to interact with the trunks bottom, being attenuated by the upper parts of the trees. Alternative microwave techniques, either aiming at measuring the tree height, such as tomography [358] or polarimetric interferometry [63], or at exploiting the tree stand extinction through specular bistatic measurements [102], have some potential in forest inventory, which is one of the crucial issues for monitoring the global carbon cycle [81, 278].

14.1.2.5 Lidar Observation of Vegetation

Lidars offer an efficient alternative to radars both in mapping the surface distribution of vegetation and in providing information on the vertical profile of the plant elements. However, the properties of the lidar measurements differ from those of radars.

Microwaves have the capability of penetrating the vegetal matter, so that the radar echo contains direct information on macroscopic parameters of the plant canopy as a whole, such as the biomass density. Instead, light waves are backscattered to a high degree from the skin of the biological materials, hence the lidar return is the superposition of individual echoes originating from the single elements of the plants. This means that lidars operate essentially as ranging systems that respond directly to the spatial arrangement, that is to the geometric structure, of the observed canopy. Parameters like biomass can be obtained indirectly by inverting the measured plant height and closeness.

Taken the above clarification into account, it has to be mentioned that the high-resolution altimetric capability of lidar systems prove quite effective in mapping forested areas [203, 211], as well as in the monitoring of plant development demanded by precision farming [361, 408].

14.1.2.6 Interferometric Coherence of Vegetation

The degree of interferometric coherence of areas containing vegetation is determined by the combined effect of the volume and surface backscattering sources outlined in Sect. 13.1. Areas with little vegetation are characterized by the prevailing surface scattering from the soil, which, when sufficiently homogeneous, is a relatively simple scatterer, characterized by a more or less high coherence. Increasing the amount of vegetation makes the dielectric structure of the scattering cells more complicated and variable from pixel to pixel, hence the coherence is expected to

Fig. 14.26 Temporal evolution of the upper crown of an acacia tree. From *top* and *left*: 10 April, 24 April, 8 May, 26 June, 18 November, 27 December. Note the fast growth of the canopy from April to May and the development of inflorescence in June; note that also the thin branch structure and arrangement undergo considerable variations across the April to December time span

decrease with the increasing quantity of plants [387], following the general trends determined by the observation parameters, in particular, by baseline, wavelength, angle of incidence and polarization, as discussed in Sect. 12.3.3.

The decrease of multi-pass coherence due to vegetation [136] is caused not only by the increasing complexity of the scattering cells, but also by the substantial time variability of plants [12]. In fact, the geometric and dielectric characteristics of vegetation change incessantly: deciduous plants, including trees, shrubs and herbaceous perennials, lose all of their leaves for part of the year; evergreen plants also lose leaves, although not all at the same time, or replace them gradually as they age and fall. In addition, developing layers of vegetal tissues, growth of boughs or twigs, and shoots continuously vary the ligneous structure of trees. Figure 14.26 highlights the dramatic changes that the crown of a deciduous tree undergoes seasonally. On their side, annual herbaceous plants change seasonally through germination, vegetative growth, maturity and decay or harvest. Therefore, vegetation is a labile scattering source, characterized by inherent low time coherence.

The multi-pass interferometric data show that, for a given time interval between acquisitions, the coherence of areas including vegetation decreases with increasing amount of vegetal biomass, because of the combined effect of the complexity of the scattering sources and of their space-time changes. From the user point of view,[20] the trend of $|\gamma|$ with the above-ground wood volume of a tree stand, such as that displayed in Fig. 14.27a, yields a simple tool contributing to the global forest biomass inventory [184], while the variation of $|\gamma|$ with the canopy thickness provides means for readily monitoring the coarse state of agricultural crops, as Fig. 14.27b suggests.

[20] As mentioned, interferometric data acquired by a polarimetric SAR provide the users with quite valuable information on the biophysical parameters of trees [363, 365] and crops [23, 214].

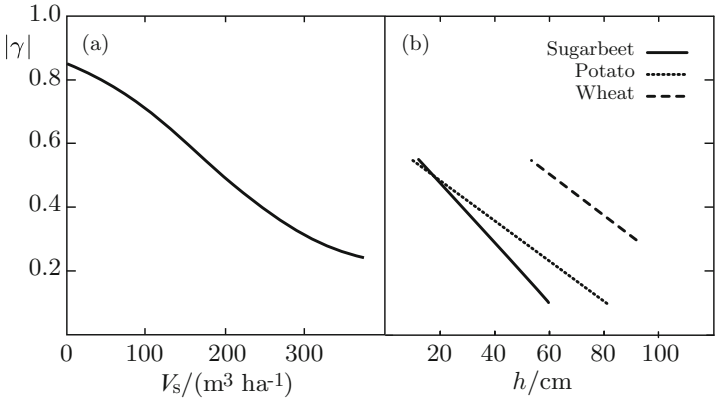

Fig. 14.27 Qualitative trends of the modulus of the C-band degree of interferometric coherence for varying amount of vegetation: (a), $|\gamma|$ of a tree stand vs. areic stem volume V_S; (b), linearized $|\gamma|$ vs. height h of three kinds of crops (Curves interpolate data from [48, 96])

14.1.2.7 Radar Observation of Snow

Section 14.1.1.3 mentions that a layer of snow is composed of an ensemble of randomly oriented ice granules in various states of aggregation, with either air or liquid water in the interstices, depending on the snow being dry or wet. Since the local microwave permittivity varies from that of ice to the one of air or of liquid water, the layer is electromagnetically inhomogeneous. The volume scattering it originates superimposes to the surface scattering contributions from the rough interfaces both at the top (air-snow) and at the bottom (snow-terrain, or snow-ice) of the layer. The results of Sect. 9.1 indicate that, given the small dimensions of the inhomogeneities, the volume scattering from snow is expected to be quite low at large wavelengths (typically, $\sigma^0 \lesssim -50\,\mathrm{dB}$, i.e., below measurement noise, at $\lambda_0 \approx 6\,\mathrm{cm}$), to increase considerably with frequency, and to become high at K_a-band. The trend of σ^0 with the incidence angle is shown in Fig. 14.28 for different frequencies.

Besides the dependence on temperature, backscattering from snow [334, 335] is sensitive both to the content of eventual liquid water[21] and to the ice volume fraction, both of which determine the SWE w mentioned in Sect. 14.1.1.3. However, a reliable relation between σ^0 and w, if at all, is hard to establish, given the entangled effects of snow thickness, wetness and ice density and of the radar frequency, which concur to set the balance between the contributions from the air-snow and snow-ground surface scattering and the one from the inhomogeneities in the volume. For certain sets of the aforementioned parameters, the backscattering coefficients of *dry* snow increase with w (Fig. 14.29), whereas, apart from the effect of the air-snow interface, the trend is opposite for *wet* snow, mainly because the *bulk* liquid water enhances the absorption in the layer, thus reducing its global albedo.

[21] Especially to the wetness of the surface layer of the snow pack [28].

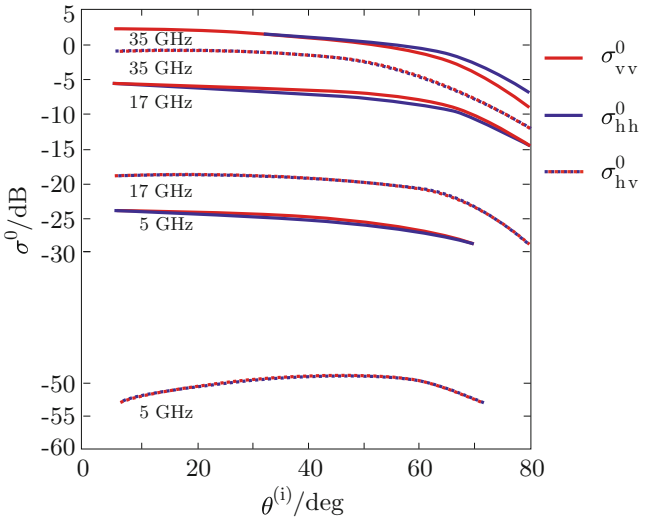

Fig. 14.28 Trend of linear co- and cross-polar backscattering coefficients of snow-covered surface vs. incidence angle $\theta^{(i)}$ for Ka, Ku, and C bands; note the quite low values (below typical system noise levels) of σ^0_{hv} at C-band (Curves interpolate data from [113])

Fig. 14.29 Co-polar backscattering coefficients at X- and Ku-band, horizontal polarization, $\theta^{(i)} = 57°$, as functions of water equivalent w of dry snow (Curves interpolate data from [368])

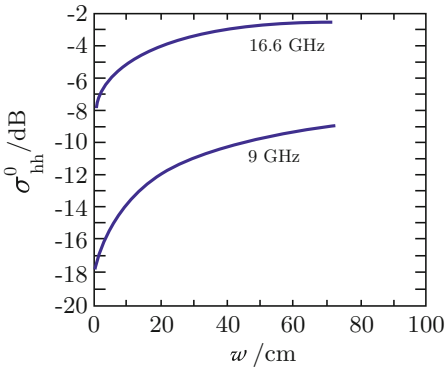

14.1.3 Observation of Land in the Thermal Infrared

Section 10.2.2 points out that the infrared wavelength range at which thermal emission is important spans the 3–100 μm interval, but, in practice, only the 3.5–4.0 μm (for *night* measurements) and the 8–14 μm spectral regions are relevant to Earth observation from high-flying or space[22] platforms, given the general atmospheric opacity at the other wavelengths. At $\lambda_0 \gtrsim 5\,\mu$m the power density emitted

[22]The 8–14 μm range is only partially available to surface observation from space, being interfered by ozone (Fig. 10.5).

spontaneously by the terrestrial environment predominates over the scattered solar radiation. In particular, more than 99 % of the power received by a radiometer looking at the Earth's surface in the atmospheric window 8–14 μm is contributed by thermal emission from the terrestrial environment.[23]

The natural or man-made media are characterized by their emissivity spectrum, that is, by their capability to radiate *spontaneously* at the various wavelengths. Since the electromagnetic reciprocity sets a complementary relation between emissivity and reflectance (Sect. 8.1.5), it is often convenient for overall consistency to make reference to this latter. Given the relatively low values of permittivity of the materials and the roughness of common surfaces, the standard deviation of which is large compared with TIR wavelengths, the emissivity is coarsely close to unity[24] [190, Chap. 1], so that the main information provided by the measurements is on the temperature of the observed areas, as mentioned in Sect. 10.2.2.1. In fact, the thermal radiation source is neither at constant nor at uniform temperature, but this latter varies according to the state of the emitting environment at the time of measurement and on previous history (stored heat), thus involving the energy budget among absorbed solar radiation, emitted radiation, and conductive and convective thermal exchanges. In many cases the TIR measurements form the input of thermal models coupled with radiative ones, which finally yield the quantities of interest to users. A suggestive example is the mapping of the bulk thermal inertia estimated from the evolution of the surface temperature derived both from radiometric data alternatively acquired at night and day, and by thermal and radiative models. The **H**eath **C**apacity **M**apping **M**ission (HCMM) [295, 386] was dedicated to this kind of observations.

Although temperature is the quantity more directly retrievable from thermal infrared measurements, identifying the spectral emissivity of terrestrials materials [92] is of great interest, since many absorption bands corresponding to specific molecular bonds occur in the TIR. Measuring the spectral features of the emissivity provides effective means to remote identification especially of those materials that are spectrally featureless in the VIS/NIR [374]. Knowing the TIR spectral characteristics of natural materials is also relevant to understand and model the energy exchange mechanisms among biosphere, lithosphere and atmosphere. However, given the overall experimental difficulties, thermal infrared measurements of good quality are less abundant than the optical and radar ones. A continuing relatively scarce availability of reliable data sets, together with the complexity of the physical models, hampers the general deeper understanding of the TIR spectral emissivity behavior of terrestrial environments and somehow restrains the use of the thermal infrared technique.

[23] Including the atmosphere.

[24] Enhancing the accuracy of surface temperature retrieval clearly requires a more precise and detailed [177, 340] knowledge of emissivity.

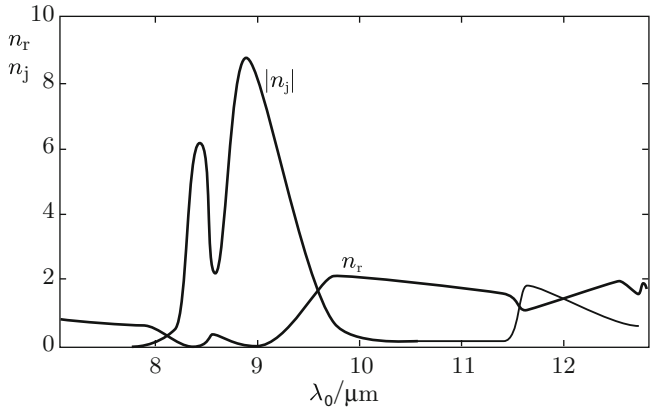

Fig. 14.30 Real (n_r) and imaginary (n_j) parts of refractive index of quartz, as defined by (4.17), vs. wavelength λ_0 in the thermal infrared (Curves interpolate data from [124])

14.1.3.1 TIR Observation of Bare Soil

The emission properties of soil are determined essentially by chemical composition and state of aggregation of the materials, as well as by their water content. The silicates form the widespread rocky material and generally imprint their features onto the spectral emissivity of bare soil [380]. Silicates show fundamental vibrational modes in the range $\lambda_0 \approx 8.5\,\mu m$ to $\lambda_0 \approx 8.9\,\mu m$, and at $\lambda_0 \approx 12.5\,\mu m$. Because of the superposition of the effects of the various resonances, the refractive index of silicates varies considerably and its module approaches the unit value at some wavelengths, around which the spectral reflectance tends to vanish, with corresponding maxima of the spectral emissivity. On the contrary, the relatively high values of $|n|$ in correspondence of the resonance wavelengths yield emissivity minima (*reststrahlen*) [194]. The spectral characteristics of the refractive index of quartz are sketched in Fig. 14.30, while main features of the emissivity of a mineral of the same group are outlined in Fig. 14.31.

It is interesting to note that the results which are readily obtained for the ideal case of an air-material plane interface are indeed indicative for the real case of granular material, at least until the surface reflection prevails, as in case of compact material or of granules large with respect to wavelength. With the exception of particular areas showing exposed rocks, bare soil is generally composed of various materials, including water, which, incorporated in the bulk matter, presents fundamental vibrational bands around $\lambda_0 = 2.9\,\mu m$ and $\lambda_0 = 6.1\,\mu m$. The sulphate ion, which has absorption bands on $\lambda_0 \approx 9.1\,\mu m$ and $\lambda_0 \approx 10.2\,\mu m$ is also frequently present. Given the heterogeneity of soil, the spectral pattern of its emissivity usually shows a rather complicated structure, although the silicate traits are often present. It is known that the spectral features of non-crystalline matter tend to be smoothed down, so that the wavelength dependence of the emissivity of

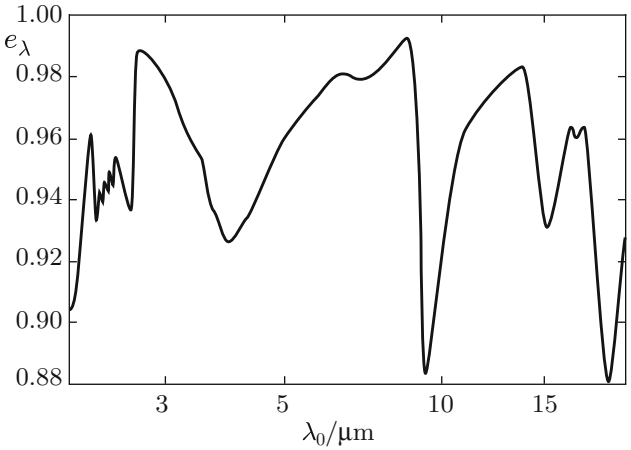

Fig. 14.31 Spectral emissivity e_λ of granular Antigorite (a silicate member of the Serpentine group) vs. wavelength λ_0 in the extended TIR; note the minimum of emissivity in correspondence of the maximum of $|n|$ in Fig. 14.30 (The curve interpolates data from [124])

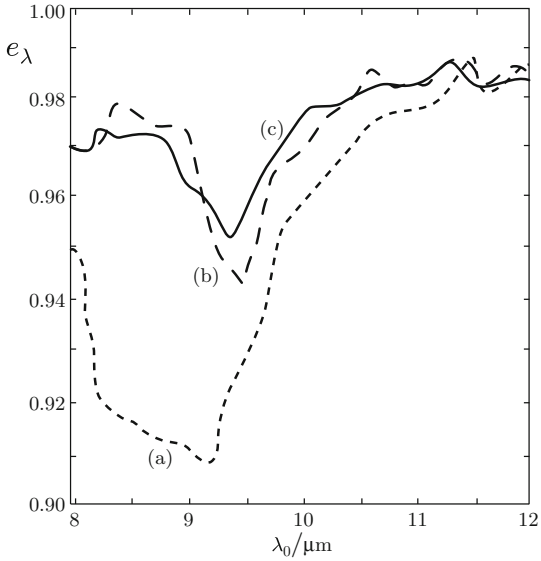

Fig. 14.32 Spectral emissivity e_λ of some earth surface materials vs. wavelength λ_0 in the thermal infrared: (a), alluvium; (b), lake sediments; (c), basaltic lava (Curves interpolate data from [217])

an amorphous material such as the terrain tends to weaken. Nevertheless, discernible peculiar features still show up, which may be sufficient to characterize the type of surface constituents, as suggested by the curves in Fig. 14.32, in which, as said, the emissivity minimum characteristic of silicates is still recognizable in the 9–10 μm wavelength range.

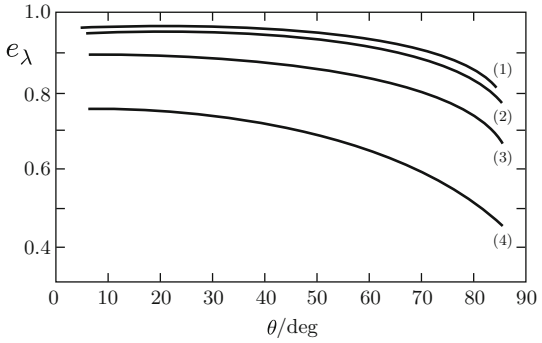

Fig. 14.33 Emissivity e_λ of Sahara dust and of granular quartz in the radiometric channels 4 ($10.5 < \lambda_0 < 11.5\,\mu$m) and 5 ($11.5 < \lambda_0 < 12.5\,\mu$m) of the NOAA AVHRR sensor as a function of observation angle θ: (1), dust, channel 4; (2), dust, channel 5; (3), granular quartz, channel 4; (4), granular quartz, channel 5 (Curves interpolate data from [354])

14.1.3.1.1 Emissivity vs. Observation Angle

Wavelengths in the thermal infrared are larger than in the visible or near infrared ranges, hence, for given surface roughness, the coherent scattering component is expected to increase, consistently with the model of Sect. 7.3.3. Correspondingly, some dependence of emissivity on the observation angle[25] (which, by reciprocity, is related to the dependence of the reflectance on incidence angle) starts appearing. As expected, a lithologically incoherent material presents angular variations which are small with respect to the ones that would occur for a homogeneous half-space of the same material and bounded by a plane surface. However, the examples in Fig. 14.33 suggest that, as the granule dimensions increase, the decrease of emissivity is accompanied by an enhanced angular dependence, in accordance with the model.

14.1.3.2 TIR Observation of Vegetation

Like the spectral reflectivity of vegetation at visible and near infrared wavelengths, the plant emission properties are affected by:

- spectral characteristics of the permittivity of the constituents of the vegetal matter;
- near-surface microstructure of the plant elements;
- global morphology of the plant canopy.

[25] A diffuse radiator tends to behave as *Lambertian* typically for observation angles $\theta \lesssim 50°$.

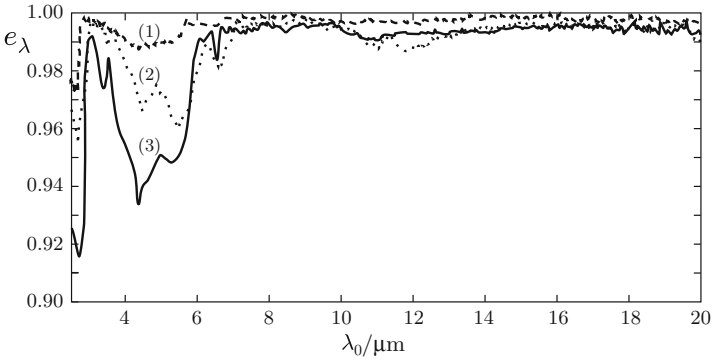

Fig. 14.34 High-resolution spectral emissivity e_λ of vegetation constituents vs. wavelength λ_0 in the thermal infrared: (1), pectin; (2), cellulose; (3), lignin (Curves interpolate data from [94])

Section 14.1.1.2 mentions the basic constituents of vegetal matter: cellulose, lignin and pectin. Emissivity of cellulose varies in the 2.5–8 μm wavelength range because of the vibrational transitions of the OH, C-H e CH_2 complexes, while the trend is smoother in the 8–14 μm window, with a slightly increasing drift at longer wavelengths. A similar behavior is shown by lignin, in which the OH, C-H and C=O complexes are responsible for the variations observed at $\lambda_0 \lesssim 8\,\mu m$ and the emissivity of which flattens at larger wavelengths. On its side, the emissivity of pectin is smoother over the whole TIR spectral range.

Relevant spectral features of the main constituents are identified in the high-resolution emissivity spectra shown in Fig. 14.34. The features of the constituents reflect into the spectral emissivity[26] of the leaves of the plants, some examples of which are reported in Fig. 14.35. The spectra show the more or less marked effects of the constituents of the vegetal tissue, interfered by the absorption bands of the hydrocarbons in the cuticle. Note that some spectral peculiarities do not derive only from the organic matter of the vegetal tissue, but also from chemical elements and inorganic compounds that the plant may have absorbed from the soil, as observed in Sect. 14.1.1.2 for the visible. As an example, the minimum of emissivity about $\lambda_0 = 9.3\,\mu m$ exhibited by Elymus leaves is due to the presence of silica in the vegetal tissue.

Figure 14.8 shows how the plant disturbances alter the spectra of reflectivity in the visible and near infrared. An analogous effect is expected in the thermal infrared for the emissivity [269]. The diagrams in Fig. 14.36 indicate that dehydration and alteration of vegetation constituents caused by senescence or disease modify the emissivity spectra, mainly in the 2.5–8 μm range, which tend to reproduce the features of cellulose and lignin.

[26]TIR transmission-like spectra, obtainable by the "attenuated total reflectance" technique, provide information on composition and structure of leaves [309], useful to identify species of plants.

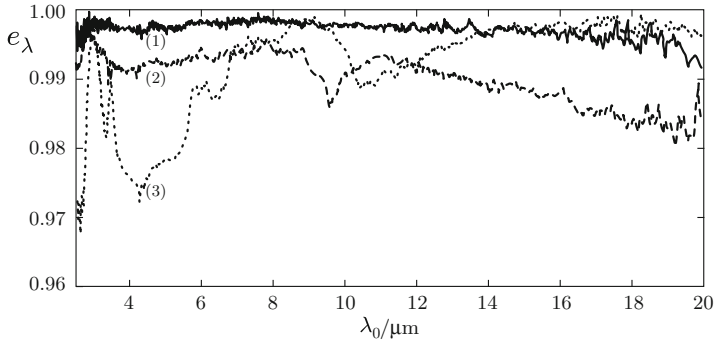

Fig. 14.35 High-resolution spectral emissivity e_λ of green shrub leaves vs. wavelength λ_0 in the thermal infrared: (1), Manzanita; (2), Elymus, (3), Artemisia (Curves interpolate data from [321])

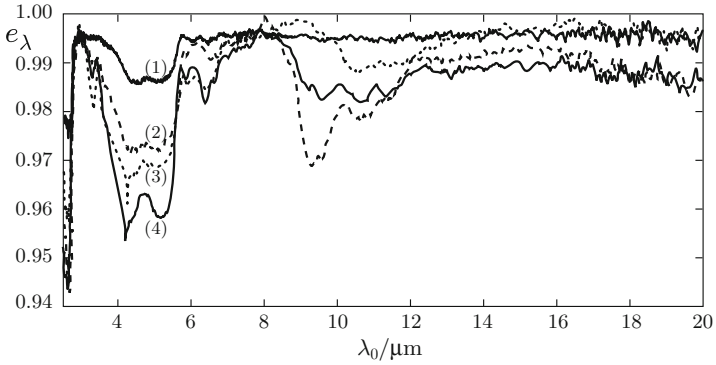

Fig. 14.36 High-resolution spectral emissivity e_λ of senescent shrub leaves vs. wavelength λ_0 in the thermal infrared: (1), Manzanita; (2), Elymus (dry); (3), Artemisia; (4), Elymus ("yellowed") (Curves interpolate data from [321])

In the 8–14 μm atmospheric window, which, as noted, is of paramount importance for applications, the emissivity spectrum of leaves is generally high and rather flat. However, some moderate diversification in the emission behavior of the various types of plants is observed in the very-high resolution measurements displayed in Fig. 14.37 referring to some types of tree. In addition to the senescent leaves considered in Fig. 14.36, the other exposed parts of plants exhibit spectral trends that essentially reproduce combinations of the spectra of basic constituents of vegetal matter. In particular, the emissivity features of wood and bark shown in Fig. 14.38 are a mixture of those of lignin and cellulose, although some characteristics peculiar of the type of plant may appear.

A word of caution is now suitable. It should be kept in mind that plants are complex assemblies of numerous different elements with random spatial distribution and orientation. Such chaotic structures tend to smooth the emissivity spectra,

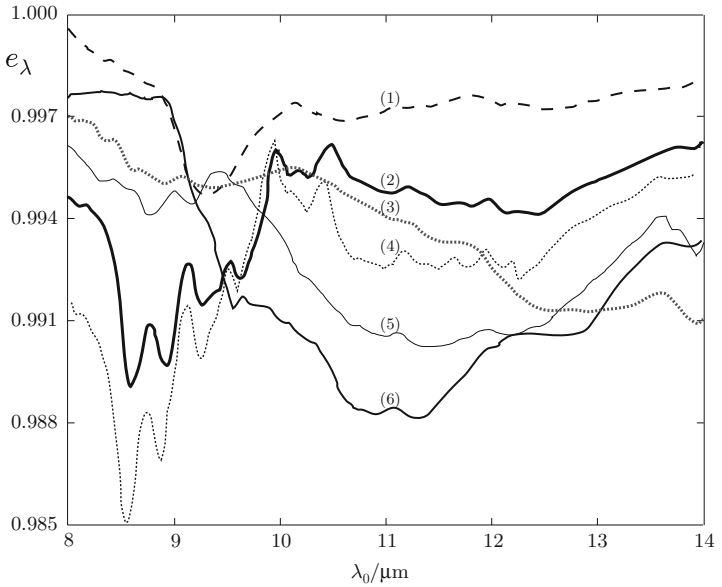

Fig. 14.37 High-resolution spectral emissivity e_λ of tree leaves vs. wavelength λ_0 in the 8–14 μm atmospheric window: (1), beech; (2), cherry tree; (3), oak; (4), senescent cherry; (5), senescent oak; (6), maple. Note the highly expanded vertical scale (Curves interpolate data from [321])

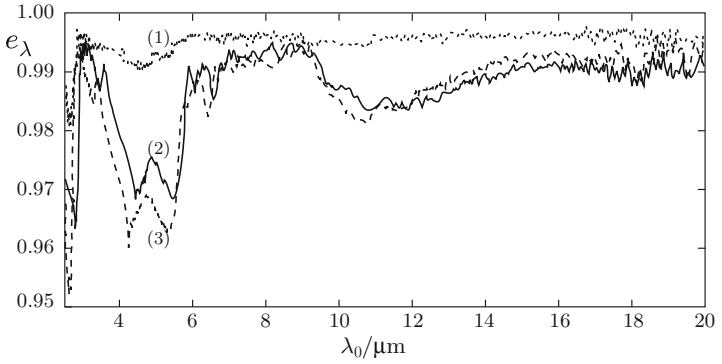

Fig. 14.38 Emissivity spectra e_λ of wood and bark vs. wavelength λ_0 in the thermal infrared: (1), Manzanita bark; (2), Manzanita wood; (3), pine wood (Curves interpolate data from [94])

mainly because multiple reflections and scattering lead to a nearly black-body behavior. This effect further reduces the spectral variations which are by themselves already scant and difficult to measure from remote locations and, in particular, from space [310]. Indeed, if spectra of vegetation are not of interest, the canopy is often assumed to be a gray body with average emissivity between 0.96 and 0.97 in the 8–14 μm atmospheric window. Moreover, as already mentioned, at least

in temperate regions the surface is only partially covered by vegetation, hence the sensed spectra are mixtures of those of soil and plants weighted by their respective cover fraction. All these features are a serious hindrance to the operational exploitation of TIR in remote monitoring of vegetation. The results presented in the Figs. 14.34, 14.35, 14.36, 14.37 and 14.38 are essentially intended to delineate some theoretical aspects as well as to suggest the potential of this observation technique, rather than to present its operational performance.

14.1.3.3 TIR Observation of Snow

Ice behaves similarly to liquid water in the thermal infrared; however, being a crystalline material, its absorption bands are narrower and the dielectric losses considerably lower. Relevant features of the ice permittivity shown in Fig. 14.39 are produced by the vibration of the O-H complex around $\lambda_0 = 3\,\mu\text{m}$, by the vibrational transitions around $\lambda_0 = 11.7\,\mu\text{m}$ and $\lambda_0 = 45\,\mu\text{m}$, as well as by the wide vibrational intermolecular band which begins at $\lambda_0 \approx 31\,\mu\text{m}$. In the 8–14 μm window $\tilde{\epsilon}_\text{r} \approx 1$. The high roughness of the air-snow interface and the dimensions of inhomogeneities combine with the almost unitary value of the refractive index of

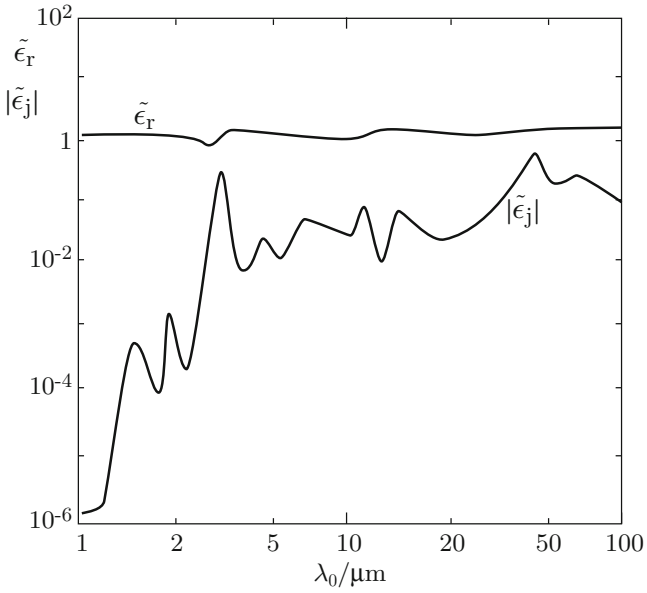

Fig. 14.39 Real ($\tilde{\epsilon}_\text{r}$) and imaginary ($\tilde{\epsilon}_\text{j}$) parts of relative permittivity of crystalline ice vs. wavelength λ_0 in the extended infrared (Curves interpolate data from [144])

ice to yield low TIR albedo, corresponding to high emissivity of the areas covered by snow,[27] in sharp contrast to the high albedo that the same areas exhibit in the visible.

14.1.4 Microwave Passive Observation of Land

At visible and near infrared wavelengths, the thermal emission from the terrestrial environment is negligible and the operational observation of the Earth from space or from aerial platforms is based on measures of reflectivity which utilize the Sun as source of radiation. The situation reverses in the TIR spectral range, where the thermal emission from the terrestrial environment predominates. At microwaves, thermal emission, although considerably reduced with respect to that in the infrared, is still measurable with sufficient signal-to-noise ratio, and, on the other side, radar systems are operationally available almost without interference[28] from the thermal environmental radiation. Therefore, both passive and active techniques are operationally available at microwaves, although with inherent differences in space resolution.

14.1.4.1 Microwave Passive Observation of Bare Soil

The theoretical curves of Sect. 8.1.3, based on electromagnetic reciprocity, effectively summarize the mechanisms that control emission from the surface of the Earth. For direction of observation locally perpendicular to the mean plane surface of the observed area, microwave emissivity depends substantially on the water content of the material: as moisture increases, permittivity increases (Sect. 2.2), with a corresponding decrease of emissivity. The dependence of microwave emissivity on polarization is apparent as the observation angle increases: emissivity at horizontal polarization decreases monotonically and tends to vanish for the limiting theoretical case $\theta \to \pi/2$; vice-versa, the vertically polarized emissivity reaches a maximum close to one at the pseudo-Brewster angle θ_{pB} before vanishing. Nevertheless, the high permittivity of moist terrain implies high θ_{pB} values (see, for instance Fig. 6.14), generally outside the angular range in which radiometric observations are carried out from elevated platforms.

Natural and man-made surfaces clearly differ from the ideal plane case, since the material is not homogeneous nor its surface is perfectly smooth: both factors act to decrease reflection and to increase emission accordingly. The values of emissivity on both horizontal and vertical polarizations increase with increasing roughness, while their difference reduces correspondingly. On its side, increasing moisture decreases

[27] Taking account of fine features such as the effects of the viewing angle [87] and of the snow-cover type [154], yields a more precise knowledge of the emissivity.

[28] Apart from the effects of direct solar radiation.

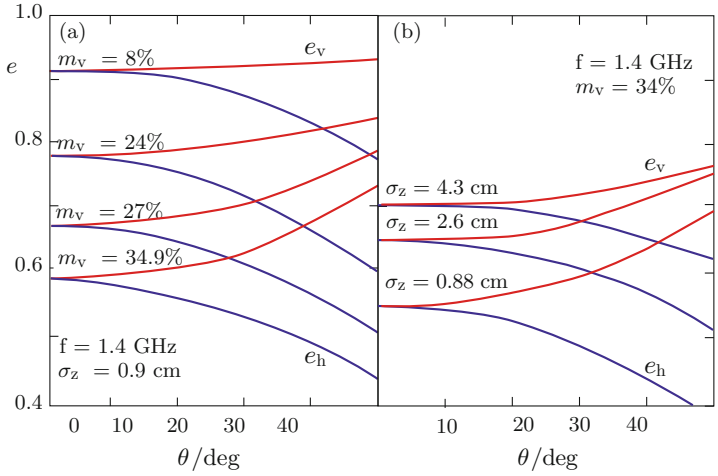

Fig. 14.40 (a) Emissivity e of rather smooth terrain with different moisture content m_v vs. observation angle θ at L-band on horizontal (*lower curves*) and vertical (*upper curves*) polarizations; (b), emissivity of moist ($m_v = 34\,\%$) terrain with different roughness σ_z vs. observation angle θ, measured on horizontal (*lower curves*) and vertical (*upper curves*) polarizations at L-band (Curves interpolate data from [368])

the emissivity of rough-surface terrain and enhances the differences between vertical and horizontal polarizations. It is worth pointing out that the values of emissivity may change, but the trends are quite analogous to those obtained for the simple plane homogeneous model of Sect. 8.1.3, which therefore is a quite useful reference for understanding the images of emissivity of the earth surface in terms of moisture distribution [72, 170, 178, 328]. Figure 14.40a shows the trend of the emissivity of soils with various moisture contents as a function of the observation angle, while Fig. 14.40b considers terrains with different roughness.

The effect of frequency on the emissivity of bare soil is mainly related to the variations undergone by permittivity, as well as to the changing effect of surface roughness. Indeed, on one side, permittivity coarsely decreases with increasing frequency and, on the other, the effect of surface geometric roughness is enhanced. Both effects act concurrently, so that the soil emissivity is observed to increase with increasing frequency and can exceed 0.95 at frequencies higher that K-band, approaching those observed in the thermal infrared.

14.1.4.2 Microwave Passive Observation of Vegetation

Emissivity of terrain covered with vegetation is usually higher that of bare soil, since the canopy of sparse lossy plant elements overlying the compact moist terrain behaves as an absorbing layer over a rather reflecting half-space. The first-order approximation outlined in Sect. 13.1.2.1 for backscattering is readily applied to

emission, by considering the emitted power made up of the one contributed by the soil and attenuated by the vegetation, added to the power originated by the plant canopy.[29] Emissivity is affected by the plant morphology and phytomass density and by the characteristics (roughness and moisture, essentially) of the underlying soil. Observed values are generally high, with some difference between denser and thinner vegetation canopies caused by the diverse extinction.

14.1.4.2.1 Microwave Emissivity of Crops

As frequency increases, the contribution from the soil decreases, given the augmenting attenuation by the canopy, while the emission by the plants increases, because the diminishing real part of permittivity (Sect. 2.2.3) reduces scattering and in turn the albedo. The counterbalancing effects act to form shallow emissivity maxima or minima at frequencies that depend on the electromagnetic thickness (Sect. 9.2) of the crop canopy. The result is displayed in Fig. 14.41 for crops with different geometric features. Plants with elements of large dimensions, hence causing higher extinction, show a moderate maximum of emissivity at frequencies lower than crops with smaller dimensions, hence more transparent at the relatively low frequencies. The combination of the soil and canopy effects is also responsible for slight emissivity minima shown by some crops, typically around X-band.

Of main interest is the sensitivity of emissivity to the PWC, which well represents the fresh biomass of crops. Given the general properties discussed previously, the emissivity is a function of PWC considerably dependent on both the radiometric frequency and on the type of plant. The diagrams in Fig. 14.42 are representative of the trends of the emissivity with the varying biomass of both wide-leaf and small-leaf crops. At low microwave frequencies, typically L-band, increasing biomass density generally implies decreasing albedo of a wide-leaf crop layer, with a corresponding increase of the overall emission from the canopy-soil system. Instead, at high frequency (X-band and beyond), the scattering from the large elements of wide-leaf plants is relatively high, hence the increasing biomass density results in a higher albedo of the crop layer, which corresponds to a decreasing trend of emissivity of the canopy-soil system. On the other side, given the prevailing absorbing characteristics of the canopies of plants with small elements, increasing biomass corresponds to decreasing albedo and to the resulting increasing trend[30] of emissivity of crops like alfalfa or small grains.

Analogous considerations may facilitate understanding the behavior of the emissivity of the more structured arboreal vegetation [101, 394], which is affected by several mechanisms, with rather complex mutual interactions [103]. In short summary, as frequency f increases, the emission from the leaves increases considerably towards a saturation value, whereas that of the underlying terrain decreases, with the result that the total emissivity increases only moderately with f, as outlined by the diagrams of Fig. 14.43.

[29] To this end, the source term in (13.7) is approximated by the thermal source (9.25).

[30] At least for frequencies up to X-band.

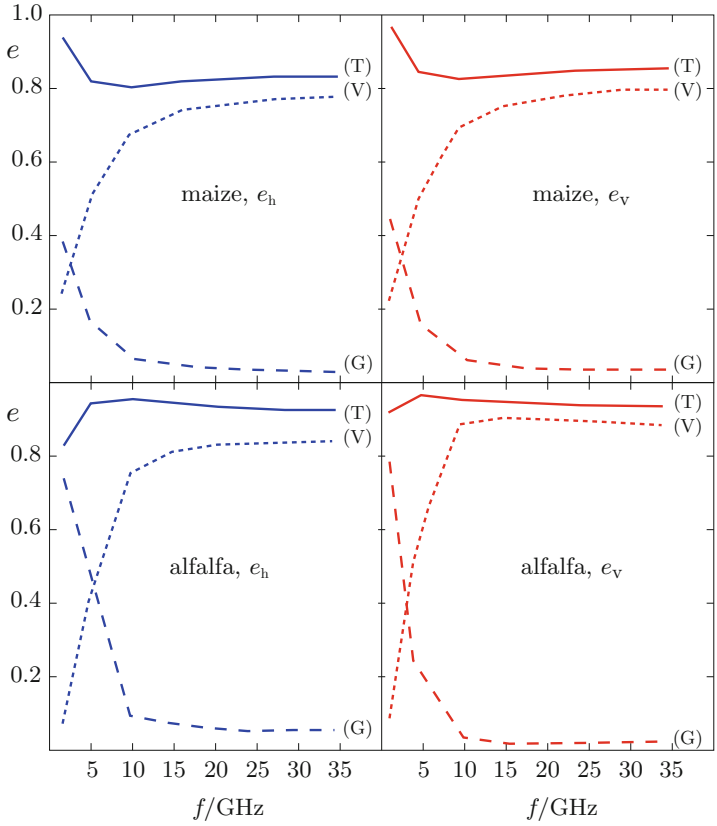

Fig. 14.41 Emissivity e of crop fields (*top*, maize; *bottom*, alfalfa) computed vs. microwave frequency f at horizontal (*left*) and vertical (*right*) polarizations: (T), total emissivity, with contribution of vegetation (V) and soil (G) (Data, courtesy P. Ferrazzoli)

14.1.4.2.2 Microwave Emissivity of Forests

Regarding the important issue of the sensitivity of the emissivity to the above-ground woody biomass of forests, the emissivity both of deciduous and of coniferous tree stands tends to increase progressively with increasing areic wood volume, as shown by Fig. 14.44. A weak dependence on the observation angle is also found.

14.1.4.2.3 Effect of Polarization on Vegetation Emissivity

Since the emission of the canopy-soil system is the superposition of that originated by the terrain shielded by the vegetation, and of the one coming fromthe canopy

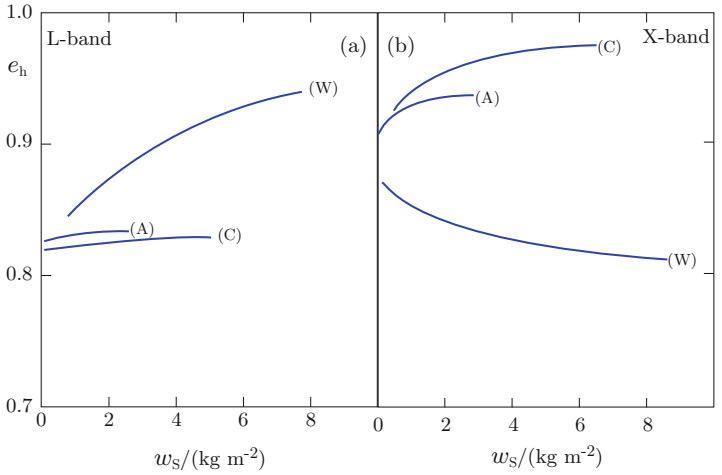

Fig. 14.42 Trends of L-band (*left*) and X-band (*right*) emissivity e of field crops vs. areic fresh biomass w_S at horizontal polarization and observation angle $\theta = 40°$: (W), wide-leaf (sunflower, maize); (A), alfalfa; (C), small-leaf cereals (wheat, barley) (Data, courtesy P. Ferrazzoli)

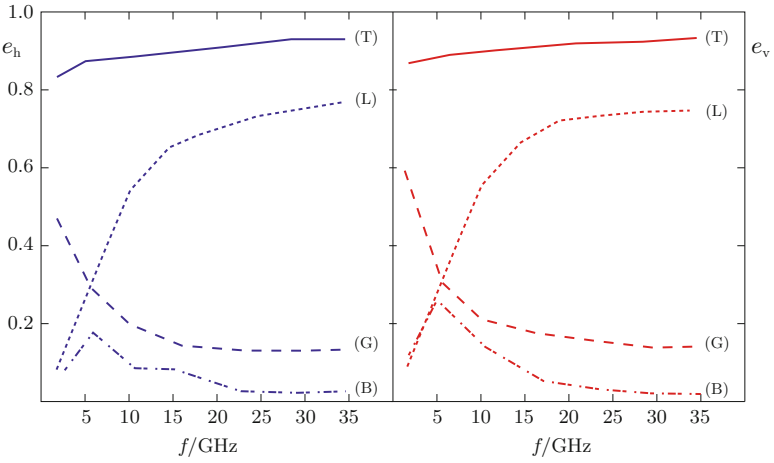

Fig. 14.43 Example of simulated emissivity e of a maple stand on horizontal polarization (*left*) and vertical polarization (*right*) linearly interpolated vs. microwave frequency f: total emissivity (T), with contributions from leaves (L), branches and trunk (B), soil (G) (Data, courtesy P. Ferrazzoli)

itself, the emissivity is expected to depend both on polarization (Sect. 8.1.3) and, as seen, on amount of vegetation. Figure 14.45 indicates that, at a given observation angle, higher emissivity is observed on vertical polarization and that the values gradually depart from those of bare soil as **l**eaf **a**rea **i**ndex (LAI) increases, i.e.,

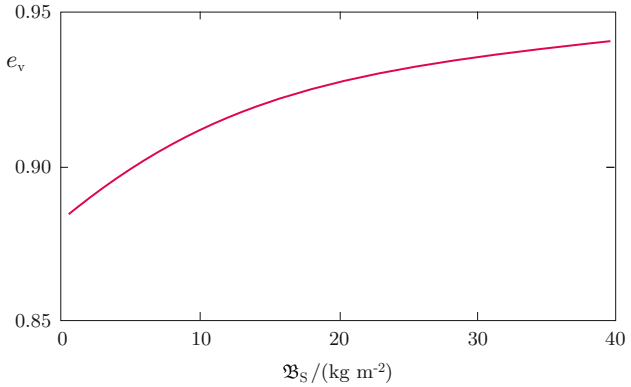

Fig. 14.44 Typical trend of L-band emissivity e at vertical polarization vs. arboreal above-ground biomass density $\mathfrak{B}_S$ for observation angle $\theta = 30°$ (The curve interpolates data from [78])

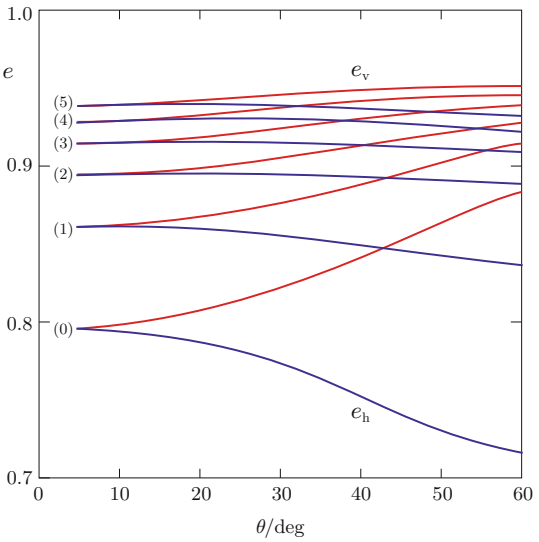

Fig. 14.45 Indicative trend of X-band emissivity e of small-leaf crop (alfalfa) vs. observation angle θ for different development stages of the plants: (0), no vegetation; (1)–(5), increasing leaf area index; *upper curves*, vertical polarization; *lower curves*, horizontal polarization (Curves interpolate data from [104])

vegetation grows.[31] The difference between the values of the emissivity e on the two polarizations correspondingly decreases with increasing LAI because, given the prevailingly random orientation of leaves and twigs, the extinction by the canopy tends to be independent of polarization and its contribution to the emission

[31]LAI, the value of which is given by the area of total green matter per unit surface ($\mathrm{m^2\ m^{-2}}$), is a further parameter commonly used to quantify the amount of fresh vegetation.

unpolarized. The polarization-dependent features of the emissivity are utilized to estimate the vegetation density from the **p**olarization **r**atio (PR), defined by[32]

$$PR := \frac{e_\mathrm{v} - e_\mathrm{h}}{e_\mathrm{v} + e_\mathrm{h}} \cdot$$

The polarization ratio PR is a normalized quantity [276, 277] analogous to (14.1), which quantifies the deviation of the emissivities at horizontal and vertical polarization from the ones of bare soil. Based on the model introduced in Sect. 13.1.2.1, PR provides information on the amount of vegetation.

14.1.4.3 Microwave Passive Observation of Snow

The permittivity of a snow layer differs appreciably both from that of the air and from the one of the soil. Therefore, wave reflection occurs not only at the bottom (snow-terrain or snow-ice) interface, but also at the top (air-snow) boundary. This implies that the microwave thermal radiation inside a snow layer results from the superposition of the waves traveling in the upward and downward directions and reflected by the top and bottom of the layer (cf. Sect. 6.5), and of the wave escaping from the lower half-space, formed by soil, rock, or ice. The emission process is related to the magnitude of these contributions, to the extinction of snow and to the reflection and scattering characteristics of the snow-air and snow-soil interfaces. Emissivity then depends on a variety of environmental parameters, including dimensions of ice granules, thickness and density of snow layer, liquid water content, roughness of top and bottom boundaries, parameters of underlying terrain, ice, or rocky bottom, possible presence of vegetation. Additional difficulties are contributed by the changes that phase in and out with the freeze-thaw cycles. These factors make difficult both modeling snow-pack emissivity [393] and establishing direct and unambiguous relations between snow parameters of interest to users [111] and measurable brightness temperature. In a simplified frame, the diagrams in Fig. 14.46 highlight the relevant features of emission from a snow layer. Given the strong volume scattering at short wavelengths, emissivity is low at 35 GHz and little dependent on the observation angle, while at 5 GHz, at which snow is fairly transparent and emission from the underlying soil prevails, vertically polarized T_B peaks moderately around 60°, i.e., in the neighborhood of the pseudo-Brewster angle of the soil-snow interface.

Like the spectral reflectance and the backscattering coefficient, also the emissivity depends in particular on the water equivalent w of the snow layer. Since the albedo of dry snow increases with w, the emissivity tends to decrease correspondingly (Fig. 14.47). The dynamic range, which depends on frequency,

[32] This quantity is also called **m**icrowave **p**olarization **d**ifference **i**ndex (MPDI) [26, 274] and can be directly related to the brightness temperatures measured at the two linear polarizations.

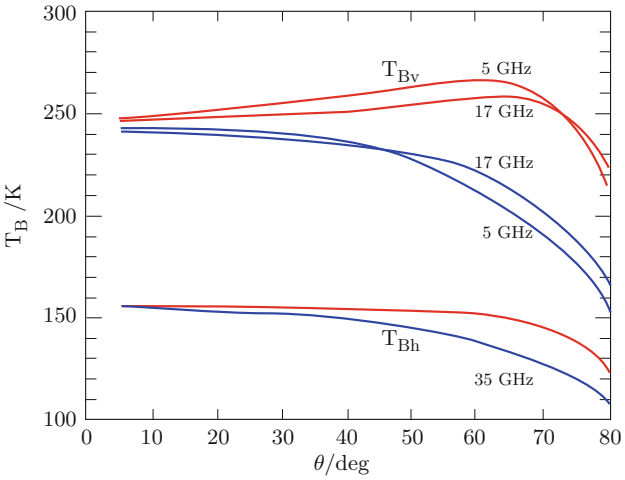

Fig. 14.46 Brightness temperature T_B at horizontal (*lower curves*) and vertical (*upper curves*) polarizations of a 50 cm thick snow layer over soil vs. observation angle θ at different frequencies for surface temperature $T = -11\,°\mathrm{C}$ (Curves interpolate data from [113, Chap. 9])

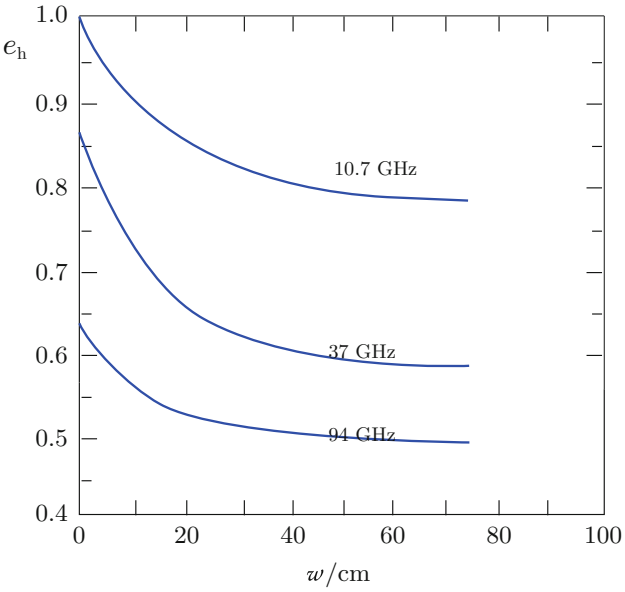

Fig. 14.47 Snow-cover emissivity e at horizontal polarization vs. water equivalent w for different frequencies at $\theta = 57°$ (Curves interpolate data from [368, Chap. 11])

shows a maximum in the K_a band, which appears an optimal[33] observational band from this point of view.

14.2 Interaction with Water Bodies

The dielectric structure of the water bodies is relatively simpler that of the land environments considered previously. The air-water interface frequently is a bare rough surface and only beyond a wind speed threshold it becomes partially covered by foam. The possible presence of oily films [8, Chap. 11] has also to be considered. The turbid bulk matter includes dielectric inhomogeneities of generally small dimensions, which affect the electromagnetic interaction only at the shorter wavelengths, typically in the visible range. The complex permittivity is clearly affected by the librational mechanism of the clustered water molecules, hence its magnitude is high at microwaves (Sect. 2.2.2.3), at which frequencies the water surfaces are highly reflecting (cf. Fig. 6.13) and the extinction caused by the bulk absorption is large.

14.2.1 Passive Observation of Water Bodies in the Optical Range

The spectral reflectance of water bodies depends on the combined effect of scattering and absorption by water itself, by the suspended particles both of organic (plankton) [352] and inorganic (sediments) [351] nature, and by thin layers (*slicks*) of oily substances of natural [142, 397] and intentional [195] or accidental [270] (oil spills) human origin possibly present on the surface [305]. The infrared intense vibrational bands make water essentially opaque at wavelengths beyond $\lambda_0 \approx 0.8\,\mu\text{m}$, thus reducing its spectral reflectance, which differs appreciably from zero only in the visible, where it exhibits a decreasing trend with wavelength. With particular reference to ocean observation, phytoplankton modifies the trend [180] by decreasing the sea reflectivity at wavelengths below $\lambda_0 \approx 0.54\,\mu\text{m}$ and slightly increasing it at larger wavelengths. Figure 14.48 indicates that at the higher concentrations of photosynthesizing plankton, the spectral features of chlorophyll appear, with the reflectance minimum around $\lambda_0 = 0.44\,\mu\text{m}$ and a second one just hinted[34] about $\lambda_0 = 0.66\,\mu\text{m}$. Although the absolute values of reflectance depend on the kind of phytoplankton, the shape of the spectrum and its variations with concentration remain fairly stable. This feature makes feasible the measurement of *phytoplankton*

[33] The aforementioned difficulties in retrieving environmental parameters such as w from microwave brightness measurements have to be taken into due account.

[34] The increase of reflectance caused by fluorescence at $\lambda_0 \approx 0.69\,\mu\text{m}$ tends to mask this latter minimum.

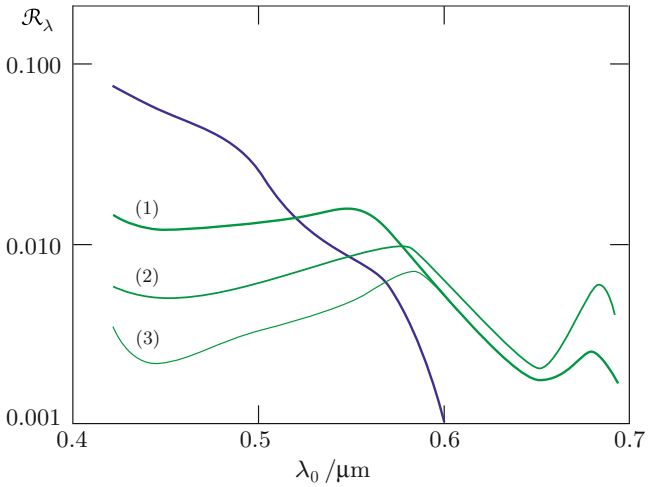

Fig. 14.48 Spectral reflectance vs. visible wavelength λ_0 of pure sea water (*blue decreasing curve*) and of water with increasing concentrations, from (1) to (3), of phytoplankton (Curves interpolate data from [314])

content from the ratio between the spectral reflectances at wavelengths at which they differ suitably [253]. Figure 14.49 highlights the dramatic change of spectral reflectance ("ocean color" [317, 399]) that may be associated with the presence of plankton.

The effect of suspended inorganic sediments [259] is different, given their large scattering section which causes the albedo, hence the spectral reflectance, to increase with increasing concentration, except that at the lower wavelengths, where the decreased albedo due to the concurrent chlorophyll absorption is generally observable (Fig. 14.50).

14.2.1.1 Passive Optical Observation of Oil Slicks

Oil forms an unmixable layer[35] on the sea surface, which modifies the spectral reflectance of this latter, given the different physicochemical properties between hydrocarbons and water. According to density, the real part of the oil refractive index ranges from $n_r \approx 1.47$ to $n_r \approx 1.55$, while the absorption coefficient varies correspondingly between $\alpha \approx 6 \cdot 10^3\,\mathrm{m}^{-1}$ and $\alpha \approx 1.5 \cdot 10^5\,\mathrm{m}^{-1}$ at $\lambda_0 = 0.4\,\mu\mathrm{m}$ and sharply decreases with increasing wavelength. Given the larger refractive index, the oil-covered sea surface tends to have an optical spectral reflectivity higher than

[35] A crude oil-sea water emulsion (*mousse*), formed by an assembly of tiny oil and water droplets and organisms, possibly including air bubbles, is also encountered.

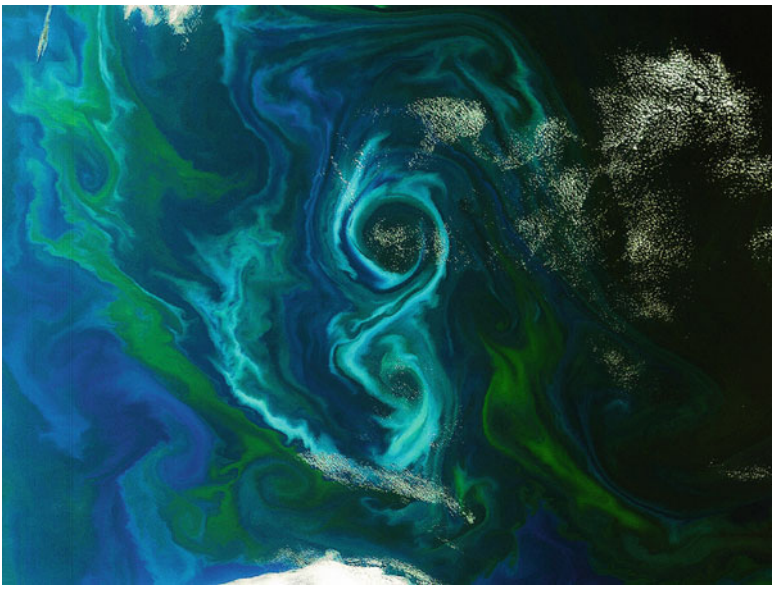

Fig. 14.49 MERIS image of algal bloom (Credits: data, ESA; image processing, courtesy C. Solimini)

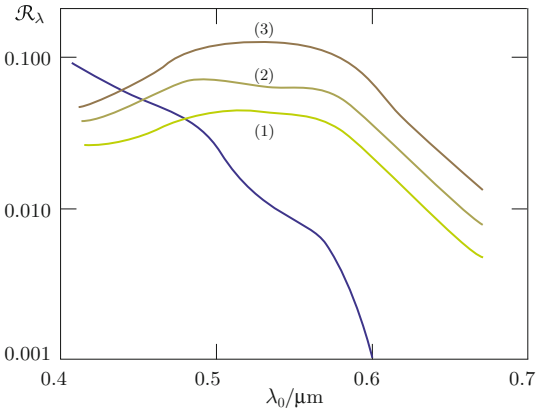

Fig. 14.50 Effect of inorganic sediment concentration on the spectral reflectance of sea vs. visible wavelength λ_0: the *blue decreasing curve* refers to pure water; (1)–(3) denote increasing sediment concentrations (Curves interpolate data from [314])

that of the clear water [11]. The radiation that penetrates into the hydrocarbon layer is correspondingly lower and further reduced by extinction. Therefore, the radiance scattered upward (Sect. 6.5.2) from the water volume below the oil surface is lower than the one from clean water.

The *contrast*, that is the difference between the upward spectral radiance coming from the oil-covered surface and the one from the clean sea provides the information for detecting and characterizing oil slicks. The balance between surface reflection and volume scattering is crucial in determining the contrast, since oil, on one side, increases the radiation reflected by the surface, while, on the other, decreases the one

scattered by the volume. The balance is made variable by several factors, including oil complex permittivity, layer thickness, density of scattering centers (i.e., slick and water turbidity), sky conditions, and mutual position of Sun, sensor and observed area. Further complexity is added by the modifications of the surface roughness [57, 58] with respect to the neighboring areas induced by the oil layer.

From the practical point of view, two coarse situations can be identified according to the thickness of the oil floating on the water.

Oil layers having thickness d_z less than a few tens of micrometers (*sheens*) are better detected and characterized in the visible images under favorable lighting and sea conditions. In particular, high contrast generally exists between oil slicks and the background water within the sun glint areas, i.e., within the regions originating specular reflection of the solar radiation: if the sensor looks at the slick about the specular direction of the Sun, *positive contrast* is observed, that is, the oil-covered area appears brighter than the oil-free water, while *negative contrast* is observed in peripheral sun glitter areas. This behavior is attributed to the above cited dampening of surface roughness [9, 68] (with ensuing increased specular reflectivity) caused by the oil film, rather than to differences in the optical properties of the surface.

The thickness d_z of the emulsion layer is typically larger than the penetration depth (6.26) at *visible* wavelengths, hence the spectral reflectance changes little with varying d_z (Sect. 7.4.7). The extinction decreases substantially with increasing wavelength, so that the reflectance becomes sensitive both to the thickness and to the NIR spectral characteristics of the matter (organic compounds and water) in the layer. Then the absorption features shown by the organic C-H bond around $\lambda_0 \approx 1.2$, 1.7 and 2.3 μm turn out useful to estimate composition and thickness of the oil-water emulsion, thus providing means for quantitatively mapping the areas of thick oil spills [60, 356].

In short summary, from the user point of view, passive optical detection of *thin* oil slicks requires some degree of sun glint for clear-water (oligotrophic) sea. On the other side, sun glint is not required when the oil layer is *thick* or overlays turbid coastal waters, where substantial volume scattering occurs.

14.2.1.2 Lidar Observation of Oil Slicks

Active sensing, being independent of solar radiation, clearly removes part of the hindrance of passive optical observation and, for instance, allows timely acquisitions, day or night. Beyond this obvious feature, the introduction to Chap. 7 hints at applications of fluorescence that utilize the re-emission spectral signatures to identify the composition of the observed target. Certain compounds of petroleum, excited by ultraviolet photons, decay through emission of visible radiation the spectral features of which are peculiar to given types of oil. Laser fluorosensors [36] operating in the ultraviolet provide information not only on the presence of the pollutant against a variety of backgrounds [105], but also on its class [280] (e.g., light, medium, heavy oil). It can be added that Raman scattering has the potential of measuring the slick thickness, which also affects the spectrum of the scattered radiation [148].

14.2.2 Radar Observation of Water Bodies

At microwave frequencies, a water body without foreign materials over it (such as foam over rough sea), or in it, is regarded as a homogeneous half-space having the permittivity of water and bounded by a rough surface. The observed field is contributed only by surface scattering (Sect. 13.1.1), which is affected by the spectrum $\mathcal{S}_\mathfrak{z}$ of the surface height deviation $\mathfrak{z}(x, y)$, as discussed in Sect. 7.4.7. The shape of the surface depends on the inertial and gravity-capillary waves, which produce components of $\mathcal{S}_\mathfrak{z}$ of corresponding periodicity, as already observed in Sect. 7.4.5. The water surface spectrum $\mathcal{S}_\mathfrak{z}(\varkappa_x, \varkappa_y)$ is the two-dimensional Fourier transform of the surface height deviation $z = \mathfrak{z}(x, y)$. Spectrum $\mathcal{S}_\mathfrak{z}$ is a function of the angular wavenumbers $\varkappa_x$ and $\varkappa_y$ in the orthogonal reference directions x and y, which can be identified in the radar image as ground range and azimuth, respectively. The spectrum is alternatively expressed by the directional spectrum $\mathcal{S}_{\mathfrak{z}\mathrm{d}}(\varkappa, \varphi)$ [145], function of angular wavenumber $\varkappa$ and of the azimuth angle φ. The directional spectrum describes the shape of the water surface as generated by the superposition of *linear* waves with angular wavenumber $\varkappa = (2\pi)/\Lambda$ traveling in the directions specified by the angle φ. An example of the shape of the water surface is shown in Fig. 14.51, in which waves of different origin traveling in different directions clearly appear. Indeed, the types of waves [189, 201] that are present on the surface of sufficiently extended water bodies, such as lakes or the sea, include:

Fig. 14.51 Gravity-capillary waves superposed to inertia-gravity waves: note that the locally wind-driven capillary waves here move in a direction (from *top left*) different from that of propagation of the inertial waves (from *top right*)

- inertia-gravity waves [288], with wavelengths Λ_0 larger than tens of centimeters and relatively high energy, which exist also in absence of local wind, since they may be generated in outer regions and propagate [181] into the observed area;
- gravity-capillary waves [407], with centimeter wavelengths, which are present only when and where surface wind blows, since their energy is not sufficient to allow them to propagate over appreciable distances.

Section 13.1.1.2.2 highlights that, consistently with the results of Sect. 7.4.5, peaks of backscattered power occur when the horizontal component $\boldsymbol{\kappa}_t$ of the scattering vector matches the spatial periodicity of the dielectric structure expressed by $\boldsymbol{\varkappa}$, hence, at usual incidence angles, when λ_0 is of the order of Λ_0. The typical gravity-capillary spatial periods Λ_0 are between 2 and 5 cm, so that, for incidence angles $30° \lesssim \theta \lesssim 60°$, the electromagnetic wavelengths satisfying the Bragg condition (13.6) fall in the range 2–9 cm. This implies that side-looking systems dedicated to the measurement of speed and direction of sea-surface wind through backscattering from gravity-capillary waves are expected to operate in the 4–15 GHz range. In particular, this important meteorological parameter is effectively retrieved from radar measurements at C-band,[36] as suggested by the detailed structure of the multi-temporal sea surface roughness field appearing in Fig.14.52.

Monitoring swell [65] through *direct backscatter* from inertia-gravity waves, the wavelength of which can attain hundreds of meters, would require low spatial resolution and much lower frequencies to satisfy the Bragg condition. Rather, the change of the backscattering intensity caused by the varying local angle of incidence on a relatively large-scale undulating surface makes swell to appear in images acquired at spatial resolution small with respect to the sea wave dimensions, at least when the waves propagate in a direction which is not parallel to the satellite ground track,[37] Figure 14.53 shows an impressive image of very high sea acquired by the ENVISAT C-band ASAR.

The coarse variation with the incidence angle of the backscattering coefficient of a water-body surface exhibits typical features of scattering from rough surfaces, with a steep decrease with θ of the nearly specular component, values of σ^0_{vv} higher than σ^0_{hh}, and low cross-polarized backscattering (Fig. 14.54). However, given the directional periodic components often embedded in the roughness spectrum, the water surface is anisotropically rough [31], what results in the dependence of σ^0 not only on θ, but also on the azimuth angle. Therefore, information on both intensity and direction of the surface wind is contained in multi-azimuth radar images of the sea surface. For a given elevation angle θ, the backscattering coefficient peaks when the horizontal component $\boldsymbol{k}_t$ of the propagation vector of the incident electromagnetic wave is parallel to the wind direction (*up–wind* or *down–wind*), whereas it has a minimum when $\boldsymbol{k}_t$ is perpendicular (*cross-wind*). A frequently used relation [80] is

[36]Indeed, the C-band frequency of the ERS SAR was selected also for its relevance to ocean observations.

[37]Note that interpretation of images of long fast sea waves requires a careful analysis of the effect of moving targets on the image features of synthetic aperture radars.

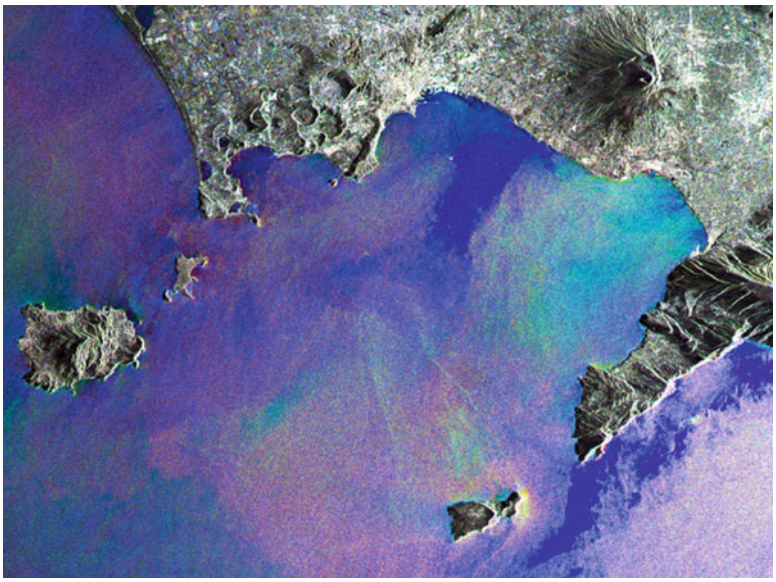

Fig. 14.52 ENVISAT ASAR RGB multi-temporal C-band image of the Gulf of Naples: coloring denotes changes of surface roughness essentially due to different wind speed fields on the dates of acquisition (Data credit: ESA; processing and image production, C. Solimini)

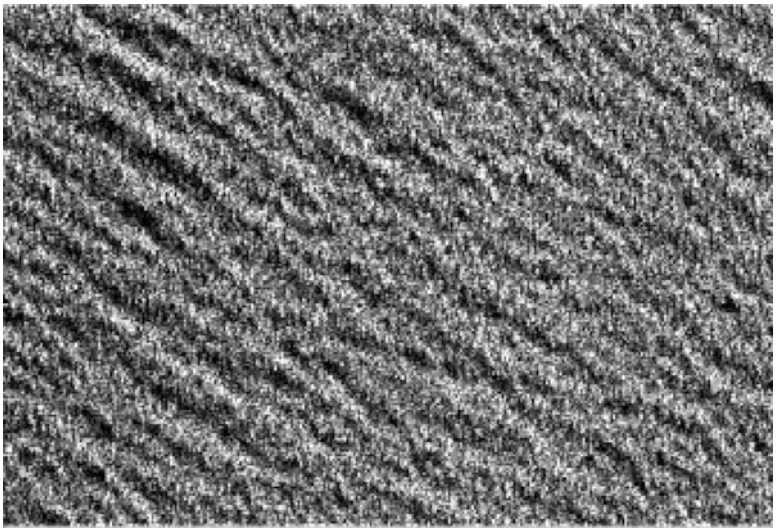

Fig. 14.53 ENVISAT ASAR C-band image of high swell waves having peak height $h_{\mathrm{sw}} \approx 15\,\mathrm{m}$, length $\Lambda_0 \gtrsim 700\,\mathrm{m}$ and speed $u_{\mathrm{sw}} \gtrsim 30\,\mathrm{m\,s^{-1}}$ (Original image credit: ESA)

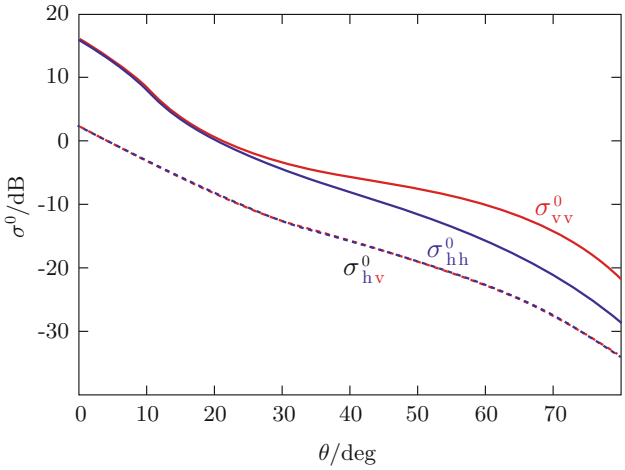

Fig. 14.54 Typical trend of backscattering coefficients of sea surface vs. angle θ at C-band for vertical (σ^0_{vv}), horizontal (σ^0_{hh}), and cross (σ^0_{hv}) polarizations (Curves interpolate data from [80])

$$\sigma^0 = a_0(\theta, v_w) + a_1(\theta, v_w)\cos\varphi_w + a_2(\theta, v_w)\cos(2\varphi_w) \ .$$

The coefficients a_i take account of the dependence of σ^0 both on the elevation incidence angle θ and on wind speed v_w; the angle φ_w is the azimuth angle between $\boldsymbol{k}_t$ and the wind velocity, with $\varphi_w = 0$ for up-wind observation and $\varphi_w = \pi$ for down-wind. Figure 14.55 highlights the behavior with the azimuth angle of the backscattering coefficients of the sea surface, which have maxima in the upwind direction, given the wave skewness.

The dependence of σ^0 on wind speed v_w, indicates that the increase of σ^0 with v_w is steeper for low v_w, while the curves tend to saturate at high speed, especially for up-wind observation. This feature is illustrated in Fig. 14.56, which suggests how the surface wind can be mapped from the intensity image of the sea backscattering.

14.2.2.1 Radar Altimetry and Lidar Bathymetry

The peculiar ranging capability of radars is exploited by climate-oriented missions such as Jason-2 [266] to measure the distance between the space platform and the *average* ocean surface. The high-precision altimetric acquisitions allow estimates of the yearly variations of the sea level [265] to a few millimeters per year, as well as of its anomalies, thus providing data crucial for seasonal-to-long-range weather and climate forecasting.

It is worth adding that, in contrast with radar systems, dual-wavelength lidars are able to provide not only the water surface topography, but also the bathymetry [168] of the water body. The measurements exploit the relatively low absorption of green

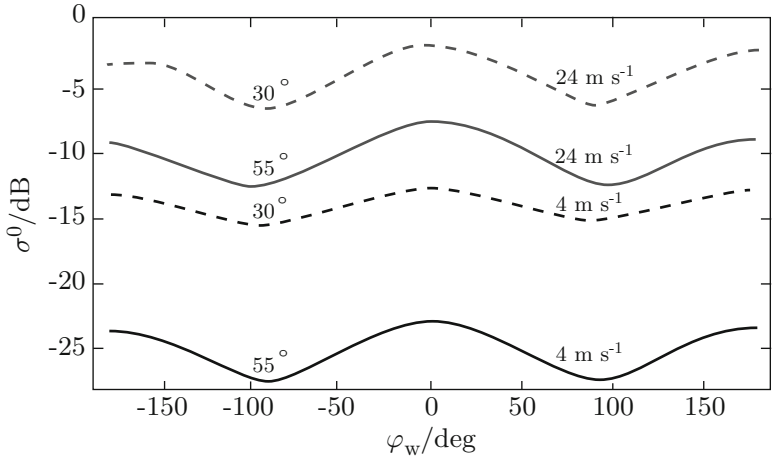

Fig. 14.55 C-band sea surface backscattering coefficient σ^0 at elevation angles $\theta = 30°$ and $\theta = 55°$ and wind speeds $v_w = 4\,\mathrm{m\,s^{-1}}$ and $v_w = 24\,\mathrm{m\,s^{-1}}$, vs. azimuth angle φ_w between horizontal direction of observation and wind direction ($\varphi_w = 0$ for up-wind observation) (Curves interpolate data from [80])

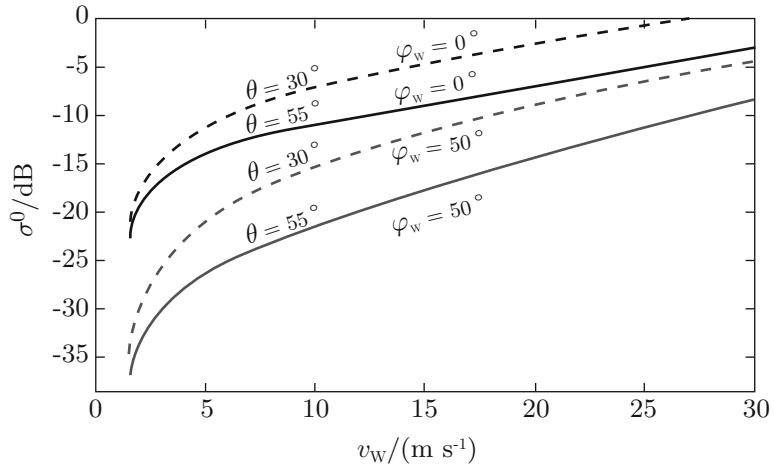

Fig. 14.56 C-band sea surface backscattering coefficient σ^0 vs. wind speed v_w for different elevation (θ), and azimuth (φ_w) angles of incidence; $\varphi_w = 0$ denotes up-wind observation (Curves interpolate data from [80])

($\lambda_0 = 532\,\mathrm{nm}$, typically) radiation, which enables echoes originating from the sea or lake bottom to reach the sensor when the local optical thickness, depending on turbidity and depth, allows a serviceable signal-to-noise ratio [132].

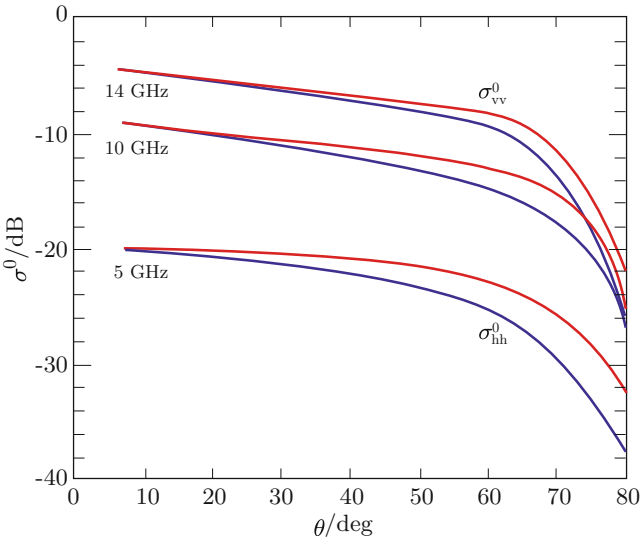

Fig. 14.57 Indicative backscattering coefficients σ^0_{hh} (*blue curves*) and σ^0_{vv} (*red*) of ice-covered sea surface vs. angle θ for different frequencies (Curves interpolate data from [113, Chap. 9])

14.2.2.2 Radar Observation of Sea Ice

Ice has dielectric properties which differ according to its origin. Polar sea ice [6] contains part of the salts dissolved in marine water, as well as inclusions of water with high salinity content, whereas fresh-water ice [21] on land includes air bubbles. The dimensions of the saline inclusions are fairly small (typically, of the order of 0.2 mm), so that the backscattering of sea ice is essentially determined by the roughness of its surface. Vice-versa, the non-negligible dimensions of the air bubbles (typically 1–2 mm) produce considerable volume scattering in land ice, which is originated by snow metamorphosis. Figure 14.57 shows that he dependence of σ^0 on incidence angle and frequency is essentially similar to the one already discussed for snow in Sect. 14.1.2.7.

14.2.2.3 Radar Observation of Oil Slicks

Section 14.2.1.1 mentions that the presence of a layer of insoluble liquid, such as oil, over the water surface, considerably damps the gravity-capillary waves, given the modification it induces on the surface tension. Indeed, even a monomolecular film inhibits the formation of small (a few centimeters) waves and wave breaking, and increases the rate of decay of capillary ripples. The ensuing reduced roughness results in decreased backscattering. Therefore, in presence of wind, the oil slicks are detectable by radar [76, 341], since they correspond to areas of the SAR image

with lower σ^0, contrasting with that of the rougher surface of the adjacent clean sea. However, it should be considered that low backscattering can be caused by a number of natural phenomena, such as particular air circulation, rain areas, or the oily biologic films produced by sea organisms. Additional features of such *look-alike* areas must be analyzed to decrease the false alarm rate in operational services.

Since monitoring oil spill by SAR exploits the contrast of backscattering between contaminated and clean sea, a minimum amplitude of the roughness spectrum, hence a minimum surface wind, is required. This implies that the observation system is not performing over low-wind areas. On the other side, in high-wind areas, typically for $v_w \gtrsim 10\,\mathrm{m\,s^{-1}}$, breaking waves, foam and fragmentation of the oil layer reduce the backscattering contrast. Some extension of the range of wind speed of operation may be expected by polarimetric systems, as well as by using cross-polarization. Notwithstanding the above limitations, SAR appears to be a relatively efficient and performing sensor for oil spills detection [19, 33, 75], though with relatively limited capabilities in direct oil thickness estimation and type recognition.

14.2.3 Observation of Water Bodies in the Thermal Infrared

Liquid water shows an ensemble of absorption bands in the thermal infrared, which are subdivided into two classes [22, 52]:

- *intramolecular* bands, associated with the structure of the single molecule and which are found also in the water vapor;
- *intermolecular* bands, which depend on the interactions between the molecules, also present in ice.

The intramolecular bands are of vibrational nature and occur at relatively short wavelengths ($\lambda_0 \approx 2.8\,\mu\mathrm{m}$, $\lambda_0 \approx 2.9\,\mu\mathrm{m}$, and $\lambda_0 \approx 6.1\,\mu\mathrm{m}$), given the separation of the energy levels involved in the transitions. The intermolecular bands are related both to *librational* motion and to relaxation, and fall in the thermal ($\lambda_0 \approx 12.5\,\mu\mathrm{m}$, $\lambda_0 \approx 14\,\mu\mathrm{m}$, $\lambda_0 \approx 18\,\mu\mathrm{m}$) and far ($\lambda_0 \approx 22\,\mu\mathrm{m}$, $\lambda_0 \approx 59\,\mu\mathrm{m}$) infrared, at temperature $T = 25\,^\circ\mathrm{C}$. Real and imaginary parts of the relative permittivity of liquid water are represented in Fig. 14.58 in an extended infrared wavelength range. Because of the superposition and interaction of the bands, both real and imaginary parts of permittivity vary appreciably with wavelength. In particular, it is important to observe that $\tilde{\epsilon}_r$ approaches one and $\left|\tilde{\epsilon}_j\right| < 0.4$ in the atmospheric window 8–14 μm. The salient consequence is that the refractive index is close to one, reflectance is low, emissivity high and the water surfaces behave approximately like black-bodies: the spectral emissivity averaged over the thermal band is $e_\lambda \approx 0.98$ for fresh water and $e_\lambda \approx 0.975$ for sea water [227]. Given the stability of these values, as outlined in Sect. 10.2.2.1, thermal infrared radiometry is used to measure

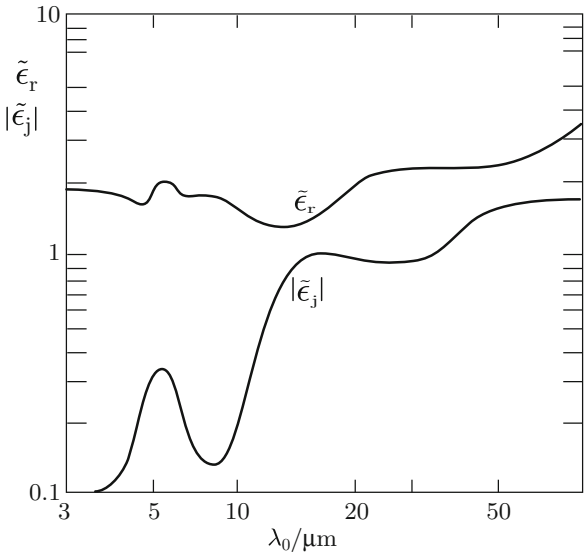

Fig. 14.58 Real ($\tilde{\epsilon}_r$) and imaginary ($\tilde{\epsilon}_j$) parts of relative permittivity of liquid water vs. wavelength λ_0 in the extended infrared (Curves interpolate data from [4])

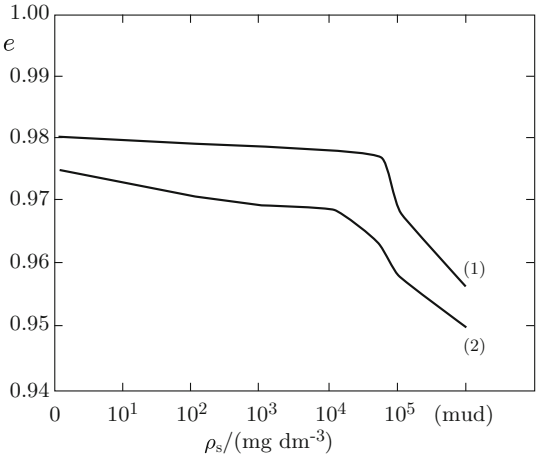

Fig. 14.59 Emissivity e averaged in the TIR 8–14 μm band of fresh water (1) and sea water (2) vs. sediment mass density ρ_s; note the expanded vertical scale (Curves interpolate data from [213])

the extremely important climatological parameter SST, as well as the water surface temperature in lacustrine [218] and riverine [140] landscapes. Only very high concentrations of sediments cause slight deviations of the emissivity of water bodies from the above values (Fig. 14.59). However, it is worth mentioning that finer values of water emissivity, possibly including polarization effects [333] are demanded by enhanced temperature estimates.

14.2.3.1 TIR Observation of Oil Spills

A contaminated sea surface has a TIR emissivity lower than the clean one, since oil has a permittivity, hence a reflectivity, higher than that of pure water [324]. On the other hand, the absorbed locally available solar radiation changes the daytime oil temperature with respect to that of the water, according to the exchanges of heat with water and air. As a consequence, a positive thermal contrast is shown by thick layers and a negative one by slicks of intermediate thickness, while no appreciable brightness difference is observed for oil films. Radiative cooling reverses the nighttime contrast for thick slicks, which appear generally cooler than the clean sea. The brightness contrast resulting from the combination of dielectric and thermal features[38] carries information on the oil layer [204]. However, oil weathering, sea state and water temperature variations caused by currents, hamper identification and characterization of oil slicks, at least if high-resolution TIR spectra are not measured.

14.2.4 Microwave Passive Observation of Water Bodies

The sea surface emissivity, which is fairly close to one in the thermal infrared, lowers considerably at microwaves, given the higher values of water permittivity, as highlighted by Figs. 10.20 and 10.21. The microwave emissivity of the sea depends on salinity [41, 234], as well as on the surface roughness [151, 164], which, as discussed in Sect. 14.2.2, is clearly a function of wind speed [235, 395].

14.2.4.1 Radiometric Observation of Ocean Salinity

Section 2.2.2.3 shows that the dissolved salts cause the sea water conductivity to differ appreciably from zero, thus further increasing the lower-frequency imaginary part of permittivity with respect to that of pure water. As a result, sea water has higher microwave reflectance and consequently lower emissivity than fresh water. Since the ion mobility decreases with increasing frequency, the feature is more pronounced at the lower microwave frequencies, typically from P- to S-band. Figure 14.60, highlighting also the effect of the water temperature, shows the sensitivity of microwave brightness temperature measurements to ocean salinity. ESA's SMOS [339] has been the first interferometric-antenna radiometric mission dedicated to map this parameter [110, 114] of quite relevant climatic importance.

[38] The properties concur to form the **a**pparent **t**hermal **i**nertia (ATI).

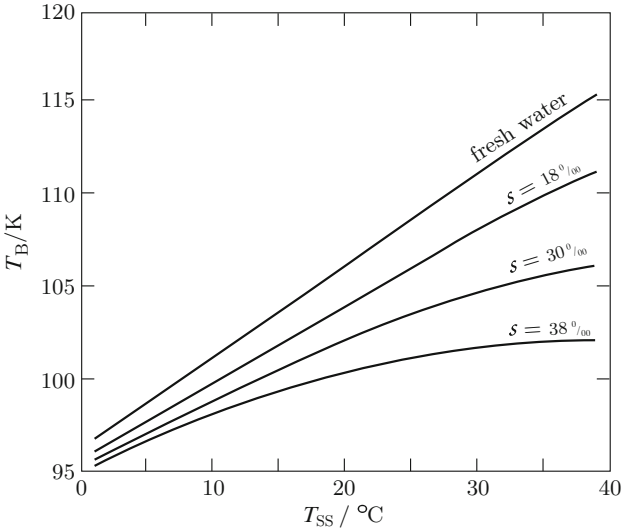

Fig. 14.60 Nadir brightness temperature T_B of sea vs. thermodynamic surface temperature T_{SS} for different values of salinity s at frequency $f = 2.65$ GHz (Curves interpolate data from [369, Chap. 18])

14.2.4.2 Radiometric Observation of Ocean Surface Wind

The surface roughness induced by the wind decreases the sea reflectance, thus increasing the emissivity, especially at horizontal polarization, high observation angles θ and high frequencies. It should be considered that high winds enhance emissivity also because they create a lossy low-permittivity foam layer over the water surface [250, 307, 377]. Figure 14.61 illustrates the sensitivity of the microwave radiometric measurements[39] to force [327] and direction [404] of sea surface wind, parameters of interest in meteorological modeling.

14.2.4.3 Radiometric Observation of Sea Ice

The emissivity behavior of sea ice [138] shows physical analogies with that of snow over land, since also in this case emission originates from an essentially layered structure, bounded by the ice-air upper interface and the ice-water lower interface. However, given the compactness of ice, volume scattering is relatively low and the reflectance is mainly affected by the features of the upper ice surface.

[39] Polarimetric measurements [405] are needed to fully characterize the polarization state of sea surface brightness temperatures, which carries information on the velocity *vector* of the surface wind.

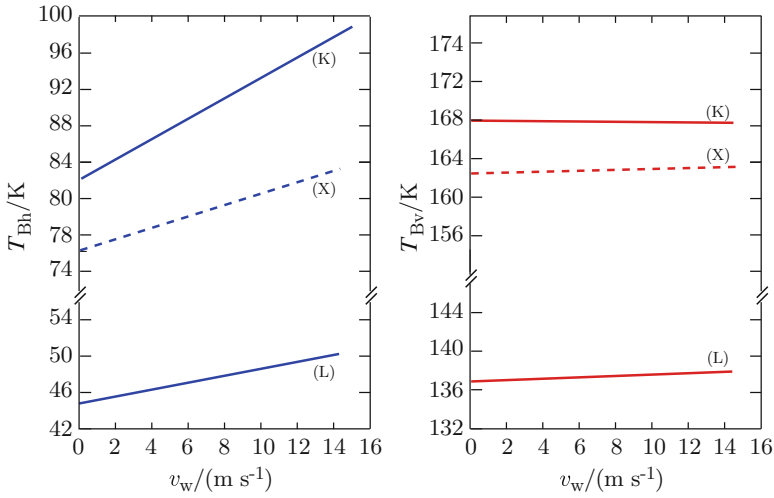

Fig. 14.61 Linearized trend of sea brightness temperatures T_{Bh} at horizontal (*left*) and T_{BV} at vertical (*right*) polarizations vs. surface wind speed v_w at different frequencies: (K), K-band; (X), X-band; (L), L-band; observation angle $\theta = 55°$; note the different ranges of T_B for the two polarizations (cf. Fig. 10.20) (Curves interpolate data from [369, Chap. 18])

Therefore, the microwave emissivity [100] of thick ice has a trend similar to that of a homogeneous half-space, being higher for vertical polarization, with a maximum in the neighborhood of the pseudo-Brewster angle (Fig. 14.62).

14.2.4.4 Radiometric Observation of Oil Slicks

An oil slick increases the brightness temperature of the water body, since the microwave permittivity of hydrocarbons (a few units for the relative real part, some hundredths for the imaginary part) is considerably lower than that of water. The oil layer forms a dielectric slab on the water half-space, as outlined in Sect. 6.5.1.1, hence a stationary field is created by the reflections from the oil-water and oil-air interfaces. Section 6.5.2 shows how the features of the stationary field depend essentially on the observation angle and frequency, as well as on the slick thickness. The emitted power, and in turn the excess emissivity over clean water, vary according to the amplitude of the field at the upper (oil-air) interface, resulting from the interference between the two waves traveling in the upward and downward directions in the oil layer. Oscillations of the brightness temperature are observed with the variation of the thickness of the slick, between a maximum value when the waves at the upper interface are in phase and a minimum when destructive interference (cf. Sect. 3.1.2) occurs. The relevant features of the trend of excess microwave brightness with the oil slick thickness are observed in the diagrams of Fig. 14.63. For this interference effect to occur, relatively thick oil layers must be observed at sufficiently high radiometric frequencies.

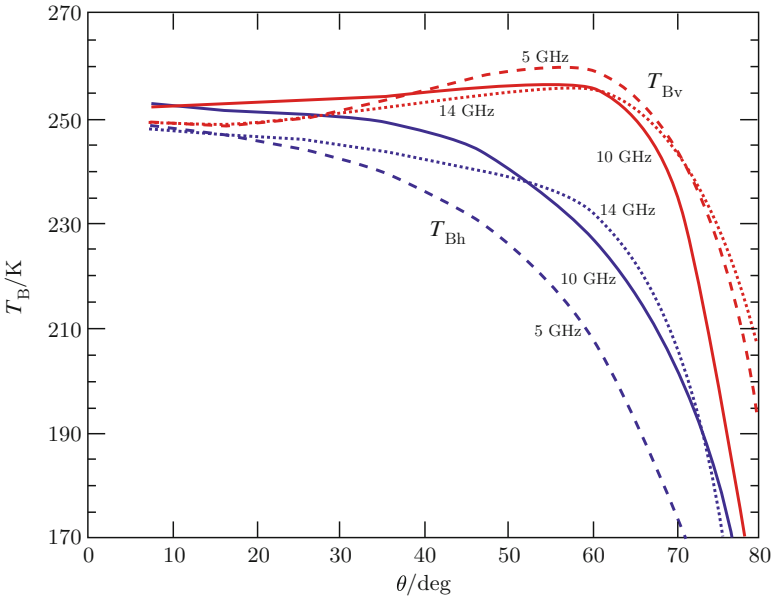

Fig. 14.62 Example of brightness temperature T_B of sea ice at horizontal (*lower curves*) and vertical (*upper curves*) polarizations vs. observation angle θ for C-, X- and K-band frequencies (Curves interpolate data from [113, Chap. 9])

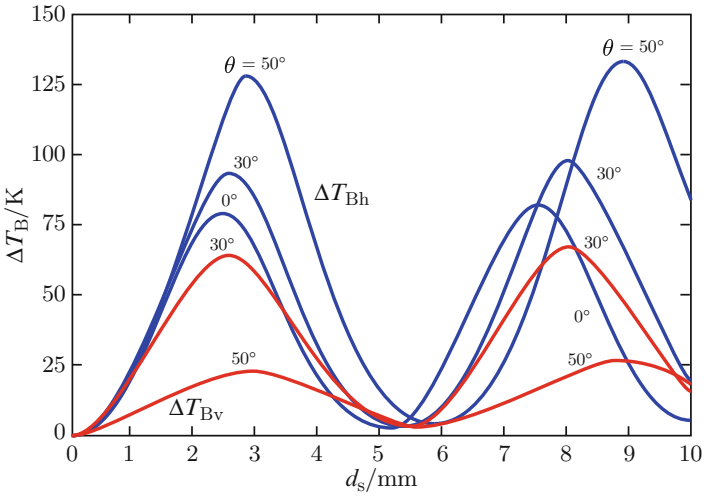

Fig. 14.63 Typical K-band excess brightness temperature ΔT_B on horizontal (*upper curves*) and vertical (*lower curves*) polarizations vs. sea oil slick thickness d_s for different observation angles θ (Curves interpolate data from [369, Chap. 18])

14.3 Interaction with the Atmosphere

The noxious role of the atmosphere in sensing the surface of the Earth from space has been discussed in Sects. 9.3 and 10.1.2.1. On the other side, Sect. 9.4 reverts the perspective by focusing onto observing the atmosphere and hinting at the complex and varied disturbing role of the surface background. In fact, the interaction between the probing electromagnetic wave and the atmosphere originating the signal exploited by the sensor is described by the same basic Eq. (9.40), the two terms of which interchange their role and have different expressions according to the type of system and of target. As for land, almost all the techniques of remote sensing are exploited, spanning the entire part of electromagnetic spectrum dedicated to EO, with less emphasis on the lower microwave range, perhaps balanced by the outreach into the **f**ar **u**ltra**v**iolet (FUV). Most of the basic wave-atmosphere interaction mechanisms that originate the useful signal clearly hold and the formalism outlined in Sect. 9.3 needs only tuning to the peculiar observation. In particular, subtle formalisms are generally required to cope at least with the three-dimensional distributed nature of the atmospheric targets.

The wave-atmosphere interaction spawns a variety of information on climatological and meteorological parameters of crucial interest to science, as well as to the everyday's life of human society [273]. The quantities observed from elevated (space-based or aerial) platforms include atmospheric temperature [156, 287, 383, 391] and moisture [150, 197] profiles, geometric and microphysical structure [38, 64, 271] and top altitude [141, 401, 403] of clouds [153, 243], precipitation [179, 344, 396], abundance of trace species [167] and aerosols [108], and air dynamics [262, 392]. On their side, weather radars are widespread ground-based systems the institutional role of which, in several countries also includes providing the community with images for public convenience and safety [258, 300].

14.3.1 Passive Observation of the Atmosphere in the Optical Range

The availability of passive sensors operating in the optical range, that is from the ultraviolet to the near infrared, with observations taken typically in the wavelength range $0.24\,\mu\text{m} \lesssim \lambda_0 \lesssim 3\,\mu\text{m}$, allows measuring the effects of the electromagnetic interaction with the various molecular species, as well as with particles of interest. The spectrum of the upwelling solar radiation observed by a space or aerial platform shows the combined absorption and scattering features of the molecules and particles present in the atmosphere, superimposed onto the "reflecting" spectral features of the Earth's surface. Information on the kind and corresponding abundance of the gas or of the particles to monitor is contained essentially in the spectral location, shape and intensity of the deviations of the observed reflectance from a reference background.

Atmospheric gas molecules, with size of the order of $D \approx 10^{-5}\,\mu\text{m}$ are sources of Rayleigh scattering (Sect. 7.2.1) in the ultraviolet and up to the blue in the visible spectral range, whereas their re-radiation becomes negligible at longer wavelengths. Aerosol and haze, the particles of which have dimensions D in the range $0.1\,\mu\text{m} \lesssim D \lesssim 1\,\mu\text{m}$, scatter from the UV up to the IR depending on their size. Scattering from cloud droplets, with dimensions up to some tens of micrometers, and from hydrometeors occur over the whole optical spectral range. In regard to the earth surface background, most natural surfaces have relatively low optical spectral reflectance (a few percent), with little angular dependence. Snow and ice, as well as some types of sand, are exceptions. The behavior of the water and land surfaces in the optical range has been outlined in the previous Sects. 14.1 and 14.2 which stress the variety of reflectances that are expected by the multiplicity of natural and man-made environments.

The reference model of interaction is the one outlined in Sect. 9.3.1, leading to the relation (9.46), which involves the contributions by the surface and by the atmosphere. The balance between the radiation "reflected" by the surface and the one originated by the atmosphere varies according to the wavelength at which the observation is carried out, because of the variations undergone by the several quantities that affect the spectral radiance that the elevated sensors measure. The information on the atmospheric parameters is contained in the albedo (9.34), the phase function (9.28) and the electromagnetic thickness (9.38). Coarsely speaking, the larger the value of the atmospheric contribution expressed by the second term in (9.46), the higher is the signal-to-noise ratio and the more accurate is the estimate of the quantities of interest, at least when the surface term is not known adequately.[40]

14.3.1.1 Observation of Trace Gases and Atmospheric Pollution

Remote spectrometry at ultraviolet, visible and near-infrared wavelengths is the basic tool to detect and monitor trace gases in the atmosphere [379]. The radiative transfer model including scattering expressed by (9.42) is clearly needed to interpret the spectra of the upwelling solar radiation in terms of abundance of trace molecules. The spectral features of absorption, which form a generally unique signature of the molecular species, must be singled out from the measured $\mathcal{I}_\lambda$ against the relatively stable spectral background of oxygen and water vapor, the scattering and absorption pedestal from clouds and aerosols and the "reflection" by the surface. It should be considered that the accuracy of the retrieval depends also on the temperature[41] profile, which is generally unknown but can be estimated from climatology and models. The general considerations and assumptions of Sect. 9.3.1 apply, bearing in

[40] It is understood that the effect of the surface requires consideration whenever assessing the measurement noise.

[41] Temperature affects the parameters of the spectral lines of the molecules, introduced in Sect. 2.2.1.

mind that the quantity of interest is now mainly contained in the optical thickness $\tau_o(\lambda)$ present in the terms of (9.42), or, alternatively, of (9.46). It is worth recalling that the second term in (9.42) represents the solar radiation scattered by the atmospheric constituents, including the contribution by the trace gases that are now the target of the observation, and that the thickness τ_o at the resonant wavelengths λ_{0tg} of the gas molecules contains the useful information, given its dependence on the abundance of these latter.

The measuring concept is that the atmospheric gaseous species interact with the electromagnetic radiation mainly through their absorption which depends sharply on wavelength, as illustrated in Sect. 10.1.2.1. Suitable techniques retrieve the quantity of interest by inverting the deviation of reflectivity observed at and outside the resonant lines of the considered molecules from the corresponding reference, or *first-guess*, values. Two main kinds of products are derived:

- the *columnar content*, that is the total amount of a molecular species contained in the normalized column of atmosphere over a given geographic location;
- the *profile*, i.e., the density of molecules as a function of height over the location.

In principle, the retrieval of a single quantity as the total content needs less data than the profiling operation, which requires measurements at a set of wavelengths at which the weighting functions defined in Sect. 9.4.1.1 are apt to generate averaging kernels (Sect. 10.2.2.2) able to scan the observed atmospheric layer.

The **d**ifferential **o**ptical **a**bsorption **s**pectroscopy (DOAS) [292] technique estimates the vertical column density of the trace gas from measurements of the reflectivity spectrum $\mathcal{R}_\lambda$ at different slant angles, corresponding to different values of air mass [139]. The DOAS combines with the Dobson's wavelength pairs method [35] based on taking measurements on pairs of wavelengths at which absorption is respectively strong and weak. Exploiting the rapid changing of the molecular absorption with wavelength reduces[42] the effects of the unknown background reflectance contributed by Mie and Rayleigh scattering, which vary with wavelength at a considerably lower rate.

Several molecules affect the properties of the Earth's stratosphere and troposphere through interrelated photochemical processes which alter the composition of the upper atmospheric layers and result in air pollution at the lower levels. Among the active species, ozone is extensively monitored, given the crucial role it plays in the biosphere evolution [349] and the concerning changes of concentration being observed both in the stratosphere and in the troposphere. Nitrogen oxides, which can severely affect air quality through oxidation mechanisms, are also subject of careful observation [225, 311]. Ozone is a major responsible of the atmospheric absorption in the ultraviolet, where the molecule presents two important bands, and in the visible range. Also NO_2 absorbs from the UV to the VIS, while NO_3 presents a pair of bands in the visible. Other trace gases of climatological relevance, such as BrO, OClO, and SO_2, present absorption bands in the UV range.

[42] Nevertheless, cloud screening is generally required.

Various space-based instruments operating in different observation modes provide spectrometric data in the ultraviolet, visible and near infrared spectral range, from which the concentrations of relevant trace gases are retrieved [30, 51, 275, 282]. The measurements at nadir [69] exploit the spectral features of the scattered and "reflected" solar radiation, as outlined above. Limb sounding [109] is based on the spectrum of the radiation scattered by the observed volume of air. On its side, the occultation technique [240] observes the absorption signatures in the directly transmitted sunlight[43] or starlight. The list of nadir-looking spectrometers in space[44] include **T**otal **O**zone **M**apping **S**pectrometer (TOMS) [263] on NASA's Nimbus [257], **G**lobal **O**zone **M**onitoring **E**xperiment (GOME) [1] on ESA's **Met**eorological **Op**erational Satellite (MetOp) [238], **Sc**anning **I**maging **A**bsorption Spectro**m**eter for **A**tmospheric **Ch**artograph**y** (SCIAMACHY) [329] on ESA's ENVISAT, and **O**zone **M**onitoring **I**nstrument (OMI) [18] on NASA's Aura [17]. SCIAMACHY has operated also as limb sounder [196, 242], a relevant example of which is the **O**ptical **S**pectrograph and **I**nfra**r**ed **I**mager **S**ystem (OSIRIS) [268] on the Swedish National Space Board's Odin [267], while **G**lobal **O**zone **M**onitoring by **O**ccultation of **S**tars (GOMOS) [126] that flew on ENVISAT, was a highly sensitive occultation-based instrument gaining information by observing the spectral features of stellar light propagating through the atmosphere. The NASA's **S**tratospheric **A**rosol and **G**as **E**xperiment (SAGE) instrument [320] on the **I**nternational **S**pace **S**tation (ISS) uses the solar occultation technique to measure not only ozone, nitrogen dioxide, and water vapor, but also stratospheric aerosols (Sect. 14.3.1.2.1).

14.3.1.1.1 Monitoring Space Weather

The physical state of the space environment surrounding the Earth, i.e., the *space weather*, impacts composition and density of the thermosphere and ionosphere [281]. Significant spectral signatures of the neutral and ionized molecules and connected processes fall in the FUV (115–180 nm) wavelength range [24], where the **G**lobal **U**ltra**v**iolet **I**mager (GUVI) [134] on the **T**hermosphere, **I**onosphere, **M**esosphere **E**nergetics and **D**ynamics (TIMED) [362] spacecraft, dedicated to the systematic exploration of the coupled ionosphere-thermosphere system, makes observations. The data [79] contain information on the morphology and dynamics of the inhomogeneities of density and composition of the ionosphere that determine the **t**otal **e**lectron **c**ontent (TEC) irregularities (ionospheric *bubbles*). It can be added that the UV observations contain information not only on the ionosphere-thermosphere system [232], but also on features of its connection with the underlying atmospheric region.

[43] The moon is also exploited as a secondary source of solar radiation.

[44] Including instruments on past missions.

14.3.1.2 Optical Passive Observation of Clouds and Aerosol

Clouds are formed by a variety of ice and/or water particles, the dimensions[45] D of which are distributed in a wide range, typically from estimated $D \approx 10^{-1}\mu\text{m}$ for condensation nuclei [90] in aerosol-to-cloud transition regions, to a few millimeters for drops[46] in rain. The broad distribution of particle size makes scattering weakly dependent on wavelength throughout the visible and near infrared interval. The upwelling radiation observed from space is the sum of the one originated by the "reflection" of sunlight from the surface and of that scattered by the crossed atmosphere. Under the assumption of low aerosol loading, the scattering contribution by the air can be neglected and the spectral radiance of a cloud-free area is approximated by the first term of (9.48):

$$\mathcal{I}_\lambda(\mathbf{s}_0) \simeq \mathcal{R}_\lambda(\mathbf{s}_0, \mathbf{s}_0^\odot)\, \mathcal{I}_\lambda^\odot(s_H)\, \mathrm{e}^{-(\tau_\mathrm{a}^\odot + \tau_\mathrm{a})} ,$$

i.e., $\mathcal{I}_\lambda$ is proportional to the spectral reflectance $\mathcal{R}_\lambda$ of the surface introduced in (8.27) and to the atmospheric attenuation, expressed by the exponential function of thicknesses over the downward and upward paths. On its side, the upwelling $\mathcal{I}_\lambda$ of a cloud-covered area is given by the second term of (9.42), if the total extinction by the cloud is sufficiently high to make negligible the contribution from the underlying surface. The observed spectral radiance originates along the electromagnetic path inside the cloud according to the profiles $\mathcal{A}_\mathrm{s}(s')$ of the albedo[47] (9.34) and $\mathcal{S}(s')$ of the phase function (9.28) determined by the local state (particle number density, size, shape and phase) of the hydrometeors in the bulk. The measured values are also functions of the spatial distribution of solar radiance $\mathcal{I}_\lambda^\odot(s')$ and of the optical thickness τ_o, which depend on extinction. When the latter is high, as it occurs in the visible if the cloud is not particularly thin, the upwelling spectral radiance originates only from the cloud's upper part, which can be identified with the *cloud top*. According to this model,

$$\mathcal{I}_\lambda(\mathbf{s}_0) \simeq \frac{\mathcal{A}}{4\pi}\, \mathcal{S}(\mathbf{s}_0, \mathbf{s}_0^\odot)\, \mathcal{I}_\lambda^\odot(s_H)\, \mathrm{e}^{-(\tau_\mathrm{at}^\odot + \tau_\mathrm{at})} , \tag{14.2}$$

where $\tau_\mathrm{at}^\odot$ and τ_at are now the optical thicknesses of the air from the top of the cloud[48] $z = z_\mathrm{t}$ to the top of the atmosphere $z = H_\mathrm{a}$, for the respective (sun and observation) directions. The radiance originated by the cloud clearly increases with

[45] A single dimension may be meaningless in case of the strongly asymmetric particles of ice clouds [16, 193].

[46] Hail is disregarded.

[47] The single-scattering approach is retained.

[48] Actually, z_t is a *radiative height*, indicative of the cloud top, given the problematic definition of the latter, especially in the diffuse case [350].

its albedo $\mathcal{A}$, but also with the height of its top, because increasing z_t reduces the optical thicknesses

$$\tau_{at}^{\odot} = \int_{z_t \sec\theta^{\odot}}^{H \sec\theta^{\odot}} \alpha_e(z)\,\mathrm{d}z; \qquad \tau_{at} = \int_{z_t \sec\theta}^{H \sec\theta} \alpha_e(z)\,\mathrm{d}z\,. \tag{14.3}$$

Scattering from clouds can be considerably higher than that from the surface.[49]

The radiance contrast readily provides a map of cloudiness of crucial interest to climatology, as well as to Earth observation [237, 248]. It can be added that the combined effect of the particles' size and nature and of the low extinction by the upper air especially highlights the loftiest cloud tops, of particular interest to meteorologists. Maps of cloudiness are acquired at short time intervals by instruments on geostationary platforms, which are able to observe the corresponding fraction of the terrestrial disc continuously. Figure 14.64 shows an example of cloud image at visible wavelengths highlighting the effect of height. The large radiance of the clouds

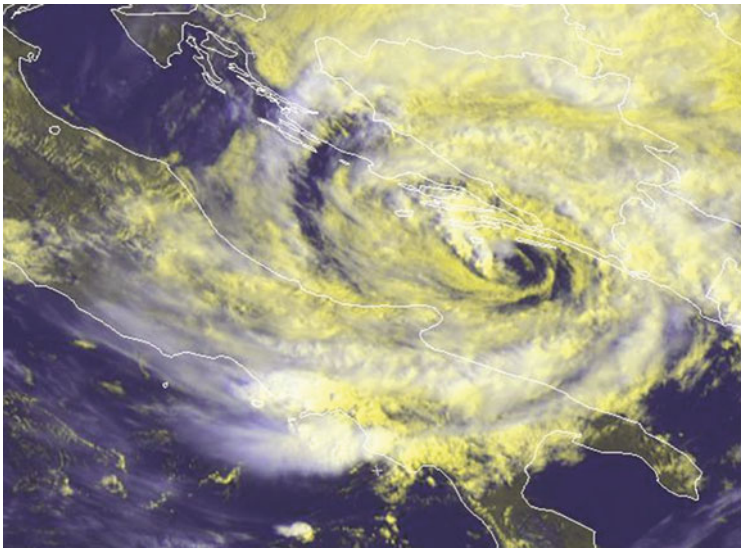

Fig. 14.64 Clouds over Italy and the Adriatic Sea mapped from observations at visible wavelengths: *bright white areas* denote high-radiance elevated clouds, lower clouds are *dull yellowish*, the low-radiance surface is *dark*; shadowing by clouds at different levels is also apparent (Credit: MSG Data, ©2013 EUMETSAT)

[49]For snow-free surface, outside sun glitter areas and with the exception of some kinds of low clouds.

stands up against the low scattering from the surface: the more elevated the cloud tops, the higher is the radiance observed through the thinner atmospheric layers.[50]

The satellite-observed radiances are interpreted not only in terms of the aforementioned macrophysical parameters, i.e., fractional cloudiness and pressure/height,[51] but also in terms of bulk cloud microphysical properties [244]. In particular, they are related to the key parameters *optical thickness*, particle (droplet or ice crystal) *effective dimension* and hydrometeor *thermodynamic phase* (liquid, melting, or frozen), which affect the reflectance of the clouds, hence, impact the Earth's radiation budget and, ultimately, the climate. The characterization of the cloud microstructure is based on the full model (9.42) or, when applicable, (9.48), relating the cloud parameters, contained in the reduced term (14.2), to its radiative properties. The latter are embodied by reflectance and transmittance,[52] which are obtainable from measurements of the downwelling and corresponding upwelling radiation at different wavelengths [62, 243].

It can be added that satellite instruments operating at the wavelengths at which the radiation emitted by the ionized air molecules are better distinguishable, detect and locate lightning [128, 293], thus providing significant information on deep convection activity in cloud systems (Sect. 14.3.2).

14.3.1.2.1 Optical Passive Sensing of Aerosols

Aerosols denote the ensemble of liquid or solid particles suspended in the atmosphere, with the exclusion of the water droplets and ice crystals forming the clouds.[53] Aerosols are of both natural (sea salt particles launched from bursting bubbles, wind-blown dust, organic matter in smoke from wild biomass combustion) and anthropogenic (mainly industrial and automotive emissions) origin and tend to concentrate in the lower troposphere. The aerosol mass concentration in the atmospheric boundary layer affects air quality [375] and the microclimatic radiative field, with possible adverse human health impacts, while the particles injected into the stratosphere mainly by volcanic eruptive events, may impact the climate evolution[54] at global scale [107].

[50] Enhanced radiance is also due to high density of ice particles, correlated, albeit coarsely, with height.

[51] The height of a cloud estimated from spectral radiance data (the radiative height) is often considerably below the "physical" height of the cloud top boundary.

[52] Clearly the radiative characterization of a cloud requires the observation and analysis also of its emissivity properties.

[53] The nucleation and growth phenomena in clouds [297] make difficult the clear-cut separation between aerosols and hydrometeors [192].

[54] The particles in tropospheric volcanic plumes also call for careful identification and mapping, given the threat they pose to air traffic [290].

Aerosols affect the upwelling optical radiation in a fashion quite similar to clouds. The mixture of akin spectral responses, superposed on the surface radiative background, may hamper the retrieval of the aerosol properties by space-based optical passive measurements [74, 225]. As for clouds, radiative transfer schemes, now including aerosol models, are the basis of the estimates [73]. It is worth cautioning that understanding cloud-aerosol interactions is a major challenging issue [345].

14.3.2 Radar Observation of Clouds and Precipitation

The inherently three-dimensional nature of the atmosphere makes active techniques particularly fit to its observation, as mentioned in the introductory Sect. 11.4.3.1. The range discrimination capability intrinsic in the radar systems allows 3-D mapping of clouds and precipitation without resorting to more or less cumbersome profiling procedures. Moreover, although scattering is the origin of information like at optical wavelengths, the coherence properties of the radar source as well as the Doppler (Sect. 3.1.1.3) and polarimetric capabilities [34] of the system can be exploited to gain a richer set of information than it is possible from the incoherent and relatively unpolarized solar radiation. The data collected by the radars both from the Earth's surface and from space platforms provide information on the initiation [29], composition and temporal and spatial features of precipitations [66, 233], as well as on the interconnected atmospheric moisture field [313] and cloud dynamics [25, 159, 208].

The basic radar operation [296] outlined in Sect. 11.4.3.1 relates the received power W_r to the backscattering cross-section σ_b of the meteorological target [133] through (11.41). The atmospheric target now consists of a three-dimensional distribution of scattering hydrometeors[55] filling the resolution cell of volume V' considered in Sect. 11.4.3.2 and sketched in Fig. 11.24. The wave radiated by the radar impinges onto a generally large ensemble of individual objects, such as rain drops, which originate the scattering in the backward direction. Given the random space-time arrangement of the scatterers, the re-radiated power is the sum of the power contributions from the single particles in V', as considered in Sect. 7.4.1. Therefore, the backscattering cross-section of V',

$$\sigma_\mathrm{b} = \sum_{i=1}^{N} \sigma_{\mathrm{b}i}$$

[55] Observation of the clear atmosphere [14], [112, Chap. 7] is not considered here.

is the sum of the average[56] backscattering cross-sections σ_{bi} of the N particles in V'. In radar meteorology, the *radar reflectivity* η is introduced as the cross-section of the unit volume

$$\eta = \frac{1}{V'} \sum_{i=1}^{N} \sigma_{bi} \ ,$$

under the assumption that the scattering particles are uniformly distributed in V'. According to the results of Sect. 11.4.3, the received average power originated by the atmospheric resolution cell at distance R from the radar is

$$\overline{W_r} \simeq \frac{\eta_A^2 A_g^2 W_T}{4\pi \lambda_0^2 R^4} V' \eta(R) \, e^{-2\int_0^R \alpha_e(\lambda_0, s)\, ds} \ , \tag{14.4}$$

The extinction coefficient α_e in (14.4) is given by the volumic extinction cross-section (7.20), dependent on the local density of scattering and absorbing hydrometeors present along the path between the radar and the scattering volume[57]:

$$\alpha_e(\lambda_0, s) = \frac{1}{V} \sum_{i=1}^{N(s)} \sigma_{ei}(\lambda_0, s) \ .$$

where $N(s)$ is the number of particles present in the generic volume V at distance s from the radar location.

The cross-sections σ_b and σ_e of a single particle are functions of its shape, dielectric structure and dimension, as well as of wave frequency and field polarization. Under simplifying assumptions, σ_b is related to the refractive index and to the diameter D_i of an equivalent sphere that represents the scattering behavior of the particle, so that, in the Rayleigh scattering regime,[58] the radar reflectivity is expressed in terms of the particle dimensions. In particular, η is proportional to the *reflectivity factor* $\mathcal{Z}$ defined by

$$\mathcal{Z} := \frac{1}{V'} \sum_{i=1}^{N} D_i^6 \ . \tag{14.5}$$

The value of definition (14.5) resides in the property of the reflectivity factor of being a function of the water contained in the unitary scattering volume, both in the

[56] Average is required because the hydrometeors, the shape of which is not spherical and changes with time, are oriented in a nearly random fashion.

[57] The air absorption is assumed negligible at the radar frequency.

[58] The radar wavelength is assumed large with respect to the dimensions of the cloud particles.

form of liquid and of ice. This feature allows mapping the precipitation intensity $\mathcal{R}$ through empirical expressions [137] of the form

$$\mathcal{Z} = A_{\mathcal{R}} \mathcal{R}^{b} \,, \tag{14.6}$$

where $A_{\mathcal{R}}$ and b are suitable parameters. Equation (14.6) is the very basic relation for producing rainfall maps over extended areas from data acquired by ground-based [13, 230, 398] and space-borne radars [127, 199].

The satisfactory retrieving of the rain parameters from the received power is subordinated to a sufficiently accurate estimation of the attenuation introduced into (14.4) by the back and forth path between radar and observed atmospheric target. Clearly, the latter is not a solitary group of particles in air, rather it is just a small portion of a large region crowded of hydrometeors, and, furthermore, the interaction mechanism originating the useful backscattered power is the same as the one causing attenuation. This implies that increasing backscattering goes along with decreasing useful signal. The hindrance can be mitigated by observing polarization and phase features of the field by multi-parameter radars. However, the model, system and calibration requirements for enhancing the accuracy of rainfall estimates are rather strict and, mainly, frequency-dependent.[59]

Large-scale measurements of rainfall are routinely performed by ground-based high-power polarimetric systems operating at relatively low microwave frequencies (C- and, especially, S-band), at which the long-range rain-path attenuation does not quench the signal. Dual-polarization X-band ground-based radars are used to detect and monitor severe weather phenomena on limited areas with enhanced sensitivity and, like systems at higher frequencies, are mainly apt to short-range observations of fine details of precipitation [185, 210], which clearly merge with the microphysics of clouds [61] mentioned in Sect. 14.3.1.2. It is worth mentioning that the scattering cloud particles, which are directly sensed, are tracers of the air motion, so that the wind field in weather systems is also retrievable by Doppler radars [299]. Indeed, besides synoptic rainfall products, radar observations yield effective information on the detailed structure of mesoscale weather systems [119, 347, 353]. At a fine scale, the time-space changes of the observed reflectivity result in three-dimensional dynamic maps of the cloud properties, from which the processes taking place in storm cells are monitored [301].

On their side, space-borne radars monitor precipitation on a global scale [355]. Given the observation geometry, the attenuation along the path is not a limiting factor, hence relatively high microwave frequencies (K-band) are employed, with ensuing enhanced response to the cloud internal processes that affect the precipitation formation. Extending the frequency range to the W-band allows also profiling the vertical structure of complex cloud systems [241]. Figure 14.65 depicts the

[59] Given the dimensions D of the rain drops, ranging from hundreds of micrometers to a few millimeters, rain backscattering, as well as path extinction, are both increasing functions of the radar frequency.

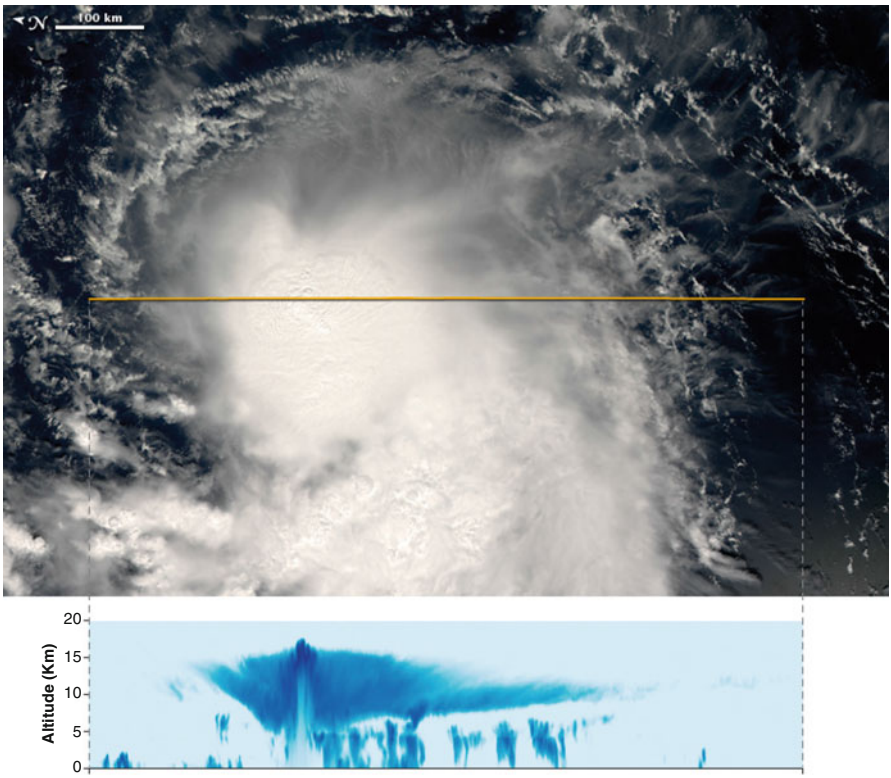

Fig. 14.65 Optical (MODIS, *top*) and 94-GHz radar (CloudSat, *bottom*) profile of Tropical Storm Leslie: the radar reflectivity (increasing from *light* to *dark blue*) along the transect highlights the detailed structure of the precipitating cloud system; the accumulation zone, where a particularly high density of water is present, corresponds to the high reflectivity vault overarching the low-reflectivity updraft large funnel (NASA Earth Observatory image by Jesse Allen, using CloudSat FirstLook August 31 2012 data, provided courtesy of the CloudSat team at Colorado State University)

impressive structure of a quite large tropical storm along a space-borne radar-imaged[60] transect across the center of the convection, where the strong updraft creates the large *vault* above which the high-water density *accumulation zone* is visible.

It can be added that radars installed on aerial platforms [378] join ground- and space-based systems in observing the three-dimensional wind field in storms, concurrently with the cloud microphysics. This latter appears to be interrelated both

[60]This radar uses a 3-mm wavelength, favoring mapping sensitivity with respect to quantitative measurement.

with precipitation and with lightining [219, 306], which is essentially located in the areas of intensive convection within extended storms.

14.3.2.1 Lidar Observation of Aerosols and Clouds

Monitoring the vertical profiles of clouds and aerosols is crucial to determining their mutual interaction as well as the impact they have on the Earth's radiative field. Section 14.3.1.2.1 mentions that the properties of aerosols are retrieved from passive measurements taken from space platforms in the optical range in cloud-free areas, whereas the overlapping of the spectral features of the clouds with those of the aerosols makes difficult untangling the respective contributions. Unlike radars, lidars operate at wavelengths at which the interaction of radiation with the aerosol particles is substantial and originates measurable backscattered power. The basic modeling is analogous to the one outlined for the radar response to hydrometeors, hence, in particular, (14.4) applies with a few straightforward substitutions. The heights of the aerosol layers are singled out from those within which the clouds develop thanks to the range discrimination capability of the active systems. Space borne sensors, such as NASA's lidars **C**loud-**A**erosol **L**idar with **O**rthogonal **P**olarization (CALIOP) [400] aboard the **C**loud-**A**erosol **L**idar and **I**nfrared **P**athfinder **S**atellite **O**bservations (CALIPSO) mission and **I**ce, **C**loud and Land **E**levation **Sat**ellite (ICESat) [165], address global-scale monitoring of aerosols.

Given the relatively high extinction by the liquid or ice particles,[61] a lidar gains information mainly on the outer (top or base, according to the position of the system) boundary of the denser clouds. Top height along transects are directly observed with enhanced spatial resolution by space-based or aerial instruments, while cloud-base data clearly refer to a limited single area in correspondence of the ground-based lidar location. The inner structure and possible layering parameters of clouds that are not opaque at the lidar wavelengths are also retrieved [146].

14.3.3 Observation in the Thermal Infrared

Space- or air-based radiometric observations in the thermal infrared exploit spontaneous emission[62] to gain information also on meteorological features and on composition and thermal structure of the atmosphere. The upwelling spectral radiance is now approximated by (9.53) within the common frame model introduced in Sect. 9.3. Analogously to the observations in the optical range introduced in

[61] Apart from cirrus clouds.

[62] Active observations by CO_2 lidars operating at wavelengths in the thermal infrared are not considered here.

Sect. 14.3.1, the information of interest is contained in the distributed atmospheric contribution of thermal radiation expressed by the second term in (9.53). Different types of parameters are extracted from the received radiance, according to the focus of the observation.

14.3.3.1 Mapping Clouds and Water Vapor

When a cloud-free area is observed at the wavelengths at which the gaseous atmosphere is sufficiently transparent, the generally large values of the emissivity e_S of the surface (Sect. 10.2.2.1) in conjunction with its relatively high temperature[63] enhances the first term of (9.53), while the second term is correspondingly low, because of the small value of the emissivity e_T of the low-loss (at these wavelengths, clearly) atmospheric constituents. The relative magnitudes of the two terms reverse when a cloudy area is observed. The extinction caused by the particles forming the clouds increases the electromagnetic thickness τ_a, thus quenching the contribution from the surface, while their absorption increases e_T, hence the emission originating from the atmospheric path. The atmospheric contribution depends on the height distribution both of the geometric features and of the density of the liquid water or ice cloud particles, as well as on the co-located temperature profile.[64] Therefore, nature and height of the clouds affect the balance between the two terms of (9.53) and the corresponding contrast between clear and cloudy areas.

Following the common approach as in Sect. 14.3.1 and assuming negligible the optical thickness of the atmospheric path, the radiance of a cloud-free area is

$$\mathcal{I}_\lambda \simeq e_S \, \mathcal{B}_\lambda(T_S) \ ,$$

while the radiance of a cloudy area is approximated by

$$\mathcal{I}_\lambda \simeq \mathcal{B}_\lambda[T(z_c)] \ , \tag{14.7}$$

if the extinction by the cloud particles is high. The quantity z_c in (14.7) denotes a *radiative* height close to the top of the cloud, as discussed in Sect. 14.3.1.2. Given the high values of the surface emissivity e_S, the difference of the measured radiance between clear and cloudy areas is essentially determined by the difference between the temperatures of the surface and those of the cloud tops. Therefore, the more direct information carried by the observations in the thermal infrared is on the cloud height [246], obviously provided approximation (14.7) holds. Ultimately, several relevant structural features of cloud systems are well rendered by thermal infrared images acquired at wavelengths at which the gaseous atmosphere is

[63] The case of extremely cold surfaces is left out.

[64] This model is oversimplified in case dense clouds are involved, because the substantial scattering occurring in the bulk requires using (9.42) in place of (9.53).

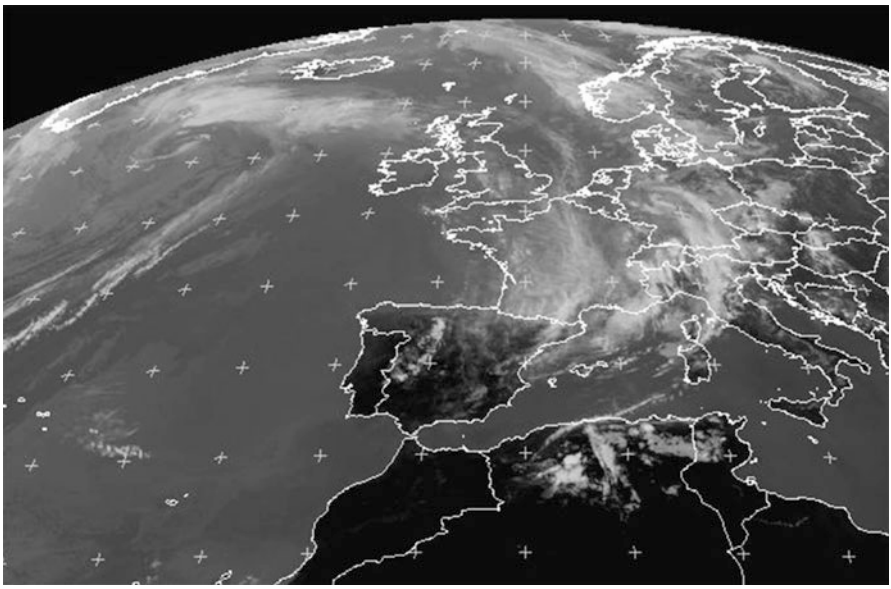

Fig. 14.66 Image acquired at $\lambda_0 \approx 10.8\,\mu\text{m}$ highlighting the distribution of clouds over parts of Europe and North Africa; *dark* denotes high-radiance (oppositely to Fig. 14.64) cloud-free areas, *light* corresponds to low-radiance high clouds (Meteosat Data ©2013 EUMETSAT)

sufficiently transparent (Sect. 10.1.2.1.1), often without need of further sophisticated processing.[65] Figure 14.66 shows an example of the map of spectral radiance in a TIR atmospheric window (cf. Fig. 10.4). The dark areas indicate high values of spectral radiance, hence they correspond to the exposed surface, while the more or less bright areas denote clouds. For a smooth understanding of this kind of images of the atmosphere, it is important to bear in mind that the relation between observed *thermal* radiance and cloud height is the opposite to the one between *optical* radiance and height seen in Sect. 14.3.1.2, given the diverse locations of the primary sources of radiation. Coarsely speaking, the lower the radiance, the higher is now the top of the cloud. It is understood that care must be exerted in interpretation, since cloud covers that are not sufficiently opaque to mask the surface contribution, or that are at low altitudes, yield lesser radiance contrast. Multi-spectral observations clearly have discrimination capability in this respect, so that the distribution of height is retrieved.

Observation at wavelengths affected by gaseous absorption results in images having similar features, since the emission by the cloud particles is replaced by the absorption by the gas molecules, roughly without modification of the radiative transfer mechanism, still modeled by (9.53). Mapping the spectral radiance in the

[65] Different heights of cloud tops are obtained by the CO_2 slicing technique, which exploits [188] the absorption increasing with wavelength around $\lambda_0 = 14\,\mu\text{m}$ (Fig. 10.6).

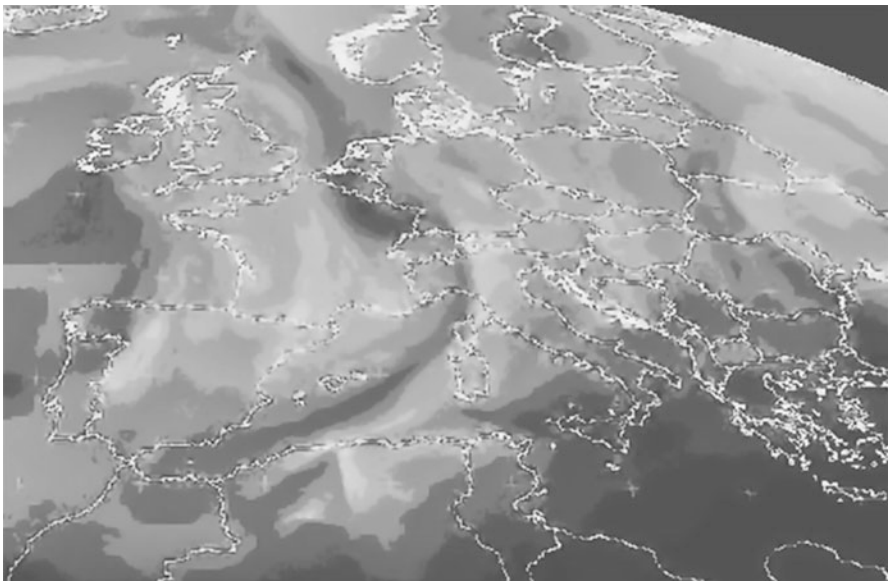

Fig. 14.67 Image acquired at $\lambda_0 \approx 6.4\ \mu$m highlighting the distribution of atmospheric water vapor over parts of Europe and North Africa; *dark gray* denotes low water vapor, *light gray* corresponds to high values (cf. Fig. 14.66) (Meteosat Data ©2013 EUMETSAT)

neighborhood of the water vapor absorption lines highlights the distribution of atmospheric moisture. Areas over which the columnar water vapor is low, essentially show the large radiance of the surface, given the small value of the "optical" thickness τ_a that weakly attenuates the first term of (9.53). An increasing moisture content reduces the surface radiance, while raising $e_T(z)$, hence the contribution originating from the "colder" atmospheric path.[66] Figure 14.67 depicts the atmospheric water vapor pattern through the radiance measured at $\lambda_0 \approx 6.4\ \mu$m (cf. Fig. 10.7). As the amount of vapor increases, the concurrently enhancing absorption and emission lower the measured radiance,[67] in accordance with the co-located temperature and vapor density profiles which affect the second term of (9.53). It is worth noting that the map of the spectral radiance at $6.4\,\mu$m in Fig. 14.67 has a general appearance more diffused than that of the contemporary $10.8\,\mu$m radiance map of Fig. 14.66. Indeed, the clouds can be considered a concentrated outcome of the excess moisture, taking place locally in the bulk of the humidity field. In particular, the water vapor tends to show a diffuse pattern with no sharp boundaries and, mainly, without more or less definite tops as the clouds do. This latter aspect suggests that the approximation (14.7) is instrumental for a simple interpretation of the cloud radiance maps, but extending it to water vapor imaging has little meaning,

[66] In the frequently encountered case $T(z) < T_s$.

[67] Again, the case of particularly cold surfaces is not considered.

given the substantially lower extinction of the vapor with respect to the one of the hydrometeors.

In addition to synoptic maps, TIR observations provide information on cloud physical properties, provided the extinction is sufficiently low to allow penetration in the bulk. The thermodynamic phase of cloud particles is identified thanks to the diverging behavior of the imaginary parts of the permittivity of liquid water and ice for wavelengths $\lambda_0 \gtrsim 10\,\mu\text{m}$ [348, 406]. Extending the wavelengths of observation into the FIR spectral region provides additional information that enhances the particle phase discrimination potential of measurements taken both from space and from ground [304].

A final remark regards the monitoring of emission of ash, aqueous aerosol and gases from volcanos [316], demanded by transportation, infrastructure and human security (cf. Sect. 14.3.1.2.1). The TIR key feature that allows discriminating the volcanic clouds against the undisturbed background is the transmissivity, which shows spectral patterns peculiar to each ejected substance [67, 385].

14.3.3.2 Atmospheric Sounding in the Thermal Infrared

The concept of weighting functions introduced in Sect. 8.1.4 and further discussed in Sect. 9.4 is the basis for collecting quantitative information on the thermal vertical structure of the atmosphere as well as on its composition.

The 15 and 4.3 μm absorption regions of the CO_2 molecule (Fig. 10.6) are mainly exploited by the satellite infrared thermal sounders, because of the relative stability of this absorbing atmospheric constituent.[68] The contribution by the atmosphere to the spectral radiance (9.53) measured in the thermal infrared at the angle ϑ is written as

$$\mathcal{I}_\lambda(\vartheta) = \int_0^H \mathcal{W}_\text{T}(\lambda_0, \vartheta, z)\, \mathcal{B}_\lambda[T(z)]\, \text{d}z\ .$$

For given ϑ, the weighting function $\mathcal{W}_\text{T}$ depends on the profile of the emission (and corresponding absorption) coefficient $e_\text{T}(\lambda_0)$. Sets of measurements are taken in the neighborhood of wavelengths at which the absorption differs so that $\mathcal{W}_\text{T}$ peaks at different heights, which means that the different receiving channels pick up the thermal information mainly from different altitudes. The height-discrimination capability is enhanced by suitable retrieval algorithms, able to synthesize *averaging kernels* [20], which maximize the sensitivity to the temperature profile.

Thermal profiling is an essential but not the only task performed by satellite thermal infrared sounders. Atmospheric moisture profiles are an additional product of great relevance to operational meteorology. The water vapordensity affecting

[68] This is a first-order approximation: indeed, the CO_2 background shows seasonal and geographical variability, in addition to its long-term trend.

the profile of the emissivity/absorption coefficient $e_T(z)$ is now the unknown quantity in (9.53). Retrieval of vapor requires measurements at wavelengths in the absorption region around $\lambda_0 \approx 6.4\,\mu\text{m}$ at which the radiation strongly interacts with the H_2O molecule (Fig. 10.7). As for the temperature, the measurement channels include spectral intervals which are especially sensitive to the vapor in layers of the atmosphere located at different altitudes. The height distribution of moisture is estimated by synthesizing the corresponding averaging kernels from the wavelength-dependent absorption. The retrieval process clearly requires at least a first-guess knowledge of the temperature profile, and often is based on a recursive scheme.

Thanks to their large number of channels, instruments such as the NASA's **G**oddard **E**arth **S**ciences **D**ata and **I**nformation **S**ervices **C**enter (NASA GES DISC) NASA/JPL's **A**tmospheric **I**nfra**r**ed **S**ounder (AIRS) [5] have the additional capability of mapping carbon trace gases such as CO_2 [221] and CO, as well as ozone and methane in the middle-to-upper troposphere on global scales. It is worth mentioning that the estimate of the various geophysical parameters and quantities is often carried out concurrently, since the profiles of the constituents and of temperature are coupled together in the radiative transfer model. Moreover, the infrared instruments are generally complemented with microwave sounders, which are able to contribute further pieces of independent information on the state of the atmosphere. The dynamics of the latter is also obtained by tracking the clouds the tops of which have been assigned to different levels, thus gaining information on the wind vectors at the various altitudes [236].

14.3.4 Passive Sounding at Microwaves

Profiles of air temperature and moisture are retrieved from microwave measurements taken from elevated or ground-based radiometers, clearly with less interference from non-precipitating clouds than TIR observations. Information on the atmosphere is gained from measurements at frequencies at which the interaction with the air gases makes the second term in (9.56) or (9.57) significant and exploitable. Radiometers aboard satellites measure the upwelling radiation at a number of wavelengths such that *stable* averaging kernels are synthesized. In particular, the **A**dvanced **M**icrowave **S**ounding **U**nit-**A** (AMSU-A) [10] instrument takes measurements in the 50–60 GHz oxygen band, in addition to the 23.4 GHz water vapor line and two frequencies at which no appreciable gaseous absorption occurs. The AMSU-A, which is primarily a temperature sounder, has operated in conjunction with sensors exploiting the 183 GHz water vapor line, such as the AMSU-B [332], the **D**efense **M**eteorological **S**atellite **P**rogram (DSMP) **S**pecial **S**ensor **M**icrowave **T**emperature-2 (SSM/T-2) [82], or the **H**umidity **S**ounder for **B**rasil (HSB), which

are essentially humidity sounders.[69] The data affected by the absorption features of oxygen, as well as of water vapor and liquid, carry information on temperature and moisture profiles, as well as on the vertical distribution of liquid water in clouds. The ground-based radiometric profilers yield the vertical distributions of temperature and water vapor from multi-frequency measurements [55, 70], although angular probing [390] is also carried out, especially for monitoring the static and dynamic state of the boundary layer [174].

Much of the preceding discussion regarding thermal infrared sounding can be extended to the microwave passive observations, which take further practical advantage of the Rayleigh-Jeans approximation (8.39). Summarizing, with respect to the observations in the TIR, the interpretation of the microwave data profits from the linear relation of the measured radiance with the thermodynamic temperature and from the negligible amount of scattering by the clear atmosphere. However, the relatively high contribution from the surface may harm the retrieval over land, given the uncertain knowledge of temperature and emissivities of the different surface types, especially under variable cloud cover [98].

A final remark regards the extension of the limb sounding technique to measure the emission in the millimeter and sub-millimeter wave spectral ranges. The **E**arth **O**bserving **S**ystem **M**icrowave **L**imb **S**ounder (EOS MLS) [222, 384] observes stratospheric parameters, trace gases and constituents, including ozone and water vapor, which present absorption/emission lines in these regions of the spectrum.

14.3.4.1 Mapping Rain by Microwave Radiometry

Section 10.2.3.1 points out that the surface of the Earth can show very low values of brightness temperature at microwaves, as it appears distinctly in Figs. 10.20 and 10.21. The figures indicate that T_B over the ocean increases in the areas where intense cloudiness occurs, as in the Intertropical Convergence Zone, which experiences considerable precipitation. The low emissivity values of the water bodies imply a high reflectance, given (8.42). Therefore, the brightness temperature observed over the water surface results from the attenuated emission by this latter and from the upwelling and reflected downwelling atmospheric radiation. The generally lower reflectivity of land weakens the contribution of the reflected downwelling radiation. The latter term is often negligible in the infrared because the surface reflectivity is generally quite low, but at microwaves, the concomitant effects of emission and reflection makes the surface a highly variable background, with emissivities in the $0.5 \lesssim e_S \lesssim 1$ range, against which the atmosphere is observed.

The microwave brightness temperature of rain-free areas is close to that of the surface, thus low over the ocean, generally high over land, consistently with the outline of Sect. 10.2.3.1. Dense clouds and rain increase the absorption, hence the electromagnetic thickness (9.58) of the atmosphere and, at the same time, its

[69] The HSB instrument broke down in 2003

emission coefficient. Therefore, on one side the first term of (9.57) decreases, while, on the other, the second term increases. The balance between the contributions from surface and atmosphere determines the difference of brightness temperature between clear and rainy areas. Apart from polarization, the difference is clearly dependent on the frequency of observation [338], which affects both the emissivity of the surface through its permittivity and roughness and the absorption/emission coefficient of the atmosphere. At frequencies lower than the oxygen band mentioned in Sect. 2.2.1, the clouds increase the brightness temperature over the ocean, while they decrease it over land, given the relatively high emissivity of this latter. The magnitude of the effect depends on nature and temperature of the land surface and on the vertical profile of the cloud density. Rain enhances the brightness temperature variability, especially when considerable amounts of large scattering ice particles gather around the tops of precipitating clouds [131].

Rainfall estimation from space can be carried out through empirical relations with the spectral radiances measured in the optical portion of the spectrum, which, as discussed in Sect. 14.3.3.1, essentially originate from the top of the clouds. With respect to the optical observations, microwave measurements are in a more direct relation with the amount of water, given the ability of relatively large wavelengths to interact with the bulk of precipitating clouds, consistently with the results of Sect. 9.1. Modeling the microwave radiation field in hydrometeors [115, 254] is made difficult by a number of factors, including the proximity of the wavelength to the particles dimensions, the wide range of sizes and shapes [84, 118], the liquid/ice coexistence [152, 336] and the complexity of the concentration and temperature spatial structures [143, 312], especially in convective complexes [158, 220].

The frequencies at which the space-based radiometric observations are carried out span the range from 10 to 183 GHz. The microwave brightness carries some information on the amount of water present at different heights. In particular, sets of dual-polarization measurements at both lower and higher K-band frequencies perform satisfactorily in measuring liquid water in precipitating cells over adequate dynamic ranges. On their side, the millimeter-wave data add information on water vapor. The NASA/JAXA's **G**lobal **P**recipitation **M**easurement (GPM), like its predecessor **T**ropical **R**ainfall **M**easuring **M**ission (TRMM), carries out the rainfall observations by actually combining microwave passive measurements[70] with K_u and K_a radar data [198, 228, 366]. Figure 14.68, depicting a product of TRMM,[71] provides an example of the precipitation mapping capability of systems of this kind [122].

With respect to TIR sensing, the coarser spatial resolution of microwave real-aperture antennas leads to *beam filling* effects [129], with more frequent occurrence of mixed pixels, resulting in less distinct image features. Dealing with the different spatial resolutions of the measurements taken at different frequencies is a quite

[70] Measurements in the visible and infrared complement the microwave observations.

[71] Additional data from other satellites and sources are merged with the precipitation radar measurements to extend the operational latitude range of the mission [162].

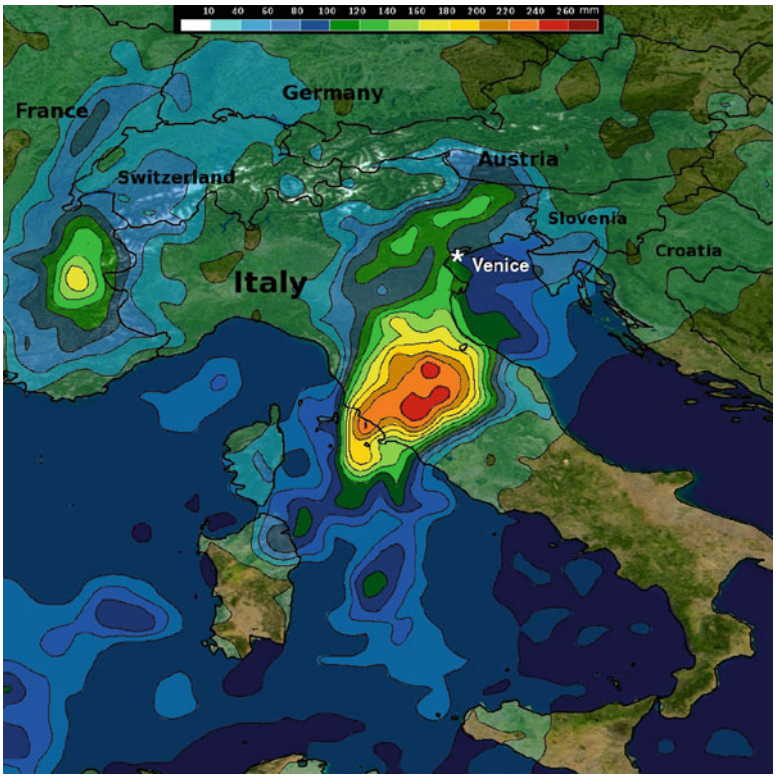

Fig. 14.68 Map of TRMM-derived cumulative rainfall over Italy for a 7-day period, showing in *red* the areas of Tuscany that received a particularly high amount of precipitation. TRMM is a joint mission between NASA and JAXA (Image produced by Hal Pierce (SSAI/NASA GSFC))

common problem to solve when retrieving cloud properties and rainfall from multifrequency passive microwave observations [303].

Paving the Road to Applications

We learned about wave-target interaction and how the systems observe the result of the interaction, so we gained some ability in comprehending the information contained in the observations. The remaining step regards the conversion of the remote measurements into the bio-geo-physical parameters that we may need for applications, in our role of EO users or decision makers. We can approach this issue with the confidence that the unified wave-medium interaction frame can reduce the risk of misinterpretation or of inadequate processing leading to dubious operational results. A number of theoretical and experimental results are displayed

and discussed on the basis both of the kind of interaction and of the type of observation technique. In a sense, we are presented with a systematic catalogue of techniques and spectral bands, to which we can anchor our enlightenment and practice. This kind of catalogue is relatively comprehensive of the basic interaction with the Earth's main materials and sceneries, but it is by far short with regard to the myriad of applications found by remote sensing data. From the users' point of view, the selection of the items in the following overview, however necessary, may appear deficitary and questionable.

Data taken on bare land are of interest to mineralogists, who exploit the spectral features of reflectance or of emission for mapping resources, including mineral identification. We got suggestions on how advanced precision farming can be grounded on data delivered by almost all kinds of remote sensing systems. Analogous considerations hold for urban planners and ecologists, as well as, on an enlarged scale, for climatologists. Observation of snow cover, the periodically evolving water reservoir of several regions of the world, is relevant to hydrology and to hydroelectric power generation. The capacity of human society to respond to emergency situations, to reduce the loss of lives and to mitigate damages, also decidedly relies on Earth observations data. From the heterogeneity of the presented results we strengthen our conviction that choosing the right EO product for the given land application demands careful analysis of the many facets of the acquisition process, from the information content of the data, linked to sensor type and wavelength, to the spatial and temporal resolutions.

The data on the ocean color originate from the wavelength-dependent interaction of solar radiation with the biological or mineral substances and particles in the water. The information they provide is used in mapping ecological and biochemical parameters of the water bodies, as well as in monitoring the onset of biological hazards. An oil spill is a type of hazard that can have heavy ecological impact on the marine environment and cause important economic losses. Almost all the available observation techniques have been tested for discovering and observing the affected areas. We now know that synthetic aperture radar imaging, even though its inherent limitations must be kept in mind, is apt to search and monitoring oil slicks over large areas. On its side, microwave emissivity is crucial for observing the distribution of the sea surface salinity, which we know affects the ocean circulation and, ultimately, the climate in which we live. Sea surface wind is another parameter of climatological interest that is obtainable by both radiometric and radar observations. Measurement of the wind on the ocean surface is clearly concurrent with the survey of the wave field, given the related mechanisms of backscattering and emissivity. As it often occurs, here the remote sensing data find dual applications: the commercial function of mapping sea waves for operational ship routing is mated by the scientific objective of providing inputs to climatological and meteorological models.

Indeed, the meteorological community has been the first to benefit operationally from data taken by open Earth observation systems. Atmospheric applications keep on widening, as sensors and models advance and mature. Absorption spectrometry helps monitoring air quality at regional scales, as well as it forms the basis for global measurements of climatological interest. Water vapor density is the key parameter

in meteorology, which, thanks to its absorption properties, is obtainable from the radiometric temperatures both in the thermal infrared and at microwaves. Scattering of solar radiation, associated with extinction, provides cloud maps, a popular EO product of prompt comprehension, able to suggest the kind of meteorological event people can expect. Radar mapping of precipitation is a main outcome of the scattering and extinction processes that microwaves undergo in hydrometeors. The accumulated precipitation is a derived product of renown value for human safety.

References

1. About GOME-2. ESA http://www.esa.int/Our_Activities/Observing_the_Earth/The_Living_Planet_Programme/Meteorological_missions/MetOp/About_GOME-2 (visited on 23 Apr 2014)
2. Adams JB (1975) Interpretation of visible and near-infrared diffuse reflectance spectra of pyroxenes and other rock-forming minerals. In: Karr C Jr (ed) Infrared and Raman spectroscopy of lunar and terrestrial minerals. Academic. ISBN:9780123999504
3. Adams JB, Adams JD (1984) Geologic mapping using Landsat MSS and TM images – removing vegetation by modeling spectral mixtures. In: International symposium on remote sensing of environment, third thematic conference: remote sensing for exploration geology, vol 2, Colorado Springs, 16–19 Apr 1984, pp 615–622
4. Afsar MN, Hasted JB (1977) Measurements of the optical constants of liquid H_2O and D_2O between 6 and 450 cm^{-1}. J Opt Soc Am 67(7):902–904. doi: 10.1364/JOSA.67.000902
5. AIRS Atmospheric Infrared Sounder. NASA Goddard Earth Sciences Data and Information Services Center. http://disc.sci.gsfc.nasa.gov/AIRS (visited on 04 May 2014)
6. All About Sea Ice. National Snow and Ice Data Center. http://nsidc.org/cryosphere/seaice/index.html (visited on 13 Apr 2014)
7. Allen WA, Gausman HW, Richardson AJ (1970) Mean effective optical constants of cotton leaves. J Opt Soc Am 60(4):542–547. doi:10.1364/JOSA.60.000542
8. Alpers W, Espedal H (2004) Oils and surfactants. In: Jackson CR, Apel JR (eds) Synthetic aperture radar marine user's manual. NOAA/NESDIS Office of Research and Applications. ISBN:9780160732140. http://www.sarusersmanual.com/ (visited on 10 Oct 2014)
9. Alpers W, Hühnerfuss H (1989) The damping of ocean waves by surface films: a new look at an old problem. J Geophys Res Oceans 94(C5):6251–6265. doi:10.1029/JC094iC05p06251
10. AMSU – Advanced Microwave Sounding Unit. NASA Aqua Project Science. http://aqua.nasa.gov/about/instrumentamsu.php (visited on 05 Apr 2014)
11. Andreou C, Karathanassi V, Kolokoussis P (2011) Spectral library for oil types. In: 34-th international symposium on remote sensing of environment, Sydney, 10–15 Apr 2011. The GEOSS Era: towards operational environmental monitoring, pp 337–340. http://www.isprs.org/proceedings/2011/ISRSE-34/ (visited on 04 Oct 2014)
12. Askne JIH, Dammert PBG, Ulander LMH, Smith G (1997) C-band repeat-pass interferometric SAR observations of the forest. IEEE Trans Geosci Remote Sens 35(1):25–35. doi:10.1109/36.551931
13. Atlas D (1964) Advances in radar meteorology. In: Advances in geophysics, vol 10. Academic. ISBN:9780080568386
14. Atlas D, Hardy KR, Naito K (1966) Optimizing the radar detection of clear air turbulence. J Appl Meteorol 5(4):450–460. doi:10.1175/1520-0450(1966)005⟨0450:OTRDOC⟩2.0.CO;2
15. Attema EPW, Ulaby TF (1978) Vegetation modeled as a water cloud. Radio Sci 13(2):357–364. doi:10.1029/RS013i002p00357
16. Auer AH Jr, Veal LD (1970) The dimension of ice crystals in natural clouds. J Atmos Sci 27:919–926. doi:10.1175/1520-0469(1970)027⟨0919:TDOICI⟩2.0.CO;2

17. Aura – Atmospheric Chemistry. NASA. http://aura.gsfc.nasa.gov/ (visited on 23 Apr 2014)
18. Aura – Ozone Monitoring Instrument (OMI). NASA. http://www.nasa.gov/mission_pages/aura/spacecraft/omi.html (visited on 23 Apr 2014)
19. Avezzano RG, Velotto D, Del Frate F, Soccorsi M, Lehner S (2011) Neural networks for oil spill detection using TerraSAR-X data. In: Proceedings of SPIE 8179 – SAR image analysis, modeling, and techniques XI, Prague, 19 Sept 2011. doi:10.1117/12.898645
20. Backus EG, Gilbert F (1968) The resolving power of gross Earth data. Geophys J R Astron Soc 16(2):169–205. doi:10.1111/j.1365-246X.1968.tb00216.x
21. Bader H (1950) The significance of air bubbles in glacier ice. J Glaciol 1(8):443–451
22. Bakker JH, Skinner LJ (2010) Vibrational spectroscopy as a probe of structure and dynamics in liquid water. Chem Rev 110:1498–1517. doi:10.1021/cr9001879
23. Ballester-Berman JD, Lopez-Sanchez JM, Fortuny-Guasch J (2005) Retrieval of biophysical parameters of agricultural crops using polarimetric SAR interferometry. IEEE Trans Geosci Remote Sens 43(4):683–694. doi:10.1109/TGRS.2005.843958
24. Barth AC (1969) Planetary ultraviolet spectroscopy. Appl Opt 8(7):1295–1304. doi:10.1364/AO.8.001295
25. Battan LJ (1973) Radar observation of the atmosphere. The University of Chicago Press. ISBN:9781878907271
26. Becker F, Choudhury JB (1988) Relative sensitivity of normalized difference vegetation index (NDVI) and microwave polarization difference index (MPDI) for vegetation and desertification monitoring. Remote Sens Environ 24(2):297–311. doi:10.1016/0034-4257(88)90031-4
27. Ben-Dor E, Chabrillat S, Demattê JAM, Taylor GR, Hill J, Whiting ML, Sommer S (2009) Using imaging spectroscopy to study soil properties. Remote Sens Environ 113 (suppl 1):S38–S55. doi:10.1016/j.rse.2008.09.019
28. Besic N, Vasile G, Chanussot J, Stankovic S, Boldo D, d'Urso G (2013) Wet snow backscattering sensitivity on density change for SWE estimation. In: 2013 IEEE international geoscience and remote sensing symposium (IGARSS), July 2013, pp 1174–1177. doi:10.1109/IGARSS.2013.6721375
29. Bodine D, Heinselman PL, Cheong BL, Palmer RD, Michaud D (2010) A case study on the impact of moisture variability on convection initiation using radar refractivity retrievals. J Appl Meteorol Climatol 49(8):1766–1778. doi:10.1175/2010JAMC2360.1
30. Bogumil K, Orphal J, Homann T, Voigt S, Spietz P, Fleischmann OC, Vogel A, Hartmann M, Kromminga H, Bovensmann H, Frerick J, Burrows JP (2003) Measurements of molecular absorption spectra with the {SCIAMACHY} pre-flight model: instrument characterization and reference data for atmospheric remote-sensing in the 230–2380 nm region. J Photochem Photobiol A Chem 157(2–3):167–184. doi:http://dx.doi.org/10.1016/S1010-6030(03)00062-5
31. Bourlier C, Berginc G, Zhang Y, Grzegorczyk TM (2002) Microwave analytical backscattering models from randomly rough anisotropic sea surface – comparison with experimental data in C- and Ku- bands. Prog Electromagn Res 37:31–78. doi:10.2528/PIER0110080a
32. Bowers AS, Hanks JR (1965) Reflection of radiant energy from soils. Soil Sci 100(2):130–138. doi:10.1097/00010694-196508000-00009
33. Brekke C, Solberg AHS (2005) Oil spill detection by satellite remote sensing. Remote Sens Environ 95(1):1–13. doi:10.1016/j.rse.2004.11.015
34. Bringi VN, Chandrasekar V (2001) Polarimetric Doppler weather radar: principles and applications. Cambridge University Press. ISBN:9780521623841
35. Brönnimann S, Staehelin J, Farmer SFG, Cain JC, Svendby T, Svenoe T (2003) Total ozone observations prior to the IGY. I: a history. Q J R Meteorol Soc 129(593):2797–2817. doi:10.1256/qj.02.118
36. Brown CE (2010) Laser fluorosensors. In: Fingas M (ed) Oil spill science and technology. Elsevier, pp 171–184. ISBN:9781856179447

37. Burlamacchi P, Cecchi G, Mazzinghi P, Pantani L (1983) Performance evaluation of UV sources for lidar fluorosensing of oil films. Appl Opt 22(1):48–53. doi:10.1364/AO.22.000048
38. CALIPSO The Cloud-Aerosol Lidar and Infrared Pathfinder Satellite Observation. NASA/CNES. http://www-calipso.larc.nasa.gov (visited on 19 Apr 2014)
39. Camilli R, Reddy CM, Yoerger DR, Van Mooy BAS, Jakuba MV, Kinsey JC, McIntyre CP, Sean Sylva P, Maloney VJ (2010) Tracking hydrocarbon plume transport and biodegradation at Deepwater Horizon. Science 330(6001):201–204. doi:10.1126/science.1195223
40. Campbell BJ, Wynne RH (2012) Introduction to remote sensing. Guilford Press. ISBN:9781609181772
41. Camps A, Corbella I, Vall-llossera M, Duffo N, Torres F, Villarino R, Enrique L, Miranda J, Julbé F, Font J, Julià A, Gabarró C, Etchetto J, Boutin J, Weill A, Caselles V, Rubio E, Wursteisen P, Berger M, Martín-Neira M (2003) L-band sea surface emissivity: preliminary results of the WISE-2000 campaign and its application to salinity retrieval in the SMOS mission. Radio Sci 38:8071. doi:10.1029/2002RS002629
42. Cannon LH (1971) The use of plant indicators in ground water surveys, geologic mapping, and mineral prospecting. Taxon 20(2/3):227–256. http://www.jstor.org/stable/1218878
43. Canuti P, d'Auria G, Pampaloni P, Solimini D (1992) MAC 91 on Montespertoli: an experiment for agro-hydrology. In: International geoscience and remote sensing symposium. IGARSS '92, vol 2, May 1992, pp 1744–1746. doi:10.1109/IGARSS.1992.578869
44. Carreiras JMB, Vasconcelos MJ, Lucas MR (2012) Understanding the relationship between aboveground biomass and ALOS PALSAR data in the forests of Guinea-Bissau (West Africa). Remote Sens Environ 121:426–442. doi:10.1016/j.rse.2012.02.012
45. Carsey FD (ed) (1992) Microwave remote sensing of sea ice. Wiley. ISBN:9780875900339
46. Carter GA (1993) Responses of leaf spectral reflectance to plant stress. Am J Bot 80(3):239–243. doi:10.2307/2445346
47. Carter AG, Knapp KA (2001) Leaf optical properties in higher plants: linking spectral characteristics to stress and chlorophyll concentration. Am J Bot 88(4):677–684. http://www.ncbi.nlm.nih.gov/pubmed/11302854
48. Cartus O, Santoro M, Schmullius C, Li Z-Y (2011) Large area forest stem volume mapping in the boreal zone using synergy of ERS-1/2 tandem coherence and MODIS vegetation continuous fields. Remote Sens Environ 115(3):931–943. doi:10.1016/j.rse.2010.12.003
49. Chaerle L, Van Der Straeten D (2000) Imaging techniques and the early detection of plant stress. Trends Plant Sci 5(11):495–501. doi:10.1016/S1360-1385(00)01781-7
50. Chamberlain JW (1961) Physics of the Aurora and Airglow. Academic. ISBN:9781118668047
51. Chance K (2005) Ultraviolet and visible spectroscopy and spaceborne remote sensing of the Earth's atmosphere. C R Phys 6(8):836–847. doi:http://dx.doi.org/10.1016/j.crhy.2005.07.010
52. Chen Y-C, Tang P-H, Wu T-M (2013) Instantaneous normal mode analysis for intermolecular and intramolecular vibrations of water from atomic point of view. J Chem Phys 139:204505. doi:10.1063/1.4829679
53. Chi G-Y, Shi Y, Chen X, Ma J, Zheng T-H (2011) Effects of metal stress on visible/near-infrared reflectance spectra of vegetation. In: Ren J-X, Pan W-G, Li Y-G (eds) Advanced materials research, vol 347–353. Trans Tech Publications, pp 2735–2738. doi:10.4028/www.scientific.net/AMR.347-353.2735
54. Chylek P, Robinson S, Dubey MK, King MD, Fu Q, Clodius BW (2006) Comparison of near-infrared and thermal infrared cloud phase detections. J Geophys Res Atmos 111:D20203. doi:10.1029/2006JD007140
55. Cimini D, Campos E, Ware RH, Albers S, Giuliani G, Oreamuno J, Joe P, Koch SE, Cober S, Westwater ER (2011) Thermodynamic atmospheric profiling during the 2010 Winter Olympics using ground-based microwave radiometry. IEEE Trans Geosci Remote Sens 49(12):4959–4969. doi:10.1109/TGRS.2011.2154337
56. Cimini D, Hewison TJ, Martin L, Güldner J, Gaffard C, Marzano FS (2006) Temperature and humidity profile retrievals from ground-based microwave radiometers during TUC. Meteorol Z 15(1):45–56. doi:10.1127/0941-2948/2006/0099

57. Cini R, Lombardini PP (1978) Damping effect of monolayers on surface wave motion in a liquid. J Colloid Interface Sci 65(2):387–389. doi:10.1016/0021-9797(78)90170-4
58. Cini R, Lombardini PP, Hühnerfuss H (1983) Remote sensing of marine slicks utilizing their influence on wave spectra. Int J Remote Sens 4(1):101–110. doi:10.1080/01431168308948533
59. Clark RB (2001) Marine pollution. Oxford University Press. ISBN:9780198792925
60. Clark RN, Swayze GA, Leifer I, Livo KE, Kokaly R, Hoefen T, Lundeen S, Eastwood M, Green RO, Pearson N, Sarture C, McCubbin I, Roberts D, Bradley E, Steele D, Ryan T, Dominguez R, the Airborne Visible/Infrared Imaging Spectrometer (AVIRIS) Team (2010) A method for quantitative mapping of thick oil spills using imaging spectroscopy. Tech. rep. U.S. Department of the Interior Geological Survey Open-File Report 2010-1167
61. Clothiaux EE, Miller MA, Albrecht BA, Ackerman TP, Verlinde J, Babb DM, Peters RM, Syrett WJ (1995) An evaluation of a 94-GHz radar for remote sensing of cloud properties. J Atmos Oceanic Technol 12(2):201–229. doi:10.1175/1520-0426(1995)012⟨0201:AEOAGR⟩2.0.CO;2
62. CLOUD ANALYSIS – PART 8: cloud Microphysics. NASA International Satellite Cloud Climatology Project. http://isccp.giss.nasa.gov/climanal8.html (visited on 25 Apr 2014)
63. Cloude RS, Papathanassiou KP (1998) Polarimetric SAR interferometry. IEEE Trans Geosci Remote Sens 36(5):1551–1565. doi:10.1109/36.718859
64. CLOUDSAT. NASA. http://cloudsat.atmos.colostate.edu (visited on 19 Apr 2014)
65. Collard F, Ardhuin F, Chapron B (2009) Monitoring and analysis of ocean swell fields from space: new methods for routine observations. J Geophys Res 114:C07023. doi:10.1029/2008JC005215
66. Collier CG (1996) Applications of weather radar systems: a guide to uses of radar data in meteorology and hydrology. Wiley. ISBN:9780471960133
67. Corradini S, Merucci L, Prata AJ, Piscini A (2010) Volcanic ash and SO_2 in the 2008 Kasatochi eruption: retrievals comparison from different IR satellite sensors. J Geophys Res Atmos 115(D2). doi:10.1029/2009JD013634
68. Cox C, Munk W (1954) Measurement of the roughness of the sea surface from photographs of the sun's glitter. J Opt Soc Am 44(11):838–850. doi:10.1364/JOSA.44.000838
69. de Beek R, Buchwitz M, Rozanov VV, Burrows JP (2004) Trace gas column retrieval from IR nadir spectra – a model study for SCIAMACHY. Adv Space Res 34(4):734–738. doi:http://dx.doi.org/10.1016/j.asr.2003.06.041
70. Decker MT, Westwater ER, Guiraud FO (1978) Experimental evaluation of ground-based microwave radiometric sensing of atmospheric temperature and water vapor profiles. J Appl Meteorol 17(12):1788–1795. doi:10.1175/1520-0450(1978)0172.0.CO;2
71. Deering DW (1989) Field measurements of bidirectional reflectance. In: Asrar G (ed) Theory and applications of optical remote sensing. Wiley. ISBN:9780471628958
72. de Jeu RAM, Wagner W, Holmes TRH, Dolman AJ, van de Giesen NC, Friesen J (2008) Global soil moisture patterns observed by space borne microwave radiometers and scatterometers. Surv Geophys 29:399–420. doi:10.1007/s10712-008-9044-0
73. de Leeuw G, Kinne S, Leon JF, Pelon J, Rosenfeld D, Schaap M, Veefkind PJ, Veihelmann B, Winker DM, von Hoyningen-Huene W (2011) Retrieval of aerosol properties. In: Burrows JP, Platt U, Borrell P (eds) The remote sensing of tropospheric composition from space. Springer. ISBN:9783642147913
74. de Leeuw G, Kokhanovsky AA, Cermak J (2012) Remote sensing of aerosols and clouds: techniques and applications (editorial to special issue in Atmospheric Research). Atmos Res 113:40–42. doi:10.1016/j.atmosres.2012.04.017
75. Del Frate F, Latini D, Taravat A, Jones CE (2013) A novel multi-band SAR data technique for fully automatic oil spill detection in the ocean. In: Proceedings of SPIE 8891 – SAR image analysis, modeling, and techniques XIII, Dresden, 17 Oct 2013. doi:10.1117/12.2031418
76. Del Frate F, Petrocchi A, Lichtenegger J, Calabresi G (2000) Neural networks for oil spill detection using ERS-SAR data. IEEE Trans Geosci Remote Sens 38(5):2282–2287

77. Del Frate F, Solimini D (2004) On neural network algorithms for retrieving forest biomass from SAR data. IEEE Trans Geosci Remote Sens 42(1):24–34. doi:10.1109/TGRS.2003.817220
78. Della Vecchia A, Ferrazzoli P, Guerriero L, Rahmoune R, Paloscia S, Pettinato S, Santi E (2010) Modeling the multifrequency emission of broadleaf forests and their components. IEEE Trans Geosci Remote Sens 48(1):260–272. doi:10.1109/TGRS.2009.2029343
79. DeMajistre R, Paxton LJ, Bilitza D (2007) Comparison of ionospheric measurements made by digisondes with those inferred from ultraviolet airglow. Adv Space Res 39:918–925. doi:10.1016/j.asr.2006.09.037
80. de Matthaeis P (1994) Overview on wind scatterometry and performance evaluation of ASCAT. Tech. rep. LI/PDM/0038/pdm. European Space Agency ESA/ESTEC, Apr 1994
81. Dixon RK, Solomon AM, Brown S, Houghton RA, Trexier MC, Wisniewski J (1994) Carbon pools and flux of global forest ecosystems. Science 263(5144):185–190. doi:10.1126/science.263.5144.185
82. DMSP. NOAA Comprehensive Large Array-data Stewardship System (CLASS). http://www.class.ngdc.noaa.gov/dataavailable/dmsp/index.htm (visited on 04 May 2014)
83. Dobson MC, Ulaby FT, LeToan T, Beaudoin A, Kasischke ES, Christensen N (1992) Dependence of radar backscatter on coniferous forest biomass. IEEE Trans Geosci Remote Sens 30(2):412–415. doi:10.1109/36.134090
84. Doherty AM, Sreerekha TR, O'Keeffe UM, English SJ (2007) Ice hydrometeor microphysical assumptions in radiative transfer models at AMSU-B frequencies. Q J R Meteorol Soc A 133(626):1205–1212. doi:10.1002/qj.84
85. Doviak JR, Zrnić DS (1993) Doppler radar and weather observations. Dover. ISBN:9780486450605
86. Dozier J (1989) Remote sensing of snow in visible and near-infrared wavelengths. In: Asrar G (ed) Theory and applications of optical remote sensing. Wiley. ISBN:9780471628958
87. Dozier J, Warren SG (1982) Effect of the viewing angle on the infrared brightness temperature of snow. Water Resour Res 18(5):1424–1434. doi:10.1029/WR018i005p01424
88. Du J, Teramoto T, Nakata K, Tokunaga E, Kobayashi T (2011) Real-time vibrational dynamics in chlorophyll *a* studied with a few-cycle pulse laser. Biophys J 101(4):995–1003. doi:10.1016/j.bpj.2011.07.011
89. Dunagan SC, Gilmore MS, Varekamp JC (2007) Effects of mercury on visible/near-infrared reflectance spectra of mustard spinach plants (Brassica rapa P.). Environ Pollut 148(1):301–311. doi:10.1016/j.envpol.2006.10.023
90. Dusek U, Frank GP, Hildebrandt L, Curtius J, Schneider J, Walter S, Chand D, Drewnick F, Hings S, Jung D, Borrmann S, Andreae MO (2006) Size matters more than chemistry for cloud-nucleating ability of aerosol particles. Science 312:1375–1378. doi:10.1126/science.1125261
91. EarthCARE ESA's Cloud, Aerosol and Radiation Mission. ESA. http://www.esa.int/Our_Activities/Observing_the_Earth/The_Living_Planet_Programme/Earth_Explorers/EarthCARE/ESA_s_cloud_aerosol_and_radiation_mission (visited on 19 Apr 2014)
92. Eastes JW (1991) Thermal infrared spectra of natural and manmade materials: implications for remote sensing. Tech. rep. ETL-0587. U.S. Army Topographic Engineering Center, Hanscom
93. Elmore AJ, Mustard JF, Manning SJ, Lobell DB (2000) Quantifying vegetation change in semiarid environments: precision and accuracy of spectral mixture analysis and the normalized difference vegetation index. Remote Sens Environ 73(1):87–102. doi:10.1016/S0034-4257(00)00100-0
94. Elvidge CD (1987) Thermal infrared reflectance of dry plant materials: 2.5–20.0 μm. Remote Sens Environ 26(3):265–285. doi:10.1016/ 0034-4257(88)90082-X
95. Emery JW, Thomson RE (2001) Data analysis methods in physical oceanography. Elsevier. ISBN:9780444507570
96. Engdahl ME, Borgeaud M, Rast M (2001) The use of ERS-1/2 tandem interferometric coherence in the estimation of agricultural crop heights. IEEE Trans Geosci Remote Sens 39(8):1799–1806. doi:10.1109/36.942558

97. Englhart S, Keuck V, Siegert F (2011) Aboveground biomass retrieval in tropical forests – the potential of combined X- and L-band SAR data use. Remote Sens Environ 115(5):1260–1271. doi:10.1016/j.rse.2011.01.008
98. English SJ (1999) Estimation of temperature and humidity profile information from microwave radiances over different surface types. J Appl Meteorol 38(10):1526–1541. doi:10.1175/1520-0450(1999)038⟨1526:EOTAHP⟩2.0.CO;2
99. Engman TE, Gurney RJ (1991) Remote sensing in hydrology. Chapman and Hall. ISBN:9780412244506
100. Eppler DT, Farmer LD, Lohanick AW, Anderson MR, Cavalieri DJ, Comiso J, Gloersen P, Garrity C, Grenfell TC, Hallikainen M, Maslanik JA, Mätzler C, Melloh RA, Rubinstein I, Swift CT (1992) Passive microwave signatures of sea ice. In: Carsey FD (ed) Microwave remote sensing of sea ice. Geophysical monograph 68. American Geophysical Union. ISBN:9781119940784
101. Ferrazzoli P, Guerriero L (1996) Passive microwave remote sensing of forests: a model investigation. IEEE Trans Geosci Remote Sens 34(2):433–443. doi:10.1109/36.485121
102. Ferrazzoli P, Guerriero L, Solimini D (2000) Simulating bistatic scatter from surfaces covered with vegetation. J Electromagn Waves Appl 14:233–248
103. Ferrazzoli P, Guerriero L, Wigneron J-P (2002) Simulating L-band emission of forests in view of future satellite applications. IEEE Trans Geosci Remote Sens 40(12):2700–2708. doi:10.1109/ TGRS.2002.807577
104. Ferrazzoli P, Paloscia S, Pampaloni P, Solimini D (1989) Modeling microwave emission from vegetation. In: Pampaloni P (ed) Microwave radiometry and remote sensing applications. VSP. ISBN:9789067641081
105. Fingas M, Brown C (2014) Review of oil spill remote sensing. Mar Pollut Bull 83(1):9–23. doi:10.1016/j.marpolbul.2014.03.059
106. Fingas FM, Brown CE (1997) Review of oil spill remote sensing. Spill Sci Technol Bull 4(4). The second international symposium on oil spills, pp 199–208. doi:http://dx.doi.org/10.1016/S1353-2561(98)00023-1
107. Fiocco G, Fuà D, Visconti G (eds) (1996) The Mount Pinatubo eruption: effects on the atmosphere and climate. NATO ASI series: global environmental change. Springer. ISBN:9783540612810
108. Fiocco G, Smullin LD (1963) Detection of scattering layers in the upper atmosphere (60–140 km) by optical radar. Nature 199(4900):1275–1276. doi:10.1038/1991275a0
109. Fischer H, Oelhaf H (1996) Remote sensing of vertical profiles of atmospheric trace constituents with MIPAS limb-emission spectrometers. Appl Opt 35(16):2787–2796. doi:10.1364/AO.35.002787
110. Font J, Camps A, Borges A, Martín-Neira M, Boutin J, Reul N, Kerr YH, Hahne A, Mecklenburg S (2010) SMOS: the challenging sea surface salinity measurement from space. Proc IEEE 98(5):649–665. doi:0.1109/JPROC.2009.2033096
111. Foster JL, Sun C, Walker JP, Kelly REJ, Chang ATC, Dong J, Powell H (2005) Quantifying the uncertainty in passive microwave snow water equivalent observations. Remote Sens Environ 94(2):187–203. doi:10.1016/j.rse.2004.09.012
112. Fukao S, Hamazu K (2014) Radar for meteorological and atmospheric observations. Springer. ISBN:9784431543350
113. Fung AK (1994) Microwave scattering and emission models and their applications. Artech House. ISBN:9780890065235
114. Gabarró C, Font J, Camps A, Vall-llossera M, Julià A (2004) A new empirical model of sea surface microwave emissivity for salinity remote sensing. Geophys Res Lett 31:L01309. doi:10.1029/2003GL018964
115. Gasiewski AJ (1993) Microwave radiative transfer in hydrometeors. In: Janssen MA (ed) Atmospheric remote sensing by microwave radiometry. Wiley. ISBN:9780471628910
116. Gates DM (1970) Physical and physiological properties of plants. In: Remote sensing with special reference to agriculture and forestry. U. S. National Academy of Sciences National Research Council Committee on Remote Sensing for Agricultural Purposes NAS Publication 1723

117. Gausman WH, Allen WA (1973) Optical parameters of leaves of 30 plant species. Plant Physiol 52(1):57–62. doi:10.1104/pp.52.1.57
118. Geer JA, Baordo F (2014) Improved scattering radiative transfer for frozen hydrometeors at microwave frequencies. Atmos Meas Tech Discuss 7:1749–1805. doi:10.5194/amtd-7-1749-2014
119. Gentile S, Ferretti R, Marzano FS (2014) Investigating Hector convective development and microphysical structure using high-resolution model simulations, ground-based radar data, and TRMM satellite data. J Atmos Sci 71(4):1353–1370. doi:10.1175/JAS-D-13-0107.1
120. Gill AE (1982) Atmosphere-ocean dynamics. Academic. ISBN:9780122835223
121. Gitelson AA, Kaufman YJ, Stark R, Rundquist D (2002) Novel algorithms for remote estimation of vegetation fraction. Remote Sens Environ 80(1):76–87. doi:10.1016/S0034-4257(01)00289-9
122. Global Precipitation Measurement/Dual-frequency Precipitation Radar (GPM/DPR). Japan Aerospace Exploration Agency – JAXA. http://global.jaxa.jp/projects/sat/gpm/index.html (visited on 06 May 2014)
123. Goel NS (1988) Models of vegetation canopy reflectance and their use in estimation of biophysical parameters from reflectance data. Remote Sens Rev 4(1):1–212. doi:10.1080/02757258809532105
124. Goetz AFH (1989) Spectral remote sensing in geology. In: Asrar G (ed) Theory and applications of optical remote sensing. Wiley. ISBN:9780471628958
125. Goetz AFH (2009) Three decades of hyperspectral remote sensing of the Earth: a personal view. Remote Sens Environ 113(suppl 1):S5–S16. doi:10.1016/j.rse.2007.12.014
126. GOMOS. ESA. https://earth.esa.int/web/guest/missions/esa-operational-eo-missions/envisat/instruments/gomos (visited on 23 Apr 2014)
127. GPM – Global Precipitation Measurement. NASA/JAXA. http://pmm.nasa.gov/node/243 (visited on 27 Apr 2014)
128. Grandell J, Dobber M, Höller H, Stuhlmann R (2012) Meteosat third generation lightning imager (MTG LI) status update. In: EUM/MTG/VWG/12/0865 GLM science team meeting, Huntsville, 19–21 Sept 2012. http://www.goes-r.gov/downloads/2012-GLM/day2/MTG-grandell.pdf (visited on 29 Apr 2014)
129. Graves CE (1993) A model for the beam-filling effect associated with the microwave retrieval of rain. J Atmos Oceanic Technol 10(1):5–14. doi:10.1175/1520-0426(1993)010⟨0005:AMFTBF⟩2.0.CO;2
130. Grey W, Luckman A (2003) Mapping urban extent using satellite radar interferometry. Photogramm Eng Remote Sens 69(9):957–961. http://info.asprs.org/publications/pers/2003journal/september/2003_sep_957-961.pdf (visited on 08 Nov 2014)
131. Grody NC (1993) Remote sensing of the atmosphere from satellites using microwave radiometry. In: Janssen MA (ed) Atmospheric remote sensing by microwave radiometry. Wiley. ISBN:9780471628910
132. Guenther GC, Grant Cunningham A, LaRocque PE, Reid JD (2000) Meeting the accuracy challenge in airborne bathymetry. In: Workshop on lidar remote sensing of land and sea, Dresden, 16–17 June 2000. Vol. 1 of the proceedings of the 20-th EARSeL symposium
133. Gunn KLS, East TWR (1954) The microwave properties of precipitation particles. Q J R Meteorol Soc 80(346):522–545. doi:10.1002/qj.49708034603
134. GUVI. The Johns Hopkins University Applied Physics Laboratory. http://guvi.jhuapl.edu/about/guvi_instrument.html (visited on 23 Apr 2014)
135. Guyot G, Baret F, Jacquemoud S (1992) Imaging spectroscopy for vegetation studies. In: Toselli F, Bodechtel J (eds) Imaging spectroscopy: fundamentals and prospective applications. Springer. ISBN:9780792315353
136. Hagberg JO, Ulander LMH, Askne J (1995) Repeat-pass SAR interferometry over forested terrain. IEEE Trans Geosci Remote Sens 33(2):331–340. doi:10.1109/36.377933

137. Hagen M, Yuter SE (2003) Relations between radar reflectivity, liquid-water content, and rainfall rate during the MAP SOP. Q J R Meteorol Soc 129:477–493. doi:10.1256/qj.02.23
138. Hallikainen M, Winebrenner DP (1992) The physical basis for sea ice remote sensing. In: Carsey FD (ed) Microwave remote sensing of sea ice. Geophysical monograph 68. American Geophysical Union. ISBN:9781119940784
139. Han Y, Westwater ER (2000) Analysis and improvement of tipping calibration for ground-based microwave radiometers. IEEE Trans Geosci Remote Sens 38(3):1260–1276. doi:10.1109/36.843018
140. Handcock RN, Torgersen CE, Cherkauer KA, Gillespie AR, Tockner K, Faux RN, Tan J (2012) Thermal infrared remote sensing of water temperature in riverine landscapes. In: Carbonneau P, Piégay H (eds) Fluvial remote sensing for science and management. Wiley. ISBN:9781119940784
141. Hanel RA (1961) Determination of cloud altitude from a satellite. J Geophys Res 66(4):1300. doi:10.1029/JZ066i004p01300
142. Hardy JT (1982) The sea surface microlayer: biology, chemistry and anthropogenic enrichment. Prog Oceanogr 11(4):307–328. doi:10.1016/0079-6611(82)90001-5
143. Harris D, Foufoula-Georgiou E (2001) Subgrid variability and stochastic downscaling of modeled clouds: effects on radiative transfer computations for rainfall retrieval. J Geophys Res Atmos 106(D10):10349–10362. doi:10.1029/2000JD900797
144. Hasted JB (1973) Aqueous dielectrics. Chapman and Hall. ISBN:9780412098000
145. Hauser D, Kahma KK, Krogstad HE, Lehner S, Monbaliu J, Wyatt LR (eds) (2005) Measuring and analysing the directional spectrum of ocean waves. Tech. rep. EUR 21367 EN. COST 714 Working Group 3. doi:9289800038
146. Heymsfield JA, Platt CMR (1984) A parameterization of the particle size spectrum of ice clouds in terms of the ambient temperature and the ice water content. J Atmos Sci 41(5):846–855. doi:10.1175/1520-0469(1984)041⟨0846:APOTPS⟩2.0.CO;2
147. Hinkelman LM, Stevens B, Evans KF (2005) A large-eddy simulation study of anisotropy in fair-weather cumulus cloud fields. J Atmos Sci 62(7):2155–2171. doi:10.1175/JAS3463.1
148. Hoge EF, Swift RN (1980) Oil film thickness measurement using airborne laser-induced water Raman backscatter. Appl Opt 19(19):3269–3281. doi:10.1364/AO.19.003269
149. Hoge FE, Wayne Wright C, Swift RN, Yungel JK (1989) Airborne discrimination between ice and water: application to the laser measurement of chlorophyll-in-water in a marginal Ice Zone. Remote Sens Environ 30(1):67–76. doi:10.1016/0034-4257(89)90048-5
150. Hogg DC, Decker MT, Guiraud FO, Earnshaw KB, Merritt DA, Moran KP, Sweezy WB, Strauch RG, Westwater ER, Little CG (1983) An automatic profiler of the temperature, wind and humidity in the troposphere. J Appl Meteorol 22(5):807–831. doi:10.1175/1520-0450(1983)022⟨0807:AAPOTT⟩2.0.CO;2
151. Hollinger JP (1971) Passive microwave measurements of sea surface roughness. IEEE Trans Geosci Electron 9(3):165–169. doi:10.1109/TGE.1971.271489
152. Hong S-Y, Dudhia J, Chen S-H (2004) A revised approach to ice microphysical processes for the bulk parameterization of clouds and precipitation. Mon Weather Rev 132(1):103–120. doi:10.1175/1520-0493(2004)132⟨0103:ARATIM⟩2.0.CO;2
153. Hong Y, Hsu K-L, Sorooshian S, Gao X (2004) Precipitation estimation from remotely sensed imagery using an artificial neural network cloud classification system. J Appl Meteorol 43(12):1834–1853. doi:10.1175/JAM2173.1
154. Hori M, Aoki T, Tanikawa T, Hachikubo A, Sugiura K, Kuchiki K, Niwano M (2013) Modeling angular-dependent spectral emissivity of snow and ice in the thermal infrared atmospheric window. Appl Opt 52(30):7243–7255. doi:10.1364/AO.52.007243
155. Horler DNH, Barber J, Barringer AR (1980) Effects of heavy metals on the absorbance and reflectance spectra of plants. Int J Remote Sens 1(2):121–136. doi:10.1080/01431168008547550
156. Houghton JT (1961) The meteorological significance of remote measurements of infrared emission from atmospheric carbon dioxide. Q J R Meteorol Soc 87(371):102–104. doi:10.1002/qj.49708737111

157. Houghton RA (2005) Aboveground forest biomass and the global carbon balance. Glob Change Biol 11:945–958. doi:10.1111/j.1365-2486.2005.00955.x
158. Houze RA Jr (2004) Mesoscale convective systems. Rev Geophys 42:RG4003, 1–43. doi:10.1029/2004RG000150
159. Houze RA (1994) Cloud dynamics. Elsevier. ISBN:9780080502106
160. Huang D, Knyazikhin Y, Dickinson RE, Rautiainen M, Stenberg P, Disney M, Lewis P, Cescatti A, Tian Y-h, Verhoef W, Martonchik JV, Myneni RB (2007) Canopy spectral invariants for remote sensing and model applications. Remote Sens Environ 106(1):106–122. doi:10.1016/j.rse.2006.08.001
161. Huffman GJ, Adler RF, Bolvin DT, Nelkin EJ (2010) The TRMM Multi-Satellite Precipitation Analysis (TMPA). In: Gebremichael M, Hossain F (eds) Satellite rainfall applications for surface hydrology. Springer. ISBN:9789048129157
162. Huffman GJ, Bolvin DT, Nelkin EJ, Wolff DB, Adler RF, Gu G, Hong Y, Bowman KP, Stocker EF (2007) The TRMM multisatellite precipitation analysis (TMPA): quasi-global, multiyear, combined-sensor precipitation estimates at fine scales. J Hydrometeorol 8(1):38–55. doi:10.1175/JHM560.1
163. Hunt GR (1977) Spectral signatures of particulate minerals in the visible and near infrared. Geophysics 42(3):501–513. doi:10.1190/1.1440721
164. Hwang P, Burrage D, Wang DW, Wesson J (2010) Ocean surface roughness spectrum and microwave brightness temperature. In: 17-th conference on satellite meteorology and oceanography, Annapolis, 26–30 Sept 2010. https://ams.confex.com/ams/17Air17Sat9Coas/techprogram/paper174297.htm (visited on 16 Apr 2014)
165. ICESat-2 Ice, Cloud, and land Elevation Satellite-2. NASA. http://icesat.gsfc.nasa.gov/icesat2/ (visited on 29 Apr 2014)
166. Imhoff ML (1995) A theoretical analysis of the effect of forest structure on synthetic aperture radar backscatter and the remote sensing of biomass. IEEE Trans Geosci Remote Sens 33(2):341–352. doi:10.1109/36.377934
167. Irion FW, Gunson MR, Toon GC, Chang AY, Eldering A, Mahieu E, Manney GL, Michelsen HA, Moyer EJ, Newchurch MJ, Osterman GB, Rinsland CP, Salawitch RJ, Sen B, Yung YL, Zander R (2002) Atmospheric trace molecule spectroscopy (ATMOS) experiment version 3 data retrievals. Appl Opt 41(33):6968–6979. doi:10.1364/AO.41.006968
168. Irish LJ, White TE (1998) Coastal engineering applications of high-resolution lidar bathymetry. Coast Eng 35(1–2):47–71. doi:10.1016/S0378-3839(98)00022-2
169. Irons JR, Weismiller RA, Petersen GW (1989) Soil reflectance. In: Asrar G (ed) Theory and applications of optical remote sensing. Wiley. ISBN:9780471628958
170. Jackson TJ, Le Vine DM, Hsu AY, Oldak A, Starks PJ, Swift CT, Isham JD, Haken M (1999) Soil moisture mapping at regional scales using microwave radiometry: the Southern Great Plains Hydrology Experiment. IEEE Trans Geosci Remote Sens 37(5):2136–2151. doi:10.1109/36.789610
171. Jacquemoud S, Baret F (1990) PROSPECT: a model of leaf optical properties spectra. Remote Sens Environ 34(2):75–91. doi:10.1016/0034-4257(90)90100-Z
172. Jacquemoud S, Ustin SL (2001) Leaf optical properties: a state of the art. In: 8-th international symposium on physical measurements and signatures in remote sensing, Aussois, 8–12 Jan 2001, pp 223–232
173. Janssen P (2004) The interaction of ocean waves and wind. Cambridge University Press. ISBN:9780521465403
174. Kadygrov EN, Shur GN, Viazankin AS (2003) Investigation of atmospheric boundary layer temperature, turbulence, and wind parameters on the basis of passive microwave remote sensing. Radio Sci 38(3):8048. doi:10.1029/2002RS002647
175. Kallel A, Verhoef W, Le Hegarat-Mascle S, Ottle C, Hubert-Moy L (2008) Canopy bidirectional reflectance calculation based on adding method and SAIL formalism: addingS/AddingSD. Remote Sens Environ 112(9):3639–3655. doi:10.1016/j.rse.2008.05.014
176. Kawamoto K, Nakajima T, Nakajima TY (2001) A global determination of cloud microphysics with AVHRR remote sensing. J Clim 14(9):2054–2068. doi:10.1175/1520-0442(2001)014⟨2054:AGDOCM⟩2.0.CO;2

177. Kealy SP, Hook SJ (1993) Separating temperature and emissivity in thermal infrared multispectral scanner data: implications for recovering land surface temperatures. IEEE Trans Geosci Remote Sens 31(6):1155–1164. doi:10.1109/36.317447
178. Kerr YH, Waldteufel P, Wigneron J-P, Martinuzzi J, Font J, Berger M (2001) Soil moisture retrieval from space: the Soil Moisture and Ocean Salinity (SMOS) mission. IEEE Trans Geosci Remote Sens 39(8):1729–1735. doi:10.1109/36.942551
179. Kidd C (2001) Satellite rainfall climatology: a review. Int J Climatol 21(9):1041–1066. doi:10.1002/joc.635
180. Kiefer DA, Olson RJ, Wilson WH (1979) Reflectance spectroscopy of marine phytoplankton. Part 1. Optical properties as related to age and growth rate. Limnol Oceanogr 24(4):664–672. doi:10.4319/lo.1979.24.4.0664
181. Kinsman B (2002) Wind waves: their generation and propagation on the ocean surface. Dover. ISBN:9780486495118
182. Klemas V (2013) Fisheries applications of remote sensing: an overview. Fish Res 148:124–136. doi:10.1016/j.fishres.2012.02.027
183. Klemas V, Yan X-H (2014) Subsurface and deeper ocean remote sensing from satellites: an overview and new results. Prog Oceanogr 122:1–9. doi:10.1016/j.pocean.2013.11.010
184. Koch B (2010) Status and future of laser scanning, synthetic aperture radar and hyperspectral remote sensing data for forest biomass assessment. SPRS J Photogramm Remote Sens 65(6):581–590. doi:10.1016/j.isprsjprs.2010.09.001
185. Koffi AK, Gosset M, Zahiri E-P, Ochou AD, Kacou M, Cazenave F, Assamoi P (2014) Evaluation of X-band polarimetric radar estimation of rainfall and rain drop size distribution parameters in West Africa. Atmos Res 143:438–461. doi:http://dx.doi.org/10.1016/j.atmosres.2014.03.009
186. Kokhanovsky AA (2008) Aerosol optics: light absorption and scattering by particles in the atmosphere. Praxis Publishing. ISBN:9783540499091
187. Kokhanovsky AA, de Leeuw G (2009) Satellite aerosol remote sensing over land. Springer. ISBN:9783540693970
188. Kokhanovsky AA, Platnick S, King MD (2011) Remote sensing of terrestrial clouds from space using backscattering and thermal emission techniques. In: The remote sensing of tropospheric composition from space. Springer. ISBN:9783642147913
189. Komen GJ, Cavaleri L, Donelan K, Hasselmann K, Hasselmann S, Janssen PAEM (eds) (1996) Dynamics and modelling of ocean waves. Cambridge University Press. ISBN:9780521577816
190. Kondratyev KY (ed) (1969) Radiation in the atmosphere. Elsevier. ISBN:9780080954479
191. Kondratyev KY, Ivlev LS, Krapivin VF, Varostos AC (2006) Atmospheric aerosol properties: formation, processes and impacts. Springer. ISBN:9783540376989
192. Koren I, Remer LA, Kaufman YJ, Rudich Y, Vanderlei Martins J (2007) On the twilight zone between clouds and aerosols. Geophys Res Lett 34:L08805. doi:10.1029/2007GL029253
193. Korolev A, McFarquhar G, Jourdan O, Wang Z, Wobrock W (2013) Properties of cloud particles. In: Ulanowski J, Flossmann A, Alexander S (eds) Workshop on measurement problems in ice clouds, Zurich, 5–6 July 2013. doi:10.1063/1.4804697. http://www.iccp-iamas.org/pdf/workshopPresentations/Topic7final.pdf (visited on 25 Apr 2014)
194. Korte HE, Röseler A (2005) lnfrared reststrahlen revisited: commonly disregarded optical details related to $n < 1$. Anal Bioanal Chem 382:1987–1992. doi:10.1007/s00216-005-3407-x
195. Kostianoy GA, Yu Lavrova O (eds) (2014) Oil pollution in the Baltic sea. Springer. ISBN:9783642384752. doi:10.1007/978-3-642-38476-9
196. Kühl S, Pukite J, Deutschmann T, Platt U, Wagner T (2008) SCIAMACHY limb measurements of NO_2, BrO and OClO. Retrieval of vertical profiles: algorithm, first results, sensitivity and comparison studies. Adv Space Res 42:1747–1764. doi:10.1016/j.asr.2007.10.022
197. Kuhn MP, McFadden JD (1967) Atmospheric water vapor profiles derived from remote-sensing radiometer measurements. Mon Weather Rev 95(8):565–569. doi:10.1175/1520-0493(1967)095⟨0565:AWVPDF⟩2.3.CO;2

198. Kummerow C, Barnes W, Kozu T, Shiue J, Simpson J (1998) The Tropical Rainfall Measuring Mission (TRMM) sensor package. J Atmos Oceanic Technol 15(3):809–817. doi:10.1175/1520-0426(1998)015⟨0809:TTRMMT⟩2.0.CO;2
199. Kummerow C, Simpson J, Thiele O, Barnes W, Chang ATC, Stocker E, Adler RF, Hou A, Kakar R, Wentz F, Ashcroft P, Kozu T, Hong Y, Okamoto K, Iguchi T, Kuroiwa H, Im E, Haddad Z, Huffman G, Ferrier B, Olson WS, Zipser E, Smith EA, Wilheit TT, North G, Krishnamurti T, Nakamura K (2000) The status of the Tropical Rainfall Measuring Mission (TRMM) after two years in orbit. J Appl Meteorol 39(12):1965–1982. doi:10.1175/1520-0450(2001)040⟨1965:TSOTTR⟩2.0.CO;2
200. Kutuza BG, Zagorin GK, Hornbostel A, Schroth A (1998) Physical modeling of passive polarimetric microwave observations of the atmosphere with respect to the third Stokes parameter. Radio Sci 33(3):677–695. doi:10.1029/97RS03318
201. LeBlond HP, Mysak LA (1981) Waves in the ocean. Elsevier. ISBN:9780080879772
202. Lee WS, Alchanatis V, Yang C, Hirafuji M, Moshou D, Li C (2010) Sensing technologies for precision specialty crop production. Comput Electron Agric 74(1):2–33. doi:10.1016/j.compag.2010.08.005
203. Lefsky MA, Cohen WB, Harding DJ, Parker GG, Acker SA, Thomas Gower S (2002) Lidar remote sensing of above-ground biomass in three biomes. Glob Ecol Biogeogr 11(5):393–399. doi:10.1046/j.1466-822x.2002.00303.x
204. Leifer I, Lehr WJ, Simecek-Beatty D, Bradley E, Clark R, Dennison P, Hu Y, Matheson S, Jones CE, Holt B, Reif M, Roberts DA, Svejkovsky J, Swayze G, Wozencraft J (2012) State of the art satellite and airborne marine oil spill remote sensing: application to the BP Deepwater Horizon oil spill. Remote Sens Environ 124:185–209. doi:10.1016/j.rse.2012.03.024
205. Lelli L, Kokhanovsky AA, Rozanov VV, Vountas M, Sayer AM, Burrows JP (2012) Seven years of global retrieval of cloud properties using space-borne data of GOME. Atmos Meas Tech 5:1551–1570. doi:10.5194/amt-5-1551-2012
206. Lenoble J, Remer L, Tanre D (2013) Aerosol remote sensing. Springer. ISBN:9783642177255
207. Le Toan T, Beaudoin A, Riom J, Guyon D (1992) Relating forest biomass to SAR data. IEEE Trans Geosci Remote Sens 30(2):403–411. doi:10.1109/36.134089
208. Lhermitte RM (1988) Cloud and precipitation remote sensing at 94 GHz. IEEE Trans Geosci Remote Sens 26(3):207–216. doi:10.1109/36.3024
209. Liang S (2005) Quantitative remote sensing of land surfaces. Wiley. ISBN:9780471723714
210. Liao L, Sassen K (1994) Investigation of relationships between Ka-band radar reflectivity and ice and liquid water contents. Atmos Res 34:231–248. doi:http://dx.doi.org/10.1016/0169-8095(94)90094-9
211. Lim K, Treitz P, Wulder M, St-Onge B, Flood M (2003) LiDAR remote sensing of forest structure. Prog Phys Geogr 27(1):88–106. doi:10.1191/0309133303pp360ra
212. Liss SP, Duce RA (2005) The sea surface and global change. Cambridge University Press. ISBN:9780521017459
213. Liu W-Y, Field RT, Gantt RG, Klemas V (1987) Measurement of the surface emissivity of turbid waters. Remote Sens Environ 21(1):97–109. doi:10.1016/0034-4257(87)90009-5
214. Lopez-Sanchez JM, Ballester-Berman JD (2009) Potentials of polarimetric SAR interferometry for agriculture monitoring. Radio Sci 44:RS2010. doi:10.1029/2008RS004078
215. Lu Y, Li X, Tian Q, Han W (2012) An optical remote sensing model for estimating oil slick thickness based on two-beam interference theory. Opt Expr 20(22). doi:10.1364/OE.20.024496
216. Luo X, Askne J, Smith G, Dammert P (2001) Coherence characteristics of radar signals from rough soil. Prog Electromagn Res (PIER) 31:69–88. doi:10.2528/PIER00052903. http://www.jpier.org/PIER/pier.php?volume=31 (visited on 09 Nov 2014)
217. Lyon RJP, Green AA (1975) Reflectance and emittance of terrain in the mid-infrared (6–25 μm) region. In: Karr C Jr (ed) Infrared and Raman spectroscopy of lunar and terrestrial minerals. Academic. ISBN:9780123999504
218. MacCallum NS, Merchant CJ (2012) Surface water temperature observations of large lakes by optimal estimation. Can J Remote Sens 38(1):25–45. doi:10.5589/m12-010

219. MacGorman RD, Rust WD (1998) The electrical nature of storms. Oxford University Press. ISBN:9780195073379
220. Maddox AR, Department of Atmospheric Science CSU (1980). Mesoscale convective complexes. Bull Am Meteorol Soc 61(11):1374–1387. http://employees.oneonta.edu/ellistd/meteorology/maddox1980.pdf (visited on 09 Nov 2014)
221. Maddy ES, Barnet CD, Goldberg M, Sweeney C, Liu X (2008) CO_2 retrievals from the atmospheric infrared sounder: methodology and validation. J Geophys Res Atmos 113(D11301). doi:10.1029/2007JD009402
222. Manney GL, Daffer WH, Zawodny JM, Bernath PF, Hoppel KW, Walker KA, Knosp BW, Boone C, Remsberg EE, Santee ML, Harvey VL, Pawson S, Jackson DR, Deaver L, McElroy CT, McLinden CA, Drummond JR, Pumphrey HC, Lambert A, Schwartz MJ, Froidevaux L, McLeod S, Takacs LL, Suarez MJ, Trepte CR, Cuddy DC, Livesey NJ, Harwood RS, Waters JW (2007) Solar occultation satellite data and derived meteorological products: sampling issues and comparisons with Aura Microwave Limb Sounder. J Geophys Res Atmos 112:D24S50:1–27. doi:10.1029/2007JD008709
223. Martin S (2014) An introduction to ocean remote sensing. Cambridge University Press. ISBN:9781107019386
224. Martin ME, Newman SD, Aber JD, Congalton RG (1998) Determining forest species composition using high spectral resolution remote sensing data. Remote Sens Environ 65(3):249–254. doi:10.1016/S0034-4257(98)00035-2
225. Martin RV (2008) Satellite remote sensing of surface air quality. Atmos Environ 42(34):7823–7843. doi:http://dx.doi.org/10.1016/j.atmosenv.2008.07.018
226. Masad E, Muhunthan B, Shashidhar N, Harman T (1999) Internal structure characterization of asphalt concrete using image analysis. J Comput Civ Eng 13(2):88–95. doi:10.1061/(ASCE)0887-3801(1999)13:2(88)
227. Masuda K, Takashima T, Takayama Y (1988) Emissivity of pure and sea waters for the model sea surface in the infrared window regions. Remote Sens Environ 24(2):313–329. doi:http://dx.doi.org/10.1016/0034-4257(88)90032-6
228. Masunaga H, Kummerow CD (2005) Combined radar and radiometer analysis of precipitation profiles for a parametric retrieval algorithm. J Atmos Oceanic Technol 22(7):909–929. doi:10.1175/JTECH1751.1
229. Mätzler C, Rosenkranz PW, Battaglia A, Wigneron J-P (eds) (2006) Thermal microwave radiation: applications for remote sensing. Institution of Engineering and Technology. ISBN:9780863415739
230. Maynard RH (1945) Radar and weather. J Meteorol 2(4):214–226. http://journals.ametsoc.org/doi/pdf/10.1175/1520-0469(1945)002/%3C0214:RAW/%3E2.0.CO/%3B2 (visited on 09 Nov 2014)
231. MEDESS-4MS Mediterranean Decision Support System for Marine Safety. European Regional Development Fund. http://www.medess4ms.eu/oil-spill-models (visited on 09 Apr 2014)
232. Meier RR (1991) Ultraviolet spectroscopy and remote sensing of the upper atmosphere. Space Sci Rev 58(1):1–185. doi:10.1007/BF01206000
233. Meischner P (ed) (2004) Weather radar: principles and advanced applications. Springer. ISBN:9783540003281
234. Meissner T, Wentz FJ (2004) The complex dielectric constant of pure and sea water from microwave satellite observations. IEEE Trans Geosci Remote Sens 42(9):1836–1849. doi:10.1109/TGRS.2004.831888
235. Meissner T, Wentz FJ (2012) The emissivity of the ocean surface between 6 and 90 GHz over a large range of wind speeds and Earth incidence angles. IEEE Trans Geosci Remote Sens 50(8):3004–3026
236. Menzel WP, Smith WL, Stewart TR (1983) Improved cloud motion wind vector and altitude assignment using VAS. J Clim Appl Meteorol 22(3):377–384. doi:10.1175/1520-0450(1983)022⟨0377:ICMWVA⟩2.0.CO;2

237. Mercury M, Green R, Hook S, Oaida B, Wu W, Gunderson A, Chodas M (2012) Global cloud cover for assessment of optical satellite observation opportunities: a HyspIRI case study. Remote Sens Environ 126:62–71. doi:http://dx.doi.org/10.1016/j.rse.2012.08.007
238. METOP. EUMETSAT. http://www.eumetsat.int/website/home/Satellites/CurrentSatellites/Metop/index.html (visited on 23 Apr 2014)
239. Metternicht IG, Zinck JA (2003) Remote sensing of soil salinity: potentials and constraints. Remote Sens Environ 85(1):1–20. doi:10.1016/S0034-4257(02)00188-8
240. Meyer J, Schlesier A, Rozanov A, Bovensmann H, Burrows J (2004) Towards O_3 and NO_2 vertical profile retrieval from SCIAMACHY solar occultation measurements: first results. Adv Space Res 34(4):744–748. doi:http://dx.doi.org/10.1016/j.asr.2003.05.053
241. Michaelides S, Levizzani V, Anagnostou E, Bauer P, Kasparis T, Lane JE (2009) Precipitation: measurement, remote sensing, climatology and modeling. Atmos Res 94(4):512–533. doi:10.1016/j.atmosres.2009.08.017
242. Mieruch S, Weber M, von Savigny C, Rozanov A, Bovensmann H, Burrows JP, Bernath PF, Boone CD, Froidevaux L, Gordley LL, Mlynczak MG, Russell JM III, Thomason LW, Walker KA, Zawodny JM (2012) Global and long-term comparison of SCIAMACHY limb ozone profiles with correlative satellite data (2002-2008). Atmos Meas Tech 5(4):771–788. doi:10.5194/amt-5-771-2012
243. Minnis P, Garber DP, Young DF, Arduini RF, Takano Y (1998) Parameterizations of reflectance and effective emittance for satellite remote sensing of cloud properties. J Atmos Sci 55(22):3313–3339. doi:10.1175/1520-0469(1998)055⟨3313:PORAEE⟩2.0.CO;2
244. Minnis P, Smith WL Jr, Young DF (2001) Cloud macro- and microphysical properties derived from GOES over the ARM SGP domain. In: Proceedings of the eleventh atmospheric radiation measurement (ARM) science team meeting, Atlanta, 19–23 Mar 2001. http://www.arm.gov/publications/proceedings/conf11/extendedabs/minnis_p.pdf?id=96 (visited on 09 Nov 2014)
245. Minnis P, Sun-Mack S, Chen Y, Yi H, Huang J, Nguyen L, Khaiyer MM (2005) Detection and retrieval of multi-layered cloud properties using satellite data. In: SPIE Europe international symposium on remote sensing, remote sensing of clouds and the atmosphere X, Bruges, 19–22 Sept 2005. http://hjp.lzu.edu.cn/publications/pdf/Minnis.SPIE.05.pdf (visited on 01 May 2014)
246. Minnis P, Yost CR, Sun-Mack S, Chen Y (2008) Estimating the top altitude of optically thick ice clouds from thermal infrared satellite observations using CALIPSO data. Geophys Res Lett 35:L12801. doi:10.1029/2008GL033947
247. Mitchell RB (1994) Intentional oil pollution at sea. MIT. ISBN:9780262133036
248. MODIS Atmosphere – Cloud Mask. NASA. http://modis-atmos.gsfc.nasa.gov/MOD35L2/ (visited on 25 Apr 2014)
249. Mohammed GH, Goulas Y, Magnani F, Moreno J, Olejníčková J, Rascher U, van der Tol C, Verhoef W, Ač A, Daumard F, Gallé A, Malenovský Z, Pernokis D, Rivera JP, Verrelst J, Drusch M (2014) 2012 FLEX/Sentinel-3 Tandem mission photosynthesis study – final report. ESA/ESTEC. http://www.flex-photosyn.ca/Reports/PS-Study_FINAL_REPORT_Full_Report_$\delimiter"026E30F$%28Public$\delimiter"026E30F$%29.pdf (visited on 03 Nov 2014)
250. Monahan CE, O'Muircheartaigh IG (1986) Whitecaps and the passive remote sensing of the ocean surface. Int J Remote Sens 7(5):627–642. doi:10.1080/01431168608954716
251. Moran MS, Inoue Y, Barnes EM (1997) Opportunities and limitations for image-based remote sensing in precision crop management. Remote Sens Environ 61(3):319–346. doi:10.1016/S0034-4257(97)00045-X
252. Moran MS, Vidal A, Troufleau D, Qi J, Clarke TR, Pinter PJ Jr, Mitchell TA, Inoue Y, Neale CMU (1997) Combining multifrequency microwave and optical data for crop management. Remote Sens Environ 61(1):96–109. doi:10.1016/S0034-4257(96)00243-X
253. Morel A (1980) In-water and remote measurements of ocean color. Boundary-Layer Meteorol 18(2):177–201. doi:10.1007/BF00121323

254. Mugnai A, Smith EA (1988) Radiative transfer to space through a precipitating cloud at multiple microwave frequencies. Part I: model description. J Appl Meteorol 27(9):1055–1073. doi:10.1175/1520-0450(1988)⟨027(1055:RTTSTA)⟩2.0.CO;2
255. Mulder VL, de Bruin S, Schaepman ME, Mayr TR (2011) The use of remote sensing in soil and terrain mapping – a review. Geoderma 162(1–2):1–19. doi:10.1016/j.geoderma.2010.12.018
256. Mulders MA (1987) Remote sensing in soil science. Elsevier. ISBN:9780080869834
257. NASA Science Missions – Nimbus. NASA. http://science.nasa.gov/missions/nimbus/ (visited on 23 Apr 2014)
258. National Doppler Radar Sites. NOAA National Weather Service. http://radar.weather.gov/ (visited on 06 July 2014)
259. Nechad B, Ruddick KG, Park Y (2010) Calibration and validation of a generic multisensor algorithm for mapping of total suspended matter in turbid waters. Remote Sens Environ 114(4):854–866. doi:10.1016/j.rse.2009.11.022
260. Neggers RAJ, Jonker HJJ, Siebesma AP (2003) Size statistics of cumulus cloud populations in large-eddy simulations. J Atmos Sci 60(8):1060–1074. doi:10.1175/1520-0469(2003)60⟨1060:SSOCCP⟩2.0.CO;2
261. Nesti G, Tarchi D, Rudant J-P (1995) Decorrelation of backscattered signal due to soil moisture changes. In: International geoscience and remote sensing symposium. IGARSS '95. Quantitative remote sensing for science and applications, vol 3. July 1995, pp 2026–2028. doi:10.1109/IGARSS.1995.524098
262. Nett H, Endemann M (2004) Atmospheric dynamics mission: Aeolus. In: 2004 IEEE International geoscience and remote sensing symposium. IGARSS '04. Proceedings, vol 2, Sept 2004, pp 1190–1195. doi:10.1109/IGARSS.2004.1368628
263. NIMBUS-7 Total Ozone Mapping Spectrometer (TOMS). Natural Environment Research Council. http://badc.nerc.ac.uk/view/badc.nerc.ac.ukATOM__dpt_dpt_TOMS (visited on 23 Apr 2014)
264. Noble SD, Brown RB, Crowe TG (2002) The use of spectral properties for weed detection and identification – a review. In: AIC 2002 meeting CSAE/SCGR program, Saskatoon, 14–17 July 2002. http://www.engr.usask.ca/societies/csae/PapersAIC2002/CSAE02-208.pdf (visited on 09 Nov 2014)
265. Ocean Surface Topography from Space. NASA/Caltech JPL. https://sealevel.jpl.nasa.gov (visited on 14 Sept 2014)
266. Ocean Surface Topography Mission (OSTM)/Jason-2. NASA/CNES. http://www.nasa.gov/mission_pages/ostm/overview/index.html#.VBVqXOdguBU (visited on 14 Sept 2014)
267. Odin. Swedish National Space Board. http://www.snsb.se/en/Home/Space-Activities-in-Sweden/Satellites/Odin/ (visited on 23 Apr 2014)
268. Odin OSIRIS. CSA. http://osirus.usask.ca/ (visited on 23 Apr 2014)
269. Oerke E-C, Steiner U, Dehne H-W, Lindenthal M (2006) Thermal imaging of cucumber leaves affected by downy mildew and environmental conditions. J Exp Bot 57(9):2121–2132. doi:10.1093/jxb/erj170
270. Oil Budget Calculator Deepwater Horizon (2010) Tech. rep. U.S. Oil Budget Calculator Science and Engineering Team. In: Lehr WJ, Bristol RS, Possolo A (eds) The Federal Interagency Solutions Group, Nov 2010. http://www.restorethegulf.gov/sites/default/files/documents/pdf/OilBudgetCalc_Full_HQ-Print_111110.pdf (visited on 09 Apr 2014)
271. Okamoto H (2012) Active remote sensing of cloud microphysics. In: Radiation processes in the atmosphere and ocean – international radiation symposium IRS2012, Berlin, 6–10 Aug 2012. AIP conference proceedings 1531. pp 19–22. doi:10.1063/1.4804697
272. Okamoto K, Manabe T, Shige S (2010) Spaceborne radar/microwave radiometer combined rain observation system. In: 6-th European conference on radar in meteorology and hydrology – ERAD 2010, Sibiu, June 19–10 Sept 2010. http://www.erad2010.org/Sibiu.htm (visited on 09 Nov 2014)

273. Olla P (ed) (2009) Space technologies for the benefit of human society and earth. Springer. ISBN:9781402095733
274. Owe M, de Jeu R, Walker J (2001) A methodology for surface soil moisture and vegetation optical depth retrieval using the microwave polarization difference index. IEEE Trans Geosci Remote Sens 39(8):1643–1654. doi:10.1109/36.942542
275. Owen T, Sagan C (1972) Minor constituents in planetary atmospheres: ultraviolet spectroscopy from the orbiting astronomical observatory. Icarus 16(3):557–568. doi:http://dx.doi.org/10.1016/0019-1035(72)90102-9
276. Paloscia S, Pampaloni P (1992) Microwave vegetation indexes for detecting biomass and water conditions of agricultural crops. Remote Sens Environ 40(1):15–26. doi:10.1016/0034-4257(92)90123-2
277. Pampaloni P, Paloscia S (1985) Experimental relationships between microwave emission and vegetation features. Int J Remote Sens 6(2):315–323. doi:10.1080/01431168508948446
278. Patenaude G, Hill RA, Milne R, Gaveau DLA, Briggs BBJ, Dawson TP (2004) Quantifying forest above ground carbon content using LiDAR remote sensing. Remote Sens Environ 93(3):368–380. doi:10.1016/j.rse.2004.07.016
279. Patino EJ, Duque JC (2013) A review of regional science applications of satellite remote sensing in urban settings. Comput Environ Urban Syst 37:1–17. doi:10.1016/j.compenvurbsys.2012.06.003
280. Patsayeva S, Yuzhakov V, Varlamov V, Barbini R, Fantoni R, Frassanito C, Palucci A (2001) Laser spectroscopy of mineral oils on the water surface. In: Proceedings of EARSeL-SIG-Workshop LIDAR, Dresden, 16–17 June 2000. EARSeL eProceedings no. 1, pp 106–114. http://www.eproceedings.org/static/vol01_1/contents.html (visited on 05 Sept 2014)
281. Paxton LJ, Morrison D, Strickland DJ, McHarg MG, Zhang Y, Wolven B, Kill H, Crowley G, Christensen AB, Meng C-I (2003) The use of far ultraviolet remote sensing to monitor space weather. Adv Space Res 31(4):813–818. doi:10.1016/S0273-1177(02)00886-4
282. Payan S, de La Noë J, Hauchecorne A, Camy-Peyret C (2005) A review of remote sensing techniques and related spectroscopy problems. C R Phys 6(8):825–835. doi:http://dx.doi.org/10.1016/j.crhy.2005.07.013
283. Penũelas J, Filella I (1998) Visible and near-infrared reflectance techniques for diagnosing plant physiological status. Trends Plant Sci 3(4):151–156. doi:10.1016/S1360-1385(98)01213-8
284. Peterson LD, Running SW (1989) Applications in forest science and management. In: Asrar G (ed) Theory and applications of optical remote sensing. Wiley. ISBN:9780471628958
285. Petrokofsky G, Kanamaru H, Achard F, Goetz SJ, Joosten H, Holmgren P, Lehtonen A, Menton MCS, Pullin AS, Wattenbach M (2012) Comparison of methods for measuring and assessing carbon stocks and carbon stock changes in terrestrial carbon pools. How do the accuracy and precision of current methods compare? A systematic review protocol. Environ Evid 1(6). doi:10.1186/2047-2382-1-6
286. Pettorelli N The normalized difference vegetation index. Oxford University Press. ISBN:9780199693160
287. Phillips N, McMillin L, Gruber A, Wark D (1979) An evaluation of early operational temperature soundings from TIROS-N. Am Meteorol Soc Bull 60:1188–1197
288. Phillips OM (1985) Spectral and statistical properties of the equilibrium range in wind-generated gravity waves. J Fluid Mech 156(1):505–531. doi:10.1017/S0022112085002221
289. Phillips OM (1980) The dynamics of the upper ocean. Cambridge University Press. ISBN:9780521298018
290. Piscini A, Picchiani M, Chini M, Corradini S, Merucci L, Del Frate F, Stramondo S (2014) A neural network approach for the simultaneous retrieval of volcanic ash parameters and SO_2 using MODIS data. Atmos Meas Tech 7(12):4023–4047. doi:10.5194/amt-7-4023-2014
291. Platt U, Perner D, Winer AM, Harris GW, Pitts NJ (1980) Detection of NO_3 in the polluted troposphere by differential optical absorption. Geophys Res Lett 7(1):89–92. doi:10.1029/GL007i001p00089

292. Platt U, Stutz J (2008) Differential optical absorption spectroscopy. Springer. ISBN:9783540211938
293. Precipitation Measurement Missions Lightning Imaging Sensor (LIS). NASA. http://pmm.nasa.gov/node/163 (visited on 29 Apr 2014)
294. Price JC (1994) How unique are spectral signatures? Remote Sens Environ 49(3):181–186. doi:10.1016/0034-4257(94)90013-2
295. Price JC (1985) On the analysis of thermal infrared imagery: the limited utility of apparent thermal inertia. Remote Sens Environ 18(1):59–73. doi:10.1016/0034-4257(85)90038-0
296. Probert-Jones JR (1962) The radar equation in meteorology. Q J R Meteorol Soc 88(378):485–495. doi:10.1002/qj.49708837810
297. Pruppacher RH, Klett JD (2010) Microphysics of clouds and precipitation. Kluwer. ISBN:9780306481000
298. Pyle DM, Mather TA, Biggs J (eds) (2014) Remote sensing of volcanoes and volcanic processes: integrating observation and modelling. Geol Soc. ISBN:9781862393622
299. Qiu X, Xu Q, Qiu C, Nai K, Zhang P (2013) Retrieving 3D wind field from phased array radar rapid scans. Adv Meteorol 2013:792631. doi:10.1155/2013/792631
300. Radar Images. Federal Office of Meteorology and Climatology MeteoSwiss. http://www.meteosuisse.admin.ch/web/en/weather/current_weather/radar-images.html (visited on 06 July 2014)
301. Radar/Storm Interpretation. NOAA. http://www.crh.noaa.gov/images/mkx/pdf/spotters/radarpt2.pdf (visited on 27 Apr 2014)
302. RAMS, the Regional Atmospheric Modeling System. Colorado State University CSU. http://rams.atmos.colostate.edu/rams-description.html (visited on 06 May 2014)
303. Rapp AD, Lebsock M, Kummerow C (2009) On the consequences of resampling microwave radiometer observations for use in retrieval algorithms. J Appl Meteorol Climatol 48(9):1981–1993. doi:10.1175/2009JAMC2155.1
304. Rathke C, Fischer J, Neshyba S, Shupe M (2002) Improving IR cloud phase determination with 20 microns spectral observations. Geophys Res Lett 29(8):doi:10.1029/2001GL014594
305. Reed M, Johansen O, Brandvik PJ, Daling P, Lewis A, Fiocco R, Mackay D, Prentki R (1999) Oil spill modeling towards the close of the 20th century: overview of the state of the art. Spill Sci Technol Bull 5(1):3–16. doi:10.1016/S1353-2561(98)00029-2
306. Reinhart B, Fuelberg H, Blakeslee R, Mach D, Heymsfield A, Bansemer A, Durden SL, Tanelli S, Heymsfield G, Lambrigtsen B (2014) Understanding the relationships between lightning, cloud microphysics, and airborne radar-derived storm structure during hurricane Karl (2010). Mon Weather Rev 142(2):590–605. doi:10.1175/MWR-D-13-00008.1
307. Reul N, Chapron B (2003) A model of sea-foam thickness distribution for passive microwave remote sensing applications. J Geophys Res 108(C 10):3321. doi:10.1029/2003JCOO1887
308. Reul N, Tenerelli J, Chapron B, Waldteufel P (2007) Modeling sun glitter at L-band for sea surface salinity remote sensing with SMOS. IEEE Trans Geosci Remote Sens 45(7):2073–2087. doi:10.1109/TGRS.2006.890421
309. Ribeiro da Luz B (2006) Attenuated total reflectance spectroscopy of plant leaves: a tool for ecological and botanical studies. New Phytol 172:305–318. doi:10.1111/j.1469-8137.2006.01823.x
310. Ribeiro da Luz B, Crowley JK (2007) Spectral reflectance and emissivity features of broad leaf plants: prospects for remote sensing in the thermal infrared (8.0–14.0 μm). Remote Sens Environ 109(4):393–405. doi:10.1016/j.rse.2007.01.008
311. Richter A, Burrows JP, Nuss H, Granier C, Niemeier U (2005) Increase in tropospheric nitrogen dioxide over China observed from space. Nature 437(7055):129–132. doi:10.1038/nature04092
312. Roberti L, Kummerow C (1995) A quantitative comparison between 3-D and plane parallel microwave radiative transfer codes applied to horizontally and vertically structured precipitating clouds. In: Solimini D (ed) Microwave radiometry and remote sensing of the environment. VSP. ISBN:9789067641890

313. Roberts R, Fabry F, Kennedy P, Nelson E, Wilson J, Rehak N, Fritz J, Chandrasekar V, Braun J, Sun J, Ellis S, Reising S, Crum T, Mooney L, Palme B (2008) Refractt-2006: real-time retrieval of high-resolution, low-level moisture fields from operational NEXRAD and research radars. Bull Am Meteorol Soc 89:1535–1548. doi:10.1175/2008BAMS2412.1
314. Robinson IS (1983) Satellite observations of ocean colour. In: Houghton JT, Cook AH, Charnock H (eds) The study of the ocean and the land surface from satellites. The Royal Society. ISBN:9780854032112
315. Robinson IS (1995) Satellite oceanography: an introduction for oceanographers and remote-sensing scientists. Wiley. ISBN:9780471954248
316. Rose WI, Bluth GJS, Ernst GGJ (2000) Integrating retrievals of volcanic cloud characteristics from satellite remote sensors: a summary. Philos Trans R Soc Lond A Math Phys Eng Sci 358(1770):1585–1606. doi:10.1098/rsta.2000.0605
317. Ruddick K, Neukermans G, Vanhellemont Q, Jolivet D (2014) Challenges and opportunities for geostationary ocean colour remote sensing of regional seas: a review of recent results. Remote Sens Environ 146:63–76. doi:10.1016/j.rse.2013.07.039
318. Rumpf T, Mahleinb A-K, Steiner U, Oerke E-C, Dehne H-W, Plümera L (2010) Early detection and classification of plant diseases with Support Vector Machines based on hyperspectral reflectance. Comput Electron Agric 74(1):91–99. doi:10.1016/j.compag.2010.06.009
319. Sabins FF (1999) Remote sensing for mineral exploration. Ore Geol Rev 14(3–4):157–183. doi:10.1016/S0169-1368(99)00007-4
320. SAGE II (Stratospheric Aerosol and Gas Experiment II). NASA. http://sage.nasa.gov/SAGE2/ (visited on 26 Apr 2014)
321. Salisbury JW (1986) Preliminary measurements of leaf spectral reflectance in the 8-14 μm region. Int J Remote Sens 7(12):1879–1886. doi:10.1080/01431168608948981
322. Salisbury WJ, D'Aria DM (1994) Emissivity of terrestrial materials in the 3-5 μm atmospheric window. Remote Sens Environ 47(3):345–361. ISSN:0034-4257. doi:http://dx.doi.org/10.1016/0034-4257(94)90102-3
323. Salisbury WJ, D'Aria DM (1992) Emissivity of terrestrial materials in the 8-14 μm atmospheric window. Remote Sens Environ 42(2):83–106. doi:10.1016/0034-4257(92)90092-X
324. Salisbury JW, d'Aria DM, Sabins FF Jr (1993) Thermal infrared remote sensing of crude oil slicks. Remote Sens Environ 45(2):225–231. doi:10.1016/0034-4257(93)90044-X
325. Sankaran S, Mishra A, Ehsani R, Davis C (2010) A review of advanced techniques for detecting plant diseases. Comput Electron Agric 72(1):1–13. doi:10.1016/j.compag.2010.02.007
326. Santos AMP (2000) Fisheries oceanography using satellite and airborne remote sensing methods: a review. Fish Res 49(1):1–20. doi:10.1016/S0165-7836(00)00201-0
327. Sasaki Y, Asanuma I, Muneyama K, Naito G, Suzuki T (1987) The dependence of sea-surface microwave emission on wind speed, frequency, incidence angle, and polarzation over the frequency range from 1 to 40 GHz. IEEE Trans Geosci Remote Sens GE-25(2):138–146. doi:10.1109/TGRS.1987.289813
328. Schmugge T, Jackson TJ (1994) Mapping surface soil moisture with microwave radiometers. Meteorol Atmos Phys 54(1–4):213–223. doi:10.1007/BF01030061
329. SCIAMACHY. ESA. https://earth.esa.int/web/guest/missions/esa-operational-eo-missions/envisat/instruments/sciamachy (visited on 23 Apr 2014)
330. Seelan SK, Laguette S, Casady GM, Seielstad GA (2003) Remote sensing applications for precision agriculture: a learning community approach. Remote Sens Environ 88(1–2):157–169. doi:10.1016/j.rse.2003.04.007
331. Seinfeld HJ, Pandis SN (1998) Atmospheric chemistry and physics: from air pollution to climate change. Wiley. ISBN:9780471178156
332. Sensors – AMSU-B Overview. NOAA STAR Center for Satellite Applications and Research. http://mirs.nesdis.noaa.gov/amsub.php (visited on 04 May 2014)
333. Shaw JA, Marston C (2000) Polarized infrared emissivity for a rough water surface. Opt Expr 7(11):375–380. doi:10.1364/OE.7.000375

334. Shi J-C, Dozier J (2000) Estimation of snow water equivalence using SIR-C/X-SAR. II. Inferring snow depth and particle size. IEEE Trans Geosci Remote Sens 38(6):2475–2488. doi:10.1109/36.885196
335. Shi J-C, Dozier J (2000) Estimation of snow water equivalence using SIR-C/X-SAR. I. Inferring snow density and subsurface properties. IEEE Trans Geosci Remote Sens 38(6):2465–2474. doi:10.1109/36.885195
336. Shupe MD, Daniel JS, de Boer G, Eloranta EW, Kollias P, Long CN, Luke EP, Turner DD, Verlinde J (2008) A focus on mixed-phase clouds – the status of ground-based observational methods. Bull Am Meteorol Soc 89:1549–1562. doi:10.1175/2008BAMS2378.1
337. Sims AD, Gamon JA (2002) Relationships between leaf pigment content and spectral reflectance across a wide range of species, leaf structures and developmental stages. Remote Sens Environ 81(2–3):337–354. doi:10.1016/S0034-4257(02)00010-X
338. Smith EA, Bauer P, Marzano FS, Kummerow CD, McKague D, Mugnai A, Panegrossi G (2002) Intercomparison of microwave radiative transfer models for precipitating clouds. IEEE Trans Geosci Remote Sens 40(3):541–549. doi:10.1109/TGRS.2002.1000314
339. SMOS. European Space Agency. http://www.esa.int/Our_Activities/Observing_the_Earth/SMOS/Mapping_soil_moisture_and_ocean_salinity (visited on 16 Apr 2014)
340. Snyder WC, Wan Z, Zhang Y, Feng Y-Z (1998) Classification-based emissivity for land surface temperature measurement from space. Int J Remote Sens 19(14):2753–2774. doi:10.1080/014311698214497
341. Schistad Solberg AH, Storvik G, Solberg R, Volden E (1999) Automatic detection of oil spills in ERS SAR images. IEEE Trans Geosci Remote Sens 37(4):1916–1924. doi:10.1109/36.774704
342. Song C (2005) Spectral mixture analysis for subpixel vegetation fractions in the urban environment: how to incorporate endmember variability? Remote Sens Environ 95(2):248–263. doi:10.1016/j.rse.2005.01.002
343. Srivastava HS, Patel P, Navalgund RR (2006) Application potentials of synthetic aperture radar interferometry for land-cover mapping and crop-height estimation. Curr Sci 91(6):783–788. http://repository.ias.ac.in/60596/ (visited on 10 Nov 2014)
344. Sorooshian S, AghaKouchak A, Arkin P, Eylander J, Foufoula-Georgiou E, Harmon R, Hendrickx J, Imam B, Kuligowski R, Skahill B, Skofronick-Jackson G (2011) Advanced concepts on remote sensing of precipitation at multiple scales. Bull Am Meteorol Soc 92(10):1353–1357. doi:10.1175/2011BAMS3158.1
345. Stevens B, Feingold G (2009) Untangling aerosol effects on clouds and precipitation in a buffered system. Nature 461(7264):607–613 doi:10.1038/nature08281
346. Stoner ER, Baumgardner MF, Biehl LL, Robinson BF (1980) Atlas of soil reflectance properties. Research bulletin 962. Purdue University Agricultural Experiment Station
347. Storm Prediction Center Mesoscale Analysis Page. NOAA's National Weather Service. http://www.spc.noaa.gov/sfctest/ (visited on 27 Apr 2014)
348. Strabala KI, Ackerman SA, Menzel WP (1994) Cloud properties inferred from 8–12 μm data. J Appl Meteorol 33(2):212–229. doi:10.1175/1520-0450(1994)033⟨0212:CPIFD⟩2.0.CO;2
349. Stratospheric Ozone. NOAA. http://www.ozonelayer.noaa.gov/science/basics.htm (visited on 22 Apr 2014)
350. Stubenrauch C, Rossow W, Kinne S (2012) Assessment of global cloud data sets from satellites. Tech. rep. WCRP No 23/2012. Global Energy and Water Cycle Experiment (GEWEX)
351. Stumm W, Morgan JJ (2012) Aquatic chemistry: chemical equilibria and rates in natural waters. Wiley. ISBN:9781118591482
352. Suthers MI, Rissik D (2009) Plankton: a guide to their ecology and monitoring for water quality. CSIRO Publishing. ISBN:9780643090583
353. Szoke EJ, Zipser EJ, Jorgensen DP (1986) A radar study of convective cells in mesoscale systems in GA TE. Part 1: vertical profile statistics and comparison with hurricanes. J Atmos Sci 43(2):182–197. doi:10.1175/1520-0469(1986)043⟨0182:ARSOCC⟩2.0.CO;2
354. Takashima T, Masuda K (1987) Emissivities of quartz and Sahara dust powders in the infrared region (7–17 μ). Remote Sens Environ 23(1):51–63. doi:10.1016/0034-4257(87)90070-8

355. Tapiador FJ, Turk FJ, Petersen W, Hou AY, García-Ortega E, Machado LAT, Angelis CF, Salio P, Kidd C, Huffman GJ, de Castro M (2012) Global precipitation measurement: methods, datasets and applications. Atmos Res 70–97. doi:10.1016/j.atmosres.2011.10.021
356. Taravat A, Del Frate F (2012) Development of band ratioing algorithms and neural networks to detection of oil spills using Landsat ETM+ data. EURASIP J Adv Signal Process 2012(1):107. doi:10.1186/1687-6180-2012-107. http://asp.eurasipjournals.com/content/2012/1/107
357. Tebaldini S (2008) Forest SAR tomography: a covariance matching approach. In: 2008 IEEE radar conference. RADAR '08, May 2008, pp 1–6. doi:10.1109/RADAR.2008.4721084
358. Tebaldini S, Rocca F (2012) Multibaseline polarimetric SAR tomography of a boreal forest at P- and L-bands. IEEE Trans Geosci Remote Sens 50(1):232–246. doi:10.1109/TGRS.2011.2159614
359. Terzaghi K, Peck RB, Mesri G (1996) Soil mechanics in engineering practice. Wiley. ISBN:9780471086581
360. Testik YF, Gebremichael M (eds) (2013) Rainfall: state of the science. Wiley. ISBN:9781118672143
361. Tilly N, Hoffmeister D, Cao Q, Huang S, Lenz-Wiedemann V, Miao Y, Bareth G (2014) Multitemporal crop surface models: accurate plant height measurement and biomass estimation with terrestrial laser scanning in paddy rice. J Appl Remote Sens 8(1):083671. doi:10.1117/1.JRS.8.083671
362. TIMED. NASA. http://science.nasa.gov/missions/timed/ (visited on 23 Apr 2014)
363. Treuhaft NR, Cloude SR (1999) The structure of oriented vegetation from polarimetric interferometry. IEEE Trans Geosci Remote Sens 37(5):2620–2624. doi:10.1109/36.789657
364. Treuhaft RN, Madsen SN, Moghaddam M, van Zyl JJ (1996) Vegetation characteristics and underlying topography from interferometric radar. Radio Sci 31(6):1449–1485. doi:10.1029/96RS01763
365. Treuhaft NR, Siqueira PR (2000) Vertical structure of vegetated land surfaces from interferometric and polarimetric radar. Radio Sci 35(1):141–177. doi:10.1029/1999RS900108
366. TRMM Tropical Rainfall Measuring Mission. NASA Goddard Space Flight Center. http://trmm.gsfc.nasa.gov (visited on 06 July 2014)
367. Tucker CJ, Newcomb WW, Los SO, Prince SD (1991) Mean and inter-year variation of growing season normalized difference vegetation index for the Sahel 1981-1989. Int J Remote Sens 12(6):1133–1135. doi:10.1080/01431169108929717
368. Ulaby FT, Moore RK, Fung AK (1982) Microwave remote sensing: active and passive. Radar remote sensing and surface scattering and emission theory, vol 2. Addison-Wesley. ISBN:9780890061916
369. Ulaby FT, Moore RK, Fung AK (1986) Microwave remote sensing: active and passive. From theory to applications, vol 3. Artech House. ISBN:9780890061923
370. Utkin AB, Lavrov A, Vilar R (2010) Evaluation of oil spills by laser induced fluorescence spectra. SPIE Proc 7994:799415–10. doi:10.1117/ 12.880750
371. Vaglio Laurin G, Chen Q, Lindsell JA, Coomes DA, Del Frate F, Guerriero L, Pirotti F, Valentini R (2014) Above ground biomass estimation in an African tropical forest with lidar and hyperspectral data. ISPRS J Photogramm Remote Sens 89:49–58. doi:10.1016/j.isprsjprs.2014.01.001
372. Vaglio Laurin G, Del Frate F, Pasolli L, Notarnicola C, Guerriero L, Valentini R (2013) Discrimination of vegetation types in alpine sites with ALOS PALSAR-, RADARSAT-2-, and lidar-derived information. Int J Remote Sens 34(19):6898–6913. doi:10.1080/01431161.2013.810823
373. Vaglio Laurin G, Liesenberg V, Chen Q, Guerriero L, Del Frate F, Bartolini A, Coomes D, Wilebore B, Lindsell J, Valentini R (2013) Optical and SAR sensor synergies for forest and land cover mapping in a tropical site in West Africa. Int J Appl Earth Obs Geoinf 21:7–16. doi:10.1016/j.jag.2012.08.002

374. van der Meer FD, van der Werff HMA, van Ruitenbeek FJA, Hecker CA, Bakker WH, Noomen MF, van der Meijde M, Carranza EJM, Boudewijn de Smeth J, Woldai T (2012) Multi- and hyperspectral geologic remote sensing: a review. Int J Appl Earth Obs Geoinf 14(1):112–128. doi:10.1016/j.jag.2011.08.002
375. van Donkelaar A, Martin R, Brauer M, Kahn R, Levy R, Verduzco C, Villeneuve P (2010) Global estimates of ambient fine particulate matter concentrations from satellite-based aerosol optical depth: development and application. Environ Health Perspect 118(6):847–855. doi:10.1289/ehp.0901623
376. Vegetation Applications: Agriculture, Forestry, and Ecology. Federation of American Scientists. https://www.fas.org/irp/imint/docs/rst/Sect3/Sect3_1.html (visited on 26 Mar 2014)
377. Villarino R, Camps A, Vall-Ilossera M, Miranda J, Arenas J (2003) Sea foam effects on the brightness temperature at L-band. In: 2003 IEEE international geoscience and remote sensing symposium, 2003. IGARSS '03. Proceedings, vol 5, pp 3076–3078. doi:10.1109/IGARSS.2003.1294688
378. Vivekanandan J, Lee W-C, Loew E, Salazar JL, Grubišic V, Moore J, Tsai P (2014) The next generation airborne polarimetric Doppler weather radar. Geosci Instrum Methods Data Sys 4:1–42. doi:10.5194/gid-4-1-2014
379. Wagner T, Beirle S, Deutschmann T, Eigemeier E, Frankenberg C, Grzegorski M, Liu C, Marbach T, Platt U, Penning de Vries M (2008) Monitoring of atmospheric trace gases, clouds, aerosols and surface properties from UV/vis/NIR satellite instruments. J Opt A Pure Appl Opt 10:104019. doi:10.1088/1464-4258/10/10/104019
380. Walter SL, Salisbury JW (1988) The basis for the spectral behaviour of silicates in the thermal infrared and applications to remote sensing. In: ESA SP-287 Spectral signatures of objects in remote sensing, Aussois, 18–22 Jan 1988, pp 337–340
381. Walter-Shea EA, Norman JM (1991) Leaf optical properties. In: Myneni BR, Ross J (eds) Photon-vegetation interactions. Springer. ISBN:9783642753893
382. Wang L, Wang Y, Mohammad L, Harman T (2002) Voids distribution and performance of asphalt concrete. Int J Pavements 1(3):22–33
383. Wark DQ, Saiedy F, James DG (1967) Indirect measurements of atmospheric temperature profiles from satellites: VI. High-altitude balloon testing. Mon Weather Rev 95(7):468–479. doi:10.1175/1520-0493(1967)095⟨0468:IMOATP⟩2.3.CO;2
384. Waters JW, Froidevaux L, Harwood RS, Jarnot RF, Pickett HM, Read WG, Siegel PH, Cofield RE, Filipiak MJ, Flower DA, Holden JR, Lau GK, Livesey NJ, Manney GL, Pumphrey HC, Santee ML, Wu DL, Cuddy DT, Lay RR, Loo MS, Perun VS, Schwartz MJ, Stek PC, Thurstans RP, Boyles MA, Chandra KM, Chavez MC, Gun-Shing Chen, Chudasama BV, Dodge R, Fuller RA, Girard MA, Jiang JH, Yibo Jiang, Knosp BW, LaBelle RC, Lam JC, Lee KA, Miller D, Oswald JE, Patel NC, Pukala DM, Quintero O, Scaff DM, Van Snyder W, Tope MC, Wagner PA, Walch MJ (2006) The Earth observing system microwave limb sounder (EOS MLS) on the Aura satellite. IEEE Trans Geosci Remote Sens 44(5):1075–1092. doi:10.1109/TGRS.2006.873771
385. Watson IM, Realmuto VJ, Rose WI, Prata AJ, Bluth GJS, Gu Y, Bader CE, Yu T (2004) Thermal infrared remote sensing of volcanic emissions using the moderate resolution imaging spectroradiometer. J Volcanol Geotherm Res 135(1–2):75–89. doi:10.1016/j.jvolgeores.2003.12.017
386. Watson K (1982) Regional thermal inertia mapping from an experimental satellite. Geophysics 47(12):1681–1687. doi:10.1190/1.1441317
387. Wegmüller U , Werner C (1997) Retrieval of vegetation parameters with SAR interferometry. IEEE Trans Geosci Remote Sens 35(1):18–24. doi:10.1109/36.551930
388. Wegmüller U, Werner CL, Nüesch D, Borgeaud M (1995) Land-surface analysis using ERS-1 SAR interferometry. ESA Bull 81, pp 30–37
389. Weng Q (ed) (2011) Advances in environmental remote sensing: sensors, algorithms, and applications. Taylor & Francis. ISBN:9781420091816

390. Westwater ER (1972) Ground-based determination of low altitude temperature profiles by microwaves. Mon Weather Rev 100(1):15–28. doi:10.1175/1520-0493(1972)100⟨0015:GDOLAT⟩2.3.CO;2
391. Westwater ER, Grody NC (1980) Combined surface- and satellite-based microwave temperature profile retrieval. J Appl Meteorol 19(12):1438–1444. doi:10.1175/1520-0450(1980)019⟨1438:CSASBM⟩2.0.CO;2
392. What is ADM-Aeolus? ESA. https://earth.esa.int/web/guest/missions/esa-future-missions/adm-aeolus (visited on 19 Apr 2014)
393. Wiesmann A, Mätzler C (1999) Microwave emission model of layered snowpacks. Remote Sens Environ 70(3):307–316. doi:10.1016/S0034-4257(99)00046-2
394. Wigneron J-P, Guyon D, Calvet J-C, Courrier G, Bruguier N (1997) Monitoring coniferous forest characteristics using a multifrequency (5–90 GHz) microwave radiometer. Remote Sens Environ 60(3):299–310. doi:10.1016/S0034-4257(96)00212-X
395. Wilheit TT (1979) A model for the microwave emissivity of the ocean's surface as a function of wind speed. Tech. rep. NASA TM 80278. NASA GSFC, Apr 1979
396. Wilheit TT, Chang ATC, Rao MSV, Rodgers EB, Theon SJ (1977) A satellite technique for quantitatively mapping rainfall rates over the oceans. J Appl Meteorol 16(5):551–560. doi:10.1175/1520-0450(1977)016⟨0551:ASTFQM⟩2.0.CO;2
397. Williams PM, Carlucci AF, Henrichs SM, Van Vleet ES, Horrigan SG, Reid FMH, Robertson KJ (1986) Chemical and microbiological studies of sea-surface films in the Southern Gulf of California and off the West Coast of Baja California. Mar Chem 19(1):17–98. doi:http://dx.doi.org/10.1016/0304-4203(86)90033-2
398. Wilson WJ, Brandes EA (1979) Radar measurement of rainfall – a summary. Bull Am Meteorol Soc 60(9):1048–1058. doi:10.1175/1520-0477(1979)060⟨1048:RMORS⟩2.0.CO;2
399. Wilson HW, Kiefer DA (1979) Reflectance spectroscopy of marine phytoplankton. Part 2. A simple model of ocean color. Limnol Oceanogr 24(4):673–682. doi:10.4319/lo.1979.24.4.0673
400. Winker DM, Hunt WH, McGill MJ (2007) Initial performance assessment of CALIOP. Geophys Res Lett 34(19). doi:10.1029/2007GL030135
401. Wu M-LC (1985) Remote sensing of cloud-top pressure using reflected solar radiation in the Oxygen A-Band. J Clim Appl Meteorol 24(6):539–546. doi:10.1175/1520-0450(1985)024⟨0539:RSOCTP⟩2.0.CO;2
402. Xiao J, Moody A (2005) A comparison of methods for estimating fractional green vegetation cover within a desert-to-upland transition zone in central New Mexico, U.S.A. Remote Sens Environ 98(2–3):237–250. doi:10.1016/j.rse.2005.07.011
403. Yamamoto G, Wark DQ (1961) Discussion of the letter by R. A. Hanel, Determination of cloud altitude from a satellite. J Geophys Res 66(10):3596. doi:10.1029/JZ066i010p03596
404. Yueh SH (1997) Modeling of wind direction signals in polarimetric sea surface brightness temperatures. IEEE Trans Geosci Remote Sens 35(6):1400–1418. doi:10.1109/36.649793
405. Yueh SH, Wilson WJ, Fuk KLi, Nghiem SV, Ricketts BW (1995) Polarimetric measurements of sea surface brightness temperatures using an aircraft K-band radiometer. IEEE Trans Geosci Remote Sens 33(1):85–92. doi:10.1109/36.368219
406. Zeng S, Riedi J, Parol F, Cornet C, Thieuleux F (2013) An assessment of cloud top thermodynamic phase products obtained from A-Train passive and active sensors. Atmos Meas Tech Discuss 6(5):8371–8411. doi:10.5194/amtd-6-8371-2013
407. Zhang X (1995) Capillary-gravity and capillary waves generated in a wind wave tank: observations and theories. J Fluid Mech 289:51–82. doi:10.1017/s0022112095001236
408. Zhang L, Grift TE (2012) A LIDAR-based crop height measurement system for Miscanthus giganteus. Comput Electron Agric 85:70–76. doi:10.1016/j.compag.2012.04.001
409. Zhou Y-S, Hong W, Wang Y-P, Wu Y-R (2012) Maximal effective baseline for polarimetric interferometric SAR forest height estimation. Sci China Inf Sci 55(4):867–876. doi:10.1007/s11432-011-4398-1

410. Zolkos SG, Goetz SJ, Dubayah R (2013) A meta-analysis of terrestrial above-ground biomass estimation using lidar remote sensing. Remote Sens Environ 128:289–298. doi:10.1016/j.rse.2012.10.017
411. Zwiggelaar R (1998) A review of spectral properties of plants and their potential use for crop/weed discrimination in row-crops. Crop Prot 17(3):189–206. doi:10.1016/S0261-2194(98)00009-X

Appendix A
Vectors, Coordinates and Operators

A.1 Recalling Vectors

A vector is usually denoted by a bold letter to be distinguished from a scalar quantity. The vector contains information on amplitude (modulus) and direction (versor) of the quantity it represents. For instance, the *position vector* $\boldsymbol{r} = r\,\mathbf{r}_0$ has modulus r (distance from the origin of coordinates) and versor $\mathbf{r}_0$ (angular position with respect to the reference system).

A.1.1 Vectors in Cartesian Coordinates

In the Euclidean space, vectors are defined by their three components. In a Cartesian coordinate system, the position vector $\boldsymbol{r}(x, y, z)$, for instance, is expressed by

$$\boldsymbol{r} = x\,\mathbf{x}_0 + y\,\mathbf{y}_0 + z\,\mathbf{z}_0 \tag{A.1}$$

while a velocity field is

$$\boldsymbol{v}(x, y, z) = v_x(x, y, z)\mathbf{x}_0 + v_y(x, y, z)\mathbf{y}_0 + v_z(x, y, z)\mathbf{z}_0$$

Note that each component v_i $(i = x, y, z)$ of the vector field $\boldsymbol{v}$ generally depends on all three coordinates.

D. Solimini, *Understanding Earth Observation*, Remote Sensing and Digital Image Processing 23, DOI 10.1007/978-3-319-25633-7

A.1.2 Vector Multiplication

A.1.2.1 Dot Product

The *dot*, or *scalar product*[1] (denoted by $\cdot$) of two vectors $\boldsymbol{A}$ and $\boldsymbol{B}$ results in the scalar quantity

$$\boldsymbol{A} \cdot \boldsymbol{B} = A_x B_x + A_y B_y + A_z B_z \ .$$

A.1.2.2 Cross Product

The *cross* or *vector product* (denoted by $\times$) between $\boldsymbol{A}$ and $\boldsymbol{B}$ results in the vector quantity

$$\begin{aligned} \boldsymbol{A} \times \boldsymbol{B} &= \begin{vmatrix} \mathbf{x}_0 & \mathbf{y}_0 & \mathbf{z}_0 \\ A_x & A_y & A_z \\ B_x & B_y & B_z \end{vmatrix} \\ &= (A_y B_z - A_z B_y)\mathbf{x}_0 + (A_z B_x - A_x B_z)\mathbf{y}_0 + (A_x B_y - A_y B_x)\mathbf{z}_0 \ , \end{aligned} \tag{A.2}$$

perpendicular to the plane containing $\boldsymbol{A}$ and $\boldsymbol{B}$.

A.1.2.3 Outer Product and Dyadics

The *outer product* between $\boldsymbol{A}$ and $\boldsymbol{B}$ (denoted by $\boldsymbol{AB}$ or by $\boldsymbol{A} \otimes \boldsymbol{B}$) generates the *dyadic tensor* $\mathbb{D}$

$$\begin{aligned} \boldsymbol{AB} \equiv \boldsymbol{A} \otimes \boldsymbol{B} = \boldsymbol{AB}^{\intercal} = \mathbb{D} = {} & A_x B_x \mathbf{x}_0 \mathbf{x}_0 + A_x B_y \mathbf{x}_0 \mathbf{y}_0 + A_x B_z \mathbf{x}_0 \mathbf{z}_0 \\ & + A_y B_x \mathbf{y}_0 \mathbf{x}_0 + A_y B_y \mathbf{y}_0 \mathbf{y}_0 + A_y B_z \mathbf{y}_0 \mathbf{z}_0 \\ & + A_z B_x \mathbf{z}_0 \mathbf{x}_0 + A_z B_y \mathbf{z}_0 \mathbf{y}_0 + A_z B_z \mathbf{z}_0 \mathbf{z}_0 \ , \end{aligned} \tag{A.3}$$

where the superscript $^{\intercal}$ denotes transpose. The dot product between a tensor $\mathbb{D}$ and a vector $\boldsymbol{C}$ generates the vector

$$\begin{aligned} \boldsymbol{E} = \mathbb{D} \cdot \boldsymbol{C} \ = {} & (A_x B_x \mathbf{x}_0 \mathbf{x}_0 + A_x B_y \mathbf{x}_0 \mathbf{y}_0 + A_x B_z \mathbf{x}_0 \mathbf{z}_0) \cdot (C_x \mathbf{x}_0 + C_y \mathbf{y}_0 + C_z \mathbf{z}_0) \\ & + (A_y B_x \mathbf{y}_0 \mathbf{x}_0 + A_y B_y \mathbf{y}_0 \mathbf{y}_0 + A_y B_z \mathbf{y}_0 \mathbf{z}_0) \cdot (C_x \mathbf{x}_0 + C_y \mathbf{y}_0 + C_z \mathbf{z}_0) \\ & + (A_z B_x \mathbf{z}_0 \mathbf{x}_0 + A_z B_y \mathbf{z}_0 \mathbf{y}_0 + A_z B_z \mathbf{z}_0 \mathbf{z}_0) \cdot (C_x \mathbf{x}_0 + C_y \mathbf{y}_0 + C_z \mathbf{z}_0) \\ = {} & (A_x B_x C_x + A_x B_y C_y + A_x B_z C_z)\ \mathbf{x}_0 \end{aligned}$$

[1] The scalar product generalizes into *inner product* in abstract vector spaces.

$$+(A_y B_x C_x + A_y B_y C_y + A_y B_z C_z)\ \mathbf{y}_0$$
$$+(A_z B_x C_x + A_z B_y C_y + A_z B_z C_z)\ \mathbf{z}_0 \equiv [\mathbb{D}]\, \boldsymbol{C}\ .$$

Note that

$$\mathbb{D} \cdot \boldsymbol{C} \neq \boldsymbol{C} \cdot \mathbb{D}\ ,$$

hence it is essential to specify the order of the product.

A.1.2.4 Double Products

The mixed double product between three vectors has commutative properties

$$\boldsymbol{A} \cdot (\boldsymbol{B} \times \boldsymbol{C}) = (\boldsymbol{A} \times \boldsymbol{B}) \cdot \boldsymbol{C} = \boldsymbol{B} \cdot (\boldsymbol{C} \times \boldsymbol{A})\ , \tag{A.4}$$

while the double vector product is expanded as

$$\boldsymbol{A} \times (\boldsymbol{B} \times \boldsymbol{C}) = \boldsymbol{B}(\boldsymbol{A} \cdot \boldsymbol{C}) - \boldsymbol{C}(\boldsymbol{A} \cdot \boldsymbol{B})\ . \tag{A.5}$$

A.1.3 Vector Circuitation and Flux

The *circuitation* (or circulation) $\mathcal{C}_{\boldsymbol{F}}$ of vector $\boldsymbol{F}$ along the closed line (*circuit*) ℓ is the line integral of the component of $\boldsymbol{F}$ tangent to ℓ

$$\mathcal{C}_{\boldsymbol{F}} := \oint_\ell \boldsymbol{F} \cdot \mathbf{s}_0\, \mathrm{d}s = \oint_\ell \boldsymbol{F} \cdot \mathrm{d}\boldsymbol{s}\ , \tag{A.6}$$

where $\mathrm{d}\boldsymbol{s}$ is the elementary oriented arc.

The *flux* $\Phi_{\boldsymbol{F}}$ of vector $\boldsymbol{F}$ across the surface S is the surface integral over S of the component of $\boldsymbol{F}$ perpendicular to S in each point

$$\Phi_{\boldsymbol{F}} := \iint_S \boldsymbol{F} \cdot \mathbf{n}_0\, \mathrm{d}S\ . \tag{A.7}$$

A.2 Recalling Curvilinear Coordinates

The rectangular Cartesian coordinate system is widely used, but spherical coordinates are quite useful in Earth observation, especially to describe radiation and scattering. Also cylindrical coordinates find use in radiation and scattering from cylinders. Thus, a short overview of the main features of curvilinear coordinates can be convenient.

A.2.1 The Metric Coefficients

Consider three continuous functions of space $f_1(\boldsymbol{r}), f_2(\boldsymbol{r}), f_3(\boldsymbol{r})$. Equations

$$f_1(\boldsymbol{r}) = q_1; \qquad f_2(\boldsymbol{r}) = q_2; \qquad f_3(\boldsymbol{r}) = q_3 \ , \tag{A.8}$$

define three surfaces. For each triplet of parameters q_i, $i = 1, 2, 3$, these surfaces have one[2] common point $\boldsymbol{r}(q_1, q_2, q_3)$, and three common lines, formed by their intersections in pairs, along which only one of the parameters q_i varies.

As in (A.1), the position $\boldsymbol{r}$ of a point P in space is specified by the triplet q_i, $i = 1, 2, 3$, which can be regarded as coordinates in the reference system formed by the considered surfaces (A.8). The intersection lines are the coordinate lines and the versors $\boldsymbol{q}_{10}$, $\boldsymbol{q}_{20}$, $\boldsymbol{q}_{30}$, tangent to the coordinate lines at the intersection P of the three surfaces, are the *coordinate axes*. If the three versors in P are mutually perpendicular, the curvilinear coordinates are *orthogonal* (Fig. A.1). Note that the coordinate axes are not in general fixed directions in space, as for the Cartesian coordinates. The elementary arc length $\mathrm{d}s_i$ of the coordinate line q_i in the neighborhood of P is proportional to the increment of the respective coordinate $\mathrm{d}q_i$ through the corresponding *metric coefficient*[3] h_i, i.e.,

$$\mathrm{d}s_i = h_i \, \mathrm{d}q_i \qquad i = 1, 2, 3 \ . \tag{A.9}$$

The metric coefficients, which are in general functions of space, determine the volume $\mathrm{d}V$ of the elementary cell (Fig. A.2):

$$\mathrm{d}V = \mathrm{d}s_1 \, \mathrm{d}s_2 \, \mathrm{d}s_3 = h_1 \, h_2 \, h_3 \, \mathrm{d}q_1 \, \mathrm{d}q_2 \, \mathrm{d}q_3 \ ,$$

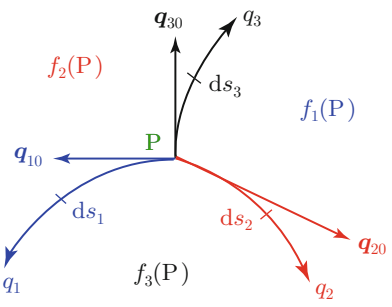

Fig. A.1 The tangents to the coordinate lines in P form a rectangular coordinate system

[2] The three surfaces must intersect in only one point.

[3] Also named *scale factors* or Lamé coefficients. The metric coefficients tend now to be replaced by the components of the metric tensor.

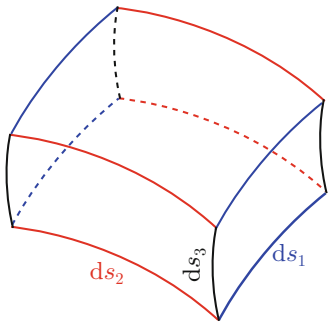

Fig. A.2 Elementary cell in orthogonal curvilinear coordinates

while the areas of the facets that delimit the cell are

$$\begin{aligned}\mathrm{d}S_1 &= \mathrm{d}s_2\,\mathrm{d}s_3 = h_2\,h_3\,\mathrm{d}q_2\,\mathrm{d}q_3\\ \mathrm{d}S_2 &= \mathrm{d}s_1\,\mathrm{d}s_3 = h_1\,h_3\,\mathrm{d}q_1\,\mathrm{d}q_3\\ \mathrm{d}S_3 &= \mathrm{d}s_1\,\mathrm{d}s_2 = h_1\,h_2\,\mathrm{d}q_1\,\mathrm{d}q_2\ .\end{aligned}$$

As the elementary volume, the areas of the facets depend on the coordinates because the metric coefficients are functions of point.

A.2.1.1 Cartesian Coordinates

The Cartesian are the simplest curvilinear coordinates. The coordinate surfaces are the planes

$$f_1(\boldsymbol{r}) = x\,;\qquad f_2(\boldsymbol{r}) = y\,;\qquad f_3(\boldsymbol{r}) = z\ ,$$

with common point $\boldsymbol{r}(x, y, z)$ and which intersect along straight coordinate lines, forming the x, y, z axes.

The arc lengths are

$$\mathrm{d}s_1 = \mathrm{d}x;\qquad \mathrm{d}s_2 = \mathrm{d}y;\qquad \mathrm{d}s_3 = \mathrm{d}z$$

with unitary metric coefficients:

$$h_1 = h_2 = h_3 = 1\ .$$

A.2.1.2 Spherical Coordinates

In a spherical coordinate system (Fig. A.3), a point is specified by the three variables r, ϑ, φ, each referring to a coordinate surface.

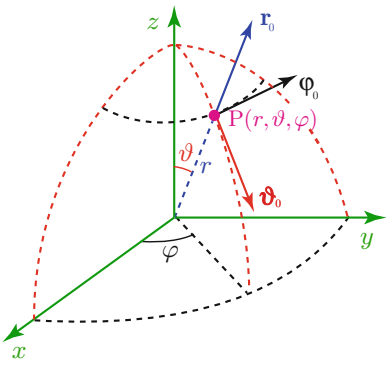

Fig. A.3 The point $\mathrm{P}(r, \vartheta, \varphi)$ in spherical coordinates is singled out by the intersection of the three coordinate surfaces $r = const$, $\vartheta = const$, $\varphi = const$. Pairs of surfaces mutually intersect along the coordinate lines, to which versors $\mathbf{r}_0$, $\boldsymbol{\vartheta}_0$ and $\boldsymbol{\varphi}_0$ are tangent

A.2.1.2.1 Metric Coefficients for Spherical Coordinates

The coordinate surfaces are:

- spheres concentric to the origin $f_1(\boldsymbol{r}) = r$,
- cones coaxial to the polar axis $f_2(\boldsymbol{r}) = \vartheta$,
- planes containing the polar axis $f_3(\boldsymbol{r}) = \varphi$.

The intersection of surfaces f_2 and f_3 are radial straight lines, along which the coordinate r varies; intersection of f_1 and f_3 are circles in *meridian* planes containing the polar axis, along which the *latitude*, or *elevation*, angle ϑ varies; intersection of f_1 and f_2 are circles perpendicular to the polar axis, along which the *longitude* or azimuth angle φ varies.

The lengths of the elementary arcs are

$$\mathrm{d}s_1 = \mathrm{d}r; \qquad \mathrm{d}s_2 = r\,\mathrm{d}\vartheta; \qquad \mathrm{d}s_3 = r\sin\vartheta\,\mathrm{d}\varphi\ ,$$

with metric coefficients

$$h_1 = 1; \qquad h_2 = r; \qquad h_3 = r\sin\vartheta\ ,$$

which, in general, are not unitary and depend on the coordinates.

When the polar axis coincides with the z axis of a Cartesian system, the relations between the coordinates of a point expressed in Cartesian and spherical coordinate systems are

$$x = r\sin\vartheta\cos\varphi; \qquad y = r\sin\vartheta\sin\varphi; \qquad z = r\cos\vartheta$$

and, inversely,

$$r = \sqrt{x^2 + y^2 + z^2}; \qquad \vartheta = \arccos\frac{z}{\sqrt{x^2 + y^2 + z^2}}; \qquad \varphi = \arctan\frac{y}{x}\ .$$

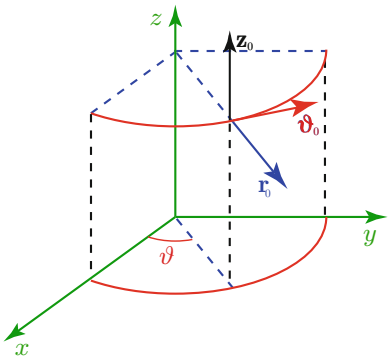

Fig. A.4 Point P(r, ϑ, z) in cylindrical coordinates is singled out by the intersection of the three coordinate surfaces $r = const$, $\vartheta = const$, $z = const$. Pairs of surfaces mutually intersect along the coordinate lines, to which the versors $\mathbf{r}_0$, $\boldsymbol{\vartheta}_0$, $\mathbf{z}_0$ are tangent

A.2.1.3 Cylindrical Coordinates

The coordinate surfaces are (Fig. A.4)

- cylinders $f_1(\boldsymbol{r}) = r$, coaxial with the z-axis,
- planes $f_2(\boldsymbol{r}) = \vartheta$, passing through z,
- planes $f_3(\boldsymbol{r}) = z$ perpendicular to z.

A.2.1.3.1 Metric Coefficients for Cylindrical Coordinates

The arc lengths are

$$\mathrm{d}s_1 = \mathrm{d}r; \qquad \mathrm{d}s_2 = r\,d\vartheta; \qquad \mathrm{d}s_3 = z\ ,$$

whence the metric coefficients

$$h_1 = 1; \qquad h_2 = r; \qquad h_3 = 1\ .$$

A.2.2 Transformation of Vector Components

In several instances, a vector expressed in one system of coordinates needs to be expressed in another system. The need typically arises when, in analyzing the field radiated or scattered by planar structures, vectors given in Cartesian coordinates must be transformed into vectors in spherical coordinates.

A.2.2.1 Transformation from Cartesian to Spherical

In spherical coordinates, the vector field $\boldsymbol{F}(\boldsymbol{r})$ at the point $\boldsymbol{r}(r, \vartheta, \varphi)$ is specified by its components along the coordinate lines r, ϑ, φ:

$$\boldsymbol{F}(r, \vartheta, \varphi) = F_r(r, \vartheta, \varphi)\, \mathbf{r}_0 + F_\vartheta(r, \vartheta, \varphi)\, \boldsymbol{\vartheta}_0 + F_\varphi(r, \vartheta, \varphi)\, \boldsymbol{\varphi}_0 \,.$$

The components are the projections of $\boldsymbol{F}$ onto each versor of the spherical coordinate lines, i.e.,

$$F_r = \boldsymbol{F} \cdot \mathbf{r}_0 \,; \qquad F_\vartheta = \boldsymbol{F} \cdot \boldsymbol{\vartheta}_0 \,; \qquad F_\varphi = \boldsymbol{F} \cdot \boldsymbol{\varphi}_0 \,.$$

If $\boldsymbol{F} = F_x \mathbf{x}_0 + F_y \mathbf{y}_0 + F_z \mathbf{z}_0$ is the expression in Cartesian coordinates, the dot products of the versors $\mathbf{x}_0$, $\mathbf{y}_0$ and $\mathbf{z}_0$ with $\mathbf{r}_0$, $\boldsymbol{\vartheta}_0$ and $\boldsymbol{\varphi}_0$ must be determined. The following results are readily obtained:

$$\mathbf{x}_0 \cdot \mathbf{r}_0 = \sin\vartheta \cos\varphi \,; \qquad \mathbf{y}_0 \cdot \mathbf{r}_0 = \sin\vartheta \sin\varphi \,; \qquad \mathbf{z}_0 \cdot \mathbf{r}_0 = \cos\vartheta$$

$$\mathbf{x}_0 \cdot \boldsymbol{\vartheta}_0 = \cos\vartheta \cos\varphi \,; \qquad \mathbf{y}_0 \cdot \boldsymbol{\vartheta}_0 = \cos\vartheta \sin\varphi \,; \qquad \mathbf{z}_0 \cdot \boldsymbol{\vartheta}_0 = -\sin\vartheta$$

$$\mathbf{x}_0 \cdot \boldsymbol{\varphi}_0 = -\sin\varphi \,; \qquad \mathbf{y}_0 \cdot \boldsymbol{\varphi}_0 = \cos\varphi \,; \qquad \mathbf{z}_0 \cdot \boldsymbol{\varphi}_0 = 0 \,.$$

Therefore, $\boldsymbol{F}$ in spherical coordinates is given by

$$\begin{aligned} \boldsymbol{F} \;=\; & (F_x \sin\vartheta \cos\varphi + F_y \sin\vartheta \sin\varphi + F_z \cos\vartheta)\, \mathbf{r}_0 \\ & + (F_x \cos\vartheta \cos\varphi + F_y \cos\vartheta \sin\varphi - F_z \sin\vartheta)\, \boldsymbol{\vartheta}_0 \\ & + (-F_x \sin\varphi + F_y \cos\varphi)\, \boldsymbol{\varphi}_0 \,. \end{aligned} \tag{A.10}$$

A.2.2.2 Transformation from Cartesian to Cylindrical

Analogously, $\boldsymbol{F}$ is given in cylindrical coordinates by

$$\begin{aligned} \boldsymbol{F}(r, \vartheta, z) &= F_r(r, \vartheta, z)\, \mathbf{r}_0 + F_\vartheta(r, \vartheta, z)\, \boldsymbol{\vartheta}_0 + F_z(r, \vartheta, z)\, \mathbf{z}_0 \\ &= (F_x \cos\vartheta + F_y \sin\vartheta)\, \mathbf{r}_0 - (F_x \sin\vartheta - F_y \cos\vartheta)\, \boldsymbol{\vartheta}_0 + F_z\, \mathbf{z}_0 \,. \end{aligned}$$

A.3 Recalling Operators

A.3.1 Gradient

Consider a scalar field $T(\boldsymbol{r})$ describing the spatial distribution of the quantity T (for instance, the temperature field in the atmosphere). If in the point denoted by the position vector $\boldsymbol{r}_1$ its value is $T = T(\boldsymbol{r}_1)$, at the point $\boldsymbol{r}_2 = \boldsymbol{r}_1 + \Delta\boldsymbol{r}$ its increment is

$\Delta T = T(\boldsymbol{r}_2) - T(\boldsymbol{r}_1)$. For sufficiently small $\Delta \boldsymbol{r} = \boldsymbol{r}_2 - \boldsymbol{r}_1 = \Delta x\, \mathbf{x}_0 + \Delta y\, \mathbf{y}_0 + \Delta z\, \mathbf{z}_0$, ΔT can be approximated by a linear function of $\Delta \boldsymbol{r}$:

$$\Delta T \simeq \frac{\partial T}{\partial x}\Delta x + \frac{\partial T}{\partial y}\Delta y + \frac{\partial T}{\partial z}\Delta z\,. \tag{A.11}$$

By introducing the *gradient* of T, defined by the vector field

$$\text{grad}\,[T] := \frac{\partial T}{\partial x}\mathbf{x}_0 + \frac{\partial T}{\partial y}\mathbf{y}_0 + \frac{\partial T}{\partial z}\mathbf{z}_0\,, \tag{A.12}$$

the increment ΔT is written in the compact notation

$$\Delta T \simeq \text{grad}\,[T] \cdot \Delta \boldsymbol{r}\,. \tag{A.13}$$

Equation (A.13) indicates that the variation of T between $\boldsymbol{r}_1$ and $\boldsymbol{r}_2$ is proportional to the first derivative of T along the direction of the (*sufficiently small*) displacement $\boldsymbol{r}_2 - \boldsymbol{r}_1$.

The gradient is a vector field the modulus of which represents the magnitude of the spatial variations of the considered quantity and that contains information on the direction and the sense in which the variations occur.

A.3.2 Divergence

Consider the vector field $\boldsymbol{F}(\boldsymbol{r})$ and a closed surface S containing the point P in Fig. A.5. The *flux* of $\boldsymbol{F}$ through S is defined by (A.7):

$$\Phi_F = \oiint_S \boldsymbol{F} \cdot \mathbf{n}_0 \, \mathrm{d}S\,.$$

If the surface S shrinks in P, the *divergence* of $\boldsymbol{F}$ in P is defined as

$$\text{div}[\boldsymbol{F}] := \lim_{V\to 0} \frac{\Phi_F}{V} = \lim_{V\to 0} \frac{\oiint_S \boldsymbol{F} \cdot \mathbf{n}_0 \, \mathrm{d}S}{V} \tag{A.14}$$

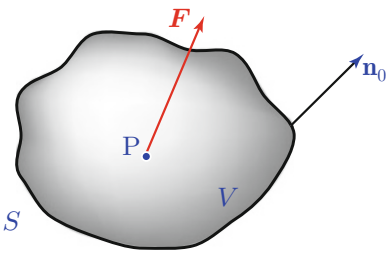

Fig. A.5 Surface S encloses the volume V around P and has outward-pointing normal $\mathbf{n}_0$

Equation (A.14) shows that the divergence is a measure of the density of sources or sinks of a vector field. The divergence in P can be visualized by the density of field (or flux) lines leaving (in case of a source) a small closed surface around P or entering (in case of sink) into it.

When $\mathrm{div}[\boldsymbol{F}] = 0$, the field $\boldsymbol{F}$ is solenoidal, and vice-versa. In this case the number of field lines leaving S equals the number of lines entering in it. Divergence vanishes in regions where the field lines are closed.

Equation (A.14) for a finite volume V expresses the *Gauss's theorem*,[4] or divergence theorem.

$$\oiint_S \boldsymbol{F} \cdot \mathbf{n}_0 \, \mathrm{d}S = \iiint_V \mathrm{div}[\boldsymbol{F}] \, \mathrm{d}V \tag{A.15}$$

The flux of vector $\boldsymbol{F}$ through *any* closed surface S coincides with the integral of the divergence of $\boldsymbol{F}$ over the volume surrounded by S.

A.3.3 Curl

Consider now a vector field $\boldsymbol{v}(\boldsymbol{r})$ (just as an example, the velocity field in a moving fluid) and a plane closed curve ℓ in the neighborhood of P in Fig. A.6. By orienting the elementary arc $\mathrm{d}\boldsymbol{s} = \mathrm{d}s\,\mathbf{s}_0$ in the counterclockwise sense with respect to the normal $\mathbf{n}_0$, the circuitation of $\boldsymbol{v}$ along ℓ defined by (A.6) is

$$\mathcal{C}_{\boldsymbol{v}} = \oint_\ell \boldsymbol{v} \cdot \mathrm{d}\boldsymbol{s}$$

The component along $\mathbf{n}_0$ of the vector $\mathrm{rot}[\boldsymbol{v}]$, named *curl* (or *rotor*) of $\boldsymbol{v}$, in P is obtained by shrinking the loop ℓ onto P:

$$\mathbf{n}_0 \cdot \mathrm{rot}[\boldsymbol{v}] := \lim_{S \to 0} \frac{\oint_\ell \boldsymbol{v} \cdot \mathrm{d}\boldsymbol{s}}{S} \tag{A.16}$$

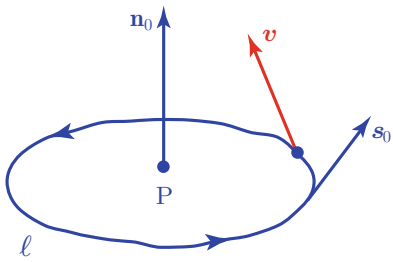

Fig. A.6 The plane closed line ℓ surrounding the point P has the tangent versor $\mathbf{s}_0$ oriented counterclockwise with respect to $\mathbf{n}_0$, normal to the plane of ℓ

[4] Originally developed by Joseph Louis Lagrange in 1762.

The three components of the curl of $\boldsymbol{v}$ in P are obtained by applying (A.16) to three mutually orthogonal loops around P.

In the example at hand, the curl of the velocity field $\boldsymbol{v}$ is a measure of the vorticity of the fluid motion. The modulus of the rotor of the velocity $\boldsymbol{v}$ in the neighborhood of the point P can be visualized by the density of closed-loop flux lines of $\boldsymbol{v}$ that wrap P. The field is *irrotational* when $\mathrm{rot}[\boldsymbol{v}] = 0$, and vice-versa. The rotor vanishes where the flux lines are radial or parallel.

Equation (A.16) for a finite surface expresses the *Kelvin-Stokes'*, or *Stokes'*, or *circulation theorem*[5]:

$$\oint_{\ell} \boldsymbol{F} \cdot \mathrm{d}\boldsymbol{s} = \iint_{S} \mathbf{n}_0 \cdot \mathrm{rot}[\boldsymbol{F}] \, \mathrm{d}S \tag{A.17}$$

The relation (A.17) indicates that the circulation of a vector field $\boldsymbol{F}$ along a closed line ℓ coincides with the flux of the rotor of $\boldsymbol{F}$ across *any* surface contoured by ℓ.

A.3.4 Operators in Orthogonal Curvilinear Coordinates

The key issue is that the spatial derivatives in curvilinear coordinates involve the metric coefficients. In fact, taking (A.9) into account, the derivatives of the scalar field $T(q_i),\ i = 1, 2, 3$, along the coordinate lines are expressed by

$$\begin{aligned}
\frac{\partial T}{\partial s_1} &= \frac{\partial T}{\partial q_1}\frac{\partial q_1}{\partial s_1} = \frac{1}{h_1}\frac{\partial T}{\partial q_1}\,; \\
\frac{\partial T}{\partial s_2} &= \frac{\partial T}{\partial q_2}\frac{\partial q_2}{\partial s_2} = \frac{1}{h_2}\frac{\partial T}{\partial q_2}\,; \\
\frac{\partial T}{\partial s_3} &= \frac{\partial T}{\partial q_3}\frac{\partial q_3}{\partial s_3} = \frac{1}{h_3}\frac{\partial T}{\partial q_3}\,.
\end{aligned}$$

The operators outlined in Sect. A.3 involve the spatial derivatives, thus their expressions depend on the system of coordinates.

A.3.4.1 Gradient

The gradient of the scalar field $T(q_i),\ i = 1, 2, 3$, is

$$\begin{aligned}
\mathrm{grad}[T] &= \frac{\partial T}{\partial s_1}\boldsymbol{q}_{10} + \frac{\partial T}{\partial s_2}\boldsymbol{q}_{20} + \frac{\partial T}{\partial s_3}\boldsymbol{q}_{30} \\
&= \frac{1}{h_1}\frac{\partial T}{\partial q_1}\boldsymbol{q}_{10} + \frac{1}{h_2}\frac{\partial T}{\partial q_2}\boldsymbol{q}_{20} + \frac{1}{h_3}\frac{\partial T}{\partial q_3}\boldsymbol{q}_{30}\,,
\end{aligned} \tag{A.18}$$

[5] Originally developed by William Thomson.

hence the *gradient* operator grad [ ] has expressions:

- in cartesian coordinates,

$$\text{grad}\,[\ ] = \mathbf{x}_0 \frac{\partial [\ ]}{\partial x} + \mathbf{y}_0 \frac{\partial [\ ]}{\partial y} + \mathbf{z}_0 \frac{\partial [\ ]}{\partial z}\ ;$$

- in spherical coordinates,

$$\text{grad}\,[\ ] = \mathbf{r}_0 \frac{\partial [\ ]}{\partial r} + \frac{\boldsymbol{\vartheta}_0}{r} \frac{\partial [\ ]}{\partial \vartheta} + \frac{\boldsymbol{\varphi}_0}{r \sin \vartheta} \frac{\partial [\ ]}{\partial \varphi}\ ;$$

- in cylindrical coordinates,

$$\text{grad}\,[\ ] = \mathbf{r}_0 \frac{\partial [\ ]}{\partial r} + \frac{\boldsymbol{\vartheta}_0}{r} \frac{\partial [\ ]}{\partial \vartheta} + \mathbf{z}_0 \frac{\partial [\ ]}{\partial z}\ .$$

A.3.4.2 Divergence

The divergence of the vector field $\boldsymbol{F}(q_i),\ i = 1, 2, 3$, is obtained by applying the basic definition (A.14) to the elementary volume shown in Fig. A.7:

$$\text{div}[\boldsymbol{F}] = \frac{\mathrm{d}\Phi_F}{\mathrm{d}V}\ . \tag{A.19}$$

The flux $\mathrm{d}\Phi_F$ of $\boldsymbol{F}$ through the elementary surface $\mathrm{d}S$ delimiting the volume $\mathrm{d}V$ is computed by adding the contributions of the three pairs of opposite facets. Flux $\mathrm{d}\Phi_1$ outgoing from $\mathrm{d}S_1$ is

$$\mathrm{d}\Phi_1 = -F_1\, \mathrm{d}s_2\, \mathrm{d}s_3 = -F_1\, h_2\, h_3\, \mathrm{d}q_2\, \mathrm{d}q_3\ , \tag{A.20}$$

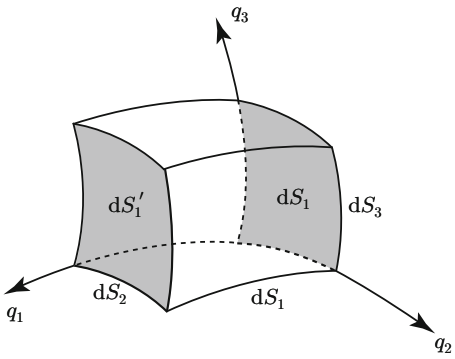

Fig. A.7 Elementary volume to compute divergence

while the flux $\mathrm{d}\Phi_1'$ outgoing from $\mathrm{d}S_1'$, opposite to $\mathrm{d}S_1$, differs from the preceding one, given both the change of sign of the outward normal and the variations undergone by F_1 and $\mathrm{d}S_1$ for the change of q_1:

$$\mathrm{d}\Phi_1' = -\mathrm{d}\Phi_1 + \frac{\partial(-\mathrm{d}\Phi_1)}{\partial q_1}\mathrm{d}q_1 \ . \tag{A.21}$$

Adding fluxes (A.20) and (A.21) yields the total flux leaving the pairs of facets $\mathrm{d}S_1$ and $\mathrm{d}S_1'$

$$\mathrm{d}\Phi_1' + d\Phi_1 = \frac{\partial(h_2\, h_3\, F_1)}{\partial q_1}\mathrm{d}q_1\, \mathrm{d}q_2\, \mathrm{d}q_3 \ .$$

By proceeding in an analogous way for the other two pairs of opposite facets, the total flux $\mathrm{d}\Phi_F$ of $\boldsymbol{F}$ through the whole elementary surface $\mathrm{d}S$ wrapping the volume $\mathrm{d}V$ is obtained as

$$\mathrm{d}\Phi_F = \left[\frac{\partial}{\partial q_1}(h_2\, h_3\, F_1) + \frac{\partial}{\partial q_2}(h_1\, h_3\, F_2) + \frac{\partial}{\partial q_3}(h_1\, h_2\, F_3)\right] \mathrm{d}q_1\, \mathrm{d}q_2\, \mathrm{d}q_3 \ ,$$

from which, by the definition (A.19),

$$\mathrm{div}[\boldsymbol{F}] = \frac{1}{h_1\, h_2\, h_3}\left[\frac{\partial}{\partial q_1}(h_2\, h_3\, F_1) + \frac{\partial}{\partial q_2}(h_1\, h_3\, F_2) + \frac{\partial}{\partial q_3}(h_1\, h_2\, F_3).\right] \tag{A.22}$$

The general form (A.22) reduces to the following expressions:

- in Cartesian coordinates,

$$\mathrm{div}[\boldsymbol{F}] = \frac{\partial F_x}{\partial x} + \frac{\partial F_y}{\partial y} + \frac{\partial F_z}{\partial z} \ ; \tag{A.23}$$

- in spherical coordinates,

$$\mathrm{div}[\boldsymbol{F}] = \frac{1}{r^2}\frac{\partial}{\partial r}(r^2\, F_r) + \frac{1}{r\sin\vartheta}\frac{\partial}{\partial\vartheta}(F_\vartheta \sin\vartheta) + \frac{1}{r\sin\vartheta}\frac{\partial F_\varphi}{\partial\varphi} \ ;$$

- in cylindrical coordinates,

$$\mathrm{div}[\boldsymbol{F}] = \frac{1}{r}\frac{\partial}{\partial r}(r\, F_r) + \frac{1}{r}\frac{\partial F_\vartheta}{\partial\vartheta} + \frac{\partial F_z}{\partial z} \ .$$

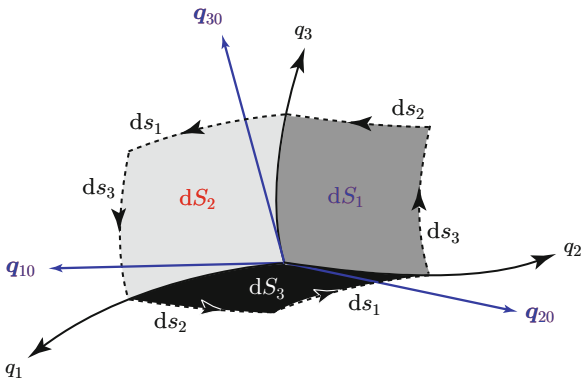

Fig. A.8 Elementary loops to compute curl

A.3.4.3 Curl

The components of the curl of the field $\boldsymbol{F}(q_i)$, $i = 1, 2, 3$, at a given point along the three orthogonal directions $\boldsymbol{q}_{i0}$ are derived by applying the definition (A.16) to each elementary facet shown in Fig. A.8

$$\boldsymbol{q}_{i0} \cdot \mathrm{rot}[\boldsymbol{F}] = \frac{\mathrm{d}\mathcal{C}_i}{\mathrm{d}S_i} \qquad i = 1, 2, 3 \,, \tag{A.24}$$

in which each elementary surface $\mathrm{d}S_i$ is perpendicular to the corresponding versor $\boldsymbol{q}_{i0}$. Consider first the component along $\boldsymbol{q}_{10}$:

$$\boldsymbol{q}_{10} \cdot \mathrm{rot}[\boldsymbol{F}] = \frac{\mathrm{d}\mathcal{C}_1}{\mathrm{d}S_1} \cdot \tag{A.25}$$

Taking into account the orientation of the integration path along the loop surrounding $\mathrm{d}S_1$ and the increments of both F_2 and $\mathrm{d}s_2$, the contribution to $\mathrm{d}\mathcal{C}_1$ from the sides $\mathrm{d}s_2$ is

$$\mathrm{d}\mathcal{C}_{12} = F_2 \, \mathrm{d}s_2 - F_2 \, \mathrm{d}s_2 - \frac{\partial}{\partial q_3}(F_2 \, \mathrm{d}s_2) \, \mathrm{d}q_3 = -\frac{\partial}{\partial q_3}(F_2 h_2) \, \mathrm{d}q_2 \, \mathrm{d}q_3 \,.$$

Analogously, the contribution from the sides $\mathrm{d}s_3$ is

$$\mathrm{d}\mathcal{C}_{13} = \frac{\partial}{\partial q_2}(F_3 h_3) \, \mathrm{d}q_2 \, \mathrm{d}q_3 \,,$$

so that

$$\mathrm{d}\,\mathcal{C}_1 = \mathrm{d}\mathcal{C}_{12} + \mathrm{d}\mathcal{C}_{13} = \left[\frac{\partial}{\partial q_2}(F_3 h_3) - \frac{\partial}{\partial q_3}(F_2 h_2) \right] \mathrm{d}q_2 \, \mathrm{d}q_3 \,,$$

whence, from (A.25),

$$\boldsymbol{q}_{10} \cdot \mathrm{rot}[\boldsymbol{F}] = \frac{1}{h_2 h_3}\left[\frac{\partial}{\partial q_2}(F_3 h_3) - \frac{\partial}{\partial q_3}(F_2 h_2)\right] . \tag{A.26}$$

After computing the other two components in an analogous fashion, the vector $\mathrm{rot}[\boldsymbol{F}]$ is formed by

$$\begin{aligned}\mathrm{rot}[\boldsymbol{F}] \;=\; & \frac{1}{h_2 h_3}\left[\frac{\partial}{\partial q_2}(h_3 F_3) - \frac{\partial}{\partial q_3}(h_2 F_2)\right]\boldsymbol{q}_{10} \\ & + \frac{1}{h_1 h_3}\left[\frac{\partial}{\partial q_3}(h_1 F_1) - \frac{\partial}{\partial q_1}(h_3 F_3)\right]\boldsymbol{q}_{20} \\ & + \frac{1}{h_1 h_2}\left[\frac{\partial}{\partial q_1}(h_2 F_2) - \frac{\partial}{\partial q_2}(h_1 F_1)\right]\boldsymbol{q}_{30} .\end{aligned} \tag{A.27}$$

Equation (A.27) yields the following specific expressions in the considered coordinate systems:

- Cartesian coordinates:

$$\mathrm{rot}[\boldsymbol{F}] = \left(\frac{\partial F_z}{\partial y} - \frac{\partial F_y}{\partial z}\right)\mathbf{x}_0 + \left(\frac{\partial F_x}{\partial z} - \frac{\partial F_z}{\partial x}\right)\mathbf{y}_0 + \left(\frac{\partial F_y}{\partial x} - \frac{\partial F_x}{\partial y}\right)\mathbf{z}_0 ; \tag{A.28}$$

- spherical coordinates:

$$\begin{aligned}\mathrm{rot}[\boldsymbol{F}] \;=\; & \frac{1}{r\sin\vartheta}\left[\frac{\partial}{\partial\vartheta}(F_\varphi \sin\vartheta) - \frac{\partial F_\vartheta}{\partial\varphi}\right]\mathbf{r}_0 \\ & + \frac{1}{r}\left[\frac{1}{\sin\vartheta}\frac{\partial F_r}{\partial\varphi} - \frac{\partial}{\partial r}(rF_\varphi)\right]\boldsymbol{\vartheta}_0 \\ & + \frac{1}{r}\left[\frac{\partial}{\partial r}(rF_\vartheta) - \frac{\partial F_r}{\partial\vartheta}\right]\boldsymbol{\varphi}_0 ;\end{aligned} \tag{A.29}$$

- cylindrical coordinates:

$$\mathrm{rot}[\boldsymbol{F}] = \left(\frac{1}{r}\frac{\partial F_z}{\partial\vartheta} - \frac{\partial F_\vartheta}{\partial z}\right)\mathbf{r}_0 + \left(\frac{\partial F_r}{\partial z} - \frac{\partial F_z}{\partial r}\right)\boldsymbol{\vartheta}_0 + \frac{1}{r}\left[\frac{\partial(rF_\vartheta)}{\partial r} - \frac{\partial F_r}{\partial\vartheta}\right]\mathbf{z}_0 . \tag{A.30}$$

A.4 Recalling Nabla and Using It

Assume a Cartesian coordinate system and define the vector operator ∇

$$\nabla := \mathbf{x}_0\frac{\partial}{\partial x} + \mathbf{y}_0\frac{\partial}{\partial y} + \mathbf{z}_0\frac{\partial}{\partial z} \tag{A.31}$$

This definition allows gradient, divergence and curl to be expressed in alternative notations.

A.4.1 Operators in Terms of Nabla

A.4.1.1 Gradient

Applying (A.31) to a scalar field T, (A.12) is obtained, so that

$$\nabla T = \text{grad}[T] \ .$$

The nabla operator applied to the scalar field T generates the grad$[T]$ vector field. Clearly,

$$\Delta T = \nabla T \cdot \Delta \boldsymbol{r}$$

A.4.1.2 Divergence

The result of the formal scalar product $\nabla \cdot \boldsymbol{F}$ coincides with (A.23):

$$\nabla \cdot \boldsymbol{F} = \nabla_x F_x + \nabla_y F_y + \nabla_z F_z = \frac{\partial F_x}{\partial x} + \frac{\partial F_y}{\partial y} + \frac{\partial F_z}{\partial z} \equiv \text{div}[\boldsymbol{F}] \ .$$

The dot product $\nabla \cdot \boldsymbol{F}$ produces the div$[\boldsymbol{F}]$ scalar field.

A.4.1.3 Curl

The formal vector product $\nabla \times \boldsymbol{F}$ coincides with (A.28):

$$\begin{aligned}
&\nabla \times \boldsymbol{F} \\
&= (\nabla_y F_z - \nabla_z F_y)\mathbf{x}_0 + (\nabla_z F_x - \nabla_x F_z)\mathbf{y}_0 + (\nabla_x F_y - \nabla_y F_x)\mathbf{z}_0 \\
&= \left(\frac{\partial F_z}{\partial y} - \frac{\partial F_y}{\partial z}\right)\mathbf{x}_0 + \left(\frac{\partial F_x}{\partial z} - \frac{\partial F_z}{\partial x}\right)\mathbf{y}_0 + \left(\frac{\partial F_y}{\partial x} - \frac{\partial F_x}{\partial y}\right)\mathbf{z}_0 \\
&\equiv \text{rot}[\boldsymbol{F}] \ .
\end{aligned}$$

The cross product $\nabla \times \boldsymbol{F}$ yields the rotor of $\boldsymbol{F}$.

A.4.2 Using Nabla

For a correct use of nabla, its vector character must be combined with that of *differential operator*. In particular, when ∇ operates on products between fields, the rules of product derivatives must be obeyed, in addition to the vector correctness of the result, as suggested by the following examples.

- If Υ and Ψ are scalar fields,

$$\nabla(\Upsilon\Psi) = \Upsilon\nabla\Psi + \Psi\nabla\Upsilon \,.$$

- If $\boldsymbol{F}$ is a vector field,

$$\nabla \cdot (\Upsilon\boldsymbol{F}) = \boldsymbol{F} \cdot \nabla\Upsilon + \Upsilon\nabla \cdot \boldsymbol{F} \,, \tag{A.32}$$

- and analogously,

$$\nabla \times (\Upsilon\boldsymbol{F}) = (\nabla\Upsilon) \times \boldsymbol{F} + \Upsilon\nabla \times \boldsymbol{F} \,. \tag{A.33}$$

- By using the properties of the mixed double product (A.4),

$$\nabla \cdot (\boldsymbol{A} \times \boldsymbol{B}) = \boldsymbol{B} \cdot (\nabla \times \boldsymbol{A}) - \boldsymbol{A} \cdot (\nabla \times \boldsymbol{B}) \,. \tag{A.34}$$

Regarding ∇ as a vector allows interesting results to be obtained with formal simplicity. For instance,

- since $\boldsymbol{B} \times \boldsymbol{B} = 0$,

$$\nabla \times (\nabla T) = 0 \,,$$

  meaning that the gradient field ∇T is irrotational;
- also, since $\boldsymbol{A} \cdot (\boldsymbol{A} \times \boldsymbol{B}) = 0$,

$$\nabla \cdot (\nabla \times \boldsymbol{F}) = 0 \,,$$

  implying that $\nabla \times \boldsymbol{F}$ is a solenoidal field;
- while

$$\nabla \cdot (\nabla T) = \nabla \cdot \nabla[T] \,. \tag{A.35}$$

A.4.3 Laplacian

Formally, in (A.35),

$$\nabla \cdot \nabla = \nabla^2 \,. \tag{A.36}$$

The divergence of the gradient forms a second-order operator denoted by ∇^2 and named *Laplacian*.

A.4.3.1 Laplacian in Cartesian Coordinates

In Cartesian coordinates,

$$\nabla \cdot (\nabla T) = \nabla_x(\nabla_x T) + \nabla_y(\nabla_y T) + \nabla_z(\nabla_z T) = \frac{\partial^2}{\partial x^2} T + \frac{\partial^2}{\partial y^2} T + \frac{\partial^2}{\partial z^2} T \,.$$

Therefore,

$$\nabla^2 = \frac{\partial^2}{\partial x^2} + \frac{\partial^2}{\partial y^2} + \frac{\partial^2}{\partial z^2} \,.$$

A.4.3.2 Laplacian in Orthogonal Curvilinear Coordinates

The expression of the Laplacian in orthogonal curvilinear coordinates is obtained from its definition (A.36), taking account of (A.22) and (A.18):

$$\nabla^2 [\,] = \operatorname{div} \operatorname{grad} [\,] = \\ \frac{1}{h_1 h_2 h_3} \left[\frac{\partial}{\partial q_1} \left(\frac{h_2 h_3}{h_1} \frac{\partial [\,]}{\partial q_1} \right) + \frac{\partial}{\partial q_2} \left(\frac{h_3 h_1}{h_2} \frac{\partial [\,]}{\partial q_2} \right) + \frac{\partial}{\partial q_3} \left(\frac{h_1 h_2}{h_3} \frac{\partial [\,]}{\partial q_3} \right) \right] \cdot \tag{A.37}$$

The expressions of ∇^2 in the different coordinate systems are obtained from (A.37) by introducing the corresponding metric coefficients defined in Sect. A.2.1:

- in spherical coordinates,

$$\nabla^2 [\,] = \frac{1}{r^2} \frac{\partial}{\partial r} \left(r^2 \frac{\partial [\,]}{\partial r} \right) + \frac{1}{r^2 \sin \vartheta} \frac{\partial}{\partial \vartheta} \left(\sin \vartheta \frac{\partial [\,]}{\partial \vartheta} \right) + \frac{1}{r^2 \sin \vartheta^2} \frac{\partial^2 [\,]}{\partial \phi^2} \,,$$

- while in cylindrical coordinates

$$\nabla^2 [\,] = \frac{1}{r} \frac{\partial}{\partial r} \left(r \frac{\partial [\,]}{\partial r} \right) + \frac{1}{r^2} \frac{\partial^2 [\,]}{\partial \vartheta^2} + \frac{\partial^2 [\,]}{\partial z^2} \cdot$$

The Laplacian is a scalar second-order linear differential operator that acts both on scalar and on vector fields. In the latter case, given its linearity, it operates on the single components. Note that in Cartesian coordinates the versors are space–invariant, hence

$$\nabla^2 \boldsymbol{F} = \mathbf{x}_0 \nabla^2 F_x + \mathbf{y}_0 \nabla^2 F_y + \mathbf{z}_0 \nabla^2 F_z \, . \tag{A.38}$$

In other coordinate systems, the Laplacian of a vector differs from (A.38), that is, it differs from the vector resultant from the Laplacians of the single components multiplied by the respective versors, because the latter generally vary with the coordinates.

A.4.3.3 The Laplacian in Some Vector Identities

In addition to those previously overviewed, some vector identities involving the Laplacian are encountered in certain theoretical issues of Earth observation.

A.4.3.3.1 Green's Lemma

Given the scalar fields Υ and Ψ, recalling (A.32)

$$\nabla \cdot (\Psi \nabla \Upsilon) = \nabla \Psi \cdot \nabla \Upsilon + \Psi \nabla^2 \Upsilon \, . \tag{A.39}$$

By integrating the two members of (A.39) over the volume V delimited by the closed surface S, and taking the Gauss's theorem (A.15) into account,

$$\oiint_S \mathbf{n}_0 \cdot (\Psi \nabla \Upsilon) \, dS = \iiint_V (\nabla \Psi \cdot \nabla \Upsilon + \Psi \nabla^2 \Upsilon) \, dV \, . \tag{A.40}$$

Equation (A.40) is named *Green's lemma*.

A.4.3.3.2 Double Curl

The double curl $\nabla \times (\nabla \times \boldsymbol{F})$ can be formally treated as a double vector product, yielding

$$\nabla \times (\nabla \times \boldsymbol{F}) = \nabla \nabla \cdot \boldsymbol{F} - \nabla^2 \boldsymbol{F} \, . \tag{A.41}$$

Identity (A.41) originates the vector Helmholtz equation.

Acronyms

AGL	**a**bove **g**round **l**evel. 347
AIRS	NASA/JPL's **A**tmospheric **I**nfra**r**ed **S**ounder. 620
AMSU-A	**A**dvanced **M**icrowave **S**ounding **U**nit-**A**. 620
ASAR	ENVISAT **A**dvanced **S**ynthetic **A**perture **R**adar. 368, 594
ASI	Italian Space Agency (**A**genzia **S**paziale **I**taliana). 384
ATI	**a**pparent **t**hermal **i**nertia. 600
ATSR	**A**long **T**rack **S**canning **R**adiometer. 377
AVHRR	**A**dvanced **V**ery **H**igh **R**esolution **R**adiometer. 575
CALIOP	**C**loud-**A**erosol **L**idar with **O**rthogonal **P**olarization. 615
CALIPSO	**C**loud-**A**erosol **L**idar and **I**nfrared **P**athfinder **S**atellite **O**bservations. 615
CloudSat	NASA/CSA's **Cloud Sat**ellite. 614
COSMO-SkyMed	ASI **Co**nstellation of small **s**atellites for **M**editerranean basin **o**bservation. 384, 403
CSA	**C**anadian **S**pace **A**gency. 386
DEM	**d**igital **e**levation **m**odel. 153, 476
DGPS	**d**ifferential **G**lobal **P**ositioning **S**ystem. 152
DinSAR	**d**ifferential **SAR in**terferometry. 153
DLR	German Aerospace Center (**D**eutschen Zentrums für **L**uft- und **R**aumfahrt). 493
DOAS	**d**ifferential **o**ptical **a**bsorption **s**pectroscopy. 606
DSMP	**D**efense **M**eteorological **S**atellite **P**rogram. 620
ENVISAT	ESA **Envi**ronment **Sat**ellite. 386, 593
EO	**E**arth **o**bservation. 3
EOS MLS	**E**arth **O**bserving **S**ystem **M**icrowave **L**imb **S**ounder. 621
ERS	ESA **E**uropean **R**emote-Sensing **S**atellite. 377, 419
ESA	**E**uropean **S**pace **A**gency. 368

D. Solimini, *Understanding Earth Observation*, Remote Sensing and Digital Image Processing 23, DOI 10.1007/978-3-319-25633-7

EUMETSAT **Eu**ropean Organisation for the Exploitation of **Met**eorological **Sat**ellites. 609

FDT **F**luctuation-**D**issipation **T**heorem. 288, 309
FIR **f**ar **i**nfra**r**ed. 356, 619
FUV **f**ar **u**ltra**v**iolet. 604
FWHM **f**ull **w**idth at **h**alf **m**aximum. 37

GNSS **G**lobal **N**avigation **S**atellite **S**ystem. 152
GO **g**eometrical **o**ptics. 528
GOME **G**lobal **O**zone **M**onitoring **E**xperiment. 607
GOMOS **G**lobal **O**zone **M**onitoring by **O**ccultation of **S**tars. 607
GPM NASA/JAXA's **G**lobal **P**recipitation **M**easurement. 622
GPS **G**lobal **P**ositioning **S**ystem. 152
GRD **G**round-**R**esolved **D**istance. 433
GSFC NASA's **G**oddard **S**pace **F**light **C**enter. 623
GUVI **G**lobal **U**ltra**v**iolet **I**mager. 607

HCMM **H**eath **C**apacity **M**apping **M**ission. 572
HSB **H**umidity **S**ounder for **B**rasil. 620

ICESat **I**ce, **C**loud and Land **E**levation **Sat**ellite. 615
IEM **I**ntegral **E**quation **M**ethod. 529
IFOV **i**nstantaneous **f**ield **o**f **v**iew. 439
InSAR **s**ynthetic **a**perture **r**adar **in**terferometry. 153
ISS **I**nternational **S**pace **S**tation. 607

JAXA **J**apan **A**erospace E**x**ploration **A**gency. 623

LAI **l**eaf **a**rea **i**ndex. 584
LANDSAT **Land** Remote-Sensing **Sat**ellite. 371
lidar **li**ght **d**etection **a**nd **r**anging. 152, 615
LTE **l**ocal **t**hermodynamic **e**quilibrium. 288

MDA **M**acDonald, **D**ettwiler and **A**ssociates, Ltd.. 386
MERIS ENVISAT **Me**dium-spectral **R**esolution **I**maging **S**pectrometer. 368, 590
MetOp **Met**eorological **Op**erational Satellite. 607
MODIS NASA's **Mod**erate-Resolution **I**magine Spectrometer. 432, 614
MPDI **m**icrowave **p**olarization **d**ifference **i**ndex. 586
MPM **M**illimeterÐwave **P**ropagation **M**odel. 362
MSG **M**eteosat **s**econd **g**eneration. 609

NASA **N**ational **A**eronautics and **S**pace **A**dministration. 11, 491
NASA GES DISC NASA's **G**oddard **E**arth **S**ciences **D**ata and **I**nformation **S**ervices **C**enter. 620
NDVI **n**ormalized **d**ifference **v**egetation **i**ndex. 551

NIR **n**ear **i**nfra**r**ed. 356, 550

OMI **O**zone **M**onitoring **I**nstrument. 607
OSIRIS **O**ptical **S**pectrograph and **I**nfra**r**ed **I**mager **S**ystem. 607

PO **P**hysical **O**ptics. 230
PR **p**olarization **r**atio. 586
PRF **p**ulse **r**epetition **f**requency. 449
PWC **p**lant **w**ater **c**ontent. 57, 582

QB DigitalGlobe Inc.'s **Q**uick**B**ird. 433

radar **ra**dio **d**etection **a**nd **r**anging. 152
RADARSAT CSA/MDA **Radar Sat**ellite. 386
RF **r**adio **f**requency. 402
RGB **r**ed **g**reen **b**lue. 594
RPAP **r**emotely **p**iloted **a**erial **p**latform. 363
RPV **r**emotely **p**iloted **v**ehicle. 338
RTE **r**adiative **t**ransfer **e**quation. 328

SAGE **S**tratospheric **A**rosol and **G**as **E**xperiment. 607
SAR **S**ynthetic **A**perture **R**adar. 49, 152
SCIAMACHY **Sc**anning **I**maging **A**bsorption Spectro**m**eter for **A**tmospheric **Ch**artograph**y**. 607
SEASAT NASA's **Sea Sat**ellite. 419
SIR NASA's **S**huttle **I**maging **R**adar. 419
SMA **s**pectral **m**ixture **a**nalysis. 551
SMC **s**oil **m**oisture **c**ontent. 62
SMOS ESA's **S**oil **M**oisture and **O**cean **S**alinity **M**ission. 419, 600
SOAR RADARSAT-2 **S**cience and **O**perational **A**pplications **R**esearch. 386
SPM **S**mall **P**erturbation **M**ethod. 529
SRTM **S**huttle **R**adar **T**opography **M**ission. 492
SSAI **S**cience **S**ystems and **A**pplications, **I**nc.. 623
SSM/T-2 **S**pecial **S**ensor **M**icrowave **T**emperature-2. 620
SST **s**ea **s**urface **t**emperature. 376, 599
SWE **s**now **w**ater **e**quivalent. 554

TanDEM **T**erraSAR-X **a**dd-o**n** for **D**igital **E**levation **M**easurement. 273, 492
TEC **t**otal **e**lectron **c**ontent. 607
TES **t**emperature **e**missivity **s**eparation. 376
TIMED **T**hermosphere, **I**onosphere, **M**esosphere **E**nergetics and **D**ynamics. 607
TIR **t**hermal **i**nfra**r**ed. 309
TOMS **T**otal **O**zone **M**apping **S**pectrometer. 607
TRMM **T**ropical **R**ainfall **M**easuring **M**ission. 622

UAV **u**nmanned **a**erial **v**ehicle. 338
UV **u**ltra**v**iolet. 356

VHR **v**ery **h**igh-**r**esolution. 338
VIS **vis**ible. 356

WKB **W**entzel-**K**ramers-**B**rillouin. 157

XIR e**x**treme **i**nfra**r**ed. 363

Symbols

A_{cir} [m^2] circular surface domain. 426
A_{e} [m^2] antenna effective area. 417
A_{ell} [m^2] elliptic surface domain. 426
$\mathrm{A_g}$ [m^2] source (antenna) geometric area. 100
A_{gt} [m^2] geometric area transverse to the observation direction. 293
A_{M} [m^2] boresight antenna effective area. 435
A'_{T} [m^2] area of surface $\Delta S'_{\mathrm{T}}$. 300
$\mathcal{A}$ attenuation. 110
$\mathcal{A}_{\mathrm{a}}$ attenuation by the atmosphere. 437
$\mathcal{A}_{\mathrm{m}}$ atmospheric attenuation for master acquisition. 488
$\mathcal{A}_{\mathrm{s}}$ atmospheric attenuation for slave acquisition. 488
$\mathcal{A}$ albedo. 219
$\mathcal{A}_{\mathrm{s}}$ single-scattering albedo. 328
$\mathfrak{A}$ [A] magnetic vector potential. 73
$\mathfrak{A}^{(\mathrm{s})}$ [A] scattered vector potential. 212
$\mathfrak{A}_{\mathrm{i}}$ [m^{-1}] magnetic vector potential impulse response. 75
$\mathcal{A}$ absorptivity. 187
$\mathscr{A}$ absorption coefficient. 170
$\mathfrak{a}$ [$\mathrm{Np\,m}^{-1}$] specific absorption. 160
a electromagnetic thickness. 226
α [$\mathrm{Np\,m}^{-1}$] attenuation constant. 106
$\boldsymbol{\alpha}$ [$\mathrm{Np\,m}^{-1}$] attenuation vector. 106
$\boldsymbol{\alpha}'$ [$\mathrm{Np\,m}^{-1}$] attenuation vector of refracted wave. 179
α_{1} [$\mathrm{Np\,m}^{-1}$] attenuation constant accounting for first-order scattering. 318
α_{e} [m^{-1}] extinction coefficient. 325
α_{ea} [m^{-1}] extinction coefficient due to absorption by inhomogeneities. 325
α_{eb} [m^{-1}] extinction coefficient due to absorption by the background. 325
α_{es} [m^{-1}] extinction coefficient due to scattering. 325
α_{S} [$\mathrm{Np\,m}^{-1}$] attenuation constant in the surface layer. 275

D. Solimini, *Understanding Earth Observation*, Remote Sensing
and Digital Image Processing 23, DOI 10.1007/978-3-319-25633-7

α_s [rad] slope angle. 126
$\alpha^{\Downarrow}$ [Np m^{-1}] attenuation constant of downward wave. 195
$\alpha^{\Uparrow}$ [Np m^{-1}] attenuation constant of upward wave. 195
α_c [$kg^2 m^{-1} s^{-1}$] conduction damping coefficient. 42
α_d [$kg^2 m^{-1} s^{-1}$] deformation damping coefficient. 35

$\boldsymbol{B}$ [T] magnetic induction. 1
B [m] interferometric baseline. 481
$B_{\perp i}$ [m] perpendicular baseline. 482
$B_{\perp C}$ [m] critical perpendicular baseline. 487
$\mathcal{B}_\epsilon$ normalized autocorrelation of relative permittivity fluctuations. 257
$\mathcal{B}_{\epsilon t}$ temporal normalized autocorrelation of relative permittivity fluctuations. 502
$\mathcal{B}_{\epsilon t}$ lateral normalized autocorrelation of relative permittivity fluctuations. 257
$\mathcal{B}_{\epsilon z}$ longitudinal normalized autocorrelation of relative permittivity fluctuations. 257
$\mathcal{B}_{\epsilon zs}$ longitudinal normalized autocorrelation of relative permittivity fluctuations in the surface layer. 275
$\mathcal{B}_\phi$ correlation coefficient of phase fluctuations. 130
$\mathcal{B}_\lambda$ [$W m^{-2} sr^{-1} \mu m^{-1}$] black-body spectral radiance. 309
$\mathfrak{B}_S$ [kg m^{-2}] above-ground tree biomass per unit area. 566
Bs Besinc function. 424
$\boldsymbol{\beta}$ [rad m^{-1}] phase vector. 106
β [rad m^{-1}] phase constant. 106
β_1 [rad m^{-1}] phase constant in single-scattering random medium. 318
$\boldsymbol{\beta}^{(i)}$ [rad m^{-1}] phase vector of incident wave. 229
$\boldsymbol{\beta}_t^{(i)}$ [rad m^{-1}] lateral component of incident wave phase vector. 228
$\boldsymbol{\beta}_z^{(i)}$ [rad m^{-1}] normal (longitudinal) component of incident wave phase vector. 228
$\boldsymbol{\beta}'$ [rad m^{-1}] phase vector of refracted wave. 166
$\boldsymbol{\beta}_t'$ [rad m^{-1}] tangential (lateral) component of refracted wave phase vector. 256
$\boldsymbol{\beta}_t''$ [rad m^{-1}] tangential (lateral) component of inner scattered wave phase vector. 256
$\boldsymbol{\beta}''$ [rad m^{-1}] phase vector of reflected wave. 166
$\boldsymbol{\beta}_f^{(s)}$ [rad m^{-1}] forward scattered propagation (phase) vector. 229
$\boldsymbol{\beta}_s^{(s)}$ [rad m^{-1}] specular scattered propagation (phase) vector. 229
β_{zs} [rad m^{-1}] vertical component of phase vector in the surface layer. 275
$\boldsymbol{\beta}^{\Downarrow}$ [rad m^{-1}] phase vector of downward wave. 191
$\boldsymbol{\beta}^{\Uparrow}$ [rad m^{-1}] phase vector of upward wave. 191

$\mathcal{C}_s$ slab factor. 196
c segment of ray. 150
c' segment of curve. 150

c_{dr} direct ray path. 150
c_{rr} reflected ray path. 150
c_o [kg $s^{-2} V^{-1}$] forcing orientation coefficient. 40
c_r [kg m $s^{-2} C^{-1}$] relaxation coefficient. 40
c_d [kg $m^{-3} s^{-2}$] restoring coefficient. 34
c_0 [$m s^{-1}$] speed of light in vacuo. 111
χ [rad] ellipticity angle. 20, 557
χ dielectric susceptibility. 32
χ_c dielectric susceptibility contributed by free charges. 42
χ_{cj} imaginary part of dielectric susceptibility contributed by free charges. 42
χ_{cr} real part of dielectric susceptibility contributed by free charges. 42
χ_d dielectric susceptibility due to deformation. 35
χ_{dj} imaginary part of dielectric susceptibility due to deformation. 36
χ_{do} dielectric susceptibility due to deformation and orientation. 41
χ_{doj} imaginary part of dielectric susceptibility due to deformation and orientation. 42
χ_{dor} real part of dielectric susceptibility due to deformation and orientation. 42
χ_{dr} real part of dielectric susceptibility due to deformation. 36
χ_o dielectric susceptibility contributed by orientation (libration). 41
χ_{oj} imaginary part of dielectric susceptibility due to orientation. 41
χ_{or} real part of dielectric susceptibility due to orientation. 41
χ_s optical susceptibility of air at reference surface conditions. 51
χ^0 static orientation susceptibility. 41

$\boldsymbol{D}$ [C m^{-2}] electric displacement. 1
D [m] lateral dimension of resolution cell. 259
D_A [m] dimension of antenna aperture. 444
D_g [m] dimension of antenna footprint. 425
D_i [m] diameter of i-th spherical particle. 224, 612
D_s [m] source transverse dimension. 89
d [m] layer thickness. 190
d_a [m] resolution in azimuth (along-track). 434
d_d [m] offset distance between prevailing scatterer and pixel center. 498
d_R [m] resolution in slant range. 464
d_r [m] resolution in ground-range (across-track). 434
d_S [m] thickness of surface layer. 274
$\mathcal{D}$ directivity. 408
$\mathcal{D}_M$ antenna gain (boresight antenna directivity). 409
ΔA [m^2] area of surface element. 219
Δf [Hz] bandwidth. 21
ΔR_g [m] difference of distance in ground range. 479
Δt [s] echo time of arrival. 444
Δt_s [s] synthetic antenna time. 449

$\Delta S'_{\mathrm{T}}$ [m^2] surface of volume V'_{T}. 295
$\Delta\tilde{\epsilon}$ deviation of relative permittivity from one. 213
$\overline{\Delta\tilde{\epsilon}}$ average deviation of relative permittivity from one. 221
$\Delta\tilde{\epsilon}\,'$ fluctuating deviation of relative permittivity from one. 221
$\Delta\Omega$ [sr] solid angle. 294
$\Delta\omega$ [$\mathrm{rad\,s}^{-1}$] deviation of angular frequency from resonance. 37
$\Delta\Phi$ [rad] phase difference between interfering waves (interferometric phase). 123, 481
$\Delta\Phi_{\mathrm{d}}$ [rad] de-ranged interferometric phase. 486
$\Delta\Phi_{\mathrm{hv}}$ [rad] phase difference between horizontal and vertical polarizations. 557
$\Delta\Phi_{ij\mathrm{f}}$ [rad] flat-earth interferometric phase. 483
$\Delta\Phi'_{j\ell}$ [rad] fluctuation of interferometric phase between pixels. 491
$\Delta\Phi'_{\mathrm{ms}}$ [rad] fluctuation of master-slave interferometric phase. 491
$\Delta\Phi_{\mathrm{R}}$ [rad] phase Rayleigh limit. 523
$\Delta\Phi_x$ [rad] horizontal phase difference. 125
$\Delta\Phi_z$ [rad] vertical phase difference. 125
$\Delta\sigma_{\mathfrak{b}}$ [m^2] radar scattering cross-section of surface element. 219
δ [m^{-3}] unitary Dirac delta function. 75
δ [rad] slope angle. 467
δn excess refractive index. 115
δn_{S} excess refractive index at the earth surface. 147
$\delta\omega$ [$\mathrm{rad\ s}^{-1}$] line width (FWHM). 37
$\delta\tau$ [s] time delay. 154
$\triangle_\epsilon$ [m^{-1}] gradient of average permittivity. 235

$\boldsymbol{E}$ [$\mathrm{V\,m}^{-1}$] electric field vector. 1
$\widehat{E}$ complex number representative of harmonic $E(t)$. 16
$\widehat{\boldsymbol{E}}$ complex vector representative of harmonic $\boldsymbol{E}(t)$. 16
$\boldsymbol{E}^{\mathrm{a}}$ representative analytic vector. 21
$\boldsymbol{E}^{(\mathrm{i})}$ [$\mathrm{V\,m}^{-1}$] incident electric field. 211
$\boldsymbol{E}^{(\mathrm{s})}$ [$\mathrm{V\,m}^{-1}$] scattered electric field. 211
$\boldsymbol{E}^{\Downarrow}$ [$\mathrm{V\,m}^{-1}$] electric field of downward wave. 191
$\boldsymbol{E}^{\Uparrow}$ [$\mathrm{V\,m}^{-1}$] electric field of upward wave. 191
$\boldsymbol{E}_{\mathrm{A}}$ [$\mathrm{V\,m}^{-1}$] electric field produced by source A. 97
$\boldsymbol{E}_{\mathrm{eA}}$ [$\mathrm{V\,m}^{-1}$] electric field produced by source A on surface S_{eA}. 98
$\boldsymbol{E}_{\infty}$ [$\mathrm{V\,m}^{-1}$] electric far field. 90
$\boldsymbol{E}_{\mathrm{LK}}$ [$\mathrm{V\,m}^{-1}$] vector term in the Luneburg-Kline expansion. 139
$\boldsymbol{E}_{\ell\mathrm{r}}$ [$\mathrm{V\,m}^{-1}$] electric field in the antenna-receiver line for receive mode. 411
$\boldsymbol{E}_{\ell\mathrm{T}}$ [$\mathrm{V\,m}^{-1}$] electric field in the source-antenna line for transmit mode. 405
E_p^{a} representative analytic p-component. 21
$\boldsymbol{E}_{\parallel}^{(\mathrm{i})}$ [$\mathrm{V\,m}^{-1}$] component of incident electric field parallel to spheroid axis. 240
$\boldsymbol{E}_{\perp}^{(\mathrm{i})}$ [$\mathrm{V\,m}^{-1}$] incident electric field perpendicular to spheroid axis. 240
$\boldsymbol{E}_{\perp}$ [$\mathrm{V\,m}^{-1}$] internal field component perpendicular to scattering direction. 214

$\overline{\boldsymbol{E}_\perp}$ [$\mathrm{V\,m^{-1}}$] average perpendicular internal field component. 221
$\boldsymbol{E}'_\perp$ [$\mathrm{V\,m^{-1}}$] fluctuating perpendicular internal field component. 221
$\boldsymbol{E}_\mathrm{s}$ [$\mathrm{V\,m^{-1}}$] electric field in the source volume. 8
$\boldsymbol{E}_\mathrm{T}$ [$\mathrm{V\,m^{-1}}$] transmitted electric field on the outer side of the antenna aperture. 406
$\boldsymbol{E}_\mathrm{t}$ [$\mathrm{V\,m^{-1}}$] tangential electric field. 173
$E_\mathrm{T}^{\square}$ [$\mathrm{V\,m^{-1}}$] truncated electric field. 428
$\boldsymbol{E}_\mathrm{TH}$ [$\mathrm{V\,m^{-1}}$] thermal electric field. 289
$\boldsymbol{E}_\mathrm{tot}$ [$\mathrm{V\,m^{-1}}$] total electric field vector. 122
$\boldsymbol{E}_0$ [$\mathrm{V\,m^{-1}}$] electric field constant vector. 104
$\boldsymbol{E}'_0$ [$\mathrm{V\,m^{-1}}$] electric field vector of refracted wave. 167
$\boldsymbol{E}''_0$ [$\mathrm{V\,m^{-1}}$] electric field vector of reflected wave. 167
E_0h [$\mathrm{V\,m^{-1}}$] horizontal component of the electric field. 118
E_0i [$\mathrm{V\,m^{-1}}$] electric field amplitude at initial abscissa. 156
E_{0p} amplitude of quasi-periodic temporal variation of p field component. 16
E_0V [$\mathrm{V\,m^{-1}}$] vertical component of the electric field. 118
e_a [$\mathrm{m^{-1}}$] emission coefficient per unit length of inhomogeneities. 326
e_b [$\mathrm{m^{-1}}$] emission coefficient per unit length of background. 326
e_f emissivity at microwave frequency f. 310
e_λ spectral emissivity. 309
$e_{\lambda\mathrm{S}}$ surface spectral emissivity. 339
e_p emissivity at p-polarization. 294
e_S surface emissivity. 437
e_T [$\mathrm{m^{-1}}$] emission coefficient per unit length of random medium. 326
$\boldsymbol{\mathfrak{e}}_\mathrm{j}$ unit vector of quadrature electric field. 19
$\boldsymbol{\mathfrak{e}}_{\ell\mathrm{r}}$ vector field transverse distribution in the antenna-receiver line. 411
$\boldsymbol{\mathfrak{e}}_{\ell\mathrm{T}}$ vector field transverse distribution in the transmit source-antenna line. 406
$\boldsymbol{\mathfrak{e}}_\mathrm{r}$ unit vector of in-phase electric field. 19
$\boldsymbol{\mathfrak{e}}_0$ unit vector of electric field. 11
$\boldsymbol{\mathfrak{e}}_0^{(\mathrm{i})}$ unit vector of incident electric field. 215
$\boldsymbol{\mathfrak{e}}_{0\parallel}$ unit vector component parallel to spheroid axis. 240
$\boldsymbol{\mathfrak{e}}_{0\perp}$ unit vector component perpendicular to spheroid axis. 240
$\mathcal{E}_\mathrm{e}$ [$\mathrm{J\,m^{-3}}$] volumic energy stored in the electric field. 10
$\mathcal{E}_\mathrm{em}$ [$\mathrm{J\,m^{-3}}$] volumic energy stored in the electromagnetic field. 10
$\mathcal{E}_\mathrm{m}$ [$\mathrm{J\,m^{-3}}$] volumic energy stored in the magnetic field. 10
$\mathcal{E}$ [m] Fourier transform of ground-range permittivity. 498
ϵ [$\mathrm{F\,m^{-1}}$] permittivity. 2
$[\boldsymbol{\epsilon}]$ [$\mathrm{F\,m^{-1}}$] permittivity matrix. 3
$\tilde{\epsilon}$ relative permittivity. 2
ϵ_b [$\mathrm{F\,m^{-1}}$] permittivity of bulk material. 234
$\tilde{\epsilon}_\mathrm{do}$ relative permittivity due to deformation and orientation mechanisms. 45
$\tilde{\epsilon}_\mathrm{doj}$ imaginary part of $\tilde{\epsilon}_\mathrm{do}$. 45
$\tilde{\epsilon}_\mathrm{dor}$ real part of $\tilde{\epsilon}_\mathrm{do}$. 45

ϵ_{j} [F m^{-1}] imaginary part of permittivity. 56
$\tilde{\epsilon}_{\mathrm{j}}$ imaginary part of relative permittivity. 37
ϵ_{r} [F m^{-1}] real part of permittivity. 56
$\tilde{\epsilon}_{\mathrm{r}}$ real part of relative permittivity. 37
ϵ^{0} [F m^{-1}] static permittivity. 56
ϵ_{0} [F m^{-1}] permittivity of vacuum. 2
$\tilde{\varepsilon}_{\mathrm{o}}$ magnitude of permittivity deviation. 497
ε_{x} range factor of permittivity deviation. 497
ε_{z} depth factor of permittivity deviation. 497
η [cm^2 m^{-3}] radar reflectivity. 612
η [Ω] intrinsic impedance. 86
η_{A} antenna aperture efficiency. 417
η_{B} antenna beam efficiency. 437
η_{ℓ} [Ω] line wave impedance. 406
η_{S2} [Ω] surface impedance. 183
η_{0} [Ω] intrinsic impedance of vacuum. 114

$\boldsymbol{F}_{\mathrm{es}}$ [N] force on source electric charges. 8
F_{e} [N m^{-3}] electric force. 35
F_{i} [N m^{-3}] inertial force. 35
F_{r} [N m^{-3}] restoring force. 35
F_{s} [N m^{-3}] frictional force. 35
f [Hz] frequency. 11
f_{D} [Hz] frequency Doppler shift. 81
f_{pr} [s^{-1}] pulse repetition frequency. 449
f_{0} [Hz] central frequency. 21
$\mathfrak{F}$ [V rad^{-1}] field radiation pattern. 91
$\mathcal{F}_{\mathrm{ell}}$ [V] radiation pattern of elliptic aperture. 426
$\mathcal{F}_{\mathrm{h}}$ horizontal factor of separable antenna angular pattern. 429
$\mathcal{F}_{\mathrm{v}}$ vertical factor of separable antenna angular pattern. 430
$\mathfrak{F}_{0}$ [V rad^{-1}] free-space scattering function. 213
$\mathfrak{F}_{0\mathrm{c}}$ [V rad^{-1}] coherent scattering function. 221
$\mathfrak{F}'_{0}$ [V rad^{-1}] incoherent scattering function. 221
$\mathfrak{F}_{\overline{\epsilon}k}$ [V rad^{-1}] scattering function of average target for k-th acquisition. 494
$\mathfrak{F}_{\epsilon' k}$ [V rad^{-1}] scattering function of target fluctuations for k-th acquisition. 494
$\mathscr{F}$ normalized line shape. 48
$\mathcal{F}^{-1}$ inverse Fourier transform. 428

$\mathbb{G}$ [m^{-1}] dyadic Green's function. 76
g_{e} [S m^{-1}] effective conductivity. 44
$\mathcal{G}$ [m^{-1}] Green's function. 76
$\overline{\mathcal{G}}$ [m^{-1}] average Green's function. 317
$\mathcal{G}'$ [m^{-1}] Green's function random component. 314
$\mathcal{G}^{\Rightarrow\circ\rightsquigarrow}$ [m^{-1}] single-scattering Green's function. 315

$\mathcal{G}^{\Rightarrow\circ\rightsquigarrow\circ\rightsquigarrow}$ [m^{-1}] double-scattering Green's function. 316
$\mathcal{G}_0$ [m^{-1}] primary Green's function. 314
$\mathcal{G}_1$ [m^{-1}] outward Green's function. 77
$\mathcal{G}_2$ [m^{-1}] inward Green's function. 77
$\mathbb{\Gamma}$ [$\mathrm{V}^2\,\mathrm{m}^{-2}$] space-time coherency dyadic. 23
$[\Gamma]$ [$\mathrm{V}^2\,\mathrm{m}^{-2}$] space-time coherency matrix. 26
Γ [$\mathrm{V}^2\,\mathrm{m}^{-2}$] coherence. 26
Γ_{12} [$\mathrm{V}^2\,\mathrm{m}^{-2}$] mutual coherence. 128
$\Gamma_{\mathcal{G}}$ [m^{-2}] Green's function correlation. 321
γ [rad] angle between $\mathbf{r}_0$ and the normal to elementary surface dA. 308
γ degree of coherence. 26
γ_{12} degree of mutual coherence. 128
γ_{a} atmospheric decorrelation factor. 513
γ_{B} geometric decorrelation factor. 513
γ_{ϵ} temporal decorrelation factor. 513
$\gamma_{\mathcal{F}}$ normalized moment of free-space scattering function. 505
γ_{p} degree of polarization. 25

$\boldsymbol{H}$ [$\mathrm{A\,m}^{-1}$] magnetic field vector. 1
$\boldsymbol{H}_{\mathrm{A}}$ [$\mathrm{A\,m}^{-1}$] magnetic field produced by source A. 97
H_{a} [m] height at the top of the atmosphere. 336, 608
$\boldsymbol{H}_{\mathrm{E}}$ [$\mathrm{A\,m}^{-1}$] Earth's magnetic field. 65
$\boldsymbol{H}_{\mathrm{eA}}$ [$\mathrm{A\,m}^{-1}$] magnetic field produced by source A on surfaceS_{eA}. 98
$\boldsymbol{H}^{(\mathrm{i})}$ [$\mathrm{A\,m}^{-1}$] incident magnetic field. 211
$\boldsymbol{H}_{\infty}$ [$\mathrm{A\,m}^{-1}$] magnetic far field. 90
$\boldsymbol{H}_{\mathrm{s}}$ [$\mathrm{A\,m}^{-1}$] magnetic field in the source volume. 8
$\boldsymbol{H}^{(\mathrm{s})}$ [$\mathrm{A\,m}^{-1}$] scattered magnetic field. 211
$\boldsymbol{H}_{\mathrm{T}}$ [$\mathrm{A\,m}^{-1}$] transmitted magnetic field on the outer side of the antenna aperture. 406
$\boldsymbol{H}_{\mathrm{t}}$ [$\mathrm{A\,m}^{-1}$] tangential magnetic field. 173
$\boldsymbol{H}'_0$ [$\mathrm{A\,m}^{-1}$] magnetic field vector of refracted wave. 167
$\boldsymbol{H}''_0$ [$\mathrm{A\,m}^{-1}$] magnetic field vector of reflected wave. 167
$\boldsymbol{H}^{\Uparrow}$ [$\mathrm{A\,m}^{-1}$] magnetic field of upward wave. 192
$\boldsymbol{H}^{\Downarrow}$ [$\mathrm{A\,m}^{-1}$] magnetic field of downward wave. 192
h [m] height above a reference (sea, ground) level. 65, 116, 345, 362
h_0 [m] refractive index characteristic height. 147
$\mathbf{h}_0$ versor of the horizontal field component. 118
$\mathbf{h}_0$ unit vector of magnetic field. 11
$\hbar$ [J s] Planck's constant. 288

$\mathbb{I}$ [$\mathrm{V}^2 m^{-2}$] dyadic interferometric product. 489
$\mathbb{I}_0$ [$\mathrm{V}^2\,\mathrm{m}^{-2}$] interferometric scattering dyadic. 494
$\mathbb{I}_{0\overline{\epsilon}}$ [$\mathrm{V}^2\,\mathrm{m}^{-2}$] component of interferometric scattering dyadic relative to mean permittivity. 494

$\mathbb{I}_{0\epsilon'}$ [$V^2\,m^{-2}$] component of interferometric scattering dyadic relative to permittivity changes. 494
I [V A] reaction integral. 95
$\mathfrak{I}$ [$V^2\,m^{-2}$] interferogram. 484
$\mathfrak{I}$ [$V^2\,m^{-2}$] field intensity. 24
$\mathcal{I}$ [$W\,m^{-2}\,sr^{-1}$] radiance. 295
$\mathcal{I}_b$ [$W\,m^{-2}\,sr^{-1}$] black-body radiance. 297
$\mathcal{I}_f$ [$W\,m^{-2}\,sr^{-1}Hz^{-1}$] brightness. 308
$\mathcal{I}_\lambda$ [$W\,m^{-2}\,sr^{-1}\mu m^{-1}$] spectral radiance. 308
$\mathcal{I}_{\lambda b}$ [$W\,m^{-2}\,sr^{-1}\mu m^{-1}$] black-body spectral radiance. 309
$\mathcal{I}_{\lambda M}$ [$W\,m^{-2}\,sr^{-1}\mu m^{-1}$] boresight spectral radiance. 435
$\mathcal{I}_{\lambda Ma}$ [$W\,m^{-2}\,sr^{-1}\mu m^{-1}$] boresight spectral radiance originated by the atmosphere. 436
$\mathcal{I}_\lambda^{\odot}$ [$W\,m^{-2}\,sr^{-1}\mu m^{-1}$] spectral radiance of solar radiation. 334
$\mathcal{I}_\lambda^{\Uparrow}$ [$W\,m^{-2}\,sr^{-1}\mu m^{-1}$] upward spectral radiance. 373
$\mathcal{I}_\lambda^{\odot\Downarrow}$ [$W\,m^{-2}\,sr^{-1}\mu m^{-1}$] downward solar spectral radiance. 373

$\mathbb{J}$ [$V^2\,m^{-2}$] polarization dyadic. 24
J Bessel function of first kind. 423
$\boldsymbol{J}$ [$A\,m^{-2}$] conduction current density vector. 2
$\boldsymbol{J}_A$ [$A\,m^{-2}$] current density of source A. 97
$\boldsymbol{J}_\epsilon$ [$A\,m^{-2}$] dielectric inhomogeneities equivalent source current. 74
$\boldsymbol{J}_{\epsilon' 1}$ [$A\,m^{-2}$] source of Green's function random component. 315
$\boldsymbol{J}_{\epsilon' 2}$ [$A\,m^{-2}$] further source of Green's function random component. 316
$\boldsymbol{J}_{eT}$ [$A\,m^{-2}$] thermal electric current density. 287
$\boldsymbol{J}_m$ [$V\,m^{-2}$] magnetic current density. 4
$\boldsymbol{J}_{ms}$ [$V\,m^{-2}$] source (impressed) magnetic current density. 4
$\boldsymbol{J}_{mT}$ [$V\,m^{-2}$] thermal magnetic current density. 287
$\boldsymbol{J}_{ob}$ [$A\,m^{-2}$] scattering object current density. 211
$\boldsymbol{J}_{ob\perp}$ [$A\,m^{-2}$] effective scattering object current density. 230
$\boldsymbol{J}_{obv}$ [$A\,m^{-2}$] vertical component of scattering object current density. 230
$\boldsymbol{J}_S$ [$A\,m^{-2}$] source (impressed) electric current density. 403
$\boldsymbol{J}_{ts}$ [$A\,m^{-2}$] total source current density. 74
$\boldsymbol{J}_t$ [$A\,m^{-2}$] current density of test source. 96
J_0 [$A\,m^{-2}$] amplitude constant of impulse source current density. 75
$\boldsymbol{\mathcal{J}}$ [$A\,m^{-1}$] local surface electric current density vector. 6
$\boldsymbol{\mathcal{J}}_{eA}$ [$A\,m^{-1}$] equivalent surface electric current for source A. 98
$\boldsymbol{\mathcal{J}}_m$ [$V\,m^{-1}$] local surface magnetic current density vector. 6
$\boldsymbol{\mathcal{J}}_{meA}$ [$V\,m^{-1}$] equivalent surface magnetic current for source A. 98
$\mathcal{J}$ [$V^2\,m^{-2}$] element of polarization matrix. 24
$[\boldsymbol{\mathcal{J}}]$ [$V^2\,m^{-2}$] polarization matrix. 24
$[\boldsymbol{\mathcal{J}}]^{(p)}$ [$V^2\,m^{-2}$] polarization matrix of polarized field component. 25
$[\boldsymbol{\mathcal{J}}]^{(u)}$ [$V^2\,m^{-2}$] polarization matrix of unpolarized field component. 25
$\mathcal{J}_a$ [$W\,m^{-2}\,sr^{-1}\mu m^{-1}$] thermal source of inhomogeneities. 326
$\mathcal{J}_b$ [$W\,m^{-2}\,sr^{-1}\mu m^{-1}$] background thermal source. 326

$\mathcal{J}_e$ [$W\,m^{-2}\,sr^{-1}\,\mu m^{-1}$] effective source function. 328
$\mathcal{J}_s$ [$W\,m^{-2}\,sr^{-1}\,\mu m^{-1}$] scattering source. 326
$\mathcal{J}_T$ [$W\,m^{-2}\,sr^{-1}\,\mu m^{-1}$] thermal source function. 326
$\mathfrak{J}$ [$W\,m^{-2}$] volume scattering source term. 532
$\mathbf{j}_0$ unit vector of electric current density. 11

$\mathcal{K}$ [m^{-8}] kernel of intensity operator. 321
K_0 [$rad\,m^{-1}$] angular wavenumber of permittivity periodic variations. 267
$\mathcal{k}$ [$J\,K^{-1}$] Boltzmann's constant. 288
$\boldsymbol{k}$ [$rad\,m^{-1}$] propagation vector. 104
κ [$rad\,m^{-1}$] propagation constant. 74
κ_1 [m^{-1}] first-order propagation constant in random medium. 318
$\boldsymbol{\kappa}_t$ [$rad\ m^{-1}$] lateral component of scattering vector. 261
κ_0 [$rad\,m^{-1}$] propagation constant in vacuo. 107
$\hat{\kappa}_x$ [rad] normalized range wavenumber. 508
κ_s [m^{-1}] scattering coefficient per unit path length. 326
$\varkappa$ [$rad\,m^{-1}$] horizontal angular wavenumber. 263
$\varkappa_\epsilon$ [$rad\,m^{-1}$] cut-off angular wavenumber. 263

$L_{\bar{\epsilon}z}$ [m] Laplace transform of vertical permittivity pattern. 498
L_S [m] length of synthetic antenna. 447
$\mathcal{L}$ [m] electromagnetic path length. 150
$\overline{\mathcal{L}}$ [m] average component of electromagnetic path length. 490
$\mathcal{L}'$ [m] fluctuating component of electromagnetic path length. 490
$\mathcal{L}_a$ [m] atmospheric excess path length. 154, 488
$\mathcal{L}_d$ [m] atmospheric dry excess path length. 154
$\mathcal{L}_w$ [m] atmospheric wet excess path length. 154
$\mathcal{L}_0$ [m] electromagnetic path length in vacuo. 154
ℓ [m] spheroid length. 239
ℓ_c [m] rough surface correlation distance. 527
ℓ_d [m] displacement of positive with respect to negative charge system. 34
$\mathcal{l}$ [m] penetration depth. 182
Λ [m] spatial period of horizontal permittivity fluctuations. 263
Λ_F [m] fringe period. 124
Λ_0 [m] spatial period of permittivity periodic variations. 267
λ_c [m] channel central wavelength. 439
λ_M [m] wavelength of maximum black-body emission. 309
λ_0 [m] vacuum wavelength. 78
λ_{0tg} [m] trace gas resonant wavelength. 606

M number of periods in a scattering cell. 530
$[\mathbf{M}]$ [m^{-2}] Müller matrix. 216
M_{ij} [m^{-2}] element of Müller matrix. 217
m_d [$g\,m^{-3}$] mass of effective charge. 34
m_e [g] mass of the electron. 65
m_c [$g\,m^{-3}$] mass of free charge per unit volume. 42

m_v [$m^3\,m^{-3}$] volumic water content. 57
$\mathcal{M}$ [$kg\,m^{-1}\,s^{-2}$] forcing torque per unit volume. 40
$\mathcal{M}_c$ [$kg\,m^{-1}\,s^{-2}$] relaxation torque per unit volume. 40
$\mathcal{M}_s$ [$kg\,m^{-1}\,s^{-2}$] damping torque per unit volume. 40
$\boldsymbol{\mathcal{M}}$ [$A\,m^{-1}$] momentum of point source. 85
$\mathcal{M}_t$ [A m] momentum of test source. 96
$\mathfrak{m}$ slope standard deviation. 528
μ [$H\,m^{-1}$] magnetic permeability. 2
$\tilde{\mu}$ relative magnetic permeability. 2
μ_0 [$H\,m^{-1}$] magnetic permeability of vacuum. 2

N refractivity. 116
N_a number of pixels in the azimuth direction. 485
N_e [m^{-3}] volumic number of free ionospheric electrons. 65
N_{H_2O} number of interaction modes of water molecule. 48
N_{O_2} number of interaction modes of oxygen molecule. 48
N_r number of pixels in the range direction. 481
N_S number of pulses in synthetic antenna time. 449
n refractive index. 109
$\overline{n}$ effective refractive index. 491
n_{ev} effective refractive index for vertical polarization. 279
n_i refractive index at initial abscissa. 156
n_j imaginary part of refractive index. 109
n_r real part of refractive index. 109
$\mathbf{n}_0$ local normal to a surface. 5
∇ [m^{-1}] nabla. 2, 661
$\nabla\cdot$ [m^{-1}] divergence. 2, 662
$\nabla\times$ [m^{-1}] curl. 2, 662
$\boldsymbol{\nu}_0$ principal normal to the ray. 145

Ω_E [rad] solid angle under which the Earth is seen. 435
ω [$rad\,s^{-1}$] angular frequency. 11
ω_D [$rad\,s^{-1}$] angular frequency Doppler shift. 81
ω_p [$rad\ s^{-1}$] plasma frequency. 65
ω_r [$rad\,s^{-1}$] dielectric relaxation angular frequency. 41
ω_s [$rad\,s^{-1}$] angular frequency of radiation at the source. 81
ω_0 [$rad\,s^{-1}$] resonant angular frequency. 35

P Point in space. 1
$\overline{\mathbb{P}}$ polarizability tensor. 237
$P_\parallel$ element of polarizability tensor relative to along-axis electric field. 239
$P_\perp$ element of polarizability tensor relative to electric field perpendicular to axis. 239
p_t [hPa] total atmospheric pressure. 50
p_w [hPa] partial pressure of water vapor. 50
$\boldsymbol{p}_{0d}$ [m] unit vector of induced dipole. 34

$\boldsymbol{\mathcal{P}}$ [$\mathrm{W\,m^{-2}}$] Poynting vector. 10
$\boldsymbol{\mathcal{P}}''$ [$\mathrm{W\,m^{-2}}$] Poynting vector of reflected wave. 169
$\overline{\boldsymbol{\mathcal{P}}}$ [$\mathrm{W\,m^{-2}}$] time-average Poynting vector. 13
$\overline{\mathcal{P}}$ [$\mathrm{W\,m^{-2}}$] magnitude of time-average Poynting vector. 13
$\mathcal{P}^{(\mathrm{a})}$ [$\mathrm{W\,m^{-2}}$] power absorbed through unit surface. 170, 187, 372
$\overline{\mathcal{P}}_{\mathrm{eS}}$ [$\mathrm{W\,m^{-2}}$] solar power density at surface of Earth. 15
$\mathcal{P}^{(\mathrm{i})}$ [$\mathrm{W\,m^{-2}}$] incident radiant flux or irradiance. 372
$\mathcal{P}^{(\mathrm{i})}_{\lambda}$ [$\mathrm{W\,m^{-2}\,\mu m^{-1}}$] incident spectral radiant flux or irradiance. 372
$\overline{\mathcal{P}'_{\mathrm{o}}}$ [$\mathrm{W\,m^{-2}}$] power per unit area entering the average scatterer. 258
$\mathcal{P}^{(\mathrm{r})}$ [$\mathrm{W\,m^{-2}}$] reflected (scattered) radiant flux or irradiance. 372
$\mathcal{P}^{(\mathrm{r})}_{\lambda}$ [$\mathrm{W\,m^{-2}\,\mu m^{-1}}$] reflected (scattered) spectral radiant flux or irradiance. 372
$\mathcal{P}^{(\mathrm{s})}$ [$\mathrm{W\,m^{-2}}$] scattered far-field power density per unit surface. 220
$\mathcal{P}_{\mathrm{t}}$ [$\mathrm{W\,m^{-2}}$] test power density incident onto $\Delta S'_{\mathrm{T}}$. 300
$\langle \mathcal{P}_{\mathrm{T}} \rangle$ [$\mathrm{W\,m^{-2}}$] thermal radiant flux or irradiance. 307
$\overline{\mathcal{P}}_{\mathrm{ta}}$ [$\mathrm{W\,m^{-2}}$] power density at the top of atmosphere. 15
$\boldsymbol{\mathcal{P}}_{\mathrm{TH}}$ [$\mathrm{W\,m^{-2}}$] thermal Poynting vector. 292
$\langle \mathcal{P}_{\mathrm{TH}\lambda} \rangle$ [$\mathrm{W\,m^{-2}\,\mu m^{-1}}$] spectral thermal radiant flux. 307
$\mathcal{P}'_{\mathrm{t}}(0)$ [$\mathrm{W\,m^{-2}}$] refracted test power density at $z' = 0$. 300
$\mathcal{P}$ [$\mathrm{W\,sr^{-1}}$] power radiation or angular power density. 87, 93
$\boldsymbol{\mathcal{P}}$ [C m] induced electric dipole. 32
$\mathcal{P}_{\mathrm{c}}$ [$\mathrm{C\,m^{-2}}$] electric dipole per unit volume associated with free charges. 47
$\boldsymbol{\mathcal{P}}_{\mathrm{d}}$ [$\mathrm{C\,m^{-2}}$] electric dipole per unit volume induced by deformation. 34
$\widehat{\mathcal{P}}_{\mathrm{d}}$ [$\mathrm{C\,m^{-2}}$] phasor of dipole induced by deformation. 35
$\boldsymbol{\mathcal{P}}_{\mathrm{o}}$ [$\mathrm{C\,m^{-2}}$] electric dipole per unit volume induced by orientation. 39
$\mathfrak{P}$ vector of geometric and physical parameters. 216
$\Phi_{\boldsymbol{F}}$ [[$\boldsymbol{F}$] $\mathrm{m^2}$] flux of $\boldsymbol{F}$. 649
Φ [rad] space-time phase. 78
Φ_{d} [rad] phase of downward or upward wave. 192
Φ_{E} [rad] phase of electric field. 11
Φ_{ES} [rad] phase of source electric field. 12
$\Phi_{\mathcal{F}i}$ [rad] phase of i^{th} scattering function. 478
Φ_{H} [rad] phase of magnetic field. 11
Φ_{h} [rad] phase of horizontal field component. 119
Φ_{hv} [rad] phase difference between horizontal and vertical field components. 118
Φ_p [rad] phase of quasi-periodic temporal variation of p field component. 16
Φ_{qv} [rad] phase of reflection coefficient for vertical polarization. 184
$\Phi_{\mathcal{R}}$ [rad] phase due to distance. 83
Φ_{v} [rad] phase of vertical field component. 119
ϕ eikonal function (normalized phase). 138
ϕ_{t} lateral component of eikonal function. 226
ϕ_{z} normal (longitudinal) component of eikonal function. 226

$\varphi^{(\mathrm{i})}$ [rad] incidence azimuth angle. 216
$\varphi^{(\mathrm{s})}$ [rad] scattering azimuth angle. 216
φ_{w} [rad] azimuth angle of surface wind velocity. 595
$\boldsymbol{\varphi}_0$ azimuth unit vector. 85
ψ [rad] angle between $\mathbf{r}_0$ and $\mathbf{r}'_0$. 90
$\psi_{\nu\mathrm{n}}$ [rad] angle between $\boldsymbol{\nu}_0$ and $-\mathbf{r}_0$. 147
ψ [rad] inclination angle. 19, 557

$\mathfrak{q}$ reflection parameter. 529
$\underline{\underline{\mathbb{Q}}}$ field transformation tensor. 215
$\overline{\underline{\mathbb{Q}}}$ average field transformation tensor. 237
$[\underline{\mathbf{Q}}_\perp]$ orthogonal-component field transformation matrix. 215
$\overline{\mathbb{Q}}_\perp$ average orthogonal-component field transformation tensor. 237
Q_{pq} element of field transformation tensor. 215
$Q_{\perp pq}$ element of orthogonal field transformation tensor. 215
q_{c} [C m^{-3}] free charge per unit volume available to conduction. 42
q_{d} [C m^{-3}] charge per unit volume available to deformation. 34
q_{E} electric field reflection coefficient. 168
$\mathrm{q_e}$ [C] charge of the electron. 65
$q_{\mathrm{E}}^{(12)}$ reflection coefficient at the interface between materials M_1 and M_2. 193
$q_{\mathrm{Es}}^{(01)}$ reflection coefficient of layered structure. 193
Q [m^{-5}] kernel of Dyson equation. 317
Q_1 [m^{-5}] first-order approximation of Q. 318

R [m] distance between source and observation point. 80
R_{g} [m] distance in ground range. 460
$\boldsymbol{R}_0$ unit vector of $\boldsymbol{r} - \boldsymbol{r}'$. 81
$\boldsymbol{r}$ [m] position vector. 1
$\boldsymbol{r}_1$ [m] location of secondary source. 315
$\mathbf{r}_{\mathrm{oe}}$ direction along which the emitted power travels. 292
$\boldsymbol{r}_{\mathrm{s}}$ [m] position vector of point source. 314
$\boldsymbol{r}_{\mathrm{t}}$ [m] location where the thermal electric field is observed. 289
$\boldsymbol{r}'_{\mathrm{T}}$ [m] position of the thermal source current. 289
$\boldsymbol{r}'_{\mathrm{t}}$ [m] position vector in the transverse (horizontal) plane. 256
$\mathbf{r}_0$ radial unit vector. 85
$\mathbf{r}_0^{(\mathrm{i})}$ unit propagation vector of incident wave. 213
$\mathbf{r}_0^{(\mathrm{s})}$ unit propagation vector of scattered wave. 213
$\mathbf{r}_{0\mathrm{f}}^{(\mathrm{s})}$ unit propagation vector of forward scattered wave. 229
$\mathbf{r}_{0\mathrm{s}}^{(\mathrm{s})}$ unit propagation vector of specularly scattered wave. 229
$\mathbf{r}_{0\mathrm{t}}^{(\mathrm{i})}$ tangential (lateral) component of incident wave unit propagation vector. 229
$\mathbf{r}_{0\mathrm{t}}^{(\mathrm{s})}$ tangential (lateral) component of scattered wave unit propagation vector. 229
$\mathbf{r}_{0\mathrm{z}}^{(\mathrm{i})}$ normal (longitudinal) component of incident wave unit propagation vector. 229

$\mathbf{r}_{0z}^{(s)}$ normal (longitudinal) component of scattered wave unit propagation vector. 229
$\mathcal{R}$ power reflection coefficient. 169
$\mathcal{R}_c$ coherent power reflection coefficient. 275
$\mathcal{R}_{ch}$ power reflection coefficient for horizontal polarization. 278
$\mathcal{R}_{cp}$ coherent reflectivity at p polarization. 303
$\mathcal{R}_{cv}$ power reflection coefficient for vertical polarization. 278
$\mathcal{R}_{ip}$ incoherent reflectivity at p polarization. 303
$\mathcal{R}_\lambda$ spectral reflectivity. 334
$\mathcal{R}$ reflectance. 303
$\mathcal{R}_\lambda$ spectral reflectance. 372
$\mathfrak{r}$ [m] mean lateral position of points in scattering volume. 258
$\boldsymbol{r}$ [m] oriented lateral distance between points in scattering volume. 258
r_ϵ [m] lateral correlation distance of permittivity fluctuations. 259
$\mathcal{R}$ [mm hr^{-1}] precipitation intensity. 613
RH relative humidity. 48
ρ [C m^{-3}] volumic electric charge. 2
ϱ [m] radius of curvature. 145
ρ_s [C m^{-3}] electric charge density in the source volume. 8
$\sqcap$ rectangle function. 423

$[\mathbf{S}]$ [m] scattering matrix. 215
$\boldsymbol{S}$ [V^2 m^{-2}] Stokes vector. 120
S' [m^2] transverse section of scattering volume. 258
S_{eA} [m^2] surface wrapping source A. 98
S_{ext} [m^2] arbitrary surface enveloping the transmit/receive antenna. 406
S_g [m^2] portion of source-wrapping surface. 100
S_i [V^2 m^{-2}] Stokes parameter. 120
S_{in} [m^2] flux tube section at initial abscissa. 156
S_∞ sphere at infinity. 95
S_{int} [m^2] arbitrary surface enveloping the internal source. 403
S_ℓ [m^2] section of the source-antenna line. 404
S_m [m] point of acquisition of the master image. 484
S_{pq} [m] element of scattering matrix. 216
S'_r [m^2] distance-transformed area. 258
$S'_{\mathfrak{r}}$ [m^2] position-transformed area. 258
S_s [m] point of acquisition of the slave image. 484
s_d [kg m^{-3} s^{-1}] deformation kinetic friction coefficient. 34
s_g [m] abscissa at the ground level along $\mathbf{s}_0^\odot$. 334
s_H [m] abscissa at the top of the atmosphere along $\mathbf{s}_0^\odot$. 334
s_i [m] initial abscissa. 156
s_o [kg m s^{-1} C^{-1}] orientation viscosity coefficient. 40
s_p [m] abscissa of aerial platform along $\mathbf{s}_0$. 338
$s^\odot$ [m] path length along $\mathbf{s}_0^\odot$. 336
$\mathbf{s}_0$ unit vector of $\nabla\phi$, perpendicular to eikonal surfaces. 138

$\mathbf{s}_{0g}$ versor of ground track. 434
$\mathbf{s}_{0M}$ direction of antenna boresight. 436
$\mathbf{s}_{0r}$ versor of ground range. 434
$\mathbf{s}_0^{\odot}$ unit vector in the direction along which solar radiation travels. 334
$\mathcal{S}_{\epsilon t}$ [m^2] lateral spectral density of permittivity fluctuations. 261
$\mathcal{S}_{\epsilon tb}$ [m^2] lateral spectral density of permittivity fluctuations in the bulk material. 275
$\mathcal{S}_{\epsilon tS}$ [m^2] lateral spectral density of permittivity fluctuations in the surface layer. 275
$\mathcal{S}_{\epsilon z}$ [m^2] spectral density of vertical relative permittivity fluctuations. 503
$\mathcal{S}_{\mathfrak{Zd}}$ [m^3] directional spectrum. 592
$\mathcal{S}$ electromagnetic frequency spectrum. 21
$\mathcal{S}$ volume scattering phase function. 327
$\mathscr{I}$ line intensity. 48
s ocean salinity. 601
σ [$W m^{-2} K^{-4} \mu m^{-1}$] Stefan-Boltzmann constant. 310
σ [m^2] bistatic scattering cross-section. 218
σ^0 [$m^2 m^{-2}$] backscattering coefficient. 219
σ_a [m^2] (total) absorption cross-section. 218
σ_{ap} [m^2] absorption cross-section for p polarization. 293
$\sigma_{\mathbf{b}}$ [m^2] monostatic (radar) scattering cross-section. 218
σ_{bi} [m^2] mean backscattering cross-section of i^{th} object. 611
σ_e [m^2] (total) extinction cross-section. 219
σ_s [m^2] (total) scattering cross-section. 218
σ_{zR} [m] Rayleigh height standard deviation limit. 523
σ_ϵ^2 covariance of relative permittivity fluctuations. 257
$\sigma_{\epsilon S}^2$ covariance of relative permittivity fluctuations in the surface layer. 275
σ_ϕ^2 [rad^2] variance of phase fluctuations. 130
ς_{12} [m] vertical distance between two points. 271
ς_e [$C m^{-2}$] local surface density of electric charge. 6
ς_m [T] local surface density of magnetic charge. 6
$\square$ two-dimensional rectangle function. 428

T [s] period of oscillation. 12
T_A [K] antenna temperature. 438
T_{AS} [K] signal temperature. 438
T_B [K] brightness temperature. 310
T_{Ba} [K] atmospheric brightness temperature. 438
T_{Bsl} [K] off-boresight brightness temperature. 438
T_C [K] temperature of cosmic background. 343
T_{env} [K] environment effective temperature. 339
T_{es} [K] effective scattered temperature. 341
T_{me} [K] environment effective microwave temperature. 342
T_N [K] noise temperature. 438
T_S [K] effective temperature of the surface. 339, 437

t [s] time. 1
t_{E} electric field transmission coefficient. 168
$t_{\mathrm{ES}}^{(01)}$ transmission coefficient of layered structure. 198
t_x conjugate angular variable in horizontal direction. 428
t_y conjugate angular variable in vertical direction. 428
$\mathcal{T}$ channel spectral response. 439
$\mathcal{T}$ power transmission coefficient. 169
$\mathfrak{T}$ transmission or direct transmittance. 117
$\mathfrak{T}_{\mathrm{a}}$ atmospheric transmissivity. 436
τ_{a} optical depth of the atmosphere for the observation elevation angle. 337
$\tau_{\mathrm{a}}^{\odot}$ optical depth of the atmosphere for the solar elevation angle. 337
τ_{ap} optical depth of the atmosphere for the aerial platform. 338
τ_{at} optical thickness of atmosphere above cloud top. 608
$\tau_{\mathrm{at}}^{\odot}$ optical thickness of atmosphere above cloud top for solar radiation. 608
τ_{o} optical thickness, or optical depth. 329
$\tau_{\mathrm{o}}^{\odot}$ optical thickness from the top of the atmosphere to s' along $\mathbf{s}_0^{\odot}$. 334
τ_{r} dielectric relaxation time. 41
τ [s] travel time. 151
τ_{p} [s] radar pulse duration. 444
τ_{pc} [s] duration of compressed radar pulse. 449
Θ [J] mean energy of quantum oscillator. 288
θ [rad] incidence angle. 172
$\theta^{(\mathrm{e})}$ [rad] emission elevation angle. 304
$\theta^{(\mathrm{i})}$ [rad] incidence elevation angle. 216
$\theta^{(\mathrm{s})}$ [rad] scattering elevation angle. 216
$\theta^{\odot}$ [rad] solar elevation angle. 336
θ_{B} [rad] Brewster angle. 177
θ_{L} [rad] limit angle. 188
θ_{ob} [rad] angle of scattering-source current. 279
θ_{pB} [rad] pseudo-Brewster angle. 184
ϑ [rad] off-nadir angle. 147
ϑ_{dl} [rad] diffraction-limited angular resolution. 426
ϑ_{h} [rad] half-power angular width in the horizontal plane. 430
ϑ_{if} [rad] linear instantaneous field of view angle. 439
ϑ_{v} [rad] half-power angular width in the vertical plane. 430
$\boldsymbol{\vartheta}_0$ elevation unit vector. 85

$\boldsymbol{u}$ [m s^{-1}] velocity. 2
u [m s^{-1}] velocity of propagation. 112
u' [m s^{-1}] propagation velocity of refracted wave. 189
u_{l} [m s^{-1}] radial phase velocity of outward Green's function. 79
u_{c} [m s^{-1}] velocity of free charge density. 43
u_{h} [m s^{-1}] velocity of propagation of homogeneous wave. 112
u_{i} [m s^{-1}] velocity of propagation of inhomogeneous wave. 112

$\boldsymbol{u}_\rho$ [m s^{-1}] velocity of the source electric charges. 8
$\boldsymbol{u}_\mathrm{s}$ [m s^{-1}] velocity of the source. 81
u_x [m s^{-1}] phase velocity along x. 174
Υ_F [m^{-1}] fringe spatial frequency. 124

V' [m^3] source volume. 76
V_g [m^3] volume of lossy material. 9
V_r [V m^{-1}] received field parameter. 411
V_S [m^3 m^{-2}] areic tree stem volume. 566
V_s [m^3] source volume. 8
V_T [V m^{-1}] transmitted field parameter. 405
$\boldsymbol{v}$ [m s^{-1}] satellite orbital velocity. 481
v_s [m s^{-1}] satellite speed. 449
v_w [m s^{-1}] surface wind speed. 595
$\mathbf{v}_0$ versor of the vertical field component. 118
$\mathcal{V}$ fringe visibility. 129
$\mathcal{V}$ [V] electric scalar potential. 74

$\overline{W}_\mathrm{d}$ total power dissipated by dielectric and conduction losses. 46
$W_\mathcal{E}$ [W] power associated with changes of stored electromagnetic energy. 10
W_es [W m^{-3}] power conveyed by electric field to current density. 8
W_g [W] electromagnetic power dissipated by Joule effect. 9
$\overline{W}_\mathrm{g}$ [W] time-average dissipated power. 14
$\overline{W}_\mathrm{gv}$ [W m^{-3}] volumic time-average dissipated power. 14
W_N [W] noise power. 437
W_ra [W] received power originated by the atmosphere. 437
W_rS [W] received power originated by the earth surface. 437
W_rs [W] synthesized received power. 449
W_s [W] power conveyed by source to electromagnetic field. 9
$\overline{W}_\mathrm{s}$ [W] time-average source power. 13
W_sc [W] total scattered power. 218
W_se [W m^{-3}] power conveyed by source current to electric field. 8
W_sl [W] stray-radiation power. 437
W_T [W] transmitted power. 403
$\overline{W}_\mathrm{T}$ [W] transmitted power averaged over the synthetic aperture time. 449
W_Tc [W] compressed-pulse power. 449
$W_{\mathrm{td}p}$ [W] power absorbed at p polarization. 291
W_tg [W] geometrically incident power. 293
$W_{tp}^{(\mathrm{i})}$ [W] power incident onto volume V'_T at p polarization. 303
$W_{tp}^{(\mathrm{s})}$ [W] power scattered by volume V'_T at p polarization. 303
w [m] spheroid width. 239
w_S [kg m^{-2}] areic plant water content or fresh biomass. 564
$\mathcal{W}$ weighting function. 301
$\mathcal{W}_T$ [m^{-1}] temperature weighting function. 344

$x_{\min}$ [m] distance of field minima. 124
$\mathcal{X}$ [m] horizontal factor of average scattering function. 497

$\boldsymbol{Y}$ [$\mathrm{V^2\,m^{-2}}$] normalized Stokes vector. 121
$\boldsymbol{Y}_{\mathrm{m}}$ [$\mathrm{V^2\,m^{-2}}$] modified Stokes vector. 121
$\boldsymbol{Y}_{\mathrm{m}}^{(\mathrm{i})}$ [$\mathrm{V^2\,m^{-2}}$] modified Stokes vector of incident field. 216
$\boldsymbol{Y}_{\mathrm{m}}^{(\mathrm{s})}$ [$\mathrm{V^2\,m^{-2}}$] modified Stokes vector of scattered field. 216

$Z_{\mathcal{P}}$ [$\mathrm{m^2}$] longitudinal permittivity factor. 258
$Z_{\mathcal{P}\mathrm{b}}$ [$\mathrm{m^2}$] longitudinal permittivity factor in the bulk material. 275
$Z_{\mathcal{P}\mathrm{S}}$ [$\mathrm{m^2}$] longitudinal permittivity factor in the surface layer. 275
z_{12} [m] average depth of two points. 271
z_{p} [m] altitude of aerial platform. 338
$\mathcal{Z}$ [m] vertical factor of average scattering function. 497
$\mathcal{Z}$ [$\mathrm{mm^6\,m^{-3}}$] reflectivity factor. 612
$\mathfrak{z}$ [m] height of random surface. 234, 525

Index

D. Solimini, *Understanding Earth Observation*, Remote Sensing and Digital Image Processing 23, DOI 10.1007/978-3-319-25633-7